Forschungszentrum Karlsruhe
Technik und Umwelt

Wissenschaftliche Berichte
FZKA 6475

Proceedings of the OECD Workshop on Ex-Vessel Debris Coolability

Karlsruhe, 15–18 November 1999
Organised in collaboration with Forschungszentrum Karlsruhe

H. Alsmeyer

Institut für Kern- und Energietechnik
Projekt Nukleare Sicherheitsforschung

Mai 2000

Forschungszentrum Karlsruhe

Technik und Umwelt

Wissenschaftliche Berichte

FZKA 6475

Proceedings of the

OECD WORKSHOP ON EX-VESSEL DEBRIS COOLABILITY

Karlsruhe, 15-18 November 1999

Organised in collaboration with Forschungszentrum Karlsruhe

Editor: H. Alsmeyer

Institut für Kern - und Energietechnik

Projekt Nukleare Sicherheitsforschung

Forschungszentrum Karlsruhe GmbH, Karlsruhe
2000

Forschungszentrum Karlsruhe GmbH
Postfach 3640, 76021 Karlsruhe

Mitglied der Hermann von Helmholtz-Gemeinschaft
Deutscher Forschungszentren (HGF)

ISSN 0947-8620

Abstract

An OECD Workshop on the Safety of Nuclear Reactors, considering Ex-Vessel Debris Coolability, was organised in Karlsruhe, Germany, from 15 to 18 November 1999, in collaboration with Forschungszentrum Karlsruhe GmbH. The international meeting was attended by more than eighty specialists from 17 countries and international organizations. Forty-eight papers were presented, three additional papers were distributed during the workshop.

In the workshop various issues were discussed which are important to control or mitigate severe reactor accidents if the corium melt would penetrate the reactor pressure vessel. A substantial increase of research and design activities to control ex-vessel melts was reported. Especially in Western Europe, this increase is related to higher safety requirements in response to technological improvements and a highly sensitive political background, and future LWRs in Europe, as the European Pressurised Reactor EPR, will include additional design features for mitigation of severe accidents involving vessel melt-through.

The papers, which are presented here, concentrate on the following topics:

- Release of corium from the pressure vessel
- Heat transfer from corium pools and particle beds
- Spreading of corium melts
- Fragmentation and quenching of melts
- Material properties and thermochemistry of melts and structure material
- Reactor application

Based on the papers and the final plenary discussion of the workshop, the Programme Committee and the Session Chairman formulated Conclusions and Recommendations which are included here. They state a substantial increase of knowledge in ex-vessel corium behaviour and control which can be used for accident management strategies, and identify areas where further research should continue.

Zusammenfassung

Konferenzberichte über den Workshop zur Kühlbarkeit von Kernmassen außerhalb des Reaktordruckbehälters

Vom 15. bis 18. November 1999 fand ein OECD - Workshop zur Sicherheit von Kernreaktoren statt, der sich mit dem Problem der Kühlung von Kernmassen nach dem Austritt aus dem Druckbehälter befaßte. Der Workshop wurde in Zusammenarbeit mit dem Forschungszentrum Karlsruhe organisiert. Dieses internationale Treffen wurde von mehr als 80 Fachleuten aus 17 Ländern und internationalen Organisationen besucht. Es wurden 48 Konferenzbeiträge vorgetragen, drei zusätzliche Papiere wurden während der Tagung verteilt.

Auf der Tagung wurden die verschiedenartigen Problemfelder diskutiert, die zur Kontrolle oder Milderung schwerer Reaktorunfälle wichtig sind, wenn Kernmassen den Reaktordruckbehälter durchdringen würden. Es wurde eine wesentliche Zunahme von Aktivitäten bezüglich der Erforschung und Auslegung von Reaktoren zur Kontrolle von Schmelzen außerhalb des Druckbehälters berichtet. Besonders in Westeuropa steht diese Zunahme in Zusammenhang mit höheren Sicherheitsanforderungen, die sich aus technologischen Verbesserungen und einem hoch sensitiven politischen Umfeld ergeben. Zukünftige Leichtwasserreaktoren in Europa, wie der Europäische Druckwasser-Reaktor, werden zusätzliche konstruktive Maßnahmen vorsehen, die zur Milderung der Folgen von schweren Unfällen mit Durchdringung des Druckbehälters dienen.

Die Konferenzbeiträge, die hier abgedruckt werden, befassen sich mit den folgenden Themen:

- Austritt von Kernmaterial aus dem Druckbehälter
- Wärmeübergang aus Kernschmelzen und Partikelbetten
- Ausbreitung von Kernschmelzen
- Fragmentierung und Abkühlen von Schmelzen
- Materialeigenschaften und thermochemisches Verhalten von Schmelzen und Strukturmaterial
- Anwendung auf den Reaktor

Auf der Grundlage der Konferenzbeiträge und der abschließenden Plenardiskussion des Workshops hat das Programmkomitee zusammen mit den Sitzungsleitern Schlußfolgerungen und Empfehlungen formuliert, die hier wiedergegeben sind. Sie konstatieren eine bedeutsame Zunahme des Wissens über das Verhalten von Kernschmelzen außerhalb des Druckbehälters und ihre Kontrolle, das für Maßnahmen zur Unfallbeherrschung genutzt werden kann. Ebenso werden Felder benannt, auf denen weitere Forschung erfolgen sollte.

Contents

Session B 2: PHENOMENA TO ACHIEVE COOLABILITY: CHARACTERISTICS OF PARTICLE BEDS
Chairman: V. Gustavson

Session B 3: PHENOMENA TO ACHIEVE COOLABILITY: SPREADING
Co-Chairmen: H.-J. Allelein and J.-C. Latché

Summary and Recommendations

of the OECD WORKSHOP on Ex-Vessel Debris Coolability

General

An OECD Workshop on Ex-Vessel Debris Coolability was organised in Karlsruhe, Germany, from 15 to 18 November 1999, in collaboration with Forschungszentrum Karlsruhe GmbH. This Summary has been prepared by the Programme Committee of the Workshop and the Session Chairmen (see Annex I).

The meeting was attended by more than eighty specialists representing thirteen OECD Member countries, the European Commission, the Republic of Kazakhstan and the Russian Federation. Forty-eight papers were presented; three additional Russian papers were distributed during the Workshop.

A first OECD Specialist Meeting on Core Debris-Concrete Interactions had been held at Palo Alto, California in September 1986, a second one in Karlsruhe in April 1992. The OECD Workshop on Large Molten Pool Heat Transfer held at Grenoble, France in March 1994 had recommended to hold in due course a workshop on ex-vessel melt coolability by spreading. More recently it had been agreed that other forms of debris coolability would also be useful to discuss, e.g. coolability by an overlying water pool (MACE experiments), and melt quenching (FARO experiments). Furthermore, a series of relatively new investigations, both theoretical and experimental, was underway in Europe, studying the basic processes to achieve coolability. This work is relevant for existing as well as for future reactors. Japan also had started COTELS experiments focused on ex-vessel corium coolability for existing plants.

Considering the large amount of work done in recent years, the Committee on the Safety of Nuclear Installations (CSNI) concluded that the time was ripe to bring all the new information together, and decided to sponsor a new workshop. The meeting organised in Karlsruhe was complementary to the OECD Workshop on In-Vessel Core Debris Retention and Coolability held in Garching, Germany in March 1998.

The objectives of the Workshop were to:

- exchange information on past, present and planned R&D activities in the area of ex-vessel debris coolability, and promote collaboration among the experts;
- review the present situation and identify areas where knowledge is adequate for plant application;
- address major uncertainties and identify remaining issues relevant to reactor safety;
- discuss future orientations of work;
- propose conclusions and recommendations to CSNI.

The Workshop had four main sessions, some of them divided into sub-sessions:

Session A: Special Modes of Corium Discharge into the Containment

Session B: Phenomena to Achieve Coolability

- B1: Natural Convection Heat Transfer with Bubbling
- B2: Characteristics of Particle Beds
- B3: Spreading
- B4: Fragmentation and Quenching
- B5: Flooding

Session C: Material Properties and Thermochemistry

- C1: Properties
- C2: Thermochemistry

Session D: Reactor Application

The Session Chairmen summaries are attached (Annex II). Each session and the meeting itself were concluded by a general discussion. Throughout the presentations of the papers and the discussions, the focus was on the application to the full size plant.

Summary

The workshop has underlined that international scientific co-operation is an important factor to assure and to increase the safety level of operating and future nuclear power plants in Western Europe, USA, Japan, and Eastern European countries as well. The similarity and convergence of the technical approaches and strategies of severe accident control and mitigation, as presented by specialists of many countries, was noted as a positive response to the requirements of safe reactor operation.

The workshop has shown a substantial increase of research and design activities to control ex-vessel melts. Especially in Western Europe, this increase is related to higher safety requirements in response to technological improvements and a highly sensitive political background. As addressed in the invited introductory paper, besides the strong interest to mitigate severe accident consequences in existing plants, future evolutionary LWRs in Europe (as the European Pressurised Reactor EPR) will include additional design features for mitigation of severe accidents involving vessel melt-through.

The following gives an overview over the current aspects in ex-vessel safety research, in the sequence of the melt-down process:

As the release mode of the corium debris from the pressure vessel is unknown to a substantial degree, bounding scenarios are addressed to quantify different possible aspects of corium release. DISCO investigations study the ejection of melt in narrow reactor cavities in case that the lower pressure vessel head fails under reduced system pressure. The dispersal and location of melt in the cavity and/or the reactor containment are important with respect e.g. to any subsequent cooling measure, and strongly depend on release pressure and location of RPV failure hole. Code development to describe melt relocation is underway.

Jet impingement is another generic question related to corium release. Experiments study the erosion rate of concrete as influenced by the properties of the jet, and will be supplemented by model development.

Candidates of concrete which are under consideration for use as sacrificial structure material for corium melts are investigated in KAPOOL experiments to quantify their erosion behaviour. Additionally, the erosion of a steel gate is investigated to assure sufficient large opening for the release of the corium melt to a dedicated spreading area.

Heat transfer from the internally heated melt during concrete erosion is investigated with model fluids especially with respect to onset of solidification. The agitation by gas bubbles provides for a more balanced upward and downward heat transfer. Other experiments show that solid particles suspended in the melt, which simulate a slurry melt after onset of partial solidification, influence the heat transfer mainly because of the higher viscosity of the dispersion.

Several contributions discussed the coupling of thermal-hydraulic and physico-chemical effects during solidification of multi-component corium melts and MCCI. Under low freezing rate, a solid layer of the refractory components of the melt would form at the cold interface, instead of a mushy fluid modelled in actual codes. As this new approach gives better understanding and description of the phenomena observed in MCCI and material interaction experiments, its implementation into codes is desirable for better predictive capability.

However, because of the complicated physico-chemical processes and the complex physico-chemical data bases, this is a very difficult task.

When a hot corium melt is introduced into a water pool, a particle bed may form. The coolability of such particle beds when flooded by water was analysed and can substantially be improved, when the water is supplied by downcomers to the bottom of the particle bed. Further experimental work is underway to characterise the influence of 3D-effects on bed coolability.

Spreading of corium to generate a shallow melt layer is of interest to generate a good condition for melt cooling. From the experiments performed within the 4th European Commission Framework Programme both with simulant (CORINE, KATS, RIT) and prototypic melts (VULCANO, FARO, COMAS) the important phenomena during spreading and the related physics are adequately understood. An important observation is that multi-component corium melts spread, even if their initial temperature is below the liquidus temperature. Immobilisation of the melt occurs when a substantial fraction of crystals has formed during cool-down of the melt and increases the viscosity of the mushy melt to virtually infinity, or when a stable surface crust is formed at the melt front. Spreading on a concrete surface slightly reduces the spreading length. The presence of a shallow water layer has minor influence on spreading and no energetic melt/water interactions were observed. It is concluded that for existing plants with their narrow cavities, spreading is sufficiently homogeneous and the spread area likely covers the entire cavity. As such, spreadability is not an issue. However, the spread depth may be large so that the debris coolability is not assured.

To better characterise the spreading processes in future reactors with possibly larger surfaces (such as the EPR), the available experimental information should be evaluated and synthesised systematically with respect to the expected accident conditions. The spreading codes have made good progress in modelling and should be further validated by systematic use of relevant experiments. In addition, the effect of concrete ablation on spreading should be quantified. At the end of the validation process a blind pretest calculation of a representative corium spreading experiment is considered to be useful. Some of the modelling problems which were discussed during the meeting may, however, not be relevant for the EPR typical spreading process as higher masses and release rates are expected.

Relations derived from dimensional analysis can be used as a guidance for the end-state of the spreading process.

Corium jets falling into water under in-vessel conditions with jet diameters of 3 to 10 cm form a particle bed of 50 % or higher on a cake of unfragmented corium. Steam explosions with very low efficiency were observed only when triggered in some of the experiments. These results, however, cannot be readily extrapolated to ex-vessel scenarios because, e.g., of the eventually different melt composition and large subcooling of the water.

Under ex-vessel conditions, fragmented jets are considered to be possible which have a good potential to be cooled. In addition to the CROTOS and FARO tests, new experiments became available from the COTELS project which also uses prototypic melts and includes UO_2, ZrO_2, Zr and steel under ex-vessel conditions. COTELS showed no occurrence of spontaneous steam explosions similar to FARO and KROTOS. However, multiple jets and the influence of a driving gas pressure were presently not considered. Furthermore, the release of steam and eventually of hydrogen upon quenching of the melt is a point of interest for the

containment atmosphere. The mechanisms of hydrogen production from purely oxidic melts during quenching as observed in FARO tests, deserves further consideration to clarify the details of corium-water interaction.

The closure of the FARO test facility leaves unresolved ex-vessel aspects and limits further investigations to the smaller KROTOS facility which is being transferred to CEA's Cadarache Centre. It is recommended to focus the future programme on ex-vessel conditions.

Besides corium jets falling into water, COTELS also cover the process of ex-vessel melts being flooded from the top. These tests, which involved collapsed corium heights from 7 to 13 cm (close to 15 cm in the MACE M0 test), for the first time indicated complete corium coolability by formation of a particulate debris bed, in contrast to the MACE experiments which showed only limited coolability for higher melts. The phenomena which influence the coolability process, such as particulate debris bed formation, crust break-up, and melt ejection from the top of the melt pool driven by gases from the decomposing concrete should be investigated in further detail. Although the final stop of concrete erosion is not assured, top flooding of the corium melt during melt concrete interaction could be beneficial during the late phase of an accident, e. g. for fission product retention. The consequences on further important implications for long term accident management strategies, e.g. due to steam release and pressurisation of the containment, must be considered.

For the flooding, no occurrence of a steam explosion was observed in the MACE, COTELS, and KATS experiments with stratified geometry.

In the COMET bottom flooding concept, water is supplied to the bottom of the melt either by injection holes or by a porous concrete layer. Experiments have shown rapid and complete solidification mainly by creation of a porous structure of the freezing melt which allows easy flooding by the steam-water coolant flow. The principle of the concept is further investigated using transparent simulant materials to show the coupling of water ingression, fragmentation and solidification. The bottom cooling concept is a promising alternative and can be readily extrapolated to reactor scale. It is applicable to future reactor designs and potentially to some existing reactors. The pressurisation of the containment by steam is, however, a consequence, which must be considered.

The physico-chemical properties of the corium melt are essential for understanding and modelling of melt behaviour. The liquidus-solidus temperatures for U-Zr-O melts with compositions typical for BWRs and LWRs were measured. This is a necessary extension and confirmation of existing phase diagrams. Viscosity measurements were also presented for these melts above and below the liquidus temperature, and show variation over several orders of magnitude depending on the composition and temperature of the melt. These data are very important to describe physical processes in which solidification is involved. To estimate the viscosity of multicomponent oxide melts also in their freezing range, a model has been proposed. Further measurements are recommended, especially in the freezing range, with inclusion of Fe and Si oxides in the melt. Additionally the influence of other components (e.g., Pu in the case of mixed oxide fuel) on phase diagrams should be estimated, if the components are expected to have significant influence on melt properties.

Another important issue to be addressed is the mechanical stability of a corium crust under thermo-mechanical loading. This is particularly relevant for the stop of melt spreading

and also for coolability investigation under top flooding condition where coolability would be improved if the crust can be breached thereby providing a path for water ingression.

Thermomechanical stability of ZrO_2 -ceramics and –concretes to resist the corium melt was investigated and conditions for stable long term retention proposed with respect to temperature gradient and oxygen potential in the melt. Differences in various models regarding the influence of temperature and oxygen potential/diffusion on the dissolution process were noted and shall be clarified. For the EPR melt stabilisation concept, the authors concluded that all requirements on the stability of the protective layer can be fulfilled. Confirmation is expected from the large scale CORESA tests.

Finally, applications to reactor plants were presented. In the framework of Spanish PSAs, MELCOR application highlighted the ex-vessel corium coolability issue. The very wide range of containment failure probability, which is related to the uncertainty of ex-vessel debris coolability, confirmed the need for further studies of ex-vessel coolability.

The GAREC group has analysed ex-vessel corium recovery for some present and future PWRs. This includes scenarios for core meltdown and corium transfer to the lower head, corium behaviour in the lower head, vessel failure, risk of steam explosion, corium-concrete interaction and coolability, corium spreading and accumulation, corium ceramic interaction, and long term corium stabilisation. The various aspects were partly discussed in the proceeding issues.

Experimental and theoretical analysis on 2-phase flow heat transfer in large scale were presented, as it may occur after surface flooding of the melt. Stable and oscillating flow conditions were observed depending on the degree of subcooling of the coolant water.

A detailed analysis of the EPR ex-vessel melt retention concept was also presented. This includes the temporary retention of the corium melt in the reactor pit to make corium recovery independent of various scenarios, the fast release of the corium to the spreading compartment, and the cooling by surface flooding. A cooled protective layer stabilises and cools the bottom of the corium melt. This EPR concept has triggered much of the research which was discussed throughout the meeting.

Conclusions and Recommendations

The following conclusions and recommendations are formulated after evaluation of the presentations and discussions. They are generally listed in the sequence of the meltdown process.

(1) The conditions of melt release at vessel failure may vary according to the variations of core melt-down in the RPV. Relevant scenarios and bounding melt release conditions, such as melt dispersal into the containment as one extreme or jet impingement as another extreme release mode, should be quantified in order to plan and assess different management procedures or countermeasures for accident mitigation.

(2) The phase diagrams and physical property data bases to characterise corium melts of various compositions should be extended, especially with respect to lower melt temperatures and in the freezing range.

(3) During solidification of the corium melt or during its interaction with structure materials, thermal-hydraulic processes related to heat transfer and movement of the melt are closely coupled to physico-chemical processes which change the constitution of the multi-component melt and its physical properties. The coupled modelling of these processes should be further developed, especially with respect to its implementation into large computer codes.

(4) Ex-vessel melt cooling by melt release into the flooded reactor cavity and resulting in major fragmentation should be further investigated, including possibly negative consequences as e.g. steam explosions.

(5) The effectiveness of cooling a corium pool by top flooding should continue to be further investigated. Key issues are particulate debris formation, melt ejection, and crust break-up as potential mechanisms for long-term debris coolability.

(6) Investigations and development of the bottom flooding concept should continue as an alternate cooling concept, including the use of porous, water filled concrete. The concept is attractive for future reactors and potentially for some existing plants.

(7) Substantial information about the spreading of corium melts is available in form of experiments and computer codes. This information should be condensed and, where necessary, completed to predict the melt conditions for which sufficient melt spreading under reactor conditions can be expected also for large areas as proposed for future reactors. A blind pretest calculation of a representative corium spreading experiment is considered to be useful.

(8) For the evolutionary containment concept of the EPR, an ex-vessel corium stabilisation concept was proposed and will be subject of the licensing procedure. Where necessary, investigations into the safe performance of this concept should continue.

(9) Melt cooling by direct water contact has important consequences on containment processes, such as pressure build-up by steam release, hydrogen concentration and fission product distribution. These processes should be further quantified for individual plants to asses the various aspects of accident management procedures.

Annex I

Programme Committee of the Workshop and the Session Chairmen

Programme Committee:

H. Alsmeyer (Chairman)	Forschungszentrum Karlsruhe, Germany
H.-J. Allelein	Gesellschaft für Anlagen- und Reaktorsicherheit, Germany
S. Basu	U.S. Nuclear Regulatory Commission, U.S.A.
J.-C. Latché	Centre d'Etudes de Cadarache, IPSN, France
J. Sugimoto	Japan Atomic Energy Research Institute (JAERI), Japan

Sesssion Chairmen:

H.-J. Allelein	Gesellschaft für Anlagen- und Reaktorsicherheit, Germany
H. Alsmeyer	Forschungszentrum Karlsruhe, Germany
S. Basu	U.S. Nuclear Regulatory Commission, U.S.A.
G. Cognet	Centre d'Etudes de Cadarache, CEA, France
V. Gustavsson	SwedPower AB, Sweden
J.-C. Latché	Centre d'Etudes de Cadarache, IPSN, France
H. Nagasaka	Nuclear Power Engineering Corporation (NUPEC), Japan
W. Scholtyssek	Forschungszentrum Karlsruhe, Germany

OECD/NEA:

J. Royen	OECD Nuclear Energy Agency

Annex II: Summaries of Session Chairmen

Session A: Special Modes of Corium Discharge into the Containment

Session Chairman: Sudhamay Basu (NRC, USA)

Four papers in this session discussed research findings on special modes of corium discharge (e.g., low pressure melt ejection, jet impingement, etc.) into the containment and consequences of such discharge on ex-vessel debris coolability and containment integrity. The results of research are particularly applicable to EPR-type cavity designs though some results can also have potential applications to current generation reactors.

Experimental investigation of corium discharge at low system pressure (<2 MPa) was reported in the first paper. The objective of the DISCO-C series of experiments at Forschungszentrum Karlsruhe (FZK) was to determine the upper bound of the RCS pressure that would result in minimum melt dispersal out of an annular cavity (e.g., EPR-type cavity design). Effects of breach size, location and failure pressure on dispersion were studied systematically using cold simulants (nitrogen/water or nitrogen/liquid bismuth alloy and helium/water). Experiments with larger holes showed more dispersal than those with smaller holes and produced higher peak pressures in the cavity.

Experiments with breach at the RPV bottom showed more dispersal than that observed in one experiment with a side breach. The threshold pressure for dispersion was found less pronounced in the annular cavity geometry than in cavities with non-annular geometry. However, more experiments are judged to be necessary, in particular, with side breach and hot simulants (e.g., thermite), before a definitive conclusion can be drawn about the optimum annular cavity design for minimum dispersal. Such experiments are planned in the current framework of activities.

During the discussion, it was clear that the results have important implications for EPR-type designs. Even though consequent direct containment heating from pressurized melt ejection is not considered a threat to EPR containment integrity, it is desirable to contain the ejected melt into a core catcher so that the inventory can be stabilized and rendered coolable. Also, for both EPR-type and operating reactors, dispersed melt trapped outside the cavity may degrade equipment and structural performance due to an imposed thermal load. Therefore, the present investigation has also implications for equipment qualification. The discussion further pointed to the fact that consideration of side breach is appropriate in the melt ejection investigation.

The second paper was an analytical complement of the first paper. The objective was to model the low pressure corium dispersal phenomenon with a computer code that combines the advantage of existing lumped-parameter models for system codes with the details of a multi-component transient fluid dynamics code. The underlying hypothesis for such code development is that the discharge of corium starts as a single phase flow for which lumped-parameter modeling is adequate but later on, switches to a two-phase flow for which detailed multicomponent, multifield modeling becomes necessary.

The analytical work at FZK utilized the Advanced Fluid Dynamics Model (AFDM) code to track water, molten corium, and gas-vapor mixture in two dimensions. Models were added to the AFDM code to describe melt oxidation and hydrogen combustion, as well as hydrodynamics of liquid films. Calculated dispersion rates using the code were found to be sensitive to transition time from the single phase to two phase. Comparison between meas-

ured (DISCO-C experiments and two SNL thermite experiments) and calculated dispersion rates showed reasonably good agreement given the early stage of code development.

During the discussion, it was clear that important dispersion processes as well as factors affecting dispersion(e.g., hole ablation, freezing, etc.) need to be considered in the code. Furthermore, it was noted that the steady-state entrainment model might not be fully valid when dealing with a transient process. Further code development addressing the above deficiencies was recommended.

Experimental investigation of corium jet discharge at low system pressure and the impingement of jet on substratum materials was the subject of the third paper. Research reported in this paper investigated corium jet interaction with sacrificial silica concrete in the KAJET experimental program at FZK, designed to gain insights into long term retention and cooling. Performance tests were carried out using water and thermite as melt simulants to obtain information on nozzle geometry and material for generating a compact melt jet. Also, two erosion tests were carried out with a melt jet which was initially metallic and then changed to oxidic. Erosion depth of the substratum was found to be higher with metallic melt than with oxidic melt. More experiments are planned with parametric variations of substratum material, melt mass, driving pressure and nozzle diameter. Results will be used to support the selection of suitable substratum materials for EPR.

During the discussion, similar work by PNC in Japan and by KTH in Stockholm was noted. A comparison of different experiments with regard to heat transfer rates would be useful. Further, it was felt that scaling studies would be required for reactor applications of the findings. Such studies are in progress at the University of Bochum, Germany.

Another aspect of the core catcher concept, i.e., stabilizing the discharged corium with a sacrificial layer before releasing it to a spreading area was the subject of the last paper of this session. The paper reported a series of KAPOOL experiments performed at FZK to investigate the erosion behavior of a sacrificial concrete layer. Iron-alumina thermite was used as a melt simulant and two different sacrificial concretes were investigated, based on borosilicate glass, and iron oxide and silica. From the limited set of experiments (three each with the two concrete compositions) conducted thus far, it appears that the borosilicate glass has a lower erosion rate. On the other hand, the transient temperature behavior of the thermite melt does not allow to discriminate between the influence of concrete type and oxidation of zircaloy which was present in two of the tests, and therefore further investigations may be necessary.

The series of KAPOOL experiments also investigated phenomena related to the failure mechanism of a steel gate, as featured in the current design of the EPR core catcher. It is important to ensure a sufficiently large opening cross-section of the steel gate under prototypic thermo-mechanical loading of the core debris. Experiments were conducted to investigate gate ablation in presence of both metallic (iron) and oxidic melts. Preliminary analysis of oxidic melt attack indicated fast temperature rise of the steel gate followed by formation of a crust. Subsequently, gaps formed between the crust and the gate resulting in large resistance to heat transfer.

During the discussion, the proof of a sufficiently large opening during gate failure was viewed by some as the most uncertain issue in the overall melt retention scheme of the EPR design. However, it relates to the design issue and those involved in design expressed confidence that the gate could be designed to melt through providing the desired opening. Further work to resolve the issue of gate meltthrough should be identified.

In the summary discussion of all four papers on special modes of corium discharge, important contributions of the FZK research team was recognized, particularly with regard to the relevance of research results to EPR-type reactor designs. The results provide important data on initial and boundary conditions for further investigation of long term coolability and retention of core melt in the EPR design. Some results can also have potential applications to current generation reactors. In order to obtain bounding data for reactor applications, a few recommendations were formulated. It was recommended that with respect to RPV failure, consequences of a side breach be investigated further as an important failure mode. Scaling studies were recommended to extrapolate the results of small-scale simulant experiments to reactor prototypic cases. Finally, the important role of physico-chemical processes was identified as an area requiring careful studies.

Session B: Phenomena to Achieve Coolability

Session B1: Natural Convection Heat Transfer with Bubbling

Session Chairman: Veine Gustavsson (SwedPower AB, Sweden)

This session consisted of three papers. The first paper dealt with heat transfer experiments from internally heated pools with and without gas injection, investigated in the BALI facility in Grenoble. The objective of this work was to quantify heat transfer coefficients at pool boundaries considering the effects of viscosity and superficial gas velocity. Water was used as corium simulant in the experiments and different weight fractions of cellulose were added to vary the viscosity. The dimension of the test section was about 3m long, 0,5m high and 0,15m wide. The single phase tests include three different cooling conditions and each test was performed for three pool viscosities. These experimental results agree well with the correlations in the literature (e.g. Reinecke and Steinberner).

The multiphase tests were performed with gas injection through the bottom ice crust with superficial velocities in the range 1 cm/s to 20 cm/s. Three different pool viscosities were investigated. The measured heat transfer coefficients, especially as influenced by the viscosity of the pool, are not correctly represented by existing correlations and large differences exist between published correlations. With respect to MCCI configurations it is concluded from the experiments that for superficial gas velocities greater than 0.5 cm/s, as e.g. existing in the MACE M3B experiment, the power split of the heat flux to the upper surface referred to the total internal heat generation is 50 % and does not depend significantly on superficial gas velocity or on pool viscosity because the bulk of the pool is well stirred.

In the development of models in this work, the coupling of thermal-hydraulic and physico-chemical effects was taken into account. The correlations derived from the BALI experiments have been used in the simulation of ACE and MACE experiments. This work was presented in the last paper of session B1.

The second paper in session B1 discussed the effects of solid particles on heat transfer in multilayered liquid pools with gas injection. This work reported experiments performed at University of Wisconsin in the US. In the experiments two fluid layers were used consisting of an upper oil layer and a lower layer of water or glycerin. Solid particles of polystyrene beads were added to the lower layer to simulate the solid and liquid slurry which may eventually form when the corium melt cools below the liquidus temperature. The addition of the beads in many cases lead to the agglomeration of a quasi solid layer at the interface between the two fluids. On this situation the report was focused.

It was observed that the viscosity of the fluid in the pool had a dominating effect on the heat transfer coefficients to the upper and lower boundaries. It was also found that the solid fraction in the pool did not have a first order effect on the heat transfer coefficient. Special attention was given to the power split of the up/down ratio which may strongly vary according to the boundary condition. It is concluded that existing models and correlations must be used with caution.

The last contribution in session B2 was about simulation of ACE and MACE experiments on molten corium/concrete interaction using a phase segregation model which was implemented in the TOLBIAC code. The phase segregation is related to solidification of refrac-

tory components UO_2 and ZrO_2 in the low temperature zone near the corium/concrete interface. This process changes the composition of the residual liquid melt.

Three components were taken into account to characterize the melt: oxides, metals, and gas, and the following phenomena were included: metal/oxide stratification, residual power, free surface heat transfer, and crust formation.

Comparison of experimental data and calculations with the phase segregation model gives a better understanding and description of late corium/concrete interaction when components of the melt start to solidify. .

There are several points in favour of the phase segregation approach for MCCI:

- the temperature traces can be recalculated, even during interaction transients,
- the material effects on melt temperature are explained,
- the effect of power variation on melt temperature is well predicted,
- the post test examinations show strong variations in melt composition,
- the composition of melt ejected in the MACE experiment M3B could be well calculated,
- the approach offers a possible explanation of periodic bursts of the crust during the test,
- the temperature-viscosity contradiction is resolved.

The confirmation of this approach is subject of ongoing analytical and experimental work, e. g. in the EC funded ECOSTAR program.

Session B2: Characteristics of Particle Beds

Session Chairman: Veine Gustavsson (SwedPower AB, Sweden)

Session B2 consisted of three contributions.

The first paper described the characterization of debris bed generated by FCI. This work was done at Professor Sehgals group at RIT, Stockholm.

In the past many investigations have been done to characterize the size distribution of particles from a debris bed generated by FCI. In the work at RIT, four types of statistical distributions were applied, namely: Weibull, log-normal, upper limit log-normal, and a distribution that resulted from the sequential fragmentation theory (SFT) from Brown. Data from experiments were fitted to each of the distributions. Two sets of data were used in this work: one set from the JRC/Ispra, KROTOS experimental program and the other set from the MIRA-20L program at RIT.

It was found that the SFT (sequential fragmentation theory) worked best. SFT is based on two parameters: mass mean diameter and a fractional dimension related to the shape of the particles.

A conclusion from this work is that the size distribution in a debris bed generated by fuel coolant interaction can be fitted to the SFT distribution, where the fractal dimension varies between two and three for the data analyzed.

The second contribution in session B2 was about an experimental investigation on dryout heat flux of a particle bed with a downcomer. Also this work was performed at RIT in Stockholm.

Many experimental and analytical studies exist world-wide which investigated the dryout heat flux in a debris bed cooled with top flooding. Important results have been

achieved, which show that the coolability of the debris bed depends strongly on particle size, shape and porosity distribution, and beds with small porosity are more difficult to cool than those with large porosity. For stratified beds, the layer on the top, where smaller particles tend to accumulate, will determine if the bed is eventually un-coolable. However, the possibilities for coolability will be improved if water is supplied at the bottom of the debris bed via a downcomer.

Two series of experiments were performed on the dryout heat flux in the POMECO (POrous MEdia COolability) facility. One was with homogenous beds and the other one with stratified beds. The porosity of the particle beds was varied from 25 to 40% and the average particle size from 0,2 to 1,0 mm. The material used in the test was made of different sand particles.

For the stratified beds the smaller particles were accumulated on the top of the bed, and dominated the dryout process.

The effect of downcomers on coolability was investigated both for homogenous and stratified beds. It was found that downcomers enhanced the dryout heat flux substantially- in the experiments in the range from 50 to 350%.

The last contribution in session B2 was an experimental investigation on particulate debris bed coolability in a multidimensional configuration. This work was performed by EdF. The experimental program is called SILFIDE, which is a French acronym for "simulation of fragmented debris with internal heat generation".

The purpose of SILFIDE is to provide data on multidimensional configurations taking into account natural circulation due to the gravity difference between liquid and vapour phase. In the experiments, corium is simulated by steel spheres heated by electrical induction heating. Water is used as coolant. The dryout heat flux is measured for different geometrical configurations and the heatup of the bed is recorded.

The experimental program is still in progress. First experiments were reported. The heating of the particle bed may, however, be not sufficiently uniform to draw conclusions at the present stage When the data for two-dimensional homogenous beds are completed, more complex heterogeneous configurations will be investigated in the SILFIDE facility.

Session B3: Spreading

Session Chairmen: H.-J. Allelein (GRS, Germany), J.-C. Latché (IPSN, France)

This session was devoted to the problem of melt spreading. Twelve papers were presented, covering experiments, code development and code validation by reactor applications.

The first presentation gave a general survey about the experimental activities (RIT and KATS simulant material experiments, FARO and VULCANO using real material) and analytical ones (improvement and validation of the spreading codes CORFLOW and THEMA) performed in the CSC-Project of the 4th European Framework Programme. Most of these work was presented in the following papers in more detail.

The next four presentations mainly dealt with the experimental findings in the test series KATS (FZK), VULCANO (CEA), COMAS (SNU), and FARO (JRC). As a result of

these experimental programs and, more generally, of the experimental work performed in Europe, a wide range of data is now available :

- from low (CORINE), medium (RIT) and high temperature (KATS) simulant experiments to real material tests (VULCANO, FARO, COMAS);
- with varied inlet conditions : low and high flowrate, temperatures ranging from below melt liquidus to large superheat;
- with inert or concrete basemat.

Melt masses spread in these experiments are generally lower than 300 kg. Masses up to 2 tons were spread in the COMAS experiments. These are still lower than in reactor accident situations, where melt masses of 100 tons and higher are considered. The main experimental results are:

- The inflow conditions (initial melt temperature, mass and composition of the melt, pouring rate) have a major influence on the spreading process.
- Different observations about the influence of the substratum material have been made in the COMAS and KATS experiments. In COMAS, no significant difference between 1D spreading on concrete and ceramic material was seen. This effect may be explained by the high pouring rate and the resulting short spreading period realized in the COMAS experiments.
  In contradiction, the one-dimensional KATS experiments 12 and 13 have shown a significant difference in the spreading length of about 30%. Also in the two-dimensional KATS experiments 8 and 17, the shape of the area covered with melt is totally different. Nevertheless, in both cases about 60 % of the surface are covered with melt.
- Following the KATS observations, the influence of an epoxy paint on a concrete surface is of minor importance for the overall spreading behaviour of the bulk of the melt.
- Only experiments with a shallow water layer (up to 1 cm) initially present on the spreading surface were performed. In all these experiments using prototypic material, only one minor energetic melt-water interaction happened. In addition, the presence of this film of water seems to have only minor influence on melt spreading.
- The porosity of the spread material after cooling was in some cases high (VULCANO) and in other cases low (COMAS, FARO). The reason for this high porosity has to be clarified as well as the occurrence of surface cracks of the solidified melt found in many experiments.
- In the COMAS and VULCANO series, the authors observed good spreadability even for oxidic melts which spread with temperatures significantly below the liquidus temperature.
- In the COMAS series it is reported that during the spreading process mixed melts separate into metal and oxide layers. .

After the presentations about these 4 experimental series, five presentations were given about the spreading codes CORFLOW, CROCO, LAVA and THEMA. These codes are based on a different modeling of the spreading process:

- LAVA and THEMA solve the mass, momentum and energy balance equations integrated over the flow height ; this approach reduces the 2D- or 3D-problem to, respectively, one or two (horizontal) dimensions. In LAVA, inertia forces are neglected.
- CROCO solves the 2D (one horizontal, either cartesian or axisymetric, and the vertical dimension) Navier-Stokes equations, either without any additional assumption or using the momentum balance simplifications arising from the thin flow approximation.
- CORFLOW solves the 2D- or 3D-Navier-Stokes equations.

LAVA, CROCO and CORFLOW are able to take into account Newtonian or non-Newtonian (Bingham) rheological laws.

The following conclusions are drawn from the calculations:

- The major part of the calculations presented was in rather good agreement with experimental data. Remaining discrepancies which are identified in comparison with experiments may be partly attributed to experimental uncertainties, such as initial conditions or material properties. Some models in the codes require further qualification which should be achieved by verification through characteristic experiments. Improvements should concentrate on those phenomena which are of primary importance for the spreading process of large melt masses in reactor scale.

- The actual understanding of the melt stabilisation process is that the stopping might be due to the growth of a low temperature, highly viscous boundary layer at the leading edge. None of the codes presently simulates the mechanical stability of the front crust, but all of them take credit from rapid increase of the viscosity (or the yield stress) near the freezing temperature.

The great number of calculations performed with these different codes, including a few sensitivity analyses, lead to the requirements of:

- a sufficiently qualified data base of material properties with special respect to the viscosity and, possibly, the yield stress, of the liquid phase,
- a high accuracy of the experimental data concerning inflow boundary conditions (temperature and mass of the melt as well as mass flow rate).

EPR spreading calculated with CORFLOW was also presented. In the calculations, different assumptions about the initial mixing or stratification of the melt phases in the pit were made. In addition, material properties of the oxidic phase, the corium initial temperature, the flow area of the sacrificial gate, and the rheological behaviour of the melt (Newtonian to Bingham) were varied. All these different calculated cases lead to an almost homogenous corium layer thickness in the completely covered spreading area in less than 60 s. But it has to be stated that some of these computations have been performed with high melt overheat, and the mass flow rates correspond to a high gate cross section of 2.4 m^2 with the exception of one calculation for 0.24 m^2 opening.

After the code presentations, a method based on dimensional analysis was presented to assess spreading characteristics. This method from RIT was first developed for spreading in

one-dimensional channels and has then been extended to spreading into an open area. In the discussion about this method, a suspected discrepancy in the theoretical assumption was discussed, which remains to be clarified.

In the last presentation, which dealt with the remelting of immobilized melt pile-ups, results obtained with a two-domain approach on moving adapting grids for the convection dominated melting problem with internal heat sources were shown. In all cases a strong convective mixing and cooling was calculated, so the temperature distribution in the liquid phase is mainly isothermal. Crust melting was predicted to appear at the top of the dome. For the moment, turbulence is not taken into account.

Session B4: Fragmentation and Quenching

Session Chairman: Werner Scholtyssek (FZK, Germany)

A necessary condition to achieve efficient quenching, cooling and stabilisation of a high melt layer in a restricted geometry is fragmentation of the melt which provides for a high heat transfer area and for sufficient void inside the melt to allow circulation of coolant. In session B4, the phenomena observed during melt injection into a coolant pool were discussed. In session B5, the results of studies of flooding of a melt layer, either from the top or from the bottom, were presented.

Four papers in session B4 presented results that were obtained in the research area of fuel-coolant interaction (FCI). The results which are of primary interest under the aspect of coolability are

- the fragmentation of a melt jet,
- the particle size and size distribution,
- the quenching rate and
- the final debris bed configuration.

Other interesting results are

- the hydrogen production during fragmentation and quenching,
- the probability of occurrence of a steam explosion and
- the thermal and mechanical loads to structures.

In the first paper, an overview of the FARO and KROTOS programs was given, including implications on FCI. Corium melt jets of 30 mm to 100 mm diameter were injected into water pools of variable height. The tests were mainly performed under in-vessel conditions, i.e. high system pressure and saturated water. Some tests were done under ex-vessel conditions, i.e. low pressure and subcooled water. UO_2-ZrO_2 melt was used, with addition of metallic Zr in one FARO-test. In all tests with pure oxidic melt, about 50% of the melt was fragmented. Complete fragmentation occurred in the test with metallic Zr. The final debris bed consisted of a solid "cake" at the bottom, overlaid by particles with mass averaged di-

ameter of 2,5 < d < 5mm. No steam explosion occurred in tests without triggering, and in those tests where steam explosion occurred, the efficiency was very low. Significant production of hydrogen was observed also in those tests with pure oxidic melt.

The second paper described modeling of coarse break-up of molten core jet. The model is part of the JASMINE code which intends to simulate FCI. It describes jet penetration into coolant, production of melt particles and their movement in the pool, and melt pool formation at the bottom. For treatment of thermal-hydraulics of the coolant, a coupling to the 3-D two-phase flow code ACE-3D will be made. The numerical behaviour of the model was tested by comparison with an analytical case. Further, the experiment ALPHA-MJB (MJB: melt jet break-up) was analysed. Reasonable agreement could be achieved after adjustment of certain model parameters. Further assessment of the parameters will be performed.

Paper 3 gave an overview of the COTELS project that started in 1995. Paper 4 described FCI tests under ex-vessel conditions within this project. COTELS is a common experimental project of Japan and Kazakhstan research organisations, oriented to FCI and MCCI. The testing complex, located in Kazakhstan, includes 3 experimental facilities, "SLAVA", "LAVA" and "LAVA-M". Corium with mass up to 60 kg and with composition UO_2-steel-ZrO_2-Zr is used, with temperatures up to 3200 K. The melt is produced in an electric induction melting furnace. To simulate decay heat, induction heating is also provided for the crucible in MCCI tests.

In the FCI tests, melt jets of 50 mm diameter were dropped into water pools of variable height and temperature. In all tests, nearly complete fragmentation of the melt occurred. Steam explosion was not observed. It was found that the first pressure peak could be correlated with the mass median diameter of the fragmented corium particles. The correlation holds also when FARO tests are included in the analysis.

Session B5: Flooding

Session Chairman: Werner Scholtyssek (FZK, Germany)

The phenomena observed during flooding of a melt layer with water, either from top or from bottom, were addressed in 7 presentations in this session. Results of primary interest concerned

- physics, chemistry and material properties important in MCCI and flooding processes
- quenching characteristics
- final debris configuration
- thermal and mechanical loads.

Other interesting results were

- probability of steam explosion
- H_2-production
- source term related phenomena.

In the first paper, ex-vessel debris cooling tests performed within the COTELS-project were described. The LAVA-M facility was used with two types of concrete crucibles with different aspect ratios. The corium melt with mass of about 60 kg and temperature of about 3200 K was dropped into the crucible which could be induction heated to simulate decay heat. 8 to 10 min after the drop water was injected at a rate of 2 l/s onto the top surface of the melt. No steam explosion was observed in 10 tests. Although fragmentation of the debris beds was not complete, and in some tests solid "ingots" were observed, cooling of the melt was achieved in all cases. This was partly attributed to formation of cracks and channels in the corium and in the concrete around and below.

The second paper reported results of structural investigation of the COTELS tests and comparison with other tests (WETCOR, MACE). Especially the absence of adhesion of the top crust to the side walls was mentioned, which helped, together with concrete erosion and formation of rubble in side walls and bottom concrete, to reach coolability and to stop concrete erosion. The particle size spectrum was analysed and found to correlate well with the Rosin-Rammler-equation.

In the third paper, an overview on the MACE test program performed at Argonne National Laboratory was given, and especially results of tests M0 and M1b were presented. The tests address the coolability - by water addition from above - of corium being in interaction with concrete. Crucibles of different cross sections and melt masses from 100 to 2000 kg have been used. The melt is heated by direct electrical heating. In all tests, crust formation and anchoring of the crust to the crucible side walls and formation of gaps between crust and the molten corium below led to significant reduction of the heat flux to the water on top so that complete quenching of the melt could not be clearly demonstrated. In prototypic, large caverns, however, the crust would very probably float on top of and remain in contact with the melt, and therefore heat transfer mechanisms identified in the tests could lead to coolability. This will be further investigated in separate tests which should increase the data base in support of model development and validation activities.

The fourth paper presented the CORQUENCH model that was developed at Argonne National Laboratory to calculate corium coolability. The modeled heat sources and sinks include decay heat, chemical reactions, heat transfer into walls and to the overlying atmosphere (gas or water). Options for 1-D and 2-D application are implemented. The model was validated on ACE/MCCI and MACE tests with reasonable success, when crust permeability was assumed. Scoping calculations for representative plant conditions showed, that, compared to the dry case, concrete erosion is significantly reduced by water addition and possibly arrested if dryout limits exceed 200 kW/m^2.

Papers five and six presented results of the COMET and COMET-PC investigations that were performed at Forschungszentrum Karlsruhe. The COMET concept proposes spreading of the melt and quenching by water injection from the bottom. This is achieved by erosion of sacrificial concrete until a system of water-bearing channels (COMET) or porous, water-filled concrete (COMET-PC) is reached. Within the program, a great number of transient tests and tests with decay heat simulation have been performed on different scales using thermite as simulant for corium. Upon passive opening of the channels, evaporating water fragments the melt and provides the conditions for rapid and efficient quenching. Tests at ANL with prototypical corium confirmed the observations. No energetic interactions of melt with water were observed; this can be attributed to the limited amount of water available at any time. High fragmentation of the frozen melt guarantees long term stabilization and coola-

bility. Consideration must be given to the pressure increase in the containment because of steam production during the quenching process.

The final paper presented results of experiments performed at the Royal Institute of Technology (Sweden) to study details of the quenching process during bottom flooding. Coolant was injected from the bottom into simulant melt, for which non-eutectic oxidic salt mixtures were used for high temperature tests, and paraffin oil for low temperature tests. The latter allowed direct visual observation of the processes. The porosity formation was studied depending on parameters including melt height, melt superheat, coolant inflow rate and pressure, and number of coolant nozzles. Important parameters governing the fragmentation process were identified to be melt viscosity, the temperature difference between melt and coolant, and the flow rate.

Discussions on Sessions B4/B5

Concerning melt injection into water, it was stated that a significant data base has been established. However, for ex-vessel situations some additional data would be needed. Also, geometric as well as material scaling considerations deserve more consideration. From the presently available data one can conclude that significant fragmentation of the melt is likely to occur when a melt jet is injected into water. The debris configuration in the cavity consists of a melt cake at the bottom and particulate debris on top which may form a coolable system. Steam explosion is not likely to occur with corium material. However for confirmation of this observation it would be necessary to put the differences that are observed between thermite and corium behaviour in the FCI process on a quantitative and mechanistic basis. As a consequence of the observations, cavity flooding before RPV failure as an accident management measure was generally considered to be beneficial.

In view of coolabity of a debris bed by top flooding, encouraging results have been obtained. It was shown that under favorable conditions coolability can be reached. However, the differences in the experimental findings on coolability in the COTELS and MACE experiments require further analysis. In any case, a benefit from water addition can be expected because erosion of the underlaying concrete layer would be slowed down and FP release would decrease. The risk of steam explosion in such a configuration was considered to be small. An enriched data base that could be used for modeling and upscaling of related phenomena could help to confirm the findings.

The concept of bottom flooding of the melt was generally considered as very effective for quenching and stabilizing of the melt. A core catcher based on this concept can provide a reliable solution for future reactors and possibly for some existing ones. A better understanding of the processes of fragmentation, debris formation, heat transfer and fission product behaviour could help to widen safety margins even further.

Session C: Material Properties and Thermochemistry:

Session C1: Properties

Session Chairman: Gérard Cognet (CEA, France)

The list of physical and thermodynamic properties which play a role in corium progression during a severe accident is quite impressive : liquidus and solidus temperatures, enthalpy, density, viscosity, thermal conductivity, emissivity, surface tension,... Moreover, most of these properties vary significantly with the composition and/or the temperature of the mixture. However, their importance not being equivalent, a prioritization can be made. Thus, the knowledge of phase diagrams and apparent viscosities is of utmost importance for the description of ex-vessel corium behaviour and cooling.

Three papers were presented in this session, one devoted to the determination of the liquidus and solidus temperatures of (U, Zr)O_{2-x} mixtures, with various oxygen contents reflecting various stages of zirconium oxidation, and 2 devoted to the estimation of corium mixture viscosity.

The solidus and liquidus temperatures of various PWR and BWR corium mixtures were measured by ANL, using a Differential Thermal Analysis technique (DTA). For PWR corium compositions (U/Zr molar ratio of 1.64), the solidus temperature was found to increase from 2005°C at 30% Zr oxidation to 2105°C at 70% oxidation. The liquidus temperatures for these compositions were nominally 400°C higher, ranging from 2465°C at 30% Zr oxidation to 2520°C at 70% Zr oxidation. For BWR compositions (U/Zr molar ratio of 0.69), the solidus temperatures were found to increase from 1930°C to 2042°C as the Zr oxidation increased from 30 to 70%. The liquidus temperature for these compositions was found to be a function of oxidation level, ranging from 2198°C at 30% oxidation to 2475°C at 70% oxidation. These 2 data sets indicate that both the liquidus and solidus temperatures decrease with increasing Zr content in the melt. Post-test analyses indicate also that Zr is soluble in the oxide phase within the range 30 to 70% oxidation.

Questions from the audience showed that some discrepancies exist between the presented values and those predicted by GEMINI / TDBCR ; Further investigations are needed.

ANL measured the apparent viscosities of some typical BWR and PWR corium compositions by measuring the spreading rate in a 1D channel. The corresponding viscosity was estimated from the analytical solution given by Huppert for the spreading of isothermal free surface flows. Tests were conducted with compositions representative of Zr oxidation of 30, 50, and 70%. Data indicates that at a roughly constant temperature of 2500 °C, viscosity increases by approximately one order of magnitude for PWR compositions and by as much as three orders of magnitude for BWR compositions. At the highest Zr oxidation state considered (i.e. 70%), there is evidence that the increased viscosity is due to the development of a solid phase within the melt as a result of the melt temperature falling below the liquidus temperature.

Questions from the audience highlighted the following points:

- The accuracy which is sometimes poor and which depends on the realization of isothermal conditions during tests;

- The use of this method to measure the apparent viscosity in the solidification range.

A general methodology, presented by the CEA, has been thoroughly investigated to calculate apparent corium mixture viscosities. This methodology, which extends the model initially proposed by Seiler and Ganzhorn (1997), is based on three main steps:

- The determination of melt compositions and phases (solid and liquid) versus temperature using a thermodynamic computer code;
- The use of either the Andrade model or the Urbain model to calculate the viscosity of the remaining liquid phase versus temperature depending on the SiO_2 content;
- The use of a modified Arrhenius law to calculate the apparent viscosity in the solidification range.

This methodology has proved its efficiency by recalculation of the evolution of the viscosity of various mixtures, in particular those of a basalt with 18% UO2 content and those of a 50% corium - 50% concrete mixture. However, complementary measurements are needed to check its validity for any corium - concrete composition. Questions were essentially oriented towards the modified Arrhenius model and its spectrum of validation. In fact, this model has been qualified on 2 types of metal melts and on 2 corium mixtures, one of which published by Skoutajan et al. (1979) and the other by Roche et al. (1993).

The general discussion which followed this session underlined some important points:

- For ex-vessel applications, other phase diagrams (U, Zr, Fe, O) and (U, Zr, Fe, Si, O) require more efforts to be made;
- Considering Mox fuel, phase diagrams with Pu could be needed;
- An effort has to be made to characterize crust stability;
- Suitable correlations or methodology should be developed for other properties such as thermal conductivity (liquid phase and crusts), emissivity and surface tension; however here, the priority is lower.

Session C2: Thermochemistry

Session Chairman: Gérard Cognet (CEA, France)

This session was devoted to the study of the compatibility of various materials regarding long-term corium collection, stabilization and solidification. Five contributions were presented, 3 of which described the results of corium ceramic interaction tests, 1, from the CEA, proposed a model for solidification and the last, from Siemens, described, in detail, the physico-chemical aspects of the EPR core-catcher concept.

The spreading area of the EPR core-catcher consists of 3 layers of different materials (from top to bottom): sacrificial concrete, sacrificial iron layer and zirconia, each of which playing a specific role. These roles were explained in detail by Dr. Hellmann, from Siemens, who also presented the results of laboratory tests which demonstrated that the target of decreasing the initially high liquidus temperature of the melt down to 1800 - 1850°C could be reached. Dr. Hellmann further reported about experiments performed at Siemens Erlangen on the thermo-chemical stability of zirconia-based protective material in contact with steel melts.

This contact mode is characteristic for the EPR melt retention concept since an interaction of the zirconia layer with oxidic melt is avoided by the addition of sacrificial material. Supported by a physico-chemical model and available knowledge in the field of metallurgy, he deduced that a zirconia protective layer is chemically stable against an EPR-type steel melt. According to his argumentation, the oxygen concentration within such a steel melt and thus the related FeO-activity remain safely below the corresponding threshold values for the formation of liquid ZrO_2-FeO phases and therefore chemical dissolution of the zirconia material cannot occur. The performed experiments confirm this dependence between FeO-activity and related extent of erosion. They also showed that at the current state of knowledge, the ZrO_2 ramming mass is one of the most promising application forms for the bottom refractory layer.

Questions from the audience pointed out that, before final conclusions, more realistic tests seem to be needed, which will be performed within the CORESA programme.

The experiments of corium ceramic interaction (2 papers: NITI and CEA) showed that the ablation of the ceramic is limited and blocked by the temperature gradient in the ceramic layer. Two dissolution models were proposed, one by S. Bechta from NITI and one by K. Froment from the CEA. The first one is based on the assumption that the ablation rate is proportional to the undersaturation degree, the second one is more complex because the authors want to take more phenomena into account. A comparison between these 2 models showed that the dependency of the ablation rate to the ΔT is not the same; Clarification seems to be needed.

Based on their experiments and their model, the Russian team from NITI claimed that the zirconia concrete (ZC) is well adapted as a protective material for core-catchers. However, based on the CEA study, any dissolution of a ceramic layer would be stopped, provided that a cooling system allows a certain temperature gradient to be maintained.

Another paper of CEA discussed the possibility of ceramic attack by oxygen which migrates from an oxidic corium layer through an iron layer. These tests proved this possibility exists, but this attack is weaker than in the case of direct contact between corium and ceramic. A theoretical estimate gives the right order of the dissolution process and shows that dissolution can be avoided by reduction of the oxygen transfer. As regards the differences found on erosion rates by Siemens and CEA, it was agreed that a common meeting will be needed to discuss in detail this issue in order to reach a joint position.

A theoretical study performed by the CEA on late phase severe accident processes has shown the importance of a strong coupling between thermalhydraulics and physico-chemistry during melt attack. This coupling leads to 2 important conclusions:

- Instead of a mushy zone the solidifying corium melt would form a layer of segregated refractory components at the cold boundary under thermalhydraulic steady state conditions;
- The current computer codes which describe corium solidification and interaction with concrete or ceramics have to be reviewed.

A first experimental proof of the coupling has been presented, however more experiments are needed, in particular with a sufficient scale to enable thermalhydraulic effects to develop; These are to be performed within the VULCANO programme.

This presentation and its consequences, in particular the coupling of chemical thermodynamic codes with thermalhydraulic codes was debated in the final discussions of this session. Discussions also highlighted that R&D efforts have to be made on dissolution phenomena and gas sparging effect.

Session D: Reactor Application

Session Chairman: Hideo Nagasaka (NUPEC, Japan)

The session D consisted of six papers. The first paper dealt with Level-2 PSA for Spanish individual nuclear power plants (CSN). The second paper was devoted to summarization of open problems of EPR core catcher and the corresponding R&D (GAREC). The third paper considered two-phase flow with possible instabilities of a natural circulation cooling system in EPR geometry (FZK). The remaining three papers dealt with the design considerations of the EPR core catcher (Siemens-KWU).

CSN has conducted independent regulatory evaluations of Level-2 PSA for all NPPs in Spain, focused on ex-vessel corium coolability issues using the MELCOR code. The effect of wet cavity flooding on MCCI suppression and the possibility of basemat melt-through were surveyed. Very wide range of containment failure probability due to the uncertainty of ex-vessel debris coolability confirmed the necessity of further enhanced study of MCCI for existing NPPs. Pool depth and subcooling should be considered in cavity flooding accident management to evaluate ex-vessel steam explosion probability.

The GAREC Working Group presented its view on major open problems with emphasis on the ex-vessel retention concept of EPR. Corresponding R&D programs were summarized extensively. This paper included scenarios for core meltdown and corium transfer to the lower head, corium behavior in the lower RPV head, vessel failure, risk of steam explosion, corium-concrete interaction and coolability, corium spreading and accumulation, corium ceramic interaction, and long term corium stabilisation. GAREC concludes that coolability during MCCI by surface flooding is difficult to be demonstrated with the present knowledge. But better understanding and modeling of the behavior of the corium melt in the freezing range would predict rather low viscosity of the residual melt instead of formation of a mushy zone. This would enhance melt ejection and thus improve corium coolability. - The main uncertainties for the EPR corium cooling concept are seen in the melt-through of the gate and the effects of late water injection.

Experimental and theoretical analysis on natural circulation and boiling induced convection related to the debris cooling after the corium is spread over the melt catcher have been conducted at FZK. It is shown that the decay heat can be removed from the flooded core by heat exchangers in the sump of the containment. Special attention is given to flow instabilities in the two-phase flow regime in the boiling induced mixed convection loop. The instabilities are caused by the transition from bubbly to slug flow by flashing phenomena. Stable and oscillating flow conditions were observed depending on the degree of subcooling of the coolant water, and a stability diagram correlates the occurrence of instabilities with the operational characteristics of the cooling loop. Analytical models consisting of six equations of the two-fluid model with the interfacial terms are expected to be validated against full height simulation in the SUCOT test facility .

Main conceptual features of the EPR melt retention concept and the designed countermeasures to several problems were well summarized by 3 papers of Siemens-KWU. The retention concept focuses on the temporary retention of the corium melt in the reactor pit to make corium recovery independent of various scenarios, the fast release of the corium to the spreading compartment, and the cooling by surface flooding. This EPR concept has triggered much of the research which was discussed throughout the meeting. To achieve the required melt stabi-

lization and cooling, the following features are described and their role for the cooling process is explained: sacrificial concrete layer and melt plug in the reactor pit, transfer channel to the spreading room, spreading room with an initially dry sacrificial concrete layer. After complete spreading of the melt and erosion of the upper concrete layer, a sacrificial steel layer would be melted which safely separates the potentially aggressive oxidic corium melt from the zirconia layer underneath. The water cooling system under the zirconia layer would be activated after melt spreading, flood the surface of the corium melt, and keep the ZrO_2 refractory layer at low temperatures, so that no thermochemical attack of the refractory layer is expected. The EPR melt stabilization concept was subject to various licensing discussions, and after some recent conceptual improvements, is considered by the industry as a sound technical solution with reasonable costs.

EX-VESSEL DEBRIS COOLABILITY
Reactor requirements and implications

OECD Workshop- November 1999

FZK - Karlsruhe

C. Lecomte
Institut de Protection et de Sûreté Nucléaire (IPSN)
F-92265 Fontenay-aux-Roses CEDEX, Fance

GENERAL SAFETY REQUIREMENTS

- **defence in-depth concept**
  - **prevention of incidents and accidents**
    - **» design, operation, maintenance**
  - **mitigation of accident consequences**
- **Design basis accidents => characteristics of safety systems**
  - **TODAY :**
    - **» LOCA, RIA**
  - **TOMORROW :**
    - **» Low pressure core-melt accident**
- **Accident management (*AM*) measures**

OBJECTIVES OF SEVERE ACCIDENTS MANAGEMENT

- TO RESTORE CONTROL OF THE SITUATION
  - **for workers and public protection**
  - **thresholds ? ? when and where ??**
- TO DELAY CORE-MELTING AND/OR CONTAINMENT FAILURE
  - **more time to implement counter-measures**
- TO MITIGATE THE CONSEQUENCES OF THE ACCIDENT
  - **radiological consequences**
  - **short, medium, long term**
- TO OPTIMISE CRISIS MANAGEMENT
  - **on-site/off-site decisions**

SEVERE ACCIDENT MANAGEMENT IN PRESENT AND FUTURE REACTORS

- TODAY :
  - **complementary procedures**
  - **non-conventional use of existing devices**
  - **limited complementary technical means**
  - **best-estimate assessment of the efficiency of these measures**
- TOMORROW :
  - **FUTURE REACTORS : evolutionary design**
  - **the design includes mitigation features for severe accidents involving vessel melt-through**

C. LECOMTE - 13/11/1999

THE EUROPEAN PRESSURISED REACTOR (EPR)

- ELIMINATION OF SITUATIONS LEADING TO EARLY CONTAINMENT FAILURE, RESULTING IN LARGE EARLY RELEASES :
  - **containment bypass**
  - **reactivity accidents**
  - **high pressure core-melt situations**
  - **energetic steam explosions, hydrogen detonations**
- LOW PRESSURE CORE-MELTDOWN : IN THE DESIGN
  - **radiological consequences : to be limited in space and time**
    - **» control of core-melt progression**
    - **» control of containment leaktightness**
    - **» control of fission products behaviour**

SEVERE ACCIDENTS PREVENTION AND MITIGATION

OBJECTIVE of FUTURE EVOLUTIONARY REACTORS

➽ IMPROVED PREVENTION

&

➽ IMPROVED MITIGATION

- **» core degradation**
- **» fission products**
- **» containment**

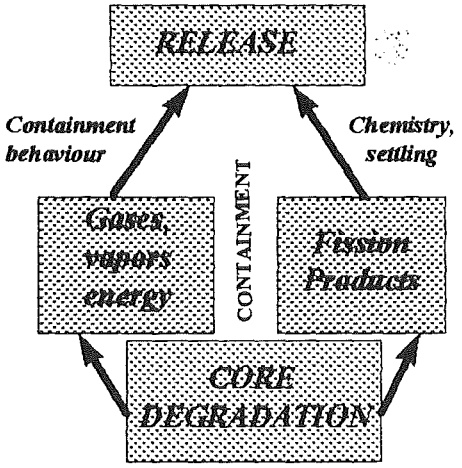

SEVERE ACCIDENTS RELATED RESEARCH

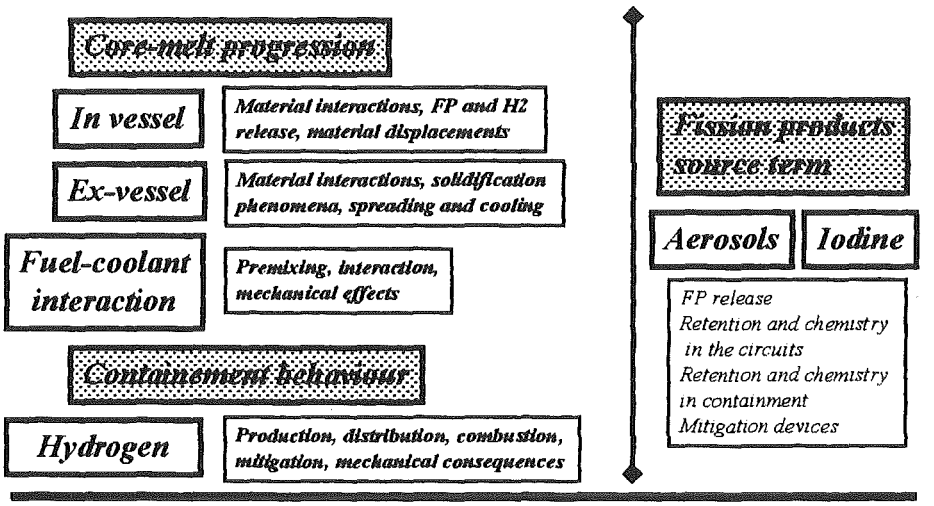

CORE DEGRADATION

➠ **THE CONTROL OF CORE DEGRADATION IS A KEY FACTOR TO CONTROL SEVERE ACCIDENTS CONSEQUENCES**

- **In-vessel core cooling**
- **Corium in the reactor pit**
- **Ex-vessel corium cooling**

POTENTIAL AM-MEASURES : Core-melt progression

- **In-vessel core-melt progression**
  - water injection inside the vessel
  - flooding the reactor pit
- **Ex-vessel core-melt behaviour**
  - spreading
  - fragmentation
    - » water injection, specific core-catcher geometries

➠ NECESSITY TO ASSESS IN EACH CASE :

- feasability
- efficiency
- potentially associated risks

➠ R&D needs

SAFETY QUESTIONS ASSOCIATED TO CORE COOLING POSSIBILITIES

- **WATER INJECTION INSIDE THE VESSEL**
  - feasability depends on the delay to restore a failed system (present reactors), or on the available systems (future)
  - efficiency is questionable (R&D focused on early degradation phase)
  - risks : H2 and FP release, FCI, thermomechanical constraints
  - no instrumentation on core status (i.e. no operator guidance)
- **FLOODING THE REACTOR PIT**
  - feasability is plant dependent (geometry, insulator)
  - efficiency : questionable for large size vessel or late flooding
  - associated risk : FCI
  - may happen in a uncontrolled way in existing plants

SAFETY QUESTIONS ASSOCIATED TO CORE COOLING POSSIBILITIES (2)

- EX-VESSEL CORIUM COOLING
  - PHENOMENA INVOLVED :
    - » corium discharge in the containment
    - » jet and erosion phenomena in the reactor pit
    - » spreading
    - » cooling by water (top or bottom contact)
    - » debris and crust formation
    - » interaction with substrate
    - » hydrogen generation
    - » fission products release

SAFETY QUESTIONS ASSOCIATED TO CORE COOLING POSSIBILITIES (3)

- SAFETY CRITERIA
  - » prevent penetration of the containment basemat by corium, in order to avoid contamination of ground water and sub-soil
  - » leaktightness with regard to contaminated sump water

- SOME CHOICES TO BE DONE FOR *AM* EITHER IN EXISTING REACTORS, EITHER FOR FUTURE REACTORS
  - priority to in-vessel vs ex-vessel cooling
  - reactor pit flooding or not
  - spreading on a large area vs dedicated core catchers
  - flooding the spreading area or not ; when ?
  - active vs passive systems ?

NECESSARY KNOWLEDGE

- **Improvement of physico-chemical knowledge**
  - spreading
  - FCI in stratified conditions
  - fragmentation mecanisms
    - » pools and shallow layers
  - heat removal capabilities and transfert to containment
  - crust formation and consequences
  - thermochemical aspects, segregation
  - long term modelling of corium-substrate interaction
  - long term thermo-mechanical behaviour
  - scaling aspects

NECESSARY KNOWLEDGE (2)

- **Improvement of models and codes**
  - mechanistic and best-estimate tools
  - integrated tools :
    - » physical models, systems behaviour
- **Necessity to study more representative situations**
  - more comprehensive initial conditions
    - » chemical composition of the corium, viscosity, solid fraction
  - complex accident scenarios
    - » successive corium discharge events, local effects
    - » understanding, repairing, management modes
  - other consequences : steam, heat, H2, FP to the containment
  - uncertainty and probabilistic studies

PERSPECTIVES

■ ON GOING RESEARCH WILL HELP TO :

- **optimise design (conceptors)**
- **contribute to safety assessment (safety organisations)**
- **validate Accident Management procedures**
- **develop guidelines to operators**
- **provide knowledge useful for on-line accident assessment**

➽ IMPORTANCE OF REVIEWING AVAILABLE KNOWLEDGE AND COMPLEMENTARY NEEDS

Session A:

SPECIAL MODES OF CORIUM DISCHARGE INTO THE CONTAINMENT

Chairman: S. Basu

OECD Workshop on Ex-Vessel Debris Coolability
Karlsruhe, Germany, 15-18 November 1999

Organised in collaboration with
Forschungszentrum Karlsruhe (FZK) GmbH

EXPERIMENTS TO INVESTIGATE THE LOW PRESSURE CORIUM DISPERSION IN EPR GEOMETRY

L. Meyer
Forschungszentrum Karlsruhe GmbH
Postfach 3640, 76021 Karlsruhe, Germany
meyer@iket.fzk.de

ABSTRACT

Experiments are being performed in a scaled annular cavity design, typical for the European Pressurized Reactor (EPR), to investigate melt dispersal from the reactor cavity when the reactor pressure vessel lower head fails at low system pressure of less than 20 bar. In the first part of the experimental program the fluid dynamics of the dispersion process are studied using simulant materials, water or bismuth alloy instead of corium, and nitrogen or helium instead of steam. The effects of different breach sizes and locations and different failure pressures on the dispersion are studied systematically. For central holes in the lower head, the dispersal rates can be correlated by a Kutateladze number based on the velocity in the annular space of the cavity.

1. INTRODUCTION

Concerning the mitigation of high pressure core melt scenarios, the design objective for future European PWRs is to transfer high pressure core melt to low pressure core melt sequences, by means of pressure relief valves at the primary circuit, with such a discharge capacity to limit the pressure in the reactor coolant system (RCS) to lower than 20 bar, at the moment of the reactor pressure vessel rupture. A failure in the bottom head of the reactor pressure vessel (RPV), followed by melt expulsion and blowdown of the RCS, might disperse molten core debris out of the reactor pit, with higher pressures at vessel failure leading to larger fractions of dispersed material. The mechanisms of efficient debris-to-gas heat transfer, exothermic metal/oxygen reactions, and hydrogen combustion may cause a rapid increase in pressure and temperature in the reactor containment and are collectively referred to as direct containment heating (DCH). Apart from the loads on the containment building due to DCH, the ejection of a considerable amount of melt debris out of the reactor cavity by itself is a problem, because the melt collecting and cooling concept of future PWRs would be rendered useless.

A large amount of work has been done to investigate the melt dispersal/DCH-phenomena for cavity designs with large instrument tunnels leading into subcompartments (Nucl. Eng. Des. 1996). Only a few experiments have been done with an annular cavity design (Blanchat, et al.,1997; Bertodano, et al.1996). Some European PWRs and the planned European Pressurized Reactor (EPR) have an annular cavity design where the only large pathway out of the cavity is the narrow annular gap between the RPV and the cavity wall (Fig.1). The past experiments focused on relatively small holes at the center of the lower head

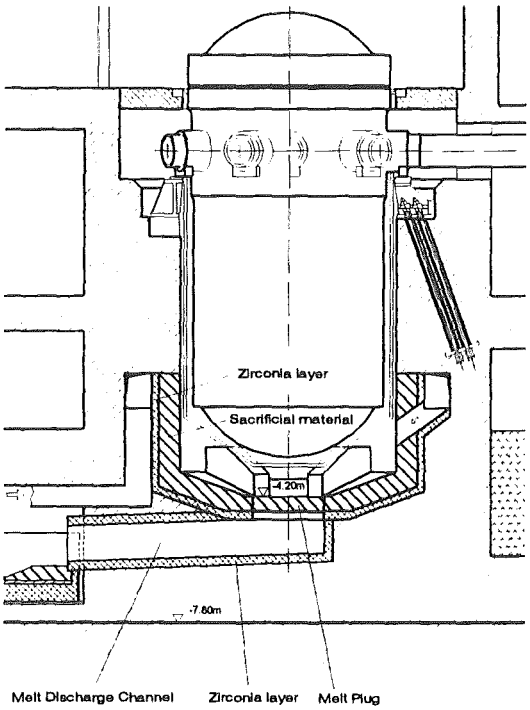

Fig. 1 The Reactor pressure vessel and cavity planned for the EPR

and high failure pressures. Our investigations have been extended to low failure pressures and larger breach sizes with a cavity design similar to the planned EPR cavity. Also, lateral breaches are being investigated.

Recently two experiments were performed at the Sandia National Laboratories (SNL) in cooperation with Forschungszentrum Karlsruhe (FZK), Institut de Protection et de Surete Nucleaire (IPSN) and the U.S. Nuclear Regulatory Commission (NRC) (Blanchat, et al., 1999). These tests were performed with thermite melt, steam and a prototypic atmosphere in the containment in a scale 1:10. For the first time, a test with a large break at low pressure was conducted. The initial pressure in the RPV-model was 11 and 15 bars, and the breach was a hole at the center of the lower head with a scaled diameter of 100 cm and 40 cm, respectively. The main results were: 78% of melt mass were ejected out of the cavity with the large hole and 21% with the small hole; the maximum pressures in the model containment were 6 bar and 4 bar, respectively.

At FZK the test facility DISCO-C has been built for performing dispersion experiments with cold simulant materials in an EPR-typical geometry in a scale 1:18. Subsequently, selected experiments in a DISCO-H facility in the same scale will be performed with thermite melt, steam and a prototypic atmosphere in the containment. The ultimate objective of the experiments is to find an upper bound of RCS pressures resulting in a minimum of melt dispersed out of the cavity in an optimized cavity geometry.

2. THE TEST FACILITY DISCO-C

A scheme of the test facility DISCO-C is shown in figure 2. There are two potential flow paths out of the test cavity. A path straight up into the refueling canal is expected not to exist in the final EPR design. The main flow path is the free flow area around the 8 main

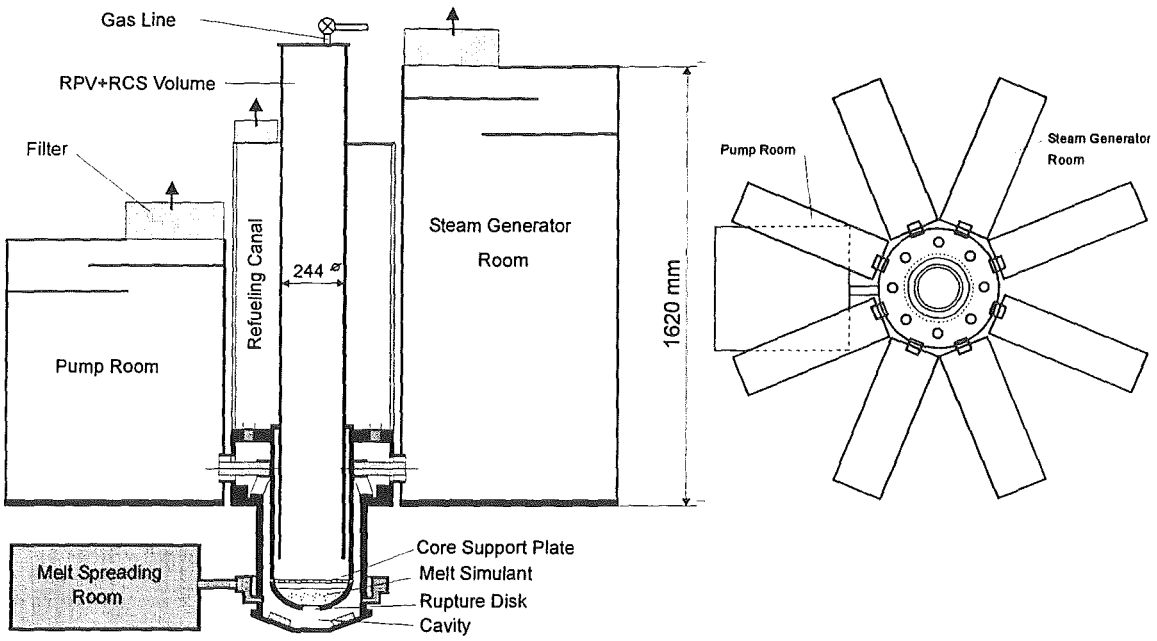

Fig. 2 Scheme of the DISCO-C-test facility

coolant lines into the pump and steam generator rooms with a total flow area of about 10 m². However, there is a flow constriction below the nozzles at the RPV support structure with an minimum flow area of only 6 m² in the present design. The other way out of the reactor pit will be through four ventilation openings in the lower part of the cavity (total flow area 1.5 m²) leading to the spreading compartment via an annular channel around the pit, and a connecting channel. This second path was closed in the first experimental series presented here. The pump and steam generator rooms are open to the dome in the prototype and open to the atmosphere in the experiment, only covered by filters for the extraction of fog or droplets. The compartments are volumetrically scaled and contain some baffles (pump room 0.131 m³, steam generator room 0.3 m³).

The dimensions of the cavity and the RPV are shown in Fig. 3. The total volume of the pressure vessel is 0.08538 m³ (scaled 498 m³), simulating the volume of both the RPV and part of the RCS. A disk holding 8 pipes (44 mm I.D., 250 mm length) separates the two partial volumes in a ratio 60:40 (RCS:RPV).

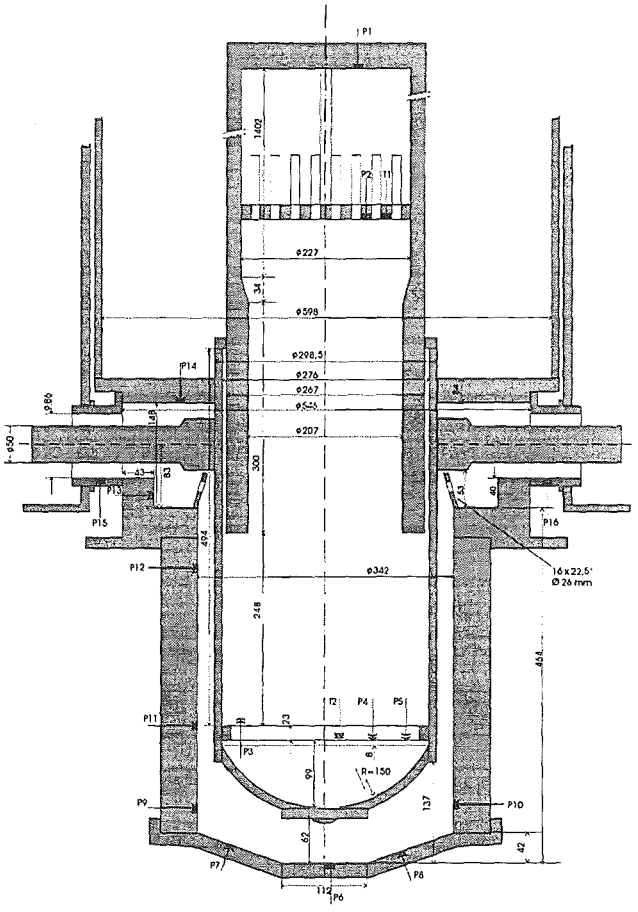

Fig. 3 The configuration of the pressure vessel with a rupture disk at the lower head (dimension in mm).

The fluids employed are water (ρ = 1000 kgm^{-3}, σ = 0.072 N/m) or a bismuth alloy (Bi-Pb-Sn-In-alloy, MCP-58®, ρ = 9230 kgm^{-3}, T_{melt} = 60°C, σ = 0.35 N/m), similar to Wood's metal) instead of corium, and nitrogen or helium instead of steam. The RPV lower head can hold 3.4×10^{-3} m^3 of liquid (liquid height in the hemisphere is 96 mm). This corresponds to 20 m^3 or 160 t of corium. The holes in all tests, except for test R-01, were at the center of the hemisphere. They were closed by a rupture disk, that had an opening diameter larger than the hole diameter. The pressure vessel was filled with gas to a pressure slightly lower than the failure pressure of the rupture disk. A small auxiliary pressure vessel, filled to a somewhat higher pressure was connected to the main pressure vessel. By opening a valve electro-pneumatically the pressure in the main vessel increased up to the failing pressure of the rupture disk and the blow down started. A break wire at the hole gave the signal for closing the valve again and for the time mark t = 0.

Table 1 Parameters and dispersed liquid fractions in DISCO-C experiments

						Liquid fraction found in				
Test	Gas	Liquid water/ metal 10^{-3} m^3	Hole Diam. (mm)	Burst Pressure abs. (MPa)	Blow through t_b (s)	Compart-ments f_d	Cavity bottom	RPV support	Cavity total f_c	RPV
D-11	N_2	3.4 w	15	0.643	0.688	0.161	0.583	0.256	0.839	0
D-10	N_2	3.4 w	15	1.141	0.419	0.382	0.387	0.231	0.618	0
D-15	N_2	3.4 w	25	0.348	0.359	0.193	0.537	0.270	0.807	0
D-07	N_2	3.4 w	25	0.620	0.106	0.518	0.224	0.258	0.482	0
D-04	N_2	3.4 w	25	1.190	0.047	0.698	0.056	0.245	0.302	0
D-13	N_2	3.4 w	50	0.353	0.032	0.551	0.212	0.237	0.449	0
D-06	N_2	3.4 w	50	0.619	0.024	0.669	0.061	0.270	0.331	0
D-05	N_2	3.4 w	50	1.200	0.018	0.759	0.012	0.229	0.241	0
D-14	N_2	3.4 w	100	0.351	0.012	0.580	0.136	0.284	0.420	0
D-08	N_2	3.4 w	100	0.613	0.013	0.717	0.052	0.231	0.283	0
D-09	N_2	3.4 w	100	1.137	-	0.741	0.021	0.239	0.259	0
D-12	N_2	3.4 w	18	0.270	-	0.000	0.950	0.050	1.000	0
H-02	He	3.4 w	25	0.388	0.335	0.123	0.621	0.256	0.877	0
H-01	He	3.4 w	25	0.641	0.104	0.350	0.399	0.252	0.651	0
H-03	He	3.4 w	25	1.156	0.065	0.616	0.123	0.261	0.384	0
R-01	N_2	1.8 w	25[#]	0.611	-	0.029	0.423	0.185	0.608	0.363
D-17	N_2	1.8 w	25	0.612	0.033	0.407	0.123	0.470	0.593	0
M-01	N_2	3.1 m	25	1.045	0.515	0.358	0.428	0.215	0.643	0
M-02	N_2	3.0 m	25	0.595	0.790	0.060	0.862	0.077[*]	0.940	0.001
M-03	N_2	3.0 m	50	0.582	0.090	0.379	0.495	0.125[*]	0.620	0.001

[*]Space behind conical ring at the support girder was filled with 0.6×10^{-3} m^3 silicon rubber up to the lower edge of the holes, so all liquid could flow back into the lower cavity, except a thin film and the frozen material at the walls.

[#] horizontal rip, 40 × 12.5 mm

3. EXPERIMENTAL RESULTS

3.1 Dispersal rates

The initial conditions of the experiments are given in table 1 together with the liquid fractions found in the compartments and the cavity after the tests. If liquid reaches the RPV support girder, approximately 0.8×10^{-3} m^3 are deposited there; 0.6×10^{-3} m^3 are kept behind a conical ring (s. Fig.3), that prevents the liquid to flow back into the lower pit. The rest stays on the horizontal surfaces in this area. Fig.4 shows the data as function of the initial pressure. For comparison, data are shown from experiments performed at Brookhaven National Laboratory (BNL) for a Westinghouse cavity design (Surry) with a large instrument tunnel (Tutu et al., 1990). These data seem to change more sharply at a threshold from low to high dispersal rates than in our case. However, for larger holes (>50 mm, >0.90 m scaled) there must be a sharp drop at very low pressure differences (0.1 – 0.2 MPa). The effect of a different driving gas (He versus N_2) is similar as found before, e.g. at BNL. The higher sound velocity of helium leads to a faster blow down, but the lower density (app. $^1/_7$ of N_2) causes less entrainment, with the net result of a lower dispersal.

One special test was run with a horizontal rip at the side of the lower head (R-01). The slot was app. 40 mm × 12.5 mm, having a 25-mm-hole equivalent flow area. The lower and the upper edge of the slot were 55 mm and 64 mm above the bottom of the lower head, respectively. The liquid volume used was only 1.8 10^{-3} m^3, and the liquid surface was at 67 mm above the bottom. In this test very little liquid was dispersed into the compartments. The small mass that was dispersed was found in the compartments on the opposite side of the break. A considerable amount of liquid remained in the lower head of the RPV. The liquid level of this rest water was at 39 mm above the bottom, or 16 mm below the lower edge of the rip opening. A comparison test (D-17) with the same amount of liquid but a center hole of 25 mm diameter gave similar results as the test with the large liquid mass (D-07). The somewhat smaller mass fraction in the compartments (0.4073 versus 0.5177) is due to the much larger (relative) mass fraction at the RPV support in D-17, but with almost identical absolute masses at the support in both tests.

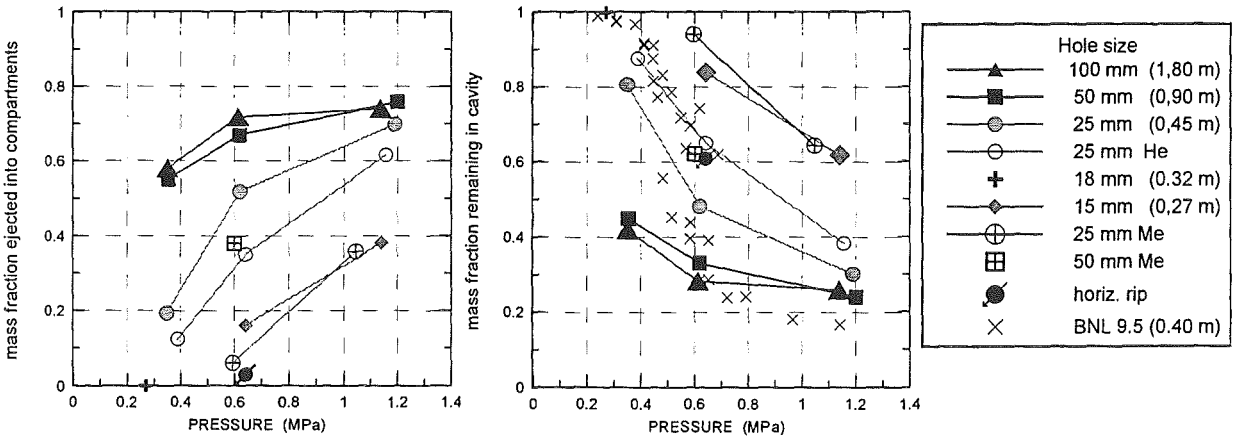

Fig. 4 Liquid mass fractions as function of the failure pressure of the rupture disk

3.2 Blow down histories

The duration of the blow down process is inversely proportional to the flow area of the hole (Fig.5). According to scaling laws it is also proportional to the length scale, so the blow down times for the reactor would be between 3 s and 120 s with hole sizes between 1.8 m and 0.27 m diameter. However, with steam and thermal effects these times would be different. Scaling laws predict a blow down time dependency on the initial pressure as $t \sim \ln (p_0/p)$ (Jacobs et al.,1997). The experiments show that the pressure effect is smaller than that. The reason is the presence of the liquid. A pure gas blow down has an entirely different trend with a steeper gradient in the beginning (Fig. 6).

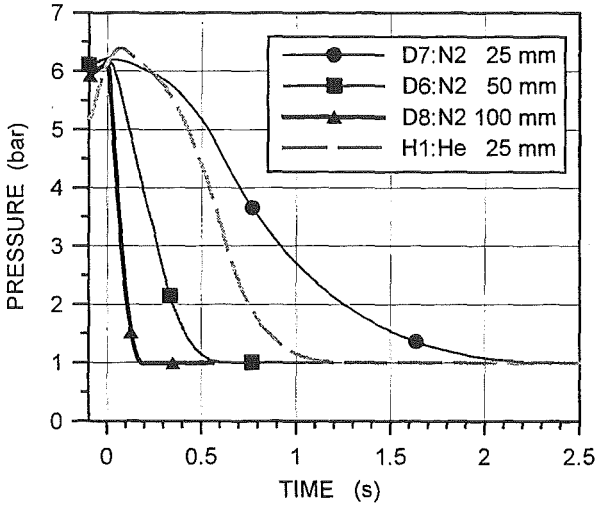

Fig. 5 Pressure histories for different hole sizes

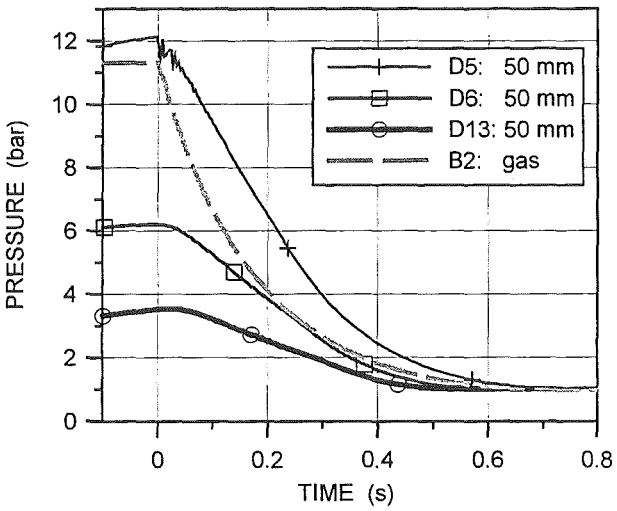

Fig. 6 Pressure histories for different initial pressures

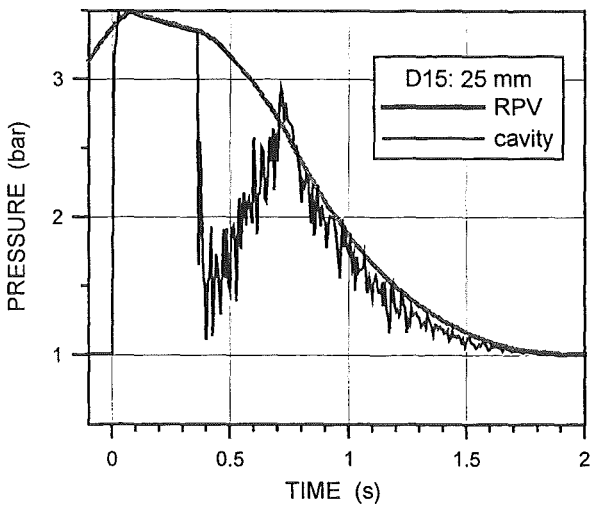

(a)

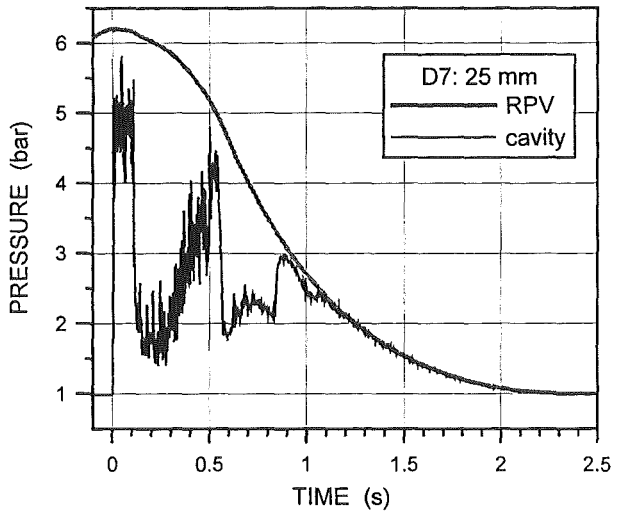

(b)

Fig.7 RPV static pressure and total pressure on the cavity floor below the hole

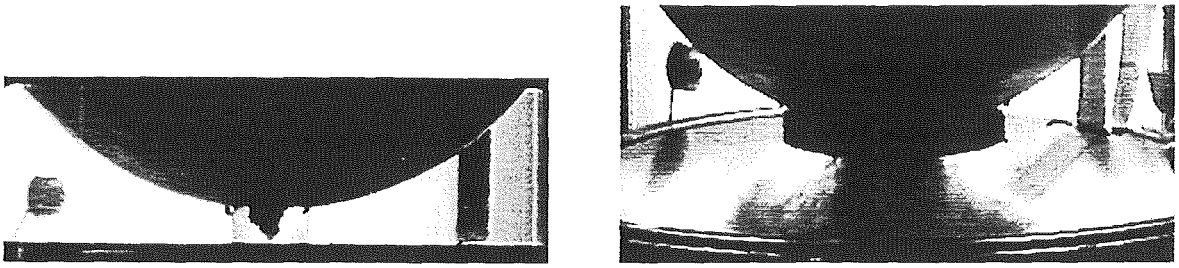

(a) (b)

Fig. 8 Water jet, (a) without fragmentation, hole was closed with a thin foil and pressure was increased with a shock, (b) with fragmentation, hole closed by a rupture disk.

Fig.7.a shows the pressure in the RPV together with the pressure (P6) measured on the cavity floor directly below the hole. The rupture disk opens at t=0 s, but the pressure still increases because the valve between the auxiliary pressure vessel and the main vessel closes not before t=0.07 s. Up to app. t=0.4 s the pressure falls only slightly. The pressure signal from P6 is identical to the RPV pressure signal up to t_b=0.362 s. This indicates that there is a single-phase liquid flow with the velocity of $u_L = (2\ \Delta p/\rho_L)^{1/2}$. At t_b=0.362 s a blow-through occurs and there is a two-phase flow up to app. t=0.78 s. From that point on there is a single-phase gas flow, probably with very small droplets, and again the pressure signal P6 gives the total pressure with $p_{dyn}=\rho_G/2\ u_G^2$. Similar signals could be observed in all tests, but in most cases the dynamic pressure in the initial liquid flow phase did not reach quite the RPV pressure (Fig.7.b); probably because of the fragmentation of the jet (Fig.8 b). The blow through times t_b are listed in table 1. More information on t_b can be found in Meyer, et al., (1999).

3.3 Analysis of the results

With the information of the pressure and the temperature in the RPV and in the cavity, and the flow cross section of the annular space around the RPV, a mean gas velocity in the annulus, u_G, can be determined. Fig.9 shows the RPV pressure and the static pressure in the cavity. Because of the choked flow at the reduced flow area below the nozzles we see a pressure peak in the cavity in experiments with large holes. This sets an upper limit to the velocities in the annulus. Fig.10 shows some typical velocity histories which were determined assuming that the whole annular cross section is available for the gas flow. Of course, this is not the case, because the liquid fills up part of the cross section. Also the velocity distribution will not be uniform. Thus, these velocities represent a lower bound. Local velocity measurements are going to be done, in order to determine the upper limit of the velocities in the annulus.

In Fig.11 we see a coarse correlation between the dispersed fraction and the maximum gas velocity in the annulus, u_G, relatively independent of the hole size. Considering the above mentioned uncertainties in the determination of the velocity, it is surprising to find such a simple relation. The tests with helium and the tests with Wood's metal lie outside this band.

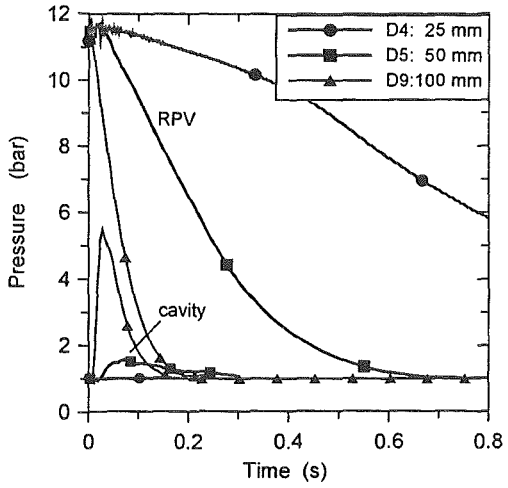

Fig. 9 Pressure in the RPV and cavity

There is no single correlation between the exit velocity of the liquid and the dispersed fraction. However, the nitrogen and helium tests collapse on one curve, if they are correlated by $\rho_G u_G^2$, and also the liquid metal tests can be joined into one curve if the dispersed mass fractions are correlated by the Kutateladze number, $Ku = \rho_G u_G^2/(\rho_L\ g\ \sigma)^{1/2}$ (Fig.12). If the threshold for droplet levitation up the annulus was applied according to the Kutateladze criterion $Ku > 14$, the velocity limit for N_2/water would be 18 m/s, and for both, He/water and N_2/Wood's metal systems it would be 47 m/s. The results, however, show no sharp threshold and dispersal occurs also at lower velocities. The above correlation should not be overrated. It is a preliminary result and does not reflect the complexity of the blow down and dispersion processes. Taking the maximum gas velocity as a correlation parameter does not seem to take account of the several stages of the blow out, the single-liquid stage, the two-phase stage and the single gas phase.

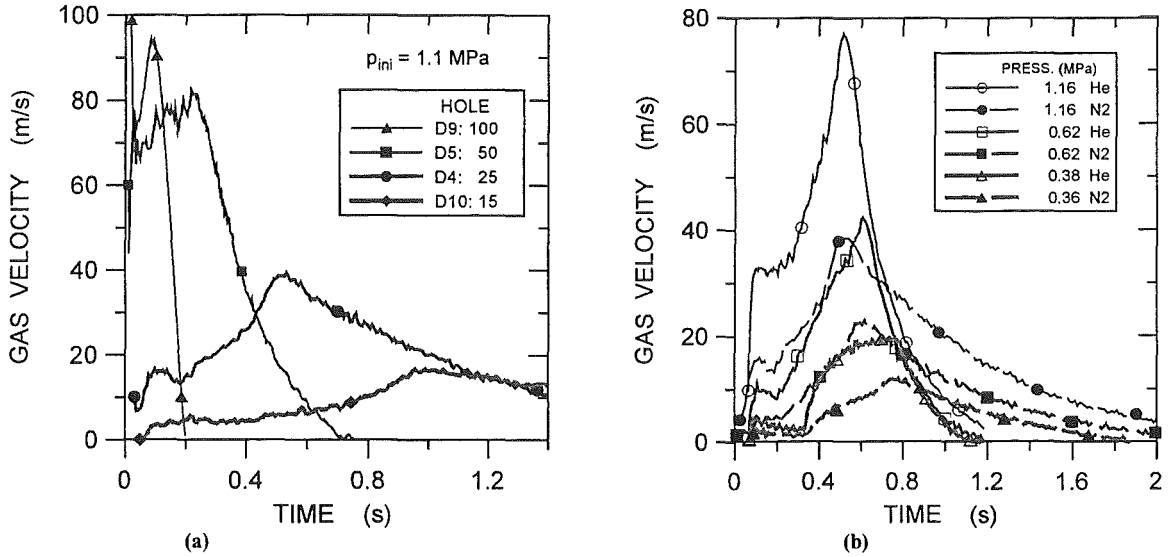

Fig. 10 Gas velocities in the annular space in the cavity; (a) at the same initial pressure with different hole sizes, (b) with an identical hole size of 25 mm, with different pressures and gases.

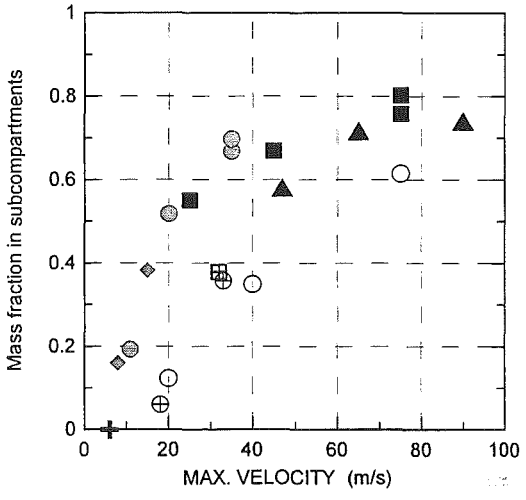

Fig. 11 Dispersed fraction f_d versus the maximum gas velocity in the annular space

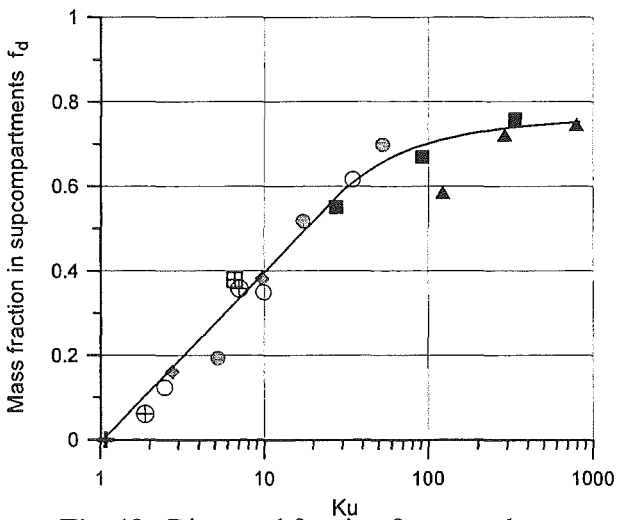

Fig. 12 Dispersed fraction f_d versus the Kutateladze-number (symbols see Fig. 4)

In the experiment the parameter $\rho_G u_G^2$ is smaller for helium than for nitrogen, which makes the f_d-data collapse on one line for both driving gases. If we assume sound velocity at the hole, $\rho_G u_G^2$ becomes proportional to κp_0. This expression is larger for helium (κ=1.667) than for nitrogen (κ=1.4). Obviously, the velocity in the experiment is smaller than theoretically possible, and more so for helium than for nitrogen. The ratio of the experimental velocities for helium and nitrogen is about 2, while the ratio of the sound velocities is 3. The reason for that difference must be the presence of the liquid phase as noted above (Fig.6).

If the gas velocity in the annulus were the governing parameter for melt dispersal, a reduction of this velocity could reduce the dispersion. Before a conclusion can be drawn for the optimum cavity design, more and special experiments are necessary, especially with lateral rips in the lower head.

4. CONCLUSIONS

A first series of 20 experiments has been performed in the DISCO-C facility with a 1/18-scale model of an EPR-typical reactor pit with simulant materials. Hole diameters between 15 mm and 100 mm (0.27 m and 1.80 m scaled) and initial pressures between 0.35 and 1.16 MPa were employed. With large holes and 1 MPa initial pressure, practically all liquid (water) was ejected out of the lower pit, however, approximately 25 % was caught in the space at the RPV support. The results of all experiments with central holes in the lower head, regarding the dispersed fractions, with material combinations nitrogen/water, helium/water and nitrogen/Wood's metal, can be correlated as a function of the Kutateladze number, $Ku = \rho_G u_G^2 / (\rho_L g \sigma)^{1/2}$, with u_G, the maximum gas velocity in the annular space around the RPV. The threshold pressure for dispersion is less pronounced in the annular cavity geometry than in cavities with a chute. The experiment with a lateral rip in the lower head showed much smaller dispersal rates than with central holes. More experiments with such a geometry will be performed.

AKNOWLEDGMENTS

This work was funded in part by the German VdEW and Siemens under the contract for the Collaboration in Research and Development for the Investigation of the Events in Severe Accidents in LWRs. The work of the team in the IKET, that performed the experiments, is gratefully acknowledged.

REFERENCES

Bertodano, M. L. de, A. Becker, A. Sharon, R. Schnider, 1996. DCH Dispersal and entrainment experiment in a scaled annular cavity, Nucl. Eng. Des.,**164,** 271-285.

Blanchat, T.K., M. Pilch, and M.D. Allen, 1997. Experiments to Investigate Direct Containment Heating Phenomena with Scaled Models of the Calvert Cliffs Nuclear Power Plant, NUREG/CR-6469, SAND96-2289, Sandia National Laboratories, Albuquerque, N.M.

Blanchat, T.K., M.M. Pilch, R.Y. Lee, L. Meyer, and M. Petit, 1999. Direct Containment Heating Experiments at Lower Reactor Coolant System Pressure in the Surtsey Test Facility, NUREG/CR-5746, SAND99-1634, Sandia National Laboratories, Albuquerque, N.M.

Jacobs, G., L. Meyer, 1997. Planned melt dispersal experiments in a scaled cavity, SMiRT 14 Post-Conference Seminar on Containment of Nuclear Reactors, CEA Sacley, France, August 25-26.

Meyer, L., G. Jacobs, D. Wilhelm, M. Gargallo, T. K. Blanchat, 1999. Experiments on Corium Dispersion after Lower Head Failure at Moderate Pressure, SMiRT 14, Post Conf. Seminar on Containment of Nuclear Reactors, Seoul, Korea, August 23-24.

Nucl. Eng. Des., **164,** 1996 (Topical Issue on DCH).

OECD Workshop on Ex-Vessel Debris Coolability
Karlsruhe, Germany, 15-18 November 1999

Organised in collaboration with
Forschungszentrum Karlsruhe (FZK) GmbH

TRANSIENT CODE MODELS FOR LOW PRESSURE CORIUM DISPERSION

D. Wilhelm
Forschungszentrum Karlsruhe GmbH
Postfach 3640, D-76021 Karlsruhe, Germany
wilhelm@iket.fzk.de

ABSTRACT

If the reactor pressure vessel of a pressurized water reactor fails, corium may be dispersed into the volumes below. The ejected corium may be subjected to chemical reactions. If pressures and breaches are large enough, the corium may be further transported into adjacent volumes without directly flowing into the core catcher. The dispersion is influenced by entrapment and entrainment of corium at the adjacent walls.

The objective of the present work is to model the associated physical phenomena with a computer code that combines mechanistic and parametric models. This is a way to take advantage of existing lumped-parameter models for system codes and of the details of a multicomponent transient fluid dynamics code. The result is a fast running code in r-z-geometry with three velocity fields and two distinct oxidization processes. Entrapment and entrainment models have been added to calculate the development of liquid corium films at the walls outside of the pressure vessel.

The code has been tested on recalculations of the SANDIA thermite and DISCO water and metal experiments which were designed to answer questions of low pressure corium dispersion (Meyer, 1999). Details of the models and the flow at the breach will be presented.

1. INTRODUCTION

If molten corium collected on the lower head of the reactor pressure vessel (RPV) causes the vessel to fail while there is still overpressure left in the reactor coolant system, the melt may be ejected in such a way that parts of it travel up in direction of the dome of the reactor containment. The melt flows through the breach, it is dispersed, a part of it may collect as a film on the adjacent walls, and parts of the film may be re-entrained into the main stream. The gas-vapor mixture blowing out of the breach oxidizes the metal components of corium. The reaction is exothermal and produces hydrogen which may burn downstream when mixing with oxygen of the containment atmosphere.

The experimental data are abundant enough to start testing theoretical models which are needed to assess conditions on prototypic scale. Besides the generally used lumped parameter models, see (Washington, 1995), the present method takes advantages of the proven technology of a multiphase code and adds specific dispersion models to it. The two theoretical approaches are used in parallel and offer to mutually influence each other. While the lumped parameter approach is justified by the lack of rigorously mechanistic models, a

multiphase code has the advantage to resolve the geometry in greater detail. For example, local velocities may have a substantial influence on how the corium is being dispersed which demands for a model that resolves major flow paths. As the code geometry approaches that of the experiment, code results can be compared to local measurements and physical details can be obtained in order to understand relationships. The code has therefore been run in parallel to the analysis of experimental results. With a detailed enough geometry, a scale-up to prototypic conditions may ultimately be possible.

2. THE TRANSIENT FLUID DYNAMICS CODE

The multiphase code chosen is AFDM (Advanced Fluid Dynamics Model, (Bohl, 1992)) which has two dimensions and three velocity fields. This allows to track water, molten corium, and a gas-vapor mixture. The code describes a multitude of energy fields and has a transient model of interfacial areas between all energy fields. The numerical solution method with its predictor-corrector method allows to add explicit models.

The AFDM cells are defined in order to model transient fluid flow on a few seconds time scale. The explicit dispersion models are superposed to the r-z-geometry of the Eulerian cell set of AFDM. There is no intention to resolve the velocity and mass concentration profiles expected in the given geometry. This would require cells of only millimeter size, and lead to inoperable cell numbers. Instead, there are only several hundred AFDM cells. This number is subject to change, especially because it governs numerical diffusion and smearing of distinct interfaces. However, it is large enough to model the main features of the given geometry which is expected to play a major role in the dispersion process.

3. THE DISPERSION MODELS

By using predefined volumes consisting of clusters of Eulerian cells of AFDM, any lumped parameter model can be imported from system codes. While AFDM distinguishes only melt, water, steam, melt vapor, and noncondensable gas, the volumes of clusters need two different kinds of melt, oxide and metal, and three different kinds of noncondensable gas, nitrogen, oxygen, and hydrogen. These new components are only recognized by the added models. AFDM receives information about the mixture of these gases and the exothermal heat. Table I shows the components of both codes sections

Table I

AFDM standard code	Velocity field	Added model
structure	-	-
melt	1	Oxide melt
Melt particles	1	Metal melt
water	2	-
Melt vapor	3	Steam
Steam	3	Nitrogen
Noncondensable gas	3	Oxygen
	3	hydrogen

There are two model sections added, the first is for the chemical reactions, and the second for the hydrodynamics in the vicinity of liquid corium films at the walls outside of the reactor pressure vessel (RPV).

For the first model section, substantial work has already been performed to describe the oxidization of melt and the combustion of hydrogen (Washington, 1995). There are two volumes of cell clusters which allows to use correlations of the two-volume equilibrium model (Pilch, 1994).

For the first model section, the volume is limited to the cavity, directly adjacent to the RPV, and the flow paths to the reactor dome. In this volume, most of the oxidization of metallic corium takes place. The second is the volume where the generated hydrogen may burn if the combustion conditions are met. The corium oxidization is supposed to be diffusion limited. This allows to introduce the necessary rate of oxidization for calculating the transient heat generation of AFDM. The combustion is supposed to be advection limited, i.e. it depends on the mass flow of hydrogen entering the oxygen-rich region of the containment.

While oxidization and combustion are important to assess system pressures and long term behavior for the SNL/Sup experiments, dispersion rates were found to be hardly affected by combustion in the present geometry. This permits to concentrate on one subject each. At present, work has concentrated on entrapment and entrainment models.

For the second model section, the volume of cell clusters is reserved to describe the formation of liquid films at the cavity walls and the entrainment of droplets out of the liquid film. This volume is a part of the cavity volume. A liquid film is defined at sections of the horizontal and vertical cavity wall. The film is supposed to have a negligible velocity. All three velocity fields of the code are already occupied, and a moving film would need a flow-regime dependent subdivision of given computational cells which are limited to use only cell-averaged values. The entrainment model is based on a modified Whalley-Hewitt correlation which depends, among others, on the liquid film thickness, δ, which happens to be an explicit value of the present model.

The entrainment rate, ε, of the modified correlation is

$$\varepsilon = C \cdot A \cdot \frac{\tau \cdot \eta_{gas}}{\sigma_{liq}} \cdot \frac{\rho_{gas}^2}{\rho_{liq}^2} \cdot \exp\left(-5 + 6.8 \tanh\left(6 \frac{\tau \cdot \delta}{\sigma_{liq}} \right) \right)$$

where C is a constant to be adjusted to fit experimental data, A is the film surface area, τ is the shear stress on the gas side of the film surface, η is the dynamic viscosity, and σ is the surface tension. To the original correlation has been added the ratio of the densities of gas and liquid, ρ_{gas}/ρ_{liq}, an addition which was found to be necessary to match water and thermite data at the same time. The exponential function is a tentative fit to a cluster of experimental points published in (Hewitt, 1979).

For the entrapment of droplets on the walls, a simple model of mass transfer rate is used which is proportional to the liquid droplet flow perpendicular to the wall. The entrapment rate is

$$\vartheta = C \cdot A \cdot v_{droplet}^{\perp} \cdot \overline{\rho} \cdot Ku^{-2}$$

where C is a constant, A is the surface area of the wall, $v^{\perp}$ is the velocity perpendicular to the wall, $\overline{\rho}$ is the liquid density per cell volume, and Ku is the Kutateladse

number which is $\rho_{gas} v_{gas}^2 / \sqrt{g\sigma(\rho_{liq} - \rho_{gas})}$ with the standard gravity g. From manipulations with experimental results, see (Meyer, 1999), the Kutateladse number was found to correlate with the fraction of liquid mass ejected out of the cavity if the velocity v_{gas} is the maximum value of the upward annular gas-vapor flow in the cavity. This led to the above formula so that at large Ku, the entrapment is reduced because the droplets are swept away by the gas-vapor flow.

As already criticized by (Williams, 1996), it is questionable whether the entrainment rate is proportional to the liquid viscosity as in the original formulation. Better results have been obtained by using a constant reference viscosity, or by the vapor viscosity as in the formula above. For low pressure corium dispersions, the shear stress may not be well represented by a formula with a two-phase friction multiplier established for annular flow in pipes. A smooth film surface shear stress has given better results.

The flow is highly transient, and the dimensions of the cavity are such that flow profiles cannot develop because of the abrupt changes of flow directions. Therefore, the steady state entrainment formula may not be fully valid. This shows also the need for adjusting the constants C in the entrainment and entrapment equations above. Local and transient measurements of flow and film parameters are difficult which limits the assessment of possible alternatives to standard entrainment models.

4. THE INFLUENCE OF GAS BLOWTHROUGH

Liquid corium is discharged through the breach in the RPV which is, for the present analysis, located at the bottom center. The flow regimes that govern this discharge may have a substantial influence on the way the liquid is subsequently being dispersed. As discussed in (Pilch, 1992), the discharge starts single phase, but may switch to two phase later. During the single phase discharge, the driving RPV gas pressure drives a solid liquid jet out of the hole into the cavity where it is subjected to break-up processes. Parts of the jet form a spray of droplets. Since the distance between the hole and the cavity bottom is small, the jet impacts on the bottom wall and is further dispersed. At a given time of discharge, the pool depth in the RPV becomes small enough to allow the high pressure gas to open a central voided channel in the jet. This may lead to higher escape rates of gas out of the RPV. The liquid is no longer pushed outside, but may also be entrained at the gas-liquid interface. However, the available liquid may not be entrained totally or may be ejected at a smaller rate so that RPV pressures come close to those in the cavity prior to total RPV voiding. This may influence the liquid dispersion from the cavity to the adjacent plena.

The gas blowthrough occurs when the ratio of remaining pool depth, h_b, to the diameter of the hole, d, falls below a threshold value. The report (Pilch, 1992) recommends the formula

$$\frac{h_b}{d} = 0.43 \frac{D}{d} \tanh\left(\sqrt{Fr}\,\frac{d}{D}\right) \qquad \text{where the Froude number is } Fr = \frac{u}{\sqrt{gd}}$$

The critical height, h_b, is large for larger holes, so the present analysis is done on the basis of the DISCO D06 experiment (water is the corium simulant) with a hole of d=50 mm. The formula is valid for upright cylinders with or without hemispherical bottoms. The inner cylinder diameter is D=276 mm. For the experiment D06, the exit water velocity, u, is about 32 m/s, and the Froude number becomes Fr=46. This yields a critical pool height of h_b=100

mm which is larger than the initial pool height of 95 mm suggesting that gas blowthrough occurs early during the transient. However, measurements indicate a later gas blowthrough. The reason for the difficulty with the analytic formula may come from the small initial pool height of DISCO. Other experiments used to validate the formula may have started with higher pools which allows a certain flow pattern to develop before the critical pool height is reached.

Experimental evidence for later gas blowthrough is coming from the pressure transducer P6 mounted flush with the cavity bottom directly below the discharge hole. Fig. 1 shows the experimental readings of the RPV pressure P1 and the cavity bottom transducer P6. The transducer P6 shows a sharp increase from 1 bar to exactly the RPV pressure shortly after hole opening. After 26 ms, the pressure falls sharply when the jet changes from single phase to two phase. Given the time for the jet to traverse the 62 mm from the hole to the cavity bottom at 32 m/s, the jet at the hole stops being single phase at 24 ms.

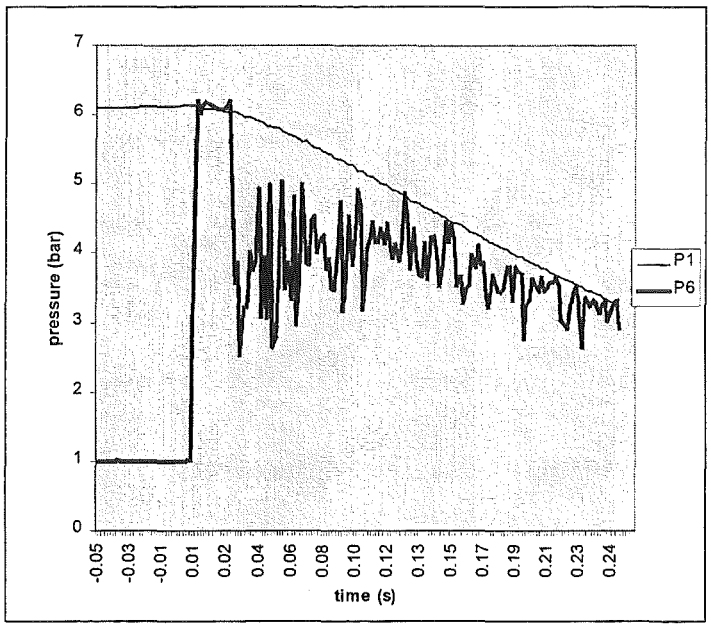

Fig.1 measured pressures of DISCO D06

The objective of modeling the fluid dynamics with the Eulerian code AFDM was to not concentrate on jet details but to model the whole discharge space, from the RPV to the reactor dome. The calculational grid was so coarse that the radial extension of the hole was modeled by only one cell. This demands additional care when setting up the geometry of the hole. Because of the staggered mesh and the associated interpolation for solving the momentum equation, the hole must be at least two cells long. In the experiment, the pressure difference across the hole is being totally transferred into kinetic energy of the liquid. At the same time, one observes the typical constriction of the jet. In order to match observed exit velocities, the upper hole cell has the nominal diameter while the lower hole cell needs to model the cross section of the constricted jet.

Dispersion rates proved to be sensitive upon the time at which the jet became two phase. As already explained, an early switch to two phase favors less dispersion of water out of the cavity. The only way to change gas blowthrough inception with an invariable grid was to specify different initial pool heights and diameters. The total initial pool mass stays always at 3.4 kg. Large pools are shallow and favor early gas blowthrough. Unfortunately, code

analyses are also influenced by the difficulty to model distinct open pool surfaces with Eulerian codes that smear given mass inventories over a whole cell. Therefore, the proper choice of the initial pool height is also a function of the chosen cell sizes. For the given coarse cells, Fig. 2 shows the liquid water volume fractions in the discharge hole over time. The hole opens at 0.05 s, see vertical line. The liquid volume fraction stays at 1.0 for the time the jet remains single phase. Upon gas blowthrough, the liquid volume fraction decreases rapidly. The time of blowthrough is specified by extrapolating the maximum downward slope up to a volume fraction of 1. The figure shows that the increase in pool height postpones the time of blowthrough.

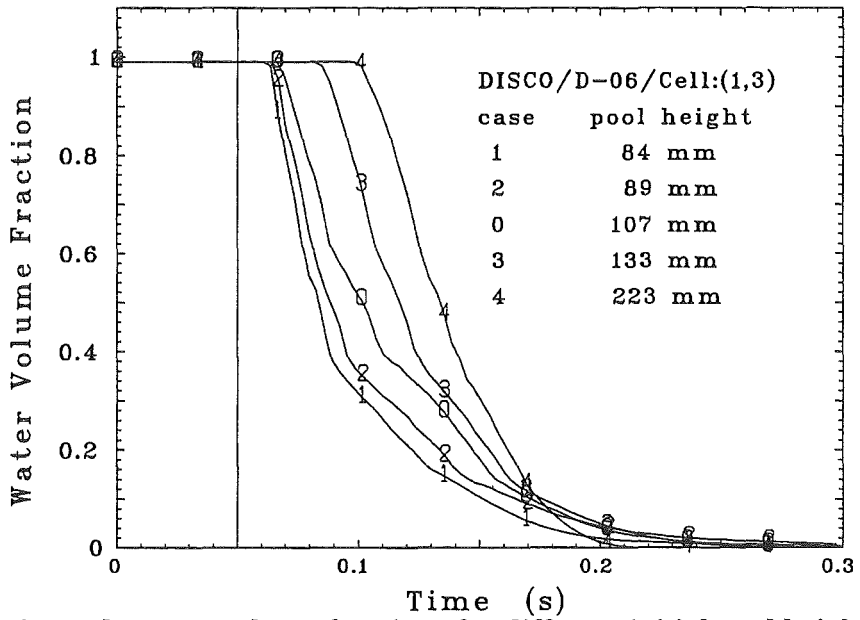

Fig. 2 code water volume fractions for different initial pool heights

Measuring the water mass dispersed out of the cavity, the dispersion increases with pool height. This increase is at least equally important as that obtained by changing entrapment and entrainment parameters of the specific melt dispersion models. Table II collects the results of the experiment and compares them to those of five code runs.

Table II blowthrough and dispersion results

CASE	pool height (mm)	time of gas blowthrough (ms)	dispersed water (kg)	dispersed water fraction
experiment	***95***	***24***	***3.19***	***0.94***
1	84	13	2.50	0.73
2	89	14	2.89	0.85
0	**107**	**18**	**3.12**	**0.92**
3	133	35	3.33	0.97
4	223	50	3.39	0.98

Table II shows that Case 0 which has the blowthrough time closest to that of the experiment produces also the best dispersion rates. The results show that prototypic conditions for corium discharge can only be met if the fluid flow inside the RPV is being modeled correctly.

5. THE INFLUENCE OF ENTRAPMEMT AND ENTRAINMENT PARAMETERS

If the pressure in the RPV is high and the breach is large enough, the dispersion of the liquid is so violent that the liquid may be ejected out of the cavity. On its way out, it may come into contact with the walls and form temporary films. Any liquid film which forms may be subjected to entrapment and entrainment at the same time. If the local mass transfer rates of both processes is equal, the local width of the film does not change. Fig. 3 shows the development of the water film for DISCO D06 and D11. Both experiments have an initial RPV pressure of about 6 bar. D06 has a hole of 0.05 m diameter, D11 of 0.015 m. For the large hole, the film develops quickly to 4 mm when entrainment starts to decrease it. Pressures are equilibrated between the RPV and the cavity after 0.5 s, but entrainment stops already at 0.3 s, so that the residual film thickness is about 0.5 mm. For the smaller hole (experiment D11), the transient is slower, and the film builds up to about 5 mm, with entrainment processes going on beyond 1 s.

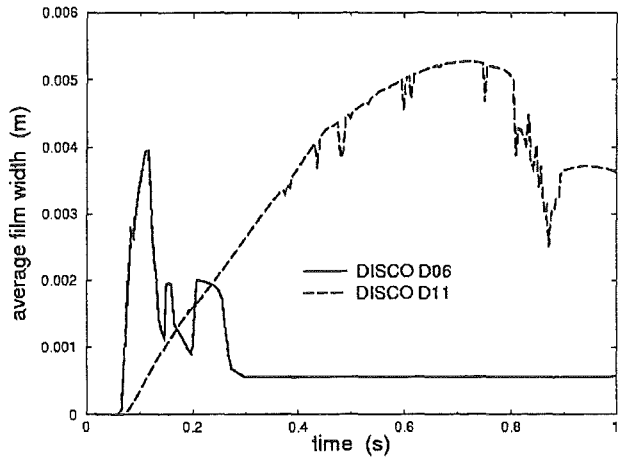

Fig. 3 Average calculated water film thickness from DISCO recalculations

Looking at the present model equations (see chapter 3.), the rates calculated for both processes depend heavily on four values: the two values of the constants C, the ratio of liquid to vapor density, and the surface tension. The objective of the dispersion model was to select equations with a single set of parameters which matches all experimental results, independent of the material combination used.

The first difficulty is to find the proper values for the surface tensions, given the possibly large influence of surfactants, especially for the thermite experiments where a chemical reaction occurs where films are being formed. The surface tension has also an influence on the transient calculation of the liquid droplet size which is governed by a standard code model using a Weber-criterion. Droplet formation may be influenced by additional physical phenomena like fragmentation upon impact and jet disintegration which are presently not represented.

The second difficulty lies in the proper selection of the constants C. The C imply also geometrical effects because the computational grid does not and could not resolve all the profiles of physical quantities needed to develop strictly mechanistic models.

An empirical approach for finding the proper parameters has been followed. Code results point towards a certain consistency of the present model equations when comparing dispersion rates with those of the experiments.

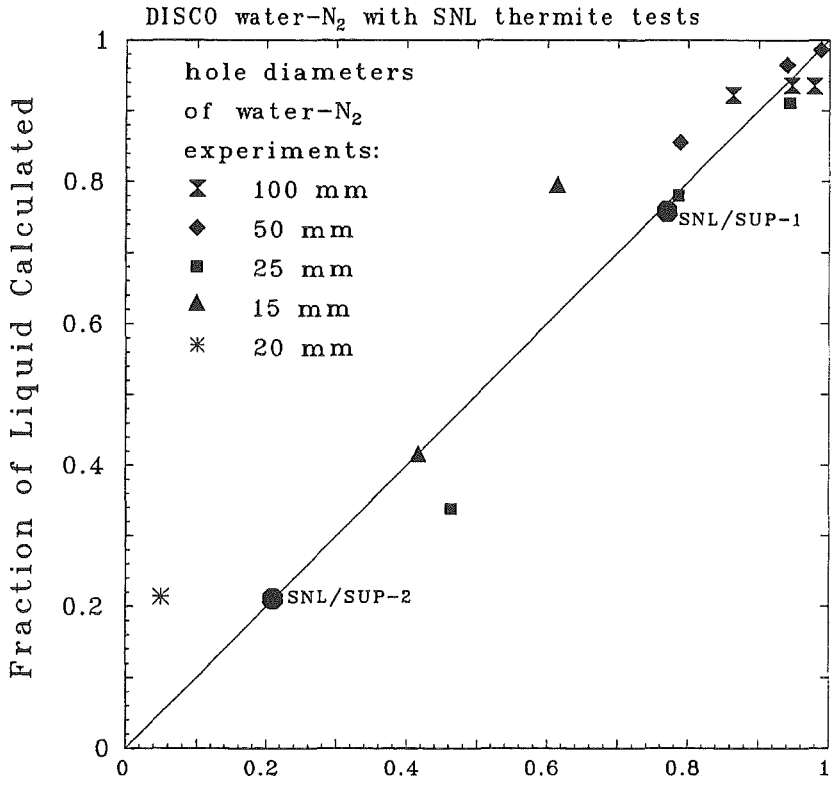

Fig. 4 Comparison between measured and calculated dispersion rates

Fig. 4 shows the comparison of measured and calculated dispersion rates. The rate is defined by the ratio of the liquid mass collected downstream of the cavity exit to the total initial mass. The cavity exit is at the upper end of the vertical annulus. Any liquid beyond the RPV pipe support structures is supposed to be dispersed. The figure collects data of the DISCO experiments and the two SANDIA (SNL) thermite tests. The DISCO experiments were run with water as corium simulant, and nitrogen as vapor simulant. Additional DISCO experiments with helium instead of nitrogen and wood's metal instead of water are not shown here because they would require a different value of C in the entrapment correlation. At this stage of the analysis, the question whether only the entrapment rate is responsible for the lack of consistency cannot be answered. It is quite possible that the processes of jet breakup (see chapter 4.) are not sufficiently well represented by the standard droplet breakup model of the AFDM code.

Summing up the experience with the present dispersion models, a set of equations and initial conditions has been found which gives reasonable results for water and thermite experiments. Several phenomena have been identified to influence dispersion rates. These are the processes leading to a disintegration of the liquid jet leaving the RPV, the formation of liquid films at the cavity wall and the entrainment of liquid from the film into the gas flow, the levitation of droplets and the movement of the film under the forces exerted by the gas

flow. For the thermite experiments, the oxidization of the metal component by steam plays an additional role because the pressures in the cavity are increased.

6. CONCLUSIONS

Low pressure corium dispersion models have been added to a multicomponent fluid dynamics code. The results show the feasibility of the approach. The phenomena at the breach through which the corium leaves the reactor pressure vessel are found to be as important as those at the liquid film which may form at the cavity walls. A set of parameters and properties has been identified to influence the film models and hence the dispersion rate. Dispersion rates of the thermite test are additionally influenced by the oxidization of the metallic component by steam. Reasonably good results for these rates can be presented at this early stage of the analysis.

REFERENCES

Meyer L., 1999, Experiments to Investigate the Low Pressure Corium Dispersion in EPR Geometry, paper to be presented at this conference

Washington K.E., Williams D.C., 1995, Direct Containment Heating Models in the CONTAIN Code, Sandia National Laboratory report SAND94-1073, August 1995

Bohl W.R., Wilhelm D., 1992, The Advanced Fluid Dynamics Model Program: Scope and Accomplishment, *Nuclear Technology*, **99**, 309-317

Pilch M.M., 1994, A Two-Cell Equilibrium Model for Predicting DCH, Appendix E of Pilch M.M., Yan H., Theofanous T.G., The Probability of Containment Failure in ZION, Sandia National Laboratory report NUREG/CR-6075, SAND93-1535, July 1994

Hewitt G.F., 1979, Liquid mass transfer in annular two phase flow, in F. Durst et.al. (Ed.), *Two-phase momentum, heat, and mass transfer in chemical, process, and engineering systems*, Vol.1, Washington 1979, p.273

Williams D.C., Griffith R.O., 1996, Assessment of Cavity Dispersal Correlations for Possible Implementation in the CONTAIN Code, Sandia National Laboratory report SAND94-0015, February 1996

Pilch M.M., Griffith G.O., 1992, Gas Blowthrough and Flow Quality Correlations for Use in the Analysis of High Pressure Melt Ejection Events, Sandia report, SAND91-2322, June 1992

OECD Workshop on Ex-Vessel Debris Coolability
Karlsruhe, Germany, 15-18 November 1999

Organised in collaboration with
Forschungszentrum Karlsruhe (FZK) GmbH

KAJET Experiments on Pressurized Melt Jets with View to their Interaction with Substratum Materials

G. Albrecht, E. Jenes, A. Kaiser, W. Schütz
Forschungszentrum Karlsruhe GmbH
Postfach 3640, D-76021 Karlsruhe, Germany
D-76021 Karlsruhe, Germany
albrecht@irs.fzk.de schuetz@irs.fzk.de

ABSTRACT

In the sequence of a core melt accident in a light water reactor it is assumed that, after melt-through of the reactor pressure vessel, the molten corium is released as a pressurized melt jet which causes erosion in the substratum material of the reactor pit. Melt jet behaviour under driving pressures of up to 2 MPa and corresponding erosion rates in various substratum materials are being investigated at Forschungszentrum Karlsruhe in so-called KAJET experiments using thermite melts (either iron or alumina) as simulant materials. Masses of up to 150 kilogrammes at temperatures of about 2100 °C can be provided for ejection. A special feature of the tests is to prevent melt dispersal due to gas break-through by sharply reducing the driving pressure before the end of melt release.

Performance tests carried out with both water and smaller melt masses (10 – 40 kg) prior to the erosion tests aimed at finding the material for and appropriate geometry of a nozzle to provide a compact melt jet. Zirconia proved to be a good material for the nozzle. Good results have been obtained with a nozzle having a length to diameter ratio of two and a contraction angle of 90°. This geometry is in good agreement with results from vessel-wall melt-through experiments at other laboratories. The first erosion test, conducted with a melt mass of 40 kg (iron and oxide in equal shares) ejected under a pressure of 0.3 MPa onto concrete plates, gives information about erosion rates concerning the target as well as the nozzle. The erosion was larger in case of iron.

1. INTRODUCTION

In the event of a postulated LWR core melt-down accident, scenarios cannot be excluded in which the reactor pressure vessel (RPV) fails and the core melt mixture (corium) is discharged into the reactor cavity (Pilch, 1994). In this context, efforts are currently directed towards ex-vessel corium behaviour with particular emphasis on long-term retention and cooling of the corium in the containment (Azarian, 1997). Various core catcher concepts for future reactors are under investigation that should prevent basemat erosion and stabilize and control the corium within

the containment (Cognet, 1997). Various modes of corium release out of the RPV may be envisaged: metal or oxide jets released by gravity or driven by overpressures resulting in low or high flow rates, respectively, liquid melts carrying solid debris, and intermittent melt discharge.

Scenario analyses performed by the GAREC group at CEA Grenoble (Micaelli, 1995) predict pressure increases of up to 2 MPa inside the RPV. In case of wall failure, melt will be released as a compact jet causing an erosion in the substratum material. The degree of erosion is determined by the following physical phenomena:

- mechanical stress caused by the impact of the jet
- melting of the substratum at the surface
- physico-chemical interaction of corium and substratum
- thermal-mechanical stress by temporary heating of the substratum
- stress by a fast decomposition of the substratum, which is particularly important in case of concrete.

The parameters that influence the erosion are the driving pressure, speed and temperature of the jet, the duration of interaction, the compositions (physical properties) of the jet as well as of the substratum material, and last but not least, the angle of inclination of the jet.

So-called KAJET experiments are being performed at the Forschungszentrum Karlsruhe to investigate erosion of reactor pit substratum material by pressurized melt jets. On basis of recommendations established by the GAREC group, several jet parameters, such as the jet velocity or a minimal time of ejection to get a noticeable degree of erosion, have been defined.

The main objective of the KAJET experiments is to investigate the features of a pressurized melt jet, e. g. its fragmentation behaviour, and its interaction with substratum materials or sacrificial layers, respectively, to be used for the lining in the reactor pit. As for the erosion, compact melt jets (rather than a spray-type melt release) are regarded to be most effective. In the experiments, simulant melt materials (iron and alumina) are applied instead of corium. The melt is provided by a thermite reaction:

$$3Fe_3O_4 + 8Al \rightarrow 9Fe + 4Al_2O_3 + 3413\ kJ/kg.$$

The theoretical temperature of the melt amounts to 2500°C if a conversion of 95% is assumed. Heat losses, however, lead to an actual melt temperature around 2100°C at the time of release.

The data obtained in the experiments are provided to validate computer codes which then are able to recalculate the experiments and transfer the results to reactor conditions.

Before the KAJET erosion experiments were started, the performance of jets under driving pressure was investigated in so-called performance tests. The first aim was to provide com-

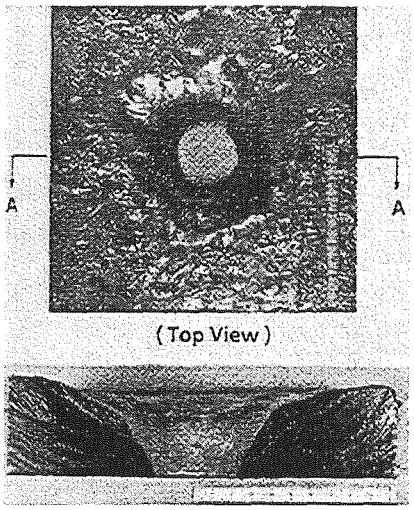

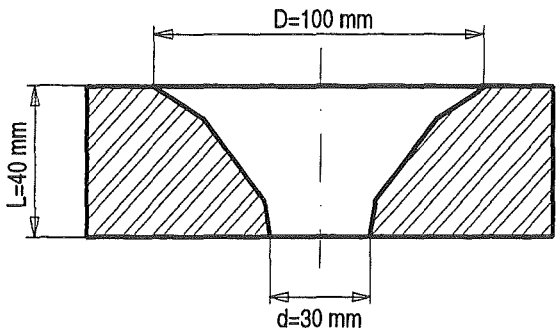

(a) PNC experiments with salt melts and tin plates

(b) KTH experiments with oxide melts and lead plates

Fig. 1 Results of wall erosion tests performed at PNC and KTH with various simulant materials.

pact melt jets. The second aim was to do this with nozzles close to realistic wall-hole geometries. In searching designs of appropriate nozzles, advantage was also taken of previous work done at other laboratories on melt/wall interactions. Experiments on wall ablation and hole enlargement have been performed using oxidic melts as the simulant materials for the corium melt. In some cases, simulant materials were used for both the melt and the wall. For example, experiments with iron-alumina melt jets were performed at Sandia National Laboraties (Pilch, 1993). Experiments were performed at PNC, Japan (Saito, 1990), and at the Stockholm KTH Institute of Technology (Dinh, 1996) with salt melts and PbO-B_2O_3 oxidic melt mixtures, respectively, acting upon test plates whose materials had much lower melting points compared with the RPV wall material. Figure 1 shows for example two typical results of these tests.

The FZK performance tests began with water. Later, small amounts of thermite melt were used. Beginning with rather long nozzles made from varying materials to provide a compact jet, we finally were able to generate compact jets using nozzles which reflect the above geometry. With this type of nozzle, we conducted the first actual erosion test in March 1999. In this paper a review of characteristic data of the performance tests is given and first results of the erosion test are reported.

Table 1 Conditions and some important data of the relevant performance tests

Test No Melt material	Water tests	VJ05 oxide	VJ06 oxide	VJ07 1.iron + 2.oxide	KJ01 1.iron + 2.oxide
Ejected mass (kg)	14	10	10	20 + 20	20 + 20
Nozzle: L/d	15 + 30	10	10	10	2.1
Temperature[1] (°C)	environm.	2000	2000	(not available)	2050
Max. driv. press. (MPa)	0.5 - 2.5	0.92	1.5	1.5 1.1	1.5 1.1
Time of ejection (s)	-	3.5	2.5	2.6 3.4	3.0 >3
Max. jet speed (m/s)	20 - 50	20.5	25	17 22.3	16.5 21.3
Jet diversion[2] D^*/d	1.5 - 2.9	2.5	3 - 5.8	2.5 5	1.5 2.5

[1]Pyrometer data in the melt cases.
[2]Jet expansion ratio at a distance of 300 mm (200 mm in the water case); D^* is the expanded jet diameter.

2. PERFORMANCE TESTS

2.1 Test conditions of the performance tests

The major test conditions together with significant results are summarized in Table 1. About 20 tests with water and eight tests with thermite melt (VJ01 - VJ07 and KJ01) have been carried out. The KJ01 performance test was carried out in the KAJET erosion test facility.

The nozzle diameter was fixed to 12 mm for the performance tests as well as for the erosion tests while considering the required jet speed, the maximum mass of melt available in the erosion tests (150 kg), and a minimum nozzle width below which the danger of a blockage due to freezing is given.

The driving pressure was increased within about one second from zero to the maximum value given in the table. The pressure was reduced in the cases when the oxide melt component was to be released after the iron. Details of the test procedures are given below.

The temperature of the melt near the nozzle exit was measured by a pyrometer. It was also estimated on basis of reaction kinetics including heat losses. The calculation gives a value of about 2100 °C at the time of release.

2.2 Performance tests with water

The nozzle geometry (Fig. 2) was composed of two sections, a contraction and a pipe section. The parameters investigated were the jet pipe length (L = 184 and 370 mm), the nozzle contraction angle (α = 30/45/60°), and the driving pressure (p = 0.5/1.5/2.5 MPa).

The jet diameter expanded over a distance of 200 mm by a factor of 1.5 – 2.9, depending on the conditions. The largest influence on the expansion ratio was exerted by the driving pressure, whereas the effect of the nozzle length was small. The smallest jet expansion ratios were achieved with the smallest contraction angle (α = 30°).

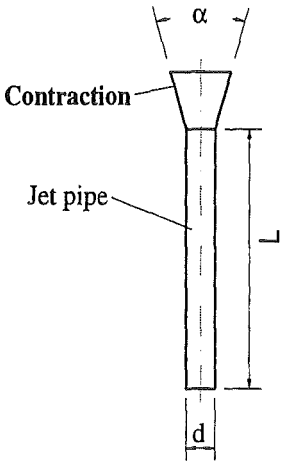

Fig. 2 Nozzle geometry used in the water tests

2.3 Performance tests with thermite melt

Experimental facility

The major parts of the experimental facility (Fig. 3) were the melt generator capable of providing 10 to 40 kg of melt, a wire netting used to measure the jet expansion and a melt catcher. Auxiliary systems were a gas pipe work and a venting system used to remove smoke from the melt release area which was filmed by a video camera.

The thermite powder was densely packed in the crucible and ignited at the top. During reaction, the two melt components separated due to their different densities. When the reaction front reached the bottom of the crucible, a steel membrane was molten that separated the thermite powder from the nozzle tube; melt release started. About at that time, opening of an argon valve was triggered which caused the driving pressure in the crucible to rise from ambient pressure to the desired pressure level.

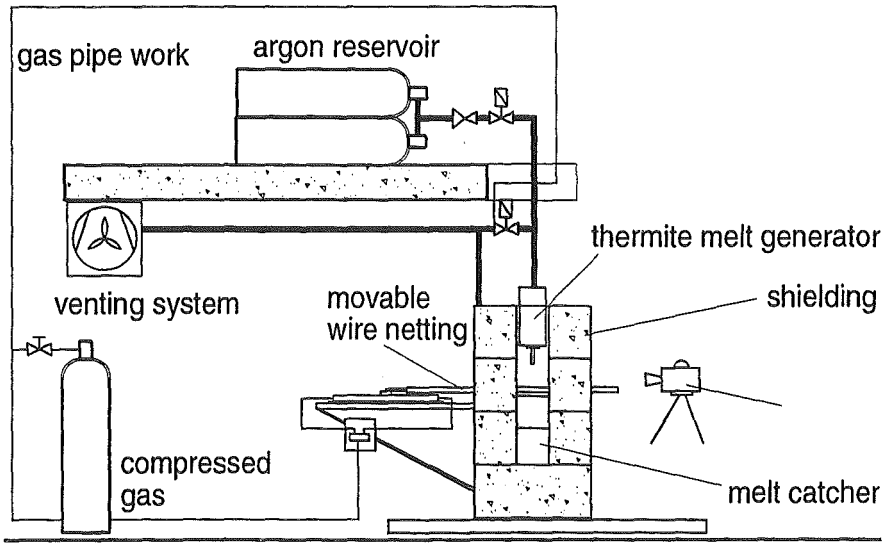

The nozzle contraction angle (30°) found suitable in the water tests was also used in the melt experiments. The l/d ratio was reduced to a value of ten (Table 1).

Tests with iron and oxide (VJ01 – VJ04)

In these tests, a total mass of about 10 kg was provided. Iron was released first because of its larger density. In the first three tests, a rather large diversion of the melt jet occurred, $D^*/d \approx 15$, caused by failing nozzles (Fig. 4). Moreover, the formation of smoke strongly handicapped the visibility. Test conditions and results have not been entered in Table 1. A few percent of alumina were added to the thermite mixture to reduce the actual melt temperature and by this the formation of smoke. To get information about the jet diameter, a fixed wire netting was mounted at a distance of 300 mm below the nozzle in VJ02. The netting was equipped in the VJ03 and VJ04 tests with melt detectors that provided better information about the jet extension versus time. The nozzles made of alumina in VJ01 andVJ02 broke during the melt release. A stainless steel nozzle used in VJ03 was almost completely molten off within one second. From the VJ04 test on, the nozzles were made of zircon oxide. With this material, the nozzles did not break any more.

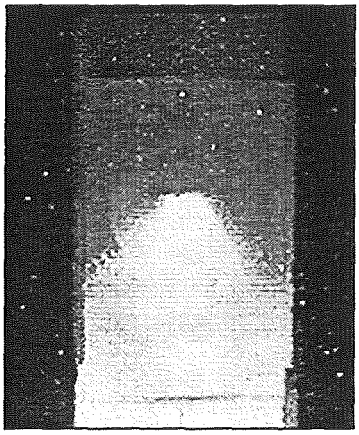

Fig. 4 Expanding melt jet

Tests with oxide only (VJ05 and VJ06)

In these tests, a melt generator was used in which the iron was retained in a compartment sunk in the crucible bottom and mostly oxide (10 kg) was released. Break-through of gas in the nozzle was prevented by sharply reducing the driving pressure well before the end of release. Measuring with the wire netting was further improved: the netting was installed on a sledge that was moved in horizontal direction (Fig. 5). The jet produced in the netting a longish hole whose width could be correlated to the pressure time history. The zirconia nozzles produced jets that had a nearly compact slim shape (Fig. 6). The jet speeds given in Table 1 were obtained for the times of maximum driving pressure. The influence of the driving pressure on the jet diversion was only weak in VJ05. In VJ06, the jet diversion ratio became larger with time, probably due to the larger ultimate driving pressure applied in this test. By restricting the release to the oxide melt

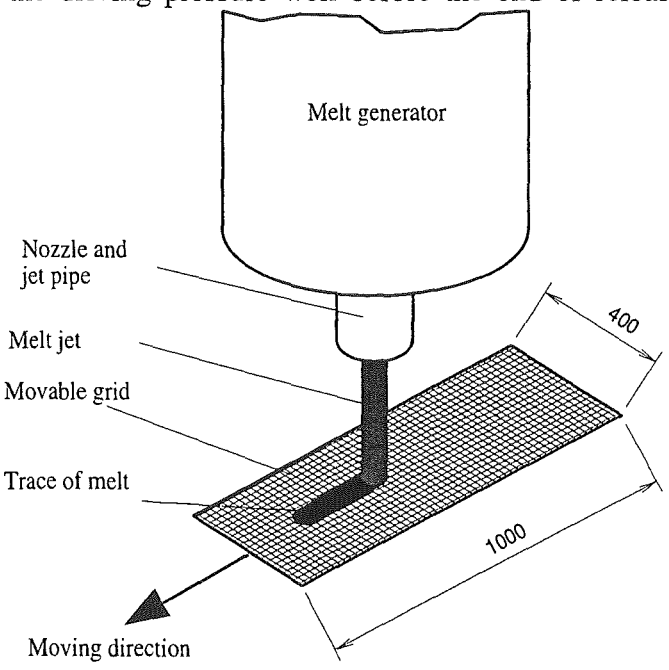

Fig 5 Detail: movable wire netting

component, no smoke was produced. We conclude from this that the smoke in the former experiments was mainly due to evaporating iron.

VJ07 test with iron and oxide

In this last test of the VJ series, a total melt mass of 40 kg was provided. Iron and oxide melt were released subsequently. The shape of the melt jet was compact during both periods of release. The expansion ratio was larger in case of oxide (Table 1). The visibility of the jet was very much improved by improving the venting system.

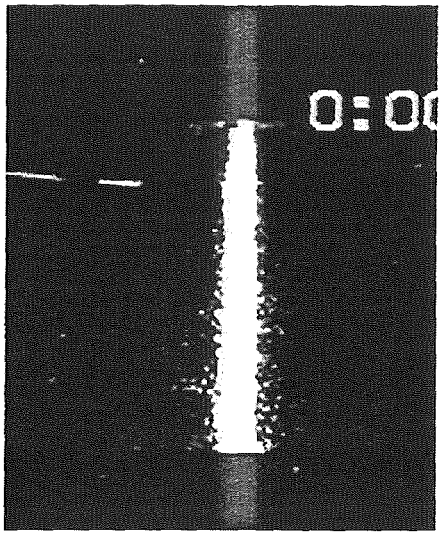

Fig. 6 Compact melt jet (oxide)

3. TESTS PERFORMED IN THE KAJET FACILITY

3.1 Test facility

The KAJET erosion test facility is shown in Fig. 7. Total melt masses of up to 300 kg can be provided by various types of melt generators. Driving pressures of up to 2.5 MPa can be established. Melt release occurs downward into a vessel which is 1100 mm in diameter and 1900 mm in height and has at its bottom layers of gravel and sand. The pressure inside the vessel can be raised up to 0.3 MPa.

3.2 KJ01 performance test

The KJ01 performance test aimed at checking the jet formation. A nozzle was used whose dimensions were more oriented to the re-

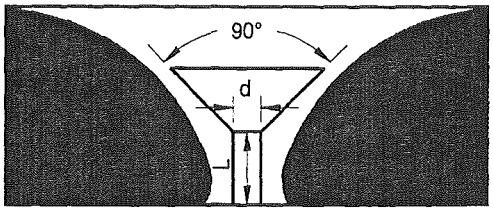

Fig. 8 Nozzle design fitting better to anticipated wall melt-through

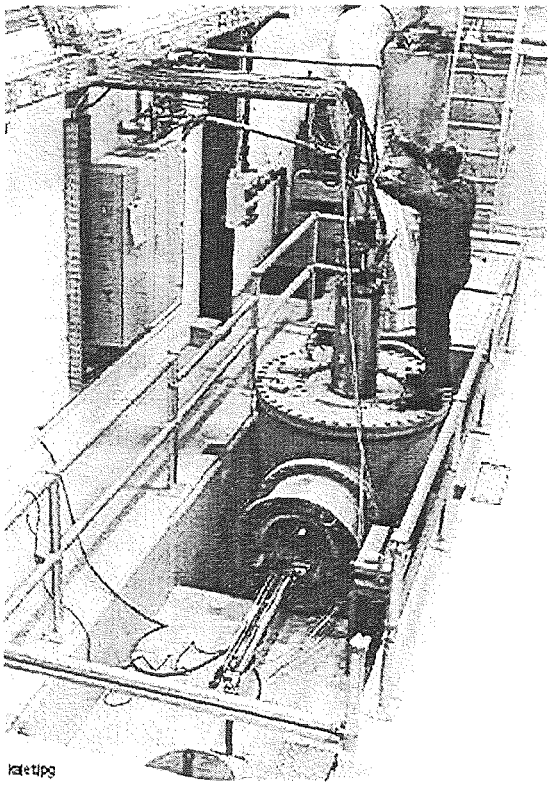

Fig. 7 KAJET test facility

sults of wall erosion tests mentioned above (see Fig. 1) than to the nozzles investigated in our VJ tests. The shape of the nozzle (Fig. 8) having an angle of 90° and 25 mm in length resembles to the hole in a pressure vessel wall (filled area in Fig. 8) generated by melt-through. Otherwise, the KJ01 test conditions agree with those of the preceding VJ07 test (see Table 1).

Figure 9 shows some characteristic measurements. Release of iron started under gravity conditions. When the driving pressure was increased at time 1.1 s, the mass flow rate grew superproportionally. After having reached a maximum of 1.5 MPa, the driving pressure continuously decreased from time 2.3 s on. At the time of three seconds, the melt material changed from iron to oxide. From time 5.3 s on, the release of residual melt occurred under gravity conditions. Movement of the netting was started at time 0.9 s.

The function of the melt speed drawn in Fig. 9 was calculated on a simple numerical model that is based on the one-dimensional flow of melt in a pipe. In the solution of the momentum equation, both the geodetic height of the melt and the overpressure in the crucible are considered as driving forces. Friction coefficients are assumed to be constant. The figure shows the melt speed is approximately proportional to the pressure.

The trace burnt in the netting (bottom of Fig. 9) gives a constant width for the time of iron release, i.e. no marked influence occurred of the pressure time history on the jet diversion. During oxide release, the trace width and with it the jet diversion became larger. The films show that the

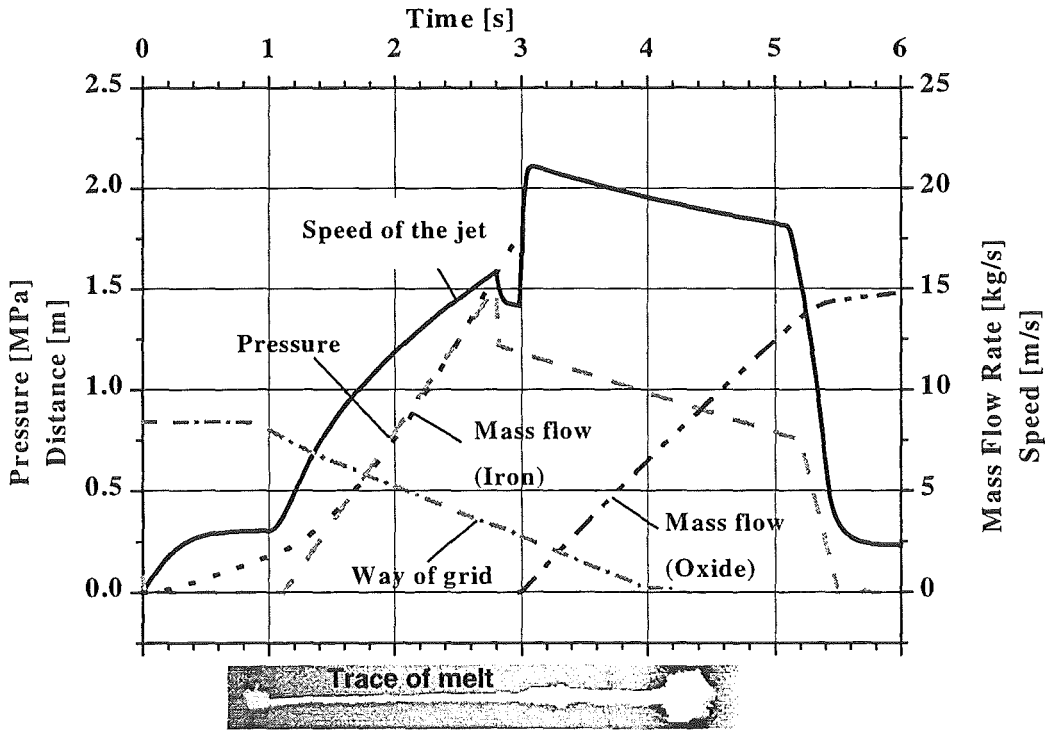

Fig. 9 Characteristic data of the KJ01 performance test showing the course of events

shape of the melt jet remained approximately constant over the pressure range applied. It is remarkable that the jet expansion ratio was even smaller than that obtained in the preceding VJ07 experiment conducted with a smaller contraction angle (30°) and longer jet pipe (110 mm) were applied (Table 1).

3.3 KJ02 erosion test

Test conditions

Test conditions together with significant results are listed in Table 2. The maximum driving pressure was 0.3 MPa. The arrangement shown in Fig. 10 helps to explain how the test was conducted. The time scale begins with the start of ejection. The first melt component to be ejected was iron. After 3 s, the plate carrier was turned by 90°. The action lasted about one second. During that time, the melt changed to oxide as the second component to be ejected.

Table 2 Conditions and results of the KJ02 test

Melt material	iron	oxide
Ejected mass, kg	18.8	21.2
Duration of ejection, s	3.6	6.3
Temperature, °C	2100	
Impact speed, m/s	7.7	11.5
Extension of erosion, mm x mm	65 x 50	55 x 70
Erosion depth, mm	25	15

The test plates consisted of concrete produced from cement, sand & pebbles (0 – 32 mm), and water mixed at a mass ratio of 1 : 5.5 : 0.4, respectively. The plates were instrumented by 25 thermocouples each. The thermocouples were arranged in five horizontal levels whose distances from the upper surface were 5, 10, ..., 25 mm. In each level, one thermocouple was in the centre, the others were crosswise arranged at distances of 25 mm to the central one. The first two seconds of the procedure were recorded by a CCD film camera. Then, the camera was destroyed by heat and/or melt impact.

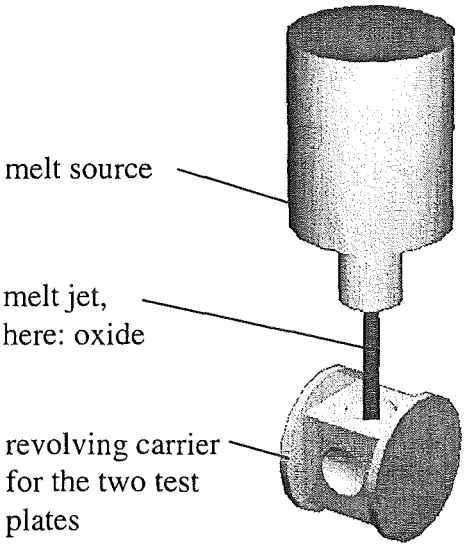

Fig. 10 Test arrangement, schematically

Results

The film taken by the camera shows a rather compact iron melt jet. In fact, the jet decomposed and sprayed when hitting the test plate; this condition temporarily deteriorated the view to the body of the jet.

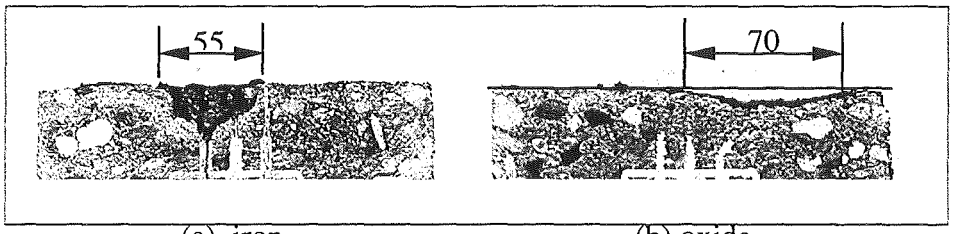

Fig. 11 Post-test vertical cuts through the test plates

Figure 11 shows the extensions of erosion in both plates caused by the consecutive jets. The cut was made along the narrow side centre line laying bare three of the thermocouple channels embedded in the concrete. The erosion in the case of iron did not occur exactly in the centre but 25 mm apart. The cut in the oxide case does not show the maximum erosion depth (15 mm, see Table 2). Crusts up to one millimeter thickness were found at the eroded surfaces. The extensions of erosion in the surface of the plates are listed in Table 2.

The progression of erosion is expressed in the destruction of thermocouples made visible in Fig. 12. Work is in progress which uses the information of the thermocouple data to evaluate the erosion volume as a function of time.

Inspection of the nozzle after the test showed that the internal wall of the nozzle had been eroded by five millimeters on average, i.e., the diameter was enlarged from 12 to 22 mm. Crusts between one and two millimeter thickness were found at the surfaces that had contacted the melt.

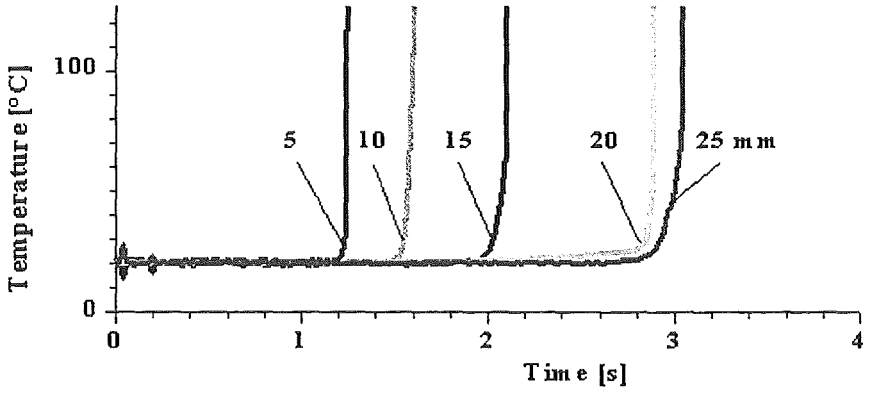

Fig. 12 Signals of thermocouples arranged vertically (erosion by iron)

4. CONCLUSIONS AND OUTLOOK

Suitable conditons to be applied in the KAJET erosion experiments, such as geometry and material of the nozzle, range of the driving pressure, have been found in performance tests. It was shown that a compact jet can be produced by longer nozzles having an L/d ratio of ten as well as by a short nozzle having a ratio of two.

Compact jets have been obtained by releasing a metal melt as well as an oxide melt with almost no influence of the driving pressure. The melt release times were in the order of three seconds. Zirconia has proved to be a stable material for the nozzle. Unstable nozzle materials, such as steel or alumina, may lead to spray-type jets.

The first erosion test, conducted with a melt mass of 40 kg (iron and oxide in equal shares) ejected onto a concrete plate, gives good information about erosion rates concerning the target plate. At the same time, the erosion of the nozzle may be studied. The erosion was larger in case of iron.

The evaluation of the data will be accompanied by theoretical investigations. The development of numerical models is under way to help in the interpretation of the phenomena observed in the tests and to allow an extrapolation of the results to large-scale reactor conditions. The parameters to be varied in future erosion tests are:

- the materials used for the substratum (protective liners and sacrificial layers)
- the melt mass (up to 150 kg, either metal or oxide),
- the driving pressure, and
- the nozzle diameter.

Among others, the data will support the selection of substratum materials for the European Pressurized Reactor EPR.

The last KAJET erosion test was performed in September 1999 using a melt mass of 112 kilogrammes. The maximum driving pressure raised from 0.3 MPa in KJ02 to 0.5 MPa in KJ03.

5. REFERENCES

Azarian, G., Bittermann, D., Eyink, J., 1997. The overall approach to severe accident mitigation, in: Kerntechnische Gesellschat (ed.), The European Pressurized Reactor EPR, Proc., Inforum, Bonn, pp.194-197.

Cognet, G., Alsmeyer, H., Morris, S., Wittmaack, R., Sehgal, B.R., Bürger, M., De Cecco, L., Ocelli, R., Azarian, G., Ranval, W., Spindler, B., 1997. Corium Spreading and Coolability (CSC Project), FISA-97 Symposium on EU Research on Severe Reactor Accidents, Luxembourg, pp. 141-151.

Dinh, T.N., Bui, V.A., Nourgaliev, R.R., Modelling of heat and mass transfer processes during core melt discharge fron a reactor pressure vessel, Nuclear Engineering and Design **163** (1996), pp. 191-206.

Micaelli, J.C., Seiler, J.M., Bung, H., Maunier, C., Humbert, J.M., Szabo, I., Valin, F., Cognet, G., Van Dorsselaere, J.P., Philipponneau, Y., Forestier, A., 1995. R&D needs related to the core-catcher concept based on corium spreading. Int. Sem. on Heat and Mass Transfer in Severe Reactor Accidents, Cesme, Turkey.

Pilch, M. M., Yan, H., Theofanous, T.G., 1994. The probability of containment failure ba direct containment heating in Zion, NUREG/CR-6075.

Saito, M., Sato, K.,Furutani, A., Isozaki, M., Imahori, S., Hattori, Y., 1990. Melting attack of solid plates by a high temperature liquid jet - effect of crust formation, Nuclear Engineering and Design **121**, pp. 11-23.

OECD Workshop on Ex-Vessel Debris Coolability
Karlsruhe, Germany, 15-18 November 1999

Organized in collaboration with
Forschungszentrum Karlsruhe (FZK) GmbH

KAPOOL experiments to simulate molten corium sacrificial-concrete interaction and gate opening in the EPR core catcher concept

G. Engel, B. Eppinger, F. Fellmoser, G. Fieg, C. Messainguiral,
H. Massier, S. Schmidt-Stiefel
Forschungszentrum Karlsruhe GmbH
Postfach 3460, D-76021 Karlsruhe, Germany
fieg@iket.fzk.de

ABSTRACT

In future Light Water Reactors special devices (core catchers) might be required to prevent containment failure by basement erosion after reactor pressure vessel meltthrough during a core meltdown accident. In the case of a postulated core melt down accident in the EPR (European Pressurized Water Reactor) the ex-vessel melt shall be retained and cooled in a special compartment inside the containment to exclude significant radioactive release to the environment. After failure of the reactor pressure vessel the core melt is retained in the reactor cavity for ~ 1 h to pick up late melt releases. The reactor cavity is protected by a layer of sacrificial concrete and closed by a steel gate at the bottom. After meltthrough of this gate the core melt should be distributed homogeneously in a special spreading room.

A series of experiments has been performed to investigate the erosion of the sacrificial concrete as well as the gate ablation using alumina-iron thermite melts as a simulant for the core melt. Two different sorts of sacrificial concrete have been studied so far: boro-silicate glass concrete and a concrete based on Fe_2O_3/SiO_2. Erosion velocities of the sacrificial concrete, the homogeneity of the melt front and steel gate ablation results are presented in this report.

1. INTRODUCTION

To exclude significant release of radioactivity to the environment even in the case of a core melt accident, next generation LWR's shall incorporate the ability to retain the core melt within the containment. In the planned European Pressurized Reactor (EPR) this shall be accomplished by spreading the core melt on a large area and cooling the spread melt by flooding with water from top (Alsmeyer, 1999). Therefore a better knowledge of core melt behaviour, especially concerning spreading and coolability is required. To achieve this, various series of experiments are performed at Forschungszentrum Karlsruhe. In all these tests the core melt is simulated by iron and alumina melts produced by the thermite reaction. Thermite melts are excellent simulants of the core melt because both, the metallic and the oxidic core melt component, are simulated, the melt temperatures (~ 2200 °C) are comparable to that of the core melt (this is important to achieve representative high radiation heat losses), and by admixture of other components (SiO_2, CaO) to the alumina melt, the characteristics of

the oxidic corium melt after admixture of concrete components (large difference between solidus and liquidus temperature) can be simulated.

After meltthrough of the reactor pressure vessel the corium melt is gathered in the cavity below the vessel. It is foreseen to hold the melt there for about one hour. This time interval is long enough to ensure that practically all corium inventory will be gathered in this cavity. The corium melt interacts with the sacrificial concrete of the cavity. This interaction changes the corium material properties drastically: metallic zirconium is oxidized, the admixture of concrete with the oxidic melt lowers the liquidus- and solidus temperatures by several hundred degrees and the density of the oxidic melt, originally above 9000 kg/m^3 distinctively higher than the metallic one ($\approx$ 7000 kg/m^3), is decreasing steadily, and eventually a flipover of the two separated phases, oxidic and metallic melts, will happen. Once the concrete erosion is finished, a steel gate will be eroded by the melt and spreading of the melt into the spreading compartment starts. The KAPOOL experiments investigate the processes (corium-concrete interaction and gate opening) inside the ractor cavity.

2. CONCRETE EROSION TESTS AND RESULTS

The corium melt is composed of a metallic (steel, zirconium) and oxidic (UO_2, ZrO_2,FeO) phase. In the KAPOOL experiments these two phases are simulated by an thermitically produced alumina/iron melt. The thermite reaction (8 Al + 3 Fe_2O_3 $\rightarrow$ Al_2O_3 + 9 Fe) produces about 50 wt% iron and 50 wt% oxidic melt. The reaction ist strongly exothermic, the maximum temperature of the melt is up to 2400 ^{0}C. As to the concrete erosion tests, the reaction is performed inside the KAPOOL containers, fig.1. The sidewalls are made of ceramics for lateral insulation. Thermocouples to measure the concrete erosion front are fed through the bottom steel plate. Due to the different melt densities the iron melt is in contact with the sacrificial concrete layer.

These concrete erosion tests are strongly transient because there is no additional heating. The temperature of the melt decreases during the test period. Therefore it has to be recorded constantly with high-temperature thermocouples which are dipped into the melt. For the detection of the erosion front in the concrete, thermocouples have been embedded in the concrete layer at different heights. The erosion front is not homogeneous, to investigate the amount of inhomogeneity across the test surface thermocouples are installed at several lateral locations in the concrete. The erosion rate, its amount of inhomogeneity and the temperature of the melt are recorded as a function of time. From this a correlation between erosion rate and melt temperature can be deducted.

The composition and size distributions of the two sacrificial concretes are shown in Table I. The grain size of the ironoxide and silica of the VM281Q concrete was < 1 mm, rather small compared to the size distribution of the boro-silicate glass concrete. Ironoxide is chosen as an oxidant for metallic zirconium. Water content of the concrete should be kept at a minimum to reduce the production of hydrogen. Samples of concrete have been made together with the concrete layer inside the KAPOOL container and underwent the same history from production until the day of the test. The weight of these samples has been controlled steadily. No mechanical properties like tensile strength have been investigated because this concrete serves only as a sacrificial layer. The container together with the samples were kept at room temperature at dry conditions for two days. The water content decreased from 10 wt% to about 7 wt%. Afterwards the containers have been heated up to 200 ^{0}C for 24 hours. The final water content at the day of the test was 2 - 3 wt%.

Table 1 Composition and size distributions of the two sacrificial concretes

	Composition in wt%	
Chemical compound of aggregates	**Borosilicate glass concrete**	**VM281Q concrete**
Fe_2O_3	-	44.5
SiO_2	45.6	39.1
B_2O_3	13.4	-
Al_2O3	2.3	-
LiO2	2.7	-
Na2O	5.4	-
CaO	4.0	-
MgO	1.7	-
TiO2	0.9	-
Portland cement	15.0	6.4
Water	9.0	10.0
	Distribution (%)	
Grain size (mm)	**Borosilicate glass concrete**	**VM281Q concrete**
0-1	30	100
1-8	70	0

Table 2 lists all relevant data of the concrete erosion experiment. Three tests have been run with the glass-concrete and three with the ironoxide/silicate concrete. In the last two tests, zircaloy has been added. In KAPOOL-7 5 kg have been deposited on top of the concrete layer, fig.1. Because no distinct change in melt temperature has been detected compared to KAPOOL-6, in KAPOOL-8 10 kg of zircaloy have been added, again deposited on top of the concrete layer, but additionally covered by a 10 mm layer of concrete. Fig. 2 shows the transient temperature curves for the metallic melt during the melt/concrete interaction for all six tests. The influence of zircaloy present in the tests (5 kg in KAPOOL 7 and 10 kg in KAPOOL 8) is only weakly to recognize. There is some systematic deviation between the data: $T_{KAPOOL8} > T_{KAPOOL7} > T_{KAPOOL\,6}$, yet the differences are not as has been precalculated under the assumption that all zircaloy metal would oxidize.

From the recorded transient erosion fronts and melt temperatures a temperature dependant erosion rate has been deducted, fig. 3. There is a rather large difference between the two different sacrificial concretes, the erosion rate of the ironoxide / silicate concrete is about twice as high than for the glass concrete. The reason may be due to the different sizes of the concrete aggregates. A linear variation of the erosion rate with the pool temperature is found for both sacrificial concretes.

Table 2 Experimental matrix of the melt/concrete erosion tests

KAPOOL #	Sacrificial concrete	Thermite (kg)	Zircaloy additives	Initial melt temperature (^{0}C)
2	Borosilicate	150	0	2100
3	"	"	0	2350
5	"	"	0	2450
6	Ironoxide/silicate	"	0	2250
7	"	"	5 kg	2250
8	"	"	10 kg	2150

3. STEEL GATE ABLATION

Several tests have been conducted to investigate the gate ablation in the presence of an iron- and oxidic melt. In these tests the gate was simulated by steel plates at the bottom of the KAPOOL containers. They have been instrumented with thermocouples at several lateral and vertical positions to detect the transient temperature fronts during the heating-up phase.

For the ablation test with an iron melt (KAPOOL-9) 150 kg thermite have been ignited inside the KAPOOL container. A layer of 10 mm sacrificial glass concrete covered the 40 mm thick steel gate, except for a hole of 20 mm diameter in the center of the plate, fig. 4. In this case early ablation starts there, where instrumentation with thermocouples was more densely than for the rest of the plate. The bottom of the plate has been recorded during the test with a video and an infrared camera. W-Re thermocouples, dipped into the iron melt, measured the transient melt temperature. Weighing cells recorded the mass losses after ablation of the plate. The results are shown in figs. 5 - 8. At the end of the thermite reaction (ca 15 s after ignition), the ablation of the steel plate began at the center, the vertical ablation was rather fast. Ten seconds later, the concrete was eroded and the attack of the steel plate began over the whole area. A thin jet was first detected at 61 s, around 65 s the jet size reached ist maximum diameter. This time was incident with the pouring end of the iron melt, the oxidic melt did not ablate the steel plate further on. An analysis of this KAPOOL-9 test has been done (Messaingueral, 1999).

In another test, KAPOOl-11, the attack of an oxidic melt onto the steel gate has been investigated. As in KAPOOL-9, the steel gate was simulated by steel plate (25 mm thickness) at the bottom of the container. It was also instrumented with thermocouples in lateral and axial positions. 300 kg of thermite have been ignited in a reaction crucible, then 120 kg of oxidic melt have been poured into the KAPOOL container, no metallic melt was present in this container. The temperature of the oxidic melt was 1980 0C at the beginning and dropped to 1900 0C within 100 s. Within that time the temperature in the steel plate rose to a maximum of 600 0C (in the center of the plate, 1 mm below the contact surface), fig. 9, the average temperature in the plate was less than 450 0C at that time. A first analysis showed a much faster temperature rise in the steel plate in contact with the hot oxidic melt and crust (Eppinger, 1999). The conclusion of this analysis is that gaps have been formed between the oxidic crust and the steel gate surface, resulting in a rather large resistance in heat transfer.

ACKNOWLEDGMENTS

This work was partly supported by a contract between FZK and EVU/Siemens.

REFERENCES

Alsmeyer, H. et al., "Simulation tests with thermite melts on erosion, spreading and cooling of melts (projects KAJET, KAPOOL, KATS, COMET)", Annual Meeting on Nuclear Technology, Karlsruhe, May 1999.

Eppinger, X., Schmitt-Stiefel, S. Analysis of KAPOOl-11, to be published

Messaingueral, C. , Interpretation of KAPOOL-9. Connection with the reactor conditions, to be published

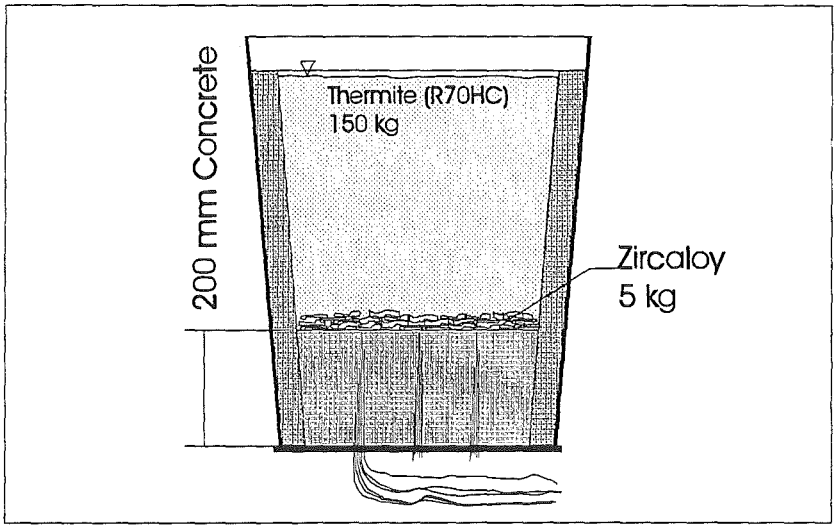

Fig. 1 Setup of the KAPOOL-7 container for melt/concrete interaction tests

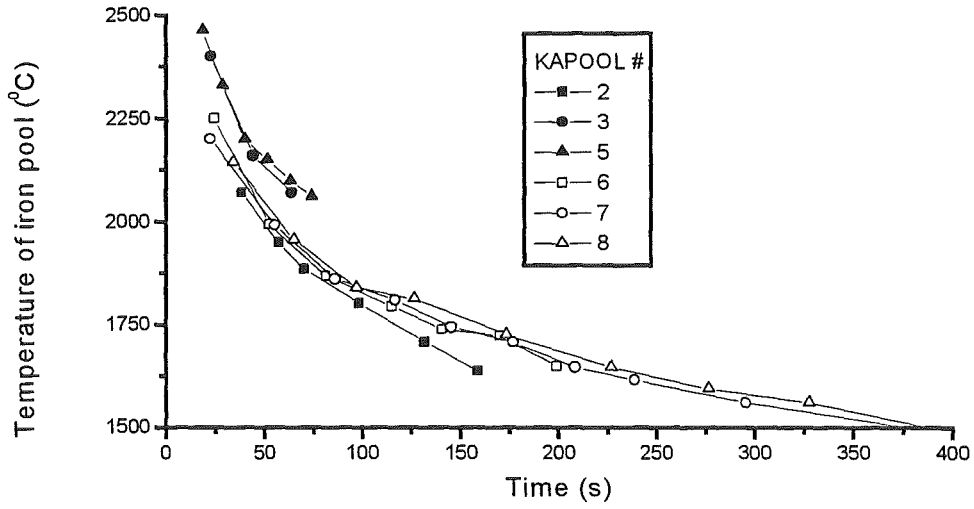

Fig. 2 Transient iron pool temperatures in the KAPOOL tests with two different sorts of concretes

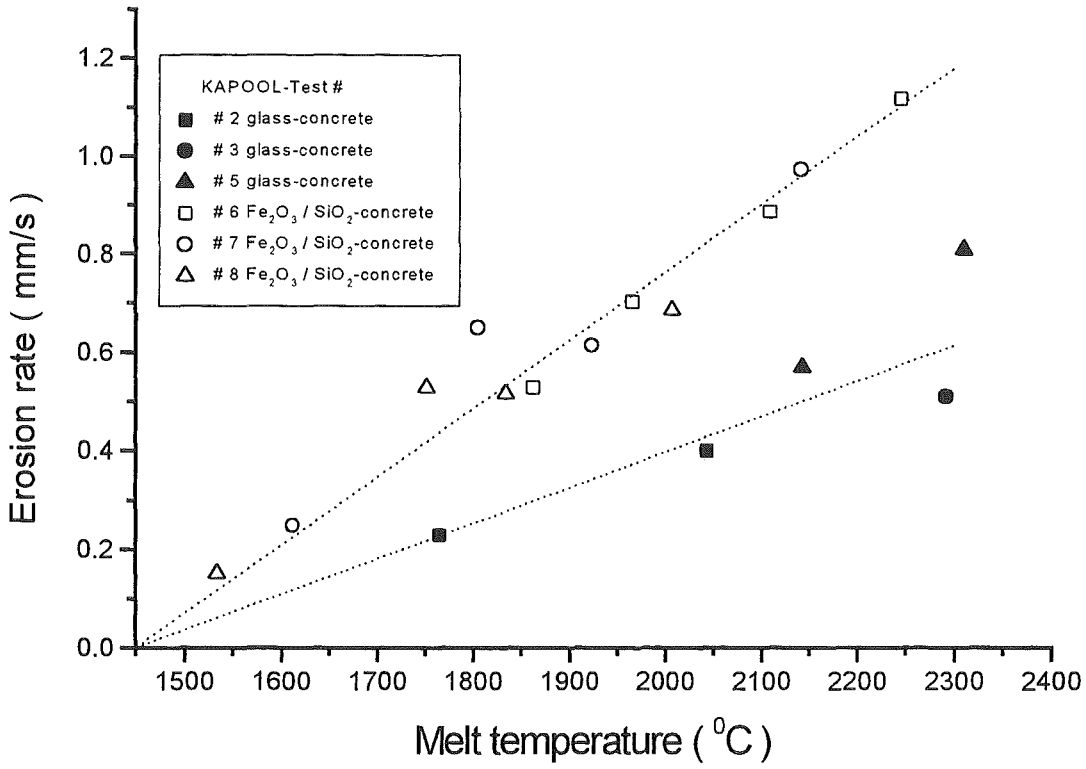

Fig. 3 Temperature dependant erosion rates for two different sorts of concrete

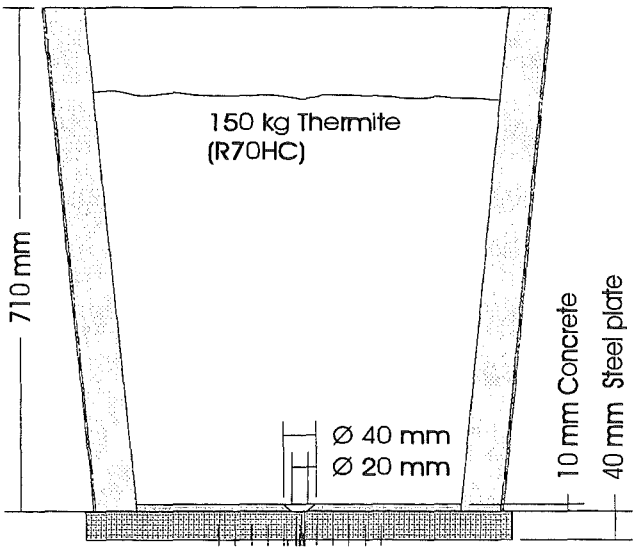

Fig. 4 KAPOOL – 9 container for iron-melt/steel gate ablation test

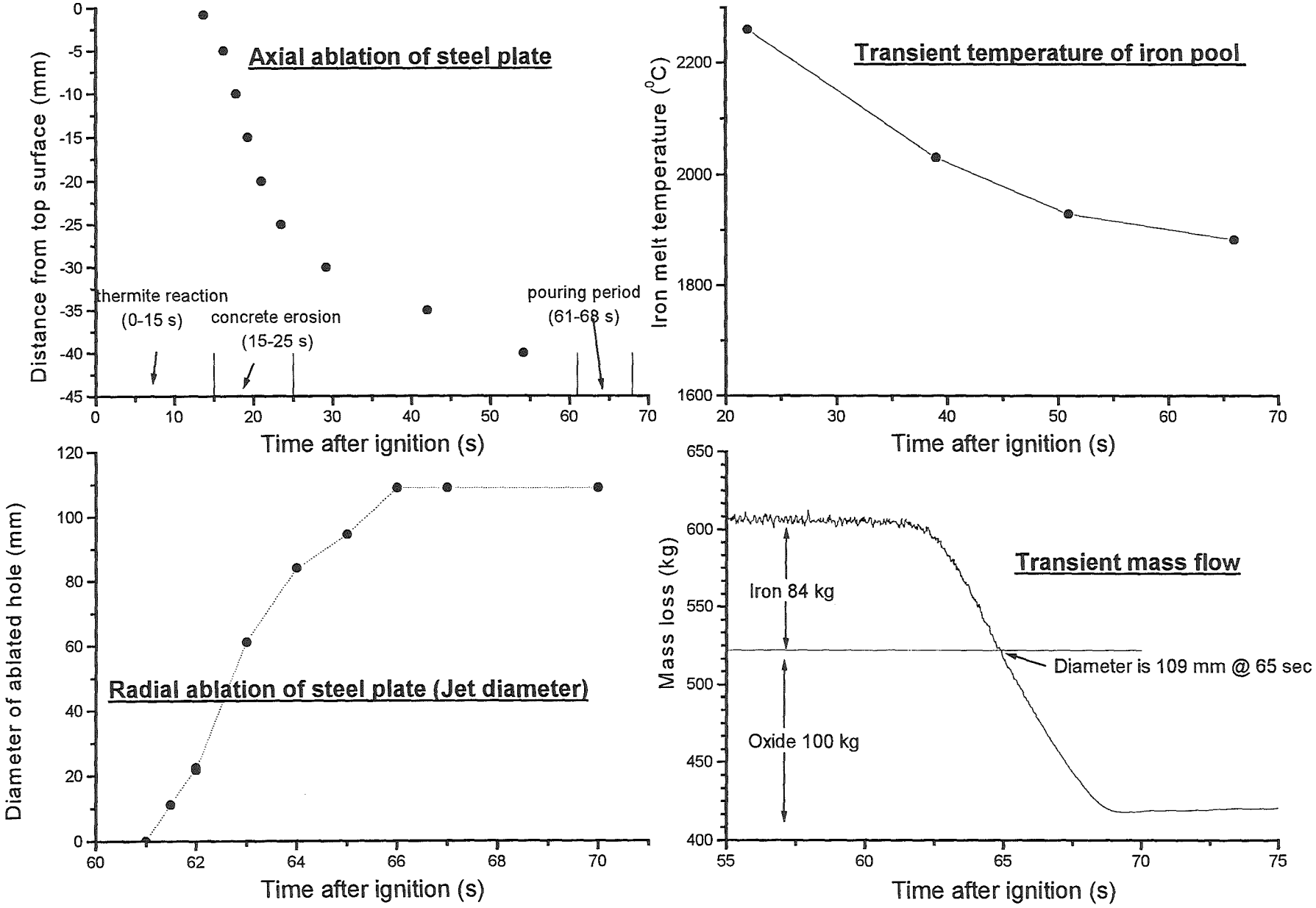

Fig. 5 Steel gate ablation in KAPOOL-9

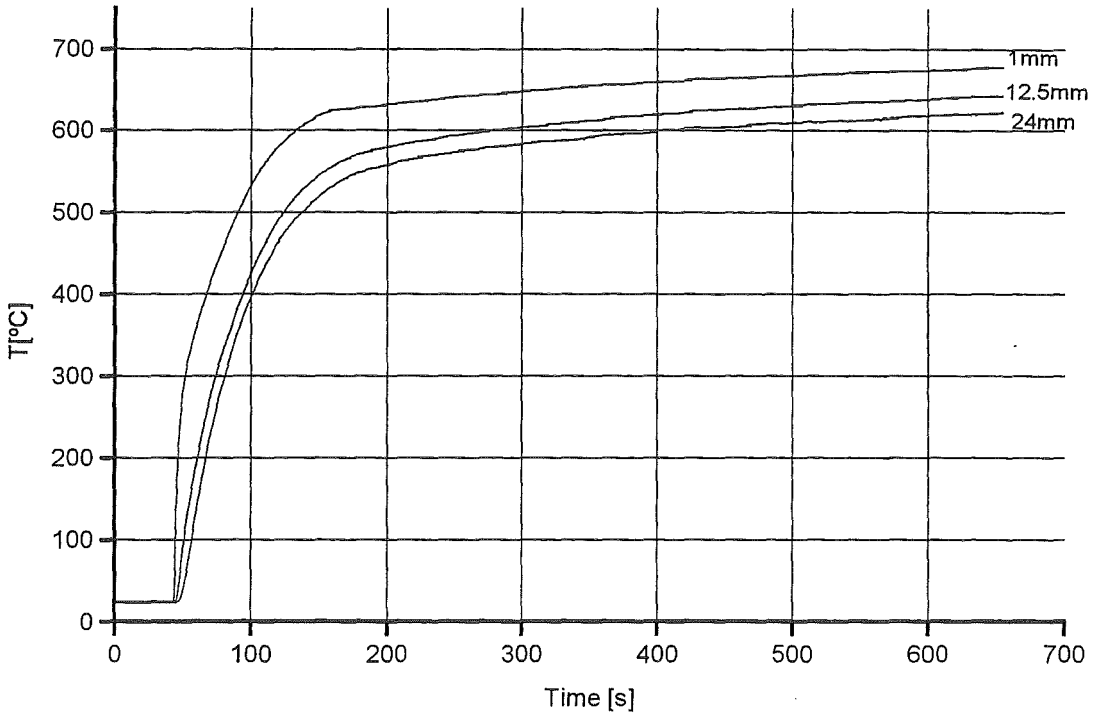

Fig. 6 Temperature transients in KAPOOL-11 at three vertical positions in the center of the steel plate (1mm under the contact surface, middle plane (12.5 mm) and bottom of plate (24 mm)

Session B 1:

PHENOMENA TO ACHIEVE COOLABILITY: NATURAL CONVECTION HEAT TRANSFER WITH BUBBLING

Chairman: V. Gustavson

THERMAL HYDRAULIC PHENOMENA IN CORIUM POOLS FOR EX-VESSEL SITUATIONS : THE BALI EXPERIMENT.

Jean Michel Bonnet

CEA Grenoble DRN/DTP/SETEX
17, rue des Martys
38054 Grenoble Cedex 9 France
Phone : (+33) 4 76 88 97 17 Fax : (+33) 4 76 88 52 51
E-mail : bonnet@dtp.cea.fr

Key word

Severe Accidents, Heat Transfer, Corium Pool, Gas Sparging

Abstract

This work concerns ex-vessel situations (with and without gas injection and for variable viscosity) and describes experimental results on heat transfer that have been obtained recently on BALI facility. After a description of the facility, results are presented and compared with existing heat transfer correlations.

Introduction

In the unlikely event of severe accident, in order to minimize the environmental consequences, the retention of molten core material in the vessel or at least in the containment is an important objective. Considering different severe accident scenarios, it appears that the heat flux distribution at the boundaries of molten material is one of the key parameters which influences directly the retention capability for both in-vessel and ex-vessel situations.

In that framework, the BALI program has been designed at CEA/Grenoble with FRAMATOME and EDF funding to improve the knowledge of heat flux distribution at corium pool boundaries. In a first time, in-vessel configurations with homogeneous or stratified pools have been considered to investigate the risk of vessel failure [1]. More recently, the program was focused on ex-vessel configurations to simulate :

- the interaction between molten corium and concrete (MCCI), situation in which concrete decomposition gases enhance significantly the heat transfer.
- the interaction between corium and ceramic which can be observed in a latest phase for the core catcher concept developed in the frame of EPR project.

The objective of this work is to quantify heat transfer coefficients at pool boundaries considering for homogeneous pool different cooling conditions, pool viscosity effects and effects related to superficial gas velocity.

Description of the facility

In the frame of severe accident studies, the use of simulant materials is the easiest way to perform large scale experiment. Nevertheless, it requires special cares to respect the dimensionless parameters of the investigated physical phenomena and the boundary conditions of reactor cases. Regarding natural convection heat transfer mechanism with volumetric heating source, three main dimensionless parameters have to be respected : the Prandtl number, the pool aspect ratio and the internal Rayleigh number.

$$\mathrm{Pr} = \frac{\upsilon}{\alpha} \quad e = \frac{H}{R} \quad Ra_i = \frac{g\beta Q H^5}{\lambda \upsilon \alpha}$$

The design of a rectangular slice test section at scale 1:1 respects the aspect ratio of the pool. Moreover, it is the only way to respect the internal Rayleigh number, due to the exponent five affecting the pool height. The use of a more convenient slice geometry introduces nevertheless a 2D aspect that has to be discussed. Dimensions of test section are about 3m long, 50cm height and 15cm wide. Transparent front and back windows permit flow visualizations. For ex-vessel situations, the Prandtl number depends strongly on corium composition. When the weight fraction of decomposition concrete oxides increases the viscosity increases. By using water with different weight fraction of cellulose compound as simulant fluid we can vary the viscosity of the pool independently from other physical properties. In this way, the Prandtl number can vary in a range from 5 to 3000. Regarding the additional convection mechanism induced by the gas sparging for MCCI, the use of water solutions respects the order of magnitude of the Laplace constant. As a consequence, same range of superficial gas velocity has been used to reproduce similar void fraction in the pool. A range from 1 to 20 cm/s for superficial velocity takes into account different concrete compositions and different phases of interaction corresponding to different ablation rates.

In the BALI program, the stress is put also on the respect of boundary conditions : residual power, uniform wall temperature or quasi-adiabatic condition and gas injection through the lower wall. By using salted water solution in a rectangular shape test section, the residual power was simulated by direct volumetric current heating from two electrode grids considering the fluid itself as a resistor. In order to reproduce the uniform cooling conditions induced by the presence of solid crust, ice crusts were produced at pool boundaries from heat exchanger cooled at low temperature, generally –60°C. For corium-ceramic interaction, the interface temperature is close to the maximum pool temperature because the thermal conductivity of the ceramic is small. It leads to a quasi adiabatic boundary condition simulated by the use of thermal insulation at the bottom of the pool and by the stop of coolant flow rate in the lower heat exchanger. Top, lateral and bottom heat exchangers were used simultaneously or independently to represent different cooling conditions.

The most challenging boundary condition was to obtain homogeneous gas injection simultaneously with ice crust formation. It has been made possible by using a multi-porous-layers plate welded on the active surface of the low temperature heat exchanger. In this way, by injecting gas during the freezing of water solution homogeneous repartition of micro- gas channels in the ice crust has been observed. The gas was released from upper heat exchanger through the 1cm gap created between heat exchanger and front or back windows.

Regarding experimental procedure, special cares have been taken to avoid water entrance in porous medium before freezing. But the technology was fragile and unfortunately the covered parameters range has been reduced by a premature destruction of the porous plate.

For each test, pool temperatures, heat flux distributions, void fraction distribution and tests parameters (coolant temperature and coolant flow rates, dissipated power and gas flow rates) were recorded.

The temperature distribution was measured from thermocouples uniformly implemented in the middle plane of the test section. Average heat flux values were obtained for each heat exchanger from classical thermal balances. The heat flux distributions at the lateral and bottom pool boundaries were deduced from measurement of temperature differences in the heat exchanger wall or by measurement of both ice crust thickness and ice temperature differences. The advantage of this latter method is to be more accurate for the lowest heat fluxes which have been achieved.

Test Results

The description of the test results is split in two parts making a distinction between tests without and with gas injection. The results presented hereafter are measurements corresponding to steady state regime. They are obtained from averaging data over 30 mn to 60 mn periods when steady state criteria (regarding global thermal balance and pool temperature evolutions) are satisfied.

Tests without gas injection

Tests without gas injection have been performed in a rectangular shape test section: 2.9m long, 15cm wide and 0.4 to 0.5m high depending on the ice crust thickness or on the presence of thermal insulation. For the tests with cooling only by the top, a 10 cm and a 10 mm thick PVC plates were added respectively at the surface of bottom and lateral heat exchangers and their coolant flow were stopped.

In this test campaign, 9 tests have been performed with different cooling conditions and different pool viscosities according to the following test matrix :

- Three different cooling conditions were investigated : -pool cooled only from the top by change of state at 0°C, -pool cooled from the top and from lateral wall by change of state at 0°C and -pool uniformly cooled by change of state at 0°C
- For each cooling conditions tests were performed for three different pool viscosities. The viscosity is increased about 10 to 100 times by addition of hydroxyethylcellulose (HEC) in water. As the salinity of HEC solutions was enough for direct current heating no additional salt was required. As the viscosity of HEC solutions depends on temperature, the following table gives order of magnitude of absolute viscosities and Prandtl numbers.

Solutions	Viscosity at 20°C	Prandtl at 20°C
V1 : water + $ZnSO_4$ ~1.3 g/l	$\mu = 1$ mPa.s	$Pr = 7$
V10 : water + HEC QP3L ~2%	$\mu = 26$ mPa.s	$Pr = 180$
V100 : water + HEC QP40 ~3%	$\mu = 340$ mPa.s	$Pr = 2400$

- For each test, the injected power was adjusted to control the maximum pool temperature. The nominal power values ranged from 5 to 15 kW

General observation

The situation where only the top of the pool was cooled is similar to the situation described by Kulacki Emara [5]. The observation of the flow pattern shows thermoconvective instabilities below the ice crust with wave lengths about 1cm. Coalescence of small

instabilities induces large scale motions with velocity of about a few cm/s which form large unstable convection cells with a radius close to the height of the cavity. These observations are consistent with the phenomenology described in the Bernaz's thesis [2,3].

The addition of lateral cooling creates a falling down boundary layer flow which impacts the bottom of the pool and spreads along the lower wall. This flow induced more instability in the large scale motion. In case of bottom cooling and for small viscosity, the local reduction of ice crust thickness is explained by this cold tongue spreading along the lower plate which increases locally the heat transfer coefficient. For higher viscosity the velocities are smaller and this effect is reduced (see figure 2).

Pool temperature distribution

Due to the thermoconvective instabilities induced by the top cooling, the upper part of the pool is well mixed and uniform in temperature. Because of the important power extracted from the top, even for uniform cooling conditions, this upper area extend over 75% of the total height. The lower zone, stratified in temperature, is reduced. Regarding the temperature evolution at middle height versus the horizontal distance from vertical cooling wall, a small "radial" temperature gradient is reported less than 1°C/m.

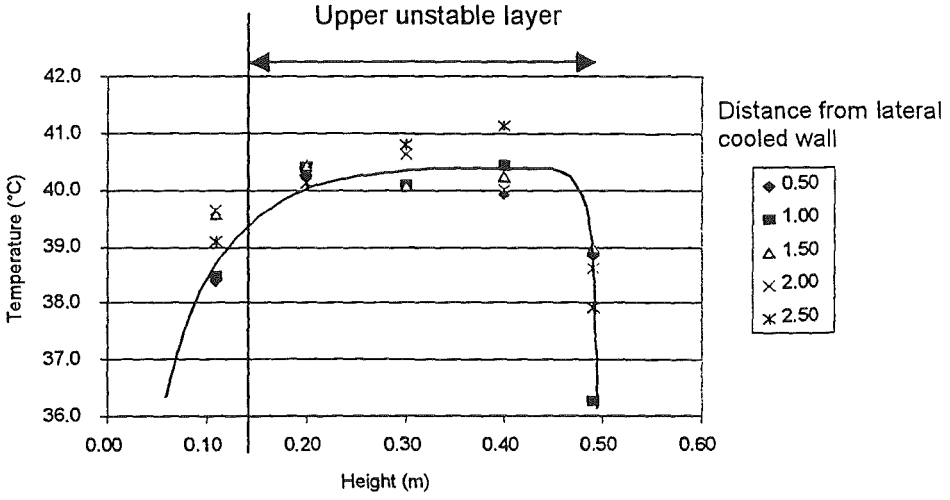

Figure 1 : Example of vertical temperature profile

Heat flux distributions

For the upward heat transfer, regarding the ice crust thickness which is uniform we conclude that the heat flux is also uniform. Results reported from COPO experiments [4] or from analyses of the heat transfer mechanism described in [2,3] support this conclusion. Furthermore, as the wave lengths of the thermoconvective instabilities, which control the heat transfer, are 10 times smaller than the test section width we can conclude that 2D results can be directly extrapolated to 3D reactor cases.

For the bottom wall, because the heat fluxes are smaller here, the best way to measure these heat fluxes was to use measurements of the ice crust thickness and measurements of the temperature difference between both sides of the ice layer. For V1 test, higher heat fluxes are observed on the first meter from the lateral cooled wall (see figure 2). This is due to the effect of the vertical cold boundary layer which impacts the lower wall and creates a cold tongue spreading on the bottom ice crust.

This phenomenon induces higher local heat transfer coefficients and consequently greater heat fluxes. For higher viscosities, the fluid velocities are smaller and this effect is less important. For V10 and V100 tests, the heat flux distributions on the bottom plate are quite uniform.

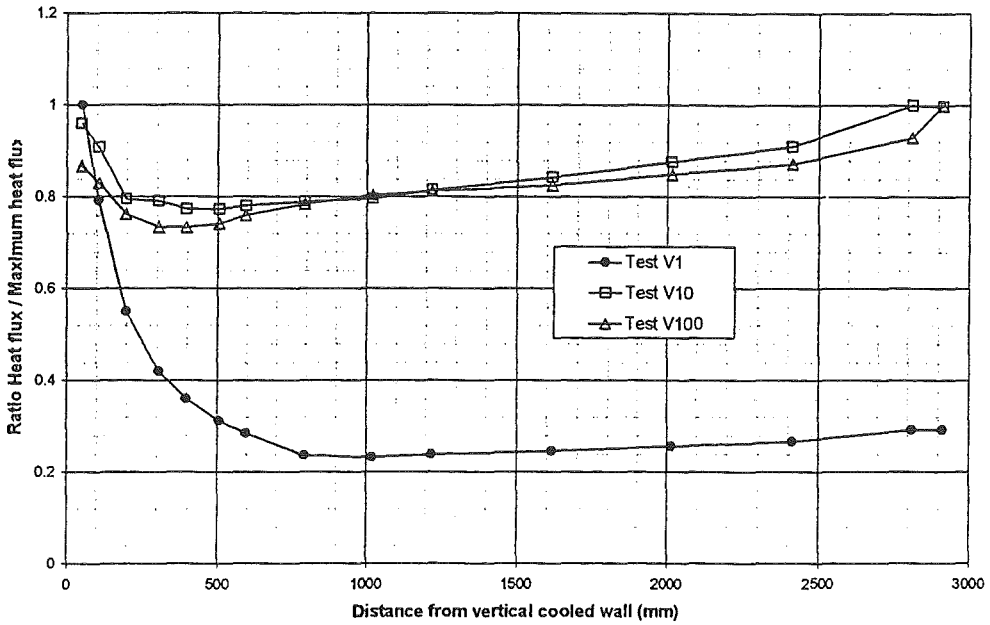

Figure 2 : lower wall heat flux profiles

Average heat transfer results

In order to compare our results with existing heat transfer correlations, we have plotted in figure 3 upward, lateral and downward Nusselt numbers as a function of internal Rayleigh number.

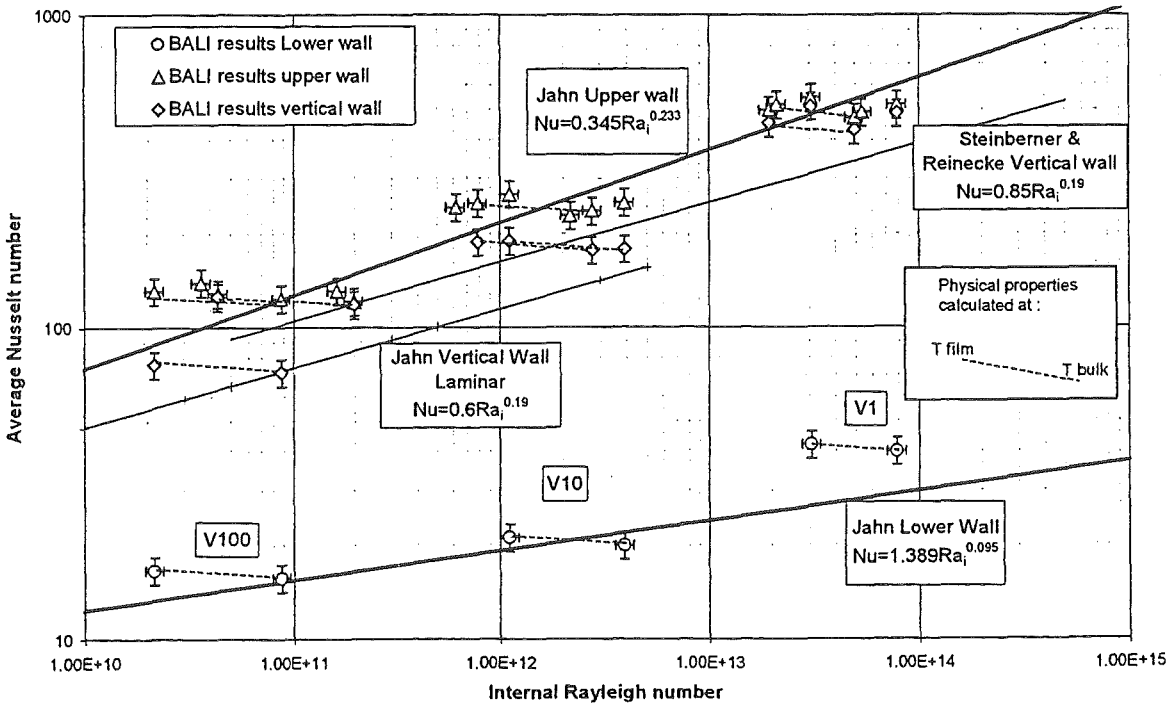

Figure 3 : Average Nusselt number as a function of internal Rayleigh number

Due to the large temperature differences observed in BALI experiment, the definition of the reference temperature for the calculation of physical properties involved in dimensionless numbers calculation is important. To check this effect, the physical properties of the fluid are calculated both at bulk pool temperature and at film temperature (at average temperature between bulk and wall temperatures). For each experimental point, both values are plotted. In figure 2, the BALI results are compared with Jahn, Steinberner and Reinecke's [6] heat transfer correlations. These correlations have been validated up to $Ra_i \leq 10^{+14}$ with experimental results obtained in a rectangular volumetric heated square cavity (800 mm in height and 35 mm in wide).

A good agreement is observed for upper and lower walls. For V1 test, the discrepancy observed for the lower wall can be explained by the effect of the cold tongue, previously described which induced a larger heat transfer coefficient over the first 30% of the plate length. If we consider only the heat flux values in the non affected area, the Nusselt number is 20% smaller and agrees better with Jahn's correlation. For vertical wall, the results obtained for V1 tests are 20 to 40% greater than Nusselt numbers calculated with vertical wall Steinberner & Reinecke's correlation. Regarding the effect of the reference temperature, a better agreement is observed when dimensionless parameters are calculated at bulk temperature.

The BALI tests have been performed at different viscosities, to observe the effect of Prantld number on heat transfer mechanisms. For the upper wall, the heat transfer mechanism has been extensively described in [2,3] and it is normal to observe that the results do not depend on Pr number. For the lower wall, if we compare our results with Jahn's or Steinberner's pure water results we can conclude also that results do not depend on Pr number.

For vertical wall, the average Nusselt numbers are also plotted in figure 4 as a function of external Rayleigh number (based on bulk-wall temperature difference) and compared with Chawla and Chan's correlations [7].

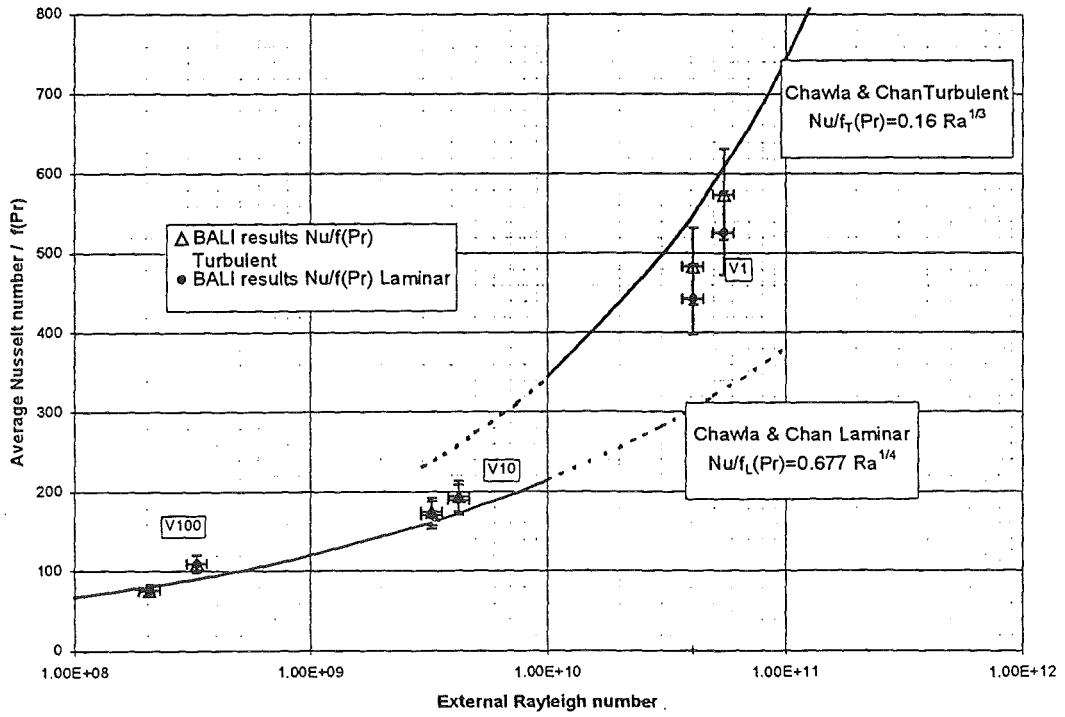

Figure 4 : Average vertical Nusselt number as a function of external Rayleigh number

Because a function f(Pr) appears in both laminar and turbulent expression of Chawla and Chan's heat transfer correlations, we have not plotted directly the average Nusselt number. We have plotted the average Nusselt number divided by $f_T(Pr)$ for turbulent regime or $f_L(Pr)$ for laminar regime. Moreover, to be consistent with Chawla's definition, the reference temperature for the calculation of physical properties is the film temperature.

In this way, we can observed in figure 4 the transition between laminar and turbulent regime which is consistent with the simple criteria $Gr \sim 10^{+9}$. Since $f_T(Pr)$ and $f_L(Pr)$ tends towards 1 when Prandtl number increases, these correction factors (13% for V1 tests) are less important for tests performed at elevated viscosity. Because of the succession of laminar and turbulent boundary layer regimes, the experimental average Nusselt value for V1 test is smaller than Nusselt number calculated for pure turbulent regime.

Tests with gas injection

Tests with gas injection have been performed in a rectangular test section: 2.4m long, 15cm wide and 0.5m high. The test section was cooled from the top and from the bottom by change of state at 0°C. Three different pool viscosities were investigated by using V1, V10 and V100 solutions. The gas was injected through the bottom ice crust with superficial velocities ranging from 1cm/s to 20 cm/s. Unfortunately, due to the premature mechanical rupture of the gas injection porous plate, the superficial velocity range was limited from 1cm/s to 5cm/s except for V100 test.

General observation

The gas injection induces greater liquid velocities and consequently enhances greatly the heat transfer. Void fraction was not homogeneous in the pool : unstable cells were observed with two phase flow chimneys and single phase returning paths.

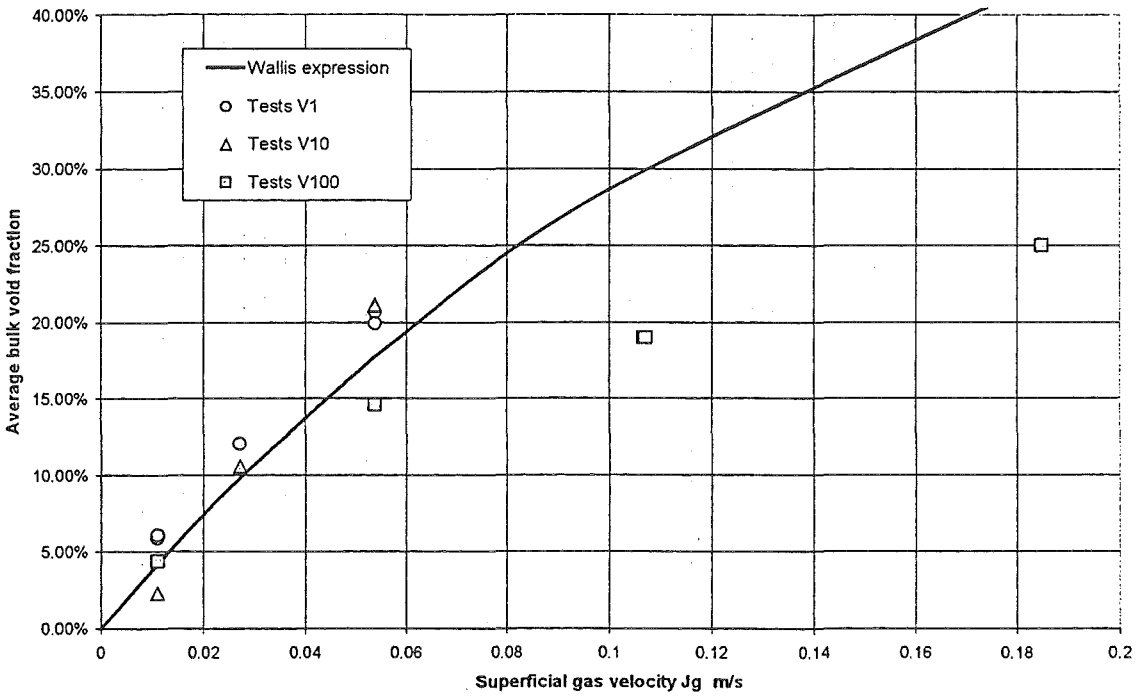

Figure 5 : Average void fraction in the bulk

The pool was very agitated and consequently the pool temperatures are uniform. Regarding ice crust on lower or upper wall, even if its "roughness" may be more important than for single phase tests we conclude that the heat flux distribution on wall surfaces is uniform. For elevated viscosity and elevated gas superficial velocities, we have observed quite large gas accumulations under the upper heat exchanger which remained nevertheless flooded. The experimental average void fractions in the bulk agree quite well with the values calculated from the Wallis expression in churn turbulent regime [13] except for elevated viscosity and elevated gas superficial velocities (see figure 5).

Wallis void fraction expression $A = \dfrac{1}{C_0 + \dfrac{U_\infty}{Jg}(1-A)^n}$. For churn turbulent regime n=0 and with C_0~1 this expression becomes $A = \dfrac{1}{1+\dfrac{U_\infty}{Jg}}$. Terminal velocity $U_\infty \approx 1.53\left(\dfrac{g\sigma}{\rho_l}\right)^{1/4}$.

Average heat transfer results

In order to compare our results with existing heat transfer correlations or recent results obtained by Bilbao y Leon and Corradini [12], upper and lower heat transfer coefficients as a function of superficial gas velocity have been plotted on figure 6.

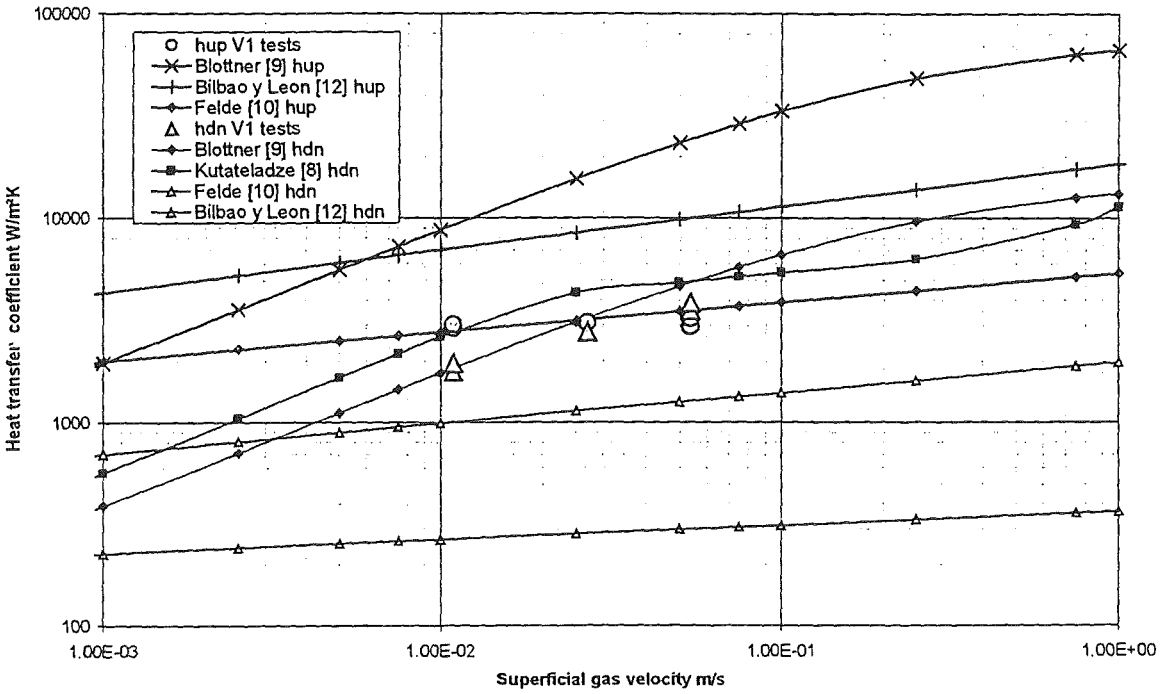

Figure 6 : Heat transfer coefficients comparison for V1 tests μ~1.5 mPa.s

Large discrepancies between the different calculated heat transfer coefficients are observed. Downward heat transfer coefficients for V1 tests agree reasonably well with Blottner [9] or Kutateladze [8] downward correlations. Regarding upward heat transfer coefficients, our results agree well with Felde's [10] upward correlation. When we compare downward and upward measured heat transfer coefficients, it is concluded that they are

similar. This result is very different than that obtained from Blottner's correlations [9], Felde's correlations [10] or more recently by Bilbao y Leon's [12] For these authors, upward heat transfer is respectively 5 times, 2.8 times and about 10 times higher than downward heat transfer.

N.B. : As the correlations presented by Felde [10], correspond to pure water tests with superficial velocities lower than 4 mm/s, we performed comparison with extrapolated correlation.

Blottner derived heat transfer correlations for bottom, vertical and upper surfaces, but he mentioned that this recommended heat transfer coefficients are probably no better than a factor two of the correct results and in some cases only within an order of magnitude. Moreover, the upper heat transfer correlation given by Blottner is valid for a liquid-liquid interface which is certainly very different from a liquid and porous crust interface.

The difference with Bilbao y Leon's results are more puzzling. For the moment, we can just mention that experimental conditions for gas injection are similar. Differences in heat transfer appear just for the upper plate; in our case the plate is not drilled and so the gas escapes only by the sides. Pure hydraulic support tests have been performed. It is observed through transparent upper plates drilled or not that gas accumulation show similar behavior in respect to bubble repartition.

Since results are not presented in dimensionless coordinates, two additional figures corresponding respectively to V10 and V100 mixtures are presented. The Bilbao y Leon's upward heat transfer correlation plotted in figure 7 or 8 corresponds to the viscous fluid correlation (validity range from 10 to 200 mPa.s).

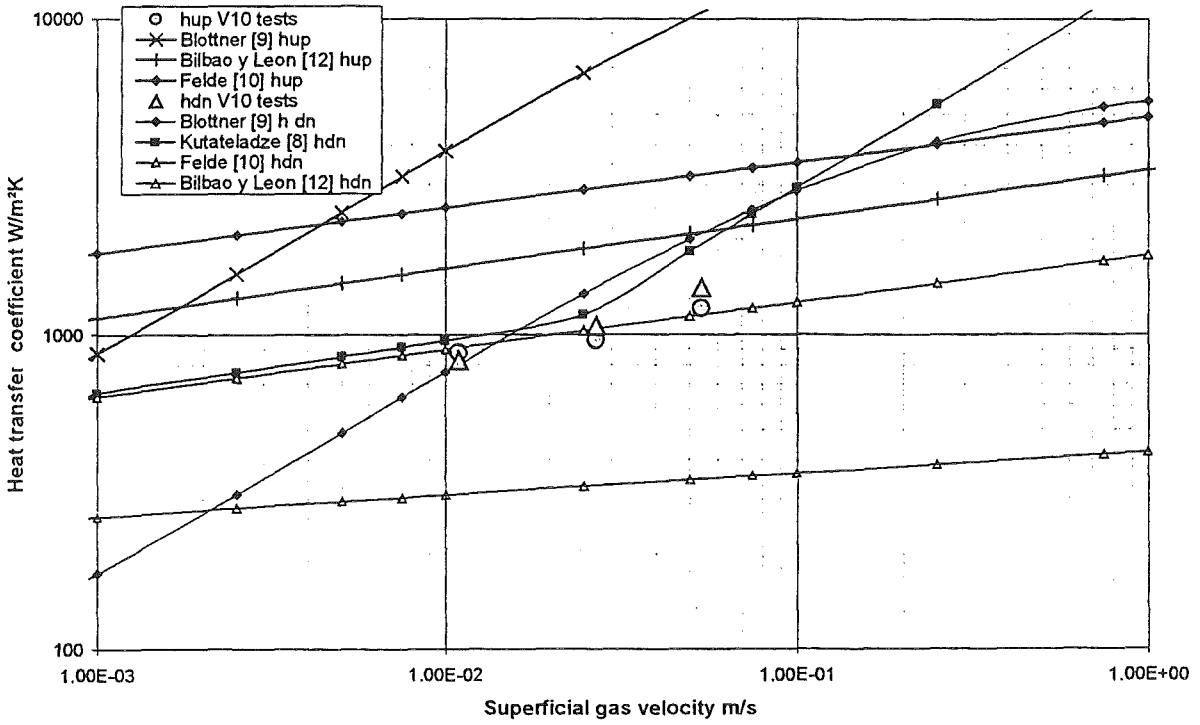

Figure 7 : Heat transfer coefficients comparison for V10 tests μ~23 mPa.s

At elevated viscosity, for V10 and V100 tests, measured downward and upward heat transfer coefficients are still similar. The V10 results agree relatively well with Blottner's, Kutateladze's, or Felde's downward heat transfer correlations. For V100 tests, the

differences are more important. However, the slope of our results (h versus j_g) are similar to those of Felde's or Bilbao y Leon's correlations.

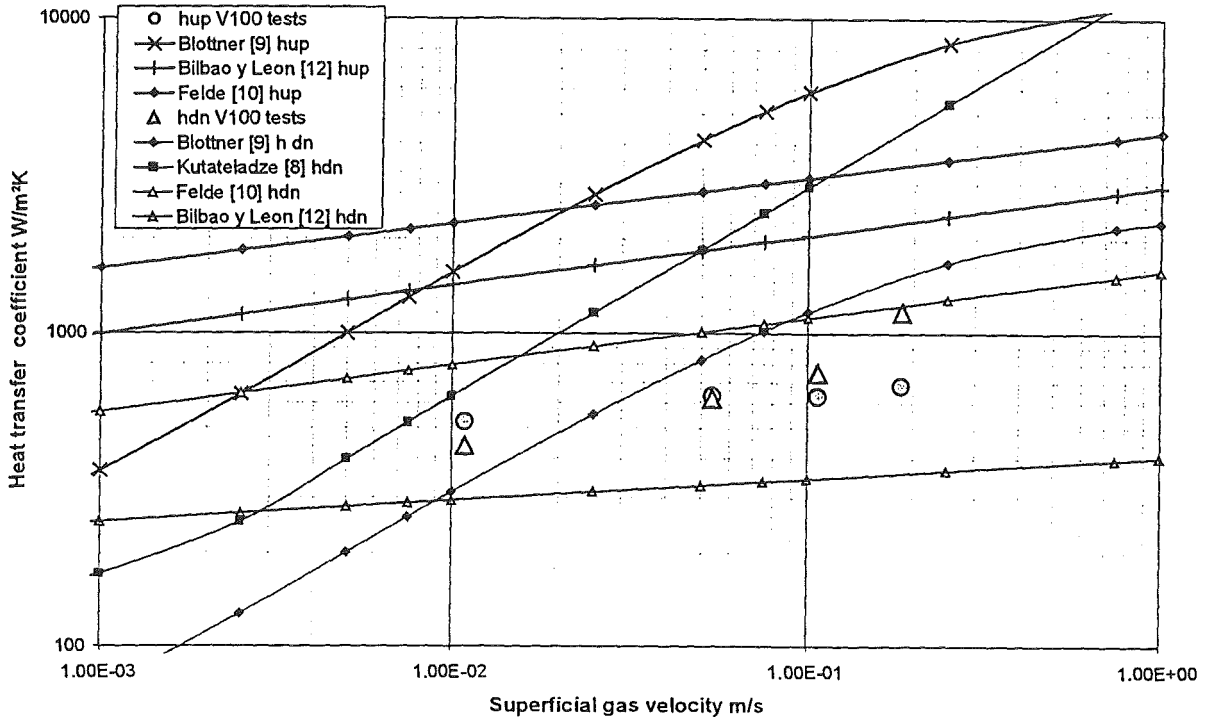

Figure 8 : Heat transfer coefficients comparison for V100 tests μ~320 mPa.s

The measured power split, which is defined by the ratio between power extracted from the top and total dissipated power, has been plotted as a function of superficial velocity in figure 9.

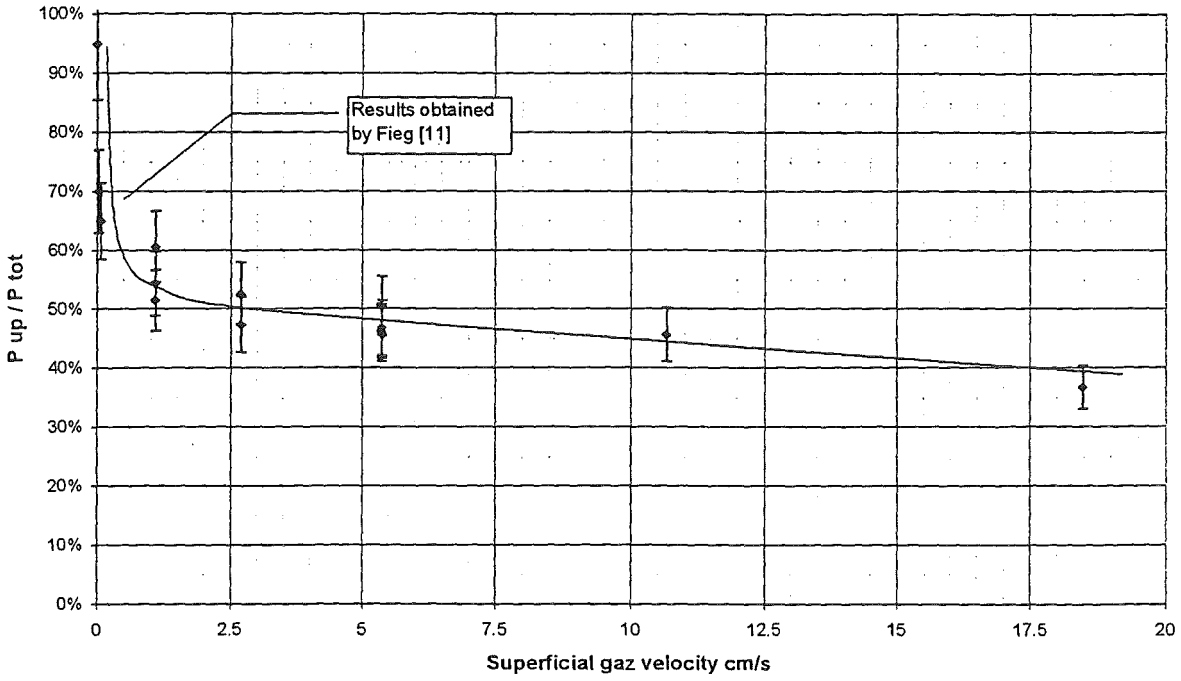

Figure 9 : Power split as a function of superficial gas velocity

We have included in this graph the power split obtained for test without gas : it ranges from 90% to 96% respectively for $Ra_i=10^{+11}$ to 10^{+14}. The power split decreases when superficial gas velocity increases. This trend has been already reported by Fieg [11] for smaller superficial gas velocities. The effect of viscosity which is taken into account in the indicated dispersion is not significant, at least up to J_g=5 cm/s. For elevated superficial gas velocities, the accumulation observed under the upper heat exchanger for V100 tests leads to the conclusion that power split may be dependant on the gas evacuation thus on the geometry of the holes in the upper boundary. If the accumulation of gas does not represent an additional heat transfer resistance, we can conclude that power split tends towards 50% when superficial gas velocity increases.

Conclusion

Regarding single phase tests, our results agree quite well with Jahn, Steinberner and Reinecke's correlations. No influence of viscosity is seen except for heat transfer on the lateral surface where we have observed indirect effect with classical transition between laminar and turbulent boundary layer regime. This transition and absolute lateral heat transfer coefficients are in good agreement with Chawla and Chan's correlations. The power split extracted from the top can reach 95% if the lateral wall is not cooled.

For MCCI configurations, large differences appear between existing correlations. From the small number of BALI experiments, our preliminary objective was not to establish new heat transfer correlations but to check, at large scale and with appropriate boundary conditions, the validity of existing correlations. Regarding absolute heat transfer coefficient values we conclude that the effect of pool viscosity is not correctly reproduced by the different correlations considered here.

On the base of our experimental investigation, we conclude that for J_g greater than 0.5cm/s the power split (W_{up}/W_{total}) is about 50% and in first approximation it does not depend significantly on superficial gas velocity or on pool viscosity. The origin of difference with the 80 to 90% reported by Bilbao y Leon has to be investigated. Nevertheless, regarding MACE M3B results, the power split seems to be about 50% during the period where the pool was maintained in contact with the crust.

Acknowledgement

This work has been performed in the frame of CEA, EDF and FRAMATOME agreement.

Nomenclature

h = heat transfer coefficient **Nu** = Nussel number, $\frac{hH}{\lambda}$ **Power split** = $\frac{W_{up}}{W_{total}}$

Ra = external Rayleigh number, $\frac{g\beta\Delta TH^3}{\nu\alpha}$ **Gr** = Grashoff number, Ra/Pr

Ra_i = internal Rayleigh number, $\frac{g\beta QH^5}{\nu\alpha\lambda}$ **Pr** = Prandtl number, ν/α

f_T(Pr) = Chawla's f(Pr) for turbulent regime, $\left(1+\left(0.492/Pr\right)^{9/16}\right)^{-16/27}$

f_L(Pr) = Chawla's f(Pr) for laminar regime, $Pr^{1/4}\left(20/21+Pr\right)^{-1/4}$

J_g = superficial gas velocity A = void fraction

References

1- Bonnet J.M., Seiler J.M., 1999. "Thermal hydraulic phenomena in corium pool : the BALI experiment", ICONE 7057, (ICONE 7) Tokyo, Japan, April 19-23, 1999

2- Bernaz L., 1998. "Etude du transfert de chaleur à la frontière supérieure d'un bain fluide avec dissipation volumique de puissance" *Thèse USMG de Grenoble*, février 1998

3- Bernaz L., Bonnet J.M., Seiler J.M., 1999,"Investigation of Natural Convection Heat Transfer to The Cooled top boundary of a heated pool", (NURETH-9) San Francisco, California, October 3-8, 1999.

4- Helle, M., Kymalainen, O., Pessa, E., 1997, COPO II-Lo Experiments, IVO Power Engineering LTD, YDIN-GT1-43. Transmitted in the frame of the MVI Project, 4th PCRD of the European Community.

5- Kulacki E.A., Emara A. A., 1975."High Rayleigh number Convection in enclosed fluid layers with internal heat sources", U.S. NRC, NUREG-75/065, 1975

6- Steinberner, U. , Reineke H.-H., 1978, "Turbulent Buoyancy Convection Heat Transfer with Internal Heat Sources" Proceedings of 6th International Heat Transfer Conference. Toronto Canada August 7-11,1978

7- Chawla, T.C., Chan, S.H., 1977, " Heat Transfer from Vertical/Inclined Boundaries of Heat Generating Boiling Pools ", In. J. Heat Mass Trans., 20 (5), pp 499-506.

8- Kutateladze S.S., Malenkov I.G., 1978. "Boiling and bubbling heat transfer under the conditions of free and forced convection" 6th Int. Heat Transfer Conference Toronto pp 281-286 (1978)

9- Blottner F.G.,1979. "Hydrodynamics and heat transfer characteristics of liquid pools with bubble agitation" NUREG/CR-0944 SAN79 1132 R3

10- Felde D.K., Kim H.S., ABDEL-KHALIK S.I., 1979. "Convective heat transfer correlations for molten core debris pools growing in concrete.

11- Fieg G., 1976. "Experimental investigations of heat transfer characteristics in liquid layers with internal heat sources" Proc. Meeting Fast Reactor Safety and Related Physics, Chicago IL VIV p2047 (1976)

12- Bilbao y Leon R.M., M.L. Corradini, 1999. "Solid particle effects on heat transfer in a molten pool with gas injection" ", (NURETH-9) San Francisco, California, October 3-8, 1999.

13- Handbook of multiphase systems Mc Graw-Hill Void fraction Chap 2.3

OECD Workshop on Ex-Vessel Debris Coolability
Karlsruhe, Germany, 15-18 November 1999

Organised in collaboration with
Forschungszentrum Karlsruhe (FZK) GmbH

SOLID PARTICLE EFFECTS on HEAT TRANSFER in MULTILAYERED MOLTEN POOLS with GAS INJECTION

Rosa Marina Bilbao y León and **Michael L. Corradini**
Nuclear Safety Research Center
Department of Engineering Physics
University of Wisconsin - Madison
1500 Engineering Drive
Madison, WI 53706
Phone: 608-265-2337; FAX: 608-262-6400
http://silver.neep.wisc.edu/~NSRC
sam@loca.neep.wisc.edu corradini@engr.wisc.edu

ABSTRACT

In the very unlikely event of a severe reactor accident involving core melt and pressure vessel failure, it is important to identify the circumstances that would allow the molten core material to cool down and resolidify, bringing core debris to a coolable state. To achieve this, it has been proposed to flood the cavity with water from above forming a layered structure where upward heat loss from the molten pool to the water will cause the core material to quench and solidify. In this situation the molten pool becomes a three phase mixture: e.g., a solid and liquid slurry formed by the molten pool as it cools to a temperature below the temperature of liquidus, agitated by the gases formed in the concrete ablation process. The present work quantifies the partition of the heat losses upward and downward in this multi-layered configuration, considering the influence of the viscosity and the solid fraction in the pool, from data obtained from an intermediate scale experimental facility that has been developed at the University of Wisconsin - Madison. Recent experimental results showing the heat transfer behavior for multi-layered pools with various viscosities and solid fractions are presented.

1. INTRODUCTION

In the design of the new generation of nuclear reactors and in the safety assessment of currently operating nuclear power plants, it is necessary to evaluate the probability of experiencing a severe accident and to identify the strategies to follow in order to mitigate the possible consequences. For example, in the unlikely event of a severe reactor accident involving core melt and pressure vessel failure, it is important to identify the circumstances that would allow the molten core material to cool down and resolidify, bringing core debris to a safe and stable state. In this type of postulated accident, the molten material which escapes from the reactor pressure vessel is expected to accumulate as a molten pool in the reactor cavity below. This material, usually called corium, is formed mainly by urania, zirconia, zirconium and stainless steel. The molten corium can thermally attack the concrete underneath and decompose it, producing gases which agitate the pool, enhancing heat losses to the boundaries as fission product decay

heat and chemical reactions continue to add energy to the process. To achieve coolability of the corium in this configuration it has been proposed to flood the cavity with water from above forming a layered structure where upward heat loss from the molten pool to the water will cause the core material to cool and solidify. The effectiveness of this procedure depends largely on the rate of upward heat loss as well as on the formation and stability of an upper crust. In this situation the molten pool can become a three phase mixture: the solid and liquid slurry formed by the molten pool cooled to a temperature below the temperature of liquidus, agitated by the gases formed in the concrete ablation process.

Because this process occurs at large scales and with materials whose physical properties are not well determined, the phenomenology involved is not completely understood. In addition, many of the currently most widely used models were not specifically obtained to simulate this phenomenology and do not always predict the experimental observations. Various attempts have been made to reproduce the problem experimentally by using either prototypic or simulant materials. Some of these are integral experiments that try to reproduce the entire scenario to pinpoint all the processes involved (Farmer et al., 1992) (Thompson et al., 1992), while others are separate effect studies focused on the more detailed analysis of very specific phenomena (Greene, 1982, 1988a, 1988b, 1991) (Felde, 1980). However, these approaches have always ignored the effects of solids within the molten pool and their impact on the apparent viscosity of the pool, as well as their effect on heat transfer.

The objective of this work is to quantify the heat losses upward and downward in this multi-layered configuration, as well as the corresponding heat transfer coefficients, considering viscosity effects, the solid fraction within the lower heated pool and the presence of an overlying solid layer. To complete this task, an intermediate scale experiment has been designed, in which simulant materials are used to model a molten pool with another liquid layer above. The design includes volumetric heating, gas injection from the bottom and solids within the pool.

2. THE EXPERIMENTAL TEST SECTION AND PROCEDURE

A diagram of the apparatus used in this study is displayed in Figure 1. It consists of a rectangularly shaped test section 6.5 in wide (16.51 cm), 8 in long (20.32 cm) and 16 in tall (40.64 cm), whose walls were made of 0.5 in (1.27 cm) thick Lexan. The fluid cell can be subdivided in two parts by insertion of a stainless steel wire mesh. The lower half of the pool holds the heating assembly, which consisted of two stainless steel electrodes, connected through a grid of high resistivity nickel-chromium heating wires wrapped into a spiral shape and connected to a DC Power Supply. Air was injected into the steel pressure box on the bottom and entered the pool through the bronze porous plate, which ensured a uniform bubble distribution in the pool.

On the top and bottom of the fluid cell there are two cooling assemblies, formed by two aluminum plates each. Machined into one of the plates was the cooling water channel, which had a double spiral water flow pattern designed to alternate the hot and cold legs of the flow, resulting in nearly isothermal cooling plates. In the bottom cooling assembly, these two plates were mounted together with the porous plate. Holes of 1/8 in (3.175 mm.) diameter were drilled in all the aluminum plates to allow for the injected air to go through.

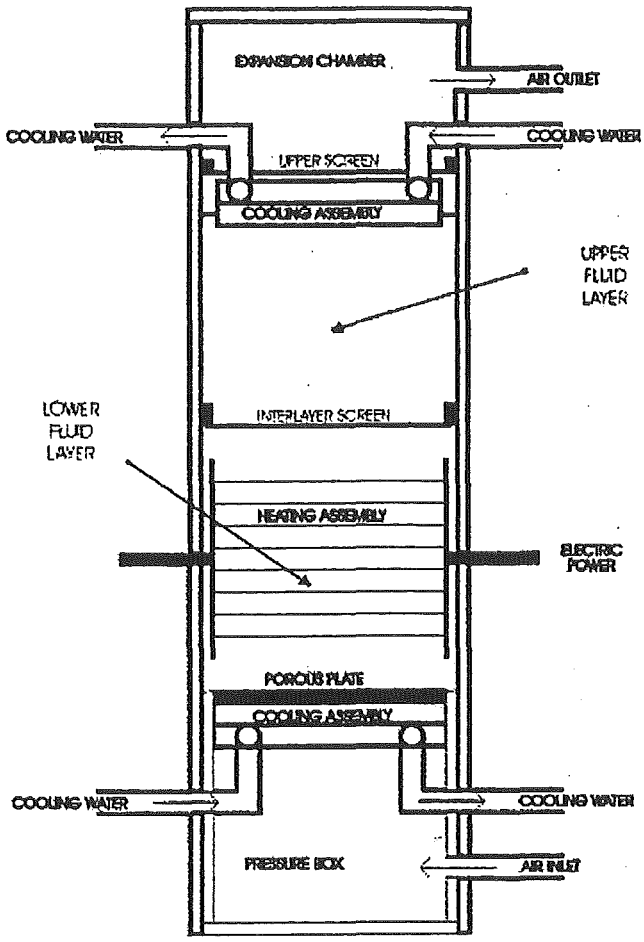

Figure 1. Schematic Diagram of the Test Section

The inlet and outlet cooling water temperature and the surface temperature in the cooling assemblies, the temperature of the pool at several heights and the inlet and outlet air temperature were measured with redundant E-type thermocouples. Flowmeters were used to measure the air and cooling water flow rates. The electrical power input by the DC power supply unit was measured by a digital multimeter and a DC current probe. The relative humidity of the inlet and outlet air was measured with a humidity and temperature transmitter. A DAS connected to a 486 PC was used to collect the voltage signals from all the thermocouples. Each data point is the result of recording 300 samples for each thermocouple at a sampling rate of 1 Hz. The simulant fluids used for this investigation were water, glycerin and white mineral oil. The solid particles were polystyrene beads, with an average size of about 0.020 in (0.5 mm), and a specific gravity of 1.04.

In order to include the effect of solids in a density stratified multi-layer configuration, it was necessary to devise a way of keeping the solids within the appropriate fluid layer. For that purpose, a stainless steel wire screen with mesh size small enough to stop the solid polystyrene beads was placed at the interface of the fluid layers. The light fluid in these tests was always low viscosity mineral oil. For the lower layer, water, a mixture of water and 10% in volume of polystyrene beads, 96% pure glycerine and a mixture of glycerine and 10% in volume of polystyrene beads were used. Only the lower layer was heated. In addition, it was of interest to simulate the effect of a

porous solid crust in between the fluids. Due to the adequate density ratio among the two fluids and the polystyrene beads, these tended to agglomerate at the interface of the fluids, and the desired configuration was achieved.

3. ANALYSIS OF THE EXPERIMENTAL RESULTS

Previous reports analyzed in detail the results of the other two series of experiments, the tests with one fluid layer (Bilbao y León et al., 1999b) and two fluid layers (Bilbao y León, 1999a). In this paper we focus on the tests involving three layers: two fluid layers with a solid interface in between.

Figure 2 shows the power split for these tests, where we observe a quite different trend from what was observed in two previous series of tests: the power split up/down has changed from 80/15 to about 60/35. This result is not surprising because of the effect of inserting the wire mesh, which collects the solid particles as a crustal layer which obstructs the process of heat and mass transfer at the interface by severely limiting the surface renewal and entrainment processes. Therefore, the increase in thermal resistance for the heat transfer upward results in a proportional increase in the fraction of the heat transferred downward. Applying this observation to the MCCI phenomenology, one may deduce that even if a full size solid crust does not form at the interface between the molten pool and the coolant, the existence of a very porous layer would substantially hinder the upward heat transfer. As for the influence of viscosity and solid fraction on the power split, we observe that the fraction of power being transferred downward is slightly larger for glycerine and its suspensions (pink symbols) than for water. This trend makes sense because as the fluid gets more viscous the screen creates a more significant obstruction to the flow and the heat transfer.

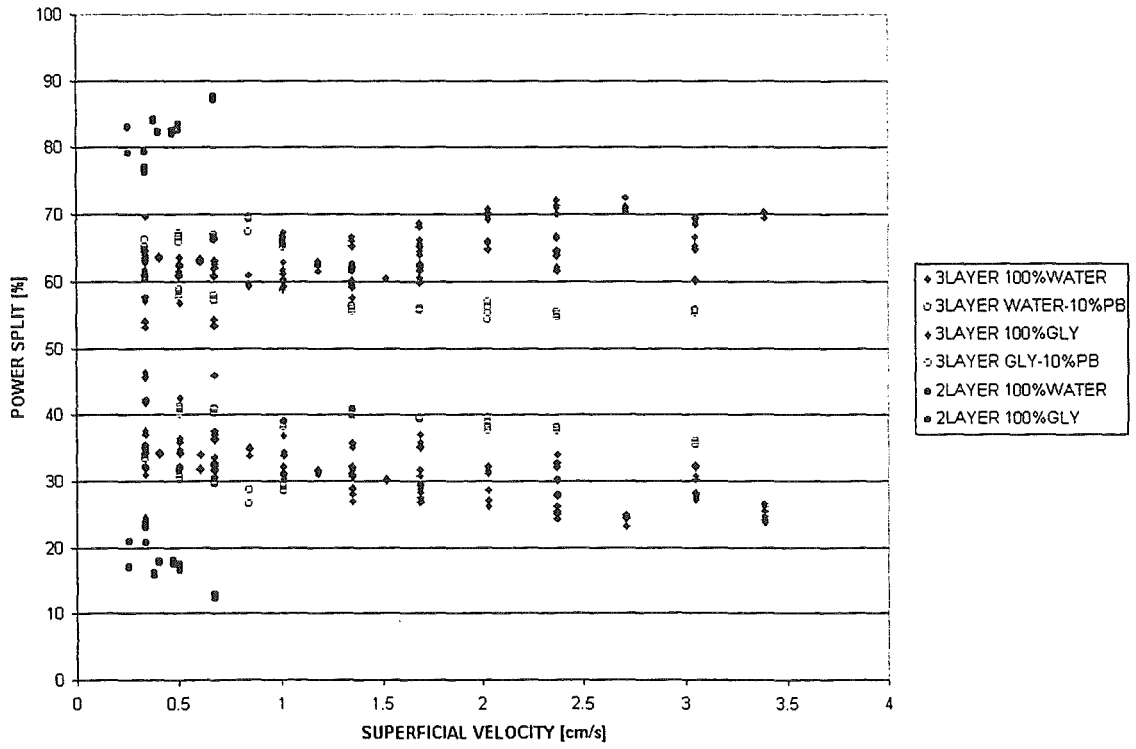

Figure 2. Power Split for all the three layer tests[1].

[1] The results for the two layers tests have also been plotted for comparison purposes

When analyzing the heat transfer coefficients (HTC), the same trends as in single layer tests were observed: overall, the HTC increases with the superficial gas velocity of the injected air and decreases with the viscosity of the fluid mixture in the lower part of the pool. No first order effect on the HTC has been detected as a direct consequence of the presence of solids in the pool, only the effect resulting from the increase in the effective viscosity due to the solids in the pool.

However, if we look at the results more closely, one observes that as the viscosity of the pool increases, the heat transfer coefficients decreases. In addition, the heat transfer coefficient decreases as the fluid in the pool changes to a different fluid of higher viscosity, but it increases as the viscosity of the pool increases for a given fluid within the pool. We explain this behavior by coupling together all the phenomena happening in the pool simultaneously: as the superficial gas velocity increases, the temperature of the pool decreases due to the improvement in the heat transfer by the agitation of the pool. At the same time, the overall viscosity of the pool increases because of the descent in temperatures, which in turn induces a decrease in the heat transfer coefficient. Furthermore, the void fraction in the pool increases with the superficial gas velocity, inducing a descent in the effective three phase viscosity of the suspension. This means that the viscosity and the superficial gas velocity induce opposite effects on the heat transfer.

Several attempts were made in order to quantify this phenomenon. First, the effective three phase viscosity of the pool, i.e. including the effect of the solids *and* the void fraction was estimated. Since no model was found in the literature to estimate the viscosity of this three-component three-phase mixture, a classical approach was taken. The suspension formed by the fluid with the solid particles was assumed to be a homogeneous fluid whose viscosity was given by Thomas equation (Seiler et al., 1996) and the overall effective viscosity of the pool was estimated as

$$\mu_{3\Phi} = \alpha \cdot \mu_{air} + (1-\alpha) \cdot \mu_{2\Phi} \tag{1}$$

where α is the average void fraction in the pool, which can be calculated using the well known drift flux model. However, this approach failed to agree with the trends found experimentally. A more successful approach was to find a way of expressing the heat transfer coefficient as a dimensionless combination of the parameters that we considered most significant to describe the phenomenology:

$$h = f(\mu_{2\Phi}, j_{sup}) \tag{2}$$

This HTC should be directly proportional to the superficial gas velocity, because we expect an increase of the HTC when j_{sup} increases. At the same time, the HTC will be inversely proportional to the viscosity of the pool, since the HTC will become smaller as the viscosity increases. Using the theorem Π for dimensionalization, we obtain the parameter:

$$\Psi = \frac{1}{\mathrm{Re} \cdot Fr} = \frac{\mu_{2\Phi} \cdot g}{\rho_{2\Phi} \cdot j_{sup}^3} \tag{3}$$

This in turn will produce correlations of the form:

$$Nu = C \cdot (\mathrm{Re}\, Fr)^b = C \cdot \Psi^{-b} \tag{4}$$

Figure 3 shows the appeareance of our experimental data for the upward and downward heat transfer coefficients when using this approach. We observe that all the data, for both fluids, with and without solids in the pool collapse very well, and behave as describe by our hypothesis. As the dimensionsless parameter Ψ increases, i.e. as the effective viscosity in the pool increases and the superficial gas velocity decreases, the heat transfer coefficient does decrease.

The interfacial heat transfer coefficients show they same trends than the upward and downward ones but they are substantially larger (Figure 4). However, these values are smaller than the ones found in the two layer series of tests due to the presence of the intermediate layer that limits the entrainment and makes the heat and mass transfer a lot less effective. Greene et al. (1982; 1988a; 1988b; 1991) and Werle (1978) performed several experiments in similar conditions, using different fluid pairs with different density ratios, which produced different levels of entrainment. In their experiments, however, there was not intermediate layer between the two fluids. The comparison between these previous data and ours is shown in Figure 5. Bilbao's data for both water and glycerine show the same trends as Greene's data for mercury but they are substantially lower. This behavior is more accentuated than expected because water and mercury have similar viscosities, but the density ratio water/mercury or oil/mercury is a lot larger than water/oil or glycerin which would translate into smaller rates of entrainment. With these premises, for a fluid pair such as water/oil we would expect to obtain larger HTCs than for mercury/oil. Therefore, it seems that the interlayer screen does have a significant effect on the HTCs. Also in Figure 5, we have plotted the correlations suggested by Greene and Szekely (1963) to represent the behavior of the interfacial heat transfer coefficient between to fluid layers. It is observed, that both numerical correlations show trends similar to our data. They predict relatively well our experimental results for glycerin while they seem to underestimate the HTC for water.

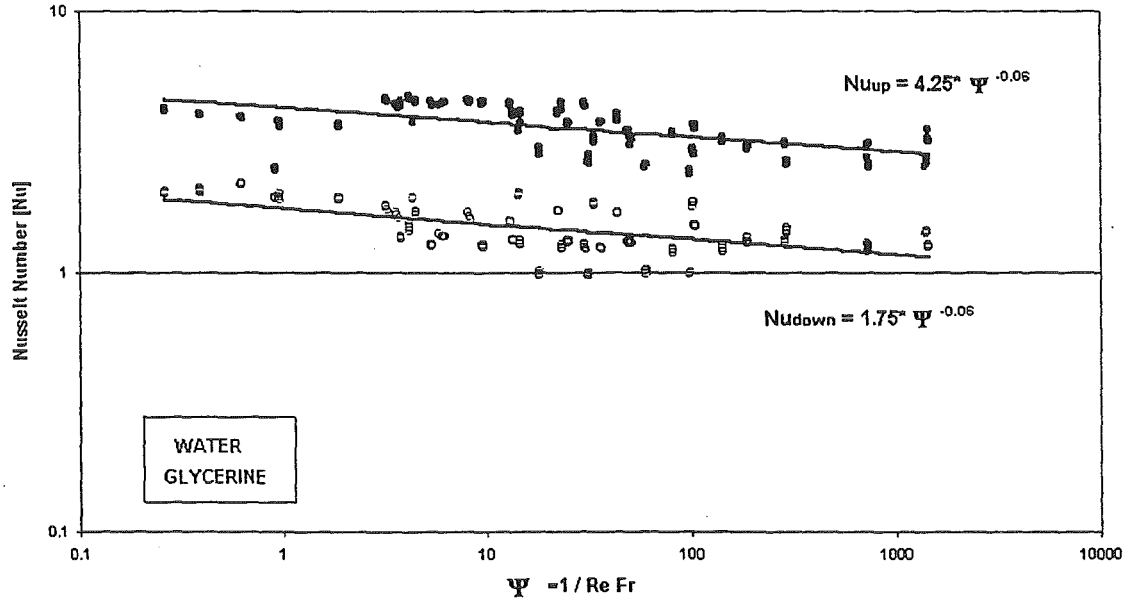

Figure 3. Upward and downward Nusselt numbers versus dimensionless number Ψ

4. CONCLUSIONS

The analysis of the experimental data obtained in the present work, and the comparison with previous models and correlations, allow us to draw some important observations:

First, we concluded that the viscosity of the fluid in the pool has a dominant effect on the obtained heat transfer coefficients to the boundaries. The heat transfer coefficient decreases as the viscosity of the pool increases. On the other hand, the solid fraction in the pool does not have a first order effect on the heat transfer coefficients. The solids in the pool increase the effective viscosity of the fluid, and in this sense the solids do have an impact on the heat transfer coefficient, but this impact is not different than the impact obtained by increasing the viscosity of the pool without adding solids.

In addition, a very imbalanced power split was found for the one and two layer tests, with 80% of the power being transferred upward and only 15% downward. The power split measured in the three layer tests is very different, with an up/down ratio of 60/35 approximately, due to the presence of a non-entraining interface between the fluid layers.

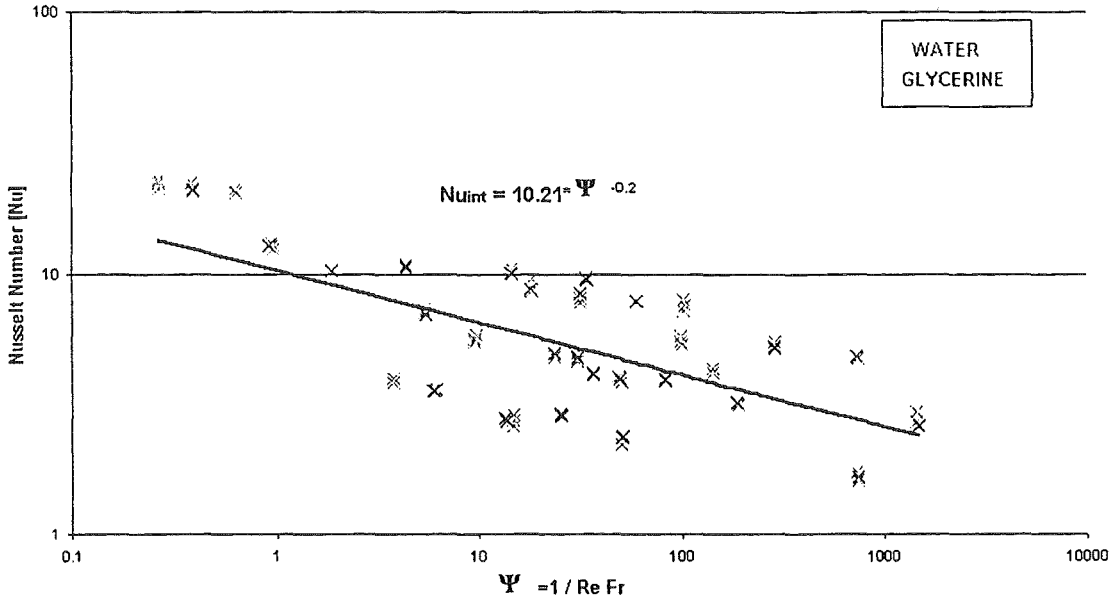

Figure 4. Interfacial Nusselt number versus dimensionless parameter Ψ

For the configurations studied here, where there is gas injection into the pool, we concluded that it is necessary to consider the overall effect. As the superficial gas velocity increases, the temperature of the pool decreases due to the improved heat transfer produced by the gas agitation. But, as the temperature of the pool decreases, the viscosity of the pool increases too, producing the opposite effect. It is necessary to account for both competing effects in order to predict successfully the behavior of the system. Furthermore, for the study of the heat transfer between density stratified fluids, the determination of the rate of entrainment between layers is of paramount importance in order to model the behavior of the system adequately.

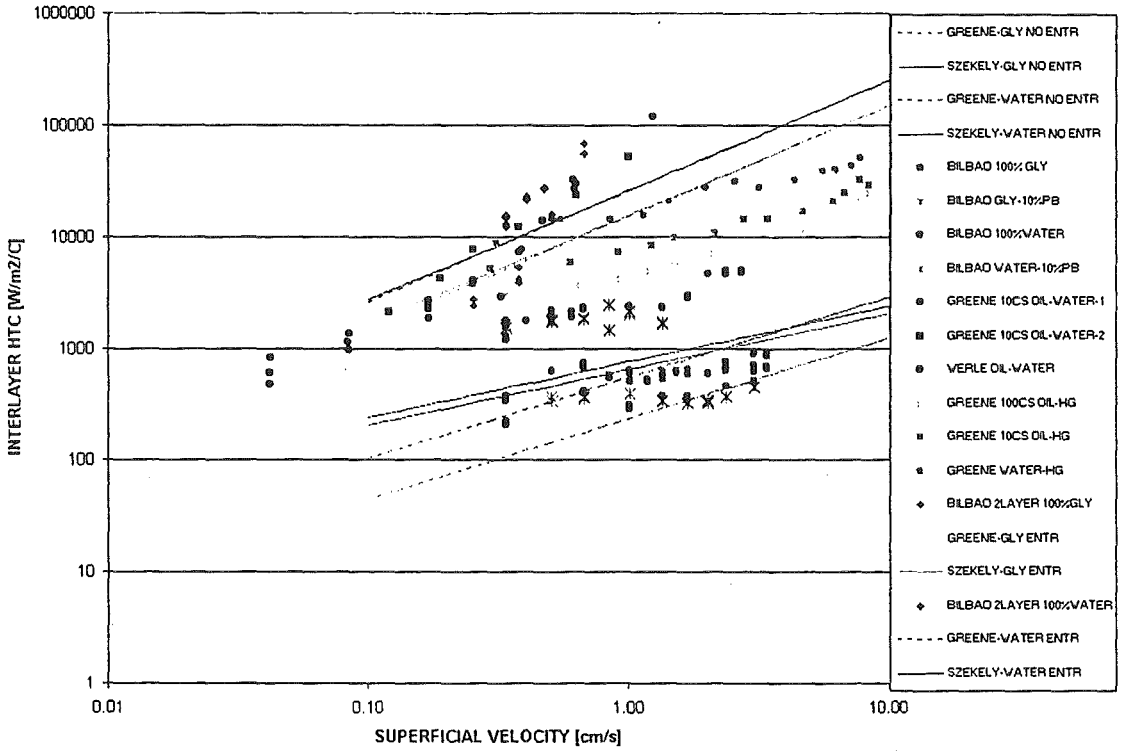

Figure 5. Comparison of Bilbao y León's data with previous experimental and numerical studies[2].

Finally, we can say that the existing models and correlations are not able to predict the new data for the entire range of viscosities and superficial gas velocities. Empirical correlations have been provided for our data (Figures 3 and 4), but these need to be used cautiously within the range of appropriate conditions.

NOMENCLATURE

A	Laplace constant [m]
g	Gravity [9.8 m/s^2]
j_{sup}	Superficial gas velocity [m/s]
k	Thermal conductivity [W/m^{2}K]
Fr	Froude number, $\rho j^2/\Delta\rho gD$
Nu	Nusselt number, hA/k
Re	Reynolds number, $\rho jD/\mu$
α	void fraction
μ	dynamic viscosity [N s / m^2]
Φ	solid fraction
ρ	density [kg/m^3]

Subscripts

air	air
l	liquid
s	solid
2Φ	two phase mixture or suspension
3Φ	three phase mixture or suspension

[2] The data from the two layer tests as well as Greene and Werle data with high entrainment have also been plotted in Figure 4 for comparison purposes.

REFERENCES

R. M. Bilbao y León, 1999a. Interfacial Heat Transfer in Multiphase Molten Pools with Gas Injection, Ph.D. Thesis, Department of Nuclear Engineering and Engineering Physics, University of Wisconsin – Madison.

R. M. Bilbao y León, M. L. Corradini, 1999b. Solid Particle Effects On Heat Transfer In A Molten Pool With Gas Injection, Ninth International Topical Meeting on Nuclear Reactor Thermal Hydraulics (NURETH-9), San Francisco, California, October 3-8, 1999.

M. T. Farmer, B. W. Spencer, D. R. Amstrong, D. J. Kilsdonk, R. A. Aeschlimann and M. Fisher, 1992. Results of MACE Test M0 and M1, Proceedings of the second OECD (NEA) CSNI Specialist's Meeting on Core Debris-Concrete Interactions, Karlsruhe, Germany.

D. K. Felde, H. S. Kim and S. I. Abdel-Khalik, 1980. Convective Heat Transfer Correlations for Molten Core Debris Pools Growing in Concrete, Nuclear Engineering Design, v. 58, pp. 65-74.

G. A. Greene et al., 1982. Heat Transfer betweeen Immiscible Liquids Enhanced by Gas Bubbling, International Meeting on Thermal Nuclear Reactor Safety, Chicago IL.

G. A. Greene and T. F. Irvine Jr., 1988a. Heat Transfer Between Stratified Immiscible Liquid Layers Driven by Gas Bubbling Across the Interface, Proceedings of 1988 National Heat Transfer Conference, Houston TX.

G. A. Greene, C. Finfrock and S. B. Burson, 1988b. Phenomenological Studies on Molten Core-Concrete Interactions, Nuclear Engineering Design, v. 108, p. 167.

G. A. Greene, 1991. Heat, Mass and Momentum Transfer in a Multifluid Bubbling Pool, Advances in Heat Transfer, v. 21, p. 277.

C. S. Miner, N. N. Dalton, et al., 1953. *Glycerol*, Reinhold Publishing Corp., New York.

J. M. Seiler and J. Ganzhorn, September 1996. Viscosities of Corium-Concrete Mixtures, 4th European Conference Thermophysical Properties INSA, Lyon, France.

J. Szekely, 1963. Mathematical Model for Heat or Mass Transfer at the Bubble Stirred Interface of Two Inmiscible Liquids, International Journal of Heat and Mass Trasfer, v. 6, p. 417.

D. H. Thompson, J. K. Fink, B. W. Spencer, D. R. Amstrong, B. R. Sehgal, 1992. Thermal-Hydraulic Aspects of the Large-Scale Integral MCCI Tests in the ACE Program, presented at the 2nd OECD (NEA) CSNI Specialists MTG. On Core Debris Concrete Interactions, Karlsruhe, Germany.

H. Werle, 1978. Experimental Investigation of Heat Transfer between Two Horizontal Liquid Layers with Gas Injection, Proc. Fourth PAHR Info. Exch. Mtg., Ispra Italy, v. 1, p.164.

The entire paper, including color figures, can be viewed at http://silver.neep.wisc.edu/~NSRC/abstracts/OECD_bilbao1999.PDF

OECD Workshop on Ex-Vessel Debris Coolability
Karlsruhe, Germany, 15-18 November 1999

Organised in collaboration with
Forschungszentrum Karlsruhe (FZK) GmbH

SIMULATION OF ACE AND MACE EXPERIMENTS WITH A PHASE SEGREGATION MODEL USING THE TOLBIAC CODE

Vandroux-Koenig Simone, Seiler Jean Marie, Spindler Bertrand, Gillot Frédéric
CEA Grenoble DTP
17 rue des Martyrs, Grenoble 38054 Cedex 09 France
svandrouxkoeni@cea.fr and seiler@dtp.cea.fr

Froment Karine
CEA Grenoble CEREM/DEM/SPCM
17 rue des Martyrs, Grenoble 38054 Cedex 09 France
Froment@chartreuse.cea.fr

ABSTRACT

The paper presents an interpretation of the ACE and MACE MCCI tests with the TOLBIAC code. The phase segregation approach has been introduced in this code. The main physical assumptions are described. Chemical reactions with Zr are believed to be achieved when the ablation of concrete begins. Mass losses from the melt due to melt splattering are taken into account, as well as formation of lateral crusts. The calculated evolution of melt temperature fits well with measurements. The model predicts well the effect of a power increase on the melt temperature; it is stated that the usual model (without phase segregation) approach for heat transfer is not able to reproduce this effect. Sensitivity calculations are performed. It is concluded that initial conditions, melt sparging and presence of lateral crusts have a significant effect on melt temperature; on the contrary, physical properties (viscosity, with reasonable variation range) and power split have a small effect on melt temperature. Finally, the points in favour of the phase segregation approach are summarised. Further development needs for TOLBIAC are also outlined.

1. INTRODUCTION

In the past, several theoretical developments have been devoted to the analysis of corium-concrete interaction [WECHSL, CORCON, COSACO,...] which are based on homogeneous model for the corium-concrete mixture (in the sense that solid and liquid phases are supposed to be well mixed). Recently a new approach based on phase segregation has been developed at CEA, which has been applied to the interpretation of limited aspects of the existing MCCI tests [Seiler, 1996] and [Froment, Seiler, 1999-1]. This approach has now been introduced in the TOLBIAC code in order to calculate the complete interaction transients. The objective of this paper is to present an interpretation of some ACE and MACE tests with this code.

2. ACE AND MACE

The ACE experiments [Wall et Sehgal, 1993] have been performed in the frame of an international programme led by EPRI, in order to determine the concrete ablation rates and release fractions of low-volatility fission product species. Researchers built a facility that melted approximately 300 Kg of UO_2 by electrical resistance heating to simulate sustained internal radioactive decay heat. The UO_2 was located on top of a concrete basemat embedded with thermocouples to measure the ablation rate. The melt temperature was measured by means of W-Re thermocouples. The interior cross section of the furnace was ~50cm by ~50cm. The space above the corium was filled with inert gas. A thermally insulated lid rested on top of the box. Different types of concretes were tested: siliceous (L2), limestone (L8), siliceous-common sand (L5, L6, L7) and composite (L4). Different initial amounts of metallic zirconium were used. Also, some amounts of iron oxides were added to the corium in some tests (L5). The test duration was variable: from ~30 minutes (L7) to, maximum, 2 hours (L4, L5).

The MACE tests have as main objective the coolability of corium during MCCI when water is added on top of the melt. These tests have generally a longer duration of MCCI (~6 hours for M3B). Also, a very large test could be performed (1,2 m by 1,2 m for M3B).

3. TOLBIAC

The purpose of TOLBIAC code [Vandroux-Koenig and Spindler, 1999] is to model, in two dimensions, the thermohydraulic of a corium pool in a structure (pressure vessel or core-catcher), in order to simulate the behaviour of the melt and of the structure. Three components are taken into account: oxides (divided into light and heavy oxides), metals and gas.

Ablation of sacrificial material is taken into account, both in the simulation of hydraulic (variable volume of cells, generation of gas and liquid) and of thermal phenomena (variable thickness for conduction calculations).

The following phenomena can also be simulated: metal-oxide stratification or mixing (depending on the presence of sparging gas), residual power, free surface heat transfer (radiation or heat transfer with a water pool), crust formation. The gas field takes into account variations in the level of the pool, and allowance is made for the geometrical volume occupied by the crust.

The constitutive laws are taken from literature or from experimental assessment.

For a first approach, the ACE and MACE experiments are modelled with only one hydraulic cell for the corium pool. A separate meshing is used for the wall thermic calculation including ablation. This enables quick calculations, and thus easy sensitivity calculations. It is however the complete version of TOLBIAC which is used. Only the data set is particular.

4. MAIN PHYSICAL ASSUMPTIONS

The heart of the model, which has been used for this work, is based on the assumption of phase segregation [Seiler, 1996]. This effect is related to the solidification of the refractory phases (mainly UO_2 and ZrO_2) in the temperature gradients (at the corium-concrete interface or on the lateral surface or, depending on heat losses, at the surface of the melt). These refractory phases are supposed to form a sort of (porous) crust in these temperature gradients. The non-refractory materials (mainly: decomposition products of concrete) are supposed to be rejected in the liquid central part of the melt.

The interface between the solid material (crust) and the residual liquid is supposed to stay at thermodynamic equilibrium. This imposes a supplementary quantitative relation between the composition of the crust, the composition of the liquid and the interface temperature. This relation is given by thermodynamic calculations which are performed with the GEMINI code (equivalent to phase diagrams) and solidification processing considerations [Froment, Seiler, 1999-2]. This supplementary equation implies for instance that, at constant power, when the concentration of decomposition products of concrete increases, then the melt temperature should decrease.

The thickness of the solid crust is also controlled by conduction heat transfer through it.

For the calculations, GEMINI has not been coupled with the TOLBIAC code. Thus, it was necessary to pre-determine the thermodynamic relations which were introduced as "pseudo-binary phase diagram". This is an important restriction for the application of TOLBIAC. In some cases (for instance when iron oxides are present, as in L5), the direct calculation was not possible with TOLBIAC due to the limited number of mass balance equations in it. Some semi-analytic methods and separate calculations were used in this case.

Another consequence from the demixtion between solid and liquid phases is that the viscosity of the liquid phase stays rather small (ranging from 0.01 to 0.2 Pa.s) [Seiler, Ganzhorn, 1997]. Due to the fact that the variation of the heat transfer coefficient inside the melt is supposed to be proportional to $\mu^{-1/3}$, only a small temperature gradient is suspected to exist in the liquid phase and the main temperature gradient is located in the solid layers.

The temperature at the interface between the concrete and the solid layers is supposed to be equal to ~1600 K. This is considered to be acceptable as the solidus-liquidus temperature interval for siliceous concrete or limestone-common sand concrete is small. There is an exception for limestone concrete for which the liquidus temperature is elevated (~2600 K) due to residual solid CaO phases . In this case, a CaO rich layer may form between the concrete and the corium as shown by the post test investigation from L8.

The chemical reactions with zirconium have been calculated separately. From GEMINI calculations, it seems that Zr may react completely with the water present in the insert concrete and with silica (SiO_2). These reactions seem to have time to take place before the initiation of the basemat ablation. As the TOLBIAC calculations start at the initiation of the basemat ablation, these reactions are not described in TOLBIAC. However, the consequent changes in the initial composition of the melt are taken into account.

A very important aspect is relative to corium splattering on the side walls of the test section. Quite all ACE post-test examinations have shown a significant splattering of corium due to gas sparging through the melt. This effect reduces the amount of liquid melt during the test. Thus, it decreases the liquid mass fraction and, as a consequence in the frame of the phase segregation model, it may reduce significantly the melt temperature. The melt splattering phenomenon has been taken into account in the model approach. The final amounts of "lost" melt are known from the post-test examinations. The hypothesis is made, that this "lost mass" varies linearly versus time. The composition of the splattered mass is supposed to be time dependent and corresponds to the instantaneous composition of the liquid melt.

The presence of lateral crusts due to heat losses through the side panels could be taken into account.

A separate analysis was performed for the investigation of heat transfers within the liquid melt [Seiler, 1998], taking into account the results from [Epstein, 1997]. It is concluded that, when usual heat transfer correlations are used in the frame of the phase segregation model, the calculations predict a up/down power split ranging from approx. 0.5 (for anchored crust situations) to maximum 5 (for melt radiating to the upper lid) which corresponds to the experimentally determined power splits. It is thus concluded that the power split is, in ACE, strongly affected by the radiation heat transfer in the top volume of the cavity which are very strongly system dependant (wall insulation, melt splattering, aerosols,...). Thus, in TOLBIAC, the top surface conditions are adjusted depending on the experiment considered.

5. RESULTS

The experimental conditions and results are taken from [Thompson et al., 1997]. Calculated evolutions of melt temperatures appear on figures 1 through 6 for L2, L6, L7, L8, L5 and M3B. There is a general agreement between experiments and calculations. However, the temperatures are initially overpredicted for L6 (by ~100 K). There is a slight underprediction at the end of the test for L7 (by ~100 K) and L8 and L2 (by ~50 K). The general decrease of the temperature as a function of time is well predicted. The temperatures calculated for L5 are really lower than for the other experiments, even if the calculation overpredicts the experiments by ~100 K; this effect is due to the presence of iron oxides.

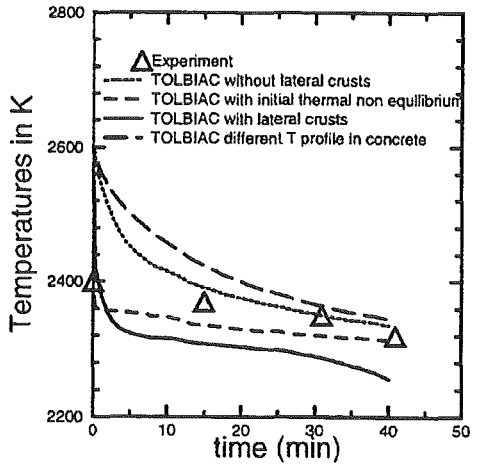

Fig. 1 Melt temperature for L2

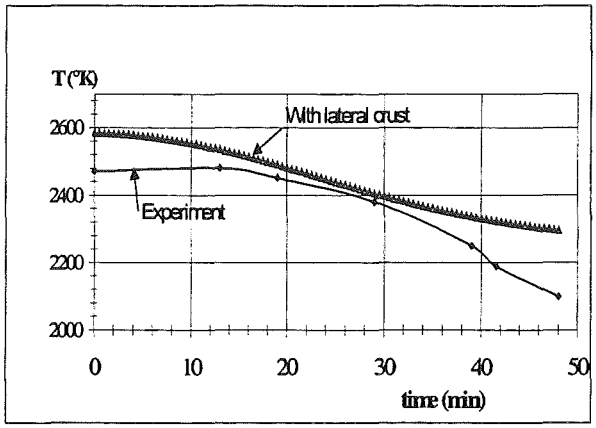

Fig. 2 Melt temperature for L6

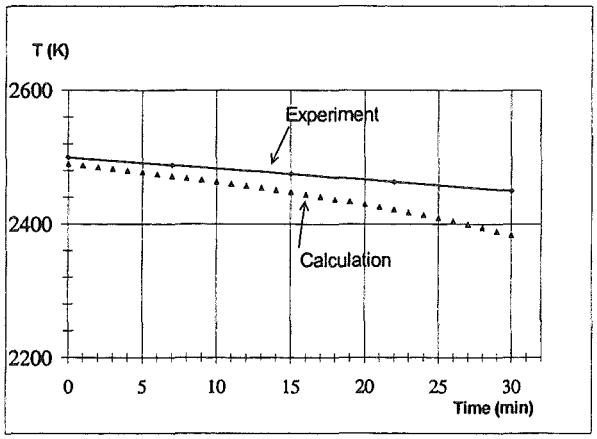

Fig. 3 Melt temperature for L7

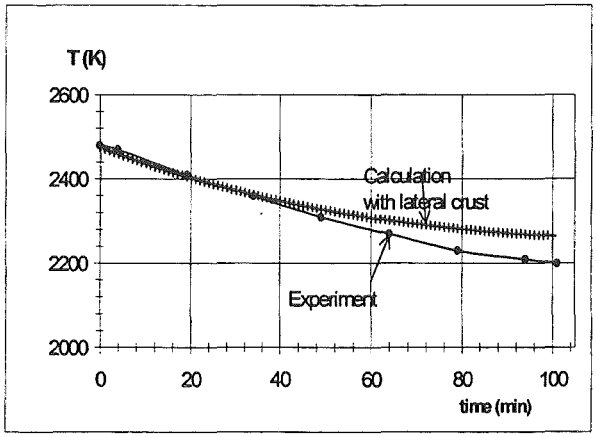

Fig. 4 Melt temperature for L8

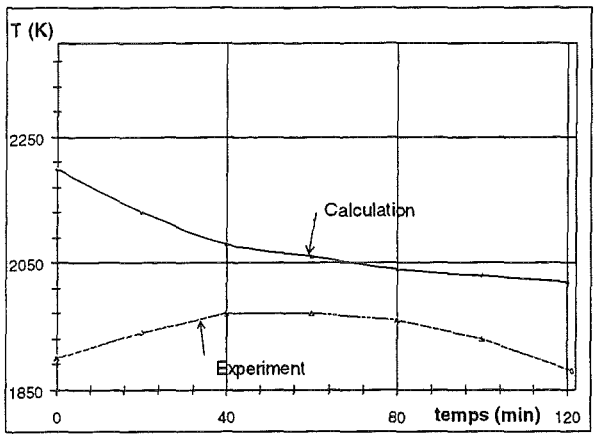

Fig. 5 Melt temperature for L5

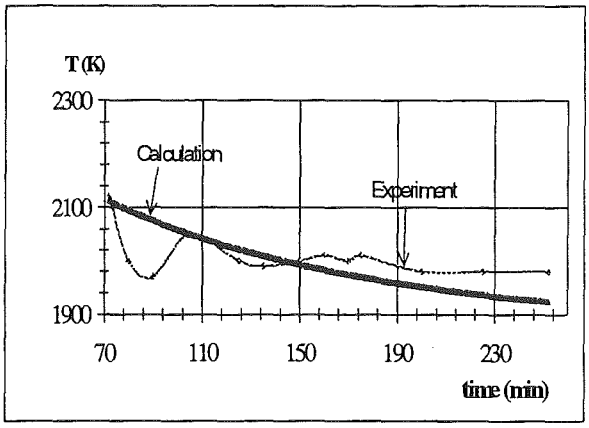

Fig. 6 Melt temperature for M3B

Figure 7 presents the results obtained from TOLBIAC and given by the experiment for a specific test: L2 with lateral crusts. It shows the evolution as a function of time of several variables. The wall (lower crust) and surface (upper crust) crust thickness almost remains constant. The melt temperature is underpredicted by -50 K. The light oxide (concrete) concentration in the melt increases with ablation. The heat flux at the surface (upper heat flux) and at the concrete wall (lower heat flux) were adjusted to fit the experimental average heat losses. Thus, the concrete thickness and the ablation rate fit the experimental valueswell.

For test M3B, a comparison between the usual homogeneous model calculation (also introduced in TOLBIAC) and the phase segregation approach has been made. In M3B an important power variation has been applied to the melt approximately at time 250 minutes. It can be seen from figure 8 that the temperature in the melt did not increase significantly as a result of this power variation

Such a power transient has been calculated with TOLBIAC, with arbitrary initial conditions and a power increase of 50% after 1200s, in order to check qualitatively the behaviour of both models. From figure 9 it is clearly seen that the phase segregation model predicts quite no temperature variation which is consistent with the behaviour observed in M3B. The usual approach (figure 9), however predicts a significant increase in temperature which is not consistent with the experimental result. This means also that attempts to correlate the heat transfer in the melt on the basis of the ratio $h = \dfrac{\varphi}{T_{melt} - T_{solidus}}$ (where φ is the heat flux) have little chance to succeed. The phase segregation model predicts that the temperature difference inside the liquid phase is small, thus the temperature in the melt is approximately equal to the interface temperature between solid and liquid. When the power is increased, the crust thickness decreases; however this decrease of the mass of solid phase does not induce a large variation of the composition in the liquid phase all the more as the power increase induces a quicker ablation of the concrete wall. As a consequence, considering the phase diagram does not induce a large variation of the interface temperature (which is the liquidus temperature in the residual liquid). In other words, the system behaves like a pure material with the difference that the melting temperature is a function of the composition of the residual liquid. This observation is considered as a supplementary validation of the phase segregation approach.

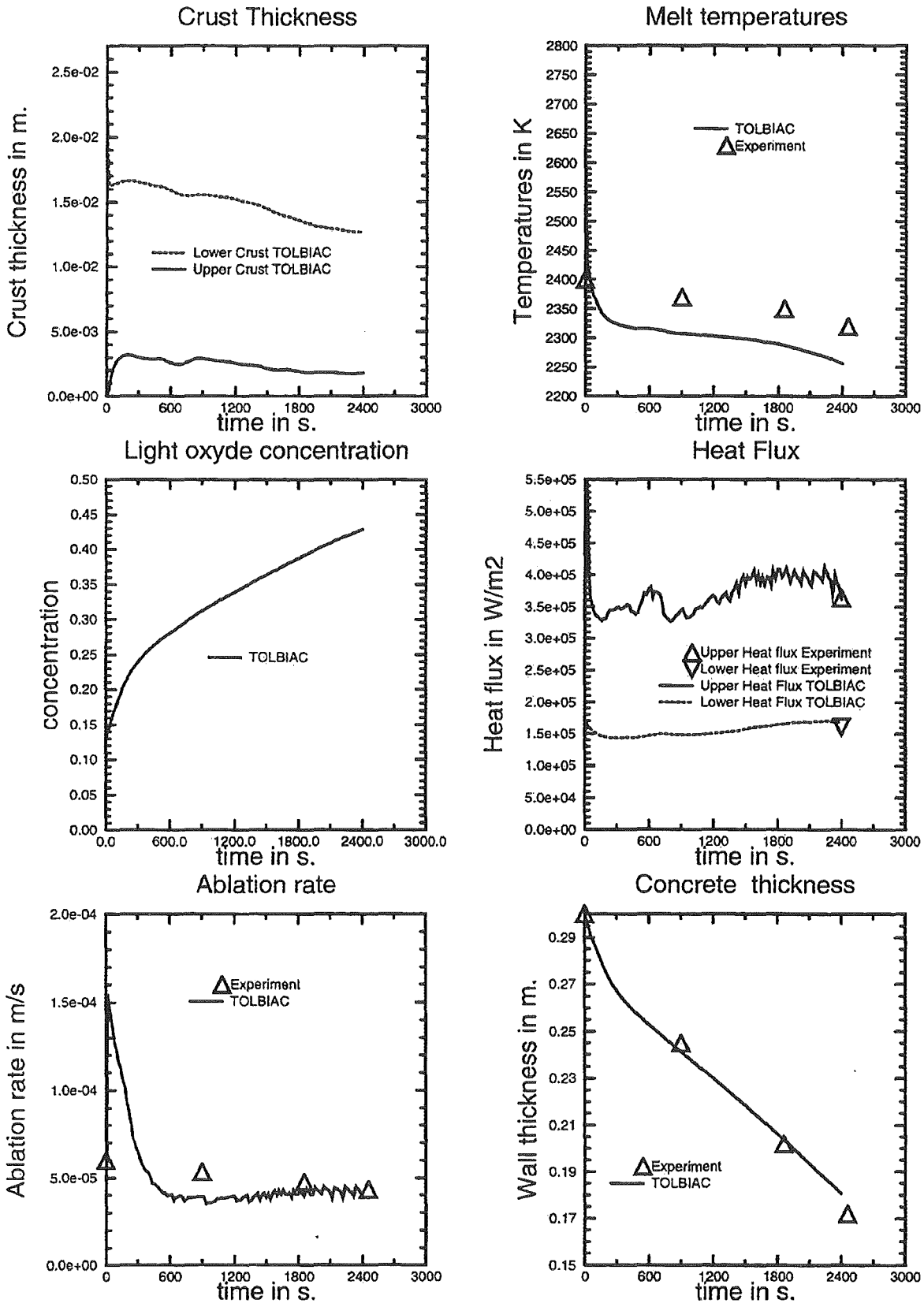

Fig. 7 Test L2 with lateral crusts: TOLBIAC results

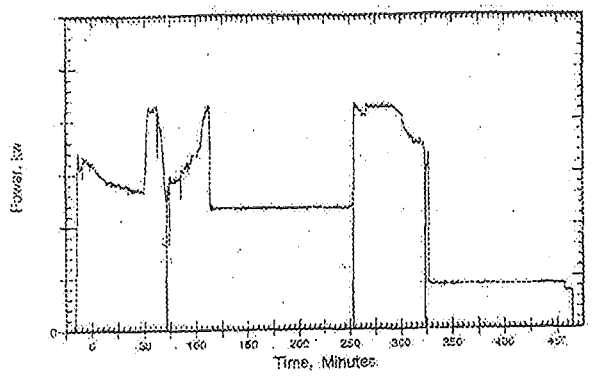

Power supply

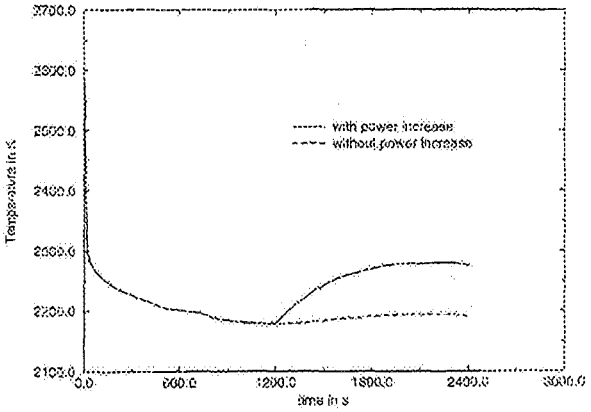

Usual model

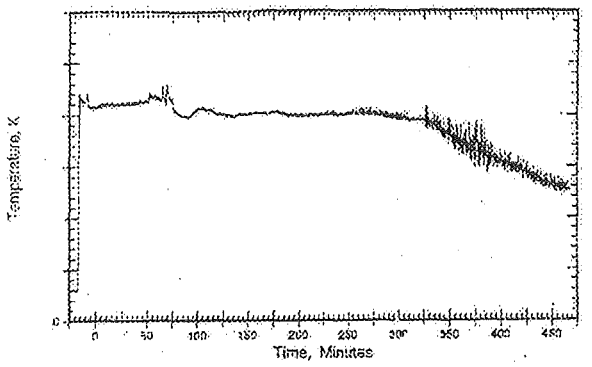

Basemat thermocouple

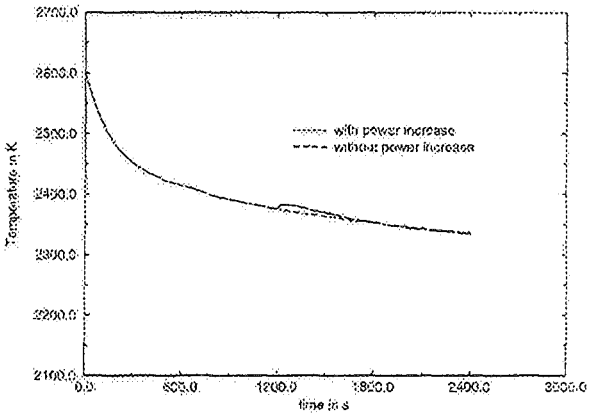

Phase segregation model

Fig. 8 Power variation in M3B and corresponding melt temperature

Fig. 9 Melt temperature as a function of time with usual model and phase segregation model, and an arbitrary power increase of 50% after 1200s on the basis of an L2 calculation.

6. DISCUSSION

Some parametric calculations have been performed in order to check the sensitivity of the model.

As stated above, the temperature prediction in the melt is not very sensitive to the viscosity of the liquid if reasonable variations ranges are considered in the frame of the phase segregation approach.

The effect of the presence of a lateral crust may be important as suggested in figure 1. The presence of a lateral crust decreases the concentration of refractory phases in the liquid and, as a consequence, decreases the liquidus temperature of the residual liquid temperature (interface temperature). The melt temperature may decrease by, approximately, 100 K.

Initial conditions may have an important effect on the transient behaviour since the characteristic time needed to reach thermal equilibrium is in the range 15 - 30 minutes. In the reference calculations (presented in figures 1 through 6) it has been supposed that thermal

equilibrium was reached at time t=0. This may not be the case in reality. Thus, sensitivity calculation was made for L2 supposing that the system was not in thermal equilibrium at time t=0: the measured initial temperature was imposed. The result appears on figure 1. During the transient, the temperature stays nearer to the measured temperatures but the ablation rate of concrete is then underpredicted.

The initial temperature profile in the concrete wall may also have an important effect. Figure 1 enables to compare two calculations without lateral crust, one with a reference profile obtained from the experimental data and one with a steeper profile. The corresponding melt temperature differences are approximately 50 K.

Separate investigations have shown that the crust may be unstable due to possible accumulation of decomposition products of concrete below this crust. The periodicity of crust ruptures has been calculated (this crust rupture corresponds, in our opinion, to the periodic bursts which have been observed in almost all ACE and MACE tests) and ranges approximately from 15 min to 50 min depending mainly on the ablation heat flux. This periodic process has not been introduced in our code. However the consequence of this is that, if the observation time is too short (an hour or less) in comparison with this period, then the obtained results cannot be interpreted as "steady-state" or "mean" values. In the frame of the phase segregation model, this phenomenon has only a slight effect on the melt temperature but has a very strong effect on the instantaneous concrete ablation rate.

It is also possible that the assumption of phase segregation is not valid during the initial phases of the MCCI (during 10 to 20 minutes). However, the comparison between test results and calculations does not allow to propose a criterion for the onset of segregation. For reactor applications the delay for MCCI is of several days. Thus, it is claimed that a precise description of the initial phase (first 30 min) is not necessary.

7. CONCLUSION

There are now several points in favour of the phase segregation approach for MCCI:

- the temperature traces can be recalculated, even during the interaction transients,
- the material effects on melt temperature are explained (L5),
- the effect of power variation on melt temperature is well predicted,
- the post-test examinations evidence strong composition variations in the melt, with an enrichment in refractory phases at the corium-concrete interface,
- the composition of the melt ejected in M3B could be well calculated,
- the approach offers a possible explanation of the periodic burst observed during the tests. Periodicity could be calculated,
- the approach solves the temperature-viscosity contradiction.

A consequence of this approach is that the prediction of the melt temperature is largely decoupled from the prediction of the power split.

To model ACE or MACE experiments with TOLBIAC, a pseudo-binary phase diagram obtained from GEMINI is used. In some cases, (for example when adding iron oxides in the melt), it would be necessary to take into account additional mass equations. This would lead to further developments in TOLBIAC.

Moreover, the phase diagram can be more complicated than a pseudo-binary, especially for the application of TOLBIAC to a real reactor case. The necessity of a coupling between TOLBIAC and GEMINI codes can be discussed.

ACKNOWLEDGMENTS

This work is performed within the frame of cooperative task between CEA-EDF and Framatome.

REFERENCES

Blottner., 1979 "Hydrodynamics and heat transfer characteristics of liquid pools with bubble agitation" Nureg/CR/0944,1979.

Epstein M., 1997 "MCCI thermalhydraulics. MCCI heat transfer models. A comparison with prototypical test data and some new ideas" ACEX TR-C-17" Internal EPRI agreement document.

Froment K., Seiler J.M. 1999-1 "On the importance of a strong coupling between Physicochemistry and Thermalhydraulics for modelling late phases of severe accidents in LWRs". Ninth International Topical meeting on Nuclear reactor Thermal-Hydraulics (NURETH-9) San Francisco, California, October 3-8, 1999

Froment K., Seiler J.M., 1999-2 "Equations for solidification of corium without sparging gas. Scaling criteria" OECD Workshop on Ex-Vessel Debris Coolability, Karlsruhe, Germany, 16-18 November 1999.

Seiler J.M.1996, " Phase segregation model and molten pool thermal-hydraulics during molten core-concrete interaction ". *Nucl. Eng. and Design,* **166**, 259-267, 1996.

Seiler J.M. & Ganzhorn J. 1997 " Viscosities of corium-concrete mixtures ", *Nucl. Eng. and Design,* **Vol 178**, n°3, December IV, pp 259-268, 1997

Seiler J.M., 1998 "Considerations about heat transfer in the ACE/MACE melts with phase segregation" internal CEA note SETEX/LTEM/98-111

Sudreau F., Cognet G . 1997 ," Corium viscosity modelling above liquidus temperature ", *Nucl. Eng. and Design*, **Vol 178**, n°3, Dec IV, 1997

Thompson, Farmer, Fink, Armstrong, Spencer, 1997 "Compilation, Analysis and Interpretation of ACE Phase C and MACE Experimental data-MCCI Thermalhydraulics Results" ACEX TR-C-14, Volume -I

Vandroux-Koenig S., Spindler B., Moreau G.M.M., Pelisson R. "TOLBIAC version 4.2: code description" internal CEA note SMTH/LM2/99-36

Wall I.B., Sehgal B.R., 1993 "Molten Corium-Concrete Interactions" EPRI Report TR-103483 dec 1993

Session B 2:

PHENOMENA TO ACHIEVE COOLABILITY: CHARACTERISTICS OF PARTICLE BEDS

Chairman: V. Gustavson

OECD Workshop on Ex-Vessel Debris Coolability
Karlsruhe, Germany, 15-18 November 1999

Organised in collaboration with
Forschungszentrum Karsruhe (FZK) GmbH

CHARACTERIZATION OF DEBRIS BED GENERATED BY FUEL COOLANT INTERACTIONS

H.Ó. Haraldsson and B.R. Sehgal
Division of Nuclear Nuclear Power Safety
Royal Institute of Technology
10044 Stockholm, Sweden
oskar@ne.kth.se

ABSTRACT

The objective of the present paper is to compare the performance of statistical distributions which are used to describe the size distributions of fragments obtained from molten fuel coolant interactions (MFCI) experiments. Four distributions namely: Weibull, log-normal and upper limit log-normal distributions are employed along with the distribution resulted from the sequential fragmentation theory (SFT) of Brown [1].The distributions are fitted to two sets of experimental data obtained from jet fragmentation experiments under FCI conditions. One set from JRC/Ispra, KROTOS experimental program and the other set from RIT/NPS, MIRA-20L experimental program, are employed.

It is found, among the distributions examined, that the SFT model, using mass mean diameter σ and a free parameter γ, which represent the fractal dimension of the debris, describe the measured data better than the other distributions. The fractal dimension is found to vary between two and three, depending on the size of the fragments (σ). In the case of corium debris the fractal dimension approaches three as the mass mean diameter decreases. For three different oxide melts, the fractal dimension varies between approximately two and three. Additionally, the paper discusses the physical background and the distribution parameters of the SFT.

1 INTRODUCTION

The introduction of a hot, molten liquid into a volatile coolant can, under certain conditions, result in explosive interactions. Such molten fuel-coolant interactions (MFCI) are characterised by an initial pre-mixing phase during which the molten liquid, metallic or oxidic in nature, undergoes a fragmentation process which significantly increase the area available for melt-coolant contact, and thus energy transfer. Although substantial progress in the understanding of phenomenology of the MFCI events has been achieved in recent years, there remain uncertainties in describing the fragmentation processes. The scale of interest can vary from a single droplet up to a large diameter, high temperature, jet falling into water. Of particular relevance to this work are those situations, during a hypothetical severe accident in a nuclear power plant in which molten oxidic-metallic melts at temperatures in excess of 2800 K interact with coolant either inside or outside the reactor pressure vessel. In addition to nuclear safety, such fuel-coolant interactions are of interest to the chemical, metallurgical and paper industries as well as to the study of volcanic eruption.

The melt jet and drop fragmentation during the premixing phase of MFCI, determines the initial conditions for debris bed coolability. Those parameters are e.g. the particle size distribution, debris bed porosity and stratification. It is essential to quantify these parameters, in order to determine whether the debris is coolable or not.

This work is focused upon analytical studies of the size distributions of the debris particles created during the fragmentation process. The fragmentation process is responsible for the interfacial area evolution during the premixing and propagation phases of steam explosion. There are many statistical distributions which have been proposed to fit the size distributions of debris fragments produced from the fragmentation processes. The most popular empirical distributions are the Weibull distribution and the log-normal (LN) distribution [2]. Fletcher [3] investigated the statistical distribution of uranium dioxide/molybdenum debris produced from MFCI experiments. He found out that the debris distribution exhibited best agreement with the upper limit log normal distribution.

Particle size distributions data from two MFCI experimental programs: KROTOS, performed at JRC/Ispra [4], employing corium and experiments performed at RIT/NPS [5], employing CaO-B_2O_3, MnO_2-TiO_2 and WO_3-CaO, are examined against four different statistical distributions; (i) the lognormal (LN) [6], (ii) the upper-limit lognormal (ULLN) [3]; (iii) the Weibull [7]; and (iv) the sequential fragmentation theory (SFT) [1] distributions. In the present work, results are reported on which of the four statistical distributions are best to fit the experimental data produced from the MFCI events. Attempts are made to investigate the fractal dimension, obtained from the SFT theory, and it's dependence on the mass mean diameter of the debris fragments.

2 STATISTICAL DISTRIBUTIONS

2.1 Empirical Fragment Size Distributions

The Weibull distribution, [7] has the following cumulative density distribution function

$$\frac{M(<l)}{M_T} = 1 - \exp\left[-(\frac{l}{\sigma})^k\right] \tag{1}$$

where $M(<l)$ is the cumulative mass of fragments of size less than l, M_T is the total mass of fragments in the distribution, σ is related to the average size of the fragments, and k is a free parameter. According to Brown [1] the Weibull distribution is identical to the Rosin Rammler (RR) distribution, given by Eq.(2).

$$\frac{M(>l)}{M_T} = \exp\left[-(\frac{l}{\sigma})^k\right] \tag{2}$$

The Rosin Rammler and Weibull distribution have been used to fit the data produced from different fragmentation processes, from crushing of geological materials, such as coals and stones, (Kittleman [8] and Geer and Yancey [9]), to the fragmentation of the universe, (Brown et.al. [10]).

The LN distribution, [6] has been used extensively to fit debris size distributions. The cumulative density function for the LN is

$$\frac{M(<l)}{M_T} = \int_{-\infty}^{l} \frac{1}{\sqrt{2\pi}x\sigma} \exp\left[-(\ln(x) - m)^2/2\sigma^2\right] dx \tag{3}$$

Here m and σ are free parameters to be fitted for the distribution. The lognormal distribution has been recommended for fragmentation processes by several authors, e.g. Kolmogorov [11].

Recently Fletcher [3] suggested that the ULLN distribution was the most preferable in fitting debris distribution produced from MFCI. The ULLN has the following cumulative density function.

$$\begin{aligned} \frac{M(<l)}{M_T} &= \int_{-\infty}^{l} \frac{x_m}{(2\pi)^{1/2}(\ln\sigma)x(x_m-x)} \exp\left[-\frac{1}{2}[\frac{\ln(x_m x/(x_m-x)-\ln\mu)}{\ln\sigma}]^2\right] dx \\ for \quad & 0 \le x \le x_m, \\ = 0 \quad & otherwise. \end{aligned} \tag{4}$$

Where x_m is the maximum particle size in the distribution and μ and σ are measure of location and scale respectively. The main difference between the LN and ULLN distributions is that the ULLN distribution tends to an asymptote at the maximum size, i.e. when x approaches x_m. It should be noted that the Weibull and the LN distributions are two parameter distributions and the ULLN is a three parameter distribution.

2.2 Sequential Fragmentation Theory

Brown [1] derived the theory of sequential fragmentation. He started with an equation for the conservation of mass.

$$n(m) = C_1 \int_m^{\infty} n(m') f(m' \to m) dm' \tag{5}$$

Here $n(m)$ is the particle number distribution, which has the dimension: number of fragments per unit mass between m and $m + dm$. The symbol C_1 is a constant. The single event mass distribution, when a particle of mass m' breakes into particles of mass m, is described by the function $f(m' \to m)$. It was shown by Austin [12] that fragmentation of any particle results in branching tree of cracks. These branching trees show a similarity and can be described as fractals, see figure (1). It is shown by Brown [13] that the following function f can be determined from the fractal theory.

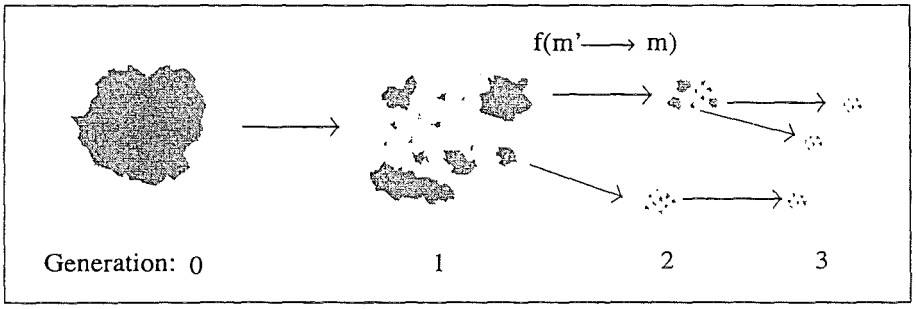

Fig. 1: *The sequential fragmentation of each particle into smaller particles.*

$$f(m' \to m) = m^{-\frac{D_f}{3}} \tag{6}$$

Where D_f is the fractal dimension, $0 < D_f < 3$. By normalising the f with average mass m_1 and setting parameter $\gamma = -D_f/3$, $-1 \leq \gamma < 0$ and $0 < D_f < 3$, function f takes the following form,

$$f(m' \rightarrow m) = (\frac{m}{m_1})^{\gamma} \tag{7}$$

By inserting Eq.(7) into Eq.(5) and choosing C_1 as m_1^{-1} the following is obtained.

$$n(m) = \left(\frac{m}{m_1}\right)^{\gamma} \int_m^{\infty} n(m') d \left(\frac{m'}{m_1}\right) \tag{8}$$

Integrating equation (8) gives,

$$n(m) = \frac{N_T}{m_1} \left(\frac{m}{m_1}\right)^{\gamma} \exp \left[\frac{(\frac{m}{m_1})^{\gamma+1}}{\gamma+1}\right] \tag{9}$$

for $(-1 < \gamma < 0)$, where N_T is the total number of particles.

$$N_T = \int_0^{\infty} n(m) dm \tag{10}$$

The mass distribution for the sequential fragmentation is obtained by multiplying Eq.(9) with the mass m, for $(-1 < \gamma < 0)$.

$$mn(m) = N_T \left(\frac{m}{m_1}\right)^{\gamma+1} \exp \left[\frac{(\frac{m}{m_1})^{\gamma+1}}{\gamma+1}\right] \tag{11}$$

The most probable mass (mode) of the distribution m_p can be obtained by differentiating Eq.(11) and setting the result equal to zero.

$$\frac{m_p}{m_1} = (\gamma+1)^{\frac{1}{\gamma+1}} \tag{12}$$

Inserting Eq.(12) into equation Eq.(11) gives,

$$mn(m) = N_T(\gamma+1) \left(\frac{m}{m_p}\right)^{\gamma+1} \exp \left[-\left(\frac{m}{m_p}\right)^{\gamma+1}\right] \tag{13}$$

The normalised mass distribution $M(< m)/M_T$, where $M(< m)$ is the cumulative mass of fragments and M_T is the total mass of all particles, is as follows.

$$\frac{M(< m)}{M_T} = \frac{\int_0^m mn(m) dm}{\int_0^{\infty} mn(m) dm} \tag{14}$$

By inserting Eq.(11) or Eq.(13) into Eq.(14), it is obtained that,

$$\frac{M(< m)}{M_T} = \frac{\Upsilon(\frac{\gamma+2}{\gamma+1}, x)}{\Gamma(\frac{\gamma+2}{\gamma+1})} = 1 - \frac{\Gamma(\frac{\gamma+2}{\gamma+1}, x)}{\Gamma(\frac{\gamma+2}{\gamma+1})} \tag{15}$$

Where γ is a free parameter and x is,

$$x = \frac{(\frac{m}{m_1})^{\gamma+1}}{\gamma+1} = (\frac{m}{m_p})^{\gamma+1} \tag{16}$$

The mass distribution can be converted to size distribution by inserting $(m/m_1 = (l/\sigma)^3)$ into equation (16). As before, σ is the mean size of the particles. The functions $\Gamma(\alpha)$, $\Gamma(\alpha, x)$ and $\Upsilon(\alpha, x)$ are the complete, the complimentary incomplete and the incomplete Gamma-functions, respectively. That is,

$$\Gamma(\alpha, x) = \int_x^\infty t^{\alpha-1} \exp(-t) dt \tag{17}$$

$$\Upsilon(\alpha, x) = \int_0^x t^{\alpha-1} \exp(-t) dt \tag{18}$$

$$\Gamma(\alpha) = \Gamma(\alpha, x) + \Upsilon(\alpha, x) \tag{19}$$

The distribution resulting from the SFT is a Gamma-like distribution. However it's parameters have a physical background. We note that a Gamma-distribution has also been largely employed to fit fragmentation data, e.g. Rubio et al. [14]. The behaviour of the cumulative mass distribution $M(< m)/M_T$ can be seen in figure (2).

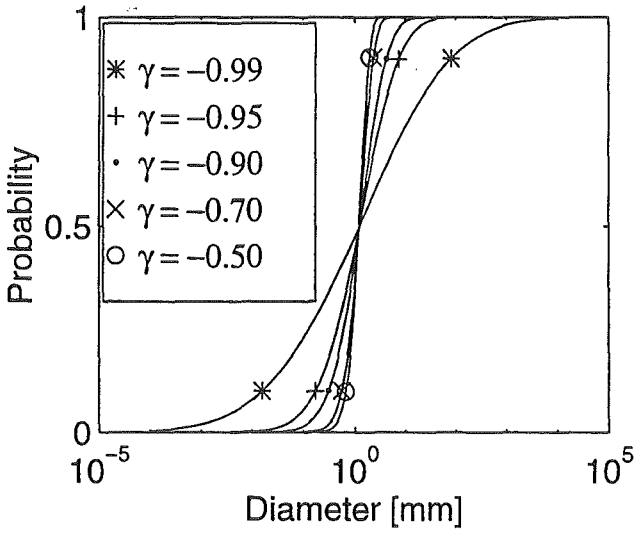

Fig. 2: *Plot of $M(< m)/M_T$ for γ values, -0.99, -0.95, -0.9, -0.7, -0.5.*

3 PERFORMANCE OF THE STATISTICAL DISTRIBUTIONS

3.1 Comparison of Statistical Distributions

To determine which of the four statistical distribution, mentioned above, is most suitable to fit debris data, two sets of MFCI experiments are used: One from KROTOS

experiments, conducted at JRC/Ispra [4], using corium and one set from MIRA-20L experiments, conducted at RIT/NPS [5], using CaO-B_2O_3, MnO_2-TiO_2 and WO_3-CaO melts, respectively.

The statistical distributions are fitted to the experimental data by using non-linear regression algorithm, the Levenberg-Marquart method, which minimises the global error function,

$$e = \sum [p_{i,exp}(l) - p_{i,fit}(l)]^2 \tag{20}$$

where $p_{i,exp}(l)$ and $p_{i,fit}(l)$ are the experimental and fitted number densities of the i-th observation. The unbiased estimate of the variance, $\sigma^2_{y|x}$ can be calculated from the following equation.

$$s^2 = \frac{\sum [p_{i,exp}(l) - p_{i,fit}(l)]^2}{N - \nu} \tag{21}$$

Here N is the total number of observed data points. The denominator, shows that ν degrees of freedom have been lost, for a ν parameter distribution. In the case of ULLN, ν is equal to three, and for SFT, LN and Weibull distributions, ν is equal to two. The variance of the fitting and the average variance can be seen in table (1) and (2). Figure (3) illustrates a typical comparison of the experimental data with the fitted distributions.

Table 1: Variance (s^2): *Fitting of corium experimental data.*

Exp.	ULLN	SFT	LN	Weibull
1	0.0064	0.0371	0.0457	0.1382
2	0.0497	0.0480	0.0551	0.1652
3	0.0206	0.0201	0.0288	0.2132
4	0.0130	0.0251	0.0332	0.1311
5	0.0496	0.0503	0.0582	0.2837
6	0.0910	0.0836	0.0867	0.0680
7	0.1211	0.0693	0.0730	0.0712
Avg.	0.0502	0.0476	0.0544	0.1529

Table 2: Variance (s^2): *Fitting of CaO-B_2O_3, MnO_2-TiO_2 and WO_3-CaO data.*

Exp.	ULLN	SFT	LN	Weibull
8	0.0030	0.0118	0.0162	0.0108
9	0.0054	0.0207	0.0306	0.0060
10	0.0082	0.0269	0.0360	0.0118
11	0.0036	0.0176	0.0235	0.0059
12	0.0037	0.0094	0.0122	0.0117
13	0.0010	0.0025	0.0063	0.0207
14	0.0044	0.0057	0.0064	0.0201
15	0.0016	0.0076	0.0057	0.0233
16	0.0035	0.0044	0.0167	0.0081
17	0.0048	0.0080	0.0200	0.0034
18	0.0210	0.0198	0.0243	0.0305
Avg.	0.0055	0.0122	0.0180	0.0138

A comparison between the variance of the three two-parameter distributions, see table (1) and (2), shows that the SFT distribution exhibits the lowest average variance, i.e. the best agreement with the distribution data. Furthermore, a comparison between the variance of the SFT and the ULLN, for corium data, demonstrates that the average variance is lower for the SFT. In the case of oxide melt data, the ULLN has a lower average variance than the SFT. In order to investigate if adding one parameter made any difference between the three parameter ULLN distribution and two parameter SFT distribution, an F-test was employed, Chatfield [15]. The F test can be formulated as,

$$F = \frac{\frac{e_2 - e_1}{n_2 - n1}}{s_2^2} \tag{22}$$

The value F follows the F distribution. The following hypothesis was then formulated,

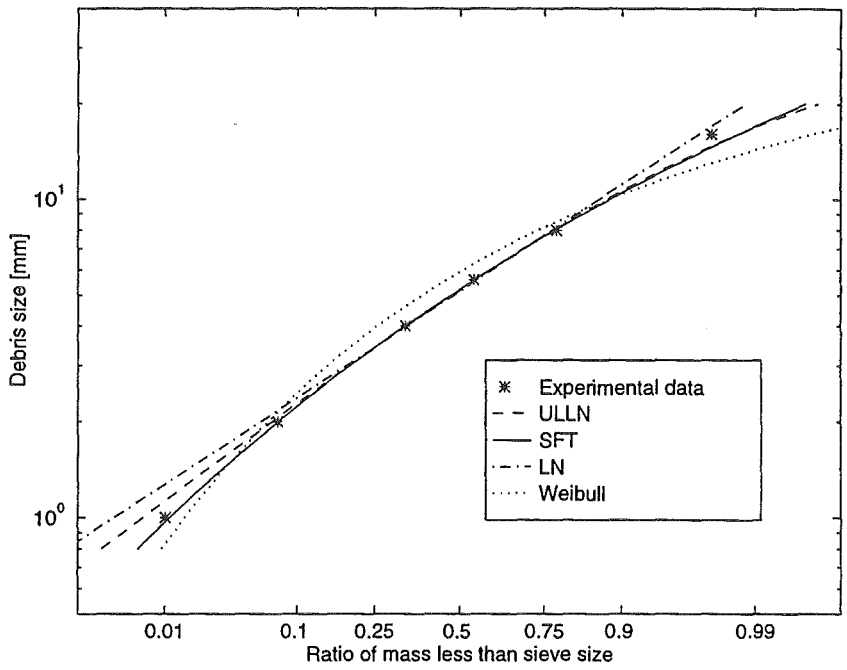

Fig. 3: *A typical comparison between the experimental and fitted distributions.*

H_o: ULLN better than SFT. $(F \geq F(\alpha, n_2 - n_1, N - \nu))$
H_1: SFT is as good or better than ULLN. $(F \leq F(\alpha, n_2 - n_1, N - \nu))$

From equation (22) it is found that F has the average value of 2.2. The values for $F(\alpha, n_2 - n_1, N - \nu)$ can be found in tables, [15]. With 95% confidence, the $F(\alpha, n_2 - n_1, N - \nu)$ values range from 5.99 to 10.13. It can be said with 95% confidence that SFT is as good or better than the ULLN distribution for data fitting.

It should be noted that for the wide range of experimental data on debris fragments, from low density $CaO - B_2O_3$ to high density corium, the SFT gives satisfactory fits to the experimental data. For experiments performed with corium at high temperature and density, γ was in the range from -0.76 to -0.90 and σ in the range from 1.71mm to 0.92mm. For oxidic melts, performed at lower temperature and with three, lower density, oxide melts, parameters γ and σ vary from -0.63 to -0.87 and 6.2mm to 1.8mm, respectively.

3.2 Parameters of the SFT

The γ parameter of the SFT is defined in terms of fractal dimension, equation (6), as $\gamma = -D_f/3$. The equation for the fractal dimension can be written as,

$$D_f = -3\gamma = \frac{\log(N)}{\log 1/r} \tag{23}$$

Where r represents fractional size and N is the number of new fragments, after each se-

quential fragmentation. From this equation it can be shown that, as $D_f \rightarrow 3$ the fragments are more volumetric. As $D_f \rightarrow 2$ a two dimensional shaped fragments are observed. Figures (4) and (5) show the fractal dimension, as a function of mass mean diameter for the corium and the three oxidic melts. The figures show that the fractal dimension varies between approximately two and three which depends on the shape of the debris. In the case of corium the particles become more volumetric as they become smaller. A jagged or rough debris is observed as the mass mean diameter becomes bigger.

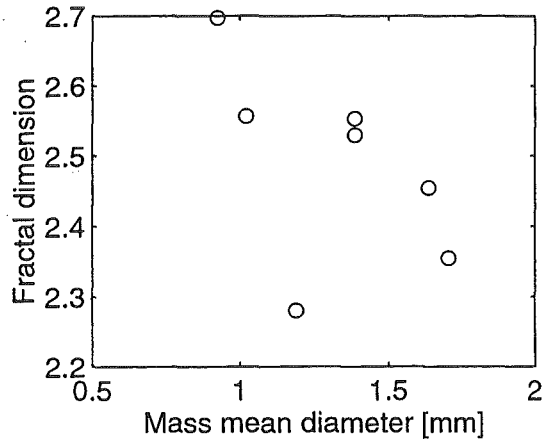

Fig. 4: *Fractal dimension as a function of mass mean diameter for corium.*

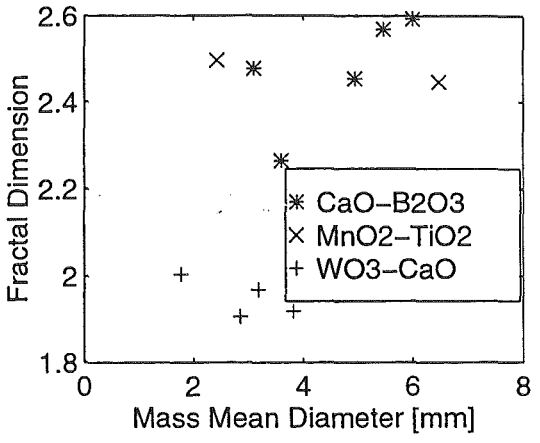

Fig. 5: *Fractal dimension as a function of mass mean diameter for oxidic melts, CaO-B_2O_3 (*), MnO_2-TiO_2 (X) and WO_3-CaO (+).*

Examination of the data, obtained from the fitting of the SFT does not give any clear correlation between the experimental conditions and the fractal dimension.

4 CONCLUDING REMARKS

Examination of four different statistical models for particle size distribution indicates that the sequential fragmentation theory of Brown [1], which results in Gamma type distribution, provides the best fit the debris distribution data. The parameter γ for the data was found to lie in the range of -0.62 to -0.9.

The fractal dimension varies between two and three for the experimental data analysed. There is no clear correlation between the experimental conditions and the fractal dimension.

ACKNOWLEDGEMENT. This work was supported by Swedish Nuclear Power Inspectorate (SKI), U.S. NRC, Swedish and Finish Power Companies, Nordic Nuclear Safety Project, Swiss Nuclear Inspectorate (HSK), and the European Union. Many thanks are due to Dr. T.N. Dinh and Dr. Z.L. Yang for their thoughtful comments and Dr. I. Huhtiniemi at JRC/Ispra for the KROTOS melt distribution data.

NOMENCLATURE

Arabic

D	Dimension
e	Global error

k	Free fitted parameter
l	Sieve size
$M(<l)$	Cumulative mass of fragments less than sieve size l
M	Mass
m	Mass
mn	Mass distribution
N	Number of fragments, total number of data points
n	Number distribution, number of points
p	Probability
r	Fractional size
s	Standard deviation

Greek

γ	Free fitted parameter
μ	Free fitted parameter, location
ν	Number of parameters
σ	Average size, scale

Subscript

$\overline{1}$	Mean
f	Fractal
$i-exp$	Experimental number density of i
$i-fit$	Fitted number density of i
p	Most probable (mode)
T	Total

REFERENCES

[1] W.K. Brown, "A Theory of Sequential Fragmentation and Its Astronomical Applications", Journal of Astrophysics, Vol 10 (1989), pp. 89-112.

[2] A.J. Yule and J.J. Dinkley, "Atomization of Melts: For Powder Production and Spray Deposition", Oxford, (1994), pp. 397

[3] D.F. Fletcher, "The Particle Size Distribution of Solidified Melt Debris from Molten Fuel-Coolant Interaction Experiments", Nuclear Engineering and Design, Vol 105 (1988), pp. 313-319.

[4] D. Magallon, I. and H. Hohmann, "In-Vessel Loads Resulting From Molten Coolant/Structure Interactions", Proceedings of Service Experience, Structural Integrity Severe Accidents, and Erosion in Nuclear and Fossil Plants, ASME, PVP-Vol. 303 (1995).

[5] H.Ó. Haraldsson and B.R. Sehgal, "Effect of Subcooled Liquid Coolant on Particle Size Generated During Fuel Coolant Interactions", CD-ROM Proceedings of Ninth International Conference on Nuclear Reactor Thermal Hydraulics (NURETH-9), ANS (1999).

[6] R.R. Irani and C.F. Callis, "Particle Size: Measurements, Interpretation and Applications", John Wiley and Sons, New York, 1963.

[7] W. Weibull, "A statistical Distribution Function of Wide Applicability", Journal of Applied Mechanics", 18 (1951), pp. 193-197.

[8] L.R. Kittleman Jr., "Application of Rosin's Distribution in Size-Frequency Analysis of Clastic Rocks", Journal of Sediment. Perol., 34, (1964) pp. 483-502.

[9] M.R. Geer and H.F. Yancey, "Expression and Interpretation of the Size Composition of Coal", Transaction of Am. Inst. Min. Metall. Pet. Eng., 130, (1938) pp. 250-269.

[10] W.K. Brown, R.R. Karpp and D.E. Grady, "Fragmentation of the Universe", Astrophys. Space Sci., 94 (1983), pp. 401-412.

[11] A.N. Kolmogorov, "Logarithmically normal distributions of fragmentory particle sizes", Dokl. Akad. Nauk. SSSR, 31 (1941), pp. 99-101.

[12] L.G. Austin, "Handbook of Powder Science and Technology", Reinhold, New York, (1984), p. 562.

[13] W.K. Brown and K.H. Wohletz, "Derivation of the Weibull Distribution Based on Physical Principles and its Connection to the Rosin-Rammler and Lognormal Distributions", Journal of Applied Physics, Vol 78(4), 1995, pp. 2758-2763.

[14] L.M. Rincón-Rubio, A. Kumar and S. Hartland, "Drop-Size Distribution and Average Drop Size in Wirz Extraction Column", Trans IChemE, Vol. 72, Part A, (1994), pp. 493-502.

[15] C. Chatfield, "Statistics for Technology", Chapman and Hall, London (1983).

OECD Workshop on Ex-Vessel Debris Coolability
Karlsruhe, Germany, 15-18 November 1999

Organised in collaboration with
Forschungszentrum Karsruhe (FZK) GmbH

EXPERIMENTAL INVESTIGATION ON DRYOUT HEAT FLUX OF A PARTICLE DEBRIS BED WITH A DOWNCOMER

Z.L. Yang, M. Konovalikhin, G.J. Li and B.R. Sehgal
Division of Nuclear Nuclear Power Safety
Royal Institute of Technology
10044 Stockholm, Sweden
yang@ne.kth.se

ABSTRACT

This paper presents the results of experimental investigation on dryout heat flux of a particulate debris bed. A series of experiments on the POMECO (POrous MEdia COolability) facility were performed for both homogeneous and stratified heated porous beds. The porous beds were made of different sand particles. The porosity of particle bed was varied from 25 to 40%, and the average particle size from 0.2 to 1 mm. Experimental results for the dryout heat flux of homogeneous beds with top flooding compare well with the predictions by Lipinski correlation. For the stratified particle beds, the fine particle layer resting on the top of another particle layer is found to dominate the dryout processes. The effect of a downcomer on the dryout heat flux was also investigated for both homogeneous and stratified particle beds. It was found that the downcomer can enhance the dryout heat flux from 50 to 350%.

1 INTRODUCTION

The Swedish BWRs employ a deep pool in the lower dry well as a severe accident management scheme to cool the melt discharged from the failed vessel. In the absence of a steam explosion, a deep debris bed may result, which maybe composed of a melt layer topped by a crust, and a particle bed, resting on it. The particle bed will have a gradation of particle sizes, with smaller size particles forming the very top layers, since they will be levitated by the steam produced during melt-water interaction event depositing later on the bed.

Numerous experimental and analytical studies have been performed to investigate the dryout heat flux of a debris bed with top flooding. Significant progress in understanding the characteristics of dryout heat flux has been achieved. For example, it was found that the coolability of debris beds depends strongly on particle size, shape and porosity distribution. Small particle size beds are more difficult to cool than the large size particle beds. Beds with small porosity are more difficult to cool than those with large porosity.

Lipinski correlation [Lipinski, 1982] appears to work well for predicting bed dry-out heat flux, with flooding, from top, of an one-dimensional debris bed. The FARO experimental results [Magallon, 1997] for a core melt jet injected into saturated water show that the resulting debris bed may be stratified with a particulate debris bed resting on top

of a "cake" of agglomerated partially-molten particles having very low porosity. Melt jets injected into subcooled water have been found to fragment into smaller size particles. In addition, stratification will occur if a small steam explosion occurs producing submicron size particles which will be blown upwards, to settle down later on top of the bed as a very low porosity debris layer. Such a bed for the conservative accident scenarios may be un-coolable [Sehgal, 1998].

Previously, Hofmann (1984) presented some results on dryout heat flux in a porous debris bed with a downcomer. The liquid was driven by natural convection from the downcomer annulus and entered the bed through a permeable base. The dryout started near the top of the bed and the dryout heat flux was more than twice as high as in a comparable top-flooded bed.

Previously, Becker (1990) also performed experimental investigations on debris bed coolability by introducing vertical tubes into the debris bed. These tubes acted as downcomers to channel water from an overlying water pool to the bottom regions of the bed. In this approach the limitations associated with counter-current flows of steam and water in a porous bed are reduced. Significant enhancement of dryout heat fluxes was found, even for a stratified debris bed of small particles, resting on top of a bed of larger particles. The database, and related theoretical background developed, however, were not sufficient to develop reliable estimates for coolability enhancement as a function of the controlling parameters.

In this paper, description and results of experiments performed to study the dryout heat flux of a particle debris bed with different configurations is provided. The focus is put on the dryout heat flux for low porosity, fine particle size, and different debris bed configurations (homogeneous and stratified particle beds, with or without downcomers).

2 EXPERIMENTAL FACILITY

A schematic of POMECO facility, constructed in the laboratory of the Nuclear Power Safety Division (NPS) of Royal Institute of Technology (RIT), is shown in Figure 1. The POMECO facility consists of a water supply system, a test section, a heater system and measurement and DAS systems.

The particle beds employed in the experiments are made of different sand samples, which have different mean particle size and porosity. Sand sample B is of 2-5 mm diameter with mean diameter of 4.01 mm and packing porosity of 0.405; Sample C is of 0.5-2 mm diameter with mean diameter of 0.92 mm and packing porosity of 0.375; and sample E is of 0-2 mm diameter with mean diameter of 0.198 mm and packing porosity of 0.38. We measured the porosities of different mixtures of these sand samples, and found that the mixture of sample B, C and E with mass ratio of 7:7:6 had the lowest porosity of 0.256. The top surface of the particle bed is covered by grids with small enough size to avoid channel formation in the particle bed and the flying-off of small size sand particles.

2.1 Test section

The test section is a stainless steel vessel of 350×350mm square cross-section and with an upper and a lower part. The height of the lower part is 500 mm and the height of upper one 900 mm. The maximum height of 450 mm is available for the sand bed. A porous plate was placed 50 mm above the bottom of the test section to provide enough space for the distribution of water, coming from the downcomer, to the sand bed. The downcomer is a tube of stainless steel with 550mm height and 30 mm internal diameter, it

Schematic of POMECO facility

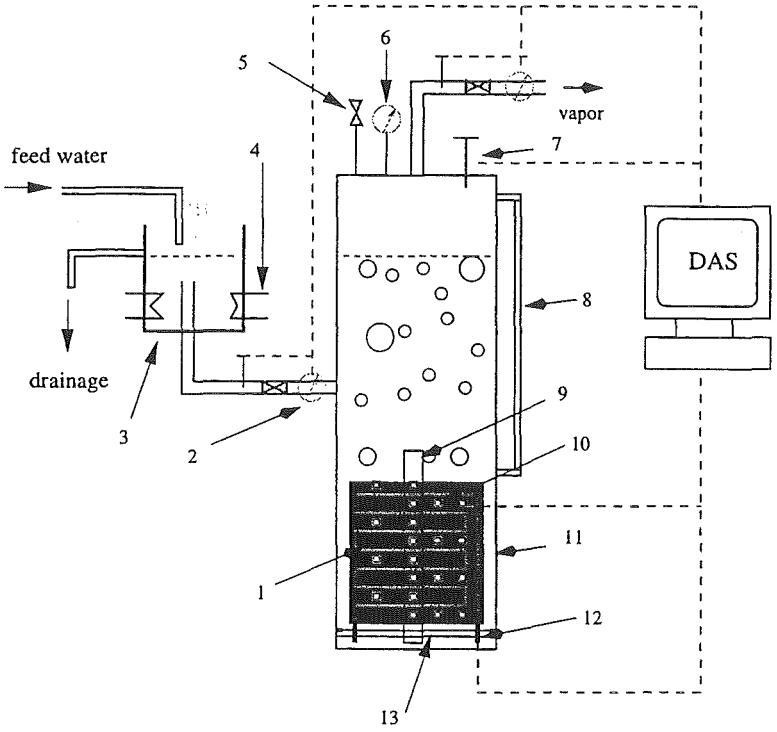

Fig. 1: Schematic of the POMECO facility.

is fixed on the porous plate. Before the sand bed is formed, a grid is placed on this porous plate in order to prevent fine sand particles from falling into the bottom space.

In the POMECO facility, the sand bed is heated internally by 22 resistance heaters with the maximum power delivery of up to 43KW.

2.2 Instrumentation and data acquisition system (DAS)

The temperature of vapor generated in the test section is measured in the steam flow line, downstream the Vortex meter. The most important measurements in this experiment are the temperatures of the coolant and the sand bed. Thirty-three thermocouples are distributed in presentative positions of the particle bed. The outputs of these thermocouple are monitored carefully in order to determine the occurrence of the dryout.

The experiments are all performed at atmospheric condition. One pressure transducer ranging from 0 to 30 psi is installed downstream the vortex meter to measure the pressure of the steam to evaluate the mass flow rate of the steam generated in the particle bed.

The steam flow rate is measured by a Vortex Flow Meter made by Omega Company, which is installed into the steam drain line (as shown in Figure 1). The range of this meter is up to 30 liter/sec. From the steam flow rate, we can evaluate the heat removal from the particle bed at the point of the dryout.

All the parameters mentioned above were sampled by using a HP data acquisition system. The sampling rate of 1 or 2 Hz is chosen.

3 EXPERIMENTAL RESULTS AND DISCUSSION

Two series of experiments have been performed for both homogeneous and stratified particle beds, respectively. The effects of porosity, mean particle size, and stratification of the particle bed on the dryout heat flux have been tested.

3.1 Homogeneous particle beds

Table 1 shows the experimental matrix and sand particle specifications for the homogeneous particle beds. Three sand particle beds were tested, in which the porosities of the particle beds are varied from 0.258 to 0.397, the mean (weight-averaged) particle sizes are smaller than 1 mm. For each sand particle bed, two experiment were performed i.e., with and without a downcomer, respectively.

Table 1: Experimental matrix for homogeneous particle beds.

Test Number	Sand Bed Type	Downcomer
Homo-1.1	Sand sample: 0-2mm diameter, Porosity = 0.397 D_{mean} = 0.198mm	No
Homo-1.2	same as Homo-1.1	Yes
Homo-2.1	Sand sample: 0.5-2mm diameter, Porosity = 0.365 D_{mean} = 0.92mm	No
Homo-2.2	same as Homo-2.1	Yes
Homo-3.1	Sand sample: sand mixture-M_B:M_C:M_E=7:7:6 Porosity = 0.258, D_{mean} = 0.8mm	No
Homo-3.2	same as Homo-3.1	Yes
M - mass fraction; Types of sand B: 2-5 mm; C: 0.5-2 mm; E: 0-2 mm		

Table 2 shows the experimental results on the dryout heat flux for the homogeneous particle beds with and without a downcomer. The predictions of dryout heat flux by Lipinski's zero-dimensional model [Lipinski, 1982] for the particle beds without a downcomer are also listed in this table. It can be seen that for the particle beds with relatively large mean particle sizes (test Homo-2.1 and Homo-3.1) and different porosities the experimental results on dryout heat flux agree quite well with the predictions by Lipinski's model. For the very fine particle bed (test Homo-1.1), the experimental result on dryout heat flux is much higher than the prediction by Lipinski's model. The porosity in this bed is not low. This indicts that the capillary force may play a part to suck the water into the bed, and results in the higher dryout heat flux. This also demonstrates that in the Lipinski's model the capillary force is weak, therefore, it underpredicts the dryout heat flux for the particle beds with fine particles.

Form Table 2 it can be also seen that the contribution from a downcomer to the dryout heat flux is significant. As the downcomer has a larger hydraulic head than that of

Table 2: Experimental results on dryout heat flux for homogeneous particle beds.

Test Number	Experiment KW/m^2	Lipinski model KW/m^2	Enhancement by downcomer
Homo-1.1	89.8	23.2	
Homo-1.2	183.0		103.8%
Homo-2.1	222.04	215.1	
Homo-2.2	331.42		49.26%
Homo-3.1	44.9	51.4	
Homo-3.2	202.04		348%

the particle bed, natural circulation can be established. Therefore, water can be channeled to the bottom of the particle bed through the downcomer. The dryout heat flux consists of two parts. The first is the contribution of the water penetrating from the top of the particle bed, which is governed by counter-current two-phase flow (CCFL), the only contribution to the dryout heat flux of the particle bed without a downcomer. The second is the contribution from the water channeled to the bottom of the particle bed through the downcomer, and rising through the bed by natural circulation.

The experimental results show that larger enhancement of dryout heat flux by a downcomer occurs for the particle beds with fine particles or low porosity. This clearly indicates that besides the hydraulic head difference in the downcomer and particle bed, the capillary force also contributes to the driving head of the natural circulation in the pool. Strong capillary force can enhance the natural circulation (increasing the mass flow rate of water), therefore, increasing the effect of a downcomer on the dryout heat flux. Basically, the stronger capillary force is observed in smaller flow channels, e.g. lower porosity or porous debris bed with finer particles. Between the experiments Homo-1.2 and Homo-3.2, experiment Homo-3.2 shows larger enhancement of dryout heat flux by a downcomer. Though the weight-averaged particle diameter in Homo-3.2 is three times larger than that in Homo-1.2, the porosity of Homo-3.2 is much less than that of Homo-1.2. We believe that the characteristic channel size in the experiment Homo-3.2 is smaller than that in the experiment Homo-1.2, therefore, the capillary force in Homo-3.2 is larger than that in Homo-1.2.

In the experiments for the particle beds without the downcomer the dryout always occurs in the upper half of particle beds, which is similar to the previous observations. However, the position of the dryout for the particle beds with downcomer is always higher than that for the particle beds without the downcomer. This indicates that the downcomer improves the mass flow rate of water in the particle bed by natural circulation.

3.2 Stratified particle beds

Table 3 lists the experimental matrix and sand particle bed configurations for the stratified particle beds. Four beds were tested. Focus of the experiments is on the effects of the configuration (such as porosity, mean particle size and the thickness) of the fine particle layer, resting on the top of another particle bed, on the dryout heat flux. In all the experiments, the lower particle layer employed the same particle configuration (mean size and porosity). Like the experiments with the homogeneous particle beds, two experiment were performed i.e., with and without a downcomer, respectively.

Table 3: Experimental matrix for stratified particle beds.

Test Number	Sand Bed Type	Downcomer
Strat-1.1	Upper layer: 0-2 mm, H = 130 mm Lower layer: 0.5-2 mm, H = 240 mm	No
Strat-1.2	same as Strat-1.1	Yes
Strat-2.1	Upper layer: sand mixture - M_B:M_C:M_E=7:7:6, H = 130 mm Lower layer: 0.5-2 mm, H = 240 mm	No
Strat-2.2	same as Strat-2.1	Yes
Strat-3.1	Upper layer: 0-2 mm, H = 240 mm Lower layer: 0.5-2 mm, H = 130 mm	No
Strat-3.2	same as Strat-3.1	Yes
Strat-4.1	Upper layer: sand mixture M_B:M_C:M_E=7:7:6, H = 240 mm Lower layer: 0.5-2 mm, H = 130 mm	No
Strat-4.2	same as Strat-4.1	Yes

Table 4 shows the experimental results on the dryout heat flux for the stratified particle beds with and without a downcomer.

Comparing the experiments Strat-2.1 and Strat-4.1 in Table 3 with the experiment Homo-3.1 in Table 1, the upper particle layer of experiments Strat-2.1 and Strat-4.1 is the same as the particle bed of experiment Homo-3.1, which has the low porosity configuration. Experimental results on the dryout heat flux in these three cases (see Table 2 and 4) show that stratification of the particle beds does not decrease the dryout heat flux below that for the homogeneous porosity layer. This is much different from the analytical and experimental observations by Lipinski (1983). Lipinski (1983) reported that the stratification of the particle bed could significantly decrease the dryout heat flux because of the much lower porosity at the interface of two different layers, which is caused by the large difference in particle size between two different particles. In the experiments Strat-2.1 and Strat-4.1, the porosity at the interface can not be lower than that of upper layer, which is the lowest to be obtained from the sand particle samples. Thicker upper layer leads to the higher dryout heat flux; this tendency agrees with the prediction of Lipinski' model (1983).

The thickness of the fine particle layer has different effect from that of low porosity. Comparing the particle bed configurations of Homo-1.1 in Table 1, Strat-1.1 and Strat-3.1 in Table 3, and experimental results on dryout heat flux for these three experiments in Table 2 and Table 4, it can be seen that the stratification decreases a little the dryout heat flux. The decrease of the dryout heat flux may be caused by the reduction of the porosity at the interface between the layers. However, as the particle size of the upper layer is too small, the capillary force aids the water penetration processes. Therefore, the thickness of fine particle layer has little effect on the dryout heat flux.

It can also be seen in Table 4 that the effect of the downcomer on the dryout heat flux is significant. Minimum enhancement of the dryout heat flux by a downcomer is about 92.6%, and maximum reaches 242%. It is found that the thickness of the fine particle layer (see the case Homo-1.2 in Table 2, Strat-1.2 and Strat-3.2 in Table 4) has little effect on the dryout heat flux for the bed with a downcomer. This phenomenon is similar to that for the bed without a downcomer. The effect of the thickness of the low porosity layer on the

Table 4: Experimental results on dryout heat flux for stratified particle beds.

Test Number	Experiment, KW/m^2	Enhancement by downcomer
Strat-1.1	87.64	
Strat-1.2	186.77	113%
Strat-2.1	53.87	
Strat-2.2	138.28	157%
Strat-3.1	55.67	
Strat-3.2	190.36	242%
Strat-4.1	122.1	
Strat-4.2	235.26	92.6%

dryout heat flux, however, is not clear for the stratified particle bed with a downcomer.

The positions of the occurrence of the dryout for the experiments Strat-2.1 and Strat-4.1 are similar to that for the experiment Homo-3.1, so do the dryout positions, for the particle beds with a downcomer. This is because the stratification in these two cases does not decrease the porosity and mean particles size which is the most important parameter in governing the dryout heat flux. However, for the experiments Strat-1.1 and Strat-3.1, the dryout always occurs close to the interface between the layers, since that location has lower porosity than the rest part of the particle bed. The position of the dryout occurrence for the particle bed with a downcomer is always higher than that for the particle beds without a downcomer. This ia similar to that in the homogeneous beds.

4 CONCLUSION

In this paper, two series of experiments performed on the dryout heat flux with different configuration of the porous particulate bed have been described. One is with homogeneous beds, another one is with stratified beds. The porosity of particle bed was varied from 25 to 40%, and the average particle size from 0.2 to 1 mm.

The experimental results show that the dryout heat flux for homogeneous particle beds, without downcomer, agrees well with the predictions by the Lipinski model. For the stratified particle beds, the fine particle layer resting on the top of another particle layer is found to dominate the dryout processes. The effect of a downcomer on the dryout heat flux was also investigated for both homogeneous and stratified particle beds. The stratification and height of fine particle layer show little effect on the dryout heat flux for the bed with downcomer. It is found that the downcomer can enhance the dryout heat flux from 50 to 350%.

More experiments are needed to verify the effect of porosity on the dryout heat flux for stratified particle beds.

ACKNOWLEDGMENTS

This work was supported by the Swedish Nuclear Power Inspectorate, the European Union, the US Nuclear Regulatory Commission, Swedish and Finish Power Companies, Nordic Nuclear Safety Project and Swiss Nuclear Inspectorate.

REFERENCES

[Becker, 1990] Becker M., Engstrom, J. and Macbeth R.V., 1990, Enhancement of core debris coolability. TIT-Report: KTH-NEL-51.

[Hofmann, 1984] Hofmann F., 1984, On the location and mechanism of dryout in top-fed and bottom-fed particulate beds. Nuclear Technology, 65, 36-45.

[Lipinski, 1982] Lipinski R.J., 1982, A model for boiling and dryout in particle beds, NUREG/CR-2646(SAND80-0765), Sandia National Laboratories, NM.

[Lipinski, 1983] Lipinski R.J., 1983, A review of debris coolability models, Proceedings of International Meeting on Light Water Reactor severe Accident Evaluation, Volume 2, P. 18.2.1-18.2.6.

[Magallon, 1997] Magallon D., I. Huhtiniemi, A. Annunziato, A. Yerkess, and H. Hohmann, 1997, The FARO programme recent results and synthesis. CSARP Meeting, Bethesda, Maryland, May 5-8, 1997.

[Sehgal, 1998] Sehgal B.R., Yang Z.L., Dinh T.N and Paladino D., 1998, Investigation of ex-vessel melt coolability by bottom coolant injection. 6th International Conference on Nuclear Engineering(ICONE-6), May 10-15, 1998.

OCDE/CSNI-Workshop on EX-VESSEL DEBRIS COOLABILITY
Karlsruhe, Germany,November 16 - 18, 1999

Experimental investigations on particulate debris bed coolability in a multi-dimensional configuration

Étienne Décossin
Électricité de France , Research and Development Division
Heat Transfer and Aerodynamics Branch
6 quai Watier 78401 Chatou, France
Etienne.Decossin@edf.fr
Phone : (33) 1 30 87 78 51 , Fax : (33) 1 30 87 79 49

ABSTRACT

Within the frame of severe accidents research at Electricité de France, coolability of particulate debris bed in multidimensional configurations is investigated, in the objective of increasing knowledge on enhancing or reducing effects of corium coolability. Up to now engineering codes like MAAP rely on zero- or one-dimensional concepts coming from small scale experiments in homogeneous beds, to model boiling and dryout phenomena in porous media with heat source term. On the contrary, real debris bed configurations may exhibit a large horizontal extension : this could favor liquid circulations to occur.

The target of the SILFIDE[1] experimental program is to provide boiling and dryout results closer to the real, multidimensional configuration taking in account natural circulation due to the gravity contrast between liquid and vapor phase. The experiment focuses on spatial and temporal dryout inception : growth, heating and stability of dry zones. The shape and size of the facility have been designed to allow for multidimensional flows. It is composed of a parallelepipedic vessel, whose width is sufficiently small to restrict the phenomena to a two-dimensional configuration. Induction heated steel spheres, diameter ranging from 1.7 to 7.1 mm are used to simulate corium particles. A condensation loop allows to evaluate mass and energy balances. The temperature field is measured during the process.

The purpose of this communication is to show the results obtained in the first dryout tests, in comparison with calculations made with the numerical model WABE-2D[2], dedicated to boiling in porous media, with internal heat sources.

KEY WORDS

severe accident, dryout experiment, porous media

INTRODUCTION

In the improbable situation of a severe accident in a nuclear reactor, the major part of the fuel and structure has melted, and results to a magma called corium. One of the investigated situations is when corium takes the form of a heat generating particulate bed, after pouring in water. Corium debris granulometry is expected to range approximately between 1 and 10 mm. The particles keep generating an important amount of heat due to radioactive decay, so it is important to know whether coolability can be attained through boiling mechanisms in the porous medium. Numerous experimental small scale tests have been performed in the early 80's to estimate coolability (see for example [Hardee and Nilson, 1977], [Dhir and Catton, 1977], [Catton et al., 1983], [Reed et al., 1985], [Tsai, 1987]. These

[1] A French acronym for "simulation of fragmented debris with internal heat generation"
[2] Two-dimensional model under development at IKE Stuttgart

studies exhibit a limit to internal heat generation, beyond which it is not possible anymore to keep a steady state boiling regime. The influence of the bed height, pressure, particle size distribution and porosity has been studied. The so-called dryout heat flux could be of the same order of magnitude as the residual heat remaining a few hours after the accident initiation. Nevertheless, regarding the great scattering of the results, the disparity of the experimental methods and the impossibility to scale the results, only simple conservative criteria have been retained and used in engineering codes. They rely mainly on the Lipinski model [Lipinski, 1984] or its derivatives, which prediction is rather good using the experimental, but 1D and small scale, database.

Compared to the small scale analytical experiments, debris beds expected in the reactor case would have reversed aspects ratios : small height and large horizontal extension. (for example piles, cakes or slices ...). Numerous of these situations can favor liquid circulation in the porous medium and enhance coolability, as shown in [Mayr et al., 1998]. In studying the effect of an inclined bottom, which represents the vessel lower head, Horner et al. observed that no dryout occur at specific power larger than the Lipinski value [Horner et al., 1998].

We have identified three ways of research about the problem of corium particulate bed cooling :

- The momentum conservation laws used for two-phase flow in a porous medium, with local vapor generation, are not clearly justified. Up to know no model, relying on theoretical or experimental basis, is known to be completely applicable in this specific situation. This point remains an open problem, even in one-phase high speed flow. Although some attempts have been done to refine the laws (see for example [Tung and Dhir, 1988] and [Vujisic et al., 1991]), the validity of the Darcy-Forscheimer formulation, with relative permeabilities and passabilities modifiers, is most of the time assumed in recent models like WABE-2D [Mayr et al., 1998].
- In general we have little information about the flow patterns in the porous media. This is not only essential for the momentum conservation laws but also for the form of the local heat transfer coefficient, that could strongly be dependent of the local void fraction, as shown by Petit [Petit, 1998]. Increasing knowledge in this field should be useful to build a model valid for all the stages of the dryout process : boiling, dryout, heat-up, quenching.
- Specific dryout data should be obtained in specific multidimensional configuration to see the effect of the geometry on dryout conditions and to identify possible margins.

In the present work we propose a contribution to the last point : we are studying, on both experimental and numerical points of view, boiling and dryout in a homogeneous 2D particulate bed. In this paper we present the SILFIDE experimental facility and the first experimental dryout results compared to the values calculated by the WABE-2D code.

1 THE SILFIDE FACILITY

The experimental setup is composed of a parallelepipedic crucible, which aspect ratio favors the onset of two-dimensional phenomena. Concerning this important feature of the experiment, a critical analysis has been done in [Décossin, 1999] to evaluate the pathological effects of heat losses through the walls of the crucible, increased porosity along the walls and non-homogeneous heating due to electromagnetic skin effect. The horizontal cross section area of the crucible is 600 mm x 100 mm (figure 1). The crucible, which can receive particulate bed up to 500 mm in height is made with epoxide resin. Corium debris are simulated by steel spheres heated by induction. Four different diameters, ranging from

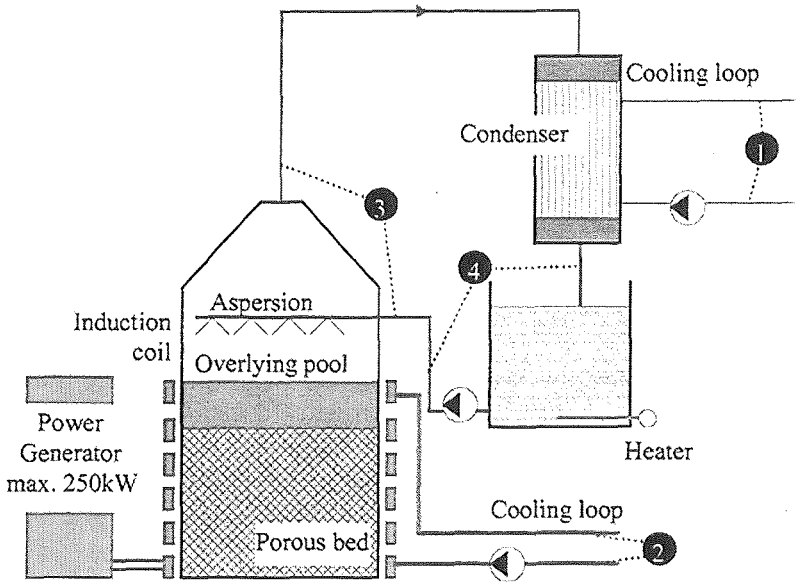

Fig. 1: Schematic of the SILFIDE facility

1.7 to 7.1 mm, are used. Water is used as the coolant, at atmospheric pressure. The generated vapor is led to a condenser. The liquid is reinjected at a controlled temperature to the crucible from a electrically heated vessel (figure 1). In the experimental procedure, it is planned to reach dryout by successive power steps, corresponding to steady-state boiling regimes. Induction power can vary between 0 and 250 kW, and frequency between 3 and 8 kHz. Temperature measurements are carried out thanks to 26 thermocouples included in the steel spheres. Pressure is measured at the top and the bottom of the porous bed. Thermal balances are performed on the condenser (**1**), the induction coil (**2**) the test section (**3**) and the hot water vessel (**4**) (figure 1). The facility is completely automated. An automaton is used to control the process and maintain the facility secured and safe. Scientific measurements are transmitted to a separated data logger connected to a workstation where the data are processed and archived. It is possible to define on the workstation level alert criteria for each channel that will be useful to detect the dryout inception (temperature excursions). Heat generation programs and movements of the thermocouples are defined on the workstation, then downloaded to the automaton that proceeds the test.

The experiment consists first in obtaining a good estimation of the heat generation distribution in the porous bed. Then the dryout heat flux for each geometrical configuration is measured and the corresponding heatup of the bed is recorded, in order to understand the phenomenology.

2 CALIBRATION TESTS

The electromagnetic heating method is simple to implement to simulate a heat generating porous bed, but it is quite difficult and even impossible to obtain a uniform heat source term, because of the electromagnetic skin effect. Although this phenomenon is very attenuated for a fragmented medium compared to a continuous metal block, it remains necessary to determine the heat generation distribution. As a matter of fact the thermal two-phase convection inside the bed could be driven by the heterogeneities of the heat source term.

In the following sections, the two stages of these preliminary calibration tests are described. In a few word the method consists of estimating separately the shape of the distribution pf and the global efficiency η of the induction heater, defined by equation (1).

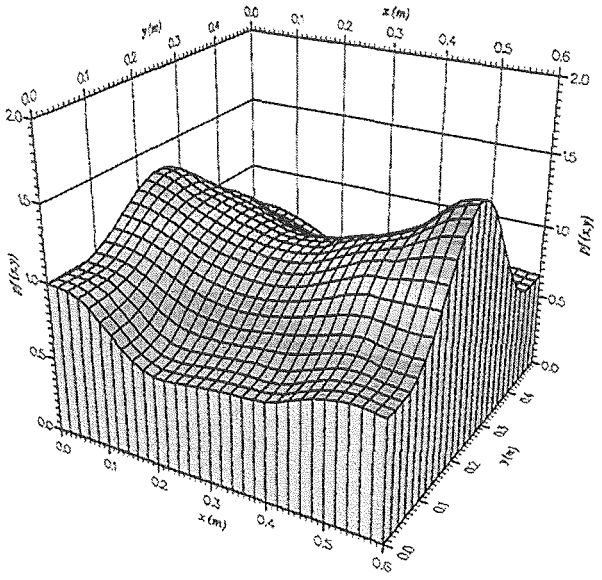

Fig. 2: Heat generation distribution - dry bed - H=500 mm - d_p=4.76 mm

$$q(\vec{x}) = \frac{Q_{elec}}{M_s}\,\eta(d_p, H)\,pf(\vec{x}) \tag{1}$$

2.1 Power distribution

The experimental procedure to estimate the heat source distribution consists of heating the bed with different induction powers, at the same frequency (2.8 kHz in the present case). The bed can be initially dry or saturated with liquid water. The conduction characteristic time through the bed is long (about 13 hours in the present case) so the local specific power is proportional to the initial temperature slope.

The aim of these preliminary experiments is not to extract a general law valid for all the configurations, because the dependence of the geometrical, physical and electrical parameters can be complicated. We simply require for each individual case the specific power spatial distribution that will be an input term for later numerical simulations. Keeping this in mind, the calibration tests have been performed for each particulate bed before the dry-out experiments, using electric powers ranging from 40 to 100 kW. They show that the heat source distribution is almost independent of the electric injected power. Moreover the same result is obtained with dry of water-filled bed, which indicates that the local heat generation does not depend of the local liquid fraction.

Both consequent axial and lateral heterogeneities have been found, with a ratio of 3 between the minimum and the maximum (figure 2). Lateral differences can be interpreted by electromagnetic skin effect : the electric eddy currents are stronger close to the border of the metallic matrix than in the center. Axial heterogeneities can be due to rapid opening-out of the field lines at the extremities of the induction coil. In fact the heat generation distribution exhibits two peaks close to the lateral walls. Their vertical position seems to be dependent of the height of the bed and even more generally to the relative position of the bed with the induction coil.

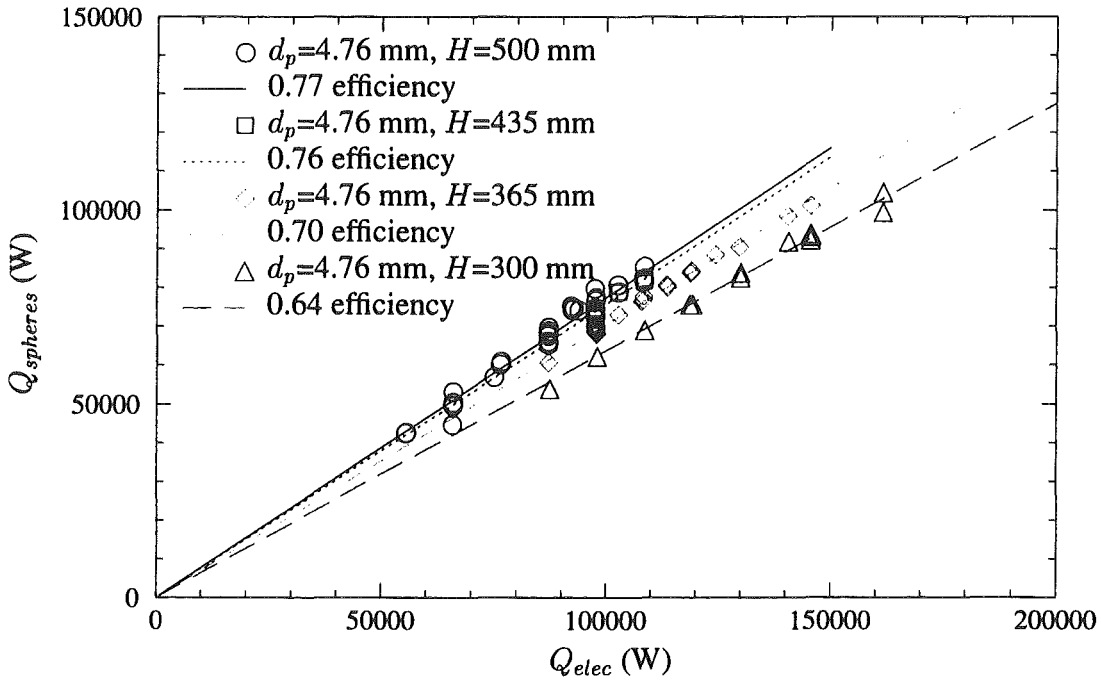

Fig. 3: Estimation of the efficiency of induction heating

2.2 Heating efficiency

In order to know the local value of the heat generation, on one hand we need the shape of the distribution, for example with the method described in 2.1, and on the other hand we need the conversion ratio between the effective mean power in the steel spheres $Q_{spheres}$ and the electric power Q_{elec}. This efficiency has been estimated for each (d_p, H) point of the test matrix using the numerous steady state boiling regimes observed before dryout during the test. A thermal balance on the condensation loops yields to the mean power generated by the steel spheres. Different measurements are plotted on figure 3. They show a linear relation which slope is the efficiency of the heating process.

3 DRYOUT TESTS AND RESULTS

3.1 Experimental method

The dryout heat flux is defined by the dryout power divided by the horizontal cross section of the bed. In the SILFIDE experimental its measurement is obtained using the following procedure :

- First, successive power steps of 10 minutes each are applied to bed. The first step where temperature excursions are detected gives a first approximation of the dryout power.
- Second, the maximum power value for which no temperature excursion are observed is used as a reference steady state boiling regime, maintained during 45 minutes. Then different power excursions are tried : the lowest value for which temperature excursions are observed correspond to the dryout power.

This method provides both a measurement of the dryout heat flux and the dryout transients (heat-up of the bed) for different power levels beyond the critical heat flux. This can be useful for comparisons with numerical simulations.

3.2 Critical heat flux

Up to now 7 dryout series have been performed. They concern the influence of bed height for particle diameter d_p=4.76 mm, and the influence of particle diameter for bed height H=500 mm. In every case the debris bed is covered with a water pool on 300 mm high. Dryout heat flux values are given on figure 4. In every case, the critical heat flux is greater than the Lipinski 1D criterion usually employed in particulate bed models. So one can expect enhancing effects on coolability in multi-dimensional configurations. As already observed in the numerous experimental and numerical studies on this subject, the measurements exhibit the same tendencies concerning the effect oh H and d_p. The dryout heat flux increases with particle diameter and decreases with bed height. However the effect of H seems to be more pronounced in the present work. Predictions of dryout heat flux have been done with the numerical model WABE-2D, using the effective heat source distribution measured for each experiments. The results, given on figure 4, are systematically lower than the experimental ones, and the effect of bed height is not predicted. The explanation for these differences is not entirely clear yet. One can suggest the following hypotheses :

- The dependency of H could not be so simple. As a matter of fact it is possible that the results depend also on the relative position of the bed with the induction coil. Complementary experiment are needed to know whether every position of a given particle bed in the coil are equivalent or not.
- Liquid circulation could be stronger in thinner beds : the ratio H_{water}/H reaches 1 for H=300 mm. One can expect an important coupling between the water reservoir and the porous bed, that we cannot take into account in the WABE-2D model.

3.3 Temperature field

Using the mesh of thermocouples, one can deduce the solid temperature field during post dryout transient. The zones where temperature excursions above the saturation value are detected correspond to the locations where the void fraction is very close to 1. Depending on the power we have identified two regimes :

- For values a little lower than the dryout power, some temperature readings have a chaotic behaviour (see figure 5). Alternative temperature excursions and fast returns to saturation are observed. This could be the signature of a flow regime where the vapour occupies most of the part of the pore space, and where non thermal equilibrium effects become important.
- For values higher than the dryout power, the temperature readings exhibit zones where the solid temperature increases fastly and reaches 200 °C over about 1 minute (figure 5). This corresponds to dry zones extension in locations where the liquid cannot replenish anymore the pore space. The local power which cannot be evacuated by boiling contributes directly to increase the temperature of the particles.

Concerning the location of the dry zones, figure 6 gives a typical example of the dryout behaviour observed in all the tests. The first dry spots appear on the two lateral borders of the test section, which are the places where the heat source, cumulated on the vertical direction, is the highest. So the explanation for this first phase of the dryout transient is straightforward. Moreover the WABE-2D code successfully predict these dry zones locations (see figure 6).

Another dry spot has been observed later in the transient ($t \geq 1800$ s on figure 6). The dry zone extends in the center, in a place where the local heat source is minimal. Up to

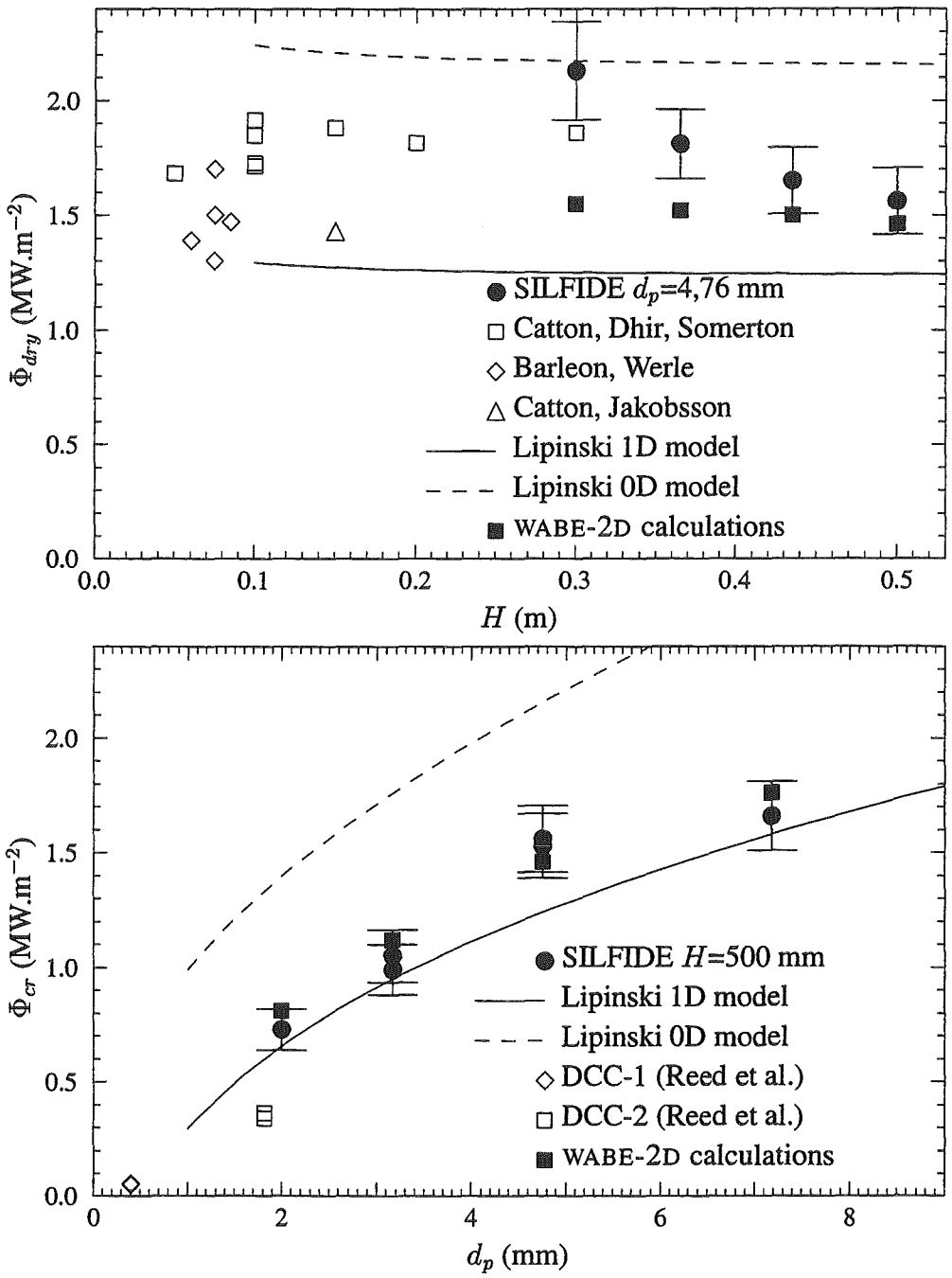

Fig. 4: Dryout heat flux measurements in the SILFIDE facility

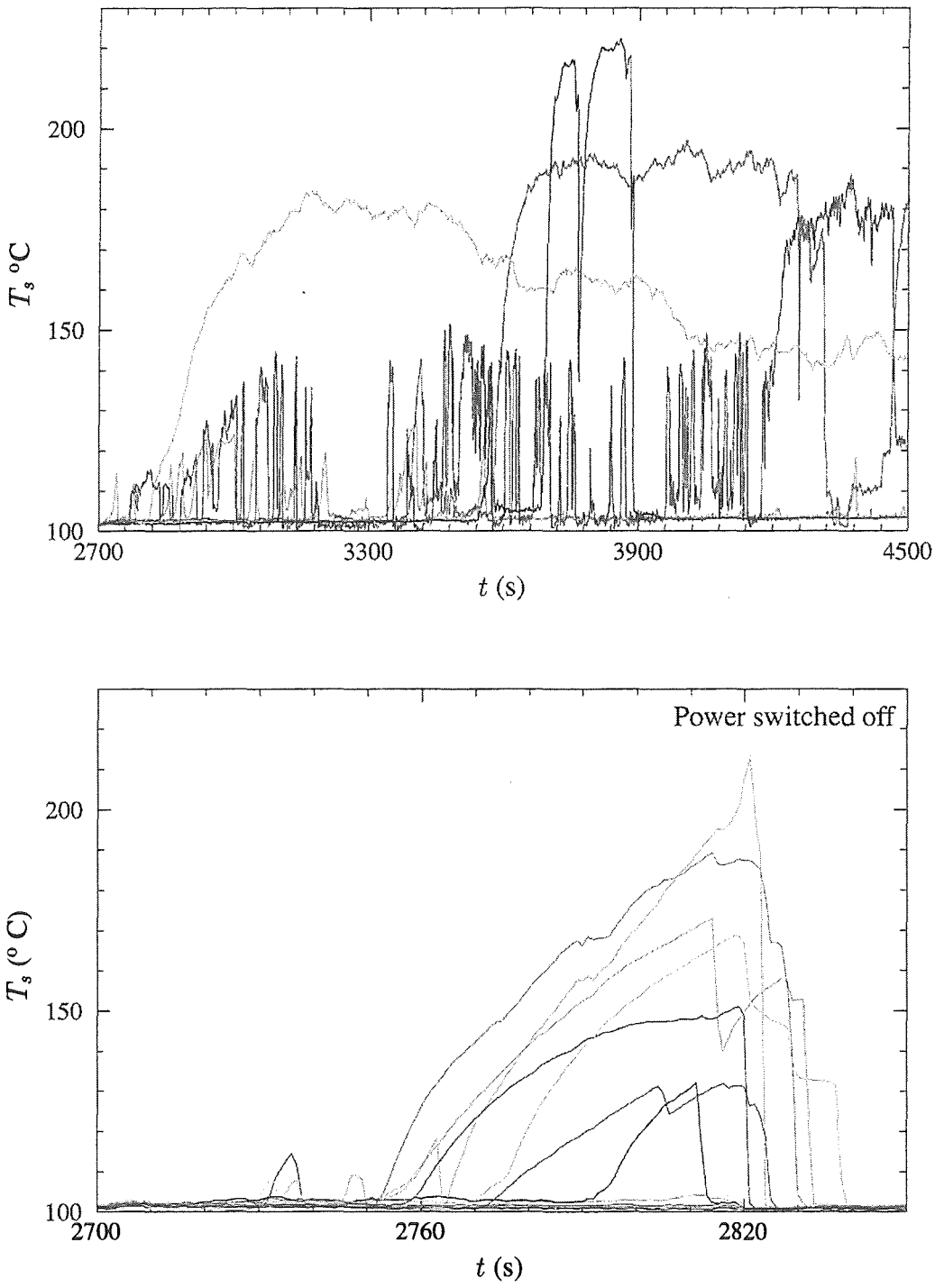

Fig. 5: Examples of solid temperature mesurements for a chaotic regime (top) and a dryout transient (bottom) - H=500 mm - d_p=7.18 mm. The different curves correspond to different locations in the porous bed.

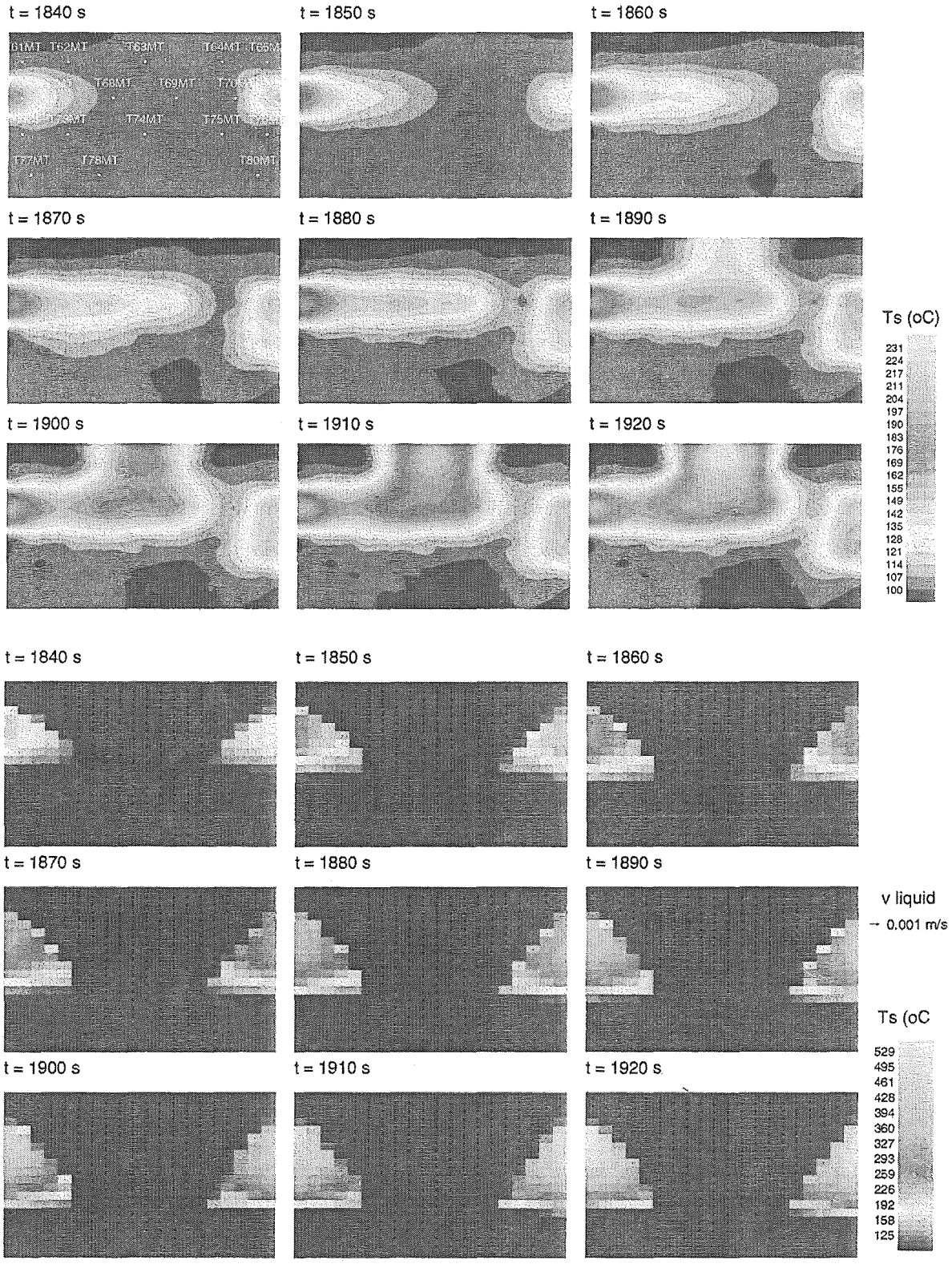

Fig. 6: Example of an experimentally measured solid temperature field (top), comparison with a WABE-2D prediction - H=365 mm - d_p=4.76 m

now, we have not found any acceptable explanation for this fact, that is not predicted by the numerical model. As we said in 3.2 about dryout heat flux, coupling with the overlying water pool may have an influence on the complete phenomenon. So we can expect stronger sub-saturated liquid currents in the center of the bed, that could induce a vapor blockage in this region. Nevertheless this has to be clarified with further investigations.

CONCLUSION

The SILFIDE experiment is dedicated to investigate boiling in porous media with internal heat sources, on order to simulate a heat generating corium particle bed that could be encountered in a severe accident of a nuclear reactor. The objective of the experiment is to provide a dryout heat flux database valid for multi-dimensional configurations, and validation results, mainly temperature fields, for 2D numerical models, like WABE-2D. Prior to the dryout tests themselves, we show that it is necessary to know the specific power distribution in the bed, that cannot be homogeneous with induction heating and can have an important influence on the results in a 2D configuration, where thermo-convective two-phase flow can be driven by the power heterogeneities. The differences in specific power can be of a factor of 3 in the present experiments. The first dryout results exhibit a margin with 1D dryout criteria, which is not not completely predicted by the WABE-2D code. The numerical model only can explain the fist part of the dryout transient, due to the lateral specific power heterogeneities. The experiment program is still in progress. Once the dryout database completed for the 2D homogeneous bed, More complex, heterogeneous configurations will be studied with the SILFIDE facility.

List of symbols

d_p	Effective particle diameter	m
H	Bed height	m
H_{water}	Height of water pool	m
M_s	Mass of particles	kg
Φ_{dry}	Dryout heat flux	$W.m^{-2}$
q	Specific internal power	$W.kg^{-1}$
Q_{elec}	electric power	W
pf	Heat source normalized distribution function	–
T_s	Solid temperature	°C
$\vec{x}$	Position vector	m

References

[Catton et al., 1983] Catton, I., Dhir, V., and Somerton, C. (1983). An experimental study of debris coolability under pool boiling conditions. Technical Report NP-3094, EPRI.

[Décossin, 1999] Décossin, E. (1999). Numerical investigations on particulate debris bed coolability : critical analysis of the silfide experimental project. In *Ninth international topical conference on nuclear reactor thermal hydraulics (NURETH-9)*, San Francisco.

[Dhir and Catton, 1977] Dhir, V. and Catton, I. (1977). Study of dryout heat fluxes in beds of inductively heated particles. Technical Report CR-0262, NUREG.

[Hardee and Nilson, 1977] Hardee, H. and Nilson, R. (1977). Natural convection in porous media with heat generation. *Nuclear Science and Engineering*, 63:119–132.

[Horner et al., 1998] Horner, P., Zeisberger, A., and Mayinger, F. (1998). Evaporation and flow of coolant at the bottom of a particle bed modelling relocated debris. In *Workshop on In-vessel core debris retention and coolability*, Garching, Germany. OECD/CSNI.

[Lipinski, 1984] Lipinski, R. (1984). A coolability model for post-accident nuclear reactor debris. *Nuclear Technology*, 65:53.

[Mayr et al., 1998] Mayr, P., Bürger, M., Buck, M., Schmidt, W., and Lohnert, G. (1998). Investigations on the coolability of debris in the lower head with wabe-2d and mesoco-2d. In *Workshop on In-vessel core debris retention and coolability*, Garching, Germany. OECD/CSNI.

[Petit, 1998] Petit, F. (1998). *Ébullition en milieu poreux et renoyage d'un lit de débris d'un réacteur nucléaire*. Thèse de doctorat ENSAM.

[Reed et al., 1985] Reed, A., Boldt, K., Gorham-Bergeron, R., Lipinski, R., and Schmidt, T. (1985). Dcc-1/dcc-2 degraded core coolability analysis. Technical Report CR-439, SAND85-1967, NUREG.

[Tsai, 1987] Tsai, F. (1987). *Dryout heat flux in a volumetrically heated porous bed.* PhD thesis, UCLA.

[Tung and Dhir, 1988] Tung, V. and Dhir, V. (1988). A hydrodynamic model for two-phase flow through porous media. *International Journal of Multiphase Flow*, 14:47–65.

[Vujisic et al., 1991] Vujisic, L., Catton, I., and Afgan, N. (1991). *Air-water two-phase flow pressure drop in large scale porous media*, pages 773–789. Convective Heat and Mass Transfer in Porous Media. Kluwer Academic Publishers, Netherlands.

Session B 3:

PHENOMENA TO ACHIEVE COOLABILITY: SPREADING

Co-Chairmen: H.-J. Allelein and J.-C. Latché

OECD Workshop on Ex-Vessel Debris Coolability
Karlsruhe, Germany, November 15-18, 1999

Organised in collaboration with
Forschungszentrum Karlruhe (FZK) GmbH

CORIUM SPREADING PHENOMENA : RESULTS OBTAINED FROM THE EU CSC PROJECT

G. Cognet[a] - W. Tromm[c&b] - D. Magallon[c] - R. Wittmaack[d] - B.R. Sehgal[e]
L. De Cecco[f] - R. Ocelli[g] - D. Pineau[h] - B. Spindler[i] - G. Fieg[b]
H. Werle[b] - C. Journeau[a] -M. Cranga[a] - G. Laffont[a]

a : CEA/DRN/DTP - Cadarache B.P. n°1 - 13108 Saint Paul lez Durance - France
b : FZK - Weberstrasse 5 - P.O. Box 3640 - D 76021 Karlsruhe - Germany
c : JRC/ISIS - T.P. 421 - 21020 Ispra (Va) - Italy
d : Siemens - KWU - NA-T - Freyeslebenstr. 1 P.O. Box 3220 - 91058 Erlangen - Germany
e : Royal Inst. Technology - Div. Nucl. Safety - Brinellvägen 60 - 10044 Stockholm - Sweden
f : ENEA - Via Martiri di Monte Sole n°4 - 40129 Bologna - Italy
g : IUSTI - Techn. de Chateau Gombert - 5 rue Fermi - 13453 Marseille Cedex 13 - France
h : EDF/DER/RNE/TTA - 6 quai Watier - 78401 Chatou - France
i - CEA/DRN/DTP - Avenue des martyrs - 38054 Grenoble Cedex - France

ABSTRACT

In the context of severe accidents, large R&D efforts throughout the world are currently directed towards ex-vessel corium behaviour. Among the mitigation means which can be envisaged, the European industries and utilities are considering the implementation of a core-catcher outside the reactor pressure vessel in order to prevent basemat erosion and to stabilize and control the corium within the containment.

The CSC project focused on two key phenomena for external core-catcher efficiency, reliability and safety : spreading and coolability. An experimental programme, covering different scenarios and including both simulant and real materials provided a lot of results which constitute now a large database and which enabled the qualification of 2 computer codes. After a brief presentation of the project, this paper presents the results obtained.

1.- INTRODUCTION

In the event of a highly unlikely core melt-down accident in Light Water Reactors, the Safety Authorities of several EU countries have requested the industries and utilities to consider severe accidents with reactor pressure vessel failure for the design of the next generation of nuclear power plants. The objective is to preserve the integrity of the containment as the main barrier of fission product release to the environment. This can only be achieved if the core melt mixture (called corium and essentially composed of UO_2, ZrO_2, Zr, Fe and fission products) is stabilized before it can penetrate the basemat. Consequently, various core-catcher concepts are under investigation for future reactors in order to prevent basemat erosion, and to stabilize and control the corium within the containment. Among those, two catchers that can potentially achieve this goal are that of the current EPR spreading concept and that of the COMET concept of volumetric quenching of the melt.

The two generic processes involved in these core-catcher concepts, namely spreading of the corium under various initial and boundary conditions and cooling of the melt by direct water contact are the main issues addressed by the CSC project (EC Contract : Cost-shared action n° FI4S-CT96-0041) which was launched on January 1, 1997 for 2.5 years. The goal of this project was the development of a sound scientific and technical basic knowledge to support both the design of a reliable core-catcher, as is presently required by the European nuclear industry, and its assessment by the Safety Authorities.
This paper presents the experimental results obtained on corium spreading with various simulant and prototypic materials as well as the work achieved on specific computer codes. A second part of the CSC Project was devoted to the COMET concept. Being extensively presented in another paper of this conference (Alsmeyer , et al., 1999), this part is not included in this paper.

2.- SPREADING PROGRAMME

Due to the various modes of corium release from the reactor pressure vessel (metal or oxide jet under pressure, low or high flowrate pouring, liquid carrying solid debris, subsequent discharge,...), a wide range of initial conditions (temperature, viscosity and composition) of the melt at the time of spreading may be envisaged. From scenario analyses performed by the GAREC group in the CEA (Micaelli, 1995) previous to this project, the spreading process could be controlled not only by flowrate but also by the onset of freezing on the melt front, by any change in the melt rheological behaviour (especially for oxidic or silica rich mixtures), by a possible melt accumulation, by subsequent discharges, by substratum erosion and by interaction with water if any. These phenomena are directly connected to the heat fluxes exchanged between the corium and its environment.
Finally, the melt layer thickness after dry spreading, which is the critical parameter for corium coolability success, would be the result of corium-concrete mixture behaviour, possible stable accumulations and/or outpourings due to decay heat.

2.1- Spreading experimental programme

From the previous MCCI project of the Reinforced Concerted Actions (RCA) in the previous Nuclear Fission Safety EC Programme (Alsmeyer, 1995), many results, obtained with low melting-temperature simulants (CORINE programme), were available for the following phenomena:

- hydraulic spreading of isothermal fluid of various viscosities;
- spreading and freezing of isothermal fluid on cooled substrata;
- spreading and freezing of hot fluid under water.

The experimental CSC programme aimed at studying, at higher temperatures and with various materials, the spreading and cooling phenomena in order to reach, via a step by step approach, the real conditions which could occur during a severe accident.
Considering the large number of thermo-physical and thermo-chemical phenomena involved in spreading processes, only the experiments carried out with real material represent reality. However, taking into account the fact that a complete analysis of all important aspects in a few experiments cannot be expected, experiments with simulant materials were performed to investigate in detail the most important phenomena. As a final step, prototypic corium melts were used to validate the observed phenomena and models.
As regards corium composition, the risk of non-spreading being more crucial for oxidic melts than for metallic melts, experiments were focused on oxidic melts. Moreover, various

compositions of melt (with and without silica) were investigated in order to assess the role of concrete erosion inside the reactor pit which should induce the spreading of a corium/concrete mixture presenting a large solidus-liquidus temperature range.
Two facilities were used for simulant material tests :

- one at the Royal Institute of Technology (RIT) of Stockholm where experiments were carried out with medium melting-temperature simulants (binary oxide mixtures);
- the other: KATS, in FZK at Karlsruhe, where a high melting-temperature simulant (alumina thermite) was used.

According to the facility characteristics, prototypic material experiments were shared between FARO of the JRC Ispra and VULCANO of the CEA Cadarache.

2.2- Spreading models and computations

Two detailed computer codes, one developed by SIEMENS (CORFLOW code) and the other by the CEA/DRN (THEMA code) were used in the CSC project for qualification and improvements of their models.

3.- EXPERIMENTAL RESULTS

¤ - *RIT experiments*

A series of experiments on spreading in both 1D and 2D channels were performed with different simulant materials (such as Cerrobend, $NaNO_3$-KNO_3 salt, CaO-B_2O_3 binary oxide mixture, etc) at temperatures varying from 100°C to 1300°C. The effects of the melt properties and substratum (concrete or steel, with or without water) were investigated. The experimental observations showed that the melt spreading into an open area is significantly different from the 1D spreading. As the melt spreads in all directions, the hydrodynamic spreading time scale is remarkably reduced, and the spreading efficiency is correspondingly enhanced. Scaling models on the spreading efficiency for both 1 and 2 D have been developed, a good agreement is obtained with all available experimental data (see Figure 1).

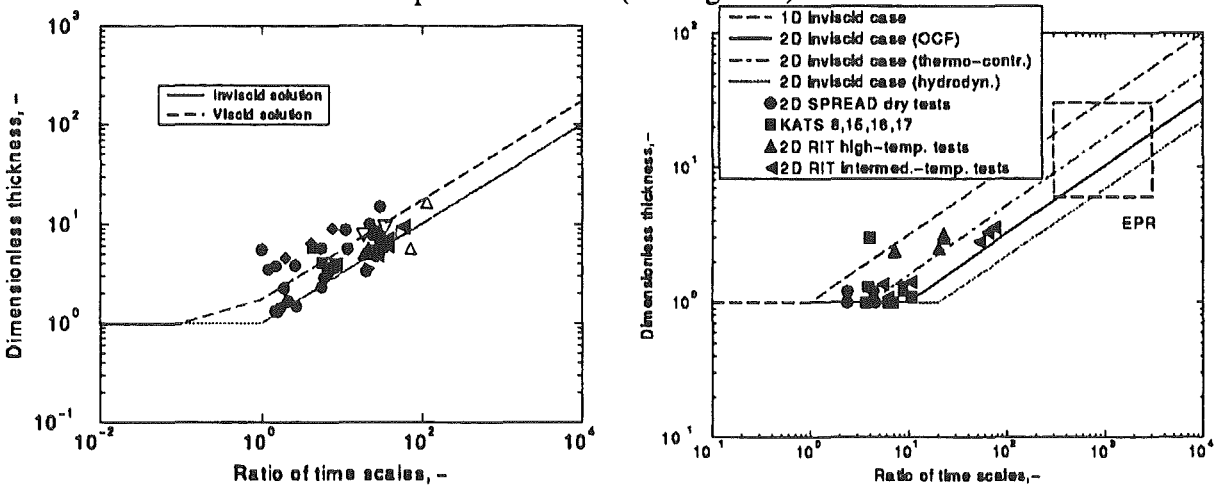

(a) one-dimensional spreading (b) two-dimensional spreading

Figure 1 : Comparison of scaling models with experimental data

The re-spreading of once spread and solidified melt pool was investigated both experimentally and analytically. The results show that the natural convection of the internally-

heated melt, contained within a crust vessel, is the controlling factor in crust remelting and break. The break location was found to be always at the upper elevations.

¤ - *KATS experiments*

In the KATS experiments, ~ 320 kg thermite were used, the two melt components were separated and spread on two different areas ; SiO_2 was added to the oxide melt to simulate corium/concrete mixtures. The following parameters : melt material properties, pouring rate and finally the material and geometry of the spreading area, were varied in the tests and their influence on spreading were determined.

In the dry spreading tests, the metallic melt is generally strongly superheated (~ 400 K). Spreading is terminated before freezing, after immobilization the iron melt front withdraws partly due to increasing surface tension. The frozen iron slag withdraws further on during cooling down to ambient temperature. The height of the melt at the time of immobilization is about 10-20 mm.

Spreading of oxidic melts may be a critical issue, if the melt temperature is in the region where viscosity increases strongly with decreasing temperature (case of melts with large liquidus - solidus temperature range). In the KATS series, spreading on concrete was observed to be remarkably less efficient than on to ceramic surfaces (see Figure 2).

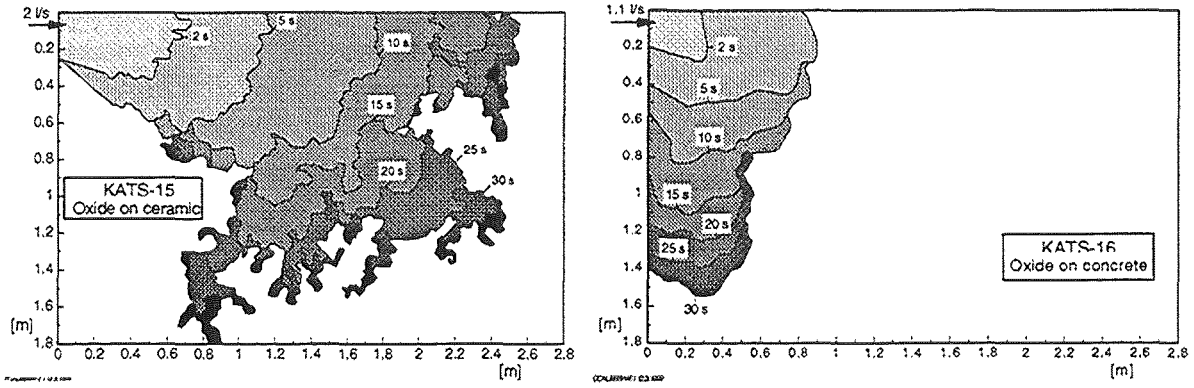

Figure 2 : 2-D spreading of oxidic melt on ceramic and concrete

As regards the presence of a shallow water on the spreading surface, three KATS tests were performed to study spreading of separated iron and oxidic melts on epoxy-painted concrete covered with 1 mm water. Only small energetic melt/water interactions were observed. The influence on the overall spreading for both metallic and oxidic melts is small.

Coolability by flooding from the top was investigated. Separated iron and oxidic melts were flooded after spreading in various KATS and KAPOOL tests. Flooding was performed by a water film (100-250 ml/s) entering at the channel end over the whole channel width. In all five tests, the water front progressed smoothly and in none of the tests any energetic melt/water interaction was observed.

¤ - *FARO experiments*

In the FARO facility, corium melts of 80 % UO_2 and 20 % ZrO_2 can be produced and released to a spreading test section named SARCOFAGO. In the 2 experiments, performed in the CSC project, the same spreading test set up was chosen. It consists of a collecting device and a spreading test plate of stainless steel separated by a 4 cm high barrier.

In the first dry experiment, 130 kg melt were spread onto the plate with a temperature of about 2950 K. The flow rate was measured to be about 16.5 kg/s, i.e. 2.1 l/s. The duration of the release was 9.7 s, the spreading time 11.5 s. The average velocity of the melt front could be

estimated from the video observation to be about 0.10 m/s. The total spreading length was 1.1m and the average height was about 70 mm.
A second spreading test was performed with the same test section, but a small water layer of 10 mm in height was added on the spreading plate up to a dam at 2 m distance from the inlet. The dam had a height of 10 mm to allow the water to flow over during the spreading of the melt. A quantity of 100 kg of corium with a temperature of about 3100 K were spread on the stainless steel plate. Only at the leading edge of the melt some evaporation was observed forming a few centimeters of pillows of the melt. But no pressure build-up in the test vessel or stronger melt/water interactions occurred. The melt spread to a distance of 80 cm. The flow rate was 18.3 kg/s, or 2.3 l/s. The spreading time and the release time were about the same, i.e. 7 s, leading to an average spreading velocity of 0.13 m/s. The average height of the melt layer was about 60 mm. During cool down of the melt, gaps were formed between the substrate and the solidified melt layer. Water flowing backwards could penetrate into these gaps and enhance cooling of the steel plate.

It was clearly observed in these 2 tests that the spreading process is strongly inhomogeneous. Crust formation and break up leading to further spreading alternated several times. But the bulk of the melt layer remained liquid over the whole spreading process. It is therefore obvious, that crust formation stops these kinds of melts with small solidus-liquidus range, and not bulk freezing. Post test investigations after a few days showed that small cracks had formed from the top to the bottom over the whole solidified melt layer. But these cracks do not seem sufficient for water to penetrate from the top throughout the cracks to enhance coolability. In both experiments with and without water the porosity of the solidified melt layer is about the same and with only a few percent very small.

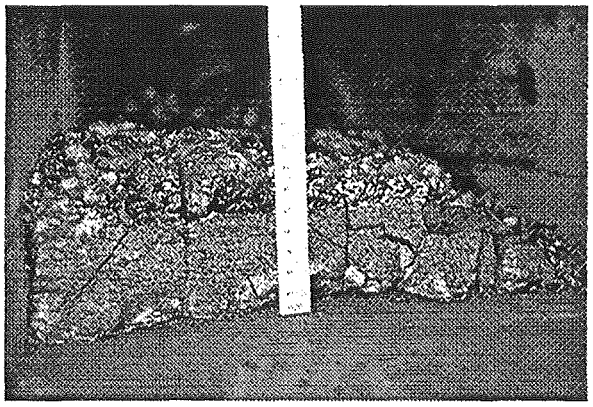

Fig. 3a : ***FARO L-26S cross section of solidified melt***

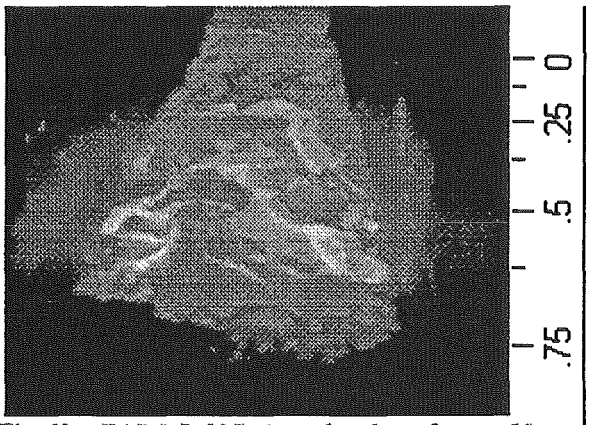

Fig. 3b : ***FARO L-32S view of melt surface at 10 s***

¤ - *VULCANO experiments*

The VULCANO facility has been designed to heat up to 3000 K and to melt roughly one hundred kilograms of corium composed of representative materials : UO_2, ZrO_2, Fe_xO_y, Zr, Fe, SiO_2... in various proportions. Since the launch of the CSC project, several tests have been performed on dry corium spreading with low flowrate and various melt compositions (both high temperature simulant and real materials) characteristic of corium discharge from the reactor pit after ablation of the sacrificial gate (EPR configuration). The most important results can be summarized as follows :

- The spreading of real corium-concrete mixtures is relatively efficient, even in unfavourable pouring conditions ; for example, in VE-U3 (composition : 60%$_w$ UO_2 + 25%$_w$ ZrO_2 + 7%$_w$ Fe_xO_y + 8%SiO_2), in spite of a low temperature at the entrance of the test section (~ 150 K below the liquidus temperature) and a low flow rate (1.2 kg/s), an early slackening

and a creeping motion of the front was observed while the melt continued to be poured. Moreover, spreading was never stopped, in any of these tests, by a crust formation at the front. The spreading capacity of such melts is certainly due to the large solidus liquidus temperature range (~ 900 K) and maybe to the physico-chemical behaviour of UO_2.

• No segregation occurred during the spreading of a melt containing a low percentage (~5%) of iron in the oxidic mixture (VE-06 test : 53%$_w$$HfO_2$ +10%$_w$$ZrO_2$ +14%$_w$$SiO_2$ +13%$_w$$Fe_xO_y$ +10%$_w$Fe). Post-test analyses revealed that iron droplets of various sizes were distributed throughout the spread melt.

• As regards the subsequent spreading, the VE-U5 test (load composition : 45.7%$_w$ UO_2 + 9.8%$_w$ ZrO_2 + 24.3%$_w$ Fe_xO_y + 19.7%SiO_2 + 0.4%$_w$ CaO + 0.1%$_w$ Al_2O_3) showed that a second corium-concrete flow can occur below the crust of the first spread melt provided that the time delay is not too great (see Figure 4b).

• Coolability of a corium/concrete spread melt would be made easier by high porosity and surface cracks if these cracks occurred early enough. The observed porous structure of cooled real material mixtures results, without any doubt, from gas bubbles stopped in their lifting motion (see Figure 4a). Among the possible explanations of the large gas release, the most likely seems to be the release of UO as gas due to a sub-stochiometry of UO_2 resulting from the reductive atmosphere of the furnace.

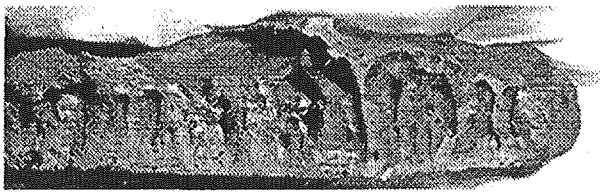

Figure 4a : VE-U1 test - View of the bottom layer

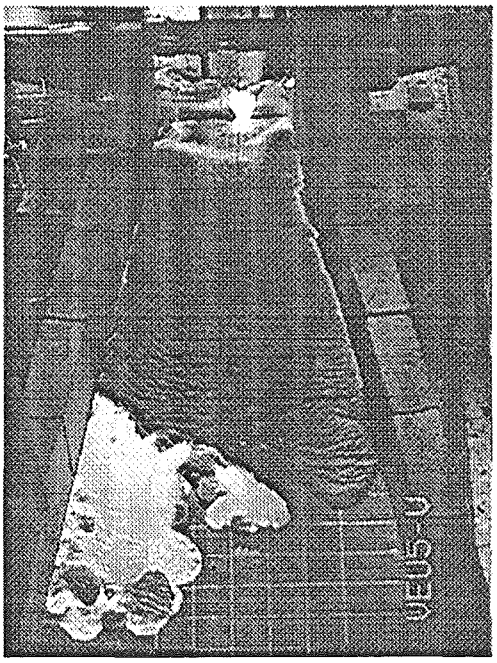

Figure 4b : VE-U5 test - View of the subsequent spreading ==>

• Post test analyses generally revealed a homogeneous structure versus spread length but the existence of five different horizontal layers. These layers have the same chemical compositions but different crystalline phases which result from different cooling rates and for the lowermost and uppermost (very thin layers of less than 50μm) from interaction with atmosphere. An attempt to re-calculate this structure with the thermodynamic computer code GEMINI and different solidification models (thermodynamic equilibrium or Gulliver-Scheil hypothesis) gave satisfactory agreement. It can be concluded that most of the corium solidifies out of thermodynamic equilibrium and that, at the opposite of what is generally admitted, the bottom part of the corium (in contact with zirconia bricks) cools with the smallest rate.

• A limited physico-chemical interaction between the corium mixture and zirconia bricks is observed in the entrance area.

4.- COMPUTATIONAL WORK

¤ - *CORFLOW improvements and calculations*

The CORFLOW computer code (Wittmaack, 1997) is designed for the simulation of free surface flow with heat transfer and phase transitions, in particular corium. The recent code development includes the introduction of a new rheology model which incorporates several types of non-Newtonian behaviour, e. g. Bingham, pseudoplastic and dilatant fluids. Namely for the COMAS EU-2b test which operated with a melt containing 15.1 % of SiO_2, the application of Bingham rheology model caused a significantly different result than a Newtonian approach. Furthermore, a dynamic geometry model was introduced to treat molten structural material as fluid ; it can be applied for the analysis of structural material erosion. Moreover, several numerical methods have been improved to make the calculations more precise and to reduce the computation time.

A variety of analytical solutions of fluid flow and heat transfer problems was used for the code verification so far (Wittmaack, 1997). In addition, for the verification of the discrete phase transition model, numerical simulations related to the analytical solutions of two Stefan problems were performed. Both solutions are fairly accurately represented by the related CORFLOW predictions.

In addition to earlier analyses, many CORFLOW simulations of simulant material and corium spreading tests were performed. These include post-calculations of the KATS-3, -5, -6 and -7 thermite spreading tests onto dry substratum, post-calculations of the COMAS-5a, -EU4 and -EU2b tests as well as post-calculations of the VULCANO VE-U1 test.

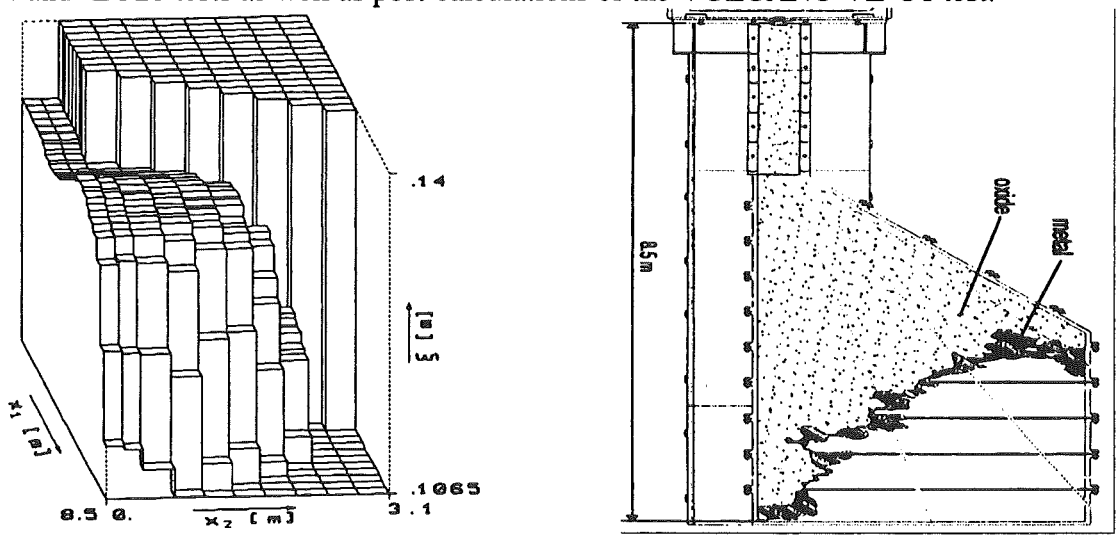

Fig. 5 : COMAS EU-4 test - Calculated (left) and experimental (right) final free surface location

In general, the predictions of the simulant material tests provide a reasonable representation of the experimental data, while the discrepancy between calculations and test data is greater for real material spreading. In the uncertainty and sensitivity analysis of CORFLOW calculations on COMAS EU-2b, the impact of the uncertainty of the input parameters on the results is studied systematically and comprehensively (Wittmaack, 1999). The uncertainty of the liquid phase dynamic viscosity is the major source of uncertainty of the calculated front propagation. Furthermore, the uncertainty related to the inflow boundary condition causes considerable uncertainty of the calculated front progression in the initial phase.

¤ - *THEMA improvements qualifications and calculations*

The THEMA computer codes simulates 1D or 2D spreading of two possible phases (metallic and oxidic) with ablation of the basemat. The mass, energy and momentum equations are integrated over the melt thickness and the variations of the physical properties, including density and viscosity are taken into account. A separate crust model is used both at the free surface and at the interface with the substrate. The thermal behaviour of the basemat is solved with a 3D conduction model.

CEA, ENEA and EDF contributed to the assessment of the code (Spindler, 1999) by calculating the following tests : KATS12, KATS14, FAROL26S, VULCANO VEU1 and VE07, RIT-3MDS-Ox-1 and RIT-3MDS-Ox-2. This work led to the implementation of many improvements in the code concerning mainly the physical properties, in particular viscosity and the closure laws (wall shear stress and heat transfer coefficient). In terms of front progression and spreading extent, discrepancy between the code predictions and the experimental data depends on the test under consideration. It appears that the best results are obtained for oxidic melts with a large solidus - liquidus temperature interval.

Thanks to a low run time, sensitivity studies have been performed with the conditions and geometry of the VE07 and VEU1 tests (see Figure 6). The influence on the spreading length of 11 parameters (melt physical properties and initial or boundary conditions) was studied. About 500 calculations were performed for each study, giving a confidence level of more than 98 %. This study pointed out that the prevailing parameters for the spreading lengths are the liquidus temperature, the viscosity model, the initial melt temperature, the melt flow rate, and the melt conductivity. The less influent parameters are the surrounding temperature, the corium emissivity and the substratum conductivity.

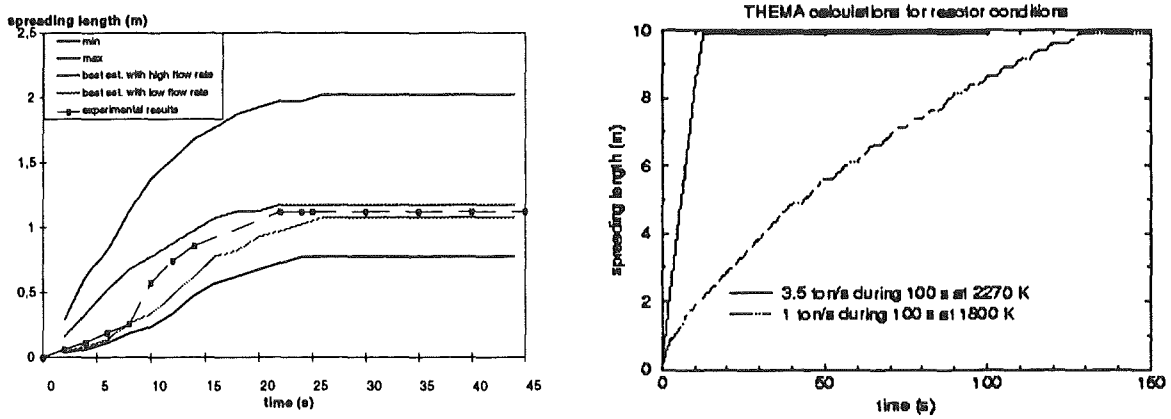

Sensitivity study on VEU1 test **EPR-like reactor conditions**

Figure 6 : THEMA calculations

The THEMA code has been also applied to reactor situations for the EPR concept. Oxidic corium was injected with different mass flow rates and initial temperatures. Spreading is observed in all cases investigated (see Figure 6). It remains however that a key issue is the definition of more numerous relevant pouring scenarios.

5.- CLASSIFICATION

A general classification of spreading regimes observed in various spreading experiments was attempted. A 2D representation, plane (P_{em}, τ) in which P_{em} is a modified Peclet number and τ a dimensionless time t which includes the cooling rate at the surface, pointed out a clear separation between iron (ψ >400000) and oxidic spreading tests (200 < ψ <10000) where ψ is a characteristic time ratio ($\psi = P_{em} . \tau$) (see Figure 7).

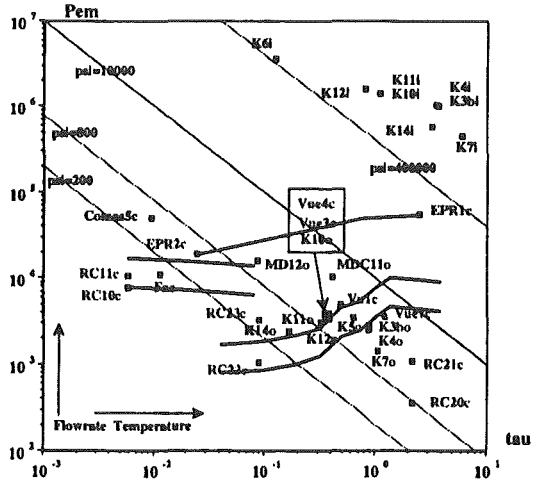

Figure 7 : Classification of spreading flows

D- CONCLUSIONS AND BENEFITS

The CSC project has enabled a great step to be made in the understanding and prediction of corium spreading and coolability phenomena. The most significant results are the following :

- Spreading progression is generally not continuous, there are formation of tongues and fingers.
- A better knowledge of the stopping mechanisms of spreading has been obtained :
  - ¤ melts with large solidus-liquidus temperature range are stopped by an increase of global viscosity which is itself due to an increase of solid fraction ;
  - ¤ melts with a small solidus-liquidus temperature range seem to be stopped by the formation of a crust.
- Spreading on concrete is remarkably less efficient than on ceramic surfaces.
- Subsequent spreading can occur after the stopping of a first spreading provided that the time delay is not too great.
- A scaling rationale has been provided which gave some interesting insight on the final parameters of spreading in particular the final average thickness of the melt.
- A large experimental data base is now available for qualification of spreading computer codes.
- Two computer codes, THEMA and CORFLOW, have been qualified ; however, some progress is still needed to reach a high level of confidence in any configuration.
- Sensitivity studies have highlighted the importance of material properties, in particular the apparent viscosity of the melt.
- A tentative of classification has been made and has given some interesting trends, but nothing appear obvious concerning fingering phenomenology.
- One of the most unknown parameters for reactor cases is the flow rate which depends directly on the melttrough of the sacrificial gate.
- Physico-chemical interaction between corium and zirconia bricks is limited ; However, in case of decay heat, this interaction could be more important and could significantly change zirconia brick properties.
- In any of the performed tests, top flooding after spreading never leads to energetic melt water interaction.

• After spreading, real material melts present cracks and a high level of porosity which could make coolability easier.

ACKNOWLEDGMENTS

This work has been partly funded out by the EC within the 5th Framework Programme (CSC Project - contract n° FI4S-CT-0041).

REFERENCES

Alsmeyer , H. et al., 1995 : « Overview on the results of the RCA project on molten core-concrete interaction », FISA-95 Symposium, Luxemburg.

Alsmeyer , H. et al., 1999 : « Corium Cooling by Bottom Flooding : Confirmation of the COMET Investigations » OECD Workshop on Ex-Vessel Debris Coolability, November 1999, Karlsruhe

Micaelli, J.C.et al., 1995 : « R&D needs related to the core-catcher concept based on corium spreading », Int. Seminar on Heat and Mass Transfer in Severe Reactor Accidents. - Cesme, Turkey, May 21-26.

Spindler, B. et al., 1999 : « Assessment of THEMA code against spreading experiments », OECD Workshop on Ex-Vessel Debris Coolability, November 1999, Karlsruhe

Wittmaack, R.,1997 : « Numerical simulation of free surface flows », Nuclear Technology, 119, pp. 158-180

Wittmaack, R., 1999 : « Uncertainty and sensitivity analysis of CORFLOW simulations of the COMAS EU-2b test »KWU NA-T/1999/E021, (1999), EXV COMAS(99)-D24

OECD Workshop on Ex-Vessel Debris Coolability
Karlsruhe, Germany, 15-18 November 1999

Organized in collaboration with
Forschungszentrum Karlsruhe (FZK) GmbH

KATS experiments to simulate corium spreading in the EPR core catcher concept

G. Engel, G. Fieg, H. Massier, U. Stegmaier and W. Schütz
Forschungszentrum Karlsruhe GmbH
Postfach 3460, D-76021 Karlsruhe, Germany
fieg@iket.fzk.de

ABSTRACT

In future Light Water Reactors special devices (core catchers) might be required to prevent containment failure by basement erosion after reactor pressure vessel meltthrough during a core meltdown accident. Quick freezing of the molten core masses is desirable to reduce release of radioactivity. In the case of a postulated core melt down accident in the EPR (European Pressurized Water Reactor) the ex-vessel melt shall be retained and cooled in a special compartment inside the containment to exclude significant radioactive release to the environment. After penetration of the lower head of the RPV the melt will first be collected in the reactor cavity and will interact with sacrificial materials. After melt-through of the steel gate the melt is released into the core catcher compartment where it will be flooded by water to extract the decay heat and solidify the melt pool. Therefore the sufficiently homogeneous melt spreading is important to ensure a large-surface and low-thickness melt distribution. KATS is an experimental programme performed at FZK to investigate the basic factors of of the spreading process by use of substitute materials for the corium melt. A series of experiments has been carried out to investigate high temperature melt spreading into 1-dim channels and on 2-dim flat surfaces using alumina-iron thermite melts as a simulant. The oxidic and metallic phases of the melt are separated and spread on different surfaces. The pouring rates and melt temperatures have been varied; furthermore, different substrates have been studied (dry, inert ceramics, silicate concrete, epoxy-coated silicate concrete). Finally, the influence of a shallow water layer on the surfaces onto the spreading behaviour has also been studied.

1. INTRODUCTION

To exclude significant release of radioactivity to the environment even in the case of a core melt accident, next generation LWR's shall incorporate the ability to retain the core melt within the containment. In the planned European Pressurized Reactor (EPR) this shall be accomplished by spreading the core melt on a large area and cooling the spread melt by flooding with water from top (Alsmeyer, 1997 and 1999).

Therefore a better knowledge of core melt behaviour, especially concerning spreading and coolability is required. To achieve this, various series of experiments are performed at Forschungszentrum Karlsruhe. In all these tests the core melt is simulated by iron and

alumina melts produced by the thermite reaction. Thermite melts are excellent simulants of the core melt because both, the metallic and the oxidic core melt component, are simulated, the melt temperatures (~ 2200 °C) are comparable to that of the core melt (this is important to achieve representative high radiation heat losses) and by admixture of other components (SiO_2, CaO) to the alumina melt, the characteristics of the oxidic corium melt after admixture of concrete components (large difference between solidus and liquidus temperature) can be simulated.

The main goal of the KATS tests is to study the effect of important initial and boundary conditions on spreading and to provide a broad basis of experimental spreading data of oxidic and metallic melts for code validation. The small-scale miniKATS experiments are complementary to the KATS tests and shall improve the understanding of important phenomena during oxide melt spreading, crust formation and immobilization.

2. EXPERIMENTAL PROCEDURES

In all test series the thermite reaction $8Al + 3Fe_3O_4 \rightarrow 4Al_2O_3 + 9Fe$ is used to provide iron and alumina melts, each with ~ 50 wt% and with temperatures up to 2400 °C. Due to the specific composition of the commercial thermite powder, the non-complete thermite reaction and erosion of the reaction crucible, the alumina melt contains small amounts of other oxides (iron oxides, SiO_2, MgO etc). In addition, in the spreading tests, generally ~ 10 wt% SiO_2 were added to the alumina melt to simulate the admixture of eroded concrete to the oxidic core melt. In the KATS tests (Alsmeyer, 1999; Ehrhard, 1998; Fellmoser, 1998), ~ 300 kg of thermite powder are ignited in a reaction crucible (fig. 1). For the spreading tests, generally ~ 20 kg SiO_2 are added to the thermite powder to tailor the characteristics of the oxidic melt to that of oxidic core melt containing eroded concrete. After the thermite reaction is completed, first the heavier iron melt (~ 160 kg) and afterwards the oxide melt is released through a nozzle. In the "low pouring rate" tests (≤ 2 l/s), the two melt components are separated during release by a swiveling pipe which directs the two components in two different containers from where they spread immediately on two spreading areas (fig. 1). In the "high pouring rate" tests (≤ 13 l/s), both melts are first stored in a container, where they separate again due to the different density. After separation, rather large windows in the upper, the central and the lower part of the container are opened one after the other to release first the oxidic melt, then a possibly mixed melt (not used in the test) and finally the iron melt on different spreading areas. The time sequence (ignition, start of data acquisition, opening of windows, etc.) of the tests is generally controlled by a PC system. The tests are instrumented with different video cameras to register the overall performance and to observe the spreading of the melts, with W/Re-thermocouples to measure the melt temperature, with type K thermocouples to detect the arrival of the melt front and finally with an infrared video system to measure the surface temperature of the spreading oxide melt. In addition, in the later KATS tests, the weight of the reaction crucible is measured during melt release, which allows to determine the pouring rate.

3. PERFORMED TESTS AND RESULTS

3.1 Dry spreading

Details of the dry KATS spreading tests are summarized in Table 1. It should be mentioned that in each test, both, the spreading of the oxide and of the iron melt is studied

simultaneously. The spreading surface consisted of ceramic (cordierite: ~ 50 wt% SiO_2, ~ 50 wt% Al_2O_3), silicate concrete or epoxy-coated silicate concrete.

In all KATS tests discussed here, SiO_2 was added to the thermite such that the composition of the oxidic melt was about 85 wt% Al_2O_3, 10 wt% SiO_2 and 5 wt% FeO. For this composition the solidus temperature (T_{sol} ~ 1577 °C), the liquidus temperature (T_{liqu} ~ 1925 °C) and the solid volume fraction between T_{liqu} and T_{sol} were calculated with the GEMINI code. Based on these data and the measured viscosity of alumina-silica mixtures above T_{liqu} (Elyutin, 1969), the temperature-dependant viscosity of the oxidic KATS melts has been estimated using the Stedman correlation.

3.1.1 Oxide melt

The 1-dim spreading behaviour of the oxidic KATS melts and the frozen slugs are shown in figs. 2, 3 and 4. The most important observations are: the spreading velocity and especially also the spreading length increase considerably with increasing pouring rate (see KATS-12 and -14, figs. 2 and 3) and the spreading length on concrete is considerably less than on ceramic (see KATS-12 and -13, fig. 4). On epoxy-covered concrete a small fraction of the melt (several ten kg) spreads in a first melt front with high velocity over a large distance, whereas the main part of melt spreads, similar as on unpainted concrete, in a second front with lower velocity over a smaller distance (KATS-11, fig. 4). This surprising spreading behaviour is due to a fast gas production during melt/epoxy contact.

Important conclusions from the small-scale 1-dim oxidic miniKATS tests concerning crust formation and its influence on spreading and immobilization are: At the top surface of the spreading melts very soon floating crusts are formed, which retard, if at all, the further spreading only slightly. Later on the crusts may stick to the walls and may be overflown by the following melt. A remarkable fraction of the melt may thus be immobilized in sticking crusts and is not available for further spreading. At the meltfront, crusts are formed much later than at the top surface, probably only if the bulk melt temperature at the front has dropped to a temperature at which the solid particle volume fraction in the melt is about 50 %. This is because at the front the melt is steadily refreshed due to melt outfreezing in bottom crusts.

In fig. 5 the results of the 2-dim spreading experiments are shown. For the oxide melts the time-dependant spreading and the final covered area is indicated. It is evident that for the oxide melt again both, the pouring rate (KATS-8 high, KATS-15 low pouring rate) and the type of substrate (KATS-15 ceramic, KATS-16 concrete) have a distinct influence on spreading. At high pouring rates, the oxide spreads faster and covers a larger area (KATS-8, 3.9 m^2) than at low pouring rates (KATS-15, 2.5 m^2). On concrete two oxide spreading tests have been performed: KATS-16 with very low flow rate and temperatures near the liquidus temperature, and KATS-17 with medium flow rate and very high temperatures. In KATS-16 the oxide melt spread only over an area of 1 m^2, whereas in KATS-17 ~ 3 m^2 were covered by the melt with very high homogeneous height distribution.

KATS-16 is especially of interest because important parameters of oxide spreading are considered to be EPR-representative (melt composition, melt temperature ~ T_{liqu}, concrete as substrate). The oxide melt spread first in the direction of the incoming melt over a distance of ~ 0.8 m. Then a dam formed at the melt front and the main part of melt spread perpendicular to the incoming melt over ~ 1.5 m.

The good spreading result of KATS-17 indicates that for sufficiently high flowrates and temperatures the negative effect of a concrete substrate (erosion, higher heat losses, out-gassing) can be compensated.

3.1.2 Iron melt

In all iron spreading tests (1- and 2-dim, on ceramic and on concrete), due to the large superheat (≥ 400 °C, Table 1), the spreading is stopped due to surface tension effects before massive freezing and the height of the spread melt (10 – 20 mm) is determined essentially by the equilibrium between gravitational and surface tension pressure. Nevertheless an interesting influence of the substrate on the spreading behaviour is visible: whereas on concrete, the melt gathers near the melt inlet, on ceramic it spreads all the way to the opposite wall.

3.2 Wet spreading

Two wet spreading tests, one with oxide and one with iron, were performed with KATS-10 and a two-dim wet spreading test with iron was done in KATS-17. For KATS-10 all characteristic data were the same as in KATS-11 (Table 1), except that the epoxy-painted concrete spreading surfaces for both, the oxide and the iron melt, were covered with a water film of 1 mm average thickness.

For iron none and for oxide only one minor energetic melt/water interaction was observed, leading to the ejection of a few kg of oxide and to a temporary stop of spreading. For both melts, the overall time-dependant spreading and the final distribution of the melts were essentially identical with those of the dry reference test KATS-11. From these results we conclude that a thin (~ 1 mm) water layer on the spreading surface has essentially no influence on the spreading of iron and oxidic melts.

In the wet spreading KATS-17 test no energetic melt/water interaction was observed. Comparing the spreading result with the dry reference experiment (KATS-16) the conclusion is that a 1 mm waterlayer has no influence on 2-dim spreading.

4. CONCLUSIONS

In a series of KATS tests, 1- and 2-dim, dry spreading of both, oxidic and metallic melts, was studied. All important parameters - melt temperature, melt pouring rate and type of substrate (ceramic and concrete) - were varied in the tests and their influence on the spreading behaviour was clearly demonstrated. A broad experimental basis for code validation is now available and first calculations of oxide spreading on ceramic with CORFLOW are in satisfactory agreement with experimental data. Wet spreading of an oxidic melt has been studied in KATS-10, the wet spreading of an iron melt in KATS-10 and –17. In all cases the spreading surfaces (epoxy-painted concrete) were covered with thin water layer of 1 mm average thickness. Only one minor energetic melt/water interaction was observed and from comparisons with the dry reference test (KATS-11) it is concluded, that thin (≤ 1 mm) water layers have essentially no influence on the spreading behaviour of oxidic and metallic melts.

ACKNOWLEDGMENT

This work was supported by the European Commission within the 4. Framework Programme on Nuclear Fusion Safety and the collaboration between the German utilities, Siemens/KWU and FZK Karlsruhe.

REFERENCES

H. Alsmeyer et al., 1997. Ex-Vessel Melt Behaviour in the EPR, Proc. SFEN/KTG Conf. on the EPR Project, Cologne, October 1997, p. 161.

H. Alsmeyer et al., 1999. Simulation tests with thermite melts on erosion, spreading and cooling of melts (projects KAJET, KAPOOL, KATS, COMET), Annual Meeting on Nuclear Technology, Karlsruhe, May 1999.

P. Ehrhard et al., 1998. Spreading of the Core Melt in the Spreading Area of the EPR, ICONE-6, May 1998.

V.P. Elyutin et al., 1969. Viscosity of alumina, Russian Journal of Physical Chemistry 43 (3), 1969.

F. Fellmoser et al., 1998. Simulation Experiments on the Spreading Behaviour of Corium Melts, Annual Meeting on Nuclear Technology, Munich, May 1998.

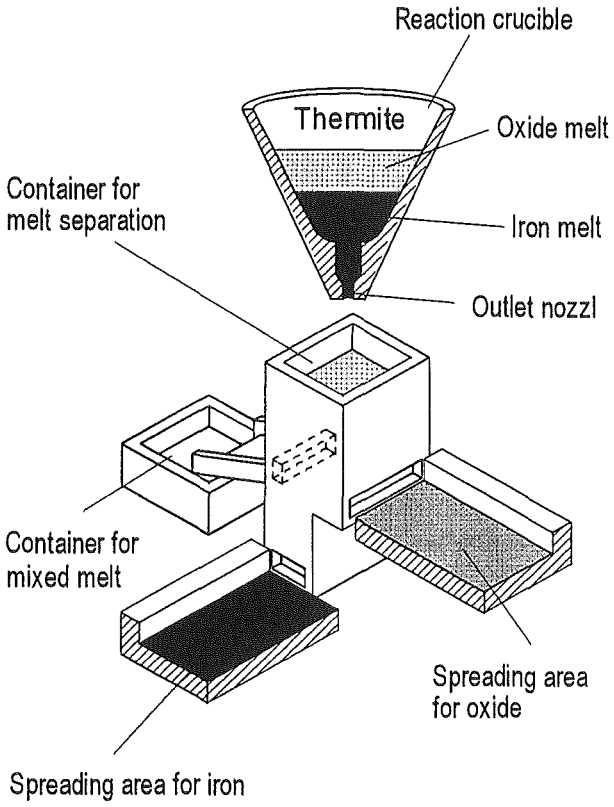

Fig.1 Experimental setup of the KATS tests

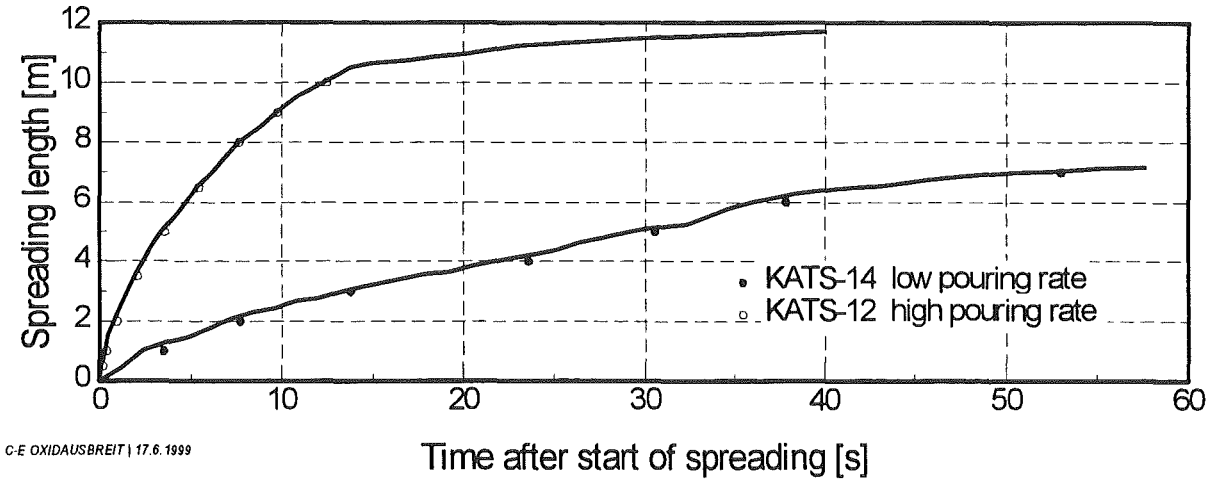

Fig. 2 Leading edge propagation of oxide melts in KATS-12 and –14

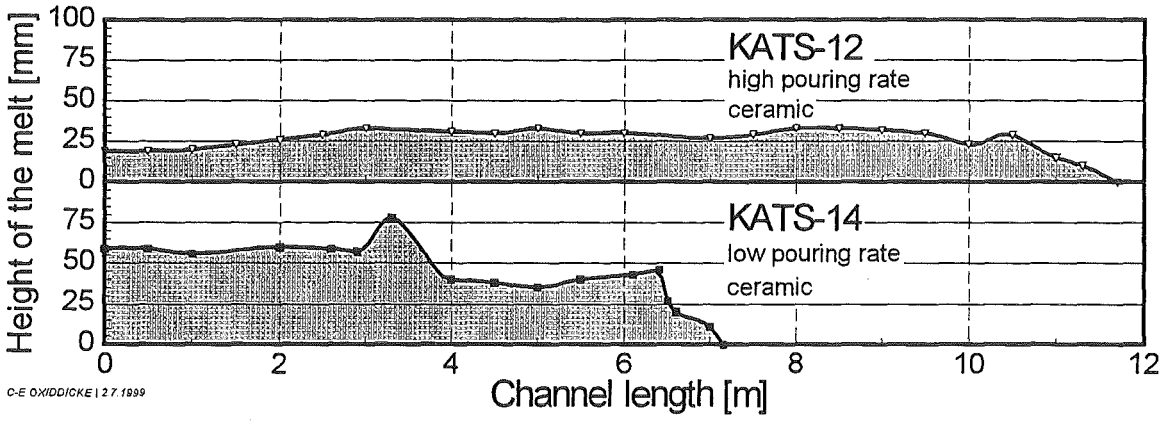

Fig. 3 Final oxide crust thickness of KATS-12 and –14

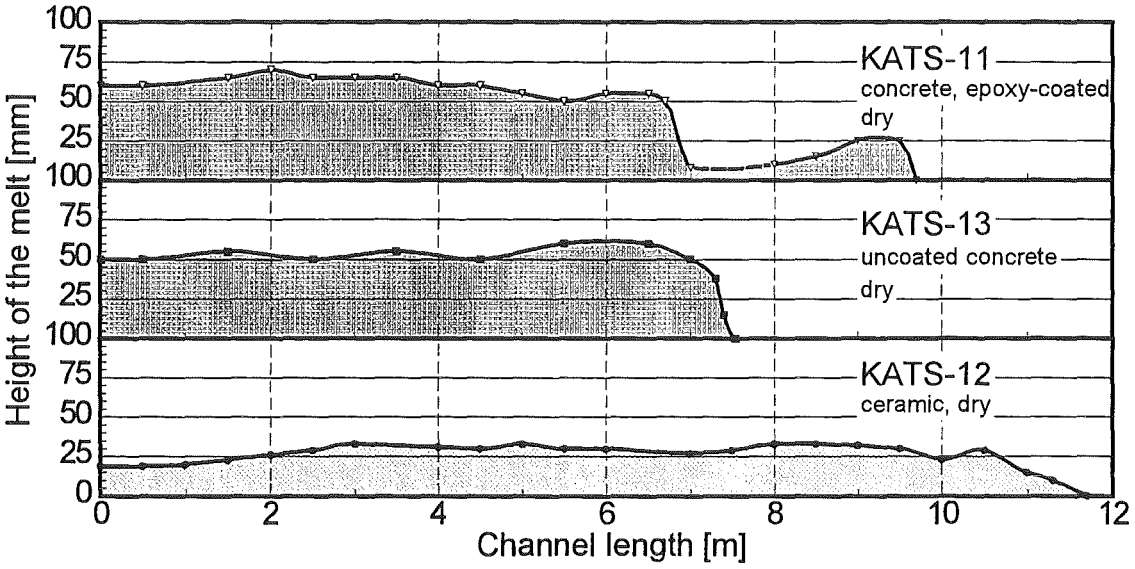

Fig. 4 Final oxide crust thickness in KATS-11, -12 and –13

KATS-8	
158 kg	
2100°C	
7.5 – 0 l/s in 16 s	
Substrate: Ceramic	

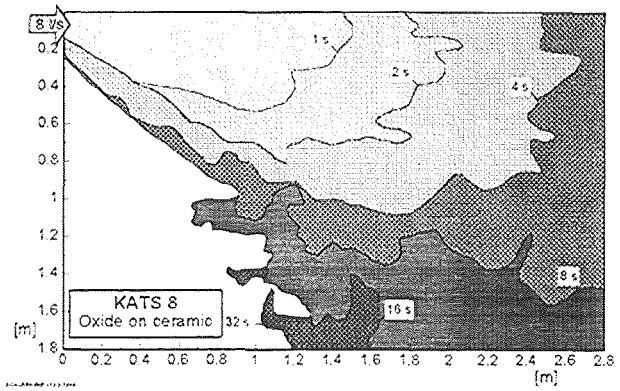

KATS-15	2.5 m²
144 kg	
2030°C	
~2 l/s in 26 s	
Substrate: Ceramic	

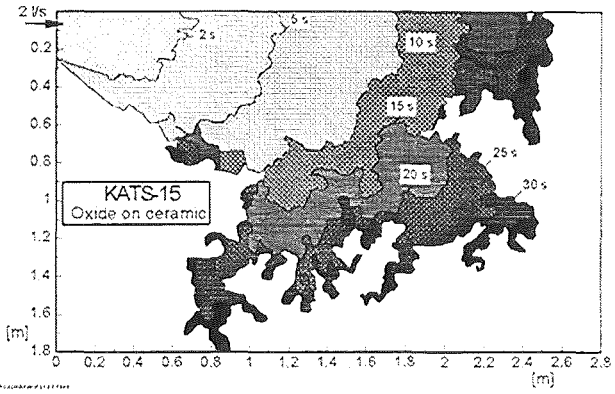

KATS-16	1 m²
129 kg	
1950°C	
~1.4 l/s in 31 s	
Substrate: Concrete	

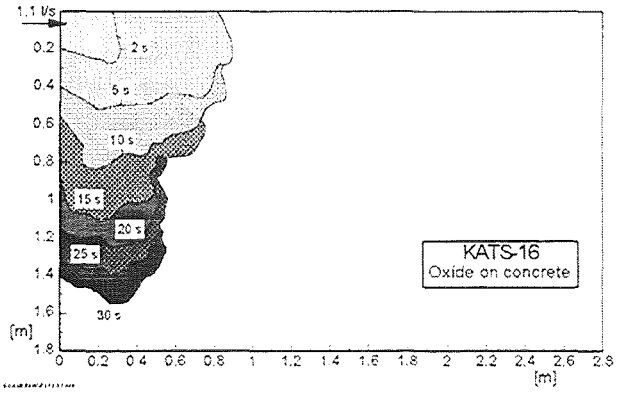

KATS-17	~3m²
121 kg	
2150°C	
~3 l/s in 15 s	
Substrate: Concrete	

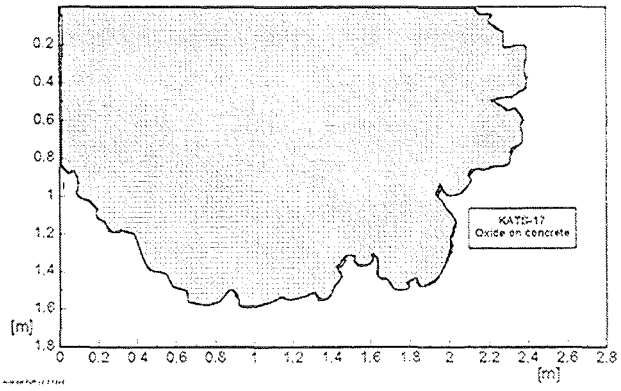

Fig. 5 2-dim spreading of oxide melts in KATS-8, -15, -16 and -17

OECD Workshop on Ex-Vessel Debris Coolability
Karlsruhe, Germany, November 15-18, 1999

Organised in collaboration with
Forschungszentrum Karlruhe (FZK) GmbH

THE VULCANO EX-VESSEL PROGRAMME

G. Cognet - G. Laffont - C. Jegou - J. Pierre - C. Journeau
M. Cranga - F. Sudreau - M. Ramacciotti

CEA
CEA Cadarache
Direction des Réacteurs Nucléaires
13108 St. Paul Lez Durance - FRANCE
gerard.cognet@cea.fr

ABSTRACT

Among the currently studied core-catcher projects, several concepts suppose corium spreading before cooling. In particular, the EPR (European Pressurised Reactor) core-catcher concept is based on mixing the corium with a special concrete, spreading the molten mixture on a large multi-layer surface cooled from the bottom and subsequently cooling by flooding with water. Therefore, melt spreading deserves intensive investigation in order to determine and quantify key phenomena which govern the spreading.

In France, for some years now, the Nuclear Reactor Division of the Atomic Energy Commission (CEA/DRN) has undertaken a large program to improve knowledge on corium behaviour and coolability. This program is based on experimental and theoretical investigations which are finally gathered in scenario and mechanistic computer codes. Within this framework, the real material experimental programme, VULCANO, conducted in collaboration with European partners, is currently devoted to the study of corium spreading.

Since 1997, several tests have been performed on dry corium spreading with various melt compositions. After a brief description of the general objectives and the facility, this paper will present the most important spreading results.

1. INTRODUCTION

In the context of severe accidents, large R&D efforts throughout the world are currently directed towards ex-vessel corium behaviour with particular emphasis on long-term corium retention and coolability in order to keep it in the containment. There are various so-called core-catcher concepts for future reactors under investigation, in order to prevent basemat erosion, and stabilize and control the corium within the containment. Although numerous patents deal with external core-catcher designs, their feasibility still has to be demonstrated as :

- they are often based on the general qualitative view of phenomena whereas very few significant quantitative results have, up to now, been obtained in representative conditions;
- they sometimes anticipate technological improvements which are supposed to be achieved in the near future;
- their implementation and passive operation in plants must be studied.

Among the most advanced core-catcher projects, the EPR (European Pressurized Reactor) is considering a core-catcher concept which is based on mixing the corium with a special concrete located in the reactor pit, spreading the molten mixture on a large multi-layer surface cooled from the bottom and subsequently cooling the spread melt by flooding with water.

Due to the various modes of corium release from the reactor pressure vessel (metal or oxide jet under pressure, low or high pouring rate, liquid carrying solid debris, stepwise discharge,...) and the uncertainties on the spreading behaviour of corium-concrete mixtures, a wide range of initial conditions (temperature, viscosity and composition) of the melt at the time of spreading may be envisaged.

The spreading process should be controlled not only by flowrate but also by the onset of freezing on the melt front and by any change in the melt rheological behaviour, especially for oxidic or silica rich mixtures. These phenomena are directly connected to the heat fluxes exchanged between the corium and its environment, for example thermal radiation, erosion of the sacrificial concrete, interaction with water....Moreover, a melt accumulation seems difficult to exclude and could induce a strong erosion even in the case of top cooling. Accumulations could result from stepwise discharges, crust formation, thermo-chemical interaction and melt fragmentation during the spreading process. Finally, the melt layer thickness after spreading would be the result of corium-concrete mixture behaviour, possible stable accumulations and/or outpourings due to decay heat.

Therefore, melt spreading, which is one of the key phenomena in achieving ex-vessel melt coolability, deserves intensive investigation.

In France, for some years now, the Nuclear Reactor Division of the Atomic Energy Commission (CEA/DRN) has undertaken a large program to improve knowledge on corium behaviour and coolability. This program (Cognet, 1997) is based on experimental and theoretical investigations, the results of which are finally used in scenario and mechanistic computer codes.

Within this framework, the VULCANO (name of an active volcano in Italy.) experimental program (Versatile UO2 Lab for Corium Analyses and Observations) has been launched with the following main objectives :

- Better understanding of the key phenomena involved in the behaviour and cooling of corium both in and out of the vessel;
- Contribution to the assessment of industrial solutions for core-catchers regarding materials and mitigation possibilities ;

• Performance of thoroughly instrumented experiments under various initial and boundary conditions with the view to providing an experimental data-base and qualifying computer codes.

In order to satisfy all the phenomena involved, in particular the evolution of corium physical properties with temperature and the physico-chemical interactions between melt and structure materials (metals, ceramics, concrete), the VULCANO experiments are performed with real materials.

The VULCANO programme, conducted within a European framework, is currently devoted to the study of corium spreading. Various situations must be considered : oxide corium on concrete, oxide/metal corium on concrete and corium/concrete on concrete with a special attention to low flowrate, crust and viscosity effects, possible phase segregations, influence of released gases and coolability.

This paper presents the first results and interpretations obtained on low flowrate corium/concrete spreading on a refractory substratum.

2. THE VULCANO FACILITY

The VULCANO facility (Figure 1) is mainly composed of a furnace and test sections, the geometry of which depends on the specific objectives of each experiment. The furnace (Jegou, 1998), which is based on a plasma arc technique, has been designed to heat up to 3000K and consequently to melt roughly one hundred kilograms of corium composed of representative materials : UO_2, ZrO_2, Fe_xO_y, Zr, Fe, SiO_2 in various proportions.

A sustained heating device based on specific induction coils is under development in order to subsequently simulate decay heat in accumulation and physico-chemical studies.

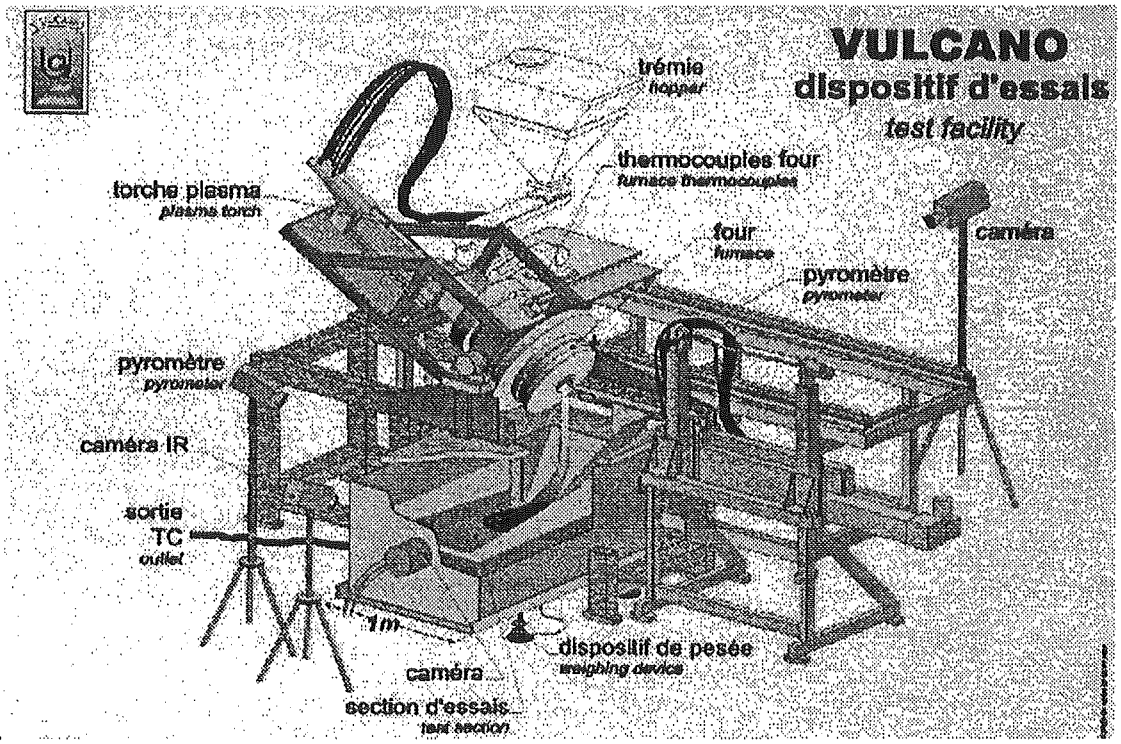

Figure 1 : The VULCANO facility

A special laboratory has also been equipped in order to carry out post-test analyses : optical and scanning electron microscopies, X-ray diffraction,...

The spreading test section substratum is horizontal and made of zirconia bricks. A truncated 19° angular sector is materialised by magnesia walls. In order to follow and record the corium flow, the test section is equipped with instrumentation composed of video cameras, pyrometers, infrared thermography, thermocouples, flowrate devices, laser telemetry.

Among the video cameras (Journeau, 1998), a Panasonic NV-S85E camera is used to obtained a zoomed view of the spreading area's first 55 centimetres (see Figure 2). This camera has been installed further away from the test section and thus was not cooled. Geometrical calibration has been made by using a 'checkerboard' installed over the test section and its walls. Contours, extracted from this image, form a regular grid which is later on added to the image of the spreading melt. This type of geometrical calibration is also used for the thermography camera although the contrast is lower.

Besides, a SONY XC999 camera has been mounted in an air-cooled jacket installed on the spreading area downstream side. Three flow systems allow this camera to operate correctly although it is located at less than 10 cm from the melt with a surface temperature of over 2000 K : a high pressure flow between the jacket double walls, an air circulation around the camera and the optics and an air stream around the porthole permit to avoid condensation. A wide angle (horizontal opening = 88°) lens is mounted on this camera so that both the slide and the spreading area end can be viewed (Figure 3).

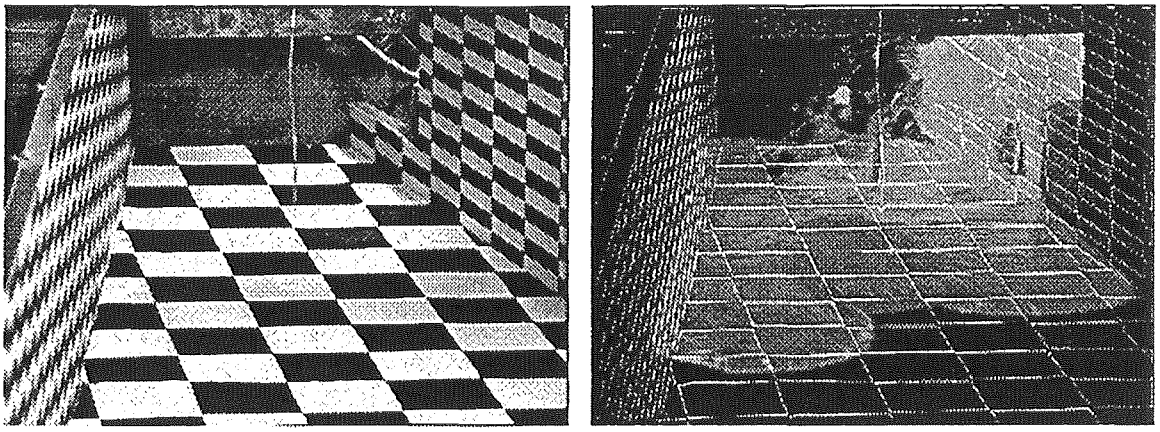

Figure 2 : Checkerboard calibration and the spreading melt of the VE-07 test

3. EXPERIMENTAL RESULTS

Since 1997, several tests have been performed on dry corium spreading with various melt compositions. According to the fact that there is no doubt on an efficient spreading in case of high flowrate, these tests were focused on low flowrates (< 1L/s).

3.1 VE-01 to VE-07 tests

Six tests were successfully performed with high temperature simulant corium in which urania was replaced by hafnia (roughly the same density and melting temperature). Several compositions were studied, all of them presenting a large solidus-liquidus temperature range (700 to 1000 K). In each of these tests, flow-rate was maintained at low values, sometimes at the limit of a discontinuous flow. The characteristics of these tests are summarised in Table 1

Table 1 Characteristics of these tests

Tests	Load composition (weight percentage)	Mass (kg)	Flowrate (l/s)	pouring temp.(K)	Main results
VE-01	50%$_w$$HfO_2$+10%$_w$$ZrO_2$+10%$_w$$SiO_2$+15 %$_w$$Al_2O_3$+15%$_w$CaO	12	0,1 discont.	2370	very limited spreading
VE-02	70%$_w$$HfO_2$+13%$_w$$ZrO_2$+7%$_w$$SiO_2$+10 %$_w$$Al_2O_3$	21	0,1 discont.	2470	length : < 30 cm thickness 5 to 13 cm
VE-03	35%$_w$$HfO_2$+5%$_w$$ZrO_2$+30%$_w$$SiO_2$+25 %$_w$$Fe_xO_y$+5%$_w$Fe	22	0,1 cont.	2420	
VE-04	70%$_w$$HfO_2$+13%$_w$$ZrO_2$+11%$_w$$SiO_2$+8 %$_w$$Fe_xO_y$	12	0,7 cont.	2620	accumulation no spreading
VE-06	53%$_w$$HfO_2$+10%$_w$$ZrO_2$+14%$_w$$SiO_2$+13 %$_w$$Fe_xO_y$+10%$_w$Fe	42	0,8 cont.	>2300	spread. length : ~45cm iron droplets throughout the oxidic phase high porosity
VE-07	34%$_w$$HfO_2$+26%$_w$$ZrO_2$+25%$_w$$SiO_2$+15 %$_w$$Fe_xO_y$	25	0,5 cont.	2270	spreading length : ~ 55 cm high compactness homogeneous structure

These tests, which are not detailed here, enabled the adjustment of furnace parameters and provided information on:

- The behaviour of complex mixtures including refractory oxides, silica, iron oxides and in one case (VE-06) iron metal. Thus, in the VE-03 test, a compound (Hf,Zr,SiO4), not predicted by thermodynamic computer code, was obtained. As regards the metallic phase, the VE-06 test showed that when iron represents a low percentage (~ 5%) of the mixture, it is transported by the oxidic phase; indeed, post-test analyses revealed that no segregation occurred and iron droplets of various sizes were distributed throughout the spread melt.
- Spreading, which was never stopped in any of these tests by a crust formation at the front. Consequently, new assumptions are required to explain progression stopping. Among all the possible hypotheses, an explanation has been proposed ; it is based on a blockage due to the formation of solid particles (dendrites or globules) throughout the fluid which induces an increase in apparent viscosity. This mechanism would be characteristic of a melt exhibiting a large solidus liquidus temperature range.
- Physico-chemical interaction between the melt and the refractory substratum (zirconia bricks) which, although quite limited, was observed on about 5 mm depth in the upstream area.

3.2 VE-U1 test

The first spreading experiment with prototypical material (VULCANO VE-U1) was performed on December 2, 1997.

The melt composition (45%$_w$ UO2, 20%$_w$ ZrO2, 20%$_w$ SiO2, 13%$_w$ Fe3O4, 2%$_w$ Fe2O3) was characteristic of corium discharge from the reactor pit after ablation of the sacrificial gate (EPR configuration). The solidus-liquidus temperature range of this composition was about 900 K with a liquidus temperature of 2250 K. During the pouring process, the corium temperature at the furnace outlet was maintained between 2450 and 2650 K. An amount of 47 kg was poured into the test section at an average flowrate of about 2.5 kg/s.

As regards spreading phenomena, video cameras showed a discontinuous progression of the melt, the formation of a skin at the free surface, the formation of hot melt protrusions (fingers and tongues) which flowed out beneath the skin and wrinkled it.

The two photos below (Figure 3) show the skin which is colder than the corium entering in the test section and hot tongues forming at the front.

In this experiment, unlike simulant material tests, spreading was quite efficient; hence, the final spreading length was 1.2 m inducing an average thickness of between 2 and 3 cm.

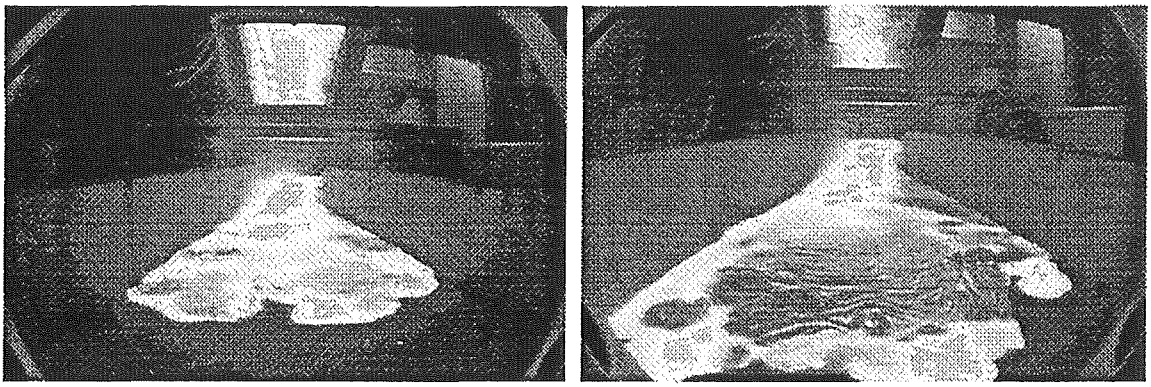

t =12h26'21 t =12h26'26

Figure 3 : VULCANO VE-U1 - View of the spreading

Thanks to the checkerboard calibration (see Figure 2), front progression history (Figure 4) is determined by image processing. Since the spreading experiments are to be compared with 1-D computer codes such as THEMA (Spindler, 1998), the radius of the 19° angular sector having, at each instant, the same area as the measured flow area, is calculated. These data are quite consistent with the measurements provided by thermocouples that were installed at the substratum surface. The time and space averaged front velocity is around 10 cm/s with a maximum at 20 cm/s.

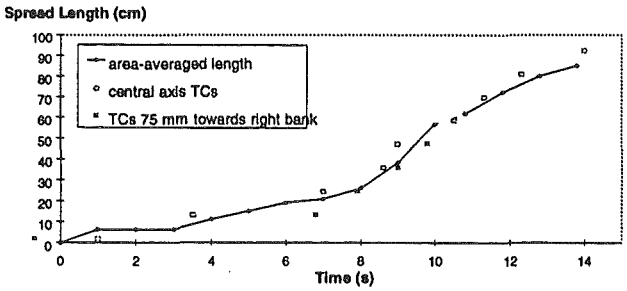

Fig. 4 : Progression of the VEU1 melt front

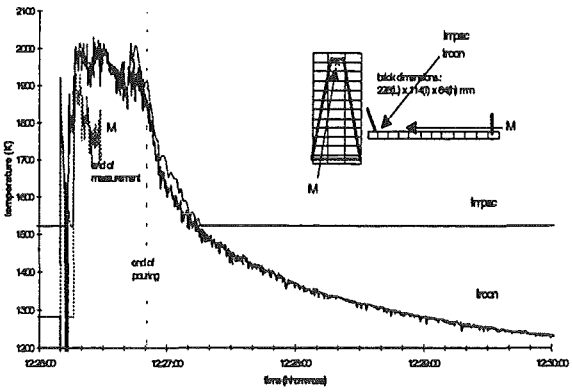

Fig. 5 : Surface temperature evolution (entrance and front pyrometers)

Figure 5 shows that the corium free surface temperature in the entrance area was always about 2000 K during the pouring process.

Thermocouples in the corium flow (Figure 6) gave, with a significant delay, a slightly higher value, but never exceeded 2100 K which is lower than the liquidus temperature of the melt. This information, if it is confirmed by other experiments, shows that the corium/concrete mixture can easily spread, certainly thanks to a large solidus-liquidus temperature range. Moreover, the front measurement pyrometer (Figure 5) points out a front temperature higher than the solidus temperature of the melt.

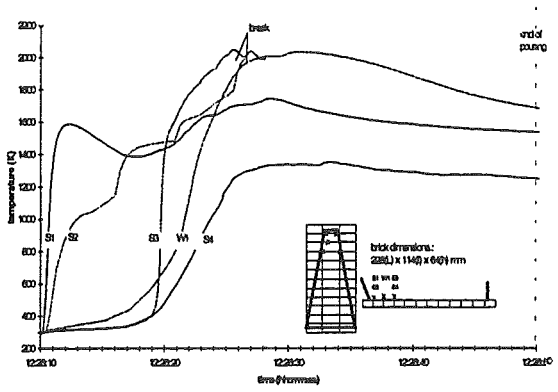

Figure 6 : Corium temperature evolution (immersed thermocouples)

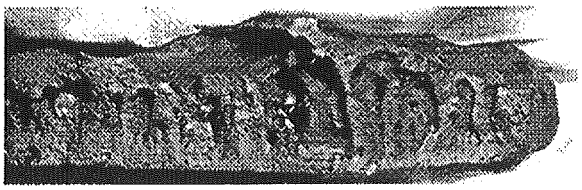

Figure 7 : VE-U1 Test View of the bottom layer

Post-test analyses showed that :

- The chemical composition of the spread melt was homogeneous and very close to that of the load ;
- The structure of the spread melt was composed of 3 layers :
  - a bottom layer of about 1 cm in thickness, in contact with zirconia bricks, presenting large vertically-elongated cavities (see Figure 7) ;
  - an upper layer of roughly the same thickness, in which there were a lot of spherical cavities ;
  - and between these two layers a lens-shaped void layer, the maximum thickness of which being about 1cm, located in the central part of the spread melt.
- A limited physico-chemical interaction (about 40 cm^2, 5 mm depth) between the corium melt and zirconia bricks at the entrance of the test section.

The cavities, observed throughout the melt, result, without any doubt, from gas bubbles stopped in their lifting motion. Among the possible explanations of the large gas release, the most likely seems to be the release of UO as gas due to a sub-stochiometry of UO2 resulting from the reductive atmosphere of the furnace.

Scanning electron microscopy revealed a homogeneous structure versus spread length but three different structures versus height :

- A thin layer (~250 μm) at the bottom, the composition of which corresponds approximately to thermodynamic equilibrium;
- The major part which is essentially composed of 2 cubic oxid solid solutions + Fe2SiO4 + silica in amorphous phase;
- A very thin layer (~40 μm) located at the top which is also composed of 2 cubic solid oxid solutions + Fe2O3 without silica.

An attempt to calculate this structure with the thermodynamic computer code GEMINI gave satisfactory agreement when only the bottom layer was supposed in

thermodynamic equilibrium. It seems that the most of the corium solidified out of thermodynamic equilibrium.

Due to the observed cavities, the porosity of the spread melt is quite high. Moreover the spread melt surface presented large cracks, which indicates that there would be no coolability problem if these cracks occurred early enough. However, the physico-chemical interaction observed in the entrance area could significantly change zirconia brick properties in case of decay heat.

3.3 VE-U3 test

The objective of the VULCANO VE-U3 test was to compare the spreading and solidification of a highly refractory oxide content corium melt with the results observed in the VE-U1 test, in which the corium melt represented the highest expected silica content after reactor pit gate meltthrough in EPR configuration.

In VE-U3, the load was composed of 60%$_w$ UO_2 + 25%$_w$ ZrO_2 + 7%$_w$ Fe_xO_y + 8%SiO_2 . Although the liquidus temperature (2520 K estimated by the GEMINI computer code) of this melt was higher than that of the VE-U1 melt (2250 K), the solidus-liquidus temperature range was kept in the same order of magnitude (about 900 K) and, more important for spreading, the difference between the liquidus temperature and the temperature at which 50% of the melt is solid was quite similar (~ 250 K).

During all the final melting process, the rate of released smokes was always very high, the most important observed up to now. In particular, it was considerably higher than in all the experiments with HfO2, thus confirming a great behaviour difference between UO2 content and HfO2 content melts and emphasizing the need for real material test.

Due to a rupture of the plasma arc during the pouring phase, only 27 kg of the melt flowed down continuously from the furnace at roughly 2570 K with an average flowrate of about 1.2 kg/s (~ half the flowrate of the VE-U1 test) and spread onto refractory zirconia bricks.

At the entrance of the test section, the melt temperature was only 2370 K, certainly below the liquidus temperature, inducing a high viscosity which limited spreading. An early slackening and a creeping motion of the front was observed while the melt continued to flow. The final spreading length was roughly 37 cm and the melt thickness varied from 2 cm at the front up to 5 cm in the back. As in the VE-U1 test, very clear folds formed at the surface during spreading.

The analyses of the recorded data and physico-chemical post-test examinations are underway for further interpretations.

The first conclusion of this test is that although pouring conditions (melt temperature and flow rate) were unfavourable, such a corium mixture effectively spread certainly because its large solidus liquidus temperature range.

4. INTERPRETATION WORK

The applications of these results on actual plant conditions need the use of computer codes which must be qualified. To reach this objective, some of these tests, in particular the VE-U1 test performed with UO_2, have been calculated with the THEMA computer code developed by CEA/DTP (Eberlé, 1997, Spindler, 1998). This code describes the spreading of a fluid of complex composition, taking into account the solidification and crust formation phenomena and conductive, convective and radiative heat losses. It solves the following equations, after having performed an averaging on the fluid melt depth: one mass balance equation for each melt material; two energy balance equations, one for metals and one for oxides; one momentum balance equation (Navier-Stokes equation) for the melt, using one velocity field. This approach is valid as long as the melt depth is small compared to the spreading distance.

4.1 Assumptions used in the viscosity model

The examination of video records and of temperature measurements (section 3.2) shows that spreading seems to be governed mainly by the melt viscosity and is not stopped by the formation of a crust at the leading edge.

The viscosity of a melt composed of corium components (UO_2, ZrO_2, Zr, Fe) and of concrete ablation products (SiO_2, CaO, Fe_xO_y) may evolve considerably in the solidus and liquidus temperature range, which may be large (up to 1100°K). The present approach used for the evaluation of melt viscosity is based on many former studies (Arrhenius, 1917, Einstein, 1911, Thomas, 1965), which give the apparent viscosity η_{app} as a function of both the liquid phase viscosity η_{liq} and the solid volume fraction ϕ of the melt, according to a relation of the following type :

$$\eta_{app} = \eta_{liq} \cdot f(\phi) \qquad (1)$$

In case of melts containing components of various melting points, the viscosity of the liquid phase itself evolves throughout solidification and can be derived from the evolution of its composition. For example, for melts containing silica, the silica content of the liquid phase increases during the corium cooling because of its low melting point, which induces an increase of the liquid phase viscosity. The thermochemistry GEMINI2 code (developed by Thermodata) is applied to determine the evolution of the solid volume fraction and of the remaining liquid phase composition versus temperature (Seiler, 1997). The model used for evaluating the viscosity of a liquid containing silica is that proposed by Urbain (1965).

In a previous paper (Ramacciotti, 1998), it was shown, from comparisons with other experimental data both on simulant and real corium material, that most of the viscosity models are inadequate for this kind of melt, giving viscosity values which are too low. Consequently, the author proposed that, for a mushy melt, the dependence of

viscosity versus solid fraction can be described by a formulation of Arrhenius type with a multiplicative factor C defined such as :

$$f(\phi) = \exp\left(2{,}5.C.\phi\right) \tag{2}$$

C being equal to 1 in the case of the nominal Arrhenius correlation. This C factor depends on experimental conditions and values between 4 and 8 are found for corium melts.

4.2 Parametrical study

The goal of this study is to assess the impact of the viscosity model on corium spreading. THEMA code calculations using a viscosity stopping model, consequently with no crust formation, and different viscosity model assumptions, are compared with experimental data from VE-U1. For the sake of simplicity, we introduce a viscosity formulation in the code which globally describes the combined effects accounting for the viscosity increase of the melt containing silica during the cooling phase.

According to a study on basalts (Shaw, 1998), viscosity can be modelled by using an empirical law such as :

$$\eta_{app} = \eta_{liq}.\exp\left[-A.\left(T - T_{liquidus}\right)\right] \tag{3}$$

A being the rheological parameter.

We use the methodology described in section 4.1 to calculate the liquid phase viscosity versus temperature, then that of the mushy melt using an Arrhenius type law with 3 values of the C factor equal respectively to 1, 5 and 6.1. We then fit, by a mean square minimization method, the viscosity law corresponding to each C factor value, using a Shaw type law with values of the A rheological parameter equal respectively to 0.01, 0.02 et 0.024 K^{-1} (see Figure 8).

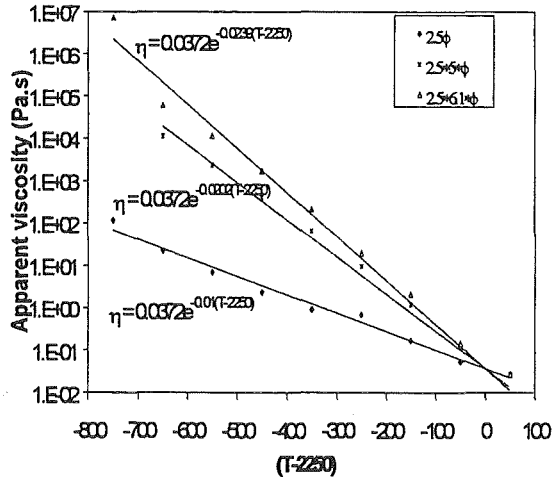

Figure 8

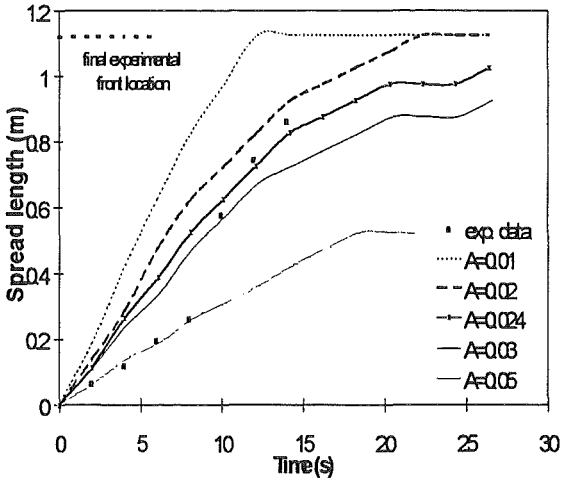

Figure 9

Figure 9 compares experimental data with the spreading length calculated versus time with the THEMA code for different values of the A parameter. The calculation performed for a rheological parameter value of 0.024 K^{-1}, corresponding to a coefficient C equal to 6.1, gives the best agreement with experimental data. The overestimation

during the first 7 seconds is thought to be related to the uncertainty on the measured mass flow-rate or to a non-Newtonian effect. So, whereas the classical Arrhenius formula does not allow the correct reproduction of the motion of the corium leading edge, a modified Arrhenius relationship with a stronger dependence on temperature enables us to obtain a rather satisfactory agreement, at least during most of the spreading phase.

5. CONCLUSIONS

These first tests provided important and encouraging information on :

- Spreading, which seems relatively efficient, even at low flowrates, for a melt presenting a large solidus-liquidus temperature range, such as a corium/concrete mixtures ;
- Coolability, which would be made easier by the high porosity and the surface cracks of a corium/concrete spread melt.

However, some questions are raised :

- The origin of the high porosity observed in spread melts after cooling, which is not well explained at the present time ;
- The stopping melt progression phenomena which is not, up to now, clearly identified ; the viscosity stopping model, combined with a modified Arrhenius viscosity model, gives a reasonable prediction of spreading kinetics in VE-U1, but will have to be checked further against other experiments ;
- What would be the physico-chemical interaction between melt and substratum in case of decay heat ?

Therefore, before concluding that there is no problem of spreading in severe reactor accident conditions, these results have to be confirmed by further experiments in order to provide answers to the remaining questions. Thus with this view, zirconia substratum will be replaced by steel and concrete, which should enable us to clarify the effect of gas release from substratum on melt porosity. The physico-chemical corium substratum interaction will be investigated in specific tests in which decay heat will be simulated by induction.

The comparison of THEMA calculations with experimental results pointed out the need of specific apparent viscosity models. Indeed, calculation results obtained with a modified Arrhenius relationship exhibit a rather satisfactory agreement.

NOMENCLATURE

ϕ	solid volume fraction
η	dynamic viscosity
C	coefficient introduced in the Arrhenius law
T	temperature

Subscripts

app	apparent (for viscosity)
liq	liquid

Acknowledgement

This work has been partially funded by the European Commission through the Contract FI4S-CT96-0041 of the 4th Framework Programme (Corium Spreading and Coolability Project) .

REFERENCES

Arrhenius, S., 1917.*The viscosity of solutions*, Biochem J., Vol.11, pp. 112-133.

Cognet, G., et al, 1997. French research programme on spreading-based core catcher designs, NUTHOS-5 Meeting, Beijing, China.

Eberlé ,P. , 1997. Modélisation physique et numérique de l'étalement d'un fluide avec solidification dans le cadre des études de sûreté pour les réacteurs à eau sous pression,. PhD Thesis, Université J. Fourier, Grenoble.

Einstein, A., 1911. *Annalen der Physik*, Vol.34, pp. 591-592.

Jegou, C., et al, 1998. Plasma transferred arc rotary furnace for corium melting. *High Temperature Material Processes* - n°3.

Journeau, C., et al, 1998. Visualisation of a 2000°C melt spreading over a plane, 8th Symp. Flow Visualisation, Sorrento.

Ramacciotti, M., et al, 1998. Propriétés de mélanges en cours de solidification, *Cahiers de Rhéologie*, Vol.16, n°1, pp 303-308.

Seiler, J.M., Ganzhorn, J., 1997. Viscosities of corium-concrete mixtures, *Nuclear Engineering and Design*, Vol. 178, pp 259-268.

Shaw, H.R., 1969. Rheology of basalt in the melting range, *Journal of Petrology*, Vol. 10 part 3, pp 510-535.

Spindler, B., Veteau, J.M., 1998. Status of the Assessment of the Spreading Code THEMA against the CORINE Experiments, SARJ-98, Japan.

Thermodata, Thermochemical equilibria calculation code complex multicomponent phases : GEMINI2, BP 66, 38402 Saint Martin d'Heres Cedex - France.

Thomas, D.G. , 1965. Transport characteristics of suspensions, *Journal of Colloid Science*, Vol. 20, pp 267-277.

Urbain, G., 1987. Viscosity estimation of slags, *Steel Research 58*, n° 3, pp 111-116.

OECD Workshop on Ex-Vessel Debris Coolability
Karlsruhe, Germany, 15-18 November 1999

Organised in collaboration with
Forschungszentrum Karlsruhe (FZK) GmbH

COMAS: REPRESENTATIVE SPREADING EXPERIMENTS WITH VIEW TO CORE MELT MITIGATION

Wolfgang Steinwarz
Siempelkamp Nuklear- und Umwelttechnik GmbH & Co.
Siempelkampstr. 45, D-47803 Krefeld/Germany
Siempelkamp@t-online.de

Wolfgang Häfner
Battelle Ingenieurtechnik GmbH
Düsseldorfer Str. 9
D-65760 Eschborn/Germany

Zeynel Alkan
RWTH Aachen
Institut für Reaktorsicherheit und -technik
Eilfschornsteinstr. 18
D-52062 Aachen/Germany

Manfred Fischer
Siemens AG - KWU
Postfach 3220
D-91050 Erlangen/Germany

ABSTRACT

Within the COMAS (Corium on Material Surfaces) project representative experimental and analytical investigations on the ex-vessel spreading behaviour of prototypic corium were performed to provide a realistic technical basis for the development of core catchers for future nuclear reactor generations.
In various large-scale experiments melts in the Mg-range with real corium compositions and temperatures around 2000°C were tested using different substratum materials (concrete, ceramics, cast iron).

The COMAS results indicate that for a sufficiently high melt release rate a quick and homogeneous coverage of an ex-vessel spreading compartment as realized in the Franco-German EPR project can be expected. Regarding the analytical assessment it can be concluded that some spreading codes have reached a sufficient level to provide guidelines for the evaluation of spreading concepts. Open questions are mainly related to segregation and immobilization of the melt.

1. INTRODUCTION

In response to more stringent legislation in some EU member states, additional safety margins are required for the development of the next generation of nuclear power plants. These include the demand to ensure the integrity of the containment - even in the case of a core melt accident - in order to render emergency measures outside the reactor plant unnecessary. One essential requirement is to prevent basemat penetration by the molten core, after failure of the reactor pressure vessel.

The related mitigation concept for the European Pressurized Water Reactor - EPR - is based on a short-term retention phase within the reactor pit to accumulate and condition the released melt, followed by its spreading over a dedicated large surface. There the melt will be passively flooded with water. Finally it solidifies.

As a contribution to the validation of the EPR-concept a number of generic spreading experiments have been performed in Europe over the last decade. Among them, the COMAS experiments are unique due to the realization of large spreading masses (Mg range), prototypic core melt compositions, realistic temperature levels and a broad spectrum of material characteristics. Furthermore, the COMAS experiments have yielded valuable data and better insight into relevant phenomena allowing the existing computer codes to be improved and validated as a basis for the development of core melt retention systems.

The work is part of the European Union's R & D Framework Programme, as well as of the German Reactor Safety Research Programme. The main project partners are Siempelkamp, Ansaldo, Aachen University, Battelle and Siemens.

2. TEST FACILITY

The large-scale COMAS experiments are carried out in the CARLA plant at Siempelkamp's Krefeld location, licensed for handling and melting of radioactively contaminated materials and equipped with a highly-qualified redundant filter system, according to nuclear standards.

The overall test arrangement for the COMAS experiments consists of the melting furnace, a feed box with a plug system and the spreading compartment. Spreading is carried out by using a 3-channel-arrangement (Fig. 1) with an overall length up to 8 m as well as a 2D-spreading area of approx. 15 m^2. For the spreading tests with pure oxidic melts, a special chamber arrangement for the feed box was developed to separate the oxidic and metallic melt fractions. As substrata for the spreading process concrete, ceramics and cast iron have been selected, in order to cover a broad spectrum of material characteristics.

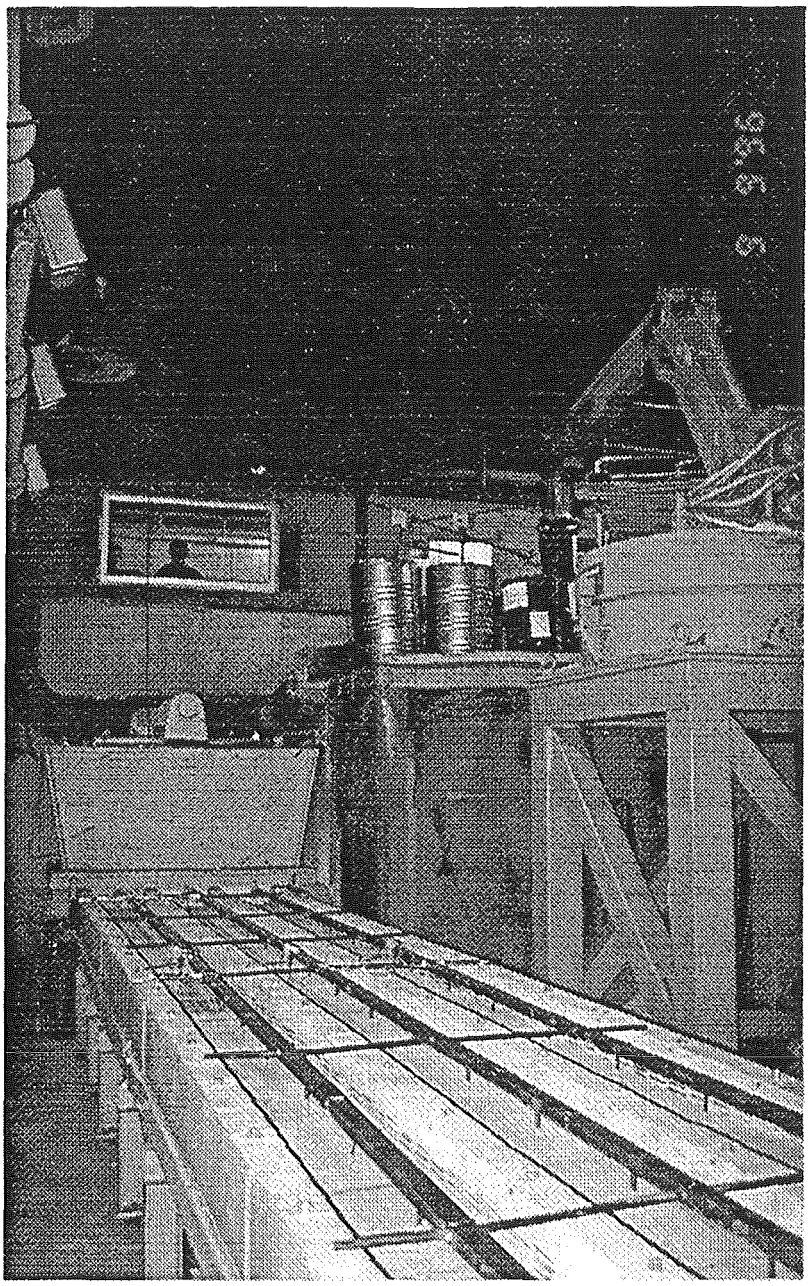

Fig. 1 Inner housing of the CARLA plant with the 1D-spreading facility

The medium-frequency induction furnace has a capacity of 3.2 Mg and allows a maximum melt temperature of roughly 2,300°C. For each test campaign, a specific furnace liner - consisting of a newly-developed material based on zirconia - is installed to adapt the furnace to the high-temperature regime. This material is similar to that foreseen for the EPR core catcher.

The measurement programme is based on a broad instrumentation equipment as well as an extended set of sampling and microanalysis technique.

For the COMAS test series, two compositions, representative of EPR conditions, have been selected to reflect the main characteristics of the chosen mitigation concept (Fig. 2).

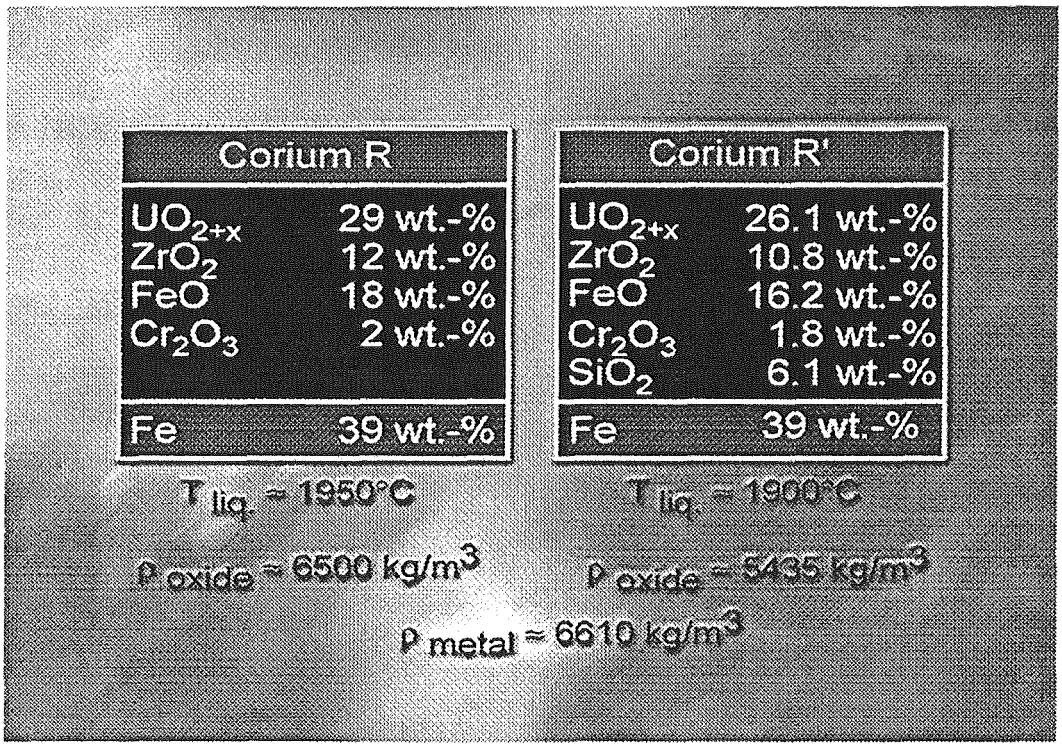

Fig. 2 Corium compositions type R and type R'

Both fully oxidized corium compositions type R and type R' are based on a ratio of oxidic to metallic melt of 60:40 weight percent. Laboratory investigations and calculations resulted in liquidus temperatures for both melts of around 1900°C. What's remarkable with a view to the spreading process are small density differences between the oxidic and metallic fractions (Hellmann, 1998).

3. EXPERIMENTS

In a total of 13 tests various mixed melts - as well as metallic and oxidic fractions separated from the reference melts were investigated since 1995. The most important new information came from the tests COMAS 5a, COMAS EU-2b and COMAS EU-4 which will now be described in more detail.

In the test COMAS 5a 1 Mg of mixed corium R-melt was spread over three 1-dimensional courses (Fig. 3). With an initial spreading temperature of 1900°C - and an average velocity of 1 to 1.5 m/s - a spreading length of roughly 5 m was reached.

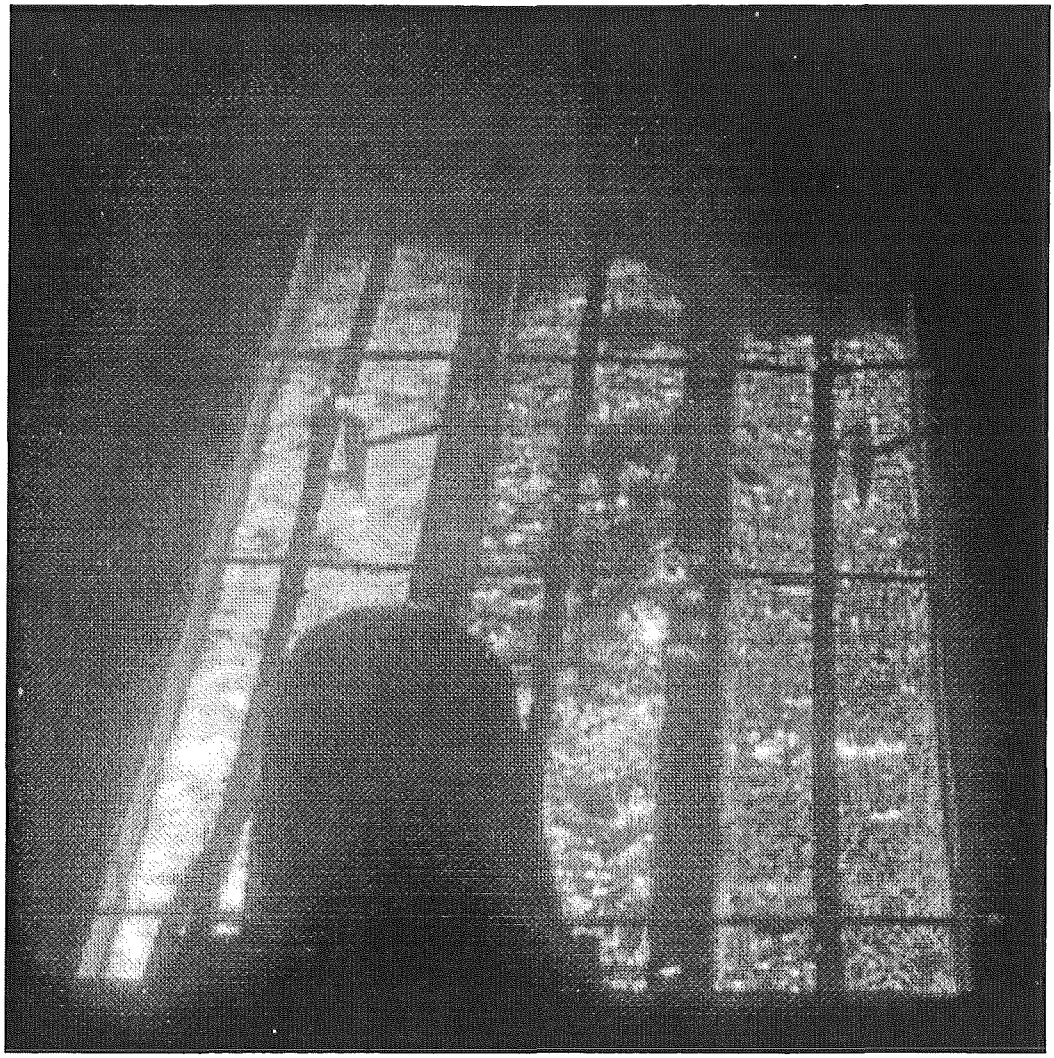

Fig. 3 COMAS 5a-test: 1D-spreading of Corium R

In the 2-dimensional test COMAS EU-2b approx. 630 kg of pure oxides - pre-separated from corium R' melt - were spread. The initial spreading temperature was monitored at 2070°C. This melt too stopped at approx. 5 m after 7 s.

Cast iron was chosen as substratum material for the 2-dimensional spreading test COMAS EU-4 (Fig. 4). Approx. 2 Mg of mixed corium R melt was spread with an initial temperature of roughly 2000°C. The maximum velocity reached nearly 2 m/s and maintained an average value of 0.7 m/s before solidification. A spreading length of about 8.5 m along the direct line was reached. This experiment can be regarded as a demonstration test for the feasibility of the EPR spreading concept, especially in view of the large-scale of approx. 1:6.

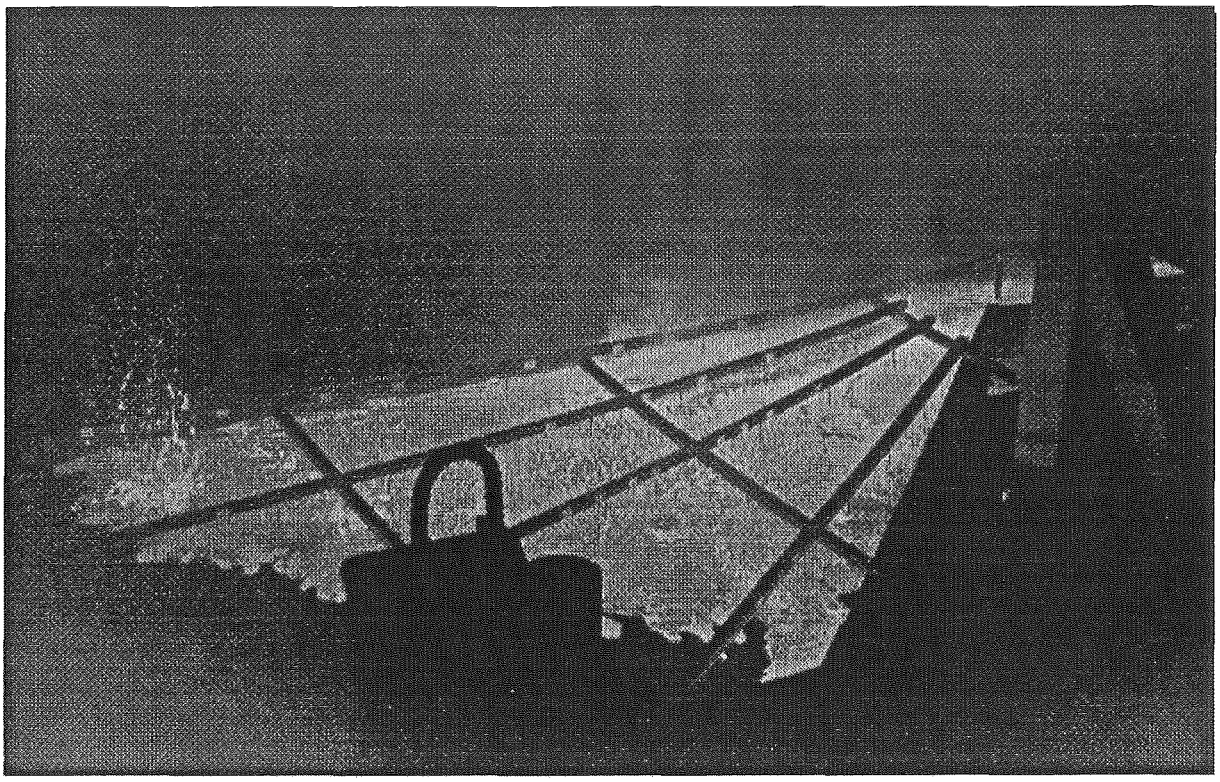

Fig. 4 COMAS EU-4: 2D-spreading of corium R

4. PHENOMENA

To gain more understanding about the complex spreading process, main emphasis within the COMAS project has been focused on investigating specific phenomena and effects governing the transport behaviour of the corium.

An interesting segregation mechanism for mixed melts was observed during the spreading process (Steinwarz, 1999). It was detected by means of the infra-red technique utilizing the largely different emissivities of the oxidic and metallic melt fraction. Using test data from COMAS 5a and in particular the channel with a cast iron substratum the evaluation revealed a clear increase of the heat flux density of the melt surface. The corresponding temperature distribution showed a rise of the peak value between 2 s after the beginning of the spreading process and 4 s in spite of the fact that the spreading melt is continuously cooling down. This effect clearly demonstrated the strong increase of th oxidic melt portion at the melt surface. Finally, the solidified melt showed a distinct separated layering of both fractions, confirmed by the metallurgical post-test examinations.

One of the predominant effects, in view of the immobilization of the melt, is the formation of crusts on all melt surfaces; on top, at the front and at the contact area between melt and substratum. Crust formation can be visualized by measuring the temperature difference between the melt surface and the melt interior, immediately after immobilization of the melt. In the case of the COMAS EU-3a test special dipping devices opened the crust. By means of the infra-red cameras temperature differences of up to 260 K were detected. The thermocouples, attached to the dipping devices, reached deep into the melt interior where they found an even higher overall difference of approx. 400 K. Especially with the cast iron crust formation at the contact surface between melt and substratum could be indirectly confirmed by the lack of melting effects at the substratum surface, combined with the generation of a thin insulating gap.

High ductility of the crust became evident in the COMAS EU-3a test when the front area of the immobilized, initially-spread melt creased - due to pressure exerted by following batches - but continued the inner melt.

5. ANALYTICAL WORK

As full-scale, real material experiments are hardly feasible, the development of computational codes for the analytical simulation of a broader spectrum of spreading scenarios is absolutely essential. These codes have to be validated by means of representative experiments. Therefore, supporting the code development was one of the most important aspects of the COMAS project, leading to detailed benchmarking using the COMAS 5a test.

By doing this, various modelling approaches with different characteristics, such as Newtonian or Bingham flow behaviour, inclusion of crust formation and multi-component melts etc. were implemented into the codes and tested.

All codes evidently had certain deficiencies when it comes to modelling the final immobilization phase of the complex spreading process.

As one of the most effective post-calculations an analytical result of the 2D-experiment COMAS EU-4 using the CORFLOW code (Wittmaack, 1998) should be shown examplary. The good fitting of the analytical and experimental result is evident (Fig. 5).

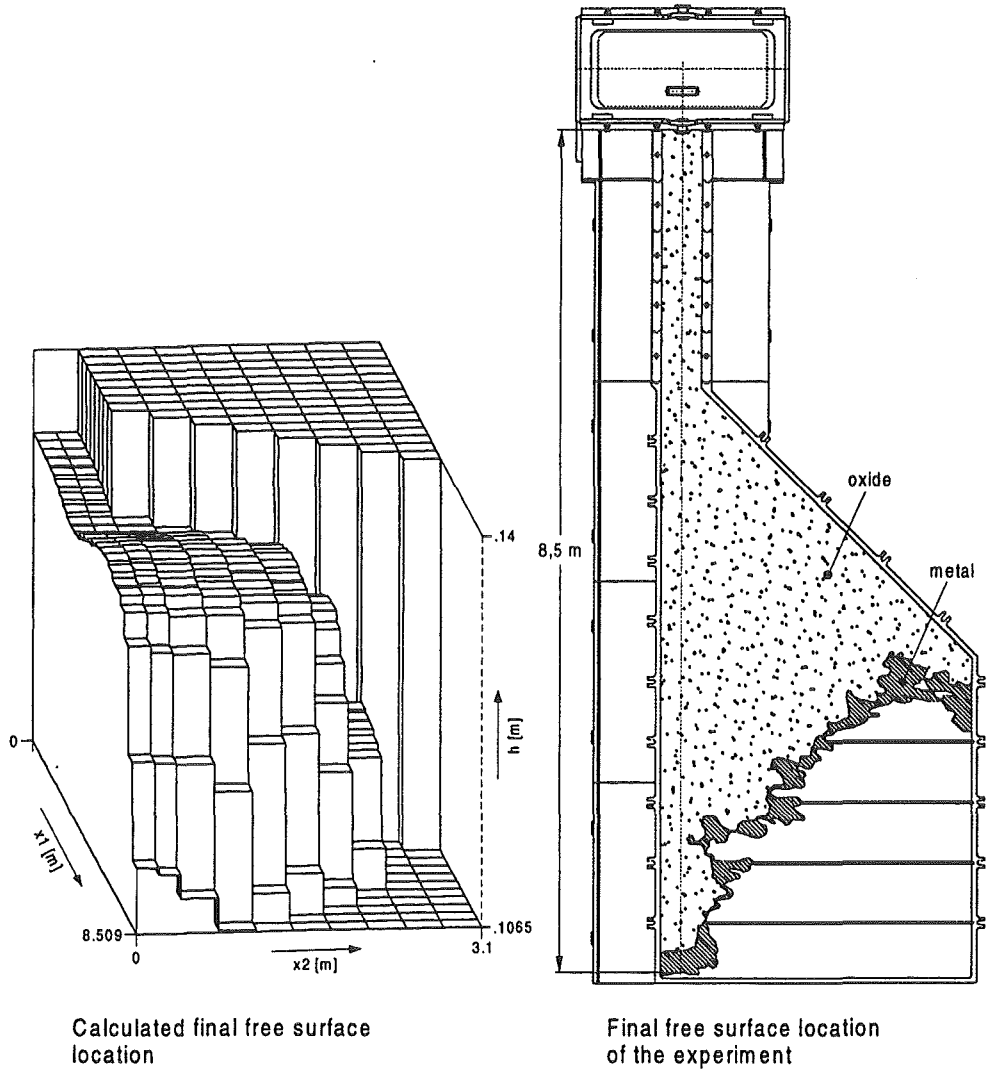

Fig. 5 COMAS EU-4: Post-test calculation with CORFLOW (2D-spreading of corium R)

6. RESULTS

In summarizing the main current results of the overall COMAS project, the following conclusions can be drawn:

- Spreading length was found to be virtually independent of the substratum, but did depend on mass flow rate, melt temperature and, for mixed melts, on metal/oxide ratio
- Even for thin melt layers of only few cm good melt distribution over the spreading area was observed
- Spreading behaviour is dominated first by inertia and later by viscous forces
- Good spreadability was observed even for oxidic melts with temperatures significantly below liquidus

- Prior to immobilization, mixed melts seperate into horizontal metallic/oxidic layers even at small metal/oxide density differences
- Front immobilization is likely caused by crust formation
- Measured heat losses to the upper and lower surfaces were in the same order of magnitude, but significantly higher than the decay heat during the spreading period
- For metal spread on cast iron the formation of an insulating gap was observed
- Analytical spreading codes have reached a sufficient quality level to provide the main design requirements for corium retention systems based on the spreading concept. The questions still open relate to segregation and immobilization of the melt.

7. CONCLUSIONS

The COMAS project has helped to identify the key phenomena which control corium spreading and has provided an important basis for the validation of theoretical models which are used to simulate melt spreading in real reactor geometries.

To improve understanding of complex spreading scenarios, further experimental research work should be concentrated on a few process-dominating phenomena such as segregation and crust formation. The results of this work should also help to finalize the validation activities for the relevant codes. In addition, large-scale demonstration tests - under representative conditions - should provide a significant contribution to final proof of a convincing corium mitigation concept.

REFERENCES

Hellmann, Lansmann, Funke, Fischer, 1998
Diverse internal reports by Siemens

Steinwarz, Dyllong, Koller, 1999
COMAS spreading experiments with prototypic oxidic corium melts for optimization of core catcher designs
Proc. ICONE-7, Tokio, April 19-23, 1999, CD-ROM No. 7196

Wittmaack, 1998
Numerische Simulation von Strömungen mit freier Oberfläche und diskreten Phasenübergängen, FZKA Report No. 6129 (August 1998)

OECD Workshop on Ex-Vessel Debris Coolability
Karlsruhe, Germany, 15-18 November 1999

Organised in collaboration with
Forschungszentrum Karlsruhe (FZK) GmbH

DRY AND WET SPREADING EXPERIMENTS WITH PROTOTYPIC MATERIAL AT THE FARO FACILITY AND THEORETICAL ANALYSIS

W. Tromm and J.J. Foit
Forschungszentrum Karlsruhe GmbH
Postfach 3640, D-76021 Karlsruhe, Germany

D. Magallon
JRC-Ispra
I-21020 Ispra (VA), Italy

ABSTRACT

With the unique opportunity of the FARO facility to investigate prototypical core melts of a UO_2/ZrO_2 weight percentage of 80/20, a first spreading experiment FARO L-26S was conducted in 1997. The objective was to obtain data on the spreading at flow rates of about 2 l/s of 160 kg prototypic high temperature oxide melt on a dry non coated stainless steel plate forming a sector of 17°. Following the objective outlined in the 4th Framework Programme (FWP) the FARO test L-32S conducted in March 1999 was a first of a kind spreading test with corium and a shallow water layer on the substrate. The test was conducted with 130 kg melt. The same spreading steel plate was chosen as in the first test L-26S. Therefore information on the spreading behaviour with a small water layer and comparison of the results with the former test was obtained.

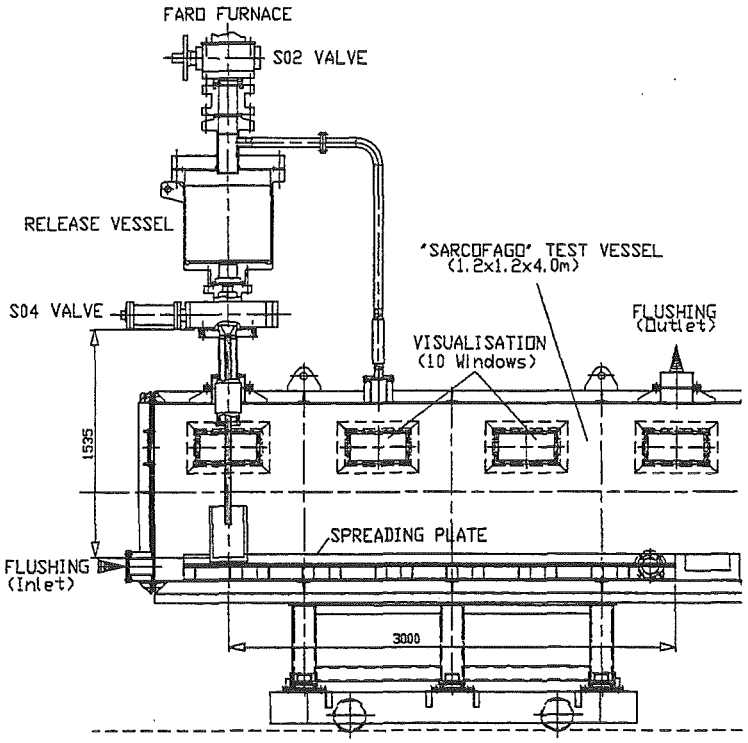

Fig. 1: SARCOFAGO test set up with FARO furnace

1. INTRODUCTION

In the FARO furnace (see Figure 1), the UO_2-ZrO_2 mixture is melted by direct heating of a compacted granulate between two electrodes. The solidus-liquidus temperature range of this melt composition of 80 wt-% UO_2 and 20 wt-% ZrO_2 was calculated by GEMINI2. The

solidus-liquidus temperature range is 50 K. In Figure 2 the solid fraction between the immobilisation temperature (defined as the temperature at which the melt is unmoveable) and the liquidus temperature is given with the related viscosity calculated by the Stedman correlation (Stedman, 1990). Table 1 shows the melt properties at liquidus temperature for the first test L-26S (Silverii, Magallon, 1998).

Tab. 1: melt properties of the FARO melt at liquidus temperature for L-26S test

property	symbol	value
Initial temperature (measured by UTS)	T_i	2950 K
Liquidus temperature	T_L	2910 K
Solidus temperature	T_S	2860 K
Density	ρ	8.0 10^3 kg/m3
Surface tension	σ	0.5 N/m
Heat conductivity	λ	3 W/mK
Heat capacity	c_p	0.5 kJ/kgK
Dynamic viscosity	μ	0.005 Pas
Initial channel width	wi	0.15 m
channel width at 0.8 m	$w_{0.8}$	0.39 m
channel width at 1.0 m	$w_{1.0}$	0.47 m

The SARCOFAGO test vessel is connected to the FARO furnace via the release tube, the intersection valve unit and the release vessel. Ultrasonic temperature sensors (UTS) are located in the release vessel to measure the initial temperature of the melt. Argon is flushed to the test vessel to perform the test in inert conditions. Initially the test section is at room temperature and atmospheric pressure. The spreading plate of stainless steel located in the SARCOFAGO vessel is shown in Figure 3. It consists of the collecting device, in which the melt was poured from the release vessel by gravity, and the spreading area forming a circular sector of 17°. A barrier of 4 cm in height divided the collection device from the spreading surface.

The principal quantities measured in the SARCOFAGO during the corium spreading were melt mass and temperature, substrate temperatures plane to the surface and at different depths and ambient pressures and temperatures. The thermocouples installed above the spreading plate were intended to monitor the horizontal progression of the melt and to give an indication of its height during the spreading phase. The whole spreading plate was mounted on weight cells to the floor of the SARCOFAGO to obtain a weight balance for detection of the melt mass versus time. Displacement transducers were installed under the steel plate to measure the plate deformation. The discharge of the melt to the collecting device via the discharge tube (127 mm above the plate) was chosen as time zero for this test. 6 video cameras and one infrared camera filmed the test.

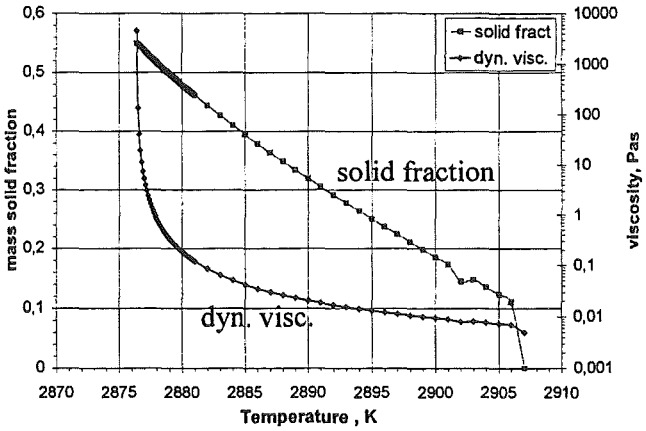

Fig. 2: mass fraction and related dynamic viscosity

2. Test FARO L-26S

About 190 kg of melt were produced and released to the test section via the release vessel. A quantity of 160.4 kg was delivered by gravity to the test section. A quantity of 30.2 kg of

material froze in the collecting device and 130.2 kg spread on the plate. Both UTS installed in the release vessel failed before reaching stable conditions.

But the initial melt temperature could be extrapolated from these signals to be about 2950 K. The duration of the release was approximately 9.7 s, deduced from the load cell signals. The mean discharge flow-rate in the period up to 9.7s was approximately 16.5 kg/s, i.e. about 2 l/s. The presence of instrumentation in the central region of the spreading plate disturbed the visualisation of melt discharge to the collecting cup by the video cameras. But the different spreading phases clearly could be observed. These observations can be seen in Figure 4 where the leading edge position is depicted. The spreading velocity was not constant. There were sudden decelerations due to crust formation followed by melt flow over the crust or by swelling of the crust until the front broke and the melt flow continued under the crust. The maximum spreading velocity was 0.502 m/s. Six different periods for the flow propagation could be distinguished from image processing and thermocouple analysis:

- First period (up to time 3.2 s). After the melt got beyond the barrier that separated the collecting device from the spreading area, the leading edge propagation was quite homogeneous. The velocity ranged from 0.15 to 0.28 m/s.
- Second period (from time 3.2 to 4.2 s). The flow stopped for about 1s as a thin crust was formed. The minimum of the leading edge

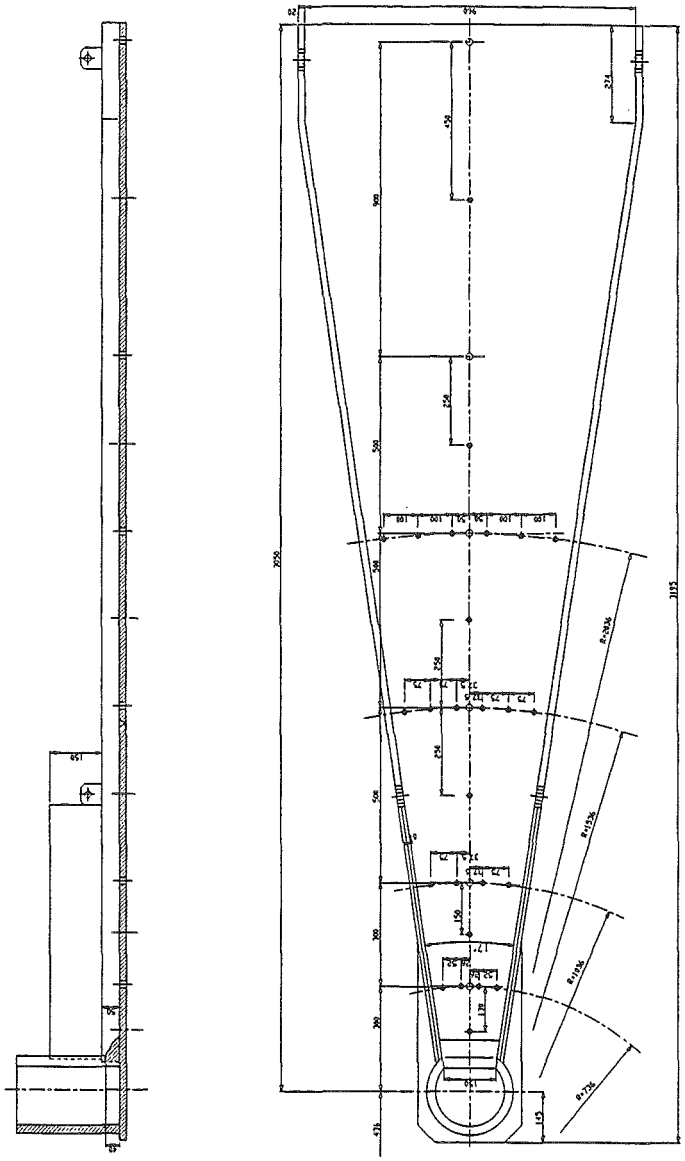

Fig. 3: test section with instrumentation

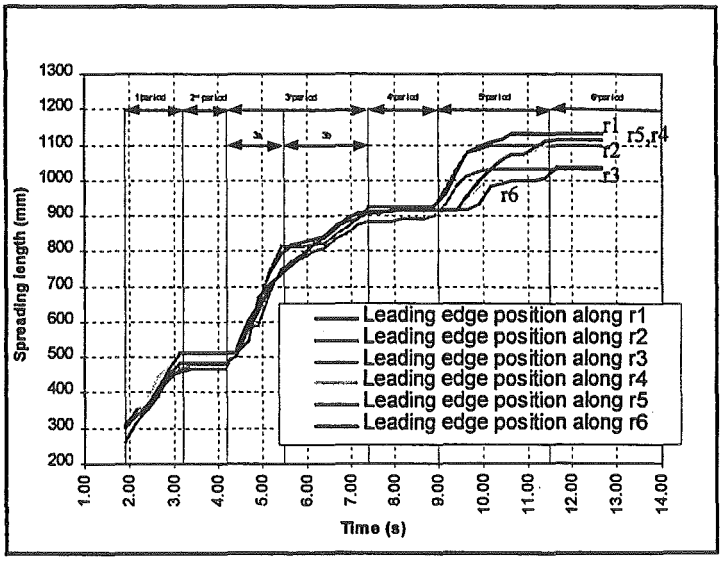

Fig. 4: Leading edge for different lateral positions

position is 460 mm, the maximum 510 mm.
- Third period (from time 4.2 to 7.4 s). The flow broke through the front of the crust. Initially (up to 9.5 s) the flow velocity was very high ranging from 0.25 to 0.502 m/s (the maximum value reached in the test). In a second phase the leading edge velocity decreased down to 0.1 m/s.
- Fourth period (from time 7.4 to 9 s). The flow stopped again due to crust formation.
- Fifth period (from time 9 to 11.5 s). The material passed below the crust. The flow velocity that initially was 0.25 m/s progressively decreased down to 0.
- Sixth period (from time 11.5 s on). The flow stopped and the corium began to cool down. The final leading edge position was between 1060 mm and 970 mm. During the cooling phase, at approximately 15.3 s, a small amount of molten material, forming a hook shape, broke through the crust. No flow was observed after 18 s.

The maximum plate surface temperature reached during the spreading phase is 720°C, see Figure 5. This temperature was reached only by one thermocouple while all the others remained at a temperature lower than 500°C. The long-term maximum plate temperature was 1085 °C and was reached approximately at 600s from time zero. The temperature gradient in the spreading plate was very high close to the plate surface. The maximum temperature difference measured was 270 K. Initially, the time dependent heat flux to the bottom was about 0.9 MW/m^2, taking into account the temperature difference in the plate and the heat up of the plate. The calculated long-term heat flux to the bottom was 0.28 MW/m^2.

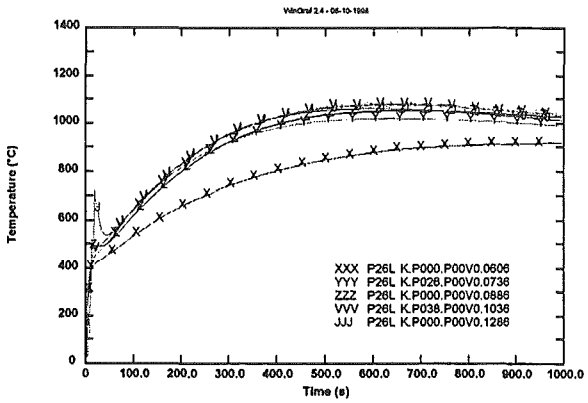

Fig. 5: Long-term surface temperatures of the spreading plate

The pressure in the SARCOFAGO did not increase throughout the test due to the venting lines. The temperature history was measured close to the SARCOFAGO ceiling. One thermocouple was located over the spread melt and was therefore heated by radiation to a maximum temperature of 450 °C. The other thermocouple was located at the end above the spreading plate. It showed a smaller increase up to 250 °C. The remarkable differences between the two temperatures showed the different radiation heat fluxes in the two regions. The debris thickness has been measured in 154 points. A mapping of the crust surface derived from these measurements is shown in Figure 6. The mean value of the debris thickness was 70 mm. The maximum spreading length was 1.05 m from initial barrier. The height of the bulk debris varied from about 10 mm at the leading edge of the melt to about 135 mm at the outlet of the collecting device.

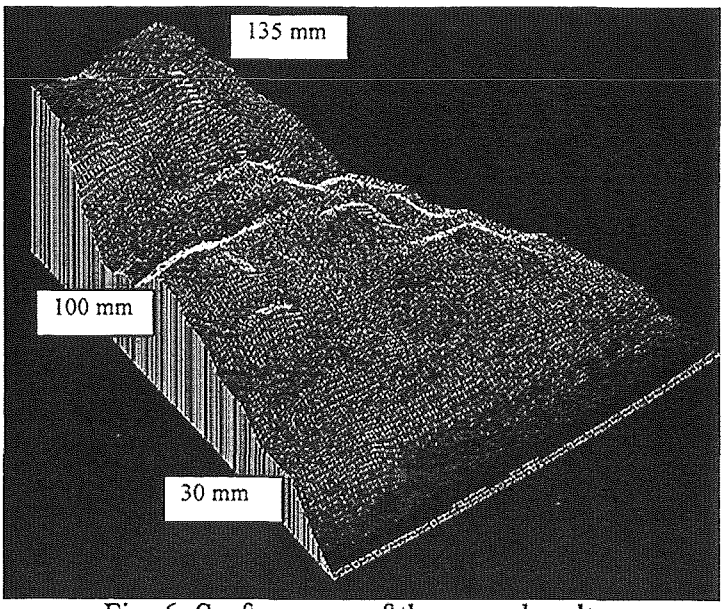

Fig. 6: Surface map of the spread melt

Figure 7 shows a cross-section through the solidified melt at 535 mm from the inlet barrier. The upper surface of the debris formed a layer with a thickness from 10 mm to 20 mm. The layer was formed of small pieces with a size of a few mm. They were completely separated from the lower debris. In the bulk, the debris consisted of discrete blocks of about 50 mm in size, separated by vertical cracks. These blocks showed a solid structure, but could be destroyed easily. The lower crust, a few millimetres in height, was formed by solidification on the spreading plate during the spreading process. The three different layers observed can be distinguished by the different brightness of the reflected light. Gaps of maximum height of 15 mm and length of about 50 mm were observed, see Figure 7 at the right part. The mean height of the gaps was about 5 mm. Neither pitting of the plate nor melt adherence or ablation of the plate was noticed.

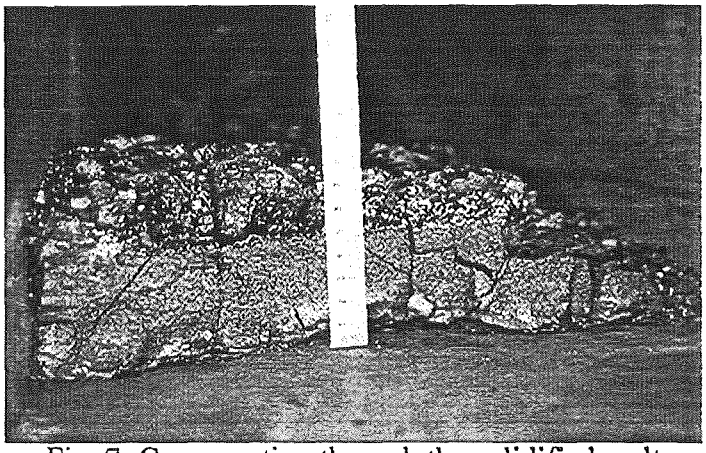

Fig. 7: Cross-section through the solidified melt

2. TEST FARO L-32S

In the second spreading test, principally the same test set up and test section was chosen. But a small water layer of 10 mm was added on the spreading plate. A small dam was welded on the steel substrate at about 1.8 m from the initial barrier to keep the water layer in the beginning at the front part of the plate between the initial barrier and this dam. Backwards, the plate was initially dry. During melt spreading the water was enabled to flow over this small dam to the backside of the plate. Therefore, the reflection of the water to the leading edge of the melt with possible melt water interactions could be prevented.

In this second test, the instrumentation of the test section was slightly changed due to the experiences gained in the first experiment. In the SARCOFAGO test vessel the temperature of the melt in the collecting device was measured by two UTS sensors additionally to the UTS sensors in the release vessel. A NiCr/Ni thermocouple was located at the barrier of the spreading plate to detect the onset of melt spreading. The surface temperature of the melt was measured by a pyrometer at a certain spot close to the barrier. An infrared camera was installed in the SARCOFAGO test vessel to get information about the temperature profile of the whole melt surface during spreading. The obtained data were compared with the pyrometer temperature measurement and with W/Re-thermocouples located at the side wall of the spreading plate. Totally, 8 W/Re-thermocouples were located 25 mm from the left side wall and 25 mm above the spreading plate. On the right side wall 8 NiCr/Ni thermocouples were located in the same position to determine the melt front progression at the outer part of the spreading compartment.

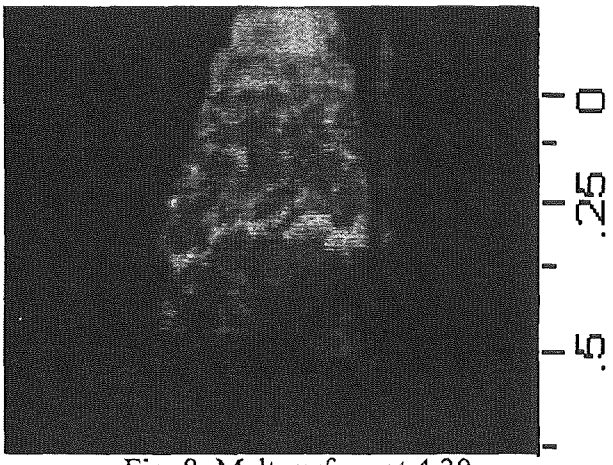

Fig. 8: Melt surface at 4.30 s

The experimental course of melt spreading was taken from the observations of the video and infrared cameras positioned in the SARCOFAGO, see Figures 8-10, and the measurement of the data acquisition system, mainly weight balance and temperature recording at the test section. Time 0.0 s for the infrared camera is equivalent to 9 s of the data acquisition system, which is the onset of melt release to the spreading plate.

About 190 kg melt was produced and at –2.5 s released to the release vessel. After 2.5 seconds, the release to the collection device on the spreading plate started. Over all, 128 kg was released to the test section. At the same time, some melt splashes started to spread over the barrier, i.e. location 0 cm at the spreading compartment. At 0.7 s this first melt had flown 25 cm on the spreading plate. But this melt spread was only a first streamlet of a small melt amount.

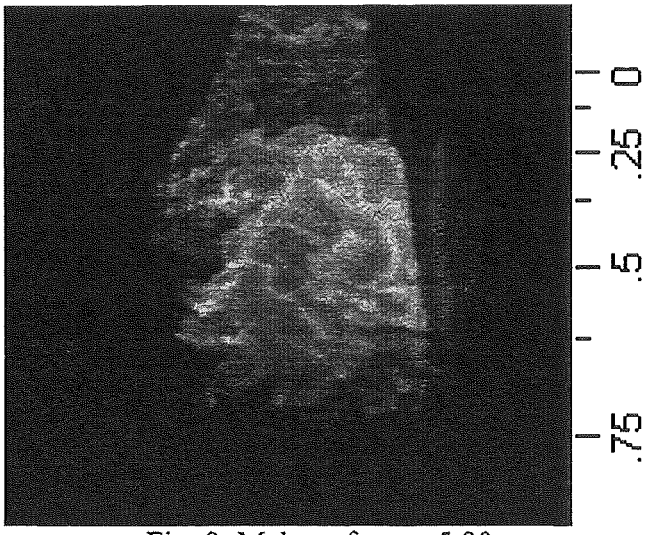

Fig. 9: Melt surface at 5.90 s

At 2 s a second melt flow started. At 4 s the melt had spread to a distance of 50 cm on the plate. Then, the melt stopped due to crust formation. For the right part of the melt, this was the final spreading position. At 4.5 s and a distance of 40 cm from the barrier, i.e. 10 cm behind the leading edge, the crusts started to break up at the left side, which led to a third spreading. This inhomogeneous spreading stopped at 75 cm at time 5.9 s. The crust broke up again at the right side of the left part of the melt and led to a more homogeneous melt front. At 7.5 s, the melt front at the right side had reached a distance of 70 cm, but only due to the left part of the melt, which continued to flow to the right side. More or less this was the final configuration of the melt. At 13.5 s two small melt tongues started to spread very slowly, one in the centre of the leading edge, one at the left side wall. They combined at about 18.5 s, forming the maximum spreading length, which was reached at about 28.5 s at 82 cm due to very slowly and small melt eruptions through the crust.

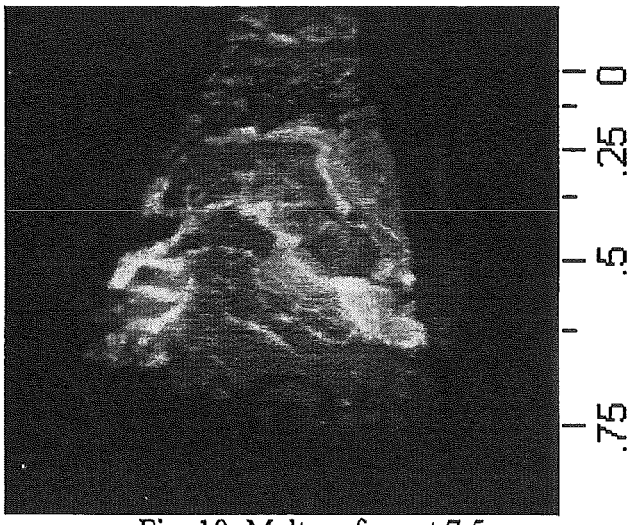

Fig. 10: Melt surface at 7.5 s

During melt spreading the water layer started to evaporate at the leading edge of the melt, and accordingly, the melt formed at the front small pillows. But the most part of the water was pushed forward and flowed over the dam at 1800 mm on the spreading plate. No melt water interactions were observed. Remarkable was the inhomogeneous spreading behaviour. On the right part, the crust stopped melt progression already 50 cm beyond the initial barrier. On the left side, the crust broke up several times and led to an overall spreading length of about 80 cm at the left part and 70 cm at the right part of the test section.

The weight measurement showed the initiation of melt release to the test section. The release started 9 s after begin of data acquisition and lasted 7 s (see Figure 11). Post test examinations showed that overall 128 kg were released to the test section, 100 kg on the spreading plate and 28 kg to the collection device. About 30 kg remained in the release vessel. The post test observations were in good agreement with the long-term weight balance. But after about 17 s the melt started to solidify in the release tube. This connection with the upper release vessel led to virtually higher melt mass and must not be taken into account. After detachment of the melt from the inlet tube due to shrinking, the weight balance showed again about 128 kg, which is the weight measured after the test. The flow from the release vessel to the test section through a tube of 1300 mm length and 30 mm diameter was observed to be nearly constant 18.3 kg/s or 2.3 l/s, considering a melt density of 8 $*10^3$ kg/m^3.

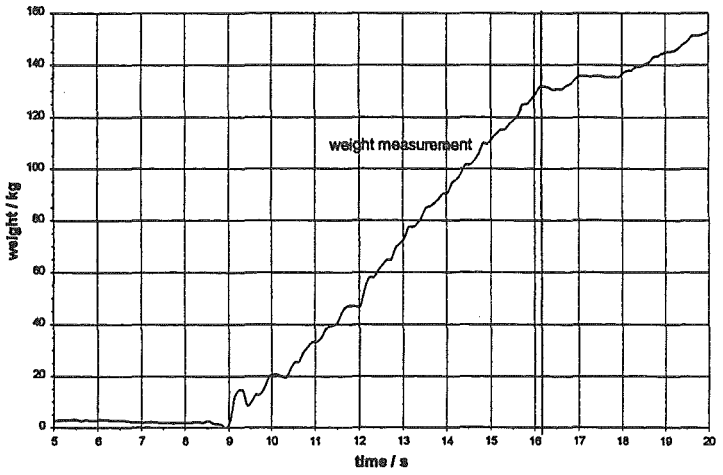

Fig. 11: weight balance at the initial phase

The spreading velocities of the leading edge of the melt were determined mainly by the video and infrared camera images. They were compared with the thermocouples located in the spreading compartment. Not taking into account the first melt splash, the first spreading process at 2 s had a velocity of 25 cm/s. The second current at 4.5 s resulted in the same spreading velocity of 25 cm/s. The melt flowed up to 75 cm which was the final spreading stage. The overall spreading velocity could be determined to about 13 cm/s. The observed spreading behaviour in this experiment was clearly two-dimensional. No homogeneous spreading over the whole channel width was observed and the left and right half of the melt behave differently. Therefore the presented results reflect only the observations at the melt front. This could also be seen by the differences observed in the thermocouple measurements. The melt tongues formed at the end of spreading were not taken into account to determine the spreading velocity, because the amount of melt was too small and the formation was very irregular.

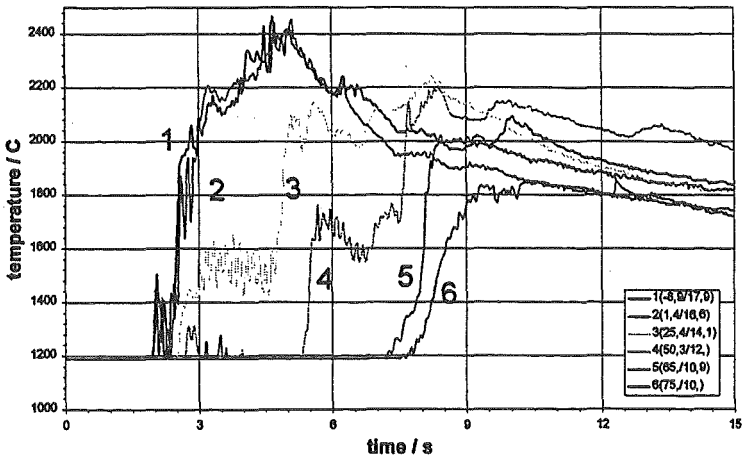

Fig. 12: Melt surface temperatures at different locations

The maximum temperature that was observed in the collecting device by the infrared camera was 2555 °C, see the surface temperatures measured by the infrared camera (Figure 12). Curve 1 and 2 cannot show these temperatures, because only average values of a certain area are depicted. Curves 3 and 4 show even the crust formation and the break up of the crusts with a continuation of spreading.

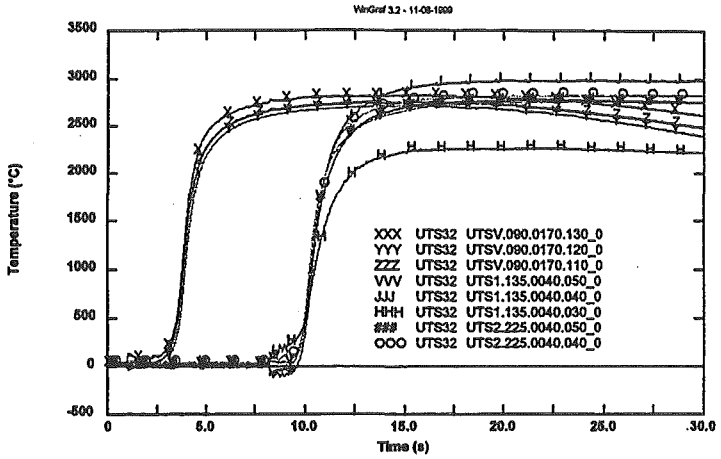

Fig. 13: UTS-temperatures in the collecting device

Two UTS sensors were installed in the collecting device additionally to the release vessel (Figure 13). The UTS sensors indicate the onset of melt release and the temperatures measured. The average measured temperatures were 3030 K in the release vessel and 3000 K in the collecting device, respectively. The melt was therefore about 90 K superheated at onset of spreading. A few seconds later, the temperature measured by the infrared camera on the surface of the melt was about 2850 K and crust formation started. In Fig. 14 the temperatures of the surface of the spreading plate are shown. They did not exceed 900 °C. At about 150–200 s water started to flow backwards due to plate distortion, which was confirmed by the displacement transducers. Some temperatures measured plane at the surface remained on 100 °C for more than 100 s. These thermocouples were located close to the final spreading length, where water still could flow to. Initially, the heat flux to the bottom was estimated to be about 0.5 MW/m^2. The long-term heat flux into the plate was about 0.2 MW/m^2. The comparison of the heat fluxes estimated for L-26S and L-32S shows that the water layer in the latest experiment lowers the

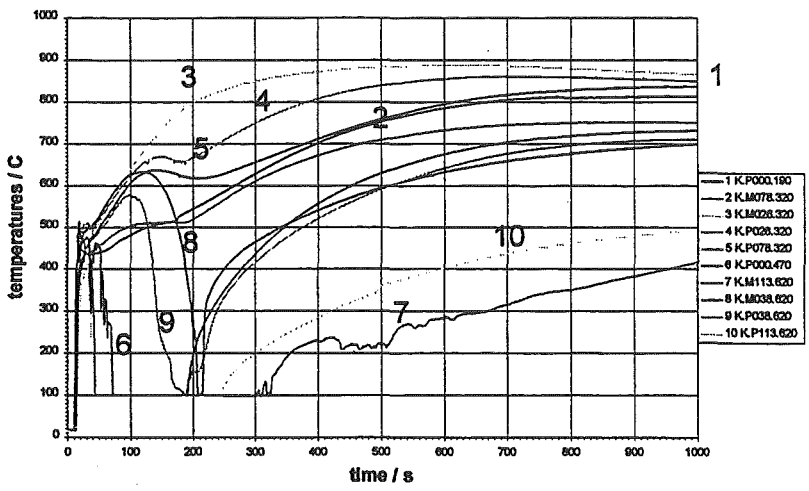

Fig. 14 Temperatures measured plane at the plate surface

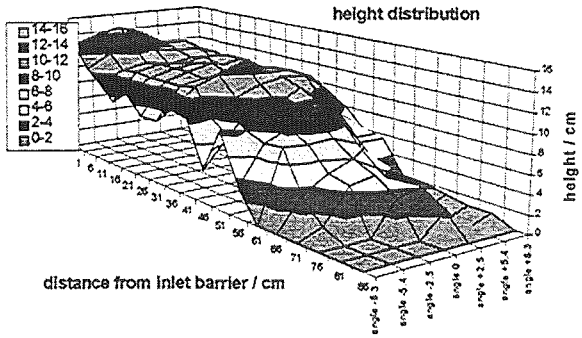

Fig. 15: Surface map of the solidified melt

temperatures in the spreading plate. But overall, the influence is small. The ambient temperatures measured in the SARCOFAGO test vessel did not exceed 350 °C, because the vessel was constantly flushed with Argon. The height of the solidified melt was determined for 9 different angle every 5 cm at the spreading plate, see Figure 15. The maximum height of 14.5 cm (including the barrier) was achieved at the inlet. The height at the final spreading length was in between 1 and 3 cm. The post test analysis showed that small caverns had been formed between the melt and the substrate close to the final spreading length. But no influence of the small water layer on this behaviour could be detected, because also in the dry spreading test small gaps were observed.

3. THEORETICAL CONSIDERATIONS

The performed numerical simulations of the FARO experiments led to pronounced discrepancies between theory and experimental results. These discrepancies may be due to experimental inaccuracy as well as to poor models in the codes and to a not sufficiently qualified data base of material properties. The following analysis of the FARO experiments will be used to identify the source of discrepancies between the THEMA (Spindler, 1995) and CORFLOW (Wittmaack, 1997) code results (DeCecco, 1999) and the experimental findings. This consideration is based on the fact that the spreading will be nearly isothermal during the first period of the melt release if the initial melt temperature is well above the immobilisation temperature. The transition time (Huppert, 1982) at which the inertial and viscous forces are equal is given by Foit (1999).

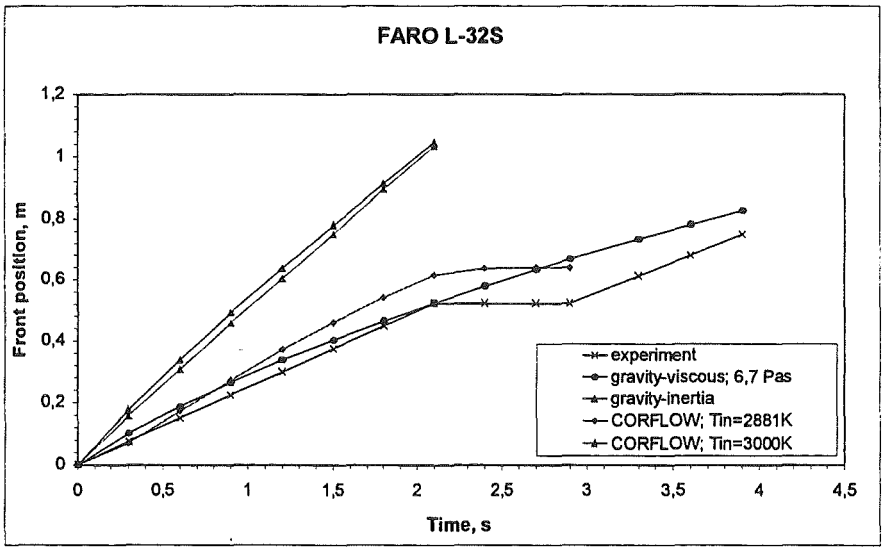

Fig. 16: FARO L-32S melt front progression

$$t_{tr;\varphi} = (2\pi/\varphi)^{1/2}\left(3^{1/2}/\pi^2\zeta_{\nu,2\pi}^4\right)\left[\dot{V}/g\,\nu(T_{in})\right]^{1/2}, \zeta_{\nu,2\pi} \approx 0.7\,, \qquad (1)$$

where $\dot{V}$ is the volume flux, φ the angle of the sector, g the gravity constant and $\nu(T_{in})$ the kinematic viscosity at the initial melt temperature. Eq. (1) yields $t_{tr} = 54\,s$ for the initial data of the experiment under consideration, i. e. the inertial forces govern the spreading and, consequently, the motion does not depend on viscosity. The front progression is described as

$$r_{f;\varphi} = \left(4g\dot{V}/\varphi\right)^{1/4}(t+t_0)^{3/4} - r_0\,, \qquad (2)$$

where $t_0 = r_0^{4/3}\left(4g\dot{V}/\varphi\right)^{-1/3}$ is the time at which the front reaches the dam at r_0. Fig. 16 shows a good agreement of the CORFLOW results for the initial temperature of 3000 K with the theoretical predictions (Eq. 2). Obviously, a variation of the melt viscosity in the temperature range between the solidus and liquidus temperature, i. e. a use of different correlations for the viscosity will not change the result of the code simulation. For the given superheat and the given flow rates, the heat losses due to radiation have no influence on the melt front progression calculated by CORFLOW. The first stop of the melt front observed in the experiment after only 2 s of motion indicates that the melt temperature cannot be much higher

than the immobilisation temperature and, consequently, the viscosity of the melt must be rather high. From this observation one can try to estimate the viscosity from the front progression of the gravity-viscous current:

$$r_{f;\varphi} = (\varphi / 2\pi)^{-3/8} \zeta_{\nu,2\pi} \left(\dot{V}^3 g / 3\nu\right)^{1/8} (t + t_0)^{1/2} - r_0 \qquad (3)$$

with the initial condition $r_{f;2\pi}\big|_{t=0} = 0$.

The time at which the front reaches the dam at r_0 is $t_0 = (\varphi / 2\pi)^{3/4} r_0^2 \zeta_{\nu,2\pi}^{-2} \left(g\dot{V}^3 / 3\nu\right)^{-1/4}$.

Using the experimental data for the melt front position at 2 s one obtains $\nu = 8 \cdot 10^{-4} \frac{m^2}{s}$ or $\mu = 6.7\ Pa \cdot s$. In this case the transition time is $t_{tr,\varphi} - t_0 = 0.6s$ and therefore the spreading is dominated by viscous forces. The front progression (Eq. 3) is also given in Fig. 16. Similar results are obtained for the former test FARO L-26S. Assuming that the GEMINI 2 results are correct, the temperature at which the melt reaches the estimated viscosity is about 2877 K if the Stedman correlation

$$\nu(T) = \nu(T_{liq}) \left(1 + 0.75 \frac{f_{sol}(T)}{f_{max} - f_{sol}(T)} \right)^2 \qquad (4)$$

is used where f_{sol} is the solid mass fraction and $f_{max} = 0.55$. The temperature for which the melt has a solid fraction of f_{max} is the immobilisation temperature. Because of the heat losses due to radiation, the melt temperature must be higher than 2877 K, estimated under isothermal conditions. CORFLOW calculations with an initial temperature of 2881 K (Fig. 16) show a good agreement with the observed melt front progression in the experiment up to the first stop. In CORFLOW, the melt front stops if almost all nodes at the free boundary reach the temperature at which the value of the viscosity becomes large and if the floating crust is connected to the basement at the melt front. For temperatures close to the immobilisation temperature, the CORFLOW results are very sensitive to a variation of the initial melt temperature. A temperature of 2881 K corresponds to a melt viscosity of 0.1 Pas (see Fig. 2), and is about 120 K lower than the average value given by the UTS. The uncertainty on the UTS measurements is normally about ±60 K.

In the opposite case, i. e. if the measured initial melt temperatures and the CORFLOW calculations are correct would mean that the freezing range of the melt and especially the immobilisation temperature are higher than that calculated by GEMINI2. The thin water layer on the substrate should not have a strong influence on the spreading process due to the thin thermal boundary layer resulting from the high Peclet-number ($>10^4$) of the melt. Consequently, the bulk temperature of the melt remains close to the initial temperature. On the other hand, questions came up whether the radiation heat losses from the upper surface would not lead to an early stop of the melt front and can give an explanation for the observed melt behaviour. However, calculations with CORFLOW with the given initial temperature of 3000 K show that even if the energy loss from the upper surface in the first 2 seconds is artificially increased by a factor 4, the melt front position at 2 s is reduced by about 10 cm only.

CONCLUSIONS

Two FARO spreading tests were performed in the 4th framework programme. The objective was to get information on the spreading behaviour of a high temperature prototypic corium melt and to investigate the spreading on a substrate covered with a shallow water layer. In the first experiment, a steel plate was used as a substrate for the spread melt, in the second ex-

periment, a shallow water layer was added on this steel substrate. This was a first of a kind experiment, where the release of a prototypic corium melt on a substrate covered with water was investigated. In both experiments, melt masses of about 150 kg were used to investigate spreading processes with flow rates of about 2 l/s. The data obtained complement those obtained with simulant materials and lower temperatures in other EU laboratories (see other papers at this workshop).

During the whole spreading process, several times crust break up and new formation of crusts could be observed. The whole spreading time lasted about the same time as the melt release. The average spreading velocity of the leading edge was about 0.1 m/s. Small tongues were formed at the leading edge in the final spreading stage. The formation of small caverns below the spread melt could be observed after solidification. Especially with the addition of a small water layer, the spreading was observed to be inhomogeneous in lateral direction. But no melt water interactions occurred. Only the formation of small pillows at the leading edge was observed. Over all the influence of this water layer was small. In both experiments the temperatures measured in the steel plate below the surface did not exceed 1400 K.

To understand the spreading process, different theoretical investigations were performed. If the temperature of the melt entering the spreading area in test L-26S and L-32S were above the liquidus temperature, the influence of the low viscosity of the melt would be negligible and the inertial forces would govern the spreading. Consequently, the motion would not depend on viscosity. Using the initial temperatures as measured in the experiments and the corresponding low viscosity, the calculated CORFLOW results are indeed in good agreement with the theoretical prediction for gravity-inertia spreading, but front progression and spreading length are considerably higher than the experimental data. To obtain a good agreement with these data the use of a viscosity in the solidus-liquidus range is required. Due to the fact that the bulk temperature of oxidic melts should remain close to the initial temperature during this short term spreading process, the observed spreading behaviour of both experiments can only be explained if a temperature in the solidus-liquidus range is assumed for the melt entering the spreading area, with the corresponding high viscosity of the melt. With this assumption, the observed spreading behaviour of these corium melts is in good agreement with the spreading behaviour of other oxidic melts and can be calculated by CORFLOW.

ACKNOWLEDGEMENTS

The tests have been co-financed by the European Commission shared cost action CSC-project in the frame of the Euratom Nuclear Safety Programme 1994-1998.

REFERENCES

Foit, J. J., 1999. To be published
Huppert, H. E., 1982. J. Fluid Mech. 121, 43.
Silverii, R., Magallon, D.: FARO LWR Programme, Test L-26S Data Report, Technical Note no. I.98.229, European Commission, Nov 1998
Spindler, B., Veteau, J.M., 1998. Status of the assessment of the spreading code THEMA against the CORINE experiment, SARJ, Tokio.
Stedman, S.J. et. al, 1990. J. Material Sci. 25, 1833.
Wittmaack, R., 1997, Nuclear Technology 119, 158.
DeCecco, L., 1999. Private communication.

SIMULATION OF CORE MELT SPREADING WITH LAVA: THEORETICAL BACKGROUND AND STATUS OF VALIDATION

H.-J. Allelein, A. Breest, C. Spengler
Gesellschaft für Anlagen- und Reaktorsicherheit (GRS) mbH
Postfach 10 16 50, 50667 Köln, Germany
spc@grs.de

ABSTRACT

The goal of this paper is to present the GRS R&D achievments and perspectives of its appraoch to simulate ex-vessel core melt spreading. The basic idea followed by GRS is the analogy of core melt spreading to volcanic lava flows. A fact first proposed by Robson (1967) and now widely accepted is that lava rheologically behaves as a Bingham fluid, which is characterized by yield stress and plastic viscosity. Recent experimental investigations by Epstein (1996) reveal that corium-concrete mixtures may be described as Bingham fluids. The GRS code LAVA is based on a successful lava flow model, but is adapted to prototypic corium and corium-simulation spreading. Furthermore some detailed physical models such as a thermal crust model on the free melt surface and a model for heat conduction into the substratum are added. Heat losses of the bulk, which is represented by one mean temperature, are now determined by radiation and by temperature profiles in the upper crust and in the substratum. In order to reduce the weak mesh dependence of the original algorithm, a random space method of cellular automata is integrated, which removes the mesh bias without increasing calculation time. LAVA is successfully validated against a lot of experiments using different materials spread. The validation process has shown that LAVA is a robust and fast running code to simulate corium-type spreading. LAVA provides all integral information of practical interest (spreading length, height of the melt after stabilization) and seems to be an appropriate tool for handling large core melt masses within a plant application

1 INTRODUCTION

Since a couple of years new design features for future reactors have been developed to ensure the integrity of these reactors even under severe accident conditions. Considering the case of a reactor pressure vessel melt-through measures to stabilize the core melt within the containment may be designed. One of these measures being part of the EPR concept includes the ex-vessel spreading of the core melt with subsequent water flooding and cooling. The basic idea followed by GRS is the analogy of core melt spreading to volcanic lava flows. One basic model assumption successfully used for the latter is the viscous thin-film-fluid theory.

2 THEORETICAL BACKGROUND

2.1 Hydrodynamics / Rheology

The subject of thin-film fluid flows, which is of strong interest in a broad variety of natural and industrial applications, has been extensively investigated up to now /1/. These investigations

have lead to numerous mathematical models and numerical simulations of the characteristic physical phenomena that can be observed in such types of flows.

One essential feature of a hot corium (or corium-like) melt which is spread onto a cold surface is the low height of the fluid film in relation to its spreading length. Gravitational forces act on the viscous material and drive the flow further before the cooling processes lead to a stabilization of the flow front. This phenomenon becomes important when the local volume fraction of solidified material increases up to a large amount so that the fluid properties are more those of a solid crust rather than those of a continuous solution of solid particles dispersed within a fluid of low viscosity.

Among the various applications in which thin-film fluid flows are important, the subject of volcanological lava-flows is very related to the problem introduced above. The most realistic methodology for numerical simulations of lava flows seems to be the method of Ishihara, which is based on Dragoni's downslope model for Bingham fluids /2, 3, 4/.

The basic idea of that theory is the assumption of 'plug'-regions in the flow domain at locations, where the shear-stress τ is smaller than the yield-stress τ_Y. Such a plug region is defined by a zero shear rate $\partial v_x/\partial z = 0$ and thus has a common velocity v_P. Since the force of gravity, which drives the flow further, causes larger shear stresses in fluid layers near the base of the flow, these plug-regions can only exist near the top surface of the fluid film. Considering a onedimensional fluid flow in direction of the x-axis the approximated velocity profile $v_x(z)$ across the fluid height and directed parallel to the main direction of flow (x-axis) has to satisfy the hydrodynamic boundary condition of zero velocity at the surface of the sbustratum:

$$v_x\big|_{z=0} = 0\,. \qquad \text{Eq. 1}$$

If the local stress at a location (x,y) on the surface of the substratum $(z=0)$, which is at the same time the maximum stress across the fluid layer, is lower than the yield stress τ_Y, then there is no flow possible within the local control volume because Eq. 1 leads to $v_P = 0$. Fluid flow is possible if $\tau(z=0) > \tau_Y$. This flow is driven by the force of gravity leading to pressure gradients caused by the curvature of the fluid layer (given by the gradient ∇H of the fluid height $H(x,y)$) and the inclination α of the spreading plane.

With the assumption that the transient character of the hydrodynamic problem can be approximated by a quasistationary approach, the stationary Navier-Stokes equation for conservation of momentum can be written as

$$\rho v_x \frac{\partial v_x}{\partial x} = -\frac{\partial p}{\partial x} + \eta\left(\frac{\partial^2 v_x}{\partial x^2} + \frac{\partial^2 v_x}{\partial z^2}\right) + \rho g \sin\alpha\,. \qquad \text{Eq. 2}$$

In case of sufficiently small fluid velocities the pressure gradient can be expressed as a function of fluid height H

$$p(z) = p_0 + \rho g(H - z)\cos\alpha\,, \qquad \text{Eq. 3}$$

leading to

$$\frac{\partial p}{\partial x} = \frac{\partial H}{\partial x}\rho g \cos\alpha\,. \qquad \text{Eq. 4}$$

If the geometry of the flow area is divided into cells of mesh size a which is chosen very small in comparison to the lengthscale for critical variations in the flow characteristic, so that

the change of the velocity component from one mesh to its neighbours in direction of the flow can be neglected $\left(\partial v_x/\partial x \approx 0, \quad \partial^2 v_x/\partial x^2 \approx 0\right)$, Eq. 2 simplifies to

$$\eta \frac{\partial^2 v_x}{\partial z^2} + \rho g\left(\sin\alpha - \frac{\partial H}{\partial x}\cos\alpha\right) = 0 \qquad \text{Eq. 5}$$

which can be integrated with respect to z along the interval $0 \le z \le H - H_c$. The neglect of the variation of velocity v_x along the x-axis (main direction of flow) is a reasonable assumption for the major part of fluid volume near the centre of the stream /5/. Only at locations near the mass source and the leading edge of the flow strong gradients $\partial v_x/\partial x$ are present for which Eq. 5 is not valid. However, the error made by using Eq. 5 is small particularly in case of low Reynolds number flows which are dominated by viscous forces rather than inertial forces. Viscous forces will become larger than inertial forces in these types of flows after a distinct period of time /1/ and this characteristic time interval shrinks if the viscosity increases quickly due to cooling of the material.

The value $z=H-H_C$ represents the z-coordinate, where the stress equals the yield stress: $\tau(z=H-H_C)=\tau_Y$, see Figure 1b. Within this interval, the flow can be characterized by a shear-rate independent plastic viscosity η according to Eq. 5. For $z>H-H_C$ only plug flow with constant velocity v_P is present. So the value of H_C is the critical height of the fluid column (depending upon local curvature of the substratum and the free fluid surface, respectively) up to which flow within a mesh is not possible due to the empircal Bingham model.

The integral of Eq. 5 is obtained by evaluation of three boundary conditions:

$$v_x\big|_{z=0} = 0 \qquad \tau_{xz}\big|_{z=H-H_c} = \tau_Y \qquad \tau_{xz}\big|_{z=H} = 0 \qquad \text{Eq. 6.a-6.c}$$

In Eq. 6 the stress τ is defined according to the Bingham model (onedimensional case, see Figure 1a):

$$\tau = \tau_Y + \eta \frac{dv_x}{dz}. \qquad \text{Eq. 7}$$

This gives the critical height H_c as function of the gradient of fluid height ∇H and the angle α

$$H_C = \frac{\tau_Y}{\rho g\left(\sin\alpha - \frac{\partial H}{\partial x}\cos\alpha\right)}. \qquad \text{Eq. 8}$$

as well as the velocity profile along the z-axis $v_x(z)$ (Figure 1b) which can be integrated over the fluid height H to calculate the mass flux $\dot{m}$ per mesh width a between two adjacent meshes:

$$\dot{m} = \rho \int_0^H v(z)dz = \begin{cases} \dfrac{\rho\sigma_Y H_C^2}{3\eta}\left(\left(\dfrac{H}{H_C}\right)^3 - \dfrac{3}{2}\left(\dfrac{H}{H_C}\right)^2 + \dfrac{1}{2}\right)\cos\alpha & \text{for } H > H_C \\ 0 & \text{for } H \le H_C \end{cases} \qquad \text{Eq. 9}$$

In the presented system the equation for continuity can be written as

$$\frac{\partial H}{\partial t} + \frac{\partial}{\partial x}\left(\int_0^H v\,(z)\,dz\right) = 0 \qquad \text{Eq. 10}$$

and thus a mass flux from one mesh to its adjacent meshes due to Eq. 9 causes updates of the local fluid heights according to Eq. 10. The updating scheme is an explicit one, the new values of variable H at time t_{n+1} are obtained from the old values at time t_n.

In order to achieve realistic simulations of fluid flows on a twodimensional surface, a cellular automaton method is applied /4/. The basic idea of that method is that the neighbouring meshes in direction of the diagonals of the cartesian coordinate system *(x,y)* are in the average more far away from the central mesh as the ones in direction of the main axes. For that reason, mass flux to meshes in direction of the main axes is more strongly weighted than mass flux in direction of the diagonals. This weighting is achieved by a stochastic selection of a mesh's neighbours to which the mass flux is being calculated. The method leads to calculation results that show isotropic spreading of the melt on an isotropic surface and no longer a strong bias towards the main axes of the system which was observed using the original algorithm of Ishihara /3/. However, the obtained approximation is not a real twodimensional solution of the Navier-Stokes equations and thus does not take the internal relationship between the velocities v_x and v_y into account. Rotating flows etc. can not be modelled, but the method consideres anisotropy (inclination, obstacles etc.) of the 2D-geometry which is assumed to have the major influence on the flow characteristic. A further benefit of this method is that it still maintains the efficiency of the basic algorithm.

For calculations of corium spreading tests temperature dependent viscosity and yield stress data are needed. Temperature dependent viscosity data are based on open literature and experiments like Rasplav /6/. The only available experimental yield stress data are found in Epstein's interpretation /7/ of Roche's measurements for a corium concrete mixture with 27.5 wt.-% SiO_2. The temperature dependence of the yield stress is approximated by an Arrhenius fit with an upper limit of 60 Pa. This fit is the basis for the adaption to other materials. Due to the lack of experimental data for other SiO_2-contents its influence on the yield stress is assumed to be linear.

2.2 Thermodynamics

Three basic heat transfer mechanisms are modelled by *LAVA*: heat transfer by mass transfer, radiation from the free surface and conduction into the substratum. The calculation of radiation and conduction is done seperately from the hydrodynamic problem and is based on empircal heat transfer correlations. The flow properties (η, τ_Y) are constant within the fluid column at location *(x,y)*, so a mean temperature *T(x,y)* has to be calculated.

Heat losses at the free surface are given by

$$\dot{q}_{rad} = \varepsilon\sigma\left(T_S^4 - T_\infty^4\right). \qquad \text{Eq. 11}$$

The surface temperature T_s can be much smaller than the maximal temperature T_{max} in the bulk of the fluid in case of crust growth at the free surface. The temperature difference is then expected to be of size $\approx 300K$ and this phenomenon requires a precise model for crust growth at the free surface which has been added to *LAVA*.

Crust growth is possible, if the surface temperature of the fluid T_s falls below the interface temperature T_i between the liquid melt and the solid crust. In this model T_i is defined by the 'softening' temperature' of the system. The softening temperature is the temperature below which convection is weak or non-existent /8/. Hence, for temperatures below the softening temperature the viscosity increases enourmously due to solidification effects and only heat conduction is effective. T_i is near T_{liq} and as a simple approach for T_i the expression

$$T_i \approx T_{liq} + \frac{3}{4}\left(T_{liq} - T_{sol}\right) \qquad \text{Eq. 12}$$

is used based on findings in /9, 10/. When a crust begins to grow, a curved temperature profile within the crust is formed because of transient heat conduction. The onedimensional temperature profile is approximated by

$$T(z,t) = T_i + (T_s - T_i)\left[\chi\left(1-\frac{z}{\delta}\right) + (1-\chi)\left(1-\frac{z}{\delta}\right)^2\right] \qquad \text{Eq. 13}$$

with $T(0,t) = T_s$ and $T(\delta,t) = T_i$. The symbol δ represents the thickness of the crust and χ is a time dependent coefficient describing the shape of the profile. Applying the Heat Balance Integral technique (HBI, /11/) and considering the Stefan boundary condition at the interface between liquid and solid the functions $T(z,t)$ and the crust thickness $\delta(t)$ are determined numerically. The convective heat transfer from the bulk of the liquid melt to the interface is expressed by a standard Nusselt correlation for convective heat transfer from a liquid to a horizontal surface /12/:

$$Nu = 0.14(Gr \cdot Pr)^{1/3} \qquad \text{Eq. 14}$$

Heat conduction in the substratum is modelled by an explicit solver for onedimensional heat conduction below each LAVA surface mesh. The convective heat flux from the moving liquid to the surface of the substratum is approximated by a standard Nusselt correlation for a hot liquid flowing on a horizontal surface /12/:

$$Nu = 0.664\sqrt{Re}Pr^{1/3} \qquad \text{Eq. 15}$$

3 Validation Calculations

3.1 Overview

LAVA is successfully validated against a lot of experiments using different materials spread (see table below).

material spread	1D spreading	2D spreading
volcanic lava	-	Ishihara reference - case A
steel / iron	COMAS - 6	TEPCO - 206
oxidic phase of thermite	KATS - 7 KATS - 14 (*)	KATS - 15 (*) KATS - 17 (*)
corium	COMAS - 5A (EU benchmark)	COMAS - EU4
corium + SiO_2	COMAS - EU2B COMAS - EU3A (*)	VULCANO VE-U1

(*) blindly pre-calculated with LAVA

A selection of validation results is shown in the following.

3.2 COMAS EU-2b

In this large-scale experiment a total mass of approximately 630 kg oxidic corium melt (31 wt.-% UO_2, 24 wt.-% ZrO_2, 19 wt.-% FeO, 15 wt.-% SiO_2, 6 wt.-% Cr_2O_3, 5 wt.-% Al_2O_3 and 1 wt.-% CaO) was spread with an initial temperature of 2090 °C into three spreading compartments (each channel is 0.4 m wide and 6.3 m long) of different substratum material types.

The data describing the exact boundary conditions were taken from /13/ and have been completed by latest and preliminary results of additional post-test analyses. The post-test calculation of the spreading on concrete performed with LAVA considers a transient mass inflow profile resulting from the analysis of the CCD camera measurements and a linear decrease of the initial temperature at the inlet which has been deduced from the experiment by evaluations of the IR-measurements.

The results of the (preliminary) post-test calculation with LAVA show that the transient character of the leading edge propagation is approximated very closely whereas the final spreading length is underestimated by 0.4 m ($\approx -8\,\%$), see Figure 2b. This might be due to several uncertainties concerning the actual melt mass on the visible section of the spreading compartments and a calculation with more exact data will have to be carried out in the future.

3.3 COMAS EU-4

The post-test calculation for the melt spreading experiment COMAS EU-4 is definitely a hard task for a numerical simulation since the experiment is characterized by a large amount of prototypic corium mass (1920 kg, composition: 29 wt.-% UO_2, 12 wt.-% ZrO_2, 18 wt.-% FeO, 2 wt.-% Cr_2O_3 and 39 wt.-% Fe) spread in a two-dimensional, large-scale geometry of about 15 m^2 ($\cong 1/6$ EPR spreading area).

In the calculation (Figure 3a-d) as well as in the experiment the melt front stops flowing in the direction of its initial momentum for a short time, in order to spread in lateral directions, before the spreading process is being continued in forward direction. Figure 4 shows the partial melt spreading on the original spreading area as a function of time calculated by LAVA. For the experiment a partial spreading about 70 % was estimated /14/. This value is in good agreement with the nearly 60 % percent given by the LAVA results.

3.4 KATS 17

A blind pre-test calculation of KATS 17 assumed 150 kg oxidic melt mass (85 wt.-% Al_2O_3, 10 wt.-% SiO_2 and 5 wt.-% FeO) to be spread with an initial temperature of about 1950 °C and predicted a maximum spreading length along the x-axis of 2.25 m. The (preliminary) post-test analysis of the experiment reports an actual temperature level of 2150 °C and a total oxidic melt mass of about 121 kg. For that reason the results of the pre-test calculation cannot be directly compared to the experimental results (Figure 5). However, the LAVA post-test calculation with the actual boundary conditions applied shows excellent agreement concerning the amount of spreading area being covered by the melt (Figure 7). The LAVA-calculation predicts symmetrical melt contours at the beginning of the spreading process (Figure 6), whereas the experiment showed a clear influence of inertia causing a bias of spread melt towards the direction of the initial momentum (Figure 5). This discrepancy is attributed to the neglect of inertial terms in the momentum conservation equation but has only marginal influence on the time-course of the melt-covered area (Figure 7).

3.5 VULCANO VE-U1

The data for the VULCANO test VE-U1 have been collected from references /15,16/. In this twodimensional spreading experiment a corium melt mass of 47 kg (45 wt.-% UO_2, 20 wt.-% ZrO_2, 20 wt.-% SiO_2, 13 wt.-% Fe_3O_4, 2 wt.-% Fe_2O_3) with an initial inflow temperature of 2100 K was spread at an average mass flow rate of 2.5 kg/s into a twodimensional test section formed as a 19° angular sector with ZrO_2 substratum material. The mass inflow rate was approximated by a parabolic profile (Figure 8a). The LAVA results demonstrate that with these boundary conditions nearly 100 % of the spreading compartment is finally covered with melt (Figure 8b, Figure 9).

4 Conclusions

All physical models considered today to be necessary for the reliable simulation of corium spreading are incorporated in LAVA. The validation results gained up to now are very encouraging. Blindly precalculated results for three KATS experiments and COMAS EU-3a confirm this. The validation process has shown that LAVA is a robust and fast running code to simulate corium-type spreading. LAVA provides the integral information of practical interest (spreading length, height of the melt after stabilization) and seems to be an appropriate tool for handling large core melt masses within a plant application.

For further validation it is necessary that the already performed experiments are analyzed self-consistently and data prepared in this way should be free available to the code users. Few future experiments indispensably need an improved instrumentation taking into account all the knowledge about experimental spreading available up to now.

5 Literature

/1/ H.E. Huppert (1982): *The propagation of two-dimensional and axisymmetric viscous gravity currents over a rigid horizontal surface. In J. Fluid Mechanics, Vol. 121, pp. 43-58.*

/2/ M. Dragoni, M. Bonafede, E. Boschi (1986): *Downslope flow models of a Bingham liquid: implications for lava flows.* In *J. Volcanology Geotherm. Res.,* Vol. 30 pp. 305-325.

/3/ K. Ishihara, M. Iguchi, K. Kamo (1990): *Numerical simulation of lava flows on some volcanoes in Japan.* In *J.H. Fink: Lava flows and domes,* Springer Berlin, pp. 174-207.

/4/ H. Miyamoto, S. Sasaki (1997): *Simulating lava flows by an improved cellular automata method.* In *Computers & Geosciences*, Vol. 23, Nr. 3, pp. 283-292.

/5/ C. Spengler, A.K. Rastogi, A. Breest and H.-J. Allelein (1999*): Ex-vessel corium melt spreading and stabilzation - physical and numerical modelling approaches.* In *Kerntechnische Gesellschaft: Annual Meeting on Nuclear Technology 1999*, Karlsruhe.

/6/ S.S. Abalin et al. (1996): *Kinematic viscosity measurement of C-100 and C-22.* Rasplav Project RP-TR-18, Russian Research Center, "Kurchatov Institute", OECD RASPLAV Project.

/7/ M. Epstein (1996): *A Bingham plastic interpretation of the ACE viscosity data.* Submitted to Electric Power Research Institute, Palo Alto, California, FAI/96-92.

/8/ G.W. Bergantz (1992): *Conjugate solidification and melting in multicomponent open and closed systems.* In *Int J. Heat Mass Transfer*, Vol. 35, No. 2, pp. 533-543.

/9/ Russian Research Center "Kurchatov Institute" (1996): *Latest findings from the OECD RASPLAV Project.* Rasplav Project RP-TR-24, OECD RASPLAV Project.

/10/ K.S. Forcey et al. (1997): *Status report on viscosities of corium mixtures.* European Commision, INV-CIT(97)-P001.

/11/ T.R. Goodman (1958): *The heat-balance integral and its application to problems involving a change of phase.* In *Transactions of the ASME*, Vol. 80, pp. 335-342.

/12/ H.D. Baehr and K. Stephan (1996): *Wärme- und Stoffübertragung.* Springer.

/13/ W. Koller (1999): *1D-spreading test COMAS EU-2b.* EXV COMAS(99)-D23

/14/ M. Sappok and W. Steinwarz (1997*): Large-scale experiments on ex-vessel core melt behaviour.* In *ARS* 1997, Florida.

/15/ G. Cognet et al. (1998): *The VULCANO spreading programme.* SARJ-98 Workshop on Severe Accident Research, Tokyo, Japan.

/16/ R. Wittmaack (1998): *Post-test calculation of the VULCANO VE-U1 test with the CORFLOW computer code.* Siemens Work Report EXV-CSC(99)-D030. KWU NA-T/1998/E098.

/17/ I. Kelmes (1997): Computersimulation des Ausbreitungsverhaltens einer Kernschmelze im Sicherheitsbehölter eines Leichtwasserreaktors. Diplomarbeit, Uni Köln.

/18/ G. R. Robson (1967): *Thickness of Etnean Lavas.* In *Nature*, 216, pp. 251-252.

6 Acknowledgements

Development and validation of the LAVA code are performed within the framework of the R&D-project RS 1042 financed by the BMBF / BMWi. The development of the LAVA code is founded on the the first steps done in this direction by I. Kelmes /18/.

Many thanks of the other co-authors are due to C. Spengler for his thoughtful and careful preparation of this paper.

BMBF: Federal Ministry for Education, Science Research and Technology
BMWi: Federal Ministry of Economics and Technology

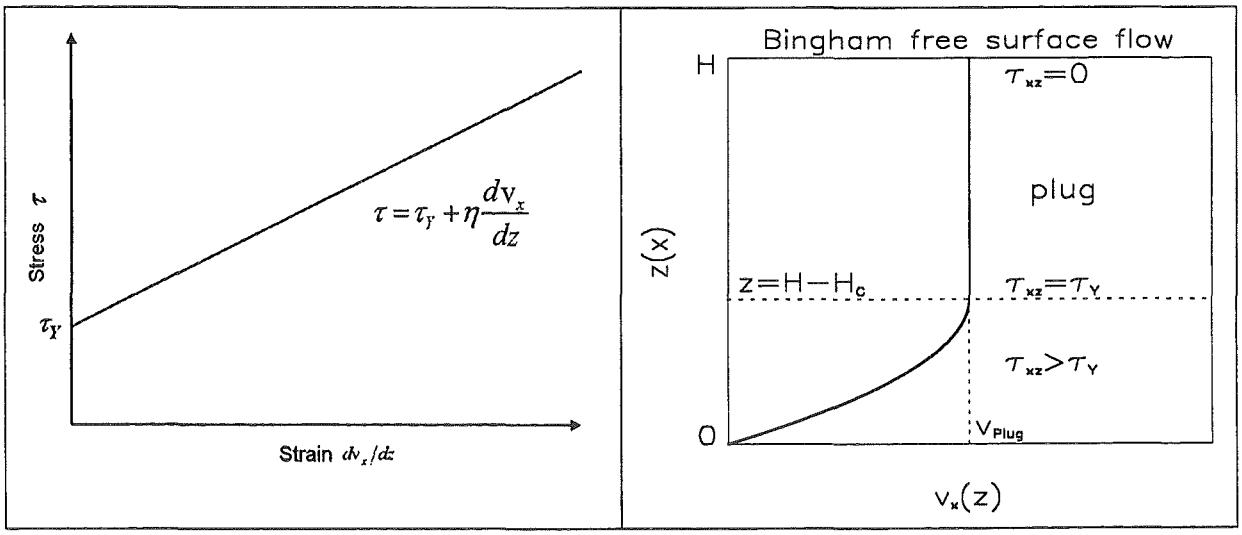

Figure 1a,1b: Stress-strain relationship of an ideal Bingham plastic and velocity profile in a free surface flow

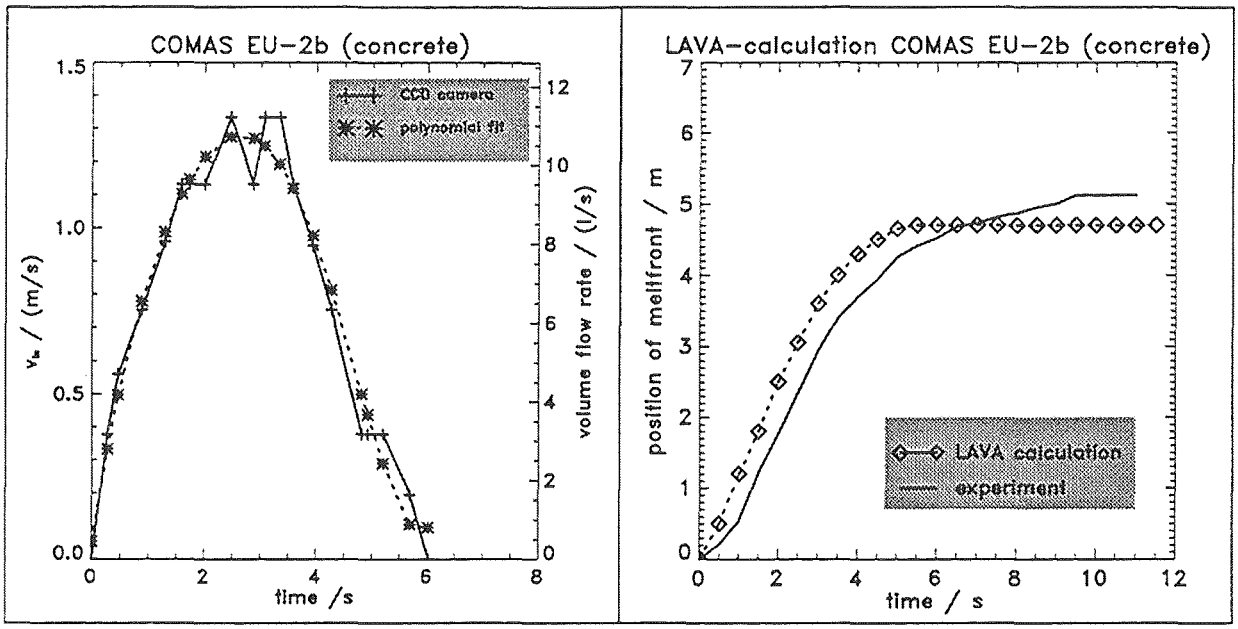

Figure 2 a-b: Volume inflow boundary conditions of COMAS EU-2b and the melt front propagation for spreading on concrete as calculated by *LAVA*

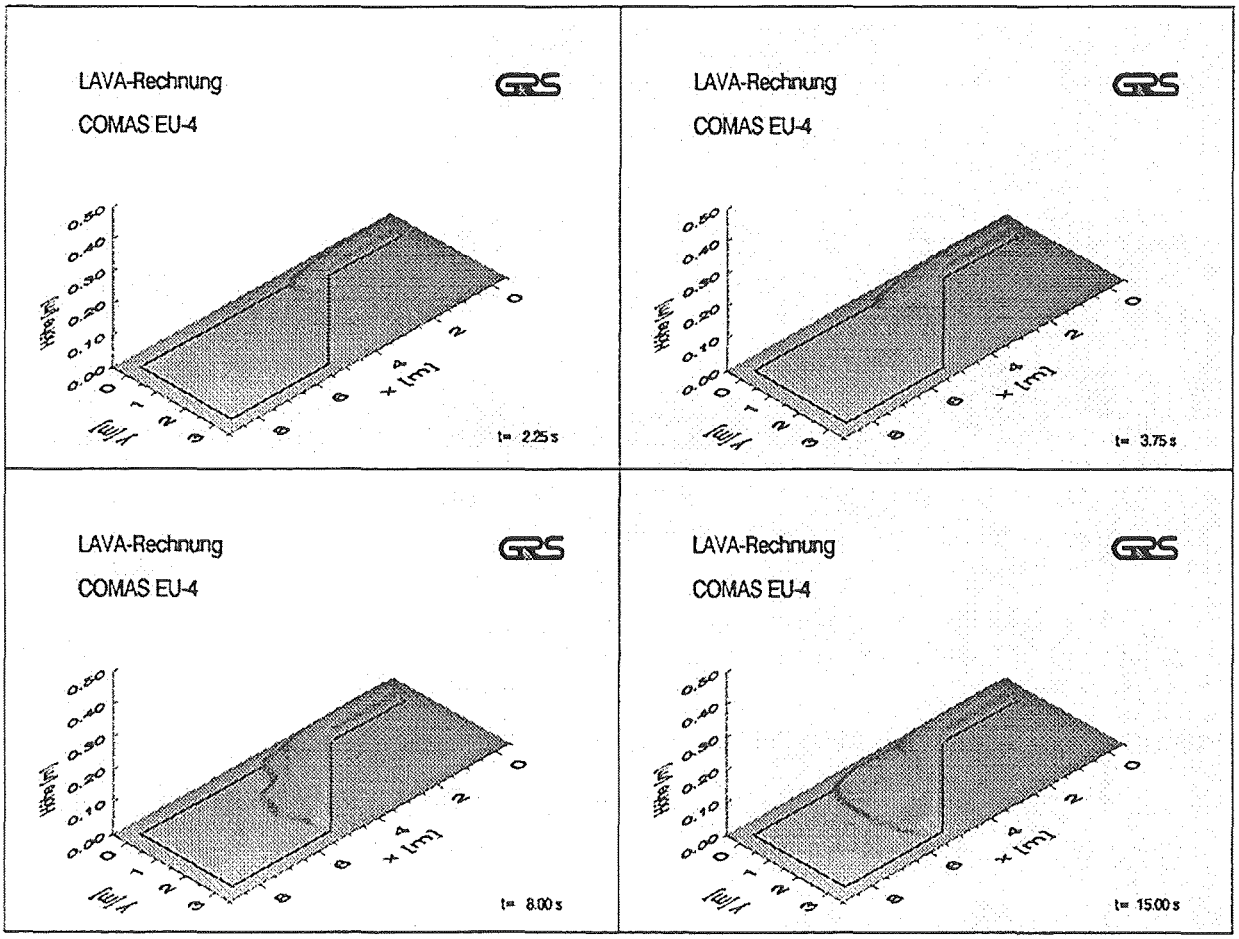

Figure 3a-d: Propagation of melt volume as calculated by LAVA for the COMAS EU-4 test.

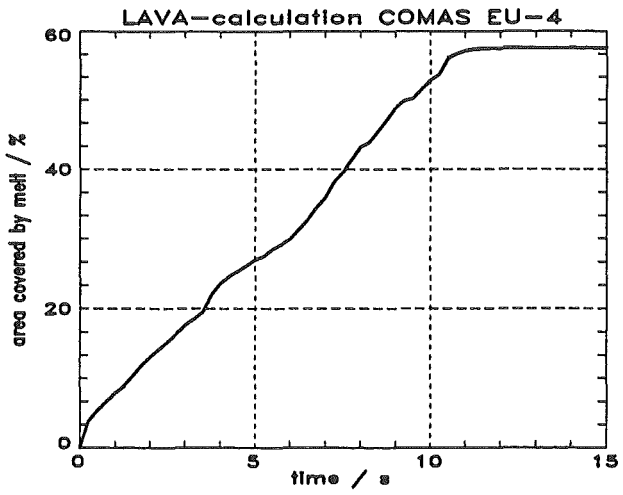

Figure 4: Part of melt-covered area versus time in the post-test calculation of COMAS EU-4

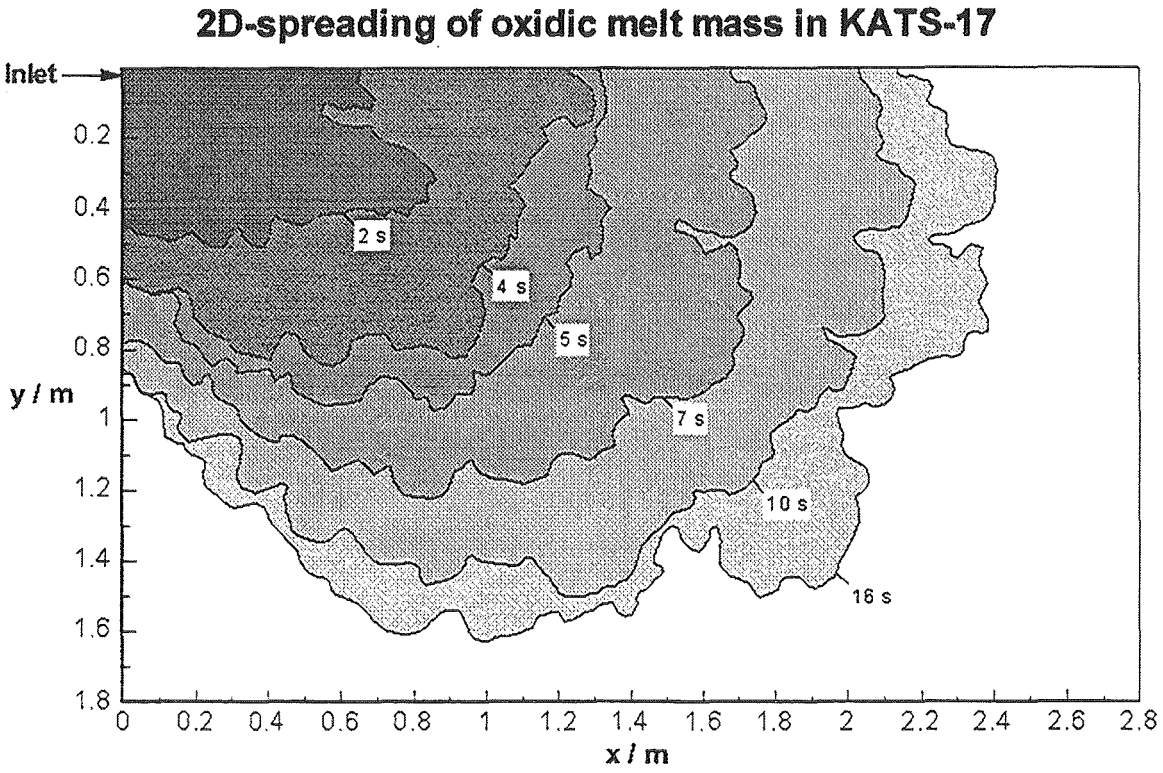

Figure 5: Propagation of oxidic melt in KATS-17 (experimental results).

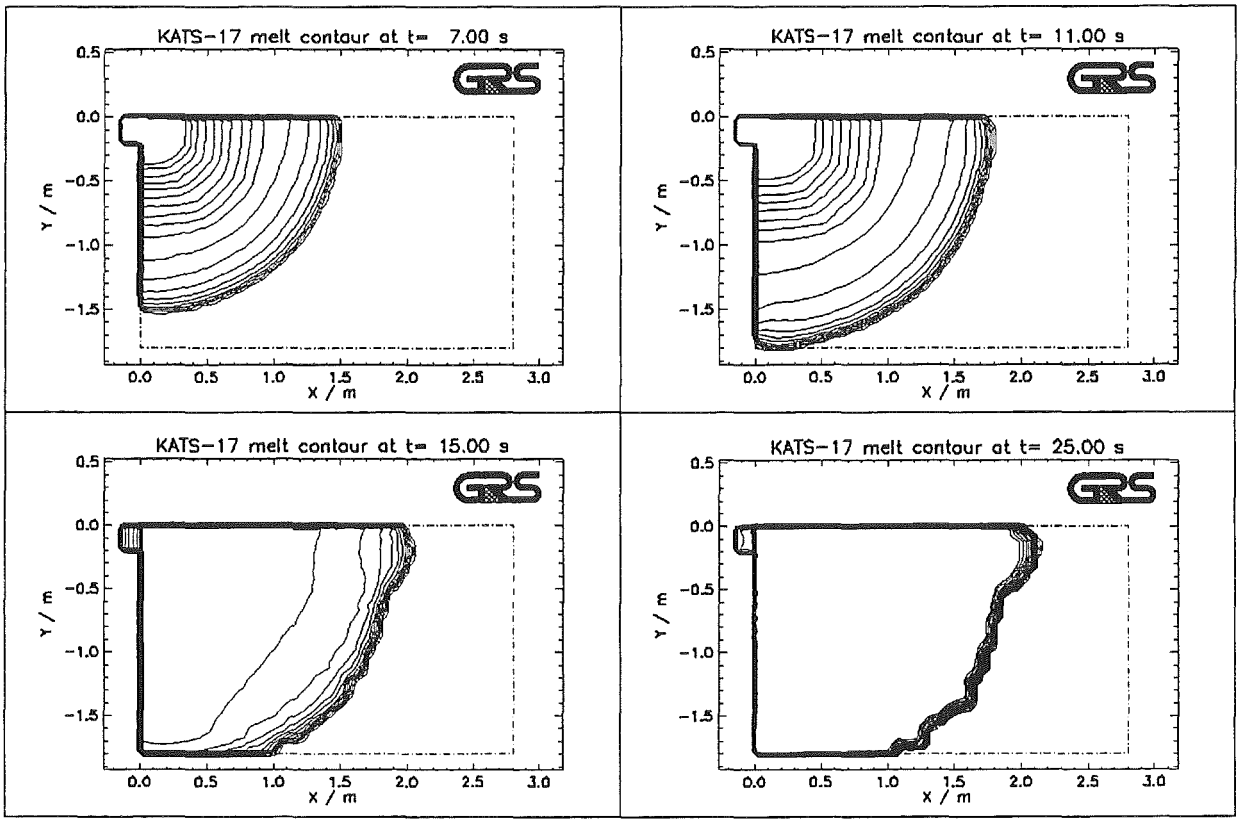

Figure 6a-d: Transient melt height contours as calculated by LAVA for KATS-17

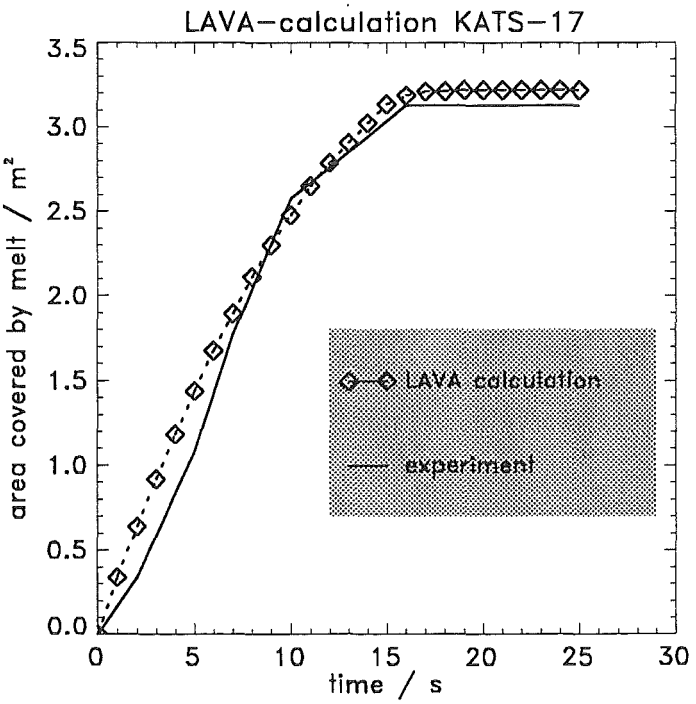

Figure 7: Melt-covered area versus time in KATS-17

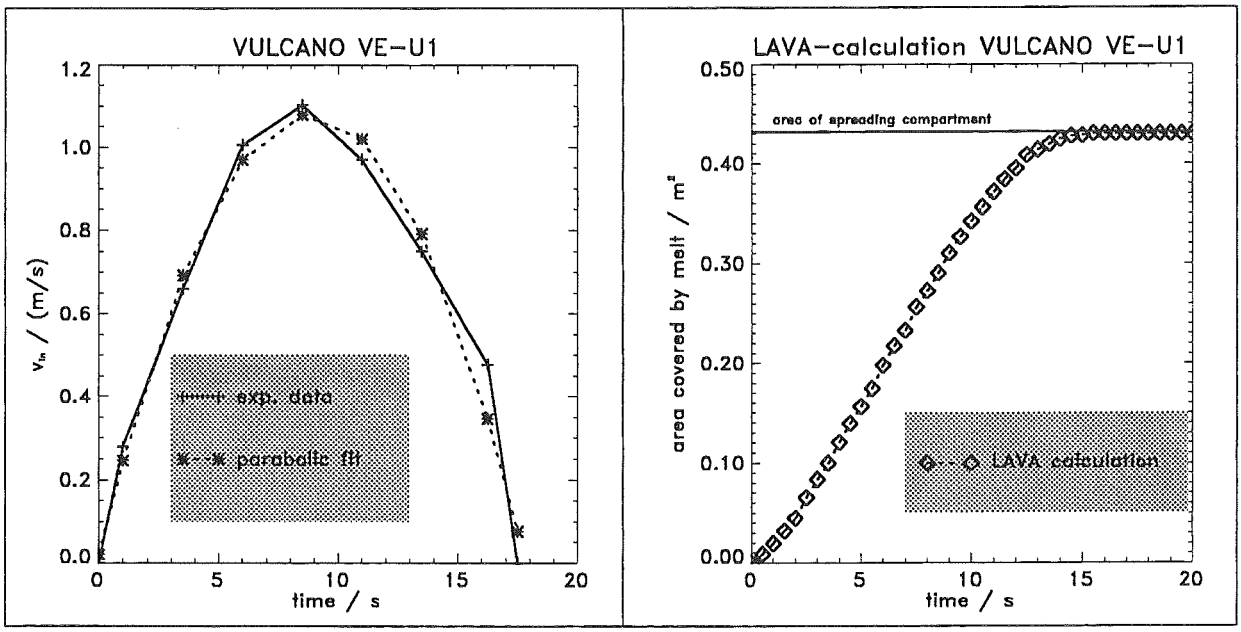

Figure 8a,b: Volume inflow boundary conditions of VULCANO VE-U1 and the melt covered area as calculated by LAVA.

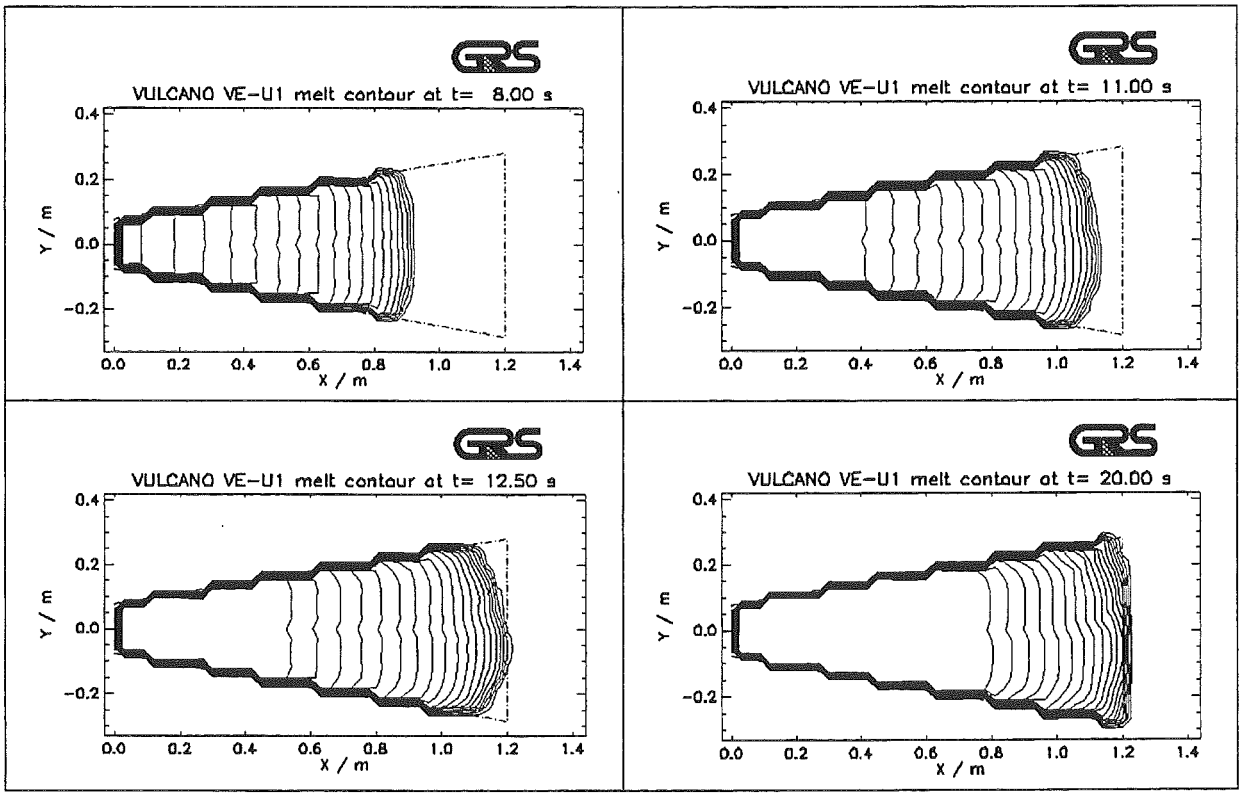

Figure 9a-d: Transient melt height contours as calculated by LAVA for VULCANO VE-U1.

OECD Workshop on Ex-Vessel Debris Coolability
Karlsruhe, Germany, 15-18 November 1999

Organised in collaboration with
Forschungszentrum Karlsruhe (FZK) GmbH

Numerical simulation of corium spreading in the EPR with CORFLOW

Ralf Wittmaack
Siemens AG, KWU NA-T
Box 3220, D-91050 Erlangen, Germany
Ralf.Wittmaack@erl11.siemens.de

Abstract

To reduce the radiological consequences of a postulated severe accident, the design of the European Pressurized Reactor (EPR) includes measures to avoid basemat penetration in case of core melt-down. The corresponding retention scheme includes a temporary retention of the debris in the reactor pit followed by the spreading of the accumulated molten corium in one event with subsequent flooding and cooling.

To contribute to the verification of this concept, numerical simulations of the spreading process with the CORFLOW code were performed. They are based on an extensive verification and validation effort summarized in the first part of this paper. It demonstrates that CORFLOW has successfully been applied to several flow, heat transfer and phase transition problems of water, glycerol, cerrotru- (low melting Bi-Sn alloy), thermite- and corium-melts.

The second part of the paper deals with calculations performed for the EPR geometry. As a result of the intermediate melt retention in the reactor pit, the conditions for melt spreading have become widely independent of the uncertainties of in-vessel melt behaviour and RPV failure modes. However, due to the complexity of the physical processes during the erosion of the sacrificial material, there remains some uncertainty related to the layering of the different corium constituents in the pit at the time of gate failure and spreading.

These uncertainties are taken into account by simulated variations of the
- release sequence of the corium fractions (metallic and oxidic corium as well as slag),
- material properties of the oxidic corium,
- corium initial temperature and
- opening cross section area of the gate between pit and channel to the spreading compartment.

From the results of earlier CORFLOW analyses for the three-dimensional COMAS EU-4 spreading test with prototypic, initially layered oxide and metal phases, it is deduced that the EPR spreading process can be represented with reasonable accuracy by the single component fluid modelling of an emulsion, with the metal phase mixed into the oxide. For this reference spreading case variations of all major assumptions were investigated.

In addition, also the subsequent spreading of the metallic and oxidic phases were analysed. Among these, the spreading of a pure oxidic corium (without slag-addition) is considered to be the most conservative case. It was found that, in all analysed spreading cases, the corium will spread into an almost homogeneous layer thickness within less than one minute.

As the shortcomings of the modelling, which are discussed in the paper, are not fundamental and taking into account the conservatism of most of the assumptions, these results are considered to verify the proper function of the spreading concept, which is, to provide a sufficiently equal final distribution of corium in the spreading room, under all considered initial and boundary conditions.

1 Introduction

As this paper presents a variety of CORFLOW calculational results, contributions to the code verification and validation as well as reactor applications, we briefly describe the physical models of the code.

CORFLOW (Wittmaack 1998b) is designed for the simulation of free surface flow with heat transfer and phase transitions. It is applicable to corium in liquid or solid state as well as to other fluids and solids. The physical models simulate the free surface flow of a single-component, incompressible, homogeneous fluid in a three-dimensional geometry. The fluid may be covered by air or an isothermal ideal fluid. In addition, several structural materials are considered as hydrodynamic obstacles or thermodynamic heat structures. Molten structural material may be treated as fluid. The fluid is assumed to have Newtonian or not explicitly time-dependent non-Newtonian rheology, e. g. Bingham plastic, pseudo plastic or dilatant.

The fluid dynamics are described by the continuity- and the momentum-equation with the Boussinesq-approximation. Papanastasiou's (1987) rheological equation is employed to simulate Bingham fluids. Volume expansion is neglected, turbulence models are not used. A free surface pressure boundary condition includes viscous stress and surface tension. The free surface is represented by a height function. Its dynamics is computed by the free surface kinematic boundary condition and integration of the continuity equation.

For temperature dependent material properties, the hydrodynamics is coupled to the thermodynamics and phase transition phenomena. For this reason, internal heat transfer and heat generation as well as heat transfer to the surroundings are modelled. At the rigid boundaries, conduction heat transfer is considered, whereas convection and radiant heat transfer are modelled at the free surface. A discrete phase transition model is available to simulate, e. g., solidification and melting of the fluid and phase transitions of the structural materials. Complex rheology and mechanical stability of crusts are not considered. A two-phase flow model describes the mushy region of the phase diagram, where the solid phase is assumed to be dispersed in the liquid phase. Below liquidus temperature it leads to fluid immobilization caused by an increase of the mushy fluid viscosity.

2 CORFLOW verification by analytical solutions

For the verification of the ***hydrodynamic code models for ideal fluids***, the oscillation of ideal fluid in an U-tube is analysed as a system where the dynamics is influenced only by inertial and gravitational forces. The numerical solution is compared to the analytical solution (Wittmaack 1998b).

Analytical solutions for isothermal plane and cylindrical viscous gravity currents on plane, horizontal surfaces have been presented by Huppert (1982, 1986). These solutions are generalized by Sakimoto and Zuber (1995) as well as by Foit (1997) to non-isothermal conditions with constant bulk temperature (bulk freezing). Huppert's solutions are used to validate the modelling of the ***hydrodynamics and free surface dynamics*** (except surface tension effects) ***in the flow regime where viscous and gravitational forces are dominant*** (Wittmaack 1997, Wittmaack 1998b). Moreover, calculations of Foit's analytical solution contribute to the verification (Foit and Veser 1999).

Analytical solutions for stationary isothermal downslope flow of Newtonian and Bingham fluids onto an inclined plane are given by Byron-Bird et. al. (1983). These are used to check the ***hydrodynamic models*** for coordinate systems where the vertical axis is rotated with respect to the gravity as well as the numerical models ***for the simulation of Newtonian and Bingham fluid*** rheology.

To verify the conduction heat transfer models, an analytical solution for ***instationary heat conduction*** in a rectangular parallelepiped (Carslaw and Jaeger 1973) is considered (Wittmaack 1998b). Three boundary surfaces of the parallelepiped are isothermal while the three other boundary surfaces are adiabatic.

For the verification of the ***discrete phase transition*** model Neumann's analytical solution for the propagation of a freezing front (Carslaw and Jaeger 1973) is simulated. It considers an instationary one-dimensional Stefan problem in Cartesian coordinates. The associated CORFLOW simulation shows a slight underprediction of the freezing front propagation. The CORFLOW solution does not suffer from smearing of the phase front due to numerical diffusion (Cognet et. al. 1999).

Analysing the EPR heavy reflector leak increase caused by corium discharge through the leak, an analytical solution was found and CORFLOW simulations were performed. Mathematically this corresponds to a Stefan problem in cylindrical coordinates with complex turbulent heat transfer boundary condition. Comparison of numerical and analytical results show that the simulation error in front propagation is less than 1 %. Furthermore, the numerical result is almost independent of the grid.

3 CORFLOW validation by calculation of spreading experiments

Isothermal broken dam experiments in cylindrical geometry with water are performed at the FZK in Karlsruhe (Maschek et. al. 1990). To validate the hydrodynamic modelling for low viscosity fluid including surface tension effects, some of these tests are post-calculated with CORFLOW.

The CEA in Grenoble, France, performs the **CORINE** spreading experiments with, e. g., water, glycerol and cerrotru (low melting Bi-Sn alloy) onto a plane substratum in cylindrical geometry. Post-test calculations are made for several tests with different inflow rate operating with water, glycerol and cerrotru (Veteau and Wittmaack 1995). The calculations of the isothermal tests with water contribute to the validation of the hydrodynamic code models for low viscosity fluids in the gravity-inertial regime. On the other hand, the isothermal glycerol tests (with a dynamic viscosity of about 0.35 Pa s) correspond to the gravity-viscous regime. The non-isothermal tests with cerrotru include spreading with subsequent freezing.

Small scale experiments in channels with a heated bottom plate with woods-metal (MCP58) and wax (canauba) are operated at the FZK in Karlsruhe (Ehrhard et. al. 1997, Kraut, Siegel and Ehrhard 1997, Ehrhard et. al. 1998). These tests are aimed at investigating the impact of crust formation at the interface to the substratum as well as the free surface. Calculations with CORFLOW contribute to the validation of the code for spreading processes with different Prandtl numbers (Ehrhard et. al. 1998).

The **KATS** spreading experiments with thermite melts (Al_2O_3 - and Fe) are made by FZK in Karlsruhe (Fieg et. al. 1996). Several tests are performed with different substratum materials, dry and water covered substratum in channels and in compartments with other geometry. To support the layout of test section geometry and thermocouple arrangement CORFLOW pre-calculations were performed. In addition, post-calculations of, e. g., KATS-5 and -6 validate CORFLOW (Wittmaack 1997, Wittmaack 1998b). In these tests liquid Al_2O_3 and Fe is spread into dry, plane channels with subsequent solidification.

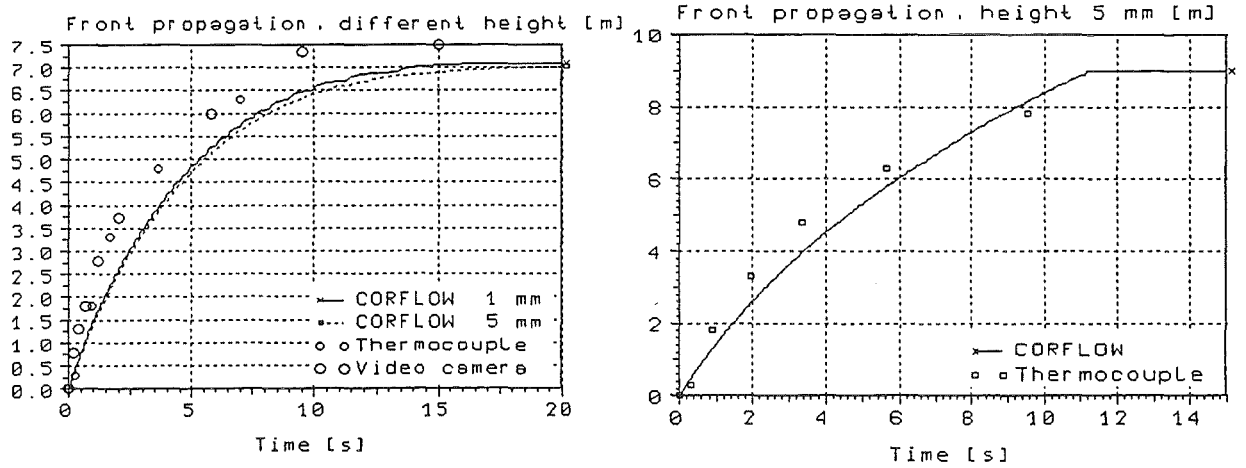

KATS-5 Al_2O_3-Test. KATS-6 Fe-Test.

Fig. 1 : Free surface (top) and front propagation (bottom).

Due to the underpredicted front velocity at the beginning, the calculated final leading edge location of KATS-5 is slightly less than the experimental value, see fig. 1. The KATS-6 calculation also underestimates the front speed at the beginning but overestimates it in the following. For this reason the experimental final front position of 8.5 m is exceeded. Moreover, KATS-7, -12 and -14 were successfully calculated by CORFLOW (Foit and Veser 1999).

In addition, **miniKATS** small scale thermite spreading tests are operated by the same team. These inexpensive tests are accompanied by CORFLOW calculations. They investigate physical processes that stop the melt progression (crust formation, bulk freezing, non-Newtonian rheology, surface tension).

At the **FARO** test facility of the JRC in Ispra, Italy, high temperature (initial temperature about 2800 K) spreading tests initiated by pouring of a UO_2-ZrO_2 mixture onto a plane substratum, as well as pre- and post-calculations with CORFLOW are performed (Wider 1998). At high temperature the radiant heat transfer to the surroundings is dominant while for low temperature tests it is less important than heat conduction into the substratum. For this reason FARO experiments are important to check the modelling of the radiant heat transfer. The calculational results compare reasonably well with the experimental data.

The **VULCANO** purely oxidic corium spreading tests are carried out by CEA in Cadarache, France. Four CORFLOW simulations are performed on VULCANO VE-U1, with different assumptions about the shear rate versus shear stress relation of the corium below the liquidus temperature (Wittmaack 1998c) : The Thomas (1965) and Stedman (1990) mushy fluid viscosity model are applied both without and with yield stress. With the Thomas model an overprediction of the front propagation is calculated, whereas an underestimation is obtained with Stedman's model. A noticeable flow retardation and rapid damping of the free surface gravity waves is observed if non-vanishing yield stress is taken into account.

At SNU in Krefeld the **COMAS** spreading tests with Fe and several corium melts onto different substratum materials (Steinwarz et. al. 1997) were carried out. Two-dimensional tests in channels and runs in three-dimensional compartments are performed. As some experiments operate with prototypic reactor corium, calculations of these tests (Fischer et. al. 1998) are important for code validation. Computations of the EU-1 Fe test provide a sufficiently accurate representation of the experimental data. On the other hand, for the -5a and -6 tests with corium the total spreading length is overpredicted. COMAS 5a was used for a benchmark, CORFLOW calculations were contributed by different organizations (Koller and Ulbrich 1997).

The final front position of COMAS EU-4 can be reproduced by three-dimensional CORFLOW simulations (Wittmaack 1998a) if linear volumetric averaging of the viscosity of the oxidic and the metallic phase is performed and if the Stedman mushy viscosity model (Stedman et. al. 1990) is used. The initial phase of the front progression is accurately predicted by the calculation, while subsequently an overestimation of the front progression is observed. However, caused by the abrupt immobilization of the fluid at the free surface the final front position resembles the experimental observation.

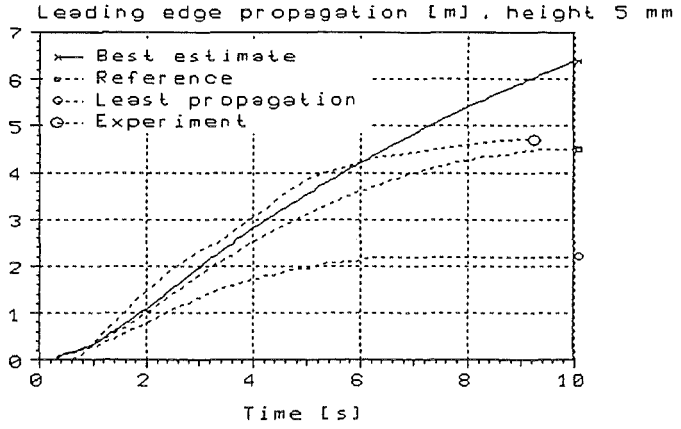

Fig. 2 : Front propagation for specific parameter combinations and test data, COMAS EU-2b.

Our uncertainty and sensitivity analysis of COMAS EU-2b simulations (Wittmaack 1999), funded by the german BMBF (project 1501213), investigates the impact of computational input parameters on the calculations results. All calculations of the **uncertainty analysis** overestimate the final melt front position of 4.73 m, predicting values from 6 to 10.6 m. However, there are input parameter combinations in the considered range of uncertainty that even lead to underprediction of the front propagation, with final front positions down to about 2.2 m, see fig. 2. Run 'Least propagation' in fig. 2 uses for all parameters those data in the range of uncertainty that hamper the spreading process. It differs from the parameter combination 'Reference' in inflow height, initial temperatures and radiation emissivities which

have best estimate values. Furthermore, the result for best estimate input parameters is given in fig. 2. Our **sensitivity analysis** of the leading edge propagation shows that the uncertainty of the inflow height in the initial phase and the uncertainty factor of the liquid phase viscosity later on have dominant impact on the uncertainty of this result. All other parameters have much less impact, e. g. parameters of non-Newtonian behaviour. Our study helps to identify the major sources of uncertainty of the key output variables based on input parameter uncertainty. It systematically shows that research on more precise estimation of the liquid phase dynamic viscosity will have high impact.

4 Simulation of EPR corium spreading

Major target of CORFLOW investigations is the corium flow from the cavity into the spreading compartment related to the EPR spreading concept. After early two-dimensional calculations with mixed oxidic-metallic corium and an inflow boundary condition, three-dimensional separate computations of oxidic and metallic corium in more detailed geometry were carried out (Wittmaack 1997). This paper presents recent EPR spreading simulations, that include the reactor pit on an enhanced height level and consider a variety of corium compositions and geometrical configurations of the oxidic, metallic and slag phases.

Our **geometry model** simulates pit, channel to the spreading compartment including the gate and spreading compartment itself, see fig. 3. Thanks to the symmetry of the reactor the model includes only one half of the real geometry. To also simulate the initial condition of a cavity filled with fluid on top of an empty channel, the model operates with two symmetry planes. Fig. 3 shows the initial condition in a side view from the vertical symmetry plane and a top view in the vertical position of the gate.

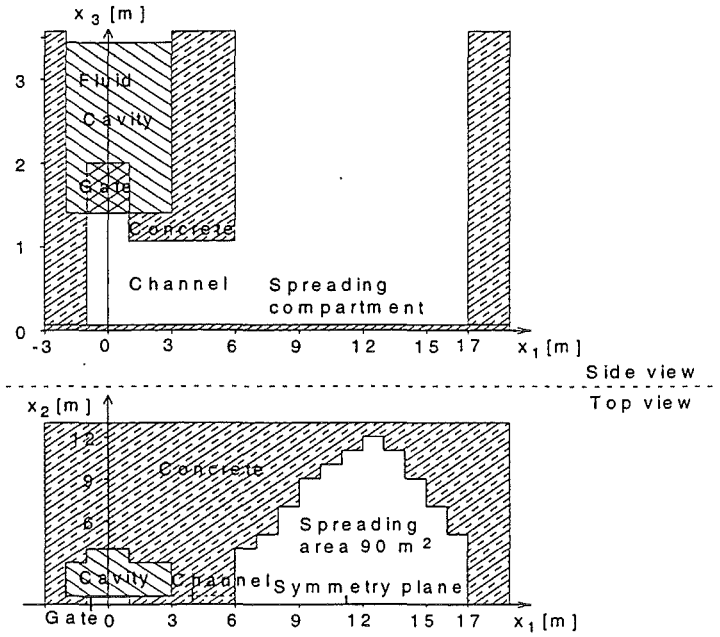

Fig. 3 : Geometry model of the EPR spreading calculations.

The model simplifies the EPR geometry, e. g., the declination of the pit bottom and the channel is neglected and round vertical pit walls as well as round and diagonal vertical walls of the spreading compartment are modelled by steps. Furthermore, as a result of the free surface representation by height functions in CORFLOW, the geometry model has a vertical gate. These simplifications are conservative with respect to front propagation, as they reduce the mechanical energy of the fluid.

Related to the geometrical arrangement of the corium constituents in the pit, we consider following **spreading scenarios** (standard scenarios) :

Case	Standard scenario
1a	Spreading of metallic corium onto the concrete in the spreading compartment and subsequent
1b	spreading of oxidic corium including slag formed by erosion of the sacrificial material onto the already spread metallic corium.

2 Spreading of oxidic corium, without slag, onto concrete.
3 Spreading of an emulsion of mixed corium (oxide, slag and metal) onto concrete.

The mixed corium spreading is considered as reference case, since it is the most probable scenario, because of the intense interaction of corium and sacrificial material in the reactor pit. In addition, it handles the entire corium mass in one run and not sequentially as in case 1, i. e. it is less conservative as the pressure in the fluid is higher than for partial corium mass and the higher heat capacity reduces the heat loss per unit mass of the fluid. Moreover, it is motivated by CORFLOW post-calculations of the COMAS EU-4 test with oxidic and metallic corium mentioned before. These computations suggest that spreading can reasonably be simulated by the single-component-fluid model of an emulsion with the metal mixed into the oxide.

Due to lack of space we do not list corium composition and all **material properties** here. For mushy corium we evaluate the dynamic viscosity by Stedman's model (1990) with $x_{sos} = 0.5$. To estimate the impact of non-Newtonian effects, we use Epstein's (1996) yield stress data (fig. 4,'outside immobile'), scaled in temperature due to the different $T_{\ell s}$ and T_{ss}, for the oxidic corium without slag. With these data and solid fractions calculated by the GEMINI code, we make a fit of k in $\tau_y = k\, x_{so}^{\,3}$, Thomas (1961), where τ_y is the yield stress and x_{so} the solid phase mass fraction. With k = 69 Pa, obtained from an average of Epstein's low temperature data, we extrapolate Epstein's data to low temperatures and obtain :

T [K]	x_{so} [-]	τ_y [Pa]	T [K]	x_{so} [-]	τ_y [Pa]	T [K]	x_{so} [-]	τ_y [Pa]
373	1	69	2688.5	0.509	21	2729	0.62	1.58
2573	1	69	2698	0.68	27.3	2745	0.58	0.26
2660	0.77	31.5	2714.5	0.65	3.75	2783	0	0
2679	0.75	26.3						

Table 3 : Estimated yield stress of the oxidic corium without slag.

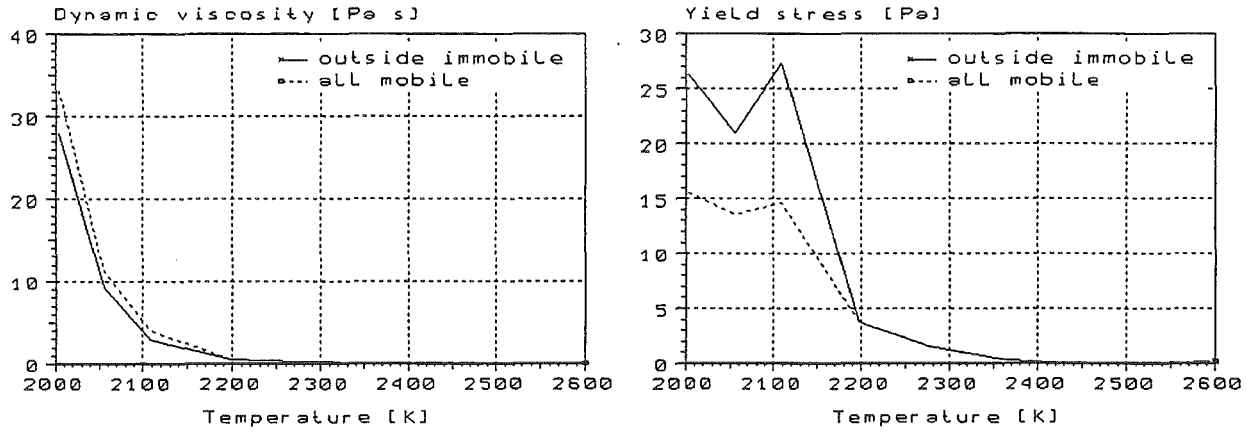

Fig. 4 : Measurements of viscosity and yield stress for oxidic corium by Roche et. al.

We model mixed corium as an emulsion of metallic and oxidic phases with the same velocity and temperature. For the density, dynamic viscosity and heat conductivity volumetric linear averaging of the properties is performed. For the specific heat, without the contribution of the latent heat, linear averaging with the mass fraction is used.

Table 4 lists initial conditions and **computational results of standard scenarios** :

Variable	Unit	Case 1a Metal	Case 1b Ox. + slag	Case 2 Oxide	Case 2 Oxide l.c.	Case 3 Mixed
Fluid mass	kg	132138	244252	200167	222900	376390
Fluid volume	m^3	20.88	36.18	24.55	33.5	56.6
Initial fluid height in pit	m	0.745	1.292	0.877	1.196	2.021
Initial fluid temperature	K	2608	2518	2715	2433	2600
Propagation time of front to outer wall of spreading compartment	s	4.9	4.4	5.2	4.9	3.7

Time of complete covering of spread. area	s	7.5	7.9	9.3	8.8	6.7
Maximum velocity in 1-direction	m / s	5.5	6.6	5.6	6.3	8

Table 4 : Initial conditions and some calculational results for different kinds of corium.

The table data indicate that in all cases the spreading area is completely covered by corium in less than 10 s. For all scenarios a spatially almost constant corium layer thickness is achieved in less than 60 s. Fig. 5 shows a sequence of free surface locations for mixed corium (view as in fig.3, height scale cut off on top of horizontal channel).

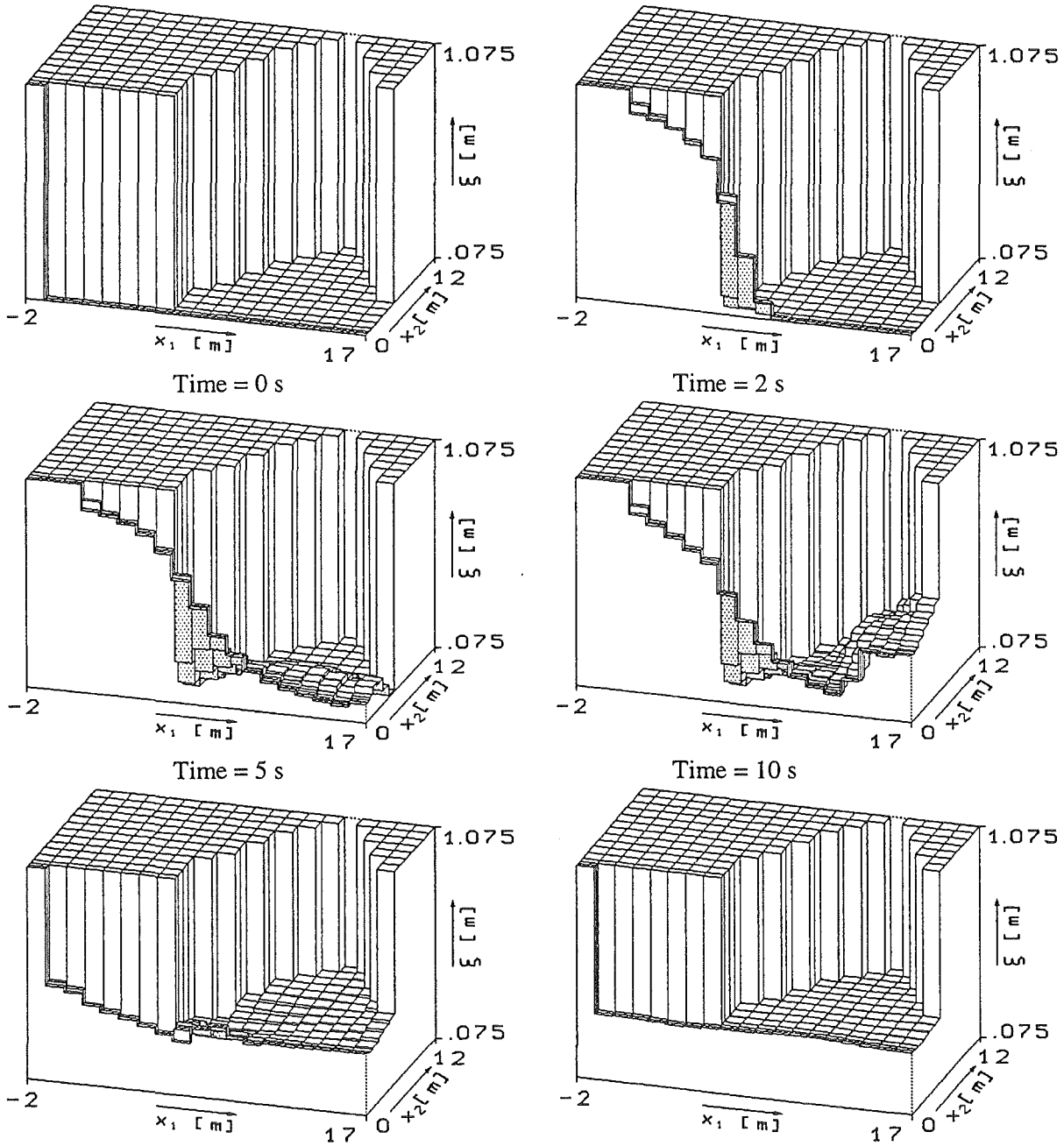

Fig. 5 : Corium flow into the spreading compartment. Free surface dynamics.

Passing the vertical gate the melt enters the channel. Propagating through the channel into the spreading compartment it reaches the outer wall earlier than the side walls. Subsequently the gravity current is reflected and redirected at vertical walls until an almost uniform free surface height is achieved. The dynamics of the other cases resemble that of mixed corium.

Due to its high heat conductivity and thanks to its low emissivity, the metal (case 1) removes the major amount of heat by conduction to the substratum. Radiation to the surroundings is the dominant process

for heat removal of the oxide, i. e. in the other standard scenarios. We neglect heatup of the ambient surface for radiation. Moreover, in the real EPR spreading process, the radiant heat transfer between melt and ambient concrete structures is reduced as a result of absorption and scattering by aerosols. These are created by burning of the epoxy coating of the concrete substratum after getting in touch with the hot corium. Therefore the used assumptions are conservative concerning melt propagation as they lead to overestimation of the heat extraction from the melt and accelerated corium cooling.

All results presented so far are calculated on a mesh with 19x14x18 nodes. To evaluate the impact of the discretization, metallic and mixed corium spreading are also computed on a horizontally refined grid with 38x15x18 nodes. Comparison of calculated results in following table shows a moderate influence.

Variable	Unit	Case 1a 19x14x18	Case 1a 38x15x18	Case 3 19x14x18	Case 3 38x15x18
Propagation time of front to outer wall of spreading compartment	s	4.9	5.3	3.7	4.3
Time of complete covering of the spreading area	s	7.5	7.5	6.7	6.8
Maximum velocity in 1-direction	m / s	5.5	5.7	8	7.6

Table 5 : Calculational results of the metallic and mixed corium spreading for different horizontal spatial discretizations.

Mixed corium spreading is also calculated with a **low corium initial temperature** of $T_0 = 2400$ K, 200 K less than the best estimate value. This influences the melt propagation only slightly, see table 6.

Variable	Unit	Low T_0	Low A_g	Case 3
Gate area	m^2	2.4	0.24	2.4
Initial fluid temperature	K	2400	2600	2600
Propagation time of front to outer wall of spreading compartment	s	3.9	7.3	3.7
Time of maximum kinetic energy	s	5.6	13.7	5.5
Time of complete covering of the spreading area	s	7.1	13	6.7
Maximum velocity in 1-direction	m / s	7.9	8.4	8
Fluid height in pit at t = 60 s	m	0.01	0.41	0.01

Table 6 : Comparison of base case with deviations from the best estimate conditions.

After the calculated problem time of one minute, bulk and minimum corium temperatures in the low initial temperature case are 2377 K and 2043 K respectively, which is significantly above the temperature where the viscosity is getting infinite (about 1960 K). Consequently there is only minor difference in the spreading behaviour between the standard scenario and the low initial temperature case.

In addition to the gate area $A_g = 2.4$ m² (reference case) also the **reduced gate area** $A_g = 0.24$ m² is considered for mixed corium spreading. The reduced flow area corresponds to a postulated improper gate opening. As seen in table 6, the reduced gate area causes considerable flow retardation. The time needed for corium to reach the outer wall and to cover the entire area of the spreading compartment is about twice as long as in the standard scenario. After 60 s the fluid height in the pit is still about 0.41 m, consequently, the spreading process lasts longer than one minute in the low gate area case. However, after 60 s the spreading area is entirely covered by mixed corium with almost constant thickness.

As indicated by table 4, **less conservative material properties** improve the spreading behaviour of the oxidic corium, compared to standard scenario properties. This can be explained as follows : Reduction of the temperature where the viscosity is getting infinite from 2673 to 2373 K and reduction of the initial temperature from 2715 to 2433 K increases the difference between initial temperature and temperature where the viscosity is getting infinite from 42 to 60 K. Furthermore, the lower initial temperature reduces the radiant and diffusive heat loss to the surroundings for the less conservative material properties. On the other hand, the decrease in heat capacity accelerates the temperature reduction of the material with less conservative material properties, which is not conservative concerning melt propagation. This effect is more than compensated by the previously mentioned ones.

Concerning **non-Newtonian rheology**, for the oxidic corium standard scenario, case 2, the calculations show no difference between the cases where Epstein's data (fig. 4) or zero yield stress are used. This leads to the suggestion that non-Newtonian effects do not significantly influence the EPR spreading process.

The EPR calculations include following **conservative assumptions** with respect to melt propagation :
- The geometry model neglects part of the corium mechanical energy, see above.
- Metal (case 1a) and oxide spreading (case 2) neglect the pressure on top of the melt related to overlying corium layers (i. e. not considered other phases).
- Radiant heat removal of the melt is overestimated as a) heatup of the surroundings is neglected and b) the radiation screening effect of aerosols generated by burning of the epoxy coating of the concrete substratum is neglected.

Our EPR spreading simulations are restricted by following **not simulated physical phenomena** :
- Interactions of the spread corium with concrete (concrete decomposition, H_2 generation due to chemical reactions of the concrete decomposition products with the corium).
- Multi-component corium flow (i. e. flow of different species with different velocity).
- Turbulence of the corium flow.

Neglecting the interactions of corium and concrete seems reasonable as there is no experimental evidence, from KATS and COMAS experiments, that their effects significantly influence the spreading. The previously mentioned CORFLOW calculations on COMAS EU-4 suggest that spreading can be simulated with sufficient accuracy by the single component fluid model of an emulsion with the metal mixed into the oxide. As EPR spreading occurs at moderate Reynolds numbers ($0.8 * 10^6$ to $2.6 * 10^6$ for mixed corium), the introduction of turbulence modelling is not essential (turbulent flow onto a plate occurs for $Re > 5 * 10^5$ (Zierep and Bühler 1991)).

5 Conclusion

The 1st part of our paper shows that most CORFLOW models are verified by analytical solutions. This constitutes a reliable basis of the code **verification**.

The pre- and post-test calculations performed for **validation** generally give a sufficient representation of most of the experimental results. Major reasons for discrepancies occurring in several simulations are
- inaccurate material properties, especially the parameters of the viscous stress tensor and
- uncertainty of boundary conditions, namely at the inflow boundary.

Our **uncertainty and sensitivity analysis** of COMAS EU-2b simulations identifies the uncertainty of the liquid phase dynamic viscosity as major source of uncertainty of the calculated front propagation.

EPR spreading calculations are performed with different assumptions about the initial mixing or stratification of the corium phases in the pit. In addition, variations of
- material properties of the oxidic corium,
- corium initial temperature,
- flow area of the gate between pit and channel to the spreading compartment and
- non-Newtonian rheological behaviour of the melt (yield stress)

were investigated. All considered spreading processes lead to an almost homogeneous corium layer thickness in the spreading compartment in less than 60 s. As these results are obtained with many conservative assumptions, the calculations indicate proper operation of the concept.

Since the oxidic corium on a microscopic scale is partially solid during the entire spreading process, the computational result depends significantly on the material properties of the melt, especially the mushy fluid viscosity and the effective specific heat during the phase transition. This is confirmed by CORFLOW calculations on COMAS EU-4 with oxidic and metallic corium modelled as emulsion. Though there is considerable uncertainty in the material properties of EPR corium, thanks to much greater corium mass and heat capacity in the EPR case compared to small scale tests, the impact on the result is much weaker. A calculation of mixed corium spreading with an initial temperature 200 K below the best estimate value demonstrates that the concept operates also with less favourable material properties.

Computations of metallic and mixed corium spreading with a finer horizontal spatial discretization show that the EPR results depend only moderately on the grid.

References

Byron-Bird, R., Dai, G. C., Yarusso, B. J. 1983 : The rheology and flow of viscoplastic materials. Rev. Chem. Eng. 1, pp. 1-70

Carslaw, H. S., Jaeger, J. C. 1973 : Conduction of heat in solids. Oxford University Press

Cognet et. al. 1999 : CSC final report, CEA Cadarache, France, to be published

Ehrhard, P., Siegel, U., Krauth, S. 1997 : Modellversuche und Simulationen mit CORFLOW zur Ausbreitung erstarrender Schmelze. Projekt nukleare Sicherheitsforschung Jahresbericht 1996, FZKA 5963, pp. 264-273, Forschungszentrum Karlsruhe

Ehrhard, P., Bunk, M., Fellmoser, F., Fieg, G., Foit, J., Huber, F., Müller, U., Siegel, U., Stegmaier, U., Werle, H., Wittmaack, R. 1998
Spreading of the core melt on the spreading area of the EPR. Proc. 6th int. Conf. on Nuclear Engineering, ICONE-6, San Diego, California, USA, May 10-14, 1998, American Society of Mechanical Engineering

Epstein, M. 1996 : A Bingham plastic interpretation of the ACE viscosity data. FAI/96-92, Fauske & Associates Inc., Burr Ridge, Illinois, USA

Fieg, G., Huber, F., Werle, H., Wittmaack, R. 1996 : Simulation experiments on the spreading behaviour of molten core melts. Proc. Natl. Heat Transfer Conf., Houston, Texas, USA, Aug. 3-6, 1996, pp. 121-130, American Nuclear Society

Fischer, M., Funke, F., Hellmann, S., Lanzenberger, K., Movahed, M., Nie, M., Petzold, K. G., Wittmaack, R. 1998 : Theoretische Untersuchungen und Grossversuche zum Nachweis der Wirkungsweise und Wirksamkeit von Reaktorsicherheitselementen. Abschlußbericht Reaktorsicherheitsforschung, Vorhabens-Nr. 15NU0963, KWU NA-T/98/080, Erlangen, 09.1998

Foit, J. J. 1997 : Spreading with variable viscosity. FZKA 6006, FZK Karlsruhe, IATF

Foit, J. J., Veser, A. 1999 : Similarity solutions for non-isothermal spreading, KATS experiments and CORFLOW results. Proc. 7th int. Conf. on nuclear Engineering, ICONE-7036, Tokyo, Japan, April 19-23, 1999

Huppert, H. E. 1982 : The propagation of two-dimensional and axisymmetric viscous gravity currents over a rigid horizontal surface. J. Fluid Mech., vol. 121, pp. 43-58

Huppert, H. E. 1986 : The intrusion of fluid dynamics into geology. J. Fluid Mech., 173, pp. 557-594

Kraut, S., Siegel, U., Ehrhard, P. 1997 : Experimentelle Untersuchung zur Ausbreitung metallischer Modellschmelzen bei gleichzeitiger Erstarrung. FZKA 6018, FZK Karlsruhe, IATF

Maschek, W., Munz, C. D., Meyer, L. 1990 : An assessment of liquid sloshing phenomena in pools based on ADFM / SIMMER-II code calculations and experiments. Proc. of the 1990 intl. fast reactor sefety meeting, pp. 395-406, Aug. 12-16, Snowbird, UT, USA

Papanastasiou, T. C. 1987 : Flows of materials with yield. J. Rheology, 31, pp. 385-404

Sakimoto, S. E. H., Zuber, M. T. 1995 : The spreading of variable-viscosity axisymmetric radial gravity currents : applications to the emplacement of Venusian 'pancake' domes. J. Fluid Mech., 301, pp. 65-77

Stedman, S. J., Evans, J. R. G., Woodthorpe, J. 1990 : Rheology of composite ceramic injection moulding suspensions. J. Mater. Sci., 25, pp. 1833-1841

Steinwarz, W., Dyllong, N., Koller, W., Langer, G., Häfner, W., Geiß, M., Hurtado, A. M., Manderbach, T., Kolb, H., Ulbrich, A., Fischer, M., Hellmann, S., Wittmaack, R. 1997 : Theoretische Untersuchungen und Grossversuche zum Nachweis der Wirkungsweise und Wirksamkeit von Reaktorsicherheits-elementen. Teilvorhaben COMAS und INKA zum Thema Beherrschung von Kernschmelzunfällen. Arbeitsgemeinschaft innovative Kernenergie, SNU Krefeld, 12.1997

Thomas, D. G. 1961 : Laminar-flow properties of flocculated suspensions. A.I.Ch.E. Journal, 7, no. 3, pp. 431-437

Thomas, D. G. 1965 : Transport characteristics of suspensions : VIII. A note on the viscosity of Newtonian suspensions of uniform spherical particles. J. Colloid Sci., 20, pp. 267-277

Veteau, J. M., Wittmaack, R. 1995 : CORINE experiments and theoretical modelling. Proc. Int. Conf. Fission Safety 1991-1995, Luxembourg, Nov. 20-22, 1995, pp. 271-285

Wider, H. U. 1998 : Pre-test calculations with the CORFLOW code for the first UO_2/ZrO_2 spreading test in FARO. Technical Note No. I.98.99, JRC Ispra, Italy, 06.1998
Wittmaack, R. 1997 : Numerical simulation of free surface flows. Nuclear Technology, 119, pp. 158-180
Wittmaack, R. 1998a : Post-calculation of the COMAS EU-4 test with the CORFLOW computer code. KWU NA-T/1998/E042, Erlangen 31.03.1998, EXV COMAS(98)-D25
Wittmaack, R. 1998b : Numerische Simulation von Strömungen mit freier Oberfläche und diskreten Phasenübergängen. University of Karlsruhe (TH), faculty of mechanical engineering, FZKA 6129, Forschungszentrum Karlsruhe GmbH, Karlsruhe, August 1998
Wittmaack, R. 1998c : Post-calculation of the VULCANO VE-U1 test with the CORFLOW computer code. KWU NA-T/1998/E098, Erlangen 04.11.1998, EXV-CSC(99)-D030
Wittmaack, R. 1999 : Uncertainty and sensitivity analysis of CORFLOW simulations of the COMAS EU-2b test. KWU NA-T/1999/E021, Erlangen 23.04.1999, EXV COMAS(99)-D24
Zierep, J., Bühler, K. 1991 : Strömungsmechanik. Springer-Verlag, Berlin

OECD Workshop on Ex-Vessel Debris Coolability
Karlsruhe, Germany, 15-18 November 1999

Organised in collaboration with
Forschungszentrum Karlsruhe (FZK) GmbH

SPREADING WITH VARIABLE VISCOSITY. CORFLOW VALIDATION AND ANALYSIS OF KATS EXPERIMENTS

J. J. Foit and A. Veser
Forschungszentrum Karlsruhe GmbH
Postfach 3640, D-76021 Karlsruhe, Germany
jerzy.foit@iket.fzk.de

ABSTRACT

The current concept of the EPR (European Pressurised Water Reactor) relies on a sufficiently homogeneous spreading of the melt in order to ensure its coolability after a passive initiation of flooding by water. The conditions under which a complete spreading can be expected are the subject of current theoretical and experimental results.

The CORFLOW code allows to treat three-dimensional non-isothermal free surface flow. The influence of cooling on the spreading is modelled by a temperature dependent viscosity. The increase of the viscosity in the thermal boundary layer of the melt can eventually lead to a stop of the melt front. The experimental findings from the KATS series are analysed and CORFLOW results are presented. In addition the available similarity solutions are also used to validate the CORFLOW code.

1. INTRODUCTION

In many applications the cooling process will lead to variable flow properties, e. g. variable viscosity and, consequently, to a coupled system of the temperature and flow equations. It is impossible to satisfactorily treat this problem analytically. The lubrication approximation leads to an equation for which similarity solutions for various conditions have been found by many authors (Zel'dovich and Kompaneets, 1950; Sakimoto, 1995; Huppert, 1982; Foit, 1997). Bercovici (1994) developed a model for an axisymmetric gravity current which accounts for thermoviscous effects, i. e., the spatial variation of the viscosity. The numerical results showed significant deviations from the similarity profiles of the constant viscosity (Huppert, 1982) as well as the time-dependent viscosity (Foit, 1997) case. A variety of experiments have been carried out to determine the effects of cooling on the flow of fluids with different properties. The influence of the crust formation rates on the fluid flow was explored experimentally by Fink and Griffiths (1993) with the aim of understanding and classifying small-scale flow surface morphology for a fluid with weakly temperature dependent viscosity (polythylene glycol 600). This study indicated that a crust does not greatly affect the fluid flow except for very high crust formation rates. Experiments which used a fluid with strongly temperature dependent viscosity (glucose syrup) were performed by M. V.

Stasiuk et al. (1993). In this case the cold, viscous fluid accumulated at the leading edge, altering the flow shape and thickness and slowing the spreading. The front became steeper and the surface behind the front was nearly horizontal. All performed experiments evolved to a stage at which the overall spreading behaviour of the flow can be approximated by a constant bulk viscosity.

2. SHORT DESCRIPTION OF THE CODE

The CORFLOW code (Wittmaack, 1997) simulates the free surface flow of an incompressible fluid in a 3-dimensional geometry. In addition to the fluid, several structure materials can be considered as hydrodynamic obstacles or thermodynamic heat sources. The fluid is assumed to possess Newtonian or non-Newtonian rheology. The free surface is determined by an equation which results from the free interface kinematic boundary condition and an integration of the continuity equation in the vertical direction. The free interface is represented as a height function either as a step function or a second-order polynomial. Internal heat transport by conduction and convection as well as heat generation (decay heat) and heat transfer to the surroundings are modelled. The material properties, except the surface tension, may depend on temperature. A discrete phase transition model is available to simulate solidification and melting of the fluid and phase transition of the structure materials. The influence of the solidification process on the spreading is modelled by an increase of the viscosity. The increase of the viscosity in the thermal boundary layer of the melt can eventually lead to a stop of the melt front.

3. CORFLOW VALIDATION

The lubrication approximation for the spreading under gravity leads to a nonlinear degenerate parabolic equation (Buckmaster, 1977). This equation admits solutions which have important properties, namely, they are zero outside a closed and bounded set and the interfaces propagate with finite speed. In many applications (e. g. the spreading of the oxidic core melt in the case of a melt down accident with a failure of the reactor pressure vessel) the cooling process will lead to an increase of the viscosity during the spreading. Assuming that the increase of the viscosity can be represented as a power law of time, i. e.

$$\nu = \gamma t^{\beta},\ \gamma = \frac{\nu_0}{t_0^{\beta}},\ \beta \geq 0. \tag{1}$$

where ν_0 is the initial viscosity of the fluid, self-similar solutions for the spreading of a given volume of liquid and the spreading of a volume of liquid which increases with time as $qt^{\alpha}, \alpha > 0$ were obtained by Sakimoto, Zuber (1995); Foit (1997) and Foit (1999). To derive the similarity solution in the axisymmetric geometry, Sakimoto and Zuber (1995) used instead the relation (1) the formula $\nu = \nu_0 t^{\beta}$ which cannot be correct for dimensional reasons.

The comparison of the evolution of the interfaces for the spreading of a constant mass flux $\alpha = 1$ and the spreading of a constant fluid volume for various values of β with the CORFLOW results are shown in Fig. 1 and Fig. 2, respectively.

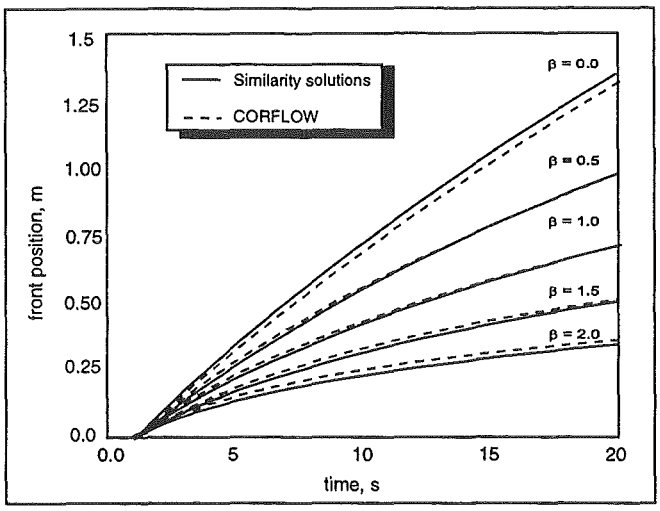

Fig. 1 Spreading of a constant volume flux.

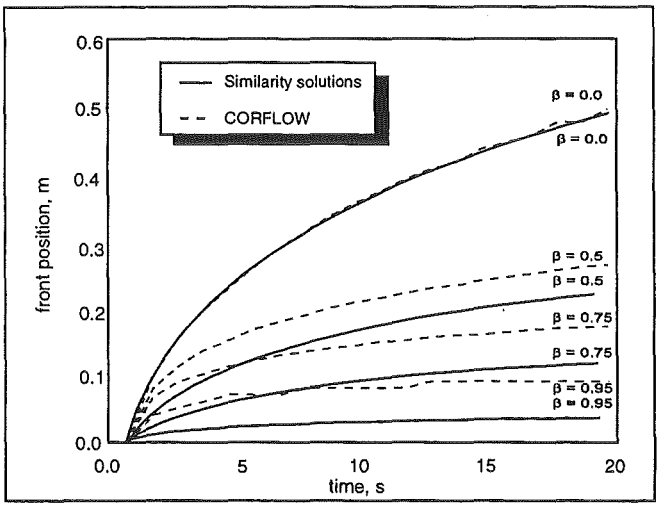

Fig. 2 Spreading of a constant fluid volume.

The CORFLOW results are in good agreement with the theoretical predictions for the spreading of a constant flux with increasing viscosity represented by $0 \leq \beta \leq 2$, whereas, the agreement in the case of the spreading of a constant volume can be stated to be good only for $0 \leq \beta < 0.5$. For faster viscosity increase, i. e. for $0.5 \leq \beta < 1$ CORFLOW overpredicts the front propagation considerably.

4. ANALYSIS OF THE OXIDIC KATS EXPERIMENTS

In the framework of large-scale KATS experiments (FZK, Germany) the non-isothermal spreading of metallic and oxidic melts on ceramic or concrete surfaces under various conditions are studied, e. g. melt overheat and melt release rates. The metallic and oxidic components of the melt are generated by the thermite reaction. The oxidic melt is composed of about 85 weight % Al_2O_3, 10 weight % SiO_2 and about 5 weight % FeO. For the above melt mixture there is only a limited data base of material properties available. Using an

estimated phase diagram, the Stedman correlation (Stedman et al., 1990) was applied to evaluate the viscosity within the solidus-liquidus range. Above the liquidus temperature the experimental data of Elyutin et al. (1969) were used (Fieg et al., 1997a). An experimental program to measure the viscosity of the oxidic KATS melts below the liquidus temperature is under way.

The KATS experiments can be classified in accordance with the melt release conditions. In KATS7 (Fieg et al., 1997a) and KATS14 (Fieg, 1998) the melt was not collected but it was poured into a cavity. As soon as the cavity was filled, the melt began to spread across the channel with flow rates defined by the diameter of the pouring nozzle. In this way an almost constant volumetric flux was achieved which lasted 12 s in the KATS7 test and 37 s in the KATS14 test. The melt front propagation ended at 49 s in the KATS7 and at 57.6 s in the KATS14 tests. In the KATS5 (Fieg et al., 1997b) and KATS12 (Fieg, 1998) experiments, on the other hand, the melts were gathered in a container before spreading into the channel was initiated by opening a gate in the container. Consequently, a linear decrease of the volumetric flow rate in time was obtained. The outflow of the oxidic melt from the container was completed after 3.7 s and 10.4 s in the KATS5 and KATS12 tests, respectively. The stop of the melt front was detected at 15 s in the KATS5 and 40 s in the KATS12 experiment.

4.1 CORFLOW results

4.1.1 Melt front progression

One can expect that the discrete phase transition model together with the variable viscosity approach used in the CORFLOW code will predict a stop of the melt front if almost all nodes at the free boundary reach the temperature at which the value of the viscosity becomes large and if the floating crust is connected to the basemat at the melt front. Because there is no crust failure criterion in CORFLOW, the results can depend strongly on the grid used for simulations. The sensitivity on the grid size will generally depend on the viscosity behaviour as a function of the temperature and the initial condition of the melt release. In Fig. 3 the CORFLOW results using a fine grid and a coarse grid with double mesh size along the channel and triple mesh size in the vertical direction for the KATS5 experiment are shown as well as the experimental findings.

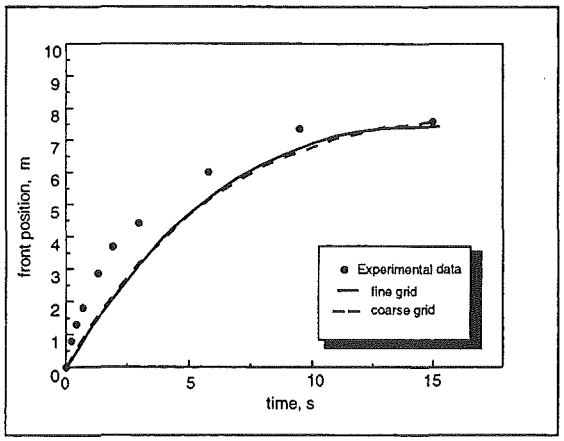

Fig. 3 Melt front progression for KATS5.

Both CORFLOW results underpredict the speed of the melt front considerably during the melt release phase. The time of the end of the front propagation and the final front position agree well with the measurements in both simulations. The simulation of the KATS12 experiment was performed using a coarser grid $((\Delta x, \Delta z) = (0.1\,m, 0.025\,m))$. The calculated front positions as a function of time are compared to the measured data in the following figure (Fig. 4).

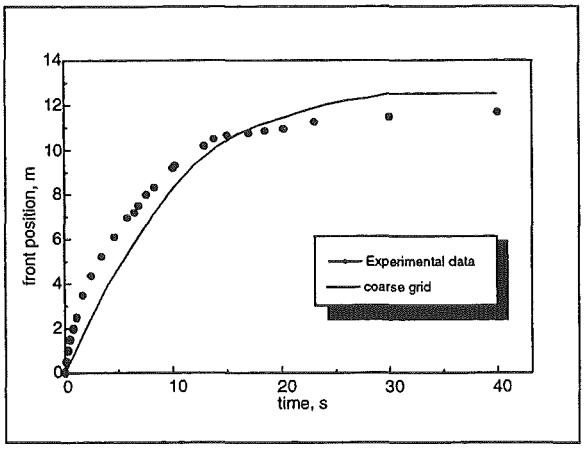

Fig. 4 Melt front progression for KATS12

As for the KATS5 experiment an underprediction of the melt front progression in the first stage of the spreading is predicted while the final front position agrees very well with the experimental one.

The results of the CORFLOW analysis of the second class of KATS experiments (experiments with an almost constant mass flux) the KATS7 and the KATS14 are shown in Fig. 5 and Fig. 6, respectively. The calculated evolution of the melt front during the melt release phase for the KATS7 agrees very well with the measured curve, in contrast to the previous cases. The time at which the melt front stops is predicted to be much shorter than detected in the experiment: 23 s for the fine grid and 27 s for the coarse grid calculation, whereas, it was measured to stop at 50 s in the experiment (Fig. 5). The discrepancies between the CORFLOW predictions and the measured front progression in the KATS14 experiment (Fig. 6) during the melt release phase might be due to the increase of the volumetric flux caused by an increase of the diameter of the pouring nozzle due to ablation. Both simulation underpredict the final front position. The stop of the melt front is predicted at 60 s for the fine grid and at 48 s for the coarse grid calculation. In the experiment the end of the melt front progression was detected after 58 s.

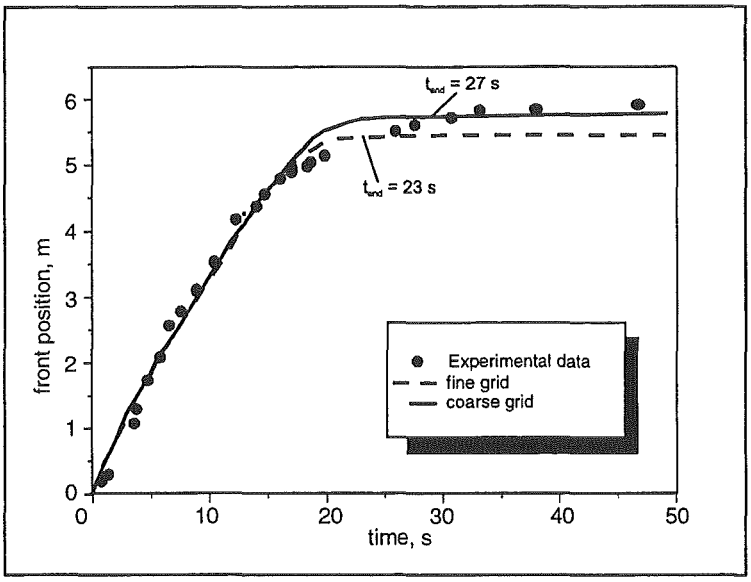

Fig. 5 Melt front progression for KATS7.

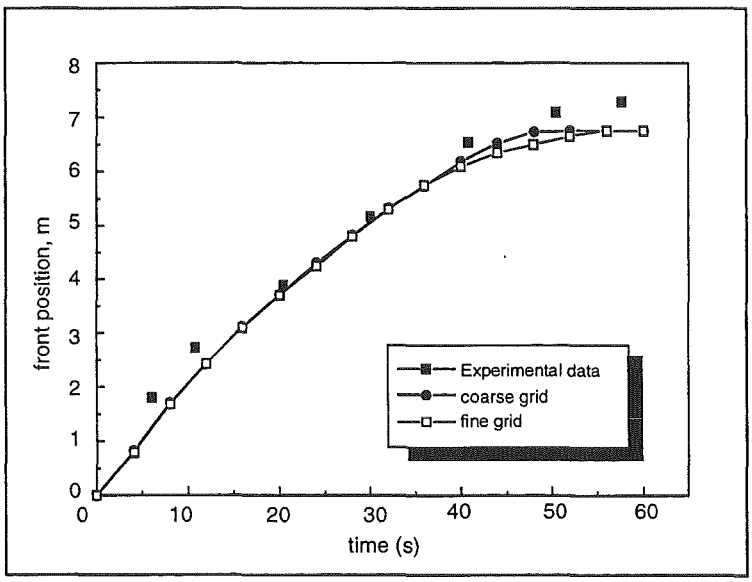

Fig. 6 Melt front progression for KATS14.

4.1.2 Temperature and velocity profiles for KATS5 experiment

The following figures (Fig. 7 - 8) show the time evolution of the thermal boundary layer in the vicinity of the melt front as predicted for the KATS5 experiment by CORFLOW. The temperature profiles are given as a function of the melt height. The mesh size in the vertical direction used in the fine grid calculation was chosen to be $1 \cdot 10^{-3}$ m. The initial melt temperature was 2393 K. The liquidus temperature and the temperature at which the viscosity becomes infinite was estimated to be 2198 K and 2050 K, respectively (Fieg et al., 1997a). The CORFLOW results show qualitatively reasonable resolution of the temperature field. While the melt continues to spread, the interface temperatures decrease and the thickness of

the thermal boundary layers increases. The central temperature of the melt decreases only slowly and is still at about 2300 K far behind the front and at about 2180 K near the melt front after the end of the melt front propagation at 16 s. The comparison with the temperature profiles obtained by the coarse grid (triple mesh size in the vertical direction) (Fig. 7 - 8) shows the necessity of using a sufficiently refined grid in order to obtain a reasonable resolution of the thermal boundaries.

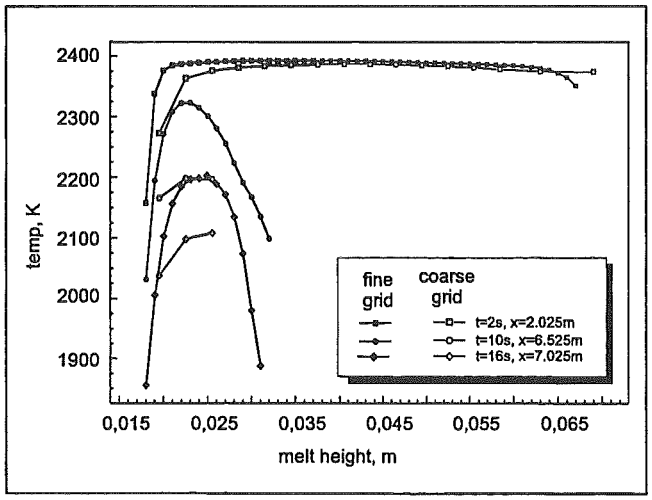

Fig. 7 Melt temperature as a function of the melt height near the melt front.

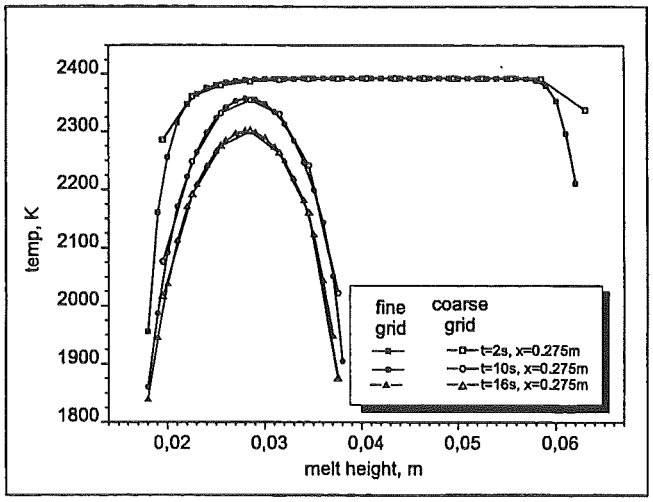

Fig. 8 Melt temperature as a function of the melt height far behind the melt front $(x = 0.275\ m)$.

5. CONCLUSIONS

After the numerical deficiencies in the treatment of non-isothermal flows with increasing viscosity have been eliminated, there is a need for validation of the achieved modifications. For this purpose the self-similar solutions for spreading with variable viscosity are used. The CORFLOW results are in good agreement with the theoretical predictions for the spreading of a constant flux for a weak as well as for a strong increase of the viscosity with

time. The agreement in the case of the spreading of a constant volume can be stated to be good only for a slow increase of the viscosity as a function of time. For faster viscosity increase CORFLOW overpredicts the front progression considerably.

Some of the KATS experiments (KATS5, KATS12) are suitable for comparison with the self-similar solutions for the isothermal spreading of a constant fluid volume in order to see the effects of the melt cooling on the front progression. In both experiments the final front position is located in the neighbourhood of the isothermal curve. Due to the fairly large Péclet number for the oxidic melt under consideration, the spreading melt develops only a thin thermal boundary layer at the cooled boundaries. Consequently, the influence of this thin crust on the front propagation is weak until the time at which the buoyancy force is balanced by the strength of the developing crust.

The variable viscosity used in CORFLOW seems to be adequate for simulations of the oxidic KATS experiments concerning the predictions of the final front position. The CORFLOW code will predict a stop of the melt front if almost all nodes at the free boundary reach the temperature at which the value of the viscosity becomes large and if the floating crust is connected to the basemat at the melt front. Because there is no crust failure criterion in CORFLOW, the results can depend strongly on the grid used for simulations. The sensitivity on the grid will generally depend on the viscosity behaviour as a function of the temperature and the initial condition of the melt release.

Even though the progression of the front and the final position of the front calculated for the oxidic KATS experiments are insensitive to the mesh size, i. e. to the resolution of the thermal boundaries and the partition of the energy losses, caution must be exercised if a much coarser grid is used. Pronounced discrepancies are observed with respect to other details of the experimental findings such as the velocity of the melt front during the melt release and the time of the end of the front progression.

When compared with the experimental database, overall, the CORFLOW code agrees well with some experimental data, and there are pronounced discrepancies with other experimental results. Discrepancy with experimental data may well be due to experimental nuances as much as poor models in the code, but, on the other hand, agreement with some experimental data should not be interpreted as justifying the underlying physical processes in the code (the data itself may not be fully qualified, and the agreement might have been obtained because of a fortuitous choice of input parameters). Therefore, additional validation is needed in order to reach a status in which one can rely on CORFLOW predictions of the spreading of the ex-vessel melt in a postulated meltdown accident. In addition, a sufficiently qualified data base of material properties for the ex-vessel core melts is required.

REFERENCES

Bercovici, D., 1994. *Geophys. Res. Lett.* **21**, 1177.

Buckmaster, J., 1977. *J. Fluid Mech.* **81**, 735.

Elyutin, V. P. et al., 1969. *Russian Journal of Physical Chemistry* **43**, 3.

Fieg, G. et al., 1997a. FZKA-Report 6605, Forschungszentrum Karlsruhe.

Fieg, G. et al., 1997b. FZKA-Report 5920, Forschungszentrum Karlsruhe.

Fieg, G.: Private communication.

Foit, J. J., 1997. FZKA-Report 6006, Forschungszentrum Karlsruhe.

Foit, J. J., 1999. Proceedings of the 7th International Conference on Nuclear Engineering, Tokyo.

Griffiths, R. W.; Fink, J. H., 1993. *J. Fluid Mech.* **252**, 667.

Huppert, H. E., 1982. *J. Fluid Mech.* **121**, 43.

Sakimoto, S. E. H.; Zuber, M. T., 1995. *J. Fluid Mech.* **301**, 65.

Stasiuk, M. V. et al., 1993. *Geology* **21**, 335.

Stedman, S. J. et al., 1990. *J. Material Sci.* **25**, 1833.

Wittmaack, R., 1997. *Nuclear Technology* **119**, 158.

Zel'dovich, Ya. B.; Kompaneets, A. S., 1950. Collection Commemorating the 70th Anniversary of A. F. Joffe, Izv. Akad. Nauk. SSR.

OECD Workshop on Ex-Vessel Debris Coolability
Karlsruhe, Germany, 15-18 November 1999

Organized in collaboration with
Forschungszentrum Karlsruhe (FZK) GmbH

ASSESSMENT OF THEMA CODE AGAINST SPREADING EXPERIMENTS

Bertrand Spindler and Jean-Michel Veteau
Commissariat à l'Energie Atomique
DRN/DTP, CEA-Grenoble, 38054 Grenoble Cedex 9, France
bspindler@cea.fr veteau@dtp.cea.fr

Claude Brayer and Michel Cranga
Commissariat à l'Energie Atomique
DRN/DTP, CEA-Cadarache, 13108 St-Paul-lez-Durance, France
cbrayer@cea.fr cranga@drncad.cea.fr

Lucio De Cecco and Piero Montanelli
Ente per le Nuove tecnologie, l'Energia e l'Ambiente
ERG/SIEC, Via Martiri di Monte Sole, 4, 40129 Bologna, Italy
dececco@bologna.enea.it

Dominique Pineau
Electricité de France
DRD/RNE/TTA, 6 quai Watier, 78401 Chatou, France
dominique.pineau@edf.fr

ABSTRACT

In the frame work of Severe Accident research, the spreading code THEMA, developed at CEA/DRN, aims at predicting the spreading extent of molten core after a vessel melt-through. The code solves fluid balance equations integrated over the fluid depth for oxidic and/or metallic phases under the shallow water assumption, using a finite difference scheme. Solidification is taken into account through crust formation on the substrate and at contact with the surroundings, as well as increase of fluid viscosity with solid fraction in the melt. A separate energy equation is solved for the solid substrate, including possible ablation.

The assessment of THEMA code against the spreading experiments performed in the framework of the Corium Spreading and Coolability project of the European Union is presented. These experiments use either simulating materials at medium (RIT), or at high temperature (KATS), or corium (VULCANO, FARO), conducted at different mass flow rates and with large or low solidification interval.

THEMA appears to be able to simulate the whole set of the experiments investigated. Comparison between experimental and computed spreading lengths and substrate temperatures are quite satisfactory. The results show a rather large sensitivity at mass flow rate and inlet temperature, indicating that, generally, efforts should be made to improve the accuracy of the measurements of such parameters in the experiments.

1. INTRODUCTION

In the event of a highly unlikely core melt-down accident in Pressurised Water Reactors, scenarios in which the reactor pressure vessel fails and the high temperature core melt mixture (corium) relocates in the reactor cavity cannot be excluded. Thus industries and utilities have been requested to take such an event into account for future reactors. Within this context, large R&D efforts throughout the world are currently directed towards various so called 'core-catchers' concepts. Among the most advanced projects, the European Pressurised Reactor includes a core-catcher which is based on first mixing the corium with concrete, then spreading the molten mixture on a large surface and subsequently cooling by flooding with water. Therefore, sufficient melt spreading is one of the key phenomena to achieve ex-vessel melt coolability and consequently deserves intensive investigations.

Considering the large number of thermo-physical and thermo-chemical phenomena involved in the melt spreading process, and the large number of spreading scenarios, the help of computer codes such as THEMA, developed by CEA in the frame of a CEA-EDF agreement, appears to be necessary.

For the sake of verification, and in the scope of investigating particular phenomena specially related to high temperatures (interaction with the substrate, physico-chemical processes), several experiments were performed. The experiments performed in the frame of the Corium Spreading and Coolability program of the 4th European Framework Program use either materials at medium temperature (RIT), or materials at high temperature (KATS), or corium (VULCANO and FARO).

After a description and discussion of the main models worked out in THEMA, this paper deals with the assessment of the code against these tests.

2. DESCRIPTION OF THEMA CODE

2.1 Melt model

The THEMA code computes 1D or 2D spreading of melt constituted of either one homogeneous phase or two stratified phases (metallic and oxidic) taking into consideration bottom and top crust formation and ablation of the substrate.

The melt model is based on 2D balance equations as a result of the integration over the melt thickness of the 3D equations (Eberlé, 1995). A single momentum equation is considered under the shallow water assumption whereas two energy equations are used, one for the metallic and one for the oxidic phase. Furthermore, several mass balance equations are used, one for each constituent of each phase.

The numerical integration of the finite difference set of equations uses a semi-implicit method with a Newton-Raphson iteration scheme. A second order discretization in space is used to get a better accuracy of the melt front progression. The time step is limited by the Courant condition. Moreover it is also controlled by the variations of the wall heat flux and the crust thickness with time. Hence the sharp variations of these variables encountered during the thermal shock, occurring when the melt comes into contact with the bottom substrate, can be satisfactorily predicted.

2.2 Crust models

Crust formation at the bottom and at the surface of the melt is taken into account with specific models. The crust thickness is not obtained by the general melt model : the conduction equation in the crusts together with the energy balance at the interfaces (contact with the substrate and the melt for the lower crust ; contact with the surroundings and the melt for the upper crust) are solved using for the temperature profile in the crust an analytical iteration procedure starting from the steady state solution, as already proposed by Savino and Siegel (1969).

2.3 Substrate model

A specific 3D heat transfer module is used, solving the heat transfer equation in the solid substrate. A fine meshing of the substrate is used near the melt-substrate interface, where the temperature gradient is large. The heat of fusion is taken into account in the specific energy of the material. These techniques enable a correct evaluation of the substrate ablation, which takes place when the substrate temperature becomes higher than its melting point. The code user imposes a thermal condition (fixed temperature or heat flux) at the external boundary, and a thermal resistance between the substrate and the melt. The system is solved using a classical alternate direction scheme.

2.4 Constitutive laws and models

The consequence of integrating the balance equations over the melt thickness is the need of constitutive laws to close the system.

As far as wall shear stress is concerned, a classical correlation is used, based on a Reynolds number with the hydraulic diameter equal to four times the melt height (free surface flow in a rectangular duct, with a small thickness in comparison with the width). For low Reynolds numbers, the laminar friction factor is 24/Re, whereas the turbulent coefficient is $0.083\ Re^{-0.25}$.

Concerning the heat transfer coefficients between melt and crusts, classical correlations are also used. For laminar flows the Nusselt number is equal to 7.6 (flow in a rectangular duct with constant wall temperature) and for turbulent flows the classical correlation $Nu = 0.023\ Re^{0.8}\ Pr^{0.4}$ is used. However, for metallic materials with low Prandtl number, specific correlations are used (Duchatelle & Vautrey, 1964) : $Nu = 6.0$ for laminar flows ; $Nu = 5.14 + 0.0127\ Re^{0.8}\ Pr^{0.8}$ for turbulent flows.

The surface tension effect is considered at the leading edge of the spreading melt. The front progression is allowed only if the melt thickness is higher than the static limiting value, $(2\sigma/\rho g)^{1/2}$, obtained by balancing the gravity forces and the surface tension forces, with the hypothesis of a radius of curvature at the front equal to the melt thickness.

3. DISCUSSION

3.1 Equations integrated over the melt thickness

The use of equations integrated over the melt thickness does not give any information concerning either the velocity or the temperature profiles. Low temperatures at the bottom and

at the surface of the melt may lead to a high viscosity at these locations, and consequently to reduced local velocities. These local phenomena are not accessible with the model implemented in THEMA. The code uses global correlations of wall shear stress and heat transfer coefficient on one hand, and separate crust models on the other hand. However a simplified temperature profile is also obtained with THEMA (fig. 1, homogeneous melt with bottom and top crust).

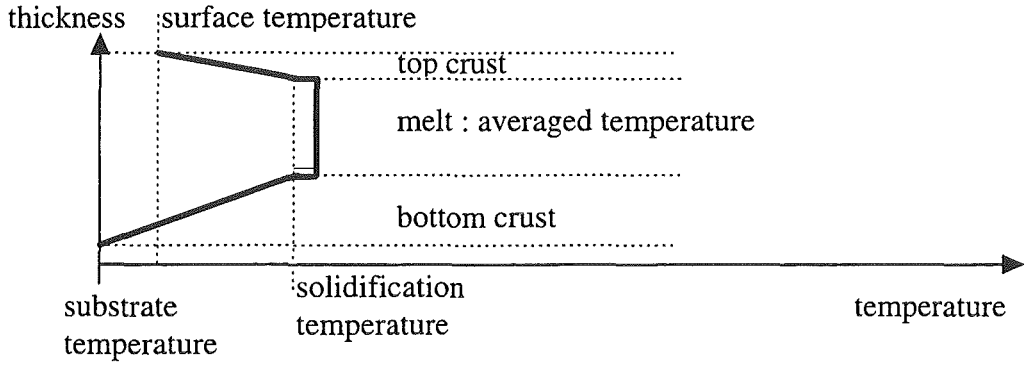

Fig.1 : Temperature profile in THEMA for a homogeneous melt with bottom and top crusts.

However a major advantage of the integrated equations is the low run times and the few numerical stability problems compared to a fully 3D model, which calculates a temperature and a velocity profile.

3.2 Solidification effects

In THEMA, solidification is accounted for both through viscosity and crust formation. The code user can select a viscosity model among several, depending on the solid fraction, which is a function of the melt temperature. At the present time the formation of crusts is restricted to a reduction of the amount of the flowing melt. Clearly specific developments are still needed concerning the behavior of the upper crust such as mechanical effects at the front. A key parameter for the solidification phenomena is the temperature at the crust-melt interface. This temperature is the melting temperature for eutectic materials and is taken as the solidus temperature for non eutectic cases. Actually a temperature between liquidus and solidus corresponding to a sufficiently high viscosity or solid fraction would be preferable, in accordance with the viscosity model.

3.3 Relevance of the constitutive laws

Classical constitutive laws are used for the wall shear stress as well as for the heat transfer coefficients. These laws are related to rectangular channels with constant physical properties of the fluid. However, during non isothermal spreading the temperature in the bulk of the melt is higher than at the boundaries and the physical properties are far from constant. In such cases, the classical constitutive laws are generally modified using either physical properties calculated at the film temperature (mean value between wall and bulk temperature), or with a correcting factor written in terms of a viscosity or a temperature ratio.

An other point is that the classical correlations used in THEMA are appropriate for fully developed flows, whereas spreading is limited in space and time. The use of correlations based upon boundary layers formulations was investigated. However for most of the situations

encountered, the boundary layer thickness is shown to reach the melt thickness within a distance corresponding to one or two times the melt thickness, then indicating that fully developed flow correlations can be used (Spindler and Veteau, 1998). These correlations are based upon a hydraulic diameter equal to four times the melt thickness (free surface flow assumption). In the presence of an upper crust it would have to be modified to account for the shear stress between the melt and the upper crust.

The surface tension effects could also be improved by using a dynamic formulation including the front velocity, and changing the radius of curvature at the front.

The assessment work under progress will show if the model and correlations are relevant enough to model the spreading phenomena, with the relevant accuracy.

4. ASSESSMENT OF THEMA CODE

4.1 Presentation of the assessment work

The classical methodology adopted for assessment of THEMA code is to validate separately the models or correlations, as far as possible. This task was started by considering hydraulic tests (without heat transfer effects) performed on the CORINE facility (CEA-Grenoble) with water-glycerol mixtures at various viscosities and with liquid metals with low melting point, to assess the friction model and surface tension effects at the front. It was found (Spindler & Veteau, 1998) that the constitutive laws used give very satisfactory agreement with experiments.

Then attention was focused on spreading with formation of a bottom crust. Comparisons were made with known solutions of different problems related to solidification of a moving warm liquid on a cold wall, thermal shock and conduction in the bottom substrate with possible surface ablation, and also with CORINE tests (Spindler & Veteau, 1998). It was very useful to adjust numerical parameters such as time steps and size of the meshes in the substrate and to check the satisfactory running of the code in computing bottom crust growth and thermal behavior of the substrate.

The logical continuation of this work would have been to validate the upper crust model using the CORINE tests with heat transfer at the top, and also to assess the viscosity models with the CORINE experiments conducted with non-eutectic materials. However the limited manpower and the constraints of the 4th Frame Work Program of the European Union lead to begin the assessment work using global tests with medium and high temperature materials, where the measurements are more limited than in the CORINE tests performed with low temperature simulating materials.

In the present paper, the assessment of THEMA (version V2.4mod1b) using different tests performed within the frame of the 4th FWP of the EU is presented. Details of these experiments are presented in the references, hence just some indications are presented here. For all the simulations, the solidification temperature (interfacial temperature between melt and crust) is the solidus temperature and the upper crust is supposed motionless. The Thomas viscosity model is used as reference (Thomas, 1965). Most of the physical properties used are those obtained from the GEMINI2 physico-chemistry code (Chevalier and Cenerino, 1992).

4.2 KATS12 and KATS14 iron tests

KATS12_I and KATS14_I are performed at Forschungszentrum Karlsruhe (Fieg et al, 1999). Due to the different injection devices for the two tests, different inlet conditions are used for the simulation with THEMA. For KATS12_I the velocity is imposed at the first cell edge, with a linearly decreasing value from 2.73 m/s (corresponding to 5.9 l/s) to 0 in 6.6 s. The initial fluid superheat is 360 K. For KATS14_I, a constant mass flow rate of 7 kg/s (corresponding to 1.1 l/s) during 22 s is imposed, with a superheat of 640 K. The basic character of these tests is spreading of a pure material, without any melting interval.

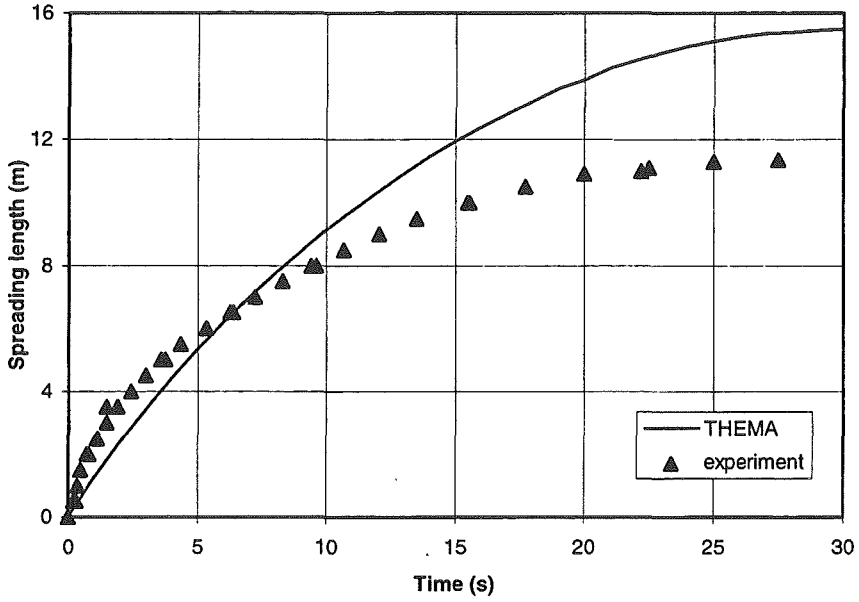

Fig. 2 KATS12-I : spreading length versus time. Experiment and THEMA.

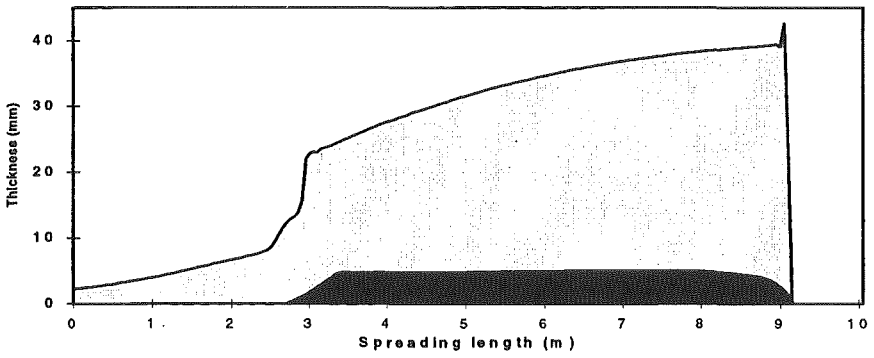

Fig. 3 KATS12_I : melt and crust thickness versus spreading length, at 10 s (THEMA).

For KATS12_I the front progression is under-predicted during the pouring duration and over predicted after (fig. 2). Due to the high thermal conductivity of metal, the bottom crust in the inlet region appears in the first seconds, then melts (fig. 3). The simulation with THEMA gives a hydraulic jump during the pouring duration (fig. 3), and a backwards flow beginning at about 12 s, which is clearly miss-predicted by the code, and then gives an overestimation of the spreading length.

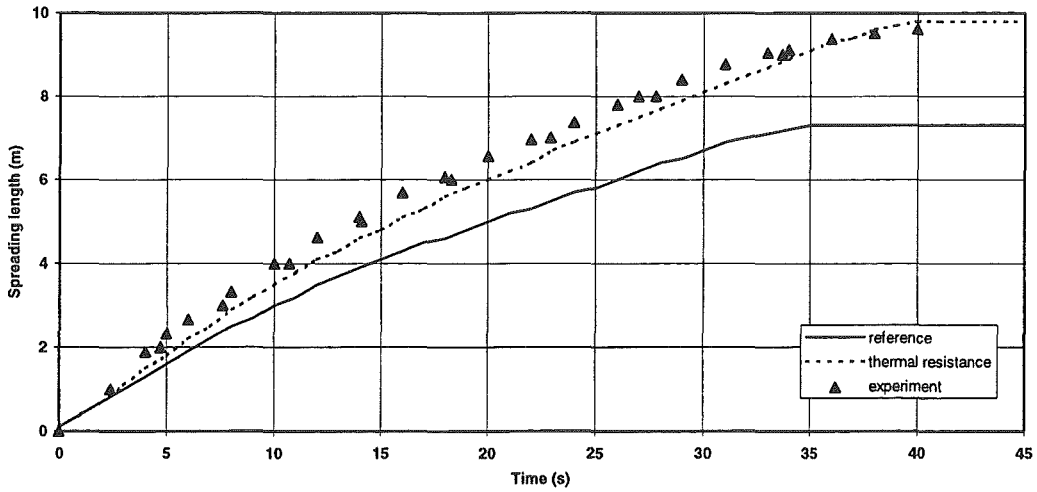

Fig. 4 KATS14-I : spreading length versus time. Experiment, THEMA reference case and THEMA with thermal resistance.

For KATS14_I the front progression is under-predicted (fig. 4). A better result is obtained with a thermal resistance (4.10^{-4} m^2.K/W) between the crust and the substrate. With the thermal resistance, the bottom crust thickness is reduced at the front and the spreading length is increased. Like for KATS12_I, no upper crust appears except at the very end of the simulation. The difference with KATS12_I concerning the thickness profiles is due to the higher mass flow rate for KATS12_I (fig. 5).

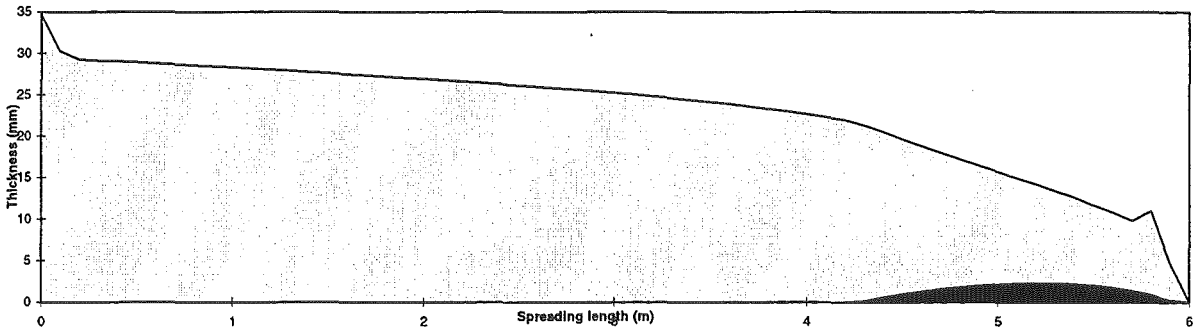

Fig. 5 KATS14_I : thickness of the melt and of the bottom crust versus spreading length, at 20 s. THEMA with thermal resistance.

4.3 KATS12 and KATS14 oxide tests

KATS12 and KATS14 are performed with alumina at Forschungszentrum Karlsruhe (Fieg et al, 1999). For KATS12 the velocity is imposed at the first cell edge, with a linearly decreasing value from 2.9 m/s (corresponding to 11.1 l/s) to 0 in 10 s. The initial fluid superheat is 100 K. For KATS14, a constant mass flow rate of 4.8 kg/s (corresponding to 1.6 l/s) is imposed during 37 s, with a superheat of 30 K.

For KATS12, the front progression is first under-predicted by THEMA but the final front position is in good agreement with the experiment (fig. 6). For the oxidic melt the bottom crust remains all along the spreading length (fig. 7). The top crust appears at about 12 s. During the pouring duration a hydraulic jump is predicted (fig. 7).

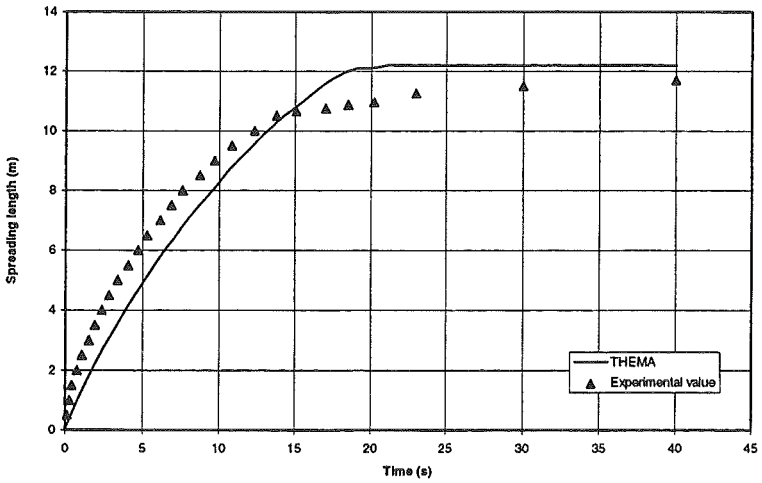

Fig. 6 KATS12 : spreading length versus time. Experiment and THEMA.

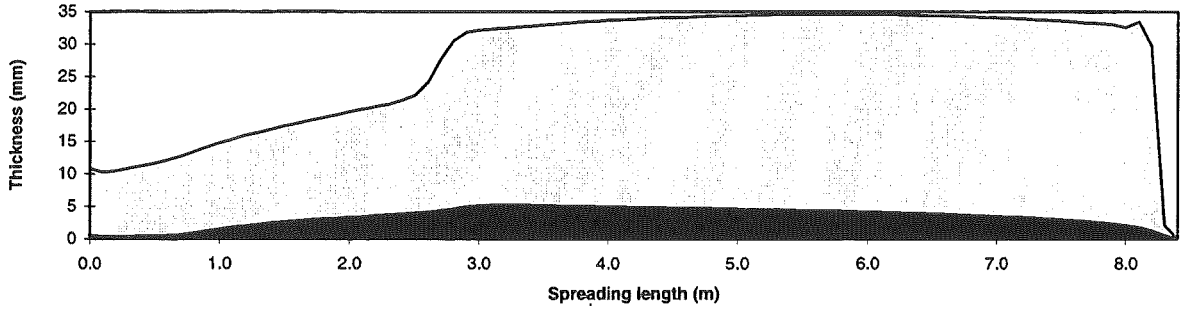

Fig. 7 KATS12 oxide : melt and crust thickness versus spreading length at 10 s (THEMA).

For KATS14 the front progression is slightly over-predicted (fig. 8). The top crust appears at about 8 s. The constant mass flow rate gives a very regular thickness profile (fig. 9). Due to the low inlet superheat, the inlet temperature is a sensitive parameter regarding the front progression unlike KATS12 test where the superheat is larger.

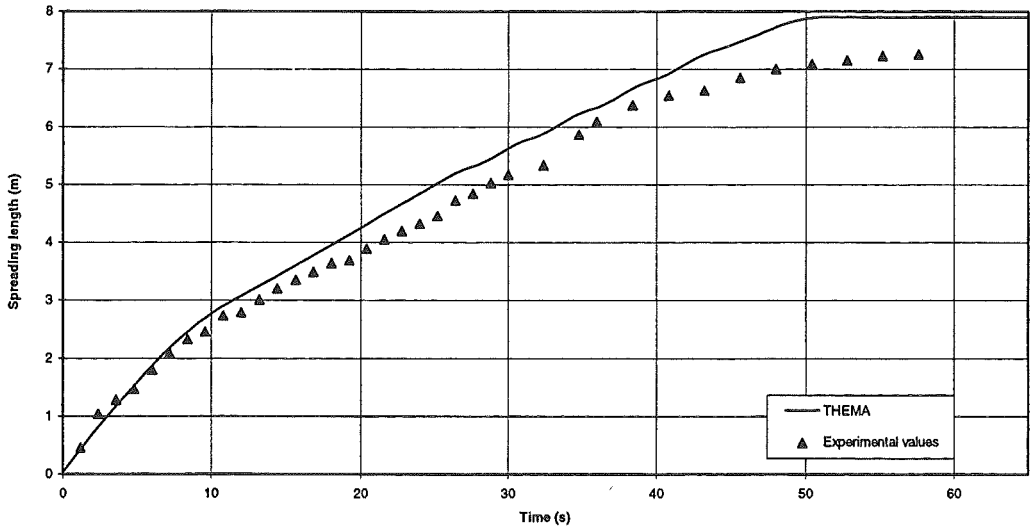

Fig. 8 KATS14 : spreading length versus time. Experiment, and THEMA.

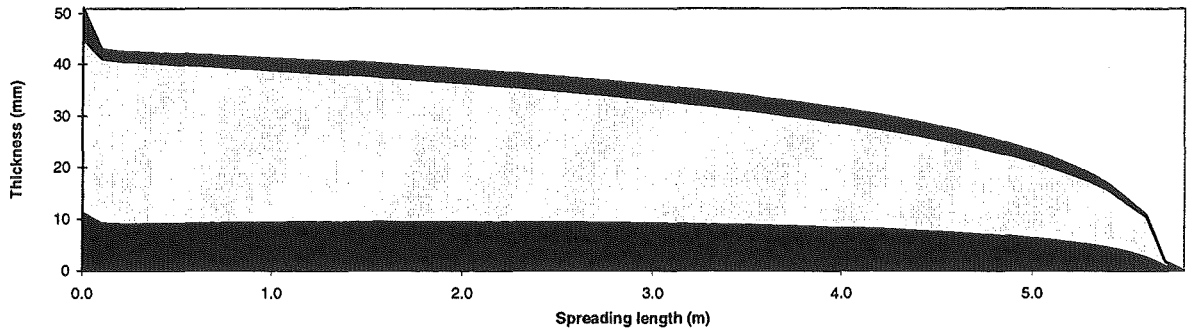

Fig. 9 KATS14 : thickness of melt and crusts versus spreading length, at 30 s (THEMA).

4.4 RIT tests

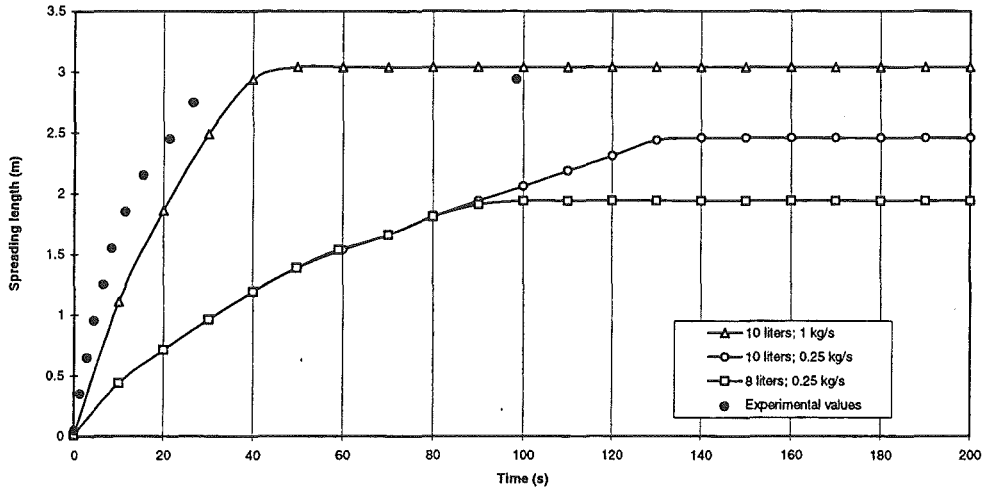

Fig. 10 RIT-3MDS-Ox1 : spreading length versus time. Experiment and THEMA (150 K superheat ; various total volume and flow rate).

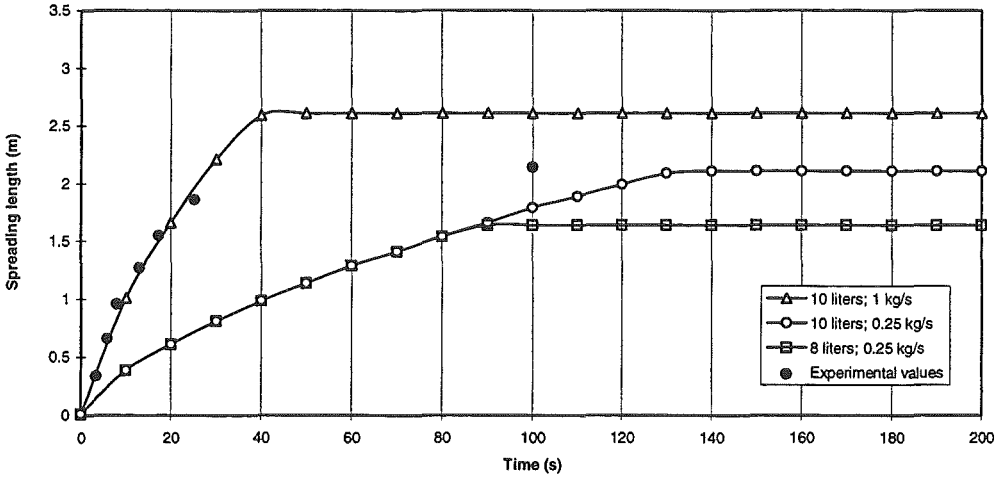

Fig. 11 RIT-3MDS-Ox2 : spreading length versus time. Experiment and THEMA (50 K superheat ; various total volume and flow rate).

RIT tests are performed with a binary oxidic salt at the Royal Institute of Technology of Stockholm (Sehgal et al, 1997). For RIT-3MDS-Ox1 test the inlet superheat is 150 K and for RIT-3MDS-Ox2 the superheat is 50 K. The simulation with THEMA has been run using different sets of conditions because some experimental data are not well known : the total amount of melt (8 and 10 liters, corresponding to 22.4 and 28 kg), and the inlet mass flow rate (0.25 and 1 kg/s). The difference between the calculated and the experimental front velocity is considerably reduced in case of higher injection rate, and the final spreading length is well predicted for the 150 K superheat case, but overestimated for the 50 K superheat case (fig. 10 and 11). The substrate temperature is well predicted during the spreading, but overestimated at the end of the simulation when all the melt is solidified (fig. 12). The models of THEMA (convection heat transfer) no more apply then.

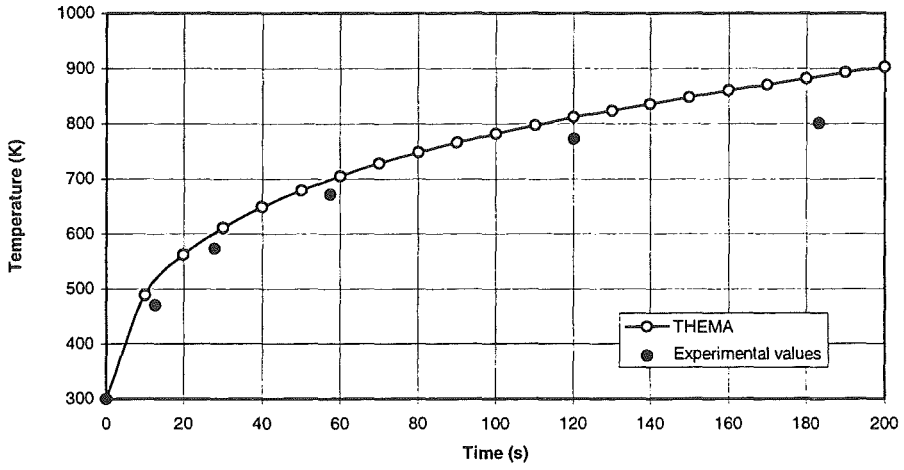

Fig. 12 RIT-3MDS-Ox1 : substrate temperature at distance 5 cm from inlet versus time. The substrate temperature is not much sensitive to the mass flow rate and superheat (THEMA with 10 liters and 1 kg/s).

4.5 FARO test

The FARO-L26S test has been performed at the Joint Research Center Ispra (Magallon and Tromm, 1999), with a mixture of 80 % of UO2 and 20 % of ZrO2. The main characteristic of this material is the low solidification temperature interval (54 K according to GEMINI2). The inlet superheat is 7 K and the total mass of corium is 130 kg. The mass flow rate is irregular ; the maximum mass flow rate is 21 kg/s and the pouring duration is 9.7 s.

Good results are obtained concerning the substrate temperature (fig. 13) with a thermal contact resistance of 3.5 m^2.K/W between the lower crust and the substrate. The spreading length is very sensitive to the inlet temperature (fig. 14). The nominal value is 2923 K, with an uncertainty of 50 K (the lowest value is then 2873 K, within the solidification interval), which is the same order of magnitude as the solidification interval. Moreover the solidus and liquidus temperatures are not well known (differences between GEMINI2 results and values recommended by the experimentalists). With a short solidification interval the solid volume fraction increase occurs within a very narrow temperature range, hence the predicted spreading length is very sensitive to the inlet temperature on one hand and to the viscosity model on the other hand (fig. 14). The Stedman (1990) correlation has an adjustable coefficient : if the solidification is supposed to occur when the solid volume fraction amounts

50 % (i.e. at 2877 K, according to GEMINI2), the melt is solid at the lowest bound (2873 K) inlet temperature. A simulation was made with THEMA using a limit of 60 % in Stedman correlation, which gives a spreading velocity close to the measured one (fig. 14).

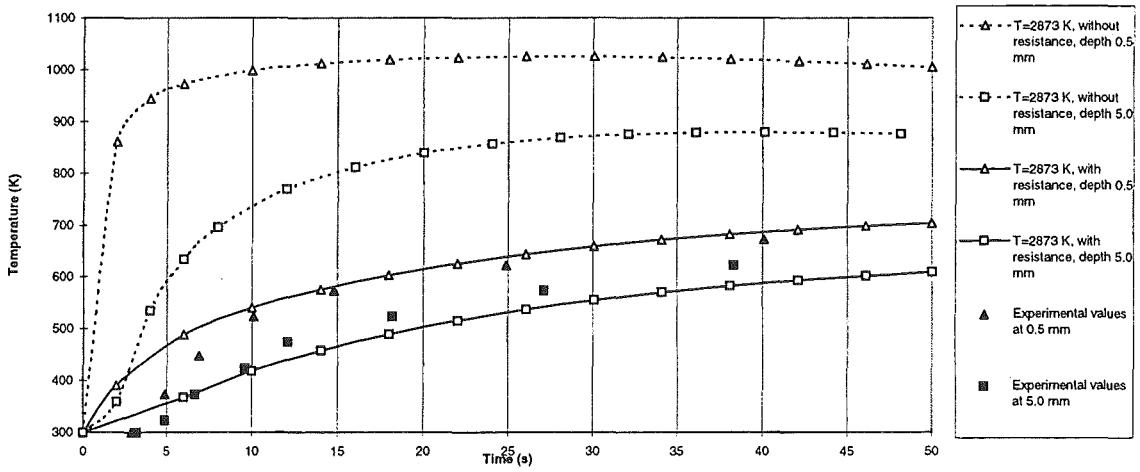

Fig. 13 FARO-L26S : substrate temperatures at two substrate depth, at distance 0.15 m from inlet versus time. THEMA with and without thermal resistance.

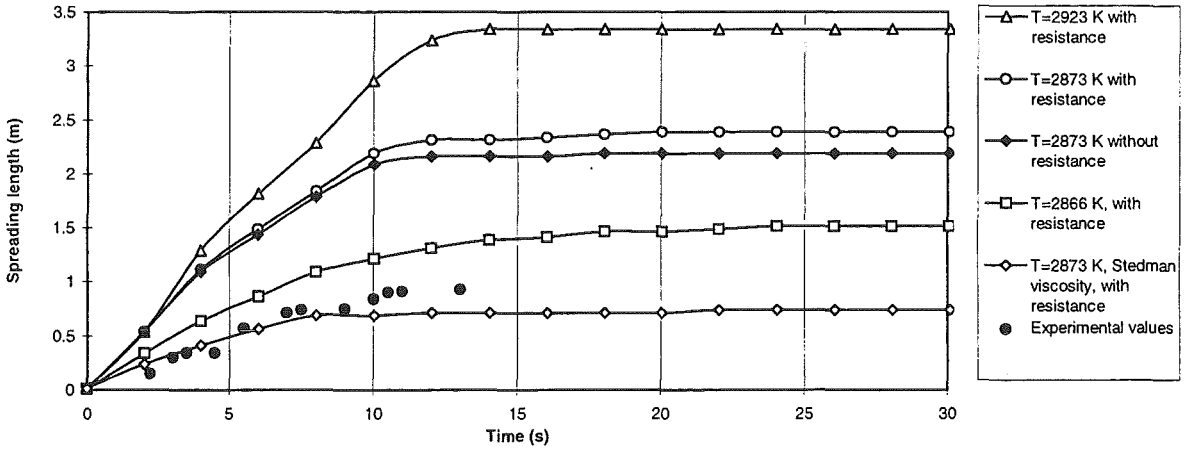

Fig. 14 FARO-L26S : spreading length versus time. Experiment and THEMA results with various inlet temperatures, thermal resistances and viscosity models.

It must be noticed that the spreading length is slightly affected by the substrate behavior, since a lower crust always forms over the substrate ; the interfacial temperature between melt and crust is independent from the substrate temperature.

4.6 VULCANO tests

Two VULCANO tests performed at CEA-Cadarache (Cognet et al, 1999) have been simulated. Test VE07 involves corium containing hafnia instead of urania, and test VEU1 involves corium containing urania. The other main components are zirconia, silica, and iron oxides. Hafnium is not included in the data base of GEMINI2 and is supposed to have the same behavior as uranium. A main feature of the materials is the large solidification interval (about 1000 K).

The number of parameters with a significant uncertainty range (corium physical properties, model parameters, experimental conditions) is quite large. Therefore an extended uncertainty analysis combining up to 11 parameters and involving 128 calculations was performed. The correlation of Shaw (1969) is used for the melt viscosity in the mushy zone $\mu = \mu_0.\exp[A.(T_{liquidus}-T)]$, fitted on an Arrhenius type model and a dependence of solid fraction versus temperature determined from GEMINI2 calculations (Ramacciotti et al, 1999). The results show that the parameters governing corium spreading are the viscosity model including the liquidus temperature on one hand, and the inlet temperature and mass flow rate (two possible high and low experimental flow rates) on the other hand

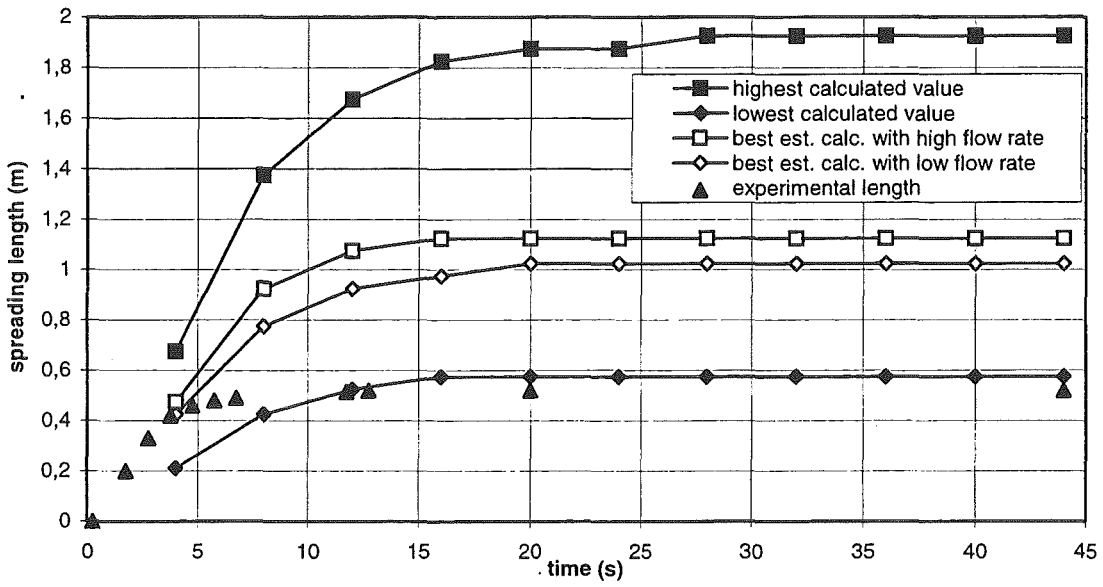

Fig. 15 VE07 : spreading length versus time. Experiment and THEMA results. The best estimate viscosity law is $\mu = 0.019.e^{0.015.(2370-T)}$ $kg.m^{-1}.s^{-1}$.

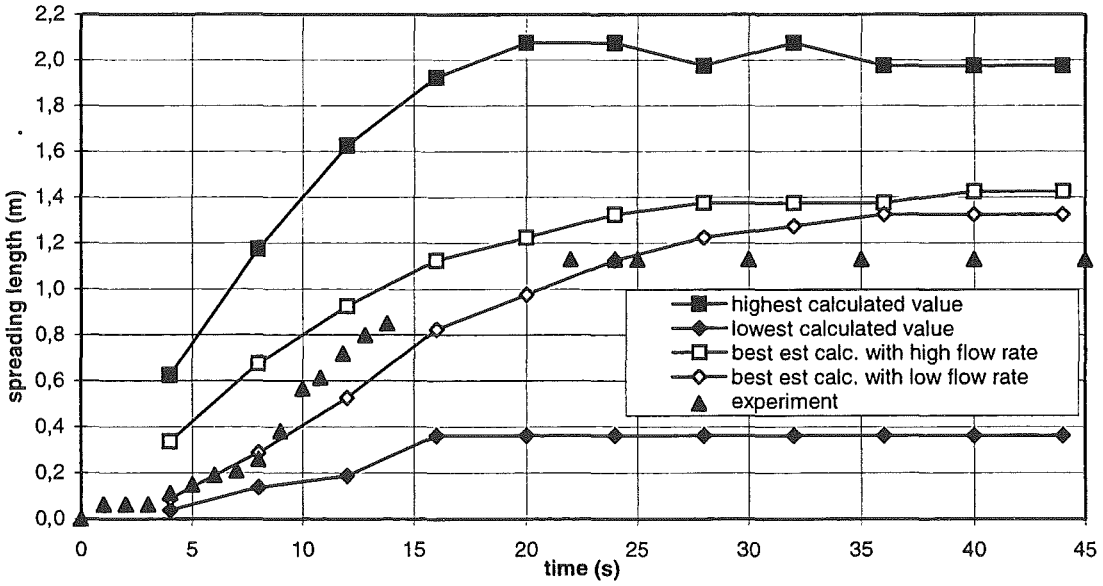

Fig. 16 VEU1 : spreading length versus time. Experiment and THEMA results. The best estimate viscosity law is $\mu = 0.037.e^{0.024.(2250-T)}$.

The highest and lowest calculated results are presented (obtained with various combinations of the different parameters), together with the results obtained with the best estimate parameters and with the high and low flow rates (fig. 15 and 16). Better results are obtained for VEU1 than for VE07. This discrepancy can be partly explained by the use of hafnia for VE07 which physical properties, and especially the liquidus temperature are not precisely known. Reasonable agreement with experiment is obtained concerning the substrate temperature (fig. 17).

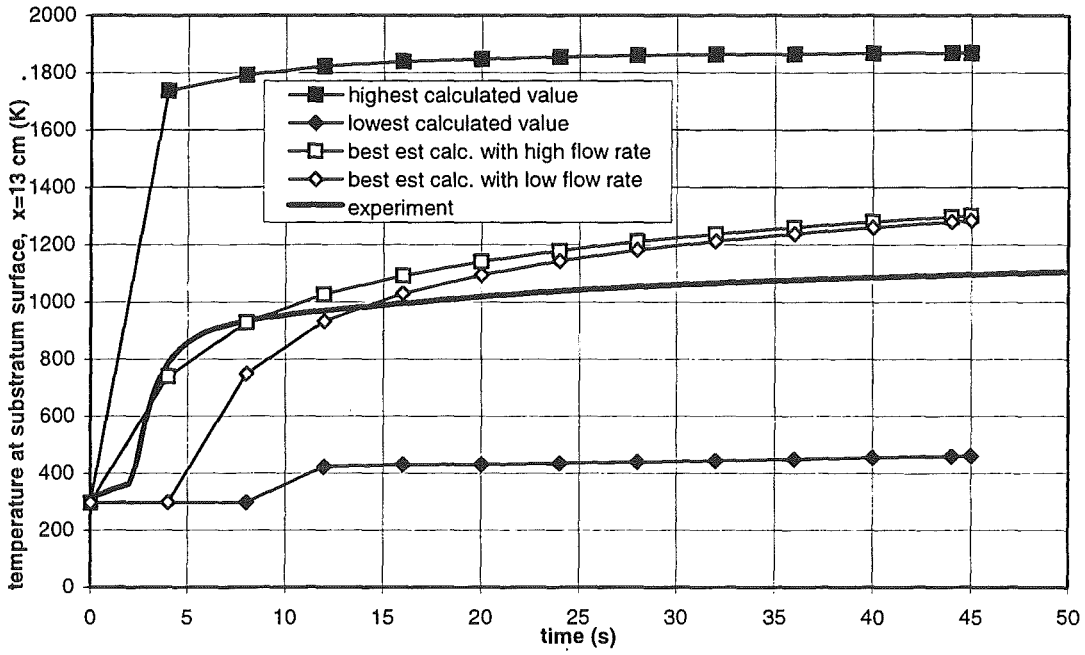

Fig. 17 VEU1 : temperature at the substrate surface at 13 cm from the inlet, versus time. Experiment and THEMA results. The best estimate thermal resistance is 3.10^{-3} K.m^2/W.

5. CONCLUSION

The THEMA code is devoted to the simulation of corium spreading. It uses equations integrated over the melt thickness. Viscosity increase and crust formation are taken into account, but not the mechanical behavior of the crust at the front. Simple constitutive laws are used. THEMA is able to simulate spreading of iron and of oxide mixtures (RIT, KATS, FARO and VULCANO tests). Encouraging results are obtained concerning the spreading velocity as well as the substrate temperatures. The code assessment needs a good accuracy of the measurements concerning the inlet conditions (temperature and mass flow rate) in the spreading experiments.

NOMENCLATURE

g	gravity acceleration	μ	viscosity
Nu	Nusselt number	ρ	mass density
Pr	Prandtl number	σ	surface tension
Re	Reynolds number		

ACKNOWLEDGMENTS

The THEMA code is developed within the frame of an agreement between CEA and EDF ; the assessment work presented here was performed in the frame of the Corium Spreading and Coolability work of the 4th Frame Work Program of the European Union.

REFERENCES

Chevalier P.Y., Cenerino G., 1992, Thermodynamic data bases and calculation code adapted to the modelling of molten core concrete interaction phenomena, OECD CSNI Specialist Meeting on Molten Core Debris-Concrete Interactions, Karlsruhe, Germany.

Cognet G., Laffont G., Jegou C., Pierre J., Journeau C., Cranga M., Sudreau F., 1999, The VULCANO Ex-Vessel Programme, OECD, NEA Workshop on Ex-Vessel Debris Coolability, November 16-18, 1999, Karlsruhe, Germany.

Duchatelle L., Vautrey J., 1964. Détermination des coefficients de convection d'un alliage en écoulement turbulent entre plaques parallèles, *Int. J. Heat Mass Transfer*, **7**, 1017-1031.

Eberlé P., 1997, Modélisation physique et numérique de l'étalement d'un fluide avec solidification dans le cadre des études de sûreté pour les réacteurs à eau sous pression, Thèse de l'Université Joseph Fourier, Grenoble 1.

Fieg G., Massier H., Schütz W., Stegmaier U., Werle H., 1999, KATS Experiments to simulate Corium Spreading in the EPR Core Catcher Concept, OECD, NEA Workshop on Ex-Vessel Debris Coolability, November 16-18, 1999, Karlsruhe, Germany.

Magallon D., Tromm W., 1999, Dry and Wet Spreading Experiments with Prototypic Material at the FARO Facility, OECD, NEA Workshop on Ex-Vessel Debris Coolability, November 16-18, 1999, Karlsruhe, Germany.

Ramacciotti M., Journeau Ch., Sudreau F., Cognet G., 1999, Viscosity model for corium melt, International Topical Meeting Nuclear Reactor Thermalhydraulics, Nureth 9, October 4-8, San Francisco.

Savino J.M., Siegel R., 1969, An analytical solution for solidification of a moving warm liquid onto an isothermal cold wall, *Int. J. Heat Mass Transfer*, **12**, 803-809.

Sehgal B.R., Dinh T.N., Green J.A., Konovalikhin M., Paladino D., Leung W.H., Gubaidullin A.A., 1997, Experimental investigation of Melt Spreading in one-dimensional Channel, RIT Report EU-CSC-1D1-97.

Shaw H.R., 1969, Rheology of basalts in the melting range, *J. Petrology*, **10**, 510-535.

Spindler B., Veteau J.M., 1998. Status of the Assessment of the Spreading Code THEMA Against the CORINE Experiments, SARJ Meeting 1998, Nov. 4-6, Tokyo, Japan.

Stedman J., 1990, Rheology of composite ceramic injection moulding suspensions, *J. of Materials Science*, **25**, 1833-1841.

Thomas D., 1965, Transport characteristics of suspensions, *J. Colloid Sciences*, **20**, 267-277.

OECD Workshop on Ex-Vessel Debris Coolability
Karlsruhe, Germany, November 15 - 18, 1999.
Organised in collaboration with
Forschungzentrum Karlsruhe (FZK) GmbH

SYNTHESIS OF THE VALIDATION OF THE CROCO V1 SPREADING CODE

B. D. Michel *, B. Piar, F. Babik, J.-C. Latché
Institut de Protection et de Sûreté Nucléaire – DRS/SEMAR/LECTA
Centre d'Études de Cadarache – 13108 St-Paul lez Durance Cedex – FRANCE

G. Guillard
Communication & Systèmes – Systèmes d'Information
Unité Opérationnelle Ingéniérie Scientifique
Centre d'Études de Cadarache – 13108 St-Paul lez Durance Cedex – FRANCE

C. De Pascale
Commissariat à l'Énergie Atomique – DRN/DTP/SMET/LMTA
Centre d'Études de Cadarache – 13108 St-Paul lez Durance Cedex – FRANCE

KEY WORDS

code assessment – severe accident – core catchers – corium spreading – free surface – semi-solid flow

ABSTRACT

A research program aimed at the modelling of the corium ex-vessel behaviour is in progress in IPSN (Institut de Protection et de Sûreté Nucléaire) since 1994, to assess the safety of future PWRs core catchers. The resulting code, named CROCO, is briefly presented here under its first version mainly devoted to the spreading phase. The numerical procedure has been verified on academic problems (namely dam break problems) exhibiting analytical solutions. Moreover, validation tests have been successfully performed against CORINE experiments using glycerol and non-eutectic Bismuth-Tin alloy simulant, KATS tests using high temperature simulants and the first real material VULCANO test. Both verification and validation tests show a satisfactory agreement between CROCO V1.0 computations and reference results.

1 INTRODUCTION

For the future European Pressurized Reactor (EPR), the corium confinement within the reactor cavity during a postulated severe accident, leading to a vessel failure, is required. Thus, a research program aimed at the modelling of the corium ex-vessel behaviour is in progress in IPSN since 1994 to assess the safety of core catcher concepts proposed by designers. To achieve this goal, the development of a code named CROCO was initiated. On completion, it should describe both the initial spreading phase and the stability or pouring of possible melt accumulations. The first version, however, is mainly devoted to spreading modelling.

*Corresponding author. E–Mail : deletie@sand.cad.cea.fr

The aim of this paper is to draw a synthesis of the validation work performed with this version, including computations of spreading academic problems (namely dam break problems), CORINE experiments using glycerol and non-eutectic Bismuth-Tin alloy simulant, KATS high temperature simulant and first real material VULCANO test.

2 THE ASSESSMENT PROGRAM

2.1 CROCO V1 description

The first version of the CROCO code is mainly devoted to the spreading phase with a particular emphasis on the modelling of the solidification processes. The key points are stressed in the following :

- The computational domain is two dimensional, either axisymmetric or cartesian.
- The fluid flow is laminar, incompressible, Newtonian, nonisothermal and exhibits a free surface. Moreover, the thermal coupling of the fluid with the basemat is taken into account.
- The fluid is a semi-solid multiconstituant mixture such that there exists a temperature interval $[T_{\text{sol}}, T_{\text{liq}}]$ for which solid phases coexist with liquid phases at thermodynamic equilibrium. The solidification is modelled using the technique of volume averaging over Representative Elementary Volumes, with the following assumptions :
  - Homogeneous model : the solidifying flow is viewed as a slurry whose viscosity increases with the solid fraction. Macrosegregation is ignored.
  - The enthalpy is a function of the temperature. No *a priori* dependence is assumed. Thus phase change is described with the enthalpy method.
  - The effective mixture dynamic viscosity is a function of the solid fraction x_{sol} and of the temperature :

$$T_{\text{sol}} < T < T_{\text{liq}} \quad : \quad \mu^* = \underbrace{\mu_{\text{liq}}(T_{\text{liq}})}_{\text{liquid viscosity}} \times \underbrace{\mu_{\text{r}}(x_{\text{sol}}(T), T)}_{\text{relative viscosity}}$$

  - The solid fraction $x_{\text{sol}}(T)$ and the enthalpy $h(T)$ have to be evaluated at the overall composition of the fluid before running CROCO.
  - The effective mixture thermal conductivity tensor is a simple scalar function of the temperature.

Two possibilities are offered to the user for solving the hydrodynamic problem : in the first one, the general equations are solved without any geometrical approximation whereas the asymptotic expansion of the momentum equation is considered under the thin flow approximation in the second one. All the computations presented here are performed using this latter hypothesis, as the flow characteristic height is always much smaller than its horizontal dimension in spreading experiments. As far as the thermal problem is concerned, the energy balance equation is always considered under its more general form since none of its term is made negligible by the thin flow approximation.

To cope with the solution of Navier-Stokes equations on a fluid domain varying with time, the CROCO code uses an original numerical method :

- The choice has been taken to use a a non-staggered *Eulerian* grid, in order to deal with flow geometry and fluid motion as general as possible.
- The equations are discretised in time by splitting each operator in its convection and diffusion part ; at each time step, the solution of the convection (advection) equations, in the explicit velocity field, by a forward characteristic technique provides an estimate of the new free surface together with an intermediate approximation of the unknowns defined on the advanced fluid domain ; then diffusion problems (Stokes problem and conduction) are solved by a modified finite element method using low order approximation spaces (Q1-Q0 discretisation for the velocity and pressure fields, Q1 elements for the temperature) on this fixed fluid area.
- A special procedure has been developped for the treatment of the meshes which are cut by the free surface ; it allows to keep the temperature approximation linear, which is of prime importance to represent sharp gradients induced by radiative cooling.

A more detailed description of the CROCO code can be found in [Piar et al., 1999]

2.2 Presentation of the assessment steps

CROCO V1.0 has been tested against a variety of problems that can be sorted in two categories : *verification tests* whose purpose is to check that the code does what it is supposed to and *validation tests* whose purpose is to determine to what extent the mathematical formulation implemented in the code represents the physical reality.

An overview of the associated tests matrix will be given below, and some of them will be discussed in the next part.

- Verification Tests exhibiting an analytical solution

  Isothermal release of a quantity of fluid (either fixed or linearly increasing with time) in vacuum by the sudden removal of a vertical barrier :

  Test 1 inertial regime [Vila, 1986].
  Test 2 viscous regime [Huppert, 1982].

- Hydrodynamical spreading

  CORINE experiments are performed at low temperature, typically less than 200°C, leading to a negligible radiative cooling at the free surface. In one of the two series studied with CROCO V1.0, the spreading area is at the same temperature as the fluid :

  Tests Series 2 : isothermal spreading of water-glycerol mixture on a plate (referenced as G95.5_1)

- Cooling Exclusively at the Basemat Interface

  The other experiment of the Test Series 2, and the other CORINE series are performed on a cold bottom plate :

Tests Series 2 : spreading tests of water-glycerol mixture on a cold bottom plate, which addresses the heat transfer mechanisms within a fluid whose viscosity is highly temperature dependent, but without solidification (referenced as G95.5_4) ;

Tests Series 4 : spreading under inert gas of a non eutectic BiSn alloy, which addresses the solidifying flow modelling and its rheological behaviour in the two phases region (referenced as Cu2Ne1, Cu2Ne2 and Cu2Ne3).

- Cooling at the Basemat Interface and at the Free Surface

  The considered experiments are performed at high temperature and the cooling rate at the free surface (mainly through radiative heat transfer) becomes comparable to the transfers at the basemat interface.

  KATS : spreading under inert gas of the oxidic phase of an alumina-iron thermite on a cold ceramic plate [Fieg et al., 1996] (referenced as KATS-12 and KATS-14)

  VULCANO : spreading under inert gas of a prototypical corium flow on a cold zirconia plate [Cognet et al., 1998] (referenced as VE-U1).

The experiments can also be classified thanks to two characteristic times : on one hand, it is possible to evaluate the transition time between inertial and viscous regimes. For a constant pouring rate, an expression is given, for a cartesian or an axisymmetric spreading, by [Huppert, 1982] :

$$t_{\text{tr}} = [\frac{q^2}{g}]^{\frac{2}{3}} \frac{\varrho}{\mu} \quad \text{or} \quad t_{\text{tr}} = [\frac{\varrho Q}{\mu g}]^{\frac{1}{2}}$$

where g ($\text{m}^2.\text{s}^{-1}$) stands for the gravity, ϱ (kg.m^{-3}) for the density, μ (Pa.s) for the viscosity, q ($\text{m}^2.\text{s}^{-1}$) for the surfacic cartesian pour rate and Q ($\text{m}^3.\text{s}^{-1}$) for the axisymmetric one.

On the other hand, an approximation of the penetration length of the temperature pertubation (at the interface between the fluid and the basemat) can be obtained by applying the model of two semi-infinite walls in perfect contact with constant thermophysical properties.

This length z_t (cf [Taine and Petit, 1989]) such that $T_{\text{fluid}}(z_t) = 0.99T^0_{\text{fluid}} + 0.01T^0_{\text{basemat}}$ is given by :

$$\text{erfc}(\frac{z_t}{2\sqrt{a_{\text{fluid}}t}}) = 0.01\frac{b_{\text{fluid}} + b_{\text{basemat}}}{b_{\text{basemat}}} \quad \text{with,} \quad \text{erfc}(u) = \frac{2}{\sqrt{\pi}}\int_u^{+\infty} \exp(-x^2)dx$$

where $b = \sqrt{\lambda \varrho C_p}$ is the effusivity and $a = \dfrac{\lambda}{\varrho C_p}$ stands for the diffusivity.

Let us then define a characteristic conduction time as the time at which the penetration length equals the average height l of the flow :

$$t_{\text{cond}} = \frac{l^2}{2 * x^2 * a_{\text{fluid}}} \quad \text{with,} \quad x \quad \text{such that} \quad \text{erfc}(x) = 0.01\frac{b_{\text{fluid}} + b_{\text{basemat}}}{b_{\text{basemat}}}$$

The comparison of these characteristic times to the spreading duration provides some information about the overall flow characteristics :

- if the inertial-to-viscous transition time is short compared to the transient duration, hydrodynamics are dominated by viscous strengths ; as a consequence, for instance with a constant inlet flow rate, the spreading velocity will significantly slow down with time while the height of the fluid increase. In the opposite case, inertia strengths are predominent and, in the same conditions, the velocity of the flow leading edge and the fluid height will approximately remain constant.
- If the conduction time is long compared to the transient duration, heat exchanges generate the development of thin boundary layers while the bulk fluid temperature remains unchanged. In the contrary case, the fluid cools down in some extent as a whole, as spreading progresses.

The main features of each test of the validation matrix are gathered in the Table 1 :

	CORINE Tests Series 2	CORINE Tests Series 4	KATS-12/14 oxidic melt	VULCANO VE-U1
geometry	axisymmetric	axisymmetric	cartesian	axisymmetric
Cooling at the bottom	G95.5_1 : no G95.5_4 : yes	yes	yes	yes
Cooling at the free surface	no	no	radiative	radiative
phase change	no	yes	yes	yes
contact resistance at the basemat	no	yes	no ?	yes
t_{tr}(s)	G95.5_1 : 2.6 G95.5_4 : 2.2	Cu2Ne1 : 27.6 Cu2Ne2 : 11.6 Cu2Ne3 : 14.7	KATS-12 : $\sim$ 100 KATS-14 : 8.1	2.7
t_{cond}(s)	1160	14.6	306	536
discharge time (s)	G95.5_1 : 43 G95.5_4 : 59	Cu2Ne1 : 14 Cu2Ne2 : 68.5 Cu2Ne3 : 38.4	KATS-12 : 10.4 KATS-14 : 37	17.5

Table 1: Validation matrix and characteristic times.

For all calculations, meshing convergence has been checked.

3 MAIN RESULTS

In this section, the results of the verification tests will be presented, then the CORINE Cu2Ne3, KATS-12 and VULCANO VE-U1 experiments. Indeed, the behaviour of these three flows is expected to be quite different :

- the conduction time of Cu2Ne3 is equal to its transition time and lower than the discharge time, so the expected spreading is viscous with overall temperature variations ;
- the conduction time of KATS-12, as its transition time, is much greater than its discharge time, so the expected spreading is inertial with thin thermal boundary layers ;
- VE-U1 is an intermediate case, with an expected viscous spreading and thin thermal boundary layers.

3.1 CROCO computation of Dam breaks

These verification tests are based on analytical and quasi-analytical solutions of the Navier Stokes equations for a two dimensional thin isothermal laminar spreading of an incompressible Newtonian fluid over a rigid horizontal surface.

Five calculations were performed :

- inertial flows : spreading of a constant volume of fluid in a rectangular channel ;
- viscous flows : spreading either of a constant volume of fluid or under a constant pour rate in an either cartesian or axisymmetric geometry.

The results are all very close to the analytical solutions. Only comparison between the free surface heights for the release of a constant volume in the case of an inertial (or viscous) spreading in a cartesian geometry are presented here (figure 1).

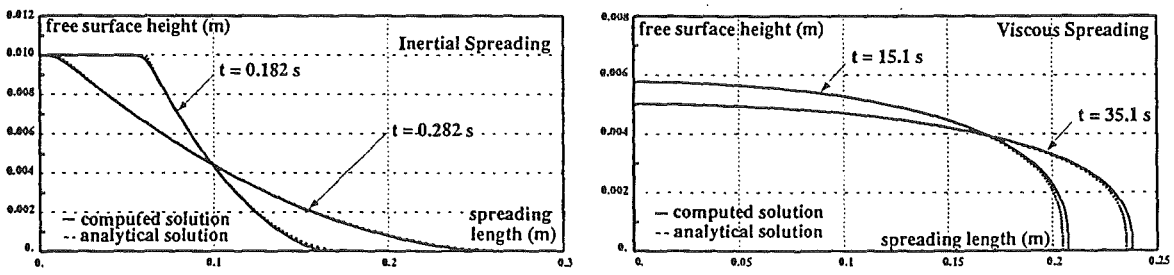

Fig. 1: Validation of CROCO V1.0 against inertial and viscous spreading.

3.2 CROCO computation of the CORINE Cu2Ne3 Test

A non eutectic Bismuth-Tin alloy is slumped, with a pouring rate of approximately 1 $\ell.s^{-1}$, in a 19° angular sector channel over an initially cold bottom plate. The spreading material is a metal at low melting point :

$$T_{sol} = 135°C = 408\,K \qquad T_{liq} = 190°C = 463\,K$$

which arrives in the spreading area at about 200 °C.

The liquidus viscosity is approximately 0.05 Pa.s, the conductivity about 35 $W.m^{-1}.K^{-1}$ and the density about 8000 $kg.m^{-3}$.

The temperature profile within the basemat and within the fluid are recorded during the experiment at various locations on the spreading area, showing and appreciable temperature drop across the interface. This effect results from the existence of a thermal contact resistance, and is modelled in CROCO by imposing the following boundary condition :

$$\left\{ \begin{array}{c} \text{conductive flux at the} \\ \text{Fluid-Basemat interface} \end{array} \right\} = h_b(T - T_b) \quad \text{with} \quad h_b = 2500\,W.m^{-2}.K^{-1}$$

where the numerical value of h_b has been fitted from the experimental temperature profiles. It should be stressed that this is the only parameter infered from the experimental results prior to the computation.

A typical comparison between the experimental results and the computed ones is given in figure 2.

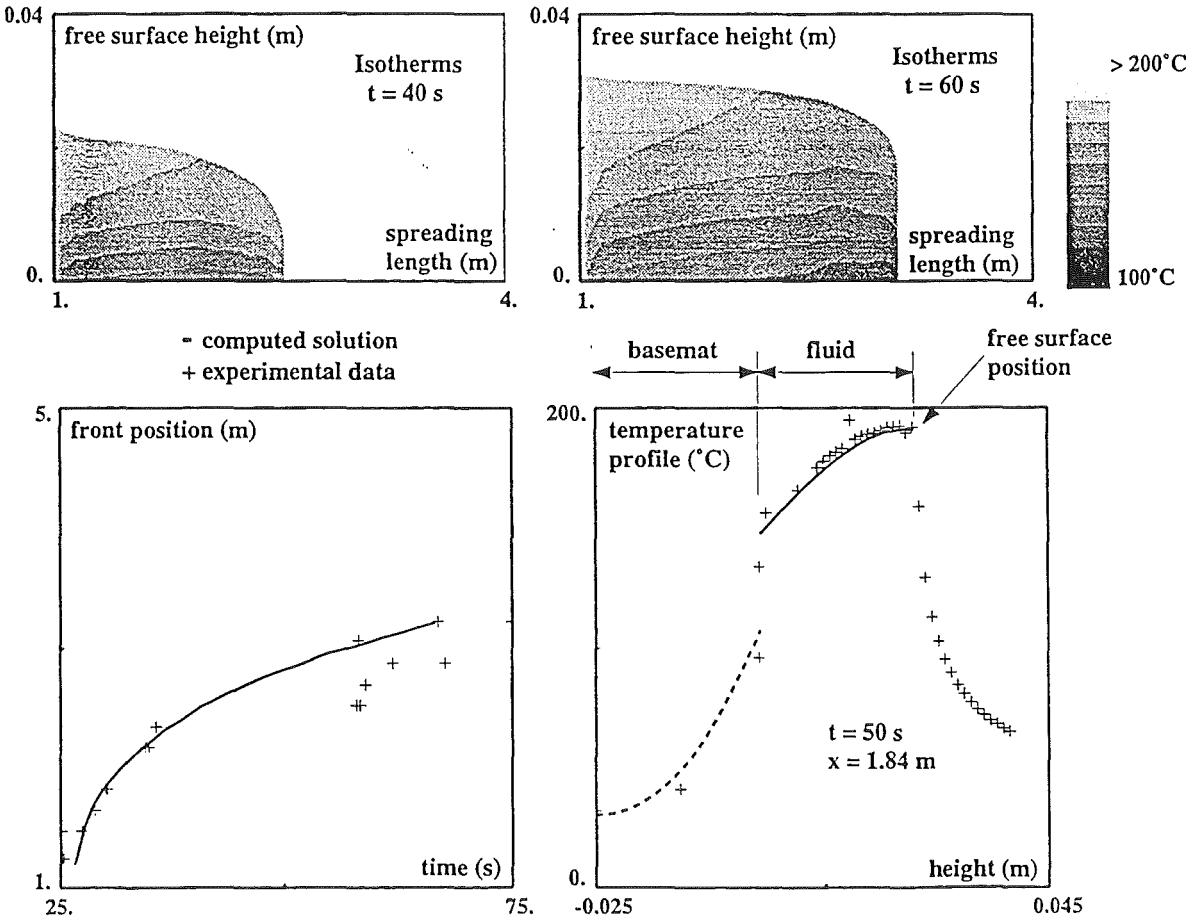

Fig. 2: Validation of CROCO V1.0 against CORINE Cu2Ne3 experiment.

3.3 CROCO computation of the oxidic KATS-12 spreading

The oxide phase of a thermite melt is slumped with a linearly decreasing pouring rate, of approximately 13 $\ell.s^{-1}$ at the beginning of the experiment, in a rectangular channel. The basemat is chemically inert. The inflow temperature is about 2300 K, which is to compare to T_{liq} = 2180 K (T_{sol} = 1888 K). The liquidus viscosity is approximately 0.2 Pa.s, the conductivity about 6 $W.m^{-1}.K^{-1}$ and the density about 3000 $kg.m^{-3}$.

A typical comparison between the experimental results and the computed ones is given in figure 3.

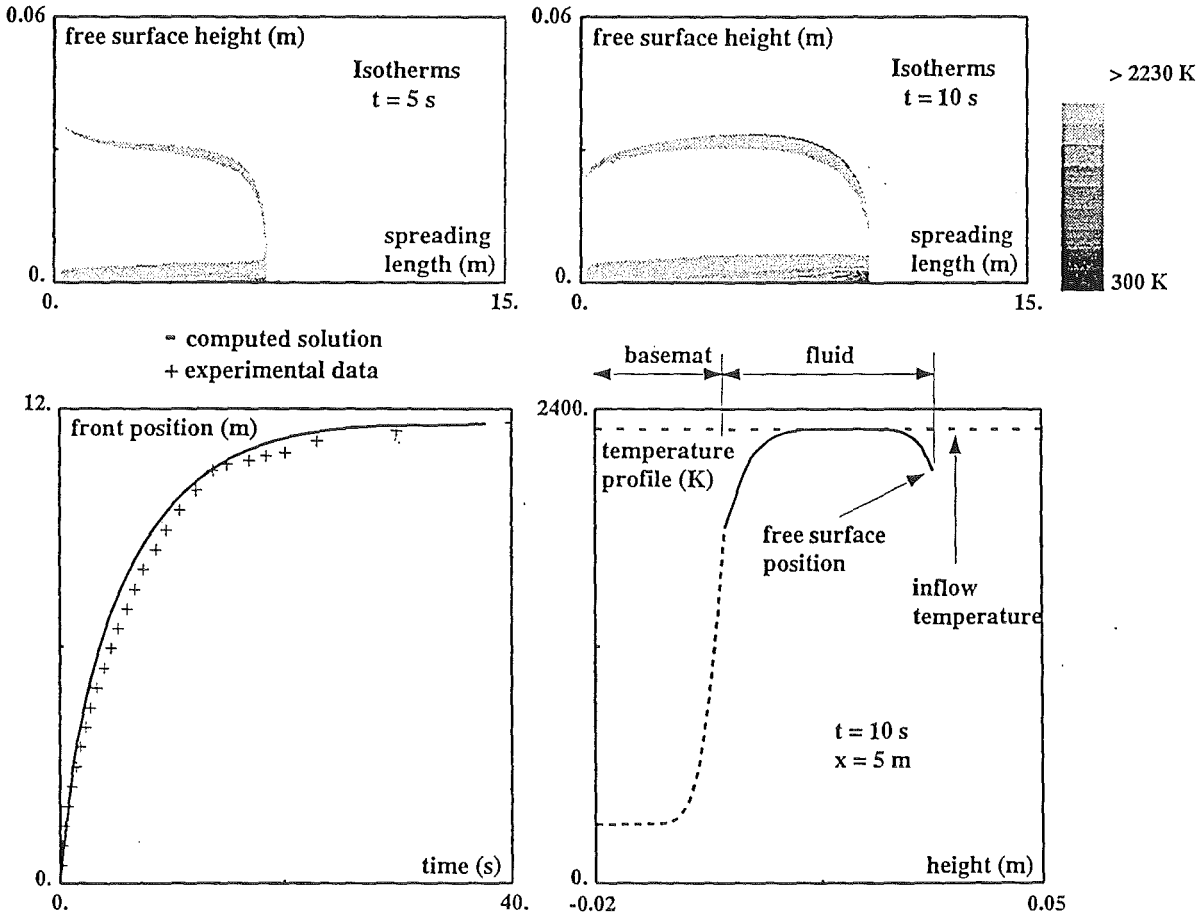

Fig. 3: Validation of CROCO V1.0 against oxidic KATS-12 experiment.

As expected, sharp temperature gradients appears at the free surface and at the melt/basemat interface.

Sensitivity studies show that :

- the estimated liquid fluid viscosity has a strong impact on the results ;
- on the opposite, the upper crust appears to be too thin to have any influence on the melt spreading.

3.4 CROCO computation of the VULCANO VE-U1 Test

A prototypical melt is slumped with non constant pouring rate of approximately $0.3\,\ell.s^{-1}$, in a 19° angular sector channel over an initially cold bottom plate. The inflow temperature at the spreading area is about 2100 K, which is to be compared to $T_{liq} = 2270\,K$ ($T_{sol} = 1300\,K$). It should then be stressed that the melt starts to spread in the liquid/solid zone so the computation will strongly depend on the model of the relative viscosity used in that zone. For the computation presented here, this parameter was evaluated using the correlation given by [Ramacciotti et al., 1999]. At 2100 K, the viscosity is approximately 2 Pa.s, the conductivity about $1.5\,W.m^{-1}.K^{-1}$ and the effective density about $3500\,kg.m^{-3}$.

As in non-eutectic Bismuth-Etain CORINE experiments, a thermal contact resistance has been put in relief. This resistance was modelled in CROCO code as described in the paragraph 3.2 with $h_b = 1000\,W.m^{-2}.K^{-1}$, which is the value recommended by experimentalists.

A typical comparison between the experimental results and the computed ones is given in figure 4.

Regarding all the uncertainties on the pouring rate and on the inflow and liquidus temperatures (and consequently on the viscosity), the computation results are rather good. Moreover, the code calculates a final spreading length which is coherent with experimental one. The melt emissivity, and so the upper crust thickness, appears to have, in the computations, a significant influence on the stop of the spreading.

4 CONCLUSION

The first version of the CROCO code is available since the beginning of 99 ; it is devoted to the description of the ex-vessel melt spreading phase, in the late stages of a postulated PWR severe accident. A rather comprehensive validation work has been performed, from which some results have been extracted and are presented here. The main conclusions which can be drawn are :

- Transients for which spreading is either isothermal or governed by solidification at the melt bottom interface are well described : a perfect agreement is obtained for dam-break problems ; CORINE computations demonstrate that the code is able to very accurately reproduce the temperature distribution within the melt, and so, provided that used melt rheological properties are realistic, flows hydrodynamics.

- As far as the computation of spreading flows with heat exchange at the melt free surface, as KATS and VULCANO experiments, is concerned, the numerical method of the code, allowing a linear description of the temperature profile everywhere in the melt, appears well suited to capture resulting steep temperature gradients induced by radiative cooling.

  However using real corium or high temperature simulants, the accurate determination of thermo-physical properties (in particular, the viscosity) is difficult and experimental measurements are compulsorily rather coarse. As a consequence, definitive statements when performing code-to-data comparison can hardly be obtained. We can nevertheless claim that one can obtain, using melt physical properties and boundary conditions within the experimental error bounds, code results which match quite satisfactorily experimental ones.

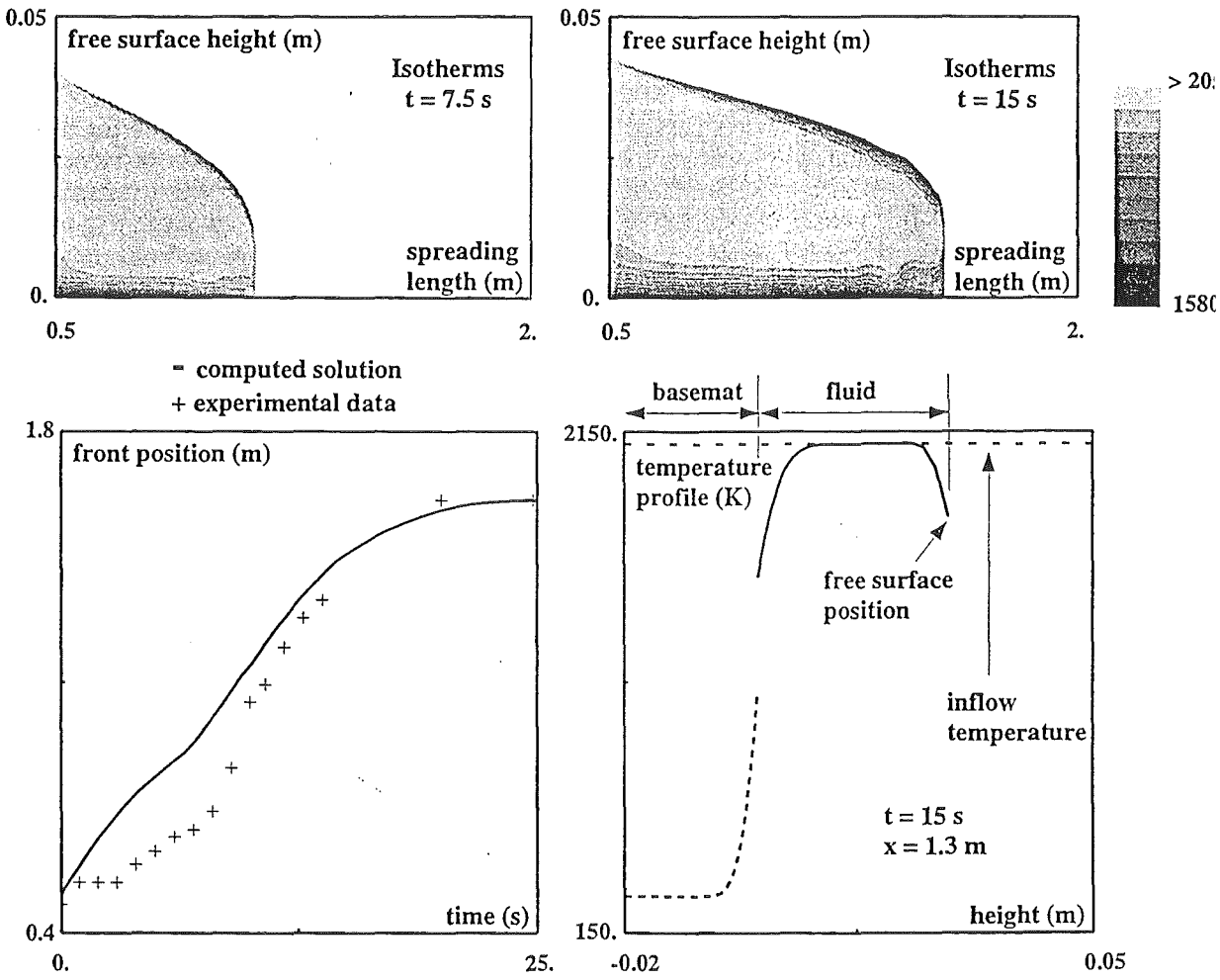

Fig. 4: Validation of CROCO V1.0 against VULCANO VE-U1 experiment.

To perform realistic reactor safety studies, further developments of the CROCO code are necessary, to deal with basemat ablation during spreading and with hydrodynamic effects of a fractured solid crust at the upper surface of the melt. They are under progress.

REFERENCES

[Cognet et al., 1998] Cognet, G., Laffont, G., Jegou, C., Journeau, C., Sudreau, F., Pierre, J., and Ramaciotti, M. (1998). The VULCANO spreading program. In *SARJ98 Workshop on Severe Accident Reasearch held in Japan, Nov 4-6, Tokyo.*

[Fieg et al., 1996] Fieg, G., Huber, F., Werle, H., and Wittmark, R. (1996). Simulation experiments on the spreading behaviour of molten core melts. In *1996 National Heat Transfer Conference, Houston, TX, August 3-6.*

[Huppert, 1982] Huppert, H. E. (1982). The propagation of two-dimensional and axisymmetric viscous gravity currents over a rigid horizontal surface. *Journal of Fluid Mechanics*, 121:43–58.

[Piar et al., 1999] Piar, B., Michel, B., Babik, F., Latché, J.-C., Guillard, G., and Ruggiéri, J.-M. (1999). CROCO : a computer code for corium spreading. In *Ninth International Topical Meeting on Nuclear Reactor Thermal Hydraulics (NURETH-9).* San Francisco, California, October 3-8.

[Ramacciotti et al., 1999] Ramacciotti, M., Sudreau, F., Journeau, C., and Cognet, G. (1999). Viscosity models for corium melts. In *Ninth International Topical Meeting on Nuclear Reactor Thermal Hydraulics (NURETH-9).* San Francisco, California, October 3-8.

[Taine and Petit, 1989] Taine, J. and Petit, J.-P. (1989). *Transferts Thermiques.* Dunod.

[Vila, 1986] Vila, J.-P. (1986). *Sur la Théorie et l'Approximation Numérique de Problèmes Hyperboliques Non Linéaires. Applications aux Équations de Saint-Venant et à la Modélisation des Avalanches de Neige Dense.* PhD thesis, UNIVERSITE PARIS VI.

OECD Workshop on Ex-Vessel Debris Coolability
Karlsruhe, Germany, 15-18 November 1999

Organised in collaboration with
Forschungszentrum Karsruhe (FZK) GmbH

THE SCALING MODEL OF CORE MELT SPREADING: VALIDATION, REFINEMENT AND REACTOR APPLICATIONS

M.J. Konovalikhin, T.N. Dinh, R.R. Nourgaliev, B.R. Sehgal and M. Fischer[+]

Division of Nuclear Power Safety
Royal Institute of Technology
Drottning Kristinas Väg. 33A
10044 Stockholm, Sweden
maxim@ne.kth.se

[+]SIEMENS Aktiengesellschaft
Power Generation Group (KWU), NA-T
Freyeslebenstr. 1, P.O. Box 3220
91058 Erlangen, Germany
manfred.fischer@erl11.siemens.de

ABSTRACT

In the current safety requirements on nuclear power plant design, specific attention has to be paid to the consequences of hypothetical severe accidents. In this respect, new designs have incorporated mitigative measures for management of such accidents. Ex-vessel core melt spreading, cooling and stabilization is proposed for the European Pressurized Reactor (EPR) plant containment design. Royal Institute of Technology - Nuclear Power Safety (RIT/NPS) is part of an European Comission joint work programme (Cognet et. al., 1997) [1], Corium Spreading and Coolability (CSC), which addresses melt spreading, both, experimentally and analytically.

A one- and two dimensional scaling methodology, which relates simulant material experiments to prototypical severe accident conditions was developed and validated at RIT. The scaling relations were then shown to be capable of predicting results of melt spreading experiments, including those at relatively large scales employing corium melts. The paper presents validation of the scaling relationships against KATS, COMAS, VULCANO, FARO, SPREAD and S3E integral experiments. The paper also applies the scaling methodology to prototypic reactor accident scenarios.

1 INTRODUCTION AND BACKGROUND

In the current EPR containment design, core melt is assumed to accumulate in an intermediate retention crucible made of a special concrete. Interactions between decay-heated core melt and concrete could then lead to ablation and rupture of the concrete bottom of the crucible. Core melt, mixed with the concrete decomposition products, is then discharged through a short sloping pathway to a two-dimensional spreading area. The time taken to ablate and rupture the bottom part of the concrete intermediate crucible should ensure relocation and accumulation of the most of the reactor core melt in the retention

crucible. This strategy of melt accumulation over time and discharge through a large hole is called the one-shot melt release, providing very high melt flow rate (10 to 20 Mg/s) with sufficient melt superheat (100K to 200K).

According to the worst-case scenario, prior to the core melt discharge, the total mass of homogeneous mixture of metal and oxide melts available for delivery to the spreading channel may range from 300 to 400 Mg (40 to 60 m^3). The objective of the work summarized here is to determine the characteristics of the core melt spreading in the EPR melt retention device. From the reactor safety perspective, it should be noted that the most important parameter for the spreading process is the terminal spread melt thickness and not its dynamics. The former is the measure of the success of spreading as an accident management strategy. In fact, the thickness of the spread core melt should be small enough to ensure the ex-vessel debris coolability. In the EPR case, the highest spreading efficiency is achieved when the open spreading area ($A_{EPR} = 180\ m^2$) of the EPR melt retention device is covered, uniformly, by a melt layer of a thickness corresponding to the total melt mass discharged from the crucible.

A number of experiments have been performed to study the phenomenology of core melt spreading on the containment floor (SPREAD, CORINE, BNL, VULCANO, KATS, COMAS, FARO, RIT/S3E). The main objective of these experiments was to provide data and observations for model development and validation. In particular, experimental programs conducted at JRC (FARO), Siempelkamp (COMAS), RIT (S3E), CEA (VULCANO) and FZK (KATS) are related to verification of the EPR melt retention scheme. Despite their non-prototypicalities (small scales, low temperatures, simulant materials, spreading channel geometry), the experiments provided invaluable insights into the physics of core melt spreading. In the KATS experiments, it was observed that even though the various (uncoated, coated, dry, wet) concrete spreading surfaces are somewhat different from that of ceramic, the spreadability i.e. spreading length is comparable. In addition, the presence of shallow water was found to have no detectable influence on spreading for high pour rate melt discharges. In the COMAS experiments, it was observed that the spreading distances were similar in channels with steel, ceramic and concrete substrate. The oxidic core melt was found to spread very well even when the melt superheat was small (up to 50K in FARO L-26) or even zero or negative (in COMAS 5a).

2 SCALING RATIONALE

2.1 Scaling principles

In general, reactor core melt spreading is a complex, thermofluid process, which is governed by

- (1) hydrodynamic motions of the spreading liquid (melt), and
- (2) solidification of melt during the spreading process.

Item (1) is affected by the gravitational, inertial, viscous and surface forces. Depending on the viscosity, the liquid spreading may be categorized into gravity-inertia and gravity-viscous regimes. Item (2) is affected by heat transfer from core melt to surrounding media, i.e. downward: $q"_{dn}$ and upward: $q"_{up}$ heat removal rates, decay heat generation rate q_{vol}, and phase change behavior of the melt. For the EPR melt retention conditions, other phenomena (e.g., molten corium-coolant and molten corium-concrete interactions,

melt stratification) are found to have negligible effect, during the very short time period (20 to 40 s) of core melt spreading, or they have been shown to be bounded by other phenomenological and scenario uncertainties.

In order to develop a scaling methodology, three major principles are maintained.

First, the scaling rationale is based on goal-oriented parameters. In this case, scaling parameters are determined from reactor safety perspectives.

Second, while seeking the simplicity of the scaling equations, it is required to conserve the (potential) effects of simulant-material physical properties on the component phenomena.

Third, equations and correlations, employed in deriving the scaling relations, are transparent and can be separately validated.

It is instructive to note that the research on the spreading process is strongly related to the ex-vessel debris long-term-coolability issue. The thinner the debris cake or bed, the more probable that it is coolable by water flooding. Thus, from the reactor safety perspective the most important scaling parameter characterizing the spreading process is the *terminal thickness* of the spread melt (debris), δ_{sp}.

2.2 Scaling laws

The RIT method was first developed for spreading in one-dimensional channels (Dinh et al., 1998) [2], but has recently been extended to cover spreading in two-dimensional channels and, more importantly, for spreading into open area (Konovalikhin et al., 1999) [3].

In the RIT method, the terminal spread melt thickness δ_{sp} is shown to be a function of the time scales of two competing processes: hydrodynamic (convective) spreading τ_{conv} and solidification τ_{sold}. In the gravity-inertia regime, the hydrodynamic spreading time scale τ_{conv} is determined as the time period required for liquid (melt) to spread to reach its capillary thickness, δ_{cap}. The characteristic solidification time, τ_{sold}, is defined as the time period needed to cool the melt to an immovable state. For this, not only the superheat, but also a fraction η of the latent heat of fusion, has to be removed from the bulk melt.

Based on the mass and momentum conservation equations, a square-root relation was established between the dimensionless length scale (representing ratio $\mathcal{L} = \delta_{sp}/\delta_{cap}$) and the dimensionless time scale (representing ratio $\mathcal{T} = \tau_{conv}/\tau_{sold}$). The square-root law was shown to be valid in both gravity-inertia and gravity-viscous regimes, employing a dimensionless viscosity number, which was analytically derived.

The following scaling model for inviscid spreading is obtained:

$$\mathcal{L} = C \cdot \mathcal{T}^{1/2} \tag{1}$$

Since the proportionality coefficients in all the equations employed have orders of unity, coefficient C should be about 1 ($C \simeq 1$). This is then confirmed by comparison to experimental data available.

In gravity-viscous spreading regime the scaling equation has similar form, but the dimensionless length and time scales should be modified to take into account the viscosity effect.

$$\mathcal{L} = C_v \cdot \mathcal{T}^{1/2} \cdot \mathcal{N}^{1/2} \tag{2}$$

where $\mathcal{N}$ is a viscosity number ($\mathcal{N} \geq 1$) defined as

$$\mathcal{N} = \frac{\nu^{1/8} \cdot V_{tot}^{1/2} \cdot g^{5/24}}{D^{1/3} \cdot G^{13/24}} \tag{3}$$

where ν, V_{tot}, g, D and G are the kinematic viscosity, total melt volume, gravitational acceleration constant, entrance width of spreading area and melt supply flow rate, respectively.

Essentially, the scaling law for spreading into 2D area is based on the concept of melt spreading in 1D channel, while accounting for the reduced hydrodynamic time scale of the boundless liquid on a horizontal surface. Exactly similar procedure as for 1D spreading was applied for deriving the relation between the time and length scales. As a result, the general viscid form can be written as follows.

$$\mathcal{L} = C_\alpha \ \mathcal{T}^{1/2} \ \mathcal{B}^{1/2} \ \mathcal{N}^{1/2} \tag{4}$$

with parameter $\mathcal{B}$ defined in the table below:

	$\mathcal{B}$
hydrodynamic regime	$\frac{1}{1+\frac{2R}{D_o}}$
open channel flow theory	$D_o \left(\frac{360\delta_{cap}}{\alpha_{ocf}\pi V_{tot}} \right)^{1/2}$
thermal-control regime	$\frac{1}{1+\frac{2\tau_{sold}U_o}{D_o}}$

Some remarks are in order concerning the development of a methodology for prediction and analysis of the melt spreading process. Clearly, the process is very complex, as evidenced by the various physical processes, and physical properties, that were considered in formulating the scaling rationale presented above.

Other approuches have been taken in developing the same methodology. These involve solutions of the melt flow equations with representation of the crust formation and the

bulk solidification process. In these methodologies (embodied e.g. in the codes THEMA, CORFLOW etc.), objective is to determine the local and time dependent thermal hydraulic conditions for the melt flow, while it is interacting with the substrate. The variation of the physical properties during the melt spreading process, in particular the viscosity, has required elaborate analysis and the development of separate material properly theories. In addition, there have been extensive discussions and debate on the subjects: (a) the melt stopping mechanisms or criteria and (b) the stopping power of a crust, which involves examination of the structural properties of the melt crust. As a result, these approaches have been only partially successful in describing and predicting, a priori, the melt spreading process.

The approach followed in our paper does not concern itself with the micro-processes, and, thus, is unable to describe the space-time evolution of the spreading process. Instead, the approach integrates these micro-processes together in an overall thermodynamic-hydrodynamic framework which predicts parameters of reactor safety significance i.e., the melt spread length, or area, and the average thickness of the spread melt. This approach makes the assumption that the melt will stop when the leading edge loses the sensible and about 50% of the fusion heat; thereby acknowledging that the increase in melt viscosity, that will occur due to the crystallization, becomes so large when about 50% of heat of fusion is removed that the melt stops. We believe that the scaling rationale presented also serves as a predictive and analysis methodology fitting the purpose. In the rest of the paper we will demonstrate this.

Needless to say the other approaches, if continued with vigour, may reach their objective in time, when detailed predictions on melt spreading dynamics, melt spread thickness profile and the detailed melt spreading surface configurations (e.g. description of melt spreading in two dimensions) can be made with acceptable certainty and accuracy. We feel that such detail is not required for the design of the EPR melt spreading device or reactor safety assessment for severe accidents.

3 VALIDATION OF THE SCALING METHODOLOGY

3.1 Validation strategy

The methodology employed for assessment was first developed as a scaling rationale for melt spreading experiments. The scaling relations were then shown to be capable of analyzing and even predicting results of melt spreading experiments, including those at relatively large scales and using prototypic core melts. A number of mechanistic equations and generic correlations were employed to enable closed form scaling equations for different regimes and geometries. As such the scaling equations serve as an integral model for assessing and predicting characteristics of melt spreading.

The strategy adopted for validation of the melt spreading model includes:

- verification of component models and correlations which were employed as the basis for the scaling methodology;
- validation of the integral model against data and observations in one-dimensional simulant-material melt spreading experiments;
- validation of the model against data obtained from two-dimensional simulant-material

melt spreading experiments; and

- validation of the model against data obtained from high-temperature melt spreading experiments employing prototypic corium melts.

3.2 Heat transfer

Heat transfer from melt largely depends on spreading regime. The upward heat removal rate in the EPR case is governed by radiation flux from the melt surface. Convective heat transfer to gas environment is small in the prototypic accident situation.

In experiments, however, both dry and wet spreading regimes were tested. Heat transfer from spreading melt to coolant in the wet case is determined by the cooling regime (convective, boiling). In the single-phase convective cooling, heat transfer from the melt crust to the coolant can be determined by using the correlation which was derived for convective heat transfer to a rough, phase change, boundary.

$$Nu = 0.0027 \cdot Pe \tag{5}$$

or

$$h_{conv} = 0.0027 \cdot \rho_{coolant} \cdot C_{p,coolant} \cdot U_{rel} \tag{6}$$

For the higher temperature, dry spreading experiments, the heat removal rate is calculated as

$$q"_{rad} = \varepsilon \sigma_B (T_m^4 - T_{env}^4) \tag{7}$$

where T_m and T_{env} are the melt temperature and the temperature of the environment, respectively, σ_B is Bolztmann coefficient $\sigma_B = 5.67 \cdot 10^{-8} W/(m^2.K^4)$, and ε is emissivity coefficient. For oxidic crust and melt, ε approaches 1.

Downward heat removal rate q''_{dn} can be evaluated as

$$q''_{dn} = h_{conv,dn} \cdot (T_m - T_{m,sold}) \tag{8}$$

provided that the bottom crust forms during the melt-substrate initial contact. The convective heat transfer from the melt flow to the crust boundary is evaluated by Eq.(5), which was shown to be valid in a large range of Peclet numbers. In a dimensional form, we have

$$h_{conv,dn} = 0.0027 \cdot \rho_{melt} \cdot C_{p,melt} \cdot U_{sp} \tag{9}$$

The above correlation was validated extensively against experimental data obtained in RIT and elsewhere. In particular, in experiments performed on jet impingement on an ablating surface, on jet impingement with crust formation and on hole ablation were shown to be governed by the convective heat transfer to a phase change boundary. Dinh and co-workers (1997) [4] have shown that the surface roughness associated with the phase change process enhances energy transfer from the melt to the ablating structure. In a series of water-ice and water-salt ice jet impingement experiments it was recognized that the surface roughness, resulting from the phase change of the melting plate material was a controlling factor in the transition from laminar to turbulent heat transfer regimes in the jet stagnation zone. Experimental observations from the jet impingement research were then extended to the vessel ablation conditions and may now be extended to calculate heat transfer between the melt flow and crust in the spreading situations, considered here. There are underlying similarities in the heat transfer mechanisms between these processes.

3.3 Melt stopping criteria

If no solidification is involved or solidification occurs much later after the spreading process is terminated, the spread melt thickness is will be equal to the liquid capillary thickness. This length scale δ_{cap} is typically 5 to 10 mm (4.1 mm for cerrobend melt, 4.9-5.3 mm for binary salt and oxide melts and 9-10 mm for thermite melt). This length scale agrees well with spread-fluid thickness observed in nearly-non-freezing or isothermal spreading tests RIT/S3E, FZK/KATS, CEA/CORINE.

In prototypical reactor cases, $\mathcal{L}$ may vary in a wide range, depending on reactor design and severe accident management schemes adopted, and on melt relocation scenarios (cavity flooding before or after melt release and spreading). A range of $\mathcal{L}$ lower than 30 (i.e. melt layer thickness less than 20 cm) is necessary for the severe accident management scheme utilizing water flooding on the containment floor to cool the debris from above.

In early experiments conducted at Brookhaven (using Pb melt spreading under water) $\mathcal{L}$ is estimated up to 10 (Greene et al., 1988 [5]). In the CORINE experiments using eutectic Pb-Sn melt, the dry spreading tests resulted in $\mathcal{L}$ up to 5, while the spreading under water tests provided $\mathcal{L}$ up to 30 (Veteau and Wittmaack, 1995 [6]). In the KATS-series (with Al_2O_3 and Fe melts) $\mathcal{L}$ varies from 1.2 to 2 (Scholtyssek et al., 1996 [7], Fieg et al., 1996 [8], Fieg et al., 1997 [9]). In dry-spreading COMAS tests (with $UO_2 - ZrO_2 - Cr_2O_3 - FeO - Fe$ melt) $\mathcal{L}$ is about 3 (Steinwarz, 1997 [10]).

The parameter η is unknown for multi-component melts, in particular, for binary oxidic and prototypic corium melts. Earlier, $\eta \simeq 0.55$ was assumed for stainless steel melt (56 K mushy zone) in order to interpret results of the SPREAD experiments (Suzuki et al., 1993, [11]). For binary oxidic melts, the latent heat of fusion is equivalent to sensible heat with superheats of about 500 K. Thus, with $\eta \simeq 0.55$ the role of heat of fusion may be comparable to the effect of melt superheat of 250 to 300K.

3.4 Summary on validation against experimental data

A large number of simulant material spreading experiments were performed using different fluids with different phase change behavior and properties and varying melt superheats, melt volume, melt flow rates and cooling conditions. It was found that the scaling relations work reasonably well in term of predicting the spreading distance.

Notably, an experimental program named scaled simulant spreading experiments (S3E) was performed at RIT (Sehgal et al., 1997 [12], Sehgal et al., 1998 [13]). The S3E

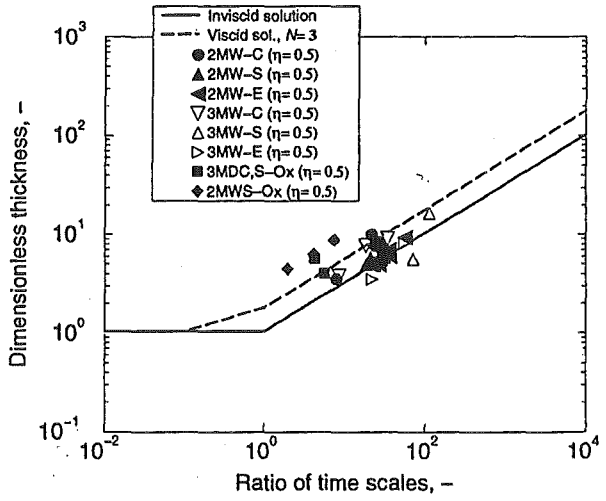

Fig. 1: Validation of the model against data from S3E spreading experiments.

data were analyzed and found to fit very well with the scaling rationale developed (Fig. 1). The RIT method was then used to predict the spreading distance in one-dimensional high-temperature oxidic melt spreading tests at RIT. Very good agreement between the pre-test prediction results and data was obtained. The validation success confirmed assumptions made in deriving the model equations (e.g., $\eta = 0.5$) and justified the use of heat transfer correlations employed.

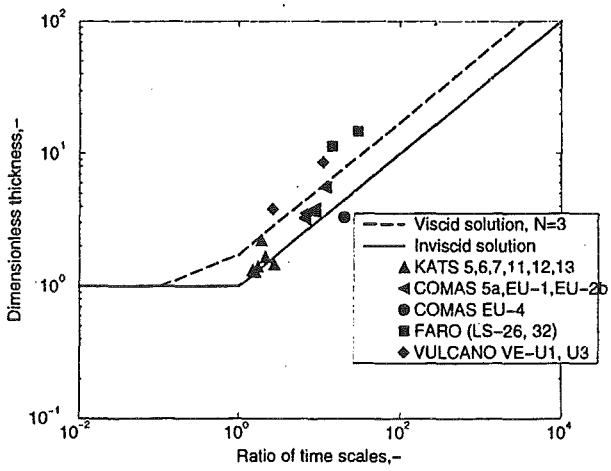

Fig. 2: Validation of the model against data from high-temperature melt spreading experiments.

Extensive validation of the RIT method was performed against experimental data from KATS, COMAS, VULCANO and FARO spreading experiments (Fig.2). The method was found to predict, with reasonable accuracy, the spreading distance in one-dimensional spreading channels and spreading into two-dimensional channels (COMAS EU-4, VULCANO and FARO). It was also found that the spreading in two-dimensional channels employed by these tests is bounded by the channel's side walls and hence essentially one-dimensional. It should also be noted that the RIT method was employed to perform pre-test

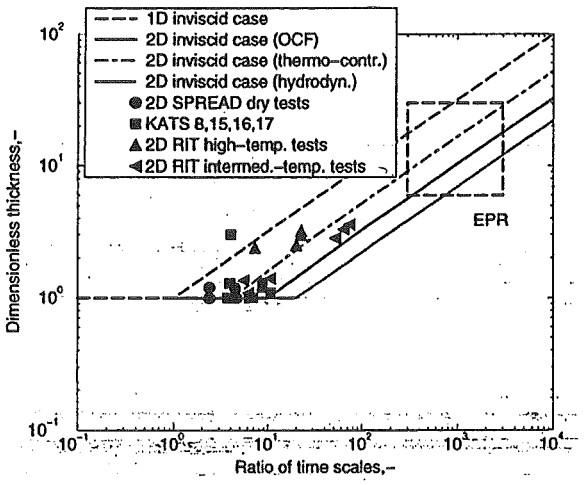

Fig. 3: Validation of the model against data from two-dimensional spreading experiments.

predictions for COMAS EU-2b core melt spreading experiment. Excellent agreement between the predicted and observed spreading distance was obtained. In general, it can be concluded that the phenomenology of one-dimensional melt spreading is reasonably well understood.

Validation of the RIT method for melt spreading into open area was also performed on the data base obtained from the RIT, KATS, SPREAD simulant-material experiments (Fig.3). Among theories tested for 2D spreading, the open-channel flow theory provides best agreement between the calculated terminal thickness and the experimental data. This theory was employed in the reactor assessment, performed, which are presented below. It should also be noted that melt spreading into an open area is significantly different from the one-dimensional spreading. As melt spreads in all directions, the hydrodynamic spreading time scale is remarkably reduced, and hence the spreading area is significantly enhanced. As a result, the spread melt thickness in the open-area spreading case may decrease by a factor of 3 to 10, compared to that for the one-dimensional spreading process.

4 REACTOR APPLICATION

4.1 EPR melt retention device

In the retention device design at the moment the walls of the reactor pit, below the RPV, are covered with a specific sacrificial concrete. If this layer is eroded the melt will face either a protective layer, in the cylindrical part, or the melt plug, at the bottom. This plug will melt through and release the corium (Fischer, 1999) [14]. Provided the melt height is 2.0 m, the discharge velocity may be up to 5 m/s. For an initial opening of 0.2 m^2, the volume flow rate of core melt discharged is estimated to be of the order of 1 m^3/s, or 7 Mg/s. This strategy of melt accumulation over time and discharge through a large hole is called the one-shot melt release, providing relatively high melt flow rate (10 to 20 Mg/s) and with sufficient melt superheat (100K to 200K), since addition of the concrete products to the corium decreases the melt liquidus and solidus temperatures considerably.

4.2 Selected scenarios of core melt accident progression

According to the worst-case scenario, prior to the core melt discharge, the total mass of the homogeneous mixture of metal and oxide melts available for delivery to the spreading channel was found to vary in the range from 300 to 400 Mg (40 to 60 m^3). Two cases are selected for design base assessment (case A and case B). In case A, minimum amount of concrete slag is assumed to mix with the oxidic core melt. In case B, maximum amount of concrete slag mixing is assumed. Parameters of these cases are provided by Siemens KWU, based on results of the Siemens study of core melt relocation and melt-concrete interactions in the intermediate concrete crucible and its rupture.

Table 1: Input parameters and uncertainties. (Base-parameters are given in bold).

%	*Parameter*	*Case A*	*Case B*
	I. Melt Delivery Conditions:		
1	Total melt mass, (Metal+Oxide) M_{melt}, t	300-**332**	300-**350**
2	Melt release temperature, T_{melt}, C°	2410-**2442**-2500	1800-**2185**-2330
3	Environment temperature, T_{env}, K	400-**800**	400-**800**
4	Decay power, Q, MW	30-**35**-40	30-**39**-45
5	Melt release time, $t_{release}$, sec	20-**30**-60	60-**90**-120
	II. Physical Properties:		
6	Mass fraction of metallic melt, φ_{met}, wt%	**40**	**36.8**
7	Density of metallic melt, ρ_{met}, kg/m^3	6000-**6350**-6500	6200-**6450**-6600
8	Density of oxidic melt, ρ_{ox}, kg/m^3	7000-**7200**-7400	6300-**6500**-6700
9	Specific heat, $C_{p,m}$, J/(kg0·K)	2500-**3000**-3500	1200-**1260**-1300
10	Dynamic viscosity, μ_m, Pa·sec	0.01-**0.02**-0.1	0.01-**0.02**-0.1
11	Surface tension, σ_m, N/m	0.45-**0.47**-0.5	0.45-**0.47**-0.5
12	Fusion heat, H_f, MJ/kg	0.6-**0.62**-0.65	1.4-**1.45**-1.5
13	Liquidus/Solidus temperature, T_{liq}/T_{sol}, C°	**2510/2300**	**2330/1180**
14	Melting point temperature, $\frac{T_{liq}+T_{sol}}{2}$, C°	**2405**	**1755**
15	Emissivity, ε	**0.8**-1	**0.8**-1
	III: Geometrical Characteristics:		
16	Total spreading area, A_{EPR}, m^2	170-**180**	170-**180**
17	Transport channel width, W_{EPR}, m	**1.2**	**1.2**
	IV: Modeling uncertainties:		
18	η	0.4-**0.5**-0.6	0.4-**0.5**-0.6
19	Coefficient C_{conv}	(2.5-**2.7**-3)·10^{-3}	(2.5-**2.7**-3)·10^{-3}
20	Coefficient C	0.5-**1**-2	0.5-**1**-2
21	Open-channel theory spreading angle α_{oct}, deg.	45-**50**-60	45-**50**-60

Table 1 shows parameters of melt delivery conditions, melt physical properties and geometrical characteristics of the melt retention device. These parameters are used in the assessment.

It should be noted here that the hole ablation and melt discharge are not modeled here. The discharge melt flow rate is time-dependent and may be significantly different for different scenarios (case A and case B). It is our judgement that addition of large amount of concrete slag makes the mixture difficult to be ejected. To enable a conservative assessment of the spreading characteristics, the melt release time period is chosen 6 times larger in case B than that in case A. The difference in melt discharge rate is however smaller (about

4 times), owing to the larger melt volume in case B (larger melt mass and smaller melt density).

Section IV of Table 1 also depicts variation range of key modeling parameters. This reflects the phenomenological uncertainties and takes into account the current understanding. While the variation range for η, C_{conv} and α_{oct} is sufficiently small, the variation range for C is rather big. In fact, the variation range of C envelopes uncertainties induced by assumptions and idealization employed in deriving the scaling methodology.

4.3 Spreading efficiency

The objective of the assessment is to determine the characteristics of the core melt spreading in the EPR melt retention device. The methodology developed at RIT is employed here to predict the core melt spreading characteristics in the EPR melt retention device. Although the prototypic situation is of spreading into open area, both the RIT method for spreading into an open area and the RIT method for one-dimensional spreading are employed. The latter is to provide the conservative lower bound estimate of the spreading area. The two methods are used to calculate the terminal spread melt thickness. Given the melt volume, the theoretical spreading area A_{theo} can be then determined. Comparison between the spreading area A_{theo} and the designed area A_{EPR} shows whether the spreading area is fully covered by core melt or the latter is piled up in only a smaller area. In reality, the maximum spreading efficiency ($\gamma = A_{real}/A_{EPR} = 1$) is achieved when $A_{theo} \geq A_{EPR}$.

4.4 Base case results

Results of the assessment employing three solutions (1D inviscid, 1D viscid and 2D viscid open channel flow models) are shown in Table 2 for the two selected base cases. In each column, one sees two values; the first results from the deterministic calculation for the conditions given and for the model parameters chosen; the second (in brackets) value is a mean value from Monte-Carlo simulations (10^6 simulations), using the uncertainty variation range specified in Table 1. As it can be seen, the two sets of values are quite close. The results indicate the very high spreading efficiency of melt spreading into an open area. Even in case B, when the melt viscosity is kept high, the melt volume is increased and the melt discharge velocity is decreased, the spreading efficiency remains about 6. As a result, the core melt is predicted to spread all over the spreading area provided in the EPR melt retention device.

Table 2: Assessment results for case A and case B (base-parameters/mean value from Monte-Carlo simulations).

%	*Result*	*Case A*	*Case B*
	1D inviscid theory:		
1	Spreading thickness, δ_s, cm	24/{32}	13/{18}
2	Spreading efficiency, ε_s	1.12/{1.04}	2.29/{1.79}
	1D viscid theory:		
3	Spreading thickness, δ_s, cm	31/{43}	21/{32}
4	Spreading efficiency, ε_s	0.87/{0.79}	1.4/{1.04}
	2D viscid open channel theory:		
5	Spreading thickness, δ_s, cm	4.6/{6.4}	3.96/{5.3}
6	Spreading efficiency, ε_s	5.84/{5.06}	7.6/{5.98}

5 SUMMARY

The paper describes the methodology developed at the Division of Nuclear Power Safety, Royal Institute of Technology (RIT, Stockholm, Sweden) to assess spreading characteristics. The RIT method was first developed for spreading in one-dimensional channels, but has recently been extended to cover spreading in two-dimensional channels and, more importantly, for spreading into open area.

In the RIT method, the terminal spread melt thickness δ_{sp} is shown to be a function of the time scales of two competing processes: hydrodynamic (convective) spreading τ_{conv} and solidification τ_{sold}. In the gravity-inertia regime, the hydrodynamic spreading time scale τ_{conv} is determined as the time period required for liquid (melt) to spread to reach its capillary thickness, δ_{cap}. The characteristic solidification time, τ_{sold}, is defined as the time period needed to cool the melt to an immovable state. For this, not only the superheat, but also a fraction η of the latent heat of fusion, has to be removed from the bulk melt.

Extensive validation of the RIT method was performed against experimental data from KATS, COMAS, VULCANO, FARO and S3E spreading experiments. The method was found to predict with reasonable accuracy, the data obtained from these test programs.

The methodology developed at RIT is employed to predict the core melt spreading characteristics in the EPR melt retention device. Although the prototypic situation is of spreading into open area, both the RIT method for spreading into an open area and the RIT method for one-dimensional spreading are employed. The latter to provide the conservative lower bound estimate of the spreading area.

The assessment was performed for two basic cases, with minimum (case A) and maximum (case B) amount of sacrificial concrete slag added to the oxidic corium before spreading. In addition, owing to the higher viscosity of the core melt-concrete slag mixture, a lower range of core melt discharge rate was chosen for a conservative evaluation of the spreading characteristics in case B. For the base selected cases, it was found that even the one-dimensional spreading model predicts complete spreading ($A_{theo}/A_{EPR} \approx 0.85$ .. 1). The spreading-into-open-area model predicts that $A_{theo}/A_{EPR} \geq 6..8$. The lower numbers (0.85 and 6) of the calculated spreading efficiency are for case B. Results of the sensitivity analysis indicate that the total melt mass and melt discharge rate are the important parameters. However, within the range of these parameters investigated, scenario and phenomenological uncertainties were found to have no profound impact on the results of the assessment.

To summarize, the results of the assessment of core melt spreading in the EPR melt retention device show that for the worst case melt delivery conditions the whole spreading area of the melt retention device can be covered by the melt uniformly with the spread melt thickness of 20 to 35 cm. It is assumed that the decay-power generated in the debris layer ($\approx$ 200 kW/m^2) can be removed by an overlying water layer to terminate the containment basemat concrete ablation and provide containment integrity during a hypothetical severe accident in the EPR plant.

Acnowledgement

This work was conducted through the support of the European Comission, SKI, USNRC, HSK, the Swedish and Finnish Utilities and the Swiss Nuclear Safety Commission.

REFERENCES

[1] Cognet, G., et al., "Corium Spreading and Coolability (CSC Project)", FISA-97, Luxembourg, November, (1997).

[2] T.N. Dinh, M.J. Konovalikhin, D. Paladino, J.A. Green, A. Gubaidulin, B.R. Sehgal, "Experimental Simulation of Core Melt Spreading on a LWR Containment Floor in a Severe Accident", ICONE-6, San Diego, USA, May, (1998).

[3] M.J. Konovalikhin, T.N. Dinh, B.R. Sehgal, "Experimental Simulation of Core Melt Spreading in Two Dimensions", NURETH-9, San Francisco, USA, October, (1999).

[4] Dinh, T.N., W.G. Dong, J.A. Green, R.R. Nourgaliev, and B.R. Sehgal, "Melt Jet Attack of the Reactor Vessel Wall: Phenomena and Prediction Method," Proceedings of NURETH-8, Tokai-mura, Japan, October, (1997).

[5] Greene, G.A., C. Finrock, J. Klages, and C.E. Schwarz, "Experimental Studies on Melt Spreading, Bubbling Heat Transfer and Coolant Layer Boiling," Proceedings of 16^{th} Water Reactor Safety Meeting, NUREG/CP-0096, pp.341-358, (1988).

[6] Veteau, J.M. and Wittmaack R., "CORINE Experiments and Theoretical Modeling", FISA-95 Proceedings, Luxemburg EUR 16896 EN, pp.271-285 (1995).

[7] Scholtyssek, W., H. Alsmeyer, and H. Werle, "Recent Results of Melt Spreading and Cooling Experiments at FZK - The KATS and COMET Projects," CSARP-96, Bethesda, MD, (1996).

[8] G. Fieg et al., "Simulation Experiments on the Spreading Behavior of Molten Core Debris", Proceedings of the 1996 National Heat Transfer Conference, in the session "Fundamental Phenomena in Severe Accidents", Houston, Texas, HTC-Vol.9, pp.121-129. August, (1996).

[9] Fieg, G., et al. PSF News, FZK Quick Look Reports from Internet, http://psf-nt-server.fzk.de/psfhome.htm, (1997).

[10] Steinwarz, W., "Investigation on the Phenomenology of Ex-Vessel Core Melt Behavior", Presented to Joint INV/EXV Clusters Meeting, Roma, 1997.

[11] Suzuki, H., et al., "Fundamental Experiment and Analysis for Melt Spreading on Concrete Floor," Proceedings of 2^{nd} ASME/JSME Nuclear Engineering Conference, Vol. 1, pp. 403-407, (1993).

[12] B.R. Sehgal, T.N. Dinh, J.A. Green, M.J. Konovalikhin, D. Paladino, W.H. Leung, A.A. Gubaidullin, "Experimental Investigation of Melt Spreading in One-Dimensional Channel", RIT/NPS Report EU-CSC-1D1-97, 86p., November, (1997).

[13] B.R. Sehgal, T.N. Dinh, M.J. Konovalikhin, D. Paladino, A.A. Gubaidullin, "Experimental Investigations on Melt Spreading in One and Two Dimensions", RIT/NPS Report EU-CSC-2D1-98, December, (1998).

[14] M. Fischer, "Main Conceptual Features of the EPR Melt Retention Concept", OECD Workshop on Ex-Vessel Debris Coolability Karlsruhe, Germany, 16-18 November, (1999).

OECD Workshop on Ex-Vessel Debris Coolability
Karlsruhe, Germany, 15-18 November 1999

Organised in collaboration with
Forschungszentrum Karlsruhe (FZK) GmbH

NUMERICAL SIMULATION OF THE STABILITY OF SOLIDIFIED CORE MELT ACCUMULATIONS

I. Wintruff and C. Günther
Forschungszentrum Karlsruhe GmbH
Postfach 3640, D-76021 Karlsruhe, Germany
ingo.wintruff@iket.fzk.de claus.guenther@iket.fzk.de

ABSTRACT

The long time behaviour of core melt accumulations under the effect of internal heat sources is investigated numerically with a new adaptive Control-Volume Finite Element Method (CVFEM) on moving triangular grids. The transient melting process of an initially solidified core melt accumulation with a sharp transition from solid to liquid is analysed. It is shown that the transient process consists of a sequence of three regimes: (a) the pure conduction regime, (b) the internal melting regime and (c) the growing liquid regime. The governing dimensionless parameters of the problem are pointed out and varied within several calculations in order to estimate the influence of geometry, of internal heat generation and of external cooling temperature. The interaction between the natural convective flow in the molten phase and the topology and propagation of the internal phase interface is pointed out. Finally, some fundamental statements about the qualitative effects of buoyancy induced flows in core melts accumulations are derived.

1. INTRODUCTION

In case of a severe core melt accident the core-catcher concept of the European Pressurized Water Reactor (EPR) aims at a complete and broad planar spreading of the molten material across the spreading area. During the transient spreading process locally limited accumulations of solidified material could emerge due to actually high cooling rates and large specific surfaces. A re-melting of such solidified masses due to decay heat is necessary to ensure the following course of spreading. Numerical simulations are presented to investigate the behaviour of the thermodynamic system. Strong simplifications are necessary in order to reduce real core-catcher conditions to a simple calculation model. Based on Huppert's (1982) similarity solution of the axisymmetric spreading of a constant volume we choose a simple symmetric geometry of the initially solidified melt accumulation in cartesian

coordinates which is characterised by the aspect ratio A. The geometry of the outer boundary is regarded as fixed (given as $h(x)$). Inside the accumulation we consider a pure substance with constant material properties. Due to internal heat generation inside the accumulation a liquid core can arise surrounded by a moving solid-liquid interface. At the outer surface $h(x)$, heat is removed by radiative heat transfer. A sketch of the transient problem is shown in figure 1.

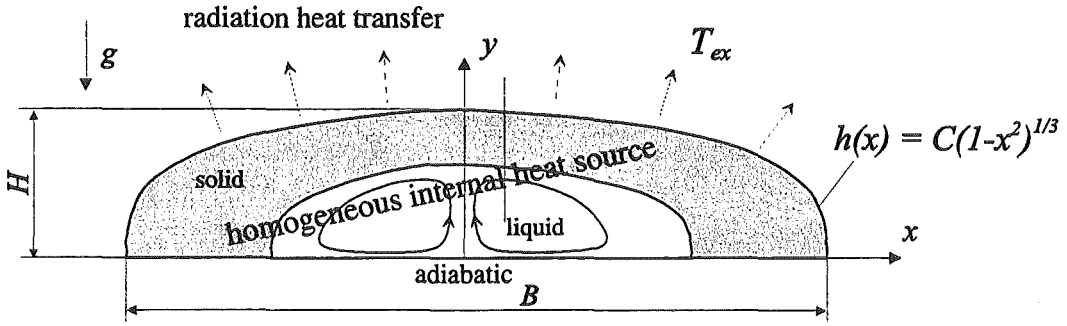

Figure 1. Sketch of the melting problem with internal heat generation.

2. THEORY

The basic equations that describe this problem under the influence of gravity are the conservation equations for mass, momentum and energy. Formally, these conservation equations have to be solved within each of the different thermodynamic phases (solid, liquid, mushy). Of course, convective fluxes can only occur in molten phases. The natural convective flow is regarded as laminar and two-dimensional. The Boussinesq approximation is used to introduce the buoyancy effect into the momentum equations. The differential equations are integrated over discrete subvolumes Ω which depend on time. The non-Eulerian formulation of the conservation equation introduces an arbitrary mesh velocity field $\vec{w}$. Consequently, an additional equation, the so called *space conservation equation* (Demirdzic und Peric 1988), has to be satisfied (eq. 1).

$$\frac{d}{dt}\int_{\Omega(t)} d\Omega = \int_{\Gamma(t)} \vec{w}\,\vec{n}\,d\Gamma \tag{1}$$

$$\frac{d}{dt}\int_{\Omega(t)} \rho\, d\Omega = \int_{\Gamma(t)} \rho\,(\vec{v}-\vec{w})\vec{n}\,d\Gamma \tag{2}$$

$$\frac{d}{dt}\int_{\Omega(t)} \rho\,\vec{v}\,d\Omega + \int_{\Gamma(t)} [\rho\,(\vec{v}-\vec{w})\vec{v} - \mu\nabla\cdot\vec{v}]\vec{n}\,d\Gamma = \int_{\Omega(t)} [\nabla p - \rho[1-\vec{g}\beta(T-T_0)]]d\Omega \tag{3}$$

$$\frac{d}{dt}\int_{\Omega(t)} \rho\, c_p T d\Omega + \int_{\Gamma(t)} [\rho\,(\vec{v}-\vec{w})c_p T - \lambda\nabla T]\,\vec{n}\,d\Gamma = \int_{\Omega(t)} S\,d\Omega \tag{4}$$

In eq.(1) - (4), Ω is an arbitrary formed discrete subvolume, Γ its surface, $\vec{v}$ the fluid velocity field, $\vec{w}$ the mesh velocity field, p the pressure, T the temperature, $\vec{g}$ the gravity vector and S a volumetric heat source. ρ, μ, λ, c_p, and β are density, viscosity, thermal conductivity, specific heat and thermal expansion of a pure substance, respectively, regarded as equal and constant in all phases. At all outer boundaries of the accumulation no-slip conditions for the

velocity are posed. The bottom of the accumulation is regarded as adiabatic, whereas heat is removed from the system at the surface *h(x)* by radiation:

$$\int_{\Gamma(t)} \lambda \, \nabla T \, \vec{n} \, d\Gamma = \int_{\Gamma(t)} \sigma \varepsilon \left(T^4 - T_{ex}{}^4 \right) d\Gamma \, , \tag{5}$$

with ε being the emissivity, T_{ex} the external radiation reference temperature and σ the Stefan-Bolzmann constant ($\sigma = 5{,}64 \cdot 10^{-8}$ W/m^{2}K^4). At inner phase interfaces the no-slip condition for the velocity holds because the density jump upon phase change is neglected. The phase change at *discrete* solid-liquid interfaces occurs at a fixed temperature $T_s = T_l = T_m$ and the Stefan condition is used to describe its propagation velocity $\vec{w}_\Gamma$ as a result of the release or absorption of latent heat L:

$$\int_{\Gamma(t)} \lambda \, \nabla T \, \vec{n} \, d\Gamma = \int_{\Gamma(t)} \rho \vec{w}_\Gamma \vec{n} L d\Gamma \, . \tag{6}$$

If phase change takes place over a range of temperature between solidus and liquidus temperature (e. g. for oxidic core melts), solid-liquid interfaces can have a very complex structure (e. g. dendritic, cellular or amorph phase transitions) and occur at microscopic length scales which does not allow the use of eq. (6). A well known one-domain enthalpy-porosity model on a fixed numerical grid (Brent, Voller and Raid 1982) with an implicit definition of a macroscopic phase separation line is used in this special case.

Beside the aspect ratio $A = B/H$ of the outer geometry the non-dimensional numbers Prandtl number, internal Rayleigh number and internal Stefan number, respectively

$$Pr = \frac{\mu}{\lambda c_p} \, , \; Ra = \frac{SH^5 \beta \, g}{\nu \kappa \lambda} \quad \text{and} \quad St = \frac{SH^2 c_p}{\lambda L} \tag{7}$$

are used to characterize the melting problem under the effect of a volumetric heat source *S*. The influence of the external temperature T_{ex} can be expressed with the non-dimensional temperature

$$\vartheta_{ex} = \frac{T_{ex} - T_m}{\Delta T_{\max,C}} = \frac{T_{ex} - T_m}{SH^2 / 2\lambda} \, ,$$

where $\Delta T_{\max,C}$ is the maximum internal temperature difference in an adequate one-dimensional pure heat conduction case.

3. NUMERICAL METHOD

The discretisation of the basic equations of fluid flow and heat transport is based on a two-dimensional Control-Volume Finite Element Method (CVFEM) on unstructured triangular grids (Prakash 1986). Unstructured triangulations are easy to build up even for complex geometries. In the context of moving boundary problems they offer the possibility to use highly graded meshes with local adaptivity. For sharp solid-liquid interfaces, we adopt a front-tracking method with many discretisation nodes on the moving boundary. As shown in

figure 2, at every time step the moving interface is explicitly resolved in the numerical grid and liquid and solid phases of the systems are strictly separated.

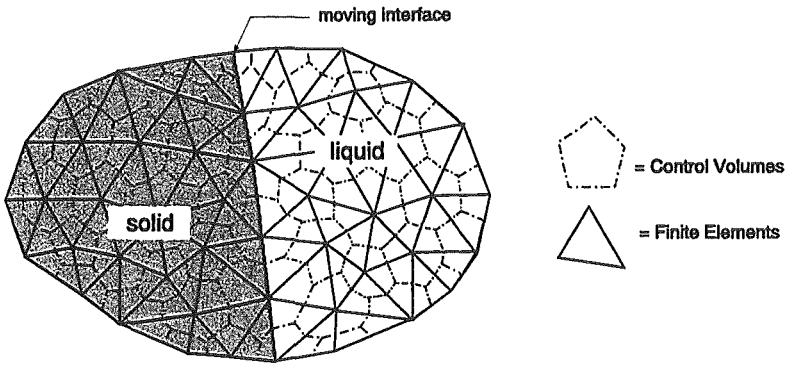

Figure 2. Two-domain discretisation around discrete solid-liquid interfaces.

Employing a moving-grid method as described above requires some computational effort for grid movement and adaptivity, but leads to a more physical implementation of the release or absorption of latent heat at a macroscopic planar solid-liquid interface. Several test cases with discrete solid-liquid phase transitions have been adopted to verify this numerical model. Results from these calculations have been compared with analytical, experimental or numerical benchmark solutions (Wintruff 1999). They demonstrate the feasibility of applying the moving unstructured grid scheme to discrete phase change problems and underline the reliability of the prediction for metallic core melt behaviour (see chapter 4).

4. RESULTS

Only results for metallic core melts are presented in this paper. Several one-component calculations are done, varying the aspect ratio A, the cooling temperature ϑ_{ex}, the internal Rayleigh number Ra and the internal Stefan number St. The Prandtl number is fixed at $Pr = 0.1$. The range of the internal Rayleigh number Ra has been chosen with respect to volumetric heat generation rates of about 500 kW/m^3 in core melt accumulations and to characteristic heights of between 10 and 20 cm. For larger accumulations the natural convective flow is expected to be turbulent (Farouk 1988).

Metallic core melts are characterised by low Prandtl numbers and a sharp transition from liquid to solid. The phase change temperature interval between solidus and liquidus temperature can be neglected, so phase change is assumed to take place at a constant melting temperature T_m. According to the situation shown in figure 1 the outer geometry of the accumulation is regarded as a fixed boundary with no slip-conditions.

Transient behaviour of the system

Starting with an isothermal temperature field below the melting temperature (solid state) the transient behaviour of the system can be divided in a sequence of three regimes (see figure 3). In the first regime, transient heat conduction is the only transport mechanism. When the core reaches the melting temperature the regime of internal melting starts. In a limited region in the core of the accumulation the internal heat is used to compensate the latent heat absorption due to transition from solid to liquid. Consequently, the liquid fraction in this core region rises continuously, creating a mushy phase inside and a discrete solid-liquid interface at its boundary to the pure solid phase. The phenomena of internal melting with a transient mushy

phase in internal heated one-component fluids has been observed earlier by Chan and Hsu (1987). The regime of internal melting is completed when the last crystal in the internal core region has been molten. Subsequently, the temperature exceeds the melting temperature and convective forces arise due to temperature gradients in the liquid phase. Afterwards, phase change occurs only at the discrete solid-liquid interface which moves outwards while the liquid phase grows. When natural convection is fully developed, internal heat is transported mainly by convection to the interface. The transient simulation terminates, if the motion of the interface has stopped (a steady state with a final crust thickness has been reached) or alternatively, if a crust break-up occurs (the local crust thickness at some place has become smaller than the typical dimension of a numerical cell).

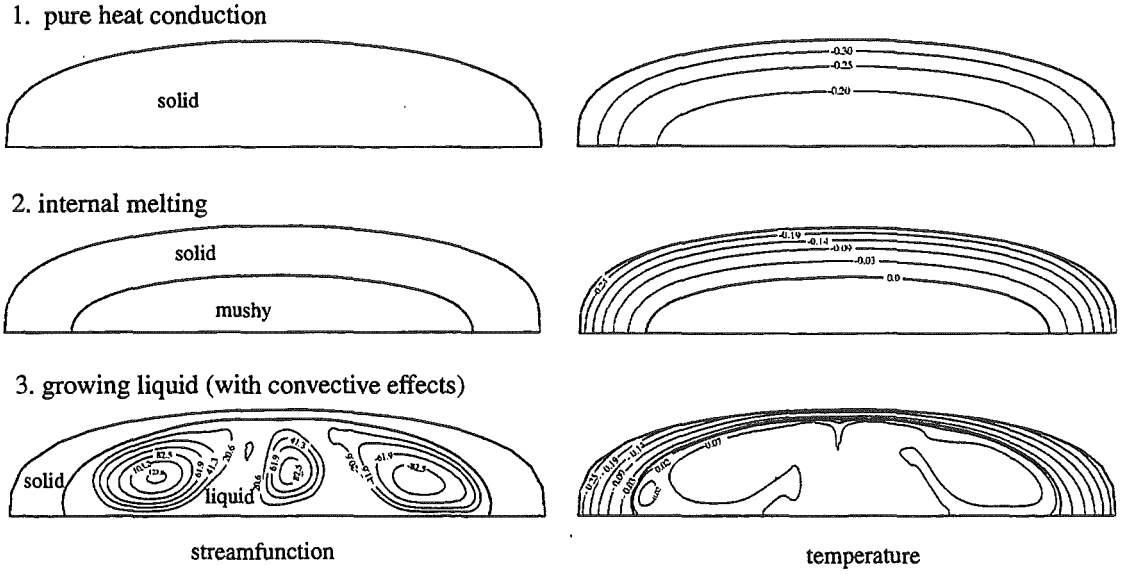

Figure 3. Three-regime model of the transient internally heated melting problem.

Several calculations were made to estimate the influence of geometry, of external cooling and of internal heating on the thermodynamic behaviour of the accumulation.

In figure 4, streamlines and isotherms of simulations with six different sets of parameters are shown. Only in case (d) (moderate external subcooling and large aspect ratio) a local crust break-up is expected. The strong mixing effect of the convective flow avoids strong interface deformations, so crust failure will occur somewhere in the most upper region of the accumulation. In cases (a), (b), (c), (e) and (f) the final crust thickness is reached.

Influence of the aspect ratio

A comparison of the results of cases (a) and (d) demonstrate the effect of the aspect ratio of the outer geometry of the accumulation. When the aspect ratio increases the dimension of the conductive heat fluxes in large parts of the accumulation is reduced to one. Heat is only transported in one spatial direction and higher temperature differences are necessary to compensate the internally-generated heat, compared to lower aspect ratio cases, where temperature gradients occur in both spatial directions. Consequently, smaller values of the aspect ratio A enlarge the minimum internal heat generation to ensure a crust break-up.

Influence of the Rayleigh number and the convective flow

Higher values of the internal Rayleigh number are equivalent to higher buoyancy forces in the liquid core. Consequently, the intensity of the fluid flow and the integral liquid fraction increase with increasing Rayleigh numbers. In all cases the fully-developed flow configuration is multicellular, unsteady and nonperiodically oscillating. The time averaged results of the different calculations (see figure 4) show that flow pattern with two and four convection rolls are favoured for the two different aspect ratios, respectively, but with increasing Rayleigh number, the flow pattern get more and more unsteady and the number and size of the rolls change continuously.

In the investigated Rayleigh number range, the increase of the liquid core volume compared with the limiting case of pure conduction is quite small (less than 10 %). The additional heat transport out of the liquid due to convective heat fluxes is reduced because of the strong convective cooling and mixing effect. In all cases, the maximum temperature in the liquid is diminished by more than 70 % compared to the value of pure conduction (see figure 5 a).

Influence of the external cooling temperature

Increasing external temperatures decrease the rest crust thickness because the average temperature level on the surface of the accumulation increases. In the limiting case of $Ra = 0$ and one-dimensional heat removal, crust failure occurs for $\vartheta > -0.5$.

calc.	*Pr*	*A*	ϑ_{ex}	*St*	$Ra \cdot 10^6$
(a)	0.1	2.5	-0.52	0.5	1.2
(b)			-0.85	1.0	2.4
(c)			-0.85	4.0	4.8
(d)		5.0	-0.52	0.5	1.2
(e)			-0.85	0.5	1.2
(f)			-0.85	2.0	2.4

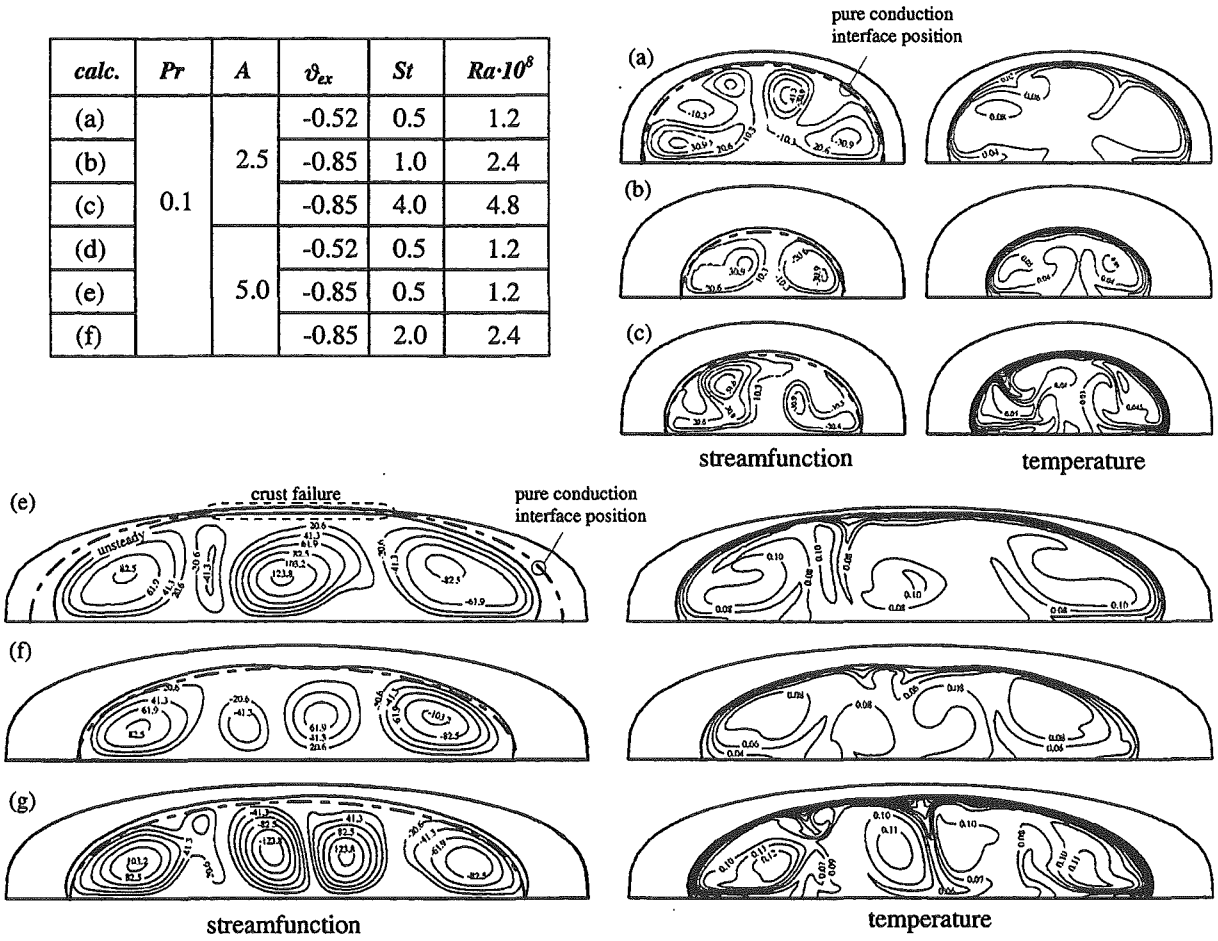

Figure 4. Streamfunction and temperature fields for metallic core melt simulations.

The wall heat flux distribution along the outer surface exhibits a configuration with two local maxima in the upper region (see figure 5 b). The position of the maxima changes in time due to the oscillating flow configuration in the liquid. Nevertheless, the influence of the convective flow on the crust thickness is small. The pure conduction limit is a good estimation of the resulting crust formation for different ϑ and A values.

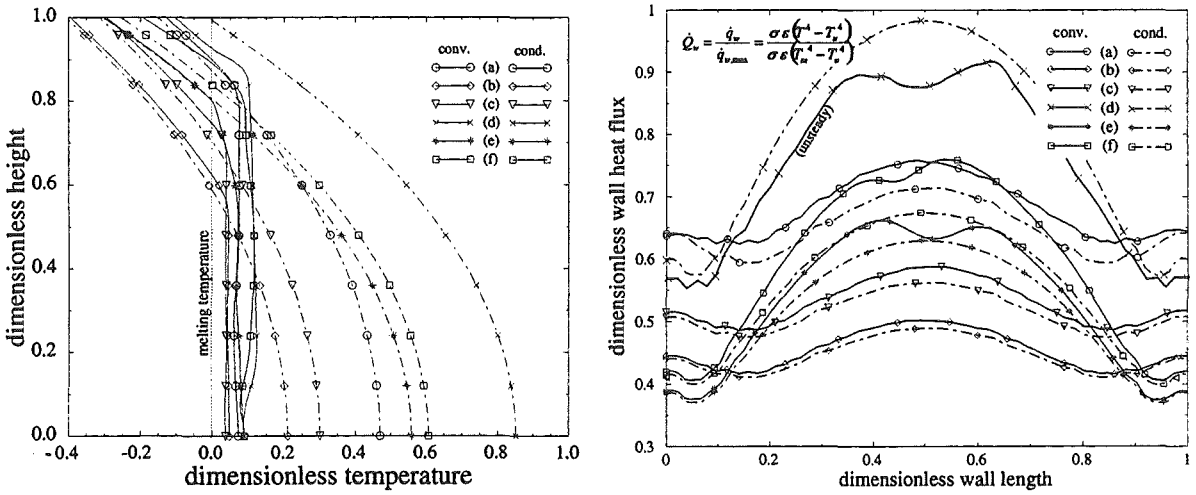

Figure 5. (a) Temperature profiles along the vertical centre line and (b) dimensionless wall heat fluxes along the outer surface for metallic core melt accumulations.

5. CONCLUSIONS

The above results demonstrate the applicability of the presented code to the convection dominated melting problem with internal heat sources. The two-domain approach on moving adaptive grids is able to track the moving solid-liquid interface in internal melting metallic core melt accumulations of arbitrary geometry. Surely, strong simplification (two-dimensional, laminar natural convective flow, homogenous one-component melts, constant material properties) have been made. The following items should therefore be interpreted as qualitative statements in consideration of the mentioned restrictions:

- Using typical material properties of metallic core melts, the natural convective flow in the liquid phase becomes unsteady and oscillatory even for flat accumulations. Effective internal Rayleigh numbers (calculated with the maximum height of the liquid core) larger then 10^7 are expected to lead to turbulent flow.

- A strong convective mixing and cooling is observed in all numerical simulations. The temperature distribution in the liquid phase is mainly isothermal with a thin thermal boundary layer near the free surface. Compared with the pure heat conduction solution the maximum temperature in the liquid phase is strongly reduced.

- In agreement with the strong mixing large local deformations of the phase interface are avoided. Convective heat fluxes cause only a small enlargement of the liquid core compared with the steady state pure conduction limit. The total volume of the liquid phase in the conduction case is always a good estimate for the final liquid fraction in the convective case.

NOMENCLATURE

A	aspect ratio, B/H
B	width
C	constant parameter
c_p	specific heat
H	height
L	latent heat
$\vec{n}$	normal vector
Pr	Prandtl number, ν/κ
Ra	internal Rayleigh number, $SH^5\beta g/\nu\kappa\lambda$
S	volumetric heat source
St	internal Stefan number, $SH^2c_p/L\lambda$
t	time
T	temperature
$\vec{v}$	fluid velocity vector
$\vec{w}$	mesh velocity vector
x,y	cartesian coordinates
β	thermal expansion coefficient
ε	emissivity
Γ	surface
κ	thermal diffusivity, $\lambda/\rho\, c_p$
λ	thermal conductivity
μ	kinematic viscosity
ν	dynamic viscosity
ϑ	dimensionsless temperature, $(T-T_m)/(SH^2/2\lambda)$
Ω	volume

Subscripts

C	conduction
ex	external
l	liquid
m	melting
s	solid
u,v	fluid velocity components
Γ	surface

REFERENCES

Brent, A. D., Voller V. R. and Reid, K., 1988. Enthalpy-porosity technique for modelling convection-diffusion phase change: Application to the melting of a pure metal. *Numer. Heat Transfer* **13**, 297 - 318.

Chan, S. H. and Hsu, K. Y., 1987. Generalized phase change model for melting and solidification with internal heat generation, *J. Thermophysics*, **1**, no. 2, 171 – 174.

Demirdzic, I and Peric, M., 1988. Space conservation law in finite volume calculations of fluid flow. *Int. J. Num. Meth. Fluids* **8**, 1037 - 1050.

Farouk, B, 1988. Turbulent thermal convection in an enclosure with internal heat generation, *Trans. of the ASME*, **110**, 126 – 132.

Huppert, H. E., 1982. The propagation of two-dimensional and axisymmetric viscous gravity currents over a rigid horizontal surface. *J. Fluid Mech.* **121**, 43 –58.

Prakash, C., 1986. An improved control volume finite element method for heat and mass transfer and for fluid flow using equal-order velocity-pressure interpolation. *Numer. Heat Transfer* **9**, 253 - 276.

Wintruff, I., 1999. An adaptive moving-grid model for melting and solidification problems. PhD thesis, University of Karlsruhe, *to be published.*

Session B 4:

PHENOMENA TO ACHIEVE COOLABILITY: FRAGMENTATION AND QUENCHING

Chairman: W. Scholtyssek

Implications of FARO and KROTOS experiments for FCI issues

D. Magallon (JRC- Ispra)
S. Basu (US-NRC)
M. Corradini (University of Wisconsin)

Abstract

The paper shortly reviews the findings from the FARO and KROTOS test programmes and shows how they contributed to the FCI issues resolution from the risk perspective. One of the most significant findings is that prototypic core melt shows no potential for generating a spontaneous steam explosion in the pouring mode as tested in FARO and KROTOS. A steam explosion could be externally triggered with corium melt, and this was done with up to 40 kg of melt in the FARO facility. However, the efficiency was so low as not to endanger the containment structures of the testing devices. Results of recent FARO tests demonstrated that 3-D conditions have a positive effect in mitigating the dynamic loads on the surrounding structures. Melt breakup by erosion of the jet column was found to be a continuous process in a stationary jet. With regard to the debris coolability issue, the results give the initial configuration and particle sizes which can be expected in the reactor case. The debris characteristics are very sensitive to the initial conditions. The debris bed can be totally fragmented, partly fragmented (re-agglomerated debris under particulate debris) or totally re-agglomerated (cake). The mean particle size obtained for the fragmented part of a debris was above 2.5 mm in quenching without propagating event and below 0.5 mm in case of a propagating event.

1. Introduction

At the time the FARO/KROTOS programme is being terminated, the objective of the paper is to analyse and summarise the implications of the FARO and KROTOS findings for the FCI related issues and to highlight the few complementary actions which would be required to definitely conclude on this item.

The FARO project is dedicated to the study of LWR severe accident issues involving melt/water interaction started in 1990. Previously, the FARO facility had been used for fuel-sodium interaction study in the field of LMFBR severe accidents. Since the beginning of the LWR project, it has been a joint venture with US-NRC, which co-financed the project, with the support and agreement of the EU Members States. The University of Wisconsin also participated in the venture, first as a NRC contractor and then as a JRC consultant on specific items.

The initial scope of the FARO-LWR programme was to determine in-vessel corium melt quenching characteristics experimentally at large scale and high pressure. Subsequently, the investigation was extended to in- and ex-vessel core melt relocation events in general: FCI, steam explosion (KROTOS), and core melt spreading. The results obtained on spreading are the subject of another paper presented at this meeting [1].

The FARO tests were designed to study the integral corium melt jet/water mixing and quenching behaviour by using 150-kg-scale of UO_2-based melt under prototypical conditions. Basically, the

penetration of molten corium into the water of the lower plenum or cavity during a hypothetical core melt down accident and its subsequent settling on the lower head or cavity floor were simulated. Twelve FARO tests completed to date involved quenching of UO_2-ZrO_2-(Zr) corium melts (melt mass from 18 kg to 176 kg) in saturated and subcooled water (see Table 1). These tests allowed the determination of the effect of system pressure (0.5, 2.0, and 5.0 MPa), water depth (1 m and 2 m), subcooling, and hydrogen generation on the quenching process. The melt quantities used in FARO were about one order of magnitude higher than in all previous work. Thus, the data represent a major contribution to the determination of the potential of water to quench the core material and to verify the corresponding computer models.

In parallel with the FARO tests, the KROTOS FCI experiments aimed at investigating the effect of fuel/coolant initial conditions and mixing on steam explosion energetics. Molten materials (both simulant and prototypic) up to 5 kg were used in a large number of KROTOS tests simulating various initial and boundary conditions. These included thirteen tests with corium of the same composition as in the FARO tests (see Table 2). The results of FARO and KROTOS tests have been reported in a number of articles [2, 3, 4, 5, 6, 7, 8].

2. Brief description of the FARO and KROTOS experiments

In the FARO facility, the corium is melted in the FARO furnace by direct heating using three power supplies form 3000V/2A to 60V/15000A. The melt is then delivered to a release vessel to ensure its controlled release. While in the release vessel, initial temperature of the melt is measured using tungsten ultrasonic sensors. Also, at this time, the furnace is isolated form the interaction vessel by a high pressure valve. The melt is released by gravity into a water pool of diameter 0.71 m and depth up to 2 m, which is contained in a pressure vessel (TERMOS or FAT) designed for 10 MPa and 573K pressure and temperature conditions. This test vessel is connected downstream to a condenser via a steam/water separator and exhaust valves, in order to vent and condense the excess of steam produced during the melt quenching. The debris is collected in a catcher put at the bottom of the test section. In one test (L-33) a trigger was applied at the bottom and induced a propagating event.

The KROTOS test facility consists of a radiation furnace, a release tube and the test section. The test material is melted is a crucible held in place in the furnace by means of a pneumatically operated release hook. The crucible is then dropped on a puncher which breaks its bottom and provides release of the melt to the water. Depending on the crucible design and melt composition, melt masses in the range of about 1 to 6 kg can be produced. Maximum achievable temperatures are 3300 K. The melt temperature is controlled by an optical bichromatic pyrometer measuring the wall temperature of the crucible. The pressure vessel is designed for 4.0 MPa at 493 K. It houses the test section, which consists of a strong stainless steel tube of inner diameter 200 mm and outer diameter 240 mm. The water level is variable up to about 1.3 m. The bottom of the test section is closed with a plate which may house a trigger device (gas or explosive charge).

The principal quantities measured in both FARO and KROTOS are the temperature of the melt, the pressures and temperatures both in the freeboard volume (static pressure measurements) and in the water (dynamic pressure measurements), and the temperatures in the debris catcher bottom plate. Visualisation of the processes is provided by a series of video cameras with rate up 1000 f/s.

Test	Corium Composition	Melt Mass (kg)	Melt Temperature (K)	Melt release diameter (mm)	Melt fall height in gas (m)	System pressure (MPa)	Gas phase	Water depth (m)	Water Temperature (K)	Water subcooling (K)	Water Mass (kg)	Date of Test
L-06	A	18	2923	100	1.83	5	Steam/Ar	0.87	539	0	120	02Dec91
L-08	A	44	3023	100	1.53	5.8	Steam/Ar	1.00	536	12	255	29July92
L-11	B	151	2823	100	1.09	5	Steam/Ar	2.00	535	2	608	02Dec93
L-14	A	125	3123	100	1.04	5	Steam/Ar	2.05	537	0	623	23June94
L-19	A	157	3073	100	1.99	5	Steam(1)	1.10	536	1	330	22June95
L-20	A	96	3173	100	1.12	2	Steam	1.97	486	0	660	30Jan96
L-24	A	177	3023	100	1.07	0.5	Steam	2.02	425	0	719	5Dec96
L-27	A	129	3023	100	0.73	0.5	Steam	1.47	424	1	536	3Dec97
L-28	A	175	3052	50	0.89	0.5	Steam	1.44	424	1	517	2Apr98
L-29	A	39	3070	50	0.74	0.2	Argon	1.48	297	97	492	2July98
L-31	A	92	2990	50	0.77	0.2	Argon	1.45	291	104	481	11Nov98
L-33	A	100(2)	3070	50	0.77	0.4	Argon	1.60	293	124	625	1July99

Table 1. FARO LWR Test Series - Main Experimental Conditions

A: 80w%UO_2 – 20w%ZrO_2
B: 77w%UO_2 – 19w%ZrO_2 – 4w%Zr
(1): >95w%steam; <5w%argon
(2): Only 40 kg in water at the time of the trigger

Test	Composition	Melt Mass (kg)	Melt Temperature (K)	Melt release diameter (mm)	System pressure (MPa)	Gas phase	Water depth (m)	Water Temperature (K)	Water subcooling (K)	Water Mass (kg)	Ext. Trigger	Date of Test
K-32	A	3.0	3063	30	0.1	He	1.08	351	22	7.1	no	01Sep93
K-33	A	3.2	3063	30	0.1	He	1.08	298	75	7.7	no	21Oct93
K-35	A	3.1	3023	30	0.1	He	1.08	363	10	7.7	yes	21Apr94
K-36	A	3.0	3025	30	0.1	He	1.08	294	79	7.7	yes	02June94
K-37	A	3.2	3018	30	0.1	He	1.11	296	77	33.9	yes	02Aug94
K-45	A	3.1	3106	30	0.1	He	1.14	369	4	34.0	yes	12Dec95
K-46	A	5.4	3086	30	0.1	He	1.11	290	83	34.0	yes	15Feb96
K-47	A	5.4	3023	30	0.1	He	1.11	291	82	34.0	yes	28Mar96
K-52	A	2.6	3133	30	0.2	He	1.11	290	102	34.0	yes	13Dec96
K-53	A	3.6	3129	30	0.36	He	1.11	290	122	34.0	yes	25Mar97
K-56	A	4.5	3033	30	0.37	He	0.98	290	123	35.1	no	13Nov97
K-58	A	4.5	3077	30	0.37	He	0.92	289	125	30.9	yes	3Mar98
K-63	A	2.0	n.a.	30	0.21	He	0.94	295	99	29.6	yes	27July99

Table 2. KROTOS Corium Test Series - Main Experimental Conditions

A: 80w%UO_2 – 20w%ZrO_2

3. Summary of findings from the FARO experiments

The influence of melt quantity, melt composition, water depth and initial pressure on quenching was assessed on the basis of twelve tests performed in various conditions [3-5]. Tests involved UO_2-based melt quantities in the range 18-177 kg at a temperature of approximately 3000 K. No spontaneous steam explosion occurred in any of the tests. In the tests at 5.0 and 2.0 MPa good mixing with significant melt breakup and quenching was obtained during the penetration in the water. At 0.5 MPa and saturated water, good penetration of the melt into the water could still be achieved, but part of the debris was ejected from the water. In long pours, e.g., FARO L-28, melt breakup by erosion of the jet column was found to be a continuous process for the duration of the jet. In this specific test, the quenching rate during the stationary phase was around 30 MW, corresponding to 1 MJ/kg of melt, i.e., 2/3 of the energy content of the melt. The addition of Zr metal in the melt in one of the tests induced a much more efficient quenching than in a similar test with no Zr metal, and produced a totally fragmented debris. It was found that significant amounts of H_2 were also produced in tests with pure oxidic melts (~0.2 kg H_2 for 100 kg of melt).

Reducing the pressure from 5.0 MPa to 2.0 MPa did not seem to affect the quenching behaviour significantly. On the contrary, the test performed at 0.5 MPa exhibited different mixing and pressurisation behaviour, comparable with what observed in the KROTOS test facility [7, 8].

The debris was generally formed of a cake and overlaying debris. Fig.1 shows that the mass averaged particle size of the fragmented part of the debris was between 2.5 and 5 mm whatever the test conditions. In some cases, no cake was found (L-11 with Zr metal in the melt, L-31 with subcooled water). In one case (L-29, conditions similar to L-31) little melt quenching occurred during melt fall in water and all the debris was a cake, indicating that the quenching process might be very sensitive to initial conditions.

In FARO L-33, last test of the series, a self-sustained propagating event was triggered by an explosive charge when about 40 kg of melt had entered the water. The maximum pressure measured at the inner vessel wall located at a radial distance of 350 mm form the centre of the test section was 8 MPa. The maximum impulse was 20 kPa.s and the mechanical energy release about 100 kJ (i.e., two orders of magnitude higher than the trigger energy), giving an efficiency of the order of and 0.2 %. This FCI, classified as a mild propagating event, caused the internal vessel to deform plastically and lift inside the FAT housing vessel. The FAT vessel itself moved 2.5 mm up and down.

4. Summary of findings from the KROTOS experiments

A number of alumina tests were performed with both subcooled and saturated water conditions in a stainless steel test section of diameter 200 mm and for water depth ~1 m [6, 8]. The subcooled tests normally resulted in spontaneous steam explosions. The tests at low subcooling were performed to confirm, on one hand, the suppression of spontaneous steam explosions under such conditions and, on the other hand, that such a system can still be triggered by using an external initiator. The other test parameters in these alumina tests included the melt superheat and the initial pressure. All the tests in the investigated superheat range (150 K - 750 K) produced a steam explosion. No evidence of the explosion suppression by the elevated initial pressure (in the limited range of 0.1 - 0.375 MPa) was observed in the alumina tests. The maximum conversion ratio (energy released/initial thermal energy) recorded in these tests was about 2.5 percent.

The corium test series included tests both under subcooled and near saturated conditions at ambient pressure and subcooled tests at an elevated pressure from 0.2 to 0.37 MPa. Corium melt masses in these tests varied from 2.4 kg to 5.1 kg (~3073 K). None of these tests with corium produced an energetic steam explosion. However, propagating low energy events with a maximum energy conversion ratio of about 0.15 % were observed when an external trigger was applied. Present experimental evidence suggests that the water depletion in the mixing zone suppresses energetic steam explosions with corium melts at ambient pressure and in the present pour geometry. On the other hand, elevated pressure reduces significantly the integral void fraction also with corium allowing better melt/water contact at triggering and generation of mild interactions. However, the coarse mixture so far has not been suitable for the mild interactions to escalate into an energetic steam explosion.

Melt penetration data and preliminary results of visualisation of melt pre-mixing in recent alumina and corium tests suggest differences in melt break-up behaviour between alumina and corium melts. The breakup behaviour determines the premixing configuration and can therefore be an important factor in determining the yield of the interaction. Fig.2 shows the particle size distribution in those KROTOS tests were a propagating event was recorded. The debris size is on average one order of magnitude lower than in the FARO quenching test (see Fig.1).

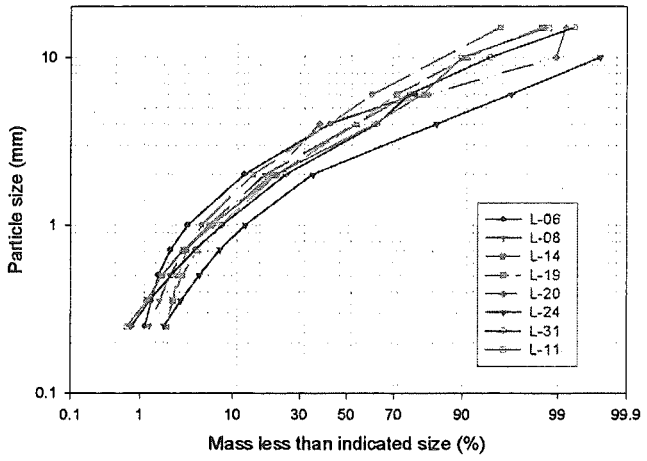

Fig. 1. Particle size distribution in FARO tests

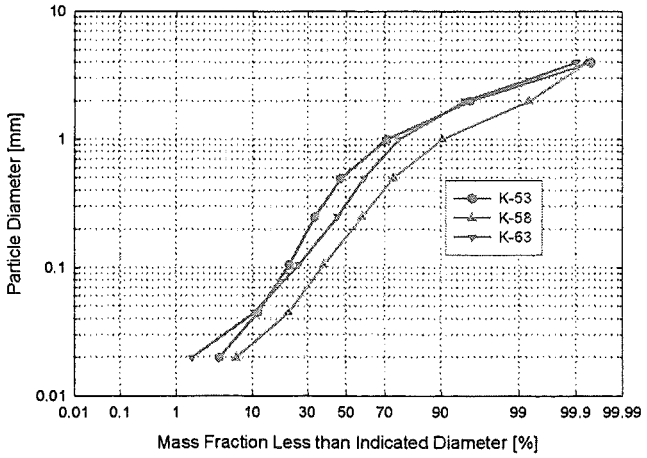

Fig. 2. Particle size distribution in KROTOS corium tests with steam explosion

5. Implication of FARO and KROTOS findings for the FCI issues

With the resolution of the alpha-mode failure issue from the risk perspective [9, 10], the remaining FCI issues are debris quenching and coolability, and energetic FCI with implications to RPV lower head integrity and reactor cavity structure integrity under shock loading. These issues are relevant to accident management strategies for operating reactors (cavity flooding in case of ex-vessel or late reflood in-vessel) as well as accident mitigation features for advanced reactors (e.g., in-vessel retention by ex-vessel cooling).

One significant finding from the risk perspective of these issues is that prototypic core melt shows no potential for generating a spontaneous steam explosion in the pouring mode as tested in FARO and KROTOS. The presence of metallic phases in the molten corium enhanced melt breakup and debris dispersal. Due to increasing void fraction and inert gas (hydrogen) production by chemical reaction during the interaction, corium melts with metallic components exhibit, from the thermodynamic point of view, even less propensity than pure oxidic corium to induce steam explosion. Thus, it may be concluded that in the absence of any external trigger mechanism, the integrity of structures is not likely to be challenged by a FCI.

Also, in these experiments, no threatening thermal load on the bottom structure was measured despite the presence of a cake in some tests. However, at low pressure and saturated water, part of the small size debris are easily rejected from the mixing zone due to the large steam volume production rate and thus does not collect on the bottom structures. Hydrogen was produced in all corium tests, the consequence of which in a reactor core melt accident would require consideration. The same applies to the debris dispersion, which may result from melt relocation at low pressure. The results for long pours suggest that erosion of the jet column may be an efficient breakup process and quenching for large (reactor-scale) pours.

The experiments performed at a system pressure of 0.1 MPa and subcooled water with small masses of prototypic core melt in the KROTOS facility did not produce an explosion even when an artificial trigger was applied. The experiments performed at higher system pressures in the range of 0.2 to 0.4 MPa showed very weak explosive events when artificially triggered. However, the debris generated by these events are much finer than those produced by non-explosive quenching, which might rise the problem of their coolability. Conversely, very energetic steam explosions easily occurred when pure alumina melt was used in similar geometrical conditions.

It may be concluded that the material characteristics plays an important role in steam explosion triggerability and explosivity, possibly explaining the low yield observed in corium tests. Leaving aside the possible role of chemical reactions during the explosion propagation, hydrogen generation during the premixing phase is believed to make the triggering of an explosion difficult (increase of void fraction and of vapour film stability) and to limit the energetics. It is noted that reliable material properties of high temperature core melt mixtures and experiments involving prototypic core melt in reactor-like configurations are crucial in extrapolating experimental findings to a real reactor situation.

Concerning the implication for modelling, the application of the various FCI codes to the FARO and KROTOS experiments has revealed that the codes have not yet achieved a stage of sufficient validation for all the phases of an FCI. One can refer in particular to the recent CSNI-sponsored International Standard Problem exercise (ISP-39) [11], where many of the FCI codes were used for the post-test prediction of FARO L-14. One general conclusion from the ISP-39 exercise is

that none of the codes performed consistently well in post-test prediction of all measured quantities. The calculated energy release to the steam/water system was in general too low with respect to the experiment. This poor performance of the codes was attributed mainly to a deficiency in modelling the energy partitioning between steam and water, and the heat transfer at the steam/water interface. Actually, most of these codes either do not have jet breakup models at all or do not have well validated models. Consequently, there is a need to improve jet breakup models and validate these models against melt jet experiments. This would help reduce the parametric uncertainties still present in these codes.

6. Suggestions for future work

The experience gained from the FARO and KROTOS FCI test series induces thinking that the consequences of a steam explosion at the reactor scale may not be as severe as previously envisioned, and that a limited additional experimental effort in some areas would be sufficient to support this conclusion. It mainly concerns ex-vessel situations, where only a limited number of tests were performed, and requires using corium with metallic phases and triggering steam explosion at small (e.g., KROTOS) and large (e.g., FARO) scale. This would complete the FCI data base and allow to definitely establish whether the mechanical loading of reactor structures due to steam explosions could jeopardise the containment integrity. This is an issue for both PWR and BWR types of plants when the cavity is flooded according to accident management strategies.

It can be concluded that from the debris quenching and coolability perspective, sufficient data has been collected for the integral behaviour of oxidic melts to allow an adequate validation of models. The data base is still lacking for prototypical melts which contain metallic phases and there is also a need to adequately instrument these future experiments so that local mixture conditions and properties can be evaluated for code validation.

References

[1] TROMM W., FOIT J., MAGALLON D., WIDER H., Dry and wet spreading experiments with prototypic material at the FARO facility and theoretical analysis, This meeting.

[2] CORRADINI M. L., HOHMANN H., Multi-phase flow aspects of fuel-coolant interactions in reactor safety research, Nucl. Eng. Des. **145** (1993), 207-215.

[3] MAGALLON D., HOHMANN H., High pressure Corium melt quenching tests in FARO, Nucl. Eng. Des. **155** (1995), 253-270.

[4] MAGALLON D., HOHMANN H., "Experimental investigation of 150-kg-scale corium melt quenching in water, Nucl. Eng. Des. **177** (1997), 321-337.

[5] MAGALLON D., HUHTINIEMI I., HOHMANN H., Lessons learnt from FARO/TERMOS Corium melt quenching experiments, Nucl. Eng. Des. **189** (1999), 223-238.

[6] HOHMANN D., MAGALLON D., SCHINS H., YERKESS A.: FCI Experiments in the aluminum oxide/water system, Nucl. Eng. Des. **155** (1995), 391-404.

[7] HUHTINIEMI I., HOHMANN H., MAGALLON D:, FCI Experiments in Corium/Water System, Nucl. Eng. Des. **177** (1997), 339-349.

[8] HUHTINIEMI I., MAGALLON D., HOHMANN H.,"Results of recent KROTOS FCI Tests: Alumina VS.Corium melts", Nucl. Eng. Des. **189** (1999), 379-389.

[9] BASU S., GINSBERG T., *editors*, Proceedings of the Second Steam Explosion Review Group (SERG-2) Workshop, NUREG-1524, August 1996.

[10] AKIYAMA M., YAMANO N., SUGIMOTO J., *editors*, Proceedings of the OECD/CSNI Specialists Meeting on Fuel-Coolant Interactions, NEA/CSNI/R(97)26, ed., , January 1998.

[11] ANNUNZIATO A. et al., *editors*, OECD/CSNI International standard problem 39, NEA/CSNI/R(97)31, 2 volumes, May 1998.

OECD Workshop on Ex-Vessel Debris Coolability
Karlsruhe, Germany, 15–18 November 1999

Organized in collaboration with
Forschungszentrum Karlsruhe (FZK) GmbH

Modeling of Coarse Breakup of Molten Core Jet in JASMINE Code

Kiyofumi Moriyama, Yu Maruyama, Hideo Nakamura, Kazuichiro Hashimoto and Jun Sugimoto
Severe Accident Research Laboratory
Japan Atomic Energy Research Institute
Tokai-mura, Ibaraki-ken, 319-1195 Japan
email: mori@sarl.tokai.jaeri.go.jp

Abstract

A new model for molten core jet breakup in a water pool was developed for JASMINE-pre, the premixing module of a steam explosion simulation code developed at JAERI. The present model was designed emphasizing two aspects: separation of the melt model from the multiphase solver, and giving finer spatial resolution for the melt. The model consists of 3 components: jet, pool and particles, and will be combined with a two-phase flow code to handle the coolant flow field. The melt jet is solved by 1-D CIP method, known for high spatial resolution, while the pool and particles are handled by 1-D FDM and Lagrangian method, respectively. It was confirmed from test calculations that the developed model can capture the profile of the jet precisely without numerical diffusion. Also, the model reproduced the results of a melt jet breakup experiment in non-boiling conditions (ALPHA-MJB16) qualitatively.

1 Introduction

In the framework of ALPHA (Assessment of Loads and Performance of Containment Vessel in Hypothetical Accidents) Program, a steam explosion simulation code JASMINE (JAERI Simulator for Multi-phase Interaction and Explosion) has been developed at Japan Atomic Energy Research Institute since 1994. JASMINE is purposed to simulate FCIs by multiphase thermohydraulics model integrating basic mechanistic models specific to the phenomena as constitutive equations, and as a final goal, to provide a real scale assessment of the influence of the steam explosion in LWR severe accidents. JASMINE has two modules to simulate premixing and propagation/escalation phases, and the present work is related to the premixing module JASMINE-pre. The molten core jet breakup behavior which plays an important role for the ex-vessel core coolability is also involved in the scope of JASMINE-pre.

The first version of JASMINE-pre [2] was designed as a three-field model handling water, vapor and melt and tested with several kinds of experimental database, including melt-coolant and particles-coolant interactions. From those test calculations, it was found the initial version had problems closely related to its basic structure, such as numerical conversion difficulty with fine grid or high melt fraction, strong effect of numerical diffusion on the melt phase, causing non-physical complexity into the basic model verification. [3] Those problems become more serious in handling a large scale geometry, i.e. a reactor scale analysis, where one needs to use a coarse grid, sometimes much larger than the actual melt jet diameter, to save the computer power within a reasonable range.

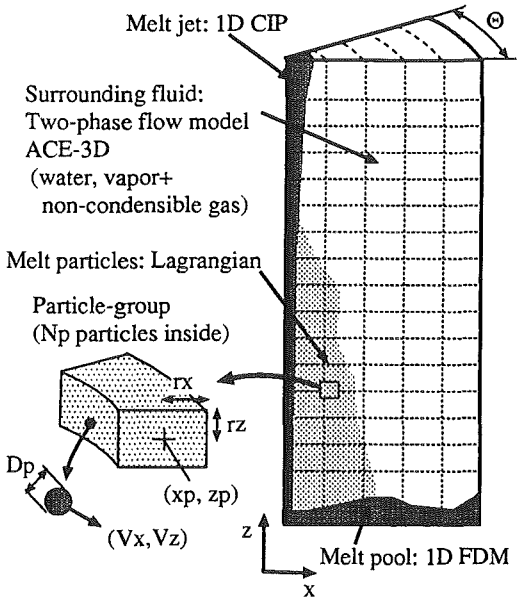

Figure 1: Concept of the new structure of JASMINE-pre

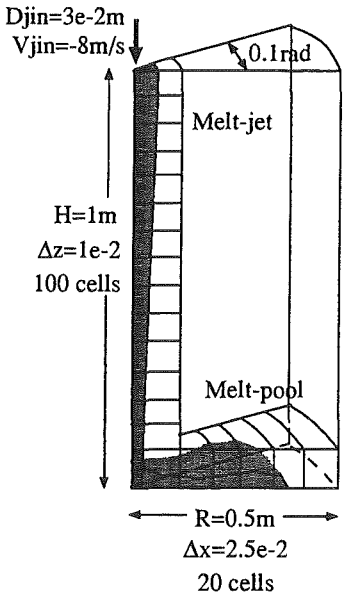

Figure 2: Test problem on free-falling liquid column

A major modification of the basic structure of JASMINE-pre was initiated in 1998 to overcome the problems and give the code a flexibility to accommodate more mechanistic models related to the melt. Separation of the melt model from the multi-field solver for easier development and maintenance, and a finer spatial resolution for the melt model were emphasized in this task.

Regarding the ex-vessel molten core coolability evaluation, relatively long term behavior should be modeled reasonably, which includes settlement of the particulate debris onto the floor and generation of molten pool by the part of the melt jet which is not fragmented. This aspect is also improved by the present modification.

In the following sections, a brief description of the new melt model and test calculations are given. The calculations here were performed with the melt model alone assuming constant surrounding fluid conditions.

2 Brief Description of the Melt Model

The new structure of JASMINE-pre is schematically shown in Fig. 1. The calculation domain considered is an azimuthal slice of a cylindrical space whose thickness is Θ. The present melt model is a 2-D cylindrical model which satisfies the minimal requirement to handle the phenomena in question.

The jet model was formulated with one dimensional conservation equations in z-direction and solved by CIP (cubic-interpolated pseudo-particle method) [7], which is known as a high resolution scheme free from numerical diffusion. The jet is assumed to reside in the central column of the two-phase flow grid and flowing from the top to the bottom. The grid for melt jet is fit in the z-direction grid of two-phase flow model, with a manner that one two-phase flow cell is subdivided into $N_{sub}(\sim 5)$ jet cells to give the jet finer resolution than the coolant flow field.

A part of the jet can be fragmented and produces melt particles. Those particles are modeled as grouped particles and tracked by Lagrangian method. When particles are generated on the jet surface, the mass, temperature, size and velocity of particles are given for each jet cell and time step.

When the jet column or a particle group reaches the bottom, it can make a pool of melt. The melt pool was modeled one-dimensionally in r-direction and solved with finite difference method. It resides in a single layer of the two-phase flow grid on the bottom. The pool model uses the same x-direction grid with the two-phase flow model. A conventional upwind scheme and SIMPLE algorithm [6] were applied. This component of melt was built mainly to accommodate the melt agglomerated on the floor as a continuous lump, which is often observed in experiments, and the spatial resolution of this part was not considered very important.

The surrounding fluid involving water, vapor and non-condensible gases is modeled with 3-D two-phase flow code ACE-3D developed by Ohnuki et al. [5] Note that the test calculation presented here was done with the melt model alone, without the link of this part.

The details of the model including basic conservation and constitutive equations were published elsewhere [4, 1].

3 Basic Test on the Jet/Pool Models

A simple test problem shown in Table 2 was solved to examine the numerical feature of the jet and pool models. A jet of 3 cm diameter was dropped into a vacant cylindrical space from the top with an initial velocity of 8 m/s, and accumulated on the bottom as a pool. The friction, heat transfer and particle entrainment were neglected.

The result for the jet and pool are shown in Fig. 3 and Fig. 4. As shown in Fig. 3, the leading edge at step 500 and trailing edge at step 2000 were in good agreement with the theoretical solution indicated with solid lines. It was confirmed that the present method for the jet has a good ability to preserve the shape as well as the position of sharp edges of the profile. It was also confirmed that the pool model reproduces the spreading of the pool qualitatively correctly.

The mass conservation error was checked. The errors in the jet, jet-pool mass transfer and pool were in the ranges of 10^{-4}, 10^{-3} and 10^{-7}. The largest error occurred at the connection from jet to pool, but still in a tolerable range.

4 Simulation of Non-Boiling Melt Jet Experiment

4.1 Experimental and Analytical Conditions

After the confirmation on the numerical feature was obtained, a test calculation was performed with an experimental data from ALPHA-MJB (Melt Jet Breakup) series. The case referred is MJB16, a non-boiling experiment. In this experiment, a low melting temperature alloy called "anatomical alloy" (Bi-Sn-Pb-In) at 110 °C was poured into a water vessel of 3 m tall and 80×80 cm cross section, as a jet with diameter of 30 mm. The density, surface tension of the melt measured by the authors were $\rho_J = 9400$ kg/m^3 and σ_J =0.46 N/m. The nominal melting temperature was 60 °C. Water temperature was set at 50 °C. Location of the melt exit was at 2.7 m from the vessel bottom and the water level was 2.3 m. From a simple calculation on the flow in the melt pot and release nozzle, the initial velocity of the jet was 3.5 m/s. With the prescribed set of the initial temperatures of melt and water, the contact interface temperature between two fluids is about 100 °C which causes neither boiling nor quick solidification upon the contact and gives relatively long time for jet breakup.

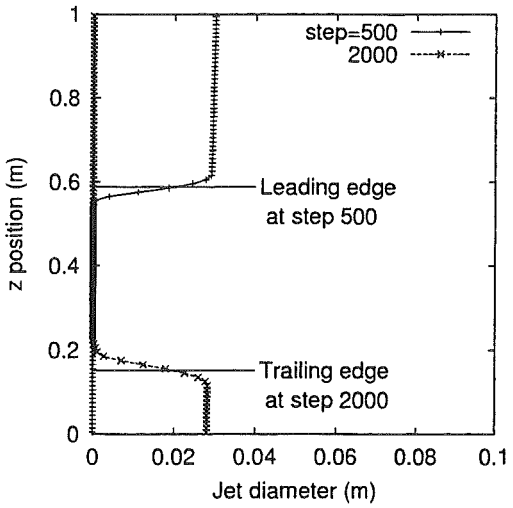

Figure 3: Calculation on the free-falling liquid column (Jet)

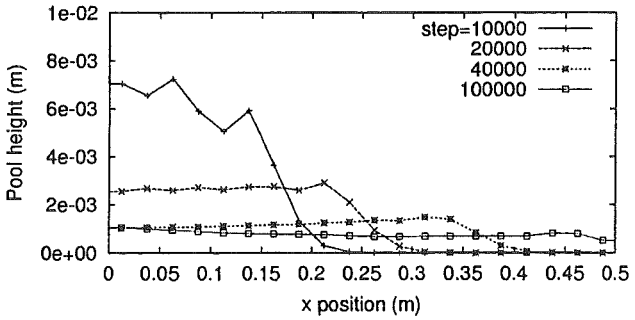

Figure 4: Calculation on the free-falling liquid column (Pool)

Figure 5 shows the melt jet observed by high speed video camera in the experiment. It was observed that the melt jet was totally broken up during flowing down in the water pool making a cloud. The position of the leading edge and the radius of the melt jet and particle cloud, as well as the debris particle size distribution were taken from the experimental result for comparison.

Conditions of the calculation are schematically shown in Fig. 6. The vessel with square cross section was modeled with a cylinder which has the same cross section, and a slice of 0.1 radian wide was taken as the calculation domain. Time step was 5×10^{-4} s. The empirical factors involved in the model [1] were tentatively set for this simulation as in Table 1.

4.2 Snapshots of the Simulation Result

Figure 7 shows some snapshots of the simulation results. The profile of the melt jet and pool are indicated with solid and broken lines, respectively. Position of the center of every particle group is plotted with cross dots.

It is seen from the figure that the jet was eroded after entering the water and totally broken up at the height about 1.6 m, the particles made a cloud of radius 0.10~0.15 m, and finally stack on the floor as a debris bed. This result is a quite good reproduction of the phenomena observed in the experiment.

In the simulation, a part of the debris agglomerated to make a continuous lump (or a frozen pool) although which was not the experimental result. The particles are assumed to freeze when its average temperature is 10 K higher than the melting point as in Table 1 but still this result was made. When the criterion was set as $T_{av} < T_{melt}$, the particles were totally merged into pool. A model of surface temperature drop and/or heat transfer from the pool will probably be necessary to improve this point.

4.3 Position of the Leading Edge and Cloud Radius

Figures 8 and 9 show the comparison of simulation (lines) and experimental (dots) results in the jet leading edge position and the radius of the particle cloud.

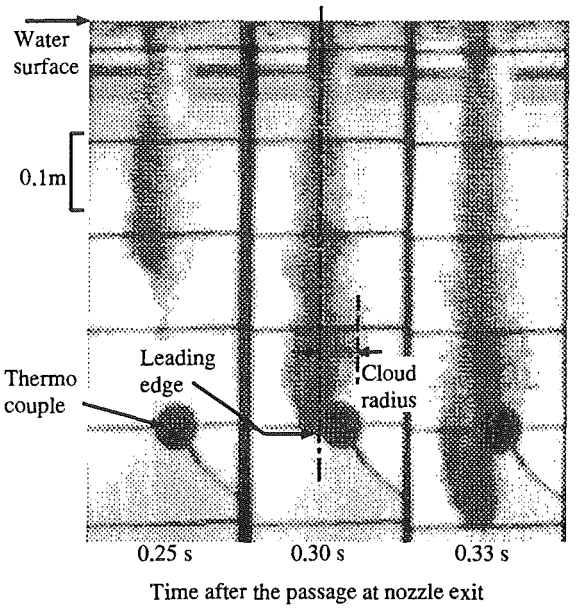

Figure 5: Observation of the melt jet with hight speed video

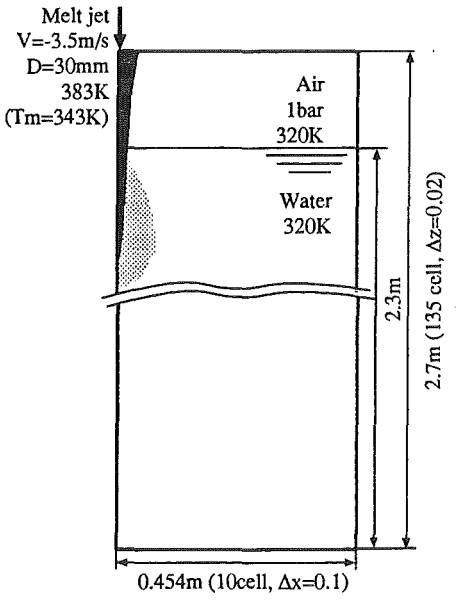

Figure 6: Conditions of MJB16 simulation

In Fig. 8, the experimental result shows that the leading edge velocity suddenly slowed at the height 1.6 m, which tells the jet column was totally broken up at this height, and the resulted particles sank making slower envelope below. The solid line, the leading edge of the jet column calculated, stopped at the height 1.6 m and reached a steady state where the mass supplied from the top and eroded in water were balanced. The broken line, the edge of the particle cloud, sank more slowly below the *breakup height* with the terminal velocity according to the particle diameter. The plot for the particle cloud was made from the average of 5 leading particle groups to moderate the effect of a few groups scattered out from the cloud seen in Fig. 7. The strange stepwise changes in the line is due to one of the leading groups disappeared by merging into the pool.

In Fig. 9, the radius of the cloud observed in the experiment (cross dots) had a tendency to continuously expand, while the simulation result showed a faster expansion in the beginning but rapid saturation later.

The discrepancy between the experiment and simulation observed in the leading edge position and cloud radius is not discussed further in this work because, to some extent, those long term behavior of the particle cloud are related to the fact that the water motion induced by the melt jet flow is not modeled in this simulation. This aspect will be looked into more detail after the coupling of the present model and two-phase flow model are done.

4.4 Debris Size Distribution

Figure 10 shows the cumulative mass fraction curves obtained from the experiment and simulation. The good agreement of the mass median diameter in the experiment and simulation is the result of setting the model constant $C_{de} = 10$ (see Table 1). It means that the present model [1] results in an order of underestimation of the diameter without correction by the empirical factor. Besides, the distribution of the debris size is too sharp compared with the experiment. Further work is required to improve the model considering the break-off process of the particle more

Jet model	
Entrainment x-velocity constant C_{vx}	: 0.10
Entrainment z-velocity constant C_{vzwt}	: 0.40
Entrainment mass flux constant C_{me}	: 0.15
Entrainment diameter constant C_{de}	: 10
Friction constant C_f	: 3.0
Heat transfer coefficient h (W/m^{2}K)	: 0
Pool model	
Friction factor with the fluid C_{fa}	: 0
Friction factor with the floor C_{fw}	: 0
Heat transfer coefficient h (W/m^{2}K)	: 0
Particle model	
Friction factor modifier C_{cfrc}	: 2.0
Damping factor for particle collision C_{dampar}	: 0.5
Damping factor at walls $C_{dampwal}$	: 0.1
Tolerance of properties to merge groups	: 20%
Pre-particle group release criterion	: $N_p > 100$ or $r_x > \Delta x/4$
Particle freeze criterion	: $T_{av} < T_{melt} + 10\ K$

Table 1: Set of empirical factors in MJB16 simulation

detail.

5 Conclusions

A new model for molten core jet breakup in a water pool was developed for the premixing module of JASMINE, a steam explosion simulation code developed at JAERI. The present melt model consists of 3 components: jet, pool and particles. It is designed to be combined with a two-phase flow code to handle the coolant flow field in a 2-dimensional cylindrical geometry.

Test calculation with the present melt model was performed assuming a constant properties and state variable of the surrounding fluid. From the results of the calculation, the followings were concluded.

- A simulation of free-falling liquid column showed that the present jet model can capture the jet profile precisely without numerical diffusion problem even at sharp edges. Also, the precision of the mass conservation in the jet and pool models was confirmed.
- In a simulation of a jet breakup experiment at non-boiling condition (ALPHA-MJB16), the present model reproduced the observed phenomena qualitatively. It was shown that the present model is capable of handling the late phase phenomena in molten core jet breakup, including particle settlement and debris bed formation.
- The adequateness of the constitutive correlations for friction, heat transfer and particle generation used in the present model need to be checked in detail after the coupling with the two-phase flow model is completed.

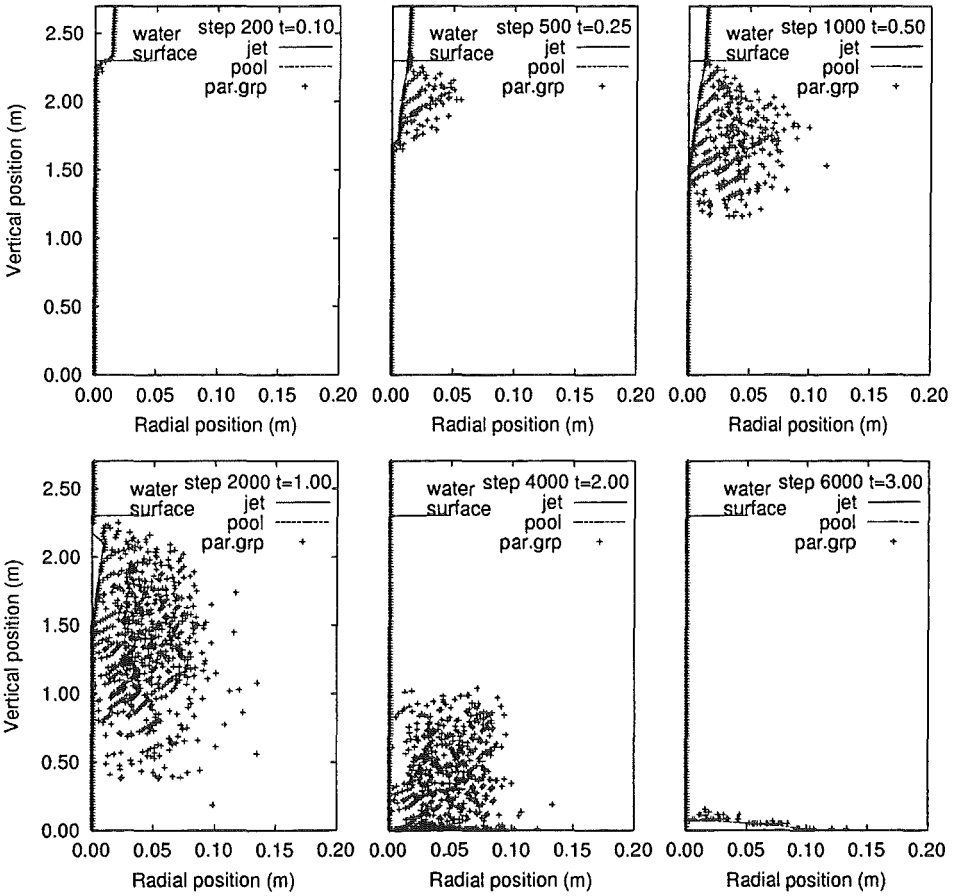

Figure 7: Snapshots of the simulation result

Acknowledgments

The experimental operation involved in this work was supported by an extensive cooperation of H. Ito, K. Komori, H. Sonobe, M. Nogami of Safety Facility Engineering Services Devision of JAERI, and M. Kojima of Nuclear Engineering, Co. The authors would like to acknowledge their devoted works.

References

[1] K. Moriyama, Y. Maruyama, H. Nakamura, and K. Hashimoto. Three-component melt jet breakup model for FCI analysis. In *Proceedings of the Workshop on Severe Accident Reseach, Japan (SARJ-99), Tokyo (To be published as JAERI-Conf)*, 1999.

[2] K. Moriyama, N. Yamano, Y. Maruyama, T. Kudo, and J. Sugimoto. Study of premixing phase of steam explosion with jasmine code in ALPHA program. In *Proceedings of 4th International Conference on Nuclear Engineering, New Orleans*, volume 1B, pages 903–915, 1996.

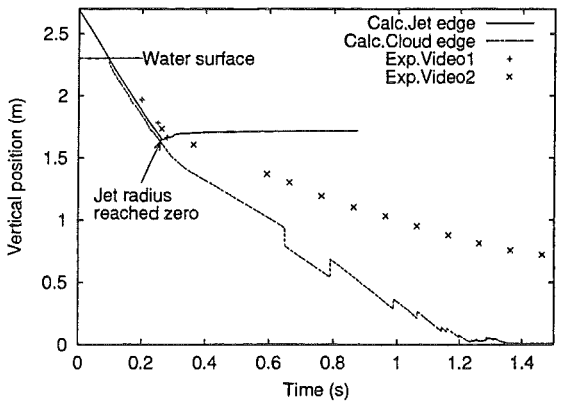

Figure 8: Leading edge position in the simulation and experimental results

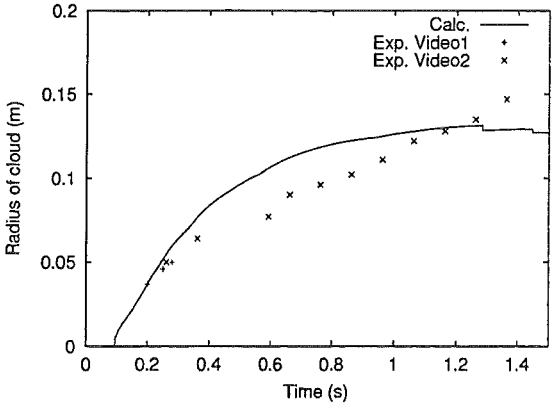

Figure 9: Radius of the particle cloud in the simulation and experimental results

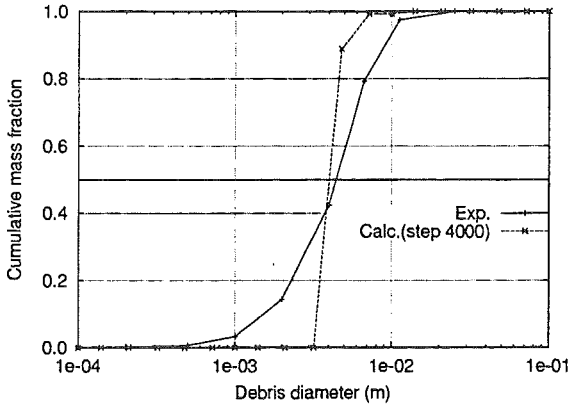

Figure 10: Debris size distribution in the simulation and experiment

[3] K. Moriyama, N. Yamano, Y. Maruyama, H. S. Park, and J. Sugimoto. FCI simulation code development in ALPHA program. In *Seminor on the Vapor Explosions in Nuclear Power Safety, Izu*, 1996.

[4] K. Moriyama, Y. Yang, Y. Maruyama, H.-S. Park, and J. Sugimoto. One dimensional molten jet model for integral FCI analysis code. In *Proceedings of the Workshop on Severe Accident Reseach held in Japan (SARJ-98), Tokyo (JAERI-Conf 99-005)*, pages 358–363, 1998.

[5] A. Ohnuki, H. Kamo, and H. Akimoto. Development of multidimensional two-fluid model code ACE-3D for evaluation of constitutive equations. Technical Report JAERI-Data/Code 96-033, Japan Atomic Energy Research Institute, 1996.

[6] S. V. Patankar. *Numerical heat transfer and fluid flow*, chapter 6. Hemisphere publishing corporation, 1980.

[7] T. Yabe and T. Aoki. A universal solver for hyperbolic equations by cubic-polynomial interpolation, I. one-dimensional solver. *Computer Physics Communications*, 66:219–232, 1991.

OECD Workshop on Ex-Vessel Debris Coolability
Karlsruhe, Germany, 15-18 November 1999

Organised in collaboration with
Forschungszentrum Karlsruhe (FZK) GmbH

COTELS Project (1): Overview of Project to study FCI and MCCI during a Severe Accident

Hideo Nagasaka, Masami Kato and Isao Sakaki
Systems Safety Department, Nuclear Power Engineering Corporation
Fujita Kanko Toranomon Bldg., 5F, 17-1, 3-chome Toranomon,
Minato-ku, Tokyo, 105-0001 Japan
nagasaka@nupec.or.jp, ms-kato@nupec.or.jp and sakaki@nupec.or.jp

Yuri Cherepnin, Yuri Vasilyev, Alexander Kolodeshnikov,
Vladimir Zhdanov and Vladimir Zuev
National Nuclear Center
Bldg. 6 Lenin St., Kurchatov City, Republic of Kazakhstan
cherepnin@nnc.kz, ysv@nnc.kz, dep240@nnc.kz, zhdv@nnc.kz and dep240@nnc.kz

ABSTRACT

Fuel coolant interaction (FCI) and molten core concrete interaction (MCCI) have been studied experimentally within the framework of COTELS project from 1995 as a joint study between NUPEC (Japan) and NNC (Republic of Kazakhstan) using one of the testing complex at NNC. The testing complex includes three experimental facilities "SLAVA", "LAVA" and "LAVA-M" for debris coolability tests. Three types of experiments were carried out.

To get the molten corium, the electric induction melting furnace (EMF) was used. The EMF produced ~60 kg of corium containing UO_2, stainless steel, Zr and ZrO_2. The temperature of the produced melt was about 3200 K. The melt was discharged into the water pool in Test A or onto the concrete trap in Test B/C. The corium in the concrete trap was heated in Test B/C by another induction melt heater.

Prior to main Test A and Test B/C, several supporting experiments were conducted. Integrity of graphite crucible with TaC sheet during producing UO_2 corium was confirmed experimentally. The induction melt heater was calibrated and the efficiency for the induction heater of "LAVA-M" facility was determined as 47%. The thermal conductivity and thermal diffusivity of concrete up to about 1073 K, and melting–solidification points of eutectics generated from corium components were determined experimentally. Discharge corium behavior, using UO_2 corium, was also observed by speed cameras in Test 01.

1. INTRODUCTION

Since WASH-1400 identified that in-vessel steam explosion (SE) was one of early containment failure scenarios (α-mode), extensive efforts to resolve this issue have been concentrated. These efforts were reviewed by the second steam explosion review group and it

concluded that α-mode failure issue was negligibly small from risk perspective (Basu, 1996). However, ex-vessel SE is still one of remaining issues mainly due to lower pressure condition under which SE is more easily to occur. Suppression of MCCI by water injection onto molten corium accumulated on the containment floor is one of the important accident management (AM) to prevent containment failure during a severe accident (SA). However, the suppression of MCCI has not been observed in former tests, such as SWISS (Blose, 1987), WETCOR (Blose, 1993) and MACE (Spencer, 1991 and Farmer, 1992) tests.

Nuclear Power Engineering Corporation (NUPEC) of Japan in collaboration with National Nuclear Center (NNC) of Republic of Kazakhstan has conducted debris cooling experiments (COTELS project), using 60 kg prototypical corium material composed of UO_2, Zr, ZrO_2 and stainless steel, under ex-vessel conditions simulating low pressure vessel failure sequence, to evaluate the validity of AM. COTELS project consists of three types of experiments: Test A, Test B and Test C. Test A focused on FCI phenomena when a molten corium fell into water pool on containment floor. Typical ex-vessel FCI conditions of SA in actual plant were pertinently simulated in COTELS project based on SA scenario analysis (Nagasaka, 1995). Test B/C were performed to investigate FCI regarding water injection onto corium (Test B) and MCCI under water injection onto molten corium (Test C), successively conducted after Test B. Main features of these tests were simulation of corium falling process before FCI/MCCI, decay heat simulation by induction heating, usage of basaltic concrete and simulation of side wall made of concrete.

Prior to the main tests, several supporting experiments were conducted to realize and to correctly evaluate the main test results. This paper summarizes the features of COTELS test facilities and the results of the supporting experiments.

2. EXPERIMENTAL FACILITIES

2.1. Description of Facilities.

"SLAVA" facility is provided for conducting the experiments in order to study the melt jet parameters simulating prototypical melt (corium) of core composition elements. Basic components of "SLAVA" facility are test vessel, removable bottom and concrete (or copper) trap. Optical windows are located on the prismatic funnel of the test vessel. Figure 1 illustrates the diagram of the "SLAVA" facility. "SLAVA" facility, connected to the water and gas supply systems, is equipped with sensors for measuring temperature and medium pressure. About 35 thermocouples are installed in the concrete trap body.

To record the melt jet parameters, a filming complex containing three speed cameras (two CKC-1M type and one-"Gladiolus-1") and a video is prepared on "SLAVA" facility. Film camera CKC-1M provides shooting speed of 150 to 4000 frame/s using 16 mm film, while "Gladiolus" camera allows shooting speed of 24 to 240 frame/s using 35 mm film.

"LAVA" facility is provided for the experiments to study FCI, including investigations of SE phenomena. Major "LAVA" facility components are test vessel and melt catcher made of concrete installed in it. The diagram of "LAVA" facility is shown in Fig. 2. "LAVA" facility housing is made of coiled steel. The technological windows are made on the lateral housing surface. All windows are sealed with technological plugs. Measuring lines and connecting branches for water and gas supply into the test vessel are connected through the plugs. A melt catcher and a cylindrical vessel allow to alter the volume and depth of the water pool without changing free space volume. Measuring items are medium pressures and temperatures, and

medium composition.

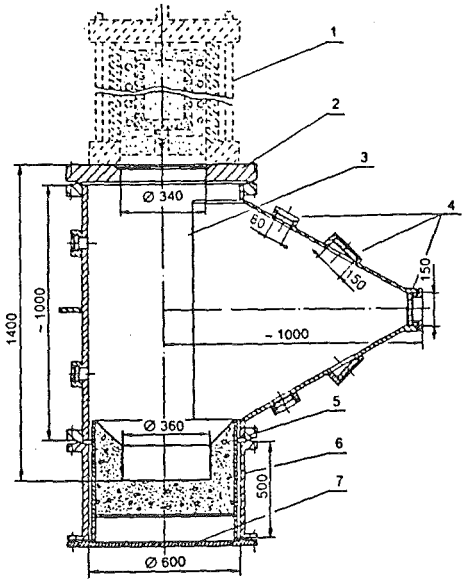

1-Electric melting furnace; 2-Test vessel lid; 3-Test vessel ; 4- Optical window; 5- Concrete trap; 6-Cylindrical adapting pipe; 7-Bottom.

Fig. 1. "SLAVA" facility

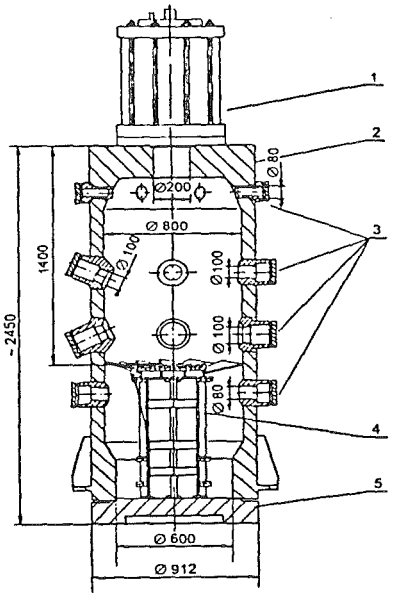

1-Electric melting furnace; 2-Test vessel; 3-Technological windows; 4-Melt catcher; 5- Removable bottom

Fig. 2. "LAVA" facility

"LAVA-M" facility is provided for the experiments to study MCCI under simulation of decay heat release. "LAVA-M" facility consists of test vessel and concrete trap with the induction heater of the melt. The diagram of "LAVA" facility is given in Fig. 3. "LAVA-M" facility housing is a thick-walled cylindrical vessel made of steel with four hardening ribs. Two types of nozzle (spray type and jet type) for water supply to the melt surface are installed on the upper end surface of the housing. Test vessel housing has a removable bottom below a concrete trap and a heater for simulating decay heat release. The melt heater is a circular coil inductor with water-cooling. The heater provides the net supply of about 75 kW power to the melt. Thirty five to forty five thermocouples are installed in the concrete trap. "LAVA-M" facility is connected to the steam condensing system to determine steam amount generated in the course of the experiment. Gas sampling systems is equipped to evaluate gas components generated in the test vessel.

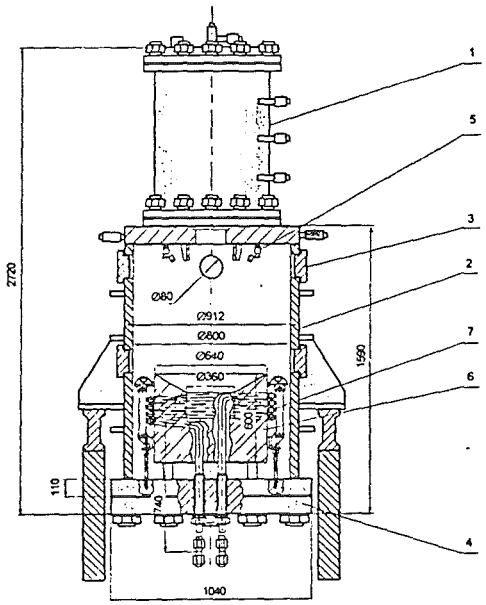

1-Electric melting furnace; 2- Test vessel; 3-Technological window; 4- Removable bottom; 5- Water supply nozzle; 6-Concrete trap; 7- Induction heater.

Fig. 3. "LAVA-M" facility

2.2. Electric Melting Furnace

EMF is one of the basic experimental facility components. EMF provides burden melting (mixture of construction materials of the core) and discharging the produced melt into

the test vessel. EMF is installed on the upper flange of the experimental facility. EMF is the induction furnace where crucible material and melted materials are heated by the induction heating. EMF diagram is given in Fig. 4. The EMF consists of crucible with a lid and breaking plug, Ta insert, multi-turn copper inductor, multi-layer thermal insulation and housing with lid and bottom. The melt is discharged through the through-hole in the crucible plug, which opens instantaneously after the plug breaking by a special mechanism. The breaking mechanism and the shutter, for closing the discharge hole in the EMF crucible after the melt discharge, are located in the housing bottom. The inductor, furnace housing and the housing lid and bottom are cooled with water. The inductor is powered from the transducer of high frequency. The EMF is equipped with means for measuring pressures, temperatures of its construction elements and cooling water and gas sampling systems. Major specifications of the "SLAVA", "LAVA" and "LAVA-M" facilities are summarized in Table 1.

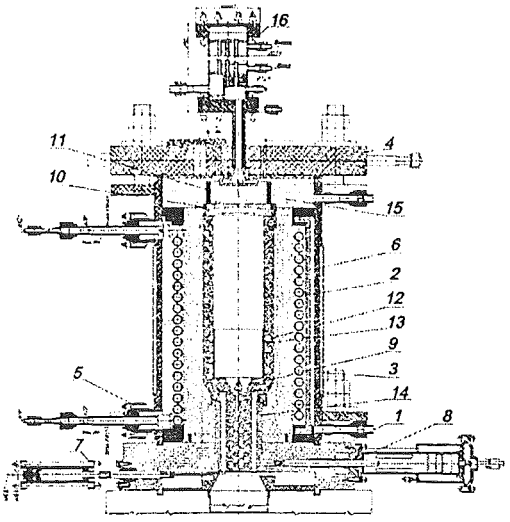

1-Hosing bottom; 2-Inductor; 3-Housing; 4-Housing cover; 5- Current supply; 6- Magnetic circuit; 7 – Shutter; 8 – Breaking plug mechanism; 9- Breaking plug; 10 – Crucible cover; 11 Ring sleeve; 12-Crucible; 13-Ta-Insert; 14 – Annulus thermal insulation insert; 15-Thermal insulation material; 16 -Heat exchanger

Fig. 4. Electric melting furnace

Table 1. Experimental facilities specifications

Parameter	SLAVA	LAVA	LAVA-M
Electric melting furnace power, kW	to 200	to 200	to 200
Melt temperature, K	to 3200	to 3200	to 3200
Maximum melt mass, kg	60	60	60
Melt falling height, m	~1.4	1...1.4	~1.3
Water depth, m^3	–	to 1.0	to ~0.1
Water volume, m^3	–	to 0.4	to 0.01
Gas volume of test vessel, m^3	~0.3	to 0.6	~0.4
Maximum medium pressure, MPa	0.2	10.0	2.0
Maximum gas medium temperature, K	to 600	to 600	to 600

2.3. Facility Operation Support Systems

The systems providing the experiments include: systems for water and steam supply to the test vessel, cooling system for the EMF, inert gas supply system, system for hot gas discharge from the EMF and the test vessel, system for gas sampling, steam condensation system, system for water drainage from the test vessel, electrical system and its cooling system.

The information-measuring system has been established on the basis of multi-purpose computation complex "Unikont UK-211" using PC. "Unikont" complex allows to make interrogation and recording ~600 measuring channels, including 500 channels of analog signal and

50 channels of inlet and outlet digital signals.

To measure the temperature field in the concrete trap, 48-channel temperature measuring complex is used on the basis of computer MicroPC, Octogen Systems, and G-5 transducers Grayhill. The independent system for measuring pressure pulse (8 channels) has been provided on the basis of speed analog-digital transducers CPN-80 and computer with "Pentium-120" processor. All measuring systems are joined into a local computation network, which provides the information exchange between the systems and operative data processing, received from all measuring systems.

3. SUPPORTING TESTS

During the stage of experimental facilities designing, a couple of problems have been raised. First of all, these were the problems associated with the production of uranium dioxide materials composition melt and discharge of the produced melt from the EMF to the test vessel. The solution of these and other problems allowed establishing the experimental facilities being capable of simulating the processes typical of SA conditions.

In addition, several supporting tests have been carried out prior to the main experiments. The most significant of them are the following: (1) the material test to develop robust crucible in producing UO_2 corium, (2) the test on calibration of the concrete trap induction heater, (3) the test on measuring some thermal and physical concrete properties under high temperature condition and (4) the test on determination of melting and freezing points of eutectics produced from corium components.

It should be noted that Test 01 was also considered as supporting experiment by its content and goals. Actually Test 01 experiments were targeted to evaluate process conditions for generating melt and determination of corium jet behavior, knowledge of which was necessary in the evaluation of the main experiments.

3.1. Material Test to Develop Robust Crucible in Producing UO_2 Corium

This group of experiments included: (1) testing technology of protective coatings application on graphite parts of the electric melting unit, (2) testing of the technology of the tantalum sheet carbiding during the melting process using model EMF at VChG-135 stand, (3) investigation of thermochemical stability of the crucible units of TaC under high temperature conditions and to the corium components at VChG-135.

The choice of tantalum carbide is explained as follows. Firstly TaC has a high melting point (~4000 K accordingly to data from different authors). Moreover, possible TaC/C interaction, bringing a change in stoichiometric carbide composition, which causes decreasing of TaC melting point only about 500 K, i.e. the melting temperature of 3400 to 3500 K. Finally, TaC has high chemical resistance with respect to corium components, which was tested experimentally at VChG -135 stand.

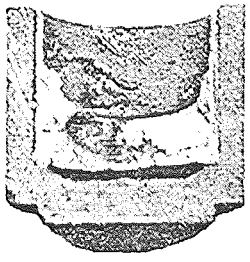

Fig. 5. Longitudinal section of the model crucible

Integrity of graphite crucible with TaC sheet during melting UO_2 was confirmed by supporting experiments and EMF, shown in Fig. 4, was developed. Figure 5 presents the slit view of "composite" crucible with UO_2-ingot, which was melted at VChG-135 stand at temperature of ~3200 K during 45 min.

3.2. Experiments on Heat Calibration of Melt Heater

The objective of the experiments on heat calibration of the melt heater is to determine the amount of net heat applied to the melt at different inductor power range. A graphite block (350 in diameter and about 100 mm in height) was used as the corium model, because the graphite electric resistance was close to corium resistance containing UO_2/metal mixture at high temperature. To minimize heat losse from the graphite block, its top surface was covered with an insulation layer (graphite felt) of 30 to 50 mm in thickness. Seven thermocouples were installed in the graphite block along the radial direction. The thermocouples layout in the graphite unit is illustrated in Fig. 6. Current and voltage in the electric heater circuit, water flow rate and water temperatures at inlet and outlet of the heater cooling path were measured.

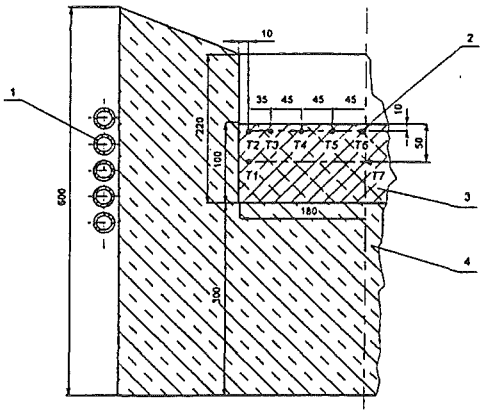

1-Induction heater; 2-Thermocouple;3-Graphite block; 4-Concrete trap

Fig. 6. Thermocouples location in the graphite block

The total energy supplied to the graphite block was determined using two independent ways. The one was the calorimetric method, using the measured data on graphite block temperature dynamics. The other was the method of heat balance between the total energy supplied to the inductor and energy released in cooling water and heater construction materials. The average electric efficiency of the heater determined by both test results was ~47%. A heat loss from the graphite block, subjected to the experiment mode, varied within the range of 10 to 20%.

3.3. Test on Concrete Thermal Properties Measurement at High Temperature

Thermal conductivity and thermal diffusivity of the concrete used in Test B/C was measured by the instantaneous heat source method. Temperature dependence of the concrete thermal conductivity was examined in the heating furnace. High-precision temperature regulator VRT-2, providing ±0.5 K accuracy for temperature control within the range of 0 to 1473 K, was used as a temperature control device. The measured thermal conductivity and thermal diffusivity of the concrete up to 1073K are given in Fig. 7.

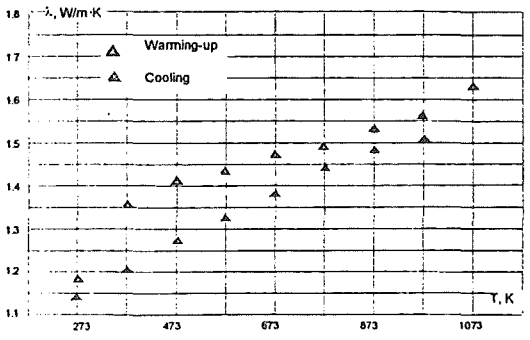

Thermal conductivity

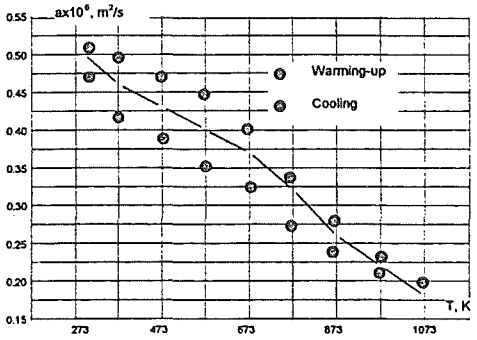

Thermal diffusivity

Fig. 7. Concrete thermal properties versus temperature

3.4. Test on Determination of Liquidus–Solidus Temperatures of Eutectics Produced from Corium Components

The experiments on determination of melting and freezing points of eutectics from corium components were carried out to get more detailed data about physical and chemical processes taken place in the EMF crucible during burden melting. These tests were carried out by induction stand VChG-135. Cooling thermograms of tested materials were recorded using spectral ratio pyrometers. Two series of experiments were conducted.

Firstly, small-chipped two-compound burden (Fe–Zr; Ta–Fe; Ta–Zr; Ni–Zr) was filled in the model graphite crucible and melted by the induction method and then was cooled. In the experiments with the study of Ta–Fe and Ta–Zr alloys, the burden was heated up to 1773 K and 2173 K, respectively, in order to obtain eutectic formation characteristics between the components. The obtained temperatures of freezing points basically agreed with the existent literature data.

The burden in the form of corium fragments with average dimensions of 1 to 2 mm in size, obtained in the results of Test A at "LAVA" facility, was loaded in the model graphite crucibles in the second experiments group. The burden was heated up to the temperature of 3073 K. The objective was to obtain temperature of eutectic melting-solidification and melting point of corium after re-melting. A series of expe-riments showed that the corium melting point was in a temperature range of 2423 to 2673 K.

3.5. Evaluation of Corium Falling Behavior

About 60 kg of melt at about 3150 K was discharged into the dry trap through 5cm hole under Ar–atmosphere using "SLAVA" facility. Three tests were conducted using the composition of 55%–UO_2, 15%–stainless steel, 25%–Zr and 5%–ZrO_2, simulating prototypical LWR corium.

By means of speed camera, the melt discharge behavior was recorded (see Figure 8). Based on the obtained cine graphs, basic geometrical parameters of corium jet, duration time of the melt discharge from the EMF and motion speed of the jet were determined. These experimental data are presented in Table 2. Flow mode behavior of falling jet was continuos turbulent jet associated with small break-up of jet surface. In case of 0.27MPa

Fig. 8. Falling corium jet

Table 2. Melt jet parameters of burden including UO_2 (Test 01)

Parameter	01-2e	01-1	01-4
1. Differential pressure between EMF and test vessel, MPa	~0.27	<0.01	0
2. Falling speed into trap, m/s	12.3	7.4	7.6
3. Falling time (up to moment of trap contact), s	0.133	0.329	0.316
4. Average flow rate, kg/s	160	122	126
5. Spraying angle, degree	~25	0	0

pressure difference between EMF and the test vessel, falling corium showed slightly diverging behavior. The corium, fallen on the concrete floor, was continuos corium with high porosity. Test 01 experimental data were utilized to evaluate test results from Test A and B/C.

4. CONCLUSION

(1) COTELS project has been conducted since 1995 to investigate ex-vessel debris coolability (FCI/MCCI), based on severe accident sequence analysis of LWR.
(2) Main characteristic features of test facilities are: (a) 60 kg molten UO_2 corium at 3200 K; (b) adjustable pool depth without changing air space volume (FCI test); (c) simulation of corium falling process and induction heating to the fallen corium for decay heat simulation (MCCI test) and (d) concrete trap totally made of basaltic concrete (MCCI test).
(3) Following several supporting experiments were successfully conducted: (a) the material test to develop robust crucible in producing UO_2 corium; (b) the test on evaluation of induction coil efficiency to simulate decay heat; (c) the test on measuring of thermal conductivity and diffusivity of concrete under high temperature conditions; (d) the tests on determination of melting and freezing points of eutectics, produced from solidified corium components.
(4) Observation of flow mode of falling corium jet and corium dispersion characteristics on concrete floor clarified the continuos turbulent jet associated with small break-up of jet surface and the accumulated continuous debris with high porosity.

5. ACKNOWLEDGEMENTS

This work was sponsored under the contract by the Ministry of International Trade and Industry, Japan.

REFERENCES

Basu, S. and Ginsberg, T., 1996. A Reassessment of the Potential for an Alpha-Mode Containment Failure and a Review of the Current Understanding of Broader Fuel-Coolant Interaction Issues, *Second Steam Explosion Review Group Workshop*, NUREG-1524

Blose, R.E., Gronager, J.E., Suo-Anttila, A.J. and Brockmann, J.E., 1987. SWISS: Sustained Heated Metallic Melt/Concrete Interaction with Overlaying Water Pools, NUREG/CR-4727,

Blose, R.E., Powers, D.A., Copus, E.R., Brockmann, J.E., Simpson, R.B., Lucero, D.A., 1993. Core-Concrete Interaction with Overlying Water Pools : The WETCOR-1 Test, NUREG/CR-5907

Farmer, M.T., Spencer, B.W., Armstrong, D.R., 1992. MACE Test M1B Data Report, Argonne National Laboratory Report, ACE-TR-D6

Nagasaka, H. Hamazaki, R and Takahashi, Y., 1995. "Scenarios of Ex-vessel Debris Cooling as Related to Nuclear Power Safety", *Proc. Probabilistic Safety Assessment Methodology and Applications*, Seoul Korea. 26-30

Spencer, B.W., Fischer, M., Farmer, M.T., Armstrong, D.R., 1991. MACE Scoping Test Data Report, Argonne National Laboratory Report, MACE-TR-D03

OECD Workshop on Ex-Vessel Debris Coolability
Karlsruhe, Germany, 15-18 November 1999

Organised in collaboration with
Forschungszentrum Karlsruhe (FZK) GmbH

COTELS Project (2): Fuel Coolant Interaction Tests under Ex-Vessel Conditions

Masami Kato and Hideo Nagasaka
Systems Safety Department, Nuclear Power Engineering Corporation
Fujita Kanko Toranomon Bldg., 5F, 17-1, 3-chome Toranomon
Minato-ku, Tokyo, 105-0001 Japan
ms-kato@nupec.or.jp nagasaka@nupec.or.jp

Yuri Vasilyev, Alexander Kolodeshnikov and Vladimir Zhdanov
Institute of Atomic Energy, National Nuclear Center
Str. Krasnoarmeyskaya –10, Kurchatov, Republic of Kazakhstan
ysv@nnc.kz dep24@nnc.kz zhdv@nnc.kz,

ABSTRACT

Extensive efforts have been performed to resolve in-vessel fuel coolant interaction (FCI) concerning α-mode failure issue. However, there are several basic differences between in-vessel and ex-vessel FCI conditions. FCI phenomena when a molten corium falls into water pool on containment floor during a sever accident (SA) were experimentally investigated in COTELS Test A. Typical ex-vessel FCI conditions of SA in actual plant were pertinently simulated in the tests based on SA scenario analysis of LWR. In the tests, about 60kg of UO_2 mixture was poured into water pool. In most tests conducted, measured pressure in the test vessel reached the first peak value as long as 0.5 s compared with the time observed in steam explosion (SE), then it gradually approached the final quasi-steady state pressure within 10 s. No violent SE was observed in any tests. Most of poured corium was broken up and only small amount of ingot corium was found on the pool bottom. The first peak pressure was well correlated by the corium particle size which was much larger than that usually observed in SE. Measured final quasi-state pressure was larger than that evaluated by the initial stored energy in corium due to non-condensible gas generation as a result of oxidation of metallic components in the corium. The non-dimensional first peak pressure was well correlated by one non-dimensional parameter not only for COTELS data but also for FARO data.

1. INTRODUCTION

Since in-vessel SE was identified as one of early containment failure scenarios (α-mode failure) in WASH-1400, not only FCI researches to understand the fundamental SE phenomena but also a systematic efforts to evaluate a probabilistic approach concerning α-mode failure have been extensively performed. These efforts were reviewed by the second steam explosion review group (SERG-2) and it concluded that α-mode failure issue was negligibly small from risk perspective (Basu, 1996) and this conclusion was supported by the recent OECD/CSNI

specialists meeting at Tokai, Japan (Akiyama, 1997). However, ex-vessel SE is still one of remaining issues mainly due to lower pressure condition under which SE is more easily to occur. Recent FARO experiments (Magallon, 1998) suggested that metallic Zr in UO_2-ZrO_2 mixture might enhance a break-up of the corium in pool. KROTOS experiments (Huhtiniemi, 1997) concluded that an energetic SE was less likely to occur for a few kg of UO_2-ZrO_2 mixture compared with molten alumina even under low pressure and highly subcooled water conditions. However, there are still a few data available under ex-vessel conditions.

This paper deals with COTELS Test A which focuses on FCI phenomena when a molten corium falls into water pool on containment floor. There are several basic differences between in-vessel and ex-vessel FCI conditions, e.g. ambient pressure and gas composition, corium jet diameter and composition, depth and temperature of water pool and pool bottom material. Typical ex-vessel FCI conditions in actual plant were pertinently simulated in COTELS project based on SA scenario analysis (Nagasaka, 1995). Dimensional analysis on the first peak pressure due to FCI was conducted based on the evaluation of the test results.

2. TEST FACILITY AND TEST CONDITIONS

The test facility (LAVA) mainly consists of an electric melting furnace (EMF), a test vessel and a melt catcher as shown in Fig. 1. The EMF has a capability to melt 60 kg of corium composed of UO_2, Zr, ZrO_2 and SS by induction heating (Nagasaka, 1999). Thermocouples and pressure sensors were installed in the test vessel. Gas sampling line was prepared to evaluate H_2 gas generation. The diameter of falling corium jet is 5 cm, corresponding to an instrumentation line of reactor pressure vessel (RPV). Pressure difference between EMF and the test vessel can be adjusted to vary corium velocity. Ex-vessel corium includes not only core structures but also structures in a lower plenum, so that the selected corium composition was UO_2 (55wt%)+Zr (25%)+ZrO_2 (5%)+SS (15%) including more metallic components.

The BWR SA scenario analysis suggested that the existence of water pool on the containment floor before RPV failure was only possible for LOCA sequence and pool depth was shallow. Thus, as reference pool conditions, the temperature is nearly saturated and the depth is 0.4 m. Five cm thickness concrete plate is laid on the melt catcher to examine the effect of interaction among corium, water and concrete considering shallow water pool. As a phase-II AM in Japanese LWRs, a reactor cavity is filled with water before RPV bottom failure to prevent a steel containment shell attack in BWR Mark-I or to suppress a molten core concrete interaction in PWR containment. Pool water is highly subcooled in both cases. In COTELS Test A, these AM conditions were also simulated.

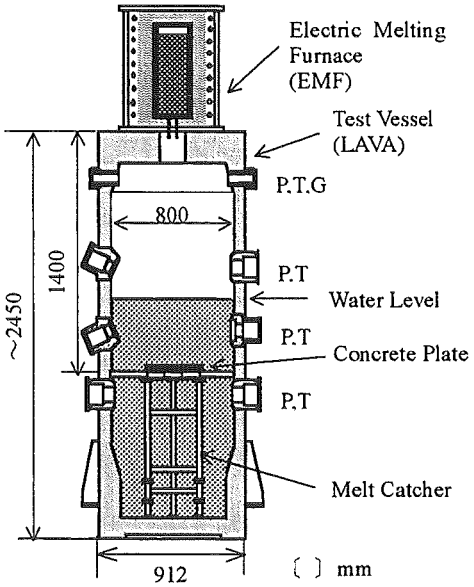

P: Pressure, T: Temperature,
G: Gas sampling line

Fig. 1 Test facility of COTELS Test A

Eight tests including one AM case were carried out. Table 1 summarizes test conditions. Test A1 is a reference case in which test conditions are 56 kg of corium, pure saturated steam conditions at 0.2 MPa, saturated pool water, 0.4 m pool depth and no differential pressure between EMF and the test vessel. Major test parameters are, corium mass (27 kg in A4), non-condensible gas existence in free space

(20% of nitrogen gas in A5), pool water subcooling (21 K subcooling in A6), differential pressure between EMF and the test vessel (A8 and A10) and pool depth (0.9 m in A9). It should be noted that the actual differential pressure in A8 might be much smaller than table value because of leakage due to crucible bearing sleeve deformation during the test. Test A11 corresponds to AM condition case, where high subcooled and deep pool was established. In this test, a concrete trap with the same dimensions as Test B/C was used instead of the melt catcher.

Table 1 Summary of initial conditions

Run No.	A1	A4	A5	A6	A8	A9	A10	A11
Corium mass, kg	56.3	27.0	55.4	53.1	47.7	57.1	55.0	53
Pool depth, m	0.4	0.4	0.4	0.4	0.4	0.9	0.4	0.8
Pool subcooling, K	0	8	12	21	24	0	21	86
Initial pressure, MPa	0.20	0.30	0.25	0.21	0.45	0.21	0.47	0.27
Ambient Gas	Steam	Steam	Steam (*2)	Steam	Steam	Steam	Steam	Ar
ΔP, MPa (*1)	0.03	0.03	0.01	~0	0.67(*3)	0.02	0.14	0.13

Corium composition UO_2:55wt%+Zr:25%+ZrO_2:5%+SS:15%
*1) ΔP: Pressure difference between EMF and test vessel to increase corium falling velocity
*2) 80 % steam +20 % nitrogen
*3) Actual ΔP might be much smaller because of leakage from deformed crucible bearing sleeve

3. EXPERIMENTAL RESULTS

3.1 Pressure Transient

Figure 2 shows a typical pressure response in free space. The pressure transient was categorised into three regions. Region 1 is a period from the time of corium contacting with pool surface to the first peak timing. In this region, the pressure rapidly increased and reached to the first peak pressure within 0.5 second. due to steam generation by heat transfer from falling corium particles in the pool. However, a pressure spike typical of steam explosion was not observed. Following to the first peak, the measured pressure temporally decreased in region 2 due to steam condensation by subcooled pool. Then, the pressure gradually approached the quasi-steady state value in region 3 usually in 10 seconds. This was caused by the heat transfer from corium accumulated on the pool bottom. The quasi-steady state pressure was larger than that evaluated by the initial stored energy in corium due to non-condensible gas generation by oxidation of metallic components in the corium in all test cases.

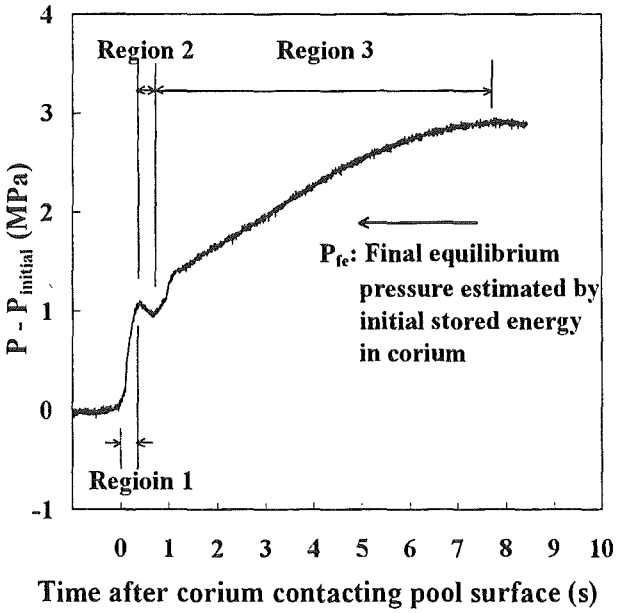

Fig. 2 Typical pressure response in test vessel (A1)

Figure 3 shows some test parameters effect on pressure transient. The initial pressurisation rate was not sensitive to poured corium mass (A4), pool depth (A9) and small pool subcooling change (A5, A6). In fact, the timing of the first peak was shorter than 0.5 second in all cases and this value was smaller than the time required for total drainage of corium from EMF. This suggested that front part of corium jet basically played an important role in region 1. The value of the first peak pressure, occurred in later stage of region 1, was more or less affected by the condensation amount of steam generated during initial phase in region 1. (Dominant mechanism of region 2 was steam condensation) More steam condensation in A5 and A6 due to subcooling, and A9 due to deep pool, caused smaller first peak compared with reference case of A1. The quasi-steady state pressure was lower than that of A1 due to a smaller amount of energy stored in the corium (A4), due to a large amount of pool mass in A9 and due to the existence of initial pool subcooling (A5, A6). The first peak pressure was sensitive to corium falling velocity which governed corium particle size. Time required to reach the quasi-steady state pressure was shorter in larger velocity cases, because of predominant initial energy release in region 1. Although higher falling velocity was imposed in AM case A11, the first peak pressure was not so high. This is because coalescence of breakup particles was caused inside of the confined geometry of concrete trap with 36 cm diameter and the generated steam was condensed by high subcooled water.

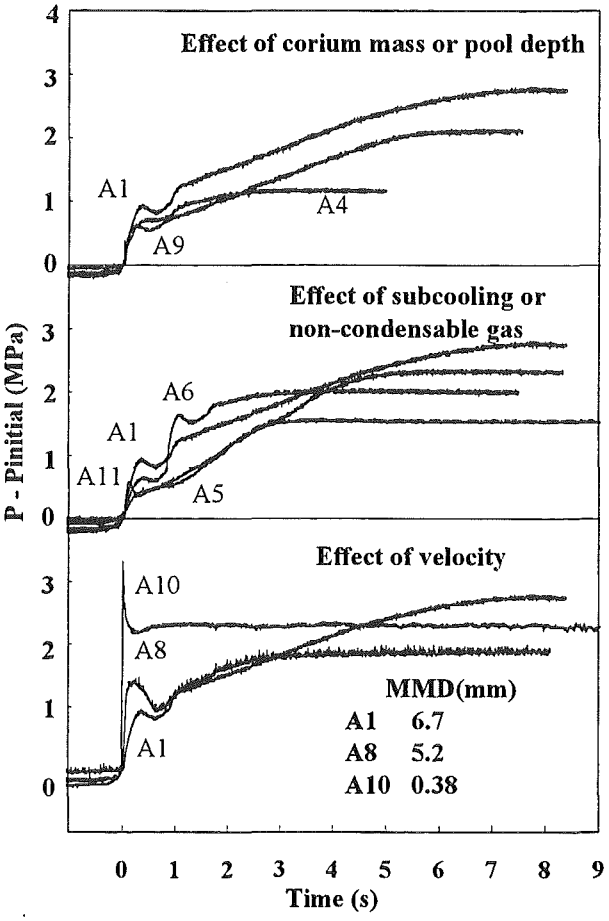

Fig. 3 Comparison of pressure transient

The first peak pressure in A10 was relatively large and measured mass median diameter (MMD) of particles was a few hundred microns different from any other cases. Figures 4 shows the measured pressure during very short period after corium pouring. A pressure spike typical of steam explosion was not observed in the free space pressure. The shape of small particles in A10 was not spherical. (Spherical shape is usually observed in SE phenomena) These data suggested that the steam explosion did not occur in A10.

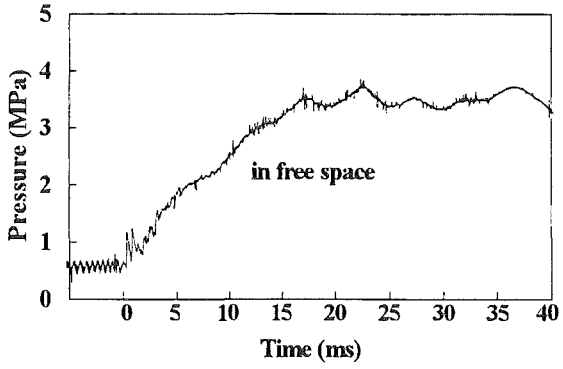

Fig. 4 Short term pressure transient (A10)

3.2 Corium Dispersion Characteristics

In all tests, most of poured molten corium was broken up in the pool. Figure 5 summarizes mass of poured corium, mass of ingot corium attached on the concrete plate and breakup ratio defined as (poured corium mass – ingot corium mass)/(poured corium mass). The breakup ratio was ranged from 0.88 to 1.0. Only a few kg corium ingot was observed in most cases. The breakup ratio was all the same except A8 and A10. No ingot corium was found under higher falling velocity (A8 and A10). This demonstrated that, in A11, coalescence of breakup particles was caused due to the 36 cm cylindrical geometry of concrete trap even under higher falling velocity (About 4 kg of ingot corium remained). The ingot corium was easily removed from the concrete floor in all cases except for A5, though the ingot mass was all the same.

L-11 of FARO, in which 4.1 % of metallic Zr was contained in oxide corium, resulted in complete breakup of the corium jet, while pancake was remained on the pool bottom in other FARO tests without metallic component. CCM tests (Spencer, 1994), in which a mixture of UO_2, ZrO_2 and SS was poured into water, showed shorter breakup length compared with that without metal component. In CCM-6, in which Froud number is close to COTELS reference conditions, (L/D) is about 14 and this corresponds to 0.7 m breakup length in COTELS. These results suggested that metallic components in corium enhanced a corium jet breakup.

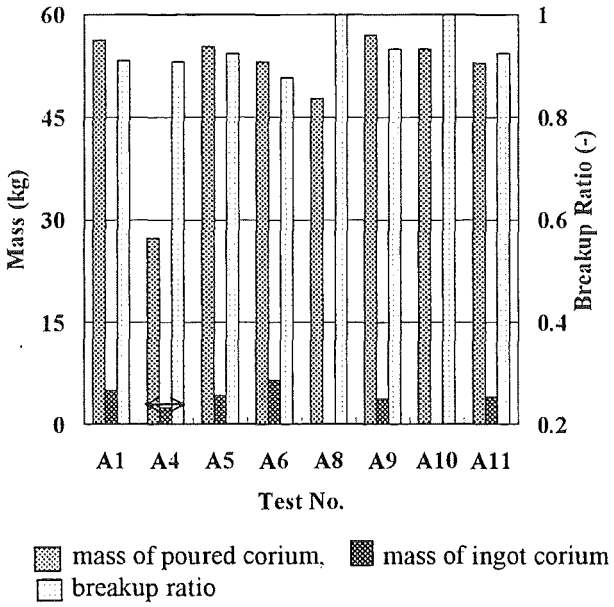

Fig. 5 Breakup ratio

Figure 6 shows photographs of particle samples and ingot corium in A1. Size of corium particles was ranged from a few hundred microns to more than 10 mm. The shape was spherical in middle size, while it was irregular in both small and large size. Each particle had many pores not only on its surfaces but also inside. Micro porosity of particles was about 10 %. These microstructure enhanced debris bed cooling. The bottom surface of ingot corium was also rough and had many small pores. No significant ablation allowed repeated use of the concrete plate. Water penetrated into the gap between the concrete surface and the ingot during quenching process.

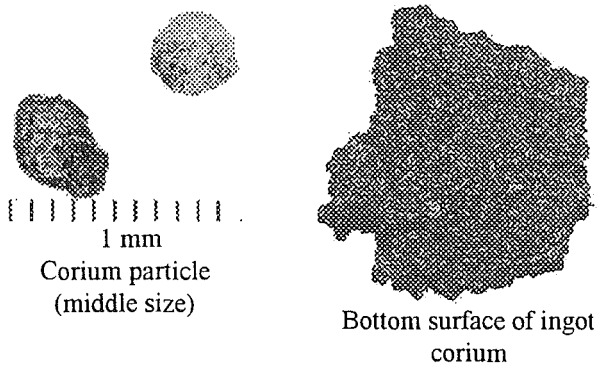

Fig. 6 Photo of particles and ingot corium (A1)

Analysis of element concentration of all particle sizes revealed that they did not depend on the particle size. This suggested that the corium was uniformly mixed and melted in EMF before pouring. Particle size was separated by sieving method and measured size distribution was well correlated by

Rosin-Rammler distribution, R=100 exp{-(x/x')^b}. Figure 7 shows a comparison of measured particle size distribution. Obtained MMD was similar except for higher velocity cases of A8, A10 and A11 so that initial pressurization rate was all the same. MMD was smaller in higher velocity cases. Figure 8 shows a relation between the first peak pressure and MMD. All data except for A11 was well correlated. Since water subcooling was very large in A11, the peak pressure was extremely suppressed by the high subcooling. Although the largest first peak pressure was observed in A10, it was well correlated with this line. This fact also implied that a SE did not occur in A10 and the first peak pressure was basically caused by heat transfer from corium particles falling in the pool.

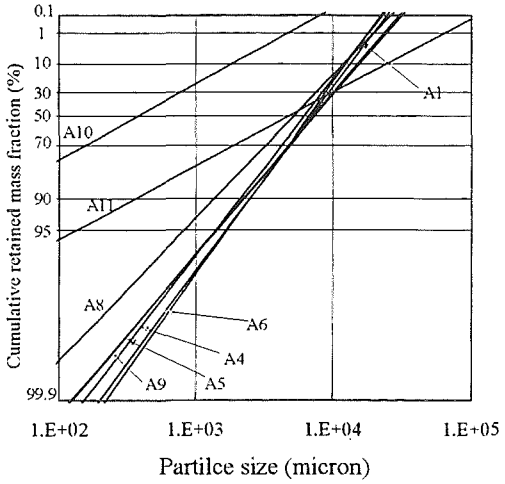

Fig. 7 Comparison of particle size distribution

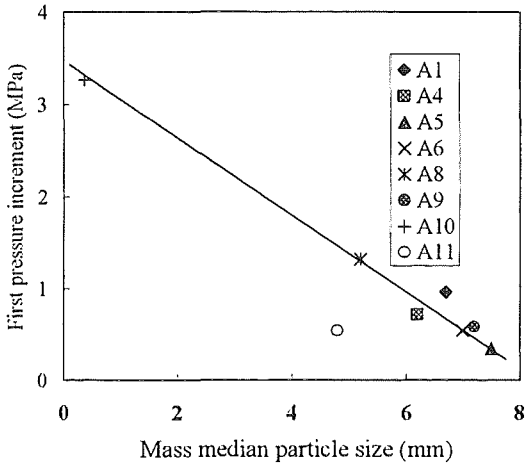

Fig. 8 Relation between MMD and first peak pressure

4. DIMENSIONAL ANALYSIS ON FIRST PEAK PRESSURE

In order to investigate the effects of tested parameters on the first peak pressure, dimensional analysis was done. In the analysis, the following assumptions were adopted based on the evaluation of Test A results to reduce the number of independent variables. Since the first pressure increase was mainly controlled by heat transfer from the falling corium particles in the pool before falling corium particles impinging on the concrete floor and dispersed particles size was small, heat conduction effect inside the particle was considered to be small. Hence, thermal conductivity of corium was deleted. Each particle was surrounded by a stable vapor film with large temperature gradient and dominant heat transfer mechanism from corium to water was considered to be radiation so that thermal conductivity and surface tension of water was also deleted. However, emissivity was not included since it was nearly common in the tests and no available data existed. Oxidation of corium components was neglected. Although gas sampling analysis suggested that metallic components in the corium were oxidized during quenching process, rate constants of oxidations under high temperature have large uncertainty and a reasonable estimation of oxidation during region 1 was difficult.

Based on the above assumptions, the first peak pressure as a dependent variable was correlated by the following 12 parameters, corium specific internal energy (instead of initial temperature and specific heat), density and surface tension, corium jet diameter and falling velocity, water specific heat, latent heat of vaporization, subcooling of water, densities of vapor and water, and volumes of pool and free space. Eight non-dimensional parameters were

determined using π theorem. One non-dimensional parameter of (ρ_j/ρ_w) was omitted due to quite small effect.

Correlation analysis was applied between a non-dimensional first peak pressure and each independent non-dimensional parameter to determine tentative exponent of each non-dimensional parameter (only COTELS data were used). The best fitting curve of a dimensional correlation based on the tentative exponent values was expressed after trial and error calculations as follows.

$$\frac{P_p}{v_j^2 \cdot \rho_g} = 1.0\times10^5 \cdot X1^{0.01} \cdot X2^{-0.2} \cdot X3^{0.01} \cdot X4^{0.01} \cdot X5^{-0.2} X6^{0.03} - 9.2\times10^3 \quad (1)$$

$\{P_p/(v_j^2 \cdot \rho_g)\}$ is non-dimensional dynamic pressure multiplied by (steam energy/corium energy). X1 is $(D/V_w^{(1/3)})$ and a ratio of jet diameter to a reference length of pool volume. Since the first pressure peak occurred in a short time and only limited water near the corium jet in the pool was heated, $X1$ is an indication of local heating of pool water. $X2$ is Weber number $(v_j^2 \cdot \rho_j \cdot D_j/\sigma_j)$ and is an indication of dispersed droplet diameter. $X3$ is a ratio of corium specific internal energy to latent heat of vaporization of water, (u_j/L). $X4$ is a ratio of free space volume to pool volume, (V_w/V_a). $X5$ is Jacob number $(1+\Delta T_{sub} \cdot c_p/L)$ and an indication of subcooling effect. X6 is a density ratio of vapor and water, (ρ_g/ρ_w).

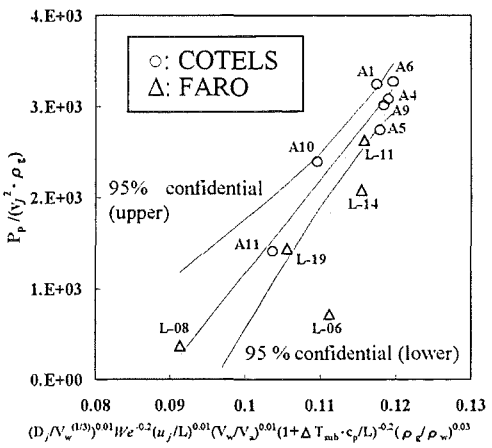

Fig. 9 Result of dimensional analysis

Figure 9 shows the non-dimensional correlation. FARO data was also plotted in this figure. Although most tests of FARO were conducted under high pressure and oxide corium condition (only L11 included 4.1 % Zr) different from COTELS, FARO test results were also well correlated except L-06, in which the pressure increase was low due to small corium mass. This agreement suggested that dominant mechanism of the initial pressure increase was same for both COTELS and FARO, and oxidation process was not significant when SE did not occur. Although the relatively large pressure peak was observed in COTELS A10, good correlation to A10 again confirmed no SE occurrence.

5. CONCLUSIONS

(1) Steam explosion was not observed not only under typical ex-vessel severe accident condition but also under AM condition.
(2) Breakup ratio was ranged 88 % to 100 % even under shallow pool. Metallic components in corium enhanced breakup of molten corium jet.
(3) The first peak pressure was well correlated by mass median diameter of breakup corium. This implied that the first peak pressure was mainly controlled by heat transfer from breakup particles. The first peak pressure was most sensitive to corium falling velocity which governed dispersed corium particle size.

(4) Quasi-steady state pressure after corium quenching was higher than that evaluated by initial stored energy in corium due to oxidization of metallic components in corium.
(5) Water penetrated into gap between ingot corium and concrete floor during quenching process.
(6) Non-dimensional correlation of the first peak pressure derived from COTELS data was well correlated for FARO.

6. ACKNOWLEDGEMENTS

This work was sponsored under the contract by the Ministry of International Trade and Industry, Japan.

NOMENCALTURE

D_j	jet diameter	u_j	specific internal energy
L	latent heat of vaporization	v_j	velocity of corium jet
P_p	first pressure increment	x	particle size
R	cumulative particle mass % retained on size x	x'	size parameter
V_a	volume of free space	ΔT_{sub}	water subcooling
V_w	volume of water pool	ρ_g	vapor density
We	Weber number	ρ_w	water density
c_p	specific heat of water	ρ_j	corium density
b	distribution parameter	σ_j	corium surface tension

REFERENCES

Akiyama, M. Yamano, N. and Sugimoto, J., 1997. *Proc. of the OECD/CSNI Specialist mtg. On Fuel Coolant Interaction*, Tokai-mura, Japan

Basu, S. and Ginsberg, T., 1996. "A Reassessment of the Potential for an Alpha-Mode Containment Failure and a Review of the Current Understanding of Broader Fuel-Coolant Interaction Issues", *Second Steam Explosion Review Group Workshop*, NUREG-1524

Huhtiniemi. I., Magallon, D. and Hohmann, H., 1997. Results of Recent KROTOS/FCI Tests: Alimina vs. Corium Melt, *Proc. of the OECD/CSNI Specialist mtg. On Fuel Coolant Interaction*, Tokai-mura, Japan

Magallon, A., Zeisberger, A. and Corradini, M., 1998. Debris and Pool Formation/Heat Transfer in FARO-LWR, Experiment and Analysis, *Proc. of IN-Vessel Core Debris Retention and Coolability*, Garching, Germany

Nagasaka, H., Hamazaki, R. and Takahashi, Y., 1995. Scenarios of Ex-vessel Debris Cooling as Related to Nuclear Power Safety, *Proc. Probabilistic Safety Assessment Methodology and Applications*, Seoul Korea

Nagasaka, H. et al., 1999. COTELS Project (1): Overview of Project to Study FCI and MCCI during Severe Accident, *Proc. of OECD/CSNI Workshop on Ex-Vessel Debris Coolability*, Karlsruhe

Spencer, B. et al., 1994. Fragmentation and Quench Behavior of Corium Melt Streams in Water, NUREG/CR-6133

Session B 5:

PHENOMENA TO ACHIEVE COOLABILITY: FLOODING

Chairman: W. Scholtyssek

OECD Workshop on Ex-Vessel Debris Coolability
Karlsruhe, Germany, 15-18 November 1999

Organized in collaboration with
Forschungszentrum Karlsruhe (FZK) GmbH

COTELS Project (3) : Ex-vessel Debris Cooling Tests

Hideo Nagasaka, Isao Sakaki and Masami Kato
Systems Safety Department, Nuclear Power Engineering Corporation
Fujita Kanko Toranomon Bldg., 5F, 17-1, 3-chome Toranomon
Minato-ku, Tokyo 105-0001, Japan
nagasaka@nupec.or.jp sakaki@nupec.or.jp ms-kato@nupec.or.jp

Yuri Vasilyev, Alexander Kolodeshnikov and Vladimir Zhdanov
Institute of Atomic Energy, National Nuclear Center
Str. Krasnoarmeyskaya - 10, Kurchatov, Republic of Kazakhstan
ysv@nnc.kz dep240@nnc.kz zhdv@nnc.kz

ABSTRACT

Test B/C in COTELS project was performed to investigate fuel coolant interaction (FCI) and molten core concrete interaction (MCCI) under water injection onto molten corium. After 60kg UO_2 corium mixture was melted in electric melting furnace (EMF), the corium was fallen into concrete trap. The molten corium in the trap was re-heated to simulate decay heat. When subcooled water was injected onto the molten debris, steam explosion was not observed. Debris was cooled about 20 minutes after water injection and MCCI was suppressed. This favorable cooling was attributed to the existence of remaining porosity inside corium due to simulation of falling process, water ingression via eroded concrete side wall clearance and channels, and the interruption of further concrete floor erosion due to the existence of pebble bed, decomposed from concrete, below the debris.

1. INTRODUCTION

Suppression of MCCI by water injection onto molten debris accumulated on a containment floor is one of the important accident management (AM) to prevent containment failure during a severe accident. However, the suppression of MCCI by water injection has not been observed in former MCCI tests, such as SWISS (Blose, R.E., 1987), WETCOR (Blose, R.E., 1993) and MACE (Spencer, B.W., 1991 and Farmer, M.T., 1992) tests.

Test B/C in COTELS project was performed to investigate FCI regarding water injection onto molten debris (Test B) and MCCI under continual water injection onto molten debris (Test C) successively conducted after Test B. Main features of this test are simulation of UO_2 corium falling process before FCI/MCCI, usage of basaltic concrete and simulation of side wall made of concrete. This paper summarizes the data evaluation results focussed on pressure increasing rate immediately after water injection onto debris (Test B) and long term debris cooling mechanism by analyzing the geometry of cross section of solidified debris and eroded concrete trap (Test C).

2. TEST FACILITY, TEST PARAMETERS AND TEST PROCEDURE

Test B/C was conducted using LAVA-M facility shown in Fig.1 (Nagasaka, H., 1999).

In this test, 60kg maximum mixture of UO_2, stainless steel, ZrO_2 and Zr was melted in EMF by electrical induction heating, located above a concrete trap. The corium was fallen onto the concrete trap inside a test vessel in order to simulate a realistic situation of a severe accident. The accumulated corium in the trap was heated to simulate decay heat by another electrical induction heater surrounding the concrete trap. Water was injected onto the molten debris by spray type or jet type nozzle. Steam condensation system to measure generated steam flow rate after the water injection and gas sampling system to evaluate gas composition due to MCCI were equipped. Temperatures and pressures of ambient gas in a test vessel were measured.

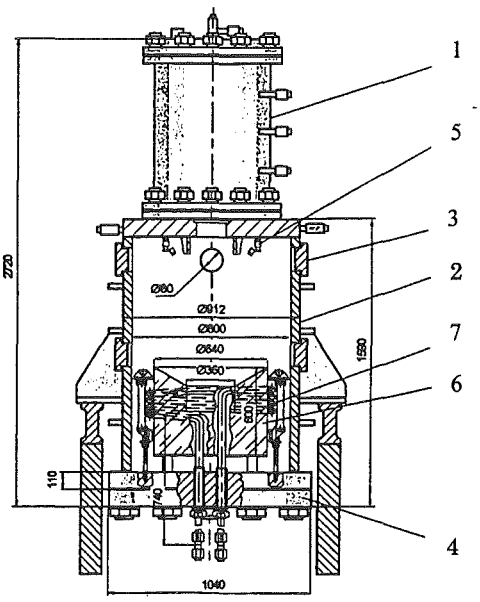

1:EMF, 2:Test vessel, 3:Instrumentation nozzle, 4:Removable bottom, 5:Water injection nozzle, 6:Concrete trap, 7:Induction heater

Fig. 1 LAVA-M test facility

Two types of concrete trap were used in the tests. One type was 36cm inner diameter trap and the aspect ratio of accumulated corium (ratio of height to diameter) was 0.19, corresponding to typical LWR severe accident condition, and another type was 26cm inner diameter and the aspect ratio was 0.5. These concrete trap were made of basaltic concrete, simulating Japanese plant cement composition, pebble size distribution and composition, strength, and field curing. Thirty five thermocouples in 36cm trap and 43 thermocouples in 26cm trap were arranged spirally inside concrete trap to measure concrete temperature transient.

As shown in Table 1, mixture composition, concrete trap diameter, power input to debris, water injection method, timing and flow rate, and differential pressure between EMF and test vessel to adjust corium falling velocity were varied. For all tests, melt mass was about 60kg, melt temperature was about 3200K slightly above UO_2 melting temperature and initial ambient gas pressure was 0.3MPa, corresponding to reactor containment pressure during a severe accident, and water temperature was room temperature. Corium type A corresponds to the mixture composition obtained from TMI-2 accident, while corium type B includes more metallic compositions, considering the existence of metal structures in lower plenum of reactor pressure vessel. Seventy five kW net heat power input corresponds to $11W/cm^3$ (about 11 times larger than decay heat), which was determined by obtaining similar transient of vertical concrete erosion depth (defined by 1650K) between reference plant and test facility based on two-dimensional unsteady heat conduction analysis. Two l/min is the minimum water injection rate to remove 75kW heat power input.

Table 1 Test B/C conditions

Varied Parameter	Test No.									
	B/C-4	B/C-6	B/C-9	B/C-5a	B/C-5	B/C-8	B/C-7	B/C-2	B/C-3	B/C-10
Corium type*	B							A	B	
Concrete trap diameter, cm	36			26	36					
Power input to debris, kW	75	~0	75	~0	75					
Condition of water injection										
- Injection method	Jet		Spray	-	Jet				Jet	
- Flow rate, l/min	2.0		2.0	0	2.0				2.0	
- Temperature, K	room		room	-	room				room	
- Injection timing delay, min.	8		8	-	8				15	
Δ P (EMF - test vessel), MPa	0					0.1	0.15	0		

Note) *Corium composition (weight %) Type A : UO_2-78, Stainless Steel-5, ZrO_2-17, Zr-0
Type B : UO_2-55, Stainless Steel-15, ZrO_2-5, Zr-25

Tests were performed during about two hours according to the following test procedure : 1) EMF and test vessel were evacuated and Ar gas was introduced under 0.05MPa, then EMF heating was initiated. 2) A few minutes before molten corium discharge, N_2 was supplied to the test vessel up to a prescribed pressure. 3) Power supply to the EMF was turned off and the corium falling device was switched on. 4) Power supply to the concrete trap induction heater was initiated. 5) Water was injected onto the molten debris about 8 or 15 min after the corium falling. 6) Steam condensation system to measure generated steam flow rate was operated. 7) The generated gas was sampled intermittently from the test vessel.

3. EVALUATION OF TEST RESULTS

3.1 Evaluation of FCI Test Results

As a typical example, Fig.2 shows pressure behavior of Test B/C-3 after corium falling for both short and long term periods. Initial rapid pressure increase immediately after corium falling was due to heat-up of ambient gas by high temperature falling corium and the accumulated corium. A dotted line in Fig.2-a is calculated test vessel pressure transient by applying P/T=constant, neglecting MCCI generation gas. The calculated maximum pressure coincided with the measured maximum pressure at 20sec. Difference between measured and calculated pressure after 20sec was due to gas generation as a result of MCCI.

When water was injected at 8min after corium falling, impulsive pressure typical of steam explosion was not observed as shown in Fig.2-b. The pressure increasing rate was only 2E-3MPa/sec which implied no steam explosion occurrence. The above results were applied to all test cases. In fact, the pressure increase rate was ranged from 2E-3 to 4E-3MPa/sec. The pressure increase rate was not affected by water injection method and corium type.

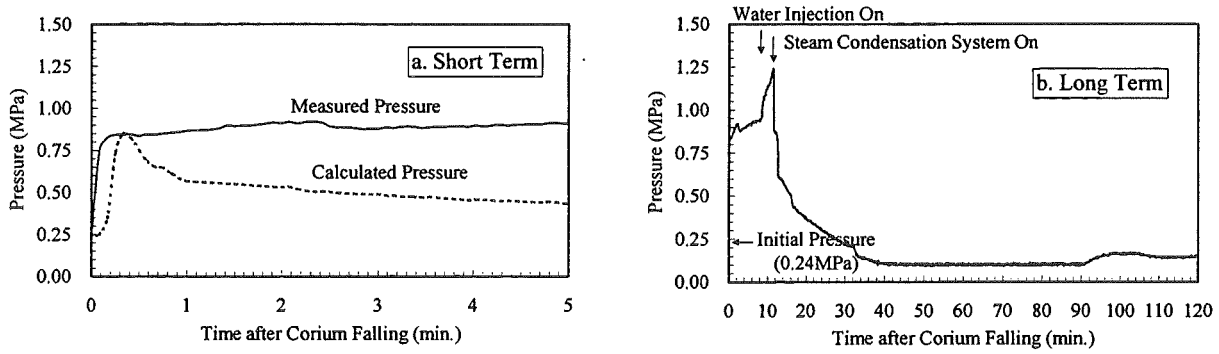

Fig.2 Test vessel pressure (B/C-3)

3.2 Effect of Several Parameters on Concrete Trap Temperature Transient

Figure 3 compares a cross section of continuous solidified debris (ingot debris) and concrete trap between Test B/C-5a and B/C-5 after removing particulate debris bed formed above the ingot debris. Debris heating period was 6min in Test B/C-5a, while 75min in Test B/C-5. Large cavities as a result of the impingement of falling corium jet on concrete trap were remained in B/C-5a due to short heating period. In Test B/C-5, such large cavities were vanished and molten debris core region was extended due to re-melting during long time heating process. In fact, the concrete in the vicinity of the ingot debris was decomposed completely and large amount of particulate debris formed due to MCCI in Test B/C-5. These observations confirmed the re-melting of debris by another induction heating.

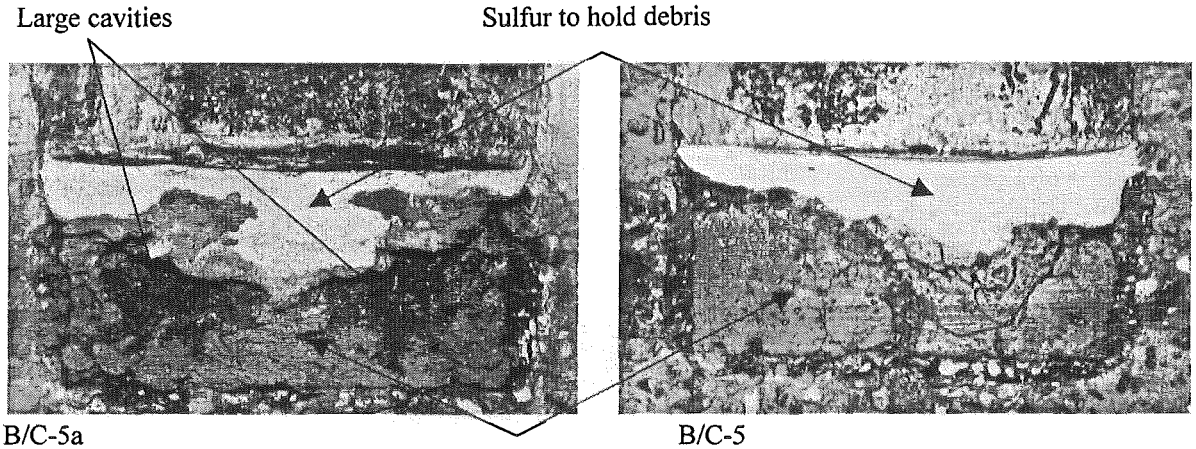

Fig.3 Confirmation of debris re-heating by induction heating (B/C-5a and 5)

Figure 4 shows the effect of aspect ratio on concrete trap temperature transient, comparing Test B/C-5 with B/C-9. Faster increase in concrete temperature and higher maximum temperature in B/C-5 (larger aspect ratio of 0.5) was observed. Figure 5 shows the effect of integrated power P_I, before water injection after corium falling, on the concrete temperature transient, comparing B/C-3 (P_I=71.2MJ) with B/C-9 (P_I=26.2MJ). Faster increase in concrete temperature and higher maximum temperature in B/C-3 was confirmed. The effect of corium type on concrete temperature transient was small. Higher temperature test cases of Test B/C-5 and B/C-3 produced large amount of particulate debris above ingot debris due to MCCI. However, the concrete temperature decreased gradually after water injection and MCCI was suppressed in any test cases.

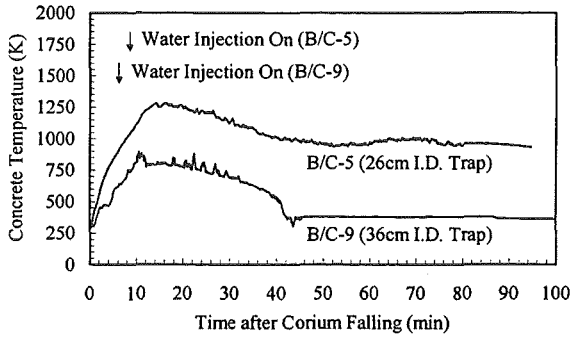

Fig.4 Effect of aspect ratio on concrete temperature (B/C-5 and 9)

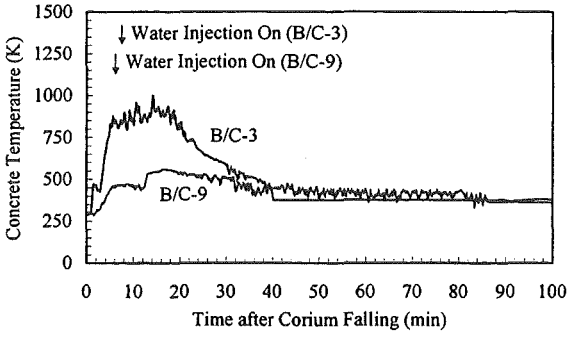

Fig.5 Effect of integrated power on concrete temperature (B/C-3 and 9)

3.3 Cooling Mechanism of Debris

Table 2 summarizes solidified debris and eroded concrete conditions. The test results were classified, depending on the amount of particulate debris bed formed above lower ingot debris, into three groups: case (1) formation of particulate debris bed, 20 to 40% of total solidified debris (case (1a) for 26cm concrete trap and case (1b) for 36cm concrete trap), case (2) formation of particulate debris bed, 70 to 80% and case (3) no formation of particulate debris bed. It is understood from this table that deeper concrete erosion was observed in the test cases with larger amount of the particulate debris bed formation.

Heat removal rate from the debris in concrete trap under nearly constant pressure condition in the test vessel was evaluated by energy balance neglecting heat loss from the

vessel and assuming saturated water reaching to pool surface. The heat removal rate per unit upper surface of solidified debris was ranged from 0.2 to 0.7MW/m^2 which was close to SWISS, WETCOR and MACE results.

Table 2 Solidified debris and eroded concrete conditions

Classification	Case (1)			Case (2)			Case (3)			
	(1a)		(1b)							
Items Test No.	B/C-5a	B/C-5	B/C-4	B/C-2	B/C-3	B/C-10	B/C-6	B/C-7	B/C-8	B/C-9
Solidified debris conditions										
-Total mass* (kg)	47	56	56	45	46	58	53	52	42	51
-Particulate debris bed (kg/%)	9/19	21.5/38	19/34	35/78	33/72	48/83	None	None	None	None
Stone like debris** (kg)	0	0	6	0	0	18	-	-	-	-
Sand like debris*** (kg)	9	21.5	13	35	33	30	-	-	-	-
Median diameter of sand like debris (mm)	0.6	0.8	2.2	1.5	1.0	0.4	-	-	-	-
-Lower ingot debris (kg)	38	34.5	37	10	13	10	53	52	42	51
Eroded concrete conditions										
-Max. erosion depth (mm) Side/bottom	13/28	10/25	25/22	15/15	15/20	48/40	8/15	10/18	8/15	~0/10
-Max. thick. of pebble bed (mm)	12	15	21	18	15	15	10	12	12	5
-Max. thick. of discolored concrete region (mm)	40	55	65	40	34	35	32	35	30	20

Note) * : Total mass of accumulated debris after test, ** : Particles larger than 16mm diameter, *** : Particles smaller than 16mm diameter

Figure 6 shows the cross section of solidified debris and concrete trap for typical test number, corresponding to each case mentioned above. In all cases concrete side wall as well as concrete floor were eroded and pebble bed decomposed from concrete, surrounding continuous solidified ingot debris, was observed. As concrete erosion depth (defined as the elevation difference between original concrete floor and the bottom elevation of ingot debris) increased, the pebble bed became deeper. A discolored concrete region existed surrounding the pebble bed, due to free water evaporation and chemical reactions in the concrete.

In B/C-5 (case (1a)) where the initially accumulated corium on the concrete trap was relatively not coolable condition due to larger aspect ratio, 10 to 12cm thickness particulate debris bed was formed, as a result of longer MCCI period, above 10 to 12cm thickness ingot debris. There were crevices and channels penetrating from bottom to top surfaces of ingot debris. The inner surface of the channels and crevices were smooth and their color was brown, which suggested the oxidation of metallic components due to steam flow through them. Small pebbles were also observed inside ingot debris due to the entrainment associated with MCCI generated gas, as shown in the right side picture of Fig.3.

In B/C-4 (case (1b)) where water injection was stopped from 26 to 56min under continual heating of debris, 34% particulate debris bed was formed in spite of smaller aspect ratio due to re-melting of partially solidified debris. The particulate debris consisted of stone-like debris larger than 16mm and sand-like debris similar to those observed in any other tests. Larger mass median diameter of this particulate debris is confirmed in Table 2. The particulate debris bed (7 to 12cm thickness) was separated from lower debris (4 to 9cm thickness) by a hard crust debris less than 5mm. The lower debris consisted of ingot debris in peripheral region and block debris in central region. The above observation suggested the outflow of stone-like debris as a result of hard crust rapture at central region associated with the reduction of crust thickness and increasing pressure below hard crust debris. In fact, slight pressure increase was observed at 68min, though steam condensation system was turned on during this period, as shown in Fig.7. Concrete temperature at 1cm below initial concrete floor still increased at 68min, which confirmed the heating of the debris.

In B/C-3 (case (2)) where the integrated power to debris before water injection was

about 2.5 times larger than that in case (1) and (3), most of debris was particulated and only small amount of ingot debris (28%) was remained in the peripheral region of concrete trap due to most violent MCCI. Lager amount of decomposed cement with white color was embedded in the ingot debris.

In B/C-9 (case (3)) where smaller integrated power was applied in smaller aspect ratio concrete trap, no particulate debris bed was formed. There were several channels penetrating bottom to top surfaces. The concrete bottom ablation depth was only 1cm.

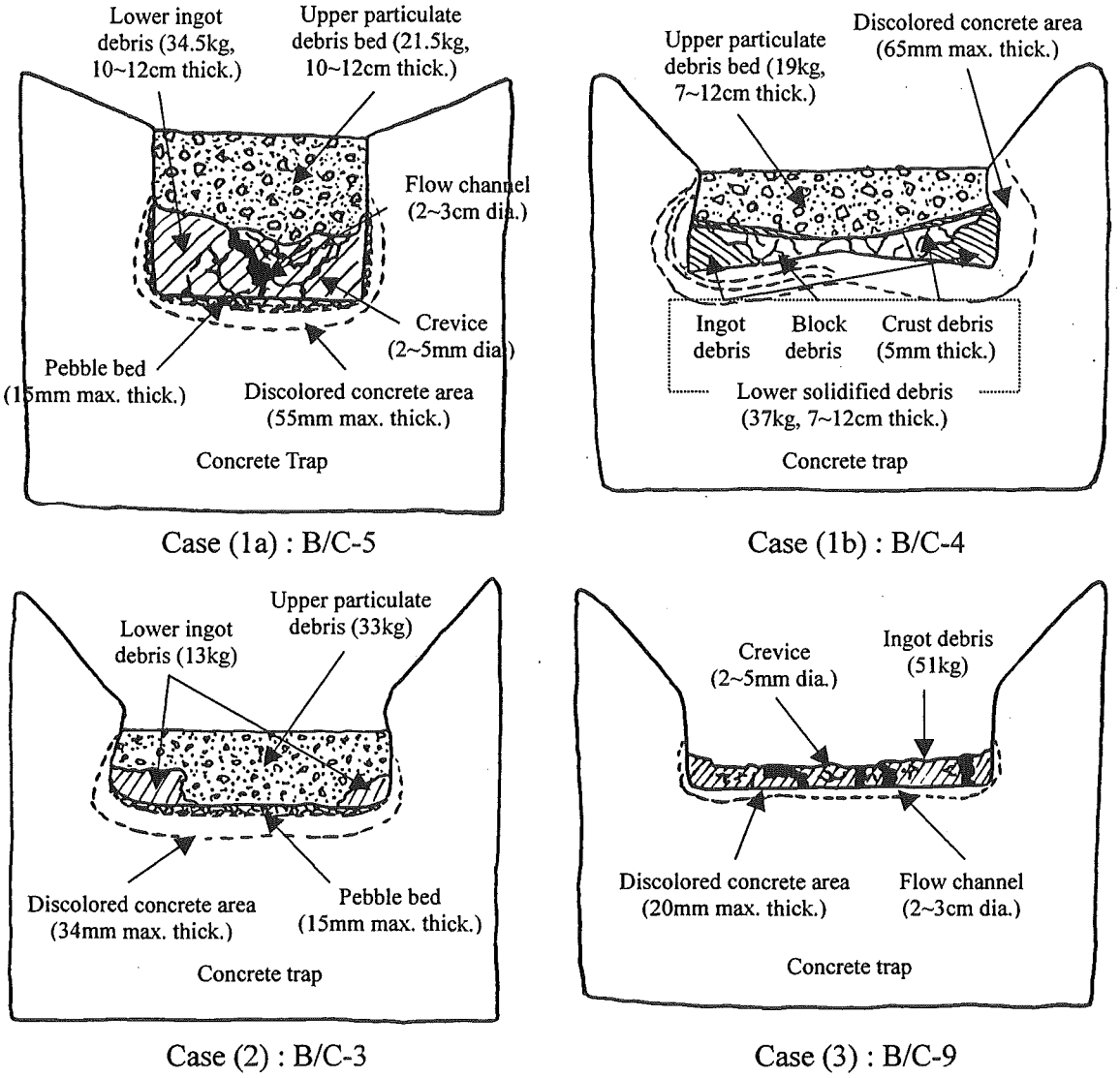

Fig.6 Typical cross section of solidified debris and concrete trap

The above observation of solidified debris condition, combined with the measured concrete temperature transients, shown in Figs.4 and 5, suggested that the favorable cooling was attributed to the remaining porosity of debris due to simulation of debris falling process and water penetration via eroded concrete side wall clearance in peripheral region and channels in central

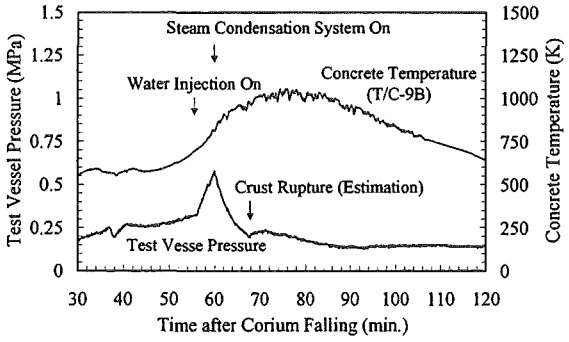

Fig.7 Test vessel pressure and concrete temperature (B/C-4)

region. Besides the accumulated pebble bed decomposed from the concrete, as a large thermal and flow resistances, interrupted the further concrete ablation.

This result was different from former test results of SWISS, WETCOR and MACE in which side wall was made of refractory except for MACE-M0 where concrete ablation was basically one-dimensional. Simulation of corium falling process not considered in WETCOR and MACE might enhance debris coolability through the initial formation of porosity inside corium in COTELS.

4. CONCLUSION

1) Steam explosion was not observed in any tests when subcooled water was injected onto the molten UO_2 debris.
2) Re-heating of molten UO_2 mixture debris in concrete trap by induction heating was confirmed.
3) Debris, in which a decay heat generation was simulated, was cooled from about 20 minutes after water injection and MCCI was suppressed in all test cases.
4) This favorable cooling was attributed to the remaining porosity of debris due to simulation of debris falling process, water penetration via eroded concrete side wall clearance and channels and the interruption of further concrete floor erosion due to the existence of accumulated pebble bed decomposed from concrete below the debris.
5) Steady state heat removal rate from upper surface of solidified debris to water pool ranged 0.2 to 0.7MW/m^2, consistent with SWISS, WETCOR and MACE results.
6) Formation of particulate debris bed above continuous solidified debris was governed by the degree of MCCI.

ACKNOWLEDGEMENTS

This work was sponsored under the contract by the Ministry of International Trade and Industry, Japan.

REFERENCES

Blose, R.E., Gronager, J.E., Suo-Anttila, A.J., Brockmann, J.E., 1987. SWISS : Sustained Heated Metallic Melt/Concrete Interaction with Overlaying Water Pools, NUREG/CR-4727, July 1987.

Blose, R.E., Powers, D.A., Copus, E.R., Brockmann, J.E., Simpson, R.B., Lucero, D.A., 1993. Core-Concrete Interaction with Overlying Water Pools : The WETCOR-1 Test, NUREG/CR-5907, November 1993.

Farmer, M.T., Spencer, B.W., Armstrong, D.R., 1992. MACE Test M1B Data Report, Argonne National Laboratory Report, ACE-TR-D6, September 1992.

Nagasaka, H., Kato, M., Sakaki, I., Cherepnin, Y., Vasilyev, Y., Kolodeshnikov, A., Zhdanov, V., Zuev, V., 1999. COTELS Project (1) : Overview of Project to Study FCI and MCCI during Severe Accident, Proceedings of OECD Workshop on Ex-Vessel Debris Coolability. Karlsruhe, 15-18 November 1999.

Spencer, B.W., Fischer, M., Farmer, M.T., Armstrong, D.R., 1991. MACE Scoping Test Data Report, Argonne National Laboratory Report, MACE-TR-D03, June 1991.

OECD Workshop on Ex-Vessel Debris Coolability
Karlsruhe, Germany, 15-18 November 1999

Organized in collaboration with
Forschungszentrum Karlsruhe (FZK) GmbH

COTELS Project (4) : Structural Investigation of Solidified Debris in MCCI

Vladimir Zhdanov, Yuri Vasilyev, Alexander Kolodeshnikov and Yuri Cherepnin
Institute of Atomic Energy, National Nuclear Center
Str. Krasnoarmeyskaya - 10, Kurchatov, Republic of Kazakhstan
zhdv@nnc.kz, ysv@nnc.kz, dep240@nnc.kz and cherepnin@nnc.kz

Isao Sakaki and Hideo Nagasaka
Systems Safety Department, Nuclear Power Engineering Corporation
Fujita Kanko Toranomon Bldg., 5F, 17-1, 3-Chome Toranomon,
Minato-ku, Tokyo, 105-0001, Japan
sakaki@nupec.or.jp, nagasaka@nupec.or.jp

ABSTRACT

Cross section of concrete trap along with solidified debris tested in COTELS Test B/C, in which the interaction among core melt, water and concrete was simulated, were structurally investigated. In 6 tests out of 10 tests, particulate debris bed was formed above continuous ingot debris. The size distribution of the particulate debris was well correlated by Rosin-Rammler equation. Large amount of smallest diameter particles was obtained due to the entrainment of molten corium, decomposed concrete and oxidation of metallic components in corium associated with molten core concrete interaction (MCCI) generated gas. The upper region of the solidified debris included more concrete compositions. The concrete erosion depth, concrete degradation condition and the structure of solidified debris were evaluated to clarify the basic difference between COTELS and former tests results. Concrete erosion depth was less than that observed in MACE, WETCOR, SWISS tests. The major differences of COTELS results compared with the former test results were: 1) absence of strong adhesion of crust to melt trap side wall: 2) water penetration into debris through both eroded side wall and channels inside ingot debris: 3) absence of large void inside ingot debris: and 4) formation of pebble bed below ingot debris. All of these promoted the suppression of MCCI.

1. INTRODUCTION

The particulate debris bed was formed above the ingot debris in 6 tests out of 10 tests in COTELS Test B/C. Although the concrete erosion depth was relatively larger than that compared with no particulate debris bed formation case, the erosion depth of concrete floor (10 to 40mm) was still smaller compared with that in former test results (50 to 229mm) of SWISS (Blose, R.E., 1987), WETCOR (Blose, R.E., 1993) and MACE (Spencer, B.W., 1991 and Farmer, M.T., 1992). In these tests large void was formed between upper crust and lower debris due to the adhesion of upper crust to side wall, which prevented water from penetrating into a corium-concrete interaction zone. The particulate debris bed was observed only in MACE-M0, as published data.

Essential differences of test conditions between COTELS Test B/C and WETCOR/ MACE, in which oxide corium was used, are summarized in Table.1. In COTELS Test B/C

initial temperature of corium was as high as 3200K and corium falling process to a concrete floor was simulated. The corium included more metallic components (about 17 to 40 weight %) which allowed effective heating of the accumulated corium on the concrete trap floor by induction heating. The side wall as well as bottom floor of the trap was totally made of basaltic concrete, simulating Japanese LWRs pebble size distribution, composition, strength and field curing.

This paper summarizes the structural investigation of the solidified debris and the eroded concrete focused on the mechanism of the particulate debris bed formation in order to clarify the cause of the differences between COTELS and the former test results.

Table 1 Comparison of COTELS, WETCOR and MACE

Test / Items	COTELS Test B/C (NUPEC/NNC)	WETCOR-1 (SNL)	MACE-M0 (ANL)	MACE-M1B (ANL)
Melt conditions				
-composition	UO_2,ZrO_2,Zr,SS	Al_2O_3,CaO,SiO_2, Fe_2O_3, MgO	UO_2,ZrO_2,Zr,SiO_2, CaO,Conc.	UO_2,ZrO_2,Zr,Fe, CaO,Conc.
-mass (kg)	60	34	109	413
-temperature (K)	3200	1850	~2000	~2300
-melting method	induction heating	induction heating of tungsten wall	direct heating (tungsten electrodes)	direct heating (tungsten electrodes)
Simulation of melt falling process	Yes	No	No	No
Simulation of decay heat				
-power density (W/g)	1.25	0.3	0.5~1.0	0~0.3
-method	induction heating	induction heating of tungsten wall	direct heating (tungsten electrodes)	direct heating (tungsten electrodes)
Concrete Trap				
-concrete type	Basaltic	Limestone /common-sand	Limestone /common-sand	Limestone /common-sand
-configuration	Cylindrical	Cylindrical (MgO side wall)	Rectangular	Rectangular (MgO side all)
-size (cm)	36 ϕ or 26 ϕ	40 ϕ	30x30	50x50
-aspect ratio	0.19 or 0.5	0.56	0.5	0.5
Water injection				
-flow rate (liter/min.)	2	57	~600	~120
-method	jet, spray	jet	jet	jet
-temperature (K)	room	295	296	296
-timing	8 or 15min. after corium falling	after 2cm concrete erosin	after 1.2cm concrete erosion	after 8cm concrete erosion

2. CONCRETE ERODED CONDITIONS

Table 2 summarizes solidified debris and eroded concrete conditions. The test results were classified, depending on the amount of particulate debris bed formed above lower ingot debris, into three groups: case (1) formation of particulate debris bed, 20 to 40% of total solidified debris (case (1a) for 26cm concrete trap and case (1b) for 36cm concrete trap): case (2) formation of particulate debris bed, 70 to 80%: case (3) no formation of particulate debris (Nagasaka, H., 1999).

The solidified debris basically consisted of lower ingot debris and upper particulate debris except for case (3), as shown in Fig.1. In general the ingot debris had many small cavities with the diameter of 1.5 to 15mm. Some cavities included small pebbles, as shown in Fig.2. The ingot had also crevices and channels, penetrating from bottom to top surfaces. In some penetrating channels, the inner surface color was blown and white which were probably

due to the oxidation of metallic components in corium and the entrainment of decomposed concrete, respectively.

Table 2 Solidified debris and eroded concrete conditions

Classification	Case (1)			Case (2)			Case (3)			
	(1a)		(1b)							
Items / Test No.	B/C-5a	B/C-5	B/C-4	B/C-2	B/C-3	B/C-10	B/C-6	B/C-7	B/C-8	B/C-9
Solidified debris conditions										
-Total mass* (kg)	47	56	56	45	46	58	53	52	42	51
-Particulate debris bed (kg/%)	9/19	21.5/38	19/34	35/78	33/72	48/83	None	None	None	None
Stone like debris** (kg)	0	0	6	0	0	18	-	-	-	-
Sand like debris*** (kg)	9	21.5	13	35	33	30	-	-	-	-
Mass median diameter of sand like debris (mm)	0.6	0.8	2.2	1.5	1.0	0.4	-	-	-	-
-Lower ingot debris (kg)	38	34.5	37	10	13	10	53	52	42	51
Eroded concrete conditions										
-Max. erosion depth (mm) Side/bottom	13/28	10/25	25/22	15/15	15/20	48/40	8/15	10/18	8/15	~0/10
-Max. thick. of pebble bed (mm)	12	15	21	18	15	15	10	12	12	5
-Max. thick. of discolored concrete region (mm)	40	55	65	40	34	35	32	35	30	20

Note) * : Total mass of accumulated debris after test, ** : Particles larger than 16mm diameter, *** : Particles smaller than 16mm diameter

The concrete erosion and degradation condition for both side wall and floor was similar in all test cases, irrespective of the particulate debris bed formation. The difference was only in erosion depth and the thickness of discolored concrete region. The maximum erosion depth of concrete floor was 48mm in Test B/C-10, where largest integrated power before water injection was adopted. However, the maximum erosion depth was still smaller than the results of SWISS, WETCOR and MACE.

Figure 3 represents the typical discolored region of concrete in Test B/C-4 as an example. Region I (5 to 7mm thickness) neighboring to the ingot debris was friable mass of solidified concrete compositions which had melted at the first contact between molten corium and concrete. The void fraction in this region was quite high. The second region II (12 to 20mm thickness) was dark-gray color compared with original concrete color and included many pebbles. The temperature in this region reached about 750K corresponding to a chemical reaction of $CaCO_3 \rightarrow CaO + CO_2$. The pebble bed was defined as region I plus region II, which had a large thermal resistance due to high porosity. Visually it looked like apparent increasing of pebble concentration due to partial or absolute absence of binding substance of cement between pebbles. Since cement and sand ingredients were melting out, partial dipping of corium and

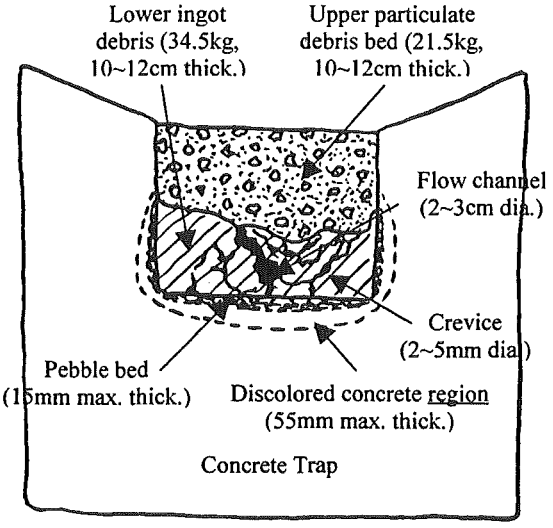

Fig.1 Typical cross section of solidified debris and concrete trap (B/C-5)

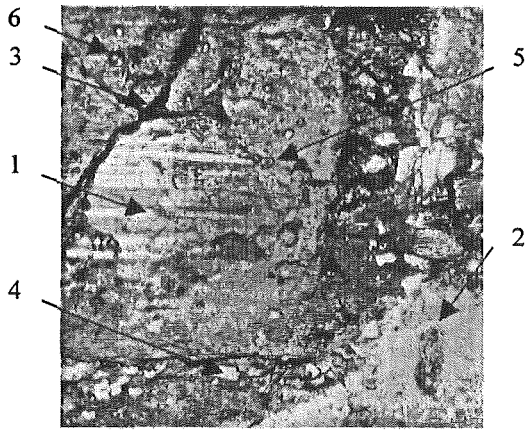

1:Ingot debris, 2:Concrete trap, 3:Crevice
4:Pebble bed, 5: Pebble, 6: Small cavity

Fig.2 Magnified photograph of cross section (B/C-5)

penetration of cooling water into region I and II occurred. The thin layer (3 to 5mm thickness) of region III was white and had low porosity. The temperature in this region reached about 650K corresponding to a chemical reaction of $Ca(OH)_2 \rightarrow CaO + H_2O$. The last region IV (15 to 20mm thickness) was solid concrete of light-gray color and the boundary between region IV and undamaged concrete was not definite. The temperature in this region reached about 400K corresponding to the evaporation of free water in the concrete.

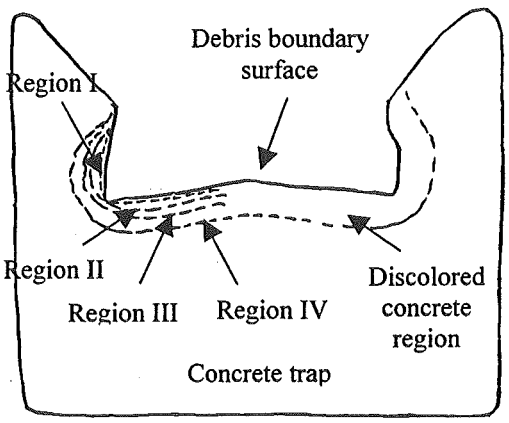

Fig.3 Discolored Concrete Region (B/C-4)

3. STRUCTURAL INVESTIGATION OF SOLIDIFIED DEBRIS

In order to clarify the mechanism of the particulate debris bed formation, size distribution of the particulate debris bed was evaluated. The particulate debris bed was removed layer by layer from the concrete trap to evaluate the vertical size distribution difference. The free fragments of each layer were divided into 12 sizes according to the cross section dimension by using sieve method. Figure 4 shows the result of size distributions for Test B/C-3. The basic difference of the size distributions among upper, middle and lower layers was more mass of the smallest particles in the upper layer.

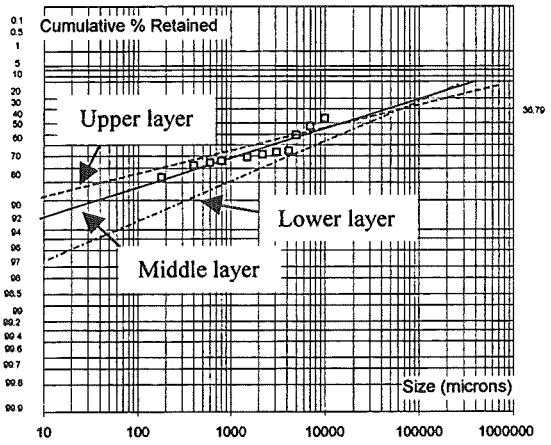

Fig.4 Vertical elevation difference of particulate debris size distribution (B/C-3)

The measured size distributions for total layers were well correlated nearly by one set of Rosin-Rammler distribution constants irrespective of case (1a) (B/C-5) and (2) (B/C-3), as shown in Fig.5. However, the distribution was completely different from the size distribution obtained in Test A-6, for example, where molten corium was fallen into water pool. In general larger amount of smallest diameter particles was contained in Test B/C.

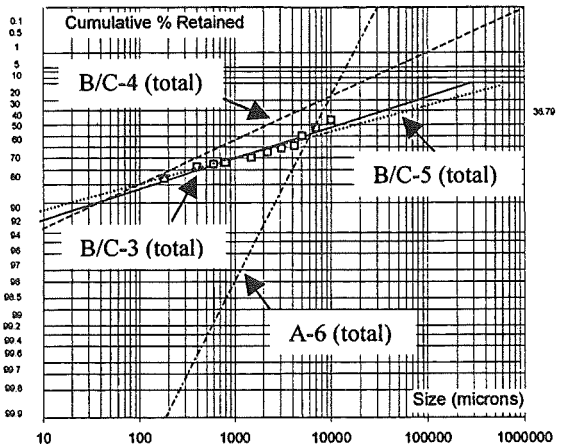

Fig.5 Rosin-Rammler correlation fitting of particulate debris size distribution compared with that in FCI test (A-6)

In this Fig.5, the size distribution of B/C-4, where a thin hard crust above the ingot debris was ruptured during re-heating process under no water injection period, was also included. The different size distribution in Test B/C-4 due to the existence of stone like debris was resulting from the combined effects of MCCI and fuel coolant interaction associated with the crust rupture.

Figure 6 compares the size distribution for the two test cases with and without water injection. In B/C-5a no water was injected, while 2l/min was

injected in B/C-5. Similar size distribution in both tests, irrespective of the amount of the particulate debris bed, suggested the continuation of MCCI even after water injection.

The amount of the particulate debris bed was strongly affected by the integrated induction power before water injection. Figure 7 shows mass of the particulate debris bed versus the integrated power for all 36cm concrete trap tests. Larger amount of the particulate debris bed was formed in B/C-2, 3 and 10 even in the concrete trap with smaller aspect ratio of 0.19. As the integrated power was increased, the more mass was observed. B/C-4 was exceptional due to long term interruption of water injection, mentioned above.

In the course of burden heating in the electric melting furnace (EMF) up to complete melting of materials, the material components were interacted to from eutectic and ceramic alloys (Hofmann, P, 1989). During this process, oxides contained in initial burden lost its oxygen partially. Since, during the heating process, gaseous components were discharged to avoid overpressure of the EMF, oxidation reactions of metal components inside EMF was less likely to occur. Thus, it should be noted that most of the metal mixture of materials remained as metal and drained into the test vessel.

During the early stage of MCCI before water injection, melted and partially vaporized concrete components tended to penetrate to the melt upper surface due to its smaller density as a result of the entrainment effect by MCCI generated gas. The entrainment to the upper surface was confirmed by the existence of channels and crevices and small cavities including pebbles, as shown Fig.2. During this process, the above mentioned metal components in corium was oxidized by H_2O and CO_2 decomposed from concrete, and the metal oxides was entrained. The molten corium was also entrained. Similar phenomena occurred in the clearance between the eroded side wall of concrete and the ingot debris. Thus, the particulate debris bed consisting of small particles was formed above the ingot debris due to the entrainment of molten corium and decomposed concrete, and oxidation components of metal associated with MCCI generated gas.

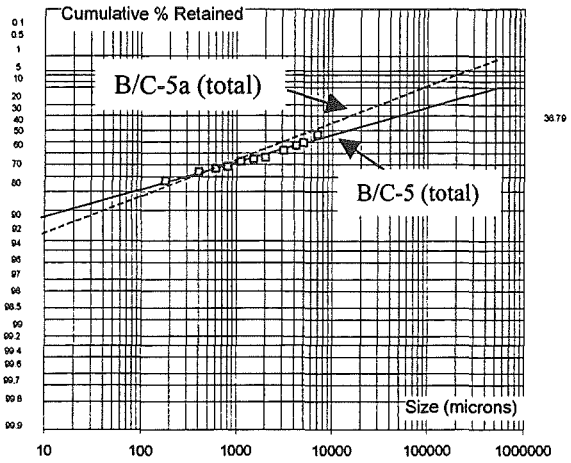

Fig.6 Effect of water injection on particulate debris size distribution (B/C-5a and 5)

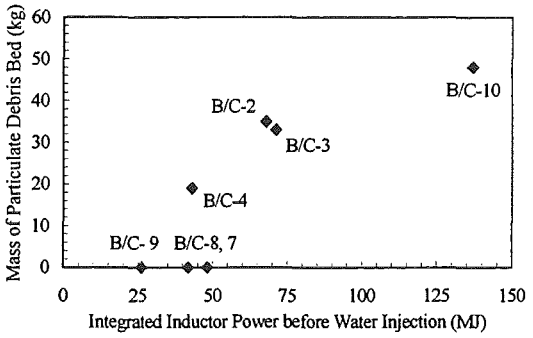

Fig.7 Mass of particulate debris bed vs integrated power

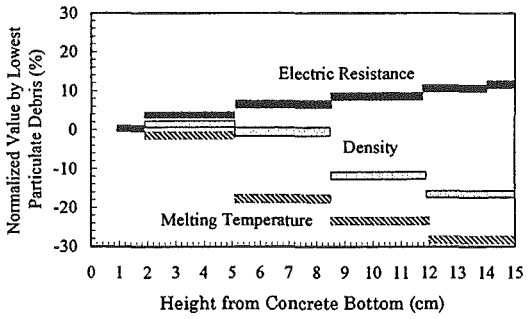

Fig.8 Vertical elevation distribution of material property of particulate debris bed (B/C-2)

The particulate debris bed formed in Test B/C-2 was sampled to study element composition of interaction products. Specific electric resistance, melting point and density of the samples were measured. To enable the pertinent comparison of the property, the samples were

powered and then sieved using a sieve with 0.1mm cell size. The normalized values of the properties, by the property value at the lowest layer, as a function of the height from the bottom of the particulate debris bed was shown in Fig.8. Decrease in density and melting temperature, and increase in electrical resistance in higher elevation suggested the existence of more concrete composition in higher elevation and more corium composition in lower elevation.

During the corium dilution with concrete components, net specific energy release in the corium was reduced, which resulted in gradual decreasing of average temperature in the entire melt volume and slowing down of concrete erosion process. Such a situation will be expected also in a severe accident of LWR. The measured pebble melting point of about 2730K, used as concrete filling compound, was remarkably higher than melting point of binding components (mortar) of about 1520K. This fact suggested that the erosion of pebble bed was controlled as long as the binding components were completely released. The pebble bed played the role of both thermal insulation and flow resistance against invasion of molten debris. The further erosion was possible only after melt entering to a new concrete layer still containing binding components.

4. COMPARISON OF CONCRETE ERODED CONDITIONS BETWEEN MACE-M0 AND COTELS B/C

MACE-M0 was selected as a comparable test with COTELS Test B/C, since the medium amount of particulate debris bed was only formed in this test as published data and rectangular trap was totally made of concrete. COTELS B/C-5 was selected as the corresponding test data, since medium amount of the particulate debris bed was formed in this case and the debris aspect ratio (0.5) was equal to that in MACE. Figure 9 shows the solidified debris and eroded concrete geometry of MACE-M0. Table 3 summarizes the differences inferred from Figs.1 and 9.

The medium amount of particulate debris bed in MACE-M0, similar to COTELS B/C-5, was attributed to larger integral power to corium before water injection time when concrete floor was already eroded 1.2cm. In COTELS initial availability of temperature difference between concrete and corium was as high as 2900K, fast heating of the concrete surface up to melting occurred. Although the rectangular trap, made of concrete, was eroded in MACE-M0, the particulate debris bed was supported by electrodes for direct heating of corium and the upper crust was stuck by the electrodes. As a result large cavity was formed. In COTELS B/C-5, the particulate debris bed fell in due to its weight, since there was no supporting structures by adopting induction heating. The sticking of ingot debris to the side wall was not observed in COTELS B/C-3 as shown in Fig.10, which was considered to be further progress of eroded concrete

Table 3 Differences between MACE-M0 and COTELS Test B/C-5

Test Items	MACE-M0	COTELS Test B/C-5
Erosion of side wall	Yes	Yes
Particulate debris bed	Yes	Yes
Upper crust debris	Yes	No
Large void under crust	Yes	No
Pebble bed	No	Yes
Water penetration path	Side wall	Side wall, Channel
Concrete erosion speed	11cm/hr	2cm/hr

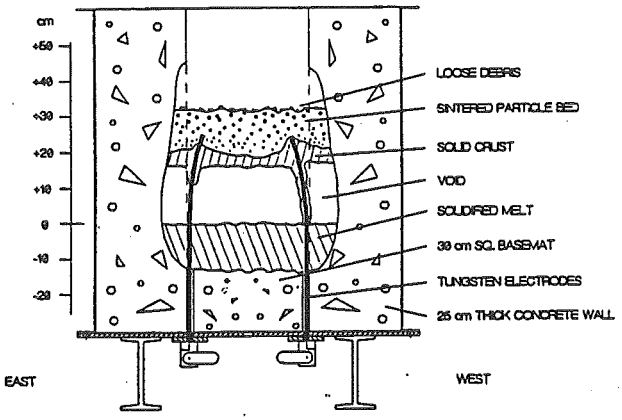

Fig.9 Geomatry of solidified debris and eroded concrete in MACE-M0

conditions from that in B/C-5. While peripheral region of corium was more heated in COTELS by induction heating, central region was more heated in MACE by direct current heating. This effect might cause different clearance condition between the concrete side wall and the ingot debris. However, basaltic concrete in COTELS is more tough than the limestone/common-sand concrete in MACE against MCCI. Hence, existence of channels inside ingot debris in COTELS, formed by the remaining porosity due to simulation of debris falling process was rather essential, which was not observed in MACE. Water penetration through two flow paths of the eroded side wall in peripheral region and the channels in central region avoided the large void in COTELS. Formation of pebble bed below ingot debris in COTELS, probably not observed in MACE, prevented the debris from further erosion of concrete.

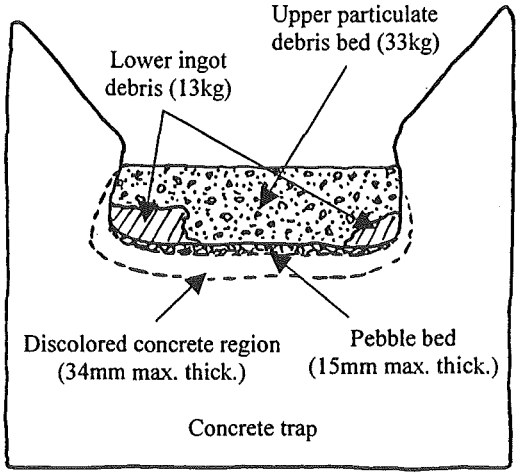

Fig.10 Geometry of solidified debris and eroded concrete in COTELS B/C-3

5. CONCLUSION

The formation of particulate debris bed was governed primarily by stored energy in corium before water supply on the melt surface. Besides, larger amount of the particulate debris bed were formed both in the case of thick corium layer and in the case of long term interruption of water supply. Large amount of smallest diameter particles was obtained due to the entrainment of molten corium, decomposed concrete and oxidation components of metal in corium associated with MCCI generated gas. The upper region of the particulate debris bed included more concrete compositions. The size distributions of the particulate debris bed were well correlated by nearly one set of Rosin-Rammler distribution constants.

The major differences of COTELS results compared with the former results of WETCOR and MACE were: 1) absence of adhesion of crust to the trap side wall by adopting induction heating to simulate decay heat in corium: 2) existence of channels in ingot debris formed by the remaining porosity due to simulation of corium falling process and high speed gas generation by MCCI: 3) better conditions for water penetration into debris via two flow paths of the clearance between eroded concrete side wall and the debris in peripheral region, and the channels in central region: 4) absence of wide void in ingot debris due to items 1), 2) and 3): 5) formation of heat resistance of pebble bed below ingot debris by simulating real size pebbles in concrete. All of these phenomena promoted the suppression of MCCI and caused smaller concrete erosion depth in COTELS Test B/C.

ACKNOWLEDGEMENTS

This work was sponsored under the contract by the Ministry of International Trade and Industry, Japan.

REFERENCES

Blose, R.E., Gronager, J.E., Suo-Anttila, A.J., Brockmann, J.E., 1987. SWISS : Sustained Heated Metallic Melt/Concrete Interaction with Overlaying Water Pools, NUREG/CR-4727, July 1987.

Blose, R.E., Powers, D.A., Copus, E.R., Brockmann, J.E., Simpson, R.B., Lucero, D.A., 1993. Core-Concrete Interaction with Overlying Water Pools : The WETCOR-1 Test, NUREG/CR-5907, November 1993.

Farmer, M.T., Spencer, B.W., Armstrong, D.R., 1992. MACE Test M1B Data Report, Argonne National Laboratory Report, ACE-TR-D6, September 1992.

Hofmann, P., Hagen, S.J.L, Schanz, G., Skokan, A., 1989. Reactor Core Materials Interaction at very high Temperatures, Nuclear Technology, vol. 87, August 1989, pp.146-185.

Nagasaka, H., Kato, M., Sakaki, I., Cherepnin, Y., Vasilyev, Y., Kolodeshnikov, A., Zhdanov, V., Zuev, V., 1999. COTELS Project (3) : Ex-vessel Debris Cooling Tests, Proceedings of OECD Workshop on Ex-Vessel Debris Coolability. Karlsruhe, 15-18 November 1999.

Spencer, B.W., Fischer, M., Farmer, M.T., Armstrong, D.R., 1991. MACE Scoping Test Data Report, Argonne National Laboratory Report, MACE-TR-D03, June 1991.

OECD Workshop on Ex-Vessel Debris Coolability
Karlsruhe, Germany, 15-18 November 1999

Organized in collaboration with
Forschungszentrum Karlsruhe (FZK) GmbH

STATUS OF LARGE SCALE MACE CORE COOLABILITY EXPERIMENTS

M. T. Farmer, B. W. Spencer, D. J. Kilsdonk, and R. W. Aeschlimann
Reactor Engineering Division
Argonne National Laboratory
9700 S. Cass Avenue, Argonne IL, USA
farmer@aeetes.re.anl.gov spencer@anl.gov

ABSTRACT

The Melt Attack and Coolability Experiment (MACE) program underway at Argonne National Laboratory is addressing the efficiency of water to cool and thermally stabilize a molten corium/concrete interaction (MCCI) when the interaction is flooded from above. Large scale reactor material tests are being conducted, in parallel with related modeling efforts, which investigate water addition to an MCCI already underway. The experiments described herein investigate the interaction of partially oxidized PWR corium with limestone/common sand concrete. Direct electrical heating is used to simulate internal heating of the corium. During the program, experiments have been conducted in test sections with cross sections ranging from 30 cm x 30 cm to 120 cm x 120 cm; melt masses have ranged from 100 to 2000 kg. The results of early tests M0 and M1b have demonstrated high initial heat fluxes (i.e., ~ 3.5 MW/m^2) which are attributable to efficient bulk cooling of the corium pool. However, a crust eventually forms which limits the heat extraction to a level of ~ 600 kW/m^2 or less. Moreover, as the tests progress, both analyses and posttest examinations indicate that the crust eventually anchors to the test section sidewalls, thereafter leading to melt/crust separation. During periods when the melt is separated from the crust, the melt/water heat flux is significantly reduced to a level of a few hundred kW/m^2 or less. However, both tests M0 and M1b provided evidence of pool swelling events which result in extrusion and ejection of melt into water above the crust, which significantly increases the quench rate by formation of porous particle bed and lava structures. Crust separation has been postulated to terminate the early, efficient quench process observed in the MACE tests. Separation is considered to be nonprototypic due to inherent crust instabilities in the large lateral span typical of most plants (~ 6 m). Thus, the current program focus is the development of separate effects tests to study crust behavior under the prototypic situation of sustained melt/crust contact.

1.0 INTRODUCTION

Reactor risk studies have focused attention on sequence specific phenomena pertaining to postulated core melt accident sequences in LWR systems. One such unresolved issue involves the coolability of molten core material (corium) accumulated on the concrete basemat of the containment. The coolability issue concerns the efficiency of water atop the corium insofar as removing the sensible energy of the melt (quench process), and also the decay heat which is a continuous source of internal heat generation. An unsuccessful outcome means that the corium pool would continue its downward migration into the concrete basemat, whereas a successful outcome would render the bed quenched and cooled by virtue of heat extracted by water, thereby terminating the accident progression.

Under the sponsorship of the ACE International Consortium, USDOE, USNRC, and EPRI, the Melt Attack and Coolability Experiment (MACE) Program is intended to provide information on the quenching behavior of prototypic core oxide material under MCCI conditions. The experiment philosophy focuses on acceptance and utilization of the database through the elimination of scale and material property questions (distortions) to the greatest extent possible. This paper provides a summary of the test apparatus and results from early MACE Tests M0 and M1b in relation to the program objectives. The current status and future direction of the program are also summarized.

2.0 EXPERIMENT DESCRIPTION

The MACE apparatus is located in a large scale test facility at ANL which consists of an explosion rated containment building to safeguard against the risk of steam explosion (hypothetical) and combustible gas (real) hazards. The facility is currently approved for melt/water interaction testing at scales up to 2000 kg molten core oxide material. The system for conducting the MACE tests consists of a test apparatus, a power supply for Direct Electrical Heating (DEH) of the corium, a water supply system, a steam collection and condensation system, a ventilation system to filter and exhaust the off-gases, and a data acquisition system. A schematic illustration of the facility is provided in Fig. 1. The apparatus for containment of the core material consists of a test section which is ~ 3 m tall with a square internal cross-section. The concrete basemat is located at the bottom of the test section. The basemat is instrumented with multi-junction Type K thermocouple (TC) arrays to measure ablation front location, and with Type C (tungsten/rhenium) TC's in tungsten thermowells to measure MCCI temperatures.

The corium powder charge is placed directly atop the basemat. In the tests described here, the charge was a mixture of crushed UO_2 pellets (unirradiated, natural and depleted) and ZrO_2 powders, plus a small amount (typically 8 wt %) of calcined concrete powders (CaO and SiO_2). The concrete is incorporated to account for concrete erosion which is expected to occur during the corium spreading phase following breach of the reactor pressure vessel (Sienicki and Spencer, 1986). The test is initiated by heating a small region of UO_2 pellets with tungsten heater elements until the oxide becomes electrically conductive. After this time, the localized zone heats up and melts, and the melted zone eventually grows to encompass nearly all the powders as the DEH input power is increased. Zirconium metal intended to be incorporated in

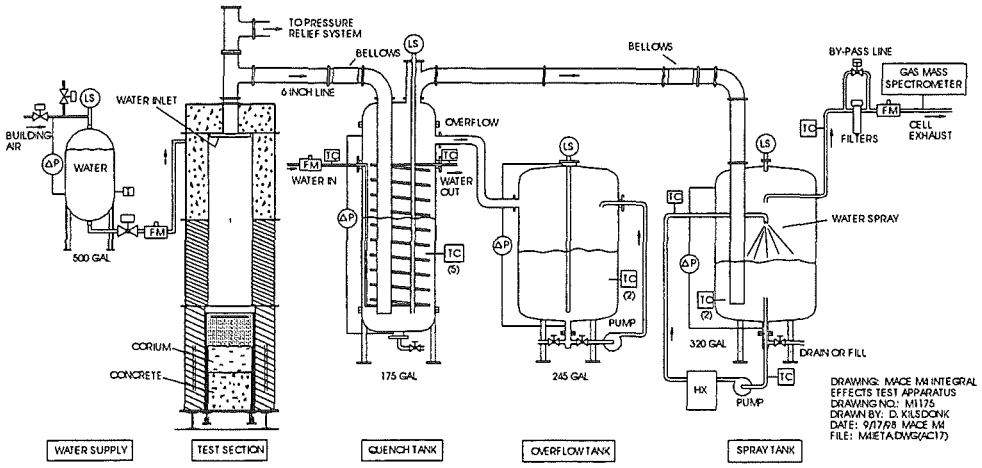

Fig. 1. Schematic Illustration of MACE Facility.

the melt is placed in distinct concrete/metal inserts located immediately over the concrete surface, so that the metal is incorporated during the last stages of the powder heatup (this approach minimizes oxidation of the Zr prior to onset of basemat ablation). Using the DEH technique, the powder melting phase of the experiment typically lasts several hours, and this long heatup phase can cause partial dryout of the underlying concrete prior to onset of ablation. For the more recent MACE tests, the DEH melt generation technique has been replaced by specially designed exothermic mixtures which, when ignited, produce prototypic core melt compositions over a timescale of ~ 20 seconds (i.e., melt generation rate of ~ 100 kg/sec at the 2000 kg core melt scale). This revised approach has satisfied one of the long-term MACE objectives of bringing core melt in sudden contact with pristine concrete, as is expected to be the case during a plant accident.

Once the melt has been established and a specified depth of concrete erosion has been achieved, water addition is initiated. Water is delivered by two weirs at the top of the test section on the sidewalls opposite those having the electrodes. The water is initially added at a steady rate to ensure that the quench process is not water-starved (i.e., sufficient to sustain a quench rate of at least 10 MW/m^2) until a 50 cm head is established. Thereafter, makeup is added to maintain the head in the range of 50 +/- 5 cm as the quench process continues. TC's in the test section measure water and covergas temperatures.

A large gas line is present in the lid of the test section to vent steam, covergas, and noncondensable MCCI off-gases to the adjacent primary quench tank, which is equipped with a cooling coil to maintain the water inventory subcooled. One or more overflow tanks are present

to collect excess condensate from the quench tank, depending on the test scale. The tanks and cooling coil are instrumented with TC's, flowmeters, level sensors, and pressure transducers to monitor transient energy deposition in the system so that the necessary heat balance information can be extracted. Downstream from the quench tank is a secondary spray tank which performs an identical condensation/gas cleanup function. While adding redundancy, the use of two tanks in series overcomes the practical limitation of attempting to resolve melt/water heat fluxes from as high as 5 MW/m^2 during the initial bulk cooling stage to as low as a few hundred kW/m^2 depending on upper crust behavior.

After passing through the quench system, the helium covergas and noncondensable concrete decomposition gases (CO, CO_2, and H_2) are vented through an offgas system which includes a demister, filters, gas flowmeters, and a gas mass spectrometer which provides information on the offgas composition versus time. The offgases are eventually exhausted through the containment cell ventilation system where it flows through a series of high efficiency filters before finally being released from the building stack.

Other significant test instrumentation includes both stationary (lid mounted) and insertable (water cooled) video cameras for observing various stages of the melt/water interaction. Insertable thermocouple and "crust busters" probe drives have also been employed at various stages of the program to investigate upper crust behavior. For each test, several fast response, high range (piezo-electric) pressure transducers are mounted at various locations within the test section to capture the pressure pulse due to a steam explosion, should one occur. Additional details regarding the facility equipment, instrumentation, data acquisition, and procedures is provided in Project documentation.

3.0 TEST RESULTS

Specifications and conditions for MACE Tests M0 and M1b are provided in Table 1. Summary results for these two tests are provided below; detailed descriptions of test results are provided in Project documentation (Spencer et al., 1991, and Farmer et al., 1992).

3.1 MACE Scoping Test M0

The objectives of the Scoping Test were to: i) provide an early indication of the mode and extent of corium quenching, and ii) provide information to aid both model development and future experiment design activities. As shown in Table 1, the experiment was conducted in a 30 cm x 30 cm test section with a corium mass of ~ 130 kg, resulting in a collapsed pool depth of ~ 15 cm. The basemat material was limestone/common sand concrete. The scale of the M0 test was chosen to be slightly larger than the 21.6 cm diameter previous SWISS tests (Blose et al., 1987) in which water was added above molten stainless steel interacting with concrete. In both these tests, an upper bridge crust formed which prevented any significant abatement of the MCCI. The Scoping test was also conducted with concrete sidewalls, based on the rationale that any crust material which formed would be unlikely to anchor to an ablating sidewall. The use of concrete sidewalls in this test is significant since the Scoping Test remains as the only two dimensional reactor material MCCI test every conducted.

Table 1 Specifications for MACE Tests M0 and M1b.

Parameter		M0	M1b
Test Section Internal Dimensions		30 cm x 30 cm	50 cm x 50 cm
Test Section Sidewall Material		Concrete	MgO
System Pressure, MPa absolute		0.1	0.1
Corium Mass, kg		130	480
Collapsed Pool Depth, cm		15	25
Corium Type		70 % oxidized PWR	70 % oxidized PWR
Corium Composition at Onset of Ablation, kg (wt %)	UO_2	73 (56)	309 (65)
	ZrO_2	14 (11)	64 (13)
	Zr	5 (4)	14 (3)
	SiO_2	4 (3)	14 (3)
	CaO	4 (3)	13 (2)
	MgO	0 (0)	63 (13)
	Concrete	30 (23)	3 (1)
Initial Melt Temperature, K		2000 (estimate)	2350
Specific Power, W/kg UO_2 (actual)		350 (2x-4x actual)	350
Basemat Type		Limestone/common sand	Limestone/common sand
Basemat Height, cm		35	55
Ablation Depth at Water Addition, cm		1.3	1.3 (5.0 actual)
Water Addition Rate, liters/second		10	2
Water Collapsed Pool Depth, cm		50	50
Water Makeup Rate, liters/second		10	2
Inlet Water Temperature, K		296	296
DEH Power Operating Mode		Constant Voltage	Constant Voltage

Water addition in the Scoping Test began when the basemat centerline TC array indicated that the concrete ablation depth had reached 1.3 cm (i.e., 4 minutes after onset of ablation was detected at the basemat centerline). The ablation front location as measured by five multi-junction TC arrays cast at various locations within the basemat is shown in Fig. 2. At this time, the melt surface video camera indicated that the pool was agitated and that there was no evidence of floating crust on the pool surface. The video also indicated that there was a partial crust (remnants of original corium powders) which had not collapsed into the pool but was cantilevered near the tops of the electrodes. This crust is estimated to have occluded ~ 1/2 the test section area, but the melt surface itself was most likely several centimeters below this crust material. The experimenters did not observe the normally intense interaction phase which accompanied the Zr ingression stage of MCCI tests (Thompson et al., 1992), and so the input DEH power was left at the heatup level of ~ 100 kW rather than reducing it to the target level of 26 kW. As a result, the input power during the Scoping Test ranged from 2 to 4 times the target level of 350 W/kg fuel. Melt temperature data is provided in Fig. 3. As is evident from this figure, no direct measurement of the melt temperature at onset of ablation was obtained. However, during posttest examinations, remnants of unmelted Zr rod initially present in concrete inserts over the basemat were recovered, which indicates that the melt temperature

was probably below the Zr melting temperature of 2130 K. Incomplete melting of the Zr rod would explain the absence of an intense initial interaction at the onset of ablation.

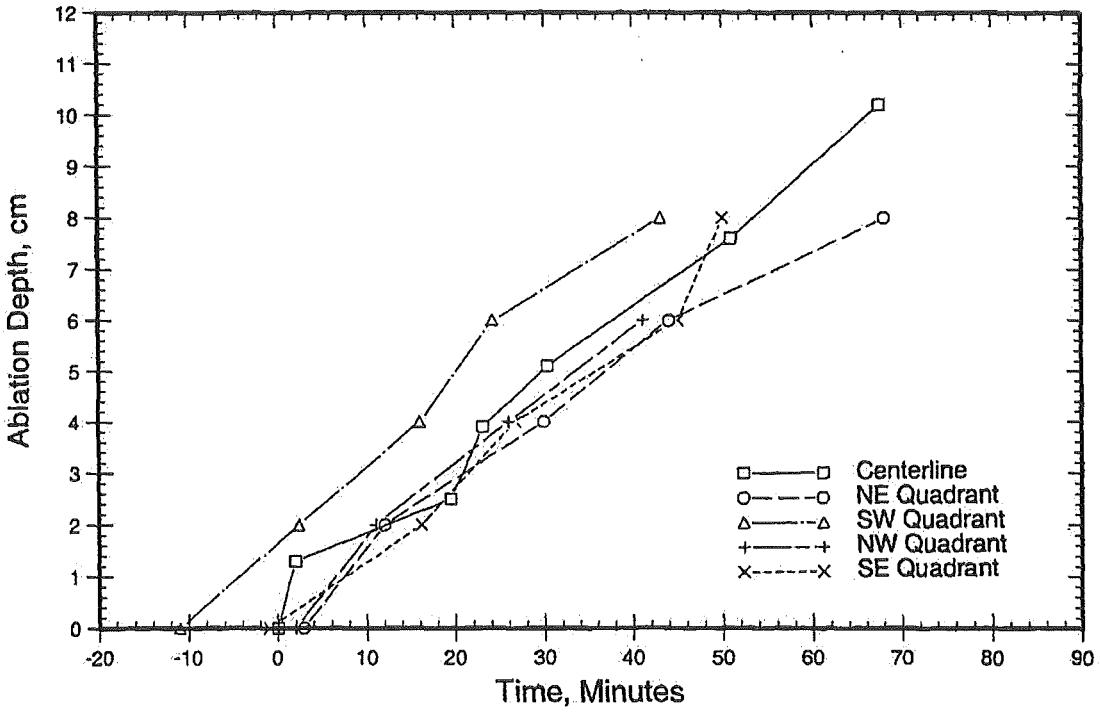

Fig. 2. M0 Basemat Ablation Data.

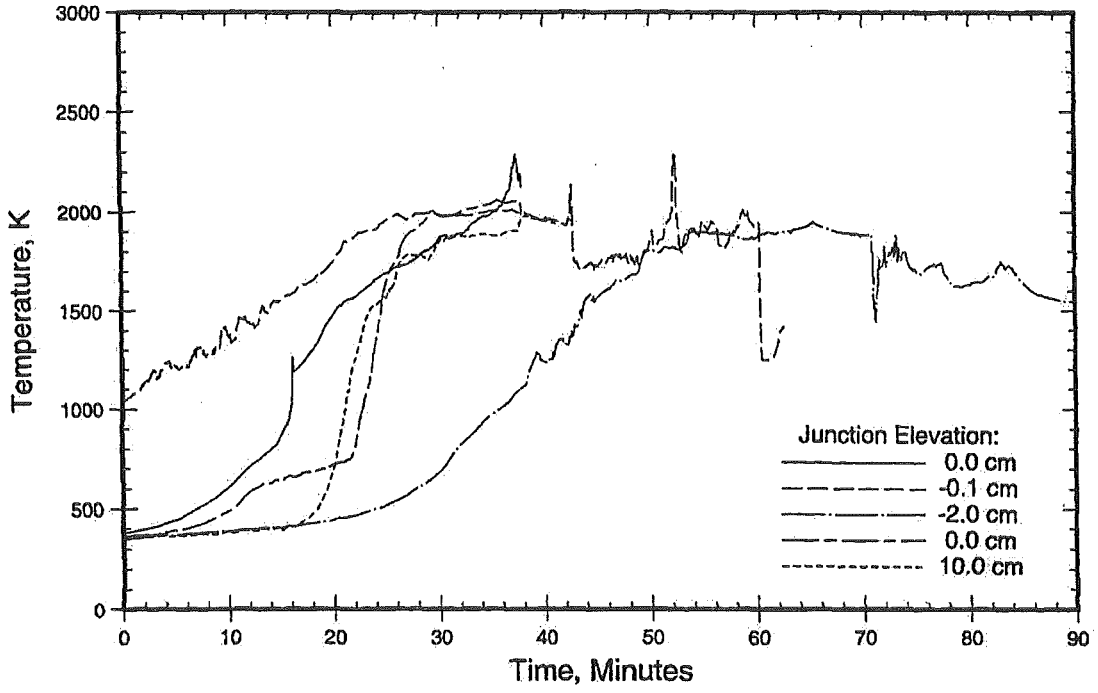

Fig. 3. M0 Melt Temperature Data.

Water was initially added to the test section at a rate of 10 l/s until the target pool depth of 50 cm was attained. Thereafter, makeup was added to maintain the depth in the range 50 +/- 5 cm. The corresponding melt/water heat flux is shown in Fig. 4; this data has been corrected for heat transfer from apparatus structure other than the melt surface itself. Also shown in the figure is the DEH input power normalized with the initial test section planar area (0.09 m^2) for direct comparison with the melt/water heat flux data. The data indicates that during the first three minutes of the interaction, a large cooling transient occurs with the upwards heat flux peaking at nearly 4 MW/m^2. The energy extraction during this phase amounted to ~ 44 MJ. Assuming a heat of fusion of 300 kJ/kg, then this amount of heat removal could theoretically have rendered the initial 130 kg corium charge as essentially a solid mass, albeit at high temperature. Due to the absence of functioning melt temperature TC's at this time, the extent of this initial interaction could not be independently verified. However, based on the upwards heat removal, it is clear that a significant cooling transient occurred.

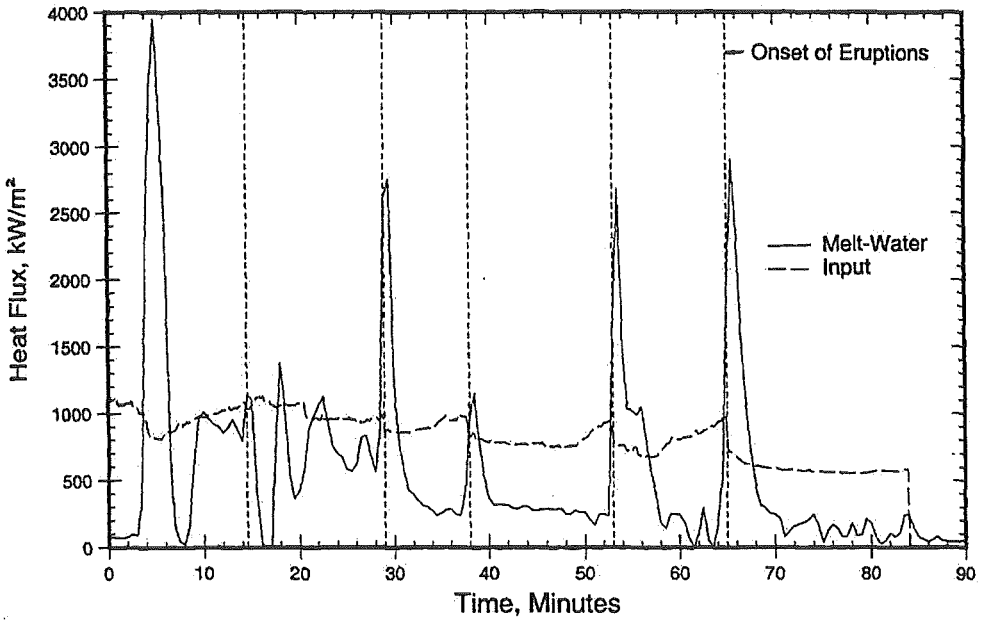

Fig. 4. M0 Melt-Water Heat Flux and Input Power.

Following the first three minutes, the heat flux fell rapidly and a quiescent period was observed. This occurrence has been attributed to the formation of a stable interfacial crust (Spencer et al., 1992); i.e., the large initial heat removal caused the melt temperature and sparging rate to decline to the point at which an incipient crust could form in the presence of the sparging gases. Although perturbations are observed, the heat flux over the next 30 minutes averages around 700 kW/m^2, which amounts to ~ 70 % of the DEH input heat flux of ~ 1 MW/m^2 during this time. After ~ 30 minutes, the average heat transfer diminished steadily to a level of ~ 150 kW/m^2 near the end of the test.

It is important to note that the crust which formed was anchored by the tungsten electrodes. Both analyses and posttest examinations indicate that the crust remained at the

elevation where it initially formed, and the MCCI resumed its downward migration. Formation of the intervening gap has been argued to terminate efficient heat transfer processes between the melt and overlying water. For this particular test, separation of the melt from the crust is believed to have occurred at ~ 30 minutes into the test sequence, as evidenced by the rapid decline in the heat transfer rate at this time.

Despite the occurrence of separation, a unique heat transfer mechanism was displayed in this test which has also been observed in subsequent MACE tests, as well as the WETCOR test conducted at SNL (Copus et al., 1992). In particular, periodic ejections of molten corium through the bridge crust were observed; the timing of these events is shown in Fig. 4. These ejections were driven by MCCI decomposition gas release, which entrained melt through the crust into overlying water in the form of dispersed droplets. These droplets quenched as they settled through the water pool and collected on the crust upper surface to form a particle bed. The M0 posttest debris distribution is shown in Fig. 5. By the end of the test, the ejected debris had formed a bed ~ 10 cm deep in which the top half was loosely packed and the bottom half was sintered agglomerate. The mass of this particle bed amounted to ~ 23 kg. Thus, this ejection mechanism lead to the rendering of ~ 20 % of the initial melt mass in the form of a quenched and coolable debris bed. As is evident from Fig. 4, these ejections occurred every 10-15 minutes, and they resulted in significant transient augmentation in the upwards heat flux to levels in the range of 1-3 MW/m^2. The power supply current was sensitive to these events. In particular, the current dropped sharply falling these events (at constant voltage), which is interpreted as a loss of conductor (melt) from the electrical path.

During disassembly, the concrete sidewalls were found to be eroded by as much as 10 cm; a rough estimate of the sidewall ablation profile is depicted in Fig. 5 (detailed measurements of the sidewall ablation profile have been made, but this data has not been released). Sidewall thermocouple data indicated that radial ablation was occurring as early as 50 minutes before onset of axial ablation. It is estimated that at onset of axial ablation, the total corium mass was ~ 130 kg, of which 23 wt % was concrete decomposition products from sidewall erosion. This large influx of concrete from the sidewalls during the preheat probably depressed the melt temperature in this test to the extent that the Zr was not significantly melted. Thus, the actual M0 test conditions reflect a 100 % oxidized PWR melt composition ~ 30 % diluted with concrete oxides run at 2 to 4 times prototypic decay heat level at 2 hours into the accident sequence.

3.2 MACE Test M1b

Following the Scoping Test, the MACE facility was upgraded to allow larger scale tests up to 75 cm x 75 cm scale. The test section was constructed with refractory sidewalls (MgO) rather than concrete to prevent early concrete dilution of the melt. The tungsten electrodes were recessed into the sidewalls to reduce the chances of crust anchoring on these surfaces. A new 0.56 MW power supply was installed, and an on-line gas mass spectrometer was added to the system. Test M1 was conducted in a 50 cm x 50 cm test section with a collapsed pool depth of 25 cm. This experiment was initially attempted in November 1991, but failed to achieve initial melt/water contact due to the presence of a preexisting upper crust which remained following the corium preheat (Spencer et al., 1992). As a result, insertable lance probes were

incorporated into the test design to dislodge the crust during the preheat if it reoccurred. Test M1 was repeated as M1b in April 1992, and this test was successful insofar as establishing initial melt/water contact.

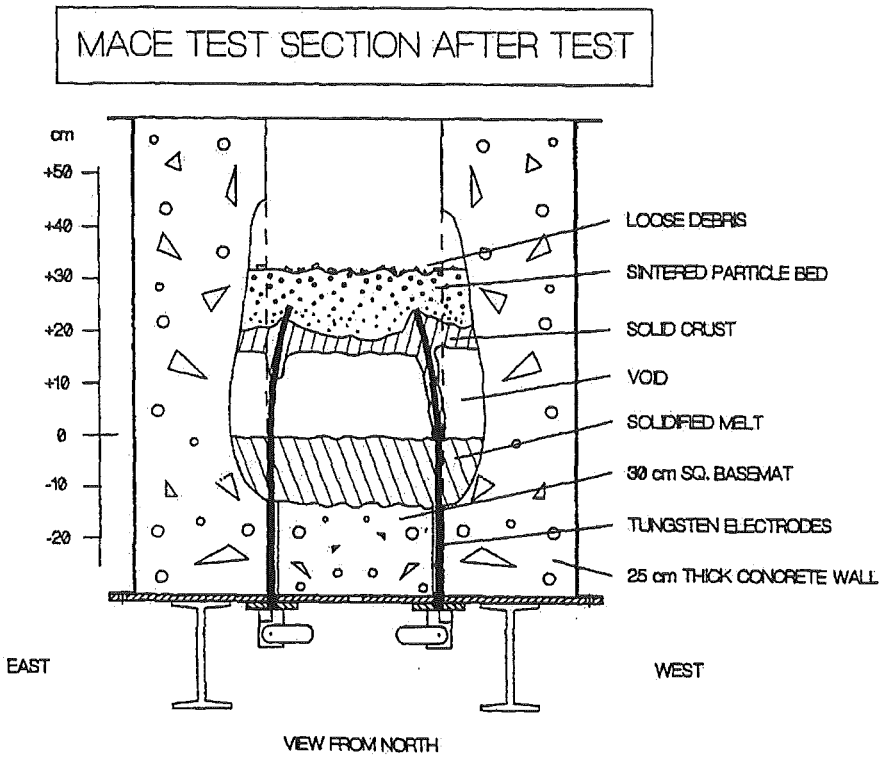

Fig. 5. M0 Posttest Debris Configuration.

Test M1b ran for six hours following onset of ablation. The experiment was terminated on the basis that most basemat TC's showed that the concrete temperature had stabilized, indicating that ablation had been arrested. The ablation front location, evaluated on the basis of basemat thermocouple measurements and also the integrated noncondensable MCCI gas release (CO/CO_2), is shown in Fig. 6. Water addition in Test M1b began when the basemat centerline ablation depth had reached a depth of 5.0 cm (i.e., 14.7 minutes after onset of ablation at the basemat centerline). As for test M1, the lid video camera indicated that a skeleton crust was present over the melt surface at onset of ablation. The lance probes were used at this time to produce several significant (i.e., ~ 10 cm diameter) holes through the skeleton crust prior to water addition. The fact that water addition was delayed until the 5 cm ablation depth was reached was a result of this action. The view of the melt surface beneath the crust at this time revealed the intense interaction characteristic of MCCI's with metallic Zr present in the melt (Thompson et al., 1992). The test data, as well as the view from the lid video camera, indicated that the remnants of the skeleton crust did not inhibit melt/water contact. Other measurements indicated that the melt temperature at the time water was added was ~ 2300 K, and the melt sparging rate was ~ 25 cm/sec.

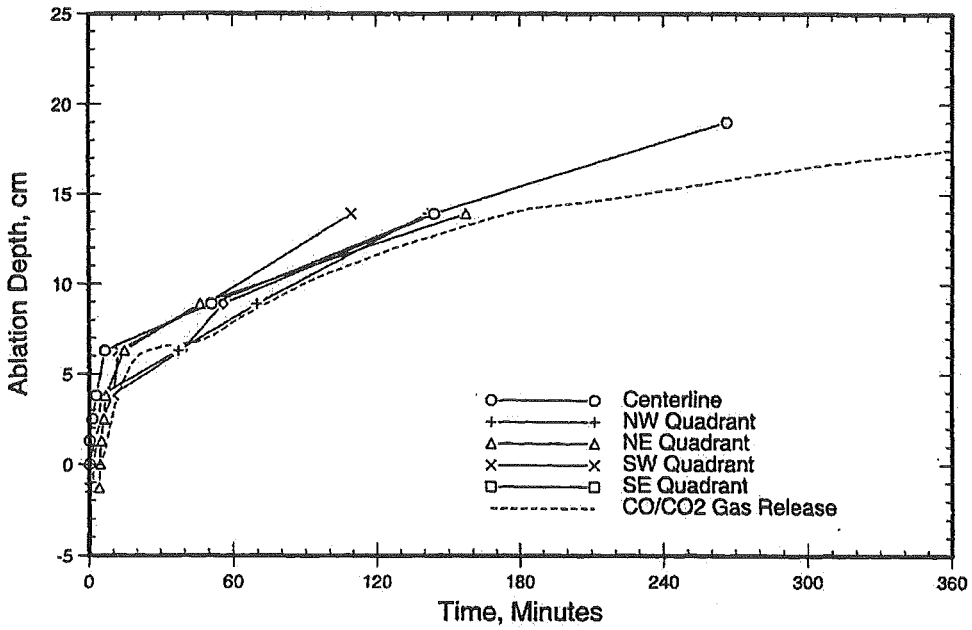

Fig. 6. M1b Basemat Ablation Data.

The water addition and makeup strategy for test M1b was basically the same as the Scoping Test, with the exception that the inlet water flowrate was reduced to 2 l/s (see Table 1). The corresponding melt/water heat flux (also corrected for heat transfer from apparatus structure) is shown in Fig. 7. The input power normalized with the test section planar area 0.25 m^2 is also shown for comparison with the melt/water heat flux data. Unlike M0, the input power was adjusted to the target level of 350 W/kg fuel at onset of basemat ablation. The melt/water heat flux data indicates that during the first 15 minutes of the interaction, a large cooling transient occurs with the upwards heat flux peaking at nearly 4 MW/m^2. Melt thermocouple measurements for M1b are shown in Fig. 8. As is evident from this figure, the initial cooling transient resulted in a bulk melt temperature decline of ~ 350 K (i.e., from 2300 K to 1950 K) before stabilizing at ~ 30 minutes. Based on the corium composition shown in Table 1, the average debris specific heat is estimated as ~ 870 J/kg•K. Given the melt mass of ~ 500 kg, then the bulk temperature decline of 350 K corresponds to 150 MJ of upwards heat removal. However, the integrated upwards heat removal over the first 15 minutes of the interaction amounted to ~ 350 MJ, which is ~ 200 MJ greater than that attributable to bulk heat removal alone. Thus, the data indicates that some amount of debris quenching at the melt/water interface must have occurred during the initial interaction. The change in the corium specific enthalpy during reduction in the temperature from ~ 2300 K to water saturation temperature is estimated as 1.7 MJ/kg for the composition shown in Table 1. Thus, the energy balance deficit of 200 MJ can be accounted for by complete quench of 117 kg of corium. Posttest analyses indicated that the mass of the skeleton crust amounted to 26 kg, which leaves ~ 90 kg of material which could have quenched and stabilized during the initial interaction. For an assumed crust density of 6000 kg/m^3, the 90 kg of core material would amount to a crust thickness of ~ 6 cm in the 50 cm x 50 cm test section. As shown in Fig. 9, this estimate from the heat balance is in reasonable agreement with the posttest measurements of the bridge crust

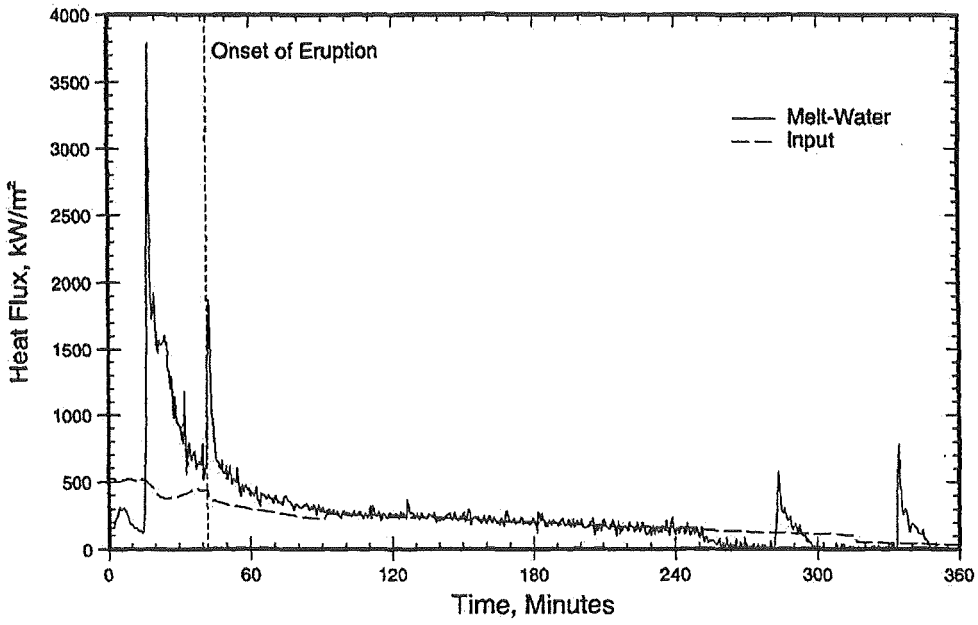

Fig. 7. M1b Melt-Water Heat Flux and Input Power.

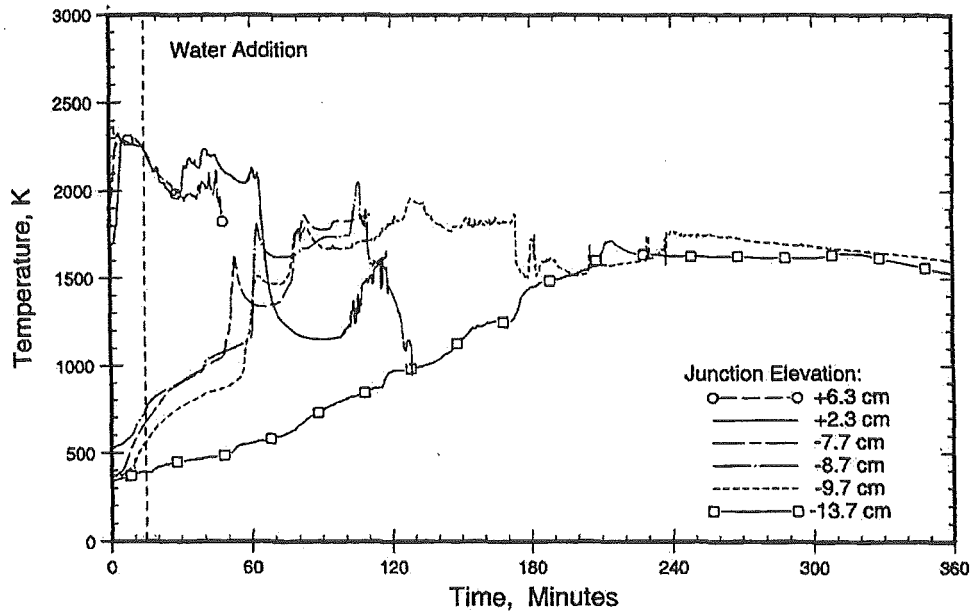

Fig. 8. M1b Melt Temperature Data.

thickness for test M1b. As shown in Fig. 8, the elevations of the thermocouple junctions in the melt were unfortunately too low to capture this postulated quenching event.

Other test data indicates that this initial interaction had a significant stabilizing effect on the MCCI. In particular, the ablation data shown in Fig. 6 indicates that the upwards heat transfer most likely caused a significant, concurrent reduction in the ablation rate. The ablation rate at onset of water addition was ~ 3.2 mm/min. During the first 15 minutes of the melt/water interaction, the ablation rate steadily declined to a level of ~ 0.2 mm/min based on the gas release rate. However, over the time interval 30-60 minutes, the ablation rate gradually increased back to a peak post-water addition level of ~ 1 mm/min. During this same time interval, the baseline melt/water heat flux declined rapidly to a level of ~ 400 kW/m^2 at 60 minutes. The thermocouple data shown in Fig. 8 indicates that the melt temperature stabilized during this period. All of these events are consistent with the formation of an interfacial crust, as described above. Assuming a crust thermal conductivity of ~ 1 W/m•K and a temperature drop of ~ 1000 K across the crust (i.e., upper surface in nucleate boiling and lower surface near corium solidus of ~ 1400 K), then the crust thickness to supply the observed heat load of 400 kW/m^2 to the overlying water is found to be ~ 3 mm assuming that the heat transfer is conduction limited. This crust thickness is more than an order of magnitude less than the actual thickness of ~ 6 cm based on both analysis and posttest examinations. Thus, this calculation indicates that the M1b crust was most likely permeable to water ingression and that the temperature drop across the crust most likely occurred across a thin thermal boundary layer located at the bottom of the crust.

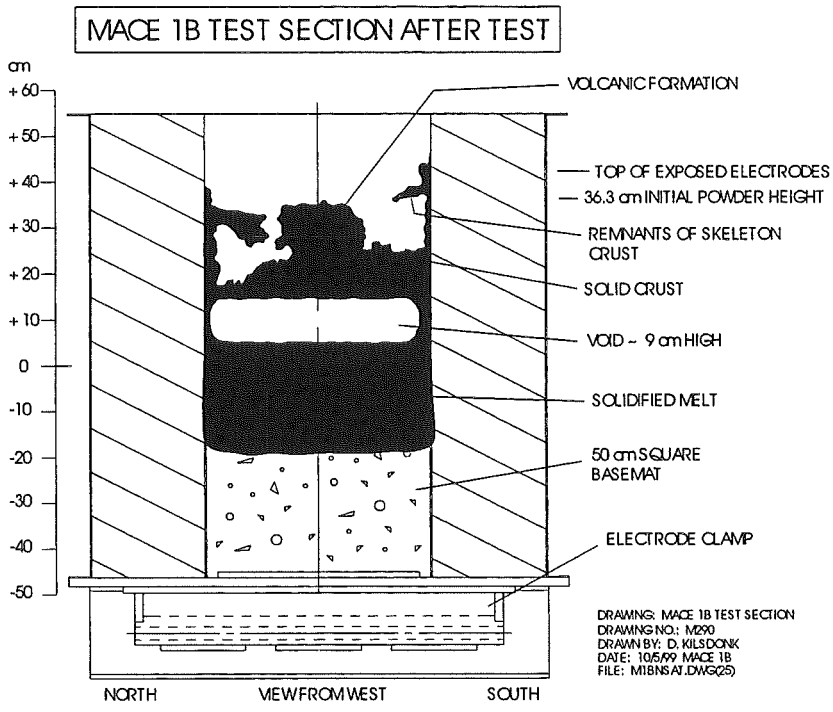

Fig. 9. M1b Posttest Debris Configuration.

As is evident from Fig. 9, the crust which formed during the initial phase of the interaction anchored to the test section sidewalls in this increased scale test, eventually leading to the formation of an intervening gap ~ 9 cm high as the MCCI continued downwards. As

discussed earlier, gap formation is believed to adversely affect efficient heat transfer mechanisms which are postulated to occur when the melt is in contact with the overlying crust. For this test, separation is believed to have occurred at ~ 50 minutes, as evidenced by the decline in melt water heat flux and the resurgence of basemat ablation after this time.

As in the Scoping Test, Test M1b provided evidence of periodic ejections of molten corium. As is evident from Fig. 7, a significant eruption was observed on video at ~ 42 minutes which lead to significant transient increase in the upwards heat flux up to ~ 1.7 MW/m^2. The heat flux data also indicates that two minor eruptions may have occurred late in the test sequence (i.e., at 285 and 338 minutes). However, these apparent eruptions were not evident on the melt surface video. The location of the volcano in M1b was very near the center of the test section. The mass of ejected material amounted to 19.1 kg, which only amounts to ~ 4 % of the initial melt mass. This fraction is noted to be significantly less than that for the Scoping Test (i.e., 20 %). However, the volcano grew axially to the extent that it contacted (and bonded with) the underside of the skeleton crust. Thus, the possibility exists that this contact could have sealed of the vent passageway(s), thereby suppressing the eruptions.

After the first 60 minutes of the interaction, the input power (at constant voltage), melt temperature, and basemat ablation rate steadily declined over the remainder of the test. This trend is most likely attributable to the fact that the upwards heat transfer rate remained very significant in comparison to the input power (see Fig. 7). The result was that after six hours of operation with water over the melt, the melt temperature had fallen significantly to near the concrete liquidus of ~ 1570 K.

During disassembly, one electrode sidewall was found to be significantly eroded. Sidewall TC measurements indicated that this interaction occurred during the ~ 6 hour corium preheat for this test, and that the interaction essentially stopped once water was added. It is estimated that at onset of ablation, the total corium mass was ~ 480 kg, of which ~ 63 kg was MgO from sidewall erosion. Thus, the actual M1b test conditions reflect a 70 % oxidized PWR melt composition ~ 23 % diluted with concrete oxides run at prototypic decay heat power at two hours into the accident sequence. The problem of melt/crucible interactions has been addressed in subsequent MACE testing. The technology has been developed to the point where there is virtually no melt/crucible interaction.

4.0 MACE PROGRAM STATUS

The MACE program was started in 1989 under EPRI sponsorship. Since the program was initiated, a total of seven integral experiments have been conducted, of which four have been operationally successful. In an effort to achieve the prototypic situation in which the crust floats atop the melt, tests have been conducted at scales up to 2000 kg core melt mass in a 120 cm x 120 cm test section. Even at this scale, the crust was found to attach to the test section sidewalls, producing a non-prototypic gap between the melt and the solidified crust/lava/particle bed structure above. Thus, the tests conducted to date have not clearly demonstrated debris coolability. However, the tests have provided evidence of heat transfer mechanisms which could lead to coolability if prototypic melt/crust contact is maintained. As a result, the current program focus is on the development of separate effects testing approaches

which will produce data on these postulated coolability mechanisms under well controlled conditions to support model development and validation activities. These models will then be used to extrapolate to plant conditions.

5.0 SUMMARY AND CONCLUSIONS

The MACE program is addressing the important safety issue of the ability of water to cool and thermally stabilize a molten corium/concrete interaction (MCCI) when the interaction is flooded from above. Early MACE Tests M0 and M1b parameterized on test section scale; these tests were performed in 30 cm x 30 cm and 50 cm x 50 cm test sections, respectively. Both tests utilized 70 % oxidized PWR corium interacting with limestone/common sand concrete. The results of these tests demonstrated high initial heat fluxes (i.e., ~ 3.5 MW/m^2) which is attributable to efficient bulk cooling of the corium pool. However, a crust eventually forms which limits the heat extraction to a level of ~ 600 kW/m^2 or less. Moreover, as the tests progress, both analyses and posttest examinations indicate that the crust eventually anchors to the test section sidewalls, thereby leading to melt/crust separation as the MCCI progresses downwards. During periods of sustained separation, the melt/water heat flux is significantly reduced to a level of a few hundred kW/m^2 or less. However, both tests M0 and M1b have revealed physical evidence of pool swelling events which result in extrusion and ejection of melt into water above the crust, significantly increasing the quench rate by formation of porous particle bed and lava-like structure.

The formation of a sustained gap between the crust and underlying melt has been postulated to terminate the early efficient quench process observed in the MACE tests. Gap formation is not considered to be prototypic due to inherent crust instabilities associated with crust anchoring in the large lateral span typical of most plants (~ 6 m). Thus, the current focus of the program is the development of separate effects tests to study crust behavior under conditions which are considered to be relevant for plant conditions.

ACKNOWLEDGMENTS

The manuscript was prepared for publication by Kathy Rank. This effort is gratefully acknowledged.

REFERENCES

Blose, R. E., Gronager, J. E., Suo-Antilla, A.J., and Brockmann, J. E. Swiss: sustained heated metallic melt/concrete interactions with overlying water pools, NRC Report, NUREG/CR-4727, 1987.

Copus, E. R., Core concrete interactions with overlying water pools, Proc. of the Second OECD (NEA) CSNI Specialist Meeting on Molten Core Debris-Concrete Interactions, KfK 5108, NEA/CSNI/R(92)10, April, 1992.

Farmer, M. T., Spencer, B. W., and Armstrong, D. R. MACE test M1b data report, Advanced Containment Experiments Report, MACE-TR-D6, 1992.

Sienicki, J. J., and Spencer, B. W., 1986. The jet impingement stage of molten core-concrete interactions. In: OECD CSNI Specialist Meeting on Core Debris/Concrete Interactions, Palo Alto, CA, September 3-5 .

Spencer, B. W., Fischer, M., Farmer, M. T., and Armstrong, D. R. MACE scoping test data report, Advanced Containment Experiments Report, MACE-TR-D03, 1991.

Spencer, B. W., Farmer, M. T., Armstrong, D. R., Kilsdonk, D. J., Aeschlimann, R. W., and Fischer, M., Results of MACE tests M0 and M1b, Proc. of the Second OECD (NEA) CSNI Specialist Meeting on Molten Core Debris-Concrete Interactions, KfK 5108, NEA/CSNI/R(92)10, April, 1992.

Thompson, D. H., Fink, J. K., Armstrong, D. R., and Spencer, B. W., Thermal hydraulic aspects of large-scale integral MCCI tests in the ACE program, Proc. of the Second OECD (NEA) CSNI Specialist Meeting on Molten Core Debris-Concrete Interactions, KfK 5108, NEA/CSNI/R(92)10, April, 1992.

OECD Workshop on Ex-Vessel Debris Coolability
Karlsruhe, Germany, 15-18 November 1999

Organized in collaboration with
Forschungszentrum Karlsruhe (FZK) GmbH

STATUS OF THE CORQUENCH MODEL FOR CALCULATION OF EX-VESSEL CORIUM COOLABILITY BY AN OVERLYING WATER LAYER

M. T. Farmer and B. W. Spencer
Reactor Engineering Division
Argonne National Laboratory
9700 S. Cass Avenue, Argonne IL, USA
farmer@aeetes.re.anl.gov spencer@anl.gov

ABSTRACT

The results of Melt Attack and Coolability Experiment (MACE) tests have identified several heat transfer mechanisms which could potentially lead to long term corium coolability. Based on physical observations from these tests, an integrated model of Corium Quenching (CORQUENCH) behavior is being developed. Aside from modeling of the primary physical processes observed in the tests, considerable effort has also been devoted to modeling of test occurrences which deviate from the behavior expected at reactor scale. In this manner, extrapolation of the models validated against the test data to the reactor case can be done with increased confidence. The integrated model currently addresses early bulk cooling and incipient crust formation heat transfer phases, as well as a follow-on water ingression phase which leads to development of a sustained quench front progressing downwards through the debris. In terms of experiment distortions, the model is also able to mechanistically calculate crust anchoring to the test section sidewalls, as well as the subsequent melt/crust separation phase which arises due to concrete densification upon melting.

In this paper, the status of the model development and validation activities are described. In addition, representative calculations for PWR plant conditions are provided in order to illustrate the potential benefits of overlying water on mitigation of the accident sequence.

1.0 INTRODUCTION

An important unresolved question in the assessment of ex-vessel severe accidents in light water reactors is the ability of water to cool and thermally stabilize molten core material accumulated on the concrete basemat of the containment building. The coolability issue concerns the efficiency of water atop the corium insofar as removing the sensible energy of the melt (quench process), and also the decay heat which is a continuous source of internal heat generation. The results of Melt Attack and Coolability Experiment (MACE) tests (Farmer et al., 1999) have provided evidence of four unique cooling mechanisms related debris coolability: i) bulk cooling, ii) water ingression through cracks/fissures in the debris, iii) melt eruptions, and iv) transient crust breach. Bulk cooling constitutes the initial phase of the interaction in which the gas sparging rate is sufficiently high to preclude stable incipient crust formation at the melt/water interface. In this regime, efficient melt/water transfer occurs due to conduction, and predominately, radiation heat

transfer across the agitated (i.e., area enhanced) melt/water interface. However, due to the efficient heat transfer, the superficial gas velocity eventually falls below the critical level required to preclude incipient crust formation, and a stable interfacial crust forms. Models for prediction of the melt/water heat transfer rate during bulk cooling have been developed (Farmer et al., 1990), as well as models for prediction of the critical gas sparging at which stable crust formation occurs, thereby terminating the stable bulk cooling phase (Farmer et al., 1992).

After a stable crust forms, film boiling eventually breaks down and water contacts the upper surface of the crust, and remains in contact. Since corium shrinkage occurs during the cooldown from a molten to a solid state, void volume will appear in the frozen material. The water ingression question concerns the ability of water to percolate down through the interstitial defects/void and augment the otherwise conduction-limited heat transfer process. There is evidence from MACE tests (Farmer et al. 1999) that water ingression does augment the melt/water heat transfer (and crust growth) rate during the early phases following bulk cooling. In addition to the observations regarding crust permeability, melt eruptions have been observed in all MACE tests conducted with limestone/common sand concrete basemats. The data indicates that dispersal occurs by the following two mechanisms: i) corium droplet ejection into overlying coolant, leading to accumulation of a permeable particle bed, and ii) single phase melt extrusions, or lava flow, which produce a porous, layered, loosely agglomerated debris formation. Substantial increases in the overall melt/water heat transfer rate are observed during these events due to quench of the ejected material. Moreover, the beds which form as a result of eruptions are porous and appear to be readily coolable. Motivated by eruptions observed in the MACE Scoping Test, Bonnet and Seiler (1992) developed a parametric model of particle bed formation by means of melt entrainment during MCCI. In this model, melt dispersal is calculated by assuming that the melt entrainment rate is proportional to the gas volumetric flowrate times an entrainment coefficient. Bonnet and Seiler found through application of this model that MCCI transformation into a quenched debris bed could be achieved for fairly modest values of the melt entrainment coefficient.

Although the above described cooling mechanisms have been postulated to provide a potential pathway for achieving long-term debris coolability, complete debris quench and stabilization by these same mechanisms has not been clearly demonstrated in any MACE test conducted to date. The reason for this is that in all tests, the crust has anchored to the test section sidewalls where it initially formed, thereby leading to the formation of a sustained gap (or void) between the melt and crust as the MCCI resumed its downward migration. Obviously, the introduction of a gap between the crust and underlying melt will terminate both water ingression and melt eruption cooling mechanisms, both of which require melt/crust contact. Moreover, if water does not flood beneath the crust, then the presence of the gap introduces an additional radiation heat transfer resistance between the melt and crust which would not present if melt/crust contact were maintained. It is important to note that sustained gap formation is not expected at plant scale, owing to inherent crust instability in the typical 6 meter span of most plants. Thus, gap formation in the MACE tests constitutes a significant experiment distortion which should be factored into the analysis of the test results.

Although sustained anchoring and separation of the crust from the melt is not expected at plant scale, the MACE test results have exhibited the following behavior which could indicate that intermittent or localized crust anchoring to the test section sidewalls is plausible: i) mechanical bonding of crust to concrete walls (Scoping Test), and ii) the development of thick crusts due to water ingression augmentation of the upwards heat transfer. These thick crusts may have sufficient mechanical strength to bond to the pedestal walls and temporarily separate from the ongoing MCCI. This configuration is not expected to be stable due to the shear weight of the crust, in addition to dead weight imposed by dispersed material accumulating above the crust. Eventually

the crust will fail, leading to rapid ingression of water beneath the crust. This transient crust breach cooling mechanism has been postulated to be a potential contributor to coolability at plant scale. There is a limited amount of MACE test data that indicates that this cooling mechanism may be plausible.

Based on the above physical observations, an integrated model of Corium Quenching (CORQUENCH) behavior is being developed. Aside from modeling several key physical processes observed in the tests, considerable effort has been devoted to modeling of test occurrences which deviate from the behavior expected at reactor scale. In this manner, extrapolation of the models validated against the MACE test data to the reactor case can be done with increased confidence. The integrated model currently addresses early bulk cooling and incipient crust formation heat transfer phases, as well as follow-on water ingression phase which leads to development of a sustained quench front progressing downwards through the debris. In terms of experiment distortions, the model is also able to mechanistically calculate crust anchoring to the test section sidewalls, as well as the subsequent melt/crust separation phase which arises due to concrete densification upon melting.

A summary description of the status of CORQUENCH model development is provided first, followed by presentation of key model validation results. Representative calculations are then provided for PWR plant conditions in order to scope the effect of bulk cooling and water ingression cooling mechanisms on mitigation of the accident sequence.

2.0 SUMMARY MODEL DESCRIPTION

The philosophy behind the development of CORQUENCH was to build a simple, modular model of MCCI behavior which could be readily adapted to incorporate melt/water heat models as they became available on the basis of experiment observations. To this end, the MCCI model within CORQUENCH is capable of performing either a 1-D or simplified 2-D ablation calculation (2-D geometry is assumed to be cylindrical, with axial and radial ablation calculated). The MCCI conservation of energy equation includes the following energy source/sink terms: i) decay heat, ii) chemical reactions between metallic melt constituents Zr, Cr, Fe, and Si (in sequence) and concrete decomposition gases H_2O and CO_2, iii) condensed phase chemical reactions between Zr and SiO_2, iv) downwards (and sidewards for 2-D case) heat transfer to concrete, including slag heat sink, and v) heat transfer to overlying atmosphere (wet or dry). The melt composition can range from fully metallic to fully oxidic; in all cases, the two phases are assumed to be well mixed (i.e., phase stratification is not modeled). The MCCI conservation of mass equations and thermophysical property subroutines consider most core and concrete metals and there corresponding oxides, so that a wide range of cases can be considered. Melt viscosity is calculated using the DaAndrade formula (see Nazare et al., 1977) with a correction for SiO_2 as developed by Shaw (1972). Viscosity enhancement due to buildup of solids within the melt is calculated using the Ishii-Zuber model (1979). Melt void fraction, which is highly relevant in the evaluation of the location where the crust anchors to the test section sidewalls in experiments, can be evaluated from one of several different correlations; the particular one used in the calculations presented below was developed by Brockmann et al. (1989).

In terms of heat transfer at the melt/concrete interface, CORQUENCH incorporates a transient concrete ablation/decomposition model based on integral thermal boundary layer theory (Corradini, 1983). The heat transfer coefficient at this interface can be selected from a variety of options; Bradley's (1988) modification to the bubble agitation heat transfer model of Kutateladze and Malenkov (1978) is used in the calculations provided below. At the melt upper surface, radiant heat transfer to overlying structure is calculated when the cavity is dry. When water is present,

bulk cooling and incipient crust formation are calculated using the models developed by Farmer et al. (1990, 1992). Following incipient crust formation, the crust growth is calculated by solving a growth rate equation; the crust material composition is treated separately from the melt material composition, which is important in long-term calculations where significant mass may be frozen in the crust. In particular, for the situation in which the crust is impervious to water ingression, the crust growth rate equation under the assumptions of uniform physical properties and decay heat distribution is of the form:

$$\rho_c \Delta e_{ls} \frac{d\delta}{dt} = k_c \frac{(T_f - T_I)}{\delta} - \frac{X_{UO2}\rho_c q_{dec}\delta}{2} - h_m (T_m - T_f) \qquad (1)$$

where the crust/water interface temperature T_I is evaluated from a suitable energy balance depending on whether or not water is present over the debris (when water is present, a full boiling curve is treated). The melt-side convective heat transfer coefficient h_m can be selected from a variety of models; the model of Kutateladze and Malenkov (1978) is used in the calculations presented below. For the case in which the crust is treated as permeable with a corresponding dryout heat flux q_d", the condition for onset of ingression is that the total heat flux from the crust upper surface falls below the dryout flux; i.e.,

$$q_d'' - \rho_v h_{lv} j_{nc}\big|_{T_{sat}} \geq k_c \frac{(T_f - T_I)}{\delta} + \frac{X_{UO2}\rho_c q_{dec}\delta}{2} \qquad (2)$$

In the development of the above equation, the assumption has been made that the MCCI noncondensable gas flow is vented uniformly across the extent of the crust[1]. Thus, the gas flow can act as a counter-current flow limitation if the flowrate is sufficiently high. Further note that the MCCI gas flowrate is evaluated at water saturation temperature based on the assumption that the debris above the dryout front is maintained at saturation temperature. After onset of water ingression, the crust growth rate equation thus takes the form:

$$\rho_c \Delta e_{sat} \frac{d\delta}{dt} = q_d'' - X_{UO2}\rho_c \delta q_{dec} - \rho_v h_{lv} j_{nc}\big|_{T_{sat}} - h_m (T_m - T_f) \qquad (3)$$

In the current work, the dryout heat flux is evaluated using the following simple model developed by Jones et al. (1984) which provides a reasonable fit to experiment data obtained with several different coolants in deep particle beds:

$$q_d'' = \frac{0.5K\rho_v h_{lv}(\rho_l - \rho_v)g}{\mu_v} \qquad (4)$$

In this highly simplified modeling approach, the debris permeability K is treated as an input constant. In reality, this property is most likely a strong function of composition, which changes appreciably over the course of the event due to ongoing concrete erosion.

Equations 1-4 provide a general framework for predicting quench front propagation due to water ingression during MCCI. However, as discussed above, the model has also been developed

[1] Note that the MACE test data indicates the MCCI gases are predominately vented at discrete locations across the extent of the crust. However, in this analysis the MCCI gases are treated as being uniformly distributed to provide conservatism in the approach.

to mechanistically calculate the important experiment distortion of crust anchoring to the test section sidewalls, as well as the subsequent melt/crust separation phase which arises due to concrete densification upon melting. The minimum crust thickness required to be mechanically stable due to the deadweight of the crust material in the given test section span is evaluated from the following first-order equation by Roark and Young (1975),

$$F = \rho_c g \delta_{min} A \sim 5.48 \sigma_f \delta_{min}^2 \qquad (5)$$

The crust failure stress, σ_f, is obviously an important input parameter in this model. Accordingly, considerable effort has been devoted to measuring this property in the MACE program. During the calculation, the crust thickness calculated from Eqs. 1-4 is compared with that predicted by Eq. 5. When the thickness exceeds δ_{min}, the crust is assumed to attach to the test section sidewalls with the upper surface elevation fixed at the location at the time of anchoring. Thereafter, the *voided* melt upper surface location is tracked relative to the crust location so that the onset of gap formation can be predicted. When a gap does form, quench front propagation by ingression ceases, and there is a corresponding reduction in upwards heat transfer due to *solidification* (latent heat) processes. Moreover, a heat transfer resistance across the gap is introduced into the upwards heat balance, which causes a further reduction in upwards heat transfer. This methodology, although first order in nature, does allow the prediction of the crust anchoring time/location in the MACE tests, as well as the subsequent gap formation process. These predictions can be compared with posttest examination results to gauge the accuracy of the model. Moreover, the model allows the prediction of the upwards heat flux both before and after separation, which can be compared with information logged during the test. Thus, the model can be more rigorously validated against test data, which increases the confidence level when the model is extrapolated to plant conditions.

3.0 MODEL VALIDATION

An important part of CORQUENCH development has been validation against both wet and dry reactor material test results. In terms of dry tests, the model has been compared to ACE/MCCI tests L2, L4, L5, L6, and L8 (Thompson et al., 1992), and also the tests SURC-1 and SURC-2 conducted at SNL (Copus, 1992). A summary of test conditions (viz. corium/concrete type) and validation results are shown in Table 1. As is evident, the validation matrix includes essentially four types of concrete (basalt and siliceous are very similar), both BWR and PWR melt compositions, and cladding oxidation states from 30 to 100 %. In all cases, the experimenter's best estimates of net input power, corium composition, and initial melt temperature were used in the calculations. The interfacial heat transfer models employed in these calculations were described in the previous section. A comparison of the model predictions of melt temperature and ablation depth with data from ACE/MCCI test L2 are provided in Figs. 1-2, respectively. Test L2 was conducted with a low gas (i.e., siliceous) concrete. The analogous comparison for the SURC-1 test is provided in Figs. 3-4; this test was conducted with a high gas (i.e., limestone/limestone) concrete. As is evident from Table 1, the end-of-test ablation depth (including concrete/metal inserts for ACE/MCCI tests; Thompson et al., 1992) is predicted to within 25 % on average for all seven tests, with a maximum deviation of 45 % (for ACE Test L5). The maximum deviation between the measured and predicted melt temperature over the course of the experiment averages 8 %. Thus, this validation exercise provides a sense of the uncertainty involved in the application of the model to reactor material test results. It is instructive to note that for these dry tests, the model predicts either no upper crust, or only thin crust segments form at the upper surface which are not mechanically stable in the presence of the sparging concrete decomposition gases.

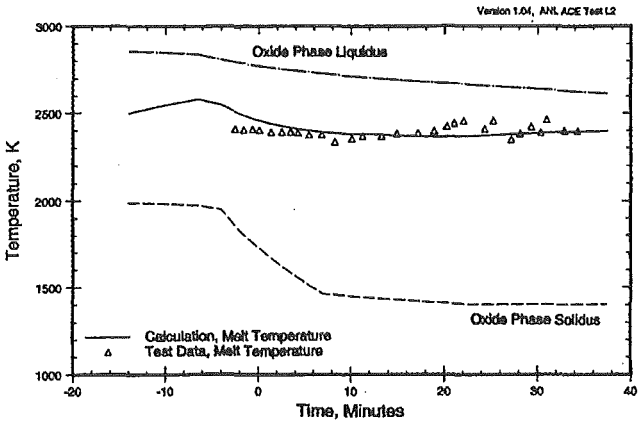

Fig. 1. Melt Temperature Predictions for ACE/MCCI Test L2.

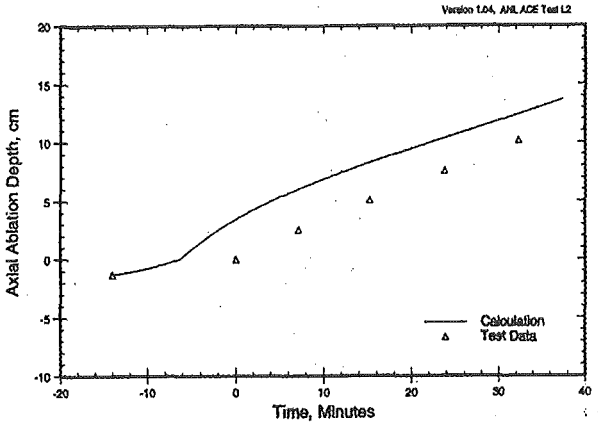

Fig. 2. Ablation Depth Prediction for ACE/MCCI Test L2.

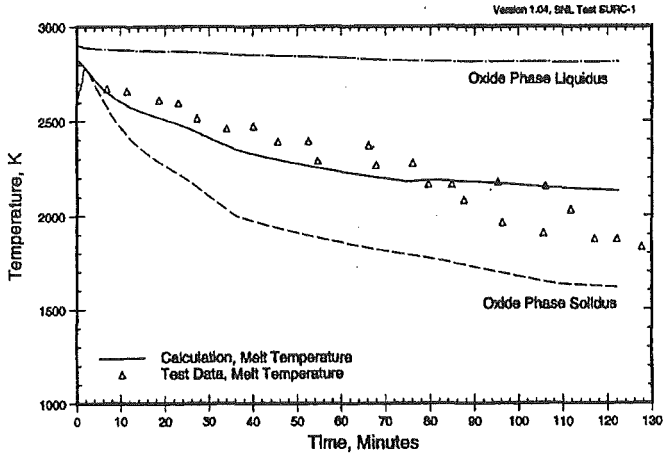

Fig. 3 Melt Temperature Predictions for the SURC-1 Test.

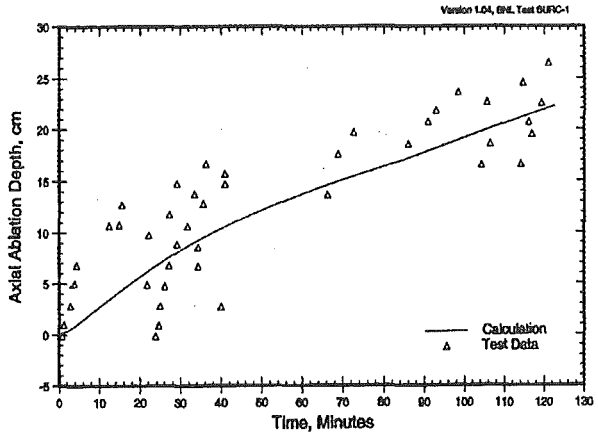

Fig. 4. Ablation Depth Predictions for the SURC-1 Test.

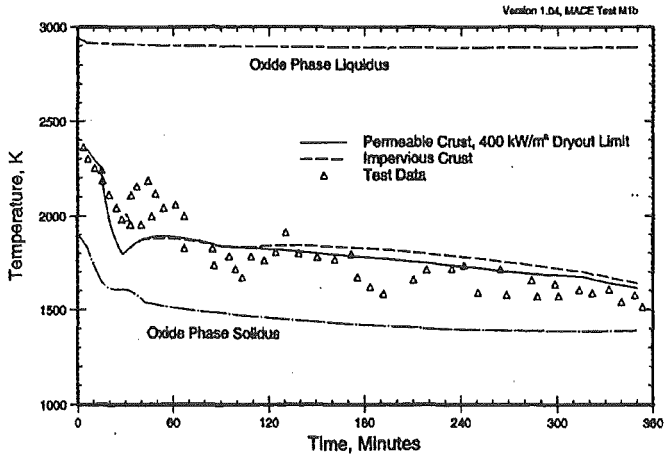

Fig. 5. Melt Temperature Predictions for MACE Test M1b.

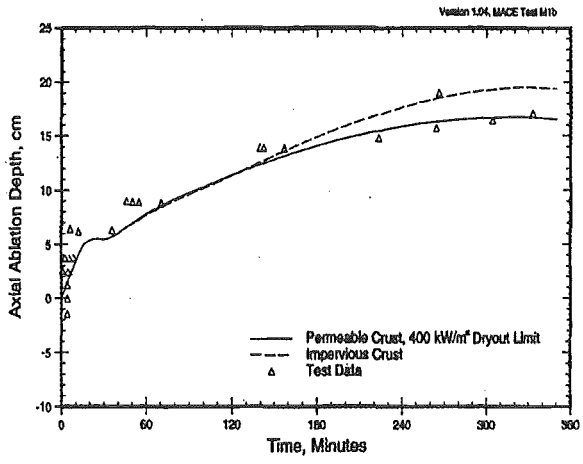

Fig. 6. Ablation Depth Predictions for the MACE Test M1b.

Table 1 Summary of CORQUENCH Validation Results for Dry Cavity Tests.

Test	Corium/ Concrete	End-of-Test Ablation Depth, cm			Melt Temperature, K		
		Actual[1]	Calculated	% Deviation	Actual (Time[2])	Calculated	Max. % Deviation
L2	70 % Ox. PWR/ Siliceous	12	14	+ 17	2450 (20)	2370	- 3
L4	50 % Ox. BWR/ Serpentine Layer over Siliceous	19	26	+ 37	2280 (130)	2020	- 11
L5	100 % Ox. PWR/ Limestone-Sand	11	16	+ 45	1800 (105)	1970	+ 9
L6	30 % Ox. PWR/ Siliceous	19	13	- 32	2420 (15)	2140	- 12
L8	70 % Ox. PWR/ Limestone	17	19	+ 11	2300 (43)	2200	- 4
SURC-1	70 % Ox. PWR/ Limestone	25	22	- 12	1900 (120)	2130	+ 12
SURC-2	70 % Ox. PWR/ Basalt	35	28	- 20	2100 (115)	1950	- 7

[1] Includes Depth of Inserts for ACE L-Series Tests
[2] Relative to Onset of Concrete Ablation

In terms of reactor material tests conducted with water, the model has been applied to all MACE tests, although the results of more recent tests M3b and M4 remain proprietary. The model is applied to MACE Test M1b in the following to illustrate the predictive capability. The interfacial heat transfer modeling assumptions are the same as those used above. The conditions for this experiment are summarized by Farmer et al. (1999). Calculations were performed for two cases: i) impermeable upper crust (i.e., K = 0 in Eq. 4), and ii) crust dryout heat flux assumed to equal ~ 400 kW/m^2 (i.e., K = $8 \bullet 10^{-10}$ m^2); the dryout heat flux for this case was selected such that the crust thickness at the end of the calculation approximates that found during posttest examinations. Consistent with the heating technique used in the MACE tests, decay heat input into the crust was assumed to equal zero, and all input heat was assumed to be deposited in the melt. The melt temperature, ablation depth, and melt/water heat flux are compared with the test data in Figs. 5-7, respectively, for both modeling assumptions. In these figures, time zero corresponds to onset of ablation, and the cavity was flooded at 14.7 minutes relative to onset of ablation. The predicted location and timing of the crust anchoring event for Test M1b is shown in Fig. 8 for the permeable crust case.

Examination of these figures indicates that the model reasonably reproduces the melt temperature/ablation/upwards heat flux during the bulk cooling transient, which lasts until ~ 30 minutes. However, following this time, the predictions differ quite substantially depending upon whether or not the crust is permeable. For the impervious case, melt crust contact is predicted to be maintained until ~ 100 minutes into the ablation sequence. Following incipient crust formation at ~ 30 minutes, the heat flux is predicted to drop rapidly to a conduction limited level in the range of 30-50 kW (120-200 kW/m^2), while the test data indicates continued high heat transfer rates in excess of 150 kW. Furthermore, the heat flux is predicted to drop in a step fashion at the time of separation by ~ 20 % due to the introduction of a radiation heat transfer resistance between the melt and crust. At the end of the test, the anchored crust is predicted to be quite thin (i.e., < 1 cm) reflecting the requirement that the heat transfer across the crust balance the upwards convective heat transfer given the conduction limitation.

As is clear from Fig. 7, the melt/water heat flux prediction for the permeable crust case is more in agreement with the test data. Following initial crust formation at 30 minutes, a brief period of film boiling is predicted to occur which lasts ~ 2 minutes. Following film breakdown, the upwards heat transfer is dominated by the freezing process as water ingresses into the crust at the specified dryout heat flux limitation of 400 kW/m^2. Note that the large spike in the upwards heat transfer rate to a level of ~ 450 kW (1.8 MW/m^2) at 40 minutes corresponds to a melt eruption (Farmer et al., 1999). As described previously, eruptions are currently not modeled in CORQUENCH, and therefore this aspect of the heat flux curve is not reproduced. However, as is evident from Fig. 8, the melt/crust separation for this case is predicted to occur at ~ 55 minutes, which is in reasonable agreement with the estimated separation time of ~ 50 minutes (Farmer et al., 1999). As described previously, the dryout heat flux limit was specified such that the crust thickness at the time of separation matches the ~ 6 cm measurement obtained during posttest examinations. Further examination of Fig. 8 indicates that the upper crust anchored at an elevation of + 23 cm with respect to the initial concrete surface, and that the height of the voided region at the end of the test was ~ 4 cm. The location of the upper surface agrees with the posttest examinations, while the gap height of 4 cm is less than the actual height of 9 cm. Part of this discrepancy is due to the fact that the model does not currently account for mass lost from the MCCI zone due to eruptions; inclusion of this affect would improve the prediction of the gap thickness.

To summarize, the incorporation of a crust dryout heat flux model into CORQUENCH has improved the model's ability to reproduce the melt/water heat flux curve for MACE Test M1b. Furthermore, the addition of the dryout limit also improves the predictions of the posttest debris configuration, including crust depth, timing/extent of gap formation, and the crust thickness. The next step in the modeling process is to develop the capability to analytically predict the crust permeability as a function of melt composition, which will remove the empirical requirement of specifying debris permeability as an input parameter.

4.0 REPRESENTATIVE PWR PLANT CALCULATIONS

Given the current state of the model, it is instructive to perform a few calculations for representative plant conditions to scope the effect of crust permeability on the accident sequence. To this end, the case of a PWR corium melt interacting with a limestone/common sand concrete basemat is considered. The cladding is taken to be 70 % oxidized, and the initial composition is assumed to contain 8 wt % concrete oxides to account for concrete erosion which is expected to occur during the corium spreading phase following breach of RPV (Sienicki and Spencer, 1986). The corresponding melt composition is thus 73.2/14.3/4.5/3.5/1.2/3.3 wt % $UO_2/ZrO_2/Zr/SiO_2/MgO/CaO$. The initial melt temperature is taken equal to 2500 K. The initial melt depth is assumed to equal 30 cm, reflecting a typical depth considered in analyses of ex-vessel sequences in existing plants. The containment pressure is assumed to be 0.4 MPa, and water is assumed to be present as an initial condition. Any limitations on water supply are neglected in this analysis, so that the quench process is not water starved. The decay heat curve is evaluated using the Revised American National Standard (1979) for a PWR at ~ 1000 days burnup. The decay heat is assumed be partitioned between the melt and crust zones depending upon the fuel mass present in each of these zones at any given time. The reactor pressure vessel is assumed to fail at two hours into the accident sequence. At this time, the decay heat level (neglecting volatiles) corresponds to ~ 300 W/kg fuel. To decouple the results from the details of any particular plant design, the calculation is performed using the 1-D modeling approach assuming 1 m^2 of containment floor area. The interfacial heat transfer modeling assumptions are the same as those utilized above. The model is applied under the assumption that melt/crust contact is maintained over the entire course of the accident sequence, as is anticipated for plant conditions.

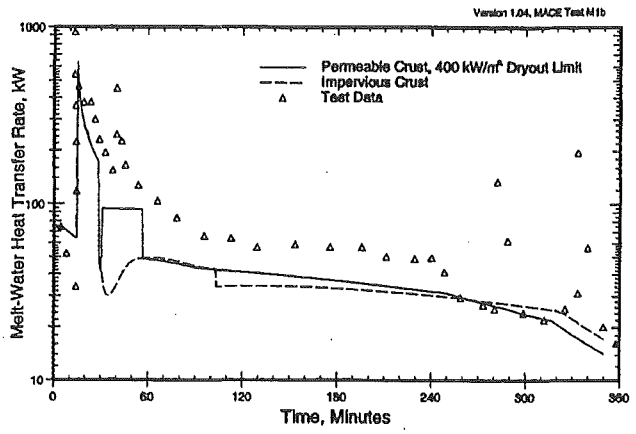

Fig. 7. Melt/Water Heat Flux Predictions for MACE Test M1b.

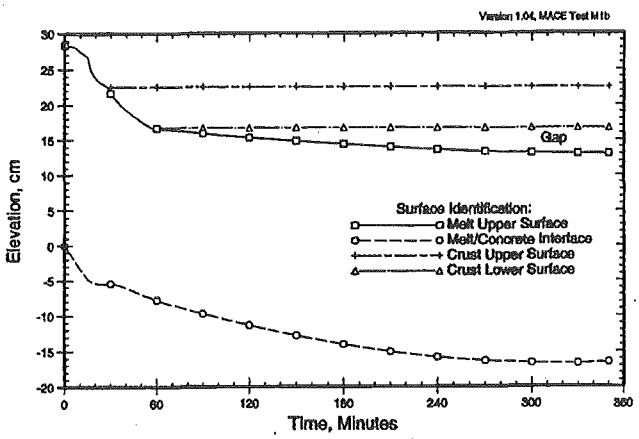

Fig. 8. Predicted Crust Upper and Lower Surface Locations for MACE Test M1b.

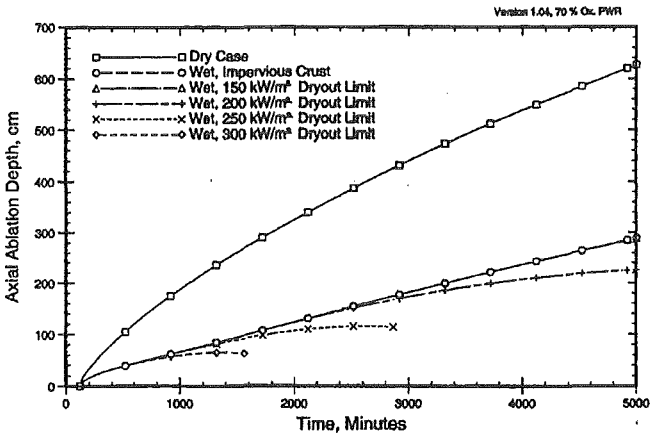

Fig. 9. Axial Ablation Depth for Various Crust Permeabilities – PWR Plant Conditions.

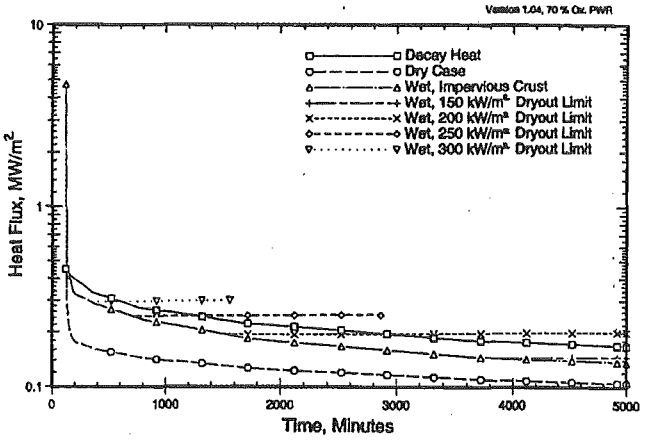

Fig. 10. Upwards Heat Flux for Various Crust Permeabilities – PWR Plant Conditions.

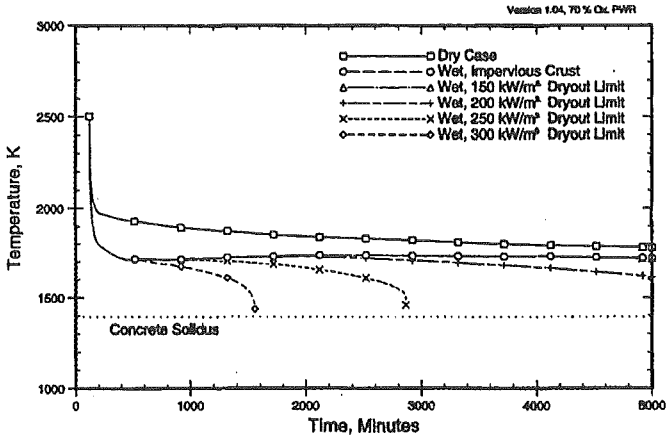

Fig. 11. Melt Temperature for Various Crust Permeabilities – PWR Plant Conditions.

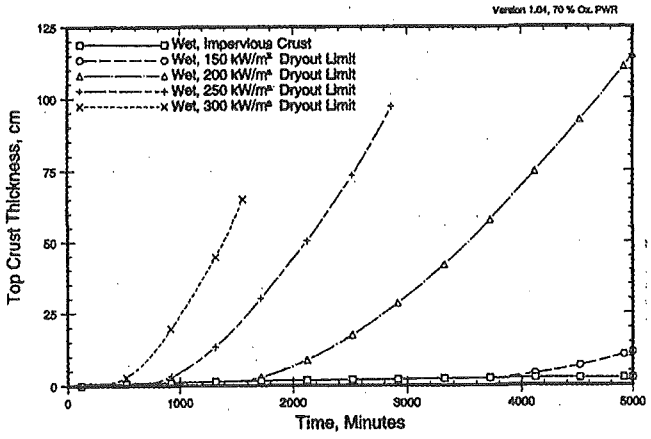

Fig. 12. Crust Depth Variation for Various Crust Permeabilities -- PWR Plant Conditions.

Calculations were carried out for the case of an impervious crust, as well as several assumed crust dryout heat fluxes ranging from 150 - 300 kW/m^2 (Corresponding range of debris permeabilities is evaluated as 1.2-2.3•10^{-10} m^2 from Eq. 4 over this heat flux range given the containment pressure of 0.4 MPa). The predicted axial ablation depth, upwards heat flux, bulk melt temperature, and crust depth for the various cases are shown in Figs. 9-12, respectively, over a calculated time interval of 5000 minutes (~ 3.5 days). The total decay heat level within the debris is shown in Fig. 10 for comparison. To provide a baseline for evaluating the effect of water on mitigating basemat attack, a calculation was also carried out for the case of a dry containment (overlying structure emissivity/temperature taken equal to 0.3/1000 K respectively). The results of this calculation are also shown in these figures. For the given set of assumptions, the dry case up/down power is predicted to be ~ 50/50, resulting in ~ 6 meters of 1-D axial erosion over 5000 minutes. For the wet impervious crust case, erosion is predicted to be reduced to ~ 3 m over the same time interval, principally as a result of the shift in the power split upwards due to lower boundary temperature (water saturation, ~ 417 K), and also the increased efficiency of nucleate boiling at the crust upper surface in comparison to radiation from melt to hot structure.

Examination of the upwards heat flux predictions in Fig. 10 indicates that water ingression does not begin to significantly influence the debris cooling rate until the dryout heat flux reaches or exceeds 200 kW/m^2. For the higher dryout heat fluxes in the range of 250-300 kW/m^2, the model predicts complete quench and thermal stabilization of the debris well within the computed time frame (i.e., at 1500 and 2800 minutes, respectively). The extent of axial ablation for these two cases is of the order of 100 cm. As is evident from Fig. 11, the remaining melt zone temperature begins to fall off rapidly as the quench process nears completion (the calculation is terminated when the remain melt zone mass falls to zero). Obviously, as the debris depth and/or decay heat level decreases, the dryout heat flux required to quench and thermally stabilize the debris will decrease. Conversely, for the same set of conditions assumed here, an increased dryout heat flux will reduce the amount of concrete erosion at the time of debris stabilization. The progression of the quench front in relation to the voided melt pool height and basemat erosion depth is illustrated in Fig. 13 for the 250 kW/m^2 dryout heat flux case. From Figs. 12-13, note that the crust growth rate increases as the time progresses, due to the reduction in decay heat level.

The results of these calculations have shown that for PWR accident conditions with an initial melt pool depth of 30 cm, the potential exists for significant abatement of the MCCI for debris dryout heat fluxes greater than ~ 200 kW/m^2 at the assumed containment pressure[2] of 0.4 MPa. Note that the model does not currently calculate the important feature of particle bed formation by volcanic eruptions, which has been found to be an important contributor to the debris cooling rate in reactor material experiments (Farmer et al., 1999). Moreover, parametric calculations conducted with the PERCOLA melt eruption model (Bonnet and Seiler, 1992) indicate that significant debris stabilization can be achieved for fairly modest values of the melt entrainment coefficient. Thus, with both water ingression and melt eruption cooling mechanisms acting together, there is a potential for significant debris quench and stabilization for fairly modest values of crust permeability and entrainment coefficient. Due to the potential importance of these two mechanisms, separate effects tests are currently under discussion within the MACE program to obtain data under well controlled experiment conditions to support model development activities for these mechanisms.

[2] For a given debris permeability, the dryout heat flux increases with increasing system pressure (Jakobsson, Catton, and Squarer, 1983).

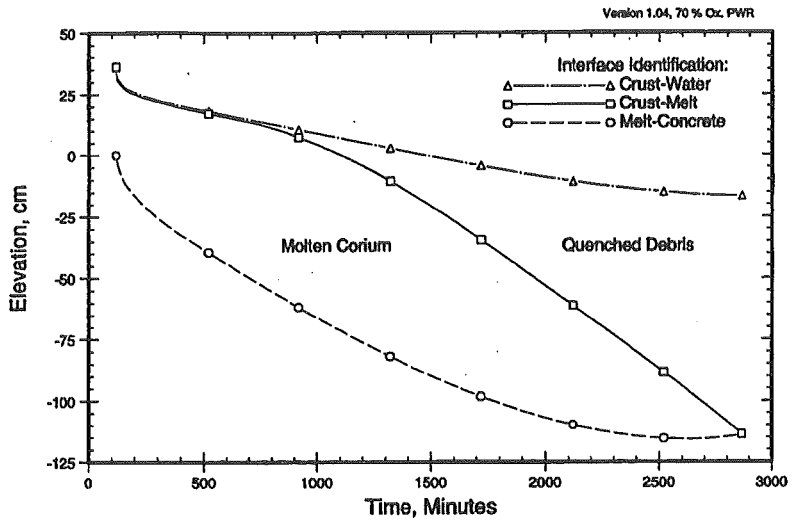

Fig. 13. Predicted Crust Upper and Lower Surface Locations for a Dryout Heat Flux of 250 kW/m^2 -PWR Plant Conditions.

5.0 SUMMARY AND CONCLUSIONS

Based on physical observations from the MACE tests, an integrated model of Corium Quenching (CORQUENCH) behavior is being developed. Aside from modeling of the primary physical processes observed in the tests, the model is also able to calculate test occurrences which deviate from the behavior expected at reactor scale. In this manner, extrapolation of the models validated against the test data to the reactor case can be done with increased confidence. The integrated model currently addresses early bulk cooling and incipient crust formation heat transfer phases, as well as a follow-on water ingression phase which leads to development of a sustained quench front progressing downwards through the debris. The model has been validated against virtually all reactor material MCCI tests (both wet and dry) available in the open literature.

The results of parametric calculations for typical PWR plant conditions indicates that there is a potential for significant abatement of the MCCI for debris dryout heat fluxes greater than ~ 200 kW/m^2 at the assumed containment pressure of 0.4 MPa. Note that the model does not currently calculate the important feature of particle bed formation by volcanic eruptions, which has been found to be an important contributor to the debris cooling rate in reactor material experiments (Farmer et al., 1999). Thus, with both water ingression and melt eruption cooling mechanisms active, the potential exists for significant debris quench and stabilization during a plant accident.

NOMENCLATURE

A	Test section cross-sectional area.
Δe_{ls}	corium latent heat of fusion
Δe_{sat}	corium change in specific enthalpy during quench to water saturation temperature
h_{lv}	water latent heat of evaporization
h_m	convective heat transfer coefficient
j_{nc}	MCCI noncondensable gas flowrate
k_c	crust thermal conductivity
q_{dec}	decay heat level (W/kg fuel)
q_d"	dryout heat flux

T_I interface temperature
T_f corium freezing temperature
T_m melt temperature
X_{UO2} weight fraction fuel in crust
δ crust thickness
K crust permeability
ρ_c crust density
ρ_v steam density
σ_f crust failure stress

ACKNOWLEDGMENTS

Support for this work was provided by the International Nuclear Safety Center (INSC) at Argonne National Laboratory. Dr. James Sienicki from Argonne provided useful technical input during the cause of this work. The report was prepared for publication by Kathy Rank. These efforts are greatfully appreciated.

REFERENCES

Bonnet, M., and Seiler, J. M., 1992. Coolability of corium spread onto concrete under water, the PERCOLA model. In: *2nd CSNI Specialist Meeting on Core Debris-Concrete Interactions*, Karlsruhe, Germany, April 1-3; KfK 5108, NEA/CSNI R(92)10.

Bradley, D. R., 1988. Modeling of heat transfer between core debris and concrete. In: *ANS Proc. 1988 National Heat Transfer Conf.*, Houston, Texas, July 24-28.

Brockmann, J. E., Arellano, F. E., and Lucero, D. A., Validation of models of gas holdup in the CORCON code, USNRC Report NUREG/CR-5433, December, 1989.

Corradini, M. L., 1983. A transient model for the ablation and decomposition of concrete. *Nucl. Tech.* **62**, 263-273.

Copus, E. R., Sustained Uranium Dioxide/Concrete Interaction Tests: The SURC Test Series, Proc. of the Second OECD (NEA) CSNI Specialist Meeting on Molten Core Debris-Concrete Interactions, KfK 5108, NEA/CSNI/R(92)10, April, 1992..

Farmer, M. T., Sienicki, J. J., and Spencer, B. W., 1990. CORQUENCH: A model for gas sparging-enhanced, melt-water, film boiling heat transfer. In: *ANS Winter Meeting on the Thermal Hydraulics of Severe Accidents*, Washington, D.C., November 11-15.

Farmer, M. T., Sienicki, J. J., and Spencer, B. W., 1992. Melt coolability model development and comparison to MACE test results. In: *2nd CSNI Specialist Meeting on Core Debris-Concrete Interactions*, Karlsruhe, Germany, April 1-3; KfK 5108, NEA/CSNI R(92)10.

Farmer, M. T., Schneider, J. P., Bonomo, B., Theofanous, G. and Spencer, B. W., 1992. Modeling and database for melt-water interfacial heat transfer. In: *2nd CSNI Specialist Meeting on Core Debris-Concrete Interactions*, Karlsruhe, Germany, April 1-3; KfK 5108, NEA/CSNI R(92)10.

Farmer, M. T., Spencer, B. W., Kilsdonk, D. J., and Aeschlimann, R. W., 1999. Status of large scale MACE core coolability experiments. In: *OECD Workshop on Ex-Vessel Debris Coolability*, Karlsruhe, Germany, 15-18 November.

Ishii, M., and Zuber, N., 1979. Drag coefficient and relative velocity in bubbly, droplet, or particle flows. *AIChE Journal* **25**, 843-855.

Jakobsson, J. O., Catton, I., and Squarer, D., 1983. The pressure dependence of dryout heat flux. In: Proc. International Meeting on LWR Severe Accident Evaluation, Vol. II, Cambridge, MA, August 28-September 1.

Jones, S. W., Epstein, M., Bankoff, S. G., and Pedersen, D. R., 1984. Dryout heat fluxes in particulate beds heated through the base. *Journal Heat Trans.* **106**, 176-183.

Kutateladze, S. S., and Malenkov, I. G., 1978. Boiling and bubbling heat transfer under the conditions of free and forced convection. In: *6th Int. Heat Transfer Conf.*, Toronto, Canada.

Nazare, G., Ondracek, G., and Shulz, B., 1977. Properties of light water reactor core melts. *Nucl. Tech.* **32**, 239-255.

Revised American National Standard, 1979. Decay heat power in light water reactors, ANSI/ANS-5.1-1979.

Roark, R. J., and Young, W. C., 1975. *Formulas for Stress and Strain*, 6th Ed., McGraw Hill, New York, pp. 480-482.

Shaw, H. R., 1972. Viscosities of magmatic silicate liquids: an empirical method of prediction. *American Journal of Science* **272**, 870-893.

Sienicki, J. J., and Spencer, B. W., 1986. The jet impingement stage of molten core-concrete interactions. In: OECD CSNI Specialist Meeting on Core Debris/Concrete Interactions, Palo Alto, CA, September 3-5.

Thompson, D. H., Fink, J. K., Armstrong, D. R., and Spencer, B. W., Thermal hydraulic aspects of large-scale integral MCCI tests in the ACE program, Proc. of the Second OECD (NEA) CSNI Specialist Meeting on Molten Core Debris-Concrete Interactions, KfK 5108, NEA/CSNI/R(92)10, April, 1992.

CORIUM COOLING BY BOTTOM FLOODING: RESULTS OF THE COMET INVESTIGATIONS

H. Alsmeyer, C. Adelhelm, H. Benz, T. Cron, G. Dillmann, ,W. Tromm, S. Schmidt-Stiefel, H. Schneider, G. Schumacher, T. Wenz
Forschungszentrum Karlsruhe GmbH
Postfach 3640, D-76021 Karlsruhe, Germany
hans.alsmeyer@iket.fzk.de walter.tromm@iket.fzk.de

F. Ferderer
Ingenieurbüro Ferderer
75228 Ispringen, Germany

ABSTRACT

The COMET concept of corium cooling serves to stabilise and cool ex-vessel corium melts in the case of core melt accidents. After erosion of a sacrificial concrete layer the melt is passively flooded by bottom injection of coolant water through a multitude of flow channels. The resulting evaporation process creates a porous structure of the melt from which the energy is easily extracted. The porous melt solidifies within one hour typical and is permanently flooded by water. For the investigations of the concept, transient experiments with high temperature thermite melts and with real corium melts are performed. Furthermore, large scale experiments with thermite melts up to 1300 kg and simulation of decay heat are conducted to study the role of inhomogeneous melt attack, the role of metallic Zr, and the influence of the coolant water pressure and melt height on coolability. The experiments show that safe short-term and long-term cooling is achieved when a reasonable pressure of the flooding water exists.

1. INTRODUCTION

The implementation of an ex-vessel corium cooling device is under consideration e. g. for future LWRs (i) to achieve safe enclosure of the ex-vessel corium in a predefined location and (ii) to remove the decay heat from the melt (Cognet, 1999). Figure 1 shows the integration of the COMET concept into a reactor design, such as the EPR, where the ex-vessel corium melt shall be collected in a predefined compartment. With respect to cooling, the concept is based on spreading of the ex-vessel core-melt on a sacrificial concrete layer, and

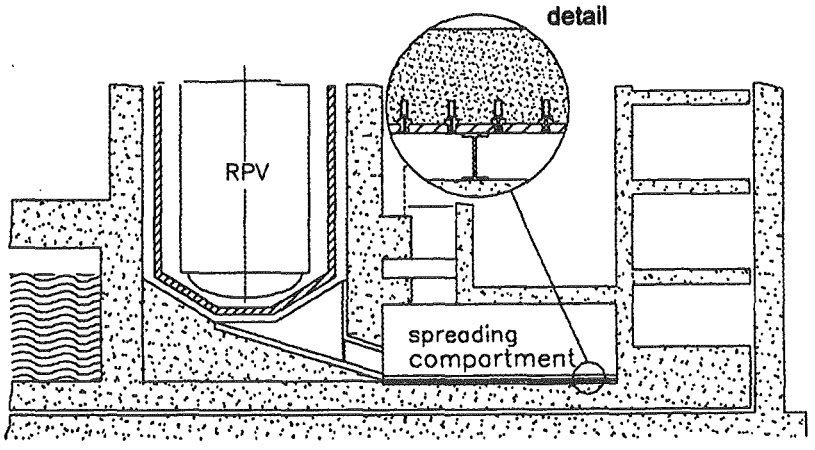

Figure 1: COMET Concept for Ex-Vessel Melt Cooling

after erosion of this layer, flooding the melt from below by totally passive water ingression through bottom injection channels. The coolant water is driven by the hydrostatic pressure of the water reservoir. Bottom injection and the fast evaporation process of the coolant water creates a porous structure of the corium melt with a multitude of flow channels and sufficient surface to extract the thermal energy and to solidify the melt in less than one hour typical. With the ongoing cooling process, the porously solidified melt is flooded by steam-water-flow and finally covered by a water layer which guarantees long term cooling. Fast solidification of the melt is a significant advantage of the concept and excludes thermal attack of important containment structures (Alsmeyer, 1999). The sequence of processes during cooling , starting with concrete erosion by the core melt up to flooding of the completely solidified melt are shown in Figure 2.

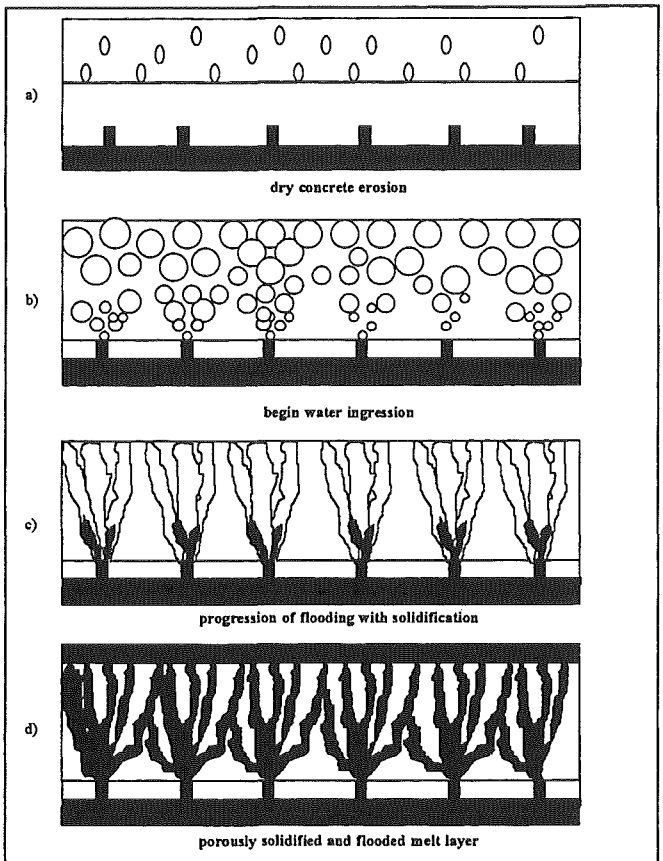

Figure 2: Formation of the coolable structure of the melt in the COMET concept

In order to prove this cooling concept and answer the questions arising from the different processes during melt cooling, a list of problems was drawn up. All the experiments performed were related to one or more questions of this list. The main problems that were answered by the experiments are:

- Occurrence of steam explosions during melt water contact
- Coolable height and related water supply pressure
- Non uniform erosion of the concrete layer
- Zirconium metal in the melt
- Hydrogen release during concrete erosion and flooding
- Steam accumulation and resulting pressure in the containment

2. EXPERIMENTAL INVESTIGATIONS

2.1 TRANSIENT EXPERIMENTS WITH THERMITE MELTS, COMET-T

Experimental Set-up

This test series use high temperature thermite melt of iron and alumina at about 2150 K, but without simulation of the decay heat. A CaO fraction of 35 wt% is added to the oxidic phase in order to reduce the solidification temperature and the viscosity of the oxide. The test set-up (Figure 3) consists of a horizontal surface area of 250 mm ∅ with a sacrificial concrete layer, into which the melting plugs for water supply are cast and onto which the hot melt is poured or generated. When the melt reaches the upper side of the plugs, they are molten and water inflow sets in. Via individual supply lines, the melting plugs are connected to a water storage tank. By the geodetic height of the storage tank, the flooding water pressure can be set for

each experiment. The geodetic height of the water column just compensates the hydrostatic pressure of the melt for 0 bar. The major physical properties of these melts and the test set-up nearly correspond to the situation in the reactor case and thus, transferability of the results is ensured (Tromm, 1998).

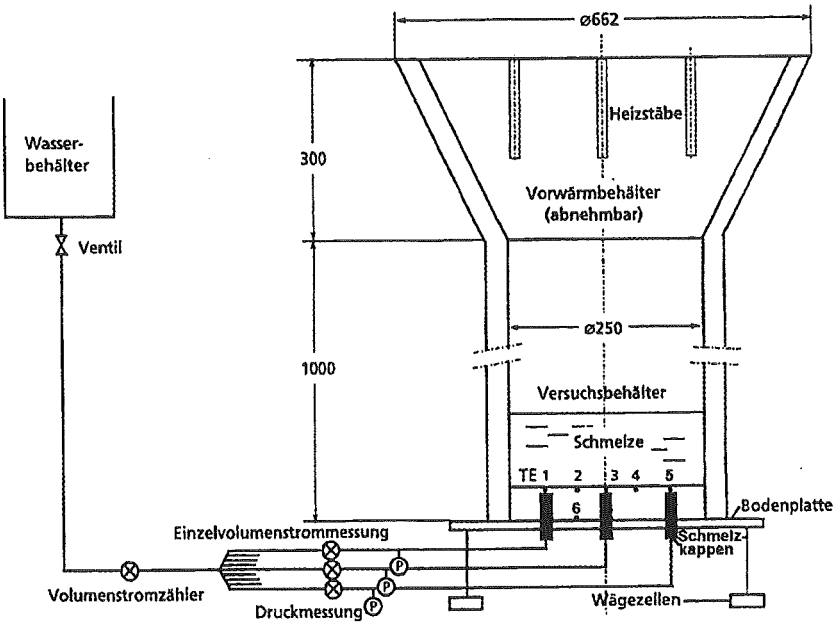

Figure 3: Set-up used for transient experiments with high-temperature melts

The volume flows and pressures of the inflowing cooling water as well as the temperatures in the melting plugs, in the concrete layer and outside of the test vessel are measured. The load cells below the test vessel serve to measure the weight changes of the crucible. The test is monitored from above and from the side by means of video cameras.

2.2 INVESTIGATIONS FOR STEAM EXPLOSIONS

As in the COMET core catcher concept water gets in direct contact with hot melt, the possibility of steam explosions under typical cooling conditions and its maximum dimension and consequences have to be determined. To provoke a steam explosion under the COMET cooling conditions and to quantify its consequences, a highly superheated melt was generated with significant water injection in the experiments COMET-T 2.1 and 2.3. This was established by a strongly reduced height of the sacrificial concrete layer of 5 mm only and a water pressure of 0.2 and 0.4 bar.

Since erosion of the 5 mm sacrificial layer takes place rather rapidly, water inflow into the melt starts after the completion of the thermite reaction after about 30 s already. The melt still has its high initial temperature resulting from the thermite reaction of about 2150 K. This value exceeds the solidification temperature by about 500 K. Furthermore, the flooding water pressure is selected to be sufficiently high to provide for a rapid water penetration into the melt and to establish an intensive contact between the melt and the water.

Only in one experiment more vigorous interactions are observed due to the reduced height of the concrete layer and the higher water pressure of 0.4 bar. Water inflow starts after 33 s. In the interval of 33-42 s, a total of six vigorous melt/water interactions take place, three of which exhibit maximum forces of up to about 10 kN (Figure 4). The strongest impact can be noticed 41.1 s after ignition or 8.1 s after start of water inflow. The measured pressure in the water supply line increases to about 1 MPa differential pressure. Momentum conservation yields a hurled-up melt mass of 5.4 kg with a kinetic energy of 530 J. The thermal energy contained in the entire melt is about 53 MJ. Consequently, a conversion efficiency of steam explosion of $\eta = E_{kin}/E_{therm} = 10^{-5}$ is obtained. This value is so small, because of the small amount of water only that may penetrate into the melt via the open melting plugs and that is available for the interaction with the melt. Another important aspect for safety assessment related to this concept is the fact that larger amounts of water may accumulate only after the melt has cooled down considerably. For this situation, however, the risk of a steam explosion does no longer exist because the viscosity of the melt is significantly increased and crusts start to form.

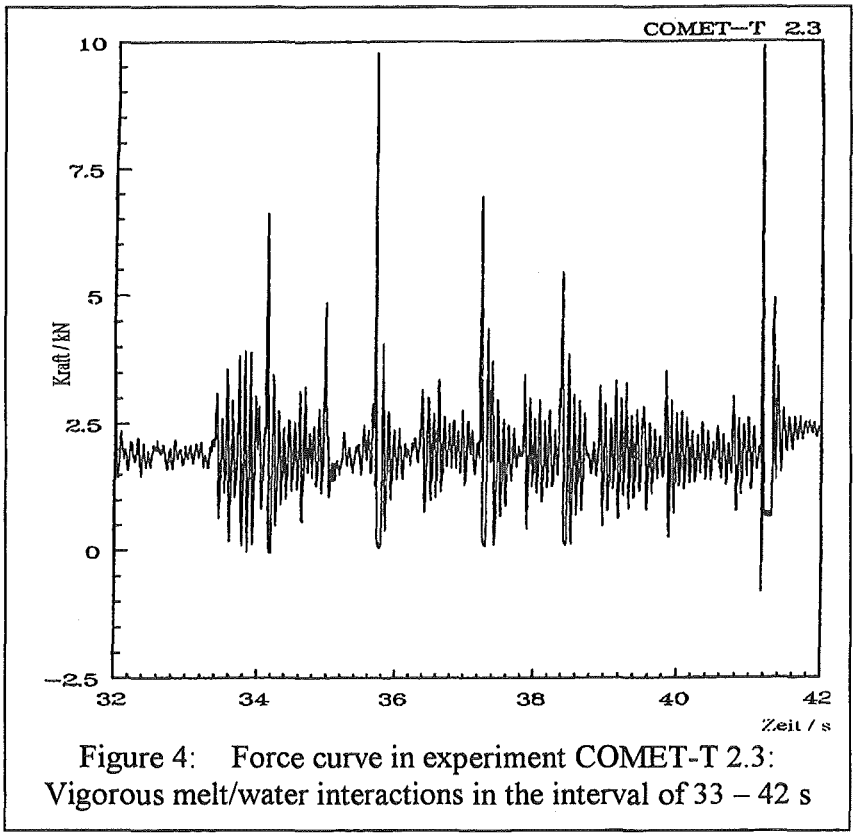

Figure 4: Force curve in experiment COMET-T 2.3: Vigorous melt/water interactions in the interval of 33 – 42 s

Further cooling tests, performed with higher sacrificial concrete layers and significantly larger melt masses, as well as tests with UO_2 dominated melts did not show the occurrence of steam explosions. The small conversion efficiency given above is therefore considered as an upper bound.

2.3 TRANSIENT COMET-U EXPERIMENTS WITH REAL UO_2-CONTAINING MELTS

The COMET-U test series performed at the ANL in Chicago (Ill), USA, are aimed at investigating the coolability of real corium melts with a high content of UO_2 as well as at evaluating the transferability of the experiments performed with iron-aluminum oxide simulation melts (thermite melts) to real corium melts (Alsmeyer, 1998). The set-up used for these transient COMET-U experiments therefore corresponds largely to that of the transient COMET-T experiments as described above. Two experiments were carried out in a test vessel of 30 cm diameter, COMET-U1 with 110 kg corium melt and COMET-U2 with 150 kg corium melt. The height of the melt without void amounted to 30 and 40 cm, respectively.

The major constituents of the melt are 52% UO_2, 16% ZrO_2, 13% SiO_2, 4% CaO and 11% Cr. Hence, the composition of the oxide fraction corresponds to that of a core meltdown accident after the erosion of the sacrificial concrete layer. Nine melting plugs are integrated in the sacrificial concrete layer and connected with the water reservoir. In the first experiment, the nine plugs are covered by a concrete layer of 5 mm, in the second experiment by 15 mm. The effective overpressure of the inflowing cooling water amounts to 0.1 bar in the first experiment COMET-U1 and to 0.0 bar only in COMET-U2.

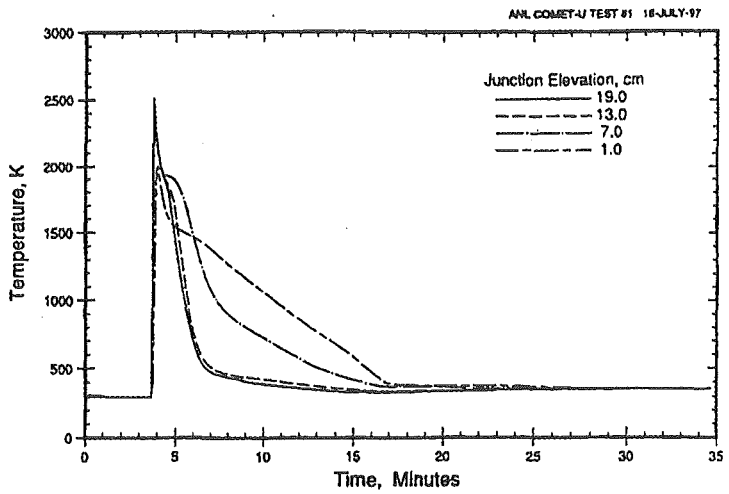

Figure 5: COMET-U1: Temperature history in the melt

The melt generated by the Uranium-thermite reaction has an initial temperature of about 2500 K (see Figure 5) and a very low viscosity. The thermocouples in the lower part of the melt do not reach 2500 K, since part of the heat is removed to the cold concrete by the tungsten sheath of the thermocouples.. In the first experiment COMET-U1, the 5 mm thick sacrificial concrete layer is eroded within a few seconds with all nine cooling channels being opened and the passive water inflow setting in. Within 50 s, a practically stationary coolant water flow of 330 ml/s (20 litres per minute) is reached such that a very efficient cooling of the melt takes place (Figure 6). 4 minutes after water inflow already, the temperatures in the melt have dropped below 1400 K. Consequently, the melt has solidified safely in a porous manner and the erosion of the sacrificial concrete is terminated. About 13 minutes after water inflow, all temperatures show that the melt has cooled down completely as the temperatures are below 100°C. After 14 minutes, water supply to the test vessel is stopped by the operator.

In the second experiment COMET-U2, because of the higher sacrificial concrete layer of 15 mm, the time for concrete erosion between the end of melt generation and the start of water inflow is extended until passive water inflow starts 1:00 min after ignition. At first, water flow amounts to 120 ml/s and then increases to its maximum value of 220 ml/s (13 litres per minute) within 2 min. Afterwards, it remains practically constant.

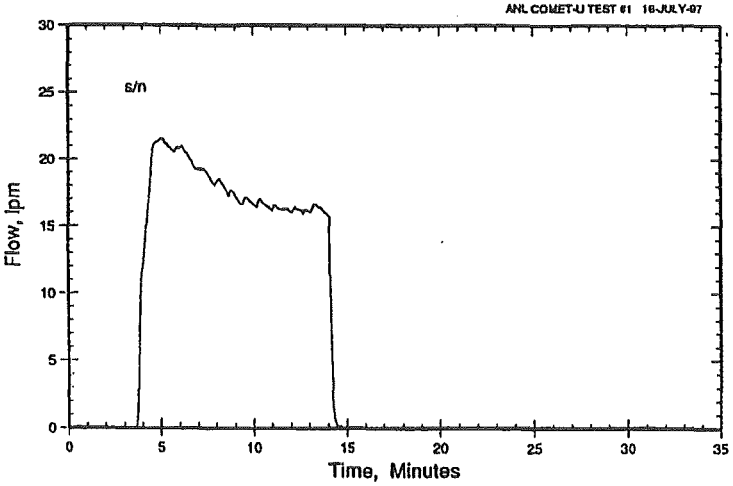

Figure 6: COMET-U1: Water inflow rate into the melt

With onset of flooding the temperatures in the melt drop very rapidly with about 5-6 K/s. About 1 min after the start of cooling, the cooling rate is slowed down to about 1 K/s. It is demonstrated by temperature measurements at the side walls and in the sacrificial concrete layer below the upper edge of the plugs that the surrounding structures remain cold. Consequently, also this experiment reflects efficient cooling of the real corium melt even at a very low effective water pressure. In this case, the initial inflow rate of flooding water is favourably affected by gas release due to concrete erosion, as a result of which flow paths are generated in the melt.

During the flooding of the corium melt, maximum pressure fluctuations of 0.2 bar were measured. Hence, no vigorous interactions between the water and the melt occurred. Post-examinations showed that all nine plugs had opened.

It is confirmed by both experiments that UO_2 rich melts behave in the same way as the simulated melts applied in the experiments at the FZK. The water inflow from below causes the melt to fragment and solidify in a porous manner. The water inflow and cooling rates correspond to those measured by the FZK in the COMET-T experiments. The high water inflow rate ensures safe short-term and long-term cooling.

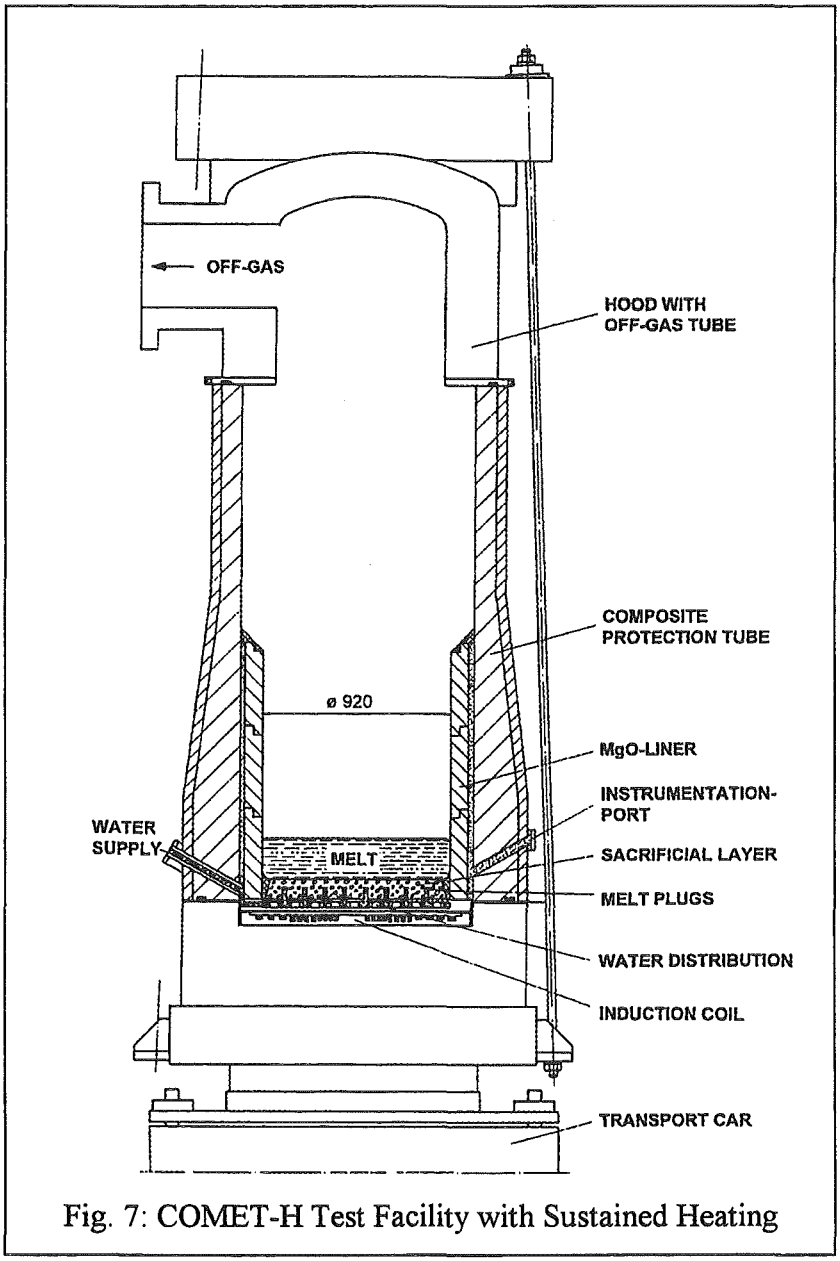

Fig. 7: COMET-H Test Facility with Sustained Heating

2.4 THE COMET-H EXPERIMENTS WITH SUSTAINED HEATING

The COMET-H experiments are large-scale experiments performed with thermite melts of up to 1300 kg. Inductive heating of the metallic phase of the melt allows to simulate the decay heat generation in the melt with a power density that is characteristic of the real core melt. The experiments represent a one-dimensional, 92 cm

diameter circular section of the large cooling facility, see Figure 7. The geometrical heights, including the heights of the melt, correspond to the real set-up. As also the melt temperatures and properties largely correspond to those of a real core melt after partial erosion of the sacrificial layer, the characteristic heat fluxes and solidification processes during cooling are represented practically 1:1.

The melts are generated by an iron-thermite reaction under the addition of further components at temperatures of about 1900°C and poured onto the cooling area. The metal melt with a mass fraction of about 50% consists of iron with a representative amount of zircaloy added depending on the objective of the experiment. The oxide melt consists of a mixture of aluminum oxide and calcium oxide, the major properties of which correspond to those of the uranium/zirconium oxide melt mixed with molten concrete in the real reactor.

The experiments are designed such that a typical power of 300 kW or a surface power density of 450 kW/m^2 is generated continuously in the melt. This represents the highest level of decay heat that has to be managed in the EPR. Inductive heating power is generated in the metal melt and transferred to the oxide phase by conduction and convection. The cooling insert above the induction coil is usually equipped with 112 water-conducting melting plugs/cooling channels, arranged in a square grid of 8 cm. These plugs are imbedded into a 5 cm high layer of castable aluminum oxide to guarantee the stability against downward melting. This layer is covered by the sacrificial layer of concrete that is produced on the basis of borosilicate glass. Both layers are equipped with thermocouples at various levels, which provide information on the progress of erosion and the cooling state of the melt. Flooding water is supplied from an elevated tank to the water distribution layer. The inflow of coolant water and its pressures are measured. Furthermore the temperatures, volumes, pressures and compositions of the exhaust gas flows are determined. Video monitoring in the crucible allows important observations of the state of the melt and the efficiency of cooling. Some of the important recent experiments are described below.

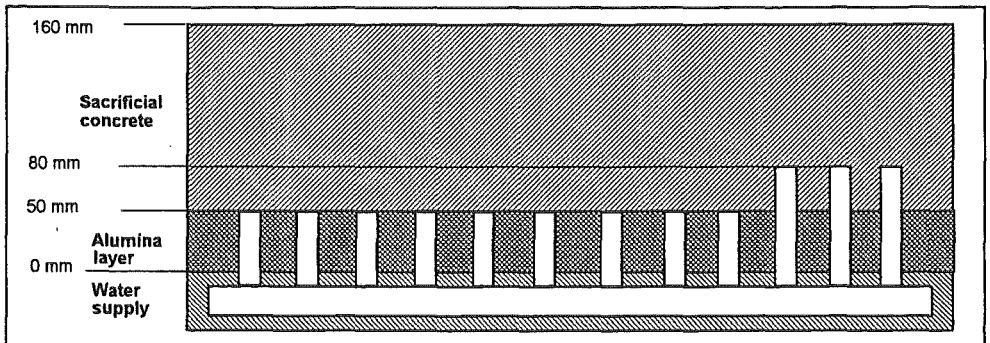

Figure 8: Schematic of Experiment COMET-H 2.2 on Inhomogeneous Melt Attack

The COMET-H 2.2 test investigates the influence of non-uniform erosion of the sacrificial concrete layer which would result in the onset of localised flooding and cooling only, while major parts of the melt are still uncooled. Such a situation cannot be excluded in the reactor case because of the large size of the necessary cooling area. Safe cooling can only be achieved when after further progression of the uncooled portions of the melt, additional cooling channels would open and foster the overall coolability.

In the experiment, the situation was simulated by a staggered array of cooling channels as shown in Figure 8. The longer channels on the right side of the surface will open earlier and water inlet and cooling starts only locally. In the experiment, the melt reaches the long cooling channels after 18 min. As expected, the local inflow of coolant water stops the melt on the right side only. Although the surface of the melt is flooded slowly, cooling of the major part of the melt remains insufficient and the erosion elsewhere continues until gradually the flow channels in the lower section open and increase the water flow to 1 l/s. This improves cooling and stabilises the melt which is completely solidified and quenched after 45 min. Heating is continued in the test for another 20 min without further erosion. Temperatures in the surrounding structures remain below 100 °C and confirm safe long term cooling of the porously solidified melt. The peak heat flux extracted from the melt was 1.5 MW during the quenching phase and exceeds the decay heat level by a factor 5, while balance of simulated decay heat and cooling by evaporation was reached after 40 min. In conclusion, the experiment has confirmed that the COMET cooling concept is sufficiently robust to ensure safe cooling and porous solidification of the melt (Figure 9) also in case of local melt attack.

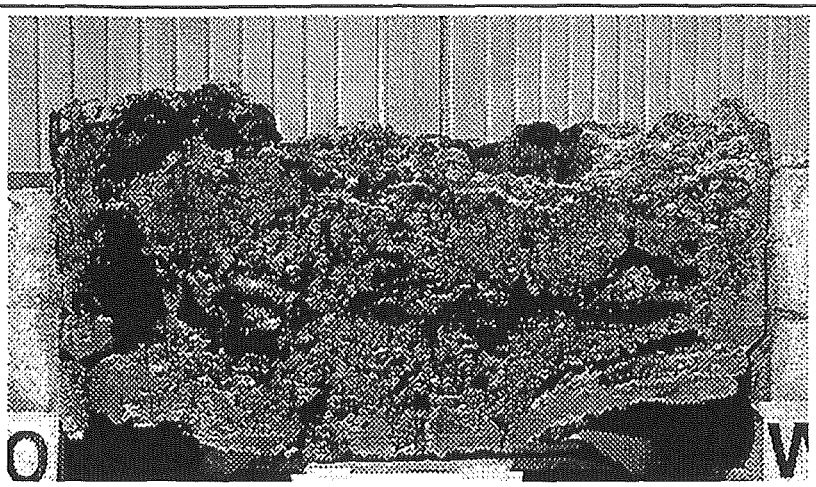

Figure 9: Section through Porously Solidified Melt (H 2.2)

The experiment COMET-H 3.1 studies the role of Zr metal during melt cooling. The thermite melt of 800 kg was mixed with 85 kg Zry and thus represents a prototypical Zr content. It is important that the chemical aggressive Zr from unoxidised fuel pins as well as the high chemical energy released during Zr oxidation does not jeopardise the cooling process. The first phase of the experiment, namely the dry erosion of the sacrificial concrete layer, is characterised by a fast erosion process during which the oxidation of the metallic Zr by the decomposing concrete was completed. This resulted in higher H_2 rates than observed for metal melts without Zr and is of course strongly influenced by the high chemical energy released during the oxidation. Passive flooding of the melt started after 7.2 min, and the melt was porously solidified and completely quenched after about 20 min. Because of the additional energy from Zr oxidation the measured peak cooling rate during flooding was 4 MW (Figure 10) which is a factor

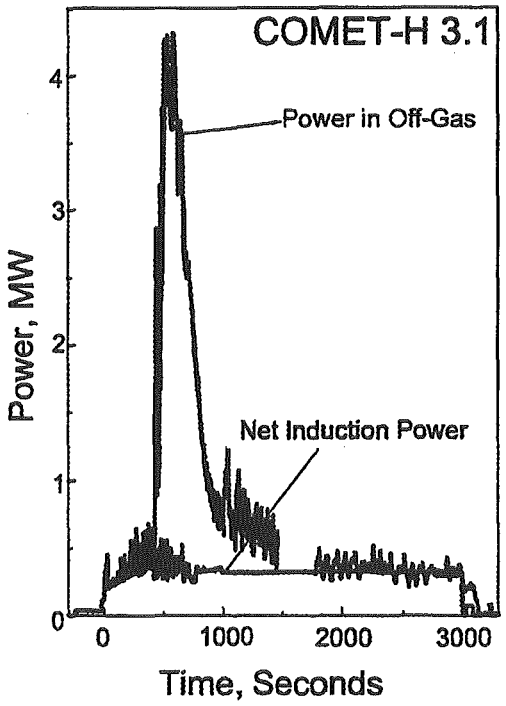

Figure 10: Simulated and removed power in COMET-H 3.1

2 higher than in the other tests. No energetic melt water interactions did occur during the flooding process. Further decay heat simulation after solidification for another 30 min confirmed safe long term cooling with temperatures of the structures below 100 °C. Post test analysis showed the high porosity of the solidified melt as found in all former tests.

The important result of this test is that the chemically aggressive Zr metal is no problem for the COMET concept as Zr is completely oxidised during the erosion of the upper sacrificial concrete layer, and the resulting melt is then safely cooled and quenched by passive water injection. The hydrogen rates are, however, higher as a consequence of Zr oxidation.

The experiments COMET-H 3.2 - 3.4 study mainly the influence of the water pressure on the cooling process, in combination with higher melts. In these tests, the effective water pressure was decreased to 0.1 bar, as opposed to 0.2 bar in the previous tests, while the mass of the melt was increased from 850 to 1300 kg resulting in a height of the melt layer from 33 to 50 cm. In spite of the reduced coolant water pressure, the water flow through the coolant channels was sufficient to generate a porous melt. Moreover, the coolant flow, in case of complete evaporation, exceeded the required rate to remove the decay heat by more than a factor 8. Good cooling and solidification was achieved in test 3.2, but penetration of a few, small melt fractions of 138 g maximum through the flow channels into the bottom water layer occurred and indicated, that limitations of safe operation might be reached. Indeed, the final test with 50 cm melt height showed these limitations. Although the total coolant flow was sufficient to cool and solidify the main portions of the melt within 20 min, the pressure of the water-steam flow was unable to create stable flow channels in all parts of the melt. In the course of the test, some of the previously open flow channels were blocked and the lack of sufficient coolant flow in some portions of the melt excluded complete solidification. Finally, 16 kg (1.2 % of the initial melt) of uncooled melt relocated through 2 coolant channels into the lower water layer after 45 min, which terminated the test. Nevertheless, most of the melt was found to be porously solidified and safely cooled. This test shows that in case of high melts and too low coolant pressure blockage and penetration of the coolant channels may occur. This is excluded by use of an overpressure for the coolant water of 0.2 bar or higher.

3. CONCLUSIONS

The cooling process according to the COMET bottom flooding concept is characterised by the following sequence of events:

- Dry erosion of the sacrificial concrete layer (10 to 15 cm high) with admixture of the concrete products to the melt. During this phase, complete oxidation of residual Zircaloy and reduction of the temperature of the melt.
- Start of bottom flooding by passive opening of the water flow channels. Evaporating water generates a multitude of flow channels in the melt. Superheated steam leaves the surface of the melt.
- Further cool-down of the melt and porous solidification as water/steam flow fills the porous melt from bottom to top.
- Completion of melt solidification after 30 to 60 min. Melt flooded and covered with water. Decay heat safely removed from the solidified corium by continuous evaporation.

The evaluation of all tests leads to the following conclusions for the COMET concept:

- Safe short term and long term cooling of melts with simulated decay heat was demonstrated over a broad parameter range and the validity confirmed also for real corium melts with UO_2 .
- The advantage of the COMET concept is the fast quenching and complete solidification of the melt which excludes major loads of important structures in the lower basement. This applies also to Zr-rich melts.
- Fast quenching of the melt, however, leads to a transient pressure increase in the containment by steam accumulation, resulting in a pressure rise of about 4 bar. This pressure is reduced by condensation of steam at containment structures.
- For melts with a height of about 50 cm, an overpressure of the coolant water of 0.2 bar is recommended.

The experiments for the COMET concept are now completed. The COMET corium cooling concept can help to recover even from the most severe core melt accidents and to keep the containment intact. A modification of the concept using a layer of porous concrete through which the water is supplied to the bottom of the melt which would simplify the construction of the core catcher will be investigated in the near future.

ACKNOWLEDGEMENT

This work is performed within the framework of the investigations for the development of the EPR by the Forschungszentrum Karlsruhe, Nuclear Safety Research Project in cooperation with and with the financial support of the German utilities and SIEMENS. The work is partially funded by the European Union under the 3rd and 4th framework programme.

REFERENCES

ALSMEYER, H., SPENCER, B., TROMM, W.; The COMET Concept for Cooling of Ex-Vessel Corium Melts, 6th International Conference on Nuclear Engineering ICONE-6, San Diego, May 10-15, 1998,New York, N. Y.: ASME, 1998, CD-ROM

ALSMEYER, H., ALBRECHT, G., FIEG, G., STEGMAIER, U., WERLE, H., Simulationstests mit Eisen- und Hochtemperaturschmelzen (Projekte KAJET, KAPOOL, KATS, COMET) in "Maßnahmen zur Beherrschung von Kernschmelze im Sicherheitsbehälter", Jahrestagung Kerntechnik '99, Karlsruhe, in press

COGNET, G. et al., Corium Spreading and Coolability (CSC Project), FISA 99 Symposium, Luxembourg, 29 Nov. - 1 Dec. 1999

TROMM, W., Experimentelle Untersuchungen zum Nachweis der langfristigen Kühlbarkeit von Kernschmelzen, FZKA 6176, FZK-Bericht, 1998

In the experiment, the situation was simulated by a staggered array of cooling channels as shown in Figure 8. The longer channels on the right side of the surface will open earlier and water inlet and cooling starts only locally. In the experiment, the melt reaches the long cooling channels after 18 min. As expected, the local inflow of coolant water stops the melt on the right side only. Although the surface of the melt is flooded slowly, cooling of the major part of the melt remains insufficient and the erosion elsewhere continues until gradually the flow channels in the lower section open and increase the water flow to 1 l/s. This improves cooling and stabilises the melt which is completely solidified and quenched after 45 min. Heating is continued in the test for another 20 min without further erosion. Temperatures in the surrounding structures remain below 100 °C and confirm safe long term cooling of the porously solidified melt. The peak heat flux extracted from the melt was 1.5 MW during the quenching phase and exceeds the decay heat level by a factor 5, while balance of simulated decay heat and cooling by evaporation was reached after 40 min. In conclusion, the experiment has confirmed that the COMET cooling concept is sufficiently robust to ensure safe cooling and porous solidification of the melt (Figure 9) also in case of local melt attack.

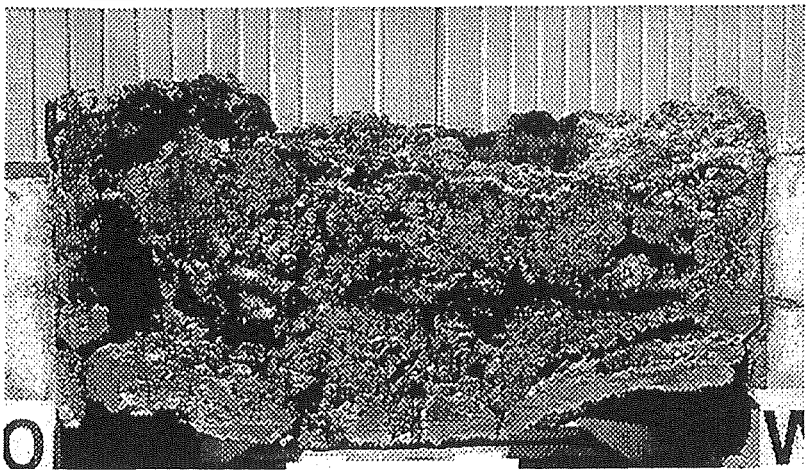

Figure 9: Section through Porously Solidified Melt (H 2.2)

The experiment COMET-H 3.1 studies the role of Zr metal during melt cooling. The thermite melt of 800 kg was mixed with 85 kg Zry and thus represents a prototypical Zr content. It is important that the chemical aggressive Zr from unoxidised fuel pins as well as the high chemical energy released during Zr oxidation does not jeopardise the cooling process. The first phase of the experiment, namely the dry erosion of the sacrificial concrete layer, is characterised by a fast erosion process during which the oxidation of the metallic Zr by the decomposing concrete was completed. This resulted in higher H_2 rates than observed for metal melts without Zr and is of course strongly influenced by the high chemical energy released during the oxidation. Passive flooding of the melt started after 7.2 min, and the melt was porously solidified and completely quenched after about 20 min. Because of the additional energy from Zr oxidation the measured peak cooling rate during flooding was 4 MW (Figure 10) which is a factor

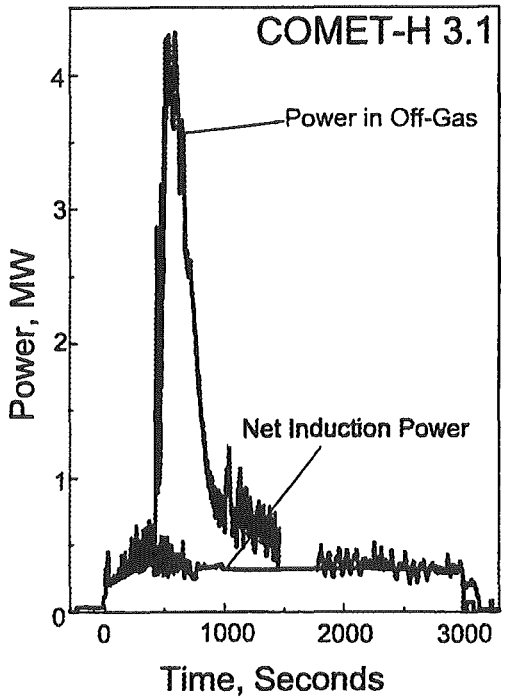

Figure 10: Simulated and removed power in COMET-H 3.1

OECD Workshop on Ex-Vessel Debris Coolability
Karlsruhe, Germany, 15-18 November 1999

Organised in collaboration with
Forschungszentrum Karlsruhe GmbH

CometPC: FIRST RESULTS FOR A SIMPLIFIED COOLING CONCEPT BASED ON POROUS CONCRETE

H. Alsmeyer, H. Benz, T. Cron, W. Tromm, T. Wenz
Forschungszentrum Karlsruhe GmbH
Postfach 3640, 76021 Karlsruhe, Germany
hans.alsmeyer@iket.fzk.de walter.tromm@iket.fzk.de

F. Ferderer
Ingenieurbüro Ferderer,
75228 Ispringen, Germany

ABSTRACT

In the modified CometPC cooling concept, the water is supplied to the bottom of the melt through a layer of porous concrete which is filled and pressurised with water from an elevated water reservoir. This layer of porous concrete replaces the array of sealed injection tubes which are used in the original COMET concept. By supply of a certain coolant water flow, a reasonable fragmentation, cooling, and complete solidification of the melt are achieved.

Five transient experiments with thermite melts are reported which were used to develop and test the required porous layers. It is found that the cooling process results in similar cooling and solidification rates of the melt as observed in the original concept. The porosity in the solidified melt is sufficiently high to safely maintain the heat removal. The first large scale test with sustained decay heat simulation in the melt resulted in lower, yet still sufficient flooding rates, as the concrete layers were fabricated in a slightly different way, and safe cooling and arrest of the melt were demonstrated over 1.6 hours.

The experiments performed so far show that the use of porous concrete layers is an attractive and economic simplification of the bottom flooding cooling concept. Additionally, an increased resistance against downward penetration of the melt even under extreme conditions is expected. Future large scale tests will concentrate on the improvement and proper design of the porous layers to optimise the coolant flow with respect to the desired porosity of the solidified melt and its solidification rate.

1. INTRODUCTION

Various concepts for ex-vessel melt cooling are under investigation to be used for accident mitigation in present and future LWRs. Cooling and arrest of a spread melt, interacting with the concrete basement, by a water overlayer alone may be successful only for shallow melt layers as water ingression through the upper melt surface was found to be limited

(Sehgal, 1999). In contrast to this, water addition to the bottom of the melt leads to fast and complete solidification also of deeper melts, as was proven for the COMET concept (Alsmeyer, 1999). In this concept, the process of cooling is strongly promoted by the evaporation of the water during its rise through the melt. This generates the required porosity of the melt with large internal surfaces to transfer the heat to the rising steam/water flow, and finally leads to a porous solidification of the melt, while the structural concrete remains cold as it is in permanent contact with the flooding water.

This paper describes experimental investigations into a modified bottom flooding concept, the CometPC concept. PC stands for porous concrete, as in this concept the water is supplied to the melt through a layer of porous concrete which in case of an accident is filled and pressurised with water from an elevated water reservoir. The use of a porous layer was initiated by a proposal of Siemens to simplify the COMET concept. The porous layers replace the array of sealed injection tubes which are used in the original COMET concept. A schema of the CometPC cooling concept is given in Figure 1.

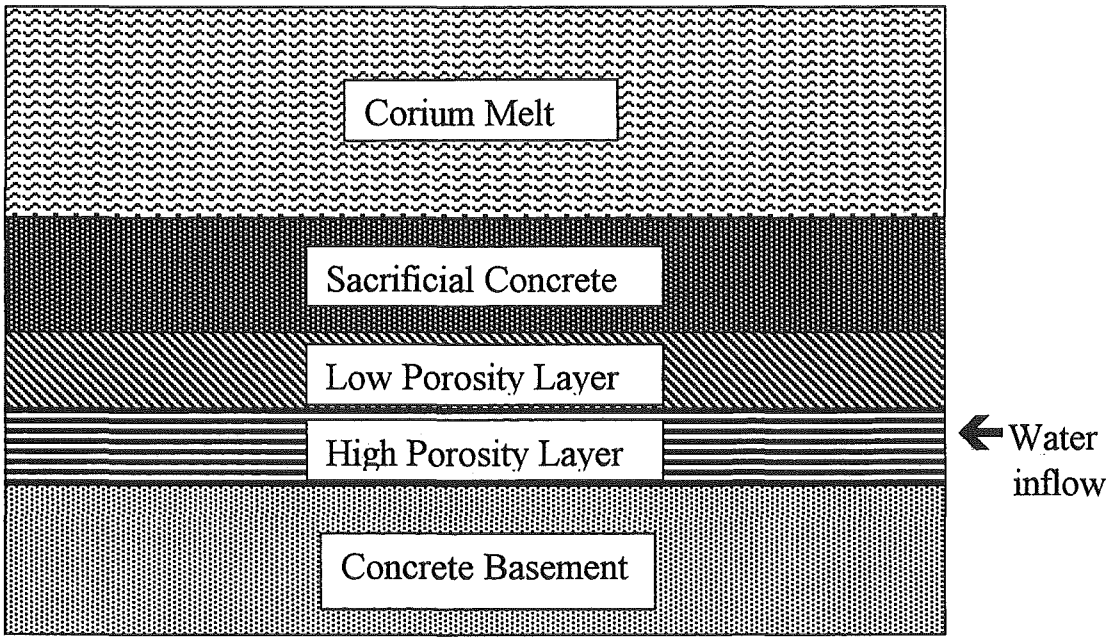

Fig.1 Schema of the CometPC cooling concept

As the coolant water is supplied from the side under the large coolant surface, a layer of high porosity is located on the basement. This layer has a sufficiently low flow resistance to allow the slightly pressurised coolant water to distribute homogeneously under the next layer which has a low porosity only and serves to limit the water inflow to the melt on top to 1 - 2 l/(s·m²). This is the water flow rate which according to the COMET experiments produces good melt fragmentation and cooling rates with acceptable steam rates. The upper sacrificial concrete layer, which can be fabricated e. g. with broken borosilicate glass, gives sufficient time for melt spreading before onset of cooling, and constitutes the melt by cooling and admixture of liquid oxides to facilitate safe cooling and the retention of fission products in the melt.

The important topics which need experimental clarification to develop the CometPC-cooling concept for its reliable use in LWRs are:

- fabrication of the required porous layers
- the required permeability of the porous layers to achieve a flooding rate of 1 – 2 l/m² s
- homogeneity of the flooding and cooling processes
- stability of the porous layers with respect to thermal and mechanical attack by the melt

The experience gained in the COMET experiments is especially useful to solve these problems.

2. Transient Cooling Tests with Thermite Melts up to 180 kg

The first experiments to investigate the feasibility of the cooling concept use thermite melts which are generated in the test vessel with an initial temperature of some 1900°C. As no decay heat is simulated in these tests, only the short term processes during the early cooling phase can be studied with emphasis on the initial water contact, melt fragmentation and quenching. This also requires that the height of the sacrificial concrete layer is reduced from 10 cm or more to a few centimetres only to maintain the elevated temperature of the melt until start of water ingression. In all tests, the thermite melt is composed of 41 wt% iron and 59 wt% oxide (Al_2O_3 + CaO). CaO is added to the oxide melt to lower the solidification temperature of the oxide and to increase the freezing range as is typical for a real corium melt after admixture of the molten concrete. Furthermore, the oxide corium melt after concrete erosion is lighter than the metal melt. Therefore, the used melt is a good representation of the real corium melt, also with respect to layering of the metallic melt beneath the oxide melt.

Figure 2 shows the experimental set-up used in most of the transient tests. The cylindrical test vessel is a 1-d section of the larger cooling device. Water is supplied from an elevated water reservoir to the bottom of the test vessel through 2 ducts and fills the porous layer. This layer is covered by the sacrificial concrete layer which is fabricated separately using broken borosilicate glass. The lower surface of the sacrificial layer is sealed by a plastic coating to prevent permeation of water into the concrete. This also ensures that porous layer and sacrificial layer do not stick together which facilitates water ingression after erosion of the sacrificial layer. The test vessel is located on a weighing platform to register reactions from the melt and its mass as well as the accumulation of water during the quenching process. Further instrumentation gives the coolant water flow and the temperatures in the layer.

Table 1 gives an overview of the main parameters of the transient tests CometPC-T 1.1 through T 1.5. The main parameters which were varied are the constitution of the porous layer and the coolant water pressure. In the first test, the porous layer consisted of a lower bed of gravel with diameter > 12 mm, 50 mm high, which has a low flow resistance and guarantees homogeneous distribution of the coolant water. To achieve the required limitation of the coolant flow, a sand bed of fine porosity, 1-2 mm grain size, 50 mm high, is located on top and finally covered by the sacrificial concrete. Although this experiment after fast erosion of the sacrificial concrete and onset of flooding showed quenching rates and coolant flows which are comparable to earlier results in the standard COMET design and therefore resulted in a porous

solidification of the melt, a strong disadvantage of the loose porous material became evident. With onset of flooding the sand and gravel bed relocated and mixed. This changes the properties of the porous layers in an undefined way and in general could result in the formation of a gap between the porous material and the sacrificial concrete.

Therefore it was decided, that the porous layers should be fabricated from mechanically stable and robust materials. This is achieved by the use of porous concrete which is fabricated by using a special grain distribution of the siliceous aggregates, i.e. by changing the relation of fine and coarse particles for the concrete. The porous concrete with the required low permeability for water has a porosity of about 15%. Its measured density is 2.0 kg/dm^3 and the compressive strength after more than 28 days is about 16 N/mm^2. This is 50 % of the strength of a standard concrete and fully sufficient for the actual application.

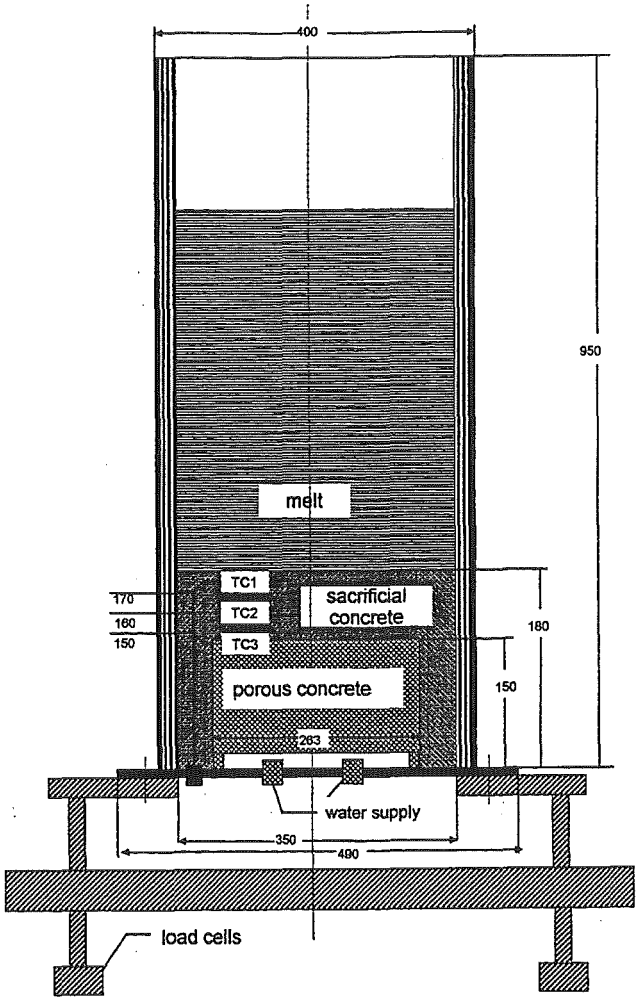

Fig. 2 Transient experiments on melt cooling

Table 1 Overview of CometPC Transient Tests.

Test	T 1.1	T 1.2	T 1.3	T 1.4	T 1.5
porous layer	sand/gravel	concrete	concrete	concrete	concrete
height of sacrificial concrete	25 mm	30 mm	30 mm	30 mm	30 mm
melt mass	54 kg	180 kg	180 kg	180 kg	180 kg
diameter of melt	25 cm	35 cm	35 cm	35 cm	35 cm
collapsed melt height	27 cm	45 cm	45 cm	45 cm	45 cm
effective water pressure	0.1 bar	0.1 bar	0.1 bar	0.1 bar	0.0 bar
onset of flooding	60 s	90 s	100 s	140 s	220 s
flooding rate	0.35 l/s	0.35 l/s	0.32 l/s	0.3 l/s	0.2 l/s

With this porous concrete, the further transient test T 1.2 through T 1.5 were performed. According to figure 2, the low porosity concrete layer is 140 mm high and covered by 30 mm sacrificial concrete. The water is supplied to the porous concrete through a gap of

10 mm underneath to allow homogeneous water inflow. In all tests, good cooling and porous solidification of the melt were observed with an adequate coolant water flow.

Experiment CometPC-T 1.3 is described here as a typical example. After ignition of the thermite powder at time 0, the formation of the melt is completed after 30 s. The thermite reaction as well as the subsequent interaction of melt with concrete and water, respectively, lead to oscillations of the load force of the test vessel over a period of about 150 s (Figure 3). The sacrificial concrete layer is eroded after 100 s, the passive water coolant flow starts, and reaches its typical value of 300 ml/s within the next 50 s (Figure 3). The slow decrease of the water inflow later on is due to the rising water level in the test vessel which reduces the driving water pressure. The load force shows that coolant water evaporates nearly completely until 220 s. Afterwards, as the melt is quenched, the water floods the porous structure and the weight of the vessel increases accordingly. As video observations of the melt surface have shown, the melt was solidified at 185 s (corresponding to the end of oscillations of the load force), and flooded at 255 s. The water inflow is interrupted by the operator at 1150 s as the water starts to spill over the test vessel. The flooding process did not result in energetic interactions of melt and water. The sequence of events as well as the structure of the solidified melt are in good agreement with the processes observed in the reference COMET concept: The melt is solidified as a porous matrix with a higher porosity in the oxidic part, and the porosity allows sufficient water flow to remove the heat.

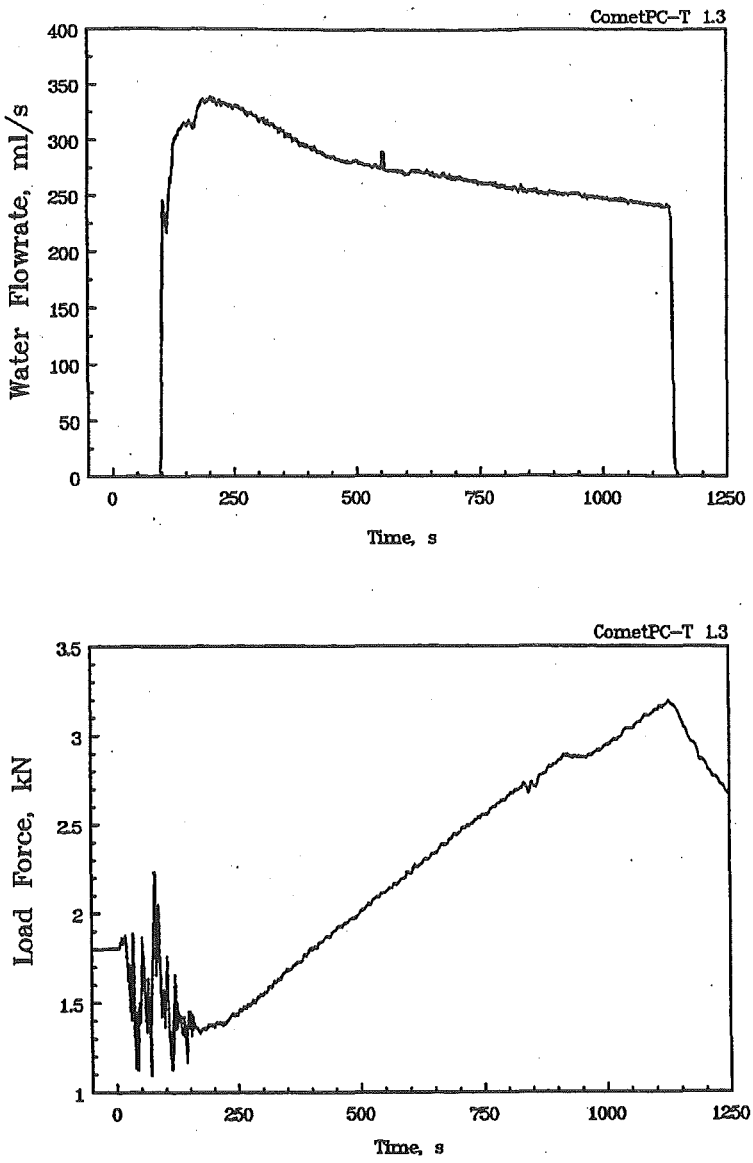

Fig. 3 Coolant water flow and load force of the test vessel in CometPC-T 1.3

Of special interest is the behaviour of the porous concrete layer. Thermocouples located 1 mm under the porous surface which comes into contact with the melt register maximum temperatures of 50°C. This means that the porous concrete, even at its upper surface, remains continuously wetted by the coolant water. Consequently, no attack of the porous concrete was observed.

While the tests CometPC-T 1.2 and T 1.4 gave very similar results, the test T 1.5, which was performed with a lower pressure of the coolant water, showed a different behaviour of the melt. During the early phase of dry concrete erosion, unexpected high steam release was observed from the radial ceramic insulation of the test vessel which may have contributed to additional early cooling of the melt. The erosion process of the sacrificial concrete was delayed and passive water ingression started after 220 s only. After about 28 s of flooding, a mild interaction of water and melt occurred and 30 % of the melt were expelled from the test vessel. Flooding continued with a rate of about 200 ml/s. This lower flooding rate is due to the lower water pressure but was sufficient to quench the melt, which was completely covered by water at 425 s. The occurrence of the mild interaction is comparable to observations which were made during former investigations of the original COMET concept: The mechanical energy conversion is indeed so low that it does not endanger the cooling device. In this experiment, less than 5 mm of the upper porous concrete layer were attacked by the melt, while the deeper porous layer is completely unaffected. Again, the melt is solidified as a porous structure with sufficient permeability for the water.

From the transient tests, the following conclusions are important: The observed flooding rate is from 2.1 to 3.6 l/(m² s), which is slightly above the desired value. The limitation of the flooding rate in these tests is mainly due to the permeability of the porous concrete layer. This layer was found to be sufficiently stable. The typical porosities in the solidified melt are 10 to 20% in the metal and 50% in the oxide.

3. Large Scale Experiment CometPC-H 1 with Sustained Heating

The COMET test facility allows the use of larger melt masses in a larger scale with a diameter of the cooling device of 920 mm. By the electrical induction heating technique, the decay heat of 300 kW is generated throughout the test in the metallic part of the simulated corium melt. The melt is produced by a thermite reaction with basically the same composition and initial temperature as described above for the transient tests. The induction coil is located under the cooling device. For the first large scale test CometPC-H 1, the test set-up is constructed with the following components (Figure 4): A bottom shell of standard concrete supports a 5 cm layer of high porosity concrete which easily distributes the inlet coolant water over the whole area. The low porosity concrete above has a height of 10 cm. Its permeability for water is some 2 l/m²·s if no further flow resistance is considered. This layer is covered by 10 cm sacrificial concrete fabricated from broken borosilicate glass. As poured and hardened on the porous layer, the sacrificial and porous concrete layers are firmly connected. This is an important difference from the transient tests. All these layers have the same heights and composition as the reactor application and therefore represent a 1 to 1 section of the cooling device in a reactor. The melt is surrounded by a set of cylindrical ceramic rings. A crucible of high temperature composite concrete with hood and off-gas tube completes the test vessel. 600 kg melt, 50 wt% Fe + Ni and 50 wt% Al_2O_3+CaO, are generated externally and poured into the test vessel. The melt forms a layer (without void) of 7 cm metal plus 17 cm oxide.

Instrumentation of the test includes measurement of power input of the decay heat. Thermocouples measure temperatures and the erosion front in the concrete layers, and temperatures in melt and coolant water. Further instrumentation gives temperatures of the off-gas and its chemical composition, and aerosol density and aerosol probes in the off-gas. Additionally, the pressures and flow rates in coolant water and off-gas are measured including possible pressure spikes which might occur in case of energetic melt/water interactions.

Observation of the melt surface by video cameras gives very important information on the status of the melt.

In the first phase of the experiment, the melt erodes the dry sacrificial concrete. The erosion of the concrete is non homogeneous, with a maximum erosion rate of 0.2 mm/s. This leads to a local onset of passive flooding after 840 s in the centre and south-east of the surface, with a low flooding rate of 0.08 to 0.1 l/s only. This rate stays nearly constant throughout the test, and is considerably lower than the designed value of 1.3 l/s which would result if the surface of the upper porous concrete layer were completely free of sacrificial concrete. The coolant water contact did not cause any energetic interaction with the melt. However, the low water flow decreases the temperature of the melt only very slowly, as the removed energy hardly overcompensates the simulated decay level. Although thermocouples indicate further removal of sacrificial concrete near the porous interface, no further increase of total coolant flow is observed. On the other side, the porous concrete layer is completely stable, as continuously flooded by water, and is not attacked by the melt.

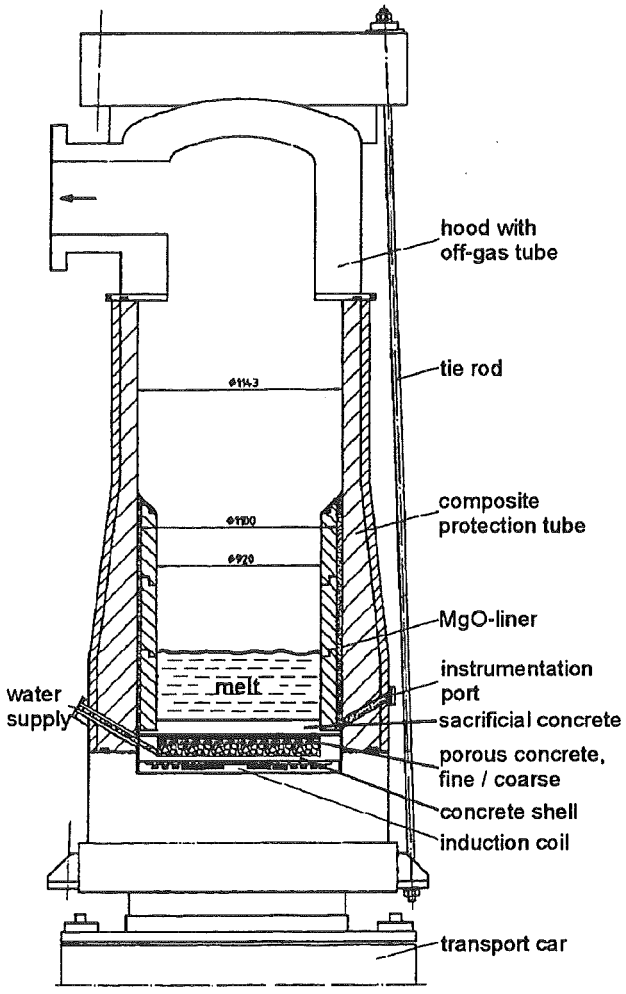

Fig4 CometPC-H1: Test facility with sustained heating

After 1100 s, the higher viscosity of the oxide melt as visible in the video indicates lower temperatures of the melt. At 1185 s, crusts on the upper melt surface grow and gradually cover the surface. The steam from the evaporating coolant flow continues to penetrate through the melt and, as surface crusts grow, lead to the formation of volcanoes which eject droplets and lava flow on the upper crust. After 4000 s, a small part of the upper crust is covered by coolant water. The water volume slowly increases, and at end of the test at 5800 s, one fifth of the melt surface is covered by water. This indicates substantial solidification processes. Figure 5 shows that the decay heat by induction heating is very close to the power which would be extracted by complete evaporation of the coolant water. As additionally some energy is transferred to the lateral crucible or radiated from the upper surface, it is evident that the extracted energy is slightly higher than the simulated decay heat and the melt solidifies. This is also confirmed by the trace of the induction power in figure 5: High frequency oscillations are due to relocations of the melt which change the coupling of the electromagnetic heating to the melt. These oscillations basically end after 3000 s which indicates that the melt is mostly solid.

This is also confirmed by the release of burnable gases in figure 6, especially of H_2. The continuous decrease of the H_2 rate after onset of flooding, which produces a minor H_2 peak at 1100 s, is due to solidification of the heated iron, as solid Fe surfaces have a considerable smaller chemical reaction rate with H_2O than liquid Fe. Furthermore, figure 6 shows that the release of methane and CO_2 is negligible as is known for concrete of the siliceous type.

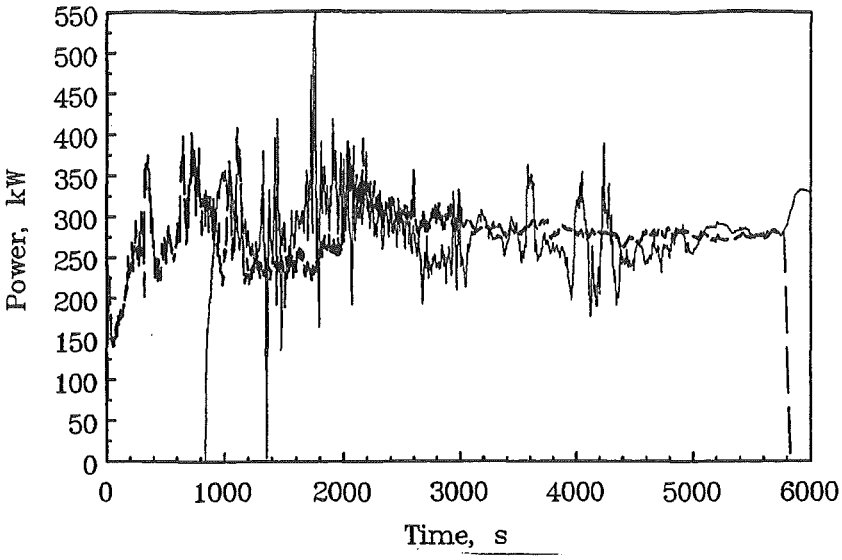

Fig. 5 CometPC-H 1: Simulated decay heat (------)and power removed by coolant flow (——)

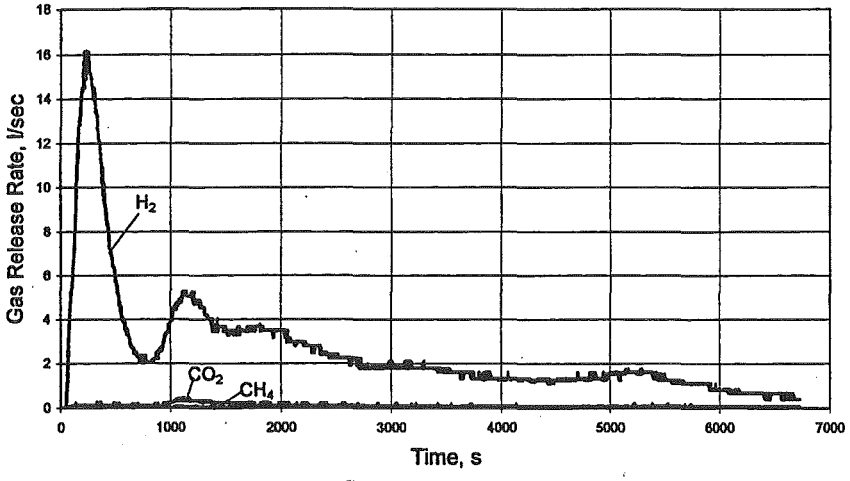

Fig. 6 Release of burnable gases in CometPC-H 1

At 5800 s, the induction heating is stopped by a safety system, as minor part of some oxide melt penetrates the test vessel radially in an area where the sacrificial concrete is not surrounded either by the MgO tube or by porous concrete. This ends the heating phase of the test and the melt cools down without any problems.

At that stage of the test, the melt is characterised by the following status: The downward penetration of the melt is stopped and the melt is safely stabilised by contact with the porous, water filled concrete layer which cools the melt by release and penetration of about 100 ml water/s. The porous concrete is in no way attacked by the liquid or solidified melt throughout the test period of 5800 s (1.6 h). The solid upper surface of the melt is partly covered by the coolant water which penetrated through the solidifying melt. The amount of water on top of the melt is slowly increasing, as the coolant flow is slightly higher than required. The bulk of the melt is largely solidified, while some minor portions of the melt are still liquid. This would not lead to problems as in reactor application the cylindrical part of the coolant device would also be fabricated from porous concrete and be flooded by water. Because of the lower coolant flow however, the small scale porosity of the solidified melt is considerably smaller than in the transient tests. Instead, the volcanic eruptions during the cool-down phase have formed large cavities which are filled with water later on.

Thus, the melt is safely arrested and cooled although the coolant water flow is by more than a factor 10 below the desired coolant rate. This small coolant rate is due to residual sacrificial concrete covering the porous concrete layer. Because of the firm interconnection of these two layers which is due to the fabrication process, the removal of the sacrificial concrete ends when balance between decay heat and coolant flow is achieved.

4. Conclusions

The current investigations have shown that by the modified bottom flooding concept the melt can be safely arrested and cooled. The use of a porous, water filled concrete layer is an attractive and economic modification of the COMET cooling concept. The porous concrete layer has excellent stability against the high temperature melt and reliably stops the progression of the melt by the release of an adequate coolant flow. Therefore, an increased resistance against downward penetration of the melt even under extreme conditions is expected. While transient tests have shown high flow rate of the coolant water to quench the melt very rapidly, the large scale test with sustained heating of the melt has shown considerably lower, however sufficient coolant flow. Further tests are planned to increase the coolant flow by higher permeability of the porous concrete and by a better separation of the porous and sacrificial concrete layers in the large scale tests.

ACKNOWLEDGMENTS

This work is performed within the framework of the investigations for the development of the EPR by the Forschungszentrum Karlsruhe, Nuclear Safety Project, in co-operation with and with the financial support of the German utilities (VDEW) and Siemens. This work is partially funded by the European Union under the 4th framework programme.

REFERENCES

Alsmeyer, H., Adelhelm, C., Benz, H., Cron, T., Dillmann, G., Tromm, W., Schmidt- Stiefel, S., Schneider, H., Schumacher, G., Wenz, T., Ferderer, F., 1999. Corium Cooling by Bottom Flooding: Results of the COMET Investigations, *OECD Workshop on Ex-Vessel Debris Coolability,* Karlsruhe, 16 -18 November 1999

Seghal, B. R., 1999. Accomplishments and challenges of the severe accident research. *Proc. Ninth International Topical Meeting on Nuclear Reactor Thermal Hydraulics,* San Francisco, California, October 3-8, 1999

OECD Workshop on Ex-Vessel Debris Coolability
Karlsruhe, Germany, 15-18 November 1999

Organised in collaboration with
Forschungszentrum Karsruhe (FZK) GmbH

EXPERIMENTAL INVESTIGATIONS ON MELT-COOLANT INTERACTION CHARACTERISTICS DURING DEBRIS COOLING BY BOTTOM INJECTION

D. Paladino, S. A. Theerthan, Z.L. Yang and B.R. Sehgal
Division of Nuclear Nuclear Power Safety
Royal Institute of Technology
10044 Stockholm, Sweden
domenico@ne.kth.se

ABSTRACT

This paper presents results of an experimental investigation of the interactions of a melt pool with coolant injected from the pool bottom. Two experimental facilities, named DECOBI(DEbris COolability by Bottom Injection)- HT (high temperature) and -V (Visualization) have been developed. On the DECOBI-HT facility, a series of experiments were performed using the non-eutectic oxide mixture $30\%CaO + 70\%B_2O_3$ (T_{liq}= 1027 °C, T_{sol}= 977 °C) and water as melt and coolant, respectively. Experimental observations showed that the channel-like porosity was formed and the volume of the porous material was dependent on the initial conditions and geometrical parameters.

The DECOBI-V facility enables visualization of the melt-coolant interaction behavior, which could not be observed in DECOBI-HT facility, and which should be important in the inter-connected porosity formation process crucial for the rapid melt coolability observed in COMET and DECOBI-HT experiments. Several series of experiments have been performed to test the influence of different parameters, e.g. viscosities of both melt and coolant, flow rate of coolant injected, pool depth, heat transfer. The flow pattern for different cases have been observed and classified. Some of the observations are very useful for the investigations on porosity formation mechanisms during debris cooling by bottom injection.

1 INTRODUCTION AND BACKGROUND

Ex-vessel melt (debris) coolability is a critical safety issue for the current and the future light water reactor plants, with respect to stabilization, and termination, of a postulated severe (core melt) accident. After vessel failure, the core melt pool attacks the concrete basemat, whose ablation can be terminated only by cooling the melt to below the concrete dissolution temperature. The core debris generates decay heat and the concrete ablation generates non-condensable gases, which together threaten the integrity of the containment structure. Containment failure and/or basemat penetration could occur if the coolability of the debris is not assured.

The most convenient accident management measure to cool the melt is to establish a water layer on top of the melt pool. This coolability scheme has been investigated in the MACE experiments ([Sehgal, 1992]), where it was found that a tough crust is formed on

the upper surface of the melt pool, which limits the access of the water overlayer to the melt. The coolability of the melt pool in the MACE experiments was not achieved, easily and readily.

Recently, achieving coolability by injecting coolant into the bottom surface of the core melt pool has been investigated in the COMET experiments at Karlsruhe [Tromm, 1993], [Alsmeyer, 1998]. In this scheme, water nozzles are embedded in the containment floor below its surface. Decay-heated core melt ablates through a sacrificial concrete layer before it reaches the water nozzles. The nozzles open as they contact the melt, thereby starting the water injection into the bottom of the melt pool. The COMET experiments using thermite melt and using prototypic core melt were performed at FZK and at ANL, respectively. In all cases, the melt was found to quench, in a relatively short time, to a porous, easily penetrable, debris with continued access of water to all regions of the previous melt pool. A limited number of experiments were performed, and it is not clear how the interconnected porosity is formed and what parameters influence the process of its formation.

A research program named DECOBI (DEbris COolability with Bottom Injection) was initiated and is being developed in Nuclear Power Safety Division of Royal Institute of Technology (NPS/RIT) ([Sehgal, 1998], [Paladino, 1999]). The major objective of DECOBI program is to understand the physics which governs the formation of the interconnected porosity and the heat transfer, in the bottom-injection coolability scheme. Two experimental facilities have been constructed, one is DECOBI-HT facility in which the non-eutectic binary oxide mixtures ($30wt\%CaO + 70wt\%B_2O_3$) and water are employed as melt and coolant, respectively. Another one is DECOBI-V facility which allows to visualize the melt-coolant interaction behavior, which we believe is important for the porosity formation process in COMET and DECOBI-HT experiments. Different parametric effect can be studied in DECOBI-V experiments. So far, only part of the experimental program on DECOBI-V has been completed. In this paper, the experimental observations made on both DECOBI-H and DECOBI-V will be presented and analyzed.

2 EXPERIMENTAL FACILITY

In this section the test facility DECOBI-HT and DECOBI-V are described. Table1 lists the the main parameters for these two facilities.

Table 1: Test facility specifications

	DECOBI-H	DECOBI-V
Dimension (cm)	I.D.= 20; H=50	B=60x30; H=100
Melt simulant	$30\%CaO + 70\%B_2O_3$	water; paraffin oil
Melt temperature (^oC)	1000-1200	25-250
Melt layer (cm)	8-20	10-40
Coolant	water	air; pentane
Number of nozzle	1-5	1-3
Diameter of nozzle (mm)	5	3-8
Measurements techniques	T;P;V	V

2.1 DECOBI-HT facility

The schematic of the DECOBI-HT facility is shown in Fig. 1. The DECOBI-HT facility consists of a cylindrical test section, a water supply system providing the water

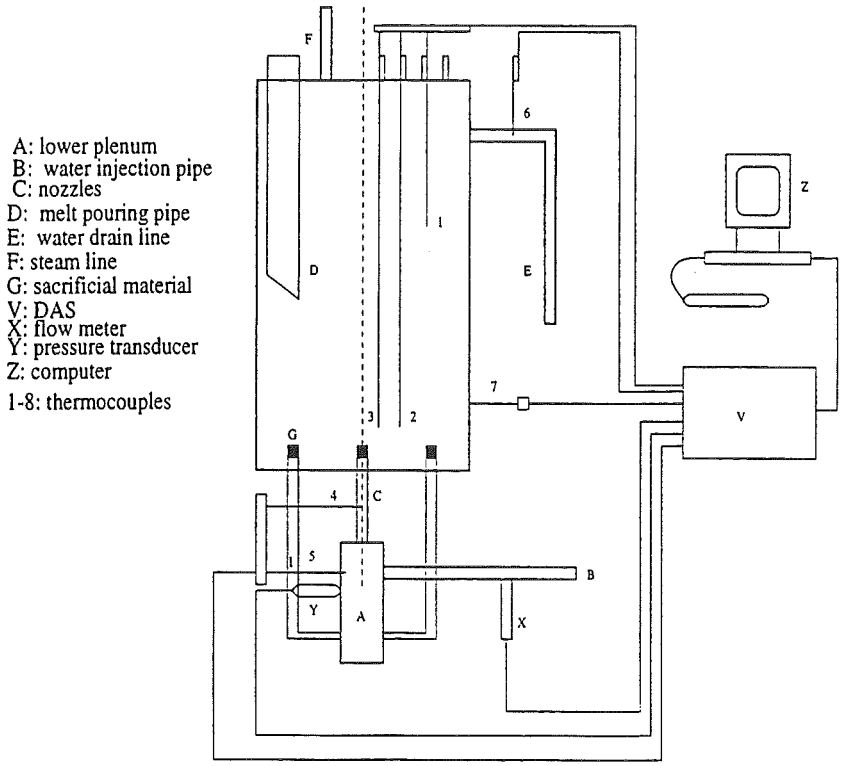

Fig. 1: DECOBI-HT Test Apparatus

coolant to the test apparatus, an induction furnace producing the melt and a DAS (Data Acquisition System). With the exception of the DAS, the entire system was housed in a containment cell. All of the test apparatuses is in modular form and the test section consists of 2 half cylindrical shells made of stainless steel sheet material (2.0 mm thick, 200.0 mm ID, 500.0 height). The nozzles for bottom coolant injection are connected to a lower plenum. These are made of steel material and copper pipes are used for their connection to the plenum. Thermocouples are inserted into the test section through the upper plate and are kept in place inside the test section with the help of guide lines in the upper plate [see Fig.1]. Water is introduced into the test section through the lower plenum. The flow rate of water is recorded by a flowmeter.

2.2 DECOBI-V facility

The schematic of the DECOBI-V facility is shown in Figure 2. The test section is rectangular in cross section with dimensions: 30×60 cm, and with a height of 100 cm. Front and back sidewalls are made of glass, the lateral and bottom sidewalls are stainless steel. The nozzles, which are made of stainless steel, are connected through a lower plenum. The coolant is injected, for each test, at constant flow-rate. Different simulants for the coolant are employed in the experiments, which are supplied differently. The air is supplied to the test section by a compressor, through a pressure reducer and a flowmeter. In the experiment performed using pentane, as coolant, a calibrated bottle is placed two meters higher than the nozzle level, so that a passive system is established. The average flow rate of pentane injected is calculated directly by measuring the liquid level variation in the bottle with time. The electric heater is installed in melt pool to obtain the melt pool with the desired temperature. The whole process is visualized by a high speed digital video system comprising of a motion scope. The recording speed was kept at 250 frames/sec.

The software OPTIMAS was used to process the image pictures.

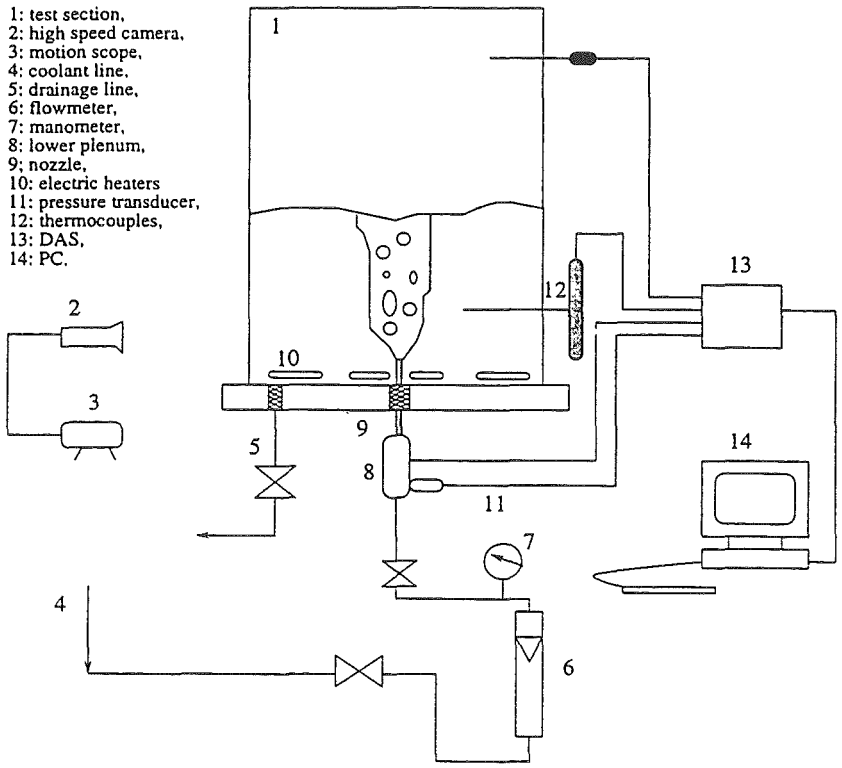

Fig. 2: DECOBI-V Test Apparatus

3 EXPERIMENTAL OBSERVATIONS

3.1 DECOBI-HT experiments

A series of experiments was performed using the non-eutectic oxide mixture $30\%CaO + 70\%B_2O_3$ (T_{liq}= 1027 °C, T_{sol}= 977 °C) as melt, and water as coolant. The main experimental conditions and results are listed in Table 2.

The experimental observations show that the structure and extension of the porosity region is strongly related to the initial melt conditions and the coolant conditions. The superheat of the melt is found to be one of the key parameters governing the porosity formation behavior. The case with low flow rate of the coolant and low superheat of the melt is shown in Fig. 3a and it is seen that the overall porosity formed is very low, with two clear non-porous regions. For the case with higher coolant flow rate and higher melt superheat, the porosity structure is found to be branched-channel-like inside the debris (Fig.3b). The melt that interacts directly with the coolant is solidified very quickly, and the rigid structure formed prevents the remaining melt from contact with coolant. Those unquenched regions of the melt are cooled slowly by conduction. For the cases with five nozzles, with greater depth of melt (~20 cm) and high flow rate of coolant, the porosity structure was quite uniform (Fig.4) and branched-channels were observed. Two of the five nozzle cases did not produce much porosity. For these cases water at $90°C$ was injected in the melt pool. From the DECOBI-HT experiments, it can be concluded that the porosity formation characteristics are related to the melt and coolant conditions, (melt superheat, coolant flow rate, coolant temperature) and the geometrical parameters (melt layer depth, nozzle diameter, distance between nozzle). A clear picture has not been obtained so far,

Table 2: Experimental Conditions and Results

TEST	Melt volume (liters)	Melt temp. (°C)	Coolant temp. (°C)	Coolant over press. (bar)	Coolant flow rate (liter/min)	Solidif. time (sec)	Porosity %
1N-I	3.6	1197	27	0.12	0.15	100	-
1N-II	2.5	1147	27	0.12	0.64	60	20
5N-III	2.5	1147	27	0.12	0.67	50	60
5N-IV	4.0	1157	27	0.13	1.50	30	41
5N-V	4.0	1157	90	0.20	1.20	90	16
5N-VI	4.0	1070	90	0.20	0.80	10	-
5N-VII	6.0	1157	27	0.80	1.50	30	38
5N-VIII	6.0	1157	27	0.20	2.30	20	44

on how the overall porosity created depends on the melt and coolant properties and other thermal hydraulic parameters. This motivated us to pursue the experimental investigation at low temperature level which allows to visualize the melt-coolant interaction behavior. In the experiments at the low temperature level, different combinations of melt and coolant can be tested and effects of more parameters be investigated.

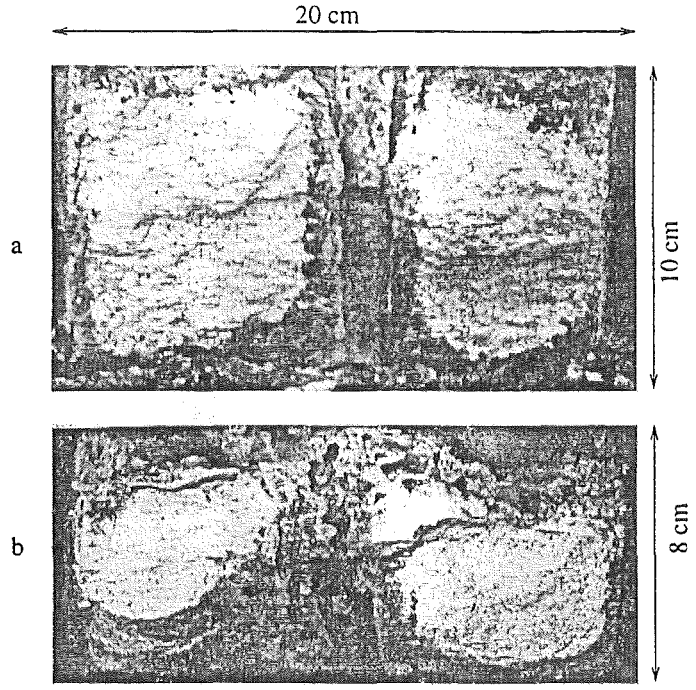

Fig. 3: DECOBI-1N-I and II. Post Test Section

3.2 DECOBI-V experiments

The research objectives of the DECOBI-V experiments is to visualize the character of the melt-coolant interactions when a coolant is injected into a melt pool.

Different series of experiments are scheduled. First one is the interaction of the melt with gas with not phase change of melt and coolant; second one is the case injecting

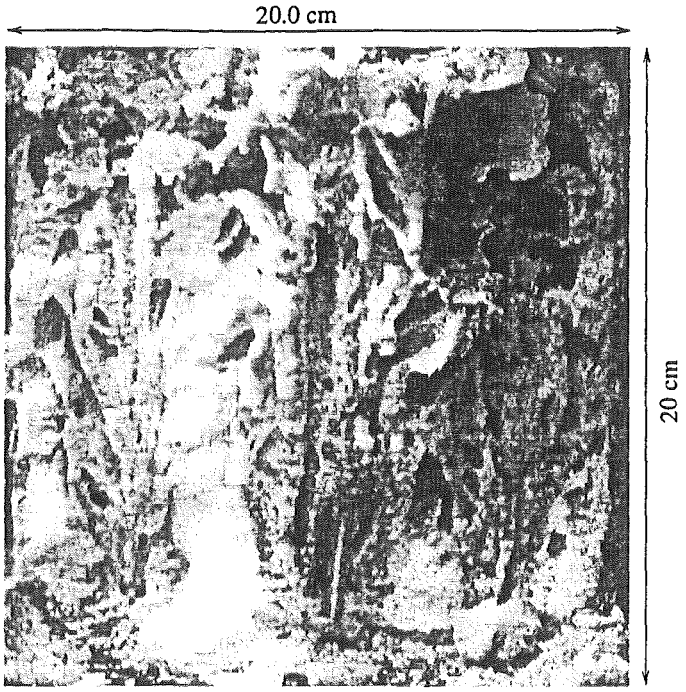

Fig. 4: DECOBI-5N-VII. Post Test Section

liquid coolant which vaporizes during the interaction process; third one is the case with melt solidification by injecting low temperature gases; the last one is the case with solidification of the melt and the vaporization of coolant. In all of these four series of experiments, separate parametric effects will be studied. So far, only first series and a part of the second series of experiments have been performed. Presently, the focus is placed on the hydrodynamic characteristics of the melt-coolant interaction. The flow patterns are analyzed and we believe that they are good precursors for further investigations.

3.2.1 Water-air experiments

The injected air flow rates vary from 1.5 to 71.0 lit/min. Sequential stages starting from the "single bubbling" and ending in the "jet formation" at the nozzle exit are observed. In Fig.5 and Fig.6 selected pictures of the flow patterns observed in 40 cm depth water pool are shown for, respectively, 3 and 8 mm nozzle diameters.

At very low flow rates, bubbles move sequentially upwards. However as the flow rate increases, they start to coalesce at some distance from the nozzle. As the flow rate is further increased, the bubbles from behind capture the front bubbles since they get accelerated in the wake behind the front bubbles. The bubble shapes in general are irregular due to the low viscosity of the melt. These observations are quite similar to those reported in literature.

For deeper pools and intermediate flow rate, the non continuous jet shows periodic bending. This phenomenon seems to be due to two factors: (1) the pressure of the melt column and (2) the non-uniform size of the bubbles formed by the jet break-up, which causes an angular momentum in the flow field. For higher flow rates, the bubble-jet stream issuing from the nozzle breaks into many small satellite bubbles which are swept away by the large scale entrainment in the liquid pool. Note that the transition from the bubble

regime to the jet regimes, occurs at a lower air flow rate when the nozzles diameter is small. That is due to the high velocity of the gas at the nozzle exit. In the axial direction, for high flow rates (Fig.7), the following flow-patterns are observed: (1) above the nozzle the bubbles coalesce and rise vertically, (2) at an intermediate level the coolant jet reaches its maximum expansion and periodic bending appears and (3) in the upper part, the coolant hits the free surface and breaks into a cloud of small bubbles.

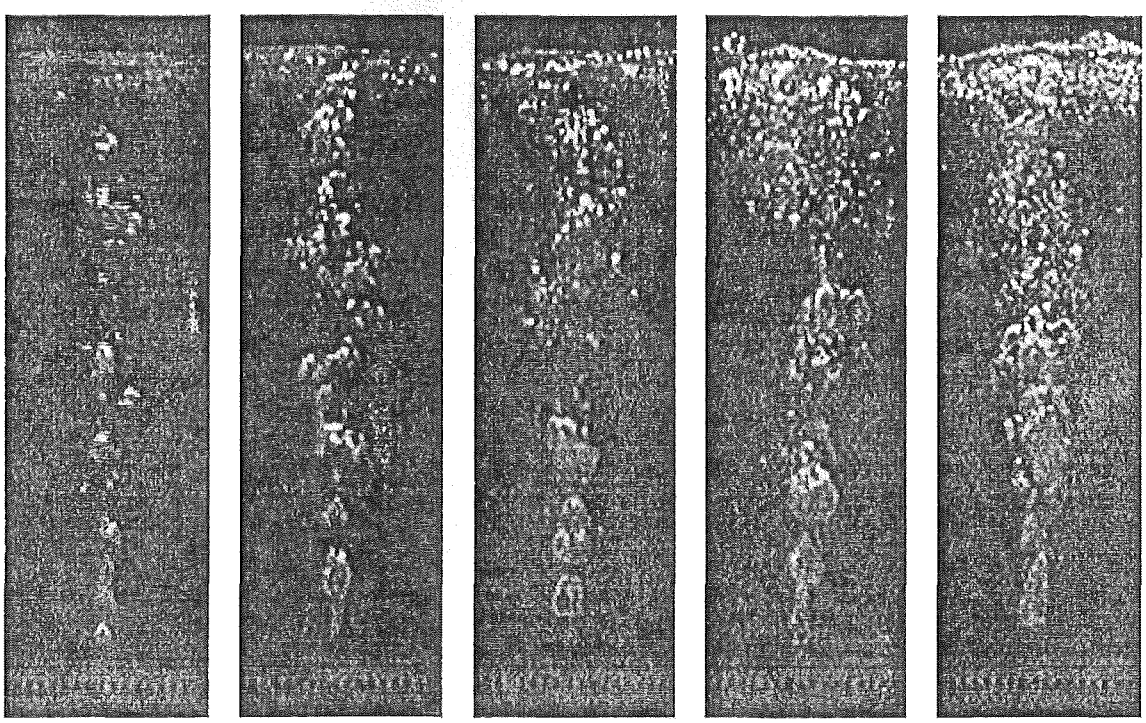

Fig. 5: Water pool 40 cm depth. Dispersed phase: air. Nozzle diameter d_n=3 mm. Flow rate (from left to right)=1.53, 6.33, 11.5, 17.0, 22.6 lit/min

3.2.2 Paraffin oil-air experiments

Selected pictures from the experiments performed in paraffin oil pool are shown in Figures8 and 9. The bubbles are rounded because of the large viscosity of the oil. The elongation along the flow direction, is due to the lower bubble joining with the upper bubble. The air jet loses much momentum due to the higher viscosity of oil, compared to that of the water pool, and hence a more regular interface in paraffin oil pool is observed compared with the water pool. At the free surface, for low flow rate, the bubbles hitting the surface do not have enough momentum to perforate the surface. For higher flow rate, the momentum of the bubbles is enough to perforate the free surface and this induces mixing, due to the drops of pool liquid falling back. Also for the higher flow rate, the jet always remains as a stream of disconnected bubbles.

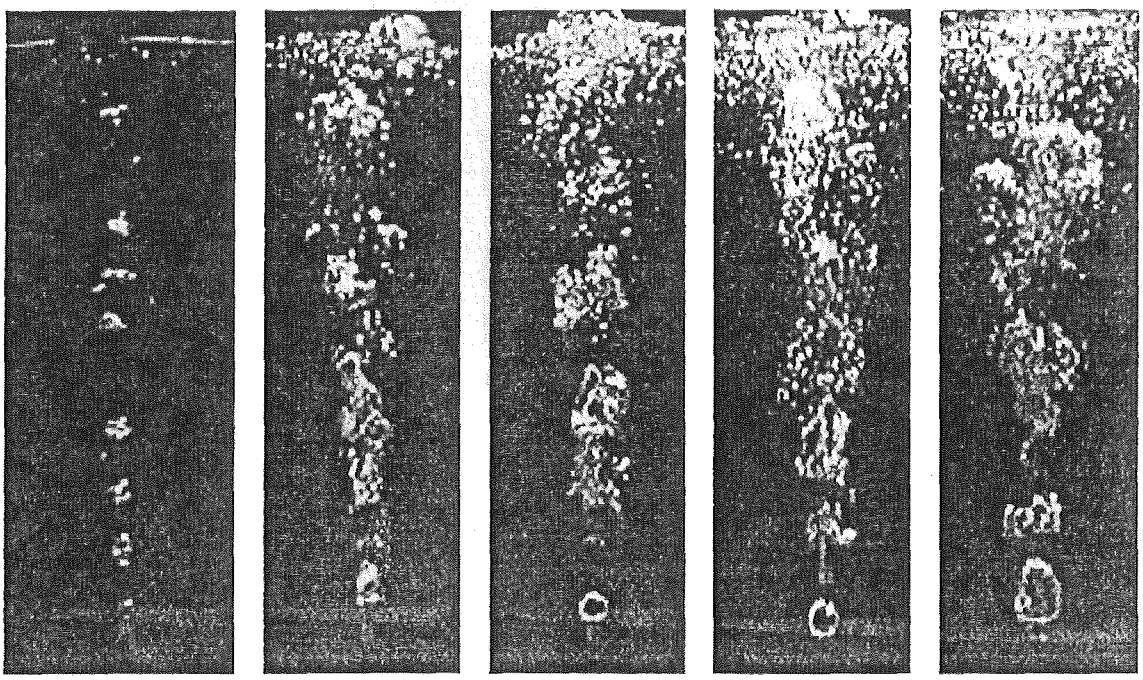

Fig. 6: Water pool 40 cm depth. Dispersed phase: air. Nozzle diameter d_n=8 mm. Flow rate (from left to right)=1.53, 6.33, 11.5, 17.0, 22.6 lit/min

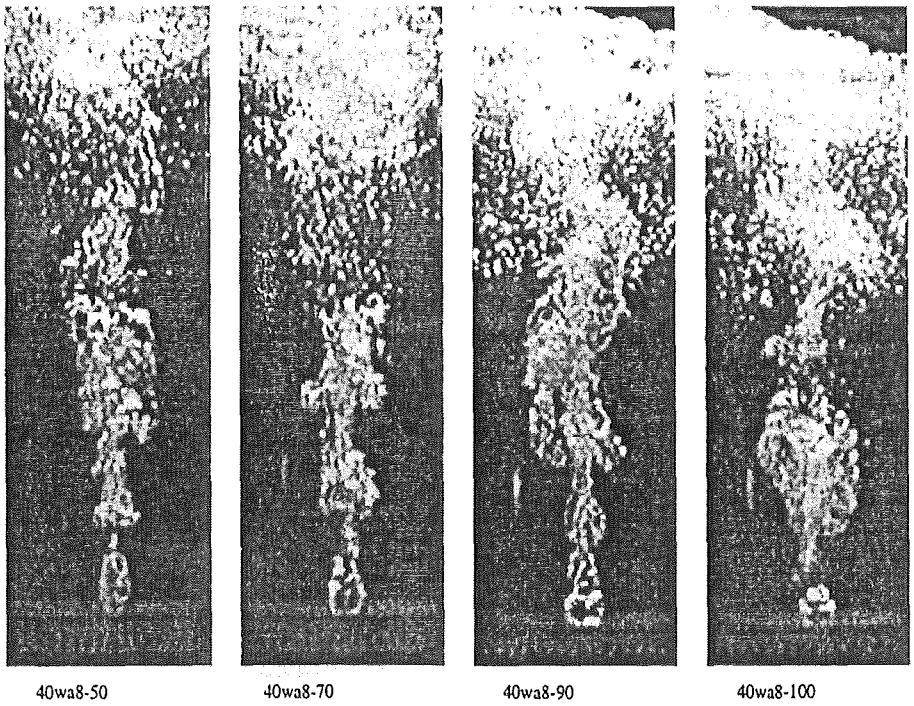

Fig. 7: Water pool 40 cm depth. Dispersed phase: air. Nozzle diameter d_n=8 mm. Flow rate (from left to right)=33.0, 47.6, 63.0, 71.0 lit/min

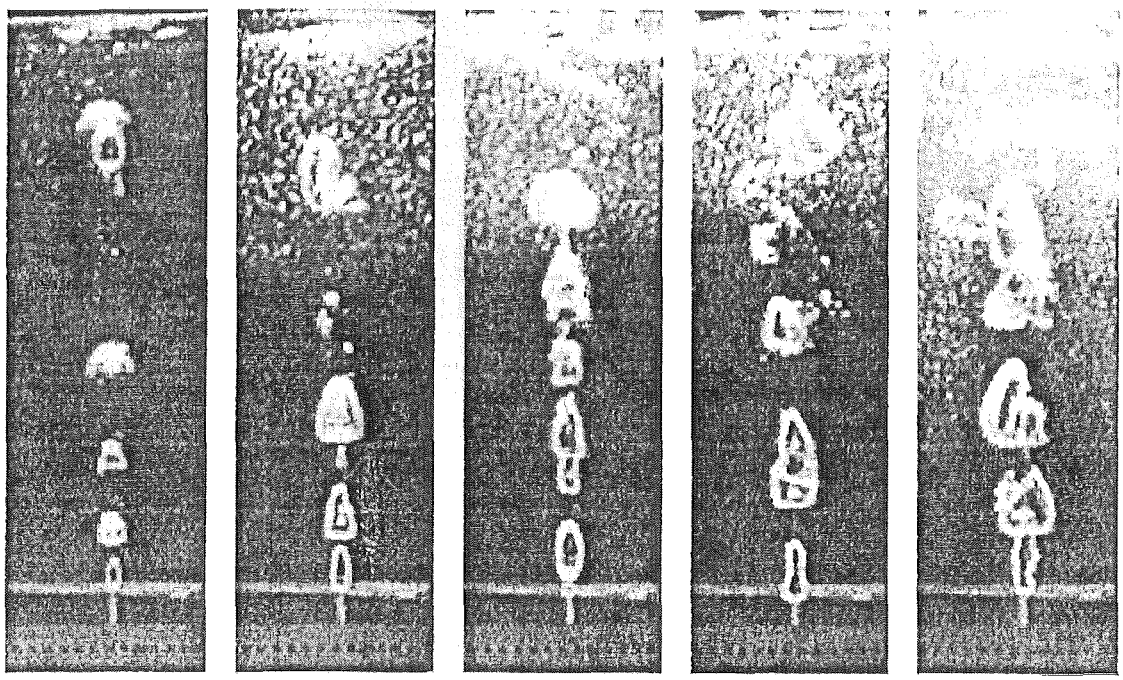

Fig. 8: Paraffin oil pool 40 cm depth. Dispersed phase: air. Nozzle diameter d_n=3 mm. Flow rate (from left to right)=1.53, 6.33, 11.5, 17.0, 22.6 lit/min

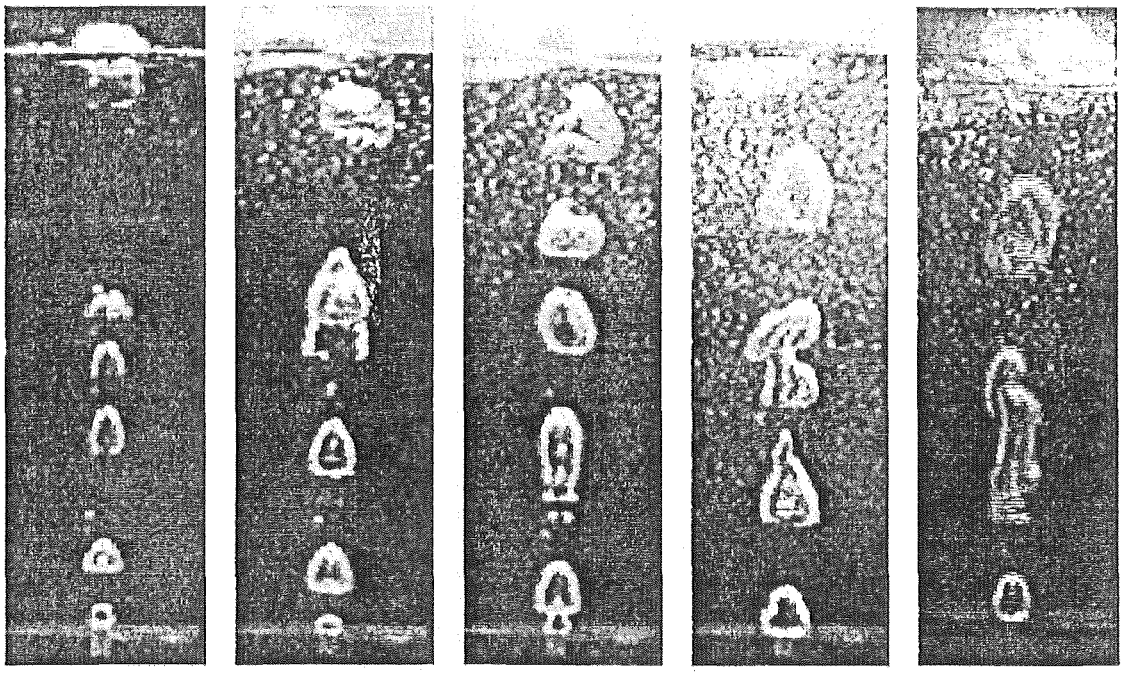

Fig. 9: Paraffin oil pool 40 cm depth. Dispersed phase: air. Nozzle diameter d_n=8 mm. Flow rate (from left to right)=1.53, 6.33, 11.5, 17.0, 22.6 lit/min

3.2.3 Two-phase coolant

A series of experiments was performed injecting a two-phase coolant (pentane) in 40.0 cm depth water and paraffin oil pool. The test matrix is reported in Table 3. Generally, it is observed that for low ΔT the core of the jet remains liquid and the phase change occurs on its surrounding region. The nucleation of the vapour is not uniform and take place in a chain at separate heights in the pool. The increase in flow rate leads to the decrease in the coolant residence time in the pool so the phase change occurs in the upper part of the pool, while for lower flow rate the phase change occurs in the lower part of the pool. In the experiments performed in the paraffin oil pool, some peculiar differences are observed. The high viscosity of the pool increases the drag force on the coolant, which leads to longer residence time and more uniform vaporization in the pool. Therefore the two-phase coolant, for low flow rate, breaks up more easily and small bubbles are formed. The disintegration of the parent droplets essentially constitutes a secondary atomization process leading to the small size droplet which vaporize readily. These effects are less pronounced in the case of high flow rate jet when the inertia of the jet dominates the drag force due to the high viscosity.

Table 3: Experiment performed using two-phase coolant pentane

EXPERIMENT	L_p (mm)	d_n (mm)	Γ_c (lit/min)	T_p (^oC)	POOL
40wp6-0.5-75	400	6	0.5	75	water
40wp6-1.0-75	400	6	1.0	75	water
40wp6-0.5-95	400	6	0.5	95	water
40wp6-1.0-95	400	6	1.0	95	water
40pop6-0.5-75	400	6	0.5	75	paraffin
40pop6-1.0-75	400	6	1.0	75	paraffin
40pop6-0.5-95	400	6	0.5	95	paraffin
40pop6-1.0-95	400	6	1.0	95	paraffin

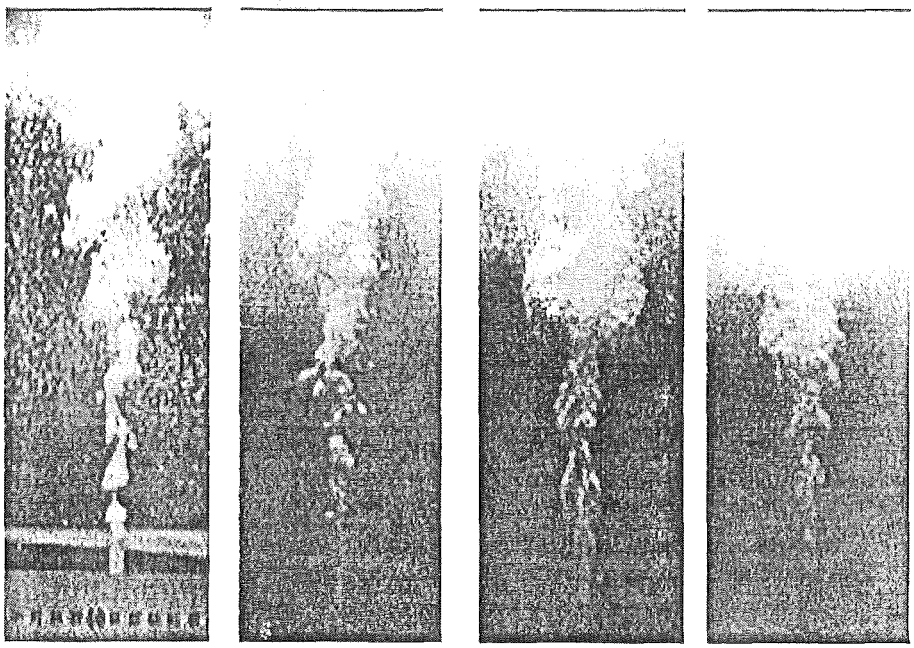

40wp6-0.5-75 40wp6-1.0-75 40wp6-0.5-95 40wp6-1.0-95

Fig. 10: Water-pentane system

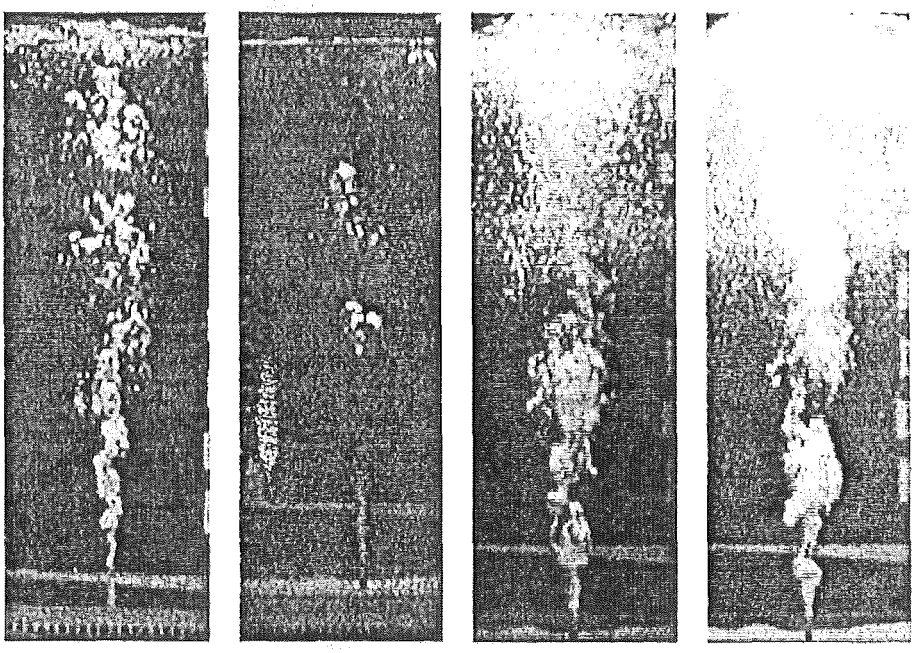

40pop6-0.5-75 40pop1.0-75 40pop6-0.5-95 40pop6-1.0-95

Fig. 11: Paraffin oil-pentane

4 SUMMARY AND FUTURE WORK

- A series of experiments were performed using the non-eutectic oxide mixture $30wt\%CaO - 70wt\%B_2O_3$ as the corium simulant and water as the coolant. In these experiments it is found that the porosity structure and extension is strongly dependent on melt and coolant conditions and the geometrical parameters.
- The experiments with single nozzle show that for low superheat of the melt, when it has high viscosity, the coolant melt pool does not develop an extented (radially) flow-pattern inside the the melt pool.
- For higher coolant flow rate a branched-porous region was observed in a portion of the debris.
- The height of the melt pool was found to have significant effect on the structure of the porosity. For a deep melt pool the coolant develops a more uniform flow-pattern and mixes better with the melt. Therefore, a more isotropic porosity may be obtained.
- On the DECOBI-V facility, single-phase and two-phase coolant jet behaviour for a wide range of experimental conditions in low and high viscosity pool have been studied. These experiments show that the expansion, fragmentation, and phase change of the coolant are strongly dependent on the viscosity of the melt pool.
- In the two-phase coolant experiments, it is seen that for low flow rate the coolant is fragmented into small bubbles readily which allows an increase in the vaporization rate.
- More experiments are undergoing, we believe that the data obtained would help to develop a parametric model describing the porosity formation process. Another series of experiments in a medium size test facility is also planned using different binary oxide melt simulant so that the effect of the melt properties on the processes of porosity formations and heat transfer can be understood.

NOMENCLATURE

d_n	Nozzle diameter, mm
g	Gravitational acceleration, m/s^2
L_p	Pool depth, mm
T_p	Pool temperature, ^oC
T_s	Pentane saturation temperature, ^oC
Γ_c	Coolant flow rate, lit/min
μ_p^4	Pool viscosity,
σ	Surface tension,
ρ_p	Pool density, kg/m^3
ΔT	$T_p - T_s$
$T; P; V$	Temperature; Pressure; Visualization

ACKNOWLEDGMENTS

This work was supported by the Swedish Nuclear Power Inspectorate, the European Union, the US Nuclear Regulatory Commission, Swedish and Finish Power Companies, Nordic Nuclear Safety Project and Swiss Nuclear Inspectorate.

REFERENCES

[Sehgal, 1992] Sehgal B.R., and Spencer B.W., 1992. ACE Program Phase D: Melt Attack and Coolability Experiments (MACE) Program. *Proc. of the Second OECD/CSNI Specialist Meeting* Karlsruhe, Germany.

[Tromm, 1993] Tromm W., Alsmeyer H. and Schneider H.,1993. Fragmentation of Melts by Water Inlet From Below. *NURETH-6* Grenoble, France.

[Alsmeyer, 1998] Alsmeyer H., Farmer M., Ferderer F., Spencer B.W. and Tromm W. 1998. The COMET-Concept for Cooling of Ex-Vessel Corium Melts. *CD-ROM Proc. of ICONE-6*. San Diego, California. pp. 437-445.

[Sehgal, 1998] Sehgal B.R., Yang Z.L., Dinh T.N and Paladino D., 1998, Investigation of ex-vessel melt coolability by bottom coolant injection. *CD-ROM Proc. of ICONE-6*. San Diego, California.

[Paladino, 1999] Paladino D., Theerthan A. and Sehgal B.R., 1999. Experimental Investigation on Debris Coolability by Bottom Injection. *Trans. ANS Annual Meeting*, pp. 167-168.

Session C 1:

MATERIAL PROPERTIES AND THERMOCHEMISTRY: PROPERTIES

Chairman: G. Cognet

OECD Workshop on Ex-Vessel Debris Coolability
Karlsruhe, Germany, 15-18 November 1999

Organized in collaboration with
Forschungszentrum Karlsruhe (FZK) GmbH

LIQUIDUS/SOLIDUS AND Zr SOLUBILITY MEASUREMENTS FOR PWR AND BWR CORE MELT COMPOSITIONS

M. T. Farmer, B. W. Spencer, and R. W. Aeschlimann
Reactor Engineering Division
Argonne National Laboratory
9700 S. Cass Avenue, Argonne IL, USA
farmer@aeetes.re.anl.gov spencer@anl.gov

ABSTRACT

Measurements have been made of the solidus and liquidus temperatures of various corium compositions using a Differential Thermal Analysis (DTA) technique. The corium in these experiments consisted of mixtures of $(U,Zr)O_{2-x}$, with the oxygen content of the mixtures varied to reflect various stages of zirconium oxidation. The melts are representative of typical in-vessel core melt sequences. For most of the tests conducted, the UO_2/Zr mass ratio was fixed at 4.86 (U/Zr molar ratio of 1.64), which is representative of most US PWRs. A few tests were also conducted with a UO_2 /Zr mass ratio of 2.05 (U/Zr molar ratio 0.69), which is representative of US BWRs, as well as Russian VVERs. Information on the solubility of unoxidized Zr in the oxide phase was obtained from both chemical and metallographic analysis of solidus/liquidus melt samples. For PWR compositions, the solidus temperature was found to increase from 2005 C to 2105 C as the extent of Zr oxidation was increased from 30 to 70 %. Similarly, the liquidus temperature was found to increase from 2465 C to 2520 C over the same oxidation range. For BWR melt compositions in the range of 30 to 70 % cladding oxidation, the solidus was found to increase from 1930 C to 2042 C, while the liquidus was found to vary more substantially from 2198 C to 2475 C. From microstructure examinations it was determined that there was no global segregation into distinct metal and oxide phases during cooldown of the samples. Therefore, it is concluded that Zr metal is soluble in the oxide phase under molten conditions for both BWR and PWR core compositions in the range of 30-70% oxidation.

1.0 INTRODUCTION

In the analysis of both in-vessel and ex-vessel core melt accident progression, accurate knowledge of the solidus and liquidus temperatures for a given melt composition is important from the viewpoint of predicting heat transfer from the melt pool to the

surrounding pool boundary, as well as the release of various fission product species from the pool by vaporization. Development of phase equilibrium models for complex multi-component oxide/metal solutions has been underway for some time in both Europe (Ball and Mignanelli, 1992; Cenerino, Chevalier, and Fisher, 1992) and the US (Powers, 1992). Validation of these models requires solidus/liquidus and phase distribution data obtained with prototypic material mixtures.

To augment the experimental database for validation of these models, measurements have been made of the solidus and liquidus temperatures of various corium compositions using a Differential Thermal Analysis (DTA) technique. Information on the solubility of Zr in the oxide phase was obtained from both chemical and metallographic analysis of solidified melt samples. The corium in these experiments consisted of mixtures of $(U,Zr)O_{2-x}$, with the oxygen content of the mixtures varied to reflect various stages of zirconium oxidation. The melts are representative of typical in-vessel core melt sequences (i.e., concrete oxides, which arise during postulated accident sequences in which the reactor pressure vessel is breached leading to melt interaction with the containment basemat, were not included in this work). Thus, in terms of ex-vessel debris coolability, the solidus/liquidus temperatures reported herein are reflective of the melt pool properties at the time of reactor pressure vessel (RPV) failure, which initiates the ex-vessel accident sequence. The UO_2/Zr mass ratios addressed in this study are reflective of both PWR and BWR core compositions.

2.0 EXPERIMENT DESCRIPTION

The experiment setup for the melting point measurements is shown in Fig. 1. The samples were heated in a 20 kVA, water cooled graphite resistance furnace capable of sustained operation at temperatures up to 2800 C. An important aspect of these tests was determining appropriate crucible material(s) which would minimize melt/crucible interactions for mixtures of $(U,Zr)O_{2-x}$ at temperatures up to 2700 C. Analysis of available literature (e.g., see Schaffer, 1964) indicated that ThO_2, TaC, and TiC (listed in order of initial preference) were the most likely candidates. ThO_2 crucibles were ruled out due to their limited availability. As a result, TaC and TiC crucibles were obtained for testing purposes. All crucibles had an outside diameter of 19.1 mm and were 19.1 mm high. The TaC crucibles had a uniform wall/base thickness of 3.2 mm, while the wall/base thickness of the TiC crucibles was 1.6 mm. The material purity was 99.5+ % for all crucibles.

As shown in Fig. 1, both the sample and reference crucibles were held in position using a graphite fixture within the furnace. The crucible containing the melt was placed in the top of the fixture, while the reference crucible was symmetrically mounted in the bottom of the fixture. The reference crucible was used for controlling the furnace temperature. Both the melt and reference crucible temperatures were measured using Ircon two-color pyrometers with operating temperature ranges of 1500 to 3500 C. The pyrometers were calibrated using standards traceable to NIST; the standard error in the temperature measurement is 1% over the operating range for these devices. The

pyrometers were focused on the melt and reference crucible surfaces through quartz window viewports located at the top and bottom of the furnace, respectively. Both viewports were purged with helium gas (2 slpm total flowrate) during the experiment to prevent aerosol deposition on the viewport windows.

As shown in Fig. 1, both crucibles were covered with heat shields containing 6.4 mm diameter holes in the center of the shields. The pyrometer measurements were made by viewing the target surfaces through these holes. Aside from minimizing radiation heat losses, the small openings which the shields provide allows the assumption of black body radiation to be made. (i.e., corrections for material emissivities are not required). The top heat shield over the melt crucible was made of Ta metal, and was intended to act as a carbon-getter should any C be present in the gas space above the melt during the tests. The heat shield over the reference crucible was made of graphite.

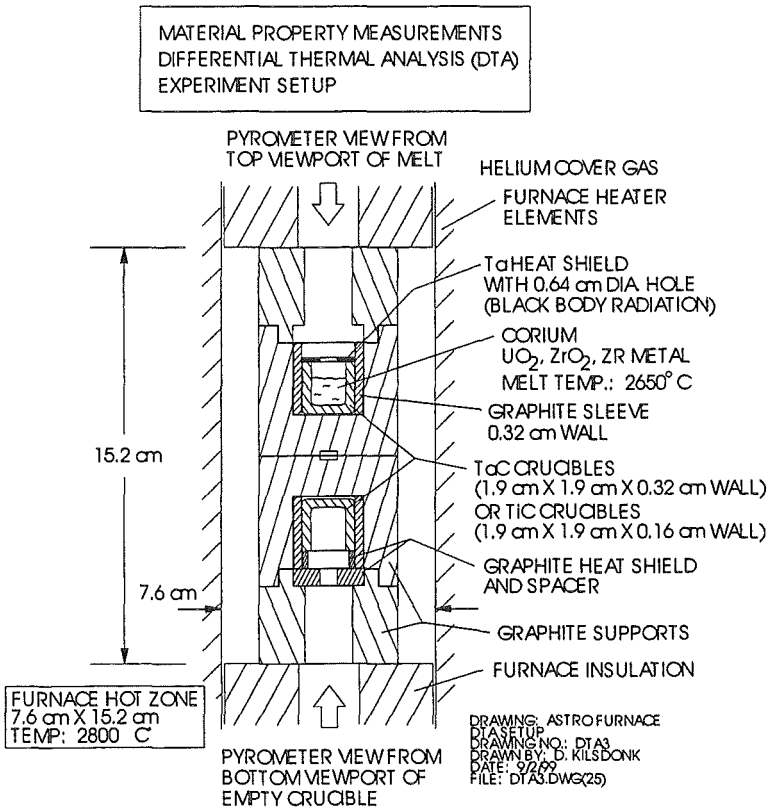

Fig. 1. Illustration of Apparatus for DTA Measurements.

Heat-up of the melt and reference crucibles was controlled by a digital programmable controller. The control signal was taken from the lower pyrometer focused on the reference crucible surface. A linear heating ramp of 25 C/min was used in the current series of tests to measure the solidus/liquidus temperatures.

The initial core compositions were made by uniformly blending appropriate proportions of UO_2 (depleted), ZrO_2, and Zr powders in a glass jar before placing the chemical mixture into the crucible. Chemical analyses of the materials used in these

experiments are provided elsewhere (Farmer et al., 1998). The UO_2 and ZrO_2 powders had purities of 99.9+ %; the Zr powder purity was 99.8 %, with the principal impurity being Fe (0.14 wt %). The particle size of the UO_2 and ZrO_2 powders was <45 μm (-325 mesh), while the particle size of the Zr was in the range 300 to 600 μm (-30 + 50 mesh). The oxygen/metal (O/M) ratio for the UO_2 and ZrO_2 powders was not determined separately. Various cladding oxidation states were simulated by introducing the appropriate proportions of Zr/ZrO_2 powders into the mixture. To ensure that the oxygen potential was preserved to the greatest extent possible over the course of the experiments, the furnace was evacuated to 10 Pascal (10^{-4} atm) and then backfilled with high purity (99.995%) helium before starting each test.

The general operating procedure for the experiments was as follows. After the crucible containing the corium powders was installed in the graphite fixture, the furnace was inerted with helium using the above procedure. The sample was then manually heated to 1600 C (i.e., slightly above lower temperature limit of 1500 C for the pyrometers). At this point, the furnace was placed in automatic control mode in which the samples were heated at a constant rate based on feedback from the pyrometer measuring the reference crucible temperature. The samples were heated at a constant rate of 25 C/min until a predefined temperature increment above the experimentally determined liquidus was reached. At this point, the power was turned off and the samples were cooled as rapidly as possible using the water cooling circuits in the furnace. The rapid cooling scheme was employed to preserve the various phases which were present in the fully molten state for later posttest examination. The typical sample cooling rate after the furnace power was turned off was 150 C/min. Note that multiple heating and cooling cycles (to look for repeatability in the observed liquidus and solidus temperatures) were not performed. This operating procedure was intended to minimize the sample time at temperature, thereby minimizing the time for melt/crucible interaction to occur. As an alternative to multiple heating/cooling cycles for a given experiment, one of the test specimens was reheated using the above procedure to look for repeatability in the observed solidus and liquidus temperatures.

Following the tests, the samples were sectioned along the axial centerline for the purpose of physical characterisation. One half of the sectioned sample was mounted and polished (through 0.05 μm Al_2O_3) for microscopic examination. A sample of the solidified melt was collected from the second half of the sectioned crucible for elemental determination by Inductively Coupled Plasma Atomic Emission Spectroscopy (ICP/AES). This method identifies the elemental composition of the samples, with the exception of carbon and oxygen. The carbon level in two selected samples was determined separately with a LECO carbon analyser. Oxygen level was also determined separately for all samples by measuring the mass gain on ignition at 900 C in an air atmosphere.

In order to verify proper operation of the apparatus, two calibration tests were conducted with Zr metal and α-Al_2O_3 standards during the program. The results of these calibration tests indicated that the experiment technique is capable of reproducing the true melting points of these two materials to within 0.8 %, which is within the 1 %

measurement uncertainty for the pyrometers. Complete information regarding calibration testing of the apparatus is provided elsewhere (Farmer, 1998).

3.0 TEST RESULTS

As summarized in Table 1, a total of six tests were conducted in the experiment series. The first three tests were conducted with PWR corium spanning the range of 30 to 70% Zr oxidation states. All these tests were conducted with TaC crucibles. Corium masses were in the range of 5.62 to 6.55 g. Following these tests, the samples were sectioned along the midplane of the crucibles. The debris was then examined under a microscope. The results indicated minimal melt/crucible interaction. On this basis, three additional tests were conducted with BWR corium spanning the range of 30 to 70% Zr oxidation states. Tests 4 and 5 were conducted with TaC crucibles, while Test 6 was conducted with a TiC crucible to determine the suitability of this material for containment of the melt. Corium masses for these tests were in the range of 5.20 to 5.88 g. Note from the table that the debris from Test 5 (30% oxidized BWR) was reheated to look for repeatability in the observed liquidus and solidus temperatures. The results of the two test series are described in sequence below.

Table 1 Summary of DTA Test Conditions.

Test Number	Representing Reactor Configuration	Melt Composition (wt%)	Melt Mass (g)	Maximum Temperature of Heating (C)
1	PWR, 50% Oxidized	80.5/11.2/8.3 $UO_2/ZrO_2/Zr$	6.550	2600
2	PWR, 30% Oxidized	81.5/6.8/11.7 $UO_2/ZrO_2/Zr$	6.126	2500
3	PWR, 70% Oxidized	79.6/15.5/4.9 $UO_2/ZrO_2/Zr$	5.620	2700
4	BWR, 50% Oxidized	63.5/20.9/15.6 $UO_2/ZrO_2/Zr$	5.20	2500
5	BWR, 30% Oxidized	64.9/12.9/22.2 $UO_2/ZrO_2/Zr$	5.85	2580
5b[a]	BWR, 30% Oxidized	64.9/12.9/22.2 $UO_2/ZrO_2/Zr$	5.85	2580
6[b]	BWR, 70% Oxidized	62.2/28.7/9.1 $UO_2/ZrO_2/Zr$	5.88	2680

[a]Reheat of Test 5 sample
[b]Conducted with TiC crucible

3.1 PWR Corium Test Series

The U/Zr molar ratio for this test series was equal to 1.64 [US Zion Nuclear Power Plant (NPP) basis]. The actual corium compositions and maximum temperature of heating for all experiments are shown in Table 1. The temperature difference between the reference and melt is plotted in Fig. 2 as a function of melt temperature during sample heatup for all the PWR tests. The "blank" sample measurement is also included in the figure for comparative purposes. For each corium composition, the solidus and liquidus temperatures deduced from the differential temperature data are also shown. All of the traces are noted to have a similar overall shape. Onset of melting is characterized by a weak inflection in the differential temperature curve. However, as the sample temperature increases, the melting rate appears to accelerate, as evidenced by the pronounced endothermic drift in differential temperature from the baseline value. Termination of melting is characterized by rapid return of the differential temperature to the baseline value. Generally, the data indicates a gradual (but fairly weak) increase in both the solidus and liquidus temperatures as the extent of Zr oxidation increases. In particular, the solidus temperature increases from 2005 C to 2105 C as the extent of Zr oxidation increases from 30 to 70 %. Similarly, the liquidus temperature increases from 2465 C to 2520 C over the same oxidation range. The solidus/liquidus data for this case is summarized in Table 2. The estimated measurement uncertainties are also shown in the table. The error range estimates include the standard error in the pyrometer reading (1%), plus an additional uncertainty which is attributable to the fact that the pyrometer measures the surface temperature of the sample as opposed to the center (or bulk) temperature. The uncertainty due to temperature lag in the center of the sample during sample heat-up (at a constant rate of 25 C/min) is estimated as - 4 C (Farmer et al., 1998).

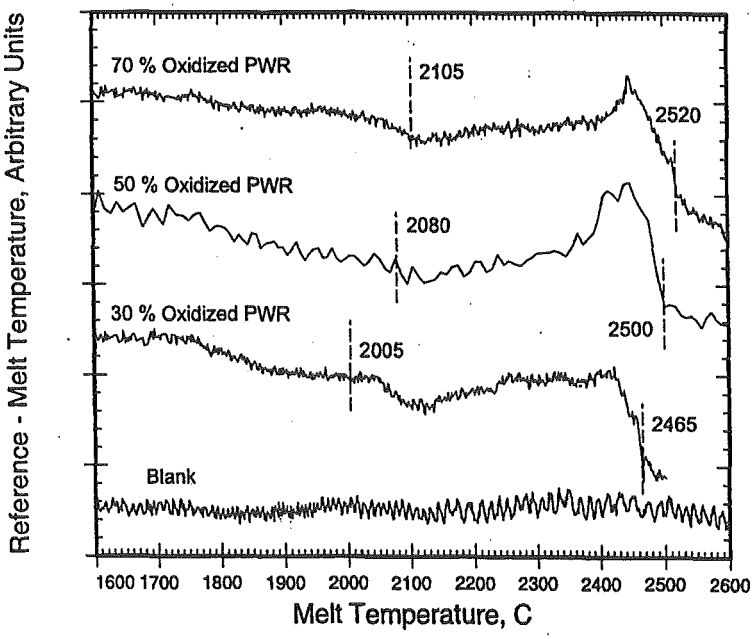

Fig. 2. Differential Temperature During Heat for PWR Test Series.

Table 2 Summary of Measured Corium Solidus and Liquidus Temperatures.

Test Number	Corium Composition	Solidus Temperature (C)	Liquidus Temperature (C)
2	PWR, 30% Oxidized	2005 -24/+16	2465 –29/+21
1	PWR, 50% Oxidized	2080 -25/+17	2500 -29/+21
3	PWR, 70% Oxidized	2105 -25/+17	2520 -29/+21
5	BWR, 30% Oxidized	1930 -23/+15	2198 -26/+18
5b[a]	BWR, 30% Oxidized	1945 -23/+15	2200 -26/+18
4	BWR, 50% Oxidized	2000 -24/+16	2330 -27/+19
6	BWR, 70% Oxidized	2042 -24/+16	2475 -29/+21

[a]Reheat of Test 5 sample to check for repeatability.

The differential temperature data obtained during rapid cooling (i.e., at ~ 150 C/min) of the samples is shown in Fig. 3. Comparison of Figs. 2 and 3 indicates that the overall shapes of the curves are reasonably well reproduced during cooldown, despite the rapid cooling rate. However, these curves were generally not used in the evaluation of the solidus/liquidus temperatures since the rapid cooling rate resulted in large temperature gradients across the samples, which were estimated to be at least 20 C (Farmer et al., 1998). Moreover, rapid cooling increases the chances of sample supercooling to occur. However, this data is provided to illustrate the reproducibility involved with the experiment technique.

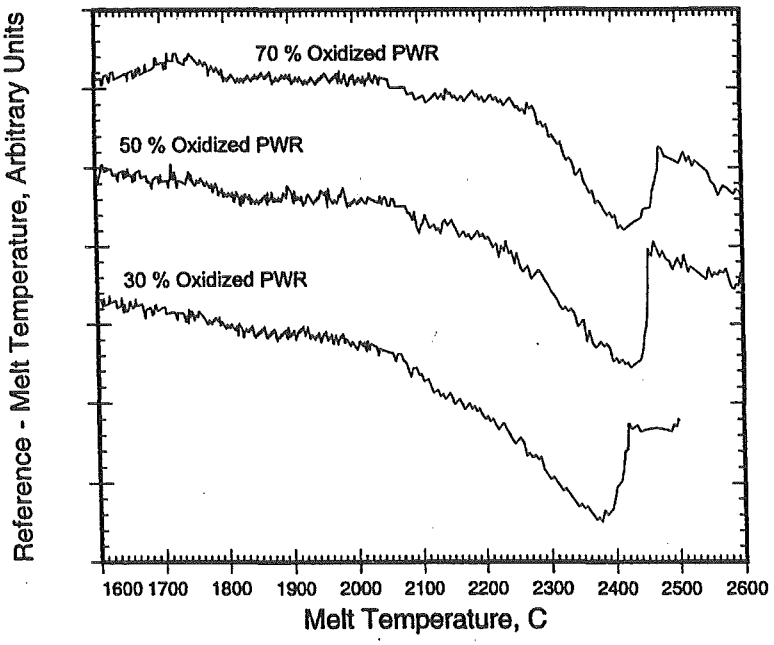

Fig. 3. Differential Temperature During Cooldown for PWR Test Series.

The results of chemical analyses performed on representative samples of solidified melt recovered following each of the tests are shown in Table 3. As noted previously, all of these tests were conducted with TaC crucibles. The Ta level in the melt samples is noted to be fairly low for all tests (i.e., <0.231 wt%). The carbon level was also measured to be 0.2 wt % for Test 3. Thus, the chemical analysis results generally indicate relatively low melt contamination levels from melt/crucible interactions.

Table 3 Raw Data from Chemical Analysis of Melt Samples from PWR Tests.

Element[a]	wt% Element for Test Number			Notes
	1	2	3	
U	70.8 ± 7.1	71.9 ± 7.2	68.9 ± 6.9	-
Zr	15.9 ± 1.6	16.9 ± 1.7	19.1 ± 1.9	-
Ta	0.053 ± 0.005	0.019 ± 0.002	0.231 ± 0.02	-
C[b]	-	-	0.20 ± 0.01	
O	12.78 ± 1.39	12.84 ± 1.42	14.12 ± 1.41	By ignition assuming U product is U_3O_8
O	9.61 ± 1.05	9.62 ± 1.06	11.03 ± 1.10	By ignition assuming U product is UO_2
O	13.05	10.98	11.57	By difference

[a]The levels of all other elements were below measurement thresholds (i.e., Al<0.1, Ca<0.005, Cr<0.01, Cu<0.01, Fe<0.01, Mg<0.005, Ti<0.005, Na<0.1, Ta <0.01, and Zn<0.005)

[b]Carbon determination performed for Test No. 3 only.

Samples from all tests were mounted and polished for microscopic examination. Axial scanning of all samples through the vertical extent of the solidified melt consistently indicated the presence of three distinct phases. The phase structure in all cases is qualitatively similar to that shown in Fig. 4, which is from the 50 % oxidized PWR case. The large continuous gray field is most likely a ceramic $(U,Zr)O_{2-x}$ phase, while the white field is most likely an oxygen stabilized, metallic Zr (α-Zr(O)) phase which precipitated out upon cooling of the sample. The third minor (black) field may be a separate (U,Zr) metallic phase, or a phase consisting of Ta/TaC from melt/crucible interactions. (Unfortunately, the exact compositions of the three phases was not determined as part of this work due to funding limitations). The axial consistency of the phase structure for the PWR test series indicates that global segregation into distinct metal and oxide phases did not occur. Global segregation would be expected due to density differences between molten Zr and the oxide phase if any Zr present as an initial condition was not soluble in the oxide phase. The fact that all Zr was soluble is verified by comparing the bulk melt composition analysis results with the initial powder composition loaded for the experiments. This comparison is provide in Table 4 for the PWR test series. To within the uncertainty in the chemical analysis results, the bulk final compositions are noted to generally agree with the initial compositions, indicating no significant oxidation or reduction took place during the tests. This is important due to the

sensitivity of thermophysical properties, especially phase changes, to changes in the oxygen/metal ratio of the samples.

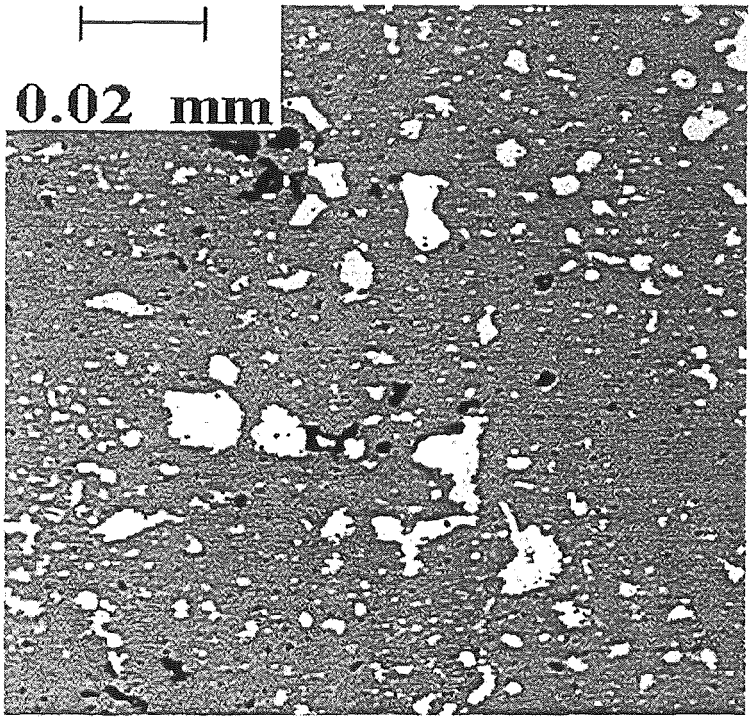

Fig. 4. Posttest Microstructure for Test 1 (50 % Oxidized PWR).

Table 4 Comparison of Pretest and Posttest Bulk Compositions for PWR Tests.

	Mole % Constituent for Test Number					
	2 (30% Oxidized)		1 (50% Oxidized)		3 (70% Oxidized)	
Element	Pretest	Posttest[a]	Pretest	Posttest[a]	Pretest	Posttest[a]
U	25.06	25.74 ± 2.6	23.67	23.11 ± 2.3	22.38	23.69 ± 2.4
Zr	15.24	15.79 ± 1.60	14.49	13.54 ± 1.4	13.68	17.13 ± 1.7
O	59.70	58.46 ± 5.9	61.82	63.35 ± 6.3	63.93	59.18 ± 5.9

[a]U, Zr based on ICP/AES results; O by difference.

3.2 BWR Corium Test Series

The U/Zr molar ratio for this test series was equal to 0.69, which is the same as a VVER/440 core inventory, as well as most US BWR's. The actual compositions and maximum temperature of heating for all experiments are shown in Table 1. The differential temperature data for the BWR test series is shown in Fig. 5. As for the PWR case, the "blank" sample temperature trace is shown for comparative purposes, and the estimated solidus/liquidus temperatures deduced from the data are

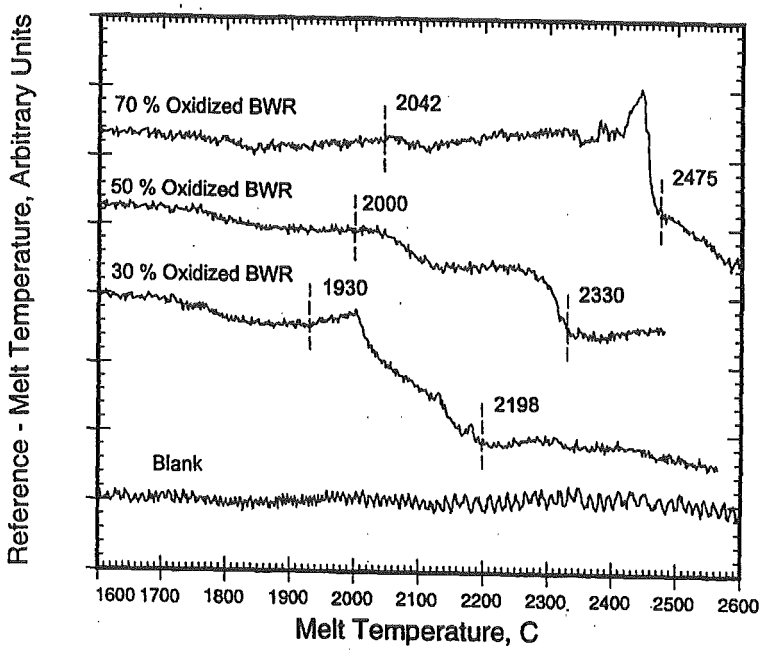

Fig. 5. Differential Temperature During Heatup for BWR Test Series.

also shown in the figure. Comparison of Figs. 2 and 5 indicates that the traces for the BWR compositions show less similarity from test-to-test in comparison to the PWR compositions. Generally, the data indicates more pronounced increases in the solidus and, particularly, the liquidus temperatures as the extent of Zr oxidation increases. The solidus temperature is noted to increase from 1930 C to 2042 C as the extent of Zr oxidation increases from 30 to 70 %. Similarly, the liquidus temperature increases from 2198 C to 2475 C over the same oxidation range. The solidus/liquidus data for this case is summarized in Table 2. To check for repeatability, the sample from Test 5 (30 % oxidized) was reheated. Note from Table 2 that the solidus/liquidus temperatures measured upon reheat are quite similar to the initially recorded values.

The results of chemical analyses performed on representative samples from the BWR test series are shown in Table 5. As noted previously, two of these tests were conducted with TaC crucibles, while the third (Test 6) was conducted with a TiC crucible. The Ta levels in the melt samples from Tests 4 and 5b are noted to be low (i.e., <0.044 wt%), reaffirming the crucible compatibility found during the PWR test series. However, the Ti level in the melt for Test 6 is significant (i.e., 2.09 wt %), indicating that TiC is not as preferable a crucible material in comparison to TaC. The carbon level was also measured to be 0.37 wt % for Test 6, which is slightly less than the level which would be expected (i.e., 0.52 wt %) assuming that the C was introduced through TiC ingression into the melt.

Table 5 Raw Data from Chemical Analysis of Melt Samples from BWR Tests.

Element[a,c]	wt % Element for Test Number			Notes
	4	5	6	
U	56.8 ± 5.7	57.1 ± 5.7	59.9 ± 6.0	-
Zr	31.1 ± 3.1	33.5 ± 3.4	28.0 ± 2.8	-
Ta	0.044 ± 0.004	0.03 ± 0.003	-	-
Ti	-	-	2.09 ± 0.21	-
C[b]	-	-	0.37 ± 0.02	-
O	14.33 ± 1.49	12.90 ± 1.56	14.51 ± 1.45	By ignition assuming U product is U_3O_8
O	11.78 ± 1.22	10.34 ± 1.25	11.85 ± 1.18	By ignition assuming U product is UO_2
O	11.86	9.17	10.61	By difference

[a]The levels of all other elements were below measurement thresholds (i.e., Al<0.1, Ca<0.005, Cr<0.01, Cu<0.01, Fe<0.01, Mg<0.005, Ti<0.005, Na<0.1, Ta<0.01, and Zn<0.005)
[b]Carbon determination performed for Test No. 6 only.
[c]TaC crucibles used for Tests 4 and 5; TiC crucible used for Test 6.

Samples from the BWR test series were also examined under a microscope. As for the PWR tests, axial scanning of all samples through the vertical extent of the solidified melt consistently indicated the presence of three distinct phases. The phase structure in all cases is qualitatively similar to that shown in Fig. 6, which is from the 50 % oxidized BWR case. The large continuous gray field is most likely a ceramic $(U,Zr)O_{2-x}$ phase, while the white field is most likely an oxygen stabilized, metallic Zr (α-Zr(O)) phase which precipitated out upon cooling of the sample. Comparison of Figs. 4 and 6 indicates the increased presence of the α-Zr(O) phase for the BWR case, which is attributable to the increased Zr content in this corium. As for the PWR tests, the axial consistency of the phase structure for the BWR tests supports the contention that all Zr was soluble in the oxide. This observation is verified by comparing the bulk melt composition analysis results with the initial powder composition; this comparison is provided in Table 6 for the BWR test series. For all tests, the posttest Zr content of the samples generally agrees with, or slightly exceeds, the Zr initial present in the powder mixture. Although the posttest chemical analysis comparison is not quite as good in comparison to the PWR data, the results nonetheless indicate that no significant oxidation or reduction took place during the tests.

4.0 DISCUSSION

The results of the solidus/liquidus measurements for the various corium compositions addressed in this study are summarized in Table 2. For the PWR melts, the solidus temperature was found to increase from 2005 C at 30% cladding oxidation to 2105 C at 70% oxidation. The liquidus for these compositions was nominally 400 C

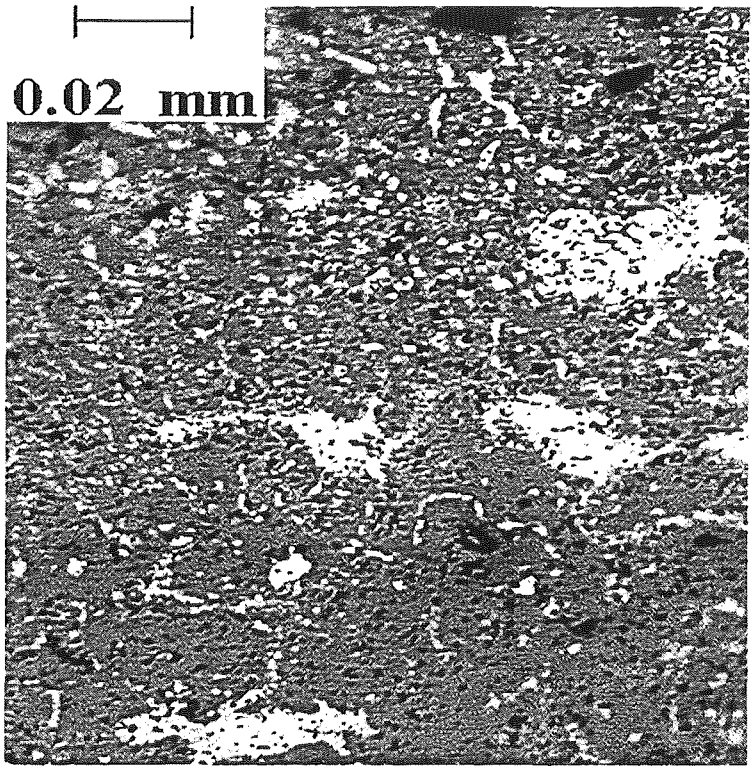

Fig. 6. Posttest Microstructure for Test 4 (50 % Oxidized BWR).

Table 6 Comparison of Pretest and Posttest Bulk Compositions for BWR Tests.

	Mole % Constituent for Test Number					
	5 (30% Oxidized)		4 (50% Oxidized)		6 (70% Oxidized)	
Element	Pretest	Posttest[a]	Pretest	Posttest[a]	Pretest	Posttest[a]
U	18.79	20.33 ± 2.0	16.97	18.07 ± 1.8	15.46	20.47 ± 2.0
Zr	27.21	31.12 ± 3.1	24.56	25.81 ± 2.6	22.34	24.97 ± 2.5
O	54.00	48.55 ± 4.9	58.48	56.12 ± 5.6	62.19	54.56 ± 5.5

[a]U, Zr based on ICP/AES results; O by difference.

higher, ranging from 2465 C at 30% oxidation to 2520 C at 70% oxidation. The results of the BWR measurements indicate that the solidus temperature increases from 1930 C to 2042 C as the cladding oxidation is increased from 30 to 70%. The liquidus for these compositions was found to be a stronger function of oxidation state, ranging from 2198 C at 30% oxidation to 2475 C at 70% oxidation. Comparison of the overall test results from the BWR and PWR test series thus indicates that both the liquidus and solidus temperatures decrease with increasing metallic Zr in the melt.

Note that the solidus temperature of 1930 -23/+15 C measured for the 30% oxidized BWR case (Test 5) is in reasonable agreement with the experimentally determined value of 1920 C measured by Skokan (1984) for mixtures of α-Zr(O) and UO_2 in the range of 0 to 30 mole % UO_2. The 30% Zr oxidation state for Test 5 (and Test 2 also) corresponds to 37.5 atom % O in the binary Zr-O system, which may be compared with 30 atom % O for α-Zr(O) (22% equivalent Zr oxidation). Note that Test 2 was conducted with 41 mole % UO_2, while Test 5 was conducted with 62 mole % UO_2. Thus, both of these tests lie outside the range of experiment data obtained by Skokan. However, the postulated phase diagram for the quasi-binary α-Zr(O)-UO_2 system produced by Skokan indicates that the solidus temperature is constant at ~ 1900 C for UO_2 contents up to ~82 mole %. The current data from Tests 5 and 2 indicate that the solidus temperature actually increases slightly as the UO_2 content increases (i.e., up to 2005 C at 62 mole % UO_2), keeping in mind the slight difference in O content for the binary Zr-O system between the two datasets. Skokan did not experimentally determine liquidus temperatures as a part of his study, so further data comparison is not possible.

The results of microscopic examinations indicate that Zr metal present in the melt was soluble in the oxide phase for both BWR and PWR melt compositions in the range of 30 to 70 % cladding oxidation (i.e., gross phase segregation into distinct metal and oxide layers was not observed in any of the tests). For these tests, the O content in the melt was sufficient to form an oxygen-stabilized Zr phase. (As discussed above, the minimum O content required to form α-Zr(O) is 30 atom % O in the binary system Zr-O, which corresponds to 22% cladding oxidation). Thus, the current data supports the concept that as long as the O content is high enough to form α-Zr(O) (i.e., cladding oxidation $\geq$22%), then a quasi-binary α-Zr(O)-UO_2 system results. Below 22% cladding oxidation, a separate metal phase may develop consisting of U or U-Zr, due to the high affinity of Zr for O. Additional testing at lower oxidation states would be required to verify this solubility limit in the range of U/Zr ratios addressed in this study.

5.0 CONCLUSIONS

For PWR corium compositions (U/Zr molar ratio of 1.64), the solidus temperature was found to increase from 2005 C at 30% cladding oxidation to 2105 C at 70% oxidation. The liquidus for these compositions was nominally 400 C higher, ranging from 2465 C at 30% oxidation to 2520 C at 70% oxidation. For BWR compositions (U/Zr molar ratio of 0.69), the solidus was found to increase from 1930 C to 2042 C as the cladding oxidation increased from 30 to 70%. The liquidus for these compositions was found to be a stronger function of oxidation state, ranging from 2198 C at 30% oxidation to 2475 C at 70% oxidation. These two sets of data thus indicate that both the liquidus and solidus temperatures decrease with increasing metallic Zr in the melt.

The results of microscopic examinations indicate that Zr metal present in the melt was soluble in the oxide phase for both BWR and PWR melt compositions in the range of 30 to 70 % cladding oxidation. For these tests, the O content in the melt was sufficient to form an oxygen-stabilized Zr phase. Thus, the data indicates that as long as the O content

is high enough to form α-Zr(O) (i.e., cladding oxidation ≥22%), then a quasi-binary α-Zr(O)-UO_2 system results. Below 22% cladding oxidation, a separate metal phase may develop consisting of U or U-Zr, due to the high affinity of Zr for O.

ACKNOWLEDGEMENTS

Support for this work was provided by the International Nuclear Safety Center (INSC) at ANL. Micrographic examination of the DTA samples was performed by Dr. John Holland and Mr. Norb Saber. Chemical analysis of samples was performed by the Analytical Chemistry Laboratory at ANL. Technical input during the course of this work was provided by Drs. Joanne Fink and Len Leibowitz at ANL. The manuscript was prepared for publication by K. Rank. These efforts are gratefully acknowledged.

REFERENCES

Ball, R. G. J., and Mignanelli, M. A. The Calculation of Phase Equilibria of Oxide Core-Concrete Systems, Proc. of the Second OECD (NEA) CSNI Specialist Meeting on Molten Core Debris-Concrete Interactions, KfK 5108, NEA/CSNI/R(92)10, April, 1992.

Cenerino, G., Chevalier, P. Y., and Fischer, E. Thermodynamic Calculation of Phase Equilibria in Oxide Complex Systems: Prediction of Some Selected Fission Products (BaO, SrO, La_2O_3) Releases, Proc. of the Second OECD (NEA) CSNI Specialist Meeting on Molten Core Debris-Concrete Interactions, KfK 5108, NEA/CSNI/R(92)10, April, 1992.

Farmer, M. T., McUmber, L. M., Aeschlimann, R. W., and Spencer, B. W. Final Report On Severe Accident Material Property Measurements, ANL Report, ANL-NT-88, October, 1998.

Powers, D. Non-Ideal Solution Modeling for Predicting Chemical Phenomena During Core Debris Interactions with Concrete, Proc. of the Second OECD (NEA) CSNI Specialist Meeting on Molten Core Debris-Concrete Interactions, KfK 5108, NEA/CSNI/R(92)10, April, 1992.

Schaffer, P.T., 1964. Plenum Press Handbook of High Temperature Materials, Materials Index No. 1, Plenum Press, New York, NY.

Skokan, A., 1984. High Temperature Phase Relations in the U-Zr-O System. In: Fifth International Meeting on Thermal Nuclear Reactor Safety, Karlsruhe, Germany, September 9-13, 2.

OECD Workshop on Ex-Vessel Debris Coolability
Karlsruhe, Germany, 15-18 November 1999

Organized in collaboration with
Forschungszentrum Karlsruhe (FZK) GmbH

ESTIMATES OF CORIUM VISCOSITY FOR PWR AND BWR CORE MELT COMPOSITIONS BASED ON SPREADING RATE

M. T. Farmer, R. W. Aeschlimann, and B. W. Spencer
Reactor Engineering Division
Argonne National Laboratory
9700 S. Cass Avenue, Argonne IL, USA
farmer@aeetes.re.anl.gov spencer@anl.gov

ABSTRACT

Viscosity estimates have been made for various corium compositions based on the spreading rate. The corium used in the measurements was a mixture of UO_2, ZrO_2, and Zr, with the oxygen content being a parameter to reflect different stages of zirconium oxidation. The mixtures used in these tests span the range of U/Zr molar ratios representative of both PWR and BWR melt compositions. The test facility consisted of a one-dimensional (3 m long by 15 cm wide), refractory lined spreading channel. The core melts were generated using exothermic chemical reactions. Spreading was initiated using a "dam break" approach (i.e., spreading was initiated following meltout of a thin stainless steel barrier). The leading edge penetration as a function of time was measured. Based on the spreading rate, the corresponding corium viscosity was estimated from a well-known analytical solution which relates spreading rate to melt mass, channel width, and viscosity for viscous flows. Tests were conducted with compositions representative of Zr oxidation of 30, 50, and 70 % for both BWR and PWR melts. The data indicates that at a roughly constant temperature of 2500 C, the viscosity varies by as much as three orders of magnitude over this range of cladding oxidation.

1.0 INTRODUCTION

In the analysis of ex-vessel debris coolability, the ability to predict the extent of corium spreading following failure of the reactor pressure vessel (RPV) is important, since the area of the spread melt is inversely proportional to the debris depth to be cooled by overlying water for a given melt volume. The spreading extent is determined by many factors, but one of the most important is the corium viscosity. Due to the general importance of this physical property in the assessment ex-vessel MCCI and debris coolability, there have been several experimental programs carried out with the objective of measuring the viscosity as a function of temperature for several different corium compositions (Roche et al., 1993; and Skoutajan et al., 1979). A

rotational (Couette) viscometer was used in these experiments to carry out the measurements. However, as discussed by Seiler and Ganzhorn (1996), the use of this technique within the solidus/liquidus range may introduce important system effects (e.g., solid phase stratification due to the effects of inertia) which may not be representative of prototypic conditions.

Based on limitations associated with measuring corium viscosity using classical techniques, viscosity estimates have been made for various corium mixtures based on the spreading rate. The corium mixtures in these tests contain $(U,Zr)O_{2-x}$, with the oxygen content being a parameter to reflect different stages of zirconium oxidation. Mixtures have been tested which span the range of U/Zr molar ratios representative of both PWR and BWR melt compositions. The core melts are generated using exothermic chemical reactions. The facility consists of a one-dimensional spreading channel. Spreading is initiated using a "dam break" approach which is readily amendable to analysis. Based on the measured spreading rate, the corresponding corium viscosity is estimated using a well known analytical solution (Huppert, 1982) which relates spreading rate to initial melt mass, channel width, and viscosity for viscous flows. Although there is increased uncertainty associated with measurement of the corium viscosity using this approach, the overall technique does provide data on the *effective* viscosity associated with corium spreading over a horizontal surface, which is important in the early stages of ex-vessel spreading and debris coolability. Furthermore, the database can be used for validation of spreading models once suitable viscosity correlations have been developed.

2.0 EXPERIMENT DESCRIPTION

A schematic illustration of the facility is shown in Fig. 1. The test apparatus consisted of a one-dimensional spreading channel which has internal dimensions of 3.58 m long by 15.9 cm wide. The melt was generated through a chemical reaction at one end of the spreading channel; details of the melt generator region are provided in Fig. 2. The powders were initially separated from the open channel by a meltout barrier (i.e., stainless steel shim stock). This barrier failed by melt through at the end of the burn, thus initiating a one-dimensional "dam break" spreading experiment. This approach for initiating the tests had the following advantages: (i) it is simple and reliable (i.e., a separate melt generator is not required) and (ii) test results can readily be analyzed to determine flow regimes and corium viscosity since the test initial conditions are consistent with those assumed by Huppert (1982) in his analysis of viscous free surface flows.

One of the key experimental objectives was to realize isothermal spreading conditions to the greatest extent possible, since corium viscosity is a strong function of temperature (Roche et al., 1993) The principal structural material for the test section was castable MgO; following placement of the MgO, the substrate surface and sidewalls were lined with a 1.3 cm thick layer of castable ZrO_2, which has a low thermal conductivity of 1.2 W/m•K at 1200 C. After placement of the ZrO_2, the channel width was equal to 15.88 cm. The top cover of the apparatus consisted of a layer of 20 mil tungsten shim stock backed up by a 1.3 cm thick layer of low density ZrO_2 insulator board (thermal conductivity of 0.3 W/m•K at 1700 C). Thus, the upper cover of the apparatus was insulated to the greatest extent possible in order to minimize upwards heat losses during the spreading phase.

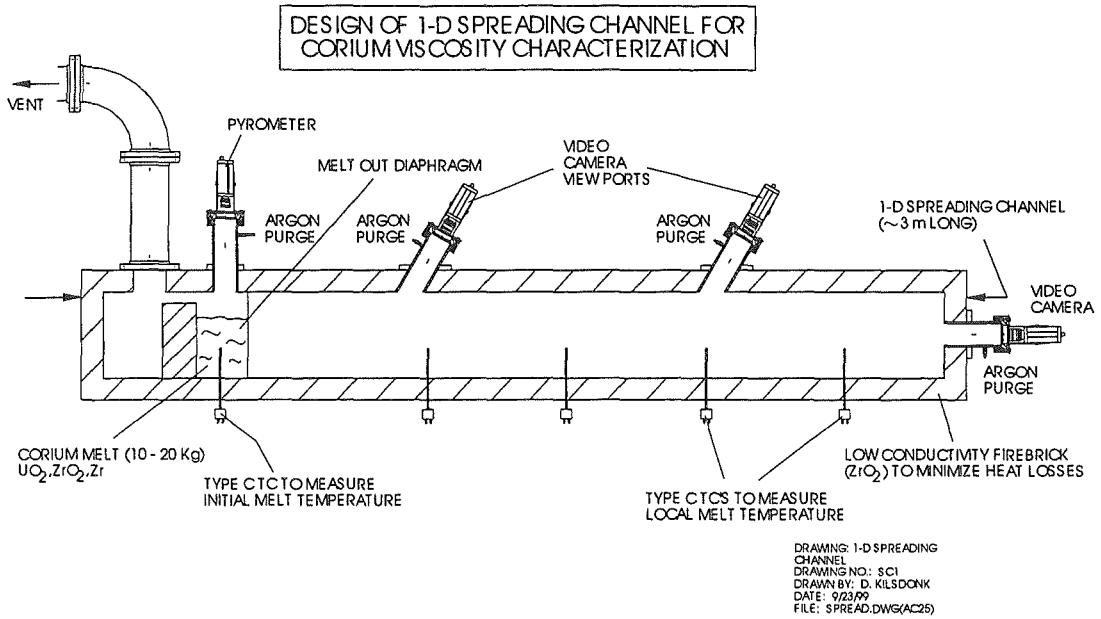

Fig. 1. Schematic Illustration of Test Facility.

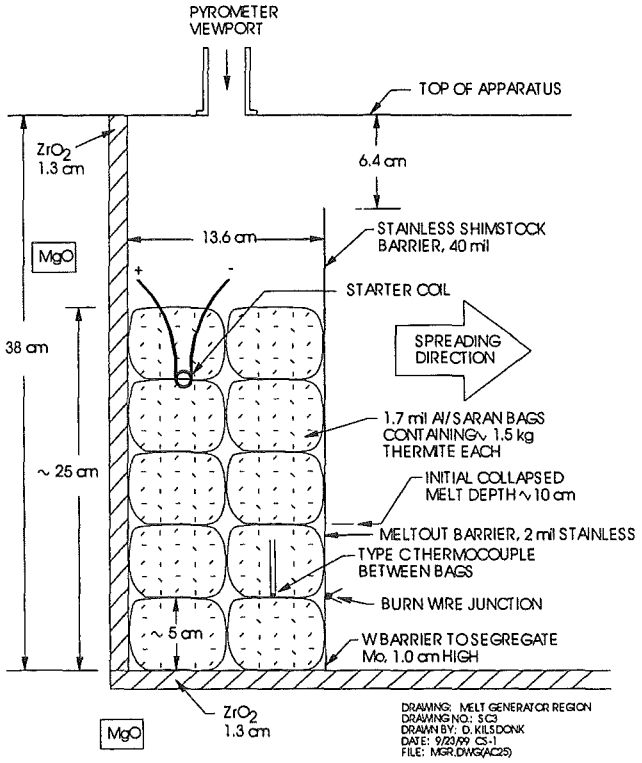

Fig. 2. Details of Melt Generator Region.

In terms of evaluating the corium viscosity, the principal data to be obtained from the tests was the melt leading edge location versus time. This was obtained through the use of an array of burn wires positioned at the center of the channel flush with the spreading surface. Melt temperatures were measured at several locations along the length of channel using 1.6 mm diameter grounded junction Type C thermocouples located 6 mm above the spreading surface. This data was used to evaluate the temperature loss as the corium spread. The initial melt temperature was also measured using a Type C thermocouple and a two-color pyrometer; the pyrometer viewport location is shown in Fig. 1. The spreading behavior was recorded by several video cameras mounted at various positions along the spreading channel. During the test, argon was purged through the video camera and pyrometer viewports to prevent aerosol deposition on the viewport windows. The purge gas, as well as any gases/aerosols generated during the experiment, exited the test section through a water cooled vent line located on the lid of the apparatus behind the melt generator region. The vent line was routed to a scrubber and then a high efficiency (HEPA) filter system for cleanup prior to discharge from the building. The vent line exit was deliberately placed near the melt generator region in an effort to remove as much aerosol as possible from the test section to improve the video data.

As noted earlier, the corium compositions were generated through exothermic chemical reactions. Prior to initiating the spreading tests, both analysis and supporting benchtop tests were performed in order to design mixtures which generate prototypic melts with 30, 50, and 70% Zr oxidation for both BWR and PWR core compositions. In these reactions, the U, Zr, and O contents were fixed at the target values for a given level of Zr oxidation. Initial powder constituents included UO_3, U_3O_8, U, Zr, and MoO_3. The reaction heat was adjusted by varying the amount of U/U_3O_8 present in the initial powder mix; Zr was always incorporated in metallic form. Molybdenum trioxide (MoO_3) was utilized as the principal oxygen provider in the reactions. The required MoO_3 content in the mixture was determined by the amount of oxygen required to obtain a particular level of Zr oxidation given the initial U/U_3O_8 content in the thermite. Mo metal was generated as a reaction byproduct. Advantages of Mo metal in this application include low vapor pressure, low solubility in the oxide phase, and rapid phase segregation due to the large density difference between the metal and oxide phases. A segregation technique was used to separate the Mo from the $(U, Zr)O_{2-x}$ phase prior to initiating spreading; the method for accomplishing this is described below. Several developmental tests were performed in order to adjust the compositions to achieve a nominal reaction temperature of 2500 C. The tests were also used to confirm Mo segregation during the reaction, and that the resultant oxide phase flowed at the reaction temperature.

As described above, the Mo metal reaction byproduct was removed from the core oxide phase prior to initiating spreading using a segregation technique. As shown in Fig. 2, this was accomplished through the use of a tungsten barrier located at the lower front edge of the melt generator region. The cross-sectional area of the generator region was configured to produce a nominal 10 cm deep melt depth after the reaction was complete for all tests. The tungsten barrier was 1 cm high, which corresponds to the depth of molten Mo metal nominally produced during the reaction for the given generator region floor area. Thus, the ideal scenario was rapid Mo separation from the oxide phase, with subsequent retention by the tungsten barrier in the melt generator region after spreading was initiated. (Data on the degree to which this approach

was successful is provided later). The powder mixtures were packed into the test section in aluminized bags which minimized the spread of contamination, and also prevented moisture infiltration into the powders as the experiment setup progressed. The reaction was initiated by a nichrome starter located at the top of the bed of powders (see Fig. 2). After ignition, the burn front proceeded downward. After the burn was completed, the lower portion of the meltout barrier (i.e., <10 cm) failed thereby initiating the spreading test. The lower portion of the barrier was constructed from 2 mil stainless shim stock. The upper portion of the barrier was constructed from heavier (20 mil) stock, which was intended to remain intact during the burn and also provide low heat capacity to minimize crust deposition on this surface.

After the test was completed, the lid of the apparatus was removed. The debris was photographed and the debris spatial distribution was measured. The solidified material was then removed from the test section. During removal, the Mo retained in the melt generator region was recovered and placed in a separate container for weighing.

During the program, a special thermite was designed to produce a 80/20 wt % Al_2O_3/SiO_2 melt at ~ 2100 C. The viscosity of this mixture is well known at the reaction temperature (Urbain et al., 1982). This composition was tested to verify that the experiment technique is able to reproduce the known viscosity; the results were positive in this regard given the measurement uncertainty. The results of this calibration test are provided in detail elsewhere (Farmer et al.; 1998).

3.0 TEST RESULTS

A summary of the target initial conditions for the eight tests conducted as part of the program is provided in Table 1. Tests 0, 2, and 3 constitute a parametric study of the effect of Zr oxidation on the corium viscosity at a nominal melt temperature of ~2500 C for BWR core melts; Tests 5-7 provide the same information for PWR melts. Test 1 was conducted to examine the effect of stainless steel on the viscosity for a PWR composition. As discussed above, Test 4 was performed as a check on the experiment technique for characterizing melt viscosity; the results of this test are described in detail elswhere (Farmer et al., 1998). All reactor material tests were conducted with an initial melt mass of 15 kg with the exception of Test 1, which was conducted with 10 kg. As shown in Table 1, the spread melt mass for all tests except Test 1 was less than the initial mass due to the fact that Mo metal segregated during the reaction and was retained in the melt generator region. Thus, the target melt spreading mass shown in Table 2 defines the actual prototypic corium mass which was intended to participate in the spreading transient. For Test 1, the spread mass equaled the initial mass since there was no Mo metal generated as a reaction byproduct (i.e., the tungsten retainer lip was not included in the melt generator for this test; see Fig. 2). The range of chemical mixtures used in these tests is illustrated in Table 2, which provides the pre- and post-reaction compositions for Tests 2 (BWR, low Zr oxidation) and 6 (PWR, high Zr oxidation). As is evident from this table, the thermites designed to produce $(U,Zr)O_{2-x}$ melts typically contained 17-18 wt % (viz. ~ 10 vol%) Mo metal as a reaction byproduct.

Table 1 Summary of Test Specifications.

Test No.	Case	Spread Melt Composition (wt%)	Initial Melt Mass (kg)	Spread[a] Melt Mass & Volume (kg/liters)	Initial Melt Temp. (C)
0	BWR, 50% Oxidized	63.5/21.0/15.5 $UO_2/ZrO_2/Zr$	15.0	12.47/1.66	2500
1[b]	PWR, 37 % Oxidized with 18 wt% Stainless Steel	57.8/10.5/13.6/14.4/3.7 $UO_2/ZrO_2/Zr/Fe/Cr$	10.0	10.0/1.33	2500
2	BWR, 30% Oxidized	65.0/12.8/22.2 $UO_2/ZrO_2/Zr$	15.0	12.29/1.63	2500
3	BWR, 70% Oxidized	62.2/28.7/9.1 $UO_2/ZrO_2/Zr$	15.0	12.65/1.70	2500
4	Calibration Test	79.9/20.1 Al_2O_3/SiO_2	10.0	8.04/2.64	2100
5	PWR, 50% Oxidized	80.6/11.1/8.3 $UO_2/ZrO_2/Zr$	15.0	12.47/1.55	2500
6	PWR, 70% Oxidized	79.6/15.5/4.9 $UO_2/ZrO_2/Zr$	15.0	12.44/1.55	2500
7	PWR, 30% Oxidized	81.5/6.8/11.7 $UO_2/ZrO_2/Zr$	15.0	12.43/1.54	2500

[a]For all tests except Tests 1 and 4, the difference between the initial and spread melt masses is due to the intended retention of metal reaction byproduct by a tungsten retainer lip in the melt generator region.
[b]The spread mass equals the initial mass for this test since a tungsten retainer lip was not included in the test design (i.e., no Mo metal reaction byproduct was produced during this test).

Table 2 Pre- and Post- Thermite Reaction Compositions for Spreading Tests 2 and 6.

	Test 6 (70 % Ox. PWR)			Test 2 (30 % Ox. BWR)		
	Reactant (wt%)	Product (wt%)		Reactant (wt%)	Product (wt %)	
Chemical		Before Mo Segregation	After Mo Segregation		Before Mo Segregation	After Mo Segregation
U	43.7	-	-	46.9		-
U_3O_8	17.1	-	-	-	-	-
UO_2	-	66.0	79.6	-	53.2	65.0
Zr	13.6	4.1	4.9	26.0	18.2	22.2
ZrO_2	-	12.8	15.5	-	10.6	12.8
MoO_3	25.6	-	-	27.1	-	-
Mo	-	17.1	-	-	18.1	-

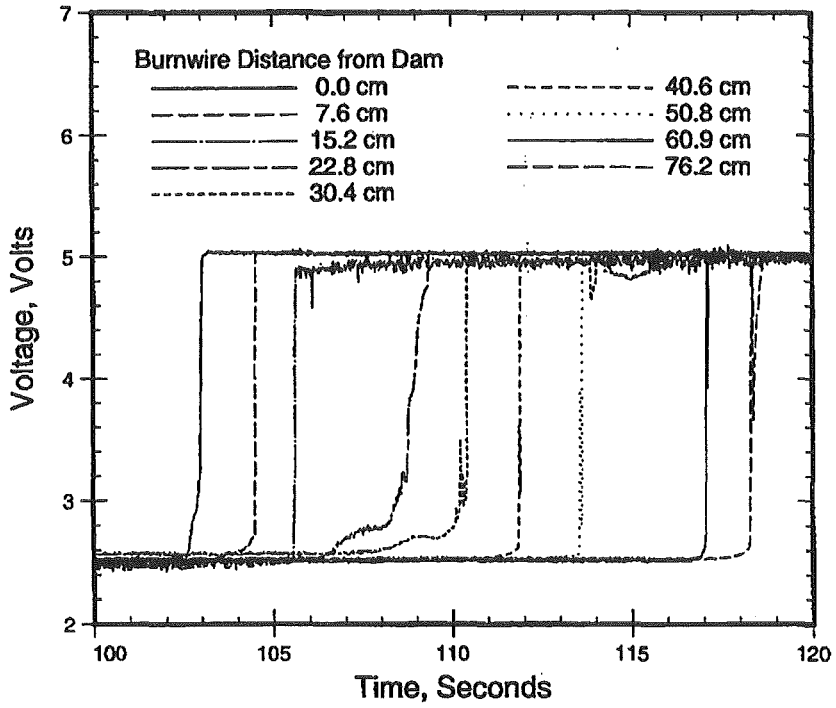

Fig. 3. Typical Burnwire Data (Test 5).

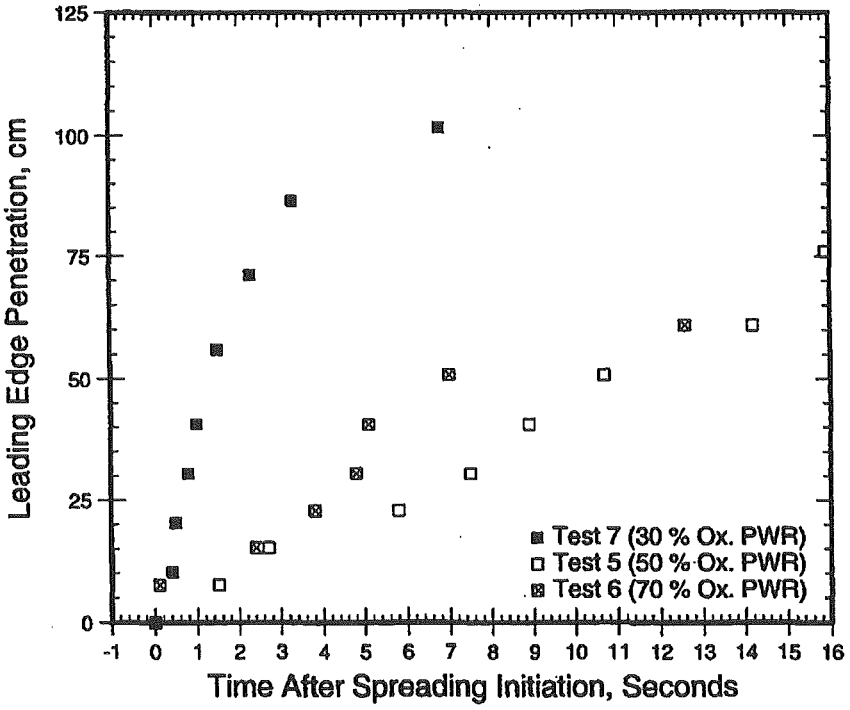

Fig. 4. Leading Edge Penetration Data for PWR Test Series.

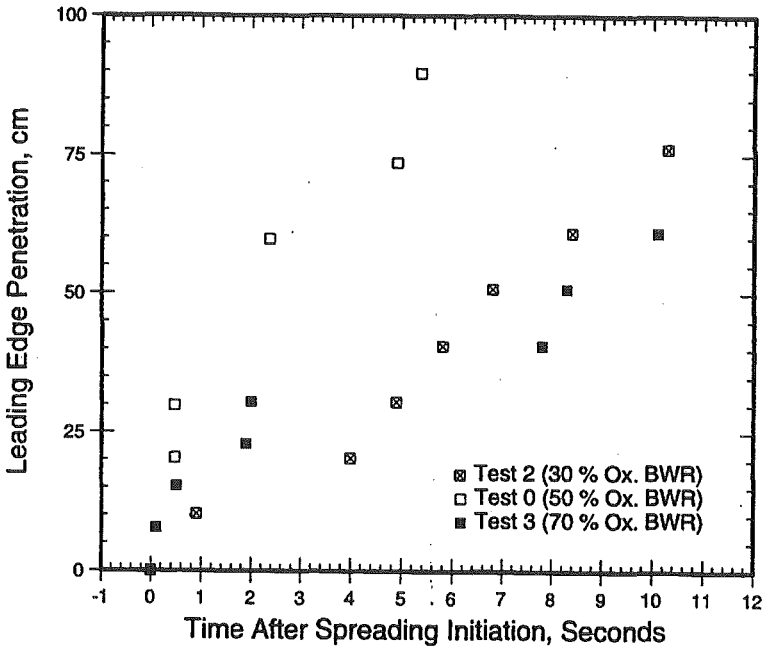

Fig. 5. Leading Edge Penetration Data for BWR Test Series.

Typical melt spreading rate data obtained for a given test is illustrated in Fig. 3, which provides the burnwire signals for Test 5 (50% oxidized PWR case). The melt leading edge location versus time was readily deduced from this information; the results are provided in Fig. 4 for the three PWR tests which parameterize on the extent of cladding oxidation. The melt arrival times in this figure (and all others) have been shifted such that t = 0 corresponds to the onset of spreading for each test, as indicated by the data from the burn wire located on the dam surface (see Fig. 2). The analogous information for the BWR test series is shown in Fig. 5.

Typical melt temperature data is illustrated in Fig. 6, which shows the response of two Type C thermocouples located downstream from the dam for Test 5. (The response of these TC's after the time the junctions failed is not shown for clarity). The actual initial melt temperature at the start of the spreading transient is shown in Table 4 for each test. An assessment of the pyrometer and Type C thermocouple data for the reactor material tests indicates that the melt temperature drop over the course of the spreading transient was nominally 50 C within the refractory test section. For the tests in which Mo metal was generated, the solidifed metal ingot at the base of the melt generator region was recovered and weighed to determine the effectiveness of the segregation technique. The data from these measurements is provided in Table 3, along with the initial Mo mass present in each mixture. Based on the discrepany between the initial and recovered Mo masses, the amount of Mo metal estimated to be present in the spread oxide phase is also shown in the table. Note from Table 3 that for four of the six tests, the segregation technique worked reasonably well, with Mo contamination levels less than ~ 1 wt %. For the other two tests, a significant fraction of the Mo (i.e., ~ 12 wt %) went downstream with the oxide during the spreading transient. For these two tests, the Mo was found to be in the form of small (several mm diameter) spheres dispersed throughout the oxide phase.

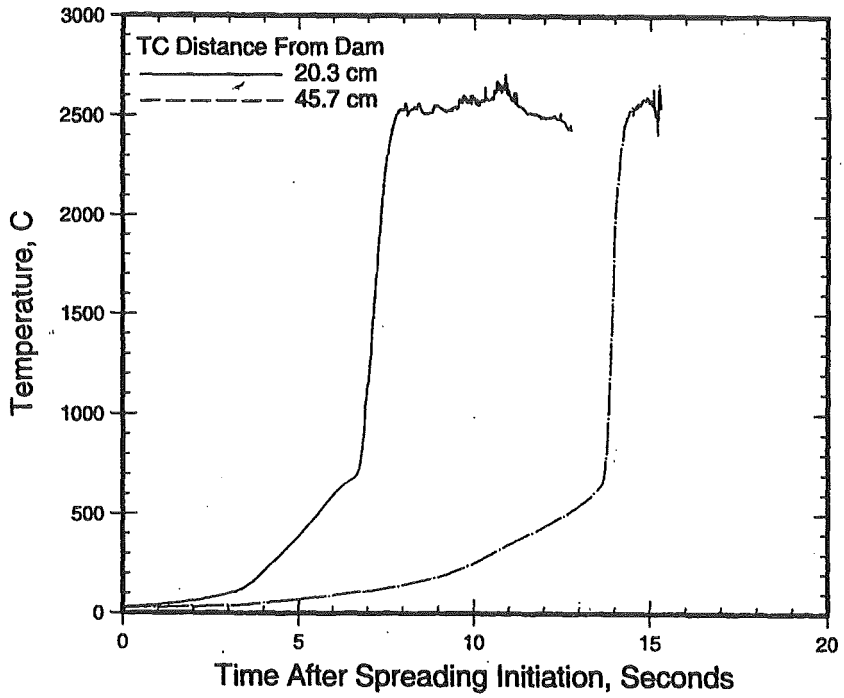

Fig. 6. Melt Temperature Measured at Two Locations for Test 5.

Table 3 Summary of Recovered Mo Mass for Spreading Tests.

Test No.	Mass Mo[b] Recovered (kg)	Theoretical Mo Mass (kg)	wt%/vol% Mo Contaminant in Spread Melt	Estimated Density[a] of Spread Melt (kg/m^3)
0	0.78	2.52	11.6/8.8	7740
2	4.01	2.72	~0/~0	7550
3	2.94	2.36	~0/~0	7460
5	2.48	2.54	0.5/0.4	8040
6	2.41	2.56	1.2/0.9	8020
7	0.80	2.58	11.8/9.6	8273

[a]In the evaluation of the spread melt density, the densities of the individual melt constituents $UO_2/ZrO_2/Zr/Mo$ were assumed to equal 8.74/5.99/6.06/10.22 g/cm^3, respectively.
[b]In all cases, a coherent, high density metal mass was recovered from the retention basin of the melt generator region; the corresponding mass is shown. Often (particularly for Tests 2 and 3), oxide was bonded to the upper surface of the metal, and therefore complete separation was not possible.

In general, the corium viscosity for all tests was estimated from the leading edge data using Huppert's solution (1982), which relates leading edge penetration to the initial fluid volume, channel width, and viscosity. For the case of one-dimensional channel flow in which a finite volume of fluid is initially present on the spreading surface at time t = 0 (i.e., dam break problem), the solution is of the form:

$$L(t) = C\left(\frac{\rho g q^3}{\mu}\right)^{1/5} t^{1/5} \qquad (1)$$

The above equation provides a general relationship between leading edge penetration distance versus time. Huppert also performed an order-of-magnitude scaling analysis to determine the transition time, t_T, at which viscous and inertial forces are comparable. For the above stated set of assumptions, the solution for the transition time reduces to

$$t_T = \left(\frac{\rho^3 q^4}{g^2 \mu^3}\right)^{1/7} \qquad (2)$$

For times greater than t_T, viscous forces dominate the flow characteristics, while for times less than this, inertial forces are dominant. For these tests, the model is thus generally applicable in the latter stages of the spreading transient (i.e., for times $t > t_T$) in which viscous forces dominate the flow behavior.

To illustrate the method for evaluating the viscosity, the leading edge penetration data for Test 5 is plotted in Fig. 7 as a function of time raised to the 1/5 power. According to Eq. 1, after inertial effects have died away and viscous forces begin to dominate the flow characteristics, the leading edge penetration should become linear on this plot. As is evident from the figure, the data for spreading distances greater than ~ 25 cm do indicate a linear relationship, in agreement with the viscous flow theory. A least squares curve fit was performed on this data over the range in which linear behavior is observed (i.e., L > 20 cm); the fit is shown on the graph. From the slope of this line, the viscosity was back-calculated using Eq. 1, the spread melt volume shown in Table 1, and the estimated melt density shown in Table 2. The results of this analysis indicate that the viscosity for 50% oxidized PWR corium at an initial temperature of 2600 C is 13 cp, with an uncertainty range of 9 to 20 cp (based on error variance of curve fit). A check on the applicability of this approach is provided by Eq. 2, which predicts an inertia/viscous flow field transition time of ~11 sec given the evaluated viscosity and other input data described above. From Fig. 4, the overall duration of the spreading transient is ~16 s, which is greater than t_T for this test. However, as described by Huppert (1982), the analysis underlying Eq. 2 is order of magnitude; the data shown in Figs. 4 and 7 seem to indicate viscous-dominated flow for times greater than ~ 6 s. Evaluation of Eq. 2 for all tests generally indicated that this equation over-predicts the time at which viscous-type flow behavior is observed. The effect of the extent of cladding oxidation on corium viscosity at a constant temperature of ~ 2500 C is qualitatively illustrated in Fig. 8, which provides the leading edge penetration data for all BWR tests plotted vs. $t^{1/5}$. As is evident from this figure, the slopes of the penetration curves systematically decrease as cladding oxidation increases. From Eq. 1, this implies that the viscosity steadily increases as cladding oxidation increases at constant temperature.

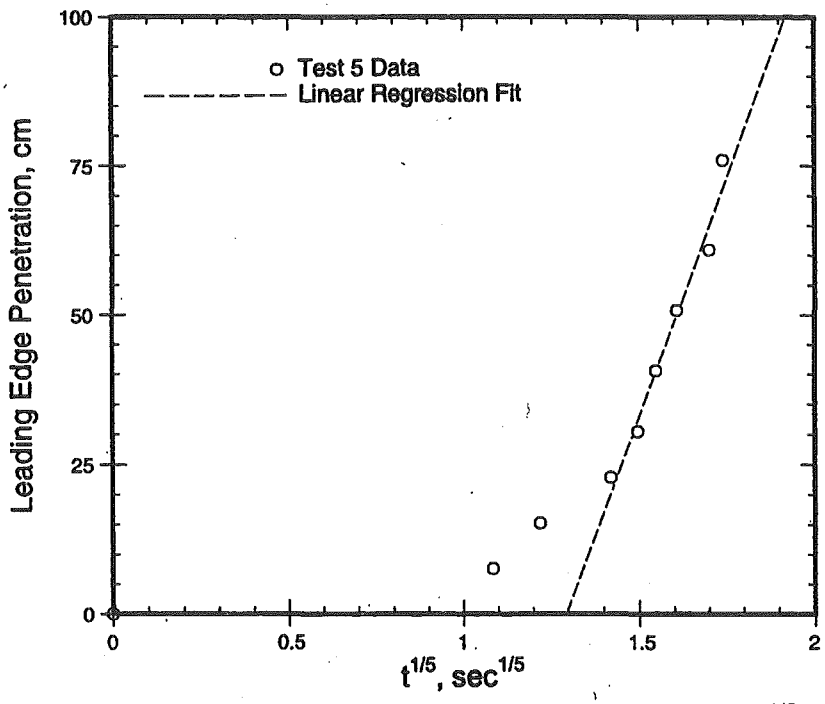

Fig. 7. Test 5 Leading Edge Penetration Data Plotted vs. $t^{1/5}$.

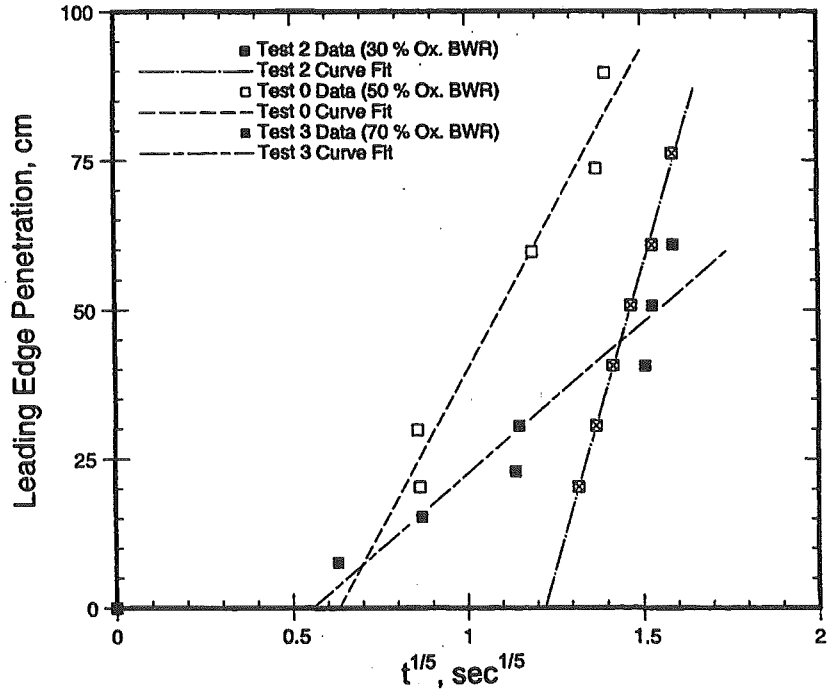

Fig. 8. BWR Test Series Leading Edge Penetration Data Plotted vs. $t^{1/5}$.

4.0 DISCUSSION

Table 4 provides a summary comparison of the melt temperature variation and estimated corium viscosity for the seven reactor material tests. Also included in this table are the measured solidus and liquidus temperatures which were obtained with the same core oxide mixtures in a companion study (Farmer et al., 1999). The target initial melt temperature for these tests was 2500 C; the realized temperatures were in the range of 2470 to 2600 C for tests conducted with corium consisting only of $(U,Zr)O_{2-x}$. Comparison of the melt temperatures with the liquidus-solidus data indicates that all tests were conducted well into the liquidus range with the exception of the 70 % oxidized tests, which were conducted at, or slightly below, the liquidus temperatures for the respective (BWR and PWR) compositions. Not suprisingly, these tests produced the highest viscosity estimates for each composition considered. This may be attributable to development of a solid phase within the melt as a result of the melt temperature falling below the liquidus during the spreading phase. A second possible explanation is the development of skin crusts which could retard the flow behavior.

Table 4 Summary of Corium Viscosity Test Results.

Test No.	Representing Reactor Configuration	Melt Temp. Variation During Spreading [a] (C)	Best Estimate Viscosity (cp)	Viscosity Uncertainty Range (cp)	Corium[b] Solidus/Liquidus (C/C)	wt% Mo in Spread Melt
2	BWR, 30% Oxidized	2520→ 2470	4.4	3.8 to 5.0	1930/2198	~ 0
1	PWR, 37 % Oxidized with 18 wt% Stainless Steel	2350→ 2300	11	2.2 to 68	---/---[c]	N/A
0	BWR, 50% Oxidized	2470→ 2420	114	65 to 218	2000/2330	11.6
3	BWR, 70% Oxidized	2530→ 2480	5070	2650 to 10700	2042/2475	~ 0
7	PWR, 30% Oxidized	2550→ 2500	8	6 to 12	2005/2465	11.8
5	PWR, 50% Oxidized	2600→ 2550	13	9 to 20	2080/2500	0.5
6	PWR, 70% Oxidized	2540→ 2490	108	57 to 227	2105/2520	1.2

[a]Estimated temperature loss during the spreading phase is ~50 C for all tests.

[b]Based on measurements with same corium compositions (minus Mo) in separate facility (see Farmer et al. 1998).

[c]Solidus/Liquidus temperature measurements were not performed for this particular composition (Farmer et al., 1998).

The viscosity data for tests in which the spread corium consisted of $(U,Zr)O_{2-x}$ is plotted in Fig. 9 as a function of cladding oxidation. The data for both the BWR and PWR test series indicates the trend of increasing viscosity with increasing cladding oxidation at roughly constant temperature. In general, the BWR melt compositions exhibit higher viscosity in comparison to the PWR compositions, particularly as the oxidation state increases. Aside from the above mentioned effect of solids within the melt, this trend could also arise if the ZrO_2 component of the oxide phase has a higher viscosity in comparison to UO_2, since UO_2 and ZrO_2 are miscible at melt conditions. However, the authors are not aware of viscosity data for pure ZrO_2, so no further conclusions in this regard can be drawn.

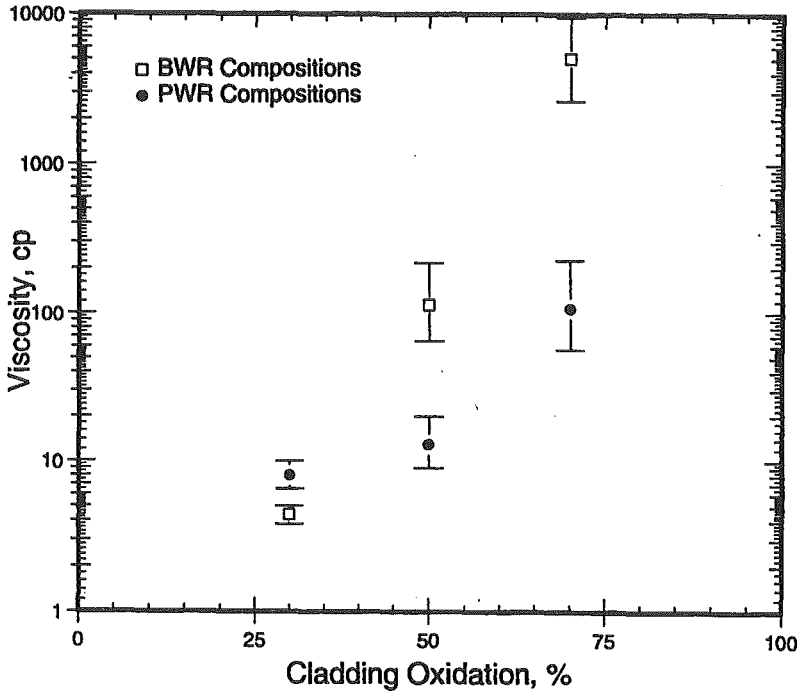

Fig. 9. The Effect of Cladding Oxidation on Viscosity for BWR and PWR Melt Compositions.

5.0 SUMMARY AND CONCLUSIONS

Viscosity estimates have been made for both BWR and PWR corium compositions based on the spreading rate. The test facility consisted of a one-dimensional (3 m long by 15 cm wide), refractory lined spreading channel. The core melts were generated using exothermic chemical reactions. Spreading was initiated using a "dam break" approach (i.e., spreading was initiated following meltout of a thin stainless steel barrier). The leading edge penetration as a function of time was measured. Based on the spreading rate, the corresponding corium viscosity was estimated from a well-known analytical solution which relates spreading rate to melt mass, channel width, and viscosity for viscous flows. Tests were conducted with compositions representative of Zr oxidation of 30, 50, and 70 % for both BWR and PWR melts. The data indicates that at a roughly constant temperature of 2500 C, the viscosity increases by approximately one order of magnitude for PWR compositions over this range of cladding oxidation. For BWR compositions, the viscosity was found to increase by as much as three orders of magnitude over the same oxidation range. At the highest cladding oxidation state considered (i.e., 70 %), there is evidence that the increased viscosity is due to development of a solid phase within the melt as a result of the melt temperature falling below the liquidus.

NOMENCLATURE

C	constant, 1.411....
g	gravitational acceleration
L	melt leading edge penetration distance
m	spreading melt mass
ρ	melt density
q	$m/\rho W$
t	time after spreading initiation
μ	kinematic viscosity
W	spreading channel width (15.88 cm)

ACKNOWLEDGMENTS

Support for this work was provided by the International Nuclear Safety Center (INSC) at Argonne National Laboratory. The report was prepared for publication by Kathy Rank. These efforts are greatfully acknowledged.

REFERENCES

Farmer, M. T., Spencer, B. W., and Aeschlimann, R. W., 1999. Liquidus/Solidus and Zr Solubility Measurements for PWR and BWR Core Melt Compositions. In: OECD Workshop on Ex-Vessel Debris Coolability, Karlsruhe, Germany, 15-18 November.

Farmer, M. T., McUmber, L. M., Aeschlimann, R. W., and Spencer, B. W. Final report on severe accident material property measurements, ANL Report, ANL-NT-88, October, 1998.

Huppert, H. E., 1982. The propagation of two-dimensional and axisymmetric viscous gravity currents over a rigid horizontal surface. *J. Fluid Mechs.* **121.**

Roche, M. F., Leibowitz, L., Fink, J.K., and Baker Jr., L. Viscosity of corium mixtures at high temperatures, Advanced Containment Experiments Report, ACE-TR-C37, 1993.

Seiler, J. M. and Ganzhorn, J., 1996. Viscosities of corium-concrete mixtures. In: 14th European Conference on Thermophysical Properties, INSA, Lyon, France, September 16-19.

Skoutajan, R., Baukal, W., Konig, R., Wagnar, W., and Walter, G. Durchfuhrung von viskositatsmessungen an oxidishcen corium-beton-schmelzen, Battelle Report, BF-R-63.556-1, 1979.

Urbain, G., Bottinga, Y., and Richet, P., Viscosity of liquid silica, silicates, and alumino-silicates. *Cosmochimica Acta*, **46**, 1982.

OECD Workshop on Ex-Vessel Debris Coolability
Karlsruhe, Germany, November 15-18, 1999

Organised in collaboration with
Forschungszentrum Karlruhe (FZK) GmbH

METHODOLOGY FOR CORIUM-CONCRETE VISCOSITY CALCULATIONS

G. COGNET, F. SUDREAU, M. RAMACCIOTTI, C. JOURNEAU, J.M. SEILER

CEA, Cadarache, Direction des Réacteurs Nucléaires,
13108 Saint Paul Lez Durance - France
gerard.cognet@cea.fr

ABSTRACT

In the case of a severe core melt accident in a nuclear power plant, the scenarios in which the reactor vessel fails and the mixture, called corium, composed of the molten core and of the vessel metallic structures, flows into the reactor pit cannot be excluded. Among the numerous physical characteristics to be taken into account in corium behavior modeling during its progression out of the vessel, viscosity plays a particularly important role.

An accurate estimation of the apparent viscosity of corium mixtures is today very difficult. Indeed, these mixtures can have very different possible compositions, in particular the concrete content can significantly vary with type of reactors, considered scenarios, and time after vessel failure . However, viscosity models are needed for the evaluation of both scenarios and mitigation devices such as core-catchers.

The work presented in this paper aims at providing a methodology for corium - concrete viscosity calculations which would be the most possible general. This methodology is based on the evolution of melt composition and various viscosity models to take into account the silica content and the presence of a solid phase.

1. INTRODUCTION

In the hypothetical event of a severe accident in a Light Water Reactor, scenarios in which the reactor pressure vessel (RPV) fails and the core melt mixture (named *corium* and essentially composed of UO_2, ZrO_2, Zr, Fe and fission products) relocates into the reactor cavity, cannot be excluded. Whatever the scenario considered, from the beginning of core melting up to the control of the accident by stopping and cooling the corium, the knowledge of corium physical properties versus temperature is essential to predict scenario evolutions with a view to managing the accident. Among the numerous physical characteristics to be taken into account in corium behavior modeling during its progression out of the vessel, viscosity (in fact, corium rheological behavior) plays a major role.

For these reasons, it is important to be able to predict an apparent viscosity of corium melts of different compositions, essentially based on refractory oxides (urania, zirconia) mixed with silica, calcia, iron oxides and in some scenarios with metals (iron, zirconium,...), not only above the liquidus temperature but also in the solidification range (solidus - liquidus temperature interval). Indeed, crystallization, which occurs within this range (for such mixtures, it can reach 1000 K), entails the formation of solid particles (globules or dentrites) and a continuous evolution of the liquid phase composition. These 2 combined effects induce an evolution of the apparent viscosity of the melt. In particular, for oxidic melts with silica, an increase of viscosity is observed which is not only due to the increase of particles in the melt but also to the increase of the residual liquid phase viscosity.

This paper presents a general methodology to calculate the apparent viscosity of corium - concrete mixtures above the liquidus temperature as well as in the solidification range. This methodology follows the approach previously developed for lavas by Ryerson et al. (1988) and firstly applied to corium by Seiler and Ganzhorn (1997).

2. VISCOSITY OF THE LIQUID PHASE

Above liquidus temperature, two models are available. For a mixture without silica, the Andrade model (1934a, 1934b) adapted by Sudreau and Cognet (1997) satisfactorily fits the experimental data and will not be described in this paper.

The viscosity of liquids containing silica (SiO_2), alumina (Al_2O_3), and/or hematite (Fe_2O_3) is generally greater than 10mPa.s, essentially due to the presence of SiO_2 which allows strong covalent bonds. According to a classification, proposed by Carron (1969), the species present in the liquid are grouped in three categories :

1. the 'glass formers' such as Si, which forms the 3-dimensional structure
2. the modifiers such as Na^+, K^+, Ca^{2+}, Fe^{2+}, Ti^{4+}, Zr^{4+}, Mg^{2+}, which contribute to decreasing melt viscosity
3. the amphoterics such as Al^{3+}, Fe^{3+}, which may act either as glass formers or as modifiers.

This classification allows the effect of the different constituents of the liquids on the viscosity to be taken into account.

A model was proposed by Urbain (1987) for the estimation of the viscosity of ternary liquids in the SiO_2-Al_2O_3-CaO system from the knowledge of its composition at a given temperature. This model described the viscosity using the Weymann relation which can be written as

$$\eta = 0.1AT\exp((1000.B)/T) \quad (1)$$

where T is the absolute temperature, A and B two parameters depending only on the composition of the melt (Urbain, 1974) which has been linked through the empirical equation

$$-\ln A = 0.29\ B + 11.57 \quad (2)$$

by studying 60 different compositions of ternary SiO_2-Al_2O_3-MO and SiO_2-Al_2O_3-M_2O mixtures (where MO and M_2O represent the bi - and mono-valent metallic oxides). A has units of Poise K^{-1} and B has units of K. The calculation of the viscosity of a silicate melt at any given temperature

thus consists of the determination of the B parameter. Urbain plotted this parameter in a diagram available for the SiO_2-CaO-Al_2O_3 system (see Figure 3) and proposed to extend it to TiO_2-A_2O_3-MO mixtures where T refers to a cation in a tetrahedral position (mainly Si^{4+}), M to Na^+, K^+, Ca^{++}, Fe^{++}, $Ti^{4+,}$ Mg^{2+} for modifiers and A to Al^{3+}, Fe^{3+} for amphoteric cations. In this diagram, the lines represent the iso-values of the B parameter versus the composition of the melt.

It is important to note that the role of Fe^{2+} and Fe^{3+} is not clearly identified but some measurements in a quaternary system seem to corroborate this classification.

We used the GEMINI thermodynamic code (Chevalier, 1992) to determine the composition of the remaining liquid phase. GEMINI calculates the thermodynamic equilibrium between materials by minimizing the Gibbs energy of the system and uses a 14 element database dedicated to nuclear safety problems. We calculate the molar fractions of formers y(F), of amphoterics y(A) and modifiers y(M) using the molar percentages of species present in the liquids calculated by GEMINI2, by applying an equivalent model for a TiO_2-A_2O_3-MO system. Parameter B is calculated with

$$B = B_0 + B_1\, y(F) + B_2\, y(F)^2 + B_3\, y(F)^3 \qquad (3)$$

$$B_0 = 13.2 + 41.5\,\alpha - 45\,\alpha^2,$$

$$B_1 = 30.5 - 117.2\,\alpha + 130\,\alpha^2, \qquad (4)$$

$$B_2 = -40.4 + 232.1\,\alpha - 298.6\,\alpha^2,$$

$$B_3 = 60.8 - 156.4\,\alpha + 213.6\,\alpha^2 \text{ with } \alpha = y(M)/(y(M) + y(A)).$$

N is the molar fraction of silica - MO stands for all modifiers and to represent this group by a single molar fraction the individual Mi moles are added according to $M = \Sigma_i\, M_i.L_i$ where Li is the number of oxygen atoms present in the i molecule. It must be noted that these coefficients have been improved by Urbain (1987) respective to a first publication (Urbain, 1982).

In the case of corium, the behaviour of zirconia (considered as a modifier by Urbain (1974, 1987)) and urania must be taken into account. We first chose to classify UO_2 as modifier because of its similarity with zirconia (it is noted that the percentage of ZrO_2 never exceeded 0.14%w in the Urbain sudies).

2.1. Application to basalts

Bottinga and Weill (1972) observed that the log-viscosity of silicate melts varies linearly with composition in simple systems and over-restricted intervals of composition. Such an arbitrarily defined composition interval in the silica mole fraction allows us to obtain an estimate of the viscosity $\eta(T)$ with the relation :

$$\ln\eta(T) = \sum D_i(T)\, y_i \qquad (5)$$

in which y_i is the molar fraction of species i, and $D_i(T)$ a constant characteristic of the i species and of the silica mole fraction. The $D_i(T)$ values are obtained by least square fitting this relation to published data.

We applied the Urbain model to about 20 different basalt compositions and obtained a better agreement with it than with the Bottinga and Weill calculations as shown in Figure 1.

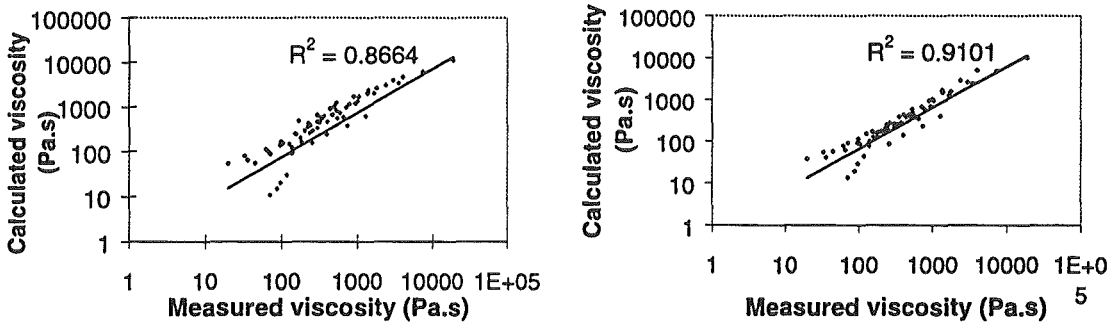

Fig. 1 **a** : comparison of measured viscosities for different basalts - viscosities calculated with the Bottinga and Weill modelling

b : Comparison of measured viscosities for different basalts - viscosities calculated with the Urbain modelling.

2.2. Application to basalts with 18%w of UO_2

If many experimental studies exist on basalts, very few data on the mixtures containing silica and UO_2 are available in the literature. The measurements used below are from a study carried out by Leibowitz et al. (1974) on a basalt (Columbia River Basalt) and on a mixture of basalt and UO_2 using a concentric viscometer of Couette type. All the viscosities are supposed to be measured at temperatures above the liquidus temperature. The composition of the different mixtures, the temperature ranges studied and the solidus and liquidus given by the GEMINI program with the TDBCR971 database are shown in Table 1. It is to be noted that the TDBCR971 base not containing Na_2O, 3%w of sodium oxide contained in the basalt have been arbitrarily added to the mass percentage of lime. The methodology presented above to calculate the viscosity of the liquid phase is applied by considering UO_2 and FeO as modifiers and Fe_2O_3 as an amphoteric. The points representing the composition of the mixture at 1800 and 2100 K with 18%w of UO_2 are located in a zone of the URBAIN diagram validated experimentally on the SiO_2-CaO-Al_2O_3 mixture.

Several measurements were made in the solidification interval estimated using the GEMINI calculations. We thus assumed that in this case, the experimental temperature is equal to the calculated liquidus temperature. In the case of the basalt mixture with 18%w of UO_2, the solid volume fraction estimated at 1800K is very low, of about 0.04, and does not therefore significantly influence the viscosity of the mixture.

It can be seen in Figure 2 that the measured viscosity decreases when the proportion of UO_2 increases in the mixture. This effect is reproduced by the calculation by considering UO_2 as a modifier or as an amphoteric. However, calculations better fit experimental data when UO_2 is consider as a modifier (Figure 2). This has also been observed by Seiler and Ganzhorm (1997) on corium-27 wt% sileceous concrete mixture. Moreover, the viscosity calculations made with the

URBAIN model provide a very satisfactory agreement with the experimental data (less than 30% deviation between experiment and calculation).

Table 1 Composition of CRB basalt and CRB basalt+UO_2 melts - Temperature range

Composition	$T_{solidus}$ - $T_{liquidus}$ (K) GEMINI calculations	Experimental range T(K)
Basalt (Columbia River Basalt)	1350 K - 1730 K	1632 K - 2205 K
Basalt + 1.6%w UO_2	1400 K - 1750 K	1922 K - 2233 K
Basalt + 18%w UO_2	1400 K - 2100 K	1805 K - 2025 K

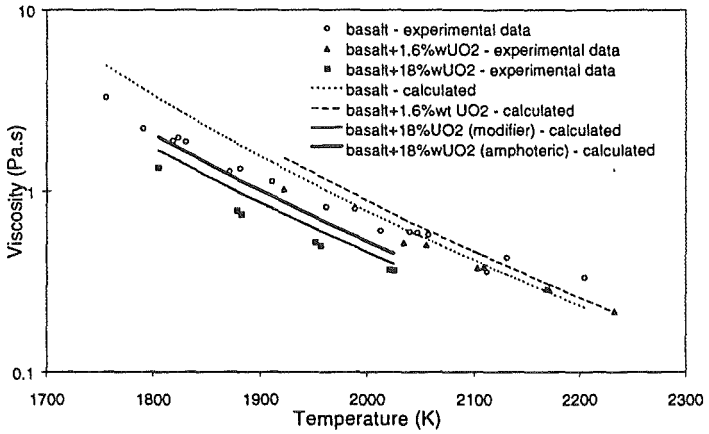

Fig. 2 Comparison of the measured and calculated viscosities for basalt containing UO_2

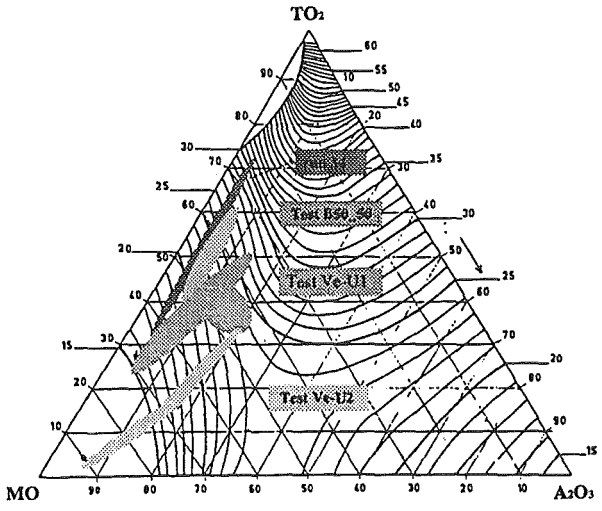

Fig. 3 URBAIN Diagram

2.3. Corium-concrete melts

It is important to underline that the compositions used above do not represent typical corium compositions considered in the case of an interaction between corium and concrete. In this last case, the quantities of silica present in the mixtures would be less as is shown in Table 2 for different corium-concrete mixtures.

In some cases, for example for the VULCANO VE-U1 and VE-U2 tests, the evolution of the composition of the residual phases could reach a field where no data exists as is represented in Figure 3 in the Urbain diagram. Nevertheless, on the basis of currently available data, we propose to use the Urbain formulation (equations (1) to (4)) to model the viscosity of silicate liquids. Indeed, its application to mixtures, the composition of which are given in Table 2, gives good results as it will be shown in the next paragraph for the Battelle corium - concrete.

However, because of the lack of direct viscosity measurements, the limitations of such a model be kept in mind when applying it to corium-concrete mixtures.

Table 2 Composition of different corium-concrete mixtures

Composition	Battelle 50%corium-50%concrete Tliq=2100K (Skoutajan, 1979)	Run 34 Tliq=2300K (Roche, 1993)	Test VE-U1 Tliq=2300K (Cognet, 1998)	Test VE-U2 Tliq=2550K
MgO	1.65	0.22		
CaO	5.85	4.2	0.7	0.8
Al_2O_3	6.3	1.26	0.1	0.2
SiO_2	34.11	21.51	19.6	2.2
Fe_2O_3	2.1	0.31	1.9	1.6
UO_2	26.7	56.55	45	60
ZrO_2	9.8	15.95	19.3	24
FeO	13.5			
Fe_3O_4			13.4	11.2

3. APPARENT VISCOSITY OF SOLIDIFYING CORIUM-CONCRETE MIXTURES

The viscosity of a melt composed of the main corium components (UO2, ZrO2, Zr, Fe...) and concrete byproducts (SiO_2, CaO, Fe_xO_y ...) can vary considerably between solidus and liquidus temperatures. The range between these temperatures can be wide (~1000K) because of the presence of concrete decomposition products such as silica, which tends to lower the solidus temperature of these mixtures. During the solidification phase, the viscosity of these compounds increases as the solid phase fraction increases.

The rheology of suspensions has been the subject of thorough research for many years, mainly because of its obvious importance in a wide range of industrial applications. The rheological models are not only dependent on the properties of the suspended and suspending materials but also on the nature of the interactions and the type of flow being experienced (Jeffrey, 1976). A large number of factors affect the rheological properties of suspensions : the concentration of the suspended particles, the particle shape, the mean size and size distribution, the properties of the continuous fluid, the ability of particles to deform, the maximum packing fraction, the mechanical properties of the particles, the physico-chemical interaction between solid and the liquid, the liquid viscosity.

Many relations express an apparent viscosity which is a function of the liquid phase viscosity and the solid volume fraction ϕ present in the melt as $\eta_{app} = \eta_l f(\phi)$.

3.1 Viscosity modellings - Literature survey

An extensive survey of the viscosity-concentration literature was made by Rutgers (1962). Most of the model developments were established for hydrodynamic isothermal non-interactive spherical particles. The first of them was proposed by Einstein (1911) :

Einstein (1911) $$\eta_r = 1 + 2.5\phi \qquad (6)$$

A lot of other models have been proposed, they always tend towards the Einstein law when $\phi \to 0$, for example :

Arrhenius (1917) $$\eta_r = \exp(2.5\phi) \qquad (7)$$

Mooney (1951) $$\eta_r = \exp\frac{2.5\phi}{1 - \phi/\phi_{max}} \qquad (8)$$

Krieger & Dougherty (1959) $$\eta_r = \left(1 - \phi/\phi_{max}\right)^{-2.5\phi_{max}} \qquad (9)$$

Thomas (1965) $$\eta_r = 1 + 2.5\phi + 10.05\phi^2 + 0.00273\exp(16.6\phi) \qquad (10)$$

where ϕ_{max} is the maximum packing fraction and $\eta_r = \eta/\eta_l$ the relative viscosity.

For non-spherical particles (dumbells, spheroids), other expressions have been proposed, for example Douglas et Garboczi (1995), in which the factor 2.5 could be modified.

In the case of concentrated suspensions, a higher-order term than ϕ^2 is important but even more difficult to analyse from a theoretical point of view. Using Einstein's result for dilute systems, Ball and Richmond (1980) introduced a development based on a technique for averaging the influence of neighbouring particles. They essentially assumed that the effect of all the particles in a concentrated suspension is the sum of the effects of particles added sequentially. The fact of taking into account the packing[1] effect (or crowding effect) yields a single generalized viscosity-concentration equation

$$\frac{d\eta}{\eta} = 2.5(1 - k\phi)^{-\sigma}\, d\phi \qquad (11)$$

Table 3 summarizes equations which give the integration of equation 11 by varying the σ coefficient and predict the form of many suspension relations given in the literature.

[1] As more and more particles are added, the suspensions "jam up", giving continous three-dimensional contact throughout the suspension, thus making flow impossible, i.e. the viscosity tends to infinity. The particular phase volume at which this happens is called the maximum packing fraction ϕ_{max}, and its value will depend on the arrangement of the particles. ϕ_{max} is controlled by the type of packing and ranges from approximately 0.5 to 0.75 for monodisperse spheres.

Table 3 Simplified form of generalized equation with the particle interaction coefficient σ

σ	Simplified form of generalized equation	Previous reference for equation derivation
σ = 0	$\ln(\eta/\eta_l)=\frac{5}{2}\phi$	Arrhenius (1917)
σ = 0.5	$\ln(\eta/\eta_l)=\left(\frac{2}{k}.\frac{5}{2}\right)(1-(1-k\phi)^{0.5})$	
σ = 1	$\ln(\eta/\eta_l)=\left(\frac{-5}{2k}\right)\ln(1-k\phi)$	Krieger et Dougherty (1959)
σ = 2	$\ln(\eta/\eta_l)=\frac{5}{2}\left(\frac{\phi}{1-k\phi}\right)$	Mooney (1951)
σ = 3	$\ln(\eta/\eta_l)=\left(\frac{5}{2}.\frac{1}{2}\right)\left(\frac{2\phi-k\phi^2}{(1-k\phi)^2}\right)$	

Thanks to its 2 parameters, this model fits the experimental viscosity data of Vand (1948) for stirred monodisperse systems, Eilers (1941) for polydisperse systems, with respectively ($1/k=\phi_{max}=0.602$ - $\sigma=1.7$) and ($1/k=\phi_{max}=0.776$ - $\sigma=1$) with a mean square method.

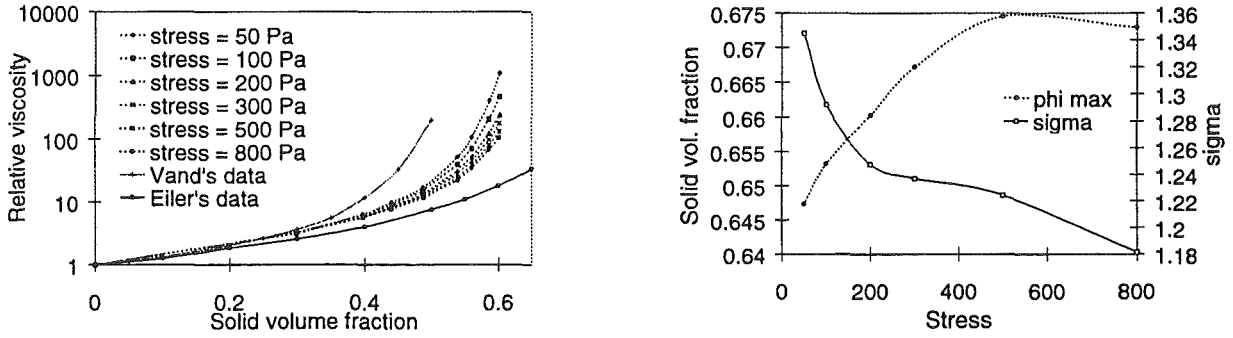

Fig. 4 **a :** relative viscosity vs ϕ for different stresses applied on latex suspensions
b : evolution with the stress of ϕ_{max} and σ parameter

This model also fits the Maron and Fok data from (Krieger, 1959) for latex suspensions with different shears as shown in Figure 4 (a and b).

3.2 Estimation of the apparent viscosity of melts in the solidification range

The effect of various parameters such as shear rate and cooling rate on the apparent viscosity of semi-solid Sn-15%Pb alloy was investigated by Joly and Mehrabian (1976) using a concentric cylinder viscometer. They mainly showed the influence of the solid volume fraction and of the shear rate on the apparent viscosity. Figure 5 shows experimental data for 2 cooling rates 0.33 and 25°C/min for different shear rates. The curves η=f(ϕ) show that the viscosity decreases with the increase of the shear rate or with the decrease of the cooling rate. This

behaviour could be linked to the morphology of the particles. The corresponding microstructures (Figure 6) show that the particles are larger, smoother, more uniform in size and therefore have less entrapped liquid. The liquid phase viscosity is equal to 1.5 mPa.s in the solidification range.

These results cannot be described by the previous viscosity models. On the contrary, a good agreement is found with the Arrhenius law (7) modified with a multiplying C factor such as

$$\eta_r = \exp(2.5C\phi) \qquad (12)$$

This relation can be compared to the exponential term of the Thomas relationship (10) which becomes predominant for ϕ>0,3.

The C factor depends on experimental conditions ; for the Sn-15%Pb alloy investigated by Joly and Mehrabian, its value varies between 4 and 8. Based on the few experimental data for which micrography analyses are available, Ramacciotti (1999) proposed a physical meaning of this parameter and a calculation model.

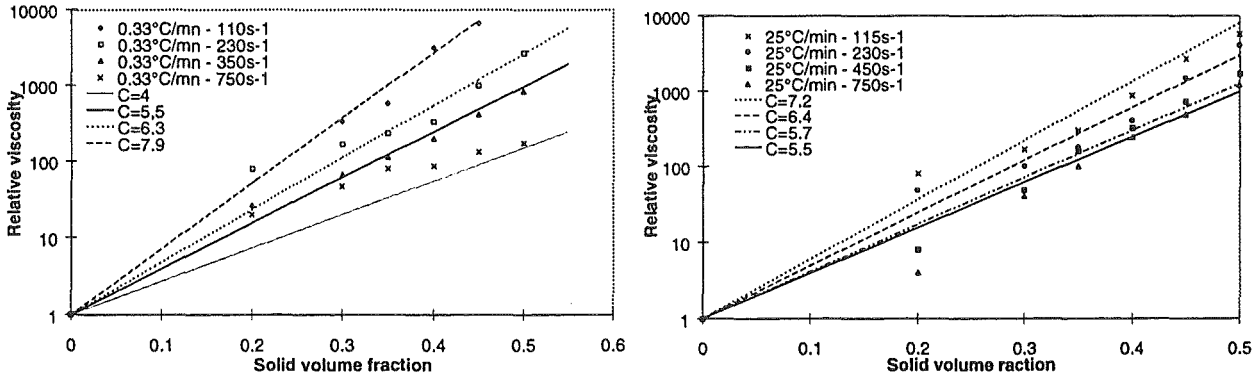

Fig. 5 **a :** relative viscosity vs ϕ for Sn-Pb alloy cooled at 0.33°C/mn
b : relative viscosity vs ϕ for Sn-Pb alloy cooled at 25°C/mn.

By plotting $\ln(\eta_r)/\phi$ versus the volume fraction ϕ, we observed that at solid volume fractions between 0.3 and 0.5, the C factor varies only between 5 and 7.

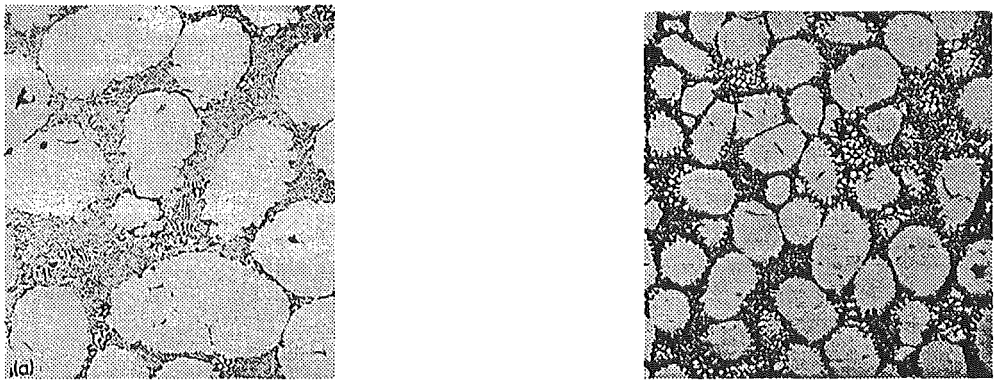

Fig. 6 Structure of Sn-15% Pb samples cooled continuously at 0,33°C/min
Shear rates : left= 230 s^{-1} ; right = 750 s^{-1}

3.3. Corium-concrete oxide melts

Experiments aiming at measuring the viscosities of corium-concrete mixtures have been performed by the BATTELLE Institute (Skoutajan, 1979). The measurements were performed using a rotational Couette type viscometer.

The results of a test composed of $50\%_w$ concrete and $50\%_w$ corium ($1.65\%_w MgO$ - $5.85\%_w CaO$ - $6.3\%_w Al_2O_3$ - $34.11\%_w SiO_2$ - $2.1\%_w Fe_2O_3$ - $13.5\%_w FeO$ - $26.7\%_w UO_2$-$9.8\%_w ZrO_2$) were compared to calculations using the Thomas equation and the modified Arrhenius law. GEMINI was used to estimate the solid volume fraction and the evolution of the residual phase versus temperature. As in §2, Urbain model is used to calculate the liquid phase viscosity. The Arrhenius formula with C equal to 4.8 gives a good agreement with experimental data (Figure 7). It can be noted that the Thomas relationship , applied by Seiler and Ganzhorm (1997) underestimates the viscosity of the melt as with Einstein, non-modified Arrhenius and Mooney equations due to the value of 2.5 which is too low.

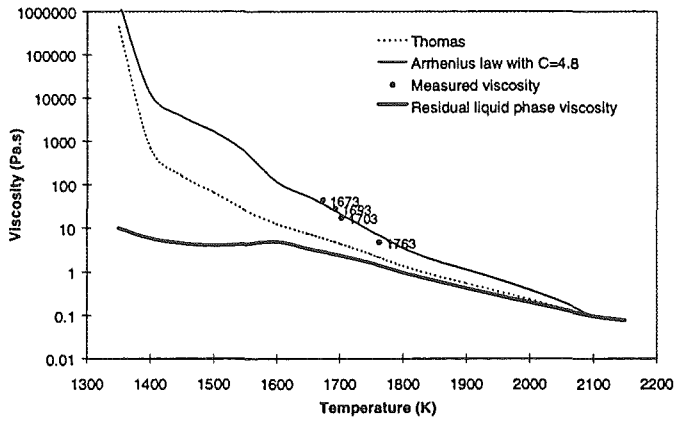

Fig. 9 Experimental data for Battelle 50/50 test

Unfortunately, neither micrographs of this test nor information on the shear rates applied during the experimentation were available.

Similar analysis has been applied on experimental results from ANL (Roche, 1993) on a corium- 27 wt% siliceous concrete mixture (Run 34) which seems to be the most reliable from this series. The best fit is obtained when using Urbain modelling with UO_2 as a modifier, and an Arrhenius law with a coefficient varying with shear rate between 3.5 and 5.5. The relationship between the C factor and shear rate is very similar to what is observed on Sn-Pb data.

4. CONCLUSION

The methodology, initially proposed by Seiler & Ganzhorn (1997), to calculate corium - concrete viscosity has been extensively investigated. Some improvements have been proposed in particular a new model, based on a modified Arrhenius law, to describe the evolution of the apparent viscosity in the solidification range. Moreover, the analysis of available data showed that the apparent viscosity, in the solidification range, cannot be described by a suspension viscosity model of non-interactive spherical particles.

This methodology is based on three main steps :

- The determination of the solid volume fraction and the composition of the residual liquid phase using thermo-chemical equilibrium calculations performed with the GEMINI code ;
- The use of the Urbain model to calculate the viscosity of the liquid phase ;
- The use of the modified Arrhenius law, $\eta_r = \exp(2.5C\phi)$ with a C factor varying between 4 and 8, to calculate the apparent viscosity in the solidification range.

The Urbain model was tested and gave good agreements between measured (Leibowitz, 1974, Bottinga, 1972) and estimated viscosities of various basalts among which one contained 18 wt% of UO_2.

As regards the C factor in the modified Arrhenius law, the available post-test analyses of melt structures after quenching show a dependence of this factor on the particle morphology. Work is currently in progress to better estimate this coefficient from micostructural data.

NOMENCLATURE

A	rheological parameter
A	Urbain's parameter in (1), (2) and (3)
B	Urbain's parameter in (1), (2) and (3)
C	multiplying factor in modified Arrhenius law
D	characteristic constant in (5)
N	molar fraction of silica
T	absolute temperature
y	molar fraction
ϕ	volume solid fraction
η	viscosity
σ	particle interaction coefficient

Subscripts

i	i^{th} component
l	liquid
liq	liquidus
r	relative
max	maximum
app	apparent

ACKNOWLEDGMENTS

This work has been partly funded out by the EC within the 5th Framework Programme (CSC Project - contract n° FI4S-CT-0041) and by SIEMENS within the framework of a CEA/SIEMENS A-G KWU Thesis Contract.

REFERENCES

Arrhenius, S., 1917. The Viscosity of Solutions. *Biochem. J.* 11, 112-133.

Ball, R.C., Richmond, P., 1980. Dynamics of colloidal dispersions. *Phys. Chem. Liq.* 9, 99-116.

Bottinga, Y, Weill, D.F., 1972.The viscosity of magmatic Silicate Liquids. *American Journal of Sciences* 272, 438-475.

Carron, J.P., 1969. Vue d'ensemble sur la rhéologie des magmas silicatés naturels. *Bulletin Soc. Minéralogie et Cristallographie*, 92, 435-446.

Chevalier, P.Y., 1992. Thermodynamic calculation of phase equilibria in a quinary oxide system Al_2O_3-CaO-SiO_2-U_2-Zr_2: determination of liquidus and solidus temperatures of some selected mixtures. *J. Nucl. Mater.* 186, 212-215.

Chong, J.S., Christiansen, EB., Baer, A.D., 1971. Rheology of concentrated suspensions. *Journal of Applied Polymer Science* 15, 2007-2021.

Cognet, G., Laffont, G., Jegou, C., Pierre, J., Journeau, Ch., Sudreau, F., Roubaud, A.,. Premiers résultats sur l'étalement de mélange d'oxydes autour de 2000°C. SFT 98 - Congrès Français de Thermique - Marseille 5-7 Mai 1998

Da C. Andrade , E.N., 1934a. Theory of the Viscosity of Liquids, Part 1. *Phil. Mag.* S7, 17, n° 112, suppl. February, 497-511.

Da C. Andrade , E.N., 1934b. Theory of the Viscosity of Liquids, Part 2. *Phil. Mag.* S7, 17, n° 112, suppl. February, 698-732.

Douglas, J.F., Garboczi, E.J., 1995. Intrinsic viscosity and the polarizability of particles having a wide range of shapes. *Advances in Chemical Physics*, volume XCI, Ed. by I. Prigogine and S.A. Rice.

Eberlé, P., 1997. *Modélisation physique et numérique de l'étalement d'un fluide avec solidification dans le cadre des études de sûreté pour les réacteurs à eau sous pression.* Ph D. Thesis, Université J. Fourier, Grenoble.

Eilers, H., 1941. Die Viskosität von Emulsionen hochviskoser Stoffe als Funktion der Konzentration. *Kolloid Z.* 97, 313-321.

Einstein, A., 1911. Investigations on the Theory of the Brownian Movement. *Annalen Der Physik* 34, 591-592.

Jeffrey, D.J., Acrimos, A., 1976. The rheological properties of suspensions of rigid particles. *AIChE J.* 22, 417-432.

Joly, P.A., Mehrabian, R., 1976. The rheology of a partially solid alloy. Journal of *Materials Science* 11, 1393-1418.

Journeau, Ch., Jung, Y., Pierre, P., 1998. Visualisation of a 2000°C melt spreading over a plane. 8th International Symposium on Flow Visualization - Sorrento, 9/98.

Krieger, I.M., Dougherty, T.J., 1959. A mechanism for non-newtonian flow in suspensions of rigid spheres. *Trans. Soc. Rheol.* 3, 137-152.

Leibowitz L., Williams, C., Chassanov, G., 1974. The viscosity of UO_2-Basalt Melts. *Nuclear Technology,* 24, 234-237

Lesty, M., 1990. Une nouvelle approche dans le choix des régresseurs de la régression multiple en processus d'intéractions et de colinéarités, *Rev. Modulad,* 22, pp. 41-77.

Mooney, M., 1951. The viscosity of a concentrated suspension of spherical particles. *J. Colloid. Sci.* 6, 162-170.

Ramacciotti, M., 1999. Etude du comportement rhéologique de mélanges issus de l'interaction corium / béton. *PhD thesis, Université de Provence (Aix-Marseille I), September 24.*

Roche, M.F., Steidl, P.F., Leibowitz, L., Fink, J.K., Sehgal, B.R. Viscosity of Corium Concrete Mixtures at High Temperatures, ANL Report ACE-TR-C37, 1993.

Roscoe, R., 1952. The viscosity of suspensions of rigid spheres. *Brit. J Appli. Phys.* 3, 267-269.

Rutgers, I.R., 1962. Relative viscosity and concentration. *Rheol. Acta* 2, 305-348.

Ryerson, F.J., Weeb, H.C., Piwinski A.J. (1988). Rheology of subliquidus magmas l. picritic compositions. *J. Geophys. Res.* , 93, pp 3421-3436.

Seiler, J.M., Ganzhorn, J. (1997). Viscosities of Corium-Concrete Mixtures. *Nucl. Eng. Des.* , 178, pp. 259-268.

Shaw, H.R., 1969. Rheology of basalt in the melting range. *Journal of Petrology* 10 part3, 510-35.

Skoutajan, R., Baukal, W., König, R., Wagmar, W., Walter, G. Durchführung von Viskositätsmessungen an oxidischen Corium-Beton schmelzen. BF-R-63.556-1, Battelle Institute, Francfort/Main, 1979.

Spindler, B., Veteau, J.M., Status of the Assessment of the Sreading Code THEMA against the CORINE Experiments, SARJ-98, Japan, 1998.

Sudreau, F., Cognet, G, 1997. Corium Viscosity Modelling above Liquidus Temperature.*Nuclear Engineering and Design*, 178, 269-277.

Thomas, DG.,1965. Transport characteristic of suspensions. *J. Colloid Sci.* 20, 267-277.

Urbain, G., 1974. Viscosité et structure de silicoalumineux liquides. *Rev. Int. Hautes Temp. Réfract.* t. II, 133-145.

Urbain, G., 1987. Viscosity estimation of slags. *Steel Research* 58 (n°3), 111-116

Vand, V., 1948. Viscosity of solutions and suspensions II. *J. Colloid Sci.* 52, 300-314.

Urbain, G., 1982. Viscosity of liquid silica, silicates and alumino-silicates. *Geochim. Cosmochim. Acta*, 46, pp 1061-1072.

Session C 2:

MATERIAL PROPERTIES AND THERMOCHEMISTRY: THERMOCHEMISTRY

Chairman: G. Cognet

OECD Workshop on Ex-Vessel Debris Coolability
Karlsruhe, Germany, 15-18 November 1999

Organised in collaboration with
Forschungszentrum Karlsruhe (FZK) GmbH

CORIUM MELT - ZIRCONIA CONCRETE INTERACTION: OXIDE MELT TESTS

S.V. Bechta, V.B. Khabensky, E.V. Krushinov, S.A. Vitol, T.Yu. Pautova, E.K. Kaliago
NITI. St. Petersburg
188540 Leningrad Region, Sosnovy Bor Russia
Phone: 7 812 69 62064
Fax: 7 812 69 62996
Niti-npc@sbor.net

Yu. B. Petrov, D.B. Lopukh, A. Yu. Petchenkov, A.M. Liubomirov
SPb GTU - LETI, St. Petersburg, Russia

I. V. Kulagin
VNIPIET, St. Petersburg, Russia

ABSTRACT

First experimental results of oxide corium melt - zirconia concrete interaction study are presented. The technique of induction melting in the cold crucible was used in tests. Experimental data on concrete ablation rate were obtained. They were used for deriving a simplified model for ablation rate evaluation. The model is based on the assumption that the rate is proportional to the melt undersaturation degree. The estimation was made of empirical dependence of the proportionality coefficient from corium temperature and initial iron oxide concentration in the melt.

1. INTRODUCTION

One of the key issues in designing the core catcher for vessel reactors of VVER type is the choice of the protective refractory material, which would ensure core melt retention. Though such corium melt characteristics as high temperature and chemical activity (it is an almost universal solvent in oxidizing atmosphere) have hindered the synthesis of melt-resistant refractory, a number of perspective materials have been proposed. Primarily they are refractory oxide-based materials (ThO_2, ZrO_2 and others). Refractory concretes are of special interest in terms of the catcher manufacturing technologies. In particular, zirconia concrete (ZC) with barium (strontium) monoaluminate bonding agent, which was developed (Pakhomov et al., 1990) for coating channels of MHD-generator and proposed (Onufriev et al., 1994) for the core catcher protective layer. Such concrete contains 94% of ZrO_2 (stabilized by yttrium oxide), 6% of barium monoaluminate and 3,5% of water (additionally to 100% of dry mass). Here and hereafter mass percentage is used.

The interaction of corium melt metal components with ZC was studied in the Institute of High Temperatures, Russian Academy of Sciences. The studies (Bakunov et al., 1995; Borodina et al., in press) have proved a high resistance of the material during its contact with iron and zirconium melts.

The objective of presented work was to get experimental data on the interaction characteristics of oxide melt UO_{2+x} - ZrO_2 - $Fe(Cr, Ni)O_y$ and zirconia concrete.

2. EXPERIMENTAL PROCEDURE

The study was carried out on the "RASPLAV-2" test facility, which comprised the furnace for induction melting of corium in the cold crucible (IMCC), (Petrov, 1983). The power was supplied by a vacuum-tube generator with 250 kVA installed capacity. The melt was produced in the crucible composed of water-cooled copper tubes (Fig. 1). A cylindrical ZC block 71.5 mm in diameter and 65 mm long was placed on the crucible bottom. Heat transfer from the block was provided by contact between the concrete and water-cooled crucible sections. 1,5 kg of oxide charge was poured on it and 3 - 8 cm melt pool was formed. Thermocouples were installed at different depths in the ceramic block. The spectral ratio pyrometer measured the color temperature in the center of the melt surface.

All tests were conducted in air.

Melt-concrete interface position was measured along the pool axis during tests . For this purpose tungsten probes were dipped into the melt.

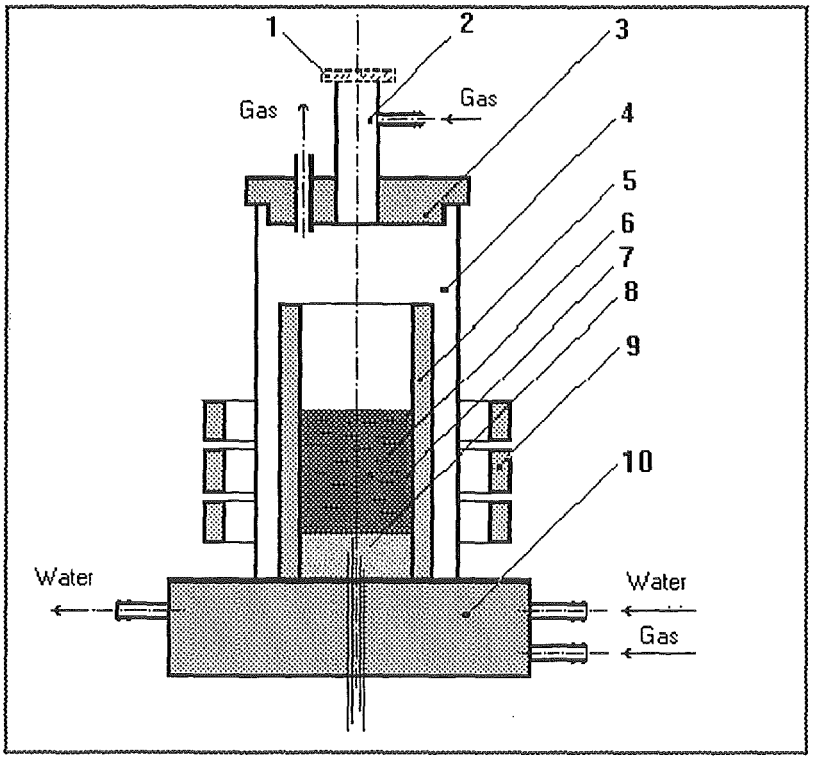

Fig. 1. Schematic diagram of the furnace
1 - glass, 2 - shaft, 3 - lid, 4 - quartz tube, 5 - crucible, 6 - melt, 7 - lining, 8 - ZC block with thermocouples, 9 - inductor, 10 - water collector.

After tests, the oxide ingot fused with ZC block was cut along the axis and the ultimate ablation depth of the block was measured.

3. EXPERIMENTAL RESULTS

Altogether, 10 tests have been made. Experimental conditions and some data are shown in Table 1.

The evident slowing down of the concrete ablation within one hour, when the melt temperature was kept constant, can be considered as the most important experimental result. When the melt temperature was increased, ZC ablation continued and after 0,5 - 1 hr it ceased again. This result became a key for further development of interaction models (Pakhomov et al., 1997, Petrov et al., 1996), which implied that wall dissolution stopped as soon as the melt reached chemical composition corresponding to liquidus temperature. On the basis of the ZC ablation data calculations were made of the melt equilibrium compositions after its saturation with zirconia (Table 1).

Along with that, a significant influence of the iron oxide concentration in the melt on the concrete ablation rate was detected.

The material study results have demonstrated that ZC ablation at its contact with oxide melt results from the following phenomena:

- Concrete wetting by the melt and its capillary impregnation by liquid iron oxide through the pores and grain boundaries;
- ZrO_2 dissolution in the melt;
- Leaching (erosion) of some zirconia crystallites and their solid phase inclusion into the the melt with subsequent dissolution in the melt pool.

Table 1 Experimental conditions and results

Characteristics obtained		Test number															
		1	2	3	4	5		6	7		8	9			10		
Corium charge composition	UO_{2+x}	60	50,5	50,5	50,5	65,8		66,5	50,5		69	30			50		
	ZrO_2	16	25,5	25,5	25,5	10,0		33,5	25,5		-	-			-		
	Fe_2O_3	15	15,0	15,0	15,0	15,1		-	15,0		31	70			50		
	Cr_2O_3	6,4	6,4	6,4	6,4	6,5		-	6,4		-	-			-		
	NiO	2,6	2,6	2,6	2,6	2,6		-	2,6		-	-			-		
Calculated melt compositions in the melt - concrete equilibrium conditions	UO_{2+x}	47,9	43,6	48,5	46,7	54,8	42,7	60,1	49,2	48,1	67,5	28,3	26,5	25,5	42,5	33,3	30,0
	ZrO_2	32,0	35,7	28,4	31,1	25,1	41,5	39,9	27,4	29,1	2,2	5,8	11,6	15,0	15	33,3	40,0
	$Fe(Cr,Ni)O_y$	20,1	20,7	23,1	22,2	20,1	15,8	-	23,4	22,8	30,3	65,9	61,9	59,5	42,5	33,3	30,0
Melt surface temperature during interaction with concrete, °C.		~ 2000	1850-1900	1950-2000	1750-1795	1700-1800	2000- 2200[1)]	2450- 2500	2060-2180	2340-2350	1600-1750	1580-1620	1600-1712	1750	1550-1680	1780-1850	1900-1950
Final concrete ablation depth along the block axis, mm		27,7	16,5	6,5	5,5	15,5	35	14,5	7	12	6	11,5	17	21,5	13	31	42
Maximum concrete ablation rate at the interaction start, mm/min.		2,2	0,32	0,3	0,045	0,54	3,0	1,41	0,375	0,25	0,3	0,7	0,56	0.33	0,14	0,21	0.33
Initial melt volume, cm^3		180	144	152	154	104[2)]		190	238		206	218			91[3)]		
Melt volume in steady power modes after its saturation, cm^3		249	181	162	173	139	198	214	250	259	215	240	265	278	118	168	190
Specific power in the melt, W/cm^3		76-80	53-58	67-71	35-41	82	91-96	105	62	95	58	56	64	73	78.5	83	87

[1)] adjusted temperature; [2)] part of the melt ejected during interaction.
[3)] part of the melt ejected at the beginning of the test.

4. DISCUSSION

Table 1 lists zirconia concentrations in melts after concrete dissolution. The volume of zirconia dissolved corresponds to the specimen mass reduction in each of the tests. Therefore it is easy to calculate the melt concentration change. As the specimen ablation actually stops by the end of the test, it can be assumed that by then thermodynamic equilibrium between liquid and solid phases is established. Consequently, the determined final concentrations of melts are the equilibrium concentrations at corresponding temperatures.

Two relationships are evident from the data presented in Table 1: the lower is zirconia concentration in the initial melt and the higher is melt temperature, the larger is the specimen ablation depth and the higher is ablation rate at the interaction start. Keeping in mind that in all tests melt temperature was below zirconia melting point (2700 °C), we cannot possibly explain the observed phenomenon by concrete melting. This definitely is the case of corrosion-erosion destruction with zirconia dissolution in liquid and a tendency to establish equilibrium.

Deviation of the dissolved component concentration C_0 from the equilibrium at a given temperature C_1 is called "undersaturation degree" (Petrov, 1983). The higher is the undersaturation degree of the melt for a given component at a chosen constant temperature, the larger is the melt dissolving impact on crystals of the component.

Let us demonstrate that the mass of concrete dissolved in the melt is proportional to the melt undersaturation degree. It is explained by the mass balance during the concrete block dissolution. If M_c is the mass of concrete dissolved in the melt, M_0 and M_1 - the initial and final melt mass, correspondingly, C_c is ZrO_2 concentration in concrete (C_c = 0,85 mass fraction), C_0 and C_1 are initial and final concentrations of ZrO_2 in the melt, then:

$$C_c M_c = C_1 M_1 - C_0 M_0 , \qquad M_c = M_1 - M_0 ,$$

Having excluded M_1 we get

$$M_c = M_0 (C_1 - C_0) / (C_c - C_1) \qquad (1)$$

Therefore, at known M_0, C_C and undersaturation degree - $(C_1 - C_0)$, the mass of dissolved concrete can be predicted in advance.

Under saturation conditions, C_1 is the concentration of ZrO_2 on the liquidus surface of the ternary diagram of uranium, zirconium and iron oxides. The hypothesis about ablation termination when corium melt reaches chemical composition corresponding to liquidus temperature was used in a method proposed for studying phase diagrams (the dissolution arrest method). Liquidus temperature is evaluated by measuring the melt surface temperature after ablation stops (the pool is assumed to be isothermal). On the basis of presented experimental results and published data on binary diagrams (Toropov et al., 1969; Gmelin, 1975) the parameters of ternary diagram UO_{2+x} - ZrO_2 – FeO_y, were evaluated (Fig. 2).

The above hypothesis is not absolutely correct from the point of view of physical chemistry. In general, chemical potentials of the liquid and solid phases must be equalized. Here equilibrium is considered for ZrO_2, the mobile component, (Korzhinsky's method) and therefore the given diagram is not a completely equilibrium one.

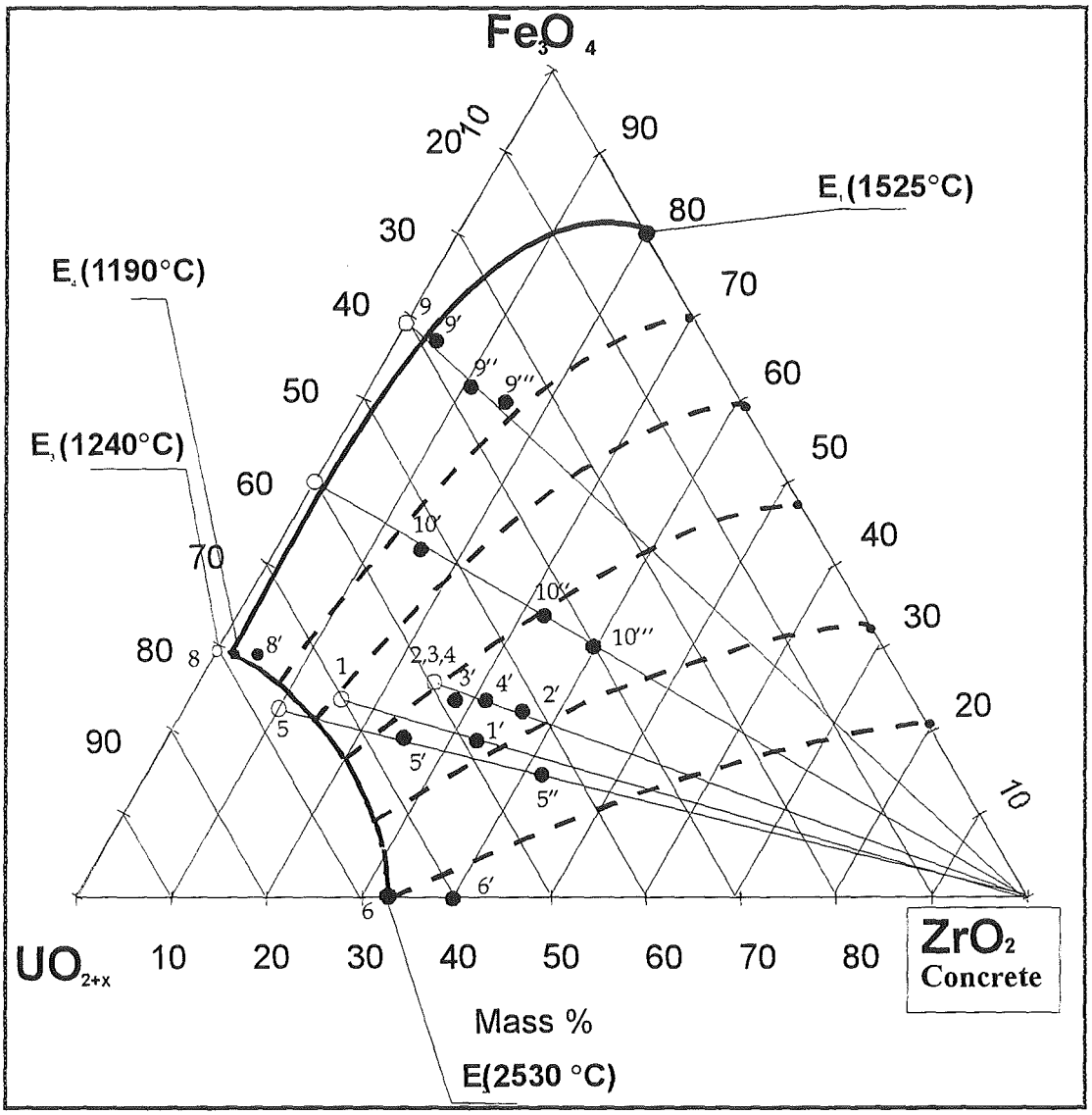

Fig. 2. The approximated phase diagram of uranium, zirconium and iron oxides. Oxygen potential in the system corresponds to conditions of melting in air.

Let us now consider the concrete dissolution rate. Assumption that dissolution rate is proportional to the undersaturation degree means that

$$\frac{dM_c(t)}{dt} = A(C_1 - C(t)) \qquad (2)$$

(2) is the equation that follows directly from the first Fick's law, where C(t) is ZrO_2 concentration in the melt at time *t*,

$$C(t) = \frac{C_c M_c(t) + C_0 M_0}{M_c(t) + M_0} \qquad (3)$$

To determine $M_c(t)$ we use the following equation:

$$\frac{dM_c(t)}{dt} = A(C_1 - \frac{C_c M_c(t) + C_0 M_0}{M_c(t) + M_0}), \qquad M_c(0) = 0 \tag{4}$$

Equation (4) is solved by:

$$A(C_c - C_1)t = -M_c(t) - M_0 \frac{C_c - C_0}{C_c - C_1} \ln(1 - \frac{M_c(t)}{M_0} \cdot \frac{C_c - C_1}{C_1 - C_0}) \tag{5}$$

Equation (5) qualitatively agrees with the experiment. Originally a quick growth of $M_c(t)$ is observed, it has the maximum rate $\frac{dM_c(t)}{dt}|_{t=0} = A(C_1 - C_0)$. Later $\frac{dM_c(t)}{dt}$ decreases and $M_c(t)$ asymptotically approaches

$M_c(\infty) = M_0 (C_1 - C_0) / (C_c - C_1)$, (See (1)).

Coefficient A in equation (2) can be calculated from the experimental results, using the measured values of the maximum concrete dissolution rate and corresponding values of undersaturation degree

$$A = \frac{(\frac{dM}{dt}|_{t=0})exper.}{C_1 - C_0} \tag{6}$$

The obtained values of A are presented in Table 2 and Fig. 3 along with other parameters characterizing experimental conditions.

The analysis of results shows that value A essentially depends on the melt temperature and FeO_y concentration in the melt. This dependence can be approximated by a simple linear expression (Fig. 3):

$$A = 0{,}6(T - 2000 + 900 C_{FeO_y}) \tag{7}$$

where T is the melt surface temperature, °C, C_{FeOy} is FeO_y concentration in the melt at the time of interaction start.

It is evident, that (7) makes sense under $T > T_{liq}$. Besides, it is clear that A should depend on the temperature on the melt-concrete boundary, which is different from the melt surface temperature. But if we assume a rough linear relation of these temperatures, the qualitative conclusions of (7) remain valid. It is seen from Fig. 3 that dependence (7) satisfactorily describes most of the tests. Still there are cases, which definitely deviate from (7), in particular 7' and 8 (Table 2). An explanation to this deviation has not been found yet.

We would like to emphasize that due to the considerable data scattering the purely empirical equation (7) can only indicate some typical tendencies of the process, which should be further studied in more detail. Besides, it is worth noting that quantitative evaluations based on tests in the cold crucible are conservative. Cooled lateral surfaces of the melt pool intensify the free-convection stirring in the melt, which results in a higher ablation rate as compared to the one typical of the core catcher conditions.

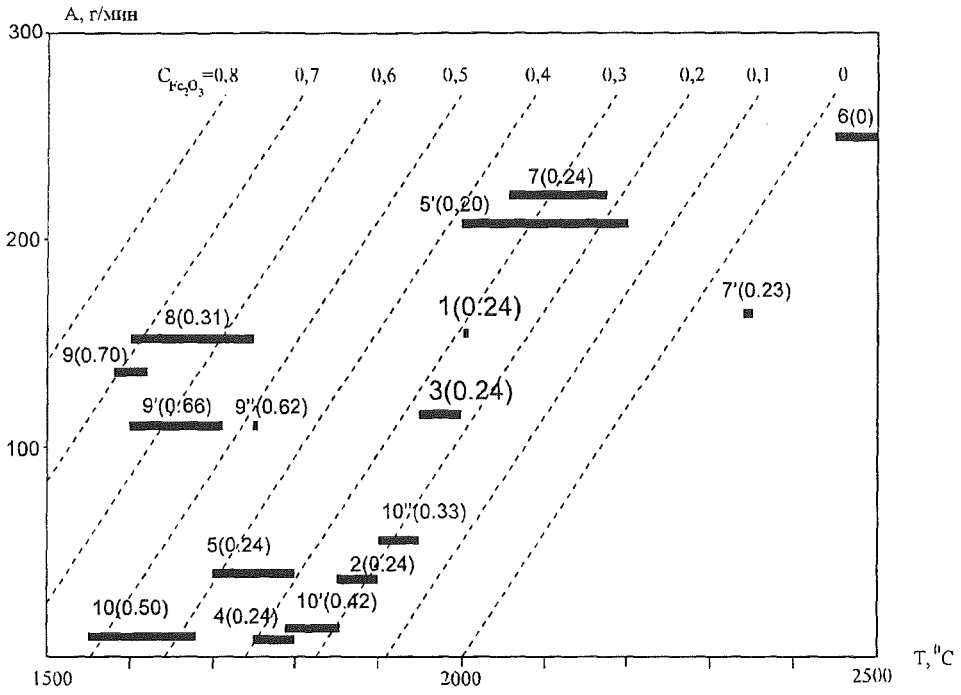

Fig. 3. Dependence of coefficient A on the melt surface temperature and initial FeO_y concentration in the melt.

A=0,6(T-2000+900C_{FeOy}). Dotted lines correspond to **A=*f*(T, C_{FeOy})**. Test numbers are indicated above experimental dots and, in parenthesis, initial concentration of iron oxides.

Table 2 Experimental conditions and results as related to the concrete ablation rate

Test №	Temperature of the melt surface, **T,°C**	Initial concentration of FeO_y, C_{FeOy}, **Mass fraction**	Maximum concrete ablation rate*, **dh/dt** $\mid_{t=0}$, **mm/min**	Undersaturation degree **(C_0 - C_1), mass fraction**	Proportionality coefficient **A, g/min**
1	2000	0,24	2,2	0,16	156
2	1850 – 1900	0,24	0,32	0,102	36
3	1950 – 2000	0,24	0,3	0,029	117
4	1750 – 1800	0,24	0,045	0,056	9,1
5	1700 – 1800	0,242	0,54	0,151	40
5'	2000 – 2200	0,201	3,0	0,164	207
6	2450 – 2500	0	1,41	0,064	249
7	2060 – 2180	0,24	0,375	0,019	223
7'	2340 – 2350	0,234	0,25	0,017	166
8	1600 – 1750	0,31	0,3	0,022	154
9	1580 – 1620	0,70	0,7	0,058	137
9'	1600 – 1710	0,659	0,56	0,058	109
9"	1750	0,619	0,33	0,034	110
10	1550 – 1680	0,5	0,14	0,15	10,6
10'	1780 – 1850	0,425	0,21	0,183	13
10"	1900 – 1950	0,333	0,33	0,067	56

5. CONCLUSIONS

The analysis has been completed of the first experimental data on the interaction of oxide corium melts and zirconia concrete in air.

The model of ceramic material ablation by corium melt was considered taking into account phase diagrams of oxide systems. The model was based on the hypothesis that ablation would cease when such a composition of the melt was established, at which its temperature was equal to liquidus. Using this model and available experimental data the approximated phase diagram of the ternary system UO_{2+x} - ZrO_2 – FeO_y was proposed.

The experimental data analysis proves the decisive influence of the melt temperature, zirconium and iron oxide concentration on the concrete ablation rate. The concept of undersaturation degree was introduced, which gives a comprehensive characteristic of temperature and zirconia concentration influence.

A simplified model was put forward for ablation rate evaluation as proportional to the undersaturation degree. Experimental data were used for estimating the empirical dependence of proportionality coefficient from corium temperature and initial iron oxide concentration in the melt.

On the basis of this and other works (Bakunov et al., 1995; Borodina et al., in press) ZC is recommended as the protective material for the core catcher.

ACKNOWLEDGMENTS

Authors would like to express their gratitude for help in the research work to Prof. V.V.Gusarov, V.R. Buligin, A.P. Martinov, V.V. Martinov, N.E. Kamensky, Dr. S.A. Patokin, Yu.A. Koriachkin.

The experimental part of the work was performed in the framework of ISTC project 64-94, Project Manager is E.P. Pakhomov.

REFERENCES

Bakunov, O.V. et al., 1995. Interaction of zirconia concrete of hydration hardening with metal melts. *Refractories*, 1995, № 11, pp. 2-7. (In Russian)

Borodina, T.I. et al. To be published. Metal melts interaction with zirconia concrete. *Refractories.* (In Russian)

Gmelin, 1975. *Gmelin Handbuch der Anorganischen Chemie Uran*, Erganzungsband Teil C3, Springer Verlag Berlin.

Onufriev, S.V. et al. 1994. Investigation of the interaction of high-temperature metal melts with refractory concrete. *High Temperatures-High Pressures.* V. 26, pp. 309-315. (In Russian).

Pakhomov, E.P. et al. 1990. Tests with ZC concrete in a high-temperature flow of burning products. *Refractories* №5, pp. 6-9. (In Russian).

Pakhomov, E.P., Krischenko, L.P. 1997. Model of interaction of the oxide corium melt and ZrO2 catcher. *Refractory materials and technical ceramics* No 3. (In Russian).

Petrov, Yu.B. 1983. *Induction melting of oxides*. Energoatomizdat. Len. Otd. (In Russian)

Petrov, Yu.B., Lopukh, D., Petchenkov, A., Bechta, S. et al. 1996. On the corrosive capacity of a superheated corium melt. *Journal of Advanced Materials*. No 3, pp. 374-378.

Toropov, N.A., Barzakovsky, V.P., Lapin, V.V., et al. 1969. *Phase diagrams of silicate systems*. Reference book. 1st issue. L. Nauka. (In Russian)

OECD Workshop on Ex-Vessel Debris Coolability
Karlsruhe, Germany, 15-18 November 1999

Organised in collaboration with
Forschungszentrum Karlsruhe (FZK) GmbH

Analysis of Ceramic Ablation by Oxidic Corium

K.Froment
CEA DTA/DEM/CEREM

B. Duret J.M. Seiler
CEA DRN/DTP/SETEX

Grenoble

Phone : 33 4 76 88 48 93
Fax : 33 3 76 88 51 17

Phone : 33 04 76 88 30 23
Fax : 33 04 76 88 52 51

17 Rue des Martyrs
38054 Grenoble Cedex France

S. Hellmann, M. Fischer
SIEMENS/KWU
Phone: 49 91 31 18 24 28
Fax: 49 91 31 18 52 34
Radiochemistry Laboratory
Freyeslebenstrasse 1, D-91058 Erlangen

S. Bechta, D. Lopukh, A. Pechenkov, S. Vitol
LSK/St Petersburg
Phone: 7 812 69 62064
Fax: 7 812 69 62996
188537 Sosnovy Bor Russia

ABSTRACT

It is well known that ceramics may be dissolved in molten oxidic corium. If ceramics are used in the design of core-catchers for Nuclear Power Plants, this dissolution must be taken into account. The thickness of the layers and the design of the cooling system of these ceramics depend on how much ceramic can disappear.

The dissolution of ceramic is usually studied at constant temperature. In the reactor case the residual power is imposed instead of the temperature. A suitable approach must take into account temperature gradients which are induced by an external cooling system. A model has been developed with this objective at CEA-Grenoble. The conclusion of calculations performed with this model is that the dissolution of ceramic is blocked by the temperature gradient and strongly reduced by the decrease of residual power. However, such calculations request some validation experiments which were not available up to now.

CIRMAT is one of the first available experiments which can be used for such validation. CIRMAT is an experiment performed by LSK (St Petersburg) on behalf of Siemens and the European Community (CIT Project in 4th FWP). The experimental results show that the ablation of zirconia increases stepwise with the dissipated power level, and a stabilised ablation depth can be associated which each power step. The model is shown to be able to recalculate the order of magnitude of ablation rates, the stabilised ablation depths and the shape of the interface between corium and ceramic.

1. ABLATION MODEL

The model which has been developed at CEA for the analysis of ceramic dissolution is based on following main physical aspects:

H1) Several physical processes may lead to the ablation of a ceramic by corium: melting, dissolution, melting of the cement, dissolution of binding material, mechanical embritlment. Here, only melting and dissolution mechanism will be considered.

H2) The basic hypothesis postulates that heat transfer is the driving mechanism of the interaction and physico-chemical diffusion mechanisms do not hinder the interaction. The reduction of the interaction kinetics due to diffusion processes can be taken into account later, if necessary.

H3) It is assumed that the interface temperature between corium and ceramic is the liquidus temperature corresponding to the liquid composition at the interface in the corium-ceramic system. A theoretical analysis of the validity of this hypothesis is proposed in annex 1.

H4) Due to the convection mixing in the liquid, the composition of the liquid is assumed to be homogeneous over the liquid volume. Thus, the interface temperature, the liquidus temperature corresponding to the local composition of the liquid, is also the liquidus temperature corresponding to the mean composition of the "residual" liquid.

H5) If a crust forms from the corium (for instance if the corium layer is in contact with water on its upper surface), the composition of the deposited solid corresponds to the solidus of the corium melt at the interface temperature. As the composition of the liquid evolves, mainly with the ablation of the ceramic layer, the composition of the different solid layers deposited in the crust may evolve as a function of time. Thus, the composition of the solid crust, at the end of the solidification process may be non-uniform.

The reader will find the detailed equations associated with this model in [Seiler et al., 1999].

2. THE CIRMAT EXPERIMENTS

The CIRMAT experiments have been achieved in the frame of the CIT project at LSK Sankt Petersburg on behalf of Siemens. CIT 9 test will be described below.

The CIT 9 test involved a corium melt of UO_2 + ZrO_2 + FeO (diameter ~7 cm, height ~4 cm) which was high frequency heated. This corium interacted with a zirconia ceramic placed at the bottom of the melt. The corium and the ceramic are laterally cooled, as shown on figure 1.

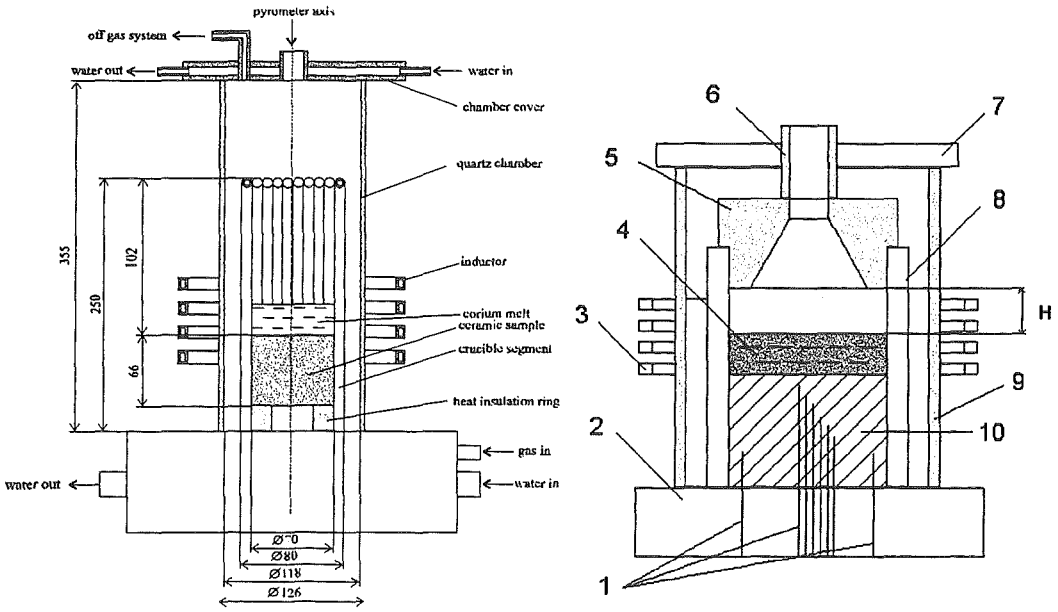

Figure 1: test device and details of the interaction zone. 1 - thermocouples; 2 – water collector of the crucible; 3 - inductor; 4- corium melt; 5 – ceramic shield; 6 – ceramic shaft of pyrometer; 7 – steel water-cooled lid of the furnace; 8 – crucible sections; 9 – quartz shell; 10 – bottom ceramic specimen. H – distance between the ceramic shield and corium melt surface.

The power level was increased stepwise as shown on figure 2.

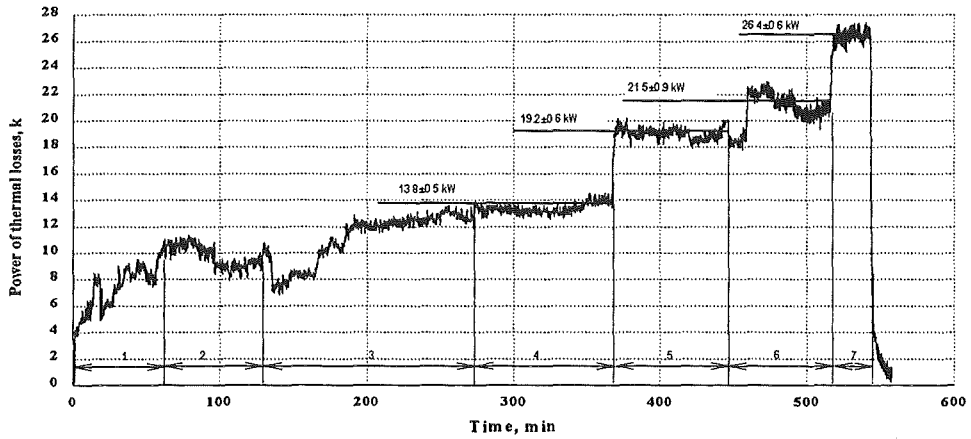

Figure 2: Power trace for test CIT 9.

The instrumentation consisted mainly in:

- measurement of HF generator power and the power extracted through the lateral cooling device,
- measurement of surface temperature of the melt with pyrometers. The surface of the melt was covered with a solid ceramic shield in order to reduce the radiative heat losses through the upper surface of the melt. Thus, it was expected that the temperature difference between the maximum temperature in the melt and the surface temperature would be significantly reduced,
- W-Re thermocouples were installed in the ceramic bottom at different heights,
- W probes were introduced in the liquid from the top, from time to time, to measure the position of the solid/liquid interface

- Tliquidus evaluation (fig.4).This measurement is performed in separate tests. The surface is cooled in a way that solid phases appear on this surface. The method consist in trying to measure the temperature at the interface between the liquid and these solid phases.

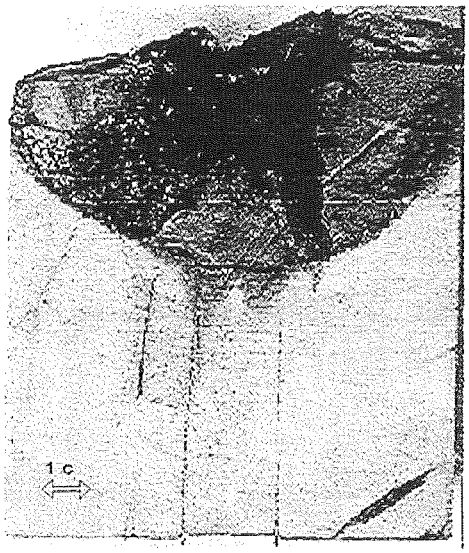

It was observed that the ablation depth of ceramic stabilises for each power level. The shape of the interface between liquid (dark) and ceramic at the end of the test appears on Figure 3.

The composition of the melt was calculated before the experiment and measured after the test.

Figure 3: Post-test examination of the corium-ceramic interface.

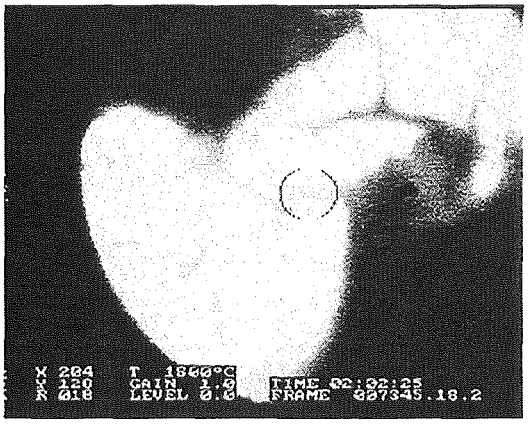

Fig.4 : Melt surface during T liq estimation with temperature measurement spot

3. COMPARISON WITH CALCULATIONS

The interaction model described in part 1 has been introduced in a numerical solver called CORAN. This code calculates transient conduction heat transfer in the ceramic coupled to convection heat transfer between corium and ceramic. The interface temperature between solid and liquid is, according to part 1, the liquidus temperature corresponding to the instantaneous composition of the liquid phase. As times evolves, the liquid becomes enriched in zirconia and, thus, the interface temperature increases versus time. This liquidus temperature is calculated with the GEMINI software and introduced in CORAN in form of a binary phase diagram as a function of the zirconia concentration in the melt. For test CIT9, this interface temperature is calculated to increase from 2050°C (at the beginning of the test) to 2200°C at the end of the test.

The heat transfer inside the liquid melt may be affected by the electromagnetic heating (Lorentz forces and their effect on the flow). Thus, separate effect calculations have been performed with the FLOTRAN code for investigating these effects. From these calculations it appears that an important temperature gradient exists along the vertical axis of the melt. A slight horizontal gradient is also calculated at the surface of the pool, with a hotter region at the periphery. The experimental value of this radial temperature difference is no more than 50°C. From these calculations a local heat transfer coefficient has been deduced, based on the calculated local heat flux and the temperature difference: $T_{surface,centre} - T_{\text{int}erface}$. This repartition of heat transfer coefficient has then been introduced in the CORAN solver. The order of magnitude of the calculated temperature difference $T_{surface,centre} - T_{\text{int}erface}$ is about 175°C for CIT9.

The calculations were able to reproduce the shape of the interface between corium and ceramic as shown by comparison between figures 3 and 4 .

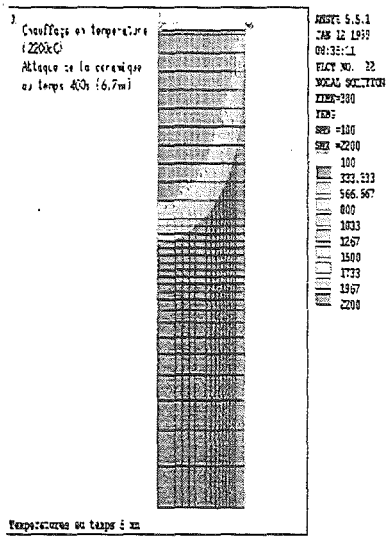

Figure 5: calculated shape of the interface (different scale)

The calculated ablations depths, corresponding to each power step, are smaller then the measured ablation depths, as shown by table 1. If the downward heat exchange coefficient in the melt is slightly increased, the exact experimental ablations can be obtained.

Ablation (mm)	1st power step	2nd power step	3rd power step	4th power step
Test	4	10	19	22,3
Calculation	3,3	8,3	10	15

Table 1: Comparison of experimental and calculated ablation depths for test CIT9

The calculated melt surface temperature is higher (+ 100°C) then the measurement at the 1rst power step and lower (- 130°C) for the last step for an overall measured temperature increase of ~ 400°C (table 2).

Temperature (°C)	1st power step	2nd power step	3rd power step	4th power step
Test	2080	2238	2395	2474
Calculated	2180	2272	2296	2346

Table 2: Comparison of experimental and calculated melt surface temperatures for CIT9

The origin of these discrepancies has been investigated and sensitivity calculations have been performed. A possible cause may be attributed to both the poor knowledge of some physical properties (electrical resistivity, thermal conductivity of the ceramic, liquidus temperature, etc...) and to measurement uncertainties (high-temperature measurements, measurement of liquid depth, etc...). There is no definitive conclusion about the origin of the discrepancies and a few other experiments will help to clarify this question.

CONCLUSION

The main conclusion is that, even if a direct contact between the oxidic melt and the ceramic is considered, the ablation of the ceramic will the limited and blocked by the temperature gradient in the ceramic layer (which is cooled, in the EPR case, at the bottom). The extend of the dissolution at constant power (in the core melt) will mainly depend on the thermal conductivity of the ceramic, the external cooling conditions and on the phase diagram of involved materials.

Ablation will be stopped provided that the cooling system is able to extract the corresponding local heat fluxes.

The model which has developed provides good agreement with the observed phenomenology and correct order of magnitude of ablation depths and melt temperatures. Some discrepancies have been observed which may be clarified with the future analysis of remaining tests performed in the frame of the CIT programme.

ACKNOWLEDGMENTS

The authors acknowledge the European Community (the work has been performed in the frame of the CIT project) and the industrial partners Siemens (Germany), LSK (Russia) EdF and Framatome (France) who supported these studies.

ANNEX 1

Simple dissolution model with boundary layer controlled mass transfer

The model considers dissolution of a solid B into a liquid containing an aggressive species A. The composition of the liquid is C_0 (mass or mole concentration of A in A+B), the composition of the solid is C_s (mass or mole concentration of A in the solid). Following assumptions are made:

1. "plane front dissolution" is considered
2. geometry is 1 D
3. the liquid is at constant temperature T

4. this temperature is above the Liquidus temperature corresponding to the concentration C_0 of the liquid in the A-B phase diagram
5. thermodynamic equilibrium is supposed at the solid/liquid interface; thus: $T_{interface} = T_{liquidus}(C_{l,I}(t))$
6. the dissolution rate R is supposed constant versus time
7. there is no density difference between liquid and solid
8. the mass transfer from the solid to the liquid is controlled by pure diffusion but in a boundary layer of reduced thickness δ_s ; the diffusion coefficient is noted D
9. outside the boundary layer, the composition of the liquid is maintained uniform, constant and equal to C_0
10. no diffusion is considered in the solid (in a mushy zone?)
11. no volumetric heating is considered

The flux of solid rejected from the interface, in terms of species B, is given by:

$$J_r = (C_0 - C_s)R \qquad \text{(Eq 1)}$$

The flux of species B leaving the boundary layer towards the bulk liquid is given by:

$$J_{bl} = (C_0 - C_{l,I})\frac{D}{\delta_s} \qquad \text{(Eq 2)}$$

where $C_{l,I}$ is the concentration of the liquid, in species A, at the solid/liquid interface.

The difference between both fluxes is stored in the boundary layer. Supposing that δ_s is constant versus time leads to:

$$\delta_s \frac{dC_{s,bl}}{dt} = J_r - J_{bl} \qquad \text{(Eq 3)}$$

with: $C_{s,bl} = 1 - C_{l,bl} = 1 - \frac{C_{l,I} + C_0}{2}$ supposing a linear concentration profile in the boundary layer

thus: $\frac{dC_{s,bl}}{dt} = -\frac{1}{2}\frac{dC_{l,I}}{dt}$ (Eq 4)

Taking into account that: $dt = \frac{dz}{R}$ (where z is the distance to the surface of initial dissolution) and $R = Cst$ (assumption 5) leads, after some manipulations, to:

$$\frac{dC_{l,I}}{dz} + \frac{2}{\delta_s \Delta} C_{l,I} - \frac{2}{\delta_s \Delta} C_0 [1 - (1 - \frac{C_s}{C_0})\Delta] = 0 \qquad \text{(Eq 5)}$$

This equation can be solved with following initial condition $C_{l,I}(0) = C_{l,I,0}$:

$$\frac{C_{l,I} - C_{I,f}}{C_{l,I,0} - C_{I,f}} = e^{-\frac{2z}{\delta_s \Delta}} \qquad \text{(Eq 6)}$$

$$z = Rt$$

and $T_{interface} = T_{liquidus}(C_{l,I}(z))$

with $C_{I,f} = C_0 - (C_0 - C_s)\Delta$ and $\Delta = \frac{\delta_s R}{D}$ (remark: $\Delta \leq 1$) (Eq 7)

Application 1

From these equations, it is seen that, when Δ is small (i.e. when the thickness δ_s of the mass transfer boundary layer is small and/or when the dissolution rate R becomes small), then $C_{l,I}$ tends towards C_0 and $T_{interface}$ is then equal to $T_{liquidus}(C_0)$, which is the liquidus temperature corresponding to the composition of the bulk liquid.

Application 2

When $z >> \frac{\delta_s \Delta}{2}$, then $C_{l,I}$ tends towards $C_{I,f}$, which depends on Δ. This parameter is, thus, the main parameter controlling the interface temperature during the dissolution transient. In this case, $T_{interface}$ may be greater than $T_{liquidus}(C_0)$.

Remark concerning δ_s

Specific developments, which are not presented in detail here, lead to the conclusion that, for natural convection situations, following relation should be valid (see N.B.):

$$\frac{\delta_S}{H} \sim (GrSc)^{-\frac{1}{3}}$$

N.B.: This paper has been shortened due to edition constraint. A detailed paper presenting assumptions and calculations can be obtained from the authors on request.

REFERENCES

Seiler J.M., Labergri F., Froment K., Valin F., "Model development for the calculation of corium-ceramic interaction during severe accidents in LWRs" 9th International Topical Meeting on Nuclear Reactor Thermal-Hydralics (NURETH-9) San Francisco, California, October 3-8, 1999

Bechta S., Lopukh D. "Reports on CIT tests" Internal LSK reports, 1998

OECD Workshop on Ex-Vessel Debris Coolability
Karlsruhe, Germany, 15-18 November 1999

Organised in collaboration with
Forschungszentrum Karlsruhe (FZK) GmbH

Small Scale Experiments on Corium-Metal-Ceramic Interaction by Oxygen Diffusion

K.Froment
DTA/CEREM/DEM
CEA Grenoble

17 Rue des Martyrs
38054 Grenoble Cedex France

Phone : 33 4 76 88 48 93
Fax : 33 3 76 88 51 17

F.Valin
DTA/CEREM/CE2M
CEA Saclay

91 191 Gif-Sur-Yvette Cedex

Phone : 33 1 69 08 25 14
Fax : 33 1 69 08 57 54

J.M. Seiler
DRN/DTP/SETEX
CEA Grenoble

17 Rue des Martyrs
38054 Grenoble Cedex France

Phone : 33 04 76 88 30 23
Fax : 33 04 76 88 52 51

ABSTRACT

It is well known that molten oxidic corium can dissolve ceramics such as zirconia if they are in direct contact. A possibility of mitigation of this direct attack is to insert a metal layer between the ceramic and the oxidic corium.

For instance, pure iron does not react with pure zirconia under inert atmosphere. However, in real reactor conditions (for core catcher applications), it is difficult to assume such an inert atmosphere : oxygen is generally present in the vessel or containment atmosphere (vapour), and also into the ceramic itself and in the molten oxidic corium layer. This oxygen may migrate through the metallic layer towards the ceramic-metal interface, form metallic oxides at this interface and then attack the ceramic.

To investigate this effect, small scale experiments have been launched at CEA/Saclay.

This paper first describes briefly the tests configurations and gives the main results concerning the ceramic ablation velocity.

A tendency analysis based on a diffusion model of oxygen through the metallic layer and thermodynamic calculations is then introduced : estimations performed with this model are shown to provide a good order of magnitude for the zirconia dissolution velocity, taking into account the diffusion phenomena and estimations of convection which may be induced by small temperature gradients inside the crucible.

A second part of the paper deals with thermodynamic estimations of the boundary oxygen potential at the metal / molten corium and metal / ceramic interfaces, which is supposed to be the driving force for the oxygen transfer through the metallic layer. Some predictions of the influence of additives into the metallic layer (chromium for instance, as an oxygen getter) on the ablation of zirconia are also examined.

EXPERIMENTS

Some small scale experiments have been launched at CEA/Saclay in order to analyse the possible attack of some ceramic by oxygen diffusion through the liquid iron layer located in between two oxidic materials :

- at the top, a molten oxidic layer composed of iron oxide (FeO) and magnesia (MgO) as a corium simulant layer,
- at the bottom, a zirconia (ZrO2) solid sample.

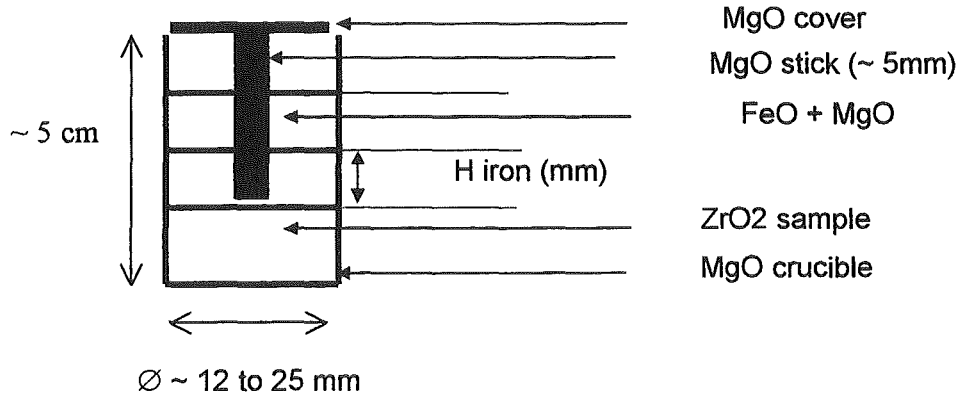

The zirconia sample is maintained at the bottom of the magnesia (MgO) crucible by a small magnesia stick (because of the relative densities of iron and zirconia).

The whole crucible is heated at different temperatures (between 1700°C and 2000°C) under inert atmosphere : as the crucible is closed, the furnace atmosphere was checked to have no influence on the studied phenomena.

The MgO amount in the liquid iron oxide is fixed according to the phase diagram MgO – FeO to the liquidus composition at the test temperature, in order to avoid any interaction with the crucible (12 at% MgO at 1700°C and 25 at% at 2000°C).

The influence of the following parameters was examined in the tests :

- the iron layer thickness (between 4 and 30 mm),
- the crucible diameter (12 and about 25 mm),
- the temperature (1700°C and 2000°C) and test duration in order to obtain the kinetics (from 1 to 7 hours)

The general observation is the attack of zirconia whatever the experimental conditions are, but resulting in different situations :

- infiltration of FeO into the ceramic porosity,
- diffusion of FeO at the grain boundaries in zirconia : corrosion led to decohesion of some individual grains or packs of grains. Some of them stay in place (it is the case for the tests performed at lower temperatures), some others are lifted towards the oxidic layer. On figure 1, some remaining zirconia can be observed below the iron layer (a part of it is infiltrated with FeO, the micrograph shows also a beginning of ZrO_2 dissolution), some corroded zirconia was lifted above the iron layer.
- The penetration of FeO in zirconia results generally in a volume expansion for the ceramic, which appears clearly in the results (table 1).

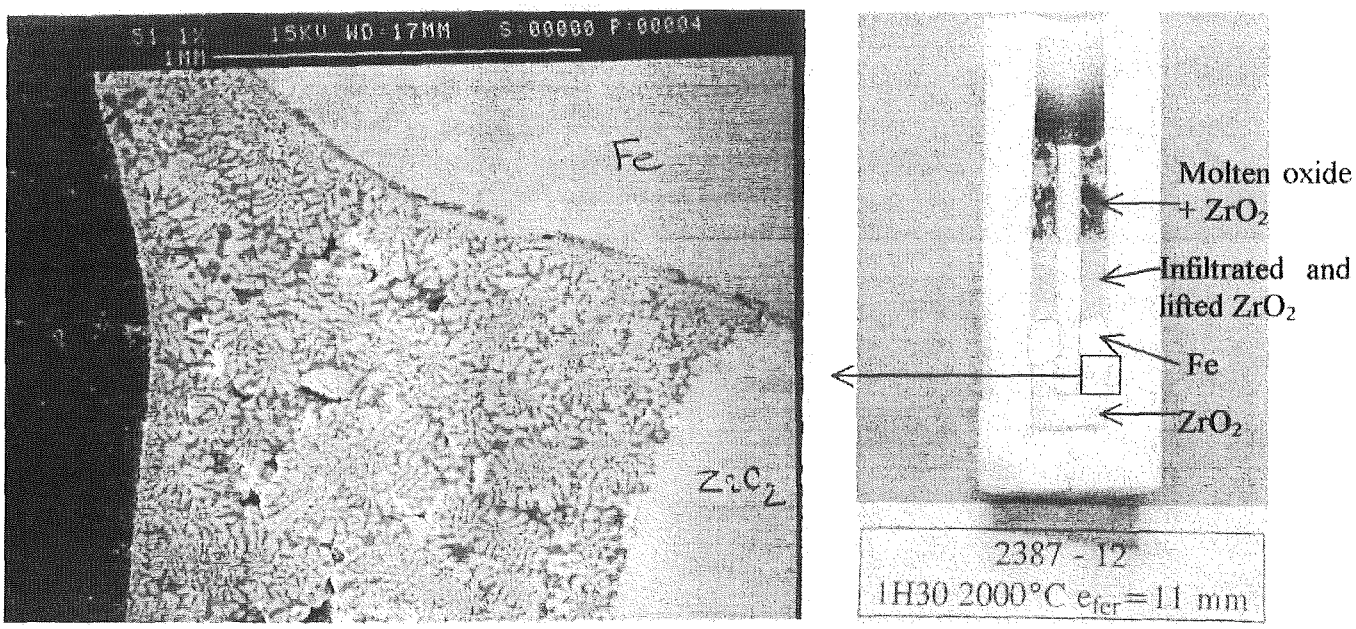

***Figure 1** : post-test examination : the zirconia infiltrated with FeO went above the iron layer and began to mix with the molten oxide. At the iron / ZrO_2 interface, the micrograph shows some attack of the ceramic (FeO/ZrO2 liquid which solidified in dendrites).*

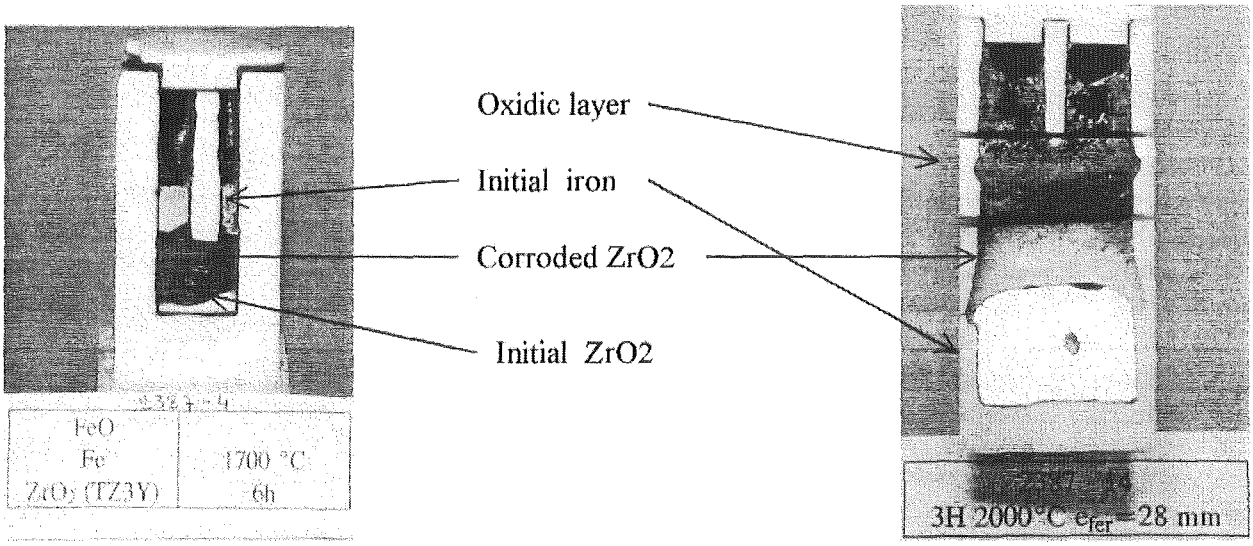

***Figure 2** : different examples of crucibles after tests*

The involved processes in these experiments can be analysed and described step by step (some of them can occur simultaneously) :

- oxygen diffusion through the metallic layer from the oxidic corium towards the ceramic due to the existence of an oxygen potential gradient,
- then possible FeO formation at the iron-ceramic interface due to the O flux coming through the metallic layer,
- diffusion in the ceramic grain boundaries
- dissolution of the ceramic itself by FeO
- solid phase diffusion (FeO-ZrO2)

The main results of these tests are summarised in the table 1 :

- initial and final height in zirconia, respectively noted $H_{initial}\ ZrO_2$ and $H_{final}\ ZrO_2$ and the deduced corresponding velocity $V^{dim}ZrO_2$ (diminution in zirconia height [$H_{initial}$ - H_{final}] divided by the test duration),
- "corrosion" velocity noted $V^{corr}(ZrO_2)$, corresponding to the ceramic thickness in which FeO penetration resulted in the decohesion of some grains or packs of grains (corroded thickness divided by the test duration).

For the tests being performed at 1700°C, the main involved process seems to be the FeO infiltration : the ceramic thickness between the beginning and the end of the test is increased (due to the expansion mentioned above), and only few zirconium (coming from ZrO2 dissolution) was found in the oxidic FeO layer by microprobe analysis. That is why $V^{dim}ZrO_2$ is assumed to be zero at 1700°C. However, the zirconia thickness affected by corrosion by FeO is significant, and the deduced velocity is given in the table 1.

For the tests being performed at 2000°C, FeO corrosion occurred simultaneously with zirconia dissolution (some ZrO_2 grains are found non totally dissolved in the molten oxidic layer). The difference in zirconia height between the beginning and the end of the experiments is then the result of both processes.

Test Reference	∅ int (mm)	T(°C) t (h)	Iron thickness (mm)	$V^{corr}(ZrO_2)$ (mm/h)	$H_{initial}\ ZrO_2$ (mm)	$H_{final}\ ZrO_2$ (mm)	$V^{dim}\ ZrO_2$ (mm/h)
2387- 4 (dense ZrO_2)	12	1700 6 h	6,3	1	10	10,5	0
2387-10 (dense ZrO_2)	12	1700 6h	17	0,45	10	10	0
2387-1b (porous ZrO_2)	12	1700 3h	4	> 3,4	10.25	8,5	0,6
2387-24 (dense ZrO_2)	12	1700 7h	18	1,4	20	23	0
2387- 23 (dense ZrO_2)	25	1700 7h	18	1,5	15.2	19	0
2387- 26 (dense ZrO_2)	25	1700 5h	12	2	14	19	0
2387-12 (dense ZrO_2)	12	2000 1h30	11,5	7,2	20	10	6,7
2387-13 (dense ZrO_2)	12	2000 1h30	30	3,7	20	7,5	8,3
2387-16 (dense ZrO_2)	28	2000 1h30	25	4,7	20	13	4,7

Table 1 : main parameters and results of the small scale experiments

TENDENCY ANALYSIS

A simple tendency analysis was developed at CEA Grenoble taking into account the oxygen diffusion through the metallic layer, in which the driving force is assumed to be proportionnal to the oxygen potential difference between the upper (molten oxidic layer / iron) and lower (iron / ceramic) interfaces.

Pure diffusion model

The oxygen diffusion flux through the metallic layer is deduced from the following equation :

$$\Phi_O = \frac{D}{H}(C_A - C_B) \qquad (1)$$

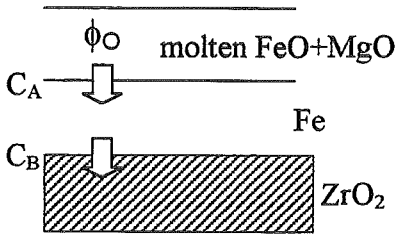

with

ϕ_O	oxygen flux (at.g/cm².s)
D	oxygen diffusion coefficient in liquid iron (cm²/s)
H	iron layer height (cm)
$C_A = C'_A\, a_O$	mobile oxygen at.g per cm³ of oxidic liquid
C'_A	oxygen at.g per cm³ of oxidic liquid
a_O	oxygen activity in liquid oxide ~ $pO_2^{1/2}$
pO_2	oxygen partial pressure at thermodynamic equilibrium
$C_B = 0$	oxygen concentration at the interface iron / zirconia (as oxygen arrives to the interface, it is consumed by Fe to form FeO and to attack or penetrate the ceramic).

The diffusion coefficient D is extrapolated from bibliography data [1, 2, 3, 4] by the relation :

$$D = D_0 \exp(-\frac{Q}{RT}) \qquad (2)$$

where Q = 10800 ± 1500 cal / mole, $D_O = 6.2\ 10^{-3}$ cm²/s

Thus D (1700°C) = $4\ 10^{-4}$ cm²/s and D (2000°C) = $5{,}5\ 10^{-4}$ cm²/s

To estimate the diffusive oxygen fluxes ϕ_O with relation (1), as D is given above and H is an experimental data, only activities values have to be calculated : we performed GEMINI2 calculations to obtain as realistic as possible values for oxygen activities.

Oxygen activities estimations

It is assumed, in this model, that the oxygen concentration at the B interface is zero : to check this assumption, we compared the oxygen activity values at the iron/ceramic (B) interface (assuming equilibrium between pure iron and ZrO2) and at the molten oxidic layer / iron (A) interface (equilibrium between pure iron and iron oxide) : the result is that the oxygen activity at the ceramic/iron interface stays 2 or 3 orders of magnitude lower than the upper interface activity, as it is shown in the following table : the assumption of oxygen concentration at the lower interface equal to zero is then acceptable.

T (°C)	Fe/ZrO₂	Fe/FeO	Fe/FeO+xMgO
1700°C	$7\ 10^{-7}$	$1.6\ 10^{-4}$	$1.4\ 10^{-4}$
2000°C	$1.3\ 10^{-5}$	$1.1\ 10^{-3}$	$9\ 10^{-4}$

Table 2 : oxygen activity at the two interfaces of the metallic layer (GEMINI2/TDBiv992 calculations).

As magnesia is added in the oxidic iron layer in order to avoid any interaction with the crucible, we also verified that this addition of magnesia in the molten oxidic layer does not modify the oxygen activity too much, as it is shown in the last column of the table 2.

Influence of convection

Convection effects may enhance the oxygen flux towards the zirconia / iron interface. For such small scale experiments, low convection levels are expected. By analogy with Nusselt (Nu) numbers for heat transfer by natural convection, it is possible to use the Sherwood (Sh) number for mass transfer. If we assume that the boundary layer thickness which mainly controls the transfers is equal for heat and mass transfers, then we get Nu~Sh. We estimated the Sherwood number to be equal to about 30 for a 10K temperature gradient.

Zirconia attack

To deduce the amount of attacked zirconia (necessary for estimating the kinetics) from the oxygen fluxes in the model, the stoichiometry of the reaction between FeO and ZrO2 has to be considered, i.e. the amount of iron oxide which is needed to dissolve zirconia.

The more simple way is to take the phase diagram [5] into account :

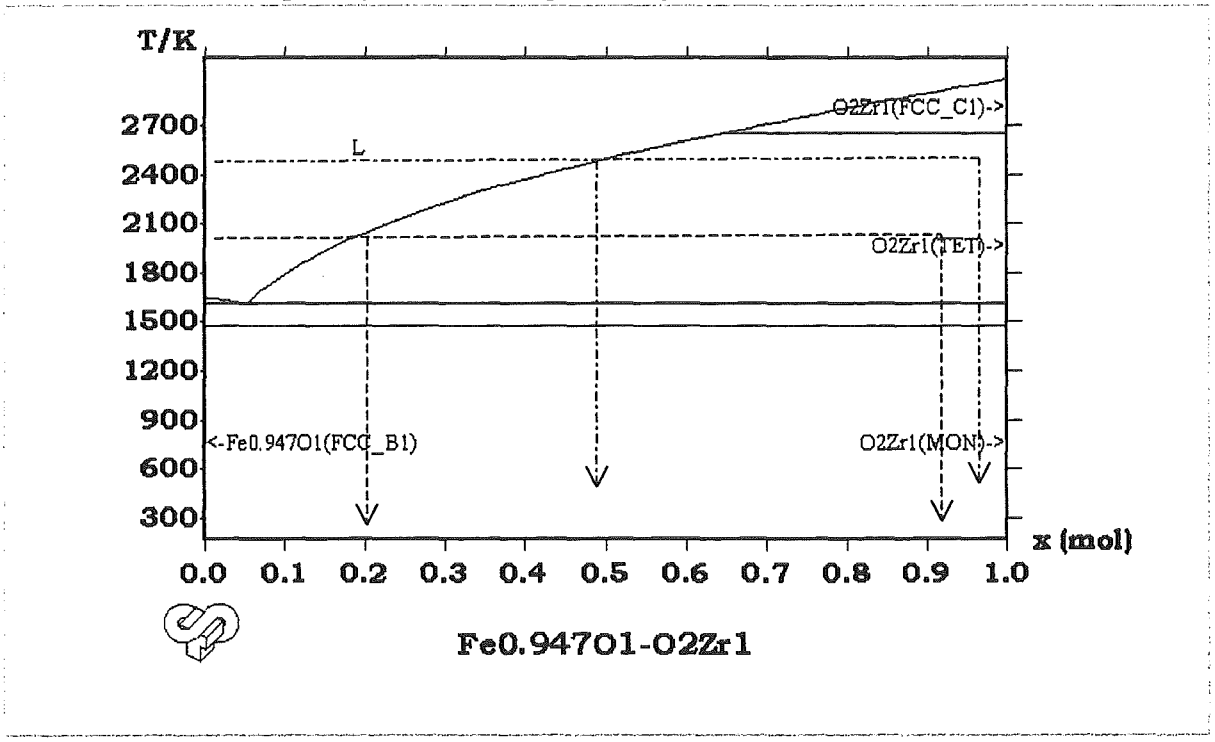

The quantities of iron oxide can be deduced from the liquidus and solidus compositions for a given temperature : for instance, at 1700°C :

- 0.8 mole of FeO can be taken as the necessary amount to obtain 100% of liquid containing 0.2 mole of ZrO2 and 0.8 mole of FeO (corresponding to the liquidus composition)
- 0.1 mole of FeO will be needed with 0.9 mole of zirconia to form a great amount of solid (nearly pure ZrO2 as no solid solution is represented, which means that FeO solubility in ZrO_2 is very small at this temperature) and a small quantity of liquid, at the liquidus composition (relative amounts of solid and liquid phases are given by the lever rule).

It is obvious that the reality will be somewhere in between these two extreme situations.

Assuming then some stoichiometry for FeO/ZrO2 reaction, it is possible to deduce from the oxygen fluxes some kinetics (2 velocities are calculated, Vmin and Vmax) and to compare estimations performed with the proposed model to experimental data.

Table 3 gives the estimations of velocities with the diffusive model and their ratio with the experimental data V^{dim} given in table 1. These values have to be compared to Sh , whose maximum value is estimated to be ~30.

T(°C)	V^{diff}_{min} (mm/h)	V^{diff}_{max} (mm/h)	V^{dim}/V^{diff}_{min}	V^{dim}/V^{diff}_{max}
At 1700°C	$7,2\ 10^{-4}$ to $3,2\ 10^{-3}$	0,03 to 0,15	0 (*)	0 (*)
At 2000°C	0,011 to 0,03	0,18 to 0,48	223 to 507	14 to 30

Table 3 : estimated kinetics of ZrO2 dissolution calculated with the diffusive model compared to the measured velocities (variation range of the results).
(*) : no dissolution is assumed at 1700°C.

This factor 30 is coherent with more accurate estimations we performed, using a boundary layer model [6] and has to be compared to the ratios of table 3 : it is clear that it might explain some of the discrepancies.

The conclusion of this model is that it allows to calculate orders of magnitude of the kinetics for dissolution processes, taking into account the maximum velocity which corresponds to a ratio 1/9 in molar composition (FeO/ZrO_2) for the FeO/ZrO_2 reaction.

The modelling of the other phenomena could be implemented (penetration of FeO into zirconia, decohesion and corrosion of zirconia grains), in order to have a full description of the interaction.

THERMODYNAMIC ESTIMATIONS

One of the major unknowns of the model is the oxygen potential at the different interfaces, which was estimated by thermodynamic calculations, and which can vary due to physico-chemical interactions.

Some additional calculations were performed with GEMINI and TDBCR [5] to look at the variation of the oxygen activity at the interfaces during the zirconia attack :

- oxygen potential variation linked to the oxygen decrease in the molten oxidic layer : as O is transferred towards the zirconia/iron interface to form FeO at this interface, the amount of oxygen can decrease in the oxidic liquid, but thermodynamics imposes a lower limit in the O content. Then, below this limit, a metallic liquid is formed, which will join the existing metallic layer, leading to a metallic liquid amount increase. Thus, both compositions of the oxidic and metallic liquid layers will not vary a lot even if their relative amounts could be modified. So, if the composition of the oxidic layer does not change, and as long as some oxidic molten layer is existing (even with a total amount decreasing), the activities in this layer will not be modified. The conclusion is that, from a thermodynamic point of view and for configurations EPR like, a decrease of the oxygen amount in the oxidic layer (as long as it exists) has no consequences on the oxygen potential into this layer, and thus, on the oxygen potential at the interface with iron.

- influence of zirconia dissolution in the molten oxidic layer : ZrO_2 dissolution can occur when corroded ceramic becomes lighter than liquid iron and is lifted towards the oxidic layer. Its dissolution means that some Zr and O are added to the inventory of the oxidic liquid and may modify the oxygen activity at the molten oxidic layer/iron interface : some slight decrease in the

O activity is actually observed, up to the layer "saturation" in ZrO_2 : beyond this amount, ZrO_2 precipitates again and no more changes in activities is predicted. Thus, the O activity in the molten oxidic layer can weakly decrease, but will always stay at least 2 orders of magnitude higher than the activity at the lower (iron/ceramic) interface.

- influence of chromium addition in the metallic layer on the oxygen potentials.

Chromium addition in the iron layer was proposed by Siemens for the EPR concept, as chromium is well known as an oxygen getter, in order to decrease or avoid any zirconia attack. Small scale experiments are planned by the end of the year with Cr to measure the effect on the reactions kinetics. We performed some GEMINI calculations to look at the thermodynamical behaviour of such a system. The calculations predict, as it is shown on the next figure, that when O is added to liquid iron at 1700°C, the (Fe,Cr,O) spinel forms first. As soon as the spinel is saturated in O (it is a solid solution at this temperature), some oxidic liquid appears. During all this process, the iron amount decreases regularly, as it is consumed by oxygen, at the beginning to form the spinel then the oxidic liquid. At the same time, the oxygen activity increases with the O amount from zero when no oxygen is present up to about the FeO/Fe oxygen activity level already calculated in the previous examples.

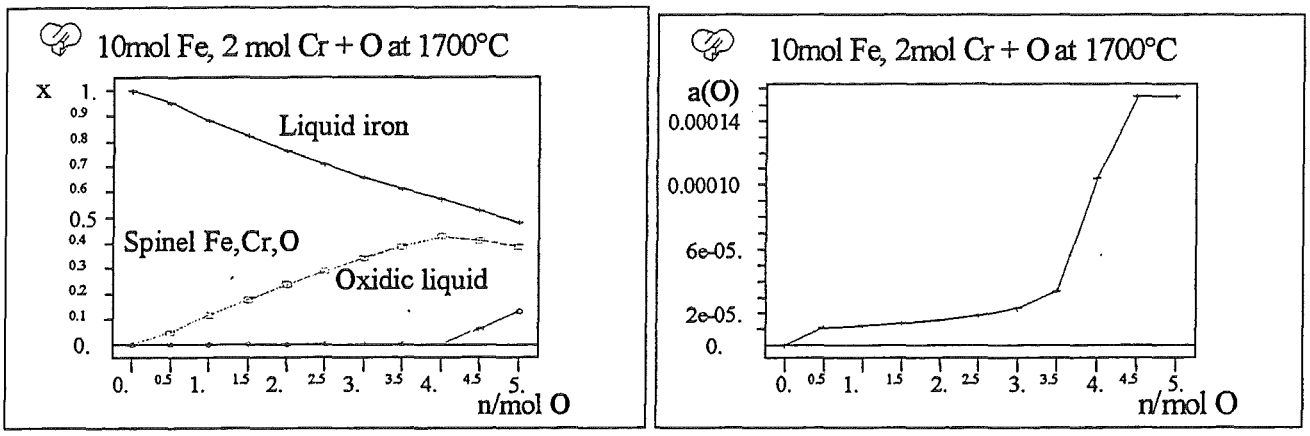

Figure 3 : thermodynamic equilibrium calculations during oxygen addition to an iron/chromium initial mixture : equilibrium phases and oxygen activity versus oxygen amount (GEMINI2-TDBiv992).

At 2000°C, the same tendency is observed, except the fact that the chromium/iron oxide is no more solid : thus, some oxidic liquid forms as soon as oxygen is added (earlier than at 1700°C) and oxygen activity increases continuously.

The main conclusion we can draw from these predictions is that the effect of chromium should be significant at rather low temperatures, when solid chromium oxide can precipitate. However, beyond the oxygen amount corresponding to the saturation of the spinel, or for higher temperatures, the activity will increase again. The zirconia attack, in these conditions, should be delayed (due both to the delay of chromium oxidation and also to the decrease in the oxygen diffusion coefficient in an iron/chromium mixture). The first pre-test performed with chromium in the small scale experiments showed actually a decrease in zirconia attack, but this has to be confirmed and precisely measured.

Remark : the thermodynamic predictions show that there is no activity threshold for zirconia attack : as soon as oxygen is added in a iron / zirconia mixture, some dissolution (even small for low temperatures) begins.

CONCLUSION

From the reactor point of view, these small scale tests evidence the possible zirconia attack, even without direct contact between the liquid oxidic corium and the ceramic, by oxygen diffusion through the metallic layer.

However, the attack is predicted to be much weaker than in the case of a direct contact between corium and ceramic : the final state will be equivalent with or whithout the presence of an iron layer, but the kinetics of the attack will be much slower.

The chromium addition is also foreseen to reduce further the zirconia attack kinetics : preliminary tests seem to confirm the thermodynamic estimations.

The tendency model provides a reasonable order of magnitude but should be completed with the other observed mechanisms such as penetration of FeO in the zirconia porosity and corrosion of the grain boundaries, decohesion of the grains from the ceramic sample... if they are finally considered as important for zirconia attack.

In any case, the modelling of the convection due to temperature inhomogeneities by the mean of the Sherwood number has to be considered with care because of the great influence of the Grashof number [6] which is itself greatly dependent on the scale : that is why realistic scale tests are necessary (they are planned in the frame of the VULCANO program). Moreover, if part of these planned experiments are performed with a temperature gradient between the molten corium and zirconia, they will provide some validation for extrapolating the results and modelling to EPR like configuration.

AKNOWLEGMENTS

This work was funded by Electricité de France (EDF) and Commissariat à l'Energie Atomique (CEA).

REFERENCES

[1] Les techniques de l'Ingénieur M.8 [M 1730]

[2] Izv. Vyssh. Uchebn. Zaved. Chern. Metall 1978 [6] 9-11

[3] Diffusion and defect data, Metals and alloys (1979) p.197

[4] Kakhanov A.D. et al., Fiz. Khim. OSM Processov Proisvod Stali 1979, 233-7

[5] TDBCR database, THERMODATA, BP66, 38402 St Martin d'Hères Cedex, FRANCE

[6] J.M. Seiler, K Froment, J.P. Garandet
Equations for Solidification of Corium and Consequences,
OECD Workshop on Ex-Vessel Debris Coolability,
Karlsruhe, Germany, 15-18 November 1999

OECD Workshop on Ex-Vessel Debris Coolability
Karlsruhe, Germany, 15-18 November 1999

Organised in collaboration with
Forschungszentrum Karlsruhe (FZK) GmbH

Physico-Chemical and Material Aspects of the Core Melt Retention Concept of the EPR

S. Hellmann, F. Funke, V. Lansmann and B. Friedrich
Siemens AG, Power Generation (KWU), Freyeslebenstr. 1, D-91058 Erlangen
Sieghard.Hellmann@erl11.siemens.de

Abstract

To maintain containment integrity and to reduce the radiological consequences of a postulated severe accident, the core melt stabilization concept of the EPR employs sacrificial materials for melt conditioning and protective materials to avoid basemat penetration.

The sacrificial materials added to the core melt fully oxidize the chemically aggressive metallic zirconium, significantly reduce the initially very high melt temperature and lead to a favorable layer inversion in the spreading room. Experimental and theoretical work shows that the sacrificial concrete lowers the liquidus temperature of the oxidic corium melt down to 1800-1850 °C. This in turn reduces the long-term temperatures of the molten corium and hence also the thermochemical challenges to the protective layer in the spreading room.

The spreading area consists of three layers of different materials (from top to bottom): (i) sacrificial concrete, (ii) sacrificial metal and (iii) zirconia (ZrO_2) as protective material. Due to the layer inversion achieved by the sacrificial material a contact between the oxidic melt and the protective layer with corresponding thermochemical interactions is avoided. The protective material is in contact with a metal melt (Fe, 3-7 w% Cr, 7 w% Ni). This metal melt is covered by a less dense oxidic melt (UO_2, ZrO_2, FeO, SiO_2, Al_2O_3, CaO, ...) which gives rise to a certain oxygen concentration in the metal melt.

The thermochemical stability of ZrO_2 is predominantly influenced by the temperature and oxygen concentration in the metallic melt. The parameter governing the stability against chemical dissolution is the activity of FeO in the metal melt which is related to the oxygen concentration. Performed theoretical and experimental investigations demonstrate that under EPR conditions this FeO activity always remains below the threshold value for the formation of liquid ZrO_2-FeO phases and therefore dissolution of ZrO_2 can be excluded. The presence of the weak desoxidant chromium in the metallic melt is beneficial and further increases the safety margin compared to a chromium-free metal melt.

Technological application forms of ZrO_2 are sinteractive ramming mass, sintered ceramic bricks or ZrO_2 concretes. At the current state of knowledge, ramming mass is the most

promising application form for the bottom area of the spreading room. Laboratory tests have shown that, when heating ramming mass by a metallic melt under EPR temperature and oxygen conditions, its high sinter activity will lead to the formation of a sealed sinter layer. This dense layer not only avoids an infiltration of the metallic melt into the ceramic material but also prevents its mechanical disintegration.

1 Introduction

In the EPR core melt stabilization concept, the core melt is first retained within the reactor pit and then distributed on a large spreading area where it is kept in a cooled state [Fischer 1999]. This concept makes use of different materials for conditioning the core melt (sacrificial materials) and for avoiding basemat penetration (protective material), cf. Fig. 1.

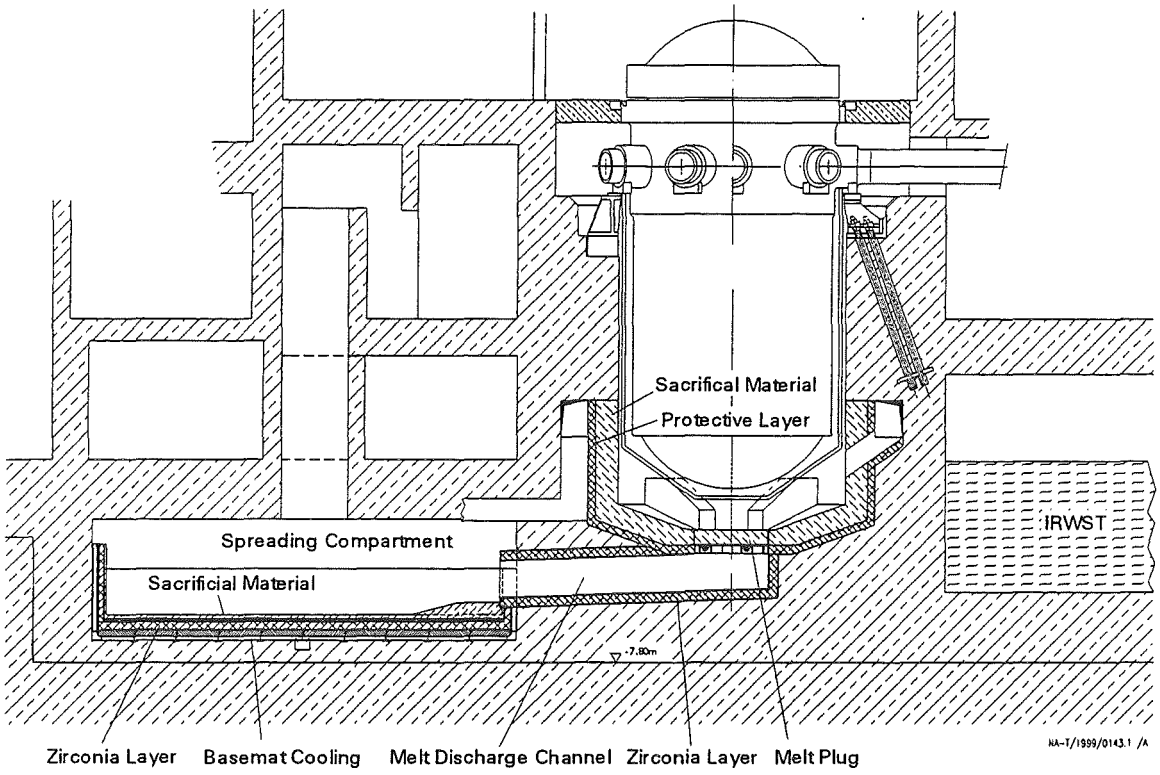

Fig. 1: Cross-section through the lower part of the EPR, showing the main components of the melt retention and stabilization concept [Fischer 1999].

An overview of the selection of relevant sacrificial concrete types and an analysis of the MCCI phase is presented in [Nie 1999]. This paper describes in the first part the contribution of the sacrificial materials for core melt conditioning and stabilization. It also outlines main physico-chemical and material aspects involved, including results from experimental and theoretical investigations.

The spreading area consists of three layers of different materials (from top to bottom): (i) sacrificial concrete, (ii) sacrificial metal and (iii) zirconia (ZrO_2) as protective material. The protective material shall prevent a further downward erosion and retain the melt in a defined shape/geometry. The protective layer is backed up with an upgraded cooling system. This heat sink underneath the protective zirconia layer is designed to prevent any postulated melt

progression [Fischer 1999]. The stability of the protective layer is in turn influenced by the temperature and the chemical nature of the resulting core melt (initial core melt mixed with sacrificial material). The physico-chemical stability of the protective layer, based on theoretical and experimental work, as well as recommended technological application forms will be discussed.

2 Conditioning of the Core Melt by Sacrificial Materials

2.1 General Considerations and Measures

Conditioning of the core melt released from the RPV takes place both in the reactor pit and in the spreading room using different sacrificial materials.

Reactor Pit

In the reactor pit the sacrificial material serves to (i) accumulate the metallic and oxidic core melt which may be successively released into the pit and (ii) transform the chemically aggressive metallic zirconium into zirconia. The intermediate MCCI phase in the pit renders the concept independent of uncertainties of the in-vessel processes, too. Based on above requirements a sacrificial concrete with iron oxide and silica as main aggregates is chosen. After the MCCI process in the pit, which is discussed in detail in [Nie 1999], about 220 Mg oxidic core melt, 130 Mg metallic core melt, and 50 Mg slag are distributed in the spreading compartment.

Spreading Compartment

In the spreading compartment a layer of sacrificial concrete rests on a layer of sacrificial metal (in form of steel). The main aim of the sacrificial concrete is to achieve a layer inversion and to reduce the long-term temperatures of the molten corium. Due to the layer inversion [Nie 1999] after which oxidic core melt rests above the metallic core melt, a contact between the oxidic core melt and the protective layer with corresponding thermochemical interactions is avoided. R&D work was carried out to optimize the sacrificial material such that for a given maximum mass the liquidus temperature of oxide melt + sacrificial material is lower than 1900°C, at best down to 1800°C. This in turn leads to similarly low temperatures at the interface of metallic core melt and protective material.

The necessary layer inversion (oxidic melt less dense than metallic melt) and the liquidus temperature reduction are achieved by a sacrificial concrete which consists mainly of technically available iron oxide grains and borosilicate glass (BSG). BSG consists of approx. 60 w% SiO_2, 12-18 w% B_2O_3 and other oxides such as Al_2O_3, CaO, MgO, TiO_2 etc.

The layer of sacrificial steel ensures that there is always a metallic melt covering the protective material, even if the spreading process should have produced local inhomogeneities in layering. The sacrificial steel consists of Fe, approx. 5-7 w% Cr, Ni and oxygen getters (Si, Al, B).

After complete erosion of all sacrificial concrete (pit + spreading room: 140 Mg) the core melt consists of about 325 Mg oxidic and 130 Mg metallic constituents. Due to the sacrificial concrete the final composition of the oxidic melt varies very little with initial Zr-oxidation level [Nie 1999]. The composition for 40 % Zr-oxidation is shown in Tab. 1.

Constituent	UO_2	ZrO_2	SiO_2	B_2O_3	Al_2O_3	CaO	MgO	FeO	Cr_2O_3
Fraction (w%)	42.4	15.7	10.0	1.6	0.7	5.0	0.2	18.5	5.9

Tab. 1: Composition of the oxidic melt from COSACO calculations after termination of MCCI in the spreading room for an in-vessel Zr oxidation level of 40 %.

After mixing of all sacrificial materials with the core melt and flooding with water the resulting configuration is **water | oxidic crust | oxidic melt | metallic melt | protective layer**.

2.2 Core Melt Chemistry

Two main aspects will be highlighted: the behavior of chromium, which plays a beneficial role for the stability of the ZrO_2 layer, and boron.

Chromium Chemistry

After all sacrificial materials are mixed with the oxidic or metallic core melts, an oxidic melt containing FeO, Cr_2O_3 etc. is in contact with a metallic melt containing Fe, Cr etc. From purely stoichiometric considerations, FeO would not be stable in the presence of Cr (FeO reduced to Fe, Cr oxidized to Cr_2O_3). However, from knowledge in the field of metallurgy it follows that FeO and Cr may coexist [Kojima 1968]. For example, Fig. 2 shows that 0.03-0.04 w% oxygen can be dissolved in a Fe/2-15 w% Cr melt at 1600°C. In other words this oxygen amount is stable against Cr and is therefore not oxidized to Cr_2O_3.

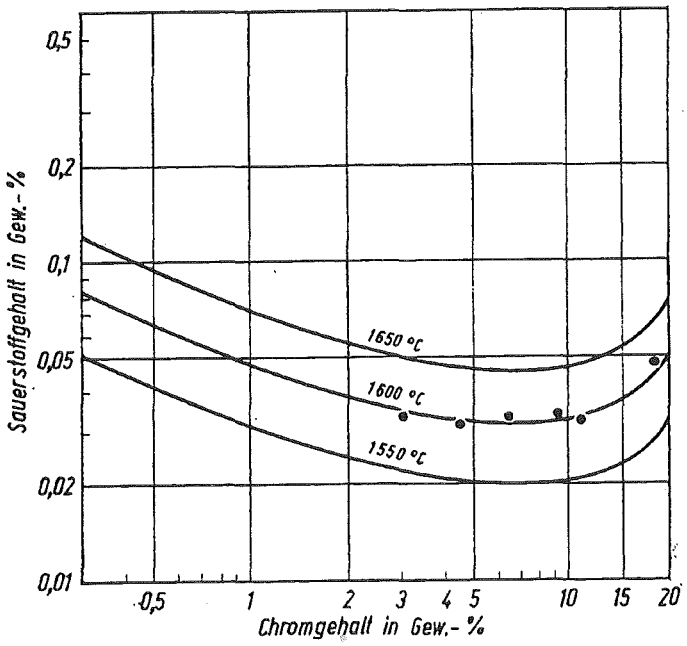

Fig. 2: Oxygen solubility in an iron/chromium melt [Knüppel 1970].
Y axis: Oxygen content in w%. X axis: Chromium content in w%.

For corium-relevant compositions the same result was qualitatively confirmed experimentally. Here an oxide melt (UO_2, ZrO_2, Cr_2O_3, FeO, SiO_2, CaO, MgO, Al_2O_3) was in contact with an initially Cr-free iron melt. After a few hours at 1900°C the metal ingot. contained substantial amounts of Cr.

For the spreading room, thermochemical calculations with CHEMSAGE/EUMCCI22 indicated that about 70 % of Cr is oxidized to Cr_2O_3 at 1800°C (54 % at 2000°C) in chemical equilibrium, see Fig. 3. According to these calculations without consideration of dissolution of the sacrificial metal layer, 3 w% Cr remain in the metal melt at 1800°C (5 w% Cr at 2000°C). No credit was taken from a Cr content in the sacrificial steel (source of additional Cr for adjusting the Cr level).

It is important to note that even in case of diffusion of external oxygen into the chemical system metallic Cr remains in the metallic melt. The long-term presence of the initial Cr concentration requires that the oxygen transport through the oxidic crust can be neglected on the time-scale of months. Estimations of the oxygen diffusion through the expected oxidic crust showed that it is very slow on the time-scale of several months.

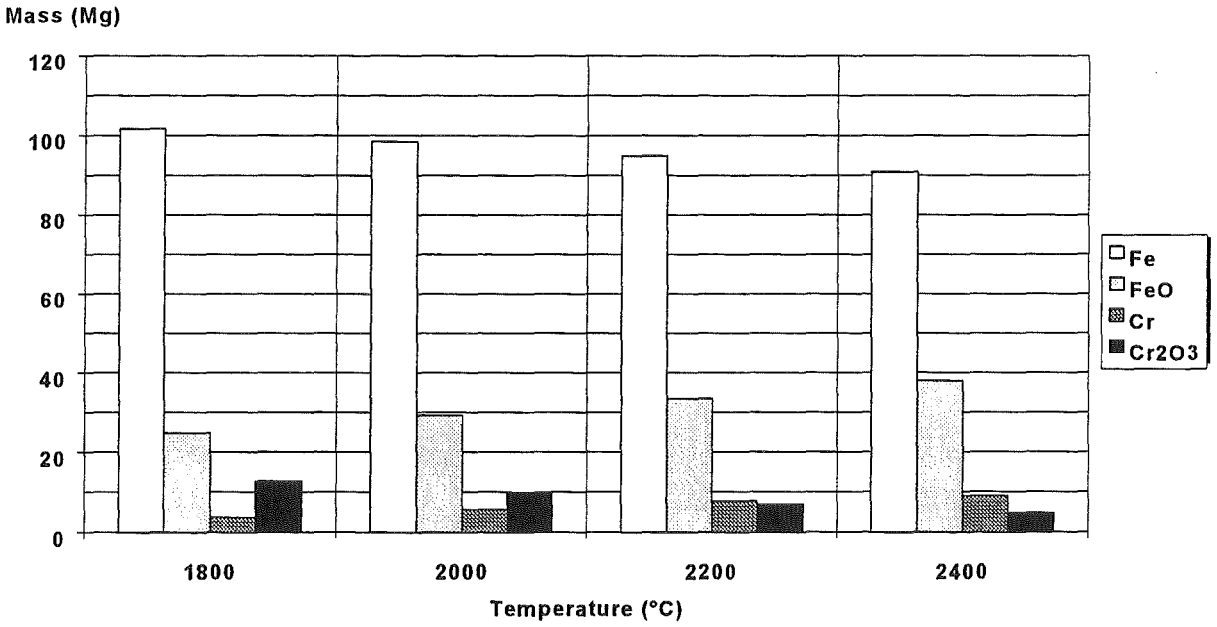

Fig. 3: Fe and Cr oxidation after dissolution of sacrificial concrete, calculated with CHEMSAGE/EUMCCI22.

Boron Chemistry

Pure B_2O_3 is volatile and would be released at 1800-1900°C . However, there are mechanisms which hinder the B_2O_3 release. The volatility of B_2O_3 is strongly reduced by its dissolution in the oxidic melt and by chemical interactions with CaO. After spreading, the crust on top of the melt will effectively retain B_2O_3. Experiments at 1800°C, i.e. just below the liquidus temperature, with a core melt which contained 2.6 w% B_2O_3 a good B_2O_3 retention was found even with an insufficient crust (1-2 mm, no closed surface). After a partial B_2O_3 release from the melt right after the start of the test the B_2O_3 concentration in the melt remained constant. For optimum B_2O_3 retention boron could also be added to the sacrificial steel which would subsequently lead to B_2O_3.

2.3 Liquidus Temperature

One of the main aims of the sacrificial material is to decrease the liquidus temperature down to, at best, 1800-1850°C. Therefore measurements of the liquidus temperature were performed at

ANL (by Differential Thermal Analysis, DTA) and at Siemens (visual observation of the temperature for complete melting of a pressed sample on an iron melt). Following an optimization of the sacrificial material composition, a reference melt was defined (Tab. 2). Starting from this melt composition the effect of composition changes on the liquidus temperature were studied. For example, a) the addition of 6 w% Cr_2O_3 and b) the elimination of all B_2O_3 (2.5 w%) on the liquidus temperature was tested.

Constituent	UO_2	ZrO_2	SiO_2	B_2O_3	Al_2O_3	CaO	MgO	FeO	Cr_2O_3
Fraction (w%)	46.9	18.2	9.8	2.5	0.8	5.1	0.4	14.6	---

Tab. 2: Composition of the reference oxidic melt in the liquidus temperature tests.

Experimental results are shown in Fig. 4. For the reference composition the observation of complete melting gave a mean liquidus temperature of 1890°C (two measurements, points 3 and 4). Using the DTA method at ANL a liquidus temperature of 1830°C +/-30°C resulted (point 2). This shows that the observation of the complete melting overrates the true liquidus temperature to some extent. For further considerations a mean liquidus temperature for the reference composition of 1860+/-30°C was taken. The addition of 6 w% Cr_2O_3 to the reference composition leaves the liquidus temperature unchanged (point 5). Boron oxide B_2O_3 contributes to decreasing the liquidus temperature of the oxide melt by about 70+/-30°C at a concentration of 2.5 w% (point 6).
For the composition of an oxidic core melt after completion of MCCI in the spreading room from COSACO calculations (Tab. 1) a liquidus temperature of 1845°C is induced (point 1). This melt contains only 1.6 w% B_2O, which means that the contribution of B_2O_3 to decreasing the liquidus temperature is only 40°C in this case.

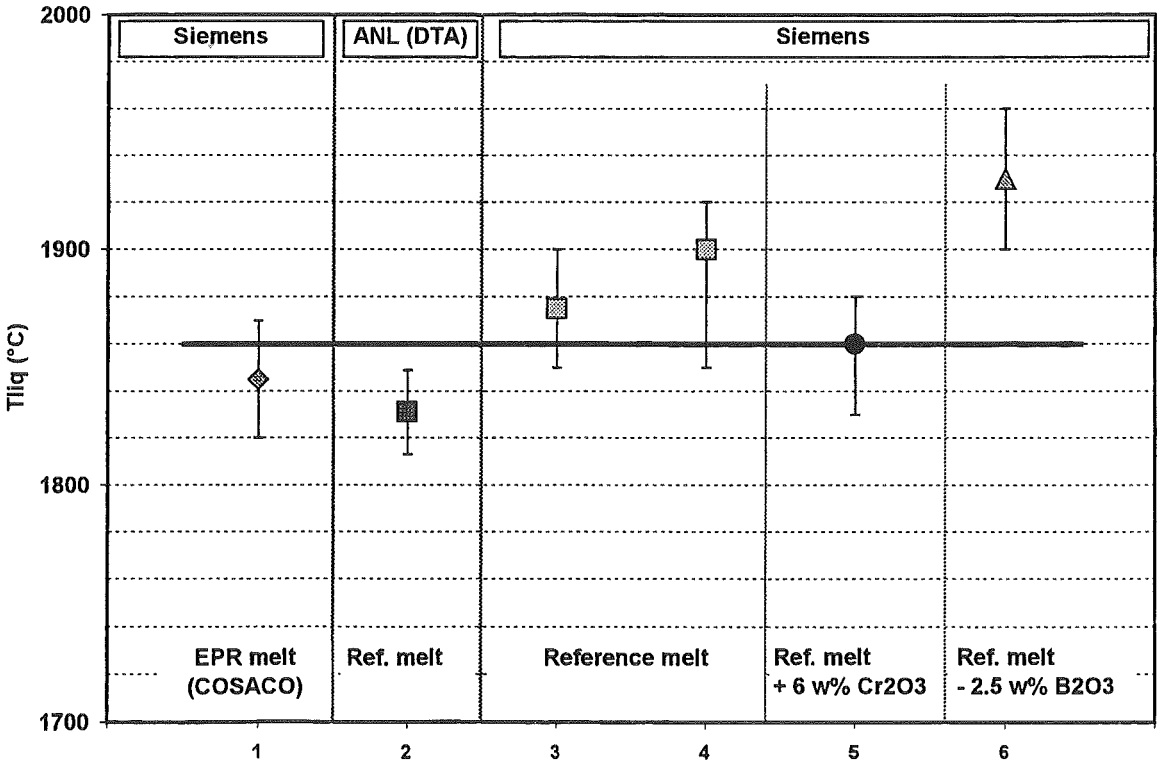

Fig. 4: Results of the liquidus temperature measurements (for details see text).

2.4 Decrease of Liquidus Temperature by Crust Formation

After spreading and flooding, the oxide melt will form a top crust. If the solidification speed is sufficiently slow, which is expected for the EPR case, the solidified melt contains predominantly the higher-melting components (UO_2, ZrO_2). This leaves the remaining liquid oxide phase with a higher concentration of lower-melting components and therefore decreases its liquidus temperature.

The corium compositions experimentally investigated in chapter 2.3 do not reflect any crust formation and therefore overestimate the liquidus temperature. The extent of the decrease in liquidus temperature due to crust formation is estimated by calculating with GEMINI2/TDBCR981 the solidification behaviour of an oxide melt having a composition as obtained by COSACO [Nie 1999]. Fig. 5 shows that the presence of a 3 cm crust reduces the liquidus temperature by about 80°C. This value has to be subtracted from the measured liquidus temperature. This yields approximately 1780°C for the liquidus temperature of the remaining oxide melt after crust formation. The best-estimate liquidus temperature of 1800°C considers the small uncertainty due to neglecting the effect of B_2O_3 in above GEMINI calculations (possibly slightly lower slope in Fig. 5).

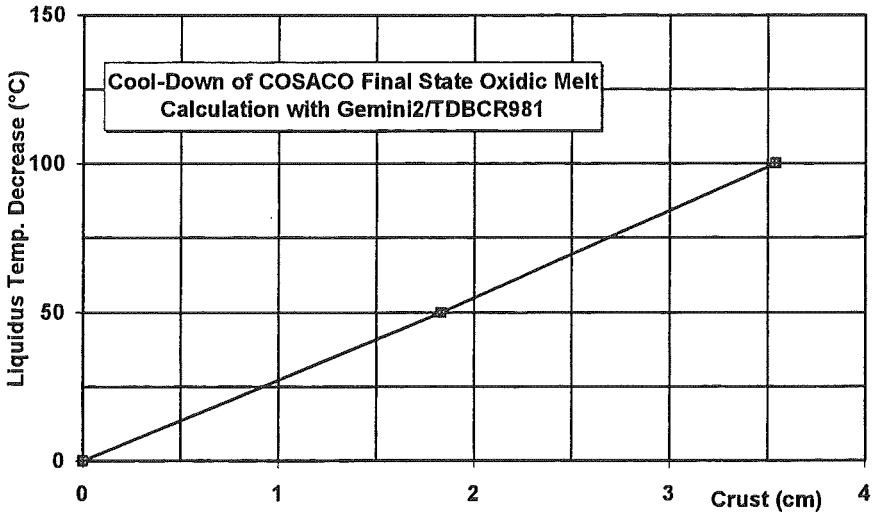

Fig. 5: Decrease of the liquidus temperature by crust formation.

3 Stability of the Protective Layer

3.1 Chemical Nature of the Contacting Metallic Melt

During the MCCI in the spreading room, the metallic core melt saturates with oxygen. After completion of MCCI it reaches the sacrificial steel and solidifies. During this freezing process the oxygen concentration in the metallic core melt decreases significantly. In the following melting/remelting process the oxygen getters (Si, Al, B) in the sacrificial steel (Fe, Cr, Ni) layer react with the residual oxygen. This ensures a very low oxygen level in the resulting new steel melt (metallic core melt + sacrificial steel) when it contacts the protective zirconia layer. Remark: Even without the oxygen decrease due to solidification the amount of oxygen getters is high enough to ensure a very low oxygen level.

After this short-term phase, the steel melt takes up oxygen from the oxidic melt on top until the thermodynamic equilibrium value is reached (equal oxygen potential in oxidic and metallic melt). During the long-term phase the zirconia layer is then in contact with a medium-oxidizing steel melt (Fe, approx. 5 w% Cr and 7 w% Ni, dissolved oxygen [O]) which is covered by a lighter oxidic slag (UO_2, ZrO_2, FeO, SiO_2, Al_2O_3, CaO, B_2O_3, ...). "Medium-oxidizing" denotes that the oxygen concentration lies between that of an oxygen-free and an oxygen-saturated iron melt. The question of chemical stability of zirconia against the contacting steel melt can be answered by chemical thermodynamics.

3.2 Physico-Chemical Concept of Zirconia Stability

The stability of ZrO_2 against chemical dissolution by an oxygen-containing iron or steel melt depends on the temperature and the chemical nature of the liquid metal [Pluschkell 1998]. Of special importance is the oxygen content [O] in either an iron (Fe) or in a steel (Fe,Cr,Ni) melt [Knüppel 1970, Kojima 1968]. The possible oxygen concentration range increases with temperature.
The saturation or maximum oxygen concentration in an iron melt under a pure FeO-slag can be calculated according to [Horvath 1970] by:

$$\log[\%O] = -\frac{6320}{T} + 2.734 \qquad (1)$$

[%O] oxygen concentration in w%
T temperature in K

Chemical dissolution of ZrO_2 takes place only if the oxygen concentration in the metal melt exceeds a critical value. The physico-chemical parameter which determines whether ZrO_2 is chemically dissolved or not is the (relative) activity of FeO, a_{FeO}, in the metal melt [Pluschkell 1998]. It is also called the "virtual" activity of FeO and is defined by

$$a_{FeO} = a_O/[O]_{max} \cong [O]/[O]_{max} \qquad (2)$$

a_O oxygen activity in the metal melt (w%)
[O] actual oxygen concentration in the metal melt (w%)
$[O]_{max}$ max. oxygen concentration in an Fe melt (w%), i.e. Fe covered by a FeO slag

Now, in order to dissolve ZrO_2 at a given temperature, the FeO activity in the metal melt has to be higher than the FeO activity in the system FeO-ZrO_2 at the liquidus composition, cf. Fig. 6 (upper part). Due to a demixing behavior (phase separation) on cooling, the FeO activity in the FeO-ZrO_2 system is higher than its mole fraction x_{FeO}. This deviation from the ideal behavior (Raoult's law) is indicated in Fig. 6, lower part, by adding a value Δa_{FeO} to the mole fraction x_{FeO}. The ZrO_2 dissolution stops when the FeO activity in the system is decreased again down to the critical value, e.g. due to the dissolution of ZrO_2 into the oxidic melt. Or, to ensure chemical stability of ZrO_2 the condition

$$a_{FeO} \text{ (in metal melt)} < x_{FeO} \text{ (liquidus composition in the FeO-}ZrO_2 \text{ system)}$$

has to be fulfilled. It is therefore a prerequisite to have a sufficiently low oxygen concentration in the metal melt which in turn leads to a sufficiently low value of a_{FeO}.

This concept is illustrated in Fig. 6 for T=1800°C: In the lower part the course of the FeO activity in the FeO-ZrO_2 system at 1800°C is shown as a function of the ZrO_2 concentration. Starting from a pure FeO melt, the FeO activity decreases with increasing ZrO_2 until the liquidus line, i.e. the beginning of the two-phase region is reached. In this FeO activity regime of a_{FeO}=1-0.8, ZrO_2 can be (partially) dissolved. Below the corresponding FeO activity of about 0.8 no more liquid FeO-ZrO_2 phases are formed, i.e. zirconia is not dissolved and only a solid solution of FeO in ZrO_2 is formed. By decreasing the FeO activity (or equivalently the oxygen concentration) further the FeO amount in the solid solution ZrO_2:FeO_{ss} is subsequently decreased, from the maximum value of about 3 w% or 5 mole% FeO eventually down to zero. Thus, if necessary, a ZrO_2 dissolution can be prevented by measures which reduce the oxygen concentration respectively the FeO activity in the iron or steel melt.

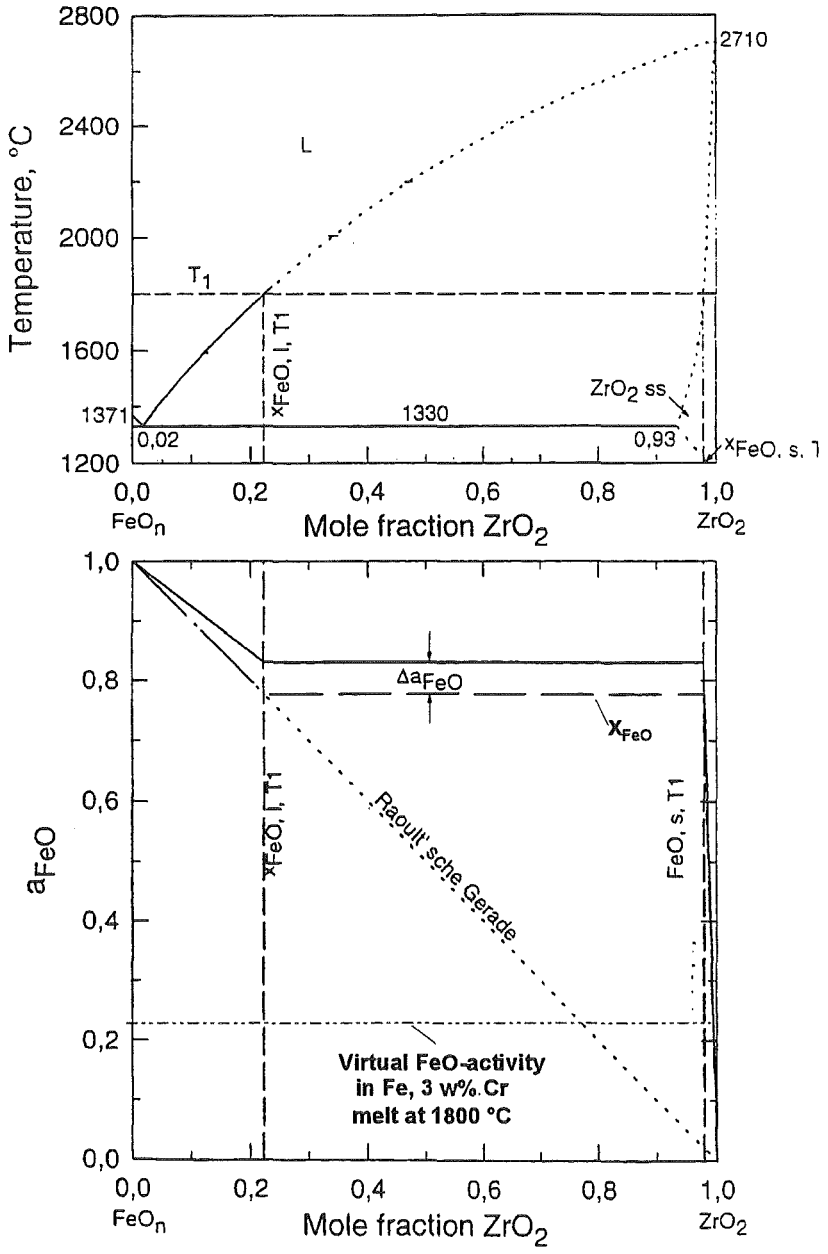

Fig. 6: Phase diagram of the system FeO-ZrO_2 (above) and derived FeO-activity at 1800°C (below) [Pluschkell 1998].

For the case of an iron or steel melt covered by a FeO-containing multi-component oxide melt the same chemical reasoning can be applied. This holds when FeO is the oxide component which gives rise to the highest oxygen concentration (activity) in the metallic melt. Again, the oxygen concentration or rather the FeO activity in the metallic melt determines whether ZrO_2 is chemically stable.

3.3 Application of the Physico-Chemical Concept to the EPR Case

In the long-term phase the oxygen concentration is determined by the presence of the mild desoxidant chromium in the metal melt (about 3w% Cr at 1800-2000°C). Such a Cr concentration decreases the oxygen concentration by a factor of about 2 at 2000°C and of about 4 at 1800°C, compared to an oxygen-saturated iron melt:
Assuming a concentration of 3 w% Cr in the metallic melt the oxygen activity a_O can be calculated according to [Knüppel 1970] using

$$\log K = \log ([\%Cr]^{0.5} a_O) = -\frac{12690}{T} + 5.41 \qquad (3)$$

K equilibrium constant (no dimension)
[%Cr] Cr concentration (w%)
a_O oxygen activity (w%)
T Temperature (K)

Tab 3 contains the saturation oxygen concentration $[O]_{max}$ in Fe (eq. 1), the oxygen activity a_O in a Fe/3 w% Cr melt (eq. 3), the derived FeO activity in the Fe/3 w% Cr melt (eq. 2) and the FeO activity necessary for ZrO_2 dissolution (derived from the FeO-ZrO_2 phase diagram, cf. Fig. 6). As the FeO activity in the Fe/3 w% Cr melt is always below the critical value for chemical dissolution no liquid FeO-ZrO_2 phases occur and only a solid solution of FeO in ZrO_2 is formed.

temperature (°C)	$[O]_{max}$ in an iron melt covered by a pure FeO-slag (w%)	oxygen activity a_O in a Fe/3w% Cr melt (w%)	(relative) FeO-activity a_{FeO} in a Fe/3w% Cr melt (-)	(relative) FeO-activity necessary for the dissolution of ZrO_2 (-)
1600	0.23	0.025	0.11	0.87
1700	0.34	0.05	0.16	0.84
1800	0.49	0.11	0.22	0.77
1900	0.67	0.21	0.31	0.72
2000	0.9	0.39	0.43	0.65

Tab. 3: Data for assessing the chemical stability of zirconia against a Fe/3 w% Cr melt.

In Fig. 6, lower part, the chemical situation described above is visualized. The FeO-activity in a Fe/3 w% Cr melt at 1800°C (a_{FeO}=0.22) is by more than a factor of 3 below the threshold value x_{FeO}=0.77 for the formation of liquid FeO-ZrO_2 phases.

To summarize, a chromium content of 3 w% reduces the oxygen concentration by a factor of about two at 2000°C, and of four at 1800°C. Oxygen concentration and FeO activity are therefore always kept below the critical limit for ZrO_2 dissolution.

Additionally it was assessed if liquid FeO-ZrO_2 phases were formed if the EPR metallic core melt did not contain chromium. For this purpose the oxygen activity of the EPR melt system was calculated by means of GEMINI/TDBCR981 (Thermodata). The database did not contain chromium. The "detour" by calculating the oxygen activity as a parameter for ZrO_2 stability was necessary because the phase field of the "solid solution" of FeO in ZrO_2 is not modeled in the database. The calculated oxygen activity is by a factor of two below the oxygen activity in the FeO-ZrO_2 system at the liquidus composition. This indicates that no liquid FeO-ZrO_2 phases are formed at the interface of metallic melt and zirconia protective layer. This result can be explained by the relatively low FeO content in the oxidic core melt. The oxygen activity induced by the oxidic melt into the metallic melt is then too low for the chemical dissolution of zirconia protective material.

3.4 Experimental Results

At Siemens crucible tests with different zirconia materials (MgO-stabilized brick material, sintered CaO-stabilized ramming mass, zirconia hydraulic-hardening concrete) were performed. Additional large-scale tests are performed at Siempelkamp in the frame of the CORESA project.

As outlined in chapter 3.1,in the EPR case the protective ZrO_2 layer is initially covered by a (Fe,Cr,Ni) melt with a very low oxygen concentration. For such starting conditions crucible experiments (2200°C, 1-6 h, Ar/0.2-0.5 % O_2, 1-6 h) were carried out with 1-1.5 kg of iron or steel (88 w% Fe, 5 w% Cr, 7 w% Ni) melts. The crucible of MgO-stabilized zirconia after 6 h at 2200°C is shown in Fig. 7. Post-test inspection by optical microscopy and scanning electron microscopy showed that no infiltration and no decrease in crucible wall thickness had occurred, i.e. the zirconia had remained stable. In this test the Cr content had decreased from 5 to 4 w% which, together with the formation of a thin slag, indicates that the oxygen concentration had reached its saturation level during the test. In tests at lower temperatures of 1850-2000°C with a more rapid oxygen saturation of the iron/chromium melt, e.g. by adding oxidic slag, the crucible in contact with metallic melt had remained stable, too.

At the current state of knowledge, (unsintered) ramming mass is the most promising application form for the bottom area of the spreading room. It has to be shown, however, that a dense, sealed sinter layer is "in-situ" formed in contact with the metallic core melt under EPR conditions.

The formation of a sinter layer and the extent of melt infiltration into the ramming mass were investigated using inductively heated iron or steel melts. The experiments were performed with 1-1.5 kg metallic melts of different oxygen potentials to establish the influence of dissolved oxygen on melt infiltration. A very low oxygen potential, as initially present in the case of the EPR, was achieved by a (Fe, 5 w% Cr, 7 w% Ni) melt in an Ar/ 0.2-2 % O_2 atmosphere. Higher oxygen potentials were achieved by a Cr-free iron melt in air or directly by FeO additions to the iron melt. Heating rates were chosen from 6°C/min (highest rate under EPR conditions) up to about 30°C/min. Generally, at lower heating rates a more favourable sintering behaviour is expected from technological experience. Therefore the higher heating rates represent more conservative conditions for the formation of a sealed sinter layer.

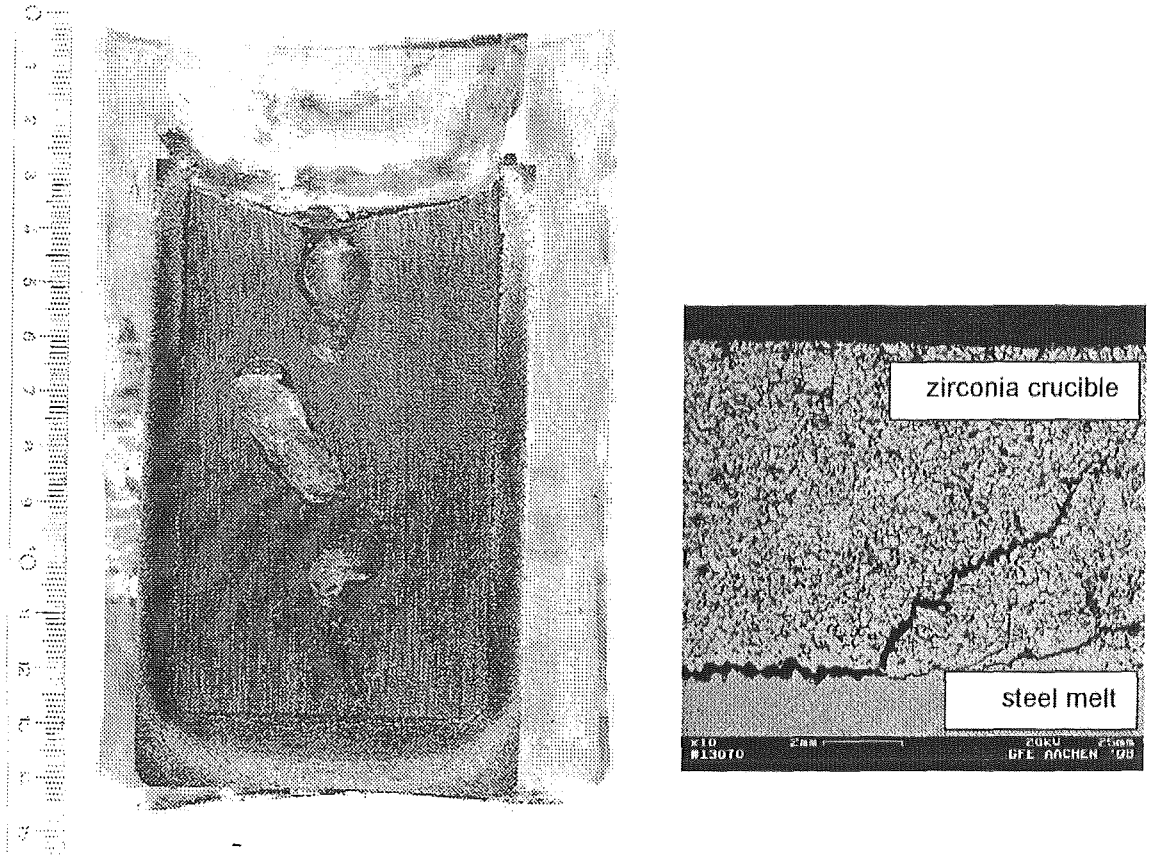

Fig. 7: Left: MgO-stabilized zirconia crucible with steel melt after heating at 2200°C for 6 h in Ar/0.2-0.5 % O_2, initial melt composition 88 w% Fe, 5 w% Cr, 7 w% Ni.
Right: SEM-micrograph of crucible wall.

Even at high heating rates, independent of the oxygen potential, a sealed sinter layer had formed which prevented infiltration of the metallic melt into the ramming mass. The experiments showed that the oxygen potential influences the thickness of a small mixed layer of metal and ramming mass formed atop of the sealed sinter layer. At the low oxygen potential initially present in the EPR case practically no mixed layer was formed. In an experiment using an iron melt with maximum oxygen potential a mixed layer of less than 5 mm had formed.

A temperature-time course typical for EPR conditions with the highest heating rate was also reproduced in tests with ramming mass (Fig. 8). After the heating up phase the melt was kept for 3 hours at 1900°C.

The steel melt consisted initially of 88 w% Fe, 5 w% Cr, and 7 w% Ni. The experiment was performed under argon atmosphere including 2 vol% oxygen. The slag layer on top of the solidified metal ingot indicated that oxygen saturation was reached during the experiment. The cross section of the crucible (Fig. 9) reveals that a sealed sinter layer had formed. There is no indication of any erosion or infiltration of steel melt into the ramming mass.

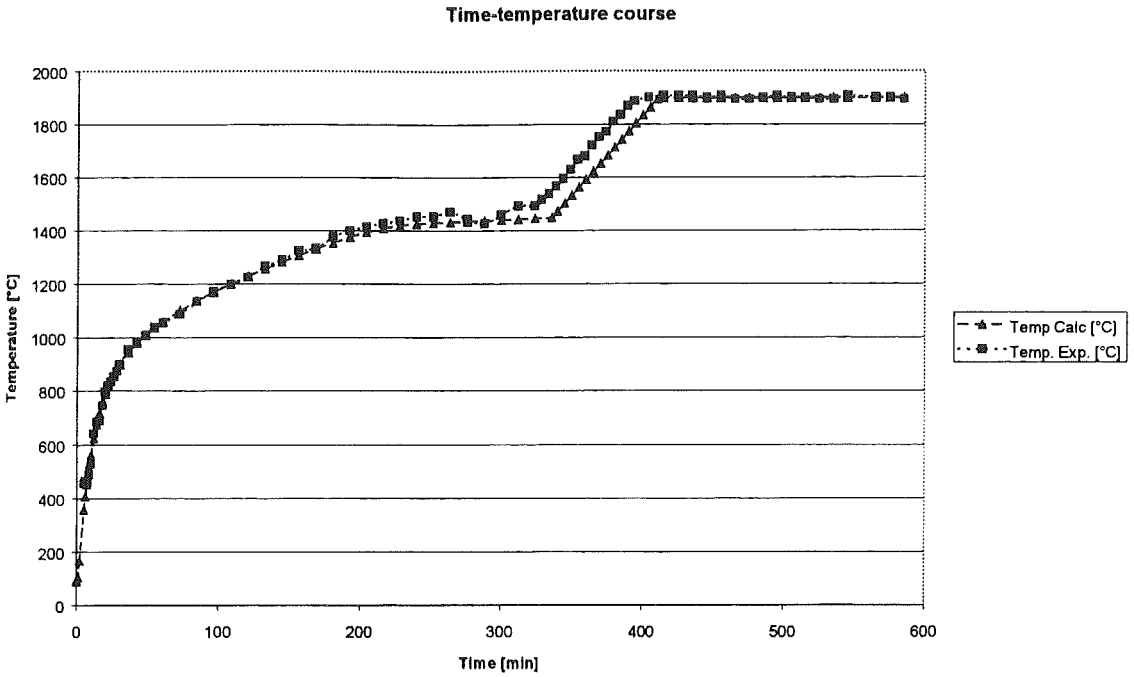

Fig. 8: Calculated and experimental temperature-time course of the experiment on sealed sinter layer formation and infiltration behaviour. Calculated: highest expected heating rate under EPR conditions.

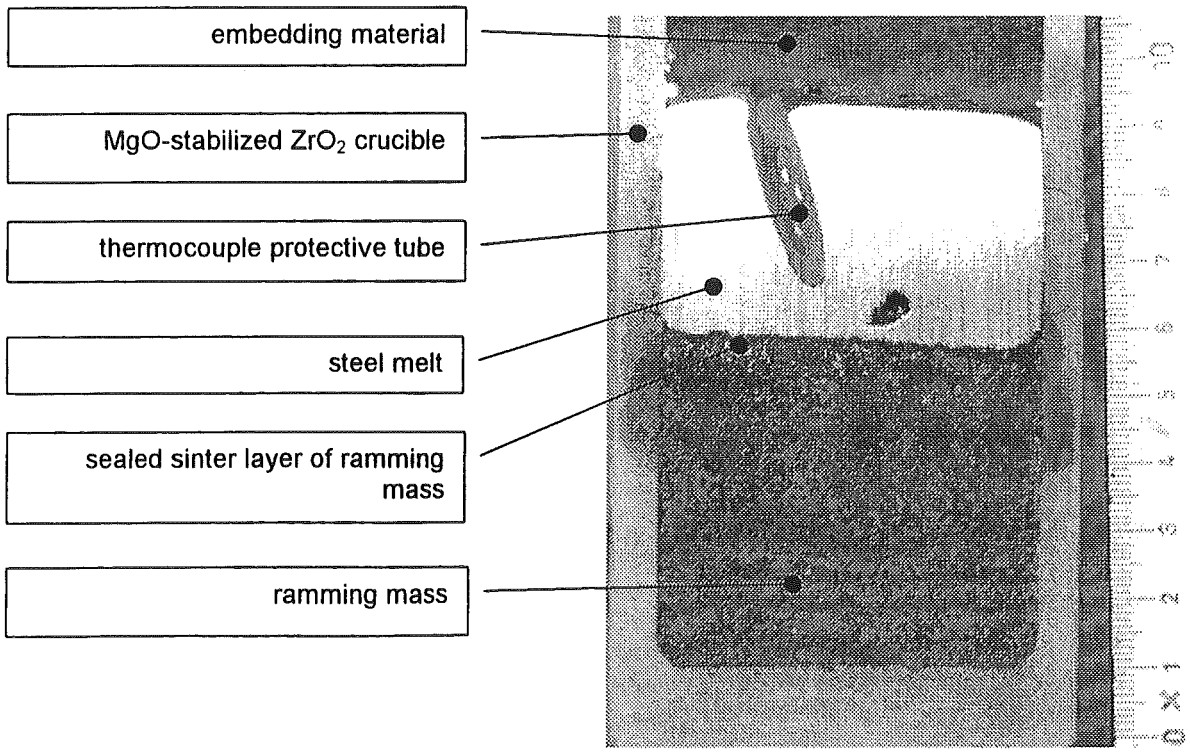

Fig. 9: Cross section of the crucible after the experiment on the sintering behaviour of ramming mass in contact with a steel melt heated up under EPR conditions.

The formation of a sealed sintered layer in the ramming mass under EPR-typical conditions was additionally confirmed by a large scale experiment (50 cm diameter) in the frame of the CORESA project. In this experiment a (Fe,Cr,Ni) steel melt contacting unsintered ramming mass was heated up to 1700°C with a heating rate expected under EPR conditions. Again no infiltration of the steel melt into the ramming mass and no erosion process was observed.

4 Summary and Conclusions

In the EPR core melt stabilization concept sacrificial material is employed for conditioning of the core melt and protective material for melt retention. Experimental results demonstrate that the target of decreasing the initially very high liquidus temperature of the melt down to 1800-1850°C is met. This liquidus temperature is also maintained when variations of the melt composition (especially chromium oxide, boron oxide) are considered. The analysis of the melt chemistry shows that chromium exists in the metallic melt which is beneficial for the stability of the protective zirconia layer in contact with the metallic melt. Knowledge from the field of metallurgy and experimental results confirm that zirconia is chemically stable in contact with the EPR steel melt. At the current state of knowledge ramming mass is the most promising technological application form for the bottom area of the spreading room.

5 References

[Fischer 1999] - M. Fischer
Main Conceptual Features of the EPR Melt Retention Concept
OECD Workshop on Ex-Vessel Debris Coolability, Karlsruhe Germany, Nov. 15-18, 1999.

[Horvath 1970] - A. Horvath
Physikalisch-Chemische Berechnungen in der Metallurgie
Akadémiai Kiadó, Verlag der Ungarischen Akademie der Wissenschaften, Budapest 1970.

[Knüppel 1970] - H. Knüppel
Desoxydation und Vakuumbehandlung von Stahlschmelzen
Verlag Stahleisen m.b.H., Düsseldorf 1970.

[Kojima 1968] - Y. Kojima, H. Sakao, K. Sano
Chromoxyd im Gleichgewicht mit Eisen-Chrom-Legierungen bei 1600°C
Arch. Eisenhüttenwes. 39 (1968) 187.

[Nie 1999] - M. Nie
Application of Sacrificial Concrete for the Retention and Conditioning of Molten Corium in the EPR Melt Retention Concept
OECD Workshop on Ex-Vessel Debris Coolability, Karlsruhe Germany, Nov. 15-18, 1999.

[Pluschkell 1998]
Prof. Dr.-Ing. W. Pluschkell, university of Clausthal-Zellerfeld, personal communication, April 1998.

Abbreviations

CORESA	Corium on Refractory and Sacrificial Material
EPR	European Pressurized Water Reactor
MCCI	Molten Corium Concrete Interaction

OECD Workshop on Ex-Vessel Debris Coolability
Karlsruhe, Germany, 15-18 November 1999

Organised in collaboration with
Forschungszentrum Karlsruhe (FZK) GmbH

Equations for Solidification of Corium and Consequences

J.M. Seiler, K Froment, J.P. Garandet
CEA Grenoble DTP and CEREM
17 rue des Martyrs, Grenoble 38054 Cedex 09 France
seiler@dtp.cea.fr

ABSTRACT

Recent developments [Froment, Seiler, 1999] have shown the importance of a strong coupling between Thermalhydraulics and Physicochemistry to describe late phases of severe accidents of LWRs. For several applications, like corium pool behaviour and Molten Core Concrete Interaction (MCCI), the solidification process of corium is an important phenomenon. The purpose of this paper is to analyse these solidification processes at the light of knowledge developed in metallurgy. Definitions of different concepts will be recalled as well as the basic equations relative to solidification processes. These concepts and equations will be applied to corium. Important consequences will be outlined, particularly for the thermalhydraulic steady state situation. The transient solidification of corium will also be analysed and some conclusions concerning macrosegregation will be discussed.

1. INTRODUCTION: SYSTEM CONSIDERED, SHORT TERM AND LONG TERM SOLIDIFICATION

In the next, we will consider a volumetrically heated layer of molten oxidic corium of finite thickness (H) and infinite width. This layer is suddenly cooled on one of its surface which is represented by a constant temperature T_{ext} as boundary condition on this surface. The opposite surface of the corium layer is supposed to be adiabatic.

Due to the contact with a cold surface, the melt is freezing and an initial solid layer is established with a characteristic time given by:

$$\tau_1 = \frac{K\rho L \Delta T_{sol}}{\varphi^2} \qquad \text{(Eq. 1)}$$

for oxidic corium and $\varphi \sim 10^5$ W/m² => $\tau_1 \sim 1320$ s = 22 mn.

The characteristic thickness of the solid layer is e_0 ~3 cm. If the thickness of the overall corium layer (H) is greater than e_0, then the remainder of the corium layer will only solidify when the residual power will decrease. The kinetics of this solidification is much smaller and may take days and months.

The solidification may, thus, be split into two main periods:

Period 1: $t < \tau_1$ for initial solidification and
Period 2: $t > \tau_1$ for long term solidification.

2. LONG TERM SOLIDIFICATION $t > \tau_1$

For the investigation of the long term solidification, we will consider as initial condition an homogeneous liquid layer of uniform composition C_0 and finite thickness $H_0 = H - e_0$. The solidification rate is given by:

$$R = -\frac{K\Delta T_{sol}}{\varphi^2}.\frac{\delta\varphi}{\delta t} \qquad \text{(Eq. 2)}$$

in which $\frac{\delta\varphi}{\delta t}$ is imposed by the decrease of residual power. Supposing a characteristic decrease period of the residual power of 1 month: R ~10^{-8} m/s. The theory developed by Favier [1981](see also transient aspects in part 3 for more details), shows that the solidification behaviour is controlled by the parameter:

$$\Delta = \frac{\delta_s R}{D} \qquad \text{(Eq. 3).}$$

In our case of interest, assuming that D varies in the range: 10^{-9} to 10^{-7} m²/s (molecular diffusivity increases at elevated temperature), taking δ_s~1 mm for natural convection (see part 5) and R ~10^{-8} m/s, the parameter Δ varies in the range 10^{-4} to 10^{-2} and is much smaller than unity. Under these conditions, Favier has shown that the composition of the solid is well approached by the Burton, Prim and Schlichter (BPS) solution [Flemings, 1974](see also part 3), which is the Gulliver-Scheil solution (part 3), but with an effective partition ratio given by:

$$k_{eff} = \frac{k}{k + (1-k)e^{-\Delta}} \qquad \text{(Eq. 4)}$$

When Δ is small, which is the case in our problem, k_{eff} is equal to k. This means that, in that case, macrosegregation takes place, liquid can be considered as well mixed and the interface temperature between solid and liquid is the liquidus temperature of the remaining liquid. Furthermore, when the solid fraction remains small (case of interest for In-Vessel corium pools with elevated residual power) the remaining liquid has approximately the composition of the considered corium layer. Thus, the interface temperature is approximately the liquidus temperature of this considered corium layer.

Validity of the hypothesis of plane front (see annex 2)

Many studies have been devoted to the analysis of the morphological stability of the solidification front. However, these studies consider generally steady state solidification (in the metallurgical sense, i.e. constant solidification rate (R)) for which the interface temperature is the solidus temperature of the considered binary mixture. For long term corium solidification, as shown above, the solidification rate is very small and the interface temperature tends to the liquidus temperature of the remaining liquid. Due to the heat transfer in the volumetrically heated corium, the temperature in the liquid will, at any point in the liquid, be higher than the liquidus temperature corresponding to the composition of the remaining liquid. Thus, cellular solidification is not possible and the assumption of plane front solidification during long term corium cooling is justified (see also Annex 2).

Effect of density ratios, viscosity and sparging gas

For corium, the ***density*** of the segregating refractory phase is higher than the density of the residual liquid. Thus, segregation is clearly reinforced for bottom cooling (for instance

for corium-concrete interaction). For top cooling, density effects may contravene phase segregation (for instance: top cooling in EPR). ***Viscosity*** may have an effect on the transport of species by convection and may increase the thickness of the mass transfer boundary layer (see annex 1 and part 5). Thus, an increase of viscosity will certainly increase the parameter Δ. However, the viscosity is not an independent function of the overall melt behaviour: segregation increases the temperature and decreases drastically the viscosity (to, about, a few 0,1 Pa.s for corium-concrete interaction) [J.M. Seiler, 1996]. ***Sparging gas*** may certainly affect the solidification process, but may be not in the long term, when the superficial velocity of gas decreases. The analysis of MACE experiments (M1B and M3B) have shown that segregation occurs clearly for corium-concrete interaction of several hours [Farmer, 1998]. The effect of gas sparging seems to be important for the short term interaction, during Period 1 ($t < \tau_1$), i.e. during crust formation.

3. SHORT TERM SOLIDIFICATION

The coherent approach in metallurgy consists in using plane front solidification models and test if the constitutional supercooling criterion (see annex 2), based on the results of the plane front solidification calculations, is reached or not, in order to know if the application of plane front solidification models is justified. If the constitutional supercooling criterion is satisfied, the plane front model should be replaced by a cellular solidification model, which is much more complex.

Even if the constitutional supercooling criterion is satisfied, plane front solidification models are expected to provide tendency results of interest.

3-1. Usual plane front solidification models

The different usual models differ by their assumptions concerning mass transfer in the solid and liquid layers.

Equilibrium solidification

It is supposed here that diffusion is infinite in the solid and in the liquid. Under these very simple conditions, the whole solid is in thermodynamic equilibrium with the whole liquid. This approach has been used for the modelling of viscosities of weel-mixed corium-concrete mixtures [Seiler and Ganzhorn, 1997]. For binary systems, the solidification process is described by the lever rule:

$$f_s = \frac{C_l(T) - C_0}{C_l(T) - C_s(T)} \qquad \text{(Eq. 5)}$$

No solid diffusion, infinite diffusion in liquid

During cooling and solidification, the liquid becomes richer in solute and so the solid that forms is of higher solute content at later stages of solidification. However, since there is no diffusion in the solid state, the composition of the solid formed in the initial stages of freezing remains unchanged. For binary mixtures and constant partition coefficient (k), this case is described by the Scheil-Gulliver equation:

$$C_{s,I} = kC_0(1 - f_s)^{(k-1)} \text{ and } C_l = C_0 f_l^{k-1} \qquad \text{(Eq. 6)}$$

Applying this model with a small partition coefficient (k) (which is a case of interest for corium solidification) provides results which are equivalent to the results which are obtained with the assumption of equilibrium solidification. This model approach has been used for the interpretation of ACE Corium-Concrete Interaction tests [Seiler, 1996] and for the interpretation of RASPLAV non-eutectic salt tests [Seiler, 1998].

Limited liquid diffusion, no convection, no diffusion in the solid

The solute rejected into the liquid is transported only by diffusion and so an enriched solute boundary layer forms. The problem has been solved when R=Constant , $C_l = \frac{C_0}{k}$ at $x = 0$ (steady state for metallurgy !) and $C_l = C_0$ at $x = \infty$ by Tiller, Jackson, Rutter and Chalmers (TJRC):

$$C_l = C_0 (1 + \frac{1-k}{k} e^{-(\frac{R}{D})x}) \qquad \text{(Eq. 7)}$$

where x is the distance from the freezing interface ($x \neq z$). The quantity $\frac{D}{R}$ may be considered a characteristic distance, the diffusion distance.

3-2. Solidification controlled by conduction in a substrate; Pure Diffusion Model by Favier & Gilly [1981] (see N.B.)

This is a case of interest for corium solidification on a basemat. The solidification process is mainly governed by the parameter

$$Y = \frac{\sqrt{\alpha_l}}{\sqrt{D}} = \left(\frac{Sc}{Pr}\right)^{\frac{1}{2}} \qquad \text{(Eq. 8)}$$

For each corium, three levels are considered for molecular diffusivity: 10^{-7}, 10^{-8} and 10^{-9} m²/s. Let us consider that the substrate has infinite thermal conductivity. By the way, this means that the interface temperature between the substrate and the melt is imposed at T_0. We suppose also that the solid oxide has the same properties as the liquid. The governing parameter Y ranges from about 1,5 (oxidic corium with elevated molecular diffusity) to about 30 (metallic corium with small molecular diffusivity). A small effective partition coefficient k_{eff} can be obtained as long as Y is smaller than approximately 5; this means as long as oxidic corium is considered with a molecular diffusion coefficient higher or equal to 10^{-8} m²/s. For elevated Y (i.e., metallic corium and small molecular diffusion coefficients), the freezing layer is calculated to have the same composition as the initial melt, in the frame of these model assumptions.

3-3. Boundary layer controlled mass diffusion

Constant solidification rate

One of the limiting assumptions of the preceding approach is the assumption of diffusion controlled mass transport in the liquid. In order to clarify the effect which may be related to a mass transport process controlled by diffusion in a small boundary layer, we have developed a simplified approach based on following assumptions :

1. Plane front solidification is considered

2. a 1D geometry is considered
3. the liquid is initially at uniform temperature T
4. this fluid solidifies at a temperature Ti (supposed constant) on a substrate
5. the freezing rate (interface velocity) (R) is first supposed constant vs time.
6. the liquid is a binary mixture characterized by a constant partition ratio (k) and a constant composition at infinite (C_0)
7. there is no density difference between the liquid and the deposited solid
8. properties are constant
9. the mass transfer in the liquid is controlled by pure diffusion but in a boundary layer of reduced thickness δ_s; the diffusion coefficient is noted D. Outside the boundary layer, liquid composition is uniform, and, inside, mass transport is by diffusion only (flux created by the concentration gradient in the boundary layer:($D\frac{dC_l}{dz} = D\frac{C_{l,I} - C_0}{\delta_s}$). The thickness of the boundary layer being small, the parameter $\Delta = \frac{\delta_s R}{D}$ is thus supposed to be small in comparison to 1.
10. no diffusion is considered in the solid layer; infinite diffusion is considered in the rest of the liquid
11. no volumetric heating is considered in the liquid.

Taking into account that $dt = \frac{dz}{R}$, the following equation controlling the composition $C_{l,I}$ of the liquid at the interface is derived (see N.B.):

$$\frac{dC_{l,I}}{dz} - \frac{2C_{l,I}}{\delta_s}\left[(1-k) - \frac{D}{\delta_s R}\right] - \frac{2DC_0}{R{\delta_s}^2} = 0 \qquad \text{(Eq. 9)}$$

The maximum thickness of the diffusion boundary layer is, in the frame of this formalism, $\delta_s = \frac{D}{R}$ (pure diffusion layer). With following initial condition: $C_{l,I}(z=0) = C_0$, the solution, derived from this simple model, is given by:

$$C_{l,I} = C_0\left[\frac{1}{1 - \frac{R\delta_s}{D}(1-k)} - \left(\frac{1}{1 - \frac{R\delta_s}{D}(1-k)} - 1\right)e^{-\frac{2z}{\delta_s}\left(k - 1 + \frac{D}{\delta_s R}\right)}\right] \qquad \text{(Eq. 10)}$$

The composition of the solid is given by:

$$C_s(z) = kC_{l,I} \qquad \text{(Eq. 11)}$$

When the exponent becomes great (steady state in metallurgy), $C_{l,I}$ tends towards $\frac{C_0}{1 - \frac{R\delta_s}{D}(1-k)}$, thus : $k_{eff} = \frac{k}{1 - \frac{R\delta_s}{D}(1-k)}$ (Eq. 12)

Burton, Prim and Slichter [Flemings, 1974] have derived a solution (without some simplifications introduced in the model described above) which is valid when the steady state (in the sense of metallurgy (i.e.: constant freezing rate and when initial or final freezing transients are omitted)) is reached. These authors have shown that the solution can, then, be written in the form of equation (Eq. 6 (Scheil Gulliver)) provided that an effective partition coefficient is used: $k_{eff} = \frac{k}{k+(1-k)e^{-(\frac{R\delta_s}{D})}}$. As $\frac{\delta_s R}{D}$ is supposed to be small in comparison to 1, it can be shown that this equation is equivalent to $k_{eff} = \frac{k}{1-\frac{R\delta_s}{D}(1-k)}$ found above.

When $\frac{\delta_s R}{D} << 1$, that is, for small growth rate, high liquid diffusivity and minimum δ_s, (case considered in part 1. For long term corium solidification governed by the decrease of residual power) solute distribution is described by the special case given earlier where infinite diffusivity in the liquid was assumed (Scheil Gulliver). When Δ ($=\frac{\delta_s R}{D}$) tends towards zero, the composition of the solid phase is equal to kC_0 and the interface temperature is equal to the liquidus temperature corresponding to the composition of the remaining liquid. The interface becomes then unconditionally stable (annex 2) since all the liquid in the boundary layer is above liquidus temperature.

Variable solidification rate and volumetric heating in the liquid

Let us now consider a simple model for crust growth controlled by heat conduction through the solid. We suppose that the crust is forming on a surface whose temperature is constant (T_0). We suppose furthermore that the temperature profile in the solid layer is linear. The temperature at the interface between solid and liquid is also supposed to stay constant (T_i). The liquid is submitted to volumetric heating and we consider that the heat flux transmitted from the liquid to the interface is constant (φ_0)(no heating in the solid).

With these assumption, the equation controlling the freezing rate is (see N.B.):

$$R = \frac{\lambda \Delta T}{z\rho L'} - \frac{\varphi_0}{\rho L'} = \frac{A}{z} - R_0 \qquad \text{(Eq. 13)}$$

with $\Delta T = T_i - T_0$; $L' = L + C_p \frac{\Delta T_{sol}}{2}$; L: latent heat of phase change; $A = \frac{\lambda \Delta T_{sol}}{\rho L'}$ and $R_0 = \frac{\varphi_0}{\rho L'}$.

The freezing rate will tend towards zero when the thickness of the solid layer z tends towards its steady state value: $z_{ss} = \frac{A}{R_0}$ (thermalhydraulic steady state). Equation (13) has following solution, supposing initial condition $z(t=0) = z_{init}$ (with: $z_{init} < z_{ss}$):

$$t^* = s_{init} - s + ln(\frac{1-s_{init}}{1-s}) \qquad \text{(Eq. 14)}$$

with: $t^* = \frac{t}{\tau_{sol}}$; $\tau_{sol} = \frac{\lambda \rho L' \Delta T_{sol}}{\varphi_0^2}$; $s = \frac{z}{z_{ss}}$ (with: $s_{init} < s < 1$); $s(t^* = 0) = s_{init}$

The differential equation (9) for $C_{l,I}$ cannot be solved analytically for the considered variation of freezing rate. However, a partial analytical solution can be found provided that:

$$z > \delta_s \left\{ \frac{A}{D\left[1-(1-k)\frac{\delta_s R}{D}\right]} \right\}^{\frac{1}{2}} \qquad \text{(Eq. 15).}$$

This solution is: $C_{l,I} = C_0 \dfrac{1}{1-(1-k)\dfrac{\delta_s}{D}\left(\dfrac{A}{z}-R_0\right)}$ (Eq. 16).

This solution shows that, when $z = z_{ss}$, then $C_{l,I} = C_0$ and the composition of the solid at the interface is $C_{s,I} = kC_0$, which means complete macrosegregation.

3-4. Effect of assumptions concerning diffusion in the liquid on final steady state (plane front solidification models)

It can also be shown that, when the partition coefficient (k) is equal to zero, the crust thickness and interface temperature obtained for the final steady state (in the thermalhydraulic sense i.e. constant power and zero freezing rate) does not depend on assumptions made about diffusion in the liquid (see N.B.). The final situation calculated by the different plane front solidification models is the same. A model based on plane front solidification and boundary layer controlled mass diffusion (and no diffusion in the solid phase) has been used by [Semenov et al., 1999] for the interpretation of the transient aspects related to RASPLAV non-eutectic salt experiments. It must be noted here that, if diffusion in the solid is neglected and if the partition coefficient is equal to zero (k=0, which is the case for the NaF - NaBF4 system used in RASPLAV salt), then all plane front solidification models predict that the solid is pure NaF. The chemical analyses performed on RASPLAV showed that the solid layer contained some NaBF4. This means that either diffusion in solid occurred from the liquid phase or that the plane front assumption is not strictly valid (cellular solidification model should then be used). Another possibility is that k is not strictly equal to zero.

3-5. Effect of density variation

In the following, the approach used for boundary layer controlled mass diffusion model at constant solidification rate will be extended (with the same basic hypotheses) to the case where the density of the solid phase is different from the density of the liquid phase. It is supposed that solid and liquid phases have constant densities, respectively ρ_s and ρ_l which do not depend on composition variations in both phases (the boundary layer is considered to belong to the liquid). Equation (9) is replaced by (see N.B.):

$$\frac{d\omega_{l,I}}{dz} - \frac{2\omega_{l,I}}{\delta_s}\left[(1-k)\frac{\rho_s}{\rho_l} - \frac{D}{\delta_s R}\right] - \frac{2D\omega_{l,0}}{R\delta_s{}^2} = 0 \qquad \text{(Eq. 17)}$$

This equation provides a first approach to the effect of density variation.

It is seen that, when the exponent becomes great (steady state in metallurgy), $C_{l,I}$ tends towards $\dfrac{C_{l,0}}{1-\dfrac{R\delta_s}{D}(1-k)\dfrac{\rho_s}{\rho_l}}$, thus $k_{eff} = \dfrac{k}{1-\dfrac{R\delta_s}{D}(1-k)\dfrac{\rho_s}{\rho_l}}$. If $\rho_s > \rho_l$, the effect of density variation will be an increase of the effective partition coefficient, which means less

segregation. As a first approximation, it can be considered that the equivalent effect of density variation is to increase the thickness of the diffusive boundary layer: $\delta_{eff} = \delta_s \frac{\rho_s}{\rho_l}$.

For more complex situations, for instance when the density is considered to depend on local composition, the more complete equations, given in annex 1, must be solved.

3-6. Specific application to corium-concrete mixtures

In the case of corium-concrete mixtures, the partition coefficient [in a pseudo-binary phase diagram based on refractory oxides (UO_2 and ZrO_2) and decomposition products from concrete] is much less than unity. This is due to the fact that melting of such mixtures always begins with the liquefaction of the decomposition materials coming from concrete, containing very small amounts of refractory materials. The solidus temperature is about 1500 K, even for small amounts of concrete. The solid at equilibrium contains, thus, mainly refractory oxides (UO_2 and ZrO_2) which corresponds to the composition of the corium when it exits the vessel and comes into contact with concrete. As a consequence, supposing that the composition of a solid crust which would form during Period 1 ($t < \tau_1$ for short term solidification) corresponds to the average composition of corium, as it arrives from the vessel, does not make a great difference when compared with the composition which would be deduced with a plane front solidification model, such as the Scheil Gulliver model. For later MCCI phases, during period 2, the liquid will be enriched in decomposition products of concrete and this, in turn, may entrain partial dissolution of the original solid layer and a decrease of the melt temperature.

4. WHAT IS LACKING ?

For further investigations what is clearly lacking is a tool able to calculate **cellular front** solidification since calculations presented above show that for **the short term solidification** (controlled by thermal resistance of the solidifying layer, such as during spreading) the assumption of plane front solidification seems generally not to be justified (see part 3). Thus, the conclusions which are drawn from actual plane front models concerning the composition of the initial solid may be questionable. However, **for long term solidification**, controlled by the decrease of the volumetric power dissipation, the freezing rate is small enough to justify actual assumptions of plane front and interface temperature equal to the liquidus temperature of the residual liquid. The effect of density variations during solidification and of sparging gas are not known and must be investigated.

5. CONSIDERATIONS ON THE THICKNESS OF THE MASS DIFFUSION BOUNDARY LAYER UNDER NATURAL CONVECTION

Specific developments, which are not presented in detail, here lead to the conclusion that, for natural convection situations, following relation should be valid (see N.B.):

$$\frac{\delta_S}{H} \sim (GrSc)^{-\frac{1}{3}} \qquad \text{(Eq. 18)}$$

ANNEX 1: General equations for solidification -The dilute alloy assumptions

Basic equations for solidification processes can be found in [Garandet et al., 1994]. According to these authors, the conservation of species at the solid/liquid boundary can be written:

$$\omega_{L,I}^{j}(1-k_0^j)V_{L,I}.n = [(\frac{\rho_{S,I}}{\rho_{L,I}})D_S^j \nabla\omega_{S,I}^{j} + D_m^j \nabla\omega_{L,I}^{j}].n,$$

and the species transport in the solution:

$$\frac{\delta\rho^j}{\delta t} + \nabla\bullet(-\rho_L D_m^j \nabla\omega^j + \rho^j V) = 0$$

It has been considered that ordinary concentration diffusion is the most important contribution to the diffusion terms. Soret effect and Dufour effect have been neglected. These effects are temperature gradient induced mass transfer (Soret) and pressure gradient induced mass transfer (Dufour). Pressure gradients are generally negligible in boundary layers; the Soret effect is an inverse function of the absolute temperature and is, thus, generally small at elevated temperatures [Moreau, 1973].

The dilute alloy approximation

It is supposed that the mixture is formed of traces of different species (2, 3, ...) in a melt consisting of nearly pure constituent 1, that the total mass density of the solution does not depend on composition, the fluid is incompressible, D_m^j does not depend on composition and temperature, k_0^j is constant (k), densities of solid and liquid are equal.

A coordinate frame moving at a rate R (solidification rate) with respect to the laboratory is considered.

Under these conditions, preceding equations simplify to:

$$\frac{\delta C}{\delta t} + (V\bullet\nabla)C = D\nabla^2 C + (R\bullet\nabla)C - D\nabla C\bullet n = C(1-k)R\bullet n,$$

With these assumptions, equations can be defined equivalently in terms of mass and mole fractions.

Remark about molecular diffusion coefficient [Moreau, 1973]

Molecular diffusion is very sensitive to the composition of a liquid melt. For liquids, D is generally increasing with the temperature. More generally, from the Stokes-Einstein equation, it is also possible to write that the product ($D\mu$) is proportional to the temperature T. Thus, at constant temperature, the molecular diffusion varies approximately as: $\frac{1}{\mu}$.

ANNEX 2: Plane front to cellular solidification. Constitutional supercooling.

A solute rich layer is present in front of a growing interface. If liquid, immediately in front of the interface is at an actual temperature that is below its equilibrium liquidus temperature (depending on local composition) the freezing front becomes unstable and cellular solidification occurs. Chalmers [Flemings, p 59] and coworkers termed this constitutional supercooling. Constitutional supercooling is absent when the actual temperature

gradient in the liquid at the interface (G) is equal or greater than $(\frac{\delta T_{liquidus}}{\delta x})$. In case of constant solidification rate (R=Cst), this criterion reduces to:

$$\frac{G}{R} \geq -\frac{m_L C_0 (1-k)}{kD} \quad \text{called Chalmer's criterion} \qquad \text{(Eq. 19)}$$

This criterion is not valid when the freezing rate is not constant and must be replaced by the more general comparison of temperature gradients $(G \geq \frac{\delta T_{liquidus}}{\delta x})$. Chalmer's approach has been refined ([Mullins-Sekerka, 1964] criterion) but equation 19 can often be taken as a "rule of thumb" definition of the morphological stability threshold.

N.B.: This paper has been intentionally shortened due to editor constraints. A detailed paper presenting all assumptions and calculations can be obtained on request.

NOMENCLATURE

C: solute composition in a dilute binary alloy (mass or mole fraction)

C_0: composition of the liquid

Cp: specific heat of solid layer (J /kg K)

D: molecular diffusivity (m^2/s)

H: height of fluid layer (m)

K: thermal conductivity of the solid layer (W/mK)

L: effective heat of solidification $L = CpDT / 2 + L_m$ (J/kg)

R: solidification rate (m/s)

g: gravitational acceleration (m^2/s)

h: effective heat transfer coefficient (W/m^2K)

n: unit vector, normal to the interface

z: distance to the surface of initial freezing (m)

x: distance from interface (m)

m_l: $\frac{dT_{Liquidus}}{dC_L}$ slope of the liquidus curve

α: thermal diffusivity (m^2/s)

β: thermal volumetric expansion coefficient (1/K)

μ: dynamic viscosity (kg/ms)

ν: kinematic viscosity (m^2/s)

δ_s: thickness of mass boundary layer (m)

δ_H: thickness of hydrodynamic boundary layer (m)

δ_T: thickness of thermal boundary layer (m)

ω^j: mass fraction of component j in solution $(\frac{\rho^j}{\rho_L})$

$\omega^j_{L,I}$: mass fraction of component j in the liquid at the interface

$\omega^j_{S,I}$: mass fraction of component j in the solid at the interface

k_0^j : equilibrium partition coefficient of constituent j ($k_0^j = \frac{\omega_{S,I}^j}{\omega_{L,I}^j}$)

k_m: effective mass transport coefficient

$V_{L,I}$: fluid advection rate (m/s)

$\rho_{S,I}$: mass density of the solid at the interface (kg/m^3)

$\rho_{L,I}$: mass density of the liquid at the interface (kg/m^3)

ρ^j : mass concentration of constituent j, i.e. mass of species j per unit volume of solution

ρ : density of the solid layer (kg/m^3)

D_S^j : solute diffusion coefficient of component j in the solid (m²/s)

D_m^j : effective binary diffusivity of the mixture (m²/s)

∇ : Nabla operator

φ : steady state heat flux transmitted through the crust (W/m²)

ΔT_{sol} : temperature difference over solid layer (K)

ΔT : superheat in the liquid (K)

T_i: interface temperature (K)

T_0: initial temperature of substrate (K)

U: velocity scale in the fluid (m/s)

Ra: Rayleigh number

Gr: Grashof number

Sh: Sherwood number

Sc: Schmidt number

Nu: Nusselt number

Pr: Prandtl number

REFERENCES

Farmer M. [1998]: Results of solidified Corium concentration on basemat vs. Distance from Concrete interface. ACE/MACE TAC Meeting, January 1997

Favier J.J., Gilly L., [1980]: Etude théorique d'une méthode simple d'élaboration de cristaux homogènes à dopage élevé. CR DMG N°107/80

Favier J.J. [1981]: Macrosegregation I. Unified analysis during non-steady state solidification. Acta Matallurgica Vol. 29, pp. 197 to 204.

Favier J.J., [1981]: Macrosegregation II. A comparative study of theories. Acta Metallurgica Vol 29, pp 205 to 214.

Flemings M.C. [1974]: Solidification Processing. Material and Engineering Series, Mc Graw Hill , 1974

Froment K., Seiler J.M [1999] On the importance of a strong coupling between Physicochemistry and Thermalhydraulics for modelling late phases of severe accidents in LWRs. Ninth International Topical meeting on Nuclear reactor Thermal-Hydraulics (NURETH-9) San Francisco, California, October 3-8

Garandet J.P., Favier J.J., Camel D. [1094] "Segregation Phenomena in Crystal Growth from the Melt" Handbook of crystal growth 2, Chapter 12 Edited by J.P. Hurle, North Holland Publishing Company

Kurz and Fisher [1992], " fundamentals of solidification" 3rd edition. Trans tech publications.

Moreau, 1973 "Transferts Thermiques" INP Grenoble

Mullins W.W., Sekerka R.F., 1964, Stability of a planar interface during solidification of a dilute binary alloy, Journal of Applied Physics, volume 35, number 2, pp. 444-451, february 1964.

Schlichting, 1968 "Boundary Layer Theory", McGraw Hill Book Company

Seiler J.M. , 1996 " Phase segregation model and molten pool thermal-hydraulics during molten core-concrete interaction ". Nuclear Engineering and Design 166 (1996) 259-267.

Seiler J.M. and Ganzhorn J., 1997 " Viscosities of corium-concrete mixtures " Nuclear Engineering and Design Vol 178 (1997) N°3 December IV 1997 pp 259-268

Seiler J.M., 1998 "Analysis of tests 55-50 and 60 from fourth series of RASPLAV salt test" Note SETEX/LTEM 98-85

Semenov V., Strizhov V., Krylov S., 1999 "Results of the Post-Test Analysis of the Non-eutectic Salt Mixture and Proposal for the Next Test", RASPLAV project RP-TR-38

Session D:

REACTOR APPLICATION

Chairman: H. Nagasaka

OECD Workshop on Ex-Vessel Debris Coolability
Karlsruhe, Germany, 15-18 November 1999

Organised in collaboration with
Forschungszentrum Karlsruhe (FZK) GmbH

SPANISH REGULATORY PERSPECTIVE ON EX-VESSEL CORIUM COOLABILITY ISSUES.

Fernando Robledo and Alfredo Lantarón
Consejo de Seguridad Nuclear
C/ Justo Dorado, 11. 28040 Madrid. Spain
frs@csn.es alg@csn.es

ABSTRACT

CSN issued a review of the "Integrated Program on Probabilistic Safety Analyses". Within this framework, 8 out 9 Spanish NPP's have finished PSA level-2 studies. CSN has made an independent assessment of these studies involving plant specific calculations with MELCOR code, the construction of Accident Progression Event Trees, the quantification of containment failure modes and uncertainty analyses of several variables based on a LHS method. The independent evaluations show that there exist plant specific containment failures modes related with ex-vessel behaviour. For PWR with dry cavity, the probability of basemat melt-through ranges from 0.002 to 0.02. For PWR with wet cavity this probability ranges from 7 E-5 to 0.01. This wide range shows the uncertainties associated to this phenomenon. "José Cabrera" shows an atypical behaviour for ex-vessel coolability. For "Santa María de Garoña", a BWR with a Mark I type of containment, the conditional probability of liner melt-through is 0.136.

1. INTRODUCTION

Light Water Reactors are equipped with a number of safety features aimed to the prevention and to the mitigation of the loads coming from the postulated Design Basis Accidents. The containment building is one of these safety features with a mitigative function: it is the last barrier to prevent the uncontrolled release of radionuclides to the environment in case of accident. Severe accidents may generate loads to the containment building in excess to those produced in Design Basis Accidents, with the corresponding threat of unacceptable radioactive releases to the environment. In case of a severe accident with subsequent failure of the reactor pressure vessel, a significant safety problem is to assure the coolability of the corium deposited outside the vessel. Corium deposited in the reactor building may challenge the containment integrity in a number of ways: basemat erosion, liner attack, containment shell failure by overtemperature etc. This paper addresses the different challenges to the containment of the Spanish Nuclear Power Plants coming from the corium deposited in the reactor building in case of a severe accident. Section 2 shows the main Spanish activities in the field of the ex-vessel corium coolability. Section 3 described the main results obtained from the plant specific PSA level-2 analyses. Finally, section 4 addresses the main conclusions obtained in this paper.

2. SPANISH ACTIVITIES IN THE FIELD OF EX-VESSEL CORIUM COOLABILITY

Table 1 shows the present Spanish NPP's along with their main relevant features related with the reactor containment building. In the field of the analytical activities, CSN approved in 1998 a review of the "Integrated Program on Probabilistic Safety Analyses". This program foresees the making of plant specific PSA level 2 studies for all the Spanish NPP's before the end of year 2000. CSN is compelled to use these results as much as possible in order to improve the safety of the Spanish NPP's. In addition, Severe Accident Management Guidelines shall be implemented in all the Spanish NPP's before the year 2000. Presently, 8 out of 9 Spanish NPP's finished their PSA level 2 study. CSN has made independent assessment of a great number of them, whose main outcomes are described in the next section.

In the field of the research activities, Spain participated in the ACE program together with several Spanish Institutions in the late eighties and early nineties. Presently, CSN together with UNESA (a consortium of Spanish Utilities) participates in the MACE program, an international research program aimed to resolve the issue of the ex-vessel corium coolability.

3. MAIN RESULTS OF THE SPANISH PSA-LEVEL 2 ANALYSES RELATED TO THE EX-VESSEL CORIUM BEHAVIOR

Eight out of nine Spanish NPP's finished their plant specific PSA-level 2 study. CSN has been making an independent evaluation of many of them. The more relevant findings related to the ex-vessel behaviour are summarised below.

3.1 .- PRESSURIZED WATER REACTORS

3.1.1. C.N. Vandellós

CSN has made an independent assessment of the PSA level 2 of C.N. Vandellós (ref. 1). This independent assessment involves the following main characteristics.

- Review and assessment of the interface between the level-1 and level-2 studies (i.e. determination of the Plant Damages States (PDS)).
- Plant specific calculations with MELCOR code.
- Construction and quantification of the Accident Progression Event Tree (APET), in order to obtain the probability of the different containment failure modes. The criteria followed for the APET quantification are the following.

Certain	1.00
Likely - Very Likely	>0.50 - < 1.00
Intermediate	0.50
Very Unlikely (Edge of Spectrum) - Unlikely	0.01 - < 0.50
Extremely Unlikely (Physical Unreasonable)	0.001
Impossible	0.00

- Determination and quantification of the radiological source terms. The outcomes obtained from the APET analyses are classified into a manageable number of release bins, which are characterized by similarities in accident progression and source term characteristics.
- Uncertainty Analyses. Several variables related with the phenomenological aspects of severe accident progression and source term calculations were submitted to uncertainty analyses by a limited Latin Hypercube Sampling (LHS) technique.

Relevant design issues for C.N. Vandellós are the following:

- C.N. Vandellós has made a specific study on the concrete composition. Table 2 shows the concrete composition.
- The reactor cavity is dry. Nevertheless, the cavity of C.N. Vandellós present one plant specific peculiarity that may result in an early containment failure mode, as it is described below. C.N. Vandellós instrument tunnel design consists of two segments; one horizontal that is practically an extension of the lower cavity

region, and the other is vertical. The vertical segment of the instrument tunnel exists into the seal table room. There are no direct flow between the seal table room and the upper containment regions. Instead, openings in the wall of the vertical part of the instrument tunnel (secondary shield wall) provide a potential path for the gases and debris transported from the cavity to enter the annular compartment. There exist a possibility of direct contact between the liner and the dispersed debris in the annular compartment. Debris and gases leaving the openings in the shield wall can also travel upwards through the annular compartment to the upper compartment. Fig.1 shows a scheme of the C.N. Vandellós containment nodalization.

The main challenges coming from the ex-vessel corium behaviour in C.N. Vandellós are debris coolability, basemat melt-through and containment liner attack.

3.1.1.1. Debris coolability and basemat melt-through

If vessel breach occurs at high pressure, DCH is the dominant phenomena. In this situation, the debris is ejected from the vessel and could accumulate in the cavity, and the blowdown of gases from the vessel at high pressure could disperse the debris from the cavity to annular compartments and the dome. At high pressures most of debris is dispersed from the cavity. If debris is highly dispersed and forms a thin film on the containment structures, the debris film may be considered coolable.

If the vessel fails at low pressure, the debris pours into the cavity and accumulates at the bottom of the cavity. Because of the cavity is dry, the interaction of the poured debris from the vessel with the cavity concrete basemat results in ablation of concrete substrate and generation of non-condensable gases (i.e. H_2, CO, CO_2). MELCOR calculations show that containment failure by over-pressurisation takes place before the containment basemat melt-through. The depth of concrete below the C.N. Vandellós cavity is approximately 3.6 m. MELCOR calculations predict a maximum penetration of 1.8 m, over a period of 2 days. Extrapolating these results, it can be concluded that basemat melt-through occurs between 4 to 5 days. The assessment of the PSA level-2 of C.N. Vandellós covers only the first 48 hours after the onset of the severe accident. Therefore, basemat melt-through within 48 hours was considered as "very unlikely" and a point estimate conditional probability of 0.01 was assigned. This variable was submitted to uncertainty analyses. A lognormal uncertainty distribution ranging from 0.001 to 0.1 is assigned to the basemat melt-through failure probability (in the absence of debris coolability), which reflects a low probability of failure, even at the upper bound of the uncertainty domain.

The results show that the conditional probability for the release category associated to basemat melt-through ranges from 0.002 to 0.02. This uncertainty is reflective of the large uncertainties in basemat melt-through probability.

An evaluation of various Severe Accident Management (SAM) strategies, and their impact on the probability of containment failure and radiological release to the environment was made. The SAM strategies considered are relatively simple in nature, and may not be identical to those to implement by C.N. Vandellós in the future, but provides some insights in terms of safety. The evaluation shows that the SAM strategy consisted in cavity flooding after vessel breach is very effective in terms of safety. The conditional late containment failure probability is reduced from 0.1683 to 0.0858 and the conditional probability of the containment remaining intact increases from 0.786 to 0.87. The probability of environmental radioactivity release also decreases in a significant way: one order of magnitude for those release categories involving basemat melt-through and containment intact.

3.1.1.2. Liner attack

This is a plant specific characteristic of C.N. Vandellós . Decomposition of the issue of liner attack is comprised of:

- Determination of the fraction of the core debris dispersed from the cavity (instrument tunnel) to the annular compartment through the openings in the instrument tunnel wall.

- Determination of the fraction of the core debris entering the annular compartment that can fall on the annular compartment floor, and accumulate next to the containment liner.

- Determination of the minimum mass of core debris that is required to melt through the liner, with and without an overlying layer of water on the containment floor.

The containment liner is 0.0065 m thick; the area of the openings between the instrument tunnel/seal table room and the annular compartment is approximately 18 m^2. The floor area of the annular compartment is approximately 481 m^2. The area of the annular compartment floor that will be covered by the dispersed debris is not known.

Heat transfer to the containment liner from the core debris is impacted by the presence of an overlying layer of water. With an overlying layer of water, a two-dimensional heat conduction analysis leads to the solution that the liner temperature is always maintained below the melting point of the steel (for that matter, at or near the saturation temperature of water at the containment pressure), as long as the depth of water is comparable to, or somewhat larger than the depth of the accumulated core debris. The debris depth, can at the most be about 0.6 m.; a better estimate of the upper bound debris depth assuming that a maximum of 20% of the core inventory spread over 20 m^2 (of the possible 481 m^2) on the annular compartment floor, is approximately 0.12 m. On the contrary, if the sprays are operating, the containment floor is flooded with water to a depth of 3.5 m over a period of 3 hours. Thus, a detailed two-dimensional analysis is not needed.

For the dry floor scenario, a one-dimensional analysis is sufficient, because of the small thickness of the liner. This one-dimensional analyses shows that the time to reach the steel melting temperature of 1700 K is estimated for various debris depths. Results are plotted in Fig. 2. This figure shows that, under dry floor conditions, liner melting is certain for debris depth-to-wall thickness ratios greater than 6. Thus, for a debris depth of greater than 5 cm. (0.05 m), liner melt-through is a certainty.

The next step is to determine the mass of debris that is necessary to melt the liner. Assuming the debris mass dispersal fraction similar to those considered in the study of the Direct Containment Heating, the minimum debris bed thick of 0.05 m. is obtained for an area spread between 18 a 36 m^2. On the other hand, there is a significant uncertainty regarding the area of the debris contacting the containment floor. If the area is much larger than 100 m^2, liner melt-through is impossible even under dry conditions. Given that due to the highly localised nature of the debris build-up, it is conceivable that the debris would reach the failure limit.

Therefore, the probability of liner melt-through is conservatively assigned a screening value of 0.75 under conditions of high-pressure melt ejection, with dry annular containment floor. The corresponding screening value for the conditional probability under wet conditions is 0.0. In addition, the screening value for the liner probability under dry conditions was submitted to an uncertainty analysis. A uniform distribution with a minimum value of 0.5 and a maximum value of 1.0 is assumed for uncertainty analysis. The results of the evaluation show that the conditional probability of containment leakage due to liner melt-through range from 1.0 E-4 to 4.0 E-4, with a mean value of 8.7 E-4; despite the assumed high likelihood of liner failure in the absence of water. It should be noted that the failure of the containment liner does not imply large releases of radionuclides to the environment, since the containment shell presents a barrier to the releases. Instead, a slow protracted release, as a result of containment leakage is expected to take place.

3.1.2. C.N. Almaraz

CSN has made an independent assessment of the PSA level 2 of C.N. Almaraz (ref. 2), whose main characteristic are described in section 3.1.1.

C.N. Almaraz has a reactor cavity type wet equipped with relief panels. Water can enter the cavity in two ways. After vessel breach, water injected into the RCS (by say, the low-pressure injection pump) will flood the cavity. If the containment spray system is working, 4.15 % of the spray flow is estimated to enter the cavity. If a spray pump operates in injection, the cavity can be flooded to a depth of 3 m. in 2500 seconds. If the spray pump operates in injection and recirculation, the cavity can be completely flooded in 10.000 seconds. It should be notice that a curb on the containment floor prevents water overflow from the sump into the cavity until the depth of the water exceeds 3.5 m. However, if the entire inventory of the RWST and the RCS are emptied onto the containment floor, the depth of the water pool will be 2 m. Hence, water overflow from the containment floor onto the cavity is impossible in C.N. Almaraz, unless one of the relief panel fails.

The main challenges coming from the ex-vessel corium behaviour in C.N. Almaraz are the following: debris coolability and basemat melt-through. Because of the characteristics of the reactor cavity, the issue of the debris coolability both on the cavity and containment floor was studied in detail within the APET. The main results of this evaluation are shown below.

If a substantial fraction of the core debris is ejected from the vessel following an in-vessel steam explosion, or the ejection is accompanied by vessel rocketing, then the debris can spread on a large area in the containment. Therefore, a conditional probability of 0.99 is assigned to long term coolability.

If vessel fail with high pressure in the RCS, the core involved in high-pressure melt ejection is likely to be widely distributed throughout the containment. Hence, long term coolability of the dispersed core debris is considered likely, and assigned a conditional probability of 0.75. It is not unreasonable to anticipate that the high pressure melt ejection dispersed debris under water will be coolable; however, since a relatively small fraction of the core debris may participate in the high pressure melt ejection, the remaining debris pouring into the cavity may not be coolable.

In case of failure of the vessel at low pressure in the RCS, the debris poured into the reactor cavity may interact with the water present in the cavity. Three possible interactions are considered:

- Ex-vessel steam explosions. The conditional probability is 0.43, according to ref. 3.

- Core debris settles on the cavity floor and quenching follows. The conditional probability is 0.285, according to ref. 3.

- Core debris does not interact with water. The conditional probability is 0.285, according to ref. 3.

Bearing in mind the above mentioned fuel-coolant interactions, the following conditional probabilities were assigned to the debris coolability:

- If vessel breach was followed by one or more energetic fuel-coolant interaction at vessel breach, then dispersal of debris as fine particles is likely. There exist uncertainties in the size and form of the melt pool/debris beds. It is assumed that due to the large cavity floor area, debris bed coolability is likely under these conditions and a conditional probability of 0.75 is assigned.

- If debris ejected from the core does not participate in ex-vessel steam explosions or high-pressure melt ejection, it is not known whether a coolable geometry can be attained. Debris coolability is uncertain and a conditional probability of 0.5 is assigned. This variable was submitted to an uncertainty analysis. A normal distribution with the most likely value, the lower and upper bounds, corresponding to 0.5, 0.01 and 1.0 was assumed.

In case of dry cavity, the interaction of the poured debris from the vessel with the cavity concrete basemat results in ablation of concrete substrate and generation of non-condensable gases (i.e. H_2, CO, CO_2). MELCOR calculations show that containment failure by over-pressurisation takes place before the containment basemat melt-through. The depth of concrete below the C.N. Almaraz cavity is approximately 3.5 m. MELCOR calculations predict a maximum penetration of about 2.2 m, over a period of 2 days. Extrapolating these results, it can be concluded that basemat melt-through occurs between 3 to 4 days. As in the case of C.N. Vandellós, this evaluation covers only the first 48 hours after the onset of the severe accident. Therefore, basemat melt-through within 48 hours was considered as "very unlikely" and a point estimate conditional probability of 0.01 was assigned. This variable was submitted to uncertainty analyses. A lognormal uncertainty distribution ranging from 0.001 to 0.1 is assigned to the basemat melt-through failure probability (in the absence of debris coolability), which reflects a low probability of failure, even at the upper bound of the uncertainty domain.

Taking into account the probabilities already explained, the results of the APET show that the conditional probability for the release category associated to basemat melt-through ranges from 7 E-5 to 0.01. This outcome reflects the great uncertainties associated both to the basemat melt-through as well as over debris coolability with an overlying layer of water.

As in the case of C.N. Vandellós, the efficiency of cavity flooding after vessel breach as a Severe Accident Management strategy was considered. The base case considers that 82% of the total core damage frequency involve a flooded cavity, whereas in this analysis it is assumed that cavity is flooded for all PDS's. Moderate benefits in terms of safety are obtained with this SAM strategy. The probability of late containment failure is reduced slightly and the risk of environmental release is reduced by about 4.5% (see Fig. 3).

3.1.3. C.N. "José Cabrera"

CSN has not made an independent assessment of this PSA level 2 analyses yet. Therefore, the results described below are taken from the documentation submitted by the plant to CSN. It should be notice that MAAP code was used for the elaboration of this PSA level 2 study.

C.N. "José Cabrera" is a unique PWR plant in many ways: it has only one loop in the RCS, the containment dome is made by steel, etc. The design of the cavity is also unique in several features. Fig. 4 and 5 show the cavity design. It can be seen that the floor of the cavity compartment is 90 cm. below the containment floor. In addition, it can be seen that the water can flow from the containment floor to the cavity floor. RCS has approximately 70 m^3 of water; therefore, the cavity has always some water in case of a severe accident; i.e. the cavity is wet. The design of the cavity favours ex-vessel corium coolability: cavity floor area is 9.4 m^2, that may be increased up to 18.65 m^2, if the area of the floor connecting to the compartment B is taken into account. In addition, the cavity design assures that, in case of failure of the reactor pressure vessel at high pressure in the reactor coolant system, all the debris expelled from the vessel will be dispersed outside the cavity compartment and deposited on the containment floor.

The main challenges to the containment integrity coming from the corium expelled outside the vessel are the following: liner attack, basemat melt-through and debris coolability.

3.1.3.1. Liner attack

As it can be seen in Fig.5, the reactor containment building is designed in such a way, that there exist walls that prevent that debris expelled from the reactor pressure vessel in case of high pressure melt ejection may impinge the containment liner. Therefore, this potential containment failure mode was discarded in this plant.

3.1.3.2. Basemat melt-through

The depth of concrete below the C.N. "José Cabrera" cavity is approximately 3.6 m. MAAP calculations show that core-concrete interaction stops 30 hours, approximately, after the onset of the severe accident, being the basemat penetration around 0.6 m. for this period of time. In addition, MAAP code was run in a very unfavourable case: dry cavity and minimum corium spreading. Under these conditions, MAAP predicts a maximum penetration of 2.4 m. over a period of 2 weeks. Therefore, it was concluded that basemat melt-through is not a credible containment failure mode.

3.1.3.3. Debris coolability

This issue was analysed by C.N. "José Cabrera" for two severe accident scenarios: those with high pressure in the reactor coolant system and those with low pressure in the reactor coolant system.

In case of a severe accident, with high pressure in the reactor coolant system, the corium expelled from the reactor pressure vessel will be deposited on the containment floor. Assuming that 100% of the core is expelled from the reactor pressure vessel, and taking into account that the containment floor area is 123 m^2, the corium depth is 2.6 cm and the heat flux required for corium quenching is 33 kW/ m^2. This is a very low heat flux, hence convection and radiation to the containment atmosphere and structures may quench the corium. Therefore, corium is considered coolable under these conditions.

For the corium poured in the reactor cavity, C.N. "José Cabrera" makes very detailed analyses in order to find out its coolability. Only some details of this analysis will be presented here. The analyses consider, among other, the following phenomena: amount of water in the cavity, core inventory deposited on the cavity floor, potential

for ex-vessel steam explosion and corium fragmentation and corium spreading. Table 3 shows the upward heat fluxes for different cases.

The probability of core debris coolability for the most relevant Plant Damage States is shown in Table 4.

3.2. BOILING WATER REACTORS

3.2.1. C.N. "Santa María de Garoña"

CSN is making an independent assessment of the PSA level 2 of C.N. "Santa María de Garoña" (ref. 4), whose main characteristics are described in section 3.1.1. Because of the evaluation is presently under way, the following results should be considered as preliminary.

C.N. "Santa María de Garoña" is a BWR equipped with a Mark I type of containment. The main challenges from the ex-vessel behaviour for this containment are the following: liner melt-through, basemat melt-through and sump-corner melt-through.

3.2.1.1. Liner melt-through

Liner melt-through is a potential containment failure mode typical of Mark I type of containment. The likelihood, timing and location of the shell failure depend strongly, among other things, on the core debris volume relative to the available in-pedestal sump volume. Containment sumps volume in C.N. "Santa María de Garoña" is 6.5 m^3 , being the ratio between the maximum core debris volume and the sump volume, 2.1. Therefore, on the basis of sump volume alone, debris contact with the drywell shell cannot be ruled out, especially under dry pedestal conditions.

The melt spreading on the drywell floor and attack on the liner can cause early failure of the containment. As it can be seen in table 5, liner submergence by ex-vessel melt can range from 0.4 to 30 cm. given various melt spreading for the drywell floor. The presence of water on the drywell floor can significantly affect to the liner heatup. The result of plant specific MELCOR calculations show that for ATWS scenarios, it takes 3 to 5 hours to boil-off water in the drywell, and following the depletion of water, thermal attack on the liner will cause liner melt-through . For cases with no water in the drywell at the time of vessel failure, the debris attack on the liner causes early failure of the containment. For the scenarios with substantial water in the drywell and availability of the drywell sprays, the liner failure is extremely unlikely. Table 6 shows the expected conditional probability of liner melt-through assessed for C.N. "Santa María de Garoña" . These values were introduced in the APET. The outcomes of APET show that the conditional probability of early containment failure by liner melt-through is 0.135. This contribution comes, mainly, from transient-2, a loss of offsite power with drywell spray inoperable. ATWS-1 and 2 lead to an early containment failure mode by drywell overpressure and ATWS-3 and 4 lead to an intermediate containment failure mode by drywell overtemperature, both, previous to a potential liner melt-through failure.

3.2.1.2. Basemat melt-through and sump-corner melt-through

The depth of concrete below the C.N. "Santa María de Garoña" in-pedestal sumps is approximately 1 m. The plant specific MELCOR calculations predicted a maximum penetration of 0.46 m. in one day. Extrapolating MELCOR results, it can be concluded that basemat melt-through occurs after 48 hours. The results of the evaluation of the PSA level-2 analyses of C.N. "Santa María de Garoña" show that the contribution to the overall conditional probability of containment failure from basemat melt-through is very low in the case of C.N. "Santa María de Garoña" .

Following, one plant specific containment failure mode is described. In addition to the drywell floor sump, C.N. "Santa María de Garoña" has two smaller sumps that are located outside of the reactor pedestal region on the drywell floor of the C.N. "Santa María de Garoña" . One of these sumps is located just outside the door connecting the reactor pedestal region to the ex-pedestal region in the drywell. The corner location of the sump just outside the pedestal doorway is only 30-35 cm. away from the drywell shell boundary. Fig. 6 provides the details of this configuration. Therefore, in case of failure of the reactor pressure vessel, there could be a high likelihood of debris build-up leading to penetration of the concrete floor at the ex-pedestal sump corner location,

and eventually reaching the drywell shell boundary (i.e. containment failure). This unique configuration in C.N. "Santa María de Garoña" leads to unique containment vulnerability during severe accidents.

The failure of the containment at this location due to core concrete interaction is expected to occur much earlier than the basemat melt-through below the in-pedestal sumps, i.e. it is estimated that this failure occur within 5 hours from the vessel breach. This containment failure mode will not prevent other containment failure modes. In addition, source term associated with this containment failure mode is expected to be small, as this failure is not expected to lead to a large direct path to the reactor building. Therefore, this failure mode is treated in the APET as subordinate to all other containment failure modes (including venting). The preliminary results shown that the conditional probability of this containment failure mode is very low: 1.E-3.

4. CONCLUSIONS

CSN issued in 1998 a review of the "Integrated Program on Probabilistic Safety Analyses". According to this program, all the Spanish NPP's will make plant specific PSA level 2 analyses before the year 2000. Also, CSN has required that all the Spanish NPP's will implement Severe Accident Management Guidelines. Presently, 8 out of 9 plants finished their PSA level 2. Except for the case of C.N. "José Cabrera", CSN has made independent evaluations of these PSA level-2 studies. This paper addresses the main features of these independent evaluations as well as the main findings obtained.

The independent evaluation involves plant specific calculations with MELCOR code, the construction of Accident Progression Event Trees, the quantification of the containment failure modes and uncertainty analyses of several variables based on a LHS technique.

The main findings obtained in these independent evaluations are the following.

- Several plant specific containment failures modes related with ex-vessel behaviour have been studied and quantified.

  1• C.N. Vandellós presents the possibility that the debris expelled from the reactor pressure vessel in scenarios with high pressure in the RCS may impinge the containment liner with the corresponding failure by over-temperature. It has been concluded, that liner overtemperature failure may be ruled out assuming flooding of the containment floor. In case of "dry" scenarios, the conditional probability of liner failure by over temperature ranges from 1.0 E-4 to 4.0 E-4. In addition, this potential containment failure mode results in low radionuclide releases to the environment, because of the presence of the containment shell.

  2• C.N. "Santa María de Garoña" has an ex-pedestal containment sump. The corner of this ex-pedestal containment sump is only 30-35 cm. away from the drywell shell boundary. The failure of the containment by sump corner melt-through takes place 5 hours after the reactor pressure vessel failure. Nevertheless, the environmental releases will be very small. In addition, this containment failure mode can not prevent other containment failure mode more relevant in terms of environmental releases.

- C.N. Vandellós is a PWR with dry cavity and the main challenge for the containment integrity comes from the basemat melt-through. The probability associated to this containment failure mode range from 0.002 to 0.02. This wide range show the uncertainties associated to this phenomenon.

  The evaluation also shows that cavity flooding as severe accident management would have important benefits in terms of reducing the plant risk.

- C.N. Almaraz is a PWR with wet cavity. A very detailed study of the issues relevant to the debris coolability and basemat melt-through was carried out in the APET, including uncertainty analyses of several phenomena. The results show that the basemat melt-through probability ranges from 7 E-5 to 0.01. This wide uncertainty band shows the great uncertainties associated to the debris coolability.

  Cavity flooding as severe accident management was also studied, concluding that only moderate benefits in terms of risk reduction are obtained.

- C.N. "José Cabrera" is a unique PWR in many ways, including several issues related with core debris coolability. PSA level 2 analyses show that the possibility of liner attack by debris dispersal after high pressure melt ejection events may be ruled out by design configurations. Also, MAAP calculations shows that basemat melt-through may be also ruled out as potential containment failure, because it takes 2 week to penetrate 2.4m the concrete basemat, whose thick is 3.6 m. Detailed studies on ex-vessel corium coolability show that debris dispersed on the containment floor are coolable. For debris deposited onto the cavity floor, it is shown that, for the most relevant core damage sequences, the probability of non-coolability ranges from 0.2 to 0.

- C.N. "Santa María de Garoña" is a Boiling Water Reactor equipped with a Mark I type of containment. Liner melt through is an early containment failure mode very relevant for these plants. The conditional probability of liner melt- through for C.N. "Santa María de Garoña" is 0.136.

5. ACKNOWLEDGMENTS

This paper was elaborated with the collaboration of the experts of the Division of Probabilistic Safety Analyses and Human Factors of CSN.

6. REFERENCES

1. ERI/CSN 97-801 " A Regulatory Evaluation of the Vandellos Probabilistic Safety Analysis (Level-2)". Final Report. December 1997.

2. ERI/CSN 98-801 " A Regulatory Evaluation of the C.N. Almaraz Probabilistic Safety Analysis (Level-2)". Final Report. September 1998.

3. NUREG/CR-4551.Vol.7. "Evaluation of Severe Accident Risks: Zion".

4. ERI/CSN 99-801 " A Regulatory Evaluation of the C.N. Santa María de Garoña Probabilistic Safety Analysis (Level-2)". First Draft. January 1999.

Table 1: Spanish Nuclear Power Plants Characteristics

PLANT	TYPE	DESIG-NER	THERMAL POWER MWth	CONTAIN MENT TYPE	FREE VOLU-ME (m^3)	CAVITY TYPE	OPERAT-IONAL DATE
José Cabrera	PWR	Westing house	510	dry	23393	wet	1968
Santa María de Garoña	BWR	General Electric	1381	Mark I	6153 (1)	wet	1971
Almaraz I,II	PWR	Westing house	2696	dry	59465	wet	1980/1983
Cofrentes	BWR	General Electric	2894	Mark III	35345(2)	wet	1985
Ascó I, II	PWR	Westing house	2696/2912	dry	62092	dry	1983/1985
Trillo	PWR	KWU	3010	dry	56811	dry	1988
Vandellós	PWR	Westing house	2913	dry	62578	dry	1988

(1) Drywell 3293 m^3; torus 2858 m^3. (2) Drywell 6822 m^3; torus 28253 m^3.

Table 2: Concrete Composition for Vandellós

SiO_2	CaO	Al_2O_3	K_2O	Na_2O	Mg, MnO, TiO_2	Fe_2O_3	Cr_2O_3	H_2O	CO_2
48.4	25.5	5.5	1.18	0.082	4.48	1.8	0.014	3.15	9.894

Table 3: "José Cabrera" upward heat flux for corium deposited in the cavity

core inventory (fraction)	Spreading Area	heat flux (kW/m^2)
0.25	9.4	109
0.50	9.4	218
0.75	9.4	327
1.	9.4	436
0.25	18.65	55
0.50	18.65	110
0.75	18.65	165
1.	18.65	220

Table 4: "José Cabrera". Probability of non-debris coolability for several plant damage states

Plant DamageState (PDS)	Contribution to CDF (%)	Probability of non-debris coolability
76	50.10	7.6 %
75	9.11	7.6%
81	8.36	17.4%
74	7.4	0.71%
53	5.25	0%
46	4.88	20,5%
69	4.38	8.6%
47	2.34	17.4%

TABLE 5

MELT SPREADING ON THE DRYWELL FLOOR AND LINER SUBMERGENCE.

	MELCOR T-2	MELCORT-3
Melt volumedischarged (m^3)	**5.5**	**14.9**
Debris volume m^3 (20% porosity)	**6.9**	**18.6**
Debris volume outside Sumps m^3	**0.4**	**12.1**
Liner submergence, cm. (25% DW coverage)	**1**	**30**
Liner submergence, cm. (50% DW coverage)	**0.6**	**19**
Liner submergence, cm. (100% DW coverage)	**0.4**	**11**

TABLE 6
"SANTA MARÍA DE GAROÑA". PROBABILITY OF LINER FAILURE.

Plant DamageState	Contribution to CDF	Early Liner Melt-through (1)	Intermediate Liner-Melt-through (2)	Water in drywell (Vw=m^3)
ATWS-1	33%	1E-4	1	6.61
ATWS-2	12%	1E-4	1	11.15
ATWS-3	1%	1E-4	1	11.17
ATWS-4	1%	1E-4	1	14.42
LOCA outside containment	3%	1	-	1.43
Small LOCA	7%	1E-4	1E-4	41.23
T-1. Transient w/o spray	21%	1E-4	1E-4	34.11
T-2. Transientwith spray	14%	1	-	0.
T-3. Transient	2%	1E-4	-	0.

(1) Early: at or around vessel breach. (2) Intermediate: at or around 5 hours after vessel breach

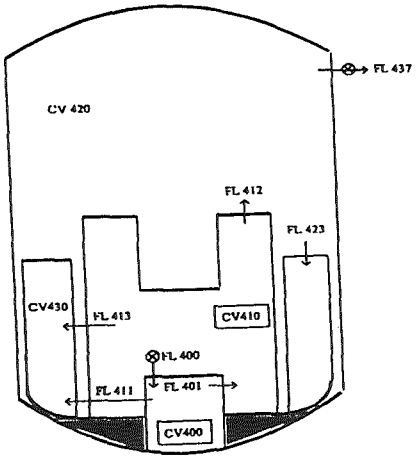

Figure 1.- C.N. Vandellós. Schematic of the containment nodalization.

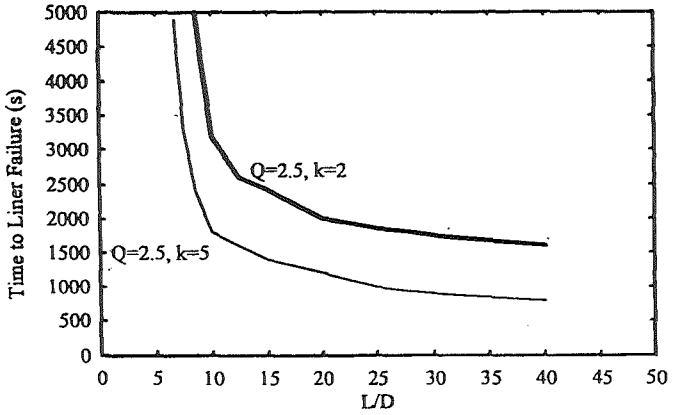

Figure 2.- C.N. Vandellós. Time for liner failure as a function of debris depth-to-liner thickness ratio.

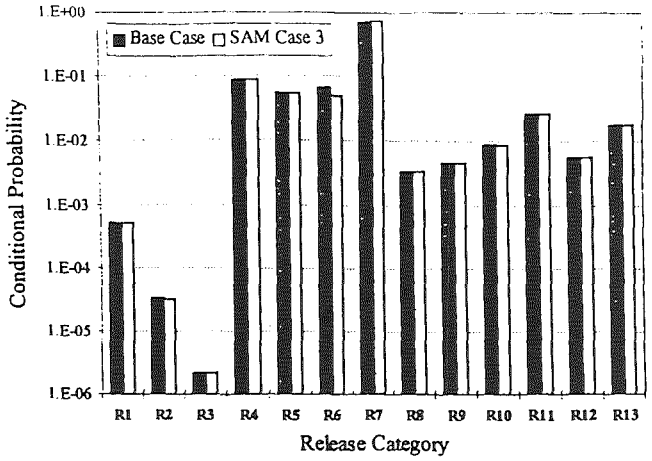

Figure 3a.- C.N. Almaraz. Impact of cavity flooding after Reactor Pressure Vessel failure as Severe Accident Management on the conditional probability of containment failure.

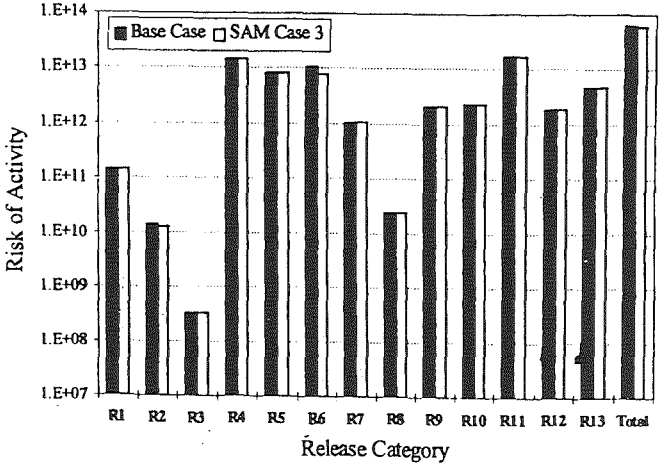

Figure 3b.- C.N. Almaraz. Impact of cavity flooding after Reactor Pressure Vessel failure as Severe Accident Management on the risk of activity (including the noble gases) associated with each release category (including the total risk).

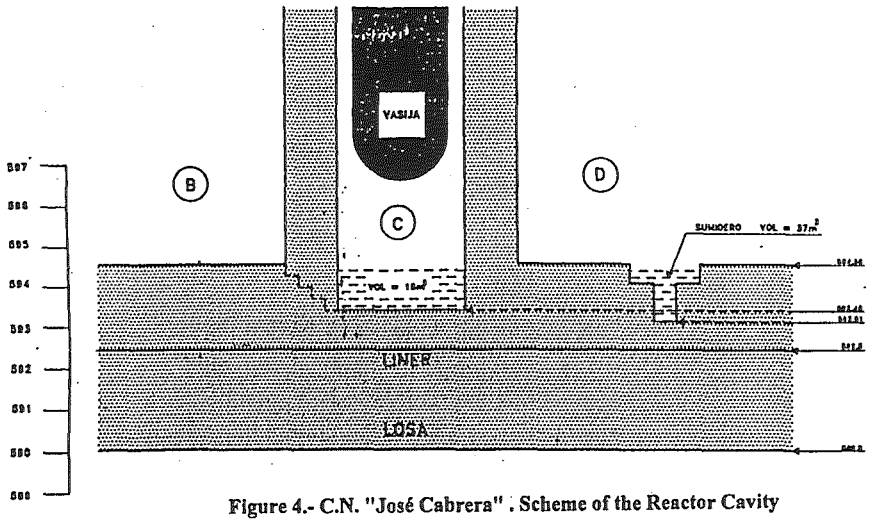

Figure 4.- C.N. "José Cabrera" . Scheme of the Reactor Cavity

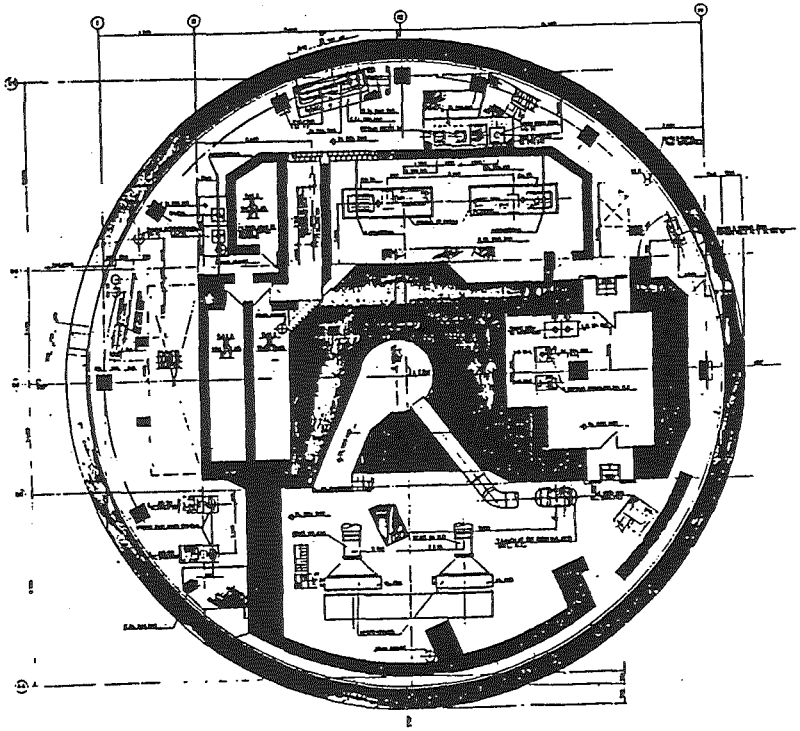

Figure 5.- C.N. "José Cabrera". Drawing of the lower part of reactor containment building.

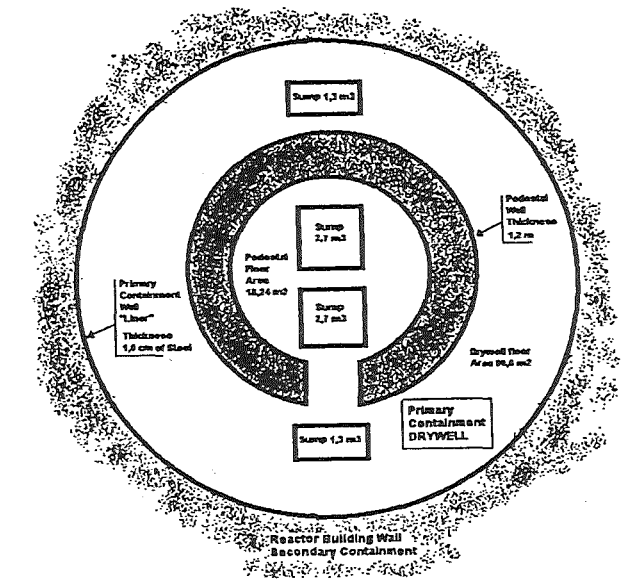

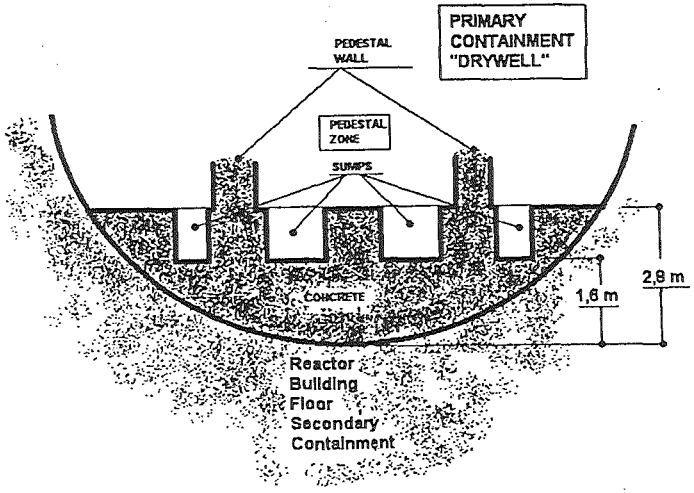

Figure 6.- C.N. "Santa María de Garoña". Containment sumps configuration.

OECD Workshop on Ex-Vessel Debris Coolability
Karlsruhe, Germany, 15-18 November 1999

Organised in collaboration with
Forschungszentrum Karlsruhe (FZK) GmbH

GAREC ANALYSES IN SUPPORT OF EX-VESSEL RETENTION CONCEPT

Participants to GAREC Working Group :
Azarian G., Gandrille P. (*Framatome*), Dumontet A., Dutheillet, Grange (*EdF*), Duriez., Goldstein G., Spindler B.., Cranga M., Cognet G., Froment K., Gatt J.M., Humbert J.M., Laporte T., Richard P., Robert G., Seiler J.M., Szabo I., Tourasse M., Valin F., Dufour P. (*CEA*)

Mailing: J.M. Seiler
CEA Grenoble DTP
17 rue des Martyrs, Grenoble 38054 Cedex 09 France
seiler@dtp.cea.fr

ABSTRACT

The GAREC group has performed an analysis of Ex-Vessel Corium Recovery capability for some actual and future PWR designs. This analysis includes : scenario analyses for core meltdown and corium transfer to the lower head, corium behaviour in the lower head (debris and corium pools), vessel failure, risk of vapour explosion, corium-concrete interaction & coolability, corium spreading, corium accumulation, corium-ceramic interaction, residual power distribution, long term stabilisation.

This analysis is based on available and most recent experimental results (ACE, MACE, VULCANO, CIRMAT, PHYTHER, etc..), on advanced calculation tools (TOLBIAC, THEMA, CORAN, CASTEM) and on engineer evaluations.

Coolability during MCCI cannot be demonstrated with the present state of scientific knowledge even if there is a great potential that it can be achieved. The paper outlines the specific aspects of the approach developed by GAREC. These aspects are based on a better knowledge of the behaviour of the corium melt. This analysis leads to the conclusion that the liquid melt in a corium pool may have rather low viscosity which in turn favours melt ejection in presence of a floating crust. The R&D program engaged by CEA in France on this subject will be outlined.

For the EPR concept, the main uncertainties are related to 1)- the melt-through of the gate, 2)- the effects of late water injections.

The progresses performed on the spreading problem (THEMA, VULCANO) are summarised. The efforts made in support of the comprehension of corium-ceramic interactions are described. These efforts involve:

- basic understanding of corium-ceramic interaction,
- model developments
- CIRMAT tests
- Test for the analysis of effect related to oxygen diffusion through a metal layer

It is concluded that the attack of the ceramic may be stabilised provided that the heat extracted from below the ceramic is sufficient.

Some aspects concerning consequences of vapour explosion in the reactor pit are also outlined.

Main open problems are discussed and the current R&D program is summarised.

1. INITIAL CONDITION: VESSEL FAILURE WITH DRY REACTOR PIT

Wet scenarios

The vessel failure conditions have a very strong impact on Ex-Vessel Corium behaviour. For dry reactor pit, the main parameters controlling the instant of vessel failure and the release of corium are the water inventory and the pressure in the RPV. Late water injection in the RPV may have a drastic influence on the vessel failure.

This is a main uncertainty in scenario analyses, with very important consequences and which must be taken into account along all the following considerations.

Corium release

Recent calculations [Eddi, 1999] have shown that, if no water is supposed to be injected in the RPV, the corium will even not be released instantaneously with the complete molten core inventory. Evaluations indicate that, depending on the scenario, at vessel failure, only 20 % to maximum 60 % of core inventory may be in liquid state, and at elevated temperature. Furthermore, for future reactors, the RPV is considered to be depressurised in severe accident situations (less than 20 bars in EPR, and probably near to the atmospheric pressure). Thus, the vessel is not expected to fail with a large opening in a very short time. A progressive and slow melting and creeping of the vessel are more probable. This implies that the mass of corium is most probably delivered sporadically over a large period of time of, possibly, several hours or even days. It may also be expected that the whole corium will not flow as a liquid, but solid chunks may drop from the vessel.

Effects of In-Vessel FCIs

As the vessel is calculated to fail before all the core inventory is gathered in a liquid form in the lower head, the risk of energetic vapour explosion following late water injection is strongly decreased. This is because the surface of any liquid corium pool (of limited molten mass) will freeze as soon as it is contacted by water. Thus, a vessel blast due to energetic vapour explosion is not expected in this phase.

If an energetic vapour explosion should occur in an earlier phase (for instance: during the first corium flow from the core into the lower head), only the inventory of liquid corium, contained at that time in the core, may be dispersed. However this scenario is not deemed to be very realistic:

- The crucible containing the corium fails at its bottom only if no water is present in the lower part of the core, thus with residual water in the lower head; under these conditions the water inventory is reduced, water is at saturation and the inertial constraint is small. This limits the efficiency of the vapour explosion. Furthermore, the vessel is still intact and is able to resist to important dynamic mechanical loads,

- If water is present at the core level, the crucible is expected to fail laterally. As a consequence, the corium flow rate and the amount of liquid corium which may flow are strongly reduced. This limits the efficiency of vapour explosion.

Corium dispersion

The problem of Corium Dispersion in the containment is also strongly dependent on the mode of vessel failure. According to the considerations developed above, the occurrence of a large vessel opening in a short time (less than a few seconds) with a large amount of molten corium under elevated pressure (10-20 bars) (these conditions are necessary to obtain a significant corium relocation in the containment) seems unlikely. Nevertheless, GAREC is concerned by this problem and follows two directions:

- survey of the R&D effort undertaken by FzK and IPSN (DISCO and modelling) and at SANDIA (LHF, Surtsey),
- actions have been launched for the evaluation of the vessel rupture kinetics under realistic thermal and mechanical loads (CEA/DMT-Saclay)

2. CORIUM-CONCRETE INTERACTION

MCCI modelling

A new approach for the modelling of corium-concrete interaction, based on phase segregation, has been developed by CEA [Seiler, 1996] and the model has been introduced in TOLBIAC [Vandroux-Koenig et al., 1999] and validated on ACE and MACE tests. This model predicts well the evolution of the melt temperature, as well as the composition and viscosity of the liquid corium [Seiler and Ganzhorn, 1997]. These data are then used for the prediction of the initial conditions for corium spreading in EPR.

However, the prediction of the power split in the corium layer (and thus, the prediction of the ablation rate of the concrete) is still an open problem. Nevertheless, the separation between solid and liquid phases (a consequence of phase segregation) provides a clear configuration (modelled in TOLBIAC) which allows to split the problem into two separate problems:

- a conduction heat transfer resistance through the solid crust,
- a convection heat transfer in a liquid layer with sparging gas.

The interface temperature between solid and liquid is imposed by the composition of the liquid phase. Several correlations for convection heat transfer exist in the literature, however with significant uncertainties. BALI experiments have been performed with a viscous liquid layer with sparging gas, which helps to make a decision [Bonnet, 1999].

Coolability

Coolability during MCCI cannot be demonstrated with the present state of scientific knowledge even if there is a great potential that it can be achieved. The MCCI specialists have produced a status of the art, under the leadership of EPRI [Levy, 1999]. This subcommittee stated that crust breach and floating, associated with water ingression and melt ejection are phenomena which are clearly able to lead to coolability. "The forecast conditions within the reactor cavity indicate that the behaviour of the crust is crucial to the coolability

issue. Furthermore, its potential for porosity, cracking, and breaching is the issue which should dominate the future strategic direction of the MACE program. Water ingression and melt ejection through those potential paths is the second area of priority". The R&D programme is mainly based on the MACE experiments. The melt ejection mechanism is examined in more detail in France with the PERCOLA programme (modelling [Bonnet and Seiler, 1992] and specific experiments for the investigation of liquid entrainment rate by sparging gases through anchored and floating crusts).

3. GATE MELT-THROUGH AND SPREADING

For EPR, the way the gate melts through (the opening kinetics) is the main effect controlling corium spreading. If the opening kinetics is fast there is no spreading problem on a dry substrate. Therefore the gate opening problem is considered as a main R&D objective. If the initial conditions are known at flow onset (temperature distribution on the gate and initial flow diameter) it is possible to calculate the evolution of the corium flowrate on the basis of models which have been developed at AEA [Dobson and Turland, 1996], RIT [Sehgal et al., 1997] and also in France. It can be demonstrated that, if a significant amount of metal flows first, the hole diameter increases rapidly which favours the spreading of the after-coming oxidic melt. If oxides flow first through a small hole in a cold plate, the hole diameter is calculated to increase much slower and, probably, not sufficiently fast. The main uncertainty is precisely the knowledge of the initial gate temperature and hole size. For the prediction of these parameters, GAREC follows the KAPOOL tests performed at FzK and continues some calculation evaluations.

Besides, it is emphasised that it is possible to demonstrate that spreading occurs even with low corium flow rates. The evaluation of this assertion was the main objective of the CORINE (simulant materials) and VULCANO (real materials) [Cognet et al., 1998] experimental programmes. The main conclusion of these tests is that there are several physical mechanisms which enhance spreading:

- the transient freezing of a highly non-eutectic material shows the formation of a viscous boundary which creeps and deforms and breaks successively, leading to outpourings [Journeau, 1999],
- due to internal heat generation a thick corium layer cannot completely solidify, and reaches a steady state with a compact crust formation. The time delay to reach this steady state is rather large (~20 minutes) [Seiler et al., 1999-1]. Meanwhile, the two phase solid-liquid zone has, basically, a viscous behaviour which favours spreading.
- . A computer code (THEMA) [Spindler and Veteau, 1999] has also been developed

However, FzK has found in KATS [Fieg, 1999] that spreading may be hindered by reaction with concrete. This problem will be investigated more precisely in the future.

4. LONG TERM CORIUM-CERAMIC INTERACTION

Interaction between oxidic corium and ceramic at imposed power and by direct contact

Corium ceramic interaction by dissolution is usually known at imposed temperature. The reactor case is different since the power dissipation is imposed instead of the

temperature. This leads to different conclusions even if the basic physics is the same. A corium-ceramic interaction model (CORAN), at imposed power, has been developed at CEA/DTP [Seiler et al., 1999-2]. This model has been validated [Duret et al., 1999] against the CIRMAT experiments performed at LSK St-Petersburg on behalf of Siemens and the European Community. The main conclusion is that, even if a direct contact between the oxidic melt and the ceramic is considered, the ablation of the ceramic will be limited and blocked by the temperature gradient in the ceramic layer (which is cooled, in the EPR case, at the bottom) [Froment et al., 1999]. The extend of the dissolution at constant power will mainly depend on the thermal conductivity of the ceramic, the external cooling conditions and on the phase diagram of involved materials.

Some particular effects like cement dissolution or thermo-mechanical embrittlment will be evaluated in the future.

Interaction between oxidic corium and ceramic at imposed power and by indirect contact

To prevent dissolution of ceramic by oxidic corium, a metallic iron layer has been introduced between ceramic and corium in the EPR concept. The efficiency of this physico-chemical barrier has been investigated by separate effect, small scale tests at CEA-Saclay. The tests showed that the ceramic could even be dissolved under these conditions by oxygen transfer from the oxidic corium to the iron-ceramic interface. The tests permitted to measure the interaction kinetics for various test parameters (thickness of iron layer, temperature, oxygen potential in the oxidic corium, etc..). It appeared that the convection within the iron layer has a very strong effect on the ablation kinetics. A theoretical model is under development. This model takes into account several physical effects like:

- dissolution of ceramic,
- existence of a mass transfer boundary layer which depends on convection,
- variation of oxygen potential in the oxidic corium layer (closed and open system),
- presence of oxygen getters (Cr, Si) in the metal layer,
- threshold criteria for dissolution and diffusion in solid phase.

It will not be possible to validate this model only on the basis of small scale experiments since convection has a very important effect. Thus, experiments at representative scales are necessary and are emphasised by Siemens and in the frame of the future VULCANO programme.

6. EFFORT FOR UNDERSTANDING OF CORIUM BEHAVIOUR

Corium is a non-eutectic material which means that it freezes (or melts) within a temperature interval. This temperature interval may vary from less than 100 K (for UO_2 + ZrO_2 mixtures, for instance) to about 1000 K (for corium + concrete mixtures, for instance) for Ex-Vessel situations. For almost all the phenomena involved in severe accidents, the temperature of corium is situated in this interval. The problem is the modelling of the behaviour of corium within this interval, in order to derive heat flux distributions, physical properties (as, for instance, viscosity for spreading) and interaction kinetics with other materials (ceramics, concrete, etc...).

The "usual approach"

The "usual" approach consists in using well-known thermalhydraulic models which have been established for pure materials, with the introduction of physical properties resulting generally from some interpolation of the physical properties known at the "extremities" of the freezing interval, in the solid state and in the liquid state. In such an approach the material is considered as "homogeneous" and its composition does not vary. This approach supposes that a mushy zone exists (under transient and steady state conditions), which rises questions about the validity of heat transfer correlations derived from simulant material experiments. Furthermore, this approach leads to several contradictions (such as the viscosity-temperature contradiction in MCCI).

The introduction of knowledge from material science led to important consequences. GAREC has considered that this is a key point for the understanding of phenomena related to severe accidents and, thus, has supported several modelling activities.

Mushy zone and steady state

The solidification theory imposes that, when the freezing rate tends toward zero (this is the case in "thermal hydraulic steady state" for severe accident situations with volumetric power dissipation and external cooling), then the mushy zone (in the sense of metallurgy) disappears [Froment and Seiler, 1999]. The freezing front becomes plane (in the sense of metallurgy) and the interface temperature becomes equal to the liquidus temperature corresponding to the composition of the liquid phase. Specific tests have been performed at CEA Saclay (PHYTHER) to verify this conclusion.

This conclusion is also valid for corium-ceramic interaction at imposed power [Froment et al., 1999] for the final steady state.

Thus, due to heat transfer within the liquid, the liquid phase has a temperature which is above its proper liquidus temperature and, in other terms, behaves as a liquid material with a defined interface temperature. As a consequence, heat transfer correlations established with simulant materials are applicable in steady state.

The issue is that, in principle, the composition of the liquid phase in the end "steady state regime" (thus, the interface temperature) depends on what happened before, on the way the considered steady state was obtained. Considering the overall amount of corium, the composition of the liquid phase depends on the composition of the solid phase, which could, for instance, be deposited during a transient freezing stage. Depending on the freezing rate, metallurgy tells that more or less phase segregation (in the sense precipitation and physical separation of refractory compounds) may occur (the solid phase is enriched in refractory compounds, like UO_2 or ZrO_2, ...). This implies, in principle, that the knowledge of the composition of the liquid phase in the final steady state requires the description of the transient behaviour of the melt, which is a quite complex task.

Solution to specific cases of interest for reactor applications

Fortunately, this problem can be overcome with simple considerations in some important reactor application cases:

1. For In-Vessel Retention, in the cases of interest, the thickness of the oxidic crust is small. In terms of solidification theory, this means that the solid fraction (in this case

"solid fraction" = $\frac{mass\ of\ crust}{total\ mass\ of\ melt}$) is small; thus, the interface temperature is practically equal to the liquidus temperature corresponding to the overall composition of the melt.

2. For Corium-Concrete Interaction (MCCI), the composition of the corium (which freezes first at the contact with concrete as it comes out of the vessel) is not very different from the composition of the solidus which is calculated to be in thermodynamic equilibrium with the mixture. Thus, the application of solidification models do not lead to very different solutions (in terms of interface temperature between solid and liquid) if it is supposed that solid layers have the composition of initial corium.

The hypothesis of segregation for MCCI leads to enhanced understanding of physical phenomena and prediction of melt temperature and viscosity [Vandroux-Koenig et al., 1999]. However, the effect of sparging gas on phase segregation is still not well understood, mainly during the first 30 minutes of interaction. Some R&D efforts should be dedicated to this objective.

Consequences on Physical properties

Another consequence is that physical properties in the solidus-liquidus range (such as viscosity) must no longer be considered as an "intrinsic" property. The viscosity must be considered as an apparent property which results from the physicochemical and rheological processes. Models have been developed which apply for liquids above their proper liquidus temperature (relevant for In-Vessel and MCCI) [Sudreau & Cognet, 1997] or for well stirred melts (the solid phase is well-mixed with the liquid phase due to mechanical stirring (example: rotational viscometer)) within the solidus-liquidus temperature interval [Seiler & Ganzhorn, 1997].

Mushy zone and transient freezing

For application to transient processes (example: freezing during corium spreading), for which the freezing rate is elevated, mushy zones (in the metallurgical sense) have clearly been evidenced, for instance on VULCANO [Journeau et al., 1999]. This work led to the concept of "rheological layer", which is under development. The behaviour of the melt must, under these conditions, be described on the basis of the "cellular solidification" theory. Some work in this sense has been initiated at CEA/DRN and at IPSN, but there is still a lot to do in this field.

Application to fission products release and corium-ceramic interaction

The thermodynamic approach proved to produce results which comply with experimental results for the release of semi-volatile fission products from degraded fuel [Froment, 1999] or during MCCI [Mignanelli et al., 1988]. Due to the partial release, from the corium, of low-volatile fission products, it is expected that the residual power may be decreased by 20% at least. Calculations also showed that the distribution of the residual power over the different phases in an oxidic corium (liquid, crusts) is practically not affected by the freezing process and that the hypothesis of uniform distribution of residual power in

these phases is reasonable (even if the different fission products are, individually, not uniformly distributed).

Experimental verification programme

An experimental programme is expected to be engaged with real materials in VULCANO for the validation of models developed for corium behaviour during solidification processes, MCCI and Corium-Ceramic Interaction. This effort is also expected to be supported by simulant material experiments (ARTEMIS). Scaling criteria have been derived from the theory and from modelling for reactor applications. These criteria include: material effects, scale effects and effects of test procedures.

7. CORE-CATCHER CONCEPTS:

CEA/DRN has performed studies in support of alternative core catcher concepts. The Dual Concept [Szabo & Richard, 1997] concerns In-Vessel Retention. A multi-crucible concept has been emphasised for Ex-Vessel [Szabo et al., 1995] as well as a single crucible concept [Blanchard et al., 1994].

REFERENCES

Blanchard V., Labatte F., David O., Yala P. Humbert J.M., 1994 "Récupérateur plan SEMT" Raport DMT/94/295

Bonnet J.M., 1999 " Thermal-Hydraulic Phenomena in Corium Pools for Ex-Vessel Situations: BALI experiments" OECD Workshop on Ex-Vessel Debris Coolability Karlsruhe, Germany, 15-18 November 1999.

Bonnet J.M., Seiler J.M., 1992 "Coolability of Corium Spread Onto Concrete Under Water" ANS Proceedings from the National Heat Transfer Conference August 9-12 San Diego, California HTC-Vol.6 pp 347-354.

Cognet G., Laffont G., Jégou, journeau C., Sudreau F., Pierre J., Ramacciotti M., 1998 "the VULCANO Spreading Programme" Proceedings of SARJ-98 Workshop on Severe Accidents, Tokyo.

Dobson G.P., Turland B.D., 1996 "The Modelling of Hole Ablation" AEAT-1033 Report EU Community

Eddi M., 1999 "Studies on heat transfer in lower head of nuclear power plant vessel during a severe accident with MAAP computer code" NURETH 9. 3-8 October 1999 San Francisco.

Fieg G., 1999 "KAPOOL" CEA-FzK Meeting 1999

Froment K., Defoort F., Baichi M., Ducros G. "Thermodynamical Calculations Applied to Fission Product Release from a degraded Fuel Pin in VERCORS and VI experiments and to Residual Power Distribution" CALPHAD XXVIII, May 2-9 1999, Grenoble

Duret B., Froment K., Seiler J.M., Hellmann S., Fischer M., Bechta S., Lopukh D, 1999. "Analysis of Ceramic Ablation by Oxidic Corium" OECD Workshop on Ex-Vessel Debris Coolability Karlsruhe, Germany, 15-18 November 1999

Froment K., Seiler J.M. "Equations for solidification of corium without sparging gas. Scaling criteria" OECD Workshop on Ex-Vessel Debris Coolability, Karlsruhe, Germany, 16-18 November 1999.

Froment K., Duret B., Seiler J.M., Fischer M., Hellmann S., Bechta S., Lopukh., Pechenkov A., Vitol S., "Analysis of Ceramic Ablation by Oxidic Corium" OECD Workshop on Ex-Vessel Debris Coolability, Karlsruhe, Germany, 16-18 November 1999.

Journeau C., Pierre J., Michaud J.C., Cognet G., 1999 "Thermal, Physico-chemical and Rheological Boundary Layers in Multi-Component Oxidic Layers" accepted for publication in the *Revue Générale Thermique*

Levy S., 1999 "Molten Corium Concrete Interaction MCCI Subcommittee Report" EPRI Report. Feb 1999.

Sehgal B.R., Dinh T.N., Green J.A., 1997 "Experimental investigations on Vessel-Hole Ablation during Severe Accidents" SKI Report 97-44

Seiler J.M. , 1996 " Phase segregation model and molten pool thermal-hydraulics during molten core-concrete interaction ". Nuclear Engineering and Design 166 (1996) 259-267.

Seiler J.M., Froment K., Garandet J.P., 1999-1 "Equations for Solidification of Corium and Consequences" OECD Workshop on Ex-Vessel Debris Coolability Karlsruhe, Germany, 15-18 November 1999

Seiler J.M. and Ganzhorn J., 1997 " Viscosities of corium-concrete mixtures " Nuclear Engineering and Design Vol 178 (1997) N°3 December IV 1997 pp 259-268.

Seiler J.M., Labergri F., Froment K., Valin F., 1999-2 "Model development for the calculation of corium-ceramic interaction during severe accidents in LWRs" 9th International Topical Meeting on Nuclear Reactor Thermal-Hydralics (NURETH-9) San Francisco, California, October 3-8, 1999

Spindler B., Brayer C., Cranga M., De Cecco L., Montanelli P., Pineau D., Veteau J.M., 199ç "assessment of THEMA code against spreading experiments" OECD Workshop on Ex-Vessel Debris Coolability Karlsruhe, Germany, 15-18 November 1999

Sudreau F., Cognet G . 1997 ," Corium viscosity modelling above liquidus temperature ", *Nucl. Eng. and Design*, **Vol 178**, n°3, Dec IV, 1997

Szabo I., Richard P., Bergamashi Y., Seiler J.M., 1995 "A multi-crucible Core-Catcher Concept" Nuclear Engineering and Design 1995

Szabo I., Richard P., 1997 "In-Vessel Retention: proposal for a "dual" strategy" SARJ 1997 Tokyo

Vandroux-Koenig S., Seiler J.M., Gillot F., Froment K., 1999 "Simulation of ACE and MACE experiments with a phase segregation model using the TOLBIAC code" OECD Workshop on Ex-Vessel Debris Coolability Karlsruhe, Germany, 15-18 November 1999.

OECD Workshop on Ex-Vessel Debris Coolability
Karlsruhe, Germany, 15-18 November 1999

Organised in collaboration with
Forschungszentrum Karlsruhe GmbH

TWO-PHASE FLOW MODELLING OF PASSIVE SAFETY COOLING LOOPS.

G. Janssens-Maenhout, J.U. Knebel, U. Müller
Forschungszentrum Karlsruhe GmbH
Postfach 3640, 76021 Karlsruhe, Germany
greet.janssens-maenhout@iket.fzk.de

ABSTRACT

In the safety concept of the European Pressurised Water Reactor the decay heat removal for the ex-vessel core melt down accident has to be analysed. For licensing purposes it has to be proved that a safety system can remove the decay heat from a flooded core in the sump out of the containment with a sufficient heat transfer rate so that the containment integrity remains unaffected. Thereby passive safety systems are envisaged because of their automatic, inherently safe operation, independent of human reliability. A passive cooling system can be designed based on boiling induced natural convection. Moreover subcooled nucleate boiling offers the potential of removing heat with a high heat transfer rate at low temperature differences. The existence of the two-phase mixture leads however to a complicated dynamical behaviour of the cooling system and the susceptibility to instabilities with non-uniform power distribution at low pressure has to be recognised.

1. INTRODUCTION

Although modern nuclear power plants reach a very high safety and availability level, modifications improving their capacity and reliability are according to Kuczera et al. (1994) still under consideration. Nowadays mainly simple systems with passive components are from Weißhäupl and Bittermann (1993) pursued for their reliable and cheap operation without human intervention. Natural circulation loops and boiling induced convection loops are in emergency core cooling systems for advanced pressurised water reactors or in emergency condensers for future boiling water reactors strongly envisaged. These loops with a complex two-phase flow and phase change in the presence of non-condensable gases need to be well understood in order to guarantee an efficient operation of their design.

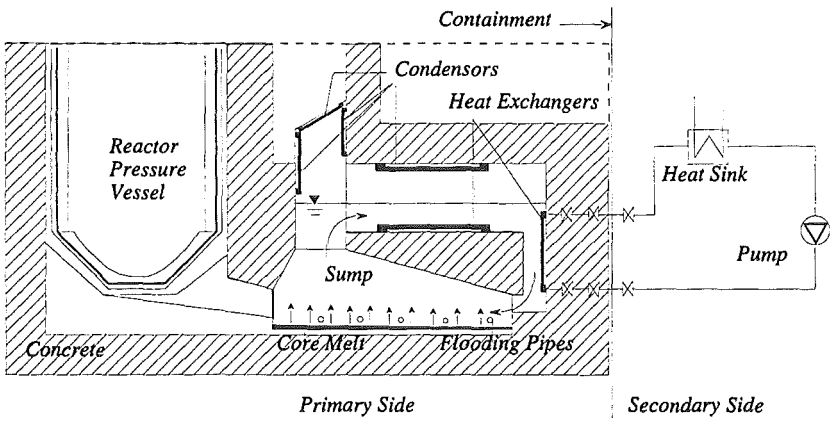

Fig. 1: First Sump Cooling Concept for the EPR.

As safety system for passive decay heat removal from the reactor sump of the European pressurised water reactor originally the sump cooling concept of figure 1 has been proposed. After being spread in the sump, the core is flooded from above by the water. The subcooled water is heated up by the core melt and starts boiling. A boiling driven mixed convection on short term and a transition from two-phase to single-phase flow on long term are expected in the cooling system.

This sump cooling concept does not fulfil the licensing requirement of a guaranteed basement integrity in case of an ex-vessel core melt accident. High long-term melt temperatures impose a potential risk for the integrity of the protective layer in the basement and it was recommended to enhance the basement cooling capacity. Therefore Siemens KWU designed the upgraded basement cooling concept for the EPR, which is represented in figure 2 .

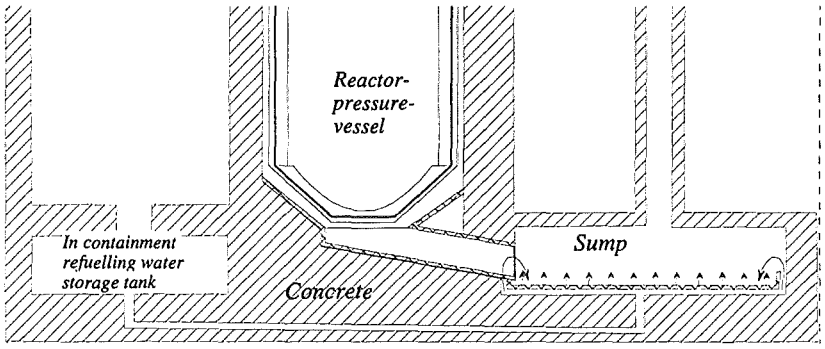

Fig. 2: Upgraded Basement Cooling Concept for the EPR.

For this upgraded basement cooling concept a heat transfer analysis of the horizontal cooling channels in the basement was performed by Schmidt et al. (1999). To guarantee the decay heat removal, the minimal water flow in the cooling channels had to be analysed. The minimal water flow was estimated by envisaging a stable, stationary, stratified two-phase-flow. Thereby the two-phase flow heat transfer calculation was reduced to the single-phase heat transfer calculation of the cooling water. For the void fraction calculation the cases of co-current and counter-current flow were considered following the Chexal-Lellouche model.

These strong simplifications give an estimation of the minimal water flow for a single active cooling channel but do not envisage the dynamic behaviour of the total system. Although the two-phase flow pattern and stability are not any more relevant under severe accident conditions, it is however important to prove that a sufficient amount of cooling channels will operate. It is not excluded that the operation of some cooling channels will be affected by flashing effects with local vapour accumulation . An irregular spreading of the core-melt leading to a non-uniform distribution of the heat load for the basement can in stagnant water induce a geyser with local high heat loads during the long incubation period and with local high pressure peaks during the short expulsion period. Probably three-dimensional effects are of significance, so that a different operation of the cooling channels may be expected for different designs of the chimneys collecting the two-phase mixture of several channels.

The upgraded basement cooling concept can be optimised by investigating the grouping of the horizontal channels. Considerable knowledge about the BWR thermal-hydraulic instabilities (of the hydrostatic head driven type or of the density wave driven type) is available in the literature. A global description of the thermal-hydraulic stability is given in terms of the Phase Change Number and Subcooling Number by Zuber (1970, 1976) or by van der Hagen (1997). However only limited research on geyser, the phenomenon that occur in stagnant water, is performed by Aritomi et al. (1992).

2. EXPERIMENT

The behaviour of a mixed convection with subcooled boiling at a heated bottom plate has been investigated by the test facility SUCOT (SUmp COoling Two-phase), constructed at FZK. The test facility scales with the full height of the prototype, so that the hydraulic behaviour of such cooling loop under fairly reactor-typical conditions can be demonstrated.

Fukuda and Kobori (1979) classified the thermal-hydraulic instabilities of such cooling loops in two major types. The first type of instability, known under flashing, is dominated by gravity effects in the riser, occurring at low mixture qualities. The second type of instability, the so-called density-wave-oscillation is driven by the interaction between the two-phase flow pressure loss, mass flux and void formation, occurring at relatively high power and low coolant-flow conditions. Experimental investigations as well as analytical and numerical modelling have been performed mainly one-dimensionally for both types by Van Bragt and van der Hagen et al. (1998), Takemoto and Aritomi et al. (1998) and especially for the second type by Ishii et al. (1970, 1976), Saha and Zuber (1974) and Yadigaroglu and Bergles (1972).

With this test facility especially the first type of instability is addressed to, since the large size of the test-facility allows to observe this flashing instability two-dimensionally. Of course the instability is system-dependent but some more general insights in the two-phase flow structure are given.

The test facility is sketched in figure 3 and consists of a L-shaped slab geometry with a length $l = 4.50\ m$, width $w = 0.94\ m$, height $h = 5.5\ m$ and depth $d = 0.12\ m$. The working fluid is water and the control parameters are the mass flow rate $M_{Lin} = \varepsilon_L u_{Lin} h\, d$, and the subcooling $\Delta T_{Sub} = T_{Sat} - T_{Lin}$ at the inlet and the wall heat source $Q_W = q_W l\, d$ at the boundary. Two operation modes, mixed convection and natural circulation, are possible. Here the mixed convection operation mode has been envisaged, with slightly forced subcooled water in the horizontal lower duct, heated up by the hot bottom plate, simulating a core melt.

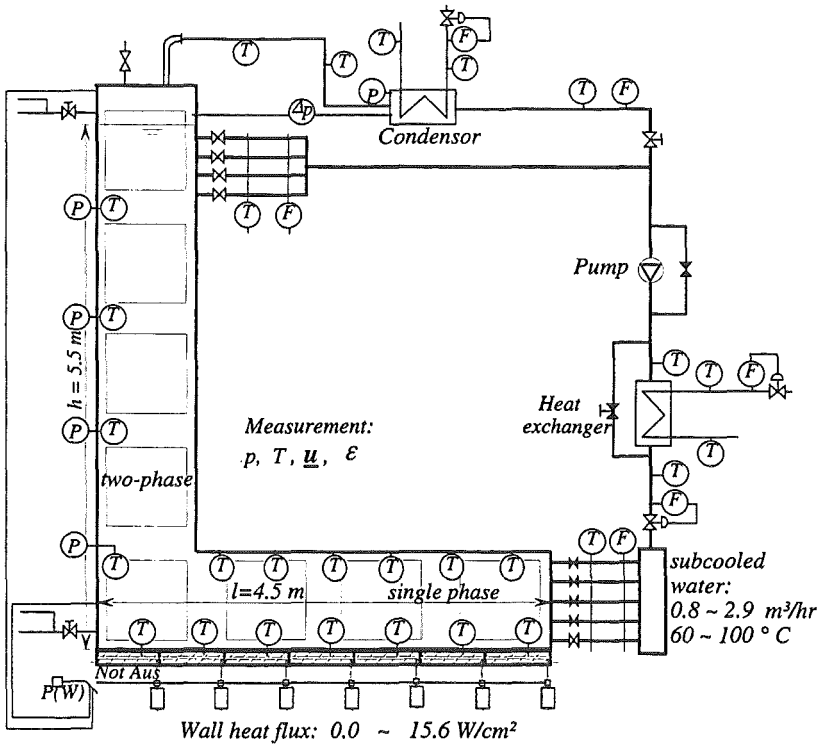

Fig. 3: Sketch of the Test Facility SUCOT.

The crust of the core melt can be smooth or fragmentised. In the experiment the surface type may vary from a smooth heated surface to a heated surface covered by a layer of small particles. In the case of a smooth heated surface, the classical boiling model at the heated bottom plate with onset of vapour generation after a single-phase entrance length can be used, whereas the case of a vaporising gravel bed can be modelled as an isothermal boundary layer with a constant vapour source term. Here the case of a heated surface has been described with an appropriate boiling model.

The bubbles generated at the heated boundary, are transferred to the bulk fluid. There the bubbles are dragged with the saturated fluid flow, establishing a disperse two-phase region. If the bubbles are not condensed in a subcooled region, they reach the chimney, where they can rise up and

continue to grow in size. The measurement techniques used are thermocouples of type K (Ni-CrNi), gamma densitometer with a ^{137}Cs source, flow meters and differential pressure sensors as described by Knebel and Janssens-Maenhout (1998).

3. ANALYSIS

3.1. Subcooled Boiling.

First subcooled boiling at a heated surface under steady state conditions has been considered. With a closed two-fluid model, described by Janssens-Maenhout (1990) boiling at a heated horizontal surface has been simulated. Thereby the two phases are described separately by two interpenetrating fields, which are coupled by closure relationships for inter-phase exchange of mass, momentum and energy. The inter-phase momentum exchange has been taken into account by interfacial forces as drag, lift, virtual mass and turbulent diffusion. The inter-phase mass and energy exchange during the subcooled boiling has been modelled with a vapour source term at the heated wall and with a condensation source term in the subcooled bulk. The detailed derivation of the six equations of the two-fluid model with the interfacial terms can be found in the Appendix.

According to Janssens-Maenhout and Müller (1990) the boiling model implemented is very sensible to the heat transfer from the hot surface towards the coolant. Here two different calculated void and temperature profiles for subcooled boiling at the heated surface are presented in figure 4. The surface which is less cooled by the water flow indicates the behaviour of pool boiling with a thicker saturated temperature layer. Whereas the better cooled surface indicates the behaviour of flow boiling with a larger change in temperature along the flow direction.

Behaviour of flow boiling

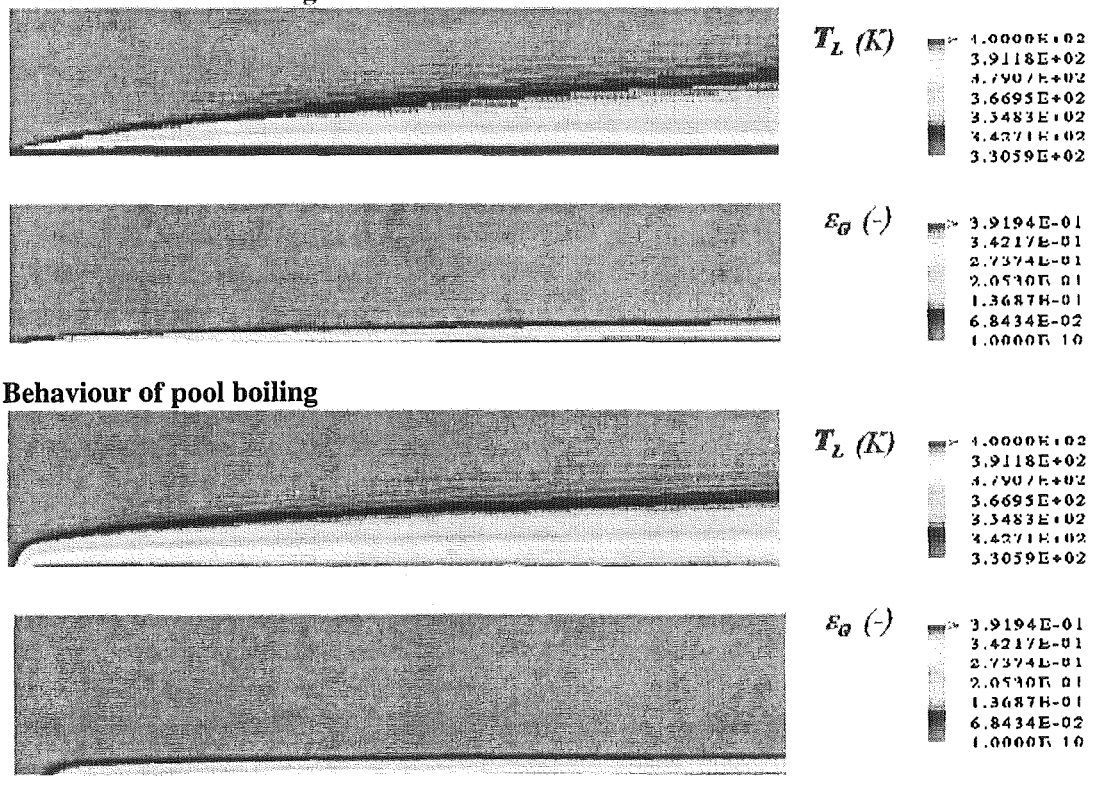

Fig. 4: Simulations of subcooled boiling with the closed two-fluid model.

3.2. Stability

Following Ishii and Zuber (1970) the behaviour of the two-phase flow can be characterised by the Subcooling Number N_{Sub}, representing the ratio of the inlet subcooling to the latent heat

$$N_{Sub} = \frac{\Delta\rho}{\rho_G}\frac{\Delta h_{Sub}}{\Delta h_{LG}} = \frac{\Delta\rho\, c_{pL}\Delta T_{Sub}}{\rho_G \Delta h_{LG}} = \frac{\Delta\rho}{\rho_G}\bigg|_{Pin} \frac{c_{pL}\left(T_{Sat}|_{Pin} - T_{Lin}\right)}{\Delta h_{LG}|_{Pin}} \tag{1}$$

and by the Phase Change Number N_{PCh}, describing the ratio of the inlet mass flux to the evaporation mass flux or the ratio of the fluid residence time to the evaporation reaction time

$$N_{PCh} = \frac{\Delta\rho Q_W}{\rho_G M_{Lin}\Delta h_{LG}} = \frac{\Delta\rho / M_{Lin}}{\rho_G / \Gamma_G} \tag{2}$$

The two dimensionless numbers N_{PCh} and N_{Sub} are coupled over the mixture quality x_{eq} by the following relationship

$$N_{PCh} - N_{Sub} = \frac{\Delta\rho}{\rho_G}\frac{\Delta h_{Out} - \Delta h_{Sub}}{\Delta h_{LG}} = \frac{\Delta\rho}{\rho_G} x_{eqOut} \tag{3}$$

For identical N_{PCh} and N_{Sub} a similar mixture quality development of the flow is preserved. In the case of $N_{Sub} < N_{PCh}$ the quality of the two-phase flow mixture is positive and vapour bubbles are present.

These definitions of N_{PCh} and N_{Sub} describe the natural convection in a one-dimensional channel. The Subcooling Number N_{Sub} describes the subcooling at the inlet and the Phase Change Number N_{PCh} describes the heat input at the wall boundary, however the pressure condition at the outlet boundary is not taken into account. Therefore the phenomenon of flashing - sudden onset of boiling due to the pressure decrease downstream - as driving force in the natural circulation loop is missing.

According to van der Hagen (1997) the Flashing Number N_{Flash} is introduced in order to describe the degree of subcooling at the outlet. This additional dimensionless number $N_{Flash,}$ which is smaller than $N_{Sub,}$ is defined as

$$N_{Flash} = \frac{\Delta\rho}{\rho_G}\frac{\left(h_{Gout} - h_{Lin}\right)}{\Delta h_{LG}} = \frac{\Delta\rho}{\rho_G}\bigg|_{Pin} \frac{c_{pL}\left(T_{Sat}|_{Pout} - T_{Lin}\right)}{\Delta h_{LG}|_{Pin}} \tag{4}$$

If $N_{Flash} < N_{PCh}$ then flashing occurs. If $N_{Flash} < 0$, then flashing occurs even without heat input.

Already Ishii and Zuber (1970) indicated a similar "Critical Subcooling Number" N_{SubC} and determined analytically the length of non-boiling region by the ratio of N_{Sub} to N_{PCh} and a stability criterion based on the thermal equilibrium model

$$N_{PCh,eq} - N_{Sub\,C} = \frac{\Delta\rho}{\rho_G} x_{eqOut} = \frac{2\left[\dfrac{\Delta p_{in}}{\rho_L u_{Lin}^2} + \dfrac{f_{2Ph} l}{2d} + \dfrac{\Delta p_{out}}{\rho_L u_{Lout}^2}\right]}{1 + \dfrac{1}{2}\left[\dfrac{f_{2Ph} l}{2d} + \dfrac{2\Delta p_{out}}{\rho_L u_{Lout}^2}\right]} \tag{5}$$

According to the experimental study of Saha, Ishii and Zuber (1976) one can only use this simplified stability criterion for the case of higher subcooling numbers. For the case of lower subcooling numbers the following criteria for the critical subcooling number are set:

$$N_{Sub\,C} = 0.0022 Pe \frac{A}{Pl} N_{PCh.eq} \quad if \quad Pe \le 70000$$

$$N_{Sub\,C} = 154 \frac{A}{Pl} N_{PCh.eq} \quad if \quad Pe > 70000 \tag{6}$$

For the test facility SUCOT, shown in figure 3, an overview of all working points ran up to now in different tests is given in the operational diagram of figure 5, representing the Subcooling Number over the Phase Change Number. During the operation of the test facility regimes with quiescent subcooled boiling as well as regimes of unstable flashing are observed. The quiescent mixed convection is indicated by triangles, the flashing effects by squares and the density wave oscillations by a rhomb in figure 5.

The structure and dynamic character of the mixed convection flow is indicated by fibre optical probes in the chimney. The oscillating onset of boiling has also been experimentally observed by the temperature fluctuations in the riser. Thereby the low frequency of the flashing phenomenon has been confirmed by the experiment.

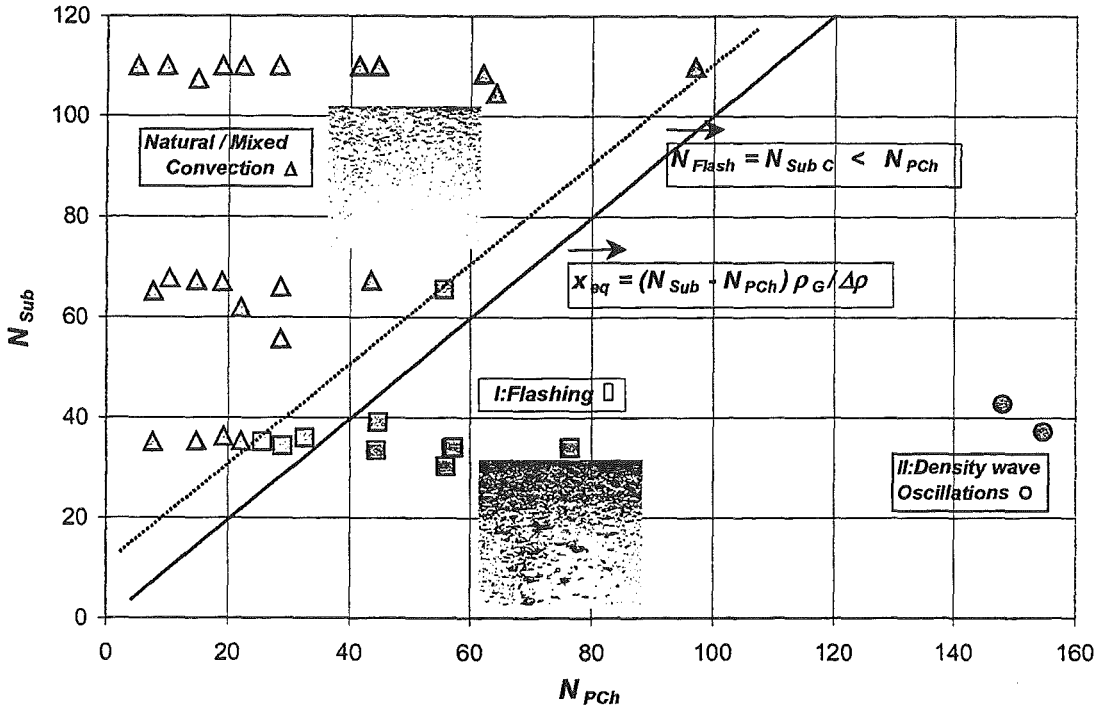

Fig. 5: Operational Stability Diagram of the Test Facility SUCOT.

This operational diagram represents the mixture quality reached in the test facility and therefore correlates with the two-phase flow pattern. As transitions of flow pattern induce instabilities from Yadigaroglu (1981), the diagram especially indicates the stable and unstable flow regimes. The stability criterion $N_{SubC}=N_{Flash} < N_{PCh}$ has been indicated with the dashed line in figure 5.

This diagram can be used to estimate flow pattern and instabilities of other boiling loops for given control parameters. For the extrapolation of this stability diagram to other applications the instabilities of phenomenological origin have to be carefully distinguished from the system dependent instabilities. Here an analytical bifurcation analysis of a simplified one- and two-dimensional boiling induced mixed convection loop is intended.

4. CONCLUSION

With the two-fluid model a wide range of two-phase flows in a cooling system can be modelled. Moreover the efficiency of heat transfer for subcooled boiling can be estimated and applied for the design of industrial cooling loops. However computational and experimental effort for the modelling of transient two-phase flow with bubbly boiling is still needed. The simulations with vapour generation indicate the sensitivity of the boiling model on the heat transfer at the hot surface. Furtheron the simulation of the dynamic behaviour of disperse two-phase flows needs a time-dependent analysis of the interfacial area.

The dynamic behaviour of disperse two-phase flow in the boiling induced mixed convection loop of the test facility SUCOT is described by the dimensionless Phase Change Number N_{PCh} and the Subcooling Number N_{Sub}. The experiments point to unstable dynamic behaviour due to the transitions from bubbly flow to slug flow by flashing phenomena. This flashing induced instability can be described by the Flashing Number. Experimentally a flow pattern map in the (N_{PCh}, N_{Sub})-diagram indicates in which range of the operational parameters flashing induced instabilities are to be expected.

REFERENCES

Anglart, H., Nylund, O., Kurul, N. and Podowski, M.Z., 1993, CFD Prediction of flow and phase distribution in fuel assemblies with spacers, *Proc. 1st CFDS Int. User Conf., Oxford*

Aritomi, M., Chiang, J.H., Mori, M., 1992, "Fundamental Studies on Safety-Related Thermal-Hydraulics of Natural Circulation Boiling Parallel Channel Flow Systems Under Start-up Conditions (Mechanism of Geysering in Parallel Channels)", *Nuclear Safety (Accident Analysis)*, Vol. **33**, No.2, April-June 1992

Bibeau, E.L. and Salcudean, M., 1994, Subcooled void growth mechanisms and prediction at low pressure and low velocity, *Int. J.. Multiphase Flow* , Vol.20(5), pp. 837-863

Cole, R. and Rohsenow, W., 1969 Correlations of bubble diameters for boiling saturated liquids, *Chem. Eng. Prog,* Vol.65, pp.211

Del Valle, V. and Kenning, D., 1985, Subcooled flow boiling at high heat flux, *Heat and Mass Transfer,* Vol. 28, pp.1907

Fukuda, K. and Kobori, T., 1979, "Classification of tow-phase flow instability by density wave oscillation model", *J. Nucl. Science & Techn,* **16,** pp.95-108

Ishii, M. and Zuber, N., 1970, "Thermally Induced Flow Instabilities in Two-Phase Mixtures", *Proc. of 4th Int. Heat Transfer Conf., Paris,* B.**5.**11

Ishii, M., Wu, Q., Assad, A. and Uhle, J., 1998, Interfacial area transport equation for two-fluid model formulation, *Proc. ImuST Meeting, Santa Barbara*

Janssens-Maenhout, G., 1999, Beiträge zur Modellierung und numerischen Simulation von Zweiphasenströmungen mit Wärmeübertragung, Ph.D thesis, Universität Karlsruhe, FzKa-6228

Knebel, J.U. and Janssens-Maenhout, G., 1998, Boiling induced mixed convection in cooling loops, *Proc. 36th Eur. Two-Phase Flow Group Meeting, Portoroz*

Kuczera, B., Eglin, W. and Weißhäupl, H.A., 1994, "Towards an enhanced quality in pressurised water reactor safety", *Kerntechnik* **59**(4-5), pp.151-155

Kurul, N., 1990 Multidimensional effects in two-phase flow including phase change, Ph.D. thesis, R.P.I.

Lahey, R.T., Jr. and Moody, F.J., 1979, *Thermal hydraulics of boiling water nuclear reactor,* A.N.S., Illinois

Lahey, R.T. Jr., 1995, The CFD analysis of multidimensional phenomena in multiphase flow, *Proc. of 2nd Int. Conf. On Multiphase Flow, Kyoto*

Malenkov, I.G., 1973, Detachment frequency as function of size for vapor bubbles, translated from *Inzhenerno-Fizicheskii Zhurnal,* Vol.20, pp.994

Ranz, W.E. and Marshall, W.R., 1952, Experimental Correlations for heat transfer between particle and fluid, *Chem. Eng. Prog.*, Vol.48, pp.141

Saffman, P.G., 1965, Lift force on small sphere in slow shear flow, *J. Fluid Mech.*, Vol.22, pp.385

Saha, P., Ishii, M. and Zuber, N., 1976, An experimental Investigation of the Thermally Induced Flow Oscillations in Two-phase Systems, *Transactions ASME, J. Heat Transfer,* nov. 76, pp.616-622

Saha, P. and Zuber, N., 1974, Point of Net Vapour Generation and Vapour Void Fraction in Subcooled Boiling, *J. Heat Transfer,* 74, *Proc. 5th Int. Heat Transfer Conf.,* Vol IV, pp.175-179

Samstag, M., 1996, Experimentelle Untersuchungen von Transportphänomenen in vertikalen turbulenten Luft-Wasser-Blasenströmungen, Ph.D thesis, University Karlsruhe, FzKa-5662

Schmidt, H., 1999, "Investigation of counter-current and co-current flow limits as bounding operational conditions for the upgraded basement cooling", *Siemens Work-Report KWU NT31/99/37, Erlangen*, proprietary info., pp.1-10

Takemoto, T., Aritomi, M., Matsuzaki, M., Usui, K. and Mori, M., 1998, "Experimental Study on the Driving Mechanism of Geysering", *CD-ROM Proc. of 3rd Int. Conf. on Multiphase flow, Lyon, June 1998*, pp.1-8

Van Bragt, D.D.B., and Van der Hagen, T.H.J.J., 1998 Stability of natural circulation boiling water reactors: Part i - description stability model and theoretical analysis, *Nucl. Techn.*, Vol.121, pp.40-51

van der Hagen T.H.J.J., Stekelenburg, A.C.J. and van Bragt, D.D.B., 1997, "Reactor Experiments on Type-I and Type-II BWR Stability", *Proc. of NURETH-8, Kyoto*, Oct 1997

Wang, C.H. and Dhir, V.K., 1993 Effect of surface wettability on active nucleation site density during pool boiling of water on a vertical surface, *Trans. ASME, J. Heat Transfer,* Vol.115, pp.659-669

Weisshäupl, H.A. and Bittermann, D., 1993, "Large Spreading of core melt for core melt retention/stabilisation", *Proc. 5th Int. Sem. Containment of Nucl. React., Karlsruhe,* pp.347-355

Wolfert, K., Burwell, M.J. and Enix, D., 1978, Non-equilibrium mass transfer between liquid and vapour phases during depressurisation process in transient two-phase flow, *Proc. 2nd CSNI Spec. Meeting*, Vol.1

Yadigaroglu, G. and Bergles, A.E., 1972, Fundamental and Higher-Mode Density-Wave Oscillations in Two-phase Flow, *Transactions ASME, J. Heat Transfer,* may 72, pp.189-195

Yadigaroglu, G., 1981, Two-phase flow instabilities and propagation phenomena, Thermohydraulics of two-phase flow systems for industrial design and Nuclear Engineering, pp.353-403

Yadigaroglu, G. and Bensalem, A., 1987, Interfacial mass generation rate modelling in non-equilibrium two-phase flow, *Multiphase Science and Techn.*, Vol.3, pp.85-127, 1987

NOMENCLATURE

A	m^2	flow cross section area	ν	m^2/s	kinematic viscosity
β	1/K	thermal expansion coefficient	p	kg/ms^2	pressure
c	J/kgK	specific heat	P	m	heated perimeter
d	m	depth	q	W/m^2	heat flux
D	m	bubble diameter	ρ	kg/m^3	density
ε	-	void fraction	σ	kg/s^2	surface tension
E	J/kg	Total spec. Energy = $h + u^2/2 - p/\rho$	t	s	time
f	1/s	bubble detachment frequency	T	K	temperature
φ	°	wetting angle	τ	kg/ms"	stress tensor
g	m/s^2	gravity	u	m/s	velocity
Γ	kg/m^2s	vapour source term	N	$1/m^2$	nucleation site density
h	J/kg	enthalpy	w	m	width
l	m	heated length	x	-	mixture quality
λ	W/mK	heat conductivity	Z	N	interfacial force
m	kg/m^2s	inter-phase mass exchange			

Subscripts

A	concerning a detaching bubble	K	of the phase k: k=L, G
B	concerning a bubble	L	of the liquid phase
C	critical for the stability	Sat	under saturation condition
Eq	in thermodynamic equilibrium	Sub	under subcooling condition
G	of the gas phase	W	at the wall boundary
i	at the interfaces	0	at initial condition
in	at the inlet boundary		

Dimensionless Numbers

C_D	Drag force coefficient	F_{2Ph}	two-phase mixture friction factor
C_L	Lift force coefficient	N_{Flash}	Flashing Number
C_{VM}	Virtual mass coefficient	N_{PCh}	Phase Change Number
C_{TD}	Turbulent diffusion coefficient	N_{Sub}	Subcooling Number

APPENDIX

Two-Fluid Model

Because of the applicability of the two-fluid model for a broad range of dispersed two-phase flows and especially for two-phase flows in large test facilities, it was chosen for the two-phase flow simulations. The following mass, momentum and energy equations for each of the phases k are used together the indicated interfacial exchange terms, derived by Janssens-Maenhout (1999).

Mass transport equation:

$$\partial_t(\varepsilon_k\rho_k)+\nabla\cdot(\varepsilon_k\rho_k\langle\mathbf{u}_k\rangle_k)=\underbrace{\Gamma_k}_{\text{Vapour source}}+\underbrace{\langle m'''_{ik}\rangle_k}_{\text{Interphase transfer}} \tag{7}$$

Momentum transport equation:

$$\partial_t(\varepsilon_k\rho_k\langle\mathbf{u}_k\rangle_k)+\nabla\cdot(\varepsilon_k\rho_k\langle\mathbf{u}_k\rangle_k^{\,2})=-\varepsilon_k\nabla p+\varepsilon_k\rho_k\mathbf{g}+\nabla\cdot\varepsilon_k\langle\boldsymbol{\tau}_k+\boldsymbol{\tau}_k^{\,\mathrm{Re}}\rangle_k+\underbrace{\sum\mathbf{Z}_{j,k}}_{\text{Interf. force}}+\underbrace{\Gamma_k\langle\mathbf{u}_k\rangle_k}_{\text{Source}}+\langle m'''_{ik}\mathbf{u}_k\rangle_k \tag{8}$$

Energy transport equation.

$$\partial_t(\varepsilon_k\rho_k E_k)+\nabla\cdot(\varepsilon_k\rho_k\langle E_k\rangle_k\langle\mathbf{u}_k\rangle_k)=\varepsilon_k\langle\rho_k\mathbf{g}\cdot\mathbf{u}_k+q'''_k\rangle_k+\nabla\cdot\varepsilon_k\langle\mathbf{u}_k\cdot(\boldsymbol{\tau}_k-\mathbf{p}+\mathbf{q}''_k)\rangle_k+\underbrace{\langle q'''_{ik}\rangle_k}_{\text{Interf. heat}}+\underbrace{\Gamma_k\langle h_{ik}\rangle_k}_{\text{Source}}+\langle m'''_{ik}h_{ik}\rangle_k \tag{9}$$

Interfacial Exchange Terms

The gas and liquid fields are interpenetrating by the interfacial forces coupling the two continuous velocity fields; by the interfacial heat, coupling the two continuous temperature fields and by the phase exchange terms at boundaries (vapour/condensate source) or internally in the bulk of the fluid (interfacial mass transfer). If a fluid particle passes from one phase to another, it not only transports it mass but also its velocity and energy to the other phase, so that these latest exchange terms give also rise to a momentum and energy source and transfer.

In Isothermal Bubbly Flows.

To close the two-fluid model in the case of an isothermal bubbly flow, constitutive relations for the interfacial forces and the Reynolds' stresses are needed. Different constitutive equations are possible but all numerical implementations to simulate interfacial forces consist in (1) a dissipative term, given by a drag tensor and (2) a dispersive term, given by a turbulent diffusion. The total sum of interfacial forces can according to Kurul (1990) be expressed by

$$\sum_j\mathbf{Z}_{j,G}=\underbrace{C_D\frac{3\varepsilon_G\rho_L}{4D_B}\left(\langle\mathbf{u}_G\rangle_G-\langle\mathbf{u}_L\rangle_L\right)^2}_{\text{Drag Force}}+\underbrace{C_L\varepsilon_G\rho_L\left(\langle\mathbf{u}_G\rangle_G-\langle\mathbf{u}_L\rangle_L\right)\times\langle\nabla\times\mathbf{u}_L\rangle_L}_{\text{Lift Force}}+\underbrace{C_{TD}\rho_L k_L\nabla\varepsilon_G}_{\substack{\text{Turbulent}\\ \text{Diffusion}}}+\underbrace{C_{VM}\varepsilon_G\rho_L\left(\left\langle\frac{D\mathbf{u}_G}{Dt}\right\rangle_G-\left\langle\frac{D\mathbf{u}_L}{Dt}\right\rangle_L\right)}_{\text{Virtual Mass}} \tag{10}$$

In stationary bubbly flows the drag tensor is deduced from the drag force on a bubble in the direction of the surrounding relative velocity field and from the lift force in shear layers which is perpendicular to this flow direction, (see Saffman (1965)). Thereby the bubble is treated as a rigid particle, which represents the real case of a bubble in non-purified water. Since the lift force is not strong enough in the vicinity of walls, an additional wall lubrication force or boundary condition for the gas phase is introduced to prohibit bubbles of penetrating

the wall. In non-steady-state cases an additional dynamic effect of the changed surrounding liquid flow field has to be taken into account by the virtual mass.

The turbulent diffusion can be modelled either by adapting the turbulence model for the Reynolds' stresses of the liquid phase or by an additional force which accounts for drifting the bubbles apart and flattening the void fraction profile as described by Anglart et al. (1993).

In Subcooled Boiling.

In the case of subcooled nucleate boiling the interfacial heat and mass exchange has to be modelled. As constitutive equation for the conductive and convective heat transfer between the two phases, the correlation of Ranz-Marshall (1952) is applied.

$$Nu_B = 2 + 0.6\,\mathrm{Re}_B^{0.5}\,\mathrm{Pr}_L^{0.3} \tag{11}$$

The modelling of the interfacial mass exchange in the bulk of the fluid is based on the energy balance and the assumption of a saturation condition inside the vapour bubble.

$$\Delta h_{LG}\frac{D}{Dt}\left(\rho_G\frac{\pi}{6}D_B^{\,3}\right) = \alpha_{Bi}\left(T_{Sat} - T_L\right)D_B^{\,2}\pi \tag{12}$$

The modelling of the vapour/condensate source by an external heat source/sink at the boundary of the fluid domain is based on a mechanistic approach, proposed by Yadigaroglu and Bensalem (1987). Thereby the vapour source term Γ_G is composed of the bubble mass with detachment diameter D_A, the detachment frequency f and the nucleation site density N. Each of those parameters is modelled by an appropriate, empirical correlation of Cole and Rohsenow (1969) for D_A, of Malenkov (1973) for f and of Wang and Dhir (1993) for N. This reads as

$$\Gamma_G = \frac{\pi D_A^3}{6}\rho_G \cdot f(q''_W) \cdot N(T_W) \tag{13}$$

The heat needed for the generation of this vapour source corresponds to the amount of the wall heat flux q_{W2} directed to the gas phase. The remaining other amount of the wall heat flux directed to the liquid phase q_{Wl} is according to the model of Lahey and Moody (1979) partially used for single phase heat transfer q_{Wla} and partially for enhanced heat transfer q_{Wlb} during the rewetting of the wall after bubble detachment. The splitting up $q_{Wl} = q_{Wla} + q_{Wlb}$ is determined by use of an empirical correlation of Del Valle and Kenning (1985).

OECD Workshop on Ex-Vessel Debris Coolability
Karlsruhe, Germany, 15-18 November 1999

Organised in collaboration with
Forschungszentrum Karlsruhe (FZK) GmbH

Main Features of the EPR Melt Retention Concept

Manfred Fischer
Siemens AG, KWU NA-T, Freyeslebenstr. 1, 91058 Erlangen, Germany
Manfred.Fischer@erl11.siemens.de

Abstract

It was one of the design targets for the European Pressurized Reactor (EPR) to ensure the long-term integrity of the containment, and thus to significantly reduce the related radiological consequences, also in case of a postulated severe accidents with core melting. It is evident that this goal can only be achieved if the interaction of the molten core with the concrete basemat is avoided.

For stabilizing the melt within the containment an ex-vessel strategy was chosen from the beginning, since the high power rating of the EPR aggravates any kind of in-vessel retention. The EPR strategy is based on the spreading of the molten core into a large lateral compartment followed by its flooding and quenching from the top. To avoid basemat penetration, the bottom of the spreading compartment is covered with a temperature resistant protective material, the long-term integrity of which is achieved by a number of diverse and redundant measures. One of these is a layer inversion caused by the incorporation of sacrificial material which makes the oxidic melt the lighter phase and therefore avoids its contact with the protective material.

Sacrificial concrete layers are provided in the pit and in the spreading compartment. In the pit, the related MCCI also results in a temporary melt retention, which

- makes the concept independent of uncertainties regarding in-vessel pool formation and RPV failure mode
- restricts and normalizes the spectrum of possible melt states at the time of spreading

The retention phase ends after the concrete cover at the bottom of the pit is eroded and after a metallic plug is destroyed which blocks the access to a transfer channel. The retained melt is expected to spread in one pour and to distribute evenly in the provided compartment. Thanks to a following hour-long phase of interaction with sacrificial material potential spreading inhomogenities are assumed to equal-out before the actual protective zirconia layer is reached. The chosen material is thermo-chemically stable in the range of given parameters. Stability is further ensured by an active cooling system at the interface with the structural concrete.

The paper summarizes the features of the actual EPR melt retention concept and gives an overview of still disputed issues.

1 Introduction

The EPR approach towards severe accident prevention and mitigation is twofold. First, scenarios, which could affect containment integrity, e.g. as a result of energetic phenomena or containment bypass, are practically eliminated by appropriate means including:

- dedicated depressurization of the primary circuit, to avoid missiles and DCH
- hydrogen control measures, to avoid DDT and global H_2-detonation
- the provision of a dry pit and spreading area, to avoid energetic FCI

Second, for the remaining low-pressure core melt scenarios, consequences are mitigated by:

- melt stabilization measures, to avoid basemat penetration
- a containment heat removal system, which prevents containment over-pressurization
- confinement measures, which ensure containment leakage <1 %/d, plus filtered release

Long-term melt stabilization is an essential precondition for the stabilization of the situation in the containment and therefore a key element of the entire mitigation scheme.

2 Main conceptual features

The concept of the EPR to stabilize a molten core in a severe accident is based on its spreading into a large lateral compartment, followed by a flooding, quenching and cooling from the top with water drained passively from an internal reservoir, the IRWST.

It is a characteristic feature that the corium is not discharged into the spreading compartment as it is released from the RPV, but first retained temporarily in the reactor pit (Fig. 1). Only after most of the core inventory is accumulated, the molten pool will be released into a lateral spreading compartment. By the described strategy a spatial separation of the functions to (1) withstand the thermo-mechanical loads during RPV failure and to (2) transfer the melt into a coolable configuration, is achieved. This separation leads to a simplification of the design of the retention device and preserves the freedom to replace it with an upgraded or even alternative solution, e.g. of COMET-type /Alsmeyer/, in case it shows better performance.

At the bottom of the spreading compartment a protective layer, made of zirconia, is provided to avoid basemat penetration. Since the long-term stability of the zirconia can only be safeguarded if it is in contact with the metallic melt fraction, a preceding layer inversion was implemented, achieved by the addition of sacrificial material in reactor pit and spreading compartment.

In the pit the provision of a sacrificial layer, introduces a phase of temporary melt retention, which will

- make the concept independent of the uncertainties of in-vessel pool formation and melt release from the RPV
- restrict and normalize the spectrum of possible melt states at the time of spreading

This way, defined initial conditions are established for the subsequent retention measures, namely for the spreading of the melt.

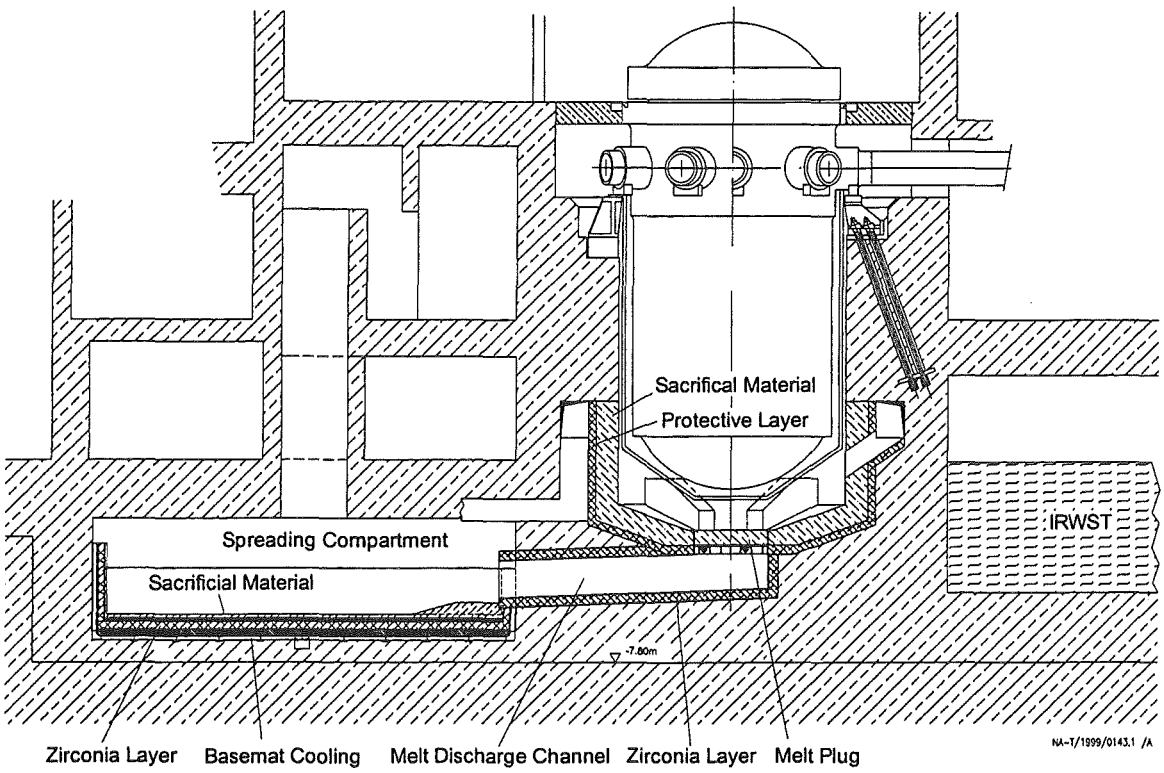

Fig. 1 Cross-section through the lower part of the EPR, showing the main components of the melt retention and stabilization concept

Spreading will start once the MCCI in the pit has exposed the melt plug and once it was destroyed by the melt. The retention time is determined by the thickness of the bottom concrete layer and will exceed the interval between assumed first and last melt release from the RPV.

Long-term stabilization of the melt is realized by a temperature resistant zirconia-layer in a dedicated lateral spreading compartment. Since the survival of this layer is crucial for the entire concept, potential thermo-chemical interactions, which may challenge its integrity, are avoided by a number of diverse measures, namely by the provision of a:

- sacrificial concrete layer as the top layer in the spreading room, the incorporation of which results in a layer inversion by reducing the density of the oxidic corium below that of the molten metal. This prevents a direct contact between oxidic corium and protective layer.
- sacrificial metal layer underneath the concrete to ensure the presence of a metallic melt at any location, independent of the characteristics of the spreading process. The slow melt-down of the steel layer guarantees a gradual heat-up of the zirconia.
- cooling system to provide a heat sink underneath the zirconia layer, which - besides keeping the temperatures in the structural concrete low - is capable to ultimately stop any postulated melt progression.

3 Components of the technical solution

The main components of the EPR melt stabilization concept, as it has evolved till the end of the EPR basic design, are shown in Fig. 1. Their characteristics are described below. Further optimization is planned in the detailed design phase.

Sacrificial concrete layer in the reactor pit

Besides fulfilling the objective to provide melt accumulation even for a postulated multi-step release from the RPV, the sacrificial concrete layer conditions the melt for spreading and ensures the complete oxidation of all zirconium, which may potentially be present in the melt. The latter is of advantage since zirconium could chemically interact with the protective layer. As a result of the oxidation, the ingredients of the sacrificial concrete, namely iron oxide and silica, will become chemically reduced. The reaction products dissolve in the metallic melt. Unreduced silica and iron oxide will be incorporated by the oxidic melt, lowering its density and liquidus/solidus temperature.

A practically carbonate free binder and a low water in the concrete content were selected to ensure a low release of non-condensable gases (CO_2, CO and H_2) during the ex-vessel MCCI-phase. Further details on the composition of this concrete are given in /Nie/.

Protective layer in the reactor pit

As an analysis of the retention phase indicates, the metallic fraction of the melt - formed from internal structures and the lower head of the RPV - will remain specifically lighter than the oxidic corium. A pool of liquid metal will thus reside atop the molten oxide and will be heated from below. The resulting "focussing effect" could lead to a pronounced sideward erosion of the concrete in the metallic region.

To ensure mechanical support for the remaining RPV plus primary circuit the surrounding structural concrete will be protected by a cylindrical shielding behind the sacrificial concrete. Since interaction time and melt temperature are lower than in the spreading room, the requirements on the selection of a suitable material are correspondingly reduced.

Melt plug

Once the sacrificial concrete at the bottom of the pit is ablated, melt will come in contact with a melt plug. It is basically a steel plate of about 2.4 m^2 cross section. The plate will first be contacted by the oxidic melt fraction.

Transfer channel

Once the melt plug is thermally destroyed, the melt will flow through a declining transfer channel into the spreading compartment. Its walls will be made of temperature resistant material. Due to the large cross-section of >1 m^2, this channel is not expected to provide a significant retardation to the melt flow.

Sacrificial concrete in the spreading compartment

Thanks to the high specific amount of concrete supplied per unit area, the consumption of the sacrificial concrete layer in the spreading room will ensure that, independent of the initial distribution of metallic and oxidic melt after spreading, the desired reduction of the oxide density will always be achieved. This way, no credit has to be taken from a long enough

retention time in the reactor pit. Lateral mixing during the following MCCI phase makes the concept widely insensitive against postulated local inhomogenities of melt spreading in respect to corium distribution and composition.

Additional advantages achieved by the incorporation of sacrificial material are (i) lower long-term melt temperatures and (ii) improved fragmentation of the top oxide layer. Though the potential extent of fragmentation is still controversially disputed, a positive assessment, e.g. as a result of new findings from the MACE program /Farmer/ can directly be credited.

Sacrificial steel in the spreading compartment

Underneath the concrete, a layer of sacrificial steel elements is provided. It ensures the presence of a metallic melt at any location, independent of the characteristics of the spreading process. The heat-up and melt-down of the elements will last several hours and will provide a gradual temperature increase and a smooth sintering of the refractory material. Since the long-term stability of the zirconia will depend on the chemical nature (oxygen content) of a metallic melt layer, advantageous initial conditions can be achieved by a suitable composition of the steel elements.

Under EPR-conditions, characterized by a relatively low percentage of FeO in the oxidic melt as well as by the permanent presence of chromium in the metallic melt, the oxygen content in the metal will always be sufficiently low to avoid thermo-chemical dissolution of the ZrO_2

Protective layer in the spreading compartment

The long-term protection of the structural concrete is provided by a layer of zirconia-based ramming mass. It is expected to sinter, from the top, during the melting of the sacrificial steel layer. The procedure is analogous to common industrial practice. It has been confirmed experimentally that zirconia is thermo-chemically stable in contact with a steel layer of EPR-specific composition and temperature /Hellmann/.

Melt flooding and basemat cooling

The basemat cooling system, initially introduced to protect the structural concrete, has recently been upgraded in respect to heat removal capacity and thermo-mechanical stability in case of postulated melt contact. It is now potentially capable to provide an effective cooling of the melt. The new solution is characterized by a "unification" of the former separate systems for melt flooding and active basemat cooling. All water, which enters the spreading room, will now have to pass the cooling channels. This ensures that, already during passive melt flooding, these channels are filled with water.

Long-term cooling of the spread melt is realized by the heat-up of water taken from the IRWST, cooled down externally and recirculated through the cooling channels into the pool atop the spread melt. From there still subcooled water flows back into the IRWST (Fig. 2).

In case the CHRS is temporarily unavailable, sufficient heat extraction is also provided passively by the evaporation from a saturated pool.

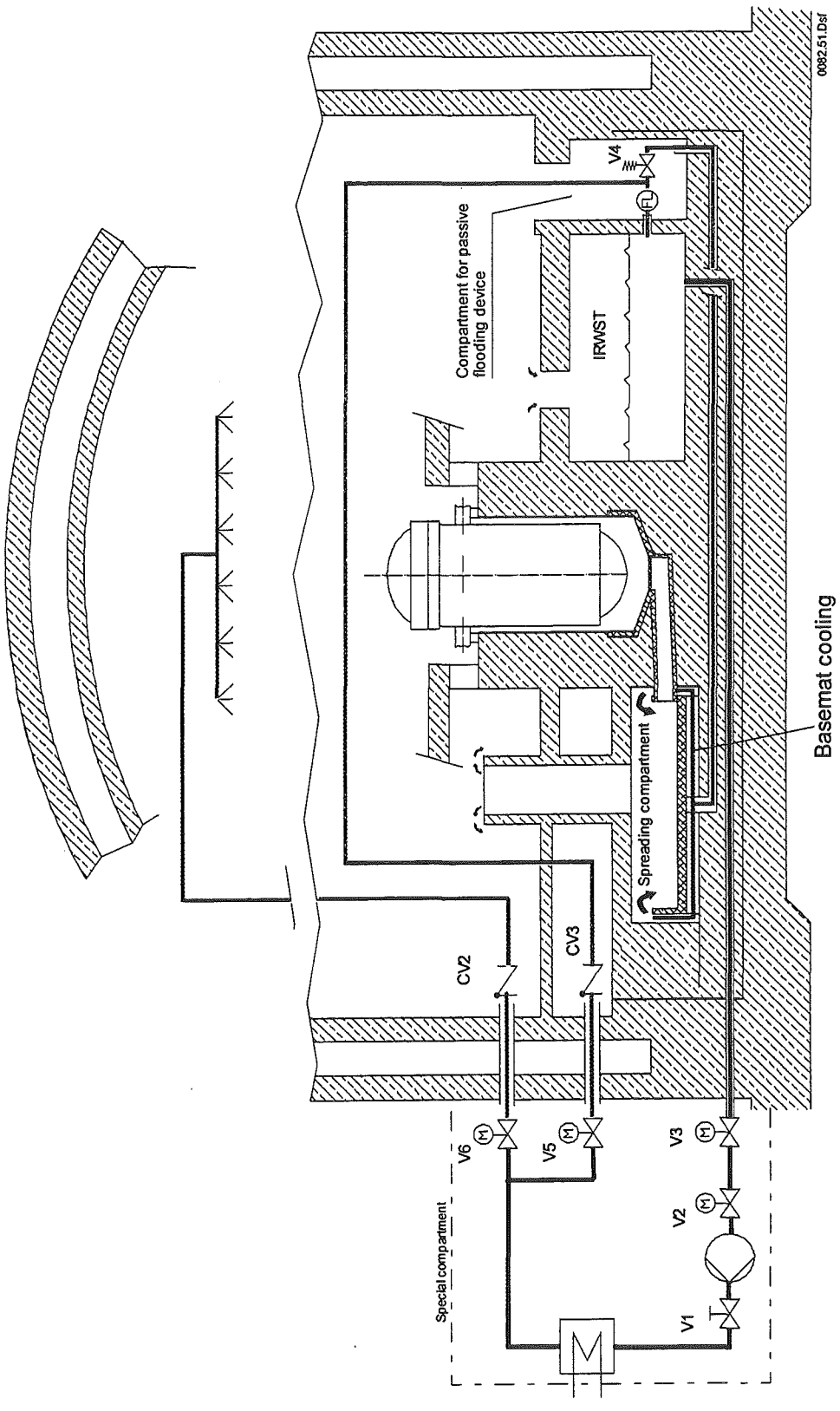

The CHRS takes water from the IRWST, cools it down externally, and supplies it to either the basemat cooling and/or containment spray system - dependent on the position of valves V5/V4 and V6. Valve V4 is triggered by the arrival of the melt in the spreading compartment, thus initiating the passive flooding of the melt via the basemat cooling channels.
Once the CHRS is available, the drainage flow is overridden by an active feed. As a result the spreading compartment (and the attached reactor room) will become submerged up to the top of the steam discharge chimney. Overflowing water will spread on the heavy floor and drain back into the IRWST, thus closing the circuit for the CHRS. The flow limiter FL is needed to prevent a bypass of the basemat cooling system during active feed.

Fig. 2 Flow diagram of the EPR containment heat removal system (CHRS) showing the distribution paths for the containment spray and basemat cooling systems

4 Status of evaluation and validation

The EPR melt stabilization concept was subject to a number of debates of the French "Groupe Permanent Réacteur" (GPR) and the German "Reaktorsicherheitskommission" (RSK) in the context of their common elaboration of recommendations for future PWR's since 1993. Their main concerns and the corresponding project position are given below:

- sensitivity of the melt retention concept with regard to various relevant scenarios

  This concern is taken care by the introduction of a phase of temporary melt retention in the pit, which eliminates the problems that result from the low predictability of in-vessel pool formation and RPV failure, and which provides defined initial conditions for spreading after melt plug failure.

- effect of the sacrificial material on the melt composition and on the thermo-chemical and thermal-hydraulic properties of the relevant corium mixtures, in particular with regard to the effectiveness of the spreading process

  The preceding accumulation of the core-melt inside the pit, as well as the fact that spreading will be into a dry compartment, relax the proof of a sufficiently homogeneous melt distribution. From the spreading experiments performed within the last decade /Cognet/, /Steinwarz/ it can be deduced that, if only the average final melt height is sufficiently high (as for the EPR), the melt can be expected to distribute evenly on the provided area.

  The application of both numerical tools /Wittmaack/ and scaling methodologies /Konovalikhin/ for the EPR situation, characterized by a total melt mass of about 350 Mg and a spreading area of about 170-180 m², did confirm this assessment. It is currently assumed that a detailed knowledge of the rheological behavior of the melt and of the phenomena that govern local front immobilization will not be required.

  Since the spreading room is a dead-end compartment it is initially "dry" in the sense that no water from any part of the containment can enter directly. Only limited condensation is possible for scenarios with a steam-rich containment atmosphere. The maximum height of a condensate layer is therefore <1 cm. Experiments within KATS /Fieg/ and FARO /Cognetl/ have proven that, under these conditions, the spreading process will not lead to results which are significantly different from the dry case.

- reliability of the opening of the steel gate

  When the oxidic melt fraction contacts the gate, the thermal inertia of the plug will immediately cause the formation of an insulating crust. After reaching its maximum thickness of a few cm, this crust will re-melt from the top as a result of the steady heat-up of the plate. Thanks to the much higher conductivity of steel, as compared to that of the oxidic crust, lateral heat conduction within the plate will provide a uniform temperature distribution. Thus, the metallic structure will become mechanically weakened at all locations at about the same time.

  After its failure, the remaining oxidic crust can not support the pressure imposed by the weight of the melt. Therefore, the melt plug is expected to open with almost the full cross-section. The described behavior is currently subject of experimental confirmation in the frame of the KAPOOL experiments /Fellmoser/.

- stability of the protective refractory layer, and the prevention of leakage to the subsoil

  The chemical stability of the refractory material depends on the temperature and chemical nature of the melt, namely on its oxygen content. It was shown that under EPR-conditions, characterized by (i) a relatively low content of iron oxide in the oxidic melt and by (ii) the permanent presence of chromium, the oxygen content in the metallic melt will always be sufficiently low to avoid thermo-chemical dissolution of the zirconia.

  Redundantly, with the recently upgraded cooling system the integrity of the protective layer is also ensured by an adequate cooling provided at the bottom. The cooling effect will progressively increase with any postulated decrease in the thickness of the zirconia. This always preserves a minimum residual layer thickness.

  Water leak-tightness of the spreading compartment is provided by a liner embedded in the structural concrete.

- risk of highly energetic corium-water interactions

  During RPV failure the reactor pit is considered dry. In addition, based on the associated low probability of this event, also a late reflooding of the molten pool before the release of the melt from the RPV is practically eliminated. Thus FCI phenomena are excluded during the initial melt release phase.

  After the formation of a molten pool in the reactor pit, the concept becomes highly insensitive against water addition from the top. Due to the expected fast radial erosion of the concrete, the lighter metallic melt will quickly be covered with a slag layer consisting of iron oxide and silica. Its high viscosity, which even exceeds that of MACE-type melts, is expected to safely prevent FCI's.

  During the following melt release from the pit, a potential water overlayer can not influence the spreading process, since the melt plug is located at the bottom of the pit. For the spreading process itself, the potential effect of a small amount of water at the floor is also not critical, since the energy release from local FCI's, if they occur at all, would generally remain small.

  As a result of the spreading process oxidic melt and the slag, formerly accumulated atop the metallic melt layer, will mix. In addition a significant content of silica in the oxidic fraction will quickly accumulate due to the area-enhanced MCCI. This will make the oxide the lighter phase and cause a layer inversion before the start of melt flooding. Fuel coolant interactions, even of low energy, have never been observed when oxidic melts of such type were flooded under MCCI-conditions.

  After the end of MCCI in the spreading room, a fragmented oxidic crust is expected to isolate the melt from the water on top.

Due to above given positive evaluation, the project considers the EPR melt stabilization concept as a sound technical solution. Nevertheless, some issues are further investigated in the frame of ongoing, as well as planned R&D.

5 Summary

To achieve the goal of long-term melt stabilization, the concept of the EPR involves design measures which ensure the distribution of the molten core on a large area followed by its afterward flooding and quenching from the top. Melt spreading is preceded by a prior melt retention phase in the pit which (i) makes the concept independent of the uncertainties of in-vessel pool formation and melt release from the RPV and (ii) restricts and normalizes the spectrum of possible melt states at the time of spreading.

The paper summarizes the actual features of the EPR melt retention concept and their intended function. It also lists the still disputed issues together with the answers provided by the project.

Abbreviations

CHRS	Containment Heat Removal System
DCH	Direct Containment Heating
DDT	Deflagration-Detonation Transition
EPR	European Pressurized Water Reactor
FCI	Fuel Coolant Interaction
IRWST	Integrated Residual Water Storage Tank
MCCI	Molten Corium Concrete Interaction
RPV	Reactor Pressure Vessel

References

/Alsmeyer/ - H. Alsmeyer, T. Cron, F. Ferderer, W. Tromm, H. Schneider and T. Wenz
CometPC: First Results for a Simplified Cooling Concept Based on Porous Concrete
OECD Workshop on Ex-Vessel Debris Coolability, Karlsruhe Germany, Nov. 15-18, 1999

/Bittermann/ - D. Bittermann
Principles of Application of Mechanical Design Measures to Control Severe Accident Phenomena, Applied to the EPR Melt Retention Concept
OECD Workshop on Ex-Vessel Debris Coolability, Karlsruhe Germany, Nov. 15-18, 1999

/Cognet/ - G. Cognet, H. Werle, D. Magallon, R. Wittmaack, B.R. Sehgal, L. De Cecco, R. Ocelli, D. Pineau and B. Spindler
Corium Spreading Phenomena: Results Obtained from the EU CSC Project
OECD Workshop on Ex-Vessel Debris Coolability, Karlsruhe Germany, Nov. 15-18, 1999

/Farmer/ - M. T. Farmer, B.W. Spencer, D.R. Armstrong, D.J. Kilsdonk, R.W. Aeschliman, and J. Chao
Status of Large Scale MACE Core Coolability Experiments
OECD Workshop on Ex-Vessel Debris Coolability, Karlsruhe Germany, Nov. 15-18, 1999

/Fellmoser/ - F. Fellmoser, G. Fieg, H. Massier, Chr. Messainguioral, H. Werle
KAPOOL Experimentsto Simulate Molten Corium Sacrificial Concrete Interaction and Gate Opening in the EPR Core Catcher Concept
OECD Workshop on Ex-Vessel Debris Coolability, Karlsruhe Germany, Nov. 15-18, 1999

/Hellmann/ - S. Hellmann, F. Funke, V. Lansmann, B. Friedrich
Physico-chemical and Material Aspects of the Core Melt Retention Concept of the EPR
OECD Workshop on Ex-Vessel Debris Coolability, Karlsruhe Germany, Nov. 15-18, 1999

/Konovalikhin/ - M.J. Konovalikhin, T.N. Dinh, B.R. Seghal, M. Fischer
The Scaling Model of Core Melt Spreading: Validation, Refinement and Reactor Applications
OECD Workshop on Ex-Vessel Debris Coolability, Karlsruhe Germany, Nov. 15-18, 1999

/Nie/ - M. Nie
Application of Sacrificial Concrete for the Retention and Conditioning of Molten Corium in the EPR Melt Retention Concept
OECD Workshop on Ex-Vessel Debris Coolability, Karlsruhe Germany, Nov. 15-18, 1999

/Steinwarz/ - W. Steinwarz, W. Häfner, Z. Alkan, M. Fischer
COMAS: Representative Spreading Experiments with View to Core Melt Mitigation
OECD Workshop on Ex-Vessel Debris Coolability, Karlsruhe Germany, Nov. 15-18, 1999

/Wittmaack/ - R. Wittmaack
Numerical Simulation of Corium Spreading in the EPR with CORFLOW
OECD Workshop on Ex-Vessel Debris Coolability, Karlsruhe Germany, Nov. 15-18, 1999

OECD Workshop on Ex-Vessel Debris Coolability
Karlsruhe Germany, 15-18 November 1999

Organised in collaboration with
Forschungszentrum Karlsruhe (FZK) GmbH

PRINCIPLES OF APPLICATION OF MECHANICAL DESIGN MEASURES TO CONTROL SEVERE ACCIDENT PHENOMENA, APPLIED TO THE MELT RETENTION CONCEPT OF THE EPR

Dietmar Bittermann
Siemens AG, KWU NA-T
Freyeslebenstr. 1, D-91058 Erlangen ,Germany
dietmar.bittermann@erl11.siemens.de

ABSTRACT

To retain and stabilize a core melt within the containment, the phenomena which principally have to be dealt with are related to melt discharge, spreading, retention and cooling, plus specific phenomena like melt dispersal and ex-vessel melt water interaction. For the elaboration of mechanical design measures provided to stabilize a melt within the containment, boundary conditions may occur which could pose extremely high thermal and mechanical loads on the structures. This file describes an approach characterized by the idea to influence the course of severe accident scenarios as much as possible in order to generate boundary conditions for mitigation means "by design", which enables the development of a mitigation concept with maximum confidence in the effectiveness of the measures provided.

1. INTRODUCTION

Mitigation means provided for design basis accidents can take benefit from the fact that the geometry of the components is more or less intact and the conditions are not so far from normal operation conditions. In severe accident situations the boundary conditions are completely different from this situation. The conditions of such scenarios are characterized by the fact that the integrity of important components like the fuel assemblies and the RPV are lost and the conditions especially the corium temperatures are extremely high and beyond that tolerable for materials normally used in the plant design. In addition, a large amount of different scenarios may be considered which may lead to an increase in the number of boundary conditions.

The designer who has to develop concepts for mitigation and control means for effects of severe accident phenomena is confronted with boundary conditions for design measures

which are far beyond of the classical design basis accident conditions especially considering the temperatures involved. In order to overcome this challenge in principle two approaches can be applied for specifying the design conditions.

One approach is to cope with such extreme situations by enveloping the entire range of potential loads and to define this as basis for the mitigation measures. This approach has two important disadvantages: first, one has to be sure that the complete range of potential scenarios and the resulting loads are covered. This has a large uncertainty since the phenomena and problems dealt with, have a very low probability at all and therefore the selected scenarios are more or less arbitrary. In addition such an "enveloping load approach" may lead to extreme requirements to the technology and the design measures to be applied with the effect of heavily burdening the capital cost of the plant.

The other approach - which is described in more detail in this paper - is a procedure which does not only provide mitigation measures for the final state of a scenario, but also intends to influence as much as possible the course of severe accident scenarios from the beginning. The idea of this procedure is to generate states with conditions which are well defined. For such states either assured knowledge already exists or can be elaborated by specific R&D work. As a consequence this approach has the potential to develop mitigation measures with maximum confidence in the effectiveness of the provisions. In this kind of approach – which is nominated as "state controlled approach", the designer must be involved in the entire process of development in order to be able to identify possibilities for design provisions which in turn may influence the R&D efforts. We are strongly convinced that this approach also leads to solutions which from the technology and the overall design point of view are more appropriate and have the potential of a minimum burdening of the capital cost of the plant.

2. CHARACTERISTIC FEATURES OF THE "STATE CONTROLLED APPROACH" PROPOSED TO BE FOLLOWED

According to this approach the task of elaboration of a concept for the control of any severe accident phenomenon is subdivided into the following steps:

- Identification of governing problems
- Analysis of correlation between relevant parameters
- Definition of design conditions

Design provisions are proposed to be foreseen for each of the individual steps. (Fig. 1) In case of the "identification"-step, such provisions can reduce the number of problems or can prevent conditions which may lead to extensive design efforts or they can lead to a minimization of thermal and mechanical loads.

In case of the "analysis"-step, design provisions can influence the range of analysis of individual parameters and consecutively the required R&D work and the relevant design conditions.

Within the "definition"-step the requirements and boundary conditions are defined which are the basis for the development of the specific concept. As a result of the entire

approach they are the concentration from a potential broad spectrum of conditions to design conditions which are able to be realized from the technology and cost point of view.

In order to identify from principally possible solutions those which are technically and economically feasible and justified, a close cooperation between analytical experts, the R&D teams and the designers is necessary. Depending on ongoing generation of R&D results, it is evident that this approach must be iterative.

3. APPLICATION OF THE APPROACH FOR THE MELT RETENTION CONCEPT

In order to retain and stabilize a core melt within the containment, the problems which principally have to be dealt with are concerned with:

- melt discharge from the reactor pressure vessel
- spreading of the melt
- melt stabilization

Each of these problems has a more or less large amount of sub-problems which all have an influence on the concept for mitigation of the core melt. Numerous questions have been raised which could result in large and time consuming R&D efforts and extraordinary design efforts. As examples, some of them are indicated as follows:

- What is the mode of corium release from the RPV? (Metal or oxide jet under pressure; low or high flow rate pouring; liquid carrying solid debris; stepwise discharge)
- How much is the portion of melt which will be dispersed during the discharge process?
- Can ex-vessel steam explosions occur and what is their effect on the stabilization of the melt?
- What kind of spreading process can be expected? Is there a potential of melt accumulation resulting from stepwise melt discharge?
- Is complete spreading on a large surface feasible?
- What about the long term thermochemical stability of the proposed protective material?
- Under what conditions can a short time for solidification of the corium be reached?

We are convinced that all these questions can only be answered satisfactorily if design measures are applied to influence the course of the whole process, starting with melt discharge from the RPV until the finally stabilized corium. The major problems, specific measures and the corresponding effects and influence on the process are described as follows.

3.1 Melt discharge from the reactor pressure vessel

For the problems resulting from melt discharge from the reactor pressure vessel in the following table the most relevant sub-problems are identified. In addition the provided design measures are indicated, together with the conditions resulting of such design measures.

Problem	Design measure	Conditions resulting from design measures
RPV failure mode and resulting mechanical and thermal loads	Separation of spreading area from reactor pit	Separation of functions: reactor pit affected from short term thermal and mechanical loads; spreading area affected from long term thermal loads
RPV failure and resulting melt discharge mode	Separation of reactor pit from spreading area by means of a plug until discharge is completed	Collection of the melt; potential of discharge in one pour and potential of complete spreading; potential of melt conditioning
Melt dispersal	RPV failure pressure reduction by means of dedicated safety valves	Low RPV failure pressure results in tolerable dispersal portion
Steam explosion within reactor pit	Prevention of open penetrations with potential of water accumulation within reactor pit as result of LOCA	Dry reactor pit
Melt jets with unacceptable erosion of structures (f. i. plug)	Provision of sacrificial and protective material within the lower part of the reactor pit;	Unacceptable erosion from jets is prevented
High mechanical load impact on plug	Provision of concrete fins at bottom of reactor pit	No direct contact between RPV bottom and plug possible; limitation of potential RPV fallheight

3.2 Melt spreading

Concerning the spreading of the melt the problems indicated in the following table must be considered:

Problem	Design measure	Conditions resulting from design measures
Dry or wet spreading	Spreading area within separate compartment; walls to protect water influx	Water inflow into spreading compartment resulting from LOCA not possible
Insufficient spreading due to low melt discharge flow rates	Provision of closure with temporary resistance against thermal loads	Accumulation of complete melt within reactor pit prior to spreading; possibility for melt conditioning by provision of sacrificial material
Insufficient spreading due to material composition and thermal conditions	Provision of temporary melt retention within reactor pit and sacrificial material	Mixture of melt and sacrificial material at temperature with sufficient low viscosity

3.3 Melt stabilization

Major problems, envisaged design measures and the resulting conditions are described in the following table:

Problem	Design measure	Conditions resulting from design measures
Interaction of melt and basemat concrete	Provision of sacrificial and protective layers and melt cooling from above and below	Stabilization of melt on spreading area above the protective layer
Risk of high energetic melt water interaction caused by flooding of the melt from above	Limitation of flow rate and flooding via the whole circumference of the spread melt; provision of delay time after flooding initiation	Contact between water and oxidic melt provided; contact of melt with small water portion resulting in crust generation
Thermochemical dissolution of the protective layer	Provision of sacrificial material to change melt conditions	Inversion of layering of the oxidic and metallic melt fractions and oxidation of metallic zirconium
High temperatures in the basemat concrete	Provision of active cooling underneath the protective layer	Basemat concrete temperatures can only reach coolant water temperatures at the maximum

With respect to the selection of mitigation means proposed for the control of the effects of core melt, the following principles are considered to be appropriate:

- separation of functions, as for instance the laterally arranged spreading area which separates the effects of mechanical loads resulting from RPV failure (reactor pit structure) from the effects of thermal loads caused by long term cooling (spreading compartment structures);
- use of passive means to appropriately consider the plant state;
- simple and robust design provisions in order to appropriately consider severe accident situations.

Details of the constructive measures provided are shown on figures 2 to 6.

4. CONCLUSION

The result of the development work performed up to now, shows that - according to our opinion - this approach focuses on a sound proposal of the melt stabilization concept for the EPR (Fischer, 1999, Nie, 1999). For the development of such a concept both knowledge driven and end user driven R&D work is necessary to be performed. Yet concerning the amount of R&D effort, such an approach minimizes knowledge driven R&D work in favor of end user driven R&D with the effect of being able to present a solution of the challenge within acceptable time and reasonable cost.

5. REFERENCES

Fischer, M., 1999. Main features of the EPR melt retention concept, OECD Workshop on Ex-Vessel Debris Coolability, Karlsruhe Germany, 15-18 November 1999

Nie, M., 1999. Application of sacrificial concrete for the retention and conditioning of molten corium in the EPR core melt retention concept, OECD Workshop on Ex-Vessel Debris Coolability, Karlsruhe Germany, 15-18 November 1999

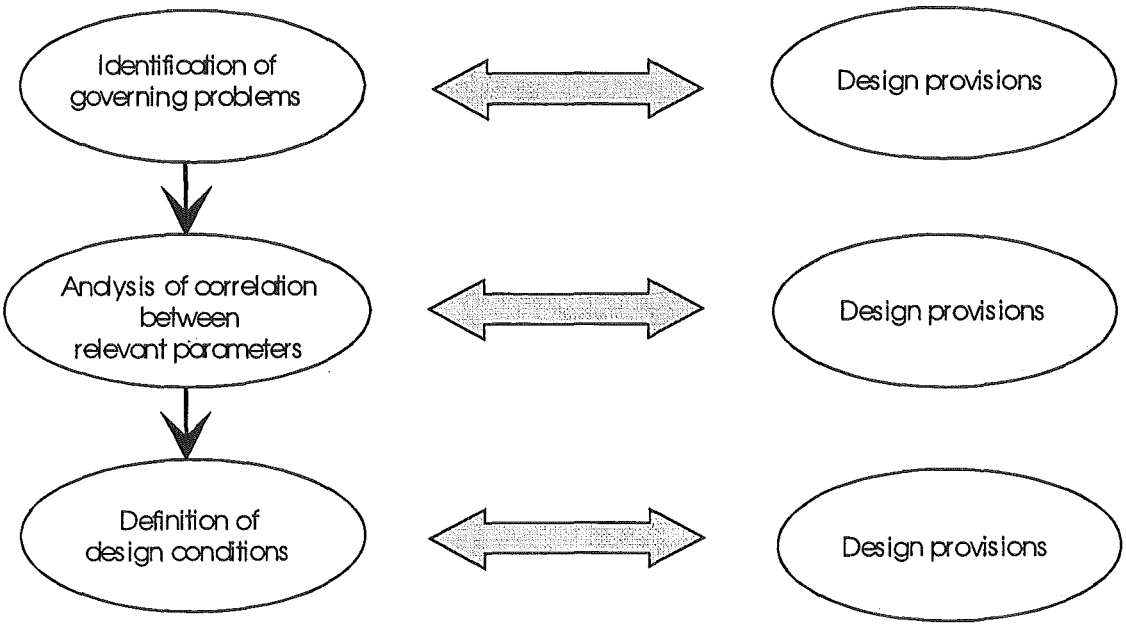

NA-T / 12.11.99
SA_Pheno.Dsf

Fig. 1 Approach for control of SA phenomena

EPR
European Pressurized Water Reactor

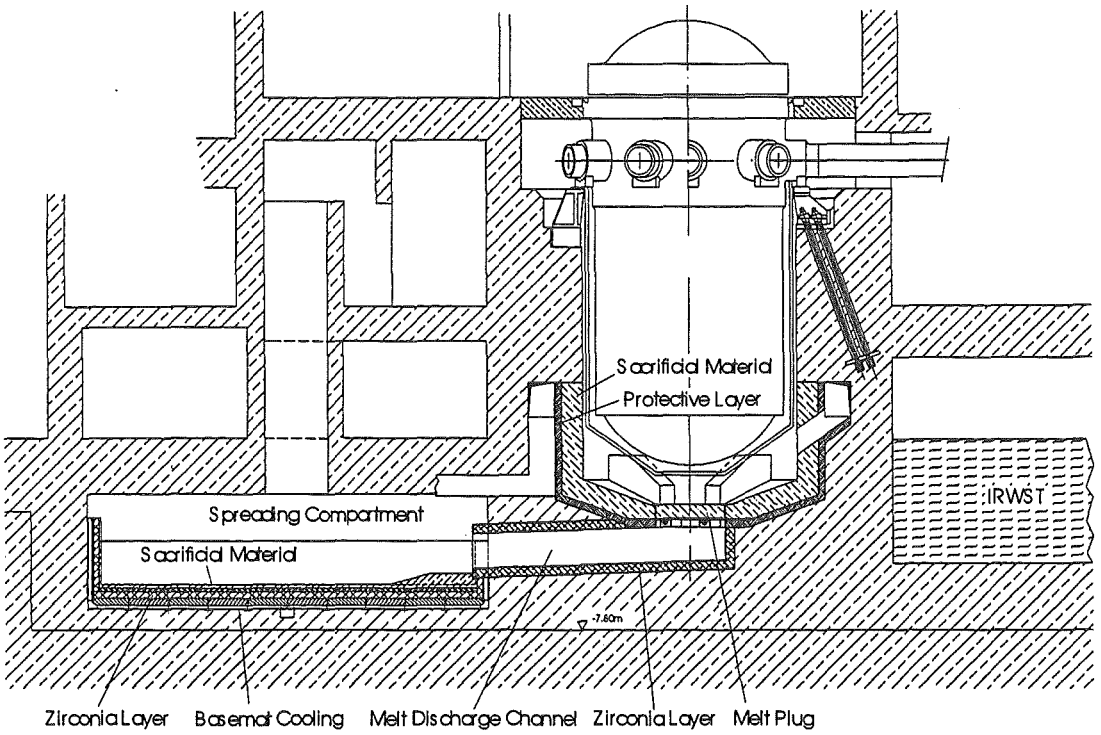

Fig. 2 Spreading Concept, Overall Arrangement

KWU NA-T/Ho.
25.10.99/Rev.A
NA-T/1999/0143.1

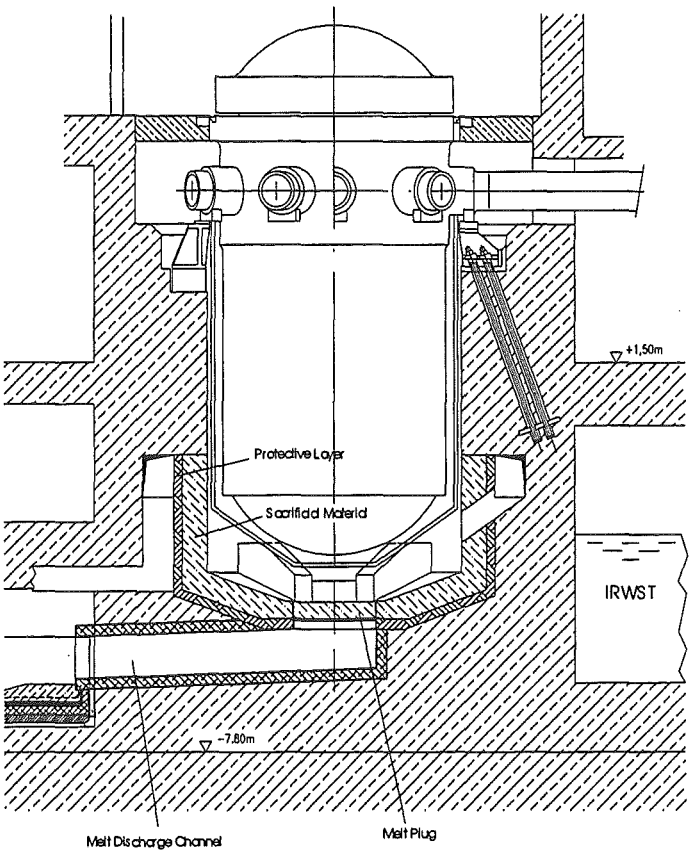

Fig.3 Spreading Concept, Reactor Pit

KWU NA-T/Ho
22.10.99/Rev.A
NA-T/1999/014.3.6

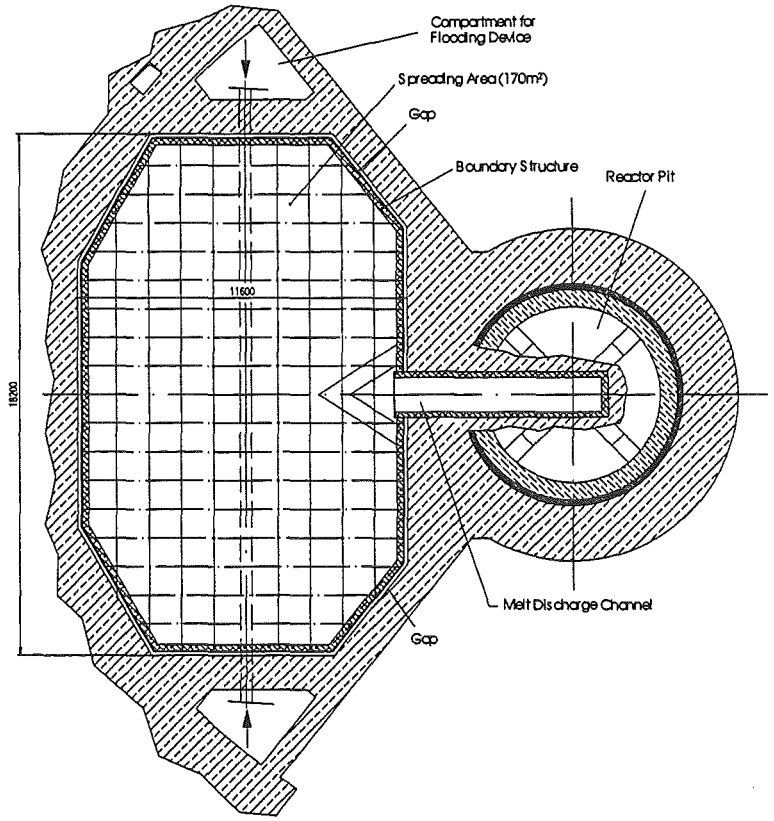

Fig.4 Spreading Concept, Spreading Area

KWU NA-T/Ho
25.10.99/Rev.A
NA-T/1999/014.3.2

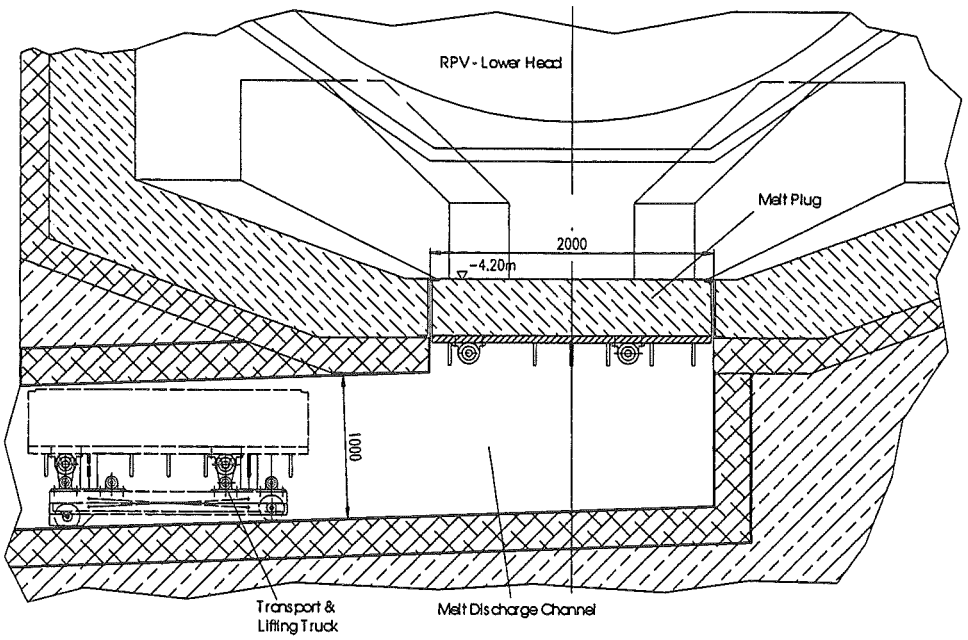

Fig. 5 Spreading Concept, Plug

KWU NA-T/Ho.
22.10.99/Rev.A
NA-T/1999/ 0143.7

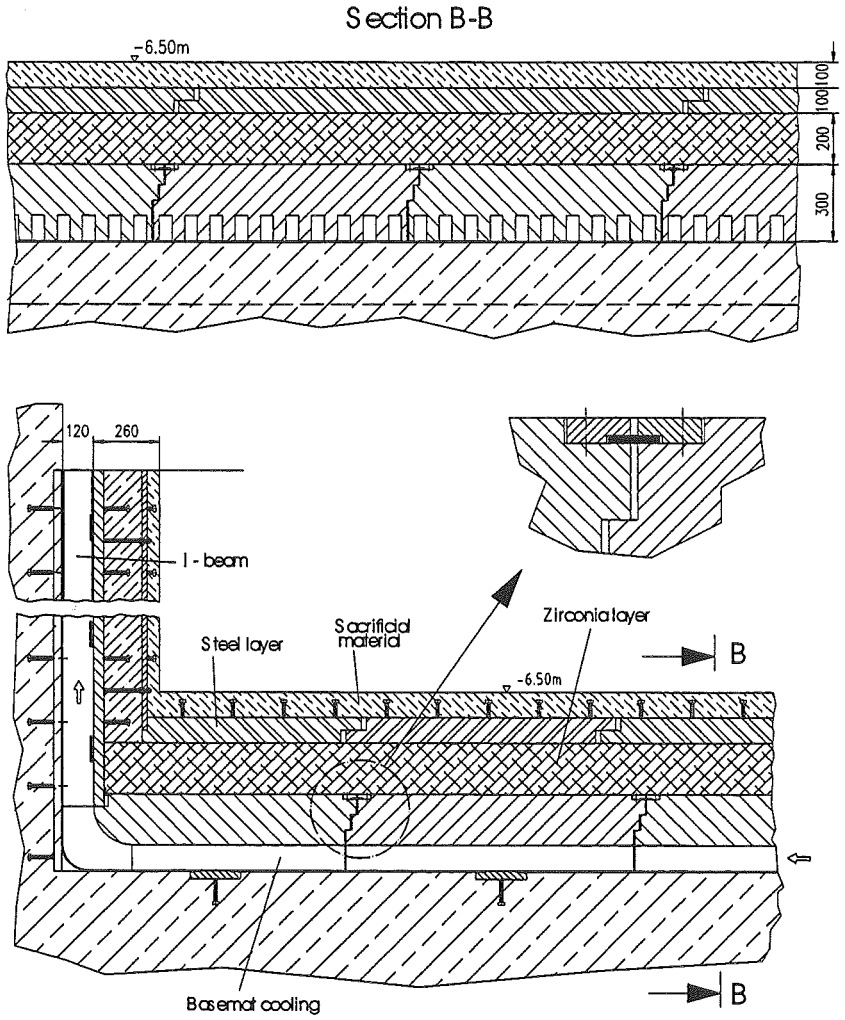

Fig.6 Spreading Concept, Layer Arrangement

KWU NA-T/Ho.
25.10.99/Rev.A
NA-T/1999/0143.4

OECD Workshop on Ex-Vessel Debris Coolability
Karlsruhe, Germany, 15-18 November 1999

Organised in collaboration with
Forschungszentrum Karlsruhe (FZK) GmbH

Application of sacrificial concrete for the retention and conditioning of molten corium in the EPR core melt retention concept

Markus Nie
Siemens AG KWU, Freyeslebenstr. 1, 91054 Erlangen
Markus.Nie@erl11.siemens.de

Abstract

The core melt stabilisation concept of the EPR involves an ex-vessel MCCI phase with sacrificial concrete for the retention and conditioning of molten corium before and after spreading. Both MCCI phases are simulated with the computer code COSACO, developed by Siemens/KWU. A brief overview of the main features of the code is given together with the results of a parametric study performed for the conservative assumption of a stepwise melt release from the RPV. This study demonstrates that the addition of sacrificial concrete in the reactor pit is an adequate means (i) to achieve a sufficient retention period and (ii) to oxidise all Zr initially present in the melt.

For the spreading compartment, COSACO calculations predict a fully oxidised melt at the end of the MCCI. Its liquidus temperature, as confirmed by supplementary DTA-tests, is about 1850 °C, and therefore significantly below the initial value of 2400°C. It is further demonstrated that the erosion of the provided sacrificial concrete will result in a density difference of about 2 Mg/m^3 between the oxidic and metallic melt and thus in a stable layer inversion. These results justify the choice made for the composition of the sacrificial concrete.

1 Introduction

In order to reduce the environmental consequences of a severe accident, the EPR concept involves design provisions to avoid basemat penetration in the case of a core melt-down (Bittermann, 1999, Fischer, 1999). The principal approach is to spread and flood the melt on a large area lateral to the reactor pressure vessel to increase the heat transfer surface, see Fig. 1.

The spreading area consists of sacrificial layers including a concrete layer on top and a protective layer made of refractory ZrO_2 at the bottom. The ZrO_2 layer and the basemat cooling system will isolate the melt from the structural concrete underneath.

Prior to spreading, the concept provides an intermediate retention in the reactor pit, realised by erosion of a sacrificial concrete lining. The primary objective of this retention is to render the long-term stabilisation independent of the uncertainties involved in in-vessel processes.

This paper describes the main aspects of the MCCI-phase and its importance for establishing favourable initial condition for the long-term melt stabilisation. The description consists of an overview of the selection of relevant sacrificial concrete types followed by an exemplary analysis of the MCCI phase with the code COSACO.

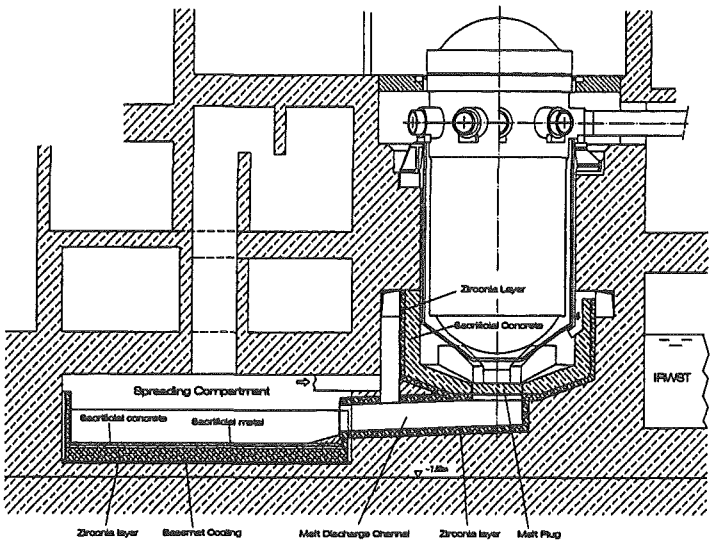

Fig. 1: Main components of the core melt retention concept of the EPR

2 Screening of sacrificial concrete aggregates

2.1 Reactor Pit

The objectives of the intermediate retention in the reactor pit are (i) the accumulation of the core melt inventory in cases of successive release from the RPV, (ii) the oxidation of chemically aggressive zirconium to avoid thermo-chemical interaction with the protective ZrO_2 in the spreading area and (iii) conditioning of the melt prior to spreading. A sacrificial concrete predominantly consisting of iron oxide and silica is deemed suitable to fulfil above requirements. Iron oxide provides a strong oxidation potential towards metallic zirconium. The reaction product Fe dissolves in the metallic core melt, where it is already the major constituent. Thus, relevant thermo-physical properties of the metallic melt remain unaffected. Moreover, unreduced iron oxide, which accumulates in the oxide melt after the zirconium inventory has been depleted, will result in an effective reduction of the oxidic melt's liquidus and solidus temperature.

Silica strongly reduces the fission product release from the melt pool. In addition, it also lowers the solidus and liquidus temperature as well as density of the oxide melt.

Fe_2O_3 and SiO_2 are favourably embedded in a concrete-type matrix, since the gas release during concrete decomposition induces a stirring effect and thus augments the mixing of the decomposition products with the melt. Owing to the application of concrete, also CaO and Al_2O_3 as the principal components of the binder, are added to the melt. They exhibit a high chemical stability against metallic zirconium and contribute to the decrease of density of the oxide.

The downward concrete ablation rate, which governs the retention time in the pit, can be influenced by the grain size of the aggregates as well as the kind of binder. Currently, it is envisaged to apply cement used to produce refractory concrete for industrial applications.
The almost carbonate free sacrificial concrete with its low water content results in a low release of condensable and non-condensable gases during the ex-vessel MCCI phase.

2.2 Spreading Area

In the EPR concept a thermo-chemical interaction between oxidic core melt and the refractory ZrO_2-layer should be avoided. This requires a layer inversion, which relocates the metallic underneath the oxidic melt. A corresponding sufficient decrease of density of the oxidic melt can be achieved by addition of light oxidic components.

Furthermore, an extra reduction of the liquidus and solidus temperature of the oxidic melt is intended to diminish the long- term thermal loads at the interface between the metallic melt and protective ZrO_2 layer. Both requirements are fulfilled applying a concrete composed of borosilicate glass and Fe_2O_3. Borosilicate glass, essentially consisting of SiO_2 and B_2O_3, has a wide variety of industrial application. A similar glass on the basis of B_2O_3 and PbO was proposed earlier as sacrificial material for the COMSORS concept (Forsberg et al, 1996). The main advantages of borosilicate glass are its low density and low glass transition temperature.

Fe_2O_3 is also an effective liquidus-reducing additive, as proven by DTA tests in the frame of the COMAS project (Steinwarz et al, 1999). In these tests, a liquidus temperature of only 1950 °C has been measured for a UO_2-ZrO_2 melt containing 32 wt% FeO. In contrast, the liquidus temperature of the native binary UO_2-ZrO_2 melt is about 2500 °C.

3 The MCCI Code COSACO

For the analysis of the ex-vessel MCCI phase, the code Corium on Sacrificial Concrete, developed at Siemens/KWU, is used. COSACO includes a 2D ablation model. The specific feature of the code is an appropriate formulation of the complex chemical interactions with sacrificial concrete. Conversely, specific long term effects, i.e. concrete erosion by solidified metal, which are not relevant for the application to the EPR, are neglected. For the modelling of chemical reactions, it is assumed that the potential oxygen providers react successively with the coexisting constituents of the metallic core melt according to the scheme depicted in Fig. 2. This scheme has been derived from considerations involving the Gibbs free energy of formation. In particular, the more negative the Gibbs free energy of formation is, the more stable the oxide, or conversely, the more aggressive the metal from which the oxide is formed, will be.

Accordingly, Zr, Si, B, Cr and Fe will be oxidised in the given sequence. In order to be consistent with the Gibbs energy consideration, a reaction order has been also introduced for the oxygen providers. Consequently, Zr as the principal oxygen reducer is oxidised first by the oxygen providers given in the adjacent box. As silica and boron-oxide have a similar stability, silica does not oxidise elemental boron and boron-oxide does not oxidise silicon.

The melt can be represented by up to three nodes, connected through mass- and energy exchange. The user may either invoke a mixed mode or a stratified layer mode. In the latter the oxidic melt is either located above or underneath the metallic melt layer, dependent on which phase is denser. If the metal melt is located above the oxide, a third layer, predominantly consisting of concrete slag, may grow atop the metal. If a certain, user-defined density difference is reached, the code simulates a layer inversion.

The heat transfer mechanism at the upper surface of the melt pool can be either radiation or, in the case of a flooded melt, boiling.

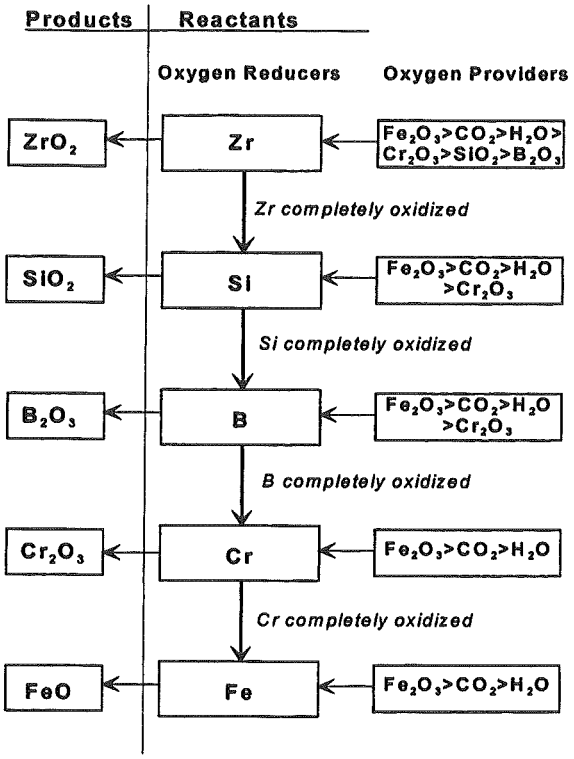

Fig. 2: Hierarchy of chemical reactions

4 Calculated Molten Pool Behaviour

4.1 Assumptions and boundary conditions

As a highly challenging initial condition for the retention function of the pit, a two-step melt release from the RPV, as illustrated in Fig. 3, has been applied. It originates from an analysis with the MAAP 4 code for a surge-line break scenario and involves a maximum required retention period of about 50 min.

The corium pool initially formed in the pit, consists of immiscible oxidic and metallic phases and is therefore assumed to be stratified. The assumption of melt pool stratification is based on the reasoning that mixing is inhibited because of (i) a low gas release from the sacrificial concrete, and (ii) the formation of a viscous layer or crust at the oxide-metal interface due to the initially high temperature difference of 550 °C between the two phases.

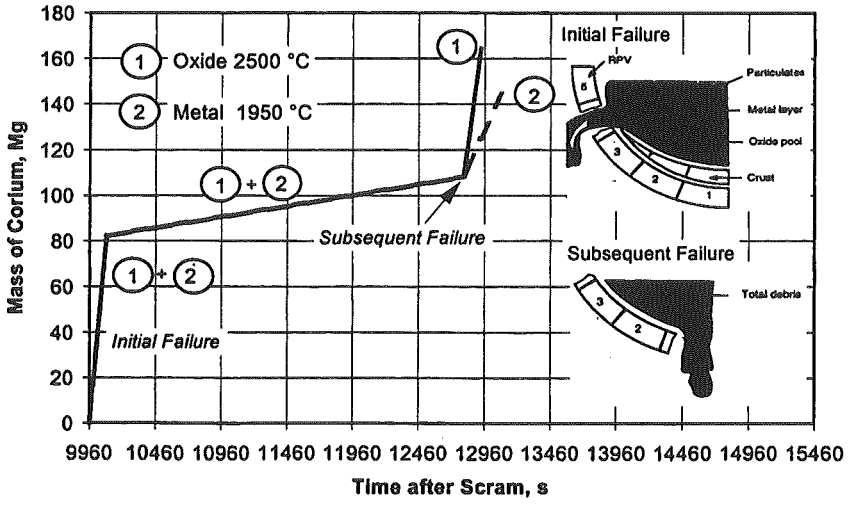

Fig. 3: Assumed two step release mode of corium into the reactor pit

Calculations have been performed for an in-vessel Zr-oxidation level varying between 30-70%. At first, the results for a best-estimate case, characterised by a 40% oxidation level and the assumption that excessive Zr will be predominantly dissolved in the oxidic melt, are discussed. Afterwards, a comparison of the downward ablation front progression for oxidation levels of 30, 40 and 70% will be presented.

The results of the best-estimate case indicate a rapid heat-up of the oxide until the depletion of the initial Zr-inventory, see Fig. 4.

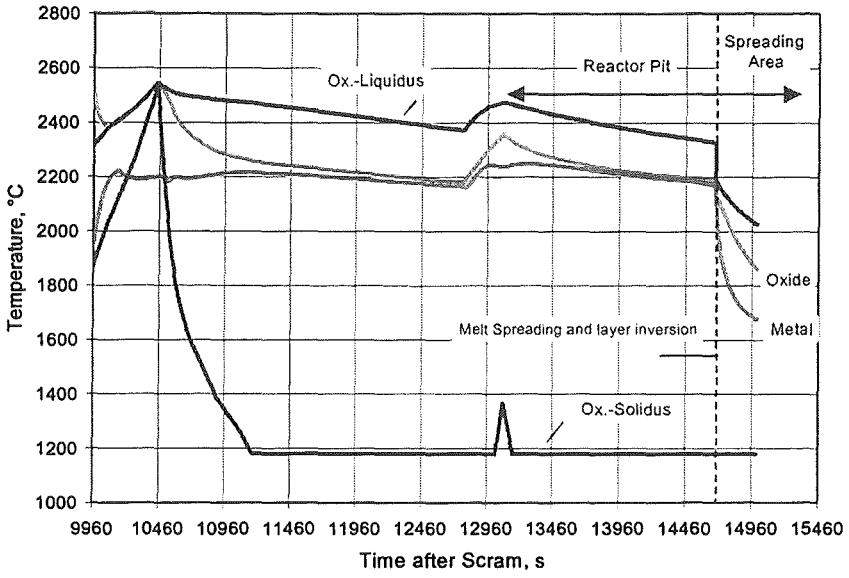

Fig. 4: Oxidic and metallic melt temperature vs. time

The maximum oxide temperature predicted in the course of the MCCI is 2535 °C, which is approximately the liquidus temperature of fully oxidised corium. The increase of the melt's temperature is attributed to the highly exothermic reactions of Zr with the concrete decomposition products. Note, that the ratio between the energy spent for the decomposition of the concrete and the chemical energy released by the reaction of its decomposition products with Zr is about 1:2,5.

After the second melt release has begun at t=12780 s, COSACO predicts a temporary increase of the melt temperatures, as well as of the liquidus and solidus temperature. Both effects are attributed to the exothermic reduction of Fe_2O_3 and SiO_2 which have been accumulated in the oxide during t=10450 s and t=12780 s, see Figs. 4 and 5, by the zirconium being newly discharged into the reactor pit.

After the in-vessel melt inventory has been collected in the reactor pit and all zirconium has been oxidised, the liquidus temperature declines to 2330 °C and the oxidic melt temperature to 2185 °C until gate failure. The density of the oxide at this time is 100 kg/m^3 higher than that of the metallic melt and thus, no layer inversion is predicted to occur in the pit. The composition of the 220 Mg oxidic melt released into the spreading area with a temperature of 2185 °C can be inferred from Fig. 5.

calculated complete decomposition of the 10 cm thick sacrificial concrete layer within 320 s. As a consequence, the metallic and oxidic melt fractions undergo a rapid cool-down to final temperatures of 1680 °C and 1880 °C, respectively. After termination of the MCCI, the density difference between the oxidic and metallic melt is calculated to be 1900 kg/m^3. The liquidus temperature of the oxide, as predicted by COSACO, is 2025 °C.

The total mass of sacrificial concrete eroded in the pit and spreading compartment is 95 Mg and 45 Mg, respectively. After the incorporation of this amount, the melt consists of 323,5 Mg oxidic and 120 Mg metallic constituents.

Table 1 lists the oxidic melt constitution at the end of the MCCI phase for in-vessel oxidation levels of 30, 40 and 70%.

Constituent [wt%]	Initial Zr-oxidation level		
	30%	40%	70%
UO_2	44,63	43,81	42,25
ZrO_2	16,47	16,17	15,6
SiO_2	10,47	10,387	10,0
B_2O_3	1,67	1,64	1,58
Al_2O_3	0,72	0,713	0,66
CaO	5,3	5,2	5,1
MgO	0,24	0,24	0,23
Fe_2O_3	8,84	9,77	13,12
FeO	5,6	6,0	4,96
Cr_2O_3	6,06	6,14	6,5
Total Oxide mass	317510 kg	323480 kg	335360 kg
Temperature	1890 °C	1860 °C	1834 °C
Liquidus Temperature	2057 °C	2025 °C	1977 °C
Solidus Temperature	1180 °C	1180 °C	1180 °C

Tab. 1: Comparison of oxidic melt condition after termination of MCCI in the spreading compartment for in-vessel oxidation levels of 30, 40 and 70%

The table shows that the final melt constitutions are almost independent of the initial in-vessel oxidation level. The total oxidic corium mass in the spreading compartment varies between about 318 Mg and 335 Mg for oxidation levels of 30 and 70%, respectively. Moreover, the calculated liquidus temperature varies only in the range between 1977 °C and 2057 °C.

Since liquidus-decreasing effects, such as the transformation of Fe_2O_3 into FeO in the presence of Fe and the influence of B_2O_3, are currently neglected in the thermal property database of COSACO, the liquidus temperatures given in Tab. 1 are approximately 150 °C higher than the experimental values obtained for these compositions by supplementary DTA analysis. This lower liquidus temperature was additionally confirmed by Siemens-tests. In these tests, pellets of the powder mixture under investigation were dropped onto the surface of a metallic melt with a definite temperature and their melting behavior was observed.

Thus, the liquidus temperature is reduced from 2400 °C for the initial ex-vessel core melt to a value below 1900 °C for the oxidic melt conditioned for long-term stabilisation. Furthermore, the characteristics of the oxidic melt after completion of MCCI in the spreading area are virtually independent of the initial Zr-oxidation level.

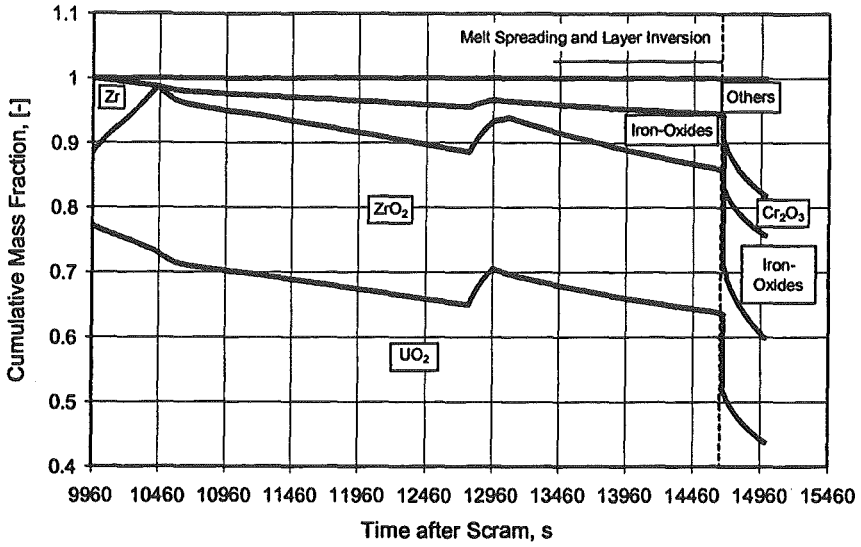

Fig.5: Cumulative fraction of oxidic melt constituents: 'Iron-Oxides' denotes $FeO+Fe_2O_3$, 'Others' denote SiO_2, CaO, Al_2O_3, MgO, B_2O_3

A contour plot of the reactor pit is depicted in Fig. 6. Clearly visible in the upper part is the focusing effect of the metal melt. As the reactor pit is backed up by a chemically resistant refractory layer, erosion does not proceed into the structural concrete.

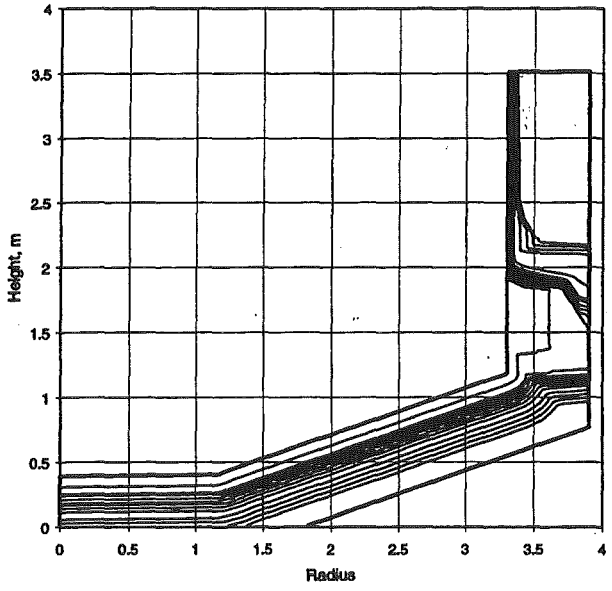

Fig. 6: Contour plot of the reactor pit, contour line acquisition interval is 500 s.

The average downward ablation rate in the pit varies between 0,21 mm/s during the initial phase until the temperature maximum is passed and about 0,08 mm/s for the remainder of the calculation. The overall retention time in the pit is predicted to be 4700 s, including a 10 min delay induced by the heat-up and melting of the melt plug located underneath the sacrificial concrete, see Fig. 1.

Immediately after onset of MCCI in the spreading compartment, the oxide's density decreases below that of the metal melt and a layer inversion occurs. During this event, 45 Mg of light oxidic slag, which have accumulated atop the metallic melt, are mixed into the oxide. The result is a steep decline of the oxidic melt's liquidus temperature, see Fig. 4. In contrast to the reactor pit, downward ablation is now governed by the metal melt. Its attack results in a

5 Summary and Conclusions

The analysis of the ex-vessel MCCI phase with COSACO shows that, even for a conservative two-step melt release from the RPV with the two releases being 50 min apart, the complete in-vessel melt inventory can be accumulated in the pit to assure spreading in one event. Moreover, owing to the presence of strongly oxidising Fe_2O_3 as a major concrete aggregate, a complete transformation of all metallic Zr to ZrO_2 can be achieved prior to melt spreading.

COSACO calculations for the spreading area indicate an oxidic melt composition at the end of MCCI which, according to DTA-measurements, has a liquidus temperature of about 1850 °C, independent of the level of in-vessel Zr oxidation. In addition, it is demonstrated that the erosion of a total of 140 Mg of sacrificial concrete in the reactor pit and spreading area will result in a density difference between the oxidic and metallic melt of about 2 Mg/m^3 which guarantees a stable layer inversion.

On the basis of these results one can conclude that the addition of sacrificial concrete is an adequate means to condition the melt for a successful long-term stabilisation independent of the uncertainties of the preceding in-vessel processes.

6 References

Bittermann, D., 1999. Principles of Application of mechanical Design Measures to control severe Accident Phenomena, applied to the Melt Retention Concept of the EPR, Proc. OECD workshop on ex-vessel coolability, Karlruhe, Germany, 16-18.11.1999, to appear

Fischer, M., 1999. Main features of the EPR melt retention concept, Proc. OECD workshop on ex-vessel coolability, Karlruhe, Germany, 16-18.11.1999, to appear

Forsberg, C.W. et al., 1996. Termination of Light-Water Reactor Core-Melt Accidents with a Chemical Core Catcher: The Core-Melt Source Reduction System (COMSORS), Oak Ridge National Laboratory ORNL-6899, 1996

Steinwarz, W. et al, 1999. Investigations on the Phenomenology of ex-Vessel Core Melt Behaviour, EC 4th Framework Programme on Nuclear Fission Safety, Contract FI4S-CT95-003, August 1999

Abbreviations

DTA	Differencial Thermal Analysis
EPR	European Pressurized Water Reactor
MCCI	Molten Corium Concrete Interaction
RPV	Reactor Pressure Vessel

Appendix A:

Late Papers

RESISTANCE OF ZIRCONIA REFRACTORIES TO THE IRON OXIDE MELT

Akopov F.A., Akopyan A.A., Barykin B.N.,Belmaz N.O., Borovkova L.B., Borodina T.I., Valyano G.E., Vlassov A.C., Lukin E.S., Mineev V.N., Chernyshov G.P.

HEDRC-IVTAN, Izhorskaya, 13/19; Moscow, 127412, Russia

Introduction

One of the most important aspects of using of the materials in the core melt catcher is their chemical resistance to the corium. We studied the resistance of the grain structured zirconia based ceramics to the oxide components of the melt under the gradient heating conditions. It was established that interaction of ceramics is more intensive with iron oxides and it is significally less intensive for the oxides of Ti, Cr, and Ni.

This report presents investigations on interactions of the iron oxide melts and stainless steel oxides melt with some modification of the zirconia ceramics and with two kinds of the zirconia concrete with binding from barium monoaluminate and with phosphoric acid.

Ceramics dissolution in the melts of iron oxides starts from dissolution of small-size fraction of the ceramics grains without decomposition of macrostructure and without destraction of mechanical contact between the coarse grains. Later on the coarse grains are partially melts. This process is defined by mass ratio of iron-oxides (M_{ox})to ceramics (M_{cer}) in zone of impregnation, $K= M_{ox}/M_{cer}$. It is shown in previous investigations, that ceramics macrostructure does not decompose at $K<1/2$ under conditions of temperature gradient of 180-360 degrees and maximum temperature of 2270 K. The coeffitient K characterizes the condition of retention of iron-oxides melts by the ceramics for catcher design. The value of K under condition of the trap-basis cooling is defined by depth-distribution of temperature from maximum value to that one for melt solidus.

Isothermal heating gives possibility to study this process more detail. The heating of ceramic layer of the catcher can be followed by a process of its interaction with oxides component of core according to one of possible assident scenario.

The purposes of this work were investigation of the interaction of iron-oxides melt with refractory materials on the basis of zirconia under isothermal conditions in nonoxidized medium as well as determination of the condition of melt retention by these refractory materials.

Experimental

The investigated materials are zirconia ceramics of different densities with two kinds of oxides for stabilizing (Y_2O_3, CaO) and zirconia concrete (ZHC, ZSC) with two kinds of binding agent, which are barium monoaluminate and zirconia binding suspension.

The composition and some properties of investigated ceramics are listed in Table 1. As is seen, these materials are generally grain-structure ceramics with large-size grains (from 0.2 to 2 mm) and fine-dispersion component of grain-size 2-5 μm. An amount of these components and a kind of fine-dispersion binder are different. The open porosity P varies from 17 to 21 %. A number of samples had height-dependent porosity, some ones had low (0.2-1.5 %) and high (about 42 %) porosity. We tested also the samples of ceramics impregnated by 50 % solution of chromium sulphate, $Cr_2(SO_4)_3 \cdot 6H_2O$. As believed, the impregnation by chromium salt will reduce of iron-oxides penetration.

Structure and some properties of concrete are submitted in Table 2. A concrete ZHC contains barium aluminate as binder, which provides hardening of a concrete and the enough high strength under hydration process /3/. In a concrete ZSC zirconia suspension (ZS) with a ortophosphoric acid is used as binding. The binding in this concrete is provided by zirconium phosphates /4/. These concretes were tested after their preliminary heat treatment at 1470 K during 2 hours in air atmosphere. Besides it, samples of a concrete ZHC and ZSC without heat treatment as well as concrete ZHC and ZSC with cover ZS (thickness of 1-1,5 mm) after preliminary heat treatment were tested too. The iron oxide consisted of FeO=55, Fe_3O_4=40, and Fe=5 of weight % (hereinafter it names the iron oxide).

It is expedient for the characteristic of a iron-oxides-melt retention by refractories under conditions of isothermal heating to enter parameter K_1, which equals to ratio of entered-oxide weight to the weight of whole refractory sample, $K_1=M_{FeOx}/ M_{sample}$.

Test conditions

All tests were realized in a vacuum furnace with tungsten heater in argon atmosphere of pressure 0.2 bar. Temperature in a furnace was measured by a tungsten-rhenium thermocouple.

Tablets of an iron oxide were placed on the top flat surface of tested samples, which, in turn, were placed on zirconia supply. The supply with samples was placed in an isothermal zone of the vacuum furnace. We have realized tests at temperatures of T=1870, 1940 and 2270 K, the times of test at these temperatures were τ=120, 30 and 45 minutes respectively. The rate of heating and cooling of a samples in a furnace was ~17 degrees/min.

Samples of refractories and tablets of iron oxides were weighed before and after experiment. The change of sample weight after tests allow to know about degree of iron-oxides retention by refractories. We shall note, that samples weights were equal to 30-50 g for K_1=1/100, 1/50, 1/30, and 100-500 g for K_1=1/50-1/4.

Depth-distribution of iron-oxides melt and its composition for samples, as well as structure of samples material after tests were studied by methods of optical and electronic microscopy, X-ray phase and X-ray micro analyses.

Experimental results

1. Dense ceramics (P=1.5 %) are impregnated by iron oxides in the least degree. A depth of impregnation is 3-4 mm (K_1=1/50, T=1940 K, τ=2 hours, and T=2270 K, τ=30 min). The area of samples was S=3 cm^2.

2. Samples of the grain ceramics (P=16-21 %) are impregnated on the depth of 9-14 mm without essential change of weights (K_1=1/50, T=2270 K, τ=30 min, S=3 cm^2, H=20 mm). Photos of samples sections for ZrO_2 / CaO after experiments with K_1=1/50, 1/25, and 1/17 are submitted on Fig. 1 (1, 2, and 3). Conditions of experiment: T=2270 K, τ=45 min, height of samples is 112 mm, S=3 cm^2. In two last cases samples are impregnated completely by iron oxides, in the first case - on the depth of 70 mm.

Despite of the different sizes of samples, relative depth of its impregnation h/H (where h is height of a impregnated zone, H is sample height) is practically identical (55 % and 63 %), that testifies to small influence of the scale factor to processes of impregnation at small K_1 ($K_1 \leq 1/50$).

The increase of K_1 up to 1/7 does not result in a total loss of samples weight for ZrO_2 / CaO (P=16 %, T=2270 K, τ=30 min), i. e. whole iron-oxide melt is retained by ceramics sample. The reduction of total weight of samples on value ~26 g is observed at K_1=1/4.5 at total weight of ceramics and iron oxide of 430 g.

3. Samples of high-porosity ceramics (P=42 %) of a grain structure from ZrO_2 / Y_2O_3 at K_1=1/50 (T=2270 K, τ=30 min) are impregnated on a depth of 14 mm (S=1 cm^2) at thickness of 16 mm.

4. Samples of a concrete ZHC by thickness of 15-20 mm at K_1=1/50 (T=2270 K, τ=30 min) are impregnated completely. At temperature of T=1870 K (τ=1 hour) the depth of impregnation is 20 mm at sample height of 30 mm.

The increase of K_1 up to 1/20, 1/7, and 1/4 (T=1870 K, τ=1 hour) results in complete impregnation of concrete samples (S≈9 cm^2). At K_1=1/4 weight loss is 17 g at total weight of a concrete and oxide of 150 g.

Removal of a crystallizing water from a concrete ZHC results to additional through porous and promotes deeper penetration of iron oxide into a concrete in comparison with ceramics.

The concrete ZSC behaves otherwise, than concrete ZHC. The impregnation of a concrete ZSC is comparable to impregnation of grain ceramics. As appear, it is associated with smaller quantity of an evaporated component, which is zirconium phosphate in this case.

5. The cover of concrete by suspension ZS does not result in change of a depth of impregnation.

6. On a surface of all refractory samples in a place of contact with iron oxide traces of a erosion are detected. The form of these traces coincides with the form of iron-oxide samples. The maximum depth of erosion is 0.1-3.5 mm for K_1=1/50-1/4 (concrete ZHC and ceramics ZrO_2 / CaO, P=16 %, T=1870-2270 K, τ=30-120 min), that corresponds to weight of FeO_x from 0.4 g up to 100 g.

7. Samples of the ceramics ZrO_2 / CaO are not practically deformed under every test conditions, whereas samples of a concrete ZHC already at T=1870 K (τ=1 hour) and K_1=1/7, 1/4 are considerably deformed.

Discussion of results

The process of interaction of investigated refractory materials with iron-oxides melt consists of melt penetration into pores of refractories as well as dissolution of ZrO_2 in FeO_x (with formation of eutectics), chemical interaction of FeO_x with binding (concrete), with impurity and stabilizing components.

We shall discuss the results of experiments on penetration of iron-oxides melt into researched refractories.

It is possible to show, that in case of complete filling of refractories pores by the iron-oxides melt, the factor K_1 and porosity $P=V_{por}/V_{refr}$ (where V_{por} is volume of porous space, V_{refr} is volume of refractory material) are connected by the expression $K_1=\rho_{ox}/\rho_{refr}\cdot P/(1-P)$.

The condition of complete filling of pores will be realized at $K_1=1/4$. Experiments in case of ceramics and concrete ZHC had shown, that iron-oxide melt is retained at $K_1 \leq 1/7$, i. e. the part of pores remains blank. However this condition will be realized for ceramics at T=2270 K, and for concrete ZHB at T=1870 K.

In the heaviest degree the processes of dissolution and chemical interaction occur on a contact surface of refractory samples with oxide melt, since through this surface all weight of melt passes. X-ray phase analysis of central sites of samples has shown, that there is iron oxide in the form of FeO only. That testifies about the reduction of Fe_3O_4 up to the lowest oxide.

As was marked above, on a surface of every sample of refractories traces of a erosion are detected, the form of these traces coinciding with the form of iron-oxide samples. It can take place only in the event, that the interaction of two materials occurs on a place of their contact among themselves, whereas as a whole the samples of FeO_x are yet in solid (nonmelted) state, as far as it is known, that the iron-oxides melt moisten of zirconia well and very quickly penetrates through pores into refractory material volume.

It is known from the diagram for system FeO - ZrO_2, that FeO will form with ZrO_2 a eutectic at 1600 K. Apparently observable pictures of a erosion of the correct geometrical form are explained just by this effect, i. e. occurrence of a liquid phase on contact surface of iron oxide and zirconia. For refinement of this assumption additional experiments were performed at 1620 K, i. e. at temperature obviously smaller than melting temperature of FeO (T_m=1700 K) as in argon, as in air. In argon atmosphere at 1620 K traces of an erosion of the regular form were detected too, reduction of iron-oxide samples in a thin surface layer (about some μm) up to a metal being thus marked.

On visible, processes of interaction of iron oxide with zirconia accompanied by surface erosion of ZrO_2 take place with formation of low-melted liquid in a place of their contact. The structure of this liquid is unknown exactly, FeO_{x-m} - ZrO_2, since reduction degree of FeO is unknown. It is not excluded, that the eutectic temperature of this structure is lower than the eutectic temperature of FeO - ZrO_2, 1600 K.

Apparently this process of a surface erosion begins about at 1600 K and is finished at melting temperature of FeO (~1700 K), when all weight of iron-oxide melt with large speed penetrates into ceramics and it concentration on the surface ZrO_2 sharply decreases. In our experiment at value of temperature-rise rate about 17 degree/min the erosion proceeds for about 6 min, i. e. the rate of formation of dimples on surface by erosion is 0.015-0.6 mm/min and depends as from kind of substrate (ceramics, concrete), as, basically, from the quantity of FeO_x. Essentially the rate of dimples formation is stipulated by the phenomena of iron-oxides restoration, that is confirmed by experiments on air, where traces of erosion was not detected at 1620 K.

The melt of FeO_x is distributed on whole refractories sample through pores after the melting of total weight of oxides. As is shown in Ref. 2, since the speed of impregnation of ceramics of 16 % porosity equals 1.2-1.5 mm/s, it is possible to affirm, that the mass-transfer velocity will depend on the ratio of weights of FeO_x and ZrO_2 (parameter K_1) and on the sample area and height. This velocity in our experiments is ~$2.0\text{-}3.0 \cdot 10^{-2}$ g $s^{-1} \cdot cm^{-2}$ for K_1=1/50, thus the given velocity depends weakly on the sample size. It is possible to affirm, that the process of impregnation, at least at small K_1, does not practically depend on the scale factor. At large K_1 (1/10-1/4) it is difficult to evaluate total mass-transfer velocity in sample because of filling of pores by melt. But if to assume, that the speed of impregnation will be the same as at small K_1, then the mass-transfer velocity for K_1=1/10-1/4 can be equal to values from $4.0 \cdot 10^{-2}$ up to $1.3 \cdot 10^{-1}$ g $s^{-1} \cdot cm^{-2}$.

The character of interaction at K_1=1/7, 1/4 is identical those for the smaller values of K_1, however the results of such interaction are expressed considerably dramatic. Iron-oxides melt fills completely the split-like pores between the zirconia grains and interacts with them, as well as initiates the processes of recrystallization of dispersible fraction, and "dissolution-precipitation", and coalescence and spheroidization of pores. Separate spherical pores, on all probability, contained gas seized during impregnation, other ones are filled in FeO, and some of them contain a metallic iron in a kind of spheres or particles of wrong form. Iron-oxide quantity fixed in samples after experiments, as a rule is 12-26 % of weights, the quantity of metallic iron can reach 4-5 %.

Chemical interaction of FeO_x melt with a solid zirconia-based solution results to impoverishment of ZrO_2 by stabilizing oxide CaO. As the consequence, after experiments in the material is fixed occurrence of monocline ZrO_2 and calcium ferrites $CaFeO_2$ and $CaFe_4O_7$. The intensity of interaction is defined by quantity of iron-oxide melts proceeded in refractory materials. So, at a ratio K=1/7, the quantity of monocline ZrO_2 in any zones does not exceed 3 % of weights. At the K=1/4 in the bottom part of refractories the quantity of monoclinic zirconia reaches 16 % of weights.

Despite essential transformation of a structure of a material of ceramics samples the preservation of zirconia skeleton and quite certain similarity to a initial structure is obviously observed, i. e. radical destruction of studied material does not occur.

Availability of traces of Si and Al impurities in ceramics and concrete ZHC results in the synthesis of $Fe_3Al_2(SiO_4)_3$, Fe_2SiO_4, Fe_7SiO_{10}.

As X-ray phase analysis has shown, an interaction of FeO_x with $BaAl_2O_4$ is not detected in concrete under any experimental conditions. However at K=1/7 the top layers of concrete samples are impoverished by $BaAl_2O_4$. Barium aluminate is moved together with melt of FeO_x to the bottom layers of samples. It is not excluded, that in these conditions there was a liquid phase of system $BaAl_2O_4$ - FeO - ZrO_2. These processes result in destruction of the concrete skeleton and as a consequence in deformation of samples.

It should notice, that at availability of barium and aluminium hydroxides in a initial concrete (that takes place at mixing of concrete ingredients with surplus water or after heat treatment of concrete samples at temperature 1200-2000 K) in a zone of impregnation the synthesis of $BaZr_2O_4$ and $FeAlO_3$ takes place. These compounds also promote the destruction of concrete skeleton.

In summary we shall note, that received data on the erosion of concrete ZHB approximately coincided data from Ref. 6, which were received under high-frequency heating.

Conclusion

The analysis of received data permits to make the following conclusion:

1. The most radical means to reduce a degree of impregnation of investigated refractories is increase of density of materials. Cover of concrete by suspension ZS, the impregnation of ceramics by a chromium salts, as well as creation of a gradient of density in samples of ceramics do not result in essential reduction of impregnation.

2. Concrete ZHC is impregnated by iron-oxides melt considerably more active, than ceramics and concrete ZSC under equal conditions. It results in material destruction with significant deformation of samples.

3. The erosion of refractories surface in a place of their contact with iron oxide occurs owing to formation of low-melted eutectics at temperatures smaller than melting temperature of FeO. The rate of formation of erosion dimples on a surface is 0.015-0.6 mm/min for different values of weights of entered iron oxides.

4. The relative depth of impregnation by iron-oxides melt at the small values K_1 (~1/50) does not practically depend on sizes of samples, that testifies to small influence of the scale factor.

5. For case of isothermal heating at 2270 K in inert gas atmosphere the zirconia ceramics of porosity ~16 % can absorb and retain without appreciable change of integrity of a structure the iron-oxide melt in quantity seven times smaller than its weight, i. e. seven weight parts of ceramics are needed on one weight part of FeO_x. At greater quantity of iron oxide the surplus over this ratio (1/7) is evacuated from ceramics.

In case of a concrete ZHC this condition will be realized at lower temperatures (1870 K).

Table 1

Composition and some properties of the zirconia ceramics.

Name of the zirconia ceramics	Grain composition, mm weght % ZrO_2					Open porosity, P %	Thermal treatment, medium, T, duration
	2-1	1-0,5	<0,2	Fine binder 2 – 5 μm			
1.Grain structure yttria stabilised ceramics.	55	-	30	cub. tetr.	7,5 7.5	16,7	Oxidazing 1900 K – 3 h.
2.Dense yttria stabilised ceramics	-	-	-	cub.	100	0,2 - 1,5	-"-
3.Grain structure yttria stabilised ceramics with variable porosity.	-	-	-	cub.	-	-	-"-
4. Grain structure yttria stabilised ceramics impregnated by chromium salt	55	-	30	cub.	15	-	One said impregnation by 50 % solution of $Cr_2(SO_4)_3 \bullet 6H_2O$
5. -"-	55	-	30	cub. tetr.	7,5 7,5	-	Thermal treatment at 1670K, 1h, air.
6. -"-	-	70	-	cub.	30	-	-"-
7. -"-	-	-	<0,5 100	-	-	-	-"-
8.Ceramics with variable porosity.	-	-	-	cub.	-	-	-"-
9.Grain structure calcia stabilised ceramics.	2 -	0,5 mm 70	-	Cub. Mon.	15 15	15,8-16,7	Oxidazing 1970K-3h
10.High porosity zirconia ceramics.	-	-	100	-	-	41,9-42,2	Oxidazing 1900K-3h
11. Grain structure yttria stabilised ceramics.	1,6-	0,6 mm 70	-	cub.	30	18	Oxidazing 2023K-13h

Table 2

Composition and some properties of the zirconia concretes.

Name and symbolism of the zirconia concretes.	Grain composition, mm weght %					Open porosity, P %	Hardening conditions, thermal treatment
	filler. ZrO_2,mm			binder			
	2-0,63	<0,63	<0,063	form	amount		
Zirconia hydrated concrete (ZHC)	50	30	14	Ba Al_2O_4	6	14-10	Hardening in air >30 days at T<300K.
2. -"-	-"-	-"-	-"-	-"-	-"-	-	Thermal treatment after hardening at 1470K-2h
3. -"-	-"-	-"-	-"-	-"- coating ZS	-"-	-	-"-
4.Zirconia slip concrete.(ZSC)	43	29	-	ZS	28	18	After hardening at 570K-3h, termal treatment 1470K-2h.
5. -"-	43	29	-	-"- coating ZS	-"-	-	Coating was made after termal treatment at 570K-3h.

ZS – zirconia suspension consisting from: 80 weight %. ZrO_2, stab. Y_2O_3,
15 % H_2O,
5 % H_3PO_4 density 1,72 g/cm^3

INVESTIGATION OF ZIRCONIUM DIOXIDE CERAMICS INTERACTION WITH FERRIC OXIDES AND MODEL CORIUM (INCLUDING URANIUM DIOXIDE).

* V.D.Slabkiy.

* O.M. Traktuev

email: traktuev@admik.com

* A.A.Khrulev

* A.A.Vedenov

email: vedenov98@hotmail.com

**F.A.Akopov.

email: akopov@hedric.msk.su

** V.N.Mineev

email: mineev@hedric.msk.su

** B.M. Barykin

(* RRC "Kurchatov Institut", Kurchatov sq.1, Moscow, 123182, Russia.

** HEDRC-IVTAN, Izhorskaya,13/19, Moscow, 127412, Russia)

KEY WORDS

Corium; ferric oxides; ZrO_2 ceramic; interaction

ABSTRACT

The results of experimental investigations of model corium compositions interaction with zirconium dioxide ceramics (ZDC) of various porosity are given. The data on influence of temperature, ratio of ferric oxides (or corium) and ZDC weights, ZDC porosity and experiment duration on process of ferric oxides melt and corium interaction with ceramics are obtained.

INTRODUCTION

At severe accident in nuclear reactor followed by melting of the core and destruction of reactor vessel the measures on environment protection

against reactor molten materials are of great significance. Environment can be effected at destruction of the reactor base constructions due to its interaction with molten fuel-containing materials of the destroyed core (corium).

Development of the concept of corium localization system (LS) contemplates solution of the complete complex of problems, one of which is the selection of high-refractory materials for the corium catcher construction.

Zirconium dioxide (ZrO_2) is considered as one of prospective materials for usage in LS [1,2], since, first of all, it is chemically rather inert, doesn't form low-melting compounds with uranium dioxide and has sufficiently high melting temperature (by estimations it can reach 2800 K).

Whereas the catcher refractory layer will be subjected to abrupt heating at contact with overheated corium, it is very important to provide high thermal stability of ceramics. Thermal stability control is implemented by creation of grain-structured materials with an opened porosity up to 20 %.

The high corrosion resistance of such ceramics is provided by use of electrical melted initial powders for its manufacturing.

The investigations have shown [3], that corrosion resistance of zirconium dioxide ceramics (ZDC) to the corium effect essentially depends on presence of ferric oxide in the corium. The ferric oxide content in the corium, depending on the severe accident progress scenario, can vary from ~ 5 weight % - in the case of insignificant destruction and melting of in-vessel constructions to ~ 35 weight % - at the reactor core complete melting and at complete oxidation of the main construction materials and considerable melting through of the reactor vessel (conservative version). The corium main component, aggressive to ZrO_2 should be $FeO \cdot [Fe_2O_3]$. Iron, in itself, practically doesn't interact with UO_2 and ZrO_2.

The corium interaction with ceramics depends on the area of corium contact with ceramics surface; apparently, at the melt contact with porous ceramics the melt - ceramics interaction, due to the melt penetration it by the pores, takes place in the whole penetration volume.

The corium penetration the ceramics occurs under gravity effect followed by capillary impregnation by the corium components. The consequences this process will render on the corium and LS protective ceramic layer condition can be specified only on the basis of results of comprehensive analysis of the interaction mechanism of both ferric oxides and model compositions of the corium containing various quantities of ferric oxides and other components with ceramics of various porosity.

INVESTIGATION OF ZIRCONIUM DIOXIDE CERAMICS AND FERRIC OXIDES INTERACTION KINETICS.

Series of experiments on studying of ZDC resistance to the ferric oxides melt were conducted under conditions of gradient one-dimensional heating in air.

The following factors influence on the process of the melt interaction with ferric oxides and ZDC was studied:

1. Interaction time.
2. Test temperature.
3. Ratio of ferric oxides and ZDC masses.

The grain-structured ZDC with grain size from 0.2 to 1.0 mm on the basis of electric molten ZrO_2, stabilized by yttrium oxide (11-12 mol %) has been selected as the material for studying of interaction with ferric oxides. The samples porosity made ~20 %, the characteristic pore size was in the range from 5 to 60 microns. The ZDC samples were made in form of cylinders 20 mm in diameter and 5 and 10 mm in height and approximately 14 and 7 g in weight, respectively.

The mixture (weight %): 55 % FeO+40% Fe_3O_4 with the small content of metallic iron (~ 5 %) was used as ferric oxides. The pellets 8 mm in diameter, 3-4 mm in height and about 0.4g in weight were pressed out of this mixture.

The one-dimensional mode of ZDC samples heating was implemented by their placement so that they were mounted by one flat surface on the surface of water cooler, in which the Ch/A thermocouple was caulked, and other surface was subjected to luminous flux of power 1.5-3 MW/m^2. Therewith, the heat flow passing the samples reached the values 0.4-0.5 MW/m^2 (dependent on the surface temperature and the sample thickness), and the temperatures gradients made ~180 degree/mm and 360 degree/mm for the samples of thickness 10mm and 5 mm, respectively.

The temporary tests were conducted on ZDC samples 10 mm in height at $T = 2270$ K. The oxides quantity in each case corresponded to ratio of $M(FeO_x)/M(ZrO_2) \approx 1/37$. The stationary hold up times at this temperature were selected as following: 6 sec., 12 sec., 20 sec., 1 min, 5 min, 15 min, 30 min, 1 hour and 3 hours. Therewith the heating modes of different time ranges frames were different.

To exclude impregnation phenomena of during reaching the stationary operation temperature (~10 min) and to register true depth of impregnation at $\tau \leq 1$ min, the ZDC samples were preliminary heated up to 2300j and only after that the pellets of the oxides were placed on the samples. The stationary hold up time was counted off from the moment of the pellet complete melting.

At $\tau \geq 5$ min the pellets of ferric oxides and ZDC samples were heated simultaneously.

The conducted tests have shown that:

- the oxides melt interaction with ZDC starts with its fast penetration by the pores deep into ceramics (during several seconds) with formation of impregnation zone which depth is determined by the temperature of ferric oxide solidus ~1800j [4]. Hereafter the processes of diffusion and chemical interaction of ferric oxides and zirconium dioxide come take place, in doing so the oxides oxidation to Fe_3O_4 and Fe_2O_3 proceeds. This is testified by gain in weight of the samples after the tests;
- average, for 20 sec, value of impregnation front motion rate doesn't exceed ~ 0.3 mm/ sec. However, at initial instants, when the front intersects the higher temperature zones its rate is much higher. The estimating calculation has shown that the impregnation initial rate under the given conditions could reach ~1 mm/sec;
- the oxides melt penetrated the ceramics not only by capillary impregnation, but also at the expense of FeO_x diffusion into crystal lattice of zirconium dioxide. As a result, the solid solutions ZrO_2-Y_2O_3-FeO_x, which have, as well as initial solid ZrO_2-Y_2O_3, cubical fluorite structure but with smaller parameters of crystal lattice were formed in the impregnation zone. The diffusion process proceeds as simultaneously with capillary impregnation, so after its completion;
- microstructure of the samples interaction zones is about the same for interaction times more than 15-20 min. It testifies that the processes of the oxides melt interaction with ZDC proceed rather fast and end within the first 15 min;
- in the top layers of impregnation zone, especially at hold up more than 15 min the microstructure transformation connected with dissolution of the small-sized (1 micron and less) grains and separate straps between the grains, with recrystallization and re-grouping of dispersed fraction grains and with pores coalescence is noticeable;
- at the tests temperature rise up to 2300K or 2670K the impregnation depth increases from 4.3 mm to 5 mm and 6.5 mm, respectively;

- at ratio of ZrO_2 weight in the impregnation area and of the oxides melt total weight, equal to 4.3 and more, only partial transformation of the structure in the top zone of impregnation with formation of interlayers of FeO -ZrO_2 fluid phase is observed. At this ratio values equal to 2 and less, the structure total transformation is observed. In this case practically all large grains are dispersed to the size ~ 50 microns in diameter and are surrounded by dispersed spongy material on the basis of ZrO_2 with small amount of ferric oxide.

INVESTIGATION OF ZIRCONIUM DIOXIDE CERAMICS INTERACTION WITH MODEL CORIUM (INCLUDING URANIUM DIOXIDE).

The experiments directed on studying of the features of ceramics density influence on character of its interaction with the corium were conducted with corium composition: UO_2 - 46.6 weight %, ZrO_2 -17.6 weight %,

Fe_2O_3 -35.7 weight % at temperature 2073K in Ar atmosphere with the crucibles samples of various density (Tab. 1).

The corium model samples in form of cylinders ~15 mm in diameter and ~22 mm in height were made of finely dispersed powders of U, Zr, Fe oxides. The powders were mixed and then were pressed at pressure ~10 MPa. These cylinders were placed inside ceramic crucibles of different porosity and geometry which, in turn, were mounted on special suspensions in the vacuum electric furnace. The samples heating and cooling was conducted with rate of ~20 degrees/min. To measure the temperature the W/Re thermocouples was used.

After the experiment termination the visual inspection of crucibles, photography, weighing, the geometrical dimensions measurement, microsections making, microstructure analysis and phase composition of the samples and auto radiography were conducted.

The samples structure was investigated using optical microscopes at magnification 400X.

To compare the observed phases metallographic image with their quality element composition (on one site of microsection) the scanning electron microscope DMS-960B with a micro-X-ray adapter MICROSPEC-2AB with 500X magnification was used.

The phases quantitative element composition on isolated points to the corium height including the corium-ceramics interaction zone (35-60 points with step 50-1000 microns), was determined by micro-X-ray analyzer CAMEBAX SX-50B

Experiment № 1

The experiment was conducted with the objective:

- to substantiate the experimental sample heating mode providing formation of the model corium from selected mixture of the oxides;
- estimations of the model corium interaction with dense ceramics.

the principal schematic diagram of three thin-wall crucibles assemblage used in this experiment is shown in Fig. 1. Fig. 2 shows the photo of microstructure of the crucibles assemblage longitudinal cut made after the experiment termination, Fig. 3 shows its autoradiography, and Fig. 4 shows the corium microstructure to the sample height.

The analysis of experimental results has shown that:

- model corium interaction with ceramics has taken place; the bottoms of two crucibles have been completely melted through, and of the third one - partially; the interaction total depth in vertical direction has made ~ 4.8 mm;
- zones of the corium intensive interaction with walls of crucibles located outside the zone of the corium direct contact with the ceramics (Fig. 3)

have been revealed; the formation of such zones is connected with ceramics interaction with the corium components; the height of the corium lift has made to ~20 mm above the corium surface in the internal crucible; the geometry of walls of the crucible impregnated by corium has been kept.

- the corium composition includes three phases: gray (matrix), lightgray and white (inclusions). The basis of white inclusions are Fe and O. The quantitative analysis of these inclusions to the corium height has shown that in investigated area their composition is close to Fe_2O_3. The composition of lightgray inclusions is enriched in comparison with white inclusions on U to ~10 weight % and Zr to ~6 weight%. The matrix is the combined product of the model corium with addition of the molten crucible elements. The elements distribution in the corium matrix to the height is shown in Fig. 3.
- the sample autoradiography (Fig. 4) demonstrates sufficiently uniform distribution of uranium in the melt whole body and its insignificant penetration into the crucibles lateral walls. The quantitative analysis of the lateral walls material composition wasn't at the given stage of investigations.

The experiments № 2 and № 3 were conducted under the same conditions as the experiment № 1, but with crucibles of porous ceramics (see Tab. 1).

Experiment № 2.

The experiment was conducted to estimate ceramics porosity influence on its interaction with model corium. The investigations were conducted on porous (Po ~30 %) crucible of cylindrical form of external diameter ~52 mm and of height ~60 mm. The internal dimensions of the crucible of cylindrical form were the following: depth 33mm and diameter ~30 mm.

Fig. 5 shows the crucible longitudinal cut macrostructure, Fig. 6 shows its autoradiography, and Fig. 7 shows the elements distribution in the corium matrix to the sample height.

Tab. 1. The crucibles parameters, the corium weight and the experiments duration.

1	Porosity (Po), %	Thickness of the crucible bottom, Mm	Corium weight, g	Ratio $l_{cor.}/l_{crucible\ bottom}$	Experiment duration , min.
1	0.6	Three thin-wall dense crucibles, inserted one into another 1 1 - 2.00 mm 1 2 - 1,86 mm 1 3 - 1,58 mm	27.5	-	15
2	30	26	27,2	0,1	15
3	17	14	45,5	0,3	30

The analysis of experimental results has shown that:

- the crucible bottom external surface has become dark colored (in initial condition the crucible is white), but the corium flowing outside hasn't taken place;
- density of crucible samples cut from the bottom central part has increased in the average ~0.7 /cm^3 at the expense of the corium pores filling, and porosity has decreased in ~19 %.
- the corium intensive interaction with the crucible material has occurred with formation of 3 main phases - matrix (gray color), lightgray phase and white inclusions in the form of thin lines on the matrix grains boundaries (Fig. 5);
- porosity character has changed essentially: the initial through channels practically have vanished, the pores have rounded and partially have coalesced with each other;
- while the corium impregnates the porous crucible the uranium contents in it reduces to zero with corresponding increase of products of corium-ceramics interaction in it, i.e. Zr and Y (Fig. 7); the depth of uranium penetration makes ~80 % of the crucible base thickness.

Experiment № 3.

The objective of this experiment consisted in check of pores size influence on character of ceramics impregnation by model corium. For this objective the crucible with porosity of Po = 17 % (approximately 2 times

lesser than in experiment N 2) was used. To boost this effect and to test feasibility of the corium flowing outside, the crucible base thickness was also reduced in half and made 14 mm, and the corium quantity was almost doubled (see Tab. 1). Other geometrical dimensions of the crucible were similar to the crucible dimensions in the 2-nd experiment.

The crucible longitudinal section macrostructure is shown in Fig. 8, and Fig. 9 shows its autoradiography.

The analysis of experimental results has shown that:

- the crucible main body has penetrated to the end of its base, but the corium hasn't flown outside;
- insignificant part of model corium has remained in the form of two mounds on the internal surface of the crucible base, i.e. the corium main body has impregnated the crucible volume;
- UO_2 distribution to the crucible height is nonuniform # the most concentration is observed in sample top part (in the mounds);
- as well as in experiment N 2 the sample has increased at the expense of the corium penetration, and the opened porosity has decreased.

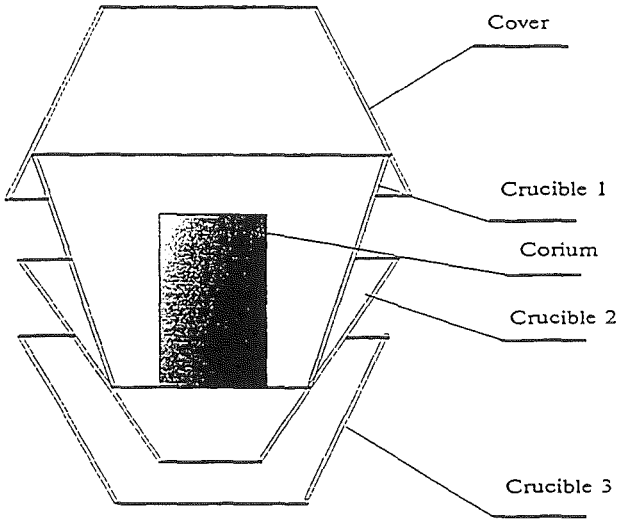

Fig. 1. The schematic diagram of crucibles assemblage (experiment N 1).

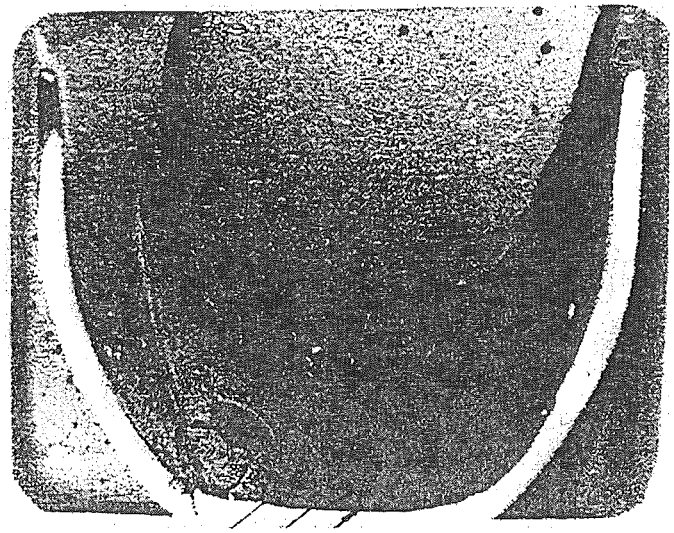

Fig. 2. Macrostructure of the crucibles assemblage longitudinal cut (experiment N 1).

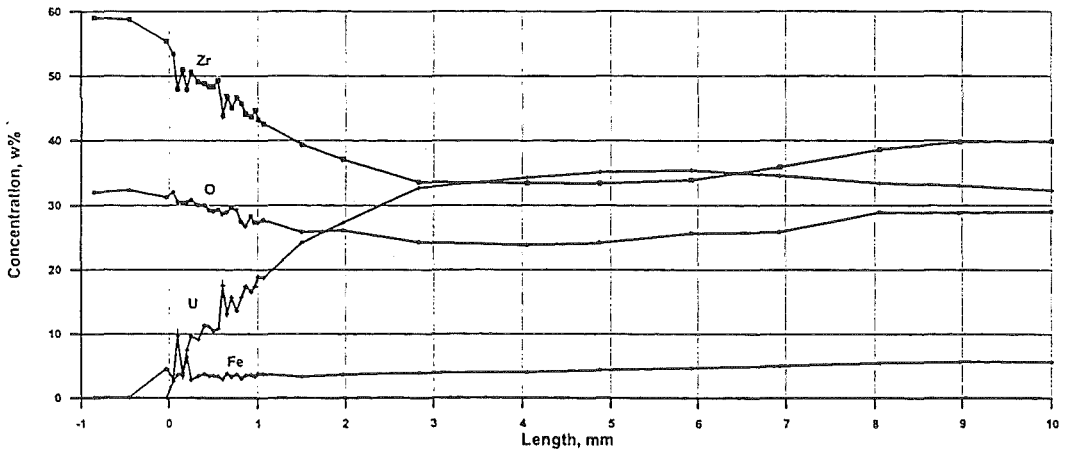

Fig. 3 The elements distribution in the corium matrix to the sample height (experiment N 1).
(0 - external surface of the crucible base).

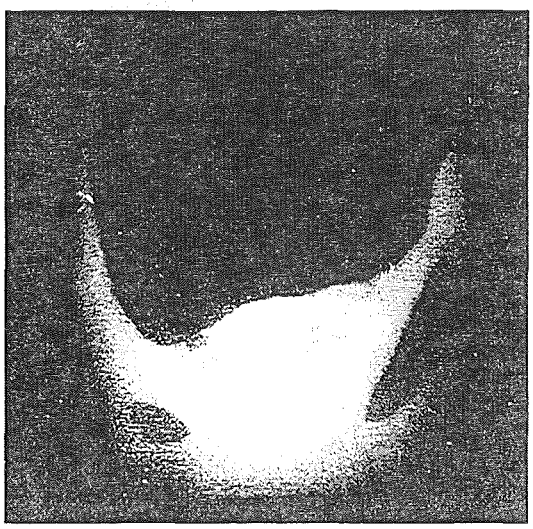

Fig. 4. Autoradiography of the crucibles assemblage longitudinal cut (experiment N 1).

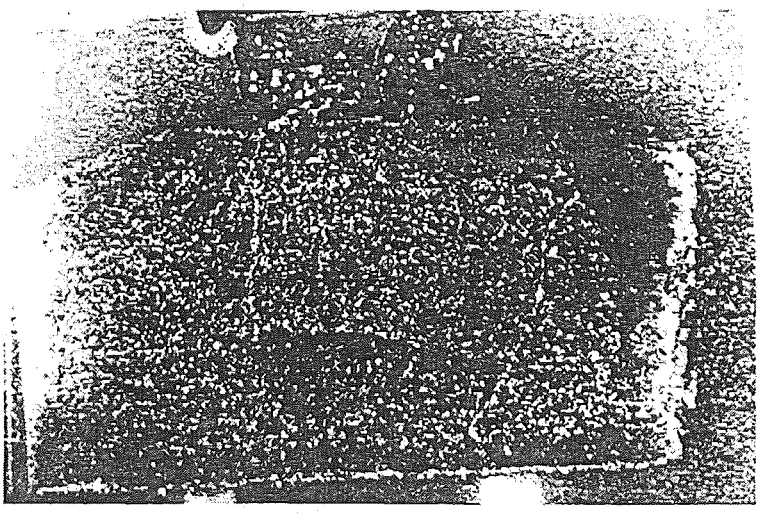

Fig. 5. Macrostructure of the crucible longitudinal cut (experiment N 2).

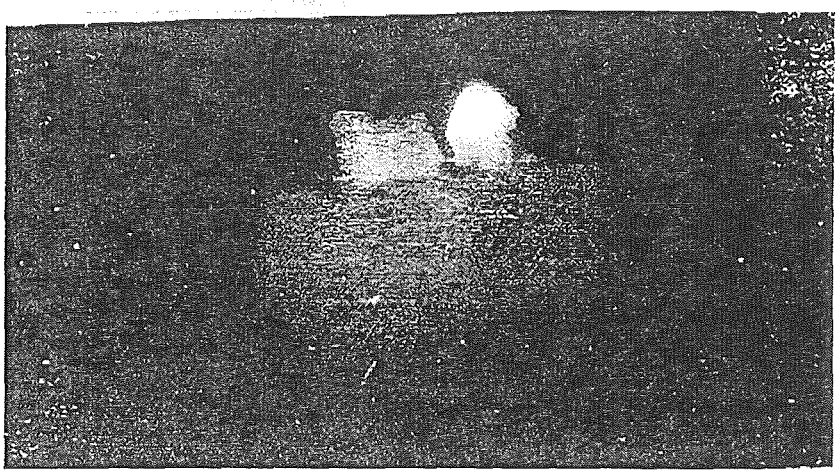

Fig. 6. Autoradiography of the crucible longitudinal cut (experiment N 2).

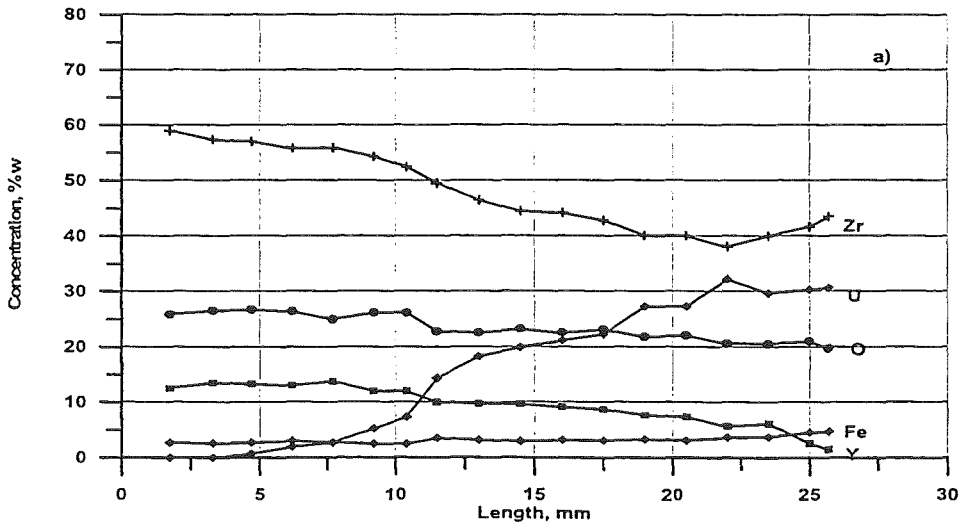

Fig. 7. The elements distribution in the corium matrix to the sample height (experiment N 2).
(0 - external surface of the crucible base).

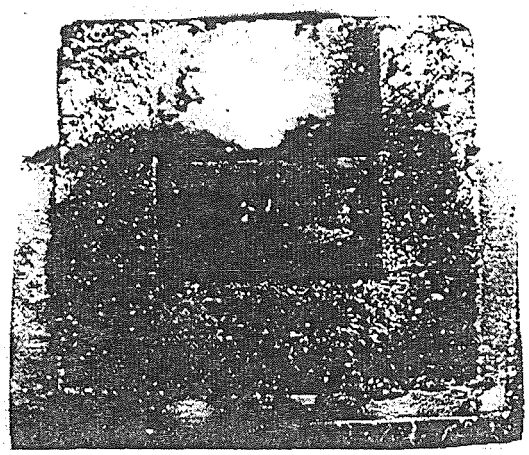

Fig..8. Macrostructure of the crucible longitudinal cut (experiment N 3).

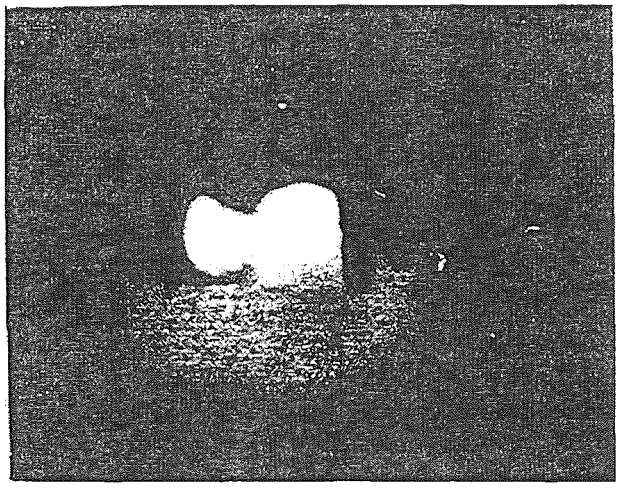

Fig.9. Autoradiography of the crucible longitudinal cut (experiment N 3).

THE MAIN CONCLUSIONS.

1. At the selected conditions of experiment the model corium is formed in the dense crucible.
2. At the model corium interaction with dense ceramics the total depth of interaction in vertical direction has made ~4.8 mm.
3. At $\overline{T}$ = 2073K during 15-30 min there isn't complete melting of the blend in the porous crucible to the model corium formation due to change of the blend composition, since the most low-melting component of the initial blend (Fe_2O_3) is partially melted out and is diluted in the crucible material, and the concentration of high temperature components in the rest of the blend is increased and by that its melting temperature is raised.

4. The zones of the corium intensive interaction with the dense crucibles walls (Fig. 3) are revealed; the formation of such zones is connected with the ceramics interaction with the corium components; geometry of the crucible walls, impregnated by the corium has been kept (it is reasonable, in further, to estimate their mechanical properties).
5. The corium molten part penetrates the ceramics pores practically to the porous crucible bottom and interacts with zirconium dioxide with formation of 3 phases:

- ferric oxide which is released at the matrix grains boundaries and has composition ($FeO_{1.4}$), close to initial composition (Fe_2O_3).
- the matrix, being the chemical combination of the corium all components and having variable composition as the melt penetrates the crucible bottom.
- The phase containing Zr, Y, O, and corresponding to the ceramics initial composition.

6. In the result of interaction the opened porosity decreases and the pores morphology changes (the most of the channels is transformed into spherical isolated pores).
7. At ratios of the corium and crucible weights used in experiments and the experiments modes the corium doesn't flow out through the porous crucible bottom, since the pores volume only in the crucible bottom makes, by our estimations, about 18 cm^3, while the corium volume doesn't exceed 4 cm^3;

REFERENCES

1. V.N.Mineev The external catcher of ceramics on the basis of zirconium dioxide. Atomic energy, v.85, iss.2., 1998.

2. F.A.Akopov Behavior of zirconium dioxide ceramics of plasma spraying at thermochemical effect of the core melt components on it. Atomic energy, v. 85, iss.2, 1998.

3. F.A.Akopov The core melt oxide components interaction with hafnium dioxide and zirconium dioxide ceramics. Atomic energy, v.84, iss.4, 1998.

4. N.A.Toropov, V.P.Barzakovsky, V.V.Lapin, N.N.Kourtseva The constitution diagrams of silicate systems. Reference book, L., Science, 1969, ps. 402-404, 460-469.

SACRIFYIRING LAYER MATERIALS COMPLEX USAGE FOR IMMOBILIZATION OF HIGH LEVEL NUCLEAR WASTES.

F.A. Akopov, A.A. Akopyan, B.M. Barikin, T.I. Borodina, M.V. Koryakina, E.S. Lukin, V.N. Mineev, A.S. Vlassov.

HEDRC-IVTAN, Izhorskaya, 13/19; Moscow, 127412, Russia

The main function of Sacrifyiring Layer (SL) of external catcher is decreasing of influence on a refractory layer. This function can be overlapped with the capability of SL to immobilize radionuclide if SL composition is identical to the Synroc composition for example. For this purpose a part of substances can be used from corium of a reactor, the other part can be complemented with substances from SL. There were studied different compositions of SL, their behavior under high temperatures and crystallization and also interaction with refractory layer. The particular attention was paid to the action of iron oxides from corium on the properties of melt, eutectic temperature, viscosity, damping, infiltration into the refractory layer from zirconium dioxide stabilized by calcium oxide bricks.

A number of projects of external catchers envisages the presence of Sacrifyiring Layer (SL) over refractory layer. The main significance of SL is decreasing of intensity of action of different shocks on the catcher in the moment of reactor destruction. The requirements to SL material are the following: support of good solubility and crystallization of corium, mitigation of heat and mechanical influence on refractory layer, heat energy absorption, control of decay products going out from corium. These principal requirements are important, but we added one more quite actual requirement - the SL ability of immobilization of High Level Nuclear Wastes (HLW). This requirement had essential influence on SL composition. Choosing SL composition we tended to find such its content that would meet all requirements mentioned above and involve elements entering in corium composition with some additives.

By literary data it was found that concretes (1), borosilicate glasses (2), glass ceramic materials (3) and ceramics without vitreous phase (4) were used for immobilization of HLW. Concretes are unsuitable in this case for action of high temperatures because the process of compacting is connected with the process of crystallization of corium melt. For the most part this process is similar to immobilization of radionuclides in matrixes formed under clinkering (5) and in glass matrixes. However investigations of radionuclide leaching in water solutions and its influence on concretes and glass have shown that ceramic matrixes were more stable and resistant (6). But all developed technologies of ceramic matrixes for immobilization of HLW are concerned with preparing of high-active powders, in which solutions of HLW were added, compacting of these powders to half-finished product with the following drying and sintering (7). Although this process differs from the

process of melt crystallization, the principles of matrix composition selection are common. The matrix must consist of atoms from different groups of Periodic Table. It is known that the presence of atoms of the first group in ceramics impairs its stability to leaching. That is why it is necessary to avoid the availability of the first group atoms in matrixes for radionuclide immobilization. In common aspect matrix composition can be written in the following way:

$$A_x^{2+}B_y^{3+}C_z^{4+}O_n^{2-},$$

where A^{2+}, B^{3+}, C^{4+} are elements of 2nd, 3d and 4th groups with large enough ionic radiuses that provides its substitution by different ions of radionuclides; O^{2-} - oxygen ions.

A range of ceramic matrixes was developed for immobilization of HLW. The materials are polyphase and composed of the compatible crystalline phases of Al_2O_3 (corundum), iron-nickel-manganese spinal (Fe, Ni, Mn)(Al, Fe)$_2O_4$, magnetoplumbite X(Al, Fe)$_{12}O_{19}$, where X=Sr, Ba, $Cs_{0,5}$+$La_{0,5}$, $Na_{0,5}$+$La_{0,5}$ and fluorite phase (U, Zr, Th)O_2. Additional phases may also be present, according to the specific tailoring additives used (9,10,12).

In such polyphase ceramics incongruent dissolution is observed. The incongruent dissolution of polyphase nuclear waste ceramics exhibits a number of characteristic features: a surface common scale reaction-product forms; certain crystalline phases selectively leach; intergranular phases, when present, preferentially dissolve; and the pH of the leachate (unless buffered) changes with time, approaching a saturation level, that is why passivating layers on the surface of the nuclear waste ceramic monolith are formed.

The group of ceramic materials called Synroc has special significance for the choice of matrixes. Synroc is the generic name for a group of titanate ceramic waste forms developed in Australia (4) to immobilize HLW. Common phases for all Synroc formulations are perovskite ($CaTiO_3$), zirconolite $CaZrTi_2O_7$), hollandite ($BaAl_2Ti_6O_{16}$) which possess the ability to incorporate radionuclides, durability with respect to leaching, and low susceptibility to radiation damage (11).

Besides the main functions, connected with damping of influence on refractory layer the SL must be able to execute the role of matrix for HLW immobilization. That is why under SL selection we were guided by the possibility of formation of new material with the composition corresponding to Synroc C as a result of interaction between corium melt and SL. It was suggested that a part of components would be used from corium. In Fig. 1 there is the scheme of using of precursor materials both from SL and corium with the purpose of creation the composition corresponding to Synroc, mentioned by K.D. Reeve (4) (Table I).

Table I. Synroc precursor components, wt % (by K.D. Reeve) (4).

TiO_2	(69,5 ÷ 71,4)
ZrO_2	(6,5 ÷ 9,8)
Al_2O_3	(5,5 ÷ 9,6)
BaO	(5,6 ÷ 8,5)
CaO	(11,0 ÷ 14,5)

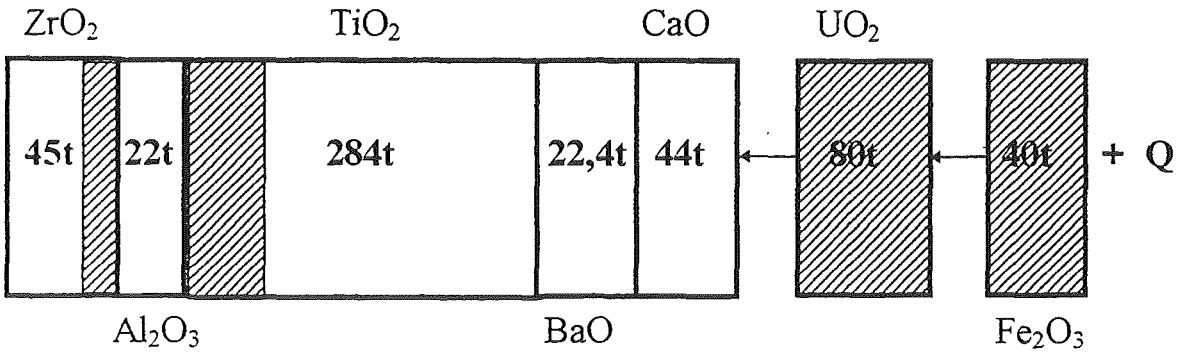

Fig.1. The scheme of precursor components sources for SL;

□ - from SL, ▨ - from corium.

The SL composition must complement the composition of corium from a reactor to form Synroc which is able to create such matrix that can absorb any ions and does not conduce increasing of solubility.

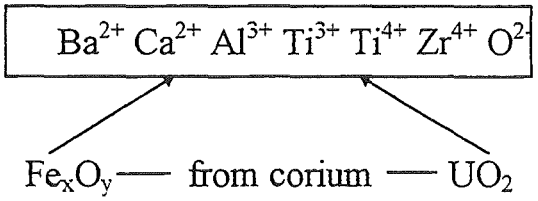

UO_2 forms solid solutions with many oxides (Table IV) and lower its melting temperature.

In the composition of crystallized SL perovskite is present. Perovskite, nominally $CaTiO_3$, is included in the phase assemblage specifically to immobilize ^{90}Sr, U and REE. Cs and Rb are fixed in hollandite-type phase ($Ba(Al, Ti)_2Ti_6O_{16}$) by substituting in the Ba site of the host phase. The strongly reducing fabrication conditions ensure that several of the waste constituents and processing contaminants are partially reduced to metal (Tc, Ru, Rh, Cd, Fe, Ni, Mo and Ti) and several alloys as have been reported (6). Magnetoplumbite-type phase ($(Ca, Sr, REE)(Al, Ti, Fe)_{12}O_{19}$) occurs as a minor phase in Synroc if the precursor material contains Al. Rutile does immobilize some Zr, but its major function is to maintain Ti - TiO_2 buffering of the oxygen potential during Synroc fabrication.

The study of interaction between SL and refractory layer was executed by means of device of light heating «URAN-1» (Fig.2). This device allowed to heat specimens by means of light stream in oxidative air atmosphere to the temperature 2500°C. The scheme of the device «URAN-1» is shown in Figure 2. Specimens of refractory layer from zirconium dioxide were prepared in a form of pill 30 mm in diameter and 5 mm in height. Specimens of refractory layer were placed onto copper sheet, cooled by water. Circulation rate of water remained constant. Specimens of SL were prepared in a form of pill 16 mm in diameter and 5 mm in height. Specimens of SL were placed onto refractory layer and heated from the side of SL.

The melt temperature was determined by means of optical pyrometer VIMP-015, the error depending on the temperature. In addition for elaboration of final crystallization temperature there was carried out a differential thermal analysis with error ±1°C at 1350°C.

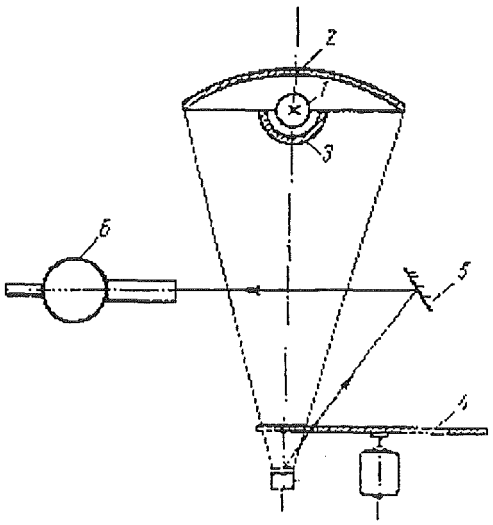

Fig.2. The scheme of device «URAN-1» : 1 - xenon lamp (10 kW), 2 - elliptical reflector, 3 - contra-reflector, 4 - modulator, 5 - flat mirror, 6 - pyrometer VIMP-015.

To study the interaction between SL and refractory layer there were made three types of SL specimens of different compositions: Synroc B (8), Synroc B with 8,75% Fe_2O_3, Synroc B with 6,47% FeO. The specimens were melted by means of device «URAN-1». The heating of specimens proceeded for several minutes till 2000°C and after some time of maintenance specimens were cooled gradually and then the xenon lamp was turned off. Specimens received after melting and containing Fe^{2+} and Fe^{3+} in initial composition do not differ in their properties. Specimens containing Fe_xO_y are characterized by deeper infiltration of melt into substrate as compared with specimens from pure Synroc B (Table II).

Table II. Infiltration Depth of SL into ZrO_2 Refractory Layer.

Initial composition of SL specimens	Composition number of ZrO_2 Refractory Layer	Maintenance after melting, min.	Infiltration Depth of SL melt into Refractory Layer, mm
Synroc B	1	5	4,6
	2	5	3,1
	3	5	2,0
Synroc B + 6,47% FeO	1	5	3,2
	2	5	2,9
	3	5	1,3
Synroc B + 8,75% Fe_2O_3	1	5	3,2
	2	5	2,8
	3	5	1,3

The increasing of period of maintenance under ultimate temperature from 5 to 20 minutes does not have considerable influence on depth of treatment of refractory layer by melt. At other equal conditions of experiment the depth of infiltration (specimen №3) has increased from 2,0 mm at 5 minutes of maintenance to 2,6 mm at 20 minutes of maintenance for specimen of Synroc B and from 1,3 mm at 5 minutes to 1,5 mm at 20 minutes for specimen of Synroc B containing FeO (t~1800°C).

Experimental data on infiltration depth also depend on magnitude of temperature gradient. Since the specimen of substrate is placed onto water-cooled copper sheet and the heating is realized from the side of SL there is considerable temperature gradient along refractory layer height that can control infiltration depth.

The process of infiltration depends on porosity and pores size of refractory material. To evaluate the influence of these properties there were made three types of refractory material samples from ZrO_2. Samples had various fractional composition and different porosity (Table III). The SL melt penetrated deeper into the samples with the highest porosity (composition №3). Samples of ZrO_2 of the composition №2 and № 3 had almost the same porosity (Table III) but thanks to more careful selection of fraction composition the pores size of the samples №3 is less than the one of the samples №2. Thus having nearly equal porosity ~20% the samples with less pores size are characterized by the least infiltration depth. One can conclude that it is not porosity but pores size has decisive influence on depth of SL melt infiltration into refractory layer.

Table III. Fraction composition and properties of refractory material samples from ZrO_2.

Fraction composition and properties	№ of ZrO_2 samples composition		
	1	2	3
Number of fraction	2	3	3
Size of small fraction, μm	2 - 5	2 - 5	2 - 5
Size of medium fraction, μm	—	71 - 125	40 - 63
Size of large fraction, μm	71 - 125	710 - 1000	400 - 710
Content of small fraction, %	15	15	15
Content of medium fraction, %	—	25	30
Content of large fraction, %	85	60	55
Open Porosity, %	30,9	19,3	20,5
Apparent Density, g/cm^3	4,08	4,77	4,70

There are dioxides of zirconium, uranium and iron which pass from corium to Synroc melt. UO_2 forms eutectics with oxides of SL. These eutectics have high melting point (Table IV).

Barium and titanium oxides form eutectics with uranium dioxide with low temperatures - 1700±50°C and 1480±30°C accordingly. It was found experimentally that the mixture of Synroc composing oxides with iron oxide melts at the temperature of 1320±1°C.

Table IV. Eutectic temperatures in oxide binary systems with UO_2.

Oxide	Eutectic melting point,°C	Oxide	Eutectic melting point, °C	Oxide	Eutectic melting point, °C
CaO	2000±50	Al_2O_3	1940±50	BaO	1700±50
REE*	2500±100	ZrO_2	2600±50	TiO_2	1480±30

*REE - rare-earth elements.

Molten pure iron does not moisten oxide refractory materials and due to their high thermodynamic strength iron can not supplant cations of oxides. That is why chemical interaction on the boundary iron melt - refractory oxide is not observed. In steels because of presence of many other cations (Ni, Si, Mn, Cr, C, N and even Fe^{2+}), anions as O^{2-}, S^{2-} and electroneutral particles there are observed chemical reactions on the boundary steel melt - oxide. What's more oxygen is most aggressive in these processes (13).

Oxygen is known to dissolve in iron. The solubility of oxygen in iron changes some orders of magnitude depending on temperature. Oxygen has great electronegativity and attracts electrons right up to the formation of oxides which are able to moisten a surface of oxide refractory materials thus providing with conditions for chemical interaction between refractory oxides

Table V. Results of X-Ray and Petrographic analysis of Synroc samples after smelting.

Initial composition (% mass)	Major phase	Minor phase	Phases in small quantity	Size and form of crystals	Pore size	Quantity of amorphous phase	Conditions of heating and cooling
Synroc B TiO_2 - 68,4 ZrO_2 - 6,5 Al_2O_3 - 5,5 $BaTiO_3$ - 8,6 CaO - 11,0	ZrO_2 (cubic)	$CaZrTi_2O_7$ $Ba_3Al_{10}TiO_{20}$	TiO_2 $BaTiO_3$ Al_2TiO_5	Homogeneous isometric form crystals with size 12 μm and round aggregations of size 8 - 30 μm, where crystal size is 2 - 4 μm	Microcracks (to 3% vol.)	Amorphous phase as discrete layers of thickness to 2 μm, spreaded inhomogeneously	Rapid heating to 1380°C, melting and heating to 1650°C for 6 minutes, then turn-off of furnace. Melt has penetrated into pores of substrate.
Synroc B with additive Fe_2O_3 - 8,75%	$CaZrTi_2O_7$ ZrO_2	$Ba_3Al_{10}TiO_{20}$ Fe_2O_3	Fe_3O_4 $BaTi_4O_9$ $Fe_2Ti_3O_9$	Phase is crystallized as large crystals of size 20 - 45 μm. There are some phases with isometric form crystals 6 - 15 μm and round crystals to 4 μm	Intracrystal-line pores to 4 μm	Amorphous phase as discrete layers around crystals of 3 μm thickness,their quantity grows at the joint of ZrO_2 substrate and Synroc. Total quantity of amorphous phase 1 - 5%	Heating to1500°C then to drop boiling on the surface to 1900°C.Heating from 1500 to 1900°C for 7 min, cooling 1850°C for 6 min, turn-off of furnace.
Synroc B with additive FeO - 6,47%	$CaZrTi_2O_7$ ZrO_2	$CaTiO_3$ $BaFe_4Ti_2O_{11}$ $Fe_2Ti_3O_9$ $BaTi_4Al_2O_{12}$	$FeAl_2O_4$ Fe_2O_3 Fe_3O_4	Fiber crystals to 4 μm and isometric crystals 4 - 10 μm	Intercrystal-line porosity, pore size to 10μm,quanti-ty of pores 4 - 5%.vol	Quantity of amorphous phase is 10%, which is spreaded homogeniously along the crystal borders	From melting point at 1400°C further heating to 2180°C for 6 min, then cooling to 2050°C for 6 min, turn-off of furnace.

and metal. The presence of oxygen in metal decreases surface tension and contact angle of refractory oxides moistened by metal. Maximum content of atomic oxygen in oxide iron is determined by equation:

$$\lg [O]_{max} = -6320/T + 2{,}734 \qquad \text{(Eq.1)}$$

The resistance of refractory layer depends on its moistening by SL melt. Under heating of samples the light stream of xenon lamp was directed in the center of SL sample placed onto refractory material sample. By this the sample was melting gradually and a drop of SL melt was formed on substrate surface. The drop of melt held its shape for some time because of surface tension forces. Under further action of light stream of xenon lamp the drop spread and oxide melt penetrated quickly into porous ceramic substrate from ZrO_2. It testifies good moistening of refractory layer by SL melt. This assumption is confirmed by data on contact angle of SL melt of different composition which are seen in Table VI.

Table VI. Contact angle θ of SL melt of different composition.

SL composition	θ, grad
Synroc B	27 - 30
Synroc B + FeO	35 - 37
Synroc B + Fe_2O_3	35 - 37

After melt cooling the polyphase systems were formed. The X-Ray and petrographic analysis carried out (Table V) have shown that this polyphase systems consist of vitreous phase and crystalline phases containing cubic zirconium dioxide (one can assume that under rapid cooling there occurs ZrO_2 solid solution formation), zirconolite, hollandite as the main phases and minor phases - barium titanate, alumoferrite, aluminium titanates, iron oxides (Table V). It is known that crystallization of melts begins from high temperature compounds and ends with the most easily fusible ones. Thus due to the temperature gradient along sample height compounds of polyphase system are crystallized successively and phase composition may vary along sample height.

If melt crystallization runs rather quickly, amorphous phase is presented as intercrystalline thin layers of thickness up to 2 μm. Pores are presented in material as intracrystalline with size up to 4 μm formed under quick growing of crystals and intercrystalline ones with size to 10 μm in amount 4 - 5%vol.

References.

1. Yu.M. Boott, V.V. Timashev, L.A. Kucenco, A.V. Gordievsky, I.E. Kozlova. Cementation of hydroxide precipitates containing some radioactive elements. Atomic energy, v. 17, № 2, 1964,p. 124-129.
2. W. D. Runcin, G.G. Wicks. Chemical Durability of Savannah River Plant Waste Glass as a Function of Waste Loading. Journal of the American Ceramic Society, June 1983, p. 417-421.
3. R.P. Turcotte, J.W. Wald, F.P. Roberts, J.M. Rusin, W. Lutze. Radiation Damage in Nuclear Waste Ceramics. Journal of the American Ceramic Society, December 1982, p. 589-594.
4. K.D. Reeve. The Synroc Process for High-Level Nuclear Waste Immobilization. Material Science Monograph. High Tech. Ceramics. Ed. P. Vincenzini. Elsiver. Amsterdam, Oxford, New York, Tokio. 1987, p. 2897-2902.
5. C. M. Jantzen, F. P. Glasser, E. E. Lachowski. Radioactive Waste - Portland Cement Systems : Radionuclide Distribution. Journal of the American Ceramic Society, October 1984, p. 668-674.
6. R.G. Dosch, C.J. Northrup, T.J. Headley. Crystalline Titanate Ceramic Nuclear Waste Forms: Leaching and Radiation Damage. Journal of the American Ceramic Society, June 1985, p. 330-337.
7. R.G. Dosch, T.J. Headley, P. Hlava. Crystalline Titanate Ceramic Nuclear Waste Forms: Processing and Microstructure. Journal of the American Ceramic Society, May 1984, p. 354-361.
8. J.L. Woolfrey, D.M. Levins, R. Smart, M. Stephenson. Effect of Hot-Pressing Conditions on the Structure and Leachability of Synroc. American Ceramic Society Bulletin. December 1987, p. 1739-1747.
9. C.M. Jantzen, D.R. Clarke, P.E.D. Morgan, A.B. Harker. Leaching of Polyphase Nuclear Waste Ceramics: Microstructural and Phase Characterization. Journal of the American Ceramic Society, June 1982, p.292-301.
10. F.J. Ryerson. Microstructure and Mineral Chemistry of Synroc D. Journal of the American Ceramic Society, September 1983, p. 629-637.
11. J.A. Cooper, D.R. Cousens, R.A. Lewis. Microstructural Characterization of Synroc C and E by Electron Microscopy. Journal of the American Ceramic Society, February 1985, p. 64-71.
12. B.S. Nikonov, B.I. Omelianenko, A.G. Ptashkin. Preparation and Characterization of Titanate Ceramics for Immobilization of Re-Actinide Fraction of HLW. 25-th Anniversary "HLW, LLW, mixed wastes and Environmental Restoration - Working Towards and Cleaner Environment" 28 февраля - 4 марта Tucson 1999, p.21.

13. K.K. Strelov. Theoretical base of refractory materials technology. Moscow. Metallurgy, 1985, 480 p.

Appendix B:

Workshop Programme

Monday, 15 November 1999

08.30 - 09.30	**REGISTRATION**
09.00 - 09.20	**WELCOME**
9.20 - 10.00 *(30 + 10)*	Invited Paper: The Role of Ex-Vessel Melt Cooling in Present and Future Reactors *C. Lecomte, IPSN France*
10.00 - 10.20	COFFEE BREAK
10.20 - 12.40	**Session A: SPECIAL MODES OF CORIUM DISCHARGE INTO THE CONTAINMENT** **Chairman: S. Basu**
10.20 - 10.50 *(20+10)*	Experiments to Investigate the Low Pressure Corium Dispersion in EPR Geometry *L. Meyer*
10.50 - 11.20 *(20+10)*	Transient Code Models for Low Pressure Corium Dispersion *D. Wilhelm*
11.20 - 11.50 *(20+10)*	KAJET Experiments on Pressurized Melt Jets with View to their Interaction with Substratum Materials *G. Albrecht, E. Jenes, A. Kaiser and W. Schütz*
11.50 - 12.20 *(20+10)*	KAPOOL Experiments to Simulate Molten Corium-Sacrificial Concrete Interaction and Gate Opening in the EPR Core Catcher Concept *G. Engel, D. Eppinger, F. Fellmoser, G. Fieg,C. Messainguiral, H. Massier and S. Schmitt-Stiefel*
12.20 - 12.40	**DISCUSSION about Session A**
12.40 - 14.00	LUNCH

14.00 - 15.30	**Session B 1: PHENOMENA TO ACHIEVE COOLABILITY: NATURAL CONVECTION HEAT TRANSFER WITH BUBBLING** **Chairman: V. Gustavsson**
14:00 - 14:30 *(20+10)*	Thermal hydraulic Phenomena in Corium Pools for Ex-Vessel Situations : the BALI Experiment *J.M. Bonnet*
14:30 - 15:00 *(20+10)*	Solid Particle Effects on Heat Transfer in Multilayered Molten Pools with Gas Injection *R.M. Bilbao y Leon and M. Corradini*
15:00 - 15:30 *(20+10)*	Simulation of ACE and MACE Experiments with a Phase Segregation Model, using a Simple Analytic Tool and the TOLBIAC Code *S. Vandroux-Koenig, F. Gillot, J.M. Seiler, B. Spindler and K. Froment*
15:30 - 15:50	COFFEE BREAK
15.50 - 17.10	**Session B 2: PHENOMENA TO ACHIEVE COOLABILITY: CHARACTERISTICS OF PARTICLE BEDS** **Chairman: V. Gustavsson**
15:50 - 16:15 *(20+5)*	Characterization of Debris Bed Generated by Fuel Coolant Interactions *H.O. Haraldsson and B.R. Sehgal*
16:15 - 16:40 *(20+5)*	Experimental Investigation on Dryout Heat Flux of a Particle Debris Bed with a Downcomer *Z.L. Yang, M. Konovalikhin, G.J. Li and B.R. Sehgal*
16:40 - 17:10 *(20+10)*	Experimental Investigations on Particulate Debris Bed Coolability in a Multi-Dimensional Configuration *E. Décossin*
17:10 - 17:30	**DISCUSSION about Sessions B 1 and B 2**
17:30 - 18:00	**Session B 3: PHENOMENA TO ACHIEVE COOLABILITY: SPREADING** **Co-Chairmen: H.-J. Allelein and J.-C. Latché**
17:30 - 18:00 *(20+10)*	Corium Spreading Phenomena : Results Obtained from the EU CSC Project *G. Cognet, W. Tromm, D. Magallon, R. Wittmaack, B.R. Sehgal, L. De Cecco, R. Ocelli, D. Pineau, B. Spindler, G. Fieg, H. Werle, C. Journeau, M. Cranga and G. Laffont*

Tuesday, 16 November 1999

08.30 - 17.20	**Session B 3 (Continued): PHENOMENA TO ACHIEVE COOLABILITY: SPREADING** **Co-Chairmen: H.-J. Allelein and J.-C. Latché**
08.30 - 09.00 *(20+10)*	KATS Experiments to Simulate Corium Spreading in the EPR Core Catcher Concept *G. Engel, G. Fieg, H. Massier, U. Stegmaier and W. Schütz*
09.00 - 09.30 *(20+10)*	The VULCANO Ex-vessel Programme *G. Cognet, G. Laffont, C. Jegou, J. Pierre, C. Journeau, M. Cranga, F. Sudreau and M. Ramacciotti*
09.30 - 10.00 *(20+10)*	COMAS : Representative Spreading Experiments with View to Core Melt Mitigation *W. Steinwarz, W. Häfner, Z. Alkan and M. Fischer*
10.00 - 10.20	COFFEE BREAK
10.20 - 10.50 *(20+10)*	Dry and Wet Spreading Experiments with Prototypic Material at the FARO Facility and Theoretical Analysis *J.J. Foit and W. Tromm*
10.50 - 11.20 *(20+10)*	Simulation of Core Melt Spreading with LAVA : Theoretical Background and Status of Validation *H.-J. Allelein, A. Breest and C. Spengler*
11.20 - 11.45 *(20+5)*	Numerical Simulation of Corium Spreading in the EPR with CORFLOW *R. Wittmaack*
11.45 - 12.10 *(20+5)*	Spreading with Variable Viscosity. CORFLOW Validation and Analysis of KATS Experiments *J.J. Foit and A. Veser*
12.10 - 12.40 *(20+10)*	Assessment of THEMA Code Against Spreading Experiments *B. Spindler, C. Brayer, M. Cranga, L. de Cecco, P. Montanelli, D. Pineau and J.-M. Veteau*
12.40 - 15.00	***LUNCH and VISIT of FZK-FACILITIES***
15.00 - 15.30 *(20+10)*	Synthesis of the Validation of the CROCO V1 Spreading Code *B. Michel, B. Piar, F. Babik and J.C. Latché*
15.30 - 16.00 *(20+10)*	The Scaling Model of Core Melt Spreading : Validation, Refinement and Reactor Applications *M.J. Konovalikhin, T.N. Dinh and B.R. Sehgal*
16.00 - 16.20	COFFEE BREAK

16.20 - 16.50 *(20+10)*	Numerical Simulation of the Stability of Solidified Core Melt Accumulations *I. Wintruff and C. Günther*
16.50 17.20	**DISCUSSION about Session B 3**
17.20 - 17.50	**Session B 4: PHENOMENA TO ACHIEVE COOLABILITY: FRAGMENTATION AND QUENCHING** **Chairman: W. Scholtyssek**
17.20 - 17.50 *(20 + 10)*	Implications of FARO and KROTOS Experiments for FCI Issues *D. Magallon, S. Basu and M. Corradini*
20.00 -	***Workshop Dinner at Heinrich-Hertz-House/ University Campus***

Wednesday, 17 November 1999

08.30 - 09.30	**Session B 4 (Continued): PHENOMENA TO ACHIEVE COOLABILITY: FRAGMENTATION AND QUENCHING** **Chairman: W. Scholtyssek**
08.30 - 08.50 *(15+5)*	Modeling of Coarse Break-up of Molten Core Jet in JASMINE Code *K. Moriyama, Y. Maruyama, H. Nakamura, K. Hashimoto and J. Sugimoto*
08.50 - 09.10 *(15+5)*	COTELS Project (1) : Overview of Project to Study FCI and MCCI during a Severe Accident *Yu. Cherepnin, H. Nagasaka, Yu. Vasilyev, A. Kolodeshnikov and V. Zuev*
09.10 - 09.30 *(15+5)*	COTELS Project (2) : Fuel Coolant Interaction Tests under Ex-Vessel Conditions *M. Kato, H. Nagasaka and Yu. Vasilyev*
09.30 - 12.50	**Session B 5: PHENOMENA TO ACHIEVE COOLABILITY: FLOODING** **Chairman: W. Scholtyssek**
09.30 - 09.50 *(15+5)*	COTELS Project (3) : Ex-Vessel Debris Cooling Tests *H. Nagasaka, I. Sasaki, M. Kato and Yu. Vasilyev*
09.50 - 10.10 *(15+5)*	COTELS Project (4) : Structural Investigation of Solidified Debris in MCCI Tests *V. Zhdanov, Yu. Cherepnin, Yu. Vasilyev, A. Kolodeshnikov and H. Nagasaka*
10.10 - 10.30	COFFEE BREAK
10.30 - 11.00 *(20+10)*	Status of Large Scale MACE Core Coolability Experiments *M.T. Farmer, B.W. Spencer, D.R. Armstrong, D.J. Kilsdonk, R.W. Aeschlimann and J. Chao*
11.00 - 11.20 *(15+5)*	Status of the CORQUENCH Model for Calculation of Ex-Vessel Corium Coolability by an Overlying Water Layer *M.T. Farmer and B.W. Spencer*
11.20 - 11.50 *(20+10)*	Corium Cooling by Bottom Flooding : Results of the COMET Investigations *H. Alsmeyer, C. Adelheim, H. Benz, T. Cron, G. Dillmann, F. Ferderer, W. Tromm, S. Schmidt-Stiefel, H. Schneider, G. Schumacher and T. Wenz*
11.50 - 12.20 *(20+10)*	CometPC : First Results for a Simplified Cooling Concept Based on Porous Concrete

	H. Alsmeyer, T. Cron, F. Ferderer, W. Tromm, H. Schneider and T. Wenz
12.20 - 12.50 *(20+10)*	Experimental Investigations on Melt-Coolant Interaction Characteristics during Debris Cooling by Bottom Injection *D. Paladino, S.A. Theerthan, Z.L. Yang and B.R. Sehgal*
12.50 - 14.10	LUNCH
14.10 - 14.40	**DISCUSSION about Session B 5**
14.40 - 15.50	**Session C 1: MATERIAL PROPERTIES AND THERMOCHEMISTRY: PROPERTIES** **Chairman: G. Cognet**
14.40 - 15.00 *(15+5)*	Liquidus/Solidus and Zr Solubility Measurements for PWR and BWR Core Melt Compositions *M.T. Farmer, B.W. Spencer and R.W. Aeschlimann*
15.00 - 15.20 *(15+5)*	Estimates of Corium Viscosity for PWR and BWR Core Melt Composition Based on Spreading Rate *M.T. Farmer, B.W. Spencer and R.W. Aeschlimann*
15.20 - 15.50 *(20+10)*	Methodology for Corium-Concrete Viscosity Calculations *G. Cognet, F. Sudreau, M. Ramacciotti, C. Journeau and J.M. Seiler*
15.50 - 16.10	COFFEE BREAK
16.10 - 18.00	**Session C 2: MATERIAL PROPERTIES AND THERMOCHEMISTRY: THERMOCHEMISTRY** **Chairman: G. Cognet**
16.10 - 16.40 *(20+10)*	Corium Melt Attack on the Zirkonia-Based Concrete : Ceramic Melt Tests *S.V. Bechta, V.B. Khabensky, E.V. Krushinov, S.A. Vitol, T.Yu. Pautova, E..K. Kaliago, Yu. B. Petrov, D.B. Lopukh, A.Yu. Petchenkov, A.M. Lubomirov and I.V. Kulagin*
16.40 - 17.10 *(20+10)*	Analysis of Ceramic Ablation by Oxidic Corium *K. Froment, B. Duret, J.M. Seiler, S. Hellmann, M. Fischer, S. Bechta, D. Lopukh, A. Pechenkov and S. Vitol*
17.10 - 17.30 *(15+5)*	Small Scale Experiments on Corium-Metal-Ceramic Interaction by Oxygen Diffusion *K. Froment, F. Valin and J.M. Seiler*
17.30 - 18.00 *(20+10)*	Physico-Chemical and Material Aspects of the Core Melt Retention Concept of the EPR *S. Hellmann, V. Lansmann and B. Friedrich*

Thursday, 18 November 1999

08.30 - 09.00	**Session C 2 (Continued): MATERIAL PROPERTIES AND THERMOCHEMISTRY: THERMOCHEMISTRY** **Chairman: G. Cognet**
08.30 - 09.00 *(20+10)*	Equations for Solidification of Corium and Consequences *J.M. Seiler, K. Froment and J.P. Garandet*
09.00 - 09.20	**DISCUSSION about Sessions C 1 and C 2**
09.20 - 12.40	**Session D: REACTOR APPLICATION** **Chairman: H. Nagasaka**
09.20 - 09.50 *(20+10)*	Spanish Regulatory Perspective on Ex-Vessel Corium Coolability Issues *F. Robledo and A. Lantarón*
09.50 - 10.20 *(20+10)*	GAREC Analyses in Support of Ex-Vessel Retention Concept *G. Azarian, P. Gandrille, A. Dumontet, Dutheillet,J.-L. Grange, Duriez, G. Goldstein, B. Spindler,M. Cranga, G. Cognet, K. Froment, J.M. Gatt, J.M. Humbert, T. Laporte, P. Richard, G. Robert, J.M. Seiler, I. Szabo, M. Tourasse, F. Valin and P. Dufour*
10.20 - 10.40	COFFEE BREAK
10.40 - 11.10 *(20+10)*	Two-Phase Flow Modelling of Passive Safety Cooling Loops *G. Janssens-Maenhout, J.U. Knebel and U. Müller*
11.10 - 11.30 *(15+5)*	Main Conceptual Features of the EPR Melt Retention Concept *M. Fischer*
11.30 - 11.50 *(15 + 5)*	Principles of Application of Mechanical Design Measures to Control Severe Accident Phenomena, Applied to the Melt Retention Concept of the EPR *D. Bittermann*
11.50 - 12.10 *(15+5)*	Application of Sacrificial Concrete for the Retention and Conditioning of Molten Corium in the EPR Core Melt Retention Concept *M. Nie*
12.10 - 12.40	**DISCUSSION about Session D**
12.40 - 14.00	LUNCH

14.00 - 15.00	**Chairmen Summaries**
15.00 - 15.20	COFFEE BREAK
15.20 - 17.30	**Final Discussion: Panel and Audience;** *invited panellists: S. Basu (USNRC), M. Fischer (Siemens/Ger), J. L. Grange (EdF/Fr), H. Nagasaka (NUPEC/Ja), M. Petit (IPSN/Fr), W. Scholtyssek (FZK/Ger), R. Seghal (RIT/Sw), Chairman: H. Alsmeyer (FZK/Ger)*

Appendix C:

LIST OF PARTICIPANTS

AUSTRIA

Dr. Gert Sdouz
Senior Scientist
Nukleare Sicherheit und Bevölkerungsschutz
Nukleartechnik
Forschungszentrum Seibersdorf

A-2444 Seibersdorf
Phone : +43 (2254) 780 3264
Fax : +43 (2254) 780 3206
E-mail: gert.sdouz @ arcs.ac.at

CZECH REPUBLIC

Dr; Bohumir Kujal
Group Leader
Department of Reactor Technology
Nuclear Research Institute Rez plc

250 68 Rez
Phone : +420 (2) 6617 3657
Fax : +420 (2) 20 94 09 60
E-mail: kub @ nri.cz

FINLAND

Ms. Ilona Lindholm
Senior Research Scientist
VTT Energy

Tekniikantie 4C, Espoo
P.O. Box 1604
FIN-0244 VTT
Phone : +358 (9) 456 5031
Fax : +358 (9) 456 5000
E-mail: ilona.lindholm @ vtt.fi

Mr Heikki. Sjövall
Nuclear Safety Engineer
Teollisuuden Voima Oy (TVO)

FIN-27160 Olkiluoto
Phone : +358 (2) 8381 3232
Fax : +358 (2) 8381 3209
E-mail: heikki.sjovall @ tvo.tvo.elisa.fi

FRANCE

Mr. Gérard Cenerino
SECCA
Reactor Core Operation and Accident Assessment Division
Département d'Evaluation de la Sûreté (DES)
Institut de Protection et de Sûreté Nucléaire (IPSN)
Centre d'Etudes Nucléaires de Fontenay-aux-Roses

B.P. 6
F-92265 Fontenay-aux-Roses CEDEX
Phone : +33 (1) 46 54 76 14
Fax : +33 (1) 46 54 95 99
E-mail : gerard.cenerino @ ipsn.fr

Dr. Gérard Cognet
Vulcano Project Manager
Commissariat à l'Energie Atomique (CEA)
Centre d'Etudes de Cadarache

F-13108 Saint-Paul-lez-Durance
Phone : +33 (4) 42 25 21 26
Fax : +33 (4) 42 25 78 70
E-mail : gerard.cognet @ cea.fr

Mr. Etienne Décossin
Engineer
Electricité de France (EDF)
DRD/TTA

6 Quai Watier
F-78400 Chatou CEDEX
Phone : +33 (1) 30 87 78 51
Fax : +33 (1) 30 87 79 49
E-mail : etienne.decossin @ edf.fr

Mr. Jacques Duco
Deputy Head
Department de Prévention et d'Etude des Accidents (DPEA)
Institut de Protection et de Sûreté Nucléaire (IPSN)
Centre d'Etudes Nucléaires de Fontenay-aux-Roses

B.P. 6
F-92265 Fontenay-aux-Roses CEDEX
Phone : +33 (1) 46 54 70 68
Fax : +33 (1) 46 54 44 37
E-mail : jacques.duco @ ipsn.fr

Dr. Karine Froment
Research Engineer
Commissariat à l'Energie Atomique (CEA)
DTA/CEREM/DEM/SPCM

17 Rue des Martyrs
F-38054 Grenoble CEDEX 9
Phone : +33 (4) 76 88 48 93
Fax : +33 (4) 76 88 51 17
E-mail : karine.froment @ cea.fr

Ms. Dominique Gayrard
Engineer
Service d'Etudes sur les Accidents (SEAC)
Département de Prévention et d'Etude des Accidents (DPEA)
Institut de Protection et de Sûreté Nucléaire (IPSN)
Centre d'Etudes Nucléaires de Fontenay-aux-Roses

B.P. 6
F-92265 Fontenay-aux-Roses CEDEX
Phone : +33 (1) 46 54 85 79
Fax : +33 (1) 46 54 85 59
E-mail : dominique.gayrard @ ipsn.fr

Mr. Jean-Louis Grange
Managerial Adviser
Electricité de France (EDF)
DRD/TTA

6 Quai Watier
F-78401 Chatou CEDEX
Phone : +33 (1) 30 87 73 11
Fax : +33 (1) 30 87 79 49
E-mail : jean-louis.grange @ edf.fr

Mr. Jean-Claude Latché
Head of Laboratory
Service d'Etudes et de Modélisation d'Accidents de Réacteurs (SEMAR)
Département de Recherches en Sécurité (DRS)
Institut de Protection et de Sûreté Nucléaire (IPSN)
Centre d'Etudes de Cadarache

Bâtiment 702
F-13108 Saint-Paul-lez-Durance
Phone : +33 (4) 42 25 61 68
Fax : +33 (4) 42 25 64 68
E-mail : jean-claude.latche @ ipsn.fr

Mme. Catherine. Lecomte
Institut de Protection et de Sûreté (IPSN)
Centre d/Etudes Nucléaires de Fontenay-aux-Roses

B.P. 6
F-92265 Fontenay-aux-Roses CEDEX
Phone : +33 (1) 46 54.81 83
Fax : +33 (1) 46 54.32 64
E-mail : catherine.lecomte @ ipsn.fr

Mrs. Bénédicte Michel
Engineer
Institut de Protection et de Sûreté (IPSN)
Centre d'Etudes de Cadarache
DRS/SEMAR/LECTA

Bâtiment 700
F-13108 Saint-Paul-lez-Durance
Phone : +33 (4) 42 25 74 79
Fax : +33 (4) 42 25 64 68
E-mail : deletie @ sand.cad.cea.fr

Mr. Marc Petit
Chef du Laboratoire et de Physique des Accidents et d'Etudes du Confinement
Service d'Etudes sur les Accidents (SEAC)
Département de Prévention et d'Etude des Accidents (DPEA)
Institut de Protection et de Sûreté Nucléaire (IPSN)
Centre d'Etudes Nucléaires de Fontenay-aux-Roses

B.P. 6
F-92265 Fontenay-aux-Roses CEDEX
Phone : +33 (1) 46 54 73 75
Fax : +33 (1) 46 54 85 59
E-mail : marc.petit @ ipsn.fr

Dr. Jean-Marie Seiler
Senior Expert
Commissariat à l'Energie Atomique (CEA)
DTP

17 Rue des Martyrs
F-38054 Grenoble CEDEX 9
Phone : +33 (4) 76 88 30 23
Fax : +33 (4) 76 88 52 51
E-mail : seiler @ dtp.cea.fr

Mr. Bertrand Spindler
Engineer
Commissariat à l'Energie Atomique (CEA)
DRN/DTP/SMTH

17 Rue des Martyrs
F-38054 Grenoble CEDEX 9
Phone : +33 4 76 88 46 87
Fax : +33 4 76 88 51 95
E-mail : bertrand.spindler @ cea.fr

GERMANY

Mr. Giancarlo Albrecht
Engineer
Forschungszentrum Karlsruhe GmbH
Institut für Reaktorsicherheit

Hermann-von Helmholtz-Platz 1
D-76344 Eggenstein-Leopoldshafen
Phone : +49 (7247) 82 2565
Fax : +49 (7247) 82 2996
E-mail : albrecht @ irs.fzk.de

Dr. Zeynel Alkan
RWTH Aachen
Institut für Reaktorsicherheit und -technik

Eilfschornsteinstrasse 18
D-52062 Aachen
Phone : +49 (241) 80 6700
Fax : +49 (241) 8888 183
E-mail : alkan @ lrst.rwth-aachen.de

Dr. Hans-Josef Allelein
Project Manager
Containment Code Development
Gesellschaft für Anlagen- und Reaktorsicherheit (GRS) mbH

Schwertnergasse 1
Postfach 10 16 50
D-50667 Köln
Phone : +49 (221) 2068 668
Fax : +49 (221) 2068 834
E-mail : all @ grs.de

Dr. Hans Alsmeyer
Group Leader
Forschungszentrum Karlsruhe GmbH
Institut für Kern- und Energietechnik (IKET)

Postfach 3640
D-76021 Karlsruhe
Phone : +49 (7247) 82 3454
Fax : +49 (7247) 82 4837
E-mail : hans.alsmeyer @ iket.fzk.de

Mr. Peter Andrae
RWTH Aachen
Institut für Reaktorsicherheit und -technik

Eilfschornsteinstrasse 18
D-52062 Aachen
Phone : +49 (241) 80 5448
Fax : +49 (241) 8888 183
E-mail : andrae @ lrst.rwth-aachen.de

Mr. Dietmar Bittermann
Team Manager
Siemens AG, KWU NA-T

Postfach 3220
D-91050 Erlangen
Phone : +49 (9131) 18 5263
Fax : +49 (9131) 18 4236
E-mail : dietmar.bittermann @ erl11.siemens.de

Dr. Axel Breest
Gesellschaft für Anlagen- und Reaktorsicherheit (GRS) mbH
Schwertnergasse 1

Postfach 10 16 50
D-50667 Köln
Phone : +49 (221) 2068 667
Fax : +49 (221) 2068 629
E-mail : bre @ grs.de

Mr. Tim Buescher
Research Scientist
Ruhr-Universität Bochum
Lehrstuhl für Nukleare und Neue Energiesysteme

Universitätsstrasse 150
D-44801 Bochum
Phone : +49 (234) 32 25984
Fax : +49 (234) 32 14158
E-mail : buescher @ nes.ruhr-uni-bochum.de

Mr. Thomas Cron
Forschungszentrum Karlsruhe GmbH
Institut für Kern- und Energietechnik (IKET)

Postfach 3640
D-76021 Karlsruhe
Phone : +49 (7247) 82 3818
Fax : +49 (7247) 82 4837
E-mail : thomas.cron @ iket.fzk.de

Miss Beatrix Eppinger
Engineer
Forschungszentrum Karlsruhe GmbH
Institut für Kern- und Energietechnik (IKET)

Hermann-von Helmholtz-Platz 1
D-76344 Eggenstein-Leopoldshafen
Phone : +49 (7247) 82 3473
Fax : +49 (7247) 82 4837
E-mail : beatrix.eppinger @ iket.fzk.de

Mr. Manfred Fischer
Siemens AG, KWU NA-T

Postfach 3220
D-91050 Erlangen
Phone : +49 (9131) 18 2577
Fax : +49 (9131) 18 4236
E-mail : manfred.fischer @ erl11.siemens.de

Dr. Jerzy Foit
Senior Scientist
Forschungszentrum Karlsruhe GmbH
Institut für Kern- und Energietechnik (IKET)

Postfach 3640
D-76021 Karlsruhe
Phone : +49 (7247) 82 3467
Fax : +49 (7247) 82 4837
E-mail : jerzy.foit @ iket.fzk.de

Miss Mireia Gargallo
Engineer
Forschungszentrum Karlsruhe GmbH
Institut für Kern- und Energietechnik (IKET)
Postfach 3640
D-76021 Karlsruhe
Phone : +49 (7247) 82 2465
Fax : +49 (7247) 82 4837
E-mail : mireia.gargallo @ iket.fzk.de

Dr. Wolfgang Häfner
Battelle Ingenieurtechnik GmbH
Düsseldorfer Strasse 9
D-65760 Eschborn
Phone : +49 (6196) 936 308
Fax : +49 (6196) 936 399
E-mail : whaefner @ battelle.de

Dr. Sieghard Hellmann
Siemens AG, KWU NT 21
Freyeslebenstrasse 1
D-91058 Erlangen
Phone : +49 (9131) 18 2428
Fax : +49 (9131) 18 5234
E-mail : sieghard.hellmann @ erl11.siemens.de

Mr. Günter Jacobs
Forschungszentrum Karlsruhe GmbH
Institut für Kern- und Energietechnik (IKET)
Postfach 3640
D-76021 Karlsruhe
Phone : +49 (7247) 82 2435
Fax : +49 (7247) 82 4874
E-mail : guenter.jacobs @ iket.fzk.de

Dr. Helmut Jacobs
Forschungszentrum Karlsruhe GmbH
Institut für Kern- und Energietechnik (IKET)
Postfach 3640
D-76021 Karlsruhe
Phone : +49 (7247) 82 2443
Fax : +49 (7247) 82 3824
E-mail : helmut.jacobs @ iket.fzk.de

Dr. Greet Janssens-Maenhout
Scientific Researcher
Forschungszentrum Karlsruhe GmbH
Institut für Kern- und Energietechnik (IKET)
Postfach 3640
D-76021 Karlsruhe
Phone : +49 (7247) 82 2253
Fax : +49 (7247) 82 4837
E-mail : greet.janssens-maenhout @ iket.fzk.de

Prof. Dr. Helmut Karwat
Consultant
Fritz Gerlichstrasse 1
D-82049 Pullach
Phone : +49 (89) 79 58 66
Fax : +49 (89) 79 00 698

Mr. Wolfgang Koller
Siempelkamp Nuklear- und Umwelttechnik GmbH & Co.
Postfach 2570
D-47725 Krefeld
Phone : +49 (2151) 8948 298
Fax : +49 (2151) 8948 457
E-mail : wolfgang.koller@siempelkamp.com

Dr. Christof Kortz
Head, Technical Transport Processes Group
Ruhr-Universität Bochum
Lehrstuhl für Nukleare und Neue Energiesysteme
D-44780 Bochum
Phone : +49 (234) 32 26364
Fax : +49 (234) 32 14158
E-mail : kortz @ nes.ruhr-uni-bochum.de

Dr. Volker Lansmann
Siemens AG, KWU NA-T
Postfach 3220
D-91050 Erlangen
Phone : +49 (9131) 18 7285
Fax : +49 (9131) 18 5234
E-mail : volker.lansmann @ erl11.siemens.de

Dr.-Ing. Leonhard Meyer
Forschungszentrum Karlsruhe GmbH
Institut für Kern- und Energietechnik (IKET)
Postfach 3640
D-76021 Karlsruhe
Phone : +49 7247 82 2469
Fax : +49 7247 82 5987
E-mail : meyer @ iket.fzk.de

Dr. Wilfred Morell
Siemens AG, KWU NA-T
Postfach 3220
D-91050 Erlangen
Phone : +49 (9131) 18 4481
Fax : +49 (9131) 18 5234
E-mail : wilfred.morell @ erl11.siemens.de

Mr. Markus Nie
Project Engineer
Siemens AG, KWU NA-T
Postfch 3220
D-91050 Erlangen
Phone : +49 (9131) 18 5657
Fax : +49 (9131) 18 4236
E-mail : markus.nie @ erl11.siemens.de

Mr. Börne Rensing
RWTH Aachen
Institut für Reaktorsicherheit und -technik
Eilfschornsteinstrasse 18
D-52062 Aachen
Phone : +49 (241) 80 5448
Fax : +49 (241) 8888 183
E-mail : rensing @ lrst.rwth-aachen.de

Mr. Werner Schmidt
Institut für Kernenergetik (IKE)
Universität Stuttgart
Pfaffenwaldring 31
D-70550 Stuttgart
Phone : +49 (711) 685 2370
Fax : +49 (711) 2010
E-mail : w.schmidt @ ike.uni-stuttgart.de

Mr. Werner Scholtyssek
Project Manager
Projekt Nukleare Sicherheitsforschung (PSF)
Forschungszentrum Karlsruhe GmbH
Postfach 3640
D-76021 Karlsruhe
Phone : +49 (7247) 82 5525
Fax : +49 (7247) 82 5508
E-mail : werner.scholtyssek @ psf.fzk.de

Dr. Wolfgang Schütz
Section Head
Forschungszentrum Karlsruhe GmbH
IRS
Postfach 3640
D-76021 Karlsruhe
Phone : +49 (7247) 82 3912
Fax : +49 (7247) 82 2996
E-mail : schuetz @ irs.fzk.de

Dr. Martin Sonnenkalb
Project Leader
Gesellschaft für Anlagen- und Reaktorsicherheit (GRS) mbH
Schwertnergasse 1
Postfach 10 16 50
D-50667 Köln
Phone : +49 (221) 2068 686
Fax : +49 (221) 2068 834
E-mail : som @ grs.de

Mr. Claus Spengler
Gesellschaft für Anlagen- und Reaktorsicherheit (GRS) mbH
Schwertnergasse 1
Postfach 10 16 50
D-50667 Köln
Phone : +49 (221) 2068 943
Fax : +49 (221) 2068 834
E-mail : spc @ grs.de

Dr. Jörg Starflinger
Forschungszentrum Karlsruhe GmbH
Institut für Kern- und Energietechnik (IKET)
Postfach 3640
D-76021 Karlsruhe
Phone : +49 (7247) 82 3445
Fax : +49 (7247) 82 5987
E-mail : joerg.starflinger @ iket.fzk.de

Dr.-Ing. Wolfgang Steinwarz
Siempelkamp Nuklear- und Umwelttechnik GmbH & Co.
Siempelkampstrasse 45
Postfach 2570
D-47725 Krefeld
Phone : +49 (2151) 8948 290
Fax : +49 (2151) 8948 457
E-mail : wolfgang.steinwarz@siempelkamp.com

Dr. Walter Tromm
Scientist
Forschungszentrum Karlsruhe GmbH
Institut für Kern- und Energietechnik (IKET)
Postfach 3640
D-76021 Karlsruhe
Phone : +49 (7247) 82 3494
Fax : +49 (7247) 82 4837
E-mail : walter.tromm @ iket.fzk.de

Dr. Dirk Wilhelm
Forschungszentrum Karlsruhe GmbH
Institut für Kern- und Energietechnik (IKET)
Postfach 3640
D-76021 Karlsruhe
Phone : +49 (7247) 82 2469
Fax : +49 (7247) 82 5987
E-mail : wilhelm @ iket.fzk.de

Mr. Ingo Wintruff
PhD Student
Forschungszentrum Karlsruhe GmbH
Institut für Kern- und Energietechnik (IKET)
Postfach 3640
D-76021 Karlsruhe
Phone : +49 (7247) 82 3464
Fax : +49 (7247) 82 4837
E-mail : ingo.wintruff @ iket.fzk.de

Dr. Ralf Wittmaack
Physicist
Siemens AG, KWU NA-T
Postfach 3220
D-91050 Erlangen
Phone : +49 (9131) 18 2145
Fax : +49 (9131) 18 4236
E-mail : ralf.wittmaack @ erl11.siemens.de

HUNGARY

Mr; Pál Kostka
Nuclear Engineering Division
Institute for Electric Power Research Co. (VEIKI)
Gellérthegy utca 17
Pf. 80
H-1016 Budapest
Phone : 36 (1) 457 8275
Fax : 36 (1) 457 8253
E-mail : kostka @ ella.hu

Dr. Zsolt Téchy
Project Manager
Nuclear Engineering Division
Institute for Electric Power Research Co. (VEIKI)

Gellérthegy utca 17
Pf. 80
H-1016 Budapest
Phone : 36 (1) 457 8245
Fax : 36 (1) 457 8253
E-mail : techy @ ella.hu

ITALY

Dr; Lucio De Cecco
Scientist
ENEA

Via Martiri di Monte Sole, 4
I-40129 Bologna
Phone : +39 (51) 60 98 475
Fax : +39 (51) 60 98 639
E-mail : dececco @ bologna.enea..it

JAPAN

Mr; Masami Kato
Senior Manager
Systems Safety Department
Nuclear Power Engineering Corporation (NUPEC)

Fujita Kanko Toranomon Blg, 5F
17-1, 3-chome Toranomon
Minato-ku
Tokyo, 105-0001
Phone : +81 (3) 3435 3402
Fax : +81 (3) 3435 3411
E-mail : ms-kato @ nupec.or.jp

Dr. Seiichi Koshizuka
Associate Professor
Nuclear Engineering Research Laboratory
Graduate School of Engineering
University of Tokyo

2-22 Shirane, Shirakata
Tokai-mura
Naka-gun
Ibaraki-ken, 319-1106
Phone : +81 (29) 287 8441
Fax : +81 (29) 287 8488
E-mail : koshi @ tokai.t.u-tokyo.ac.jp

Dr. Hideo Nagasaka
Senior Manager
Systems Safety Department
Nuclear Power Engineering Corporation (NUPEC)

Fujita Kanko Toranomon Bldg, 5F
17-1, 3-chome Toranomon
Minato-ku
Tokyo, 105-0001
Phone : +81 (3) 3435 3402
Fax : +81 (3) 3435 3411
E-mail : nagasaka @ nupec.or.jp

Mr. Masaki Nakagawa
Director, General Manager
Nuclear Power Department 1
Marubeni Utility Services, Ltd

1F, Palace Side Building
1-1, Hitotsubashi 1-chome
Chiyada-ku
Tokyo 100-0003
Phone : +81 (3) 3214 9065
Fax : +81 (3) 5218 8711
E-mail : nakagawa @ marinet.or.jp

Dr. Hideo Nakamura
Principal Engineer
Severe Accident Research Laboratory
Department of Reactor Safety Research
Japan Atomic Energy Research Institute
Tokai Research Establishment

2-4 Shirakata-Shirane
Tokai-mura
Naka-gun
Ibaraki-ken, 319-1195
Phone : +81 (29) 282 6163
Fax : +81 (29) 282 5570
E-mail : nakam @ lstf3.tokai.jaeri.go.jp

REPUBLIC OF KAZAKHSTAN

Miss Tatiana Bolgova
Engineer
Analysis and Co-ordination Division
National Nuclear Centre of the Republic of Kazakhstan

Ul. Lenina, 6
Kurchatov
Phone : +7 (3272) 33 85 85
Fax : +7 (3272) 33 85 85
E-mail : bolgovat @ nnc.kz

Prof. Dr. Yury S. Cherepnin
Director General
National Nuclear Centre of the Republic of Kazakhstan

Ul. Lenina, 6
Kurchatov
Phone : +7 (3272) 33 85 85
Fax : +7 (3272) 33 85 85
E-mail : cherepnin @ nnc.kz

Mr. Vladimir S. Jdanov
Chief of Laboratory for Testing Fuel and ... (?)
Institute of Atomic Energy
National Nuclear Centre of the Republic of Kazakhstan

Ul. Krasnoarmeyskaya, 10
Kurchatov
Phone : +7 (3272) 33 85 85
Fax : +7 (3272) 33 85 85
E-mail : zhdv @ nnc.kz

Mr. Alexandre A. Kolodeshnikov
Chief of Laboratory for Thermal Reactor Physics
Institute of Atomic Energy
National Nuclear Centre of the Republic of Kazakhstan

Ul. Krasnoarmeyskaya, 10
Kurchatov
Phone : +7 (3272) 33 85 85
Fax : +7 (3272) 33 85 85
E-mail : dep240 @ nnc.kz

Mr. Yury S. Vasilyev
Chief of Department for Reactor Testing
Institute of Atomic Energy
National Nuclear Centre of the Republic of Kazakhstan

Ul. Krasnoarmeyskaya, 10
Kurchatov
Phone : +7 (3272) 33 85 85
Fax : +7 (3272) 33 85 85
E-mail : ysv @ nnc.kz

REPUBLIC OF KOREA

Dr. Hee-Dong Kim
Head, Severe Accident Research Team
Korea Atomic Energy Research Institute (KAERI)

150 Duckjindong Yusonggu
Taejon, 350-353
Phone : +82 (42) 868 2664
Fax : +82 (42) 868 8256
E-mail : hdkim @ kaeri.re.kr

RUSSIAN FEDERATION

Mr. Felix Akopov
Institute for High Temperatures

Izhorskaya, 13/19
Moscow, 127412
Phone : +7 (095) 484 1622
Fax : +7 (095) 485 7990
E-mail : akopov @ hedric.msk.su

Dr. Sevostian Bechta
Head of Department
Research Institute of Technology (NITI)

188540 Sosnovy Bor
Leningrad Region
Phone : +7 (812) 69 62064
Fax : +7 (812) 69 62996
E-mail : noti-npc @ sbor.net

Mr. Alexandre S. Kozlov
Interpreter
Intourist

Milyutinskyi per., 13/1
Moscow
Phone : +7 (095) 797 3048
Fax : -----
E-mail : -----

Mr. Vladimir Mineev
Institute for High Temperatures

Izhorskaya, 13/19
Moscow, 127412
Phone : +7 (095) 484 1622
Fax : +7 (095) 485 7990
E-mail : mineev @ hedric.msk.su

Mr. Oleg Traktouev
Russian Research Centre "Kurchatov Institute"

Kurchatov Square, 1
Moscow, 123182
Phone : +7 (095) 196 7847
Fax :
E-mail : traktuev @ base 1.dhtp.kiae.ru

Mr. Anatoli Vlassov
Institute for High Temperatures

Izhorskaya, 13/19
Moscow, 127412
Phone : +7 (095) 484 1622
Fax : +7 (095) 485 7990
E-mail : vlassov @ hedric.msk.su

SPAIN

Mr; Fernando Robledo
Division of Modeling and Simulation
Consejo de Seguridad Nuclear

C/ Justo Dorado, 11
28040 Madrid
Phone : +34 (91) 3460 249
Fax : +34 (91) 3460 588
E-mail : frs @ csn.es

SWEDEN

Dr. Veine Gustavsson
Senior Consultant
SwedPower AB

P.O. Box 527
SE-162 16 Stockholm
Phone : +46 (8) 739 5346
Fax : +46 (8) 739 6900
E-mail : veine.gustavsson @ swedpower.vattenfall.se

Mr. Maxim Konovalikhin
PhD Student
Royal Institute of Technology
Nuclear Power Safety Division

Drottning Kristinas Väg, 33A
SE-100 44 Stockholm
Phone : +46 (8) 790 6983
Fax : +46 (8) 790 9252
E-mail : maxim @ ne.kth.se

Mr. Domenico Paladino
PhD Student
Royal Institute of Technology
Nuclear Power Safety Division

Drottning Kristinas Väg, 33A
SE-100 44 Stockholm
Phone : +46 (8) 790 9295
Fax : +46 (8) 790 9252
E-mail : domenico @ ne.kth.se

Prof. Bal Raj Sehgal
Royal Institute of Technology
Nuclear Power Safety Division

Drottning Kristinas Väg, 33A
SE-100 44 Stockholm
Phone : +46 (8) 790 9252
Fax : +46 (8) 790 9197
E-mail : sehgal @ ne.kth.se

SWITZERLAND

Dr. Jonathan Birchley
Scientist
Laboratory for Safety and Accident Research
Paul Scherrer Institut

CH-5232 Villigen PSI
Phone : +41 (56) 310 2724
Fax : +41 (56) 310 21 99
E-mail : birchley @ psi.ch

UNITED STATES OF AMERICA

Dr. Sudhamay Basu
Safety Margins and Systems Analysis Branch
Office of Nuclear Regulatory Research
U.S. Nuclear Regulatory Commission

Washington, D.C. 20555-0001
Phone : +1 (301) 415 6774
Fax : +1 (301) 415 5160
E-mail : sxb2 @ nrc.gov

Dr. Rosa Marina Bilbao y Leon
Research Associate
Nuclear Safety Research Center
Department of Engineering physics
University of Wisconsin-Madison

1500 Engineering Drive
Madison, Wisconsin 53706
Phone : +1 (608) 265 5091
Fax : +1 (608) 265 4546
E-mail : sam @ loca.neep.wisc.edu

Dr. Mitchell Farmer
Reactor Engineering Division
Argonne National Laboratory

9700 South Cass Avenue
Argonne, Ill. USA 60439
Phone : +1 (630) 252 4539
Fax : +1 (630) 252 6080
E-mail : farmer@ aeetes.re.anl.gov

Dr. David Squarer
Consultant
Energy Technology

1193 Beechwood Blvd.
Pittsburgh, PA 15206
Phone : +1 (412) 441 5390
Fax : +1 (412) 441 5390
E-mail : squarer@ att.net

EUROPEAN COMMISSION

Dr; Daniel Magallon
Sector Head
Institute for Systems, Informatics and Safety (ISIS)
European Commission
Joint Research Centre
Ispra Establishment

T.P. 421
I-21020 Ispra (Varese)
Italy
Phone : +39 (0332) 78 9703
Fax : +39 (0332) 78 5412
E-mail : daniel.magallon @ jrc.it

OECD NUCLEAR ENERGY AGENCY

Dr. Jacques Royen
Deputy Head
Nuclear Safety Division
OECD Nuclear Energy Agency

Le Seine - Saint Germain
12 Boulevard des Iles
F-92130 Issy-les- Moulineaux
France
Phone : +33 (1) 45 24 10 52
Fax : +33 (1) 45 24 11 29 or 11 10
E-mail : jacques.royen @ oecd.org
royen @ nea.fr

Appendix D: Origins and Purposes of the OECD, NEA, and CSNI

OECD

The Convention establishing the Organisation for Economic Co-operation and Development (OECD) was signed on 14th December 1960.

Pursuant to Article 1 of the Convention, the OECD shall promote policies designed:

-- to achieve the highest sustainable economic growth and employment and a rising standard of living in Member countries, while maintaining financial stability, and thus to contribute to the development of the world economy;

-- to contribute to sound economic expansion in Member as well as non-member countries in the process of economic development; and

-- to contribute to the expansion of world trade on a multilateral, non-discriminatory basis in accordance with international obligations.

The original Member countries are Austria, Belgium, Canada, Denmark, France, Germany,
Greece, Iceland, Ireland, Italy, Luxembourg, the Netherlands, Norway, Portugal, Spain, Sweden, Switzerland, Turkey, the United Kingdom and the United States. The following countries became Members subsequently through accession at the dates indicated hereafter : Japan (28th April 1964), Finland (28th January 1969), Australia (7th June 1971), New Zealand (29th May 1973), Mexico (18th May 1994), the Czech Republic (21st December 1995), Hungary (7th May 1996), Poland (22nd November 1996) and the Republic of Korea (12th December 1996). The Commission of the European Communities takes part in the work of the OECD (Article 13 of the OECD Convention).

NEA

The OECD Nuclear Energy Agency (NEA) was established on 1st February 1958 under the name of the OEEC European Nuclear Energy Agency. NEA membership today consists of all European Member countries of OECD as well as Australia, Canada, Japan, the Republic of Korea, Mexico and the United States. The Commission of the European Communities takes part in the work of the Agency.

The primary objective of NEA is to promote co-operation among the governments of its participating countries in furthering the development of nuclear power as a safe, environmentally acceptable and economic energy source.

NEA works in close collaboration with the International Atomic Energy Agency (IAEA), with which it has concluded a Co-operation Agreement, as well as with other international organisations in the nuclear field.

CSNI

The NEA Committee on the Safety of Nuclear Installations (CSNI) is an international committee made up of senior scientists and engineers, with broad responsibilities for safety technology and research programmes, and representatives from regulatory authorities. It was set up in 1973 to develop and co-ordinate the activities of the NEA concerning the technical aspects of the design, construction and operation of nuclear installations insofar as they affect the safety of such installations. The Committee's purpose is to foster international co-operation in nuclear safety amongst the OECD Member countries. CSNI's main tasks are to exchange technical information and to promote collaboration between research, development, engineering and regulation organisations; to review the state of knowledge on selected topics of nuclear safety technology and safety assessments, including operating experience; to initiate and conduct programmes to overcome discrepancies, develop improvements and reach consensus on technical issues; to promote co-ordination of work, including the establishment of joint undertakings.

PWG4

CSNI's Principal Working Group on the Confinement of Accidental Radioactive Releases (PWG4) has been given two tasks : containment protection, and fission product retention. Its role is to exchange information on national and international activities in the areas of severe accident phenomena in the containment, fission product phenomena in the primary circuit and the containment, and containment aspects of severe accident management. PWG4 discusses technical issues/reports and their implications, and the results of International Standard Problem exercises and specialist meetings, and submits conclusions to the CSNI. It prepares Technical Opinion Papers on major issues. It reviews the main orientations, future trends, emerging issues, co-ordination and interface with other groups in the field of confinement of accidental radioactive releases, identifies necessary activities, and proposes a programme of work to the CSNI.

SAC

The Task Group on Severe Accident Phenomena in the Containment (SAC) is a specialized extension of PWG4. Its main tasks are to exchange information, discuss results and programmes, write state-of-the-art reports, organise specialist workshops, and perform International Standard Problem exercises in the field of ex-vessel severe accident phenomenology.